Numerical Modelling of Mesoscale Atmospheric Dispersion

by
Michael D. Moran

Department of Atmospheric Science
Colorado State University
Fort Collins, Colorado

Roger A. Pielke, P.I.

Department of
Atmospheric Science

Paper No. 513

NUMERICAL MODELLING OF MESOSCALE ATMOSPHERIC DISPERSION

Michael D. Moran

Department of Atmospheric Science
Colorado State University
Fort Collins, Colorado
Fall 1992

Atmospheric Science Paper No. 513

ABSTRACT

NUMERICAL MODELLING OF MESOSCALE ATMOSPHERIC DISPERSION

It was once thought that the atmosphere's capacity to dilute the concentration of air pollutants is effectively without limit, and that for pollutant dispersion over mesoscale distances, the dilution will be large enough that there is little practical need to predict pollutant concentrations. More recently, it has been recognized that if pollutant sources are strong enough or numerous enough or long-lasting enough, or if the pollutants themselves are sufficiently toxic or active enough in some way, then pollutant concentrations or dosages may still be of concern even after mesoscale dilution. The multi-country radionuclide contamination experienced during the 1986 Chernobyl disaster is one recent example. Others include regional-scale acidic deposition, volcanic plume dispersion, photochemical oxidant episodes, airborne pathogen dispersal, and visibility degradation and heavy-metal and pesticide accumulation in remote areas.

Mesoscale atmospheric dispersion is more complicated than smaller-scale dispersion because the mean wind field can no longer be considered steady or horizontally homogeneous over mesoscale time and space scales. Wind shear also plays a much more important role on the mesoscale. Horizontal dispersion can be enhanced and even dominated by vertical wind shear through either the simultaneous or delayed interaction of horizontal differential advection and vertical mixing over one or two diurnal periods. In addition, vertical wind shear associated with the diurnal cycle can be augmented by shear produced by physiographically- or synoptically-forced mesoscale circulations.

The CSU mesoscale atmospheric dispersion modelling system has been used in this study to simulate the transport and diffusion of a perfluorocarbon tracer gas for episodic

releases made during two North American mesoscale dispersion field experiments, the 1980 Great Plains mesoscale tracer experiment and the 1983 Cross-Appalachian Tracer Experiment (CAPTEX). Ground-level and elevated tracer concentrations were measured out to distances of 600 km from the source in the first experiment and 1100 km in the second. The physiography of the two experimental domains was quite different, permitting isolation and examination of the roles of terrain forcing and differential advection in mesoscale atmospheric dispersion.

Suites of numerical experiments of increasing complexity were carried out for both case studies. The experiments differed in the realism of their representation of both the synoptic-scale flow and the underlying terrain. Ground-level concentration 'footprints' predicted by the various numerical experiments were found to be sensitive to both inhomogeneities in terrain elevation and other land-surface properties and to the structure and evolution of the synoptic-scale flow. Many of the differences were due to differences in predicted wind shear and differential advection. The Great Plains nocturnal low-level jet played an important role in the first case study while temporal changes in the synoptic-scale flow were very significant in the second case study. The contributions of differential advection and mesoscale deformation to mesoscale dispersion dominated those of small-scale turbulent diffusion for both case studies, and Pasquill's (1962) delayed-shear-enhancement mechanism for lateral dispersion was found to be particularly important.

This study has added significance in that it is the first quantitative evaluation of the CSU mesoscale dispersion modelling system with episodic mesoscale dispersion field data. The modelling system showed considerable skill in predicting quantitative tracer-cloud characteristics such as peak concentration, maximum cloud width, arrival time, transit time, and crosswind integrated exposure. Model predictions also compared favourably with predictions made by a number of other mesoscale dispersion models for the same two case studies.

Michael D. Moran
Department of Atmospheric Science
Colorado State University
Fort Collins, Colorado 80523
Fall 1992

ACKNOWLEDGEMENTS

It is a pleasure to acknowledge the help and support that I received from many individuals during the course of this research. Prof. Roger Pielke, my adviser, gave me more than enough rope to hang myself but at the same time was a continuous source of support, insight, suggestions, and constructive criticism. I have also benefitted from interactions with and comments from all of my other committee members: Profs. William Cotton, Richard Johnson, and Prof. Robert Meroney of the Department of Civil Engineering. Dr. Walter Lyons also served as a committee member and Adjunct Professor in the Department of Atmospheric Science during much of my Ph.D. program.

Prof. Richard McNider of the University of Alabama at Huntsville taught me much about Lagrangian particle models and has been a wonderful collaborator. Chap. 2 is as large as it is because of discussions we had on the mesoscale energy spectrum. Dr. Raymond Arritt and Mr. Moti Segal patiently answered my many questions about the Pielke–Mahrer mesoscale numerical model when I first arrived at CSU. Drs. Craig Tremback and Robert Walko answered my even more numerous questions about the many components of RAMS; in addition, they have provided an invaluable service to all RAMS users through their development of and improvements to the RAMS code. I have also benefitted from discussions with Drs. Roni Avissar, Mark Hadfield, William Physick, and Marek Uliasz.

In the more distant past, Prof. Maurice Danard, now at the University of Victoria, whet my interest in atmospheric science while I was an undergraduate at the University of Waterloo, and later, Prof. T.N. Krishnamurti kept me interested during my studies at Florida State University. I also owe thanks to Prof. George Young, now at The Pennsylvania State University, for convincing me that Colorado State University was a good place to study.

My officemates at different stages, Jennifer Cram, Cathy Finley, Tsengdar Lee, Douglas Wesley, and Xubin Zeng, put up with me and made life in a crowded office both enjoyable and stimulating. Other students, faculty, and staff within the Department of Atmospheric Science also contributed to a dynamic research environment and pleasant workplace.

Mrs. Dallas McDonald helped in numerous ways, including word processing, textual criticisms and consistency checks, dissertation format control, and LaTeX troubleshooting. I also received assistance with manuscript preparation from Mr. Bryan Critchfield, Ms. Tara Pielke, and Mr. Tony Smith. Mrs. Fredi Boston came through again and again on requests for obscure articles based on questionable citations and never once complained about my single-handed efforts to improve the Atmospheric Science library circulation statistics. And Ms. Donna Chester did her best to keep various group computers and workstations running, networked, and backed up.

I am indebted to the scientists at NOAA's Air Resources Laboratory in Silver Springs, Maryland, at Brookhaven National Laboratory in Upton, New York, and elsewhere for their vision, scientific and technical excellence, and old-fashioned hard work in the execution of the two mesoscale tracer experiments modelled herein and in the subsequent analysis and dissemination of their results. Dr. Jerome Heffter of the Air Resources Laboratory and Dr. Richard Carhart of the University of Illinois at Chicago generously answered a number of questions I had about their work related to these experiments. And Dr. Francis Binkowski of the U.S. Environmental Protection Agency and Mr. Chris Walcek of the State University of New York at Albany graciously made the extended EPA land-use data set available to me (and to the National Center for Atmospheric Research).

I am also obliged to the following companies and organizations for permission to reproduce previously published illustrations: the Air and Waste Management Association, publisher of the *Journal of the Air and Waste Management Association*, for Fig. 1.11; the American Geophysical Union, publisher of the *Journal of Geophysical Research, Radio Science,* and *Water Resources Research,* for Figs. 2.14, 2.16, 2.17, 2.19, part of Fig. 3.27, and parts of Fig. 4.5; the American Meteorological Society, publisher of the

LIST OF TABLES

Bulletin of the American Meteorological Society, Journal of Applied Meteorology, Journal of the Atmospheric Sciences, and *Monthly Weather Review* for Figs. 1.7, 1.9, 2.1–2.12, 2.13a, 2.15, 2.18, 2.20, 2.24, 2.26, 2.28, 3.25, parts of Fig. 3.27, Figs. 4.22a and 4.24a-b, and Fig. 5.4; The Institute of Mathematics and its Applications, Southend-on-Sea, England, for Fig. 1.8; Kluwer Academic Publishers, publisher of *Boundary-Layer Meteorology*, for Fig. 2.13b and part of Fig. 3.27; Pergamon Press, publishers of *Atmospheric Environment*, for Figs. 1.1, 1.2, 1.10, 2.23, 2.25, 2.31, 2.33, and 3.12; Plenum Press for Figs. 1.3, 2.35, and 3.11; the Royal Meteorological Society, publisher of the *Quarterly Journal of the Royal Meteorological Society* and the *International Journal of Climatology*, for Fig. 2.21 and part of Fig. 4.5; and the Swedish Geophysical Society, publisher of *Tellus*, for Fig. 1.5.

I received financial support during my residence at Colorado State University from the Electric Power Research Institute, Inc. under Contract No. RP-1630-53, the National Park Service under Contract NA81RAH00001, Amendment 17, Item 15, and the Office of Naval Research under Contract N00014-88-K-0029. My visit to the University of Alabama at Huntsville in August, 1988 was supported by Cray Research, Inc. Much of the computational work described in this dissertation was performed at the National Center for Atmospheric Research; NCAR is supported by the National Science Foundation. NCAR Scientific Computing Division and Data Support Service personnel were also very helpful in answering questions on a number of occasions.

Finally, on a personal note, my parents and my Aunt Nancy stood behind me throughout a long program of study. Their unwavering support helped to keep me going. Dr. Keith Puckett of the Atmospheric Environment Service in Toronto showed far more patience than a slow-finishing graduate student had any right to expect, but for which I am grateful. And towards the end of my program, Ms. Lee Benson provided advice, encouragement, help with figures, and extra incentive to finish.

LIST OF FIGURES

PREFACE

In the preface to his chronicle of British history, the monk Nennius declared "I have heaped together all that I found" (Fleischman, 1992). You, the reader, may wonder if something similar has occurred here. I will readily admit that this dissertation has grown far beyond my original expectations or intentions. It represents some years of self-education and it expanded as I learned more. But I also believe that all of the material discussed herein is relevant to the topic of mesoscale atmospheric dispersion in general and to the two case studies in particular.

To begin with, I have been forced to go back to first principles. The two most fundamental concepts in this study, those of *turbulence* and *dispersion*, are not absolutes but instead are situational — they are defined in the context of their application. It is thus critical to understand the meaning of mesoscale turbulence and to recognize the extent to which it is possible and even desirable to parameterize it for the purpose of modelling mesoscale dispersion. The concepts of averaging and scale, and expectation and realization, are all integral to the understanding of turbulent dispersion. I took a long time to come to grips with the idea of an ensemble average in an unsteady flow, to sort out the roles of release time, travel time, sampling time, averaging time, and filtering time in mesoscale dispersion, and to distinguish between a 'Lagrangian' and an 'Eulerian' eddy diffusivity. I also struggled to appreciate the difference between mesoscale relative diffusion and mesoscale absolute diffusion and to understand the limitations on the use of a 'one-particle' model for simulating the former.

Moreover, mesoscale dispersion, to the extent that it has been studied at all, has been analyzed using concepts and methods developed for small-scale dispersion. But mesoscale flows are, in general, nonstationary, inhomogeneous, and anisotropic, precluding, or at the very least demanding reexamination of, the application of many smaller-scale theories and approaches. Mesoscale 'eddies' can be dramatically different in structure and behaviour from the familiar small-scale eddies of the wind tunnel. The mesoscale energy spectrum also differs from the small-scale energy spectrum. All of these complicating factors will influence the phenomenon of mesoscale dispersion, and I have addressed them in this dissertation to the best of my ability. I hope these considerations will excuse, or at least help to explain, the range and depth of the background material discussed here.

TABLE OF CONTENTS

LIST OF ABBREVIATIONS

Acid MODES	Acid Model Operational Diagnostic Evaluation Study
ACURATE	Atlantic Coast Unique Regional Atmospheric Tracer Experiment
AEC	Atomic Energy Commission
AES	Atmospheric Environment Service (Canada)
AGL	above ground level
ALPEX	Alpine Experiment
AMS	American Meteorological Society
ANATEX	Across North America Tracer Experiment
APE	available potential energy
ARAMS	Advanced Regional Atmospheric Modeling System
ARL	Air Resources Laboratory
ARRPA	Air Resources Regional Pollution Assessment
ASCOT	Atmospheric Studies in Complex Terrain
ATAD	atmospheric transport and dispersion
BAO	Boulder Atmospheric Observatory
BATS	Brookhaven atmospheric tracer sampler
BVF	Brunt-Väisälä frequency
CAG	concentration analysis grid
CAPTEX	Cross-Appalachian Tracer Experiment
CAT	clear-air turbulence
CBL	convective boundary layer
$CBrF_3$	bromotrifluoromethane (Freon-13B1)
CCMS	Committee on Challenges of Modern Society
CDT	Central Daylight Time (GMT - 5 h)
CISK	conditional instability of the second kind
CL	centerline
CPU	central processing unit
CWIC	cross-wind integrated concentration
CWIE	cross-wind integrated exposure
DNS	direct numerical simulation
DOD	Department of Defense
DOE	Department of Energy
DOPPTEX	Doppler Acoustic Sounder Tracer Experiment
DSS	Data Support Section (part of NCAR Scientific Computing Division)
ECMWF	European Centre for Medium-Range Weather Forecasts
EDT	Eastern Daylight Time (GMT - 4 h)
EMEFS	Eulerian Model Evaluation Field Study
EPA	Environmental Protection Agency
EPRI	Electric Power Research Institute
FAO	Food and Agriculture Organization

FGGE	First GARP Global Experiment
fl	femtoliter ($= 10^{-15}$ l)
FM-CW	Frequency Modulation–Continuous Wave
GARP	Global Atmospheric Research Programme
GASP	Global Atmospheric Sampling Program
GCM	general circulation model
GFDL	Geophysical Fluid Dynamics Laboratory
GISS	Goddard Institute for Space Studies
GLADIS	Greater Los Angeles Distant Impact Study
GLC	ground-level concentration
GM	Garrett-Munk
GMT	Greenwich Mean Time
HF	high frequency
HHI	horizontally-homogeneous initialization
hPa	hectoPascals (1 hPa $\equiv$ 1 mb)
Hz	hertz (= one cycle per second)
IGW	internal gravity waves
INEL	Idaho National Engineering Laboratory
IR	infrared
ISAN	isentropic analysis
ISDME	International Sulfur Deposition Model Evaluation
IWEX	Internal Wave Experiment
KDE	kernel density estimation
KE	kinetic energy
KfK	Kernforschungzentrum Karlsruhe GmbH
KH	Kelvin-Helmholtz
KHI	Kelvin-Helmholtz instability
LBC	lateral boundary condition
LES	large-eddy simulation
LASL	Los Alamos Scientific Laboratory
lidar	light detection and ranging
LORAN	long-range navigation
LPDM	Lagrangian particle dispersion model
LRT	long-range transport
LRTAP	long-range transport of air pollutants
LST	Local Solar Time
MAD	mesoscale atmospheric dispersion
MASS	Mesoscale Atmospheric Simulation System
MATEX	Massive Aerometric Tracer Experiment
MCR	mesoscale compensation region
Me	methane (Me-16 = $^{12}CH_4$; Me-20 = $^{12}CD_4$; Me-21 = $^{13}CD_4$)
METREX	Metropolitan Tracer Experiment
MHz	megahertz
MLPDM	mesoscale Lagrangian particle dispersion model
MONEX	Monsoon Experiment
MST	mesosphere-stratosphere-troposphere
MU	middle-upper
NAPAP	National Acid Precipitation Assessment Program

NCAR	National Center for Atmospheric Research
NEROS	Northeast Regional Oxidant Study
NGM	Nested Grid Model
NMC	National Meteorological Center
NOAA	National Oceanic and Atmospheric Administration
NPP	nuclear power plant
NPS	National Park Service
NSSL	National Severe Storms Laboratory
NWP	numerical weather prediction
NWS	National Weather Service
OA	objective analysis
PBL	planetary boundary layer
PDCB	perfluorodimethylcyclobutane
PDCH	perfluorodimethylcyclohexane
PE	potential energy
PGF	pressure-gradient force
PGS	power generating station
pibal	pilot balloon
PMCH	perfluoromethylcyclohexane
PMCP	perfluoromethylcyclopentane
PMVD	Plume Model Validation and Development
PSI	parametric subharmonic instability
PTCH	perfluorotrimethylcyclohexane
radar	radio detecting and ranging
RADM	Regional Acid Deposition Model; Random-walk Advection and Dispersion Model
RAMS	Regional Atmospheric Modeling System
RMS	root-mean-square
RSDM	regional-scale dispersion model
SCCCAMP	South Central Coast Cooperative Aerometric Monitoring Program
SCD	Scientific Computing Division (of NCAR)
SCENES	Subregional Cooperative Electric Utility/DOD/NPS/EPA Study
SEADEX	Shoreline Environment Atmospheric Dispersion Experiment
SESAME	Severe Environmental Storm and Mesoscale Experiment
SGS	subgrid-scale
SIESTA	SF_6 International Experiments in Stagnant Air
sodar	sound detecting and ranging
SST	sea-surface temperature
ST	stratosphere-troposphere
STATE	Sulfur Transport and Transformation in the Environment
SURE	Sulfate Regional Experiment
TKE	turbulence kinetic energy
TLH	transport-layer height
TULLA	Transport und Unwandlung von Luftschadstoffen im Lande Baden-Württemberg und aus Anrainerstaaten
TWERLE	Tropical Wind, Energy conversion and Reference Level Experiment
UBC	upper boundary condition
UHF	ultrahigh frequency

UNESCO	United Nations Educational, Scientific and Cultural Organization
USDA	U.S. Department of Agriculture
UTC	Universal Time Coordinated
VAD	velocity-azimuth display
VAN	visualization & analysis
VHF	very high frequency
VI	variable initialization
WHITEX	Winter Haze Intensive Tracer Experiment
WMO	World Meteorological Organization
4DDA	four-dimensional data assimilation

LIST OF SYMBOLS

$A(\lambda)$	cloud work function
A_l	universal constant for D_l
A_t	universal constant for D_t
c	total concentration; instantaneous concentration; phase speed; complex wave speed
$\overline{c}$	mean concentration
c'	concentration fluctuation
c_g	group velocity
c_i	imaginary component of complex wave speed
c_p	specific heat of air at constant pressure; phase speed; peak concentration
c_r	real component of complex wave speed
C_n	refractive-index structure-function parameter
C_T	temperature structure-function parameter
Co^2	cospectrum
Coh	coherence
$d\xi_t$	Gaussian stochastic process
D	molecular diffusivity; disturbance length scale
D_l	Eulerian longitudinal velocity structure function
D_r	radial or cross-stream molecular diffusivity
D_t	Eulerian transverse velocity structure function
D_v	virtual along-stream diffusivity
D_x	along-stream molecular diffusivity
$\overline{D^2}$	plume centerline variance
E	kinetic energy spectral density; exposure
E_1	longitudinal spectral density of horizontal wind speed
f	Coriolis parameter; frequency; unspecified flow quantity; characteristic frequency
F	Fourier number
F_1	longitudinal spectral density of longitudinal velocity
Fr	Froude number
Fr_D	internal Froude number; disturbance Froude number $[= U/ND]$
g	acceleration due to gravity; unspecified flow quantity
G_1	longitudinal spectral density of lateral velocity
h	obstacle height
H	density scale height; vertical scale length
H_1	longitudinal cospectral density of horizontal velocity components
i	relative turbulence intensity
k	von Kármán's constant; x-direction wavenumber; planar wavenumber; spherical wavenumber
k_d	dissipation-range wavenumber

k_e	energy-containing-range wavenumber
k_1	longitudinal wavenumber
k_2	latitudinal wavenumber
K_e	effective eddy diffusivity
K_h	eddy diffusivity of heat
K_H	horizontal eddy diffusivity
K_m	eddy diffusivity of momentum
K_x	along-stream eddy diffusivity; x-direction eddy diffusivity
K_{xe}	eddy-driven along-stream diffusivity
K_{xs}	shear-driven along-stream diffusivity
K_{xz}	XZ eddy diffusivity
K_{yz}	YZ eddy diffusivity
K_z	vertical eddy diffusivity
l	y-direction wavenumber
ℓ	Scorer parameter; vertical mixing length; cloud length scale
L	horizontal length scale; Monin-Obukhov length; integral turbulence length scale
L_b	buoyancy length
L_{MO}	Monin-Obukhov length
L_R	Dougherty-Ozmidov length
L_x	length scale in x-direction
L_y	length scale in y-direction
L_ϵ	Kolmogorov microscale (see also η)
m	longitudinal wavenumber; vertical wavenumber; order of spherical harmonic
M	mesh spacing; number of flight segments
n	degree of spherical harmonic; two-dimensional spherical wavenumber; cyclic frequency
N	Brunt-Väisälä frequency; number of vertical levels
$O(\ )$	order of magnitude
p	pressure
p_s	surface pressure
p_{00}	10^5 Pa (1000 mb)
P	particle position probability density function
P_{ij}	projection tensor
P_n^m	associated Legendre polynomial
q^2	turbulence kinetic energy
Q	source strength
Q^2	quadrature spectrum
r	distance; separation distance
r_v	water vapour mixing ratio
R	gas constant for dry air; autocorrelation function
Re	Reynolds number
Re_λ	turbulence Reynolds number $[= \lambda U/\nu\,]$
R_E	Eulerian velocity correlation function
RH	relative humidity
Ri	gradient Richardson number
Ri_f	flux Richardson number

R_L	Lagrangian velocity correlation function
Ro	Rossby number
Ro_D	disturbance Rossby number $[= V'/fD]$
R_t	Eulerian vector velocity temporal correlation
R_u	space or time Eulerian longitudinal velocity correlation function
R_v	space or time Eulerian meridional velocity correlation function
R_V	space or time Eulerian speed correlation function
s	slope; geometric stretching ratio; averaging time
t	time
t_e	time scale for most effective separating eddy
t_i	integral time scale
t_l	Lagrangian advective time scale
t_r	release time
T	travel time or diffusion time
T_I	integral time scale
T_L	Lagrangian turbulent integral time scale
T_{Lu}	horizontal Lagrangian turbulent integral time scale
T_{Lw}	vertical Lagrangian turbulent integral time scale
T_S	slow-variation time scale
u	total u-velocity component
$\overline{u}$	mean u-velocity component
u'	u-velocity fluctuation
u_*	friction velocity
U	horizontal velocity scale; 1D KE spectral density; mean speed of fluid relative to sensor; Taylor advection velocity
U_g	geostrophic wind speed
U_t	mean translation velocity
v	total v-velocity component
v_o	RMS turbulence velocity
v_1	longitudinal velocity component
v_2	lateral velocity component
V'	horizontal velocity disturbance scale
$\vec{V}$	wind velocity vector
V_g	geostrophic wind speed
V_R	line-of-sight velocity; target volume
w	total w-velocity component
w_i	relaxation weights
w_*	convection velocity
w^*	terrain-following vertical velocity (cf. σ_z)
W	cloud width
x_1	x-coordinate
x_2	y-coordinate
x_3	z-coordinate
$\overline{X^2}$	along-wind particle position standard deviation
$\overline{Y^2}$	cross-wind particle position standard deviation
Y_n^m	spherical harmonic
z	Cartesian height; geopotential height
z_i	planetary boundary layer height

z_s	surface height
z^*	terrain-following vertical coordinate
α	specific volume; unspecified constant
Γ^2	spectrum function
Δt	time interval
Δx	horizontal grid interval
Δz	height interval; vertical grid interval
Δz_G	elevation difference between adjacent grid points
ϵ	turbulence energy dissipation rate per unit mass
η	Kolmogorov microscale length $[= \nu^{3/4}\epsilon^{-1/4}]$; enstrophy cascade rate
θ	potential temperature; latitude
θ_{il}	ice–liquid water potential temperature
θ_v	virtual potential temperature
κ	three-dimensional scalar wavenumber; R/c_p
$\vec{\kappa}$	three-dimensional vector wavenumber
κ_H	horizontal scalar wavenumber
λ	longitude; Taylor microscale length; cloud fractional rate of entrainment
Λ	integral turbulence length macroscale
ν	kinematic viscosity
ξ	separation/lag time
π'	perturbation Exner pressure
Π	Exner pressure $[= c_p(p/p_{00})^\kappa]$; potential vorticity
ρ	density
ρ_0	base-state density
σ	standard deviation; vector velocity standard deviation
σ_l	longitudinal temporal variability
σ_p	normalized pressure coordinate p/p_s
σ_t	transverse temporal variability
σ_u	RMS turbulent u-velocity component; zonal temporal variability
σ_v	RMS turbulent v-velocity component; meridional temporal variability
σ_w	RMS turbulence vertical velocity
σ_x	along-wind puff width
σ_y	cross-wind puff or plume width
σ_z	vertical puff width; terrain-following vertical coordinate (cf. z^*)
σ_V	Eulerian vector wind time variability
σ^2	variance
$\sigma^2_{T,s}$	variance over finite duration T for averaging time s
τ	sampling period; relaxation time
τ_{adj}	adjustment time
τ_{BV}	Brunt–Väisälä period
τ_{LS}	large-scale time scale
ϕ	latitude; generic model interior value
ϕ'	phase angle

ψ	Montgomery streamfunction $(= c_p T + gz)$
ψ_n^m	spherical harmonic coefficient
ω	frequency; dp/dt
ω_i	intrinsic frequency $[= \omega - \vec{V} \cdot \vec{\kappa}]$
$\vec{\omega}$	absolute vorticity

In the laboratory, the phenomena accompanying the mixture of two fluids are so commonplace that they do not seem to merit investigation. In the ocean and atmosphere, the phenomena are presumably very similar, but the lack of a good theory on which to base calculations complicates the problem much more than in the laboratory.

It is useful to consider a trivial experiment by way of introduction: the mixing of coffee and cream. Three more or less distinct stages can be observed:

1. *The initial stage,* in which rather large volumes of cream and coffee are distinctly visible; there are sharp gradients at the interfaces between the volumes, but elsewhere the gradient is practically zero. Averaged over the entire volume, this state persists for a considerable time.

2. *The intermediate stage,* after motion has been induced by stirring the liquids; the masses of cream and coffee are distorted, with a rapid increase in the extent of the interfacial regions having high concentration gradients. The average value of the gradient is correspondingly increased.

3. *The final stage,* in which the gradients disappear, apparently quite suddenly and spontaneously, with the liquid becoming homogeneous.

Carl Eckart (1948)

Chapter 1

INTRODUCTION

The smoke trails from cities have been observed by aviators to be hundreds of miles long. If aviators would also take note of the horizontal breadth of the trail at various distances from the source, and of the speed of the mean wind, it might be possible to extract a measure of the horizontal diffusivity.

L.F. Richardson (1922, p. 220)

Atmospheric *dispersion* is the irreversible process by which a cloud of tracer or pollutant expands, mixes, and is diluted by atmospheric motions acting on the cloud[1]. It may be thought of as the result of two processes or components, *advection* and *diffusion*. Oceanographers often refer to these two processes as *stirring* and *mixing* (e.g., Eckart, 1948). The advective (or transport or stirring) component can in turn be divided into two subcomponents: (a) mean or whole-body advection, which determines the trajectory of the center of mass of the tracer cloud; and (b) differential advection, in which the tracer cloud is deformed and even fragmented as a result of horizontal and vertical shear (Pielke et al., 1987a).

Differential advection (or stirring) leads to streaks and stronger concentration gradients while diffusion (or mixing) results in weaker concentration gradients and smaller concentration maxima (e.g., Garrett, 1983). This separation of dispersion into two separate processes is somewhat artificial, however. As I will discuss a number of times in

[1] Unless otherwise noted, the word 'cloud' will be used herein to refer to a cloud of tracer or pollutant material and not to a cloud of water droplets or ice crystals.

this dissertation, the interaction of differential advection with turbulent diffusion results in enhanced diffusion or mixing. Csanady (1973, p. 137) suggested the term *turbulent dispersion* to distinguish such augmented diffusion from 'pure' turbulent diffusion. Following Csanady, and Pielke et al. (1987a), I will use the term *turbulent diffusion* to refer to pollutant dispersal due to unresolved or subgrid-scale motions and the term *turbulent dispersion* to denote dispersal due to both turbulent diffusion and differential advection.

Diffusion is a macroscopic concept, a statistical description of unresolved small-scale advective transport (e.g., Hinze, 1975, Sec. 1.9). *Molecular* diffusion results from the aggregate movements of individual molecules. Like other quasi-continuous macroscopic fluid properties of statistical mechanics such as pressure, density, and temperature, molecular diffusion is defined based on an average over a large number of molecules in a small volume, and like pressure, density, and temperature, it can be measured directly without knowledge of the details of molecular motions. Much of our present theory of turbulence is based on an analogy to statistical mechanics and the kinetic theory of gases. *Turbulent* diffusion thus corresponds to the mean advective transport due to turbulent velocity fluctuations. As in the molecular case, the details of individual turbulent velocity fluctuations are not known; rather, our description is confined to only a few of the statistical properties of the turbulent fluctuations. The distinction between the processes of advection and turbulent diffusion thus depends critically upon the specification of the *averaging operator* and the *averaging scale* (see Sec. 1.4).

What then is *mesoscale* atmospheric dispersion? Atmospheric motions occur over a wide range of scales from a few millimeters to thousands of kilometers. All of these flow scales will affect the dispersion of atmospheric pollutants to some degree. However, the majority of atmospheric dispersion studies to date have been concerned with the *local* scale, that is, dispersion within a few kilometers of a source. Micrometeorological atmospheric turbulence as defined for averaging periods on the order of 30–60 minutes is the dominant dispersion mechanism over these distances. More recently, a number of studies have dealt with the *long-range* transport and diffusion of air pollutants over regional-scale, synoptic-

scale, and even global-scale distances. Synoptic-scale eddies such as extratropical cyclones constitute the primary mechanism for dispersion on these scales. Mesoscale atmospheric dispersion falls between these two extremes. Small-scale turbulent diffusion is important for mesoscale dispersion but so are temporal and spatial variations in the mean wind field, including mesoscale 'eddies', caused by changing surface characteristics, diurnal forcing, and large-scale atmospheric dynamics.

This dissertation describes a numerical investigation of mesoscale atmospheric dispersion with a coupled pair of numerical models. A basic tenet of this work is that over mesoscale distances and travel times, differential advection, especially that due to vertical shear, contributes to additional pollutant mixing and dilution and plays an even more important role than it does in short-range atmospheric dispersion. Where necessary I have gone back to first principles in this study because (a) implicit and explicit assumptions about atmospheric dispersion that have proven useful on smaller and larger scales may not hold on the mesoscale (e.g., Frenkiel, 1952; Pasquill, 1974), and (b) inherent 'compatibility' questions arise when comparing mesoscale dispersion theory, observations, and model results.

In this first chapter, I give an overview of the phenomenon of mesoscale atmospheric dispersion, introduce some basic concepts such as types of averaging, intrinsic time and space scales for mesoscale flows and dispersion, absolute and relative diffusion, and shear effects on dispersion, summarize some fundamental issues, present my hypothesis, and outline the organization of the rest of the dissertation.

1.1 Definition of Mesoscale

First of all, what exactly do I mean by the term 'mesoscale'? The atmospheric mesoscale can be defined in several ways. The first definition, introduced during the 1950s, was a utilitarian or operational one, namely those atmospheric scales that cannot be observed with contemporary observing systems (Emanuel, 1986). In the 1950s the atmospheric mesoscale thus fell between the cumulus scale, resolved by early weather

radar, and the cyclone scale, resolved by the operational synoptic observing network. However, observing system technologies have improved greatly over the past three decades, effectively shrinking this definition of mesoscale with each advance.

Orlanski (1975) suggested a simple geometric definition based on horizontal space scales. In his scheme the atmospheric mesoscale covers three spatial decades: the meso-γ scale (2–20 km), the meso-β scale (20–200 km), and the meso-α scale (200–2000 km). Orlanski recognized that time scales and vertical space scales also need to be considered but argued that his scheme provided precision of terminology and less ambiguity than a comparable definition based on time scales alone. Although somewhat arbitrary, Orlanski's geometric definition has been widely adopted.

A third definition has been offered based on dynamic similarity. Pielke (1984) proposed that the term 'mesoscale' be used to refer to horizontal scales large enough that vertical accelerations can be neglected (i.e., hydrostatic) but small enough that the Coriolis force does not balance the horizontal pressure force (i.e., ageostrophic). Emanuel (1986) categorized atmospheric phenomena on the basis of Lagrangian Rossby number, the ratio of the 'pendulum day' $(2\pi/f)$ to the Lagrangian *advective* time scale t_l, the time required to move through one wavelength of an atmospheric structure if it is periodic or to move through the entire structure if it is aperiodic. His mesoscale corresponds to "processes with Lagrangian time scales between the period of a pure buoyancy oscillation and a pendulum day and includes inertia-gravity waves and slantwise convection" (Emanuel, 1986, p. 17). Pielke's definition thus corresponds to Orlanski's meso-β scale while Emanuel's corresponds to the meso-γ and meso-β scales (in the tropics, both of these dynamical definitions will include some of Orlanski's meso-α scale, too).

In the rest of this dissertation, the term 'mesoscale' will refer to Orlanski's full three-decade range although the emphasis will be on the meso-β scale. The term 'regional-scale' will also be used as a synonym for 'meso-α scale'. Mesoscale atmospheric dispersion (MAD) will be defined herein as the transport and diffusion of an air pollutant or other atmospheric constituent over horizontal distances of between 2 and 2000 km and time

periods ranging from 1 to 48 hours. It thus falls between what might be termed local or small-scale dispersion on the one hand, and synoptic-, continental-, and global-scale atmospheric dispersion on the other.

1.2 Examples of Mesoscale Atmospheric Dispersion

Early studies of atmospheric dispersion after World War I focused almost exclusively on local dispersion, motivated by civilian concerns over the effects of industrial air pollutants on public health and by military concerns over the impact of smoke, poison gases, and biological agents on the battlefield. The conventional wisdom of the time held that since the atmosphere's capacity to dilute air pollutants is effectively limitless, maximum ground-level concentrations (GLC) close to the pollutant source should be the main concern of the air pollution meteorologist. For pollutants transported over mesoscale or larger distances, it was argued, sufficient dilution will have taken place that there is little practical need to know pollutant concentrations at these distances.

In the last fifteen or twenty years, however, there has been increasing recognition that in situations where (i) pollutant sources are either strong enough or numerous enough or long-lasting enough or (ii) where the pollutants themselves are sufficiently toxic or active enough in some way, e.g., bioaccumulative or catalytic, then pollutant concentrations or dosages even far from the source may be of concern. The multi-country radionuclide contamination experienced during the 1986 Chernobyl disaster in the Soviet Union is one recent example of mesoscale and synoptic-scale pollutant transport (Persson et al., 1987; Smith and Clark, 1988; Wheeler, 1988). Earlier significant releases and transport of radionuclides occurred during the Windscale reactor accident in England in 1957 and during numerous atmospheric tests of nuclear devices in the 1950s (Crabtree, 1959; Feely et al., 1966; List et al., 1966; Reiter, 1978).

Regional-scale (i.e., meso-α-scale: 200–2000 km) acidic deposition, ozone, and haze episodes are the result of the transport and mixing over long distances of chemical compounds emitted by numerous large and small sources (Lyons, 1980; NRC, 1983;

Vukovich and Fishman, 1986; Lefohn and Krupa, 1988; Mohnen, 1988; Whelpdale et al., 1988). Even remote regions of the planet without local sources of pollutants have been affected by air pollution in recent years. For example, present-day air pollution impacts in the Arctic and Antarctic include wintertime haze episodes, diminution of polar stratospheric ozone concentrations, and uptake and accumulation of pesticides and other chemicals by Arctic flora and fauna (Stonehouse, 1986; Stolarski, 1988; Trivett et al., 1988; Barrie et al., 1989; Maenhaut et al., 1989). The behaviour of urban-scale plumes downwind of large, industrialized cities is another example of mesoscale atmospheric dispersion (e.g., Trout and Panofsky, 1974; Aguado, 1990; Bastable et al., 1990; Lamb et al., 1990).

Significant mesoscale transport of natural aerosols also occurs from time to time as a result of volcanic eruptions, forest fires, or sandstorms (Chung et al., 1981; Crabtree and Kitchen, 1984; Chung, 1986; D'Almeida, 1986; Segal et al., 1989; Ferrare et al., 1990). Biological organisms, including pollens, seeds, bacteria, spores, viruses, and harmful insects such as locusts and spruce budworms, can also be transported over mesoscale or greater distances (Blackall and Gloster, 1981; Stinner et al., 1982; Pedgley, 1982).

1.3 Basic Features of Mesoscale Atmospheric Dispersion

Mesoscale atmospheric dispersion is of interest for its own sake as well as for its effects and impacts. It is an even more complex phenomenon than smaller-scale atmospheric dispersion due to the additional physical processes that may play a role and to the greater number of characteristic time and space scales (e.g., Pasquill, 1974). Consider the following six differences between small-scale dispersion and mesoscale dispersion.

(1) In the case of small-scale, near-source, or local dispersion, dilution occurs due largely to turbulent diffusion. To a first approximation, both the mean transport wind and turbulence may be considered *steady* and *horizontally homogeneous* although they may vary vertically. Under such atmospheric conditions, simple, semi-empirical diffusion models such as Gaussian plume models and similarity-theory models have been applied with some

success to small-scale dispersion in flat, uniform terrain and with less success to small-scale dispersion in complex terrain (e.g., Hanna et al., 1982; Pasquill and Smith, 1983).

However, over mesoscale travel times and distances, this approximation of steady, horizontally homogeneous flow no longer holds (e.g., Wendell, 1972; Pasquill, 1974; Smith, 1979). Instead, a large number of mesoscale flow modes are possible, including terrain-forced and synoptically-forced mean mesoscale circulations and mesoscale fluctuations, with a wide range of attendant temporal and spatial scales (discussed in more detail in Sec. 2.1). Pollutants can even be trapped by recirculating mesoscale cells, a phenomenon sometimes referred to as 'negative dispersion' since concentrations may actually increase due to advection (e.g., Lyons and Cole, 1976).

(2) The relative importance of vertical diffusion vs. horizontal diffusion differs between mesoscale dispersion and shorter-range dispersion. Over short distances, say 10 km or less, vertical and horizontal diffusion will be comparable in magnitude under neutral or unstable conditions. Once a tracer has mixed through the depth of the planetary boundary layer (PBL), however, additional dilution can only result from either further horizontal dispersion or from leakage out of the PBL due to mechanisms such as cloud venting, mesoscale venting by fronts or mesoscale convective systems, large-scale convergence, and surface deposition. Under stable conditions, vertical motions will be constrained by buoyancy forces whereas horizontal motions will not be so constrained. Horizontal diffusion will thus dominate both short-range dispersion in stably stratified flows and mesoscale atmospheric dispersion. And as will be described in Sec. 1.7, shear processes can greatly augment horizontal diffusion.

(3) One important consequence of Taylor's (1921) statistical theory of diffusion (see Sec. 2.3.1) is that in statistically *stationary, homogeneous* turbulence, the crosswind concentration standard deviation σ_y of the ensemble-mean plume from a continuous point source will initially grow linearly with travel time T, but then as T becomes large compared to the Lagrangian integral time scale T_L, σ_y will asymptotically approach a square-root dependence on T (Pasquill and Smith, 1983). Hanna (1981) reported aver-

age values for T_L of 60–90 s in the daytime boundary layer. Thus, the parabolic $T^{1/2}$ regime for lateral plume spread should be approached after travel over several kilometers if the appropriate T_L is the PBL convective time scale.

However, observations of a number of mesoscale plumes suggest that the linear time regime may persist out to mesoscale distances of 500 km or more (e.g., Pasquill, 1974; Panofsky, 1978; Clarke et al., 1983; Gifford, 1983, 1986; Pasquill and Smith, 1983). Fig. 1.1 shows a composite of three different sets of mesoscale plume observations which illustrate this behaviour (other comparable figures are presented in Sec. 2.2.2). In addition, many Lagrangian-puff regional-scale dispersion models (RSDMs — see Sec. 2.4) use Pack et al.'s (1978) formula for lateral plume spread, $\sigma_y = 0.5T$, where σ_y is in units of meters and T is in seconds, for all mesoscale travel times (e.g., Heffter, 1980; Carhart et al., 1989). See the discussion of Eq. 2.40 for more details. As described in Sec. 1.7, the augmentation of horizontal dispersion by the simultaneous interaction of vertical shear and vertical diffusion is largely responsible for this continued linear dependence during the first few hours. At longer travel times when the flow can no longer be considered steady, Gifford (1983, 1984, 1989b) has argued that the inertial period may be the appropriate T_L for mesoscale dispersion, and McNider et al. (1988) have suggested that the combined influence of two mesoscale time scales, the diurnal period and the inertial period, is important for mesoscale lateral dispersion in the PBL.

(4) Another difference is the treatment of vertical motions. Small-scale dispersion models neglect vertical motion. Over mesoscale distances, however, the effects of mesoscale and larger-scale vertical motions associated with convergence and divergence in the horizontal wind field may have a significant impact on dispersion. Mean vertical velocity ($\overline{w}$) values on the synoptic scale may range from 1 cm s^{-1} downward in an intense anticyclone to a few cm s^{-1} upward in extratropical cyclones (Pasquill, 1974). Much larger vertical velocities can occur in thunderstorms and mesoscale convective systems and along frontal surfaces. A vertical velocity of 1 cm s^{-1} will displace a parcel 36 m in an hour or 864 m in a day. Even net vertical transport due to active nonprecipitating convective clouds

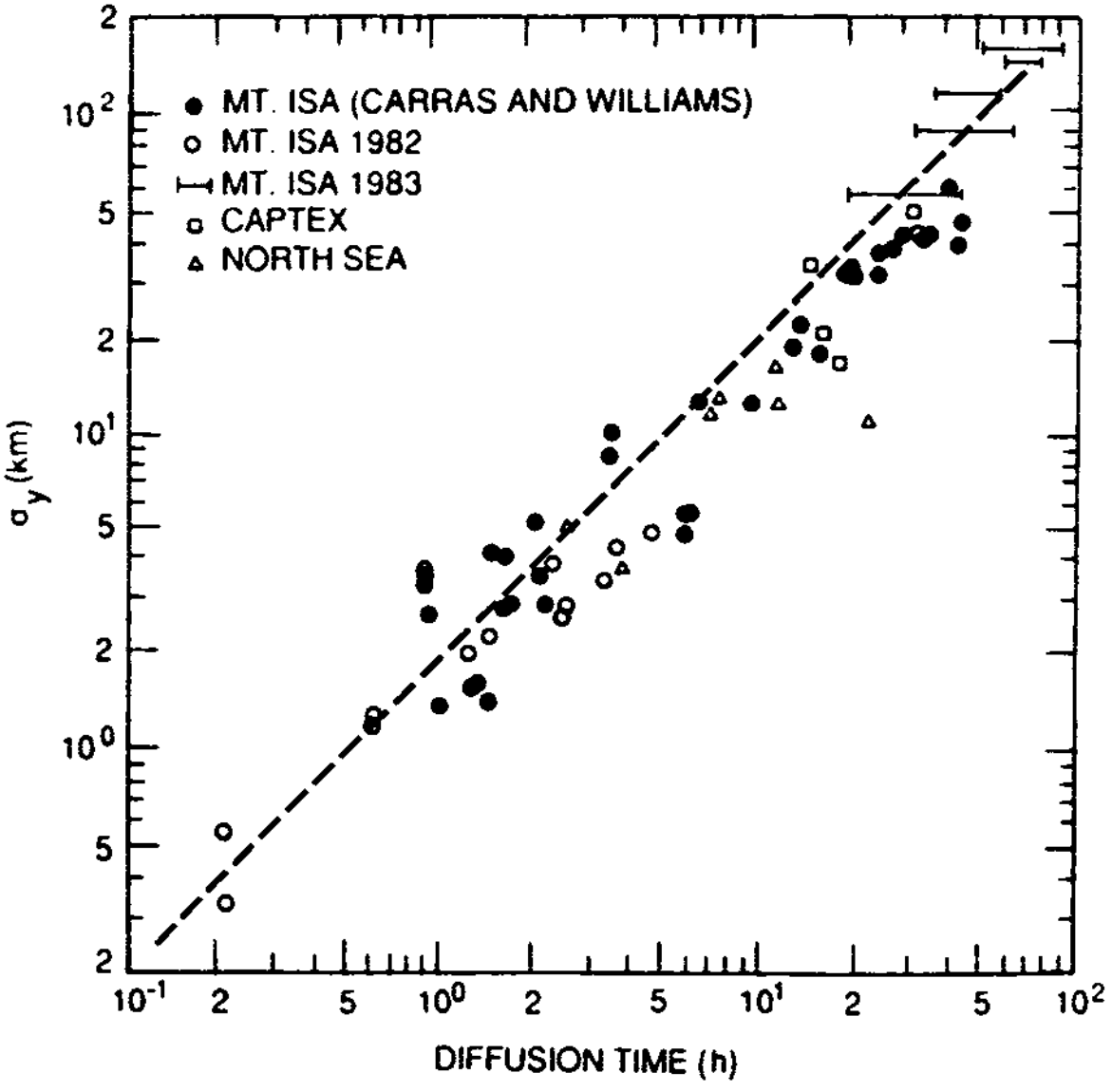

Figure 1.1: Composite of plume width observations for mesoscale travel times as compiled by Gifford (1986) [adapted from McNider et al., 1988]. Mt. Isa observations were made by aircraft of an isolated sulphide smelter plume in northern Australia during several winters; CAPTEX observations of a perfluorocarbon tracer plume were made by a network of surface monitors in autumn, 1983; the North Sea observations of an SF_6-labelled English power plant plume over the North Sea were made by aircraft in 1980. The dashed line shows the relationship $\sigma_y = 0.5T$ proposed by Pack et al. (1978).

can exchange significant amounts of PBL and free-tropospheric air, a process known as *cloud venting* (e.g., Ching and Alkezweeny, 1986; Dickerson et al., 1987; Ching et al., 1988; Martner and Kropfli, 1989; Vukovich and Ching, 1990). Studies of the impact of vertical motions on mesoscale transport and dispersion include Moran et al. (1986), Draxler (1987), Haagenson et al. (1987), Martin et al. (1987), Segal et al. (1988), and Uliasz (1990b).

(5) Contrary to the idealization for smaller-scale dispersion[2], non-Gaussian, multimodal cross-plume concentration profile are often observed at mesoscale travel distances. Carras and Williams (1988) have presented plots (reproduced here as Fig. 1.2) of five multimodal plume cross-sections for the plumes from the Mt. Isa smelter in northern Australia and the Kalgoorlie smelter in southwestern Australia at downwind distances ranging from 230 km to 1200 km. A common feature of all five cross-sections is that in each case the plume has experienced at least one morning or evening PBL transition prior to the measurement. What is especially interesting about the Mt. Isa measurements is that transport has taken place across fairly flat, homogeneous terrain, suggesting that terrain-forced mesoscale circulations due to mesoscale physiographic inhomogeneities are not responsible for the cross-plume mesoscale structure, yet there is significant cross-plume mesoscale structure.

A second example may be found in the set of three-hour-average measurements of perfluorocarbon surface concentration made along an arc of samplers 600 km from the release site during the 1980 Oklahoma mesoscale tracer experiment (Sec. 3.1.1). Measurements along this sampler arc for each of the first two 3-hour observing periods showed three relative concentration maxima across the tracer puff (Fig. 3.8). The westernmost peak was approximately two orders of magnitude smaller than the other two peaks but was still at least five times greater than background levels. Csanady (1972) also reported measurements of two peaks even after travel over distances of only 30 km in some tracer

---

[2]And the Gaussian model *is* an idealization for small-scale dispersion from elevated sources, at least. Moore et al. (1988) reported that only 35% of hourly-averaged ground-level concentrations measured during many hours of SF_6 tracer releases at the PMVD plains site at Kincaid, Illinois could be judged to be Gaussian in shape.

trials carried out in rural Arkansas. He attributed these features to the effect of wind shear and to expected irregularities in individual tracer clouds.

(6) A sixth difference is the occurrence of along-wind multimodal surface concentrations. A simple Gaussian dispersion model would predict a single GLC maximum and then monotonically decreasing concentrations at greater downwind distances. A Lagrangian-puff RSDM with a Heffter-type parameterization of horizontal diffusion would predict similar behaviour. However, in the mesoscale Cross-Appalachian Tracer Experiment (CAPTEX; see Sec. 3.2.1) in 1983, some six-hour-average surface concentration fields and time-composited maximum concentration fields showed two or more concentration relative maxima (Fig. 3.22 and Ferber et al., 1986, Figs. 2, 4, 11). Multimodal surface concentration patterns were also measured in the Oklahoma experiment (Fig. 3.10) and in the Across North America Tracer Experiment (ANATEX) in 1987 (e.g., Draxler, 1989, Figs. 2–5).

It would appear from this discussion and from other observations of mesoscale dispersion that additional physical processes must come into play in atmospheric dispersion at mesoscale space and time scales, even over flat, uniform terrain under simple synoptic conditions. Over complex terrain, terrain-forced mesoscale circulations can add further complexity to pollutant dispersion as can complicated and changing synoptic conditions.

1.4 Averaging and Turbulence

Let us now consider the fundamental concept of turbulence. The term 'turbulence' as used by most fluid dynamicists implies an irregular fluid flow produced by small-scale three-dimensional motions which show a random variation with space and time but for which statistically distinct average values can be discerned (Hinze, 1975; Mellor, 1985). By randomness, we are referring to irregular, aperiodic behaviour due to the complex

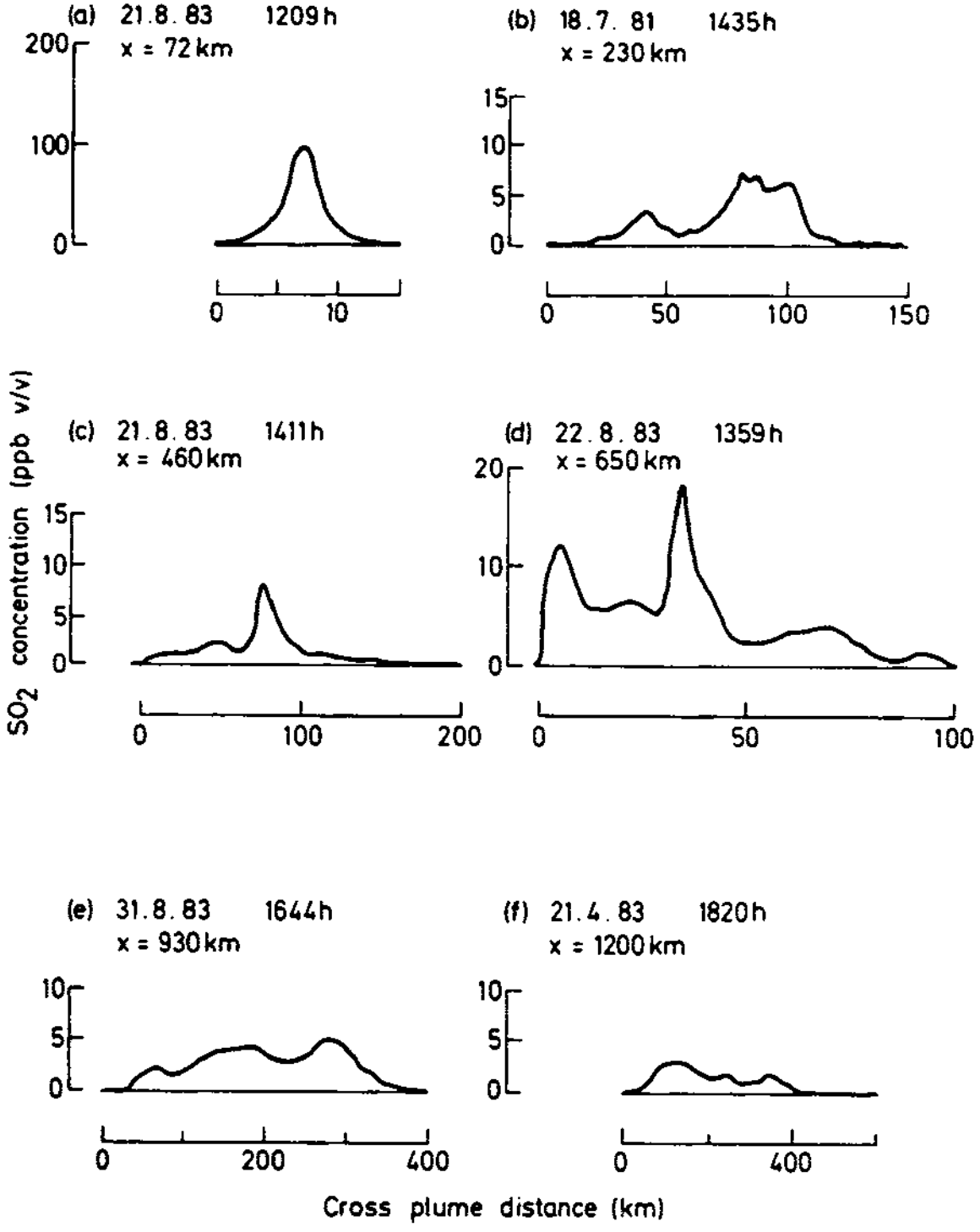

Figure 1.2: Variations of Mt. Isa plume SO_2 crosswind concentration distributions with distance from source as measured by aircraft (from Carras and Williams, 1988).

dynamics of a continuous spectrum of eddies[3] embedded in the mean flow. Batchelor and Townsend (1956, p. 352) have observed that "the most striking property of turbulent motion is its ability to disperse fluid particles that initially are grouped together". Yet despite such apparently concrete definitions and descriptions, the concept of turbulence may mean different things to observationalists, theoreticians, and modellers.

Stommel (1949, p. 215) stated that "*the term 'velocity' is meaningless unless accompanied by some indication of the mode of averaging employed in its determination*", and he repeated this statement in discussing 'eddy viscosity'. Richardson (1952, p. 2) observed that "... the motion of numerous particles is not naturally divided into a mean motion and a residuum; but that the mean is a mental artefact, and may be variously apprehended, so that the motion of the residuum is a compensatory artefact; and that therefore different types of mean may need to be compensated by different laws of diffusion." Thompson also noted that Reynold's formal definition of turbulence depends on the mode of averaging assumed and concluded that turbulence "... is not a real and distinctive physical phenomenon, but is simply a formal and rather useful concept for dealing with fluid systems whose state is not completely known" (Thompson, 1954, p. 152). In a somewhat similar vein, Lamb (1984) argued that since the continuous atmosphere has an infinite number of degrees of freedom, its state at any time cannot be determined completely. That is, for any finite set of observations, there is an infinite subset of atmospheric states which could fit the observations. Thus, rather than attempting to divide the atmospheric flow field into a deterministic mean component and a stochastic turbulent component, Lamb advocated that in regional-scale modelling, atmospheric flow should be considered as a single nondeterministic class of possible atmospheric states which he termed 'metulence'.

---

[3]Note the confusion arising from the use of the term 'eddy' to describe turbulence structure in *both* physical and spectral space (e.g., Gifford, 1968, p. 86). In discussions of turbulence spectra, 'eddy' is often used to denote a Fourier component with characteristic time and length scales: "Let it be said firmly and right at the beginning, that the word 'eddy' does not refer to any particular local distribution of velocity. It is merely a concise term for a component of motion with a certain length scale, i.e., an arbitrary flow pattern characterized by size alone." (Batchelor, 1950, p. 133). However, Corrsin (1959, p. 2136) noted that the 'traditional' usage of the term "implies a spatially local blob of fluid, usually swirling."

Nevertheless, the classical Reynolds treatment of three-dimensional turbulence is based on the concept of a rapidly fluctuating turbulent component superimposed on a stationary, or at least slowly varying, mean flow. For example, the u-component of velocity can be decomposed into mean and turbulent components

$$u = \bar{u} + u' \ , \tag{1.1}$$

where the overbar denotes an average of some sort over some scale and the prime denotes a fluctuation from that average. By introducing averaging, we can concentrate on mean values and ignore many flow details just as individual molecular behaviour is ignored in the kinetic theory of gases. However, an averaging operator must be chosen, bearing in mind that the use of different operators may lead to different decompositions of the flow and hence to different mean and turbulence fields.

1.4.1 Types of averages

The main types of averages are time averages, space averages, space-time averages, and ensemble (or statistical or probability) averages (e.g., Frenkiel, 1953; Hinze, 1975; Wyngaard, 1982; Cotton and Anthes, 1989). Kampé de Fériet showed in the 1930s that the derivation of the Reynolds-averaged equations of motions (Reynolds, 1895) requires the averaging operator to satisfy the following Reynolds conditions (Kampé de Fériet, 1951, 1954, 1974; Monin and Yaglom, 1971):

$$\overline{f+g} \ = \ \overline{f} + \overline{g} \ , \tag{1.2}$$

$$\overline{\alpha f} \ = \ \alpha \overline{f} \ , \ \alpha = \text{constant}, \tag{1.3}$$

$$\overline{\overline{f} g} \ = \ \overline{f}\,\overline{g} \ , \tag{1.4}$$

and

$$\overline{\partial f / \partial s} = \partial \overline{f} / \partial s \ , \ \text{where} \ s = x_1, x_2, x_3, \text{ or } t \ . \tag{1.5}$$

It then follows that $\overline{\overline{f}} = \overline{f}$ and $\overline{f'} = 0$. Kampé de Fériet (1974) also noted Oseen's observation in 1930 that neither a time average over a finite interval of time nor a space

average over a finite volume of space exactly satisfies the Reynolds conditions. Monin and Yaglom (1971) pointed out that it is Eq. 1.4 that causes the problem but also noted that a time or space average can satisfy this condition *approximately* provided that the averaging interval is chosen to be large compared to the characteristic periods or length scales of f' but small compared to the characteristic periods or length scales of $\overline{f}$.

An ensemble average, on the other hand, can be shown to satisfy the Reynolds conditions exactly. Accordingly, the modern theory of turbulence has adopted a statistical or probability-theory approach in which fields of fluid dynamical variables in a turbulent flow are assumed to be random fields and ensemble averages are used instead of time or space averages (e.g., Chap. 3 of Monin and Yaglom, 1971). Consideration of a single turbulent flow is replaced by consideration of the statistical ensemble of all flows with the same set of *fixed external* conditions. One experiment then reduces to a single sample value or realization, and ensemble averages are taken over an infinite number of such independent realizations. No intrinsic time or space scales are involved.

1.4.2 Applications of different averages

These various types of averages are appropriate to different situations. Clearly, a true ensemble average taken over an infinite number of realizations only has theoretical utility, although, as will be discussed in the next subsection, a sample ensemble average can be calculated based on only a finite number of realizations. Time averages, on the other hand, are commonly used for measurements made over a sampling interval τ at a fixed point in space by *in situ* instruments such as hot-wire anemometers, instrumented towers, or tethered balloons. Space averages are more demanding for practical applications since they require knowledge of instantaneous variable values over one, two, or three spatial dimensions. Nevertheless, some measurements made by remote-sensing techniques such as photography, laser interferometry, radar, sodar, and lidar yield space averages. Strictly speaking, moving *in situ* probes such as airborne, balloon-borne, or carriage-mounted instruments give *space-time* averages but, if the probe velocity is large relative to the internal time scales of the flow, these averages will approximate instantaneous

space averages. Obviously, measurements from remote-sensing instruments over a finite sampling time will yield space-time averages.

The fundamental average used in numerical models is also a space-time average, namely a grid-volume—time average (e.g., Pielke, 1984). Lamb (1984) has noted that we can generate a system with any desired number of degrees of freedom from a continuous fluid flow with an infinite number of degrees of freedom by performing suitable space-time averaging. This is what is done in a finite-difference model, for example, when we represent a continuous flow by values at a finite number of discrete grid points. Mesoscale meteorological models frequently use two different time averages. The obvious one is the time average over the model time step, but a second, longer time average over 15–60 minutes is implicit in the use of ensemble-average-based turbulence parameterizations (e.g., Pielke, 1984; Mahrt, 1987). Cotton (1986) argued that such 'generalized ensemble' averages are different from grid-volume—time averages and in fact are the fundamental averaging operators actually used in mesoscale and larger-scale meteorological models.

It has been suggested that the horizontal grid scale of mesoscale meteorological models provides a natural demarcation between turbulence and the mean flow (e.g., Lewellen, 1987). According to this view, turbulence consists of subgrid-scale flow motions while the mean flow corresponds to grid-resolved motions. Unfortunately, this appealing definition does not always coincide with common notions of turbulence. In some mesoscale models, larger PBL turbulence scales will be grid-resolvable, while in others, even some mean mesoscale circulations will be subgrid-scale in size. Moreover, the form of the model's turbulence parameterization scheme must be considered. As discussed by Wyngaard (1982) and Lamb (1982), boundary-layer turbulence models may be divided into two broad classes: (i) ensemble-average models and (ii) volume-average models. Ensemble-average boundary-layer models parameterize *all* PBL turbulence; they are unable to generate large eddies even though such scales of motion may be grid-resolvable. Thus, equating turbulence to subgrid-scale motion is not consistent with the formulation of ensemble-average boundary-layer models.

The best known volume-average boundary-layer models are the large-eddy simulation (LES) models. In these *three-dimensional, nonhydrostatic* models with *inertial-range grid spacing* in *both* horizontal and vertical directions[4], subgrid-scale motions are parameterized but eddies larger than a few grid lengths in size are resolved explicitly. However, most boundary-layer meteorologists would deem these large eddies to be 'turbulent' motions. As the size of the averaging volume increases, however, the fraction of eddies which can be explicitly resolved decreases. Mesoscale meteorological models with horizontal grid resolution of several kilometers or more will be incapable of resolving any PBL eddies. In fact, most volume-average mesoscale meteorological models employ an ensemble-average boundary-layer model (e.g., Mellor, 1985). Continuing upscale, synoptic-scale meteorological models with horizontal grid spacing on the order of several hundred kilometers will be unable to resolve even terrain-forced meso-β-scale circulations such as sea breezes that a boundary-layer meteorologist would likely deem to be 'mean' motions. Thus, in the case of volume-average turbulence models, equating turbulence to subgrid-scale motions does provide an operational though sometimes nontraditional definition of turbulence. It is also in keeping with Gifford's generalized definition of turbulence as motions that cause relative diffusion (Gifford, 1984, 1989b).

1.4.3 Relationships between different averages

Although the use of ensemble averages and the techniques of modern mathematical probability theory provide a powerful tool with which to investigate turbulence theoretically, there is still a need to compare theoretical deductions with laboratory or atmospheric measurements and with numerical model calculations. From a practical viewpoint, then, it is necessary to invoke an ergodic[5] hypothesis of some sort to relate various kinds of averages and to determine how close empirical mean values obtained by physical measure-

---

[4] All of the italicized characteristics must be present in an LES model.

[5] "Of or relating to a process in which every sequence or sizeable sample is equally representative of the whole (as in regard to a statistical parameter)" (Webster's New Collegiate Dictionary, 1975).

ment or numerical simulation are to the ensemble mean value (Hinze, 1975; Panofsky and Dutton, 1984).

Ensemble-average turbulence statistics can be approximated (a) as the ensemble average of a spatially and temporally local variable (i.e., an instantaneous point measurement) taken over a *finite* number of flow realizations, or (b) as the time average of a spatially local variable in a single stationary flow realization, or (c) as the space average of a temporally local variable in a single homogeneous flow realization (averaged and homogeneous in one, two, or three dimensions). In each case the accuracy of the sample estimate is improved by maximizing sample size (see Eq. 1.6). For instance, turbulence measurements made at a fixed point in a wind tunnel or at a certain height on an instrumented tower are averaged over as long a time as is practical without violating the assumption of flow stationarity (typically 30–60 minutes) in order to obtain an estimate of the ensemble average at that point. Similarly, aircraft measurements of turbulence quantities are averaged over as long a spatial 'leg' as is possible without violating the assumption of spatial homogeneity. Large-eddy-simulation (LES) model results are usually averaged over both time and the full horizontal domain (e.g., Moeng and Wyngaard, 1989; Hadfield et al., 1991; Walko et al., 1991).

Wyngaard (1973) discussed the averaging times used to estimate ensemble averages in the atmospheric surface layer at a fixed point. He used the expression

$$\tau = 2t_i\overline{f'^2}/(a^2\overline{f}^2) \tag{1.6}$$

to examine sampling fluctuations, where τ is the sampling time required to determine the ensemble average $\overline{f}$ to an accuracy a, t_i is the integral scale of the time-dependent function f, and $\overline{f'^2}$ is the ensemble variance of f about $\overline{f}$. τ is assumed to be much larger than t_i (e.g., Tennekes and Lumley, 1972, p. 212). To estimate the mean horizontal wind speed $\overline{u}$ to 1% accuracy (i.e., $a = 0.01$) for a typical value of relative turbulence intensity $\overline{u'^2}/\overline{u}^2$ of 0.05, τ should be equal to approximately $1000t_i$. For an integral time scale of 1 second, this corresponds to a sampling period of about

15 minutes, a typical value for surface-layer measurements. However, Wyngaard then showed that averaging times for a given accuracy increase with the order of the statistical moment of interest and with height. For example, to measure stress $\overline{u'w'}$ with the same accuracy at 200 m as at 20 m, τ must be about 50 times larger.

In a similar vein, Mellor (1985) has discussed the minimum sampling *distances* required to obtain ensemble-mean statistics from data in both the atmosphere and the ocean. If Λ is the integral turbulence length macroscale and if we accept a 10% error in our estimate, then for second-order moments, the measurement distance should be at least 100Λ, assuming Gaussian probability distributions. For a 1% error, this distance increases to $10,000\Lambda$. If U_t is a translation velocity relative to the turbulence field being observed, then a corresponding sampling time would be $100\Lambda/U_t$. If we further assume that Λ for the PBL is one-half the PBL height, then for a 1 km deep PBL the measurement distance should be at least 50 km. For a translation velocity U_t of 10 m s^{-1}, the corresponding measurement time would be about an hour and a half. For these same assumptions in a numerical model with square horizontal grid cells, each areal cell should be at least 5 km on a side for cell values to represent ensemble-average values. This is consistent with recent results of Moeng and Wyngaard (1989, p. 2325), who suggest that the largest PBL-scale eddies will not be resolvable on a 5 km by 5 km grid. Wyngaard (1973) also briefly considered spatial averages for fixed arrays of sensors, for aircraft measurements, and for remote sensing techniques.

1.4.4 Averaging and flow realizations

As already alluded to, one crucial difference between ensemble and volume averages is that ensemble averaging completely removes randomness whereas volume averaging does not (Wyngaard, 1982; Mellor, 1985; Cotton, 1986). Since an ensemble average is in principle taken over an infinite number of realizations, it samples all possible eddy sizes, phases, and amplitudes so that all transient eddies are averaged out (e.g., Yule, 1980). Stationary, surface-forced eddies may not be removed by ensemble averaging, but then these structures are by definition not random or transient. Grid-volume averages may,

however, retain transient eddies or coherent structures larger than the averaging length employed since such fields represent single flow realizations. Wyngaard has the following to say on this point (Wyngaard, 1982, p. 71):

> ... while the ensemble averaging operation removes all the turbulence, the volume averaging operator removes only those components of turbulence having spatial scales smaller than the averaging scales. In a statistically homogeneous, stationary, unbounded turbulent flow, the volume average converges to the ensemble average in the limit as the averaging volume increases. Thus one can think of the volume-averaged field as being the sum of the ensemble-averaged field and the large-scale turbulence.

Note that Wyngaard implicitly defines turbulence based on an ensemble average. If a volume-average definition is used instead, then what he refers to as large-scale turbulence must instead be interpreted as the resolved mean flow for the single flow realization being considered.

Under what conditions will volume-average model predictions closely resemble ensemble-average model predictions? If the volume-average model grid scale is much larger than the turbulence integral scale and the flow is both homogeneous and stationary, then volume-average and ensemble-average models become identical since both schemes will parameterize all turbulence. As discussed above, ensemble-average models always parameterize all scales of turbulence. For very large averaging volumes, volume-average models will be unable to resolve any eddy-scale motions and hence must also parameterize all eddy effects. If the horizontal resolution is considerably coarser than the vertical resolution as is usually the case in mesoscale meteorological models, any eddies which are resolved will be unrealistically long and flat (Lilly, 1989a). Moreover, if the model is hydrostatic, it will be unable to produce turbulent eddy motions even for a small averaging volume. Similarly, two-dimensional models of any resolution will effectively be ensemble-average models since real boundary-layer turbulence is three-dimensional and hence must be entirely parameterized in these models. In fact, Deardorff (1973, p. 429) states that "the use of a two-dimensional model to simulate three-dimensional flows is scarcely justifiable unless the problem is one in which continuous and strong forcing in two dimensions occurs".

1.4.5 Nonstationarity

What about nonstationary flows? Hinze (1975, p. 6) discusses the case of a turbulent flow with slow, nonturbulent variations. If the turbulence integral time scale is T_L and the time scale for the slow, nonturbulent variations is T_S, then the averaging time T should be chosen so that $T_L \ll T \ll T_S$. Problems arise, however, if T_S is itself small, since a time average based on a short time sample may be quite different from the corresponding ensemble average, resulting in a large sample variance (e.g., Tennekes and Lumley, 1972; Sykes, 1984). Such fluctuations can be reduced if averaging is extended over multiple realizations under identical external conditions in an analogous manner to the conditional sampling and compositing techniques used to study coherent flow structures (e.g., Yule, 1980; Elsberry, 1989; Ruscher and Mahrt, 1989; Narasimha and Kailas, 1990).

Nonstationarity is a particular problem in the atmosphere with its many time scales, including the diurnal cycle and cyclone–anticyclone lifetimes and passage times[6] (Frenkiel, 1952; Csanady, 1973). In the case of a convective boundary layer (CBL) with a depth z_i of 1200 m and a convection velocity w_* of 2 $\mathrm{m\,s^{-1}}$, one large-eddy turnover time will take about 10 minutes. An averaging time of 30 minutes would sample three large-eddy turnover times but would still be considerably shorter than the significant variations over one diurnal period. On the other hand, Wyngaard (1973) and Millán (1987) noted that even three or four hours of measurement in a CBL may not be long enough to obtain a stable sample. Turbulence time scales will be smaller in neutral and stable boundary layers. Csanady (1973, Sec. 3.13) argued that 3–60 minute PBL measurements have to be considered within the context of a geophysical turbulence continuum in which the 'mean wind' will itself depend on larger-scale eddies. He pointed out that micrometeorologists often reject data obtained during periods when the mean wind had 'shifted' midway through the observing period or showed an upward or downward trend or even complete

---

[6] Lagrangian and Eulerian time scales, respectively.

fluctuation cycles. Clearly, turbulence scales are much larger in the atmosphere than in a wind tunnel. This topic will be explored in the next section.

How can ensemble-average parameterizations or models handle nonstationary conditions? In the cumulus parameterization scheme of Arakawa and Schubert (1974), the time change of the cloud work function $A(\lambda)$ is divided into two parts, one due to cumulus-scale processes with an adjustment time scale τ_{adj} and one due to large-scale processes with a time scale of τ_{LS} (λ is the cloud fractional rate of entrainment). Arakawa and Schubert demonstrated that the adjustment time τ_{adj} for the environment to return from an unstable state to a neutral state is usually much smaller than τ_{LS}. Given this efficient adjustment, the cumulus ensemble, that is, the subgrid-scale cumulus-cloud field, will follow a sequence of near-equilibrium states as the large-scale environment slowly changes so that the time scale of the statistical properties of the cumulus ensemble is equal to the time scale of the large-scale processes τ_{LS}.

A similar approach can be followed when using ensemble-average equations to simulate a complete PBL diurnal cycle (Wyngaard, 1973). We assume that the turbulence time scales are much smaller than our averaging time which is in turn much smaller than a diurnal period. Given this wide scale separation, the diurnally-varying surface forcing can be assumed to carry the slowly-evolving PBL through a sequence of quasi-equilibrium states over the course of a day (e.g., Nieuwstadt and Brost, 1986). In fact, Mellor and Yamada's Level 2, Level 2.5, and Level 3 ensemble-average turbulence-closure schemes ignore most or all of the local time rate of change terms in the governing equations because these time scales are much larger than the time scale of turbulence (Mellor and Yamada, 1974). Only after the morning transition, when the PBL is growing rapidly, does this simplification cause problems (Helfand and Labraga, 1988). The overall success which ensemble-average models have had in simulating the full PBL diurnal cycle supports the application of the quasi-equilibrium assumption to this case.

1.4.6 Correlations, spectra, windows, and filters

As already discussed, sampling fluctuations are to be expected when estimating the characteristic statistics of either a chaotic or a random process from a finite sample. However, another limitation imposed by finite sampling duration or distance is that scales longer or larger than the sample size will not be fully accounted for in statistics calculated from the finite data record. Moreover, the smallest scales will be smoothed out due to instrument inertia in continuous measurements or will not be resolved due to the finite sampling rate in discrete measurements. Thus, both sampling duration τ and averaging time s will influence the apparent statistical properties of the physical property being measured[7].

Consider again a measurement made of the u-component of velocity, $u(t)$. Under statistically *stationary, homogeneous* conditions, we can define the temporal autocorrelation function $R(\xi)$ as

$$R(\xi) = \frac{\overline{u'(t)\,u'(t+\xi)}}{\overline{u'^2}} \quad , \tag{1.7}$$

where ξ is the time lag and $\overline{u'^2}$ is the variance. If the u-component is measured at a fixed point in space, then Eq. 1.7 defines an Eulerian autocorrelation function R_E, whereas if the u-component is measured for a tagged particle moving through the flow, then Eq. 1.7 defines a Lagrangian autocorrelation function R_L. An integral time scale T_I may then be defined for the u-component by the integral[8]

$$T_I = \int_0^\infty R(\xi)\,\mathrm{d}\xi \quad . \tag{1.8}$$

T_E is the Eulerian value of T_I (based on R_E) while T_L is its Lagrangian value (based on R_L).

---

[7]The rest of this subsection is largely an attempt to summarize the excellent treatment of this topic given in Chap. 2 of Pasquill and Smith (1983).

[8]Tennekes (1982) noted that very often in practice $R_L < 0.01$ for $\xi > T_L$ so that this integral converges rapidly to its asymptotic value.

Since $R(\xi)$ is a real and symmetric function (e.g., Tennekes and Lumley, 1972, p. 214), its Fourier transform $F(n)$ reduces to a cosine transform. The Fourier transform–inverse pair R–F thus has the form

$$F(n) = 4\int_0^\infty R(\xi)\cos 2\pi n\xi \,\mathrm{d}\xi \quad , \tag{1.9}$$

$$R(\xi) = \int_0^\infty F(n)\cos 2\pi n\xi \,\mathrm{d}n \quad , \tag{1.10}$$

where n is the cyclic frequency (in Hertz or cycles per second). $F(n)$ is sometimes referred to as the *normalized* power spectrum function since

$$\int_0^\infty F(n)\,\mathrm{d}n = 1 \quad . \tag{1.11}$$

Now in the case of a running average over a time interval s, instead of an instantaneous velocity u we are actually dealing with an averaged or smoothed velocity $\overline{u}$ where

$$\overline{u}(t) = \frac{1}{s}\int_{t-s/2}^{t+s/2} u(t')\,\mathrm{d}t' \quad . \tag{1.12}$$

Let $\sigma^2_{\infty,s}$ represent the variance of $\overline{u}$ for an *infinitely* long sample; assuming an ergodic system, $\sigma^2_{\infty,s}$ will thus equal the ensemble or probability statistic value. Let $\sigma^2_{\infty,0}$ represent the corresponding variance of u, that is, the true variance without signal averaging (so that $s = 0$). It can then be shown (Kahn, 1957) that for the 'boxcar' or 'top-hat' average assumed in Eq. 1.12,

$$\sigma^2_{\infty,s} = \sigma^2_{\infty,0}\int_0^\infty F(n)\frac{\sin^2\pi ns}{(\pi ns)^2}\,\mathrm{d}n \quad . \tag{1.13}$$

Since the positive-definite weighting function $\sin^2\pi ns/(\pi ns)^2$ in Eq. 1.13 has magnitude less than one at all non-zero frequencies n and decreases approximately as n^2 with increasing n, it acts as a low-pass spectral filter function. Accordingly, $\sigma^2_{\infty,s}$ will be

less than $\sigma^2_{\infty,0}$ for any averaging time s. As the averaging time increases, more and more of the power spectrum function $F(n)$ will be filtered and the value of $\sigma^2_{\infty,s}$ will become smaller and smaller.

The use of a finite sampling time τ will produce a complementary filtering of low-frequency contributions (Ogura, 1957, 1959). Consider an infinitely-long record of mean zero divided into a series of contiguous records, each of finite length τ. The ensemble variance of the entire record is again represented by $\sigma^2_{\infty,0}$. This value is equal[9] to the sum of the mean of the squared sample means for all of the individual finite-length records ($\sigma^2_{\infty,\tau}$) plus the mean of the finite-sample variances about the individual sample means, that is,

$$\sigma^2_{\infty,0} = \sigma^2_{\infty,\tau} + [\sigma^2_{\tau,0}]_\infty \quad , \tag{1.14}$$

where the symbol $[\ ]_\infty$ represents the mean value of the individual sample variances from consecutive periods of length τ over the entire (infinite) record. Rearrangement of the terms of Eq. 1.14 and use of Eqs. 1.11 and 1.13 then yields

$$[\sigma^2_{\tau,0}]_\infty = \sigma^2_{\infty,0} \int_0^\infty F(n) \left(1 - \frac{\sin^2 \pi n\tau}{(\pi n\tau)^2}\right) \mathrm{d}n \quad . \tag{1.15}$$

Thus, the *average* variance of a finite-length data record will be equal to the integral of the high-pass-filtered *full* power spectrum $F(n)$.

The combined effects of finite sampling duration τ and averaging time s on the mean sample variance can then be expressed by the equation (Smith, 1962)

$$[\sigma^2_{\tau,s}]_\infty = \sigma^2_{\infty,0} \int_0^\infty F(n) \left[1 - \frac{\sin^2 \pi n\tau}{(\pi n\tau)^2}\right] \frac{\sin^2 \pi ns}{(\pi ns)^2} \mathrm{d}n \quad . \tag{1.16}$$

The net result is that the true spectrum is bandpass-filtered by the combination of the two sampling effects. As a 'rule of thumb', Pasquill and Smith (1983) suggested that

---

[9] By the parallel-axis theorem for moments of inertia (e.g., Csanady, 1973, p. 86).

frequencies corresponding to periods between τ and $10s$ are well represented while frequencies corresponding to those periods $> 10\tau$ and $< s$ are effectively excluded (see Eq. 2.66 as well).

It is also worth considering Eq. 1.13 a little further. An important property of the Fourier transform is that multiplication in the time domain transforms to convolution in the frequency domain and vice versa (e.g., Jenkins and Watts, 1968). $F(n)$ and $R(t)$ are a Fourier transform pair. The Fourier transform of $\sin^2 \pi ns/(\pi ns)^2$ is the function

$$\begin{cases} \frac{1}{s}\left(1 - \frac{|n|}{s}\right), & |n| \leq s \\ 0, & |n| > s. \end{cases} \tag{1.17}$$

Use of the convolution property and Parseval's theorem then gives (Jenkins and Watts, 1968, p. 56)

$$\int_0^\infty F(n) \frac{\sin^2 \pi ns}{(\pi ns)^2} \, \mathrm{d}n = \frac{2}{s^2} \int_0^s (s - \xi) \, R(\xi) \, \mathrm{d}\xi \quad . \tag{1.18}$$

Eq. 1.18 is of interest because Taylor's theorem is easily derivable from it (see Sec. 2.3.1).

The convolution of the triangular function $1 - t/s$ with $R(t)$ in the time domain of Eq. 1.18 is one example of what is sometimes called a 'lag window' since it operates on the correlation function $R(t)$ while its counterpart $\sin^2 \pi ns/(\pi ns)^2$ in the frequency domain is referred to as a 'spectral window'[10] (e.g., Jenkins and Watts, 1968). Similarly, Eq. 1.12 can be viewed as the convolution of the boxcar function

$$w(t) = \begin{cases} 1, & |t| \leq s/2 \\ 0, & |t| > s/2, \end{cases} \tag{1.19}$$

with the instantaneous velocity u. The Fourier transform of $w(t)$ is the function

---

[10] These particular functions are sometimes referred to as the Bartlett filter in the literature (e.g., Jenkins and Watts, 1968, p. 242).

$$W(n) = s\frac{\sin \pi n s}{\pi n s} \quad . \tag{1.20}$$

The Fourier transform of Eq. 1.12 would thus yield the product of $W(n)$ with the Fourier transform of u. If we instead define $w(t)$ in terms of a fixed finite interval $(-s/2, s/2)$, then the product of $w(t)$ with $u(t)$ will result in a truncated or finite-length record. This definition of $w(t)$ is sometimes called a 'data window'. The Fourier transform of $w(t)\,u(t)$ will then consist of the convolution of $W(n)$ with the Fourier transform of $u(t)$.

1.5 Mesoscale Flow Scales

Echoing Csanady (see p. 21), Pasquill and Smith (1983; p. 359) have observed that "at longer scale(s) and over longer durations, the mean wind itself becomes variable and is part of the spectrum of turbulence". The implication, of course, is that mesoscale flow scales and flow structures which can be neglected when studying small-scale dispersion must be considered for mesoscale atmospheric dispersion. Such mesoscale flow variability can be characterized by a number of natural time and space scales.

1.5.1 Time scales

Within the PBL, changes in vertical stability and vertical mixing resulting from the diurnal heating cycle modify the vertical mean wind and turbulence profiles and give rise to oscillations in both wind speed and wind direction even over flat, uniform terrain. One striking example of such oscillations is the frequent formation of a low-level jet over land on clear nights (e.g., Blackadar, 1957; Bonner, 1968; Crawford and Hudson, 1973; Thorpe and Guymer, 1977; Mahrt et al., 1979; Lenschow et al., 1988a; Parish et al., 1988). Fig. 1.3 shows mean hodographs in which the presence of the low-level jet as a *climatological* feature is easily seen. Although the timing of the formation and subsequent erosion of the nocturnal jet is controlled by the diurnal cycle, the jet itself can be explained as an inertial oscillation. Thus, *two* natural mesoscale time scales need to be considered for travel times of more than one or two hours: the 24-hour diurnal period and the

latitude-dependent inertial period $2\pi/f$, where f is the Coriolis parameter (Moran et al., 1987; McNider et al., 1988). The inertial period may be longer than, equal to, or shorter than the diurnal period; for instance, the inertial period is 35 h at 20° latitude, 24 h at 30° latitude, 18.6 h at 40° latitude, and 13.8 h at 60° latitude. In addition, the *shape* of the diurnal forcing, i.e., the relative duration of night and day, is dependent upon latitude and season.

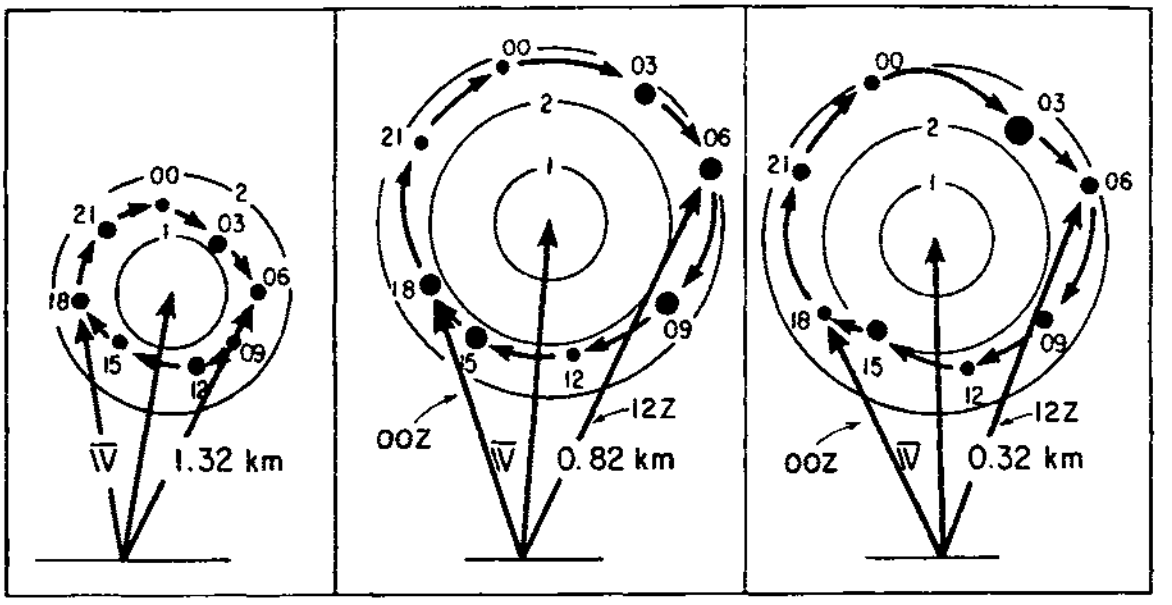

Figure 1.3: Hodographs of the summertime diurnal wind variation at three levels for Fort Worth, Texas including the mean wind vector and wind vectors at the two standard synoptic observing times (0000 GMT/1800 CST, 1200 GMT/0600 CST). Speeds are in meters per second. The size of the solid circles for each observing time is proportional to the magnitude of the probable error in determining the deviation vector at that time (adapted from Bonner and Paegle, 1970).

For horizontally-limited mesoscale circulations forced by differential surface heating (or cooling) such as sea (land) breezes, the natural circulation time scale is the forcing time scale, that is, the duration of heating (or cooling). Depending upon latitude and season, this time scale may vary from 1 to 24 hours. Short-duration forcing is less likely than longer-duration forcing to generate a mesoscale atmospheric response, but

some shallow circulations such as drainage winds can form in as little as one or two hours (Atkinson, 1981; Arritt, 1985; Whiteman, 1990). In contrast, mesoscale circulations resulting from the mechanical forcing of stably-stratified flows by topographic features (see below) will have the time scale of the larger-scale flow even though they are mesoscale in spatial extent. Still other mesoscale time scales will be associated with internally-forced mesoscale phenomena such as fronts and jet streaks and latent-heat-driven phenomena such as mesoscale convective complexes or mesoscale rainbands. These time scales will often be comparable to or larger than the inertial or diurnal periods, but they can also be shorter, especially if internal gravity waves are important.

Internal gravity waves are the free oscillation modes of a stably stratified fluid. There is a continuum of time scales associated with internal gravity waves, whose intrinsic period can lie anywhere in the range from the Brunt-Väisälä period $2\pi N^{-1}$ and the inertial period $2\pi f^{-1}$. Recent observations suggest that such modes are frequently present throughout the troposphere and stratosphere (see Sec. 2.1.8).

1.5.2 Space scales

Boundary forcing

If atmospheric flows are seldom steady over mesoscale time periods, then neither are they normally horizontally homogeneous over mesoscale distances. Many mesoscale circulations are atmospheric responses to externally-imposed *boundary* forcing. The presence of such topographic features as mountains, plateaus, and valleys can result in mesoscale flow phenomena such as mountain waves and rotors, lee waves, vortex shedding, upstream blocking, mesoscale gyres, and channeled flow due to *mechanical* forcing (e.g., Wendell, 1972; Durran, 1986, 1990; Baines, 1987; Smolarkiewicz et al., 1988; Wilczak and Glendening, 1988; Etling, 1989, 1990b; Meroney, 1990; Snyder, 1990) and slope winds and mountain-valley circulations due to *thermal* forcing (Atkinson, 1981; Pielke and Segal, 1986; Whiteman, 1990). Variations in other terrain properties may also affect atmospheric flows. Horizontal inhomogeneities in roughness length or surface temperature can generate internal boundary layers, and horizontal inhomogeneities in such

surface properties as water cover, soil moisture, vegetation type, vegetation cover, and snow cover can have a pronounced effect on dispersion by forcing mesoscale atmospheric circulations such as land-sea breezes through differential heating (Pielke and Segal, 1986; Dalu et al., 1991; Segal et al., 1990).

These various surface-forced mesoscale circulations possess a number of natural spatial scales. In the case of mechanically-forced circulations, the horizontal and vertical scales will depend on obstacle height h, obstacle width L, horizontal flow speed U, vertical stratification (represented by the Brunt-Väisälä frequency $N = [g\theta_v^{-1}(\partial\theta_v/\partial z)]^{1/2}$), and density scale height H $[= \rho_0(\partial\rho_0/\partial z)^{-1}$, where ρ_0 is the base state density]. Relevant combinations of these parameters include the Rossby number Ro $(= U/fL)$, the internal Froude number Fr $(= U/Nh)$, the nondimensional scale height NH/fL, the Scorer parameter ℓ^2 $(= N^2/U^2 - U^{-1}d^2U/dz^2)$, the Rossby radius of deformation based on scale height NH/f, and the Rossby radius of deformation based on obstacle height Nh/f. For instance, for $Ro > 1$ and $Fr < 0.5$, upstream flow below the height h of a two-dimensional ridge will be strongly blocked for a horizontal distance on the order of the obstacle-based Rossby radius of deformation[11]. For larger Froude numbers, a deep, vertically propagating, upstream-tilting hydrostatic mountain wave may form if the ridge width L is much greater than ℓ^{-1}, but only a weak shallow flow perturbation will occur if L is much less than ℓ^{-1} (Durran, 1986). In general, the vertical scale of mechanically-forced mesoscale circulations will range between the height of the obstacle h and the density scale height H while the horizontal scale will lie between the horizontal scale of the obstacle L and the Rossby radius of deformation based on obstacle height Nh/f.

---

[11] The upstream-propagating disturbances correspond to horizontally-propagating 'columnar disturbances' whose influence is limited in a rotating fluid by geostrophic adjustment; the fundamental vertical wavelength of the columnar modes, and hence their phase speed, is proportional to the mountain height (Pierrehumbert and Wyman, 1985; Pierrehumbert, 1986)

In the case of thermal forcing, thermally-forced mesoscale circulations tend to be shallow so that the PBL height z_i is a reasonable vertical scale while the Rossby radius of deformation Nz_i/f is a limiting horizontal scale (e.g., Dalu and Pielke, 1989).

Differences in surface heating due to surface inhomogeneities may also trigger moist convection; convective clouds in turn may vent pollutants up out of the PBL or deposit them on the ground through precipitation scavenging and washout. Convection tends to be cumulus-scale although organized mesoscale convective systems can be much larger, resulting in *mesoscale* venting and washout/rainout (e.g., Lyons et al., 1986).

Internal forcing

Spatial variations in atmospheric fields may also arise due to *internal* flow dynamics and instabilities. Mesoscale circulations can be generated by synoptic-scale dynamical or thermal forcing: examples of such circulation systems include frontal and dryline circulations, density currents, squall lines, jet streaks, and mesoscale gravity waves (e.g., Bluestein, 1986; Keyser, 1986; Schaefer, 1986; Simpson, 1987; Uccellini and Koch, 1987) . In addition to geostrophic adjustment (and flow over topography), internal gravity waves with horizontal wavelengths ranging from several hundred meters to several hundred kilometers can be generated by Kelvin-Helmholtz instability, frontal surges, convective activity, and restratification processes (e.g., Gossard and Hooke, 1975, and Sec. 2.1.8 of this study). Quasi-horizontal *vortical* modes may be generated by three-dimensional turbulence decay and upscale energy transfer in a stratified fluid (e.g., Lilly, 1983a; Etling, 1990a; Sec. 2.1.9 of this study). Synoptic-scale baroclinicity can also modify vertical profiles of mean wind and turbulence within the PBL by imposing additional vertical shear (McBean et al., 1979; Pielke et al., 1987a; McNider et al., 1988). Mesoscale or synoptic-scale vertical motions resulting from internal flow dynamics may concentrate pollutants near the Earth's surface or lift them out of the PBL (e.g., Martin et al., 1987).

Clearly, mesoscale circulations and atmospheric fluctuations can be complicated and can directly influence mesoscale dispersion. The work described herein concentrates on mesoscale flow features and mesoscale dispersion associated with surface forcing and PBL

transport but mesoscale circulations and fluctuations can also contribute to dispersion in the free atmosphere.

1.6 Dispersion Scales

Besides the mesoscale flow scales just discussed, the transport and diffusion of a passive scalar introduce additional spatial and temporal scales.

1.6.1 Source characteristics

A pollutant source may be categorized according to its geometry as a point source, line source, area source, or volume source. Pollutant sources are often approximated as point sources; this approximation becomes increasingly valid as the distance at which pollutant concentration is measured becomes large with respect to the actual source dimensions. Whatever the source shape, the size of the source introduces new spatial scales. The location of the source may do the same. For example, the distance from a pollutant source to a major terrain inhomogeneity such as a large body of water or a mountain range may be important. In the case of an elevated source, the heights of the source above the ground and below the PBL capping inversion are frequently important spatial scales.

Pollutant releases range in duration from instantaneous *puff*-type releases at one extreme to continuous, long-term *plume*-type releases at the other. Accordingly, *release time* constitutes an important dispersion time scale since instantaneous releases and continuous releases must often be treated quite differently for purposes of analysis and simulation. In the intermediate case of a point release made over a finite time interval t_r into a flow of mean velocity U, the longitudinal cloud length will be Ut_r (ignoring longitudinal diffusivity K_x).

This release length scale can be important because the *relative* diffusion of a cloud is scale-dependent (see below). The size of the release time relative to the travel time to a downstream receptor will also affect the fraction of time that non-zero concentration levels measured at that receptor are quasi-steady. If the release time is large compared to the travel time, then unsteady concentration levels associated with the passage of the

leading and trailing edges of the pollutant cloud will constitute only a small fraction of the total concentration trace. If, however, the release is terminated well before the leading edge of the cloud reaches the downstream receptor site, then the concentration trace will likely 'ramp up' to a maximum value and then 'ramp down' with no period of quasi-steady concentration levels (e.g., Pasquill, 1961; Draxler, 1988).

Before discussing these two primary types of pollutant releases in detail, let us jump ahead for just a minute. There are two basic forms of turbulent diffusion: (i) diffusion from a fixed emitting source and (ii) diffusion of a cloud about its center (e.g., Batchelor, 1949, 1950). The former, which is often referred to as *absolute* diffusion, requires an Eulerian analysis framework[12] while the latter, which is often referred to as *relative* diffusion, requires a Lagrangian analysis framework[13]. While puff releases are generally associated with relative diffusion and plume releases are usually associated with absolute diffusion, what actually distinguishes these two[14] basic types of turbulent diffusion from each other is the analysis reference frame rather than the release type. This distinction should become clearer from the discussion of the next few pages.

Puff releases

For tracer puffs or clouds, the natural frame of reference is a coordinate system that *moves* with the puff center of mass, i.e., a Lagrangian reference frame, and the puff characteristic of greatest interest is the *size* of the puff. The simplest representation of the diffusion of such a puff is the rate of separation of a pair of particles or fluid elements released simultaneously from the same source (Batchelor, 1950, 1952). For this reason, the

---

[12] "... in the sense that one enquires into the probable concentration of the diffusing substance at various points relative to the fixed source" (Batchelor, 1950, p. 139).

[13] "... in the sense that we are concerned with the distribution of probable concentration relative to a center which moves with the fluid" (Batchelor, 1950, p. 139).

[14] As will be discussed in Sec. 2.3.3, Herterich and Hasselmann (1982) have introduced a third, intermediate form of turbulent diffusion which they term 'patch diffusion'.

growth and spreading of a puff about its center of mass is often referred to as *two-particle* or *relative* diffusion.

The manner in which a puff release disperses will be determined by the size of the puff relative to the spatial scale of the dominant motions of the flow field in which it is embedded. If the dominant elements of the flow field are large relative to the puff, then the puff will tend to be transported as a whole and will experience little growth and dilution due to mixing, although velocity gradients associated with these large flow scales may deform the puff (Fig. 1.4a). If the dominant flow field elements are comparable in size to the puff, then deformation, mixing, growth, and dilution of the puff will be rapid (Fig. 1.4b). If the dominant flow field elements are small relative to the puff, then the puff will experience only slow growth at its boundaries (Fig. 1.4c). Thus, a fundamental property of relative diffusion, first recognized by Richardson (1926), is that the rate of growth of a puff depends directly on the size of the puff. This means that the growth of a large cloud cannot be represented as the superposition of the growth of component elements.

In spectral terms, the spatial scale of a puff or cloud defines a high-pass filter; spatial spectral scales larger than the scale of the puff cannot contribute to puff growth (e.g., Smith and Hay, 1961; Mikkelsen et al., 1988). The problem of defining a sampling time and hence of specifying the operational definition of turbulence[15] which complicates plume growth (see below) is avoided for puff growth since the sampling time is of necessity the puff travel time. On the other hand, the characteristics of the 'high-pass filter' change in time as the puff grows (Smith and Hay, 1961).

Even flow structures on the scale of extratropical cyclones can act to 'stir' and deform a tracer puff, drawing the puff out into a long, narrow 'streak' and increasing concentration gradients (e.g., Garrett, 1983). Fig. 1.5 shows an example of large-scale horizontal

---

[15] "... one man's turbulence is another man's mean motion" (Sheih, 1980, p. 557).

deformation due to the 500 hPa flow field. As in Fig. 1.4b, puff scale and dominant eddy scale are comparable so that deformation is both rapid and pronounced.

Plume releases

A plume release is an extended continuous release of a pollutant from a fixed or stationary source. The resulting downstream plume, which is sometimes described as a concentration 'wake', remains connected to the source. Thus, the natural reference frame for a plume release is a coordinate system that is *fixed* with respect to the source (e.g., Batchelor, 1949, 1950). In such an Eulerian reference frame, it is easy to vary the period of time over which the resulting pollutant plume is sampled. A photograph of a plume taken with a shutter speed of a fraction of a second will tend to show a long, narrow, sinuous plume, in effect a plume realization or instantaneous plume (e.g., Nappo, 1981). However, if a time exposure of several minutes is made, the resulting plume will tend to appear broader, smoother, and more symmetric about its mean axis[16].

This behaviour is illustrated schematically in Fig. 1.6a; as cross-plume concentration measurements are made for longer and longer sampling times, the resulting concentration distribution becomes broader and smoother and peak values become smaller (Fig. 1.6b). *Observing time* or *sampling time* is thus an important quantity when studying continuous releases. This dependence of plume concentration on sampling time is the result of averaging over flow fluctuations or eddies with time scales shorter than the sampling period. Since eddy time scales are normally directly proportional to spatial scale, increasing the sampling time incorporates a greater and greater proportion of all eddy contributions and hence a greater range of plume displacements. The role of sampling time is discussed in more detail in Sec. 2.3.3.

Atmospheric motions larger than the plume dimensions tend to transport the plume intact, a process known as *meander*, while smaller motions tend to act at the plume boundary, resulting in further mixing, growth, and dilution. For a plume, *all* scales of

---

[16] Gifford (1968) and Nappo (1983) show plume photographs taken over different exposure times

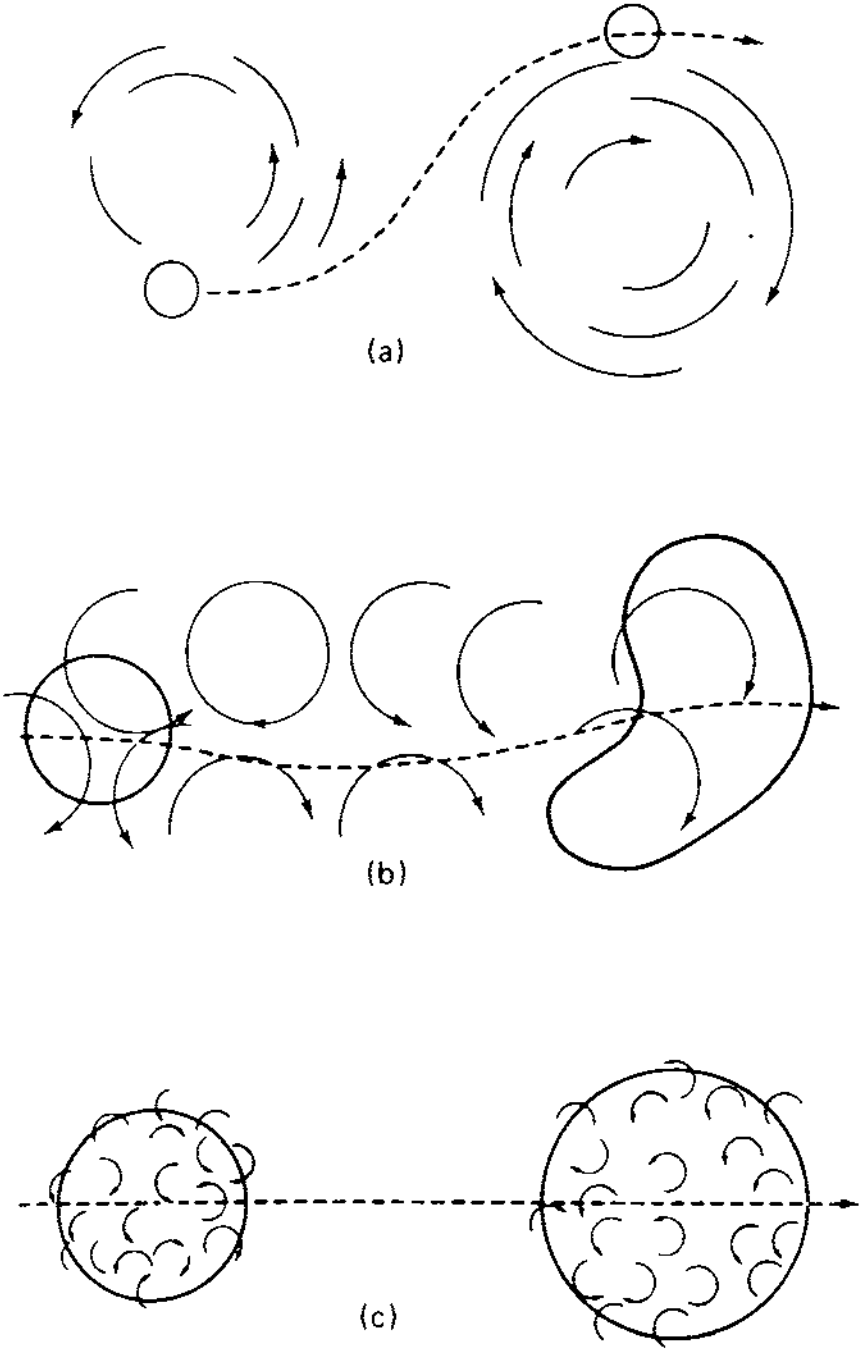

Figure 1.4: Idealized dispersion patterns of a pollutant 'cloud' for three dominant scales of motion: (a) uniform field of eddies large in size compared with size of pollutant cloud; (b) uniform field of eddies comparable in size to pollutant cloud; (c) uniform field of eddies small in size compared to size of pollutant cloud (from Slade, 1968).

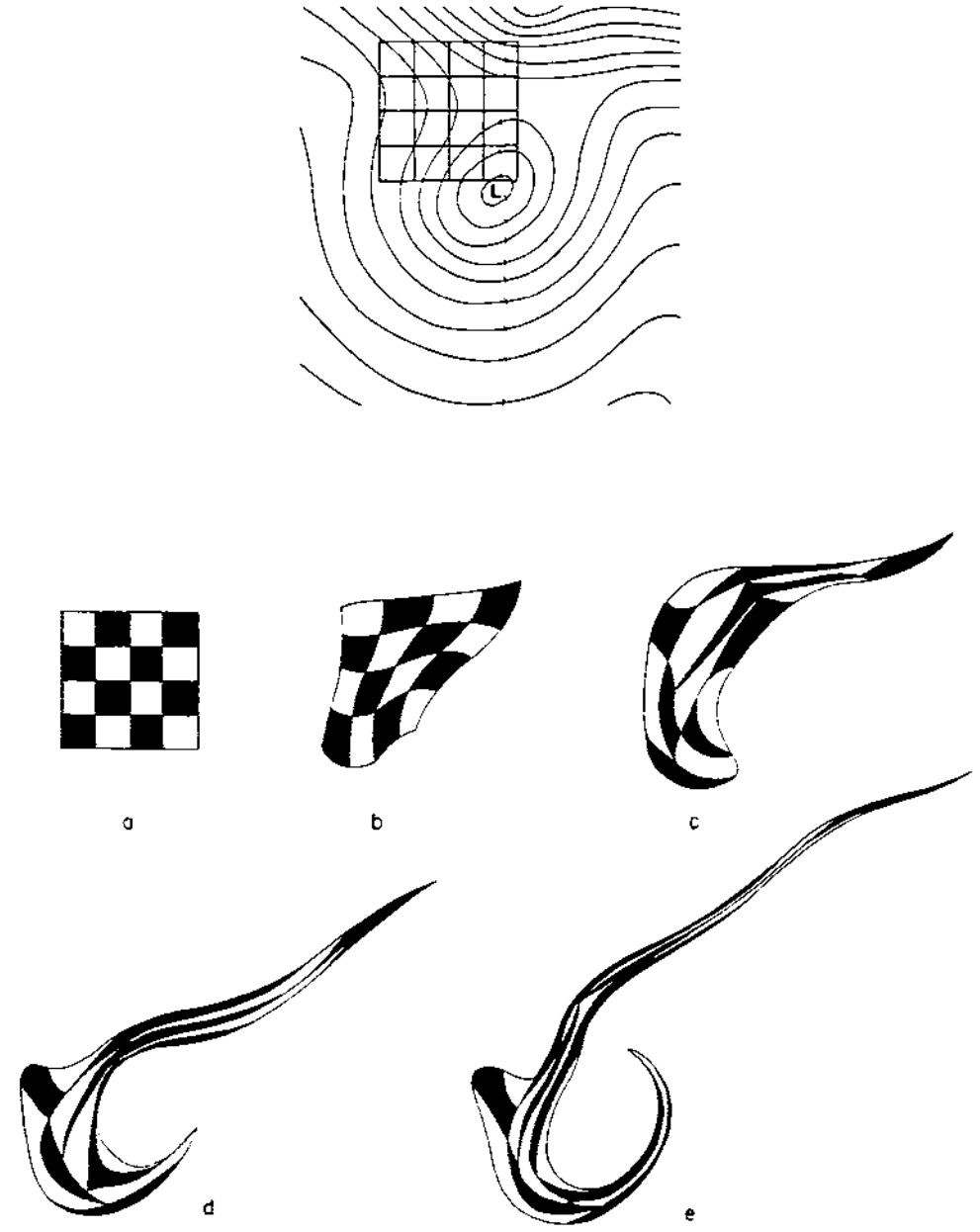

Figure 1.5: Horizontal deformation of a large-scale parcel by two-dimensional incompressible flow at 500 mb as predicted by a barotropic numerical model: (a) 0 h; (b) 6 h; (c) 12 h; (d) 24 h; and (e) 36 h. The initial streamline pattern is shown at the top. The sides of the coloured grid squares are 300 km (from Welander, 1955).

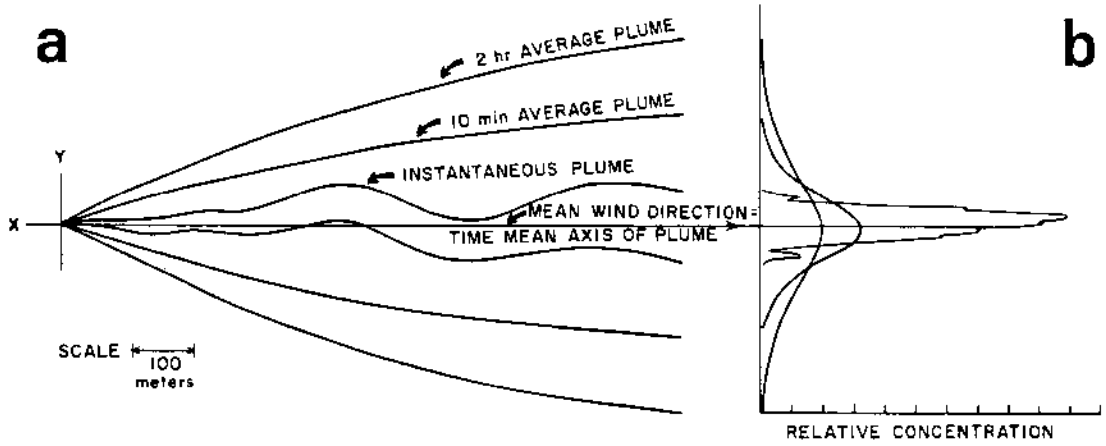

Figure 1.6: Effects of averaging time on plume shape and intensity: (a) outlines of a pollutant plume viewed from above at an instant in time, over a 10-minute period, and over a 2-hour period; (b) corresponding cross-plume relative concentration (from Slade, 1968).

motion contribute initially to mixing, but as the plume grows, the smaller scales contribute less and less to dilution of the plume, instead acting merely to oscillate fluid elements back and forth (see Sec. 2.3.1). On a scale of days, synoptic-scale flow fluctuations can change the direction of plume transport, a process referred to by Smith (1979a) as 'synoptic swinging' (see Sec. 2.2.1).

Under stable conditions, plume meander can dominate the reduction of mean concentrations due to increased sampling time[17] (e.g., Kristensen et al., 1981; Hanna, 1986a; Etling, 1990b). Meander is also responsible for most concentration fluctuations in the early stages of *elevated* plume transport (e.g., Hanna, 1984, 1986b; Moore et al., 1988; Fackrell and Robins, 1990; Peterson et al., 1990). Fig. 1.7 shows one example of a horizontal wind component trace with mesoscale oscillations capable of causing significant plume meander.

---

[17] A simple analogy is to consider the effect on the resulting spray pattern of waving a garden hose back and forth versus holding it steady.

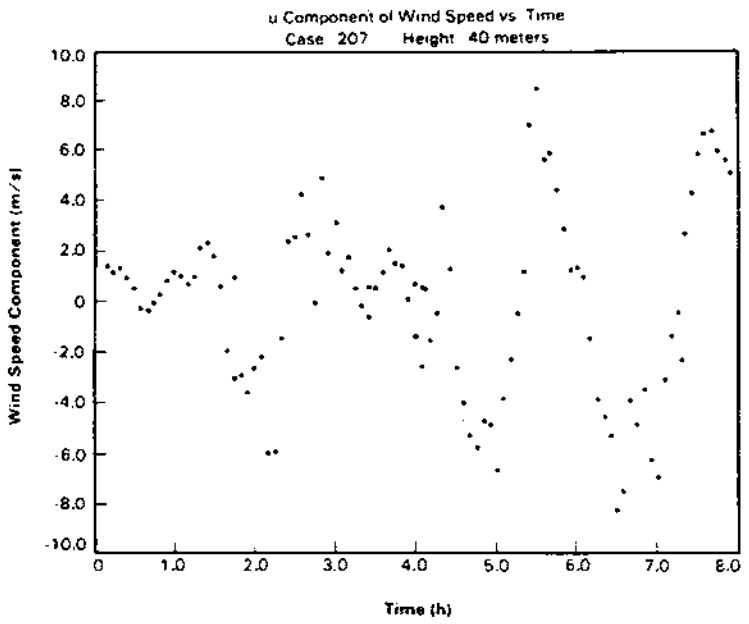

Figure 1.7: Detrended 40-meter u-component time series (5-minute averages) measured at Cinder Cone Butte, Idaho from 0000 to 0800 LST on October 25, 1980 (from Hanna, 1983).

For stationary flows, the limiting mean value of time averaging will be the Eulerian ensemble-mean plume, that is, the mean plume resulting from the average of an infinite number of instantaneous and independent plume realizations for identical source characteristics and flow conditions. Recognizing this, Nappo (1981) employed another photographic technique to estimate the Eulerian ensemble-mean plume. He overlaid four plume snapshots taken at approximately 15-minute intervals from an overflying aircraft to produce a fixed-reference-frame composite plume consisting of nearly independent, instantaneous plume samples or realizations. Both plume growth and widening and plume meander were accounted for by this technique (see also Groll and aufm Kampe, 1983).

A plume can also be approximated as the *sequential* release of many small puffs (e.g., Frenkiel, 1952, 1953). Plume diffusion can thus be studied by considering the behaviour of a train of puffs as they pass a given fixed point. Unlike the three-dimensional growth of a puff, however, plume dispersion is basically a two-dimensional process in the crosswind

and vertical directions[18]. The greater the number of puffs considered (assuming a fixed puff release rate), the greater the effective sampling time. Successive plume sections may follow different trajectories as a result of larger-scale flow fluctuations so that, as mentioned before, mean concentrations downwind from a source will depend inversely on sampling time. In an Eulerian reference frame, the emphasis will be on the positions of the centers of mass of this sequence of *independent* fluid elements relative to a fixed point or axis rather than on the separation of such a set of elements relative to their common center of mass and to each other. Plume diffusion viewed from an Eulerian perspective is thus frequently referred to as *one-particle* or *absolute* diffusion since it can be studied by considering an ensemble of independent marked-fluid-parcel trajectories (e.g., Batchelor, 1949; Sec. 2.3.1 of this study).

1.6.2 Relative diffusion vs. absolute diffusion

The distinction between absolute and relative diffusion (or one-particle and two-particle diffusion) is a fairly subtle one. In fact, the study of atmospheric dispersion was well established before Batchelor (1949, 1952) and Brier (1950) discussed this difference and its relation to the choice of observing reference frame. Batchelor and Brier showed that absolute diffusion is properly studied in an Eulerian reference frame while relative diffusion must be studied in an Lagrangian reference frame. Csanady (1973, p. 51) summed up the difference in this way:

> The 'ensemble mean' concentration is a fairly subtle concept the theoretical advantages of which fail to impress experimentalists unless there is a tolerable resemblance between theory and experiment. One way to ensure such resemblance is to tailor the precise definition of this mean (and of the particle displacement probabilities to which it is proportional) to the particular experimental situation. Thus one may consider the average of many concentration readings taken at a *fixed point* $\mathbf{x}$ in space, or else that obtained at fixed distances $\mathbf{y} = \mathbf{x} - \mathbf{c}$ from the *center of gravity* $\mathbf{c}$ of

[18] And this is a significant difference when considering the dilution of a pollutant release. A puff can be diluted by growth in both the crosswind and alongwind directions whereas alongwind expansion is not a factor for the dilution of a plume. In a shear flow, the effective diffusivity in the shear direction can be greatly enhanced (e.g., Csanady, 1973, p. 136), and vertical shear is usually most pronounced in the alongwind direction (see next section).

a diffusing cloud. The two approaches lead respectively to the theory of 'absolute' and 'relative' diffusion, and provide more or less satisfactory models for different experimental findings.

To appreciate this difference, let us return to puffs and plumes. A puff release was used at the beginning of this section to illustrate the phenomenon of relative diffusion while a plume release was used to illustrate the phenomenon of absolute diffusion. However, it is also possible to calculate the absolute diffusion of a puff or the relative diffusion of a plume; neither type of release is uniquely associated with one type of diffusion or the other (e.g., Csanady, 1973, Sec. 4.1).

Absolute diffusion of a puff

To consider the absolute diffusion of a puff, the observer's frame of reference is chosen to be fixed relative to the release point, contrary to the usual practice of following the puff. A composite or ensemble-average puff for a particular travel time can then be constructed by superposing a set of independent puff realizations corresponding to that travel time. Rather than superposing puff centers, superposition is carried out by lining up, or registering, the source and other background reference points. The concentration field of the resulting Eulerian ensemble-average puff then corresponds to the probability density function describing the likelihood that a particle released from the instantaneous source will be found at each point in space after traveling for the specified travel time (Batchelor, 1949; Batchelor and Townsend, 1956; Csanady, 1973). This Eulerian puff concentration field for absolute diffusion will be much larger in spatial scale and will have a lower peak value than the Lagrangian center-of-mass-based puff concentration field for relative diffusion since the scatter of the *positions* of the puff centers of mass is considered as well as the growth of each individual puff about its center of mass (e.g., Garrett, 1983). In the Lagrangian average, only the growth of each puff relative to its center of mass, that is, the *shape* and *size* of the cloud, is considered (Batchelor, 1952). Basically, relative diffusion results only from mixing while absolute diffusion results from *both* transport and mixing (Durbin, 1980).

It should be noted that *neither* of these ensemble-average puffs is likely to match a single puff realization very well (e.g., Garrett, 1983). An ensemble-average puff concentration field will be much smoother, larger, and more symmetric than that of any puff realization. A Lagrangian ensemble-average puff may also have what Chatwin and Sullivan (1979a, 1980) have termed a "core-bulk" structure with a high-concentration core enveloped by a low-concentration outer layer (see Fig. 1.8). No puff realization is likely to have a comparable structure. Chatwin and Sullivan (1979a,b) suggested that two advantages of the Lagrangian ensemble average over the Eulerian ensemble average are that (i) the Lagrangian average involves less 'smearing', that is, the Lagrangian ensemble puff will be closer in size to a 'real' puff, and (ii) the effects of flow unsteadiness on ensemble averaging are minimized. Gifford et al. (1988) have also noted that for complicated flow fields, a single measure such as σ_y may not be sufficient to describe the shape of a strongly distorted, non-Gaussian puff or cloud.

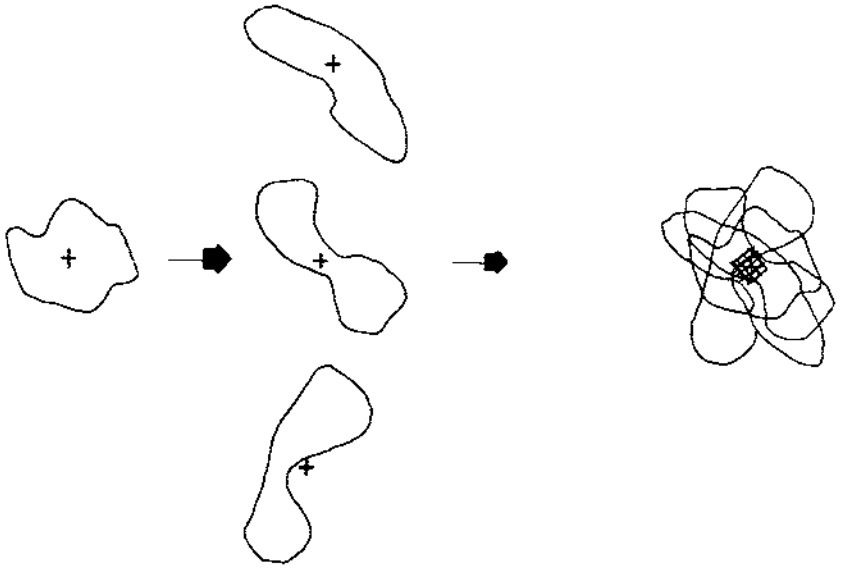

Figure 1.8: Sketch of core-bulk structure resulting from the superposition of the centers of mass (indicated by 'plus' signs) of four puff realizations. The small cross-hatched area marks the core region (from Chatwin and Sullivan, 1979a).

The concept of the absolute diffusion of a puff has considerable relevance for this study. Two mesoscale tracer experiments have been modelled for which observations of the movement of a tracer cloud across a surface-based (i.e., Eulerian) observing network are available. The numerical dispersion model that has been employed in this study is a one-particle model suitable for calculating Eulerian ensemble-average concentration fields. However, as will be discussed later, complications arise in the form of finite release time, flow nonstationarity, flow inhomogeneity, and inherent uncertainty due to comparing observed realizations against model-predicted ensemble means.

Relative diffusion of a plume

To consider the relative diffusion of a plume, it is necessary (i) to examine *instantaneous* plumes *and* (ii) to perform ensemble averaging *relative* to the centerlines of the instantaneous plumes, that is, relative to a moving reference frame. Nappo (1981) measured plume relative diffusion by superposing four plume snapshots relative to their centerlines, a Lagrangian superposition carried out in addition to the Eulerian superposition already discussed on p. 39 and then measuring plume widths. Other plume measurements made with short sampling times (e.g., aircraft, boat, or van traverses over, under, or through a plume) will also measure near-instantaneous plume widths and hence will describe relative rather than absolute diffusion (e.g., Murthy and Csanady, 1971; Gifford, 1977; Chatwin and Sullivan, 1979c; Carras and Williams, 1981, 1988; McElroy et al., 1981; Groll and aufm Kampe, 1983; Groll et al., 1985). If a plume cross-section can be assumed to be composed entirely of marked fluid released at the same time, then cross-plume widths at different distances will correspond to puff widths at different travel times. However, this assumption will not hold in shear flows, where marked fluid at different locations in the cross-section will likely have been released at different times (e.g., Uthe et al., 1980; Carras and Williams, 1981).

Knowledge of plume relative diffusion is important when studying concentration fluctuations. One example is odour studies, where near-instantaneous concentrations are important (e.g., Högström, 1972; Csanady, 1973; Fackrell and Robins, 1982). Plume

meander, on the other hand, will affect odour intermittency or frequency, i.e., whether the plume is present at a particular location or not. Interestingly, one effect of relative diffusion is to reduce concentration fluctuation variance $\overline{c'^2}$ by increasing plume width and hence reducing the number of zero concentrations due to meander and the peak-to-mean concentration ratios (Durbin, 1980).

The role of sampling time in plume measurements should now be clearer. Sampling over a long period at a fixed point in a stationary flow is one way to estimate a local ensemble average. In the same way, observing a plume with long-exposure photographs or other extended-sampling-period technique will permit estimates of absolute plume diffusion and the Eulerian ensemble-average plume over an area or volume. Plume σ_y's based on time-averaged measurements will thus be larger than instantaneous σ_y's because meander effects will also contribute (e.g., Moore et al., 1988). Sampling time does not play a comparable role in puff observations since time averages in a moving reference frame will have no comparable connection to ensemble averages (e.g., Csanady, 1973, Sec. 4.1). However, another way to estimate an ensemble average is by averaging over a number of independent measurements or realizations. In this case, near-instantaneous plume measurements can be used to estimate *either* Eulerian or Lagrangian ensemble averages depending on the choice of reference frame used for averaging (e.g., Nappo, 1981).

1.6.3 Travel time

A third dispersion time scale is *travel time*, the length of time that the tracer is carried by the flow. For mesoscale atmospheric dispersion, this quantity will vary between several hours and several days. In general, the longer the travel time, the greater the impact that flow inhomogeneities, both spatial and temporal, will have on dispersion because of the greater likelihood that fluid elements will encounter such fluctuations (e.g., Fig. 1.2). Theory also suggests that relative and absolute diffusion become less and less distinguishable and peak-to-mean ratios approach unity at longer travel times (see Sec. 2.3.1). This is an important consideration for mesoscale travel times since (a) most dispersion models do not handle relative diffusion very well and (b) many mesoscale

diffusion measurements are near-instantaneous and thus correspond to relative diffusion rather than absolute diffusion.

The roles of each of these three dispersion time scales — release time, sampling time, and travel time — are discussed in greater detail in Chap. 2 (along with averaging time and filtering time). Mesoscale dispersive behaviour will depend on both the absolute values of these three time scales and their sizes relative to each other.

1.6.4 Concentration variables

Three different measures of concentration may be used in practice: (i) instantaneous concentration c; (ii) average concentration $\bar{c}$; and (iii) exposure[19] E. Following Islitzer and Slade (1968) and Draxler (1984), we can define these quantities as follows:

$$c = \frac{\text{mass of pollutant}}{\text{volume of air}} \quad , \tag{1.21}$$

$$\bar{c} = \frac{1}{\tau}\int_{t_0}^{t_0+\tau} c\,\mathrm{d}t \quad , \tag{1.22}$$

$$E = \int_{t_0}^{t_0+\tau} c\,\mathrm{d}t \qquad = \tau\bar{c} \quad , \tag{1.23}$$

where τ is the sampling time.

Practical considerations in atmospheric diffusion field programs formerly dictated that exposure be measured rather than average concentration since the times when samplers were started and stopped were known but not the tracer transit time past a sampler. When average concentrations were reported, they were usually based on the tracer *release* time even though the tracer transit time is generally greater due to the along-wind spreading effects of along-wind turbulent diffusion and vertical wind shear (Islitzer and Slade, 1968). Development of sequential sampler technology has removed this restriction in some cases.

---

[19] There is some confusion over terminology, unfortunately. Csanady (1973, p. 49) and Pasquill and Smith (1983, p. 185) refer to exposure as defined below as 'dosage' whereas Islitzer and Slade (1968) and Draxler (1984) define dosage as the *product* of exposure and wind speed.

Exposure or time-integrated concentration is also the variable of primary interest in many radiological studies. In addition, there is a degree of duality between concentrations in steady-state plumes and exposure in instantaneous puffs. Exposure is a natural measure of the impact on a receptor subjected to the passage of a cloud of contaminant. But as noted by Pasquill (1961) and Gifford (1968, p. 115), the analytical expression in a Gaussian model for ground-level exposure due to the passage of a puff overhead has the same mathematical form as the expression for the *concentration* of a continuous plume with the same source location as the puff.

1.7 Shear Effects

The presence of velocity gradients further complicates flow dynamics and dispersion, whatever the scale. For example, many flow instabilities occur at least partly as a result of the presence of flow shear, and velocity gradients introduce differential advection into the dispersion problem. Flow shears may enhance turbulent diffusion by increasing turbulence intensities. In addition, velocity gradients provide another mechanism for dispersion through the *interaction* of differential advection and turbulent diffusion. In the PBL, for example, vertical shear of the horizontal flow may result in pollutant at different levels being advected at different speeds (speed shear) or in different directions (direction shear). Vertical diffusion will then mix the pollutant through a larger volume than if no shear were present. Such mixing can occur *at the same time* as the differential advection or *at a later time*. Differential advection with *simultaneous* mixing has been recognized for many years as a contributing factor to dispersion in shear flows (e.g., Eckart, 1948; Taylor, 1953, 1954a,b; Aris, 1956; Pasquill, 1961; Saffman, 1962; Högström, 1964; Smith, 1965; Tyldesley and Wallington, 1965; Csanady, 1969, 1972; Maul, 1978; Taylor, 1982; Millán, 1987; Lamb et al., 1990), but it appears that Pasquill was the first to mention the combination of differential advection with *subsequent* or *delayed* vertical mixing as a mechanism in mesoscale atmospheric dispersion (Pasquill, 1969, p. 72):

> There is, however, a fairly obvious inference to be drawn regarding the effect of shear when the vertical mixing is temporarily inhibited (as, for example, with the onset

> of stable conditions on a clear night). In this case the distortion of the cloud can proceed without opposition, yielding horizontal displacements which are *potentially* effective at other levels, and merely require the revival of vertical mixing to become actually effective. Thus one would expect horizontal spread, unlike vertical spread, to be effectively maintained in spite of a diurnal reduction of turbulence.

Pasquill alluded to the differences in the contribution of vertical shear to dispersion between nighttime and daytime in his paper. In the daytime for unstable conditions, vertical turbulent mixing acts to reduce vertical wind shear and hence also reduces shear-enhanced dispersion. However, vertical shear will be still present due to surface friction, baroclinicity, and other sources (e.g., Kahl and Samson, 1988c), and its interaction with vertical diffusion results in simultaneous mixing. At night under stable conditions, much larger vertical shears are possible but vertical turbulence levels are lower, resulting in potential or delayed shear dispersion. That is, differential advection of the pollutant is followed later by vertical mixing and dilution either through turbulent bursts due to Richardson-number breakdown or during the growth of the daytime convective boundary layer after sunrise. Note that this mechanism will also apply to PBL transitions from stable to unstable conditions due to advection as in the case of advection from cold land to warm water in winter or from cold water to warm land in summer[20].

1.7.1 Analytical models of shear-enhanced dispersion

G.I. Taylor was apparently the first to study the effect of the interaction between flow shear and diffusion on total dispersion[21]. Taylor (1953) considered both theoretically and experimentally the longitudinal or along-stream diffusion of a parcel of dye carried by a slow-moving, laminar flow through a long uniform pipe. He first obtained an analytical solution which suggested that in a reference frame moving with the mean flow velocity, the

---

[20] Barr and Kreitzberg (1975) have discussed the equivalence of local changes due to periodic surface forcing in horizontally homogeneous flows and advective changes in stationary flows over periodically-varying terrain in considerable detail.

[21] Corrsin (1953) gave a mathematical analysis for dispersion in an unbounded shear flow at about the same time but his work was not much noticed by the meteorological and oceanographic communities (Smith, 1965).

coupling of the cross-stream molecular diffusion and the cross-stream velocity shear would result in an enhanced 'virtual' along-stream diffusivity D_v if the diffusion time scale was shorter than the shear time scale. His analytical solution had several other surprising features. First, the expression for the along-stream 'virtual' diffusivity D_v varied *inversely* with the *cross-stream* molecular diffusivity D_r. Second, the asymptotic concentration distribution was predicted to be symmetrical in the along-stream direction in spite of the asymmetry of the parabolic velocity profile. And third, fluid in the center of the pipe, whose flow speed was twice the mean flow speed, would pass *unaltered* through the dye cloud. That is, a dye-free centerline parcel initially upstream of the dye cloud would enter the dye cloud, dye would diffuse into the parcel, reach a maximum concentration as the parcel passed through the cloud center, and then decrease to a negligible value as the parcel exited from the downstream end of the dye cloud. This last prediction in particular was so remarkable that Taylor set up a series of laboratory experiments to test his mathematical solution. These experiments confirmed the analytical solution, including the result that the effective along-stream diffusivity D_v could be considerably larger than the molecular along-stream diffusivity D_x.

Taylor (1954a) found qualitatively similar behaviour for *turbulent* flow through a pipe (see also Batchelor and Townsend, 1956, and Chatwin, 1971). He also showed that the shear-driven along-stream diffusivity K_{xs} would be additive with the eddy-driven along-stream diffusivity K_{xe}. One limitation of Taylor's work was his assumption of uniform cross-pipe dye concentration. He made this assumption in order to obtain a closed-form analytical solution but it restricted the applicability of his solution to times after the initial dye distribution had mixed uniformly across the pipe (Young et al., 1982). Taylor also assumed a constant along-stream concentration gradient, again to simplify the mathematics (Csanady, 1969). Aris (1956) applied a different analytical technique, the method of moments, to Taylor's pipe dispersion problem. This technique provides information about the time evolution of integral moments of the tracer distribution (e.g., center of mass, moment of inertia). It is considerably more complicated mathematically

and does not give a complete closed-form solution but at the same time is not subject to the same restrictions as Taylor's solution. Aris's solution both supported and extended Taylor's analytical results. As discussed below, Aris's method of moments has been used in many subsequent studies. Batchelor and Townsend (1956) described still another approach in which a Taylor-series solution was obtained for small diffusion times in a lateral shear flow (see also Tennekes and Lumley, 1972, and Hinze, 1975). Elder (1959) extended Taylor's work, both theoretical and experimental, to the case of steady, turbulent open-channel flow. Consideration of a wide channel removes the lateral constraint on fluid particles. This extra degree of freedom allowed Elder to examine some of Taylor's approximations directly. Elder's experiments in a water flume agreed quite well with his analytical solution for shear dispersion in an open channel, adding support for Taylor's approach. Longitudinal dispersion in the flume was about five times greater than lateral dispersion for a shallow flow about 1 cm deep.

Atmospheric models

Saffman (1962) applied Aris's concentration moment method to the atmospheric dispersion problem of the horizontal dispersion of an instantaneous ground-level source in a linear, vertically-sheared flow with constant eddy diffusivity. He considered two geometries, a neutral PBL bounded by a capping inversion and a semi-infinite or semi-unbounded atmosphere (unbounded above but bounded below by the Earth's surface). For the case of a layer of finite thickness, Saffman's asymptotic solution for large times agreed with Taylor's principal results for turbulent shear dispersion in a pipe: (a) the interaction of vertical shear with vertical diffusion resulted in an enhanced longitudinal diffusivity coefficient; and (b) cloud length σ_x depended linearly on time t at large times and was *inversely* proportional to the vertical eddy diffusivity K_z.

This inverse proportionality of spread to turbulent diffusivity is different from the usual direct proportionality encountered in atmospheric dispersion, but in this case the two quantities lie along perpendicular directions, i.e., *longitudinal* spread and *vertical* diffusivity. To get a better grasp on this inverse dependence, consider two extreme cases.

If K_z is very large, then as soon as a vertical concentration gradient is created by differential horizontal advection, it will immediately be mixed out by vertical diffusion. In this extreme case, any enhancement of along-stream horizontal diffusion due to shear would be insignificant since it would be dwarfed by the horizontal turbulent diffusivity K_x. At the other extreme, if K_z is very small, then it would appear that the enhanced horizontal diffusivity should become very large. However, Taylor's solution is an asymptotic one and is only valid for $t \gg z_i^2/K_z$; it would not apply as $K_z \longrightarrow 0$. In this case, little actual mixing and dilution would occur, only stirring and deformation.

For the second case of a semi-infinite atmosphere, however, Saffman's analytical solution displayed quite different properties: longitudinal spread σ_x at any level[22] depended *directly* on the magnitude of the vertical diffusivity K_z and was proportional to a t^3 term as well as to a linear t term. This implied (a) that horizontal spread could not be described by an effective horizontal eddy diffusivity which is independent of time as in the molecular case (see Sec. 2.3.1) and (b) that after some initial period the shear interaction contribution to horizontal spread would overwhelm the horizontal diffusion contribution.

Subsequent studies by Högström (1964) and Smith (1965) for the fully unbounded atmosphere supported Saffman's results. In contrast to previous studies, Högström (1964) considered the effect of cross-wind shear on puff dispersion due to a change in wind *direction* rather than wind speed. Smith (1965) extended Saffman's and Högström's results by obtaining a solution for all travel times rather than just for large travel times and by including the off-diagonal diffusivities K_{xz} and K_{yz} neglected in the earlier studies. To do this, Smith used a statistical approach based on Taylor's (1921) classical one-particle model for $\overline{y^2}$. Pasquill (1969) applied Smith's treatment to data from two field experiments in which measurements were made out to 5 km and 25.6 km, respectively.

---

[22] Taylor (1953, 1954a,b) only considered the spread of the entire tracer cloud because of his assumption of uniform cross-stream concentrations. Saffman considered both horizontal spread at individual levels and vertically-integrated horizontal spread.

He found evidence in both data sets of (a) plume distortion by shear 2 to 3 km downwind of the source and (b) shear-enhanced dispersion at the measurement point 5 km downwind in the first data set (elevated release) and at 12 km and beyond in the second data set (ground-level release). Recently, Moore et al. (1988) presented a lidar scan of an elevated power plant plume distorted by directional wind shear.

Csanady (1969) and Taylor (1982) applied Aris's concentration moment method to shear dispersion in a classic (i.e., idealized) Ekman layer. This was a significant advance since the earlier analytical models had considered wind fields of varying speed but uniform *direction* or varying direction but uniform *speed*. Adoption of an Ekman spiral permitted consideration of a wind field in which wind direction as well as wind speed varied with height. [Csanady (1966) had previously considered dispersion in the oceanic Ekman layer qualitatively.] Csanady's (1969) analytical solution was quite complicated and included terms involving error functions and associated functions of the Fresnel integral. Csanady suggested that Saffman's (1962) t^3 solution could be explained by the constant growth in maximum velocity differences encountered by the growing cloud. He then showed that his own solution for σ_y also exhibited t^3 dependence for small diffusion times but approached t dependence at large diffusion times because of the decreasing velocity gradient with height. He concluded that Saffman's semi-unbounded model with a linear velocity gradient was only appropriate early in the shear dispersion regime[23].

Csanady also concluded that (a) at large travel times the lateral cloud spread is about two orders of magnitude larger than it would be if only horizontal diffusion were acting, (b) his analytical solution agreed well in its general features with corresponding results obtained in a numerical model of dispersion in an Ekman layer by Tyldesley and Wallington (1965), including their finding that the shear-term dominance of horizontal dispersion begins about 5 to 10 km downwind of the source, and (c) the asymptotic 'effective' horizontal diffusivity is *not* dependent on K_z because the Ekman-layer scale

---

[23] The velocity gradient at low levels in a classical Ekman spiral is linear to a first approximation (Csanady, 1969, p. 421).

depth is also dependent on K_z in a compensatory fashion. Fig. 2.27 shows a comparison of a sample lateral diffusion curve for long travel times based on Csanady's analytical model with four observed curves of tropospheric mesoscale lateral diffusion. The model appears to predict very reasonable values.

Csanady (1969) confined exploration of the behaviour of his analytical solution to the ground-level motion of the cloud and to the spread of the cloud in the direction perpendicular to the geostrophic wind at very short and very long times. Taylor (1982) extended Csanady's results and described first and second moments for the cloud at all heights, directions, and times. Fig. 1.9 shows Taylor's solution for the time evolution of the growing cloud through approximately three periods ($t = 9.5 \approx 3\pi$). At each time shown the cloud is represented by a stack of ellipses at evenly-spaced height intervals corresponding to the 'one-sigma' concentration contours of a bivariate Gaussian distribution. Taylor used an 'equivalent' Gaussian distribution because only the first and second moments of the cloud concentration field at each height were available from the analytical solution. The sizes of the ellipses depend both upon the amount of material and the horizontal variances σ_x and σ_y at each level.

Several effects of shear are evident in this figure. Initially, centroids at different levels follow the wind approximately at that level but eventually the centroids at all levels tend to move along parallel parabolic paths, 'freezing' the centroid axis into a fixed form. The cloud becomes elongated in a direction at a 45° angle to the geostrophic wind direction in line with the mean Ekman-layer wind shear. Horizontal spread is also much enhanced along this axis at each level due to shear but pure horizontal diffusion is still important along the 'narrow' axis.

Oceanographic models

Oceanographers have also devoted considerable attention to the role of flow shear in turbulent dispersion. This is understandable in view of the stable stratifications, strong shears, and weak turbulence intensities commonly found below the thermocline. While meteorologists have emphasized the steady-shear case, oceanographers have concentrated

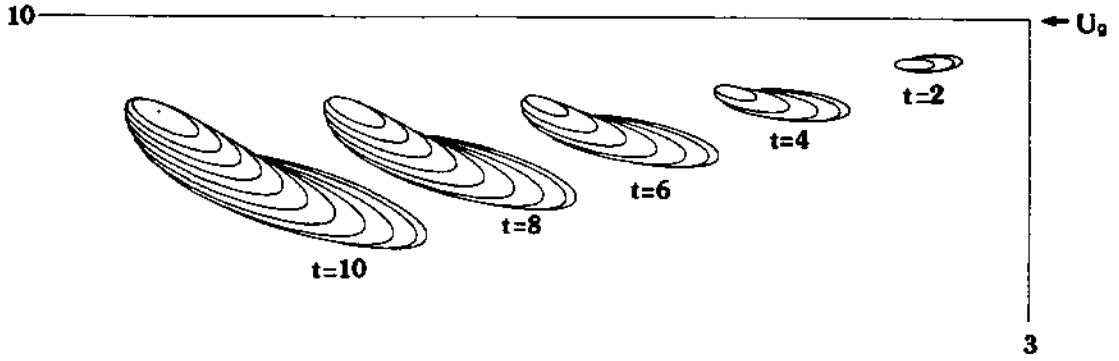

Figure 1.9: Plan view of the time evolution of the equivalent Gaussian representation of an ensemble-average puff from an instantaneous ground-level release into a classical Ekman boundary layer. Contours show elliptical one-sigma concentration isopleths corresponding to an exp(-0.5) reduction from the bivariate Gaussian peak value at each height. Time increments $\Delta t = 2$ are nondimensionalized by an $f/2$ time factor, height intervals $\Delta z = 0.5$ are nondimensionalized by an $(f/2K_z)^{1/2}$ depth factor, and horizontal coordinates are nondimensionalized by an $f/2U_g$ advective factor. See Taylor (1982) for details.

on oscillatory flows because of the importance of tides and other sheared oscillatory currents such as internal gravity waves and inertial oscillations in the ocean. Their solutions for oscillatory shear flows definitely have relevance for mesoscale atmospheric dispersion given the occurrence of periodic atmospheric shear flows such as the nocturnal low-level jet and mountain-valley circulations.

Novikov (1958) considered the case of an instantaneous point release into a time-dependent horizontal flow with linear vertical shear of the form

$$U_m(x_3, t) = u_m(t) + a_m(t)x_3, \quad m = 1, 2. \tag{1.24}$$

He used a Laplace-transform approach to obtain a general solution and then considered the stationary case in some detail. Novikov concluded that in the stationary case the shear effect would dominate over purely horizontal diffusion after an initial period. Bowden (1965) extended Taylor's method to shearing currents in estuaries and coastal regions by considering both steady and oscillatory currents in the longitudinal direction in a bounded sea. He noted that horizontal mixing due to the 'shear effect' is more determinable

than that due to turbulent diffusion since such current shears are more representable. Bowden's analytical solution for an oscillatory current was restricted to the case where vertical mixing has a much shorter time scale than that of the oscillatory current [i.e., Taylor's (1953) condition B].

Csanady (1966) applied Taylor's and Saffman's methods to dispersion in both the steady oceanic Ekman layer (simultaneous nonlinear speed and direction shear) and to an unsteady, inertially-oscillating current. He argued that such shear-enhanced dispersion could explain the accelerated diffusion that he observed in diffusion experiments with dye plumes in a large lake. Okubo (1967) generalized Bowden's work to include any combination of vertical diffusivity and current time scales in both unbounded and bounded flows. Okubo (1968) discussed a simple advection-diffusion model for an instantaneous point source in an unbounded current with *steady* linear shear in *both* the vertical and cross-current directions. He also applied the concentration moment technique to the same problem in a bounded sea. Okubo and Karweit (1969) extended this model to a *continuous* point source in an unbounded flow. Numerical solutions were required since the solution could not be integrated analytically in time.

Kullenberg (1972) , following Okubo (1967), used a generalized concentration-moment technique involving (a) Fourier transformation of the advection-diffusion equation, (b) solution of the transformed equation for the moment-generating function corresponding to the concentration field, and (c) calculation of concentration-field moments by differentiation of the moment-generating function. Kullenberg's flow field consisted of a mean ocean current varying only in the vertical with a superimposed, time-dependent rotary current intended to represent an inertial oscillation. The tracer source was an instantaneous line source of unit length oriented across the mean current. For his particular parameter space, Kullenberg found that the oscillating current was overwhelmed by the steady sheared current for dispersion in the longitudinal or along-current direction but dominated dispersion in the lateral or cross-current direction.

Young et al. (1982) gathered together and generalized much of the previous work on shear-enhanced dispersion in an *unbounded* medium. They considered three basic current structures: (i) oscillatory longitudinal flow with linear vertical shear ($\alpha z \cos \omega t$, 0); (ii) elliptically-polarized horizontal flow with linear vertical shear ($\alpha z \cos \omega t$, $\beta z \cos[\omega t + \phi]$); and (iii) oscillatory longitudinal flow with sinusoidal vertical shear ($u_0 \cos mz ; \cos \omega t$, 0). These simple current profiles are analytically tractable and yet are still applicable to the shear-enhanced mixing in the ocean interior due to internal waves and inertial oscillations. They also served as models for horizontal stirring by mesoscale eddies in the limit as $\omega \to 0$. Young et al. concluded that horizontal mesoscale stirring begins to dominate internal-wave-shear dispersion in the ocean interior at horizontal scales larger than 100 m.

1.7.2 Low-level jets and shear-enhanced dispersion

Numerical studies by Moran et al. (1987) and McNider et al. (1988) have suggested that delayed mixing can play an important role in lateral mesoscale dispersion in the PBL in conjunction with the development of the low-level jet. Moran et al. (1987) carried out idealized simulations of the mesoscale behaviour of the Mt. Isa plume in northern Australia using a 1D meteorological model coupled with a Lagrangian particle dispersion model[24]. Fig. 1.10 shows the increasingly complicated simulated mesoscale plumes obtained for four increasingly realistic simulations. Despite the use of horizontally homogeneous meteorological fields, a realistic Mt. Isa plume was simulated which displayed both linear horizontal growth over mesoscale travel times and multimodal cross-plume concentration patterns (McNider et al., 1988). As can be seen in Fig. 1.10a, the simulated plume was unrealistically narrow when only turbulent diffusion was considered in the absence of vertical shear and differential advection.

McNider et al. (1988) attributed the success of this simulation to the shear-enhanced dispersion resulting from the combination of time-dependent vertical shear and time-

---

[24] Described in Sections 2.3.4 and 4.4.

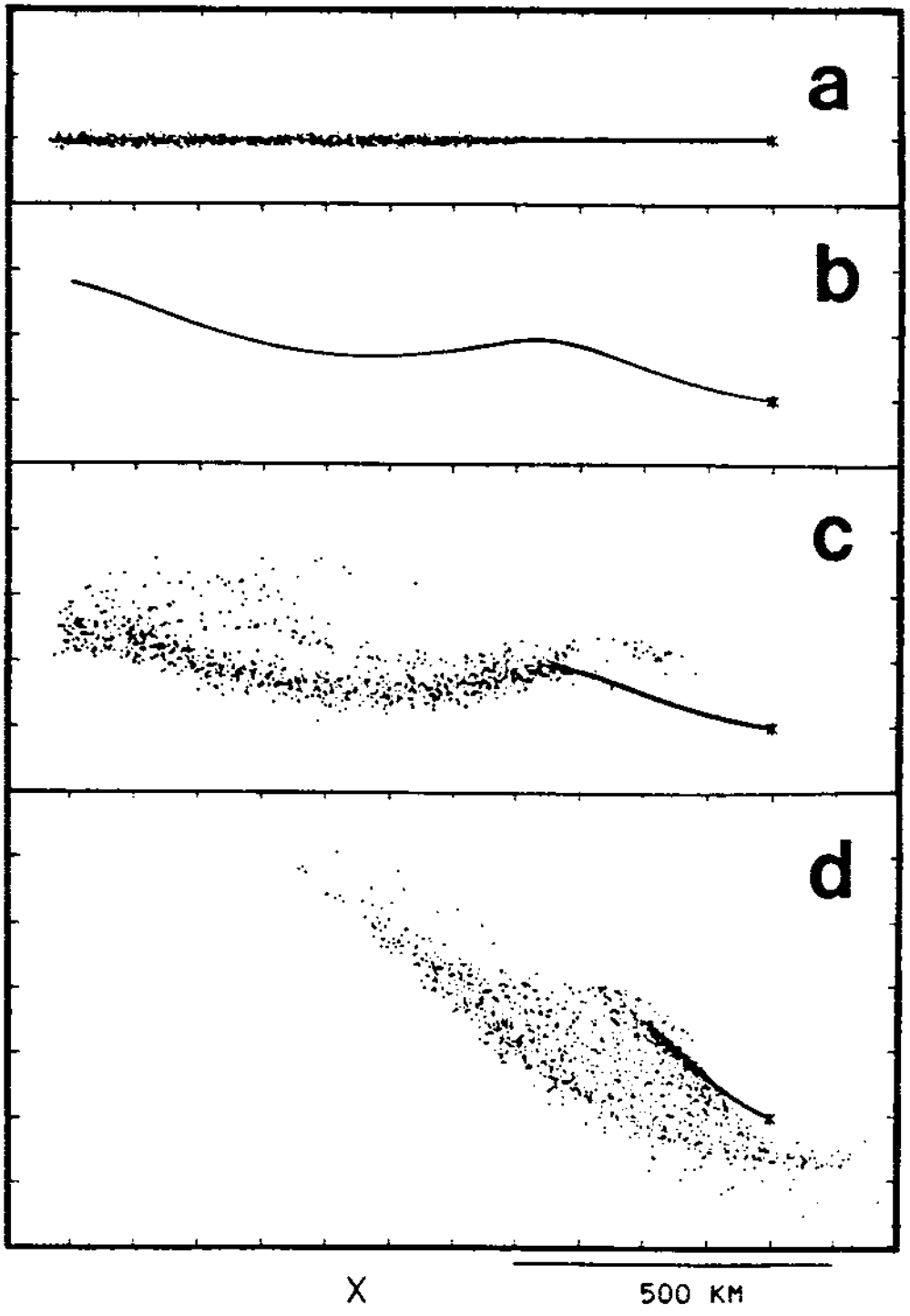

Figure 1.10: Instantaneous depiction of Mt. Isa plume simulation after 42 h for four increasingly realistic flow fields: (a) PBL turbulence but no PBL shear, Coriolis force, or horizontal temperature gradient; (b) Coriolis force and PBL shear but no PBL turbulence or horizontal temperature gradient; (c) PBL turbulence, PBL shear, and Coriolis force but no horizontal temperature gradient; (d) same as (c) except with a north-south horizontal temperature gradient (from McNider et al., 1988).

dependent vertical mixing, with the nocturnal low-level jet playing a crucial role. At night, the formation of a nocturnal surface inversion due to longwave radiational cooling decouples the nocturnal boundary layer from the remainder of the well-mixed daytime PBL above (termed the residual layer by Stull [1988]). The wind speed in the nocturnal boundary layer decreases and the wind direction backs due to the new force balance between the pressure gradient force, Coriolis force, and weakened friction force (e.g., Thorpe and Guymer, 1977). The residual layer begins to sweep through an inertial oscillation, clockwise in the Northern Hemisphere and counterclockwise in the Southern Hemisphere, resulting in the formation of a nocturnal low-level jet. Increased stratification reduces turbulent mixing but vertical variations in horizontal advection due to the wind-direction and wind-speed shear caused by the inertial oscillation distort the pollutant cloud. When morning arrives and the daytime PBL begins to grow anew, the shear-distorted cloud again mixes in the vertical, resulting in a wider, ground-level plume 'footprint'. This process is accentuated in the presence of additional vertical shear due to a synoptic-scale horizontal temperature gradient (e.g., Fig. 1.10a vs. 1.10b).

Carras and Williams (1981) found similar shear contributions to the lateral dispersion of the Mount Isa plume using a simpler empirical approach. They calculated a set of constant-height forward trajectories starting from Mount Isa for eight levels within the daytime PBL based on a time sequence of observed three- or six-hourly winds at four meteorological stations located across northern Australia. They then selected one trajectory for each level from a set of sequential releases so that the *arrival* time at the downwind distance of interest was the same even though the eight trajectories selected could have different *release* times. The predicted plume width then corresponded to the cross-wind width of the envelope of trajectories. All levels could be assumed to contribute to the predicted near-surface concentrations since most observations were made at midday when a well-mixed PBL would be expected. Predicted plume widths using this approach agreed with measured values to an accuracy of about $\pm 30\%$.

Uthe et al. (1980) presented four lidar scans of a shear-distorted elevated power plant plume about 40 km downwind of its source which are consistent with McNider et al.'s conceptual model. Fig. 1.11 shows their schematic representation of their observations; they also had to assume that the stack plume rise varies somewhat because of changing meteorological conditions in order to have the pollutant distributed through a finite vertical depth.

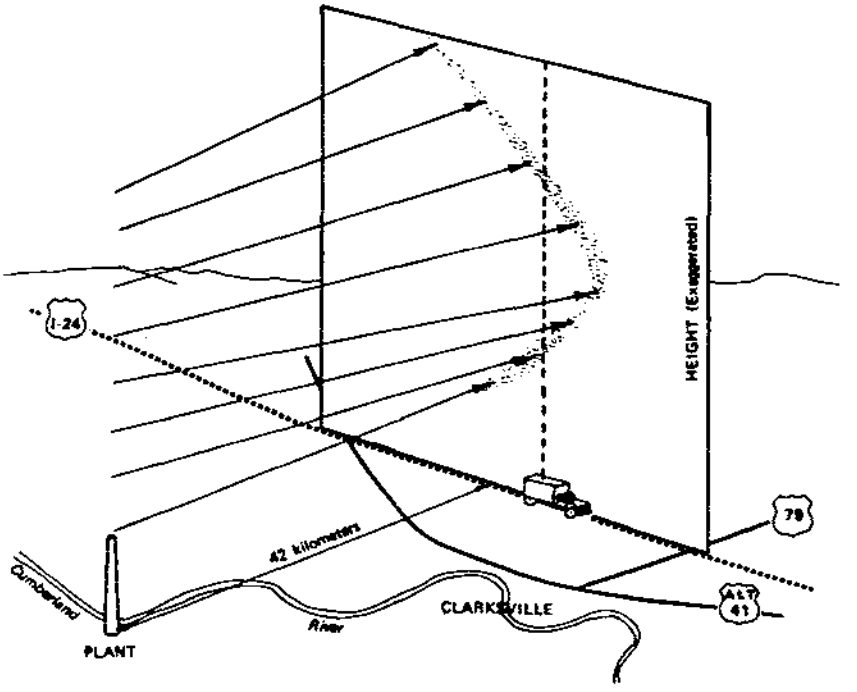

Figure 1.11: Schematic representation of the effects of directional wind shear and varying plume rise on an elevated power plant plume under stable conditions (from Uthe et al., 1980).

In summary, numerous studies have indicated that atmospheric dispersion will be enhanced by the interaction of wind shear with turbulent diffusion. Although the case of the simultaneous interaction of these two processes has received the most attention, the other possible case of sequential or delayed interaction in which differential advection is *followed* by turbulent mixing is likely to be more important for mesoscale travel times in which a pollutant cloud experiences one or more full diurnal cycles. However, as discussed in Sec. 2.4, relatively few LRTAP models treat vertical wind shear explicitly, despite

Smith and Hunt's (1978, p. 477) conclusion that "the effects of wind shear, combined with the diurnal cycle of stability, on lateral dispersion" are one of the three most pressing aspects of LRTAP requiring further study. This problem is explored in some detail in the remainder of this dissertation.

1.8 Numerical Modelling, Hypothesis, and Issues

1.8.1 Use of numerical models

Some examples of mesoscale atmospheric dispersion have been presented in this chapter and some of the physical mechanisms and temporal and spatial scales that play a role in this phenomenon have been described. Enough observations from field studies of mesoscale atmospheric dispersion are now available to permit description of many aspects of mesoscale atmospheric dispersion (Sec. 2.2), but the varied and complex nature of these field programs makes it difficult to relate available real-world observations to our current theoretical understanding of mesoscale atmospheric dispersion under very idealized conditions. Numerical models provide a tool to bridge this gap. They can be used to conduct a series of controlled, repeatable experiments for both simple and complex surface and atmospheric conditions, thus permitting an examination of both individual contributions from and interactions between the different proposed physical mechanisms.

In general, mathematical models vary widely in complexity and completeness. Simple *idealized* models can be used to strip a problem to its essentials. The success of such models depends on how well they represent the fundamental processes governing the real phenomenon. At the other extreme, complicated *comprehensive* models serve to integrate and synthesize our best understanding of all of the processes which may affect the phenomenon of interest (e.g., Venkatram, 1990). Idealized models are frequently analytical; comprehensive models almost always require numerical solution. Idealized models can be used to isolate the contributions of particular processes; comprehensive models allow the interactions of a variety of competing or complementary processes to be studied. In an even more philosophical vein, Lamb (1984) has given a thought-provoking

discussion of air pollution models in which a model is viewed as a 'universal statement' and a complementary set of 'singular' statements.

1.8.2 Hypothesis

A natural step then is to consider how well mesoscale atmospheric dispersion can be modelled mathematically. As will be discussed in the next two chapters, a number of numerical models have been used with limited success to simulate cases of mesoscale atmospheric dispersion. Even the simplest of these models is fairly complicated in keeping with the complexity of the problem. Nevertheless, the poor performances of many of these models may be explicable by their neglect or poor treatment of several physical processes important in mesoscale atmospheric dispersion, namely vertical shear, inertial oscillations, terrain-forced mesoscale circulations, and mesoscale vertical ascent and descent. *It is the hypothesis of this study that such mesoscale atmospheric flow features contribute significantly to dispersion in the PBL over mesoscale and longer distances over all types of terrain through shear processes, differential advection, and delayed mixing.*

Many factors may play a role. For example, latitude affects both the inertial period and diurnal forcing. Time of year affects the diurnal forcing. Time of day affects the dynamics of the turbulent boundary layer into which pollutant is released. Large-scale baroclinicity and large-scale vertical motions affect the local structure and dynamics of the planetary boundary layer. Terrain inhomogeneities can force mesoscale flow inhomogeneities as can synoptic-scale forcing.

Given the complexity of mesoscale influences on atmospheric dispersion described in the previous sections, a numerical mesoscale atmospheric dispersion model should (i) be capable of predicting three-dimensional, time-dependent atmospheric mean flow and turbulence fields over complex terrain in an unsteady synoptic environment with sufficient resolution to account for mean vertical PBL structure and significant terrain and atmospheric inhomogeneities, and (ii) be able to use this information to predict the transport and diffusion of a pollutant released from a specified source or sources into an unsteady and horizontally and vertically inhomogeneous turbulent flow. The

CSU mesoscale atmospheric dispersion modelling system, which consists of a mesoscale meteorological model, RAMS, coupled with a mesoscale Lagrangian particle dispersion model, has these capabilities and has been used in this study to investigate the above hypothesis.

Of course a numerical model is only an approximate surrogate for the real atmosphere. The degree of success of any mathematical or physical model in simulating a real phenomenon will be an indication of the relative importance of the scales and processes that the model can represent well versus those that it can represent only poorly or not at all. Even before carrying out any MAD[25] simulations, it is possible to anticipate some likely issues and problem areas.

1.8.3 Modelling issues

Representability of the mesoscale energy spectrum

In the real atmosphere, mesoscale energy is distributed over a variety of flow modes, including mean mesoscale circulations, internal gravity waves, and, likely, quasi-horizontal vortical modes or mesoscale eddies (Secs. 2.1.8 and 2.1.9). Given the synoptic scale of the meteorological fields used to initialize mesoscale meteorological models, none of this flow energy will be included in the initial model state. Moreover, some of the sources of these mesoscale flow modes will be subgrid-scale and hence unrepresentable as will be much of the atmospheric vertical fine structure which can modulate these modes (Sec. 2.1.6). Certain model characteristics may also preclude representation of these mesoscale eddies (Sec. 1.4).

This study concentrates on mesoscale dispersion within and immediately above the planetary boundary layer in situations when moist convection, an important source of small-scale energy and structure, is not important. *A priori* we might expect representability problems to be less important in this layer than in the free atmosphere above

---

[25] But not crazy.

because of the dominant role of boundary forcing in the PBL and its ability to generate mesoscale flow features (e.g., Paegle et al., 1990). Nonetheless, representability of the full mesoscale energy spectrum is a real concern.

By representability problems I refer to the inability of a numerical model to represent adequately one or more atmospheric processes or features important to the problem being considered. Representability problems may be due to (a) insufficient model resolution, (b) incomplete model physics or dynamics, or (c) inadequacies in the physical parameterizations employed. A parameterization may be thought of as an *implicit* representation of a process or its effects.

(a) Consider model resolution. Numerical modelers have found that the smallest temporal or spatial features that can be realistically treated in a numerical simulation are those $4\Delta t$ or $4\Delta x$ in size (e.g., Mesinger and Arakawa, 1976; Avissar, 1990). $2\Delta t$ or $2\Delta x$ features are impossible to handle accurately with any available numerical solution techniques. For temporal resolution, then, Δt can be no larger than 6 h if the 24 h diurnal cycle is to be resolved even crudely. As for spatial resolution, the smallest resolvable feature for a horizontal grid increment Δx of 50 km would be 200 km in size; if the horizontal grid increment is increased to 400 km, only flow features larger than 1600 km could be resolved. Even a regional-scale meteorological model with 50 km horizontal grid spacing will be unable to resolve such common meso-β-scale circulations as sea and land breezes and mountain-valley winds. The CSU mesoscale atmospheric dispersion modelling system has been used in this study with $\Delta t \sim 30$ s, $\Delta x \sim 5$ km, and $\Delta z \sim 200$ m. It is thus well able to resolve mesoscale time scales and many meso-β-scale mean circulations. If the study hypothesis is correct, resolving such mesoscale flow features should produce improved MAD simulations compared to models with only synoptic-scale resolution.

(b) As an example of incomplete model physics and dynamics, it is well known that flow in the convective PBL is frequently organized into large-scale coherent structures called longitudinal rolls (e.g., LeMone, 1973; Brown, 1980). The vertical scale of these

rolls is the depth of the PBL, z_i, while their horizontal scale is about $3z_i$. A typical value of z_i is 1 km. It is extremely rare for mesoscale meteorological models to be run with horizontal resolution sufficient to represent such circulations explicitly. Longitudinal rolls are significant for another reason: they represent an upper bound for classical, three-dimensional turbulence in the atmosphere. In fact, given their horizontal anisotropy, they cannot be considered to be true three-dimensional turbulence. Larger-scale atmospheric flow structures will have even smaller aspect ratios (i.e., ratio of vertical length scale to horizontal length scale) than longitudinal rolls and hence will be even more nearly quasi-horizontal. This implies that mesoscale 'eddies' contributing to mesoscale dispersion will be more two- than three-dimensional, another fundamental difference between small-scale and mesoscale dispersion (e.g., Tennekes, 1978, 1985). Mesoscale flow modes and energetics, including two-dimensional turbulence and mesoscale turbulence, are discussed in greater detail in the next chapter, but it is worth raising the question now as to whether such mesoscale eddies will be adequately represented in a MAD model.

As another example of incomplete physics or dynamics, cloud venting has been identified as a process that can inject significant amounts of boundary-layer air into the stratified free atmosphere above (Sec. 1.3). In order to treat this process in a mesoscale model which cannot resolve individual clouds, some sort of cumulus parameterization scheme would have to be employed which accounts for PBL—free troposphere exchanges of air. Otherwise, the PBL will be capped by an impermeable lid as far as PBL pollutant is concerned. Very few mesoscale meteorological models even include this process let alone handle it well. As already mentioned, mesoscale venting may also be important but this process *may* be resolvable in a mesoscale model.

(c) Turning to inadequacies in physical parameterizations, the representations of subgrid-scale turbulent diffusion in both the meteorological and dispersion components of the CSU mesoscale atmospheric dispersion modelling system are based on ensemble-average parameterizations (e.g., Mahrt, 1987; Garratt et al., 1990). As discussed in Sec. 1.4, one characteristic of ensemble averages is that all random characteristics are re-

moved. Thus, an ensemble-average turbulence parameterization does not resolve subgrid-scale motions explicitly but instead attempts to represent the grid-volume-average diffusive effects of such motions. For example, to represent realistically flows in which longitudinal rolls are present, ensemble-average horizontal eddy diffusivities should have a directional dependence with larger values in the crosswind direction than in the alongwind direction. Most turbulence parameterizations currently being used do not consider effects due to such organized subgrid-scale structures.

The parameterization of mesoscale eddies is even more problematic. In the stable free atmosphere, RAMS, the mesoscale meteorological model developed at CSU, uses a nominal vertical diffusivity of 1 $cm^2 s^{-1}$ (although the possibility of convective overturning can be included). Transport due to explicitly resolved mesoscale fluctuations such as large internal gravity waves generated by resolved topography or convection or terrain-forced circulations will thus be represented but not advection and mixing due to individual, random pancake eddies or smaller-scale internal waves (the recent paper by Pleune [1990] describing a parameterization of vertical diffusion in stable conditions which accounts for subgrid-scale vertical finestructure and Kelvin-Helmholtz instability is one step in this direction). Comparison of the results of MAD simulations against observations will then provide an indication as to how important the effects of the unresolved flow modes are.

The 1984 Øresund mesoscale dispersion experiment (see Table 2.4) may provide one illustration of this problem. The general synoptic conditions on two Øresund release days, June 4 and June 5, were quite similar but ground-level concentrations measured on June 4 were one-third to one-half those measured on June 5 (Andrén, 1990a). Andrén also noted that pibal observations on June 4 indicated the presence of a low-level jet in the lowest 100 m which wasn't observed on June 5 nor predicted by any of the numerical dispersion models which attempted this case.

Sampling and averaging

Sampling and averaging considerations are also an issue in this study as in any modelling study since observations and model predictions almost always have *different* asso-

ciated time and space scales. One familiar example of this problem is the comparison of volume-averaged model grid-point predictions against real-world point measurements (e.g., Pielke, 1984). In addition, some observations must be considered to be single realizations while others approximate ensemble-averaged values as a result of averaging over large temporal or spatial ranges. In this study, observations from two mesoscale tracer experiments have been compared against the results of numerical simulations. The individual tracer releases are single MAD realizations[26] whereas the Lagrangian-particle-dispersion-model (LPDM) concentration predictions are ensemble averages, thus introducing inherent uncertainty and intersample variability as factors in the evaluation (see Sec. 4.6). The difference between the Øresund tracer releases on June 4 and June 5 mentioned above is an example of this problem. Accordingly, a model cannot be validated against only one or two cases. Any single case may be an outlier due either to inherent statistical fluctuations or, even worse, to processes and phenomena not well represented in the model.

Another complicating factor is that ensemble averages require identical external conditions. The ergodic hypothesis is normally invoked for quasi-homogeneous, quasi-stationary turbulence such as wind-tunnel flows. For the mesoscale dispersion case, however, the external flow conditions are both time-dependent due to the diurnal cycle and synoptic evolution and space-dependent due to terrain forcing and synoptic structure. Actual time of tracer release thus becomes an important parameter since tracer material is being dispersed by an unsteady but quasi-periodic flow. Daytime releases will likely behave differently from nighttime releases (e.g., Moran et al., 1986) and interpretation of LPDM predictions must take these variations into account.

In a sense, mesoscale dispersion models have to predict the external conditions of the ensemble average itself, that is, the large-scale flow variations in time and space. While this is obviously more complicated than the small-scale-dispersion case where these

---

[26] Even though they are tracked and sampled for several days.

conditions are fixed, there is also a greater degree of determinism involved due to our knowledge of some of the external conditions, e.g., time of year, latitude, topography, surface conditions, and synoptic environment. If mesoscale-flow realizations fluctuate less from the model-predicted ensemble-average mesoscale flow (e.g., Lamb, 1984; Lamb and Hati, 1987) than do smaller-scale turbulent flow realizations about the local, short-term, quasi-stationary, quasi-homogeneous mean flow, and if resolvable mesoscale flow features are important for MAD as is hypothesized here, then MAD models may perform reasonably well despite not being able to represent the full mesoscale energy spectrum or particular mesoscale flow realizations.

Finally, tracer releases were several hours long in the two experiments considered in this study, corresponding to 'long puffs' or 'short plumes', while sampling times were also on the order of several hours, quite short relative to mesoscale variations. Travel times over the experiment observing networks, on the other hand, were as long as three days. These long travel times force the use of ensemble averages with unsteady, inhomogeneous external conditions. In effect two ensemble averages are involved since the subgrid-scale turbulence parameterization used in RAMS is associated with an ensemble average over quasi-stationary and quasi-homogeneous conditions as discussed in Sec. 1.4. The long travel times also raise the important issue of the difference between relative and absolute diffusion for such release, sampling, and travel times, especially because the Lagrangian particle model used in this study is a 'one-particle' model. That is, it cannot simulate *subgrid-scale* turbulent relative diffusion although it can simulate relative dispersion due to resolved differential advection. I will return to this topic in Chap. 2, but it appears that the distinction between relative and absolute diffusion is less important on the mesoscale than on the local scale since most of the correlation between two particles will be due to representable and resolvable motions (e.g., Pasquill, 1974).

The preceding discussion is not intended to denigrate the CSU MAD modelling system in any way. As should become clear in the next chapter, it is a much more complete and sophisticated package than most being used today to simulate mesoscale atmospheric

dispersion. Nevertheless, no numerical model can represent the real atmosphere perfectly. Assessment of what has been left out of a model as well as what has been included can help in understanding the degree of success of a model and hence the physical phenomenon itself.

1.9 Summary

Mesoscale atmospheric dispersion has been defined in this chapter as the transport and diffusion of air pollutants or other atmospheric constituents over horizontal distances of 2 to 2000 km and time periods of 1 to 48 hours. Conventional wisdom used to hold that the atmosphere's capacity to dilute the concentration of air pollutants is effectively without limit and that for pollutant dispersion over mesoscale distances, sufficient dilution will have taken place that there is little practical need to know pollutant concentrations at these distances. More recently, however, it has been recognized that (a) if pollutant sources are strong enough or numerous enough or long-lived enough or (b) if the pollutants themselves are sufficiently toxic enough or active enough in some way, then ambient pollutant concentrations or long-term dosages may still be significant even after mesoscale dispersion and dilution.

The multi-country radionuclide contamination experienced during the 1986 Chernobyl disaster in the U.S.S.R. is one recent example. Other anthropogenic pollutants or their precursors are responsible for regional-scale acidic deposition, oxidant episodes, and visibility degradation even after transport and diffusion over mesoscale distances. Heavy metals in aerosol form and synthetic organics such as pesticides can be transported to, and then accumulate in, sensitive regions. In all of these cases, even remote areas such as the Arctic, which are far away from the sources of such pollutants, can be affected. Natural aerosols produced by volcanic eruptions, forest fires, or sandstorms, and biological organisms such as pollens, seeds, bacteria, spores, viruses, and insects, can also affect regions far from the source.

Mesoscale atmospheric dispersion was shown in this chapter to be a more complicated process than small-scale dispersion. Over mesoscale time and space scales, the mean wind field can no longer be considered steady or horizontally homogeneous. In fact, it is very important to specify the type of averaging and scale of averaging employed when differentiating between mean and fluctuating quantities on these scales since neither the ergodic hypothesis nor the Reynolds conditions are likely to hold. Distinguishing between absolute and relative diffusion is also more difficult on the mesoscale because four different time scales — release duration t_r, travel time T, sampling time τ, and the relative diffusion time scale t_e — are relevant.

Horizontal dispersion is usually more important[27] than vertical dispersion on these scales due to the limited vertical extent of the planetary boundary layer and the troposphere. Horizontal dispersion can be enhanced by vertical shear through either the simultaneous or delayed interaction of horizontal differential advection and vertical mixing over one or more diurnal periods. Low-level vertical shear is nearly always present in the atmosphere as a result of surface friction and synoptic-scale horizontal temperature gradients. Mesoscale circulations driven by terrain or synoptic forcing may also produce vertical or horizontal shear and differential advection. Characteristic time scales for mesoscale atmospheric dispersion include the diurnal period and daylight[28] period, inertial period, release duration, relative diffusion time scale, and travel time. Characteristic space scales include the external length scale associated with physiographic or synoptic forcing, the Rossby radius of deformation, the source size, and travel distance.

The literature on the role of shear in turbulent diffusion in the laboratory, atmosphere, and ocean was also reviewed in this chapter. Like much else in fluid dynamics, the study of shear-enhanced diffusion was initiated by G.I. Taylor, but many others have since con-

---

[27] In the absence of cloud venting and mesoscale venting.

[28] That is, the length of daylight, which will modulate convective mixing and low-level vertical coupling and decoupling. This value might be though of as representing higher harmonics of the equinoctial diurnal period.

tributed. There is a considerable oceanographic literature on shear-enhanced diffusion which provides a valuable complement to the meteorological literature. A number of analytical solutions to various forms of the problem have been obtained. In general, they fall into one of three categories depending on the type of domain considered: bounded, semi-infinite, or infinite. The character of the solutions is quite different for each domain type. Pasquill (1962) appears to have been the first to mention the combination of differential advection with *delayed* vertical mixing as a mechanism in mesoscale atmospheric dispersion. The role and importance of this mechanism forms the central theme of this study.

This chapter concluded with a brief discussion of the philosophy of numerical modelling, the study's hypothesis ("... that ... mesoscale atmospheric flow features contribute significantly to dispersion in the PBL over mesoscale and longer distances over all types of terrain through shear processes, differential advection, and delayed mixing"), and various philosophical issues raised by the methodology. The latter include incomplete representation of the mesoscale energy spectrum by the mesoscale dispersion modelling system, the extension of ensemble averages to environments with time-dependent external conditions, and the distinction between mesoscale averages and mesoscale realizations.

1.10 Outline

The influence of resolvable mesoscale shear on mesoscale atmospheric dispersion is investigated in this study with a mesoscale meteorological model used in conjunction with a mesoscale Lagrangian particle dispersion model. This CSU mesoscale dispersion modelling system has been used to run suites of numerical simulations of tracer releases made during two mesoscale atmospheric dispersion field experiments. Tracer measurements are available out to 600 km from the release site for one of these experiments (the 1980 Oklahoma mesoscale tracer experiment) and out to 1100 km for the other (the 1983 Cross-Appalachian Tracer Experiment). Such observations of the transport and diffusion of a passive tracer on the mesoscale contain valuable information concerning the impact of

vertical shear, the diurnal cycle, inertial oscillations, and terrain-forced mesoscale circulations on this process. The suites of numerical sensitivity experiments were designed to investigate the roles of various atmospheric processes, especially the diurnal heating cycle and surface processes, by including them or excluding them in various combinations.

Observational studies, theoretical studies, and computer- and laboratory-based modelling studies relevant to the phenomena of mesoscale variability, mesoscale 'turbulence', and mesoscale atmospheric dispersion are surveyed in Chap. 2. The fact that this is a long chapter attests to both the complexity and novelty of the topic. Where possible I have tried to refer the reader to appropriate review articles, but much of the material reviewed here is recent and no comparable overview appears to have been published elsewhere. The two mesoscale atmospheric dispersion tracer experiments examined and simulated in this study are described in Chap. 3. Chap. 4 provides a description of the CSU mesoscale atmospheric dispersion modelling system, the actual model configurations used, and an overview of available evaluation procedures. Chaps. 5 and 6 are the two results chapters: the suites of numerical experiments are described along with the results of the experiments for the two mesoscale tracer experiments. Finally, implications of the numerical results are summarized in the form of conclusions in Chap. 7 and some suggestions are made for further research on this topic.

Chapter 2

BACKGROUND

There is the tale of a philosopher who succeeded in reducing the whole of physics to a single equation H= 0, *but the explanation of the meaning of* H *occupied twelve fat volumes.*

L.F. Richardson (1922, p. 220)

The subject of atmospheric dispersion may be well established for small-scale three-dimensional turbulent flows, but even fundamental assumptions have to be reexamined when extending this subject to larger scales at which the existence of flow nonstationarity, inhomogeneity, anisotropy, and intermittency can no longer be ignored. Nor can the mesoscale be viewed in isolation. As a somewhat arbitrary 'middle region' of the atmospheric energy spectrum, the mesoscale is influenced by both smaller and larger flow scales and processes. Flow dynamics are also more varied and complex on the mesoscale than at smaller scales. For example, density stratification plays a more important role on the mesoscale. Consonant with this view of greater complexity, observations and theory discussed in Sec. 2.1 suggest the existence of *two* mesoscale inertial ranges with very different dynamics than those of the small-scale Kolmogorov inertial range.

Batchelor (1949, p. 437) observed that "diffusion can be regarded as almost wholly a kinematic problem, depending only indirectly on the dynamics of turbulent motion." As noted in Chap. 1, however, nonturbulent motions can also contribute to mesoscale dispersion through stirring so that a wide range of flow phenomena and circulations may play a role. Accordingly, this chapter begins with a review of the kinematics, dynamics, and energetics of mesoscale flows. One underlying theme of Sec. 2.1 is the much broader

definition of the term 'turbulence' that must be employed on the mesoscale. Secs. 2.2, 2.3, and 2.4 in turn review observational, theoretical, and numerical studies of mesoscale dispersion itself. A historical, chronological perspective has generally been followed in order to portray the evolution of our current understanding of this subject, the interplay between different approaches, and the connections to related topics.

2.1 Kinematics, Dynamics, and Energetics of Mesoscale Flows

In order to understand the dispersion of atmospheric trace constituents or pollutants over mesoscale travel times and distances, it is first necessary to understand the behaviour of atmospheric flows on these scales. For example, what types of mesoscale forcing, mesoscale instabilities, and mesoscale circulations are possible, how frequently do they occur and under what conditions, and how do the various mesoscale circulations interact with smaller, larger, and comparable circulation systems? What is the statistical structure of mesoscale flow fields, and what are the statistical properties of energy, vorticity, and momentum transport on the mesoscale?

Only in the last few decades have answers to the above questions begun to emerge. Historically, many advances in meteorology have resulted either directly or indirectly from improved means of observation: consider the impact of such inventions as the thermometer, barometer, deep-water sailing ship, telegraph, and radiosonde on our understanding of the small-scale and large-scale behaviour of the atmosphere. For this reason, until recently the study of mesoscale meteorology lagged behind micrometeorology and synoptic meteorology due to a lack of suitable observational tools. However, the advent since the 1940s of such new observing methods as instrumented aircraft, constant-height balloons, earth-orbiting satellites, dense networks of surface stations ('mesonets'), microbarographs, and remote-sensing electromagnetic probes (radar, sodar, lidar) has revolutionized mesoscale meteorology and provided an ever-increasing data stream of mesoscale observations (e.g., Atkinson, 1981; AMS, 1986).

It was therefore somewhat ironic that just as detailed observations of such mesoscale phenomena as severe thunderstorms, squall lines, surface fronts, and sea breezes were becoming available for the first time in the 1950s, the first published atmospheric energy spectra to include the mesoscale indicated the existence of a broad spectral minimum or 'gap' centered in the mesoscale, suggesting to one author "the lack of a physical process that could support wind-speed fluctuations in this frequency range" (Van der Hoven, 1957, p. 164).

The horizontal wind-speed frequency spectra of Panofsky and Van der Hoven (1956) and Van der Hoven (1957) were based on long-record instrumented tower measurements. These spectra showed major energy peaks at frequencies (periods) of 0.28×10^{-5} Hz (4 days) and 0.02 Hz (1 minute) bracketing a spectral energy gap[29] centered at a frequency ranging from 0.28×10^{-3} Hz (1 hour) to 0.28×10^{-2} Hz (6 minutes). The existence of such a mesoscale energy gap would have significant implications for (a) the predictability of large-scale atmospheric motions (Tennekes, 1978, 1985), (b) the parameterization of small-scale motions in terms of the characteristics of the large-scale motions on the other side of the gap (Robinson, 1967; Fiedler and Panofsky, 1970; Leith, 1971), and (c) the statistical stability of atmospheric turbulence measurements (Monin, 1972; Wyngaard, 1973; Monin and Yaglom, 1975). Since a spectral energy minimum on the mesoscale generally simplifies matters, this apparent demonstration of the existence of a mesoscale gap was embraced by many meteorologists.

More recent observations and theoretical developments, however, have led to the quite different view of a continuous mesoscale energy spectrum of disordered wave and eddy motions transferring energy between the cumulus and cyclone scales with *intermittent* mesoscale and microscale spectral '*humps*' appearing due to organized mesoscale events and turbulent bursts (Atkinson, 1981; Emanuel, 1986). This new view of the

---

[29] Monin (1972, p. 8) noted that the advective length scale corresponding to the spectral minimum at 20 minutes or so is on the order of the effective thickness of the atmosphere $H \sim 10$ km and that this minimum could be thought of as separating small-scale, three-dimensional atmospheric turbulence from large-scale, quasi-two-dimensional atmospheric turbulence.

mesoscale as a crucial link in the atmospheric energy spectrum is discussed in this section, beginning with the macroscale and working down through the mesoscale. The question of a mesoscale gap is then revisited in Sec. 2.1.10.

2.1.1 Mesoscale sampling and representativeness

A case can be made that flow dynamics in Orlanski's three-decade mesoscale range (see Sec. 1.1) are inherently the most complex of any within the atmospheric flow continuum. Every atmospheric dynamical process operating on scales larger than molecular dissipation and smaller than the latitudinal variation of the Coriolis force can play a role in mesoscale circulations. Mesoscale flows may be hydrostatic or nonhydrostatic. Both ageostrophic advection and Coriolis acceleration can be important. Mesoscale topography may block low-level flows or excite a range of internal gravity waves (IGW). A wide spectrum of internal gravity waves may also be generated by a number of other processes (Sec. 2.1.8). Differential surface heating can drive thermally-direct mesoscale circulations. Moist processes can also be very important: symmetric instability or slantwise convection is a natural mesoscale instability, and cumulus-scale convection may also develop mesoscale organization and structure as it evolves (e.g., squall lines, mesoscale convective complexes, mesoscale cellular convection, tropical cyclones, mesoscale rainbands). Synoptic-scale wave-wave interactions may produce higher-wavenumber circulations or flow features. And finally, there is also evidence that quasi-horizontal vortical modes or 'pancake eddies' may evolve from smaller-scale turbulence in stably-stratified conditions (Sec. 2.1.9).

Clearly this wide range of often intermittent dynamical processes and mesoscale circulations makes generalization about mesoscale flows difficult. Short-term energy frequency spectra will frequently have preferred modes and more structure than longer-term spectra (e.g., Desbois, 1975; Balsley and Carter, 1982). Accordingly, *if* a statistical approach is to be used or representative mean values are required, then sampling periods should be months long or sampling domains thousands of kilometers in size in accordance with Eq. 1.6. (The other possible approach is to resolve the mesoscale phenomenon of interest

explicitly, that is, to consider a single realization even if smaller scales are still parameterized.) Other sampling factors such as the location of measurement and time of year can also be significant. For example, changes in mean jet-stream position, tropopause height, mean vertical stability, and strength and frequency of convection with season can affect spectral amplitudes and shapes.

The sampling *methods* used may also introduce biases or uncertainties into mesoscale statistics. For example, commercial aircraft will alter flight paths to avoid severe weather and probable areas of clear-air turbulence when possible. Clear-air Doppler radars (i.e., wind profilers) give line-of-sight radial velocities; if an oblique beam angle is used, then assumptions must be made in order to calculate horizontal or vertical wind components. Profiler beams pointed in different directions will also sample different atmospheric volumes at different distances from the profiler site. Balloons cannot obtain instantaneous profiles at a fixed location but instead rise at a finite rate and are carried downwind of their release site. The use of photographs from a suspended camera to determine balloon ground position requires cloud-free conditions (Mantis, 1963). Similarly, precipitation echoes make tracking tetroons by radar problematic if not impossible if the tetroons are not equipped with transponders or beacons (Angell and Pack, 1960).

Accordingly, estimates of mean flow statistics such as KE spectra must be interpreted and applied cautiously, with due allowance made for measurement technique, measurement location, sample length and resolution, heterogeneity of data sources, and probable observational biases or analysis errors. Qualitative and quantitative estimates of spectral *variance* are also very important in view of the intermittency of mesoscale phenomena and questions of representativeness. To give one example, Vinnichenko (1970) included three curves at the high-frequency end (periods of less than a few minutes) in his composited KE frequency spectrum corresponding to light, moderate, and strong clear-air turbulence measurements.

2.1.2 Macroscale turbulence

The dynamics of large-scale, horizontal transports of heat and momentum by approximately two-dimensional, planetary- and cyclone-scale atmospheric waves are obviously different from those of small-scale heat and momentum transport by microscale, three-dimensional turbulence. Nevertheless, and somewhat remarkably, techniques and concepts from the statistical theory of microscale turbulence which were first developed in aerodynamic laboratories have been applied fruitfully to large-scale atmospheric flows. In turn, observational and theoretical studies of large-scale atmospheric energetics have contributed significantly to our understanding of mesoscale energetics.

According to Hutchings (1955) and Saltzman (1957), Defant (1921) was the first to consider synoptic-scale anticyclonic and cyclonic circulation systems as large-scale atmospheric eddies or turbulence elements. Clearly, this is macroscale or climatological turbulence. For individual eddies several thousand kilometers in size and persisting for a week or more, the sampling domain should be hemispheric or global in scale and the sampling period should be on the order of years in order to obtain a statistically significant sample.

Support for the usefulness of this approach was subsequently provided by observational studies of the statistical properties of large-scale tropospheric disturbances which indicated apparent similarities between large-scale and small-scale spectral flow characteristics. Syono and Gambo (1952), Kubota and Iida (1954), and Syono et al. (1955) calculated Fourier series for 500-hPa geopotential heights along entire latitude circles (10–14 day samples, 5°–7.5° resolution) and found the slope of the mean-square amplitudes of harmonic components plotted against wavenumbers greater than four to be approximately $-7/3$. Pressure spectra in the inertial subrange of an isotropic three-dimensional turbulent flow have the same slope (e.g., Ogura, 1958). Considering another statistical measure, Hutchings (1955) reported similar functional forms between the autocorrelation functions of free-troposphere wind velocity fluctuations and surface pressure up to 24 h

and 72 h, respectively, to the autocorrelation functions predicted by isotropic turbulence theory for the Kolmogorov inertial range .

Ogura (1958) considered wintertime 300-hPa u- and v-component power spectra along three latitude circles and found evidence of horizontal quasi-isotropy for wavenumbers greater than four, although the kinetic energy (KE) spectral slopes, which ranged from -2.3 to -3.5, were *steeper* than the $-5/3$ value predicted by three-dimensional isotropic turbulence theory. White and Cooley (1956), Benton and Kahn (1958), and Saltzman (1958) showed that the standard deviations of the daily one-dimensional KE spectra are of the same order of magnitude as the mean longitudinal KE spectra based on one to three months of data and 5° to 10° longitudinal resolution[30]. Saltzman and Fleisher (1962) presented detailed KE spectral statistics for one year (1951) broken down by season and latitude and by stationary vs. transient components. A number of other early observational studies of large-scale atmospheric energetics in terms of longitudinal wavenumber are listed in Saltzman (1970).

Finally, Horn and Bryson (1963) and Wiin-Nielsen (1967) presented a number of longitudinal KE spectra in which the spectra showed a -2.7 or -2.8 power-law relationship with longitudinal wavenumber m in the higher wavenumber range ($8 \leq m \leq 15$). These results were significant as they supported Ogura's (1958) results and contradicted the earlier indications that large-scale atmospheric wavenumber spectra followed the same power-law relationships as small-scale, three-dimensional, inertial-range turbulence spectra. Instead, an entirely different mechanism of turbulent scale interaction appears to operate on the large scale (Charney, 1971). The period just described may be thought of as the early or empirical stage of the study of large-scale atmospheric turbulence. A single theoretical paper by Kraichnan (1967) ushered in the next stage.

---

[30] Note that the spectral description of turbulent flows discards detailed phase information. An alternative 'episodic' description of turbulence, which focuses on turbulence 'events' and coherent structures, has been introduced by wind-tunnel researchers over the last twenty years and may also be useful in describing large-scale atmospheric eddies (e.g., Yule, 1980; Narasimha and Kailas, 1990).

2.1.3 Two-dimensional turbulence

Theorists also began to apply spectral analysis to the study of large-scale atmospheric turbulence after the Second World War. Given the very large aspect ratios of horizontal scales to vertical scales, it was only natural to view large-scale atmospheric flows to a first approximation as quasi-horizontal and hence to investigate the properties of two-dimensional turbulence. Two-dimensionality imposes a powerful constraint on flow-field dynamics and scale interactions through vorticity conservation. In a barotropic, incompressible, inviscid fluid, *enstrophy* (one-half the squared vorticity) will be conserved in addition to KE. The two-dimensional behaviour of the flow disallows vortex-tube stretching and hence the kind of energy cascade towards higher wavenumbers that occurs in three-dimensional flows (e.g., Onsager, 1949; Lee, 1951; Ogura,1952; Batchelor, 1953). In fact, Tennekes (1985) has distinguished two-dimensional turbulence from three-dimensional turbulence by referring to the former as *vorticity-advecting* chaos and to the latter as *vorticity-stretching* chaos. Batchelor (1969), however, noted that the two basic properties of turbulence, *randomness* and *nonlinearity*, are present in two-dimensional turbulence as well as in three-dimensional turbulence (see also Table 2.3).

Fjørtoft (1953) investigated nonlinear scale interactions in a two-dimensional nondivergent flow on a sphere and showed that the transfer of KE from one flow scale to a smaller one must be accompanied by the simultaneous flow of KE to a *larger* flow scale if both energy and enstrophy are to be conserved[31]. To see this, consider the problem in wavenumber space. The twin constraints of energy and enstrophy conservation will then be equivalent to the invariance of the two integrals $\int_0^\infty E\,\mathrm{d}k$ and $\int_0^\infty k^2 E\,\mathrm{d}k$, where E is the KE spectral density at a two-dimensional wavenumber k and k^2E is the

---

[31] In fact, Fjørtoft concluded erroneously that a *larger* amount of KE must always flow upscale. Merilees and Warn (1975) proved that this was not necessarily so but was true in about 70% of possible triad interactions.

corresponding enstrophy spectral density. Rhines (1975, 1979) suggested[32] thinking of the first integral as the 'mass' of $E(k)$ in wavenumber space and of the second integral as its spectral 'moment of inertia' about $k = 0$. It then follows that any transfer of KE towards higher wavenumbers, which corresponds to a widening of $E(k)$, must be accompanied by a simultaneous transfer of KE towards lower wavenumbers in order to leave the second moment of E unchanged.

Physically, this corresponds to fluid elements with similarly signed vorticity grouping together to create larger eddies (Batchelor, 1953). At the same time, the shear of the larger eddies distorts vorticity contours, straining them out into thin filaments. In two-dimensional turbulence, then, some turbulent energy must flow upscale during inertial interactions and will tend to collect at the largest scales. Although counterintuitive, this view is consistent with early studies of large-scale atmospheric energetics which showed that the KE of the mean zonal flow (wavenumber 0) is maintained against friction by the transfer of KE from large-scale horizontal eddies (e.g., Starr, 1954). Starr referred to this phenomenon as "negative viscosity" since the flow of energy is directed towards larger scales (Starr, 1968; Kraichnan and Montgomery, 1980).

Lorenz (1953) also considered a two-dimensional flow field, consisting of a mean flow with superposed random disturbances, as an analogue with which to study the maintenance of KE in the Earth's atmosphere against frictional dissipation. Using a statistical hydrodynamic approach, he discussed conditions under which such disturbances could transfer KE to the mean flow. Thompson (1954) discussed temporal and spatial *weighted* averaging of the governing equations for large-scale flow and introduced a mixing-length hypothesis to handle the Reynolds terms. He noted two main differences in behaviour between large-scale and small-scale turbulence: "the eddy transport of vorticity is directed normal to the mean vorticity gradient" rather than down the gradient, and "the

---

[32] Mesinger and Arakawa (1976, p. 40) attribute this mechanical analogy to a 1966 report by Jule Charney.

coefficient of eddy transfer depends on the correlation between eddy displacements in one direction and eddy velocities in the direction normal to it."

Saltzman (1957) derived equations for the rate of change of KE and available potential energy (APE) of individual longitudinal Fourier components. These equations provided a theoretical framework within which to study the generation, transfer, and dissipation of KE and APE among various scales of eddies and have since been employed in many observational studies [see Saltzman (1970) for a list].

Inertial ranges in two-dimensional flows

The next big advance was the extension to two-dimensional flows of Kolmogorov's (1941) assumption that in certain wavenumber ranges the turbulence KE spectrum $E(k)$ may depend only on the two-dimensional wavenumber k and the spectral transfer rate of either KE or enstrophy. In 1967, Kraichnan postulated in a seminal paper that the constraints imposed on homogeneous, isotropic, two-dimensional, *inviscid* flows by the conservation of *two* quadratic quantities, KE and enstrophy, admit *two* formal inertial ranges with wavenumber-independent spectral fluxes for a single energy source. Neither of these inertial ranges, however, will be exactly analogous to the three-dimensional, downscale energy cascade of Kolmogorov (1941) in which only KE is conserved. The first of Kraichnan's two-dimensional inertial ranges corresponds to a downscale *enstrophy* cascade in which the *two-dimensional* KE spectral density $E(k)$ has the form $E(k) \sim \eta^{2/3}k^{-3}$, where k is a *two-dimensional* wavenumber and η is the enstrophy cascade rate. This k^{-3} downscale inertial range occurs at scales *smaller* than the scale of energy insertion (the rate of which is assumed to be continuous: Lilly, 1983a). The second of these two-dimensional inertial ranges corresponds to an *energy* cascade where $E(k)$ has the form $E(k) \sim \epsilon^{2/3}k^{-5/3}$ and ϵ is the rate of cascade of KE per unit mass. However, this $k^{-5/3}$ inertial range occurs at scales *larger* than the energy-insertion scale and thus is directed *upscale*, making it a backward or reverse energy cascade compared to the classic Kolmogorov cascade. Moreover, the transfers of KE in the downscale two-dimensional

inertial range and of enstrophy in the upscale two-dimensional inertial range are identically zero.

Mathematically, the possibility of two inertial cascades in two-dimensional turbulence is a consequence of the integral quadratic constraints on both energy and enstrophy. As shown by Fjørtoft (1953), net transfer of both energy and enstrophy must be either away from or toward the *middle* wavenumber for any triad interaction, and nonlinear interactions transfer energy over an increasingly wide range of wavenumbers (Batchelor, 1953; Rhines, 1975). In terms of a physical picture, Kraichnan (1967, p. 1422) described the double-cascade transfer process "as a clumping-together and coalescence of similarly signed vortices with the high-wavenumber excitation confined principally to thin and infrequent shear layers attached to the ever-larger eddies thus formed". Enstrophy dissipation is proportional to the squared vorticity *gradient*, whose enhancement by the stretching of vorticity contours is analogous to the energy-dissipation enhancement by vortex stretching in three-dimensional turbulence (Rhines, 1979; Tennekes, 1985). Concerning the reverse energy cascade, Kraichnan and Montgomery (1980, p. 592) proposed the following mechanism: "The large scales (wavenumber k) strain the small scales (wavenumber q), drawing them into elongated shapes with constant enstrophy and decreased energy. At the same time a secondary flow associated with the small scales grows on scales $\sim 1/k$ and gives destructive interference with the excitation at wavenumber k, thereby maintaining energy balance. The net result of this process, with stochastic variation of the straining time taken into account, is the negative viscosity."

Leith (1968), who had been working along similar lines to Kraichnan, developed a closure hypothesis for two-dimensional inviscid turbulence which was consistent with both inertial ranges. Batchelor (1969) considered the case of decaying, two-dimensional, isotropic turbulence at large Reynolds number[33]. Kraichnan (1971) and Leith and Kraichnan (1972) used a simple dynamical argument to suggest a logarithmic correc-

---

[33] Tennekes (1985) has summarized the complications introduced by viscosity in both two- and three-dimensional turbulence and noted that inviscid flow is a *singular* limit of the viscous case as $\nu \to 0$.

tion factor $(\ln k)^{-1/3}$ for the k^{-3} enstrophy-transfer range in order to achieve consistency with the test-field model closure approximation and to ensure convergence of the enstrophy transfer integral. The log correction shows that the enstrophy inertial range is non-local: straining comes equally from all wavenumber octaves below a given wavenumber of interest k. Note that the enstrophy spectrum $2k^2E(k)$ has the form k^{-1} in the enstrophy inertial range, apart from the log correction. This is the same spectral slope as in the viscous-convective range, a small-scale regime in which 'blobs' of passive *scalars* such as temperature are advected by turbulence (Batchelor, 1959; Tennekes and Lumley, 1972). "The small blobs (in the present case blobs of vorticity) are drawn into filaments and the resultant statistical distribution of filament widths gives the k^{-1} spectrum" (Kraichnan and Montgomery, 1980, p. 586). Note though that Kraichnan and Montgomery (1980) emphasize that the log correction to the enstrophy spectrum has by no means been shown to be valid.

Supporting evidence

Observational studies supportive of the ideas of Kraichnan, Leith, and Batchelor soon appeared. As already mentioned, one-dimensional KE spectra calculated by Horn and Bryson (1963) and Wiin-Nielsen (1967) had exhibited power-law relationships close to m^{-3} for longitudinal wavenumbers $m > 10$. Large-scale KE spectra published by Kao and al-Gain (1968), Julian et al. (1970), Kao and Wendell (1970), Kao et al. (1970), Desbois (1975), Chen and Wiin-Nielsen (1978), Lambert (1981), and Boer and Shepherd (1983) after the publication of Kraichnan's paper provided additional evidence[34] for a k^{-3} enstrophy-cascading inertial range for cyclone-scale wavenumbers (although, as will be discussed shortly, there is some question regarding the form of the spectral wavenumber used). Lilly (1969, 1971, 1972a,b) carried out numerical simulations of two-dimensional planar turbulence which resulted in modelled flow behaviour consistent with the theories

[34] Although Yang and Shapiro (1973) noted that some of these results were likely influenced in part by the observations and analysis procedure used and may have given overestimates of the spectral slope as a result.

of Kraichnan, Leith, and Batchelor, including back transfer of energy to larger scales and a small-scale energy spectrum approximately proportional to k^{-3}.

The existence of a k^{-3} KE spectrum at atmospheric scales smaller than those of principal baroclinic instability (i.e., the large-scale energy-injecting wavenumbers) has important implications for studies of atmospheric predictability and the limits of deterministic forecasting. Subgrid-scale energy, which cannot be resolved in numerical atmospheric models, will eventually propagate to all scales through nonlinear interactions. The rate of this energy transfer depends critically on the shape of the KE spectrum (Lorenz, 1969), and the propagation of subgrid-scale uncertainty will be slower with a -3 spectrum than a $-5/3$ spectrum. Leith (1971) and Leith and Kraichnan (1972) considered the predictability problem assuming a -3 spectrum at higher wavenumbers. For an overview of more recent work in this area, see Kraichnan and Montgomery (1980), Holloway and West (1984), Ghil et al. (1985), Tennekes (1985), and Anthes (1986).

Choice of scalar wavenumber

During the 1950s and 1960s, spectral analyses of large-scale atmospheric energetics employed the *one*-dimensional longitudinal wavenumber m (e.g., Saltzman, 1957). In three-dimensional turbulence, however, energy dissipation is proportional to the *three*-dimensional Cartesian wavenumber $\kappa = |(k_x, k_y, k_z)|$ while in two-dimensional planar turbulence, energy and enstrophy dissipation are proportional to the *two*-dimensional Cartesian wavenumber $k = |(k_x, k_y)|$ (e.g., Tang and Orszag, 1978; Pasquill and Smith, 1983). For two-dimensional turbulence on the sphere, a comparable two-dimensional wavenumber for spherical geometry is required; m is not suitable because it is a one-dimensional index and does not incorporate large-scale curvature effects (Leith, 1971; Baer, 1972; Tang and Orszag, 1978).

The appropriate characteristic functions or normal modes on a sphere are the spherical harmonics $Y_n^m(\phi, \lambda)$, where n is the degree and m is the order of the spherical harmonic, ϕ is latitude, λ is longitude, and

$$Y_n^m(\phi, \lambda) = P_n^m(\cos\phi)e^{im\lambda} \quad , \tag{2.1}$$

where $P_n^m(\cos\phi)$ is the associated Legendre polynomial. Baer (1972) and Wiin- Nielsen (1972) were the first to argue that the appropriate two-dimensional spectral index to characterize spatial scales on a spherical surface is n, the degree of the associated Legendre polynomial. Baer based his argument on the fact that in spherical geometry, dissipation of a normal mode of unit amplitude is proportional to $\nabla^2 Y_n^m = -n(n+1)Y_n^m$. This corresponds to the case of Cartesian or planar geometry in which dissipation is proportional to $k^2E(k)$ (Tang and Orszag, 1978).

More recent observational studies of large-scale atmospheric turbulence have used n as the two-dimensional spectral index (e.g., Chen and Wiin-Nielsen, 1978; Boer and Shepherd, 1983; Shepherd, 1987). One advantage of using a two-dimensional wavenumber is that flow anisotropy is automatically accounted for.

One-dimensional vs. two-dimensional spectra

There is another problem with the use of one-dimensional longitudinal wavenumbers and one-dimensional spectra in observational studies. Kraichnan's theory for two-dimensional inertial ranges is expressed in terms of a *two-dimensional* wavenumber and *two-dimensional* energy and enstrophy spectra just as Kolmogorov's theory for the three-dimensional inertial range was expressed in terms of a three-dimensional wavenumber and a three-dimensional energy spectrum. Inertial-range theory also requires the turbulence field to be homogeneous and isotropic at least locally.

To see the difference between one- and two-dimensional energy spectra, consider a two-dimensional wavenumber vector $\vec{k}$ with components (k_1, k_2) and two-dimensional velocity vector $\vec{v}$ with components (v_1, v_2). The one-dimensional spectral functions usually measured are, following the notation of Leith (1971),

$$\frac{1}{2} < v_1^2 > \;=\; \int_0^\infty F_1(k_1)\,\mathrm{d}k_1, \quad , \tag{2.2}$$

$$\frac{1}{2} < v_2^2 > \;=\; \int_0^\infty G_1(k_1)\,\mathrm{d}k_1, \quad , \tag{2.3}$$

$$\frac{1}{2} < v_1 v_2 > \;=\; \int_0^\infty H_1(k_1)\,\mathrm{d}k_1, \quad , \tag{2.4}$$

$$E_1(k_1) \;=\; F_1(k_1) + G_1(k_1) \quad , \tag{2.5}$$

where F_1 and G_1 are respectively the longitudinal Fourier transforms of the longitudinal and lateral velocity correlation coefficients $f(x)$ and $g(x)$ (Ogura, 1952).

For *isotropic* turbulence all second moments will be characterized by a one-dimensional spectral function $U(k)$ dependent only on the scalar two-dimensional wavenumber $k = (k_1^2 = k_2^2)^{1/2}$:

$$< v_i v_j >= \int\int P_{ij}(k_1, k_2)\, U(k)\,\mathrm{d}k_1\,\mathrm{d}k_2 \quad , \tag{2.6}$$

where the projection tensor $P_{ij}(k_1, k_2)$ has the form

$$P_{ij}(k_1, k_2) = \delta_{ij} - \frac{k_i k_j}{k^2} \tag{2.7}$$

as a consequence of the nondivergence of the velocity field (Leith, 1971). The isotropic two- dimensional energy spectral density $E(k)$ is then obtained by integrating $U(k)$ over an annular ring of radius k and width dk:

$$E(k) = \pi k U(k) \quad . \tag{2.8}$$

The one-dimensional spectral densities F_1, G_1, H_1, and E_1 can also be expressed in terms of $U(k)$ and k (Leith, 1971):

$$F_1(k_1) \;=\; 2\int_{k_1}^\infty (k_2/k)\, U(k)\,\mathrm{d}k \quad , \tag{2.9}$$

$$G_1(k_1) \;=\; 2k_1^2 \int_{k_1}^\infty (1/kk_2)\, U(k)\,\mathrm{d}k \quad , \tag{2.10}$$

$$H_1(k_1) \;=\; 0 \quad , \tag{2.11}$$

$$E_1(k_1) \;=\; 2\int_{k_1}^\infty (k/k_2)\, U(k)\,\mathrm{d}k \quad . \tag{2.12}$$

Leith (1971) then showed the important result that if the two-dimensional energy spectrum satisfies a -3 power law, i.e., $E(k) = Ak^{-3}$, the one-dimensional energy spectra will satisfy similar power laws in terms of the one-dimensional wavenumber k_1:

$$F_1(k_1) = (1/8)Ak_1^{-3} , \tag{2.13}$$

$$G_1(k_1) = (3/8)Ak_1^{-3} , \tag{2.14}$$

$$E_1(k_1) = (1/2)Ak_1^{-3} , \tag{2.15}$$

These equations provide the link between observed one-dimensional energy spectra and two-dimensional theory.

Isotropy

Given the important role that isotropy plays in two-dimensional turbulence theory, how close to isotropic is the real atmosphere? Using the Kármán-Howarth equation for two-dimensional nondivergent turbulence, it can be shown (Ogura, 1952) that

$$G_1(k_1) = -k_1 \frac{d}{dk_1} F_1(k_1) . \tag{2.16}$$

Ogura (1958) used this relationship to compare observed G_1 spectral densities with ones computed from observed F_1 densities. He found fairly good agreement for the two curves at wavenumbers k_1 of 6 and greater based on one-dimensional longitudinal spectra at 20°N, 40°N, and 70°N for the months of January and February, 1949. Values of the cospectrum function $H_1(k_1)$ were an order of magnitude smaller than $G_1(k_1)$ at these wavenumbers. Leith (1971) performed a similar comparison on longitudinal spectra published by Kao and Wendell (1970) and found approximate isotropy for wavenumbers $k_1 > 10$.

Boer (1983) showed that the spherical harmonic coefficient ψ_n^m for the random two-dimensional streamfunction ψ will be independent of the order m if ψ is isotropic. He also showed that homogeneity and isotropy are equivalent conditions on the sphere. Boer and Shepherd (1983) found ψ_n^m to be roughly independent of m for $n \gtrsim 10$

for KE and to a lesser degree for APE. Shepherd (1987) extended this analysis further by decomposing the flow field into stationary and transient components. He found the transient modes to exhibit approximate isotropy even at the largest scales of motion for FGGE January 1979 global data.

Morel and Larcheveque (1974) examined this question from a quite different perspective. They considered the relative dispersion of Eole experiment balloons and concluded that isotropy was a good assumption for scales of less than 1500 km but that anisotropy became significant at larger scales. Desbois (1975) obtained similar conclusions from an Eulerian analysis of balloon-derived winds based on the Eole experiment data set. Kao (1974) also reported evidence for large-scale anisotropy based on the analysis of simulated isobaric trajectories constructed for clusters of particles advected and dispersed using gridded, objectively-analyzed NMC 500-hPa wind fields.

2.1.4 Geostrophic turbulence

Despite the apparent support from spectral analyses of large-scale meteorological data for the existence of a k^{-3} enstrophy cascade as postulated by Kraichnan (1967), it was not clear that two-dimensional turbulence was the best model of large-scale atmospheric energetics. Baroclinic instability, an important large-scale energy source, requires three-dimensional motions. The 'equivalent barotropic' models employed in early numerical weather prediction (NWP) efforts were essentially two-dimensional models but were soon superseded by more realistic three-dimensional baroclinic models (e.g., Haltiner, 1971). To quote Charney (1971, p. 1088):

> Observations show that the main synoptic-scale motions in the atmosphere are decidedly baroclinic, with vertical variations in velocity, temperature, etc., through the depth of the troposphere as great as the horizontal variations. In general, changes in the vertical vorticity component are as much due to vertical stretching of the vortex tubes of the Earth's rotation as to horizontal advection. The similarity observed between the observed spectrum and that of two-dimensional flow would thus seem to be somewhat fortuitous.

However, Charney (1971) pointed out a deeper similarity between three-dimensional, *quasi-geostrophic* flows and purely two-dimensional flows. Quasi-geostrophic flows, like

two-dimensional flows, are governed by the conservation of two scalar invariants. For quasi-geostrophic flows these invariants are *pseudo-potential vorticity*, a combination of potential vorticity and potential temperature, and *total energy*, i.e., KE plus available potential energy (APE). Charney then went on to show that the conservation of pseudo-potential vorticity forbids a downscale energy cascade under certain conditions. Once this analogy was established, all other theorems applying to energy exchanges amongst spectral components in two-dimensional flows could then be shown to apply to three-dimensional quasi-geostrophic flows as well, including a k^{-3} downscale enstrophy cascade.

Charney derived several additional properties of what he termed 'geostrophic turbulence'. He showed that by proper scaling the vertical coordinate $\zeta = Nf_0^{-1}z$ could be made to appear completely symmetric with the horizontal coordinates, except for boundary conditions. This then suggested that in the k^{-3} inertial range, the energy spectrum for each of the three components would have the same form and same fluctuation energy. Upon rescaling, this symmetry implies that (i) the APE will be one-half the KE and (ii) temperature variance will also have a k^{-3} spectrum in the enstrophy-cascade inertial range. The problem of the temperature variance spectral slope had been raised by Saunders (1972) but could not be addressed by simple two-dimensional turbulence theory. Charney also showed that, assuming local isotropy, $G_1(k_1)$, the longitudinal spectral density for the transverse (or meridional) velocity component v, should be larger than $F_1(k_1)$, the longitudinal spectral density of the longitudinal (or zonal) velocity component u, by a factor of three as a result of the Kármán–Howarth relation (see Eq. 2.15). Lesieur (1990) gives a short overview of this topic.

Observational evidence

Since two-dimensional and geostrophic turbulence theory both predict k^{-3} spectral slopes for KE in the enstrophy inertial range, the supportive observational studies listed in the earlier section on two-dimensional turbulence apply equally to geostrophic turbulence. What about the unique properties of geostrophic turbulence? Charney (1971) cited the results of Kao (1970), which showed a k^{-3} spectrum for temperature variance, and

plotted some results of Kao not shown in Kao's paper. Charney also presented analyzed temperature spectra from a 10-day simulation made with a six-level general circulation model (GCM) which were consistent with a k^{-3} slope.

Baer (1974), Chen and Wiin-Nielsen (1978), Lambert (1981), and Boer and Shepherd (1983) have each carried out hemispheric or global spectral analyses of APE variance (which is proportional to temperature variance; see Charney, 1971). Fig. 2.1 shows vertically-averaged global KE and APE spectra obtained by Boer and Shepherd (1983) using two months of data from 1979 (see also Shepherd, 1987). There is an APE power-law range evident at higher two-dimensional wavenumbers but it is less steep than -3. Boer and Shepherd pointed out too that the slope steepness tends to increase with increasing atmospheric height, reaching a maximum in the upper troposphere. Fig. 2.2 compares their results with those of Baer (1974) and Chen and Wiin-Nielsen (1978); it is evident that spectral slope over a restricted wavenumber range is sensitive both to height and to differences in the data used in different studies. It is also worth noting the following cautionary comment made by Boer and Shepherd (1983, p. 172) in discussing their results:

> It must be emphasized, however, that the enstrophy-cascading inertial range is not really a prediction for the atmosphere but is a possible solution to the spectral equation in an unforced subrange which may or may not have some correspondence to the situation in the real atmosphere. Consequently, the fact that the spectra obey power laws at all may be considered to be a striking, although by now well known, feature of the atmosphere.

Interestingly, Morita and Uryu (1989) recently reported temperature spectra from geostrophic turbulence simulations in a laboratory rotating annulus which obeyed an f^{-3} power law over frequency in the enstrophy inertial range, providing independent support for this phenomenon.

Charney (1971) further proposed an equipartition of energy between the two horizontal components of KE and APE based on local isotropy. He presented u, v, and T spectra from both Northern Hemisphere observations and GCM simulations which indicated approximate energy equipartition. The results of Boer and Shepherd (1983),

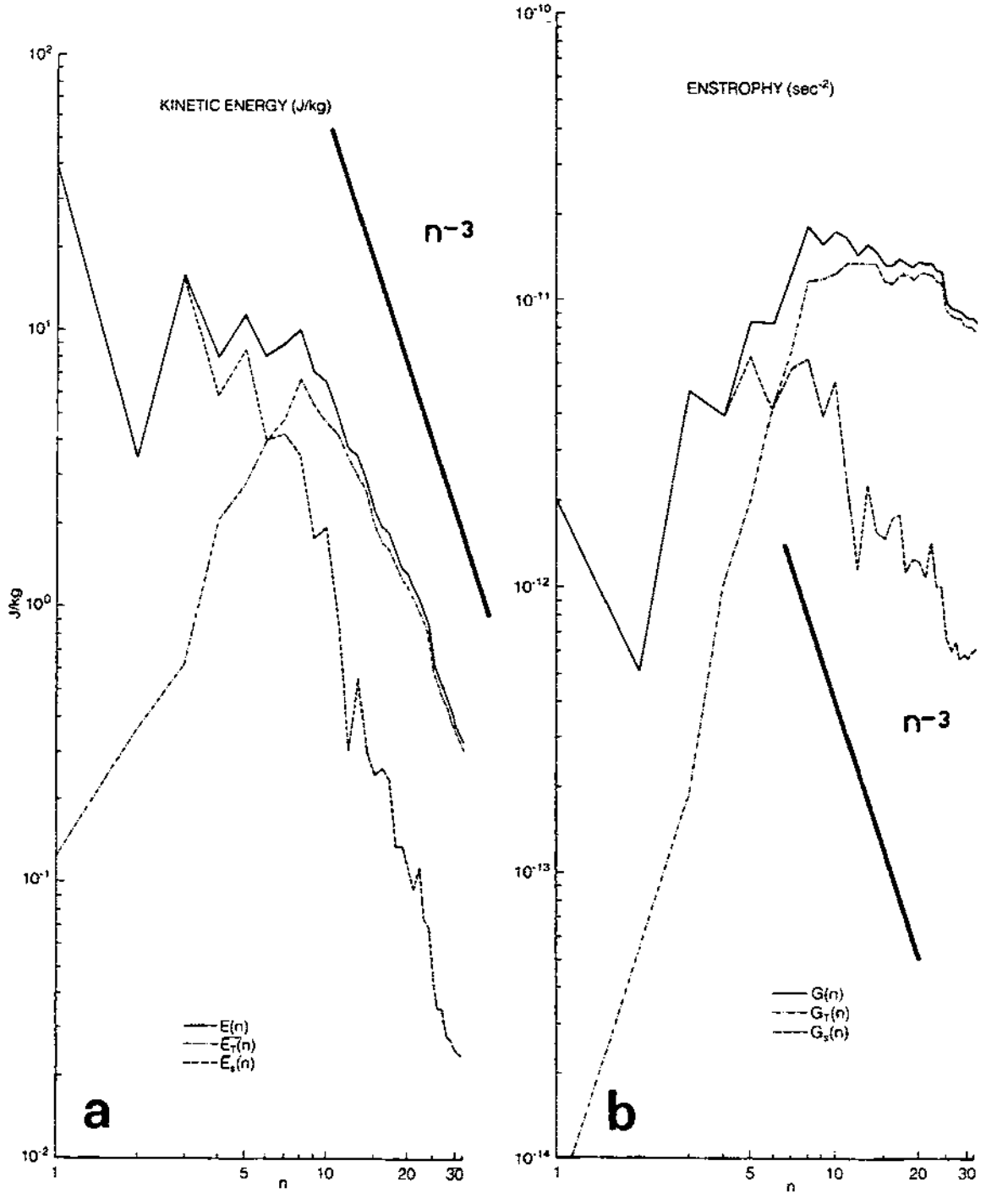

Figure 2.1: Vertically-averaged (1000-50 hPa) wavenumber spectra of (a) KE and (b) APE for January and July 1979 from FGGE-IIIa global data set. The abscissa is in terms of spherical two-dimensional wavenumber n. Lines with n^{-3} slope have been added for purposes of comparison (adapted from Boer and Shepherd, 1983).

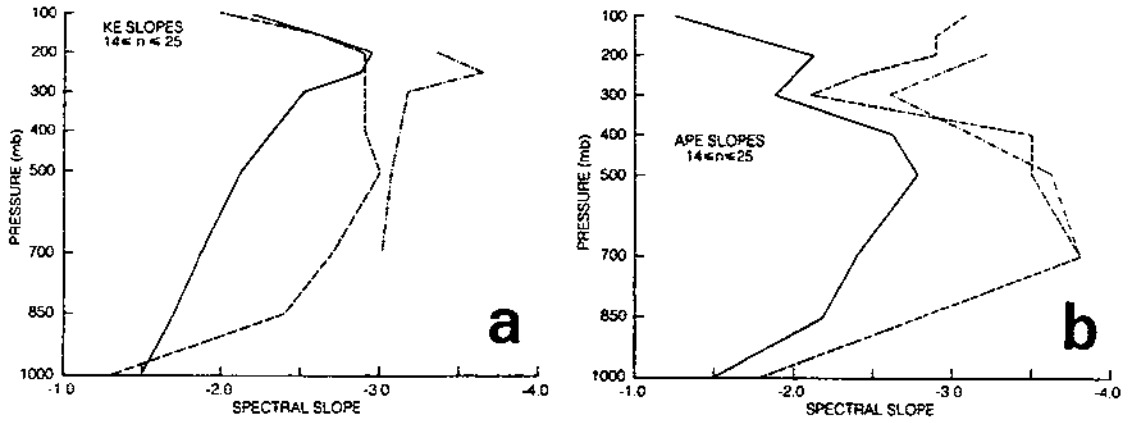

Figure 2.2: Comparison of slopes of straight lines fitted to (a) KE spectra and (b) APE spectra in the wavenumber range $14 \leq n \leq 25$ in three large-scale spectral energetics studies: dash-dotted line – Baer (1974); dashed line – Chen and Wiin-Nielsen (1978); solid line – Boer and Shepherd (1983) (from Boer and Shepherd, 1983).

based on more extensive observations, also indicated approximate energy equipartition. Boer and Shepherd showed in addition that the uv cospectrum term is small at higher wavenumbers (n = 10–30), providing additional support for the existence of an approximately homogeneous and isotropic large-scale turbulence regime. Hutchings (1955), Buell (1957), Ogura (1958), and Shepherd (1987) also presented observations in support of large-scale horizontal *quasi*-isotropy. However, it must be borne in mind that the poleward horizontal fluxes of angular momentum provided by large-scale horizontal eddies and required to maintain the atmospheric general circulation (e.g., Starr, 1968) would be zero in a perfectly isotropic flow field.

Besides a k^{-3} KE spectral slope, energy equipartition, and isotropy, a two-dimensional enstrophy-cascading inertial subrange also requires a spectral region with no sources and sinks of energy, zero spectral KE flux, and a constant spectral enstrophy flux. Chen and Wiin-Nielsen (1978) and Boer and Shepherd (1983) calculated KE, enstrophy, and APE nonlinear interaction terms and fluxes in two-dimensional wavenumber space. Their results showed that KE and enstrophy are exported from intermediate scales (say $8 \leq n \leq 14$) with a large sink of KE at low wavenumbers and of enstrophy of high

wavenumbers, consistent with the concepts of Fjørtoft (1953) and Kraichnan (1967). Chen and Wiin-Nielsen (1978) concluded that zero KE flux and constant enstrophy flux are not evident at higher wavenumbers, but Boer and Shepherd (1983) pointed out that the use of a truncated harmonic expansion in the analysis resolved only a portion of the nonlinear interactions and fluxes. By applying a parameterization suggested by Leith (1971) to estimate the unresolved high-wavenumber contributions, Boer and Shepherd determined that the estimated net (i.e., sum of resolved and parameterized unresolved components) KE flux is quite close to zero for higher wavenumbers while the estimated net enstrophy flux appears to be flattening out at $n = 32$. In contrast to the high-wavenumber regime, which varies little between summer and winter, Boer and Shepherd's results showed that the low-wavenumber regime $(1 \leq n \leq 5)$ is dominated by the stationary component of the flow, shows significant anisotropy and lack of energy equipartition, and changes markedly from summer to winter. None of the features expected of a reverse-cascade energy inertial range are evident at these planetary scales except for a strong upscale flux of KE.

2.1.5 Mesoscale turbulence

To this point we have discussed theoretical models for three spectral subregions of atmospheric turbulence: a three-dimensional downscale energy inertial range ($k^{-5/3}$ law), a two-dimensional downscale enstrophy inertial range (k^{-3} law), and a two-dimensional upscale energy inertial range ($k^{-5/3}$ law). The characteristics and spectral locations of any inertial range will be determined by the characteristics and spectral locations of its source and sink regions.

The small-scale, three-dimensional Kolmogorov inertial range is, in general, limited to spatial scales on the order of 100 m or smaller (Batchelor, 1950; Kaimal et al., 1976; Gage, 1979), although this range may be expanded upscale somewhat under strongly convective conditions when vertical velocities are significant. Energy is injected by large anisotropic eddies associated with boundary-layer thermals, cumuliform clouds, and wind shear, cascades through the isotropic $k^{-5/3}$ Kolmogorov inertial range, and is dissipated

on scales of millimeters and centimeters. The k^{-3} enstrophy-cascade inertial range obtains its energy from transient extratropical cyclones generated by baroclinic instability at planetary longitudinal wavenumbers m between 4 and 10–15 (i.e., 2000–7000 km range in midlatitudes) and cascades down through the mesoscale. Indirect evidence from 200 hPa balloon pairs has suggested a k^{-3} law down to 100 km (Morel and Larcheveque, 1974), although as will be discussed shortly, a lower limit of 500 km appears more likely. Observations do not support the existence of a $k^{-5/3}$ reverse-energy-cascade inertial range at scales larger than those of baroclinic instability (e.g., Boer and Shepherd, 1983). However, a rapidly increasing body of evidence supports the existence of such an inertial range at the *lower* end of the mesoscale from several kilometers to several hundred kilometers.

The existence of such a mesoscale $k^{-5/3}$ reverse-cascade inertial range was apparently first inferred by Golitsyn (1974) and Gage (Gage and Clark, 1978; Gage and Jasperson, 1979; Gage, 1979) based upon both previous studies and newly available measurements. I use the term 'inferred' because nearly all of the supporting evidence was time- or frequency-based. At this stage only a few Eulerian spatial velocity spectra were available, and these were somewhat unrepresentative, being based on aircraft measurements made in or near the tropospheric jet stream during clear-air turbulence (CAT) studies (see Table 2.1). However, these few spatial energy spectra did roughly follow a $k^{-5/3}$ law in the 50–500 km range (Pinus et al., 1967). Gage (1979) offered three types of evidence consistent with the existence of a mesoscale $k^{-5/3}$ law inertial range; two of these were also discussed by Golitsyn (1974).

Frequency spectra

First, mesoscale frequency spectra of atmospheric KE based on time series of winds from standard rawinsonde releases showed $f^{-5/3}$ law behaviour. If Taylor's 'frozen turbulence' transformation $x = Ut$ is used to convert these frequency spectra into wavenumber spectra, then the corresponding wavenumber or spatial spectra will exhibit $k^{-5/3}$ law behaviour (e.g., Taylor, 1938; Monin and Yaglom, 1975; Larsen et al., 1982). Gage refer-

enced the work of Pinus (1968) for Moscow area rawinsonde measurements. Vinnichenko and Dutton (1969) and Vinnichenko (1970) reported similar results for rawinsonde data from Kharkov in Ukraine. Note that this evidence hinges upon the validity of the the Taylor hypothesis at these scales (see Sec. 2.1.7). Vinnichenko and Dutton (1969) and Vinnichenko (1970) also included Lagrangian frequency spectral measurements made by Mantis (1963).

Temporal variability

Gage's second set of evidence (also briefly discussed by Golitsyn) was based on observations of mesoscale atmospheric variability $\sigma_l(\xi)$. This quantity is defined as

$$\sigma_l^2(\xi) \;=\; D_l(\xi) \;=\; \overline{[u(t) - u(t+\xi)]^2} \quad , \tag{2.17}$$

where ξ is a lag time, $D_l(\xi)$ is the Eulerian temporal structure function for the longitudinal velocity component and the overbar denotes a time average. Comparable expressions may be written for the transverse and vertical velocity components. For stationary turbulence, Eq. 2.17 may be written as

$$\sigma_l^2(\xi) \;=\; D_l(\xi) \;=\; 2\overline{(u')^2}\,[1 - R_u(\xi)] \quad , \tag{2.18}$$

where $u' = u - \overline{u}$ and the Eulerian velocity autocorrelation function $R_u(\xi)$ is defined as

$$R_u(\xi) = \frac{\overline{u'(t)\,u'(t+\xi)}}{\overline{(u')^2}} \quad . \tag{2.19}$$

One consequence of Kolmogorov's (1941) first[35] and second[36] similarity hypotheses is that in the three-dimensional inertial range the Eulerian *spatial* structure functions for

---

[35] "At sufficiently high Reynolds numbers there is a range of high wavenumbers where the turbulence is statistically in equilibrium and uniquely determined by the parameters ϵ and ν. This state of equilibrium is *universal*" (Hinze, 1975, p. 223; also Batchelor, 1950).

[36] "If the Reynolds number is infinitely large, the energy spectrum in the subrange satisfying the condition $k_e \ll k \ll k_d$ is independent of ν, and is solely determined by one parameter ϵ" (Hinze, 1975, p. 226; also Batchelor, 1950)

the longitudinal and transverse components of velocity will have the following form (e.g., Batchelor, 1950; Monin and Yaglom, 1975; Gage, 1979):

$$D_l(r) = A_l \epsilon^{2/3} r^{2/3} , \tag{2.20}$$

$$D_t(r) = A_t \epsilon^{2/3} r^{2/3} , \tag{2.21}$$

where A_l and A_t are universal constants ($A_t = 4A_l/3$ in an incompressible fluid), ϵ is the eddy dissipation rate per unit mass, and r is the separation distance. These so-called 'two-thirds' laws for the Eulerian inertial-range structure functions are equivalent to the 'five-thirds' law followed by the inertial-range KE spectrum (Monin and Yaglom, 1975). If we now employ the Taylor transformation $r = \overline{u}\xi$, where ξ is the separation time, we can rewrite the Eulerian temporal structure functions as

$$D_l(\xi) = A_l \overline{u}^{2/3} \epsilon^{2/3} \xi^{2/3} , \tag{2.22}$$

$$D_t(\xi) = A_t \overline{u}^{2/3} \epsilon^{2/3} \xi^{2/3} , \tag{2.23}$$

implying that in the three-dimensional inertial range the temporal variabilities σ_l and σ_t will follow a $\xi^{1/3}$ power law provided that the Taylor transformation is valid (see Sec. 2.1.7).

A number of studies have shown that temporal variability $\sigma(\xi)$ follows a $\xi^{1/3}$ power law even over mesoscale periods (Hutchings, 1955; Ellsaesser, 1969b; Gage and Clark, 1978; Gage and Jasperson, 1979). Assuming the Taylor transformation to be valid, this suggests that the spatial 'two-thirds' law is also valid and hence that a $k^{-5/3}$ inertial range exists at these larger scales. Hutchings (1955), Ellsaesser (1969b), and Gage and Jasperson (1979) analyzed time series of winds from the surface to 300 hPa obtained by successive balloon releases while Gage and Clark (1978) used a VHF Doppler radar to sample winds at 1 km intervals from 5 to 13 km. These papers are discussed in more detail in Sec. 2.1.6.

Scale-dependent diffusion

The third type of evidence presented by Gage (and Golitsyn) in support of a two-dimensional mesoscale inertial range were observations of scale-dependent atmospheric diffusion at mesoscale distances (see also Sec. 2.3.2). Both scale-dependent eddy diffusivities $K \propto L^{4/3}$ (Richardson, 1926) and dispersion $\overline{x^2} \propto t^3$ are consistent with a $k^{-5/3}$ law inertial range (e.g., Batchelor, 1950; Monin and Yaglom, 1975). However, many of the relative diffusion observations following these relationships corresponded to scales far larger than the classical three-dimensional inertial subrange (e.g., Gifford, 1977, 1983).

Supporting frequency-domain measurements

Gage's hypothesis received qualified support as papers presenting tropospheric KE frequency spectra obtained from Doppler radar measurements began to appear in the literature. These instruments are also referred to as wind profilers, ST (stratosphere-troposphere) radars, or MST (mesosphere-stratosphere-troposphere) radars, depending upon their operating characteristics. They are discussed further in Sec. 2.1.6. Table 2.1 provides a summary of such wind-profiler spectral measurements to date as well as mesoscale energy spectra determined by other measurement techniques.

Balsley and Carter (1982) found a good fit to a $f^{-5/3}$ power law for a smoothed composite frequency power spectrum of zonal winds averaged over a 2.2 km thick layer centered at 8 km. The winds were measured by the Poker Flat MST radar in Alaska for an 83-day summer period (5 June–27 August 1979). The frequency range was roughly 3 minutes to 8 days. Larsen et al. (1982), in a complementary study, presented zonal and meridional KE frequency power spectra for five 2.2 km thick layers centered at 6.0, 8.2, 10.4, 12.6, and 14.8 km. The wind-component time series in this study were also obtained using the NOAA MST radar at Poker Flat, Alaska but for a different period: 42 days from 23 February to 5 April 1979. The resulting frequency range extended from 2 to 40 hours. Least-squares linear fits to the log-log spectral plots gave average slopes of -1.6 for both zonal and meridional spectra, very close to a $f^{-5/3}$ power law, while

Table 2.1: Summary of mesoscale velocity spectral measurements.

Variable	Spectrum Type	Measurement Method	Atmospheric Region	References
u, v	horizontal wavenumber	aircraft	PBL	Pinus et al. (1967), Lenschow et al. (1988b)
		aircraft	troposphere	Kao & Woods (1964), Pohle et al. (1965), Reiter & Burns (1966), Pinus et al. (1967), Hsueh (1968), Pinus (1977), Nastrom & Gage (1983, 1985), Lilly & Petersen (1983), Nastrom et al. (1984, 1987), Jasperson et al. (1990)
		aircraft	stratosphere	Axford (1971), Lilly & Lester (1974), Dewan (1979), Pinus (1979), Nastrom & Gage (1983, 1985), Nastrom et al. (1987), Jasperson et al. (1990)
		sodar	PBL	Masmoudi & Weill (1988)
		balloon	troposphere	Julian et al. (1970), Julian & Cline (1974), Desbois (1975), Brown & Robinson (1979)
		dual Doppler radar	PBL	Doviak & Berger (1980), Eilts et al. (1984)
		lidar	PBL	Eilts et al. (1984)
u, v	vertical wavenumber	balloon	troposphere	Endlich et al. (1969)
		smoke trail	stratosphere	Dewan et al. (1984)
u, v	frequency	balloon	PBL	Hess & Clarke (1973)
		balloon	troposphere	Mantis (1963)
		rawinsonde	troposphere	Kao (1965), Pinus (1968), Vinnichenko & Dutton (1969), Vinnichenko (1970)
		tower	PBL	Panofsky & Van der Hoven (1956), Van der Hoven (1957), Oort & Taylor (1969), Hwang (1970), Fiedler (1971), Lyons (1975), Smedman-Högström & Högström (1975), Courtney & Troen (1990), Mori (1990)

* radial line-of-sight velocity

Table 2.1: (cont'd) Summary of mesoscale velocity spectral measurements.

Variable	Spectrum Type	Measurement Method	Atmospheric Region	References
		wind profiler	troposphere/ stratosphere	Nastrom & Gage (1990), Frisch et al. (1991)
V_r^*	radial wavenumber	wind profiler	troposphere/ stratosphere	Larsen et al. (1982, 1986), Scheffler & Liu (1985), Fritts et al. (1988)
		wind profiler	mesosphere	Smith et al. (1985)
V_r	frequency	wind profiler	troposphere	Balsley & Carter (1982), Larsen et al. (1982, 1986), Scheffler & Liu (1985)
		wind profiler	stratosphere	Larsen et al. (1982, 1986)
w	horizontal wavenumber	aircraft	PBL	Young (1987), Lenschow et al. (1988b)
		aircraft	troposphere	Reiter & Burns (1966), Kuettner et al. (1987)
		aircraft	stratosphere	Axford (1971), Lilly & Lester (1974)
w	vertical wavenumber	balloon	troposphere/ stratosphere	Sidi et al. (1988)
		wind profiler	troposphere/ stratosphere	Larsen et al. (1987)
		wind profiler	mesosphere	Smith et al. (1985)
w	frequency	balloon	PBL	Hess & Clarke (1973)
		balloon	troposphere/ stratosphere	Sidi et al. (1988)
		wind profiler	troposphere	Balsley & Carter (1982), Ecklund et al. (1986), Gage et al. (1986), Larsen et al. (1987)
		wind profiler	stratosphere	Ecklund et al. (1986), Gage et al. (1986), Larsen et al. (1987)
		wind profiler	mesosphere	Balsley & Carter (1982), Gage et al. (1986)
$\partial V/\partial z$	vertical wavenumber	balloon	stratosphere	Barat & Cot (1989)

plots of temporal variabilities $\sigma_u(\xi)$ and $\sigma_v(\xi)$ were fit reasonably well by a $\xi^{1/3}$ power law.

Possible energy transfer mechanisms

Note again that *a priori* there is no theoretical reason to expect $f^{-5/3}$ or $\xi^{1/3}$ power laws, but *if* the Taylor transformation is valid for this mesoscale frequency range, then such results imply a $k^{-5/3}$ power law in wavenumber space. A $k^{-5/3}$ law mesoscale spectrum could in turn imply a mesoscale reverse-energy-cascade inertial range as suggested by Gage (1979). However, a competing hypothesis based on a spectrum of propagating, interacting internal gravity waves may also explain this spectral shape (Dewan ,1979; VanZandt, 1982).

Although mean power spectra 'average out' a large amount of temporal variability, they still provide considerable insight into the dominant dynamics at the measurement level. Balsley and Carter (1982, p. 467) noted that "...the continuous distribution of spectral energy over the complete range of observed frequencies suggests strongly that local nonlinear coupling processes are operative throughout the atmosphere at periods between a few minutes and many hours" since "...(in the absence of local energy sources) a constant spectral slope cannot be maintained over such a height range in a real, dissipative atmosphere without continuous energy exchange between wavelengths". They then discussed two mechanisms which could drive such energy exchanges: turbulent cascade processes as suggested by Gage (1979) and nonlinear interactions between propagating gravity waves as suggested by Dewan (1979). Larsen et al. (1982) raised the same two possibilities and referred to theoretical advances by VanZandt (1982) and Lilly (1983a).

Both of these energy-exchange mechanisms gained adherents and for the rest of the 1980s the two competing camps struggled to enshrine their respective mechanism as orthodoxy. While an explanation invoking turbulent processes might seem more familiar to most meteorologists initially, the reverse turbulent cascade mechanism poses some conceptual problems. For example, if we assume a $20\ \mathrm{m\,s^{-1}}$ mean advecting flow, then by Taylor's transformation a 10^{-4} Hz oscillation ($\sim$ 3 hours) corresponds to a spa-

tial scale of 200 km (Balsley and Carter, 1982). 'Turbulence' on this scale must be strongly anisotropic yet unlike Charney's quasi-two-dimensional geostrophic turbulence with its k^{-3} power spectrum. Moreover, a cumulus-scale source of energy which is quasi-continuous and widely distributed is needed to drive this upscale energy cascade. Lilly (1983a) proposed a theoretical model of mesoscale two-dimensional turbulence which addresses these concerns. He hypothesized that a fraction of the three-dimensional turbulent energy created at small scales by convective and shearing instabilities 'leaks' upscale to form quasi-two-dimensional 'stratified turbulence' or 'vortical modes' in a process analogous to the 'wake collapse' phenomenon in a stratified environment (e.g., Lin and Pao, 1979). Vortical modes and the Gage–Lilly model are discussed in more detail in Sec. 2.1.9.

The alternate model suggested by Dewan (1979) is based on an internal-gravity-wave energy cascade. Dewan argued that the Kelvin-Helmholtz instability, the primary source of turbulence in the upper troposphere and lower stratosphere, will typically have a maximum inertial-range wavelength of 20 m in the stratosphere, far too small to explain mesoscale stratospheric $k^{-5/3}$ law velocity fluctuations as measured, for instance, by a U-2 aircraft (see Dewan's Fig. 1). He proposed instead that propagating internal gravity waves (IGW) could be trapped or ducted inside finite layers through the combined effects of wind and Brunt-Väisälä frequency variations with altitude and then trigger Kelvin-Helmholtz instability through the enhanced shear at wave crests and troughs. To summarize this concept, Dewan (1979, p. 834) paraphrased Richardson's (1922) famous rhyme about the Kolmogorov inertial range (which predated Kolmogorov by 20 years): "big waves have little waves that feed on deformation, and little waves have lesser waves to turbulent dissipation (in the eddy sense)." If Kolmogorov's dimensional arguments are applied, then this IGW downscale energy cascade will also produce a $k^{-5/3}$ inertial range.

Building upon Dewan's model, VanZandt (1982) noted the resemblance of available atmospheric mesoscale fluctuation spectra to oceanic mesoscale (or fine-structure) spectra, the latter which had recently been explained by a model based on IGW theory (Garrett and Munk, 1972, 1975, 1979). VanZandt then modified the Garrett–Munk model slightly

to describe atmospheric mesoscale spectra in terms of a universal IGW spectrum. The spectral frequency range of relevance is from the inertial period $2\pi/f$ to the Brunt-Väisälä period N. This IGW model is discussed further in Sec. 2.1.8.

Conceptual mesoscale energy spectrum model

Although the exact nature of the dominant energy exchange mechanism operating in the $-5/3$ mesoscale inertial range was unknown, Larsen et al. (1982) presented a schematic mesoscale energy spectrum illustrating this new view of mesoscale energetics (Fig. 2.3).

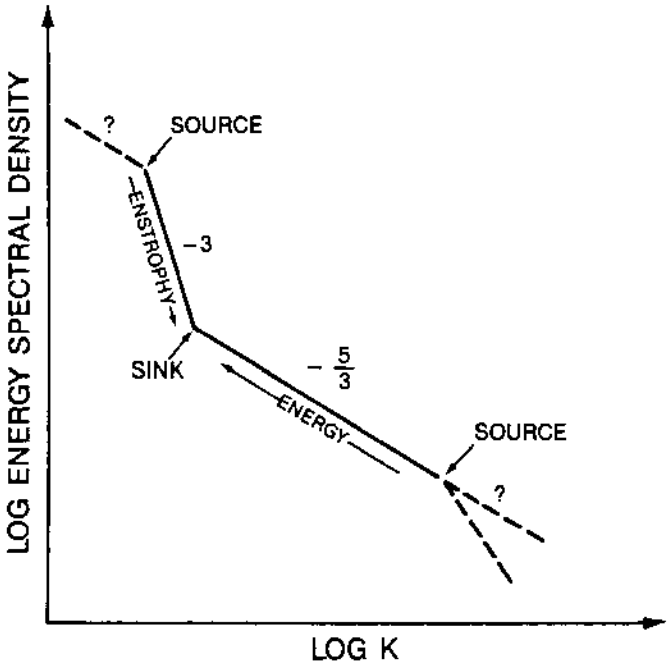

Figure 2.3: Schematic representation of spectral ranges in quasi-two-dimensional turbulence (from Gage and Nastrom, 1986a, after Larsen et al., 1982).

This schematic spectrum included two primary energy input regions (cyclone-scale and cumulus-scale) and two inertial ranges (k^{-3} law enstrophy cascade and $k^{-5/3}$ law reverse energy cascade). One important consequence of the existence of the $k^{-5/3}$ reverse-cascade inertial range is that much more KE is present at higher mesoscale wavenumbers than can be explained by the decay of geostrophic turbulence (Lilly, 1983a). Gage and Nastrom (1985b) argued that the mesoscale energy spectrum is important for a number of

reasons. First, it reveals much about mesoscale wave and turbulence dynamics. Second, it is important for numerical weather prediction (NWP) from the point of view of predictability and subgrid-scale parameterization. Third, it provides a quantitative measure of the 'noise' background against which the representativeness of all atmospheric wind measurements are evaluated (Lilly, 1984). Such mesoscale spectra also provide a description of mesoscale variability (Lilly, 1983b). The nature and exact spectral location of the transition region connecting the two mesoscale inertial ranges was unclear in the early 1980s. However, more recent mesoscale turbulence measurements have provided strong support for this conceptual model and have cleared up some of the uncertainties.

Wavenumber-domain measurements

In 1983, the first two of a now sizeable number of papers describing direct aircraft measurements of 'climatological' mesoscale spatial spectra for various parameters were published. Some aircraft-based mesoscale velocity spectra had been published previously but these were obtained from short-term, geographically-fixed studies, often in support of clear-air turbulence research (Kao and Woods, 1964; Pohle et al., 1965; Hsueh, 1968; Axford, 1971; Pinus, 1977, 1979; Dewan, 1979; Vinnichenko et al., 1980). Nastrom and Gage (1983) and Lilly and Petersen (1983) presented preliminary analyses of atmospheric KE wavenumber spectra based on wind velocity measurements collected by long-haul commercial jet airliners. Since then additional papers based on more extensive commercial flight data have been published by Nastrom et al. (1984, 1986a, 1987), Nastrom and Gage (1985), Gage and Nastrom (1986a,b) and Jasperson et al. (1990). Table 2.1 provides a listing of published mesoscale velocity spectra based both on aircraft measurements and on other observational techniques.

All of the recent aircraft measurements were made by Boeing 747 airliners in routine commercial service. Horizontal wind measurements were taken from the standard aircraft navigation system based on data from the inertial navigation system and conventional dynamic and static pressure sensors. Winds were recorded to the nearest knot (about 0.5 $\mathrm{m\,s^{-1}}$) and degree and have a random error of about 5% (Nastrom and Gage,

1985). No side-slip angle measurements were available. With the exception of the data analyzed by Lilly and Petersen (1983), all of these long-haul aircraft data were collected from 1975–1979 during the observational phase of NASA's Global Atmospheric Sampling Program (GASP).

GASP measurements. GASP research instruments were placed aboard up to four Boeing 747s to measure *temperature* (Rosemount temperature sensor), *ozone* (ultraviolet absorption photometer), *water vapour* (chilled-mirror dew/frost-point hygrometer), and *carbon monoxide* (infrared absorption analyzer using dual-isotope fluorescence) (Nastrom et al., 1986a). The GASP data were recorded on cassette tapes at all times during aircraft flight above 6 km. Most measurements (about 80%) were collected at cruising altitudes between 9 and 14 km, corresponding to either the upper troposphere or lower stratosphere depending upon latitude and season (Nastrom et al., 1984). The GASP data set contains records from over 6900 flights. These are distributed evenly amongst the twelve months. The flight tracks, however, tend to be clustered along certain geographic corridors (i.e., standard air routes) and about 80% of the data lies in the zonal band between 30°N and 55°N (Nastrom and Gage, 1985). Fig. 2.4 shows the global frequency distribution of GASP flights at least 2400 km in length (311 flights were over 10,000 km long).

On most flights, measurements were recorded every five minutes (a 75 km spacing for a nominal airspeed of 250 $\mathrm{m\,s^{-1}}$) while on 97 special flights, measurements were recorded every 4 s (nominal 1 km intervals). In addition, data were recorded every 4 s when the aircraft encountered moderate or stronger turbulence, defined as conditions when the vertical accelerometer reading fell outside the $0.8g$ to $1.2g$ range, where g is the acceleration due to gravity (Nastrom and Gage, 1983). Note that even these jet aircraft measurements were not true Eulerian spatial measurements since they were not gathered across the flow field instantaneously. It was still necessary to apply Taylor's transformation to obtain a spatial representation (this topic is discussed further in Sec. 2.1.7).

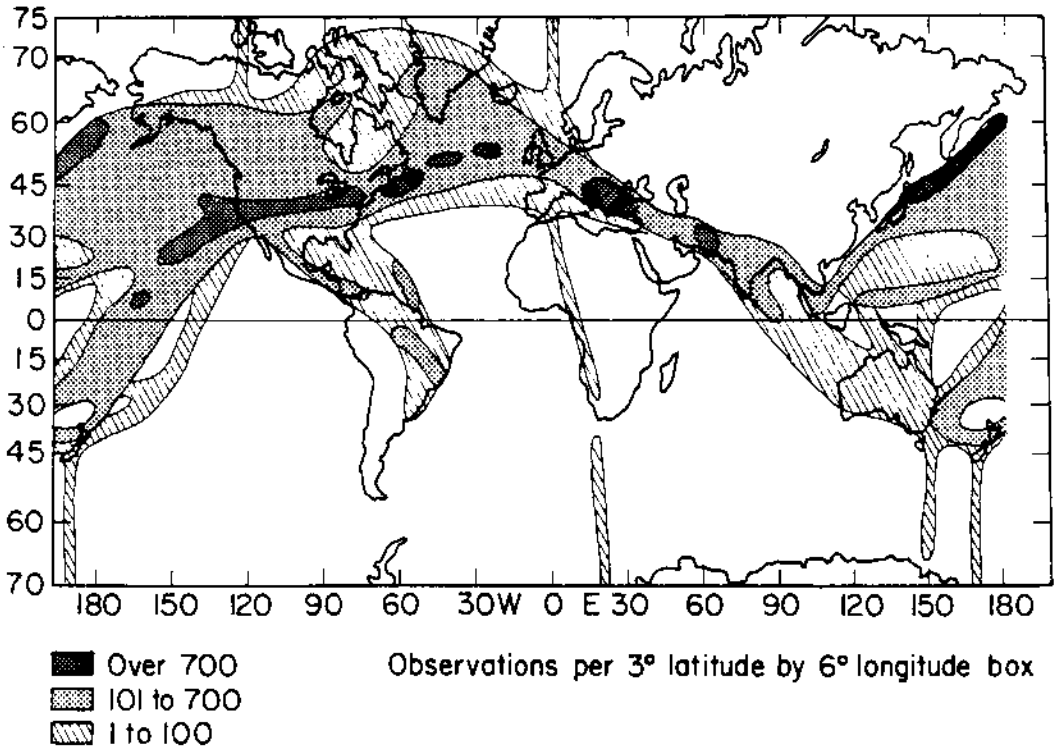

Figure 2.4: Geographical distribution of GASP observations from flight segments at least 2400 km long and with nominal spacing of 75 km (from Nastrom and Gage, 1985).

Measurement characteristics. A few peculiarities of the GASP measurements should be mentioned before considering the resulting spectra. In addition to the wind-speed measurement errors of about 5%, the wind speeds contain a sinusoidal (Schuler) error of period 84 minutes and random amplitude between 0 and 2.5 $m\,s^{-1}$ which arises from the electronic tuning of the inertial-navigation-system gyroscopes and accelerometers. According to Nastrom and Gage (1985), this error is not evident in the velocity spectra. However, the wind direction measurements also contain a spurious periodicity with near 30 s period (nominal 8 km wavelength), apparently connected to the one revolution per minute of the inertial navigation system platform; this effect does lead to an artificial local peak at high wavenumbers (Nastrom and Gage, 1983, 1985).

At high frequencies (on the order of 0.1 Hz or greater), the inertial and aerodynamic response of a large aircraft to small wind changes is less than 100% but the effect of this partial response is likely to be relatively small compared to the 5% measurement errors and one-half knot speed resolution (Nastrom and Gage, 1983). High-altitude aircraft also tend to 'bob', moving up and down as much as a few tens of meters with a period of about 20 minutes (nominal 300 km wavelength). This bobbing effect introduces spurious energy into the temperature and potential temperature spectra at high frequencies that cannot be corrected without detailed knowledge of local vertical temperature gradients. Both Nastrom and Gage (1985) and Nastrom et al. (1986a) investigated this problem. The latter determined that, outside of the tropics, the effects of aircraft bobbing will be overwhelmed by horizontal temperature variations and will contribute less than 10% of the total spectral energy, though the problem is more significant for tropical flights. Accordingly, no corrections were attempted.

Another complicating factor is that upon reaching cruising altitude, commercial aircraft tend to fly along a constant pressure surface for several hours, then climb about 600 m to a higher altitude after sufficient fuel has been burned. As a result, long flights are composed of between two and four constant pressure altitude segments. These altitude changes introduced discontinuities into the temperature and trace constituent data but

not the horizontal velocity data, restricting analysis of the former quantities to constant pressure altitude segments (Nastrom and Gage, 1985; Nastrom et al., 1986a). Finally, GASP data points were located relative to the tropopause (i.e., above or below) based on space-time interpolations from NMC 2.5° by 2.5° latitude-longitude analyses (Nastrom and Gage, 1985). This information permitted separate spectral analyses to be carried out for the troposphere and stratosphere, an important consideration since the roughly four times greater stratification of the stratosphere (Gage and Nastrom, 1986a) is likely to influence some flow fluctuations. However, the NMC grid values are relatively smooth and hence represent only large-scale fluctuations in tropopause height (Nastrom et al., 1986a).

GASP wavenumber spectra. Fig. 2.5 shows composite mean variance power spectra of zonal wind component, meridional wind component, and potential temperature based on measurements from selected GASP flights. Three sets of flight segments of different lengths and spatial resolution were analyzed in preparing this figure. The first set consisted of the 311 flights that were more than 10,000 km long. The average orientation of these flights was east-west and the average latitude was 50°N. The flight data were interpolated to 75 km intervals, single-flight power spectra were calculated, and then these spectra were averaged over all 311 flights for wavelengths between 150 km and 10,000 km. The second set consisted of 1492 flight segments of 150 km length from the 97 special GASP flights with high-frequency sampling (every 4 s). These data were interpolated to 1.3 km intervals and single-segment power spectra were calculated and then averaged over all segments for wavelengths between 2.6 km and 150 km. The average latitude of these 97 flights was 30°N. The third set of flight segments was selected to illustrate the continuity between the first two sets. It consisted of 39 flight segments of 1500 km length from the high-data-frequency flights. Average power spectra were calculated for wavelengths from 25 km to 1500 km. See Nastrom et al. (1984) and Nastrom and Gage (1985) for additional details.

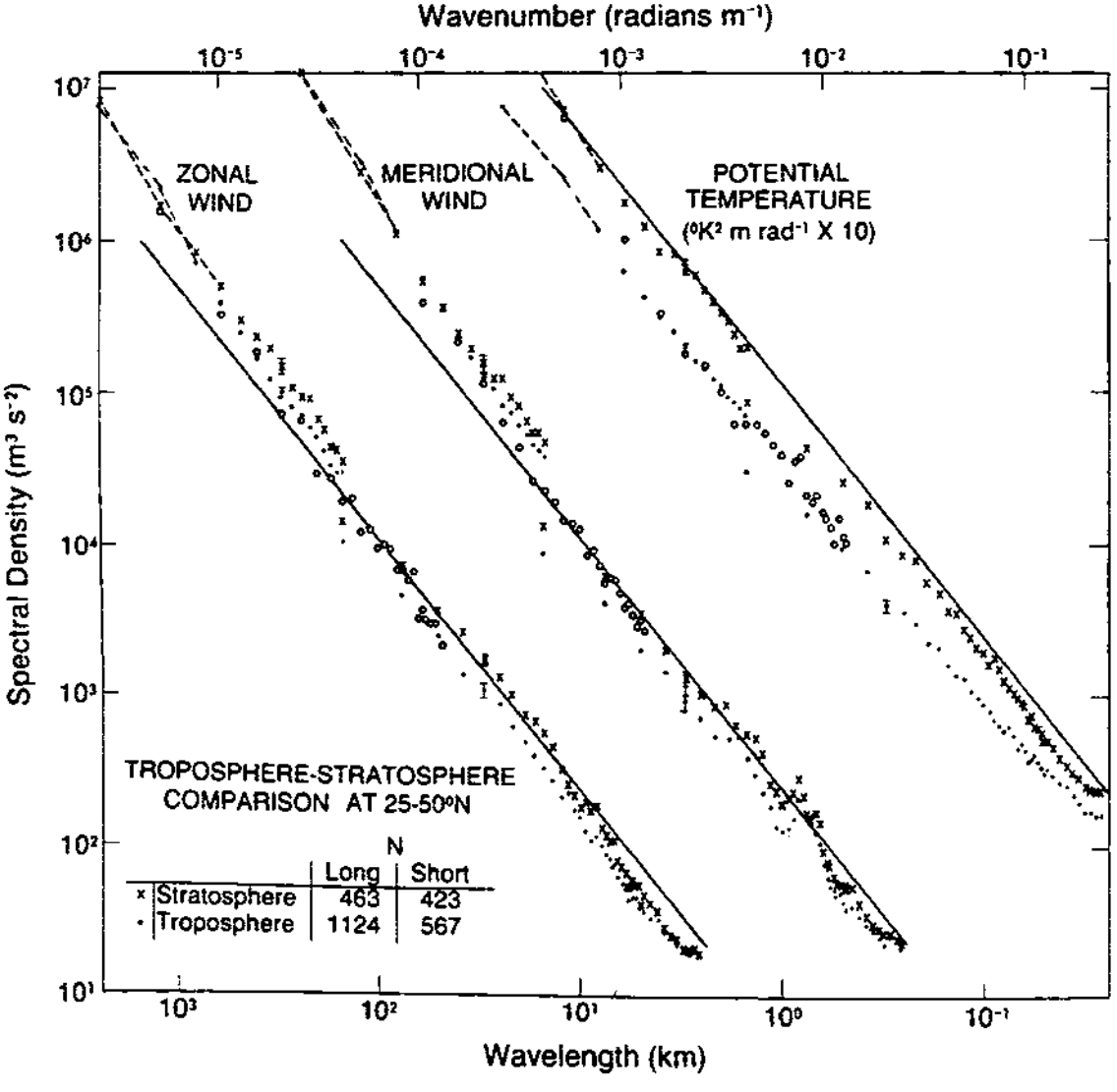

Figure 2.5: Variance power spectra of zonal and meridional wind components and potential temperature near the tropopause (both upper troposphere and lower stratosphere) from selected GASP aircraft data. The spectra for meridional wind and potential temperature are shifted one and two decades from the right, respectively. Lines with slope of -3 and $-5/3$ are entered at the same relative coordinates for each variable for comparison. Error bars are indicated for the 3000 km wavelength. Filled circles denote long-segment (150–10,000 km) data, plain crosses denote intermediate-segment (25–1500 km) data, and circled crosses denote short-segment data (from Nastrom and Gage, 1985; see also Nastrom et al., 1984).

Examining Fig. 2.5, we note first of all that the spectra are smooth and continuous over their entire range; there is no evidence of a broad spectral gap. There are also four spectral subregions evident. At the longest wavelengths, the spectral slopes do not obey an obvious power law. These scales correspond to the cyclone scales of baroclinic instability. In the wavelength range from about 1000 km to 3000 km, all three spectra have a slope of about -3. This is consistent with the downscale enstrophy-cascade inertial range of geostrophic turbulence proposed by Charney (1971). At wavelengths smaller than about 400 km, the spectra are fit very well by a $-5/3$ slope, consistent with Gage's hypothesized reverse-energy- cascade inertial range (see Fig. 2.3). The remaining wavelengths between about 400 km and 1000 km constitute a transition region between the 2 two-dimensional inertial ranges. Overall, these spectra agree very well with the conceptual model of Larsen et al. (1982) and are consistent with previous results (Fig. 2.6). Gifford (1988) recently proposed a simple model of the tropospheric turbulence KE spectrum based on the GASP data.

Standard deviations of the mean spectral estimates are about the same magnitude as the mean values at all wavelengths (Nastrom et al., 1984; Nastrom and Gage, 1985). Error bars approximating the 95% confidence intervals at all wavelengths are plotted in Fig. 2.5 for the 3000 km wavelength; they extend $\pm 2\sigma/M^{\frac{1}{2}}$ from the mean, where σ is the standard deviation of the spectral estimates over M flight segments (Nastrom and Gage, 1985; Nastrom et al., 1986a). Nastrom and Gage (1983) also prepared a special small-scale KE spectrum using only recorded episodes of moderate turbulence more than 17 km long in order to compare spectra for 'quiet' and 'turbulent' periods. As expected, the magnitude of the spectrum for the turbulent episodes was larger than for the quiet periods but the slope of the turbulent spectrum more nearly followed a k^{-1} line.

In constructing the zonal and meridional wind-component spectra shown in Fig. 2.5, Nastrom et al. (1984) used all suitable flight segments without regard to latitude, season, or location relative to the tropopause. Nastrom and Gage (1985) stratified the GASP data with respect to each of these factors to investigate their influence. They found the velocity

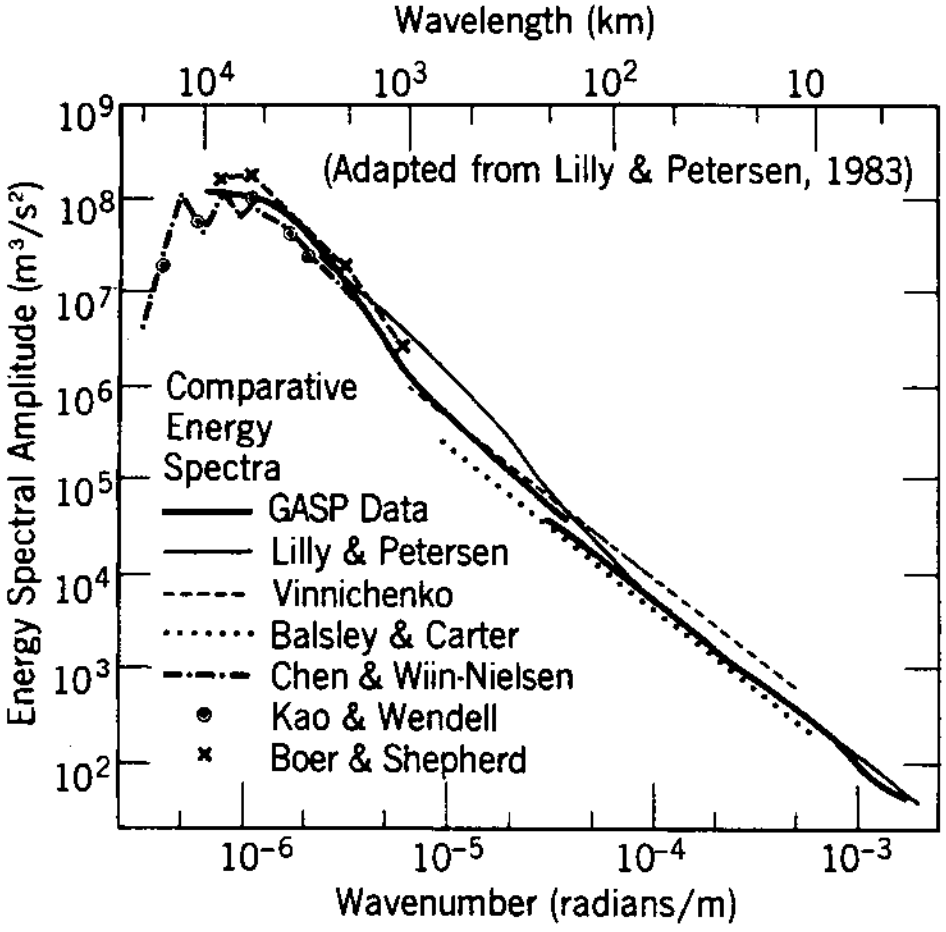

Figure 2.6: Composite horizontal kinetic-energy spectrum from Nastrom and Gage (1985) compared to the previous results from Kao and Wendell (1970), Vinnichenko (1970), Chen and Wiin-Nielsen (1978), Balsley and Carter (1982), Boer and Shepherd (1983), and Lilly and Petersen (1983) [from Nastrom and Gage, 1985.]

component and temperature spectra to have nearly the same universal shape regardless of data stratification. The velocity component and temperature spectral amplitudes, on the other hand, did show some variability with latitude, season, and vertical location, but differences were usually less than a factor of three. Potential temperature spectral amplitudes were larger in the stratosphere than the troposphere by a factor ranging from 1.5 to 4.

Influence of vertical displacements. Gage and Nastrom (1986a) examined further the striking similarity in shape between the horizontal velocity component and potential temperature spectra (Fig. 2.5). The potential temperature spectrum thus differs from the behaviour expected of a *passive* scalar quantity in two-dimensional turbulence, where the slope of the spatial spectrum of a passive scalar should be -1 in the enstrophy-cascade range and $1/3$ in the energy-cascade range (e.g., Lesieur and Herring, 1985). In contrast, the potential temperature spectrum exhibited a -3 slope in the enstrophy-cascading geostrophic turbulence range, consistent with Charney's (1971) theory, and a $-5/3$ slope in the energy-cascading mesoscale turbulence range. This suggests that the potential temperature spectrum may be governed by the same dynamics which determine the horizontal velocity component spectra in both wavenumber ranges.

Gage and Nastrom (1986b, p. 13213) argued that "fluctuations in any conservative passive scalar quantity will be produced whenever there is a component of motion parallel to the gradient of the scalar quantity". In the atmosphere, most scalar quantities such as potential temperature and ozone tend to have much larger vertical gradients than horizontal gradients. Defining 'vertical displacements' as displacements orthogonal to *isentropic* surfaces, Gage and Nastrom (1986b) showed that the vertical displacement spectrum could be deduced from the potential temperature spectrum if the background potential temperature gradient is known. Since the potential energy (PE) spectrum is also related to the vertical displacement spectrum, the potential energy spectrum can then be deduced directly from the PE spectrum (Gage and Nastrom, 1986a,b).

Gage and Nastrom (1986a) used this approach to calculate tropospheric and stratospheric PE spectra and then compared these spectra to the corresponding KE spectra. They found an amplitude ratio of approximately one-half at all wavelengths from 150 km to 4800 km. This result was consistent with Charney's (1971) prediction for geostrophic turbulence but had not been predicted for the mesoscale turbulence regime. It suggested that the GASP temperature and horizontal velocity spectra are linked closely by dynamics and that the differences between the tropospheric and stratospheric potential temperature spectra found by Nastrom and Gage (1985) can be explained by the need to maintain an equilibrium between the PE and KE spectra.

Gage and Nastrom (1986b) suggested as a further consequence that the fluctuation spectra of such atmospheric trace species as ozone, water vapour, and carbon monoxide could also be related to the vertical displacement spectrum in the same way as potential temperature provided that their background vertical gradients were known. These relationships were based on the simple physical model of an ensemble of quasi-horizontal eddies flowing along surfaces inclined slightly to surfaces of constant mixing ratio of a trace species (or to isentropic surfaces). The slight inclination between the flow surface and the other surface would result in a vertical component of scalar transport. Gage and Nastrom (1990) later proposed that over complex terrain, lee waves could also contribute to the tilting of isentropic surfaces. A field of quasi-horizontal eddies is also likely to have non-zero vertical velocities. For example, Ruscher (1988) and Ruscher and Mahrt (1989) have presented aircraft measurements consistent with the presence of quasi-horizontal eddies or vertical modes which showed upward 'ejections' of fluid, possibly as a result of random 'collisions' of individual eddies.

Nastrom et al. (1986a) calculated horizontal variance power spectra of ozone, water vapour, and carbon monoxide from GASP measurements. They found that at wavelengths less than 500–800 km, the horizontal spectra of these three trace constituents all followed a $k^{-5/3}$ power law. Comparison of observed tracer species spectral amplitudes with values predicted from potential temperature spectral amplitudes also showed

reasonable agreement. These results supported the hypothesis that mesoscale horizontal tracer fluctuations arise from a spectrum of vertical displacements acting upon vertical tracer gradients. Nastrom et al. also found that the spectral amplitude of ozone has an approximate lognormal frequency distribution, consistent with the lognormal frequency distributions of wind and potential temperature spectral amplitude found by Nastrom and Gage (1985).

Table 2.2 lists published mesoscale spectra of a number of atmospheric scalars, including pressure p, potential temperature θ, vertical displacement δ, specific humidity q, trace species mixing ratio χ, and radio refractivity structure function C_n^2.

Topographic effects. Lilly and Petersen (1983) found somewhat steeper velocity variance spectral slopes in the 100–1000 km wavelength range than did Nastrom and Gage (1983) and suggested that this steepening might be due in part to the effects of topography in the mountainous western United States. Nastrom and Gage (1985) showed that the variance associated with scales less than about 400 km is somewhat greater over land than water, with values over the western United States being from two to four times larger than those from over the ocean. However, they did not give any details regarding changes in the shape or amplitude of the variance power spectra as a function of underlying topography or synoptic weather conditions. Ecklund et al. (1986) presented vertical velocity frequency spectra for 'active' periods over complex terrain which also inidcated the presence of much more energy than during light-wind 'quiet' periods.

Nastrom et al. (1987) and Jasperson et al. (1990) carried out more detailed evaluations of terrain effects on mesoscale spectra. In both studies, flight segments were grouped by underlying topography (ocean, mountaiins, plains), vertical stability (troposphere, stratosphere), and flight- level wind speed (< 25 m s^{-1}, > 25 m s^{-1}). Nastrom et al. (1987) showed that for horizontal scales from 4 to 80 km, wind and temperature variances at flight level were up to six times larger over mountainous regions than over oceans in both troposphere and stratosphere and for both low and high flight-level wind

Table 2.2: Summary of mesoscale atmospheric scalar spectral measurements.

Variable	Spectrum Type	Measurement Method	Atmospheric Region	References
p	frequency	microbarograph	surface	Gossard (1960), Herron & Tolstoy (1969), Herron et al. (1969), Canavero & Einaudi (1987)
θ	horizontal wavenumber	aircraft	PBL	Young (1987), Lenschow et al. (1988b)
		aircraft	troposphere	Nastrom & Gage (1985)
		aircraft	stratosphere	Vinnichenko & Dutton (1969), Axford (1971), Lilly & Lester (1974), Nastrom & Gage (1985)
		balloon	troposphere	Julian & Cline (1974)
θ	vertical wavenumber	balloon	troposphere	Mantis & Pepin (1971), Fritts et al. (1988), Sidi et al. (1988)
		balloon	stratosphere	Mantis & Pepin (1971), Fritts et al. (1988), Sidi et al. (1988), Cot & Barat (1989), Sidi & Dalaudier (1989)
θ	frequency	radiosonde	stratosphere	Vinnichenko & Dutton (1969)
		thermograph	surface	Kolesnikova & Monin (1965), Goff & Duchon (1974)
δ	horizontal wavenumber	aircraft	troposphere	Gage & Nastrom (1986a)
		aircraft	stratosphere	Gage & Nastrom (1986a)
r_v	horizontal wavenumber	aircraft	PBL	Nicholls et al. (1982)
		satellite	troposphere	Manney & Stanford (1990)
	frequency	microwave radiometer	troposphere	Rogers & Schwartz (1990)
χ^*	horizontal wavenumber	aircraft	troposphere	Nastrom et al. (1986a)
		aircraft	stratosphere	Nastrom et al. (1986a)
$\ln C_n^2$	frequency	Doppler radar	stratosphere	Nastrom et al. (1986b)
$\partial\theta/\partial z$	vertical wavenumber	balloon	stratosphere	Barat & Cot (1989)

* trace species (ozone, water vapour, carbon monoxide)

speeds. At scales from 80 to 500 km, variances over mountainous regions were also larger than over oceanic regions but differences were smaller and less consistent.

Jasperson et al. (1990) found similar results based on an analysis of a greater number of flights and also demonstrated that differences in mean total variances were statistically significant at the 99% level. For most data groupings, flight-level wind speed did not show a significant correlation with total variance; the one exception was tropospheric flight segments over mountainous terrain. Fig. 2.7 shows the horizontal spectra of zonal wind for flight segments grouped by underlying topography. The largest differences in spectral amplitude occur at wavelengths between about 10 and 80 km. Jasperson et al. also showed that spectral variances over mountainous terrain are positively correlated with objective measures of 'orographic roughness'. These large-scale roughness parameters were calculated on the basis of such quantities as terrain height variance, number of ridges, and minimum, maximum, and modal terrain elevations. Nastrom and Gage (1990) recently reported wind-profiler frequency spectra consistent with enhanced horizontal velocity energy in the vicinity of rough terrain.

To explain these observations, Gage and Nastrom (1985a, 1990) and Nastrom and Gage (1990) proposed a simple model in which (a) horizontal velocity variances are enhanced by the launching of a spectrum of vertically propagating gravity waves due to stratified atmospheric flow over rough terrain, and (b) vertical velocity variances are enhanced both by these vertically-propagating IGW and by the tilting of isentropic surfaces by lee waves which then 'contaminates' the observed vertical velocities by adding a contribution due to the normally horizontal vortical modes (see Sec. 2.1.9).

2.1.6 Vertical fine structure

The atmospheric mesoscale structure and fluctuations discussed to this point have almost all been horizontal in nature. Let us now consider mesoscale *vertical* variability and structure. Both direct and indirect atmospheric measurements reveal widespread, coherent, small-scale variations of temperature and velocity in the vertical. Such vertical

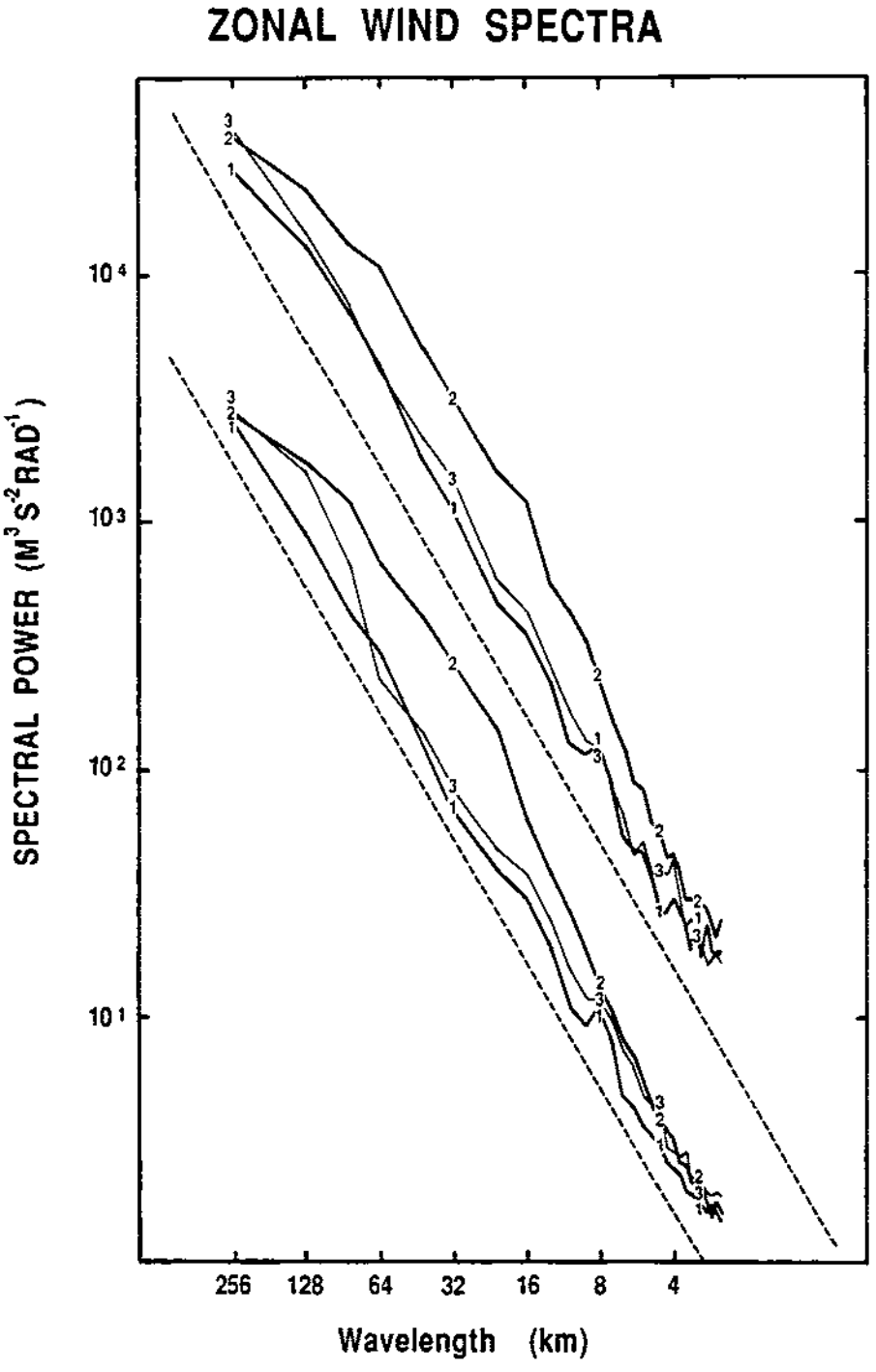

Figure 2.7: Average horizontal variance spectra of zonal wind component for flights over (1) oceans, (2) mountainous regions, and (3) plains. Values on ordinate axis apply to stratospheric flights; tropospheric spectra are shifted down one decade. Two $-5/3$ lines have also been drawn (dashed lines) one decade apart (from Jasperson et al., 1990).

'fine structure' or 'microstructure' appears to be similar to the vertical fine structure[37] observed in the ocean (e.g., Woods, 1968, 1969a; Woods and Wiley, 1972; Munk and Garrett, 1973; Phillips, 1971, 1977; Gregg and Briscoe, 1979). In studying the vertical structure of the oceanic thermocline, an approximate oceanic analogue to the PBL capping inversion, oceanographers have frequently found a complex vertical stack of approximately homogeneous 'layers' separated by thinner 'sheets' of high static stability. For example, measurements made using dye tracers in the summer thermocline of the Mediterranean Sea near Malta revealed sheets 10–30 cm thick and tens of kilometers in horizontal extent separating layers several meters thick (Woods, 1968, 1969a). The 'layers' or low-gradient zones are the sites of earlier mixing events while the 'sheets' or high-gradient zones are the boundaries between these mixed regions (Müller, 1984).

A related concept from oceanography is that of 'fossil turbulence'. In fossil turbulence, scalar fluctuations are present on a scale and at an intensity that cannot be accounted for by the existing velocity field (Woods, 1969b). Gibson (1987, p. 5383) defines this term for the ocean as "a remnant fluctuation in any hydrophysical field produced by active turbulence which persists after the fluid is no longer actively turbulent (overturning) on the scale of the fluctuation." The concept of fossil turbulence is helpful in trying to explain the origins of atmospheric vertical fine structure.

The presence of vertical fine structure has significant implications for the calculation of spatial and temporal spectra in such a 'layered' medium. Phillips (1971) showed that spatial spectra calculated from traverses of such a layered medium will have a κ^{-2} form simply due to the random distribution of discontinuities. Similarly, the whole-body movement of such structure past a fixed measurement point, due for example to IGW passage, will yield a f^{-2} frequency spectrum. This suggests that spectra with such spectral slopes can arise from the *mean* structure of a stable medium and not from short-

---

[37] Oceanographers use these two terms in a complementary fashion: 'fine structure' refers to 1–100 m scales while 'microstructure' refers to 0.001–1 m scales (e.g., Gregg and Briscoe, 1979).

term fluctuations, an important caveat since a -2 slope lies right between the -3 and -5/3 slopes discussed in the previous sections.

The rest of this section summarizes both the wide variety of observing technologies that have been used to measure vertical atmospheric structure and some of the relevant results and significant findings. It should be clear from this material that the atmosphere as well as the ocean possesses significant vertical fine structure and microstructure.

Direct measurements

Temperature structure. Danielsen (1959) reanalyzed standard NWS radiosonde records and found many narrow zones of large hydrostatic stability separated by layers of near neutral stability in the troposphere. Based on vertical cross-section analysis, isentropic maps, and isentropic trajectories, Danielsen showed that these stable zones, which he called 'stable laminae' to emphasize their small vertical dimension and large quasi-horizontal extent, displayed considerable spatial and temporal continuity even though they were frequently omitted from radiosonde reports. Woods (1969a) presented one plot of gradient Richardson number fine structure derived from a Liverpool (England) atmosperic sounding which supported this view.

Research balloon launches have revealed more details of tropospheric and stratospheric vertical temperature structure. Mantis and Pepin (1971) and Camp (1971) described fast-response thermometers designed to be carried by balloon to obtain high-resolution vertical profiles of temperature. Mantis and Pepin noted that their temperature measurements showed numerous shallow layers with near adiabatic lapse rates in both the troposphere and stratosphere. On the basis of power spectra of vertical temperature variance, they concluded that there is more fine-scale temperature structure in the stratosphere than troposphere. Camp reported that a sequence of four balloon launches made over a seven-hour period indicated persistence of the resolved fine-scale temperature structure between launches. More recently, Fritts et al. (1988) presented a three-day sequence of three-hourly, high-resolution ($\sim$ 30 m) temperature soundings

made by balloon in November 1986 in Japan which again showed this persistence but also upward and downward phase progressions of some of the dominant features.

Dalaudier et al. (1985), Dalaudier and Sidi (1987), and Sidi and Dalaudier (1989) have described very-high-resolution (< 1 m) temperature and velocity profiles obtained by an instrumented high-altitude balloon. Fig. 2.8 shows the 'sawtooth' vertical microstructure observed in profiles of both quantities in one lower-stratospheric turbulent layer. They then used these measurements to calculate vertical spectra in order to investigate the characteristics of the buoyancy subrange adjacent (at longer wavelengths) to the inertial subrange (see Sec. 2.1.9) and claimed that the resulting spectra provided support for their theory of the buoyancy subrange, which includes the prediction of a reverse or upscale cascade of PE and its possible role in producing the vertical microstructure.

Measurements have also been made of the vertical structure of other scalar quantities. Lane (1969) and Coulman (1973) carried out balloon-borne measurements of refractive-index structure function parameter C_n and temperature structure function parameter C_T, respectively, in the troposphere. Fairall et al. (1991) recently presented profiles of Brunt-Väisälä frequency and Richardson number as well as wind shear. Table 2.2 summarizes all of the studies that reported vertical spectra. Secs. 2.1.8 and 2.1.9 describe some of the mechanisms responsible for this small-scale and mesoscale vertical structure.

Velocity structure. Vertical wind profiles obtained by balloon display considerable vertical structure too. Sawyer (1961) described quasi-periodic wind variations with height in the lower stratosphere over England. Wind measurements were taken at approximately 50 m height intervals with radar-sonde theodolite. The wind variations had vertical dimensions on the order of one kilometer and were frequently persistent for a sequence of measurements made over a six-hour period. Weinstein et al. (1966), DeMandel and Scoggins (1967), and Endlich et al. (1969) used a tracking radar to follow a rising balloon and obtain detailed vertical wind profiles. Spherical Mylar balloons were used in the first study while the latter two studies employed 'Jimspheres', balloons de-

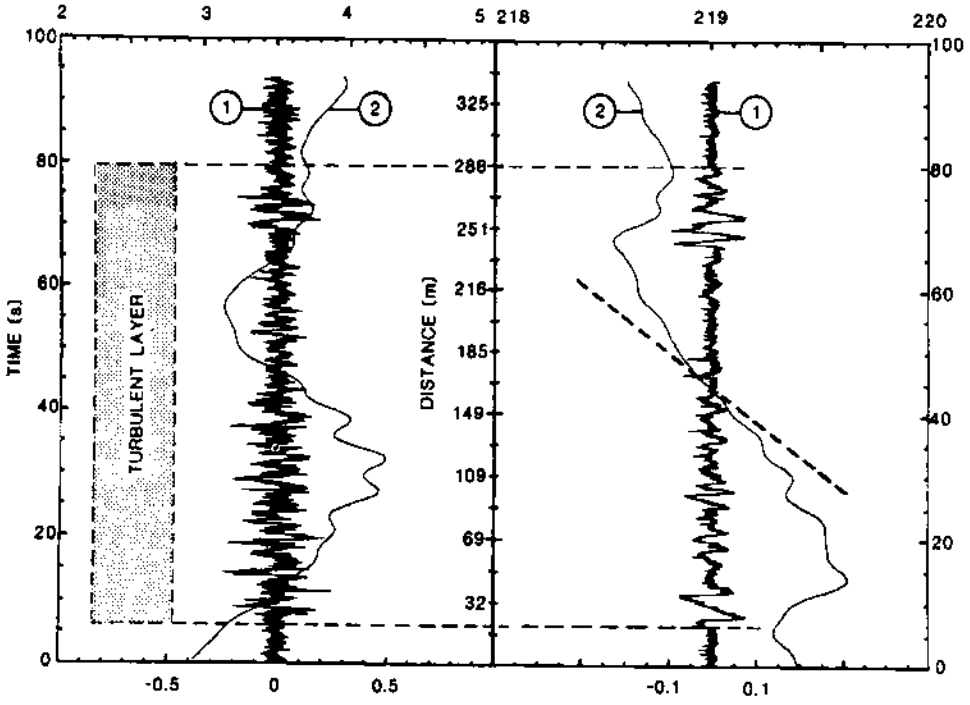

Figure 2.8: Vertical profiles of vertical velocity (left panel) and temperature (right panel) measured in a stratospheric turbulent layer at about 14 km over southern France on May 4, 1984. The two curves marked (1) show the high-frequency component while those marked (2) show the low-frequency component (the mean vertical velocity profile corresponds to the balloon ascent velocity) based upon partitioning with a numerical filter. The sampling rate was 0.016 Hz (64 measurements per second). The lower abscissa scales correspond to the curves marked (1) while the upper scales correspond to the curves marked (2). The slanted dashed line on the right panel indicates the adiabatic lapse rate (from Dalaudier and Sidi, 1987).

signed to minimize wobbling due to aerodynamic forces (Murrow and Henry, 1965; Scoggins, 1965). These balloon/radar wind-profiling systems were developed for use in aerospace vehicle studies. Sequences of Jimsphere wind profiles with 100 m resolution showed considerable fine structure and time continuity, and some features could be seen to move upwards or downwards with time. Mesoscale oscillations with periods between 1 and 24 hours and vertical wavelengths of 2 km or less are frequently observed.

For example, Fig. 2.9 shows a sequence of nine Jimsphere wind profiles made over a twelve-hour period in the spring at Cape Canaveral, Florida. The profile macrostructure is nearly constant through the observing period whereas several mesoscale perturbations with amplitudes of more than 5 $m\,s^{-1}$ are evident near the 7 and 10 km levels. Weinstein et al. (1966) reported similar findings and suggested that the free atmosphere be envisioned as a stack of thin horizontal layers undergoing a multitude of oscillating motions. They proposed either internal gravity waves or inertial oscillations coupled with the laminated thermal structure of the atmosphere as possible explanations of this behaviour.

Gage and Jasperson (1979) and Jasperson (1982) described an economical, ground-based radio-location system for balloon tracking which could be used to obtain high-resolution, sequential wind profiles in the lower troposphere. Wind estimates were made every 100 m and maximum absolute errors were less than 1 $m\,s^{-1}$. Persistent and continuous features with amplitudes of 1–2 $m\,s^{-1}$ and vertical wavelengths of only 200–400 m were very evident above the PBL in the sequence of soundings shown in Fig. 2.10.

Barat (1983) described a balloon-borne system in which direct measurements are made of vertical wind *shear*; the wind profile can then be obtained by integration. Vertical fine structure was observed in both troposphere and stratosphere with this technique, which Barat claimed was considerably more accurate than the tracking radar/Jimsphere technique described above. Axford (1968) also obtained stratospheric vertical shear profiles by using an instrumented *aircraft* with a high-quality inertial navigation platform; measurements were made along alternating ascending and descending flight 'legs'.

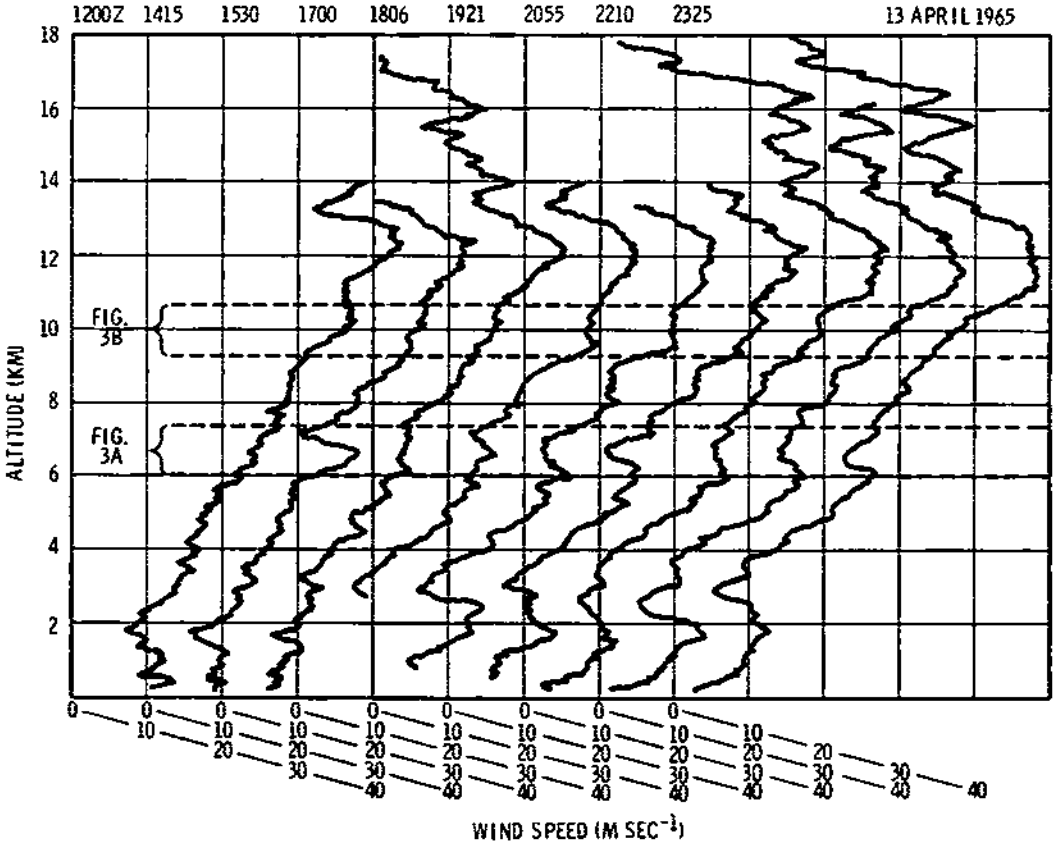

Figure 2.9: Successive wind-speed profiles measured at Cape Canaveral, Florida by FPS-16 radar/Jimsphere technique on 13 April 1965 (from DeMandel and Scoggins, 1967).

Continuous profiles of low-level vertical fine structure can also be measured by making vertical traverses with either tethered balloons (e.g., Readings and Butler, 1972; Morris et al., 1975) or movable instrument carriages installed on meteorological towers (Kaimal and Gaynor, 1983). Studies of multiple stable layers in the nocturnal atmosphere based on such carriage traverses include Li et al. (1983) and Gossard et al. (1984, 1985). The use of a continuous traverse can reveal microstructure not detectable by fixed-level tower measurements. For example, Gossard et al. (1984) commented that even 50 m vertical resolution may not be adequate to capture some significant features.

One last direct technique that has been used to determine high-resolution vertical wind profiles is the photogrammetric analysis of rocket smoke trails (e.g., Tolefson and Henry, 1961; Cooke, 1962; Gill et al., 1963; Scoggins, 1965). The smoke-trail technique has the advantage that an instantaneous vertical profile of winds directly over the launch site can be determined for the full length of the smoke column. In contrast, balloon techniques produce profiles *integrated* in both space and time; a balloon may require 30 minutes or more to traverse the depth of interest and will drift away from the release point during this time. Tolefson and Henry (1961) showed wind profiles between 1.5 and 12 km with considerable fine structure that were produced by photogrammetric analysis of pairs of simultaneous photographs taken at different locations separated by a known baseline. Smoke trails also offer immediate visual evidence of any gross inhomogeneities or changes from previous profiles (Cooke, 1962). However, this technique also has some drawbacks. Determination of wind speeds by photogrammetric analysis requires computations comparable in difficulty to those for double-theodolite pilot balloon analysis so that profiles take some time to calculate. Use of this method is also limited to the daytime and manpower requirements are high. For example, Gill et al. (1963) described a five-man launch team consisting of rocket-launcher operator, communications specialist, rocket retriever, and two cameramen. Nevertheless, the smoke-trail technique can provide valuable data. Dewan et al. (1984) described a state-of-the-art application in which

vertical profiles of horizontal wind speed with 10 m resolution were obtained in the 13 to 37 km region of the stratosphere.

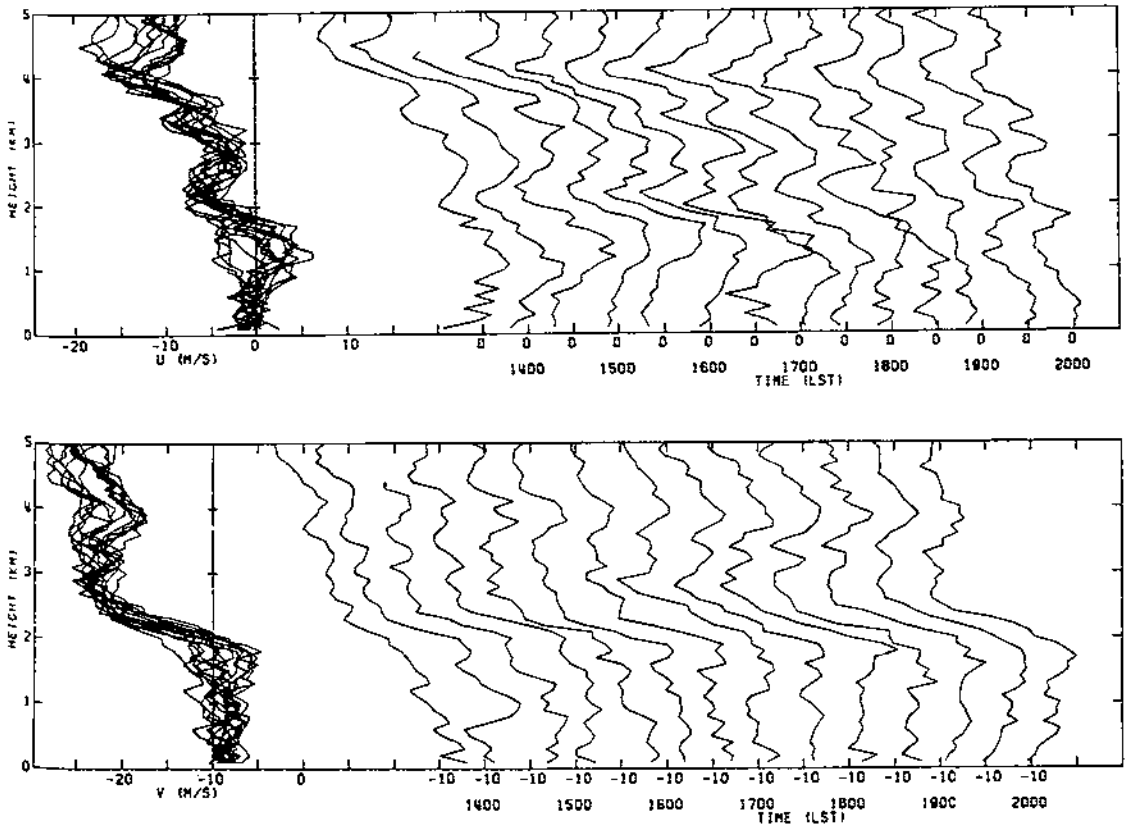

Figure 2.10: Sequential vertical profiles of the u- (upper panel) and v-component (lower panel) winds from 14 balloon launches over a six-hour period on 31 March, 1976 at St. Cloud, Minnesota (from Gage and Jasperson, 1979).

Indirect measurements

In addition to direct or *in situ* measurements, indirect or remotely-sensed measurements made by radar, sodar, and lidar have provided a wealth of information about atmospheric fine structure. In fact, Munk and Woods (1973, p. 201) stated that "it is remarkable that so much of what is known of atmospheric structure has been learned by its scattering properties, whereas nearly all of the corresponding oceanographic information has been derived by direct sounding".

Noncoherent radars. Early weather radar revolutionized the study of clouds and precipitation systems, but during this period researchers often noted mysterious anomalous returns from regions of the sky with no apparent 'targets'. Such returns gave rise to a fairly substantial literature on 'angels', 'ghosts', and 'pixies' (James, 1980; Chadwick and Gossard, 1986; Hardy and Gage, 1990). In fact, clear-air echoes had been observed even earlier by long-wavelength (10–200 m) radars used for ionospheric studies. Colwell and Friend (1939) used aircraft measurements to show that some of these high-frequency (HF) tropospheric reflections were associated with the large refractive-index gradients found in low-level temperature inversions. After considerable controversy, most of the so-called 'dot angels' or 'dot echoes' were attributed to backscattering from birds or insects while the 'angel layers' and other types of clear-air echoes were attributed to reflections from atmospheric radio refractive index gradients (James, 1980; Hardy and Gage, 1990).

Refractive-index variability, which results from fluctuations in temperature, water vapour content, and wind, causes scale-selective scattering of both radio waves and acoustic waves (Woods, 1969b; Ottersten et al., 1973; Gage, 1990). Appreciable radar backscattering occurs when a radar beam encounters significant three-dimensional refractive-index structure on a scale equal to *half* the radar wavelength. For HF (3–30 MHz) radar, then, scattering scales will be of the order of 5 m to 50 m, for VHF (30–300 MHz) radar 0.5 m to 5 m, and for UHF (300–3000 MHz) radar 0.05 m to 0.5 m. Higher-frequency, shorter-wavelength radars are less likely to sense refractive-index irregularities since their operating wavelengths are close to the tropospheric inner scale of turbulence, that is, the Kolmogorov scale or dissipation scale (Ottersten et al., 1973; Gage and Balsley, 1978; Gage, 1990). Conventional S-band weather radar is represented by a 3 GHz frequency and 10 cm wavelength beam, C-band weather radar by a 6 GHz frequency and 5 cm wavelength beam, and X-band weather radar by a 10 GHz and 3 cm beam (e.g., Chadwick and Gossard, 1986). On the other hand, these smaller wavelengths are closer to the backscatter cross sections of single birds and insects.

Sharp vertical gradients of radio refractive index can also cause partial *reflections* of radar beams. This process is called quasi-specular reflection and is often present in vertical-incidence radar soundings made with VHF radars of 6–7 m wavelength (Gossard, 1990). Such partial reflections will be coherent whereas turbulent Bragg scattering is incoherent (Lane, 1968). Strong temperature inversions such as occur with the capped PBL under anticyclonic conditions, tropospheric fronttal zones, the tropopause, and the lower stratosphere can be detected based on quasi-specular echoes (Colwell and Friend, 1939; Saxton et al., 1964; Larsen et al., 1986; Gossard, 1990; Hardy and Gage, 1990). Dester et al. (1990) recently reported the simultaneous detection of several horizontally stratified atmospheric layers, one tropospheric and one stratospheric, by two ST radars located 25 km apart. There are also indications that multiple, thin, partially-reflecting layers can give rise to quasi-specular echoes as well (Beran et al., 1973; Gage and Balsley, 1980; Green and Gage, 1980; James, 1980; Gossard et al., 1984; Gage, 1990; Gossard, 1990; Röttger and Larsen, 1990).

The development of powerful and sensitive pulsed radars in the 1960's made possible routine observation of the clear convective boundary layer and of turbulent layers in the free troposphere. This quickly led to the use of these radars in clear-air turbulence (CAT) research. Radar scans were able to show the 'braided structure' associated with shear-induced Kelvin-Helmholtz billows (Ottersten et al., 1973; Hardy and Gage, 1990). The development of FM-CW (Frequency Modulated Continuous Wave) radar with vertical resolution as fine as one meter by Richter (1969) permitted detection of thin multiple layers, some exhibiting regular vertical spacing, in the first two kilometers of the atmosphere (e.g., Gossard et al., 1973; Ottersten et al., 1973). Sodar records also show complex vertical structure in the stably stratified PBL with lamina often only a few meters thick (e.g., Beran et al., 1973; Davis and Peltier, 1976; Hooke and Jones, 1986).

Coherent radars. Noncoherent radars only outline the strongest echoing regions and hence have been used primarily for qualitative morphological studies (Gage and Balsley, 1978). Coherent or Doppler pulsed radars also retain information on the phase of

signal returns, enabling the frequency spectrum of the incoming signal to be measured in addition to the signal intensity. Since the mean frequency of the return signal will usually be Doppler-shifted, the Doppler equation $\delta\omega = -2V_R/\lambda$ can be used to infer the mean outward radial or line-of-sight velocity of the target volume, V_R, where λ is the wavelength of the signal and $\delta\omega$ is the difference in frequency between transmitted and received signals (Chadwick and Gossard, 1986). Complete vector winds can be measured by moving the radar beam to three noncoincident directions although the calculation is subject to errors resulting from flow variability over the spatial separation between beams (Hogg et al., 1983; Larsen et al., 1986; Röttger and Larsen, 1990). Vertically-pointing Doppler radars can measure vertical velocity directly with a single beam while returns from two azimuthally-orthogonal, off-vertical beams can be used to infer horizontal velocity if vertical velocity is assumed to be negligible. Another advantage of coherent pulsed radars is the improved signal-to-noise ratio made possible by coherent integration of the return signal (Strauch et al., 1984; Chadwick and Gossard, 1986; Röttger and Larsen, 1990).

A wide variety of clear-air Doppler radars have measured vertical wind profiles in the troposphere, stratosphere, and even mesosphere over the past decade. Both monostatic (co-located transmitter and receiver) and bistatic (transmitter and receiver at separate sites) techniques, different antenna configurations (steerable dish, fixed dish/steerable feed, phased dipole array, phased Yagi array), and a wide range of radio wavelengths in the VHF and UHF bands have been used (Balsley and Gage, 1982; Röttger and Larsen, 1990). Wind profiles with vertical resolution of 150 m have been measured by clear-air radars employing 1 μs pulse widths (Strauch et al., 1984; Augustine and Zipser, 1987). The combination of vertical resolution comparable to or better than rawinsondes, excellent time resolution (5–15 minutes), unattended operation, and high reliability demonstrated over the past decade by prototype operational 'wind profilers' has resulted in this technology being chosen for the new generation of operational tropospheric sounding systems. Low manpower requirements help to balance the capital costs of these

new profilers; it has been estimated that the costs of labour and expendibles incurred in the operation of a standard NWS rawinsonde station will pay for a profiler in about seven years (Hogg et al., 1983).

Wind profilers are already a major source of data on mesoscale flow variability and mesoscale frequency spectra based on wind-profiler data sets were discussed in the previous section (see also Table 2.1). Fig. 2.11 shows a sample time series of wind-profiler-measured vertical wind profiles made during the 1985 Oklahoma-Kansas PRE-STORM experiment. One limitation of low-VHF profilers such as the three deployed during PRE-STORM is their minimum height resolution of one kilometer or more (note the near-surface measurement gap in Fig. 2.11). Ecklund et al. (1988) recently described a new boundary-layer wind profiler designed to overcome this problem. Multiple Doppler radars can also be used to obtain wind fields with high three-dimensional spatial resolution (e.g., Doviak and Berger, 1980; Kropfli and Hildebrand, 1980; Eilts et al., 1984; Gossard, 1990).

2.1.7 Taylor transformation

The Taylor transformation has already referred to a number of times in this chapter when discussing the conversion of frequency spectra to wavenumber spectra for aircraft, rawinsonde, and wind-profiler measurements. This coordinate transformation, also known as Taylor's hypothesis or the 'frozen turbulence' hypothesis, was first employed by Taylor (1938) to derive a time correlation function $R_u(t)$ from wind-tunnel measurements of the longitudinal velocity spatial correlation function $R_u(x)$. Since the mean wind-tunnel velocity U was much larger than the longitudinal turbulent fluctuations u', Taylor assumed that turbulent eddies were transported by the mean flow without appreciable distortion or evolution. In other words, he assumed the turbulent flow structure to be independent of time in the reference frame moving with velocity U, suggesting the term 'frozen turbulence'. It then followed that

$$R_u(x) = R_u(Ut) \ . \tag{2.24}$$

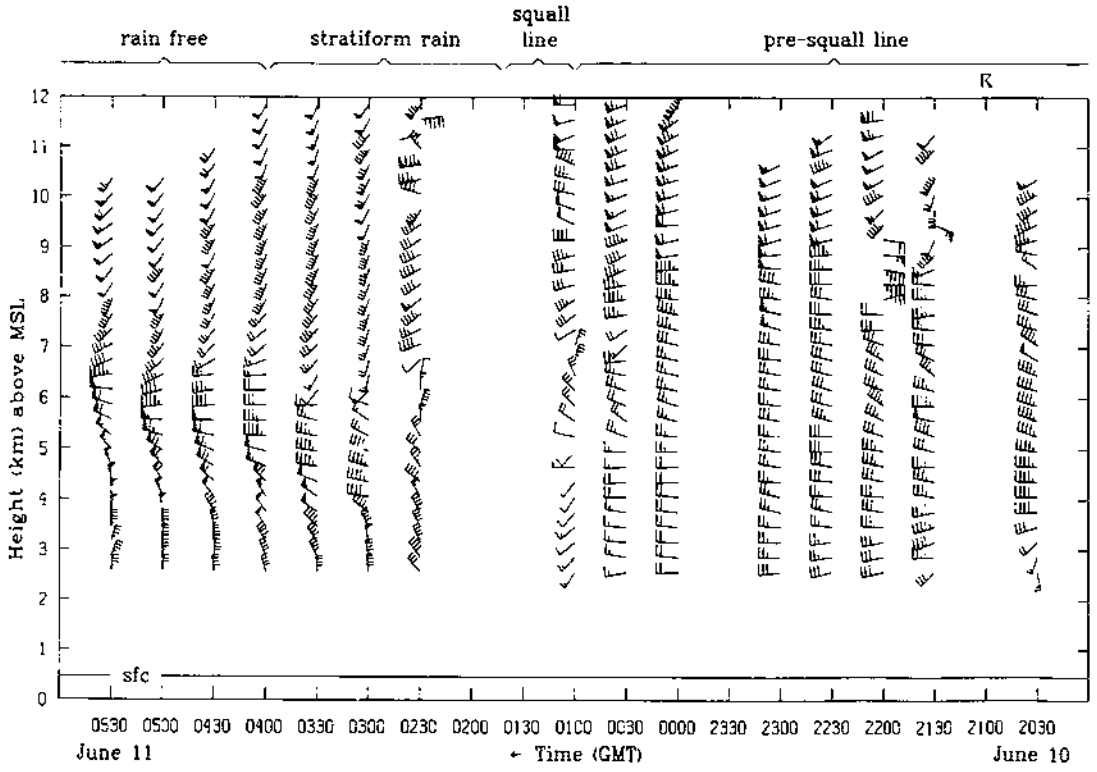

Figure 2.11: Time-height cross section of wind profiles for a nine-hour period from measurements made by a phased-array 49.25 MHz Doppler profiler at McPherson, Kansas on June 10–11, 1985. Profiles correspond to half-hour averages. Each half barb is 2.5 $m\,s^{-1}$, each full barb 5 $m\,s^{-1}$, and each flag 25 $m\,s^{-1}$. Current weather is marked at the top of the frame. The profiler was turned off from 0130–0230 GMT on June 11 due to frequent lightning strikes accompanying the squall line (from Augustine and Zipser, 1987).

This simple transformation allows *statistical properties* such as Eulerian one-point correlations or variance spectra to be converted from the time domain to the space domain or vice versa, e.g., from frequency to wavenumber or from wavelength to period. Moreover, if we view U as the mean speed of the air relative to the sensor, then the sensor could be fixed in space or attached to a moving platform such as an airplane. In either case the resulting spatial correlation function or spectrum is one-dimensional and *along* the mean flow direction.

Application to small-scale turbulence

If the Taylor hypothesis is to be satisfied exactly, then the equations of motion reduce to the form

$$\frac{\partial u_i}{\partial t} + U\frac{\partial u_i}{\partial x_1} = 0 \quad , \quad i = 1,2,3, \tag{2.25}$$

where $u_i = \overline{u}_i + u_i'$ is the total velocity and $U = \overline{u}_1$. Clearly this relation will not hold in a real turbulent flow. However, in a homogeneous, high Reynolds number flow, it can be shown that

$$\frac{\partial u_i}{\partial t} + U\frac{\partial u_i}{\partial x_1} \approx 0 \tag{2.26}$$

if the (relative or normalized) turbulence intensity $i = \left[\overline{u_1'^2} + \overline{u_2'^2} + \overline{u_3'^2}\right]^{1/2}/U$ is much less than unity[38] (e.g., Lin, 1953; Monin and Yaglom, 1975, p. 364). Taylor's hypothesis thus implies that for high Reynolds number flows, the material derivative $\mathrm{D}u_i/\mathrm{D}\,t$ is a small difference between two large terms describing the local acceleration $(\partial u_i/\partial t)$ and the inertial acceleration $(u_1\partial u_i/\partial x_1)$. Monin and Yaglom (1975, p. 259) suggest that this is because "the velocity $u_i(t)$ at a fixed point in isotropic turbulent flow is determined mainly by the large-scale disturbances from the energy range, which are transferred past the point

---

[38] Comte-Bellot and Corrsin (1971) suggested that an equivalent local requirement might be that a turbulent structure of size k^{-1} should have a spectral coherence time much longer than its convective passage time $(Uk)^{-1}$.

and thus lead to rapid changes in the Eulerian velocity." Eq. 2.26 has been verified by many wind-tunnel studies (e.g., Frenkiel and Klebanoff, 1966; Comte-Bellot and Corrsin, 1971) for lag times corresponding to eddy time scales smaller than the time scale of the energy-containing eddies (i.e., $\xi \leq T_E$: Baldwin and Johnson, 1974). In the atmosphere, however, turbulence intensities are frequently on the order of 0.1 or larger. Gifford (1956) argued, based on a turbulence model of Ogura (1953), that Taylor's hypothesis was still a reasonable approximation in the atmosphere for values of i less than 0.3. Willis and Deardorff (1976) found a similar limit based on water-tank diffusion experiments. Atmospheric measurements also suggest that the frozen turbulence hypothesis is *not* valid at low wavenumbers or frequencies even for small turbulence intensities since these modes are unlikely to move at the mean convection velocity (e.g., Pasquill and Smith, 1983).

The applicability of Taylor's hypothesis is even more restricted in *inhomogeneous* flows because additional terms such as $w'\partial U/\partial z$ must also be neglected. In general, Taylor's hypothesis will only be satisfied for frequencies considerably higher than the characteristic frequency associated with the mean shear, dU/dz. Lin (1953) suggested that application of Taylor's transformation be restricted to the frequency range

$$2\pi n \gg \frac{dU}{dz} \ , \tag{2.27}$$

where n is the cyclic frequency, or, equivalently, since $n = U/\lambda = Uk/2\pi$ (e.g., Fisher and Davies, 1964; Powell and Elderkin, 1974), to the wavenumber range

$$k \gg \frac{1}{U}\frac{dU}{dz} \gg 1 \ , \tag{2.28}$$

so that the velocity gradient across the eddies of interest is negligible compared to the mean convection velocity U [an analysis of atmospheric surface-layer data by Powell and Elderkin (1974) suggested that these conditions could be relaxed somewhat]. Lumley (1965) extended Lin's analysis and experimental work by Fisher and Davies (1964) by listing four conditions which must be met in extending Taylor's hypothesis to shear flows.

He based these conditions on violation of "... isotropy of the convection field, isotropy of the convected field, and lack of correlation between the two."

Heskestad (1965) also studied the use of Taylor's hypothesis in shear flows and suggested a rough shear correction to the mean advection velocity proportional to the magnitudes of the three velocity variances $\overline{u_i'^2}$. Wyngaard and Clifford (1977) extended Lumley's work and showed how convective velocity fluctuations affect both small-scale velocity and scalar spectral statistics. They also noted that aircraft measurements were preferable to tower-based measurements in this regard. Wacongne and Babiano (1982) examined space-time correlations of longitudinal velocity in the atmospheric surface layer and compared the performance of two definitions of mean advection velocity. Other papers on the application of Taylor's hypothesis in micrometeorology include Ropelewski et al. (1973), Panofsky et al. (1974), Mizuno and Panofsky (1975), and Hayashi (1991).

Extension to larger scales

Somewhat surprisingly, despite these various restrictions on the application of Taylor's hypothesis to even the atmospheric microscale, Taylor's hypothesis has been successfully employed on much larger scales, though not without encountering considerable skepticism. Brown and Robinson (1979, p. 271) quoted a reviewer who wrote of their initial study proposal, "...it is nearly incredible that anyone could take seriously the results of the frozen turbulence hypothesis at these [synoptic] scales." Nevertheless, Brown and Robinson argued heuristically that if the frozen turbulence hypothesis applies to a pattern of motion which is fixed in time and space, then it should also apply to the average of many samples of 'statistically frozen', that is, stationary and homogeneous, turbulence. An attendant requirement for any scale of application is that the time scale or length scale used in determining the mean advection velocity U should be large in comparison with the spectrally analyzed scales so that the scales of interest do not themselves contribute significantly to U.

Possibly the earliest application of Taylor's hypothesis to large-scale atmospheric flows was made by Hutchings (1955). He argued that the fundamental requirement for

the equivalence of space and time correlation functions to hold is that individual turbulence elements undergo only minor internal changes as they move past the point of observation. The facts that (i) the large-scale turbulent horizontal velocity fluctuations are likely to be of the same order of magnitude as the mean horizontal flow speed and (ii) the eddy translation speed may differ from the mean flow speed are secondary. To test this hypothesis, Hutchings calculated longitudinal and lateral Eulerian-time velocity correlation functions $R_u(\xi)$ and $R_v(\xi)$ for three months of six-hourly, 500 hPa wind measurements at Larkhill, England and three months of six- hourly, 300 hPa wind measurements at Auckland, New Zealand and then compared them against the Taylor-transformed theoretical form of the Eulerian-space velocity correlation functions $R_u(r)$ and $R_v(r)$ for a two-dimensional, homogeneous isotropic inertial range, $[1 - R(\xi)] \sim \xi^{2/3}$. He found good agreement out to 48 h for the three months of Larkhill data and less good agreement out to 24 h for the three months of Auckland data. In both cases U was taken to be the mean zonal wind component value for the entire period. Later studies of $R_u(\xi)$ and $R_v(\xi)$ for synoptic-scale flows (both the Eulerian and Lagrangian forms) include Angell (1961), Kao and Bullock (1964), Kao (1965), and Murgatroyd (1969).

Gifford (1956) replotted Hutching's Larkhill data against his own analytical formula for $R_u(t)$ [based on a $k^{-5/3}$ energy spectrum, Ogura's (1953) simple turbulence model with eddy translation, growth, and decay, and Taylor's hypothesis] and found slightly better agreement compared to the $\xi^{2/3}$ power law used by Hutchings. Gifford took this approach to avoid the restriction to turbulence intensities smaller than commonly observed in the atmosphere in either small-scale, three-dimensional turbulence or large-scale, quasi-two-dimensional turbulence. For example, Gifford assumed a turbulence intensity value $i = \sigma_u/U$ of 0.7 for the Larkhill data over the three-month period, a value considerably larger than the 0.1 limit often specified for application of Taylor's hypothesis.

Ellsaesser (1969a) employed Taylor's hypothesis to derive a formula for the Eulerian vector wind time variability, $\sigma_V(\xi) \propto \xi^{1/3}$, where $\sigma_V(\xi)$ is the square root of the Eulerian vector wind temporal structure function $2\sigma^2[1 - R_V(\xi)]$, from the Kolmogorov inertial-

range Eulerian velocity spatial structure functions for locally homogeneous, isotropic turbulence, $\sigma_u^2(x) = C(\epsilon x)^{2/3}$ and $\sigma_v^2(x) = (4C/3)(\epsilon x)^{2/3}$. σ is the vector velocity standard deviation, R_V is the Eulerian vector-velocity temporal correlation function, C is a universal constant, ϵ is the rate of KE dissipation per unit mass, and x is the longitudinal separation distance. Ellsaesser (1969b) then examined published wind variability data from sites in California, Nevada, Britain, and the South Pacific and found them to be consistent with this formula for lag periods of 4 to 6 hours and even 24 to 36 hours in some cases.

Planetary-scale restrictions. Despite these successes, Taylor's hypothesis will not apply at all atmospheric scales. Kolesnikova and Monin (1965) suggested on the basis of simple scaling considerations that the frozen turbulence hypothesis should not be expected to hold at the planetary scale. If turbulent flow is to be approximated as 'frozen', then eddy transport times should be considerably smaller than eddy lifetimes. At planetary scales, however, if U is assumed to have a value of $10\ \mathrm{m\,s^{-1}}$, then at mid-latitudes it will take about a month for an eddy to complete one global revolution, considerably longer than the lifetime of typical synoptic disturbances. Moreover, space spectra, unlike time spectra, will be limited at small wavenumbers by the finite size of the Earth. Taking the maximum possible wavelength to be 40,000 km and U again to be $10\ \mathrm{m\,s^{-1}}$, the maximum period for which time spectra can be transformed to space spectra will be about one month.

Vinnichenko (1970) also considered the validity of Taylor's hypothesis on the planetary scale and argued that it cannot be used on this scale since the phase speed of planetary-scale eddies (i.e., Rossby waves) depends on wavenumber and not on a mean advection velocity. He suggested that the relationship between space spectra and time spectra at these scales is best described in terms of *group* velocity. Comparison between a pair of large-scale KE space and time spectra provided qualitative support for this view (Vinnichenko, 1970). Kao and Wendell (1970) and Kao et al. (1970) provided additional evidence of the inapplicability of Taylor's hypothesis to the largest atmospheric scales,

including KE wavenumber and frequency spectra with markedly different power-law dependencies.

Recent mesoscale applications. Brown and Robinson (1979) examined daily 500 hPa wind values at 72 rawinsonde stations in eastern Europe from July 1966 as an indirect means to investigate the 200–2000 km KE spectral range. Their novel investigation included separate analyses for spatial and temporal variance and covariance functions and addressed both separation-distance and directional contributions to spatial covariance. Based on comparison of time- and space-based empirical variance spectra and correlation functions, Brown and Robinson concluded that the Taylor transformation worked well in the 500–1000 km range and could be applied with some success to scales as large as 2500 km.

Gage and Jasperson (1979) and Jasperson (1982) extended Ellsaesser's (1969a,b) work on mesoscale temporal variability with a field program in which hundreds of pilot balloons were launched to measure low-level winds in conjunction with a ground-based radiolocation system. Most launches were sequential launches of single balloons spaced 30 minutes apart to study time variability but some space variability experiments were also conducted. In these latter experiments, pairs of balloons were released simultaneously separated by either 20 m, 4.4 km, or 20.9 km in a sequence of launches with 30 minute temporal separation. Results supported Ellsaesser's finding of a $\xi^{1/3}$ power law for the Eulerian wind time variability $\sigma(\xi)$ for the u and v components, in this case out to 5 hours lag except for the u wind component under cyclonic synoptic patterns (see Fig. 2.12). Again, such a power-law relationship is consistent with the Taylor transformation of the spatial structure function for a $k^{-5/3}$ inertial range. Additional observational support for a $\xi^{1/3}$ power law out to 4 hours was provided by a Doppler radar study of jet-stream winds by Gage and Clark (1978). All three of these studies also provided valuable information about low-level vertical fine structure (see Sec. 2.1.8).

Lilly and Petersen (1983) applied the Taylor transformation on a larger scale (10–1800 km) to convert KE frequency spectra calculated in earlier studies to wavenumber

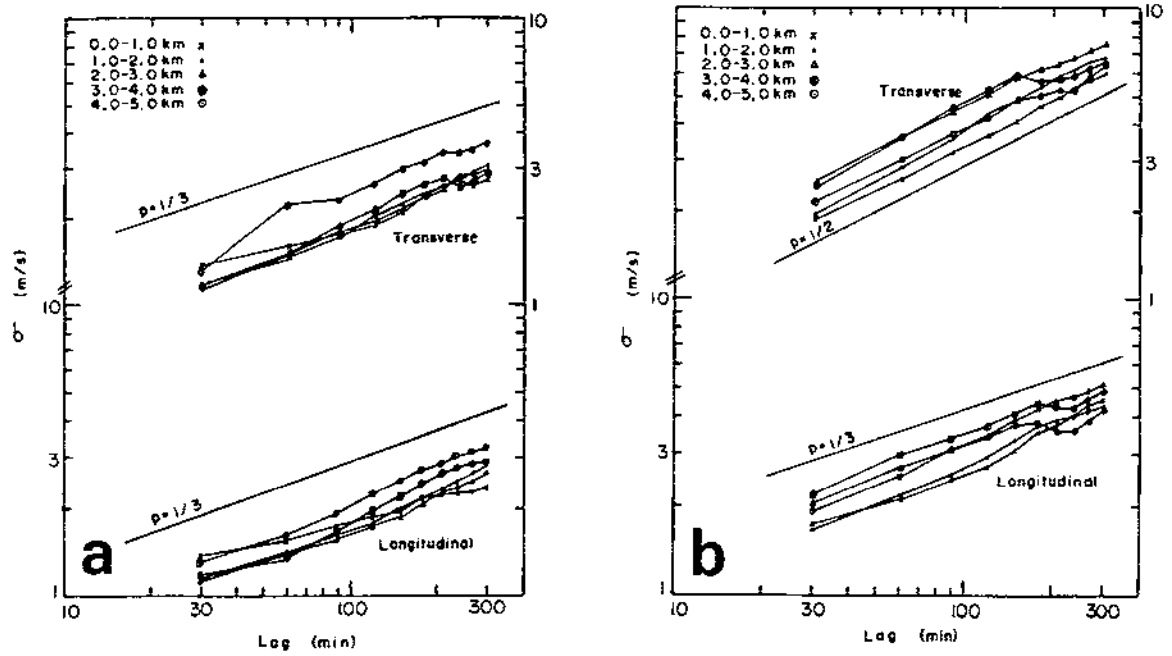

Figure 2.12: Longitudinal and transverse wind component temporal variabilities $\sigma_l(\xi)$ and $\sigma_t(\xi)$ averaged over 1 km intervals for balloon launch sequences under (a) anticyclonic and (b) cyclonic weather patterns (from Jasperson, 1982).

spectra for comparison with their aircraft-measured mesoscale KE wavenumber spectrum. Two mesoscale KE frequency spectra had been published previously by Vinnichenko (1970) and Balsley and Carter (1982). To convert these frequency spectra to wavenumber spectra, Lilly and Petersen employed the group velocity value of 23 $\mathrm{m\,s^{-1}}$ suggested by Vinnichenko (1970) as the Taylor advection velocity for the Vinnichenko spectrum and an average of the climatic mean *vector* wind speed and climatic mean *scalar* wind speed of 10 $\mathrm{m\,s^{-1}}$ for the appropriate period for Fairbanks, Alaska as the Taylor advection velocity for the Balsley–Carter spectrum. Lilly and Petersen then plotted these two Taylor-transformed mesoscale KE spectra against their own KE wavenumber spectrum plus those of Chen and Wiin-Nielsen (1978) and Nastrom and Gage (1983). Nastrom and Gage (1985) extended this comparison by including additional KE wavenumber spectra from Kao and Wendell (1970) and Boer and Shepherd (1983) (see Fig. 2.6). The reasonable agreement between these seven independent spectra, despite wide differences in data sources and analysis methods, gives support for the use of the Taylor transformation on these scales. In fact, Lilly and Petersen (1983) and Nastrom and Gage

(1983, 1985) also used the Taylor transformation themselves implicitly to convert their space-time series of aircraft measurements to a spatial measurement series. Both pairs of investigators assumed that the aircraft air speed was much greater then the propagation velocity of atmospheric disturbances. Given their nominal air speeds of $240\ \mathrm{m\,s^{-1}}$ and $250\ \mathrm{m\,s^{-1}}$, this assumption will usually be satisfied. Gage and Nastrom (1986a, p. 734) also noted that "the success of the Taylor transformation is a strong indication that the GASP spectra represent a nondispersive turbulence-like process".

Recently, Masmoudi and Weill (1988) described analyses of mean horizontal wind speeds obtained in the southwestern corner of France with a network of four Doppler sodars during the 'Mesogers 84' boundary-layer experiment. The sodars were arranged in a quadrilateral pattern with a distance of between 15 and 38 km separating each sodar pair. Both temporal and spatial velocity structure functions averaged over the lowest 350 m were calculated for a three-day undisturbed period during September 1984. Assuming the two velocity structure functions to be equal through the Taylor transformation gave a Taylor advection velocity value U of $8\ \mathrm{m\,s^{-1}}$. This value was very close to the mean observed wind speed averaged over the 350 m layer, all four stations, and all three days, suggesting that the Taylor transformation was valid in this case as well.

In summary, the Taylor transformation has been employed with some success on the mesoscale as well as on much smaller scales. Both theoretical considerations and observational evidence suggest that spatial scales on the order of 2000 km are likely to be the upper limit of applicability. At slightly smaller scales, the Taylor transformation should be viewed as an empirical tool which may give approximately correct answers under some circumstances. While potentially very useful, it should not be relied upon exclusively but rather used in conjunction with other approaches and data sources and with due regard for previous successes and failures. The best chance for success occurs when the mean speed U of the air relative to the measuring instrument is large compared to velocity fluctuations as in the case of a jet aircraft.

2.1.8 Internal gravity waves and 'undulance'

Until recently, internal gravity waves (IGW) were lumped together with acoustic waves by most meteorologists as interesting but dynamically insignificant atmospheric free oscillations. This view has changed drastically, largely as a result of the development of new observing techniques (e.g., Gossard et al., 1970; Ottersten et al., 1973). It is now recognized that gravity or buoyancy waves (a) cause much of the clear-air turbulence encountered in the upper troposphere by jet aircraft, (b) produce downslope windstorms, (c) trigger convective activity, (d) transport momentum between different atmospheric regions, (e) contribute directly and indirectly to spectral energy transfer, and (f) affect the transport and diffusion of air pollutants.

Einaudi et al. (1979, p. 632) observed that "while planetary waves are responsible for significant meridional transport of momentum and energy, gravity waves are the ones that provide efficient vertical transport of these quantities with accompanying rearrangement of the atmospheric structure." Moreover, IGWs modulate virtually every atmospheric variable, including wind speed, wind direction, temperature, density, humidity, pressure, chemical composition, and particulate concentration (Hooke, 1986). And internal gravity waves are ubiquitous: to quote Hines (1972, p. 74), "... the atmosphere from its lowest levels to its highest must be suspected of being permeated by gravity waves". Such considerations motivated Court (1965) to propose the term 'undulance' to describe a fluid "in which particles (or 'parcels') oscillate more or less regularly, in contrast to turbulence, in which the motions are irregular, random, or chaotic."

It wasn't until the 1960s that enough observational evidence was gathered, largely as a byproduct of research into clear-air turbulence (CAT), to suggest that internal gravity waves were a significant component of atmospheric subsynoptic motions. In a review article, Panofsky (1969, p. 540) discussed CAT and "mesoscale, quasihorizontal structures which have been discovered in vertical wind soundings made with precision radar, and by accurately navigated flights on constant- pressure surfaces." He concluded

that these mesoscale structures with vertical dimensions of order of 1 km were probably gravity waves.

Finally, as discussed in Sec. 2.1.5 (see p. 99), IGW activity has been suggested as one possible explanation for the observed spectrum of mesoscale fluctuations in the free atmosphere. What are the characteristics of internal gravity waves which make them a candidate?

Basic characteristics of internal gravity waves

First, internal gravity waves are mesoscale atmospheric free oscillations, the simplest and most fundamental motions on the mesoscale (Hooke, 1986). They are long-lived, propagating disturbances that can transport both momentum and energy over long distances. Their presence results in *mesoscale* fluctuations in wind speed and direction, temperature, pressure, and density. Internal gravity waves have a large number of sources and source mechanisms and are almost always present in the density-stratified free atmosphere, unlike turbulence, which is intermittent in both time and space. They can both generate turbulence (e.g., CAT) and be generated by turbulence, and internal gravity waves often act as 'triggers' for convective activity. They can also interact with each other, resulting in energy transport in wavenumber-frequency space as well as in physical space. Table 2.3 lists some of the characteristics that distinguish internal gravity waves from turbulence.

Dispersion and polarization relations. Like other classes of atmospheric waves, internal gravity waves obey a dispersion relation which relates wave frequency to wavenumber or wavelength. For plane progressive internal gravity waves in a continuously stratified, rotating medium with constant Brunt-Väisälä frequency N, the dispersion relation will be

$$\omega_i^2 = \frac{(k^2 + l^2)N^2 + f^2 m^2}{k^2 + l^2 + m^2} \quad , \tag{2.29}$$

Table 2.3: Physical differences between internal gravity waves and turbulence†.

Internal Waves	Turbulence
Weakly nonlinear	Strongly nonlinear
Weak mixing	Strong mixing and diffusion
Non-local	Local
Propagating	Non-propagating
Long-lived	Short-lived
Weakly dissipative	Strongly dissipative
Coherent	Incoherent
Obey dispersion relation	No dispersion relation

† adapted from Dewan (1985)

where ω_i is the *intrinsic* wave frequency, $\vec{\kappa}=(k,l,m)$ is the wavenumber vector, and $\kappa_H = (k^2+l^2)^{1/2}$ is the horizontal wavenumber (e.g., Gill, 1982).

The intrinsic wave frequency ω_i is the frequency of the wave relative to the air or sensed by an observer moving with the *undisturbed* air. ω_i is also known as the Doppler-shifted frequency. Doppler-shifted that is to an observer moving with the undisturbed flow (Gill, 1982). It is related to ω, the wave frequency relative to the ground or the wave frequency in a *fixed* frame of reference, by the relation

$$\omega_i = \omega - \vec{V}\cdot\vec{\kappa} \quad , \tag{2.30}$$

where $\vec{V}$ is the speed of the undisturbed flow. This distinction between types of wave frequencies is important when applying the theory of oceanic IGW spectra to the atmosphere (see p. 172).

We can see from Eq. 2.29 that the IGW intrinsic frequency ω_i will lie between a minimum value of f (when $\kappa_H = 0$) and a maximum value of N (when $m = 0$).

If ω_i is larger than N, internal gravity waves cannot propagate away from their source; instead, disturbances remain local and their amplitudes fall off exponentially with distance from the source. Such solutions are said to be 'evanescent' (Turner, 1973; Gossard and Hooke, 1975; Gill, 1982). Note that ω_i depends only on the angle ϕ' that $\vec{\kappa}$ makes with the horizontal and not on the magnitude of $\vec{\kappa}$ (unlike surface gravity waves, which are dependent on $|\vec{\kappa}|$ but independent of ϕ'). In fact, the IGW dispersion relation can be rewritten as $\omega_i = N\cos\phi'$. For a typical tropospheric Brunt-Väisälä frequency of $0.01\ s^{-1}$, the corresponding period $\tau_{BV} = 2\pi/N$ will be about 10 minutes. In the stratospheric case, a typical value of N of $0.02\ s^{-1}$ gives a τ_{BV} value of 5 minutes or so (e.g., Gill, 1982; Gage and Nastrom, 1986b). Thus, atmospheric IGW periods range from a few minutes to a few hours. When ω_i approaches f, on the other hand, Coriolis effects must also be considered. Such low-frequency internal waves are called inertia-gravity waves (Holton, 1972) or rotating waves (Gill, 1982).

The relationships between the perturbation quantities u, v, w, ρ', and p' for an internal gravity wave are often called 'polarization relations' (e.g., Gossard and Hooke, 1975; Gill, 1982). Substitution of progressive plane-wave solutions of the form $V_0\exp[i(\vec{\kappa}\cdot\vec{r} - \omega_i t)]$ for $\vec{V} = (u, v, w)$ into the incompressible continuity equation yields $\vec{\kappa}\cdot\vec{V} = 0$, implying that particle motions are perpendicular to the wavenumber vector, and hence to the IGW phase velocity vector $\vec{c}_p = (\omega_i/k^2)\vec{\kappa}$ (Turner, 1973; Gill, 1982). Particle motions will thus be parallel to wave crests and troughs as shown in Fig. 2.13a. When the vertical wavenumber m is zero, then $\omega_i = N$, $\phi' = 0$, $\vec{\kappa}$ and $\vec{c}_p$ will be horizontal, and particle motions will be vertical. At the other extreme, when $k^2 + l^2 \ll m^2$, then $\omega_i \ll N$, $\phi' \approx \pi/2$, $\vec{\kappa}$ and $\vec{c}_p$ will be nearly vertical, and particle motions will be nearly horizontal.

If a disturbance frequency ω_i is imposed externally, then the resulting atmospheric response will be that for which $\omega_i = N\cos\phi'$. That is, the atmosphere 'picks out' a response direction ϕ' which allows it to match the forcing motion. The angle $\pi/2 - \phi'$ defines the angle followed by an oscillating particle and $N\cos\phi'$ is the natural frequency

of such a displaced particle (Turner, 1973). Note that if $\omega_i > N$, that is, if the external forcing has a higher frequency than the Brunt–Väisälä frequency N, then there is no value of ϕ' which will satisfy the relation $\omega_i = N\cos\phi'$ (i.e., the evanescent case).

Group velocity. The group velocity $\vec{c}_g$ determines the propagation speed and direction of the wave envelope, wave packet, or wave group and hence also the propagation of wave energy. It has the form

$$\vec{c}_g = \nabla\omega_i = \left(\frac{\partial\omega_i}{\partial k}, \frac{\partial\omega_i}{\partial l}, \frac{\partial\omega_i}{\partial m}\right) \quad . \tag{2.31}$$

Since ω_i depends only on the direction of $\vec{\kappa}$ and not on its magnitude, $\vec{c}_g$ must be normal to $\vec{\kappa}$ and hence to $\vec{c}_p$ (Turner, 1973). Thus the group velocity will be parallel to wave crests and to particle motions. The magnitude of $\vec{c}_g$ is $(N/\kappa)\sin\phi'$ and its direction is at an angle ϕ' to the *vertical.* Since the phase-velocity vertical component $\omega_i/m = (N/\kappa)\cos\phi'\sin\phi'$ and the group-velocity vertical component $\partial\omega_i/\partial m = -(N/\kappa)\cos\phi'\sin\phi'$, when the phase velocity $\vec{c}_p$ has a downward (upward) component, the group velocity $\vec{c}_g$ will have an upward (downward) component (e.g., Gill, 1982). On the other hand, while the vertical components of $\vec{c}_p$ and $\vec{c}_g$ have opposite senses, their horizontal components will have the *same* sense or direction. The κ^{-1} dependence of $\vec{c}_g$ means that internal gravity waves will be dispersive, with low-frequency (small κ) waves having the largest group velocities.

Influence of atmospheric structure. To this point, only a uniform atmosphere has been considered. Gravity wave propagation depends upon both atmospheric temperature structure *and* velocity structure: gravity waves can be refracted or reflected due to changes in either N or $\vec{V}$. The simplest example is that of a two-layer, horizontally homogeneous atmosphere at rest where the lower layer has buoyancy frequency N_1 and the upper layer has buoyancy frequency N_2. Where for a uniform medium there were two possibilities, $\omega_i < N$ or $\omega_i > N$, for this two-layer piecewise-uniform medium there are now four solution possibilities: (a) $\omega_i < \min(N_1, N_2)$; (b) $\omega_i > \max(N_1, N_2)$; (c) $N_1 < \omega_i < N_2$; and (d) $N_2 < \omega_i < N_1$.

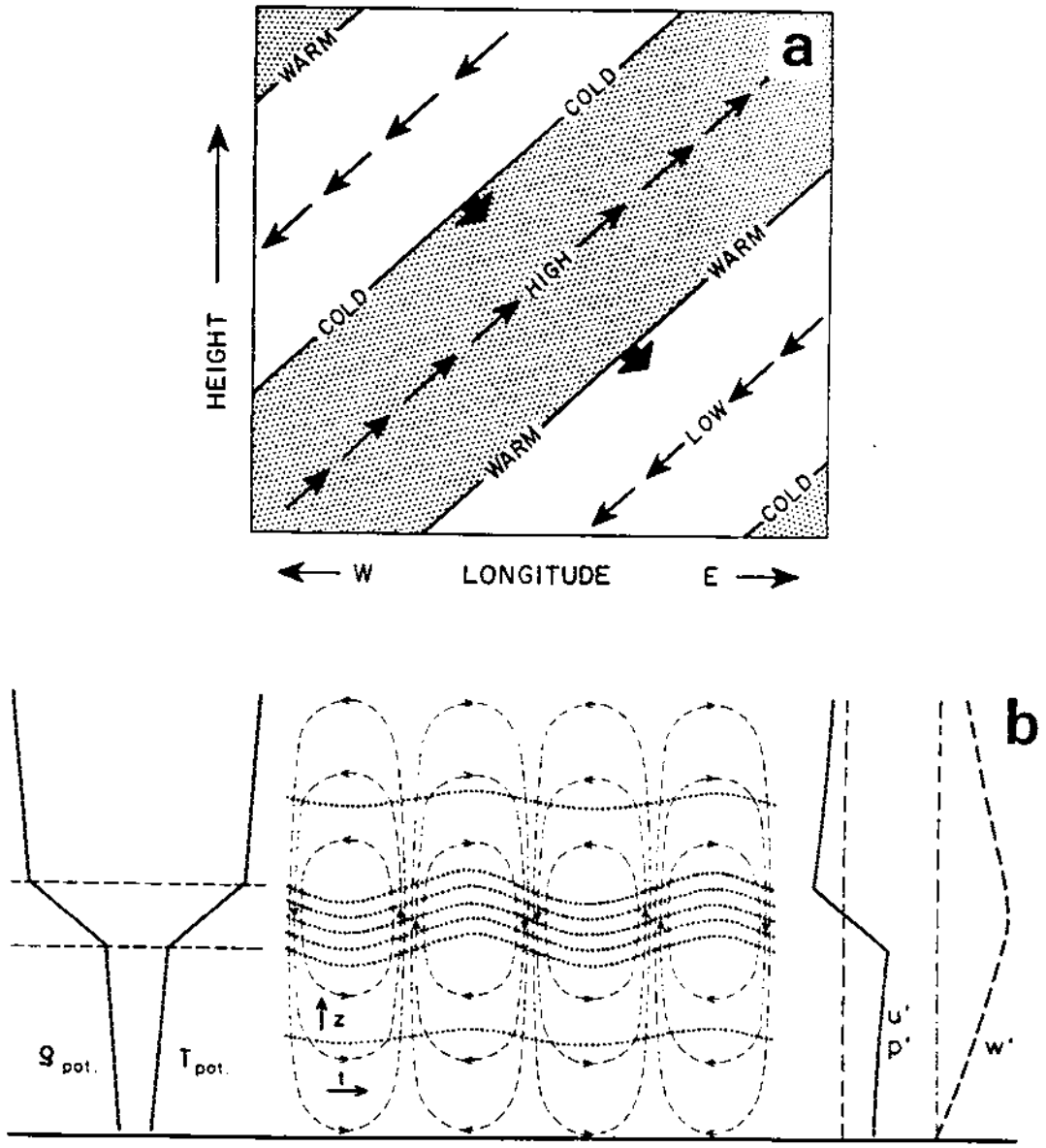

Figure 2.13: (a) Sketch showing phase relationships in vertical plane for plane progressive internal gravity wave with downward phase velocity. Solid lines denote lines of maximum and minimum pressure perturbations while dashed lines denote lines of maximum and minimum density perturbations. Thin arrows denote particle motions while thick arrows indicate phase velocity (from Wallace and Kousky, 1968); (b) Three-layer model of lower atmosphere with leftward-propagating ducted gravity waves (fundamental mode): (left) vertical profiles of potential density and potential temperature; (middle) displacement contours and particle streamlines; and (right) vertical profiles of u, w, and perturbation pressure p' (from Stilke, 1973; see also Gossard and Hooke, 1975).

In the first case, freely propagating gravity waves can be supported in both layers, but since by the dispersion relation

$$m^2 = (k^2 + l^2)\left(\frac{N^2}{\omega_i^2} - 1\right) \quad , \tag{2.32}$$

and since $k^2 + l^2$ must be the same in both layers, then both vertical wavenumber m and propagation angle ϕ' must be larger in the layer with larger N. An IGW law of refraction reminiscent of Snell's law in optics,

$$N_1 \cos\phi_1' = N_2 \cos\phi_2' \quad , \tag{2.33}$$

then follows because ω_i will also be the same in both layers. If we apply this simple model to the troposphere-stratosphere system, we see that the phase velocity of internal gravity waves entering the stratosphere from the troposphere will become more vertical and vertical wavelength will decrease. In addition, part of the wave energy will be reflected at the medium interface, leading to constructive or destructive interference in the lower layer (see Sec. 6.9 of Gill, 1982, for details).

In the second case, disturbances will be evanescent in both layers with the rate of decay depending upon N. In the third and fourth cases, internal waves will be freely propagating in one layer and evanescent in the other. In such cases, waves may be said to be 'trapped' since they are viable in only one layer. Three-layer models of the atmosphere in which a strongly stable layer is 'sandwiched' between two moderately stable layers are also very common. Such models are frequently applied to describe gravity waves propagating in the capping inversion at the top of the PBL. Fig. 2.13b shows particle streamlines and vertical profiles for a trapped or 'ducted' mode in the middle layer.

Wave frequency and the choice of reference frame. The presence of even a uniform atmospheric flow introduces another factor, the appropriate frame of reference. There are two natural reference frames for describing atmospheric waves, that of an observer moving with the air and that of an observer fixed relative to the ground. The former is appropriate

for studying wave properties *in situ* since wave propagation is usually described relative to the supporting medium. The intrinsic wave frequency ω_i will thus be the appropriate wave frequency in a moving reference frame (see p. 139). However, ground-based measurements of internal gravity waves by radar, instrumented tower, or microbarograph are made in the latter reference frame and waves generated by stratified flow over hills and mountains are commonly described relative to the ground. The ground-relative wave frequency ω is used in fixed reference frames.

It is ω which is imposed at fixed sourcea and which must remain constant following a wave *packet* (Turner, 1973). Wave phase velocities and group velocities can be expressed relative to either the air (see p. 140 and 141) or ground, depending upon whether ω_i or ω is used. For example, the Taylor–Goldstein equation for IGW vertical motion w (Taylor, 1931; Goldstein, 1931),

$$\mathrm{w}_{zz} + \left[\frac{N^2}{(U-c_p)^2} - k^2 - \frac{U_{zz}}{U-c_p}\right]\mathrm{w} = 0 \quad , \tag{2.34}$$

which is the starting point for most analyses of the effect of wind shear on gravity waves and which was introduced into meteorology by Scorer (1949), is formulated in a ground-based reference frame since $c_p = \omega/k$, where ω is the wave frequency relative to the ground (e.g., Booker and Bretherton, 1967). [Note that in Scorer's study of standing waves forced by topography, c_p was equal to zero.] However, we can also express the Taylor–Goldstein equation in terms of intrinsic wave frequency ω_i as

$$\mathrm{w}_{zz} + \left[k^2\left(\frac{N^2}{\omega_i^2} - 1\right) + \frac{kU_{zz}}{\omega_i}\right]\mathrm{w} = 0 \quad , \tag{2.35}$$

since $U - c_p = -\omega_i/k$ (e.g., de Baas and Driedonks, 1985).

Examining this equation qualitatively, it is evident that wind shear can affect wave propagation in several ways. First, ω_i is dependent upon the local value of velocity $U(z)$. If the quantity $N^2/\omega_i^2 - 1$ changes sign, then wave reflection and trapping can occur. This quantity depends upon both ambient temperature and velocity profiles. Second, the equation is singular when $\omega_i = 0$. Levels at which this occurs are called 'critical

levels' and require very careful mathematical treatment. Moreover, it has been found by both analysis and experiment that internal gravity waves encountering critical levels are partially or entirely absorbed so that such levels can play a very significant dynamical role (Eliassen and Palm, 1961; Booker and Bretherton, 1967; Hazel, 1967; Jones, 1967; Bretherton, 1969b; Lindzen and Tung, 1976; Merrill and Grant, 1979; Thorpe, 1981; and Clark and Peltier, 1984). Critical levels are also important in the theory of shear generation of Kelvin-Helmholtz waves and internal gravity waves (Gossard and Hooke, 1975).

Sources and source mechanisms

Convection and flow over orography have already been mentioned as sources of atmospheric internal gravity waves but there are a number of other source mechanisms as well. The following material expands upon a review of this topic by Gossard and Hooke (1975). Thorpe (1975) and Garrett and Munk (1979) have considered the same topic for the oceanic case.

(a) *Orography.* The generation of mountain waves or lee waves by stably stratified flow over orography is easily the best known and most studied manifestation of atmospheric internal gravity waves. The frequent occurrence of distinctive ordered cloud patterns to the lee of orography reveals the presence of these waves to the surface observer as do the less common but no less noticeable downslope windstorms. For example, Gill (1982) quotes an 1839 description of one well-known damaging wind, the Helm wind on the west side of the Pennines in England. Quantitative observations were first made of mountain waves during the 1920s and 1930s using balloons and gliders. Since then, considerable progress has been made in theoretical, observational, and modelling studies of mountain waves. Good reviews include Queney et al. (1960), Smith (1979b), Atkinson (1981), Gill (1982), and Durran (1986).

The significance of mountain waves for tropospheric dynamics has only recently been recognized. It was well known that internal gravity waves could transport momentum from the surface to the upper atmosphere (e.g., Fritts, 1984a). However, wave breaking

and momentum absorption in the lower stratosphere will affect tropospheric winds and temperatures by inducing an ageostrophic mean meridional circulation. Palmer et al. (1986) and McFarlane (1987) showed that inclusion of an orographic wave drag parameterization in operational numerical weather prediction models and general circulation models can reduce systematic westerly biases in the Northern Hemisphere wintertime flow and also improve systematic errors in the mean thermal structure.

Gossard and Hooke (1975) have noted that most studies of mountain waves to date have concentrated on the steady state case. When the flow is nonstationary, *progressive* waves should be produced rather than a wave pattern fixed with respect to the ground, thus widening the region of influence of the topography. And as discussed in Sec. 2.1.5, Gage and Nastrom (1985a, 1990) and Ecklund et al. (1986) have described mesoscale velocity frequency spectra in the vicinity of mountainous terrain which seem to have been enhanced due to the generation of a spectrum of vertically-propagating IGW by stratified flow over topographic obstacles.

(b) *Penetrative convection.* Rising convective elements, including boundary-layer thermals, cumulus clouds, and thunderstorms, can excite buoyancy waves when they penetrate an overlying stable layer. Townsend's (1965, 1966, 1968) theoretical work on penetrative convection suggested that the resulting gravity 'ripples' in the stable layer would propagate horizontally in the absence of wind shear. Stull (1976) demonstrated that penetrative convection would excite both horizontally propagating interfacial waves at the base of the inversion and vertically propagating internal gravity waves, and Gossard et al. (1971) showed FM/CW radar sounder records of convective cells generating gravity waves on the marine inversion. Deardorff (1969, 1974), Deardorff et al. (1969), and Carruthers and Moeng (1987) carried out laboratory or numerical simulations of the excitation of internal gravity waves in the capping inversion above a growing convective boundary layer. In a complementary study, Carruthers and Hunt (1985) investigated the resulting velocity statistics and spectra in a capping inversion.

Clark et al. (1986) and Kuettner et al. (1987) have argued that in the presence of vertical wind shear, both rising thermals and cumulus clouds can excite tropospheric IGW through a combination of impulsive penetration and acting as obstacles to the horizontal flow. Kuettner et al. (1987) reported aircraft measurements of these 'convection waves' up to 9 km over central Nebraska. This is an important result since convective boundary layers and fields of fair-weather cumuli are a common occurrence. Thus, even over flat terrain, the presence of a fair-weather convective boundary layer effectively replaces the rigid ground with a pulsating 'hilly' surface as a lower boundary for flow in the free atmosphere. Observations reported by Pennell and LeMone (1974) for the free atmosphere above a convective trade-wind boundary layer are consistent with this model. In addition, Clark et al. (1986) and Huang and Källén (1990) have proposed that gravity waves generated by convection can create mesoscale structures by acting to organize boundary-layer eddies and cumulus convection, and Bretherton and Smolarkiewicz (1989) have suggested that IGW are the agents responsible for adjusting environmental buoyancy to match convective buoyancy through compensating subsidence.

Observations also show the occurrence of internal gravity waves in association with deep convection (e.g., Erickson and Whitney, 1973; Gedzelman, 1983; Lu et al., 1984; Larsen et al., 1986; Einaudi et al., 1987; and Gage, 1990). Interestingly, the relationship is not as clear-cut as one might expect. For instance, Gedzelman (1983) asked, but did not answer, why relatively few cases of gravity waves associated with stratosphere-penetrating thunderstorms have been observed in light of the frequent occurrence of such deep convection. Lu et al. (1984) discussed three other mechanisms besides penetrative convection by which thunderstorms might generate IGW. It has also been suggested that IGW can interact with deep convection to create self-sustaining, propagating convective systems [see discussion of source mechanism (d)]. A good review of this 'wave-CISK' model is given in Cotton and Anthes (1989).

(c) *Shear instability.* The generation of internal gravity waves by dynamic instabilities of the wind profile is one of the most common if not the most common IGW source

mechanisms (e.g., Gedzelman and Rilling, 1978; Einaudi et al., 1979). Study of this phenomenon began in the 19th century with investigations by Helmholtz, Rayleigh, and Kelvin: their pioneering contributions are recognized today in such terms as Kelvin-Helmholtz instability (KHI), Kelvin-Helmholtz waves, the Rayleigh inflection-point theorem, and the Rayleigh stability equation. Reviews of this early work may be found in Drazin and Howard (1966) and Gossard and Hooke (1975). Since then, shear instability mechanisms in the atmosphere, oceans, and even the Sun's outer regions have been investigated by remote and *in situ* measurements and by theoretical, numerical, and physical models. Much of the atmospheric work was motivated by concerns over clear-air turbulence. Results from these studies suggest that shear instability (or Kelvin-Helmholtz instability) is 'robust'; that is, it does not depend strongly on the exact form of the velocity and density profiles involved (Fritts and Rastogi, 1985).

Mathematical models of shear instability have provided considerable insight into the nature of this phenomenon. These models are nearly all linear and so are concerned with infinitesimal disturbances, that is, with the initiation phase of shear instability (e.g., Howard and Maslowe, 1973). They may be grouped based on the characteristics of their velocity and density profiles into four main types: discontinuous profile models; continuous profile models; smooth profile models; and 'real' profile models. The first three types of models have analytical solutions while the fourth type generally requires the use of the WKB approximation for an inhomogeneous medium and numerical solution of the resulting eigenvalue problem (e.g., Gossard and Hooke, 1975; Gill, 1982).

The *discontinuous profile models* correspond to idealized layer models in which different layers have different properties with instantaneous 'jumps' in these properties occurring at the interfaces between layers. Correspondingly, in the continuous models, *gradients* of model properties have discontinuities at layer interfaces. Neither of these two types of models is likely to be realized exactly in the real world; molecular diffusion will tend to smooth out such jumps and discontinuities. They can be regarded as limiting cases, however, and many of the properties of their solutions are similar to those of more realistic

profiles and of observations. They also have the advantage of (relative) mathematical simplicity.

The very simplest mathematical model for shear instability is that of two deep uniform layers moving with different velocities (the *Helmholtz model*). Such a model would be applicable to the real world when vertical shear is concentrated over a vertical layer which is thin relative to the vertical wavelengths of interest. If both layers have the same density, then disturbances of any horizontal wavelength are unstable (Turner, 1973). If stratification is introduced, that is, if the upper layer is less dense than the lower layer, then only short disturbances will be unstable. The exact 'cutoff' wavelength will depend upon the size of the velocity and density jumps (e.g., Turner, 1973; Gossard and Hooke, 1975). Note that viscosity and surface tension are neglected in this model.

More complicated layer models have also been formulated. A two-layer model with a linear wind profile (i.e., constant shear) and one density jump is absolutely stable (Gossard and Hooke, 1975). However, a three-layer model with a linear wind profile and two density jumps (the *Taylor model*) is unstable for an intermediate wavenumber range. Motion consists approximately of two waves, one propagating along the upper density interface and one along the lower density interface at such velocities so as to stand still relative to the center of the middle layer (Howard and Maslowe, 1973). Howard (1963) discussed a 'double Helmholtz' model, a three-layer model with velocity and density jumps at both interfaces. Like the Helmholtz model, this double Helmholtz model is unstable at shorter wavenumbers but has *two* unstable subregions, one with stationary modes and a second with propagating modes.

The *Holmboe model* (Holmboe, 1962; Smyth and Peltier, 1989) has a piecewise-smooth velocity profile consisting of a constant velocity layer, a constant shear layer, and a second constant velocity layer with a density jump in the middle of the shear layer. This model is unstable for intermediate wavelengths and also has two unstable subregimes with stationary and propagating modes, respectively (Howard and Maslowe, 1973). One last discontinuous layer model, the well-known *Taylor-Goldstein model*, has a velocity profile

like that of the Holmboe model but has *two* density jumps, one at each of the velocity gradient discontinuities. Like the Taylor model, it is unstable for an intermediate-wavelength range centered on modes propagating along the two interfaces at the same speed (Turner, 1973).

The *continuous profile models* have some qualitative differences from the discontinuous profile models. The simplest of the continuous-profile models is the *Rayleigh model*, which consists of the same three-layer velocity profile as the Holmboe and Taylor-Goldstein models but in a constant-density fluid. The Rayleigh model is unstable only at shorter wavelengths (Gossard and Hooke, 1975), unlike the Helmholtz model in a homogeneous fluid. The other frequently discussed continuous, piecewise-smooth profile model is a stratified version of the Rayleigh model with density decreasing linearly across the central shear layer and constant density in the two outer layers (see Fig. 2.14). This *Goldstein* model was first analyzed by Goldstein (1931) and later by Miles and Howard (1964). Like some of the stratified discontinuous models (Taylor model, Holmboe model, Taylor-Goldstein model), only an intermediate wavenumber range is unstable for the Goldstein model. However, unlike any of the discontinuous profile models, which are unstable no matter how large the density differences, the Goldstein model only has unstable modes for layer gradient Richardson number Ri of 0.25 or less. When Ri is reduced below 0.25, the first unstable horizontal wavelength λ is approximately equal to $7.5h$, where h is the thickness of the center layer.

Smoothly-varying profile models represent the limits of analytical tractability. Many employ a hyperbolic-tangent velocity profile. However, depending upon the choice of velocity and density profiles, they may display behaviour qualitatively similar to some of the simpler models, including the Taylor, Holmboe, and Goldstein models (see discussions in Drazin and Howard, 1966; Howard and Maslowe, 1973; Turner, 1973; and Gossard and Hooke, 1975). The specification of smoothly varying velocity and density profiles also results in continuous profiles of Ri and N since these quantities depend on the first derivatives of the velocity and density (or potential temperature) profiles, respectively.

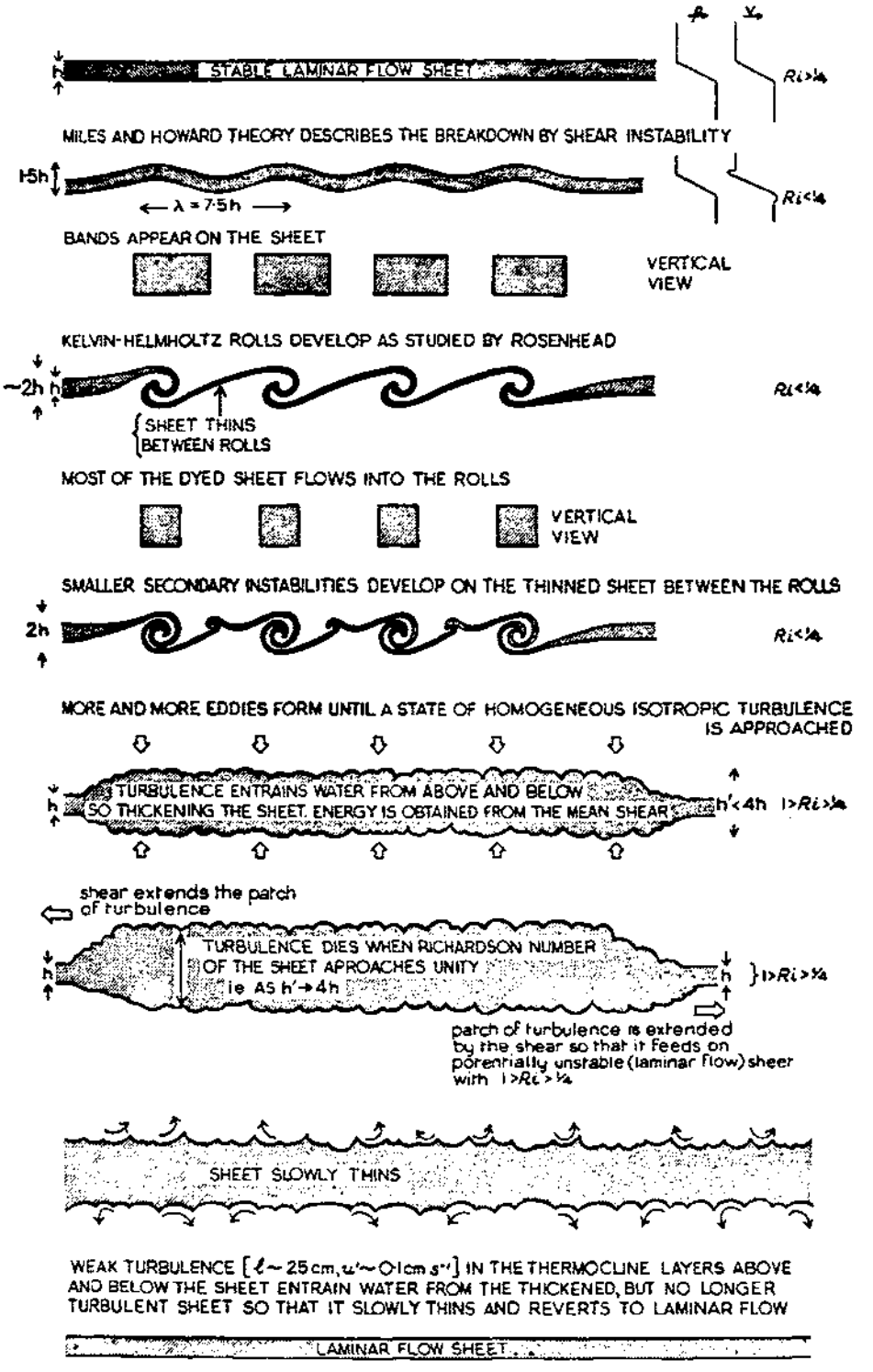

Figure 2.14: Schematic representation of the development of spontaneous KH billows on a thermocline sheet and subsequent transition to turbulence in conditions where the density and velocity differences across the sheet do not change during the lifetime of the turbulence (from Woods, 1969a).

Three general criteria relevant to shear instability have also been developed. First, Rayleigh showed in 1878 that a *necessary* condition for instability in a *homogeneous* fluid with a monotonic velocity profile is that the velocity profile have at least one inflection point. The inflection point in turn corresponds to a vorticity extremum. Second, Howard (1961, p. 510) proved for an inviscid, continuously stratified fluid that "the complex wave velocity c for any unstable mode must lie inside the semicircle in the upper half-plane which has the range of U for diameter", i.e., the semicircle on the complex plane (c_r, c_i) with center $0.5\,(U_{\max}+U_{\min})$ and radius $0.5\,(U_{\max}-U_{\min})$ [see Fig. 4.6 in Turner, 1973]. This *necessary* condition for shear instability in an inhomogeneous fluid is often referred to as Howard's semicircle theorem (e.g., Gossard and Hooke, 1975). Third, Miles (1961) proved that the *sufficient* condition for an inviscid, continuously stratified flow to be *stable* to small disturbances is that the *local* gradient Richardson number Ri be larger than $1/4$ *everywhere* in the flow. Howard (1961) also showed how his semicircle theorem, Miles's stability theorem, and Synge's (1933) generalization of Rayleigh's inflection-point theorem for stratified flows can be obtained from the same integral relation.

Laboratory models have been used to generate Kelvin–Helmholtz instabilities (KHI) on interfaces between fluid layers. Thorpe (1969, 1973a) carried out a series of classic experiments to investigate the stability of stratified shear flows. He used a closed tube of rectangular cross-section which contained a homogeneous layer of fresh water overlying one of brine. Other KHI laboratory studies include those of Delisi and Corcos (1973) using a wind tunnel and Koop and Browand (1979) using a water channel.

Woods (1968, 1969a) used scuba divers and tracer dye releases to study KHI in the seasonal Mediterranean thermocline off Malta. Fig. 2.14 shows his conceptual model for the evolution of KHI on a thin 'sheet' of fluid[39] (i.e., a Helmholtz profile modified by interface diffusion). Thorpe (1973b) presented a very useful summary table comparing

---

[39] The later stages of this model will be referred to shortly in the discussion of wake collapse and restratification in mechanism (g).

characteristic KHI parameter values measured in laboratory experiments, atmosphere, and ocean.

Successful *numerical simulations* of KHI and the development of finite-amplitude Kelvin-Helmholtz 'billows' have been carried out by Patnaik et al. (1976), Davis and Peltier (1979), Fritts (1982), Sykes and Lewellen (1982), and Klaassen and Peltier (1989), among others. Such simulations have allowed the investigation of nonlinear interactions not amenable to mathematical analysis.

Many *observational atmospheric studies* have also found evidence of KHI and shear-induced internal gravity waves. Ground-based arrays of microbarographs have recorded numerous instances in which internal gravity waves detected at the surface appear to be associated with jet-stream winds (e.g., Madden and Claerbout, 1968; Herron and Tolstoy, 1969; Herron et al., 1969; Hooke and Hardy, 1975; Keliher, 1975). That is, IGW phase speeds and directions correlate well with the mean wind speed and wind shear direction, respectively, of the most unstable upper tropospheric layer in accordance with the Wegener hypothesis[40]. Herron and Tolstoy (1969) showed that good correlations could persist for weeks and Keliher (1975) estimated that between one-third and one-half of the 280 IGW events which he analyzed from Colorado and Washington, D.C. microbarograph array data appeared to be associated with upper-level wind shear.

Hooke and Hardy (1975) described a case in which jet-stream-associated gravity waves were measured simultaneously by a microbarograph array and a 10-cm wavelength radar. Gage (1990) has summarized numerous other radar observations of Kelvin-Helmholtz waves and clear-air turbulence in the upper troposphere made by UHF and VHF radars over the past twenty years. Similar studies of wave propagation and wave breaking within the elevated marine inversion have been carried out using FM-CW radar (e.g., Richter, 1969; Gossard et al., 1970, 1973; Metcalf, 1975b). KHI was shown to occur

---

[40] States that cloud billows produced by wind-shear-generated IGW will tend to have their wave fronts perpendicular to the wind shear and will tend to be advected with the mean wind speed of the unstable shear layer (Keliher, 1975; Gossard and Hooke, 1975).

in vertical layers only a few meters thick in some cases. Gossard (1990) recently reviewed many of these PBL radar studies. Finally, Fritts and Rastogi (1985) have reviewed a large number of observational studies of atmospheric shear instability, including studies based on visual observations, radar, sodar, and aircraft-, rocket- and balloon-borne instruments.

Although KH waves are the fundamental shear instability mode, other unstable and neutral modes can occur. KH waves are *evanescent* both above and below their level of generation, are *stationary*, and are *restricted in horizontal extent* by the depth of the shear layer that generates them. However, many observations of jet-stream-associated gravity waves indicate the existence of *propagating* waves with horizontal wavelengths of several kilometers or more. Drazin and Howard (1966), Jones (1968), Lindzen (1974), Acheson (1976), Grimshaw (1976), and McIntyre and Weissman (1978) have observed that discontinuous or piecewise continuous velocity profiles in an *unbounded*, stratified fluid can support *neutral* internal gravity waves as well as KH modes. The presence of a rigid boundary will introduce additional unstable modes through the mechanism of *over-reflection* (e.g., Jones, 1968; Acheson, 1976; Davis and Peltier, 1976; Lalas et al., 1976; Lalas and Einaudi, 1976; Lindzen and Rosenthal, 1976; Klemp and Lilly, 1978; Lindzen and Tung, 1978; Smyth and Peltier, 1989). Some of these modes are propagating ones while others are evanescent. Jones (1968), Kogan and Shakina (1973), Lalas and Einaudi (1976), Mastrantonio et al. (1976), Davis and Peltier (1976), and Chimonas and Grant (1984a) considered realistic velocity and static stability profiles and found propagating unstable modes as solutions in addition to the KH mode. Fua et al. (1976) and Davis and Peltier (1976) examined the stability of inflection-free velocity profiles.

All of the studies listed above were based on linear theory. In every case, the KH mode was found to be the fastest-growing, which suggests that this mode will dominate the other modes and hence preclude the development of finite-amplitude propagating shear modes. Nonlinear processes, however, provide a path by which other shear modes may still occur. Two main mechanisms have been suggested to date. In one, the *vortex-pairing*

or *subharmonic interaction* mechanism, propagating gravity waves are excited by the nonlinear interaction of pairs of the fastest growing KH mode (McIntyre and Weissman, 1978; Davis and Peltier, 1979; Fritts, 1984b). In the second, the *envelope radiation* mechanism, the nonlinear interaction of two KH modes of similar wavelength excites a propagating unstable mode of much longer wavelength (Fritts, 1982, 1984b; Chimonas and Grant, 1984b). Fritts (1984b) compared these two mechanisms and concluded that the envelope radiation mechanism will occur under a much wider range of conditions than the subharmonic interaction mechanism [see also the discussion of wave-wave interactions in source mechanism (e)].

(d) *Squall lines, frontal systems and density currents.* A number of studies since early work in the 1950s (e.g., Williams, 1953) have associated the occurrence of some internal gravity waves with squall lines and various frontal systems. Recently, Schmidt and Cotton (1990) used observations and a mesoscale meteorological model (RAMS: see Chap. 4) to examine the coupling between internal gravity waves generated by a squall line and the structure and maintenance of the squall line itself in a sheared environment. Cram (1990) and Cram et al. (1992a,b) also used RAMS in a real-data case study of the development and propagation of a squall line which had formed and moved ahead of an advancing cold front. They proposed that the observed propagation of the squall line at a velocity greater than that of the cold front was due to the propagation of a deep, tropospheric internal gravity wave in a wave-CISK-like process. Lin and Goff (1988) described a solitary mesoscale gravity wave which was generated by a squall line north of the Gulf of Mexico and then propagated over 1000 km to New England along a midtropospheric inversion.

Ley and Peltier (1978) used an analytical model and Gall et al. (1988) used another nested-grid numerical model to study IGW generation during frontogenesis. Hobbs (1978) has suggested that internal gravity waves propagating ahead of a cold front may be the cause of the warm-sector rainbands sometimes observed in extratropical cyclones. Both Gossard and Sweezy (1974) and Caughey and Readings (1975) have considered cases of

internal gravity waves associated with a frontal system. Gedzelman and Rilling (1978) noted that very large amplitude gravity waves often accompany the passage of cold fronts.

Donn et al. (1956) have described the propagation of large-amplitude internal gravity waves on a *sea-breeze* front and Gossard and Munk (1954) also mentioned sea-breeze fronts as a source of internal gravity waves. Geisler and Bretherton (1969) referred to internal gravity waves progagating inland ahead of the mean sea-breeze front as the sea-breeze 'forerunner'. Noonan and Smith (1987) have proposed colliding sea-breeze fronts as one generation mechanism for the 'Morning Glory', interface waves (or 'bore waves') at the leading edge of an internal undular bore which are often observed in northern Australia, and Haase and Smith (1984) speculated that an observed Oklahoma morning glory was initiated by a thunderstorm outflow impinging on a pre-existing low-level stable layer [see Smith (1988) for a review of the morning glory phenomenon and Simpson (1987) for a summary of the literature on atmospheric internal bores].

(e) *Wave-wave interactions.* Internal gravity waves are weakly nonlinear and hence can interact with other gravity waves. A quadratic interaction between two sinusoidal waves with phases $\vec{\kappa}_1 \cdot \vec{x} - \omega_1 t$ and $\vec{\kappa}_2 \cdot \vec{x} - \omega_2 t$ can be approximated by including forcing terms in the linearized dispersion equation with sum and difference phases $(\vec{\kappa}_1 + \vec{\kappa}_2) \cdot \vec{x} - (\omega_1 + \omega_2)t$ and $(\vec{\kappa}_1 - \vec{\kappa}_2) \cdot \vec{x} - (\omega_1 - \omega_2)t$ (Bretherton, 1969a). These terms will excite new modes with wavenumbers $\vec{\kappa}_3 = \vec{\kappa}_1 \pm \vec{\kappa}_2$ and frequencies $\omega_3 = \omega_1 \pm \omega_2$. However, forced modes will grow very slowly unless $\vec{\kappa}_3$ and ω_3 also satisfy the dispersion relation, in which case energy transfer to the new mode will be more rapid until energy is partitioned equally among the three modes. Such interactions are termed resonant and the three modes are called a 'resonant triad'.

Note that the excited mode $(\vec{\kappa}_3, \omega_3)$ may be either smaller or larger in scale than the two initial modes, thus allowing the possibility of complex spectral interactions. When generalized to the case of a random wave field, this theory of resonant interactions yields a continuous energy spectrum (Bretherton, 1969a). Cubic and even higher-order resonances are also possible. The essential mathematics of wave–wave interactions was first

developed for quantum field theory, and such tools as Feynman-path-integral formalism can be directly applied to internal wave interactions (Hasselmann, 1966, 1967; Müller et al., 1986). McComas and Bretherton (1977) identified three types of dominant resonant triads: (i) induced diffusion, (ii) elastic scattering, and (iii) parametric subharmonic instability — (or PSI). PSI is closely related to Orlanski's (1973, 1976a) 'trapeze' instability.

(f) *Geostrophic adjustment.* Large-scale extratropical atmospheric flow above the PBL is generally close to a state of geostrophic balance. When ageostrophy occurs, the atmosphere undergoes mass and momentum adjustments to restore geostrophy; inertial-gravity waves are excited which carry energy away from the region of imbalance (e.g., Matsumoto, 1961; Blumen, 1972, and references therein; Schubert et al., 1980). Such behaviour is frequently observed in the early stage of NWP model runs unless the initial fields are balanced by a technique such as nonlinear normal mode initialization.

Uccellini and Koch (1987) have reviewed thirteen case studies of mesoscale wave disturbances which consisted either of single waves of depression or wave packets with periods of one to four hours and horizontal wavelengths of 50 to 500 km. They argued that most or all of these wave events appeared to share a similar large-scale synoptic pattern with wave initiation occurring within the exit region of a jet streak propagating towards an upper-level ridge and suggested geostrophic adjustment as the generation mechanism. They also concluded that the coherence and long lifetimes of these events could be explained by the presence of a tropospheric wave duct (basically a low-level stable layer capped by a convectively-unstable upper layer containing a critical level; see Lindzen and Tung, 1976, for details).

Fritts and Luo (Fritts and Luo, 1992) noted recently that the major tropospheric IGW sources, orography, penetrative convection, and shear instability, excite predominantly high-frequency gravity waves whereas the IGW spectrum at many altitudes is dominated by inertio-gravity waves, that is, gravity waves with frequencies close to the

inertial frequency. They surggested that geostrophic adjustment of the jet stream is likely to be a major source of such low-frequency gravity waves.

(g) *Restratification.* Mixed-region collapse occurs in a stably stratified fluid when a vertically well-mixed region, which has an excess of potential (and possibly kinetic) energy relative to the surrounding fluid, equilibrates intrusively at its level of neutral buoyancy by collapsing vertically and expanding horizontally. The resulting displacements of the surrounding fluid generate internal gravity waves and solitary waves (e.g., Amen and Maxworthy, 1980). Mixed regions can be formed by convective or shear-instability mixing and occur naturally in both the atmosphere and the oceans. Laboratory studies of the gravitational collapse of mixed regions include those of Wu (1969), Pao (1973), Lin and Pao (1979), Amen and Maxworthy (1980), Dickey and Mellor (1980), Maxworthy (1980), Stillinger et al. (1983), Broward and Hopfinger (1985), Liu et al. (1987), and Itsweire and Helland (1989). Gibson (1981, 1987) has discussed restratification in the context of oceanic fossil turbulence and Amen and Maxworthy (1980) have suggested that restratification may contribute to the fine-scale structure of the oceanic thermocline. In the atmosphere, Lilly (1983, 1988) and Etling (1990a) have investigated the collapse of thunderstorm cirrus outflows (see also Sec. 2.1.9). Presumably restratification also plays a role in the decay of isolated free-troposphere turbulent patches generated by shear instability (e.g., CAT).

IGW Climatology

A number of studies have been published concerning the frequency of occurrence of internal gravity wave fluctuations at the Earth's surface. Such studies provide what amount to lower-bound likelihood estimates since many downward propagating internal waves are damped and filtered in the lower troposphere before reaching the ground (Gedzelman, 1983).

Gossard (1960), Herron and Tolstoy (1969), and Herron et al. (1969) presented surface pressure frequency spectra that included the 3–60 minute range in which tropospheric IGW activity might be expected. Gossard (1960) mentioned convection and sea-breeze

fronts as sources of IGW activity for his southern California observations, while Herron and Tolstoy (1969) and Herron et al. (1969) mentioned jet-stream instability and generation by synoptic fronts as sources for their New England observations. Stilke (1973) reported detection of internal gravity waves 10% of the time during a four-year period by a German microbarograph station network. The waves occurred most frequently at night and showed similar seasonal behaviour to the frequency of occurrence of low-level temperature inversions. Keliher (1975) analyzed 181 gravity wave events detected at Boulder, Colorado by a microbarograph array during a four-month winter period (154 events) and a three-month summer period (27 events) and another 99 gravity wave events detected with another microbarograph array located in Washington, D.C. Based on analysis of twice-daily rawinsonde data from nearby rawinsonde stations, Keliher concluded that at least one-half of the events were due to upper-level shear.

SethuRaman et al. (1982) prepared an IGW climatology using two years of measurements from two sites on Long Island, New York, one on the eastern shore at Tiana Beach and one 15 km inland at Brookhaven National Laboratory. The inland station showed a pronounced diurnal variation with nighttime maximum whereas the coastal station showed little diurnal variation, but total IGW activity was comparable at the two sites. Raynor and Hayes (1984) extended the work of SethuRaman et al. (1982) and compiled a variety of IGW statistics for the Tiana Beach station, including frequency distributions of wave duration, wave period, wave angular amplitude, and number of waves. Gedzelman (1983) used one year of measurements from an array of four microbarograph stations to prepare an IGW climatology for Palisades, New York. He found that wave amplitudes increased markedly when extratropical cyclones approached the study area, suggesting upper-tropospheric shear generation as a source (see also Gedzelman and Rilling, 1978, and Gedzelman and Donn, 1979).

Canavero and Einaudi (1987) have calculated surface pressure frequency spectra at two stations in northern Italy from 60 days of high-frequency observations made during the 1982 Alpine Experiment (ALPEX), and Einaudi et al. (1989) produced a climatology of

gravity waves and other coherent disturbances at the Boulder Atmospheric Observatory (BAO) during a one-month period in the spring of 1984. Such disturbances included density currents, thermals, turbulence patches, downdrafts, and cloud bands in addition to internal gravity waves, all with periods ranging from 1 to 20 minutes. Overall, Einaudi et al. found coherent motions to be present about 25% of the time for 1–5 minute periods and more than 80% of the time for 10–20 minute periods, with the percentages rising even higher when only nighttime measurements were considered.

Wave breaking and turbulence

One important dynamical role played by internal gravity waves is to trigger flow instabilities which then produce isolated patches of turbulence, even in the interior of stably stratified fluids. Two types of wave-induced flow instability are the most common: *Kelvin-Helmholtz* (or KH or shear) instability and *convective* instability (also known as advective or Rayleigh-Taylor instability). KH instability can only occur when the local gradient Richardson number Ri falls below a value of 1/4. Internal gravity waves can induce this instability because they simultaneously generate shear and modify local stability by tilting isopycnals or isentropes. Convective instability occurs when wave motions have sufficiently large amplitude, either alone or superposed with others, to advect heavy fluid over lighter fluid. This mechanism is often referred to as 'wave breaking' and requires a negative Richardson number. Thus, KH instability is the more common of these two types of flow instability.

Wave-induced KH instability occurs preferentially in regions where large gradients of density and velocity are present but can also occur in uniformly stratified fluids due to low-frequency waves (Fritts and Rastogi, 1985). The layering associated with vertical fine structure can thus control where KH instability occurs. Fig. 2.15 shows a wind direction trace from a coastal location which recorded wind direction meander and turbulent bursts due to breaking internal gravity waves.

Wave-induced convective instability tends to occur due to high-frequency waves with large vertical group velocities. The high wave amplitudes required by this instability are

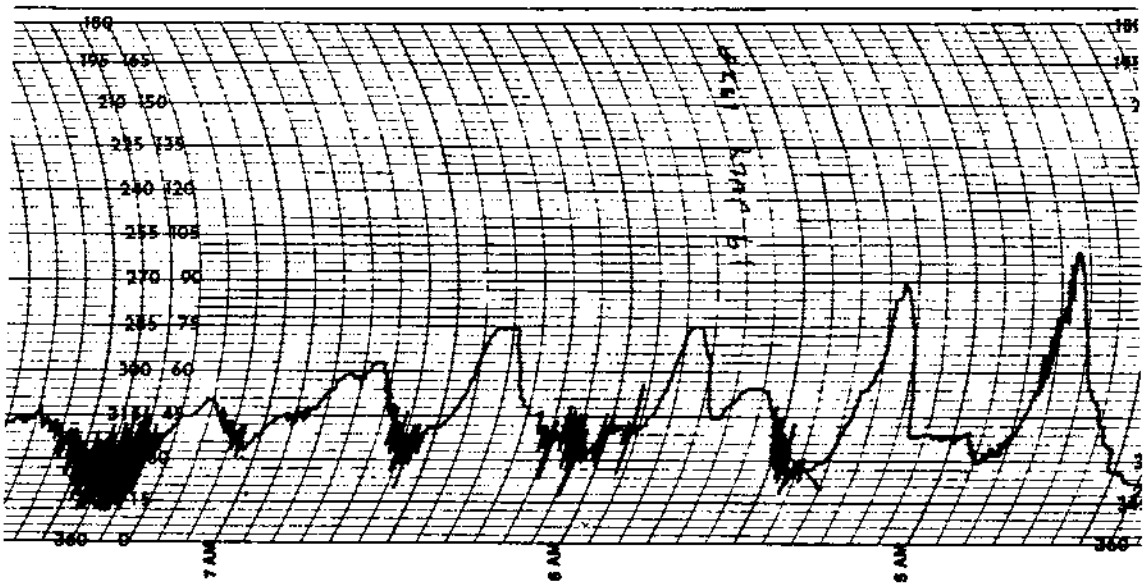

Figure 2.15: Section of a wind direction chart from a 23-m tower at Tiana Beach, Long Island from 0430-0730 EST, 19 July 1978 (from Raynor and Hayes, 1984).

most likely to be found near strong sources or critical levels or at high altitudes. One example of a strong IGW source is a resonant mountain wave (e.g., Lilly and Kennedy, 1973; Lilly, 1978). Another is a region of reduced stability such as the underside of the tropospheric jet stream.

Either of these instabilities can result from reduced Richardson numbers caused by constructively interfering waves in a random wave field. Such a random superposition of internal gravity waves is common in both the atmosphere and ocean. In such cases, however, the term 'wave breaking' is no longer strictly applicable since the instability is not associated with a particular internal wave train (Gregg and Briscoe, 1979). Turbulence generated by flow instabilities in a random wave field will obviously be both intermittent in time and patchy in space. Bretherton (1969a) suggested an approximate formula to estimate the degree of intermittency. Recent discussions of wave-induced instabilities in the ocean include those of Sherman et al. (1978), Olbers (1983), Gibson (1987), Gregg (1987), and Gargett (1989). In the atmosphere, clear-air turbulence is often the result of wave-induced instabilities (e.g., Pinus et al., 1967; Vinnichenko et al., 1980).

Shear instability and convective instability impose important limits on upward-propagating internal gravity waves, leading to wave 'saturation'[41] in the stratosphere and mesosphere. Downward-propagating waves can also induce flow instabilities. Gossard et al. (1973), SethuRaman (1977), Merrill and Grant (1979), Finnigan et al. (1984), and Finnigan (1988) have discussed cases in which instabilities occurred in stable layers near the Earth's surface as a result of Richardson-number perturbations induced by downward-propagating internal waves.

Influence on vertical fine structure

The action of internal gravity waves has been suggested as one mechanism contributing to the formation of atmospheric vertical fine structure (see Sec. 2.1.6). Hines (1960) proposed that the smaller-scale vertical variations in ionospheric wind profiles revealed by meteor-trail shearing could be explained by the random superposition of propagating internal gravity waves. Later investigators suggested that the same mechanism could also explain wind-profile fine structure in the troposphere and stratosphere as well (e.g., Sawyer, 1961; Weinstein et al., 1966; Axford, 1968; Endlich et al., 1969; Gage and Jasperson, 1979; Barat, 1983; Fritts et al., 1988; Fairall et al., 1991).

The presence of internal gravity waves may also help to explain some of the observed *density* fine structure in the ocean and *potential temperature* fine structure in the atmosphere. Orlanski and Bryan (1969) and Woods and Wiley (1972) suggested that the 'sheets' and layers observed in oceanic profiles could be a result of episodic turbulent mixing initiated by IGW breaking and followed by mixed-layer collapse (e.g., Wu, 1969; Amen and Maxworthy, 1980; Browand and Hopfinger, 1985). Gossard et al. (1985) have proposed that a similar mechanism produces atmospheric step structure. Desaubies and Gregg (1981) compared reversible oceanic microstructure produced by IGW strain with irreversible microstructure resulting from turbulent mixing and found that IGW strain

---

[41] Any IGW field in which wave amplitudes are limited by instabilities or interactions arising from large-amplitudemotions (see review in Fritts, 1984a).

contributed significantly to larger features but not to fine structure at scales smaller than a few meters.

Radar and sodar observations of the stably-stratified PBL often show the presence of multiple, thin, horizontal lamina or strata which are sometimes regularly spaced in the vertical (Gossard et al., 1971; Beran et al., 1973; Ottersten et al., 1973; Davis and Peltier, 1976; James, 1980). Gossard et al. (1971) suggested that these strata might represent the nearly horizontal wave-phase surface of downward-propagating gravity waves impinging upon the stable PBL. Davis and Peltier (1976) suggested an alternative mechanism in which local PBL shear instability produces long-wavelength gravity wave modes *in situ*. Recently, Hooke and Jones (1986) offered a third explanation: they proposed that the interaction of externally-generated IGW encountering the stable PBL and rough, rigid Earth's surface could excite short-wavelength viscous and thermal-conduction *dissipative* waves. Such waves are generated in order to satisfy the no-slip and thermal boundary conditions at the Earth's surface. Given the short wavelengths of these waves together with amplitudes comparable to those of their parent gravity waves, dissipative waves can create large shears and thermal gradients which lead in turn to dynamic and convective instabilities and turbulent breakdown. Useful reviews of the origins of atmospheric and oceanic fine structure include Gregg (1987), Gage (1990), and Gossard (1990).

Influence on atmospheric dispersion

There are relatively few references to internal gravity waves in the air pollution literature[42]. Although internal gravity waves can transport momentum and kinetic and potential energy, to first order they cannot contribute to net mass transport. Nevertheless, internal gravity waves can influence the atmospheric dispersion of trace gases and pollutants in several ways.

Gifford (1959) proposed a mathematical model of a fluctuating plume that separated total lateral dispersion into two components: (i) lateral diffusion; and (ii) center-

[42] One exception is Högström's (1964) brief discussion of 'wave turbulence'.

line fluctuation or meandering. Changes in horizontal wind direction, whether due to random fluctuations or periodic oscillations, cause plume meander and result in lower time-averaged concentrations (e.g., Fig. 1.6). Kristensen et al. (1981) investigated the effect of plume meander in a very stable atmosphere and found that meandering can easily decrease mean ground-level concentrations by a factor of five.

One important characteristic of internal gravity waves is the oscillating variation that they can induce in either wind speed or wind direction depending upon their direction of propagation relative to the mean wind (see Fig. 2.13b). In fact, the occurrence of wave-like changes in surface wind direction has been used to identify IGW events (e.g., SethuRaman et al., 1982; Raynor and Hayes, 1984). Such periodic variations[43] in wind direction will cause plume meander (e.g., Etling, 1990b). In one of the earliest studies of atmospheric IGW, Gossard and Munk (1954) analyzed surface oscillations of wind direction, wind speed, and surface pressure for seven IGW events recorded over a 13-month period in southern California. Crest-to-trough wind direction swings ranged from 78° to 318° under conditions of generally light background winds. SethuRaman et al. (1982) found mean monthly horizontal directional amplitudes (crest to trough) of between 10° and 25° during gravity wave events at the two stations in their IGW climatology. Raynor and Hayes (1984) extended this work and examined almost 700 cases of wind direction meander that occurred during onshore flow over a three-year period at the Tiana Beach site. They found event-mean directional amplitudes ranging between 4° and 68° with an average of 14° and maximum amplitudes as large as 125°. The wave events measured at this site lasted between 4 and 438 minutes with an average duration of 94 minutes. Meander with angular amplitudes greater than 3° occurred 15% of the time during onshore flow.

---

[43] Note that the velocity records used to calculate velocity variance in atmospheric turbulence measurements are typically discarded if either time trends or slow oscillations are present, effectively screening out IGW contributions (e.g., Högström, 1964; Csanady, 1973, Sec. 3.13)

Internal gravity waves can also influence diffusion under stable conditions by increasing turbulence intensity levels through wave breaking (Einaudi et al., 1979). For example, SethuRaman (1977) reported a hundredfold increase in turbulence intensity compared to background levels during a wave-breaking event in the marine boundary layer off Long Island, New York. SethuRaman (1980) made direct measurements from an aircraft of KE dissipation rate ϵ during a very long-lived wave-breaking event and found values two orders of magnitude larger than values usually observed over water under conditions of stable stratification and moderate wind speeds (i.e., 200 cm^2s^{-3} vs. 1 cm^2s^{-3}). Gossard et al. (1973), Merrill and Grant (1979), Finnigan and Einaudi (1981), Finnigan et al. (1984), and Finnigan (1988) have also studied cases where downward-propagating waves from levels above the PBL both *generated* and *modulated* PBL turbulence. Other studies of shear breakdown in the stable nocturnal boundary layer over land include those of Caughey and Readings (1975), Lu et al. (1983), de Baas and Driedonks (1985), and Nappo (1990).

Wave-breaking generation of turbulence is also common in the free atmosphere but is very intermittent. Climatological studies of clear-air turbulence and tropospheric energy dissipation rate may be useful in parameterizing turbulent diffusion occurring *above* the PBL. A recent paper by Pleune (1990) outlines one possible approach to this problem. On a related topic, the role of internal waves in laboratory and oceanic mixing has been discussed by Thorpe (Thorpe, 1973b), Sherman et al. (1978), Garrett (1979), and Young et al. (1982).

Identification of waves and turbulence

One important problem in the study of stably stratified flows is the degree to which turbulent motions can be distinguished from internal gravity waves when both are present. These two types of flow motion have very different transport and mixing properties (e.g., Table 2.3), and estimates of transport, diffusion, or dissipation made from measured variances may be grossly incorrect if the wrong motion type is assumed. Moreover, in a stably stratified flow, both waves and turbulence will generally be present and will modify

each other (Busch, 1969). Stewart (1969) considered this problem and concluded that a rigorous general solution seemed impossible. However, he proposed several experimental criteria that would allow an approximate identification and separation.

Among these, Stewart suggested that cross-spectral analysis could be used for this purpose based on the different physical and spectral properties of turbulence and internal gravity waves. Turbulent motions are strongly diffusive and can transport passive scalars such as heat. In linear gravity waves, on the other hand, vertical velocity fluctuations and temperature (or density) fluctuations are 90° out of phase (i.e., in quadrature) so that the covariance $\overline{w'\theta'}$ will be negligible for wave-dominated flows. In terms of cross-spectra, the vertical velocity–temperature squared coherence[44] Coh^2 will be large and a relative maximum and the phase angle will be near $\pm 90°$ at one wavelength if monochromatic waves are present, whereas for turbulence the vertical velocity–temperature squared coherence will be smaller and the phase angle will be close to 0° or $\pm$ 180°. In terms of other cross-spectral quantities, for monochromatic waves the vertical velocity–temperature cospectrum Co^2 will be small and a relative minimum while the quadrature spectrum Q^2 will be large and a relative maximum. However, since the quadrature spectrum is an odd function, its integral is zero and it does not contribute to the total covariance (Metcalf, 1975a). Vertical mixing is considered because of the near horizontal homogeneity in the stratified atmosphere (Dewan, 1985), although this will often not hold true over complex topography.

Cross-spectral analysis has been used in a number of studies of stratified flows, including Axford (1971), Pao (1973), Caughey and Readings (1975), Metcalf (1975a), SethuRaman (1977), Lu et al. (1983), de Baas and Driedonks (1985), and Hunt et al. (1985). Axford (1971) analyzed lower-stratospheric aircraft measurements from a 100 km flight through essentially 'smooth' air; there was no observable turbulent energy in the wavelength range from 10–230 m. He found evidence for the presence of three

---

[44] $\mathrm{Coh}^2_{w\theta}(f) = \frac{\Gamma^*_{w\theta}\Gamma_{w\theta}}{\Gamma_w\Gamma_\theta} = \frac{Co^2+Q^2}{\Gamma_w\Gamma_\theta}$, where Γ is the spectrum function, Co^2 is the cospectrum, and Q^2 is the quadrature spectrum.

different IGW wavelengths but still had to deal with problems of noise and measurement errors even in the absence of turbulent fluctuations. Metcalf (1975a) discussed differences in expected polarization relationships between trapped and freely propagating waves for his analysis of aircraft measurements taken in the marine inversion off southern California. His measurements indicated a fairly wide range of dominant horizontal wavelengths and frequencies for different flight 'legs'. In general, unless internal gravity waves are linear, of large amplitude, monochromatic, and separated spectrally from turbulent fluctuations, their cross-spectral signature is usually ambiguous. Hunt et al. (1985) illustrated this problem by comparing three cases, one with weak wave activity, one with moderate wave activity, and one with strong wave activity, selected from nighttime measurements at the BAO tower in eastern Colorado. Finnigan et al. (1984) also discussed this problem. Recently, Finnigan (1988) concluded that waves cannot be separated from turbulence by means of frequency spectra because of nonlinear wave behaviour and wave–turbulence interactions.

Several other analysis techniques are also available. Caughey and Readings (1975) plotted low-pass-filtered signal traces and SethuRaman (1977) and Hunt et al. (1985) plotted various correlograms. Axford (1971), Caughey and Readings (1975), Metcalf (1975a), and SethuRaman (1977) also examined coherence and phase angles for $\overline{u'v'}$, $\overline{u'w'}$, and $\overline{v'w'}$ and their consistency with the polarization relationships as an independent diagnosis for wave activity. Stewart (1969) and Busch (1969) suggested another diagnostic tool, the quantity $Q = fE(\partial E/\partial t)^{-1}$, where f is a characteristic frequency associated with a given motion, E is its KE, and $\partial E/\partial t$ may be taken as the rate of spectral energy transfer through the frequency band f. Q thus indicates the number of cycles it takes to change the energy of the motion an amount comparable with E. For small-scale turbulence, where $\partial E/\partial t$ corresponds to the dissipation rate ϵ, Q is on the order of unity whereas for waves, $Q \gg 1$. SethuRaman (1977, 1980) estimated Q values on the order of 100 for internal gravity waves propagating in a stable marine surface layer compared to values of 1 to 2 during wave-breaking events.

Metais and Herring (1989) recently used Ertel's theorem[45] as a means to differentiate between wave and turbulent motions. Müller (1984) had noted that internal gravity waves have zero potential vorticity. Metais and Herring (1989) took the 'vortical' velocity to be that portion of the velocity field with vorticity normal to constant–ρ surfaces while the 'wave' velocity was that portion of the total velocity field normal to the vortical velocity and with vorticity tangential to constant–ρ surfaces[46]. Müller et al. (1988) used a similar normal-mode decomposition to separate the contribution of IGW and vortical modes to IWEX current data.

Finnigan and Einaudi (1981), Finnigan et al. (1984), and Finnigan (1988) have employed the method of phase averaging to separate mean flow, wave, and turbulence components in the time domain. This method requires a reference signal to define the period used by the phase-averaging operator; Finnigan et al. (1984) used a ground-level microbarograph trace as the reference oscillator. This approach is also restricted to cases of nearly monochromatic waves. Dewan (1985) discussed a test based on vertical coherency to differentiate between internal waves and quasi-two-dimensional turbulence. Finally, Olbers (1983) has discussed the problem of distinguishing waves from turbulence for oceanic measurements.

Internal gravity wave spectra

Two competing explanations for the $k^{-5/3}$ reverse energy cascade that has been observed on the atmospheric mesoscale were discussed in Sec. 2.1.5 (see p. 99). One of these explanations was that of a nonlinear IGW energy cascade (Dewan, 1979). This hypothesis has been quantified by VanZandt (1982) and others for the atmosphere based

---

[45] Ertel's theorem states that for non-dissipative and non-diffusive flows, the potential vorticity $\Pi = \rho_0^{-1}\vec{\omega}\cdot\nabla\rho$ is conserved along fluid-parcel trajectories, where ρ_0 is the volume-averaged value of the mean density profile $\overline{\rho}(z)$ and $\vec{\omega}$ is the absolute vorticity (Metais and Herring, 1989).

[46] See also Fig. 1 of Müller (1984).

on previous work on oceanic IGW spectra. Let us consider these IGW spectral models, first for the ocean and then for the atmosphere.

Oceanic spectra. Internal gravity waves are also important oceanic modes of motion. They account for a significant fraction of oceanic flow variability, transfer momentum and energy, exert stress on larger-scale motions, induce mixing, and advect and disperse chemical and biological tracers such as phytoplankton (Garrett and Munk, 1979; Müller et al., 1986). A wide variety of sensors have been used to collect data on oceanic internal waves, including (i) moored sensors, (ii) towed or self-propelled sensors, (iii) dropped or lowered sensors, and (iv) remote sensors such as sonar[47]. Garrett and Munk (1972) synthesized a large number of oceanic internal wave measurements made during the 1960s with a variety of sensors in almost all oceans in all seasons at various depths into an empirical model spectrum. This first IGW wavenumber-frequency model spectrum, usually called GM72 by oceanographers, was subsequently revised by Garrett and Munk (1975) to incorporate additional IGW data from the early 1970s; naturally, the revised model is known as GM75.

GM72 and GM75 are thus *empirical* spectral models based on observations and a number of simplifying assumptions. They apply to time scales from the inertial frequency f to the buoyancy frequency N and to length scales from O(10 m) to O(1000 m). Garrett and Munk assumed the deep-sea flow field to be wave-like over the wavenumber range considered. The Boussinesq approximation was made and the ocean was assumed to be horizontally homogeneous and exponentially stratified. The internal wave field was assumed to be composed of a random-phase superposition of elementary linear wave trains which satisfy the linear dispersion and polarization relations. Internal wave energy was assumed to be equally distributed in all horizontal directions (i.e., horizontally isotropic) and vertical symmetry was also assumed (equal amounts of upward and downward propa-

---

[47] Atmospheric analogues include (i) instrumented towers, (ii) aircraft, (iii) rawinsondes, dropwinsondes, and tethered balloons, and (iv) radar, sodar, and lidar, respectively

gating energy). Currents and their associated Doppler shifts were assumed to be negligible and neither internal tides nor vortical modes were considered. The assumptions of horizontal isotropy and approximately linear dynamics each reduce the dimensionality of the problem by one so that the spectral density function depends only on two of the three independent variables κ_H, m, and ω[48] (Sidi et al., 1988). Finally, the three-dimensional, wavenumber-frequency energy spectral density $E(\kappa,\omega)$ was assumed to be separable in κ and ω. By using the dispersion relation, $E(\kappa_H,\omega)$ can easily be transformed into forms $E(\kappa_H,m)$ or $E(m,\omega)$.

The frequency spectrum obtained by integrating $E(\kappa,\omega)$ over κ has a peak at the inertial frequency f and an ω^{-2} dependence down to a sharp cutoff at the Brunt-Väisälä frequency N. The horizontal wavenumber spectrum varies as κ_H^{-2} at low wavenumbers at low wavenumbers and as $\kappa_H^{-5/2}$ at high wavenumbers while the vertical wavenumber spectrum is independent of m at low m and varies as $m^{-5/2}$ at high m.

Garrett and Munk (1972) made no great claims for GM72 but rather described it as a "contrived" model cobbled together "to get some hold on the distribution of space *and* time scales of internal waves." Briscoe (1975) described GM72 as a "strawman" that "workers could use to compare measurements and design experiments, in fact, a model that was not expected to contain all the answers." Despite these modest beginnings, GM72 and GM75 turned out to describe the deep-ocean IGW energy spectrum very well. In fact, except for anomalous spectra in the vicinity of possible source regions of wave energy, the GM75 model spectrum seemed to apply universally. This is especially noteworthy because oceanic (and atmospheric) IGW sources are not distributed uniformly. The reason for this universality, particularly of spectral shape, appears to be due to a combination of wave propagation over long distances and the effects of weak nonlinear interactions (McComas and Müller, 1981). Reviews and evaluations of the Garrett-Munk spectrum

---

[48] Horizontal wavenumber, vertical wavenumber, and frequency, respectively.

have been given by Garrett and Munk (1979), Olbers (1983), Holloway (1986), and Müller et al. (1986).

Atmospheric spectra. VanZandt (1982) proposed that a modified form of the Garrett-Munk IGW energy spectrum can be used to describe the *atmospheric* mesoscale energy spectrum. He argued that atmospheric mesoscale fluctuations above the PBL are dominated by internal gravity waves and that observed atmospheric mesoscale spectra "exhibit a considerable degree of universality versus season or meteorological conditions" (VanZandt, 1982, p. 575). He also noted that atmospheric mesoscale spectra "bear a striking resemblance to the shapes of spectra of oceanic fine structure." Following the approach employed by Garrett and Munk (1972), VanZandt arrived at his atmospheric mesoscale energy model spectrum by fitting selected spectral shapes to observed atmospheric mesoscale spectra. He used $\omega^{-5/3}$ for his frequency spectrum and a wavenumber spectral slope which approached -2.4 for both high horizontal and vertical wavenumbers. Resulting root-mean-square properties of the atmospheric IGW field from VanZandt's model spectrum include a $(\overline{u^2})^{1/2}$ value of 4.4 $\mathrm{m\,s^{-1}}$, $(\overline{v^2})^{1/2}$ value of 0.6 $\mathrm{m\,s^{-1}}$, RMS horizontal displacement of 22 km, and RMS vertical displacement of 360 m.

VanZandt's original model spectrum had some weak points. He based his empirical spectral density function on far fewer observed spectra than had Garrett and Munk. Although he used frequency spectra and horizontal and vertical wavenumber spectra of horizontal velocity, he did not have two-point coherence data available comparable to those used by Garrett and Munk nor did he have vertical velocity spectra available. Also, VanZandt followed Garrett and Munk and assumed that Doppler shifting of frequency due to the mean flow could be neglected (see Eq. 2.30). While this approximation is reasonable in the deep ocean where currents are usually no more than 1 or 2 $\mathrm{m\,s^{-1}}$, it is clearly not applicable in the free atmosphere where flow speeds can be much larger and intrinsic frequencies ω_i quite different from ground-relative frequencies ω. One practical problem with VanZandt's model spectrum was that it could not be compared

directly against the *radial* velocity spectra measured by monostatic Doppler sounding systems, at present the most common source of mesoscale fluctuation observations.

Since VanZandt's original paper (hereafter referred to as VZ82) appeared, however, VanZandt (1985) and Scheffler and Liu (1985) have extended VZ82 to permit direct comparison with line-of-sight measurements made by monostatic Doppler sounding systems such as MST radar, Doppler lidar, and Doppler sodar for both radial wavenumber and frequency spectra, and Scheffler and Liu (1986) and Fritts and VanZandt (1987) have accounted for Doppler-shift effects. Scheffler and Liu (1985) also noted that VanZandt's model spectrum implies that line-of-sight velocity spectra will change slope as a function of zenith angle and suggested this as one test of the model's applicability.

Comparison with atmospheric observations. VanZandt's model spectrum provides a good fit to horizontal and vertical wavenumber and frequency spectra of *horizontal* velocity fluctuations. This is to be expected since the model is based on an empirical fit to such spectra. For example, VanZandt and Fritts (1989) have suggested modifying one of the model spectrum parameters to better fit more recent observations of vertical wavenumber spectra of horizontal velocity. Thus, observations of the spectra of atmospheric variables other than horizontal velocity are required to test this model (Larsen et al., 1986, 1987). As shown in Table 2.1, only a limited number of vertical and radial velocity spectra are available.

In general, these spectra provide some support for VZ82 but also indicate that observed mesoscale atmospheric spectra cannot be explained solely by a spectrum of random internal gravity waves. For instance, Ecklund et al. (1986) calculated frequency spectra of *vertical* velocities in both the troposphere and stratosphere based on time-series analysis of vertically-oriented clear-air Doppler radar measurements from sites in Alaska, Colorado, France and Pohnpei (South Pacific). For conditions with weak background winds, they found the 'quiet-period' vertical velocity spectrum to be very similar at all four sites and to resemble closely the GM75 oceanic model spectrum in shape. For strong background winds, however, the 'active-period' vertical velocity spectra approached the

$\omega^{-5/3}$ spectral slope observed for horizontal motions. Ecklund et al. suggested that the 'quiet-period' frequency spectra are due to a nearly universal spectrum of internal waves while 'active-period' spectra contain additional energy due to tilting of quasi-horizontal stratified turbulent motions, analogous to the explanation of mesoscale horizontal tracer spectra offered by Gage and Nastrom (1986b) and Nastrom et al. (1986a).

It should be noted that most observations made with wind-profiling Doppler radars to date have been made using radars located in valleys. At one time such sites were considered desirable since the surrounding hillsides would suppress radar sidelobes (Gage, 1990). However, since mountainous areas are a strong IGW source, orographically-generated IGWs may swamp other sources and processes under high-wind conditions, especially for the vertical velocity component. Such conditions would correspond to Ecklund et al.'s 'active' periods. Results from a new wind profiler, which is located in very flat terrain near Urbana, Illinois, suggest that 'quiet-period' vertical velocity spectra obtained near mountains are similar to vertical velocity spectra obtained under most conditions far from mountains (Green et al., 1988; Gage and Nastrom, 1990).

Gage and Nastrom (1985a, 1990) tested VanZandt's model spectrum by using the Garrett-Munk theory to calculate the horizontal-velocity frequency spectrum corresponding to one of the vertical-velocity frequency spectra of Ecklund et al. (1986). They found the predicted horizontal velocity spectrum to contain about an order of magnitude *less* energy than several observed horizontal-velocity frequency spectra. Larsen et al. (1986) analyzed radial velocity measurements made at different zenith angles by the Arecibo Observatory 430 MHz radar in Puerto Rico. They examined both frequency spectra and vertical wavenumber spectra of vertical velocities and concluded that the spectral slopes obtained were inconsistent with VanZandt's model spectrum. Larsen et al. (1987) found similar discrepancies in a 15-day record of vertical velocity profiles measured by the SOUSY-VHF-Radar wind profiler in Germany. This data set had the advantage that vertical winds were measured directly. The observing period was synoptically active and was "characterized by a series of frontal passages, including two occlusions, two cold

fronts, three warm fronts, and two upper level disturbances." Barat and Cot (1989) and Cot and Barat (1989) have also reported discrepancies between stratospheric spectra of wind shear, temperature, and vertical temperature gradient based on balloon-sounding observations and VanZandt's model spectrum.

Recently, Sidi et al. (1988) derived what they claimed to be an improved version of the VZ82 model spectrum. They modified VanZandt's (1982) model-fitting procedure in two important ways: (i) they used only observed vertical wavenumber spectra for fitting spectral parameters in order to minimize possible contributions from coexisting vortical modes (see next section); and (ii) they required the model spectrum to represent a *saturated* internal wave field at its high wavenumber limit. One shortcoming of their IGW spectrum was their use of data from a single balloon ascent to determine the model-spectrum parameters. However, Sidi et al. derived these parameters based on vertical velocity and temperature spectra in contrast to VanZandt's use of horizontal velocity spectra. They found reasonably good agreement between their proposed atmospheric IGW model spectrum and published spectra but found it necessary to use two sets of parameters for best results, one set corresponding to quiet periods and the other to active periods.

Gage and Nastrom (1985a, p. 1346) argued that "these results strongly suggest that the radar spectra of vertical and horizontal velocity are indicative of different processes." The vertical velocity spectra are dominated by IGW while the horizontal velocity spectra contain the contributions of both IGW and quasi-two-dimensional turbulence. The latter, also referred to as *pancake turbulence*, *blini*[49], *stratified turbulence*, or *vortical modes*, is discussed in the next section. Somewhat ironically, at the same time that some meteorologists were championing the application of the GM model to atmospheric mesoscale fluctuations, some oceanographers were concluding that the GM model was incomplete due to its neglect of the vortical mode. A primary reason is that internal gravity waves,

---

[49] Russian for 'pancakes' (e.g., Bretherton, 1969a).

unlike horizontal vortices, cannot carry potential vorticity (Müller, 1984). Riley et al. (1981), Müller (1984), and Müller et al. (1986, 1988) discuss this point in detail, and Dong and Yeh (1988) and Yeh and Dong (1989) have investigated IGW—vortical mode interactions. Finally, Fritts (1989) has observed that universality of IGW spectra may not strictly hold in the atmosphere since IGW sources will vary considerably in space and time and the atmospheric environment, which interacts with and filters internal gravity waves, is itself geographically and seasonally variable.

2.1.9 Vortical modes and stratified turbulence

Let us now consider these less well known vortical modes. As discussed in Sec. 2.1.5, Gage (1979) pointed out that much more energy exists on the mesoscale than can be explained by the k^{-3} spectral decay of geostrophic turbulence. One possible explanation, that a spectrum of internal gravity waves is responsible for the observed mesoscale energy distribution, was discussed in the previous section. Gage (1979) offered another explanation, that some small-scale turbulent energy could be transferred upscale into quasi-two-dimensional motions through the effects of atmospheric stratification. Lilly (1983a) put this hypothesis on a much firmer foundation by extending the scale analysis of Riley et al. (1981) for the decay of homogeneous turbulence in a stratified fluid to the atmospheric case.

Laboratory experiments (e.g., Lin and Pao, 1979) and numerical simulations (e.g., Riley et al., 1981) of turbulence in stably stratified fluids had shown that stratification introduces wave-like characteristics into the flow field, inhibits the growth of vertical scales, and tends to enhance the growth of horizontal scales, including the development of quasi-horizontal vortices (or vortical modes). Lilly (1983a) referred to this phenomenon as 'stratified turbulence' and proposed that decaying convective clouds and thunderstorm anvil outflows could contribute energy to the atmospheric mesoscale through the mechanism of 'wake collapse' (p. 158). This section discusses some theoretical analyses, laboratory and numerical-model simulations, and atmospheric and oceanic observations of stratified turbulence.

Characteristic length scales in stratified fluids

Fluid particles moving vertically in a vertically-stratified fluid experience Archimedean (or buoyancy) forces. Consequently, turbulence in a stably stratified fluid has to work against negative buoyancy fluxes which generate PE at the expense of KE. Despite this handicap, turbulence is widely observed in the stably stratified atmosphere although it is usually 'patchy' and intermittent.

Density stratification introduces new length scales even in an unbounded domain. The well-known Monin-Obukhov length L_{MO} in atmospheric surface-layer similarity theory, which is defined as

$$L_{MO} = -\frac{\overline{\theta_v} u_*^3}{kg\left(\overline{w'\theta_v'}\right)_{sfc}} \quad , \tag{2.36}$$

is a measure of the importance of diabatic effects close to the Earth's surface, where $\overline{\theta_v}$ is the average near-surface virtual temperature, u_* is the friction velocity, k is von Kármán's constant, and g is the acceleration due to gravity (e.g., Monin and Yaglom, 1971; Tennekes and Lumley, 1972). L_{MO} indicates the height in the atmospheric boundary layer at which buoyancy production of turbulent KE balances shear production. Closer to the ground, shear effects dominate buoyancy effects.

Dougherty (1961) and Ozmidov (1965) suggested a length scale L_R at which buoyancy and inertial forces become of equal importance in the *interior* of a stably stratified fluid. First, define the buoyancy length scale L_b to be the vertical distance travelled by a fluid particle in converting all of its vertical fluctuation energy into PE in a stably stratified fluid[50]. Then,

$$L_b = \frac{(\overline{w'^2})^{1/2}}{N} \quad , \tag{2.37}$$

---

[50] Simply the work done in raising unit mass adiabatically through the height L_b, namely $N^2 L_b^2/2$ (Dougherty, 1961)

where $(\overline{w'^2})^{1/2}$ is the root-mean-square vertical fluctuation velocity and N is the Brunt-Väisälä frequency (Stillinger et al., 1983). L_b is thus an upper limit to the largest vertical scale of turbulent overturning in a stably stratified fluid. Larger-scale eddies would instead oscillate as internal gravity waves. Note that this vertical buoyancy length scale does not limit horizontal scales in any way.

If we then assume that (i) for fully turbulent flow w'^2 is proportional to the total turbulent KE per unit mass $q^2 = (u'^2 + v'^2 + w'^2)$ for the energy-containing eddies, i.e., the largest turbulent scales, (ii) the turbulent KE dissipation rate per unit mass ϵ can be expressed as

$$\epsilon = C\frac{q^3}{L} \quad , \tag{2.38}$$

where C is a proportionality constant and L is the characteristic length scale for the energy-containing eddies, and (iii) $C = 1$ and $L = L_b$, then the buoyancy length scale L_b can be rewritten as the Dougherty-Ozmidov length scale L_R :

$$L_R = \left(\frac{\epsilon}{N^3}\right)^{1/2} \quad . \tag{2.39}$$

Another way to obtain the above expression for L_R is to assume that the inertial-range eddy of length scale L and KE $(\epsilon L)^{2/3}$ is the largest eddy with sufficient momentum to overturn in the vertical plane against the torque supplied by the buoyancy force. Since overturning a vertical distance L in a stably stratified fluid requires KE of order L^2N^2, equating energies and setting $L = L_R$ will produce the required expression (Browand and Hopfinger, 1985; Lilly, 1989b).

The buoyancy length scale L_b is more general than the Dougherty-Ozmidov length scale L_R since the former may be used for either pure turbulent flows or for combined fields of turbulence and internal gravity waves or for pure random IGW fields. Given its derivation, L_R values will be misleading if q^2 contains internal-wave contributions. Metais and Herring (1989) have pointed out, however, that these two length scales can both be defined by equating the Brunt-Väisälä period N^{-1} with a vertical inertial period

to $L_b(\overline{w'^2})^{-1/2}$ for the buoyancy length scale and to $(L_R^2/\epsilon)^{1/3}$ for the Dougherty-Ozmidov length scale. Note that when L_R approaches the Kolmogorov microscale $L_\epsilon = (\nu^3/\epsilon)^{1/4}$, no inertial range can exist and turbulence collapses (e.g., Itsweire et al., 1986; Hopfinger, 1987; Lilly, 1989a). Other characteristic length scales can also be defined: Table 2 in Gibson (1987) lists *eleven* length scales employed in studies of stratified turbulence (see also Yoon and Warhaft, 1990).

Characteristics of mesoscale vortical modes

On the large scale, the quasi-horizontal, potential-vorticity-carrying vortical modes discussed by Müller (1984) correspond to familiar geostrophic and quasi-geostrophic modes. For these small Rossby number cases, the Coriolis force is important and the vortical modes are approximately horizontally nondivergent and in geostrophic and hydrostatic balance.

However, Müller (1984) noted that such modes could also exist in the *nonrotating* case $f = 0$ but would *not* be in geostrophic balance. For such large Rossby number flows, in which rotation is not important, the vortical mode of motion (i) will consist of horizontal vortices, (ii) have no vertical motion (to first order), (iii) have local and advective time scales shorter than the inertial period, (iv) have horizontal scales much smaller than the internal Rossby radius of deformation Nh/f, (v) have a basic horizontal momentum balance between the pressure gradient force and nonlinear advection term (i.e., cyclostrophic balance: Müller et al., 1988), (vi) be unaffected by rotation, and (vii) lack vertical coupling (Lilly, 1983a; Müller, 1984).

Fig. 2.16 shows the difference between the horizontal wind vector fields for two-dimensional IGW and vortical modes. The former field is divergent but irrotational while the latter is rotational but nondivergent.

Although vortical modes have very different characteristics from internal gravity waves, nonlinear interactions between these two flow modes are still possible. Dong and Yeh (1988), Yeh and Dong (1989), and (Lelong and Riley, 1991) have investigated both resonant and nonresonant interactions of this kind.

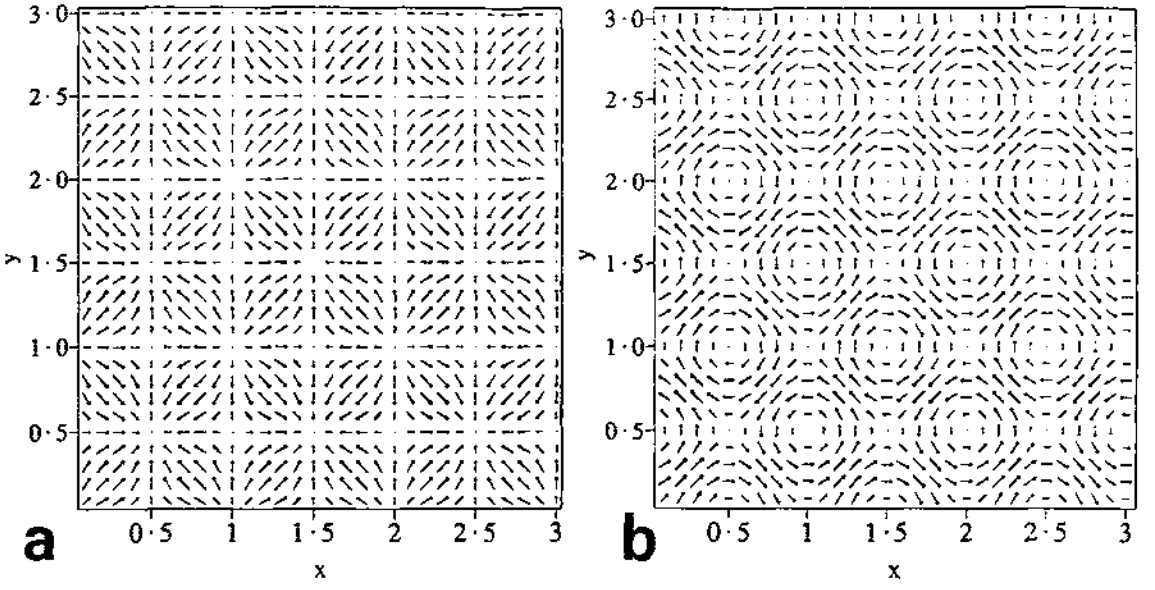

Figure 2.16: Vector fields corresponding to horizontal wind oscillations of (a) two orthogonally-aligned internal gravity waves and (b) two orthogonally-aligned vortical modes. Abscissa and ordinate units are in units of wavelength (adapted from Vincent and Eckermann, 1990).

Laboratory experiments

Lilly (1983a) remarked that his theoretical investigation of quasi-two-dimensional atmospheric turbulence was sparked by his interest in thunderstorm anvil outflows and their apparent analogy to the stratified 'wake collapse' phenomenon (see also p. 158). A wake is the non-propagating disturbance produced by a body moving through a fluid (e.g., Lin and Pao, 1979). The term 'wake collapse' refers to the sudden change in the behaviour of such a wake as it decays in a stratified fluid. Initially, the wake grows by turbulent mixing (cf. Fig. 2.14). In a stably stratified fluid, however, vertical mixing will result in a decrease of turbulent KE and an increase in turbulent PE[51]. After a certain period of time, a threshold is reached and the decaying wake collapses vertically, generating internal gravity waves and inducing lateral motions which result in a faster horizontal

[51] PE gained through the creation of interleaved density microstructure by vertical turbulent flux of buoyancy $g\rho_0^{-1}\overline{w'\rho'}$ (e.g., McEwan, 1983; Stillinger et al., 1983).

expansion than in a comparable unstratified wake (Lin and Pao, 1979). Etling (1990b) recently suggested that decaying KHI-induced turbulence could be a source of vortical modes (Fig. 2.14). Such a local turbulent 'patch' is not a true wake, but like a wake it is a non-propagating disturbance in the flow interior.

Grid-generated turbulence. The first studies of the decay of turbulence were carried out for grid-generated turbulence in *unstratified* wind-tunnel flows. For an observer moving with the mean speed of the flow, such turbulence can be viewed as wake turbulence created by the movement of a grid through a quiescent fluid. Even in an unstratified fluid, viscous stresses will cause a decrease in turbulent KE with time through dissipation. These wind-tunnel investigations indicated that the grid-wake turbulent KE decreases with time according to a power law while the integral length scale of the turbulence L *increases* as a function of time due to the decay of the smallest eddies and persistence of larger eddies. Reviews of these studies may be found in Hinze (1975) and Monin and Yaglom (1975).

A natural extension of these early studies was to consider the decay of grid-generated turbulence in *stratified* fluids. Hopfinger (1987) has reviewed a number of such studies using salt-stratified water from 1973 onwards and Yoon and Warhaft (1990) discuss recent work in stratified wind tunnels. Normally, the spatial integral length scale L of the nearly homogeneous turbulence behind the grid will at first be smaller than the buoyancy length L_b or Dougherty-Ozmidov length L_R of the flow so that buoyancy effects are not important. As the turbulence decays, however, L will grow with time while both L_b and L_R shrink (since both $\overline{w'^2}$ and ϵ decrease with time). Buoyancy effects will thus play a larger and larger role as the turbulence weakens.

Dickey and Mellor (1980) described an experiment in which a horizontal grid was towed upwards through a linearly stratified fluid in a columnar tank. Their results showed a distinct break (i.e., slope change) in the decay rate of the fluctuation KE which they attributed to the collapse of three-dimensional turbulence at nearly all scales and the emergence of an internal-wave regime. Results from another study carried out by Stillinger et al. (1983) of unsheared grid-generated turbulence in a closed-loop, salt-

stratified water channel indicated a less evident break in the fluctuation KE decay rate but showed a clear break in the $\overline{\rho'^2}$ decay rate. Stillinger et al. also measured $\overline{\rho' w'}$ (vertical density flux) values decreasing to zero, indicating complete turbulence collapse. Previous studies had not made simultaneous single-point measurements of vertical velocity and density, but the vertical buoyancy flux $g\rho_0^{-1}\overline{\rho' w'}$ is a good indicator of the presence of turbulence since linear internal gravity waves do not contribute to it (Stewart, 1969).

Itsweire and Helland (1989) extended the work of Stillinger et al. (1983) and found spectral evidence for a reverse energy cascade produced by the development of quasi-two-dimensional eddies as the original, grid-generated, three-dimensional turbulence decayed and collapsed. Maxworthy et al. (1990) performed visualization studies of the time evolution of grid-generated turbulence in a continuously stratified fluids for very small local disturbance Froude numbers $Fr_D = (\overline{u'^2})^{1/2}/ND \sim 0.01$, where D is a characteristic disturbance length. As illustrated by Fig. 2.17, the initial three-dimensional turbulence (panel A) decays into a quasi-two-dimensional flow structure with marked vertical vorticity (panel B). This latter stage persists for a very long time and is still relatively intense at $Nt = 1500$ (Hopfinger, 1987).

Wake collapse. Laboratory experiments have also been carried out in stably stratified fluids to study the wake-collapse phenomenon behind cylinders and axisymmetric towed or self-propelled bodies (see reviews by Thorpe, 1973b, Lin and Pao, 1979, and Hopfinger, 1987). Such studies have relevance to thunderstorm anvils, aircraft, submarines, and flow past mountains. Several of these studies have produced striking flow visualizations that illustrate the development of quasi-two-dimensional vortical modes following wake collapse. Fig. 2.18 shows the upscale evolution of the wake behind a towed slender body while Fig. 2.19 shows the upscale evolution of the wake behind a towed sphere. Pao and Kao (1977) presented similar photographs of the wake evolution behind a towed sphere in a stably stratified fluid.

Following Lilly's (1983a) suggestion of a close analogy between thunderstorm anvil outflows and turbulent wakes, Etling (1990a) has applied laboratory results to estimate

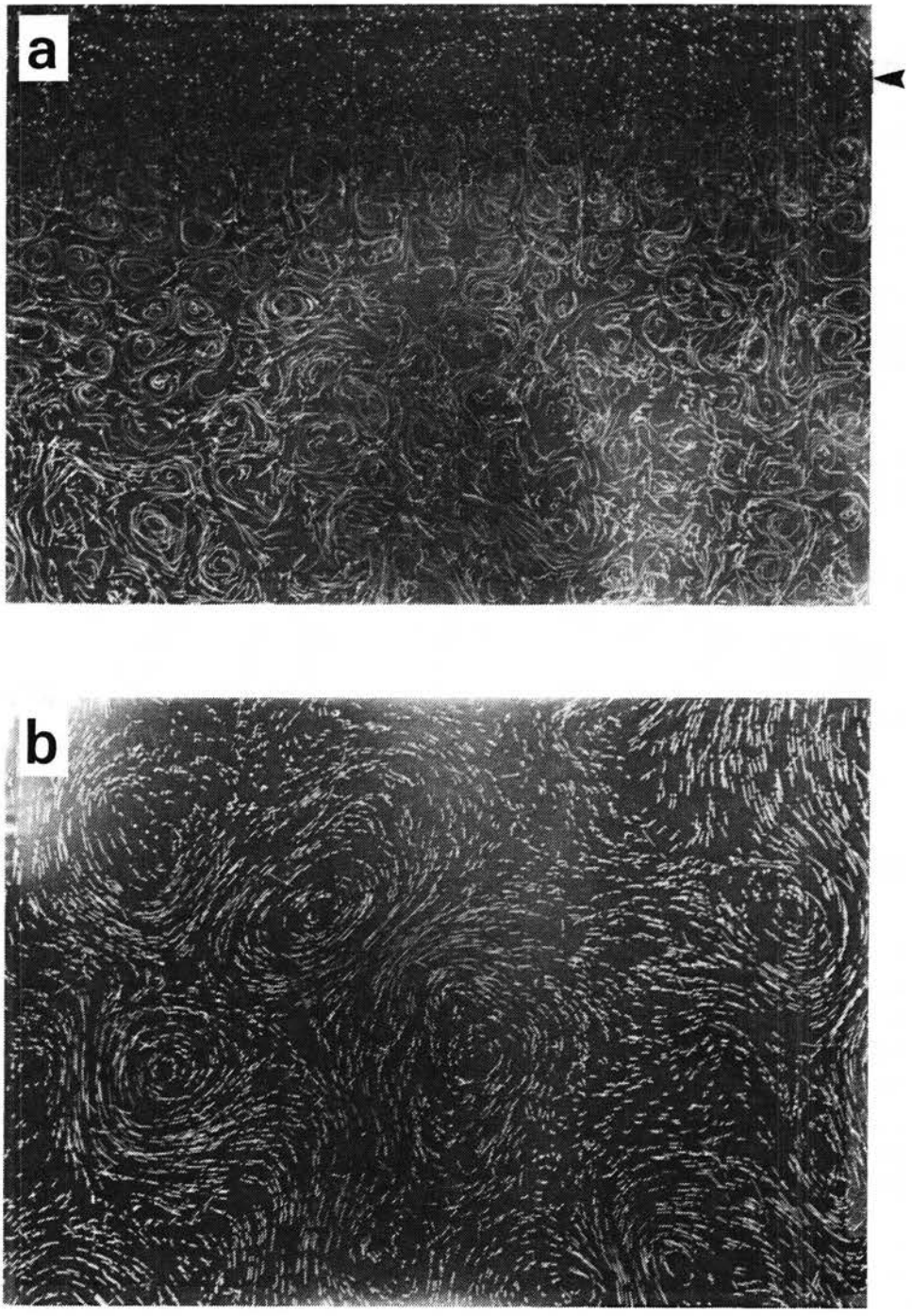

Figure 2.17: Streak-line photographs (plan view) of flow structure of decaying grid-generated turbulence in a continuously stratified fluid at travel times (a) $Nt = 25$ and (b) $Nt = 540$, where N was 2.5 rad s^{-1}, grid velocity U was 5.9 cm s^{-1}, grid mesh spacing M was 15.2 cm, grid bar size was 3.8 cm (square), and tank dimensions were 2.4 m $\times$ 2.4 m $\times$ 0.2 m. The arrow to the right of (a) marks the location of the mesh (from Maxworthy et al., 1990; reproduced in Hopfinger, 1987).

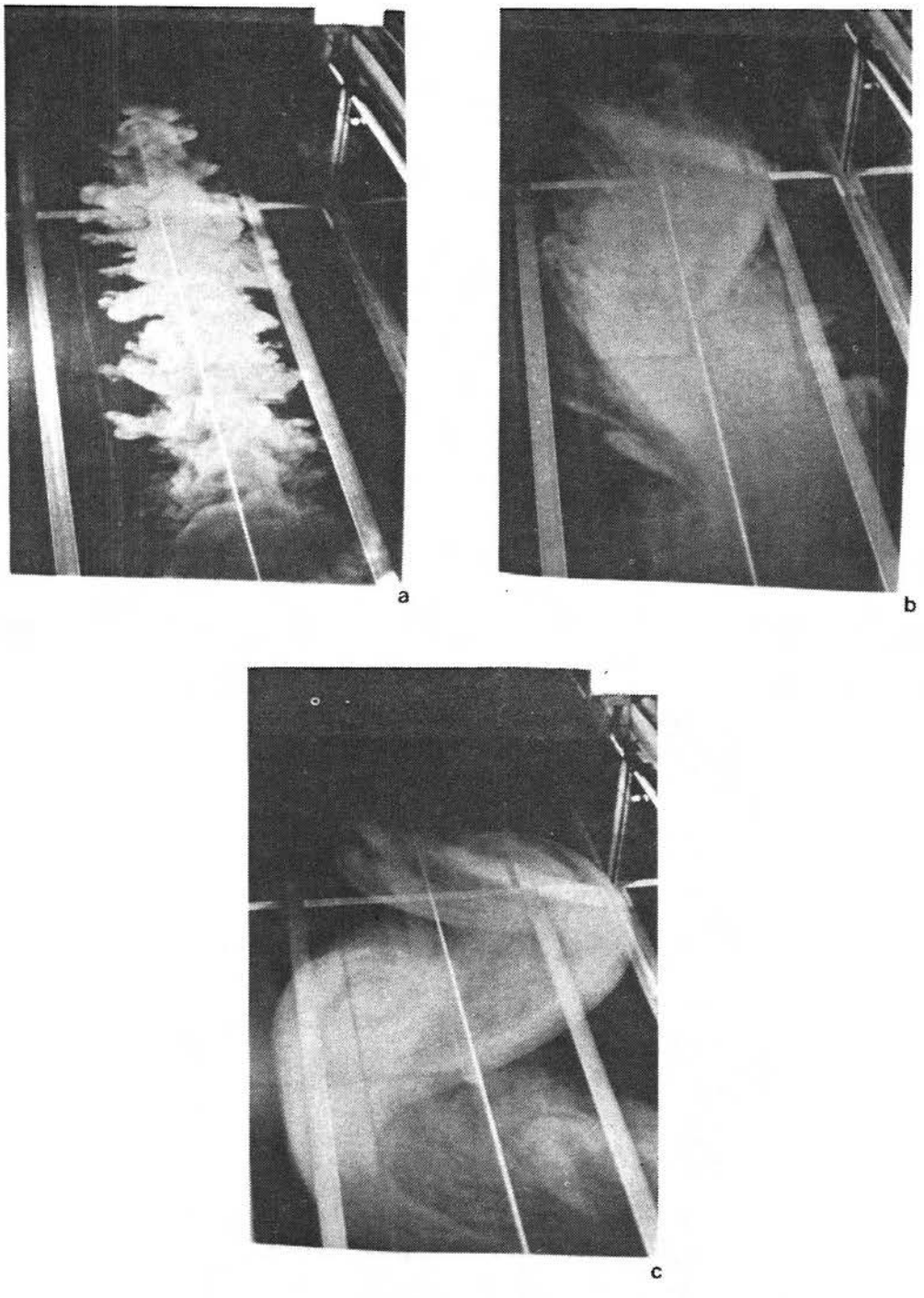

Figure 2.18: Oblique views of a dye visualization of the wake behind a towed slender body in a stratified fluid (internal Froude number $Fr_D = U/ND = 103$, Reynolds number $Re_D = UD/\nu = 3 \times 10^4$, where D is a characteristic length scale for the towed body): (a) $Nt = 0.82$, after wake collapse; (b) $Nt = 2.57$, wake meandering; (c) $Nt = 5.99$, formation of horizontal eddies (from Lilly, 1983a, after Pao and Lin, 1973, and Lin and Pao, 1979).

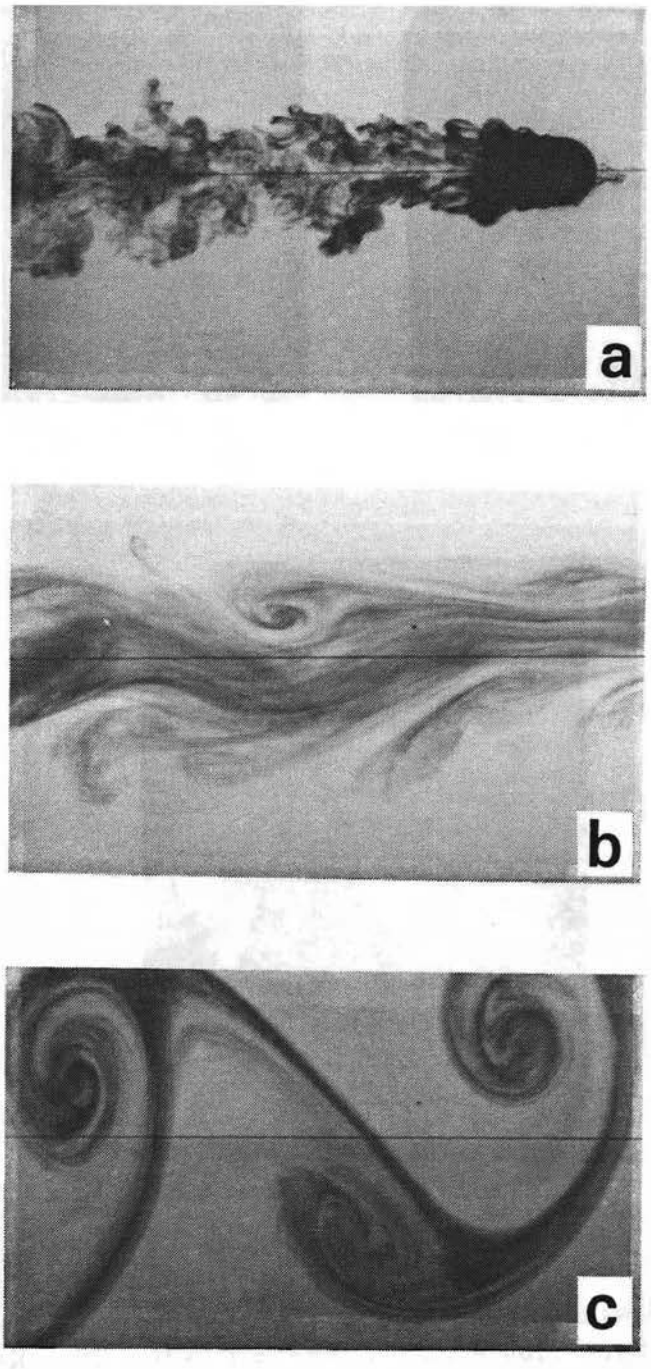

Figure 2.19: Top views of wake collapse following the passage of a towed sphere through a continuously stratified fluid ($Fr_D = 1.6$): (a) $Nt = 0.8$; (b) $Nt = 26$; (c) $Nt = 135$ (from Hopfinger, 1987; see also Etling, 1990a).

characteristic atmospheric values. If initial wake collapse as defined by vanishing mean vertical buoyancy flux occurs for $Nt \approx 3$ and organized horizontal vortical modes have formed by $Nt \approx 100$, then for a typical atmospheric lapse rate of 3.5 K km^{-1}, the onset of wake collapse and the formation of vortical modes would occur in the upper troposphere after roughly four minutes and after two hours, respectively.

Theoretical analysis and scale separation

If internal gravity waves and quasi-two-dimensional turbulence can coexist on different time scales in stratified turbulence, how can these two regimes be identified in the governing equations? Phillips (1977) discussed an extended form of Reynolds decomposition in which the mean flow, waves, and turbulence are separated by averaging over different spatial length scales. Finnigan et al. (1984) and Finnigan (1988) performed a time-domain decomposition of PBL observations by using a phase-average operator defined in terms of a reference oscillator. Müller et al. (1988) used the decomposition of an incompressible Boussinesq flow into its three eigenmodes to decompose observed oceanic velocity and density fields into IGW and vortical modes; this normal-mode decomposition is unique and complete at any scale.

Riley et al. (1981) introduced two separate time scales in their scaling analysis of the equations governing the decay of homogeneous turbulence in a stably stratified fluid. This approach was suggested by the variety of physical phenomena observed in laboratory studies of grid-turbulence decay and wake collapse in stratified fluids, including three-dimensional turbulence, quasi-horizontal vortices, and internal gravity waves (e.g., Lin and Pao, 1979; Hopfinger, 1987).

By using two time scales, a buoyancy time scale N^{-1} and an advective time scale D/V', to scale the Boussinesq incompressible flow equations, Riley et al. obtained two different sets of dimensionless equations (viscous and turbulent diffusive terms were neglected for convenience). Nondimensionalized individual terms were either of order $O(1)$, $O(Fr_D)$, or $O(Fr_D^2)$, where $Fr_D = V'/ND$ is a disturbance Froude number, V' is a horizontal disturbance velocity scale, and D is a horizontal disturbance length

scale. As an initially turbulent flow decays in a stably stratified fluid, the disturbance Froude number becomes small. If the $O(Fr_D)$ and $O(Fr_D^2)$ terms are neglected, one of the dimensionless systems reduces to a linear set of equations from internal-wave theory. If Fr_D is then used as an expansion parameter, higher-order solutions of this system are forced nonlinearly by the lower-order solution through resonant wave-wave interactions (Lilly, 1983a). The lowest-order solution for the second dimensionless system is a horizontally nondivergent, nonlinear, hydrostatic flow composed of almost independently evolving horizontal layers (a 'pancake street': Lin and Pao, 1979). Higher-order solutions may be horizontally divergent, inducing internal gravity waves. Thus, Riley et al.'s analysis admits a collapsed state of coexisting, weakly coupled internal gravity waves and quasi-horizontal vortical modes.

Atmospheric case. Lilly (1983a) extended Riley et al.'s (1981) analysis by adding a Coriolis term to the Boussinesq incompressible equations, thus introducing a disturbance Rossby number $Ro_D = V'/fD$ as a second dimensionless parameter. He then nondimensionalized the governing equations for three different scale regimes: (a) isotropic three-dimensional turbulence (Fr_D large, Ro_D large); (b) isotropic Riley et al. scaling (Fr_D small, Ro_D large); and (c) anisotropic Charney–Rossby scaling (Fr_D small, Ro_D small).

To scale the first regime, Lilly used only one length scale and one velocity scale and assumed that horizontal and vertical divergences were comparable in magnitude. All of the terms in the resulting dimensionless equations were of order $O(1)$ except for the buoyancy term in the vertical velocity equation, which was of order $O(Fr_D^{-2})$. Thus, for weak stratification (Fr_D large), buoyancy effects are weak and the solutions correspond to three-dimensional isotropic turbulence.

Lilly followed Riley et al.'s study closely in his analysis of the second scale regime. He assumed horizontal and vertical length scales to be of comparable magnitude but considered two time scales, a buoyancy time scale and an advective time scale. The resulting dimensionless systems of equations for wave and vortical modes were identical

to those of Riley et al. except for the additional Coriolis terms. Lilly referred to the quasi-horizontal vortical-mode solution as 'stratified turbulence'.

In the third scale regime, Lilly considered anisotropic, small Rossby number flows where the horizontal length scale L is much larger than the vertical length scale H. This regime required new scaling assumptions. The relevant time scale for the wave-like flow is a stretched buoyancy time scale L/HN, and the horizontal pressure gradient and Coriolis terms are of the same order in the horizontal equation of motion. The resulting wave system has inertio-gravity waves as solutions, while in the small Fr_D limit the turbulence system equations are "formally identical to those of Charney's (1971) geostrophic turbulence" (Lilly, 1983a, p. 754). The mathematical difference is that in Lilly's system the two-dimensional Laplacian of a streamfunction is conserved whereas in geostrophic turbulence it is the three-dimensional Laplacian which is conserved. McWilliams (1985) extended Lilly's analysis even further and suggested a scaling for the advective-time-scale or 'turbulence' nondimensionalization which spans all values of Rossby number. He called this system, which includes both stratified turbulence and geostrophic turbulence, 'balanced turbulence'.

Implications of Lilly's conceptual model. Lilly's analysis indicates that two types of motion fields with very different time and amplitude scales can coexist for flows with an aspect ratio L/H in the range between f/N and unity when $Fr \ll 1$. The IGW and stratified turbulence will be significantly decoupled, and the IGW will exhibit much larger horizontal divergences and vertical accelerations. The IGW are only weakly nonlinear while the stratified turbulence is strongly nonlinear (e.g., Gage and Nastrom, 1986a). The propagation characteristics of the wave and turbulence modes are also very different. IGW energy will propagate in space away from its source region whereas turbulence energy remains near its source region. In wavenumber-frequency space, however, the wave component propagates little while turbulence energy may migrate both upscale and downscale. The time tendency is thus one of greater separation between these two modes in both physical and wavenumber space.

Lilly's scale analysis also suggested that the time required for the local disturbance Froude number to decrease to order unity from even a large value is less than one Brunt-Väisälä period (i.e., N^{-1}), and he remarked that this appeared to be consistent with laboratory experiments. Regarding the partitioning of the energy in an initially imposed isotropic disturbance between waves and stratified turbulence, Lilly determined that small-amplitude, isotropic forcing of the velocity field will tend to produce equal amounts of wave and turbulence energy while forcing by buoyancy can only produce wave-like flow. This implies that mixed forcing such as would be expected with a thunderstorm outflow or decaying convective cloud would tend to yield more wave energy than turbulence energy. The magnitude of the time scale for the injection of turbulence relative to N^{-1} is also important. If the injection time scale is much smaller than N^{-1}, then internal waves will be the dominant mode (Lilly, 1989b).

In applying this theory to the atmospheric KE spectrum, Lilly (1983a) also had to address the facts that (a) the injection of turbulent energy by decaying convective elements is sporadic in time and space and (b) initially independent turbulent "events" will experience interactions with other events as upscale growth occurs, leading to a "quasi-homogeneous domain of forced turbulence". Other authors have suggested breaking internal waves and shear-induced turbulence as additional sources of energy (e.g., Gage and Nastrom, 1986a), but these mechanisms are also sporadic in space and time. Lilly showed that the average energy spectrum for "temporally isolated" decay elements has a k^{-2} form. However, as the spectra associated with initially independent decay elements begin to overlap with time and interact, a shallower spectral slope approaching a $k^{-5/3}$ law results.

Another complicating factor is the question of the vertical coherence of stratified turbulence. If the quasi-horizontal vortical modes at different levels are decoupled, then the decorrelation of the vertical flow structure will inevitably produce locally small Richardson numbers and Kelvin-Helmholtz instability. The resulting three-dimensional turbulence will then modify the evolution of the stratified turbulence. Lilly pointed out, however,

that (a) the vertical mixing caused by the generation of three-dimensional turbulence must limit or at least slow down vertical decorrelation, and (b) as the stratified turbulence grows upscale, it must approach the geostrophic turbulence regime. The vertical coupling present in geostrophic turbulence will tend to minimize shear instability. One consequence of the vertical decoupling is that if horizontal gradients of any scalar quantity are present in the flow, decorrelated horizontal advection will create persistent vertical fine structure (Gage and Nastrom, 1985b).

Finally, Lilly (1983a) evaluated his conceptual model for the two-dimensional scalar atmospheric KE spectrum with respect to observed spectra and dissipation rates. He concluded that only a few percent of observed small-scale turbulent energy must 'leak' upscale in order to maintain the observed mean mesoscale $k^{-5/3}$ law spectrum.

In a recent paper, Lilly (1989a) used a theoretical model to investigate the spectral transition zone between the $-5/3$ and -3 inertial ranges at wavelengths near 500 km (see Figs. 2.3 and 2.5). He assumed the existence of two spectral energy source regions with negligible forcing and dissipation in the spectral region between them. Applying two different diffusive approximations for the transfer functions of the spectral entropy and energy equations of two-dimensional turbulence to model the transition region, Lilly found that the two opposing inertial ranges could coexist over the same spectral region with limited interaction. No enstrophy or energy sink is required to avoid a 'pile-up' of variance in the transition zone. However, this approach depends on the validity of the two spectral closure schemes employed and does not say anything about the nature or structure of the turbulent eddies involved. Lilly suggested that high-resolution numerical models would probably be the best means to investigate this topic further. Gifford (1988) has also considered this question of the transition region between the energy- and enstrophy-cascade regimes using a simple energy spectrum model and similarity theory arguments. He also compared his calculations against GASP-based energy spectra (e.g., Fig. 2.5).

Numerical simulations

Very few numerical modelers have attempted simulations of the evolution of homogeneous turbulence in a stably stratified fluid. Riley et al. (1981) considered the decay of initially isotropic, homogeneous three-dimensional turbulence in a linearly stratified Boussinesq fluid. Their study was motivated by the laboratory experiments of Lin and Veenhuizen (1975) and Dickey and Mellor (1980). The homogeneous case has the advantage that stratification effects on turbulence can be considered without the additional complicating factors of turbulence generation and diffusion.

Numerical simulations, in turn, have advantages over laboratory experiments since "(i) much more statistical information of interest can be obtained (since the entire flow field is known at every step in time), (ii) parameters can be easily varied, and (iii) experimental conditions are most controllable" (Riley et al., 1981, p. 80). The main disadvantage of numerical simulations of turbulent flow is the limited spatial resolution available, which limits the range of scales which can be represented. Flow features smaller than four model grid intervals or larger than one-quarter of the domain will be represented only poorly or not at all (e.g., Avissar et al., 1990).

Riley et al. (1981) used the direct numerical simulation (DNS) technique[52] so as to avoid the use of closure assumptions or subgrid-scale models. As a result, they were quite limited in the maximum Reynolds number that they were able to consider; for their $32 \times 32 \times 32$ grid, their initial Taylor-scale (or 'turbulence' or 'dissipation-scale') Reynolds number Re_λ [$= \lambda U/\nu$] was equal to 27.2, where the Taylor longitudinal microscale λ is bigger than the grid spacing. [In comparison, laboratory values of Re_λ are usually not much larger than 100 (Hinze, 1975, p. 253).] Riley et al. made three runs, one unstratified and two stratified. The two stratified simulations did not show a break in the

[52] DNS is also referred to as 'full-turbulence' simulation. The Navier-Stokes equations are solved directly with only molecular diffusivity used in the dissipation terms. Grid resolution is finer than the Taylor microscale so that even the larger energy-dissipating eddies are represented explicitly (e.g., Orszag and Patterson, 1972; Herring et al., 1974; Siggia and Patterson, 1978; Rogallo and Moin, 1984; Yeung and Pope, 1990).

fluctuation energy decay rate but did evolve to a mixture of internal waves and horizontal vortical modes as the turbulence decayed. The simulations also provided a more complete description of the energetics of the decay than did the laboratory experiments. Good reviews of Riley et al.'s pathbreaking simulations are given by Müller et al. (1986) and Gregg (1987). Müller et al. (1986) also review 4 two-dimensional numerical studies of decaying turbulence.

Metais and Herring (1989) noted that the effective Taylor-scale Reynolds number for Riley et al.'s simulations was too low to allow for a long period of decay or direct comparison with laboratory experiments. In their own numerical simulations of the decay of homogeneous turbulence in a stratified flow, they used fine enough spatial resolution (64^3 periodic box) to give effective Taylor-scale Reynolds numbers comparable with laboratory experiments ($\mathrm{Re}_\lambda \leq 45$)[53]. Metais and Herring compared their simulation results against laboratory measurements of freely evolving, unsheared, grid-generated turbulence in a ten-layer, closed-loop, salt-stratified water channel (Itsweire et al., 1986) and reported overall qualitative agreement. Some of the differences may have been attributable to large Prandtl-number differences (1:200).

Additional numerical experiments employing different initial proportions of vortical and wave modes indicated a lack of universality in subsequent flow evolution. These results suggest that the initial energy partition between wave and vortical modes could determine the final state of the flow field. In one simulation in which initial fields contained only vortical modes, the vortical modes continued to dominate as the flow evolved but vertical shear resulting from the juxtaposition of independent layers produced both smaller-scale turbulence and internal waves. This simulation was also much more dissipative than comparable simulations for purely two-dimensional turbulence.

In a related paper, Herring and Metais (1989) reported results from direct numerical simulations of *randomly forced*, stably stratified, homogeneous turbulence. They found a

---

[53] Vincent and Meneguzzi (1991) recently reported results from DNS runs at resolution 240^3 and $\mathrm{Re}_\lambda \approx 150$.

degree of reverse energy cascade to large scales, although the spectral slope was shallower than $k^{-5/3}$. However, they noted that their $64 \times 64 \times 64$ grid resolution may still have been too coarse to simulate an inverse energy cascade correctly. Nieuwstadt and Brost (1986) used a large-eddy model to study the decay of convective turbulence in an unstable atmospheric boundary layer when upward surface sensible heat flux is suddenly stopped. This is a more complicated case because the vertical stratification is nonuniform and evolves with time due to entrainment and the decaying turbulence is confined from above by the capping inversion and from below by the Earth's surface. It is also the only simulation to include rotation; Riley et al. (1981), Metais and Herring (1989), and Herring and Metais (1989) considered non-rotating cases since they were comparing their simulations against laboratory experiments.

Related studies of the decay of two-dimensional and geostrophic turbulence include Lilly (1971), Herring et al. (1974), Herring (1980), Bennett and Haidvogel (1983), Brachet et al. (1988), and McWilliams (1989, 1990a,b).

Atmospheric and oceanic observations

As might be expected given the recent nature of the interest in vortical modes by meteorologists and oceanographers, very few observations supportive of these modes have been reported to date. Larsen et al. (1986) discussed an evening case of deep convection in Puerto Rico during which wind measurements were made by the Arecibo Observatory Doppler radar. Comparison of frequency spectra calculated for two observing periods, one from the period of active convection and one from a period two hours later when the convective activity had diminished, showed a redistribution of power towards lower frequencies over time. Such behaviour is consistent with Lilly's (1983a) model of thunderstorm outflow decay but is not definitive since advection could also have been important. Etling (1990a) has suggested that examination of satellite photographs of supercell thunderstorms might reveal wake-like cloud features although none appear to have been identified to date. Aircraft measurements of thunderstorm outflows would also be helpful.

Mahrt and Frank (1988), Ruscher (1988), and Ruscher and Mahrt (1989) have presented analyses of aircraft measurements made at the top of a strong nocturnal surface inversion on a synoptically quiet day during the 1979 SESAME experiment which support the presence of 400-meter-long quasi-horizontal modes. Mahrt and Frank also speculated that the spotty turbulence observed during the flight legs might have been generated locally by vertical shear induced by the independent movement of these vortical modes at different heights. Mahrt (1988) suggested that multiple high-resolution lidars and/or Doppler radars could provide additional observational evidence of such horizontal modes in the stable PBL.

Etling (1990b) proposed that earlier observational studies of the stably-stratified boundary layer could be re-examined for evidence of vortical modes. He gave the study of Maitani et al. (1984) as one possible example. In this study, wave-like wind fluctuations were observed in the nocturnal surface layer over a rice canopy with about an 8-minute period, behaviour suggestive of propagating internal gravity waves. But in addition, these fluctuations were modulated by a slower oscillation with a period of about 30 minutes. This longer-period oscillation was apparent in both wind direction and wind speed traces. The wind direction trace actually went through five full anticlockwise rotations. Measurements from another station 10 km away exhibited similar oscillations. Etling pointed to the studies of Sethuraman (1980), Zhou and Panofsky (1983), and Raynor and Hayes (1984) as other candidates for re-examination.

Satellite photos frequently show cloud 'vortex streets' on the leeward side of large islands (e.g., Chopra, 1973; Scorer, 1986; Etling, 1990b). Vortices shed by topographic obstacles are most likely to be generated by the interaction of the obstacle with a stably stratified flow. These are not vortical modes *per se* but like vortical modes are mesoscale vortices with vertical axes. Etling (1988) has also speculated, however, that in instances when such organized vortices only appear at larger distances from the island, i.e., 'far-wake' cases, turbulent wake collapse might be the responsible generating mechanism.

For the ocean, Müller has argued that current fine structure observed during the Internal Wave Experiment (IWEX) was due to vortical modes (Müller, 1984; Müller et al., 1986). In a more recent analysis of the IWEX data set, Müller et al. (1988, p. 415) found the vortical modes to dominate "the total energy and shear spectrum in the resolved horizontal scale range from 5 to 260 m." They also cited previous oceanic observational studies in which (a) horizontal KE spectra exhibited higher energy levels than predicted by IGW theory, (b) horizontal KE was found at frequencies greater than the local Brunt-Väisälä frequency, and (c) vertical coherence between horizontal currents was smaller than between vertical displacements, all findings consistent with the presence of vortical modes.

The available geophysical observations are thus supportive of the existence of vortical modes in the atmosphere and ocean but are not definitive. Dedicated observational campaigns may be required to demonstrate conclusively the existence of geophysical mesoscale vortical modes and to reveal details of their structure and behaviour.

2.1.10 Mesoscale gap

More than three decades after the first publication of horizontal wind-speed frequency spectra which indicated the existence of a mesoscale energy minimum (Panofsky and Van der Hoven, 1956; Van der Hoven, 1957), what is the present status of the so-called *mesoscale gap*? Unquestionably there is considerable observational evidence to support the existence of a mesoscale spectral minimum of horizontal wind speed, temperature, and humidity in the *surface layer* over homogeneous terrain some of the time (Kolesnikova and Monin, 1965; Oort and Taylor, 1969; Fiedler and Panofsky, 1970; Hess and Clarke, 1973; Smedman-Högström and Högström, 1975; Olesen et al., 1984; Courtney and Troen, 1990). Over inhomogeneous terrain, however, diurnally-varying, terrain-forced mesoscale circulations can introduce mesoscale spectral 'spikes' (e.g., Fiedler and Panofsky, 1970; Lyons, 1975). Moreover, free-atmosphere spectra do not show such a gap. In fact, a spectral minimum is not always observed in the surface layer even over homogeneous terrain (Bushnell and Huss, 1958; Hwang, 1970; Atkinson, 1981; Gifford, 1989b). It

is also worth remembering Eriksson's (1975) warning that when the ordinate axis of a frequency spectrum shows spectral density multiplied by frequency, spectral 'peaks' and 'gaps' may be obtained even when the spectral density is a *non-increasing* function!

Rather than being a universal feature, the mesoscale gap must be viewed as an anomalous, near-surface feature resulting from boundary effects. The presence of a rough, rigid, lower boundary will create vertical shear, mechanically-induced turbulence and mixing, and weaker stratification, thus providing a source of microscale turbulent energy and reducing the ability of the near-surface atmosphere to support IGW activity. Surface heating will also reduce stratification and the rigid boundary will reflect internal gravity waves (e.g., Lalas et al., 1976; Finnigan and Einaudi, 1981; Hooke and Jones, 1986). As well, mesoscale frequencies in the free atmosphere usually contain much more energy than near-surface spectra (Fiedler and Panofsky, 1970; Vinnichenko, 1970). Instead of a mesoscale gap, then, current thought favours an interpretation in terms of an intermittent microscale maximum or 'hump' or 'bump' (e.g., Gifford, 1988).

For example, many of the early mesoscale KE frequency spectra were constructed by 'patching' together a set of heterogeneous wind observations. Van der Hoven's (1957) famous microscale maximum corresponded to the spectrum of a short time series made during a hurricane! Courtney and Troen (1990) have argued that construction of a composite spectrum based on such non-representative meteorological conditions is very misleading. Other articles which discuss sample-dependent microscale 'humps' include Mantis (1963), Hwang (1970), and Vinnichenko (1970). Reviews of the mesoscale gap may be found in Bretherton (1969c), Fiedler and Panofsky (1970), Monin and Yaglom (1975), and Atkinson (1981).

2.1.11 Waves vs. turbulence

Although there is still controversy over the mechanisms responsible for observed mesoscale atmospheric spectra and variability, the combined results of observational, theoretical, and numerical and laboratory modelling studies appear to support the view of a complex flow field composed of coexisting and interacting organized mesoscale cir-

culations, internal gravity waves, quasi-horizontal stratified turbulence or vortical modes, and dry and moist three-dimensional turbulence. As discussed above, the intermittent existence of a mesoscale gap in the PBL does not appear to be representative of the rest of the atmosphere but is rather the result of the influence of the Earth's surface and the emphasis by micrometeorologists until recently on the daytime PBL over homogeneous terrain.

Prior to 1960, mesoscale variability in the free troposphere and above was explained by classical three-dimensional turbulence. This view changed following the publication of Hines's seminal paper and it soon appeared that internal gravity waves were the sole responsible mechanism. VanZandt's (1982, 1985) application of the Garrett-Munk oceanic IGW spectrum to the atmosphere may be viewed as the logical extension of this viewpoint. However, while internal gravity waves appear to be responsible for most of the mesoscale variability observed in *vertical* velocity, observations suggest that IGW activity can explain only a fraction of the observed horizontal velocity variability (Gage and Nastrom, 1985a, 1988). Stratified turbulence appears to offer the best explanation for most of the observed meoscale horizontal variability, but this hypothesis is still unproven. As discussed in Sec. 2.1.9, there is considerable indirect evidence for this mechanism from laboratory experiments, theory, and numerical simulations but conclusive direct observational evidence is not yet available.

It is worth remembering Lumley's comment that the difference between random internal waves and turbulence is in a sense a semantic question that depends critically on our definition of 'turbulence': "if [turbulence] is taken to be any random, three-dimensional velocity field with a continuous spectrum, displaying spectral transfer and dissipation at high wave numbers, then the case of internal waves is also included" (Lumley, 1964, p. 101). Dewan has argued similarly that "waves and turbulence can be viewed as two extremes of a continuum of possibilities" (Dewan, 1985, p. 1301). Given also the multiple interactions possible between waves and turbulence and the difficulty in distinguishing

between these two flow modes (Sec. 2.1.8), it is clear that the distinction between waves and turbulence is not a simple one.

2.1.12 Implications for mesoscale dispersion

Contrary to earlier views of a mesoscale gap, the atmosphere has been observed to contain significant mesoscale motion, structure, and variability. Mesoscale spectra can be described by simple power-law formulations for large enough samples, though short temporal or spatial samples may deviate significantly from these simple forms (e.g., Larsen et al., 1982). Not all of this spectral energy can contribute to diffusion, however. Nonbreaking linear internal gravity waves will only induce oscillatory advection but not direct mixing. Nevertheless, as discussed by Sanderson and Okubo (1988), the superposition and interaction of random internal waves may still result in lateral dispersion via a random-walk process analogous to that described by Herterich and Hasselmann (1982) for surface water waves.

In the planetary boundary layer, internal gravity waves are frequently observed under stable conditions, including internal gravity waves propagating downwards from upper-level sources and breaking near the surface (e.g., SethuRaman, 1977; Finnigan et al., 1984). There is also some evidence that quasi-horizontal vortical modes can occur in the PBL under stable conditions (e.g., Ruscher, 1988). Both modes can contribute to vertical shear, meander, KH instability, and convective overturning, increasing effective diffusivity in stably stratified flows. Such mesoscale 'eddies' clearly have different properties than microscale three-dimensional eddies but may have comparable influence on mesoscale dispersion, particularly lateral dispersion. If mesoscale eddies are present, sample averaging times will have to be much larger than the eddy characteristic time scales in order to estimate ensemble averages (e.g., Mellor, 1985). Also, such mesoscale eddies pose problems for gradient-transport diffusion models since these models assume that the diffusing turbulent eddies are much smaller in scale than the tracer cloud being modelled.

The above suggests that the mechanism of delayed mixing, that is, stirring or differential advection followed by turbulent mixing, is important for dispersion in both the intermittently turbulent free atmosphere and the diurnally-varying boundary layer. In fact, in the free atmosphere this mechanism can contribute to both vertical and horizontal dispersion whereas it is usually only important for horizontal dispersion in the PBL. In a sense, the free atmosphere is more dispersive *on the mesoscale* than the PBL is. The two primary mesoscale turbulent flow modes, internal gravity waves and quasi-horizontal vortical modes, require stable stratification and are not viable in the well-mixed boundary layer. There are thus more ways for *mesoscale* stirring to occur in the free atmosphere. However, this stirring is largely two-dimensional (i.e., quasi-horizontal). In addition, aside from deep moist convection, vertical mixing is a local, intermittent phenomenon in the free troposphere, unlike the continuous nonlocal mixing which occurs in the well-mixed convective PBL.

2.2 Observational Studies of Mesoscale Atmospheric Dispersion

Observations of mesoscale atmospheric dispersion form the foundation of most of our current understanding of this phenomenon and have provided the impetus for many theoretical and numerical studies. Relatively few MAD observations exist, however, compared to the large number of observations of short-range dispersion experiments made since World War I. There are a number of reasons for this difference, including an early lack of interest on the part of both the scientific community and various funding agencies, a lack of suitable technologies for observing atmospheric dispersion over larger scales, and the high costs and organizational and logistical demands associated with mounting a MAD experiment. A well-designed MAD field program requires coordinated and extensive sensor networks deployed over a large area to measure both meteorological variables and tracer concentrations or locations[54]. A variety of Lagrangian marker systems have been

[54] In the case of balloons or other Lagrangian point markers

employed in MAD experiments to date, but basically these all fall into one of two main categories: *balloons* and *tracer gases.*

2.2.1 Balloons and tetroons

Balloons[55] have been used to study mesoscale dispersion in three ways: (i) in isolated releases as Lagrangian markers of pollutant trajectories for atmospheric flow over complex terrain or long distances (e.g., Angell et al., 1972; Pack et al., 1978; Clarke et al., 1983); (ii) in sequential releases to provide one-particle diffusion estimates (e.g., Richardson and Proctor, 1925; Edinger and Rapp, 1957; Angell, 1962; Vogt and Thomas, 1985; Thomas and Vogt, 1990) ; and (iii) in simultaneous or cluster releases to study relative diffusion (e.g., Sakagami, 1961; Angell and Pack, 1965; Morel and Larcheveque, 1974; Er-El and Peskin, 1981). Usually, constant-level, constant-volume, superpressure balloons, which tend to travel on isopycnic surfaces, are used in these studies (Cadet, 1978; Clarke et al., 1983). These balloons are either spherical or tetrahedral in shape; the latter are often called *tetroons.* They may be tracked by means of aircraft, radar, LORAN, or satellite. Angell (1961) has provided a good overview of the early days of constant-level ballooning.

Balloon characteristics

Although balloons, and especially tetroons, have been widely used in atmospheric transport and diffusion studies, they are not perfect Lagrangian markers (Clarke et al., 1983). If we neglect entrainment, we would expect unsaturated air parcels to follow isentropic trajectories. Tetroons, on the other hand, are designed to follow isopycnic (i.e., constant air density) surfaces. In regions of significant vertical motion, isopycnic and isentropic trajectories will swiftly diverge. Tetroons are also subject to physical forces which do not act on corresponding air parcels. Because of the radiative properties of the tetroon skin material (usually Mylar film), the tetroon surface, and hence the gas inside,

---

[55] Or their oceanic counterparts, drogued drifter buoys (e.g., Mackas et al., 1989; Thomson et al., 1990).

will heat up during the day and cool off at night, changing the volume of the tetroon by a small but significant amount. This property leads to a complex diurnal height variation of the order of 250 m for a tetroon with a 300-m equilibrium altitude (Hoecker, 1981). Moreover, if expansion due to heating is too great, the tetroon skin material may be stretched beyond a critical limit and will not return to the same equilibrium volume upon cooling (Clarke et al., 1983). This hysteretic effect thus results in an increased equilibrium altitude.

In contrast, gas diffusion and leakage will also occur during a flight, leading to lower superpressures and reduced equilibrium altitudes on long flights. Dramatic fluctuations in tetroon altitude can also result from dew formation or precipitation collection on the tetroon surface. Any of these effects will result in a "constant-level" balloon changing its altitude during a flight and experiencing a wide range of altitude-dependent winds, especially at night. Loss of altitude can also end with the loss of the tetroon due to grounding, especially for tetroons with low initial equilibrium altitudes.

Another balloon characteristic which must be kept in mind is that one balloon is only a single Lagrangian particle. That is, it is only a single realization of particle motion in a (usually turbulent) atmospheric flow. Most Lagrangian statistics assume averages over a set of particles rather than over a single particle trajectory for an extended time or distance. This is a particular problem in inhomogeneous turbulent flows such as the convective PBL where variances are large and a single realization may deviate greatly from the mean (cf. Eq. 1.6). However, despite these limitations, balloons can still serve as *single-realization* Lagrangian markers, even in the well-mixed daytime PBL, provided balloon position and velocity data are used in an appropriate fashion.

Trajectories

The most common use of balloon and tetroon trajectories by the air pollution community has probably been to estimate the mean or maximum likelihood trajectory and the transport speed and direction for a cloud of pollutant in a given flow (e.g., Islitzer and Slade, 1968). The statistical significance of the cloud trajectory estimated from tetroon

trajectories will depend, however, on the number of tetroons launched. A single tetroon trajectory may not be very representative, particularly in situations with strong wind shear. In the convective PBL, a tetroon trajectory may be strongly influenced by its relative residence time in various updrafts and downdrafts associated with turbulent eddies, thermals, longitudinal rolls, or Bénard-type convection cells. Under stable conditions, wind direction and speed often vary significantly with height and for greatest representativeness, the tetroon flight level should correspond to the mid-point of the vertical extent of the transport layer of interest or else 'bracket' that layer (i.e., by using multiple tetroons with different equilibrium levels). Averaging over multiple trajectories from a simultaneous tetroon release may also give a mean trajectory quite different than one based on trajectories from sequential releases or releases from different days with similar conditions due to the difference in effective sampling time (see Sec. 2.3.3).

Some studies have been carried out to compare tetroon trajectories with trajectories predicted by (i) hand analysis from meteorological maps (subjective approach), (ii) objectively-analyzed wind fields based on observations (kinematic approach), or (iii) three-dimensional wind fields predicted by prognostic numerical models (dynamic approach). In general, the tetroon trajectories have been treated as 'truth', although as already discussed they have certain limitations, especially due to sampling fluctuations.

Two basic types of comparisons are possible. The first is to determine a tetroon's trajectory throughout its flight. Tetroons are seldom followed out to distances beyond 100 km due to radar limitations if only a single radar is used for tracking. Longer trajectories can be constructed if the tetroon or balloon is large enough to carry a transmitter or transceiver, thus permitting use of a radio positioning network or satellite navigation system (e.g., Angell, 1961; Morel and Bandeen, 1973; Gage and Jasperson, 1976), or a camera (e.g., Mantis, 1963) or if the balloon's flight is 'shadowed' by an aircraft (e.g., Moore et al., 1954). It is also possible to obtain tetroon recovery-point data if 'return tags' or 'mail-back cards' are attached to the tetroon or to the tetroon-borne radar transponder or reflector and are subsequently returned by the finder (e.g., Pack et al., 1978; Clarke

et al., 1983). This alternate approach is clearly haphazard and less informative but may still provide useful data.

Pack et al. (1978) have reviewed both types of comparisons for tetroon trajectories and a number of different trajectory calculation methods, including both subjective and kinematic approaches. They found large and sometimes systematic errors for some of the trajectory calculation techniques. For trajectories out to 100 km, errors ranged from 10–54% of the trajectory length were reported for low-level tetroon flights while standard vector deviations of about 55–60% were reported for low-level tetroon flights out to 650 km. Clarke et al. (1983) and Reisinger and Mueller (1983) have carried out similar comparisons of the kinematic approach with tetroon trajectories from the STATE and NEROS air quality studies. Clarke et al. reported that errors in prediction of tetroon trajectories was a factor of five or larger than observed plume dimensions for comparable travel times based on Mount Isa data. Stocker et al. (1990) compared predictions made by the ARL–ATAD trajectory model against balloon end-point data obtained after a unique simultaneous release of approximately 190,000 helium balloons by schoolchildren from about 800 sites scattered across the United States in May 1986. The authors were able to infer large-scale dispersion characteristics and evaluate ARL–ATAD model performance associated with different synoptic conditions from analysis of this data set.

Comparison of longer-range constant-level balloon trajectories in the free troposphere with 'geostrophic' trajectories calculated by subjective or kinematic analysis has been of considerable interest because of the much greater ease with which the latter can be obtained and their applicability to large-scale atmospheric dispersion (see next section). Angell (1961) mentioned *eight* different subjective approaches but concluded that, on average, they were all about equally successful. He reported errors on the order of 30% for these schemes for flight ranges of about 1000 km and upper-tropospheric flights. He also pointed to synoptic patterns with strong anticyclonic shear as a particularly difficult situation for trajectory calculation from meteorological observations. Moore et al. (1954) reported trajectory *forecast* errors of about 23% of the distance traveled for 300 mb

constant-level balloon flights ranging from 1300 to 2500 km for a group of experienced meteorological analysts using a standard subjective method. More interestingly, *hindcast* errors made by the same group of analysts for the same balloon flights were only reduced to 20% on average, causing Angell (1961, p. 158) to remark that "apparently there are times in meteorology when the blame for an incorrect result does not rest solely on the forecaster." Durst et al. (1959) estimated that errors in their 36–48 h geostrophic trajectories were probably not more than 10% on average.

Warner (1981) and Warner et al. (1983) have compared trajectories predicted based on wind fields calculated by a three-dimensional mesoscale meteorological model with tetroon trajectories from the STATE and NEROS studies, respectively. Warner et al. (1983) concluded that the dynamic approach produced a more accurate trajectory prediction because of its ability to handle nonlinear variations of the transport wind field in space and time, although they also conceded that forecast errors would gradually degrade this advantage.

Lateral diffusion estimates

In addition to providing estimates of mean centerline or center-of-mass positions and mean transport flow speeds and directions, position and velocity data from even a single tetroon release can also be analyzed to provide estimates of lateral diffusion. These are usually expressed either in terms of lateral standard deviation σ_y or lateral eddy diffusivity K_y. Anticipating the discussion of Taylor's theorem in Sec. 2.3.1, let us consider each of the three approaches mentioned by Islitzer and Slade (1968) as well as several others. Note that a number of studies (e.g., Durst et al., 1959; Kao and Bullock, 1964; Murgatroyd, 1969) adopted a similar analysis approach for estimating larger-scale atmospheric diffusion based on observed trajectories but instead considered sequences of hand-analyzed geostrophic isobaric trajectories[56].

---

[56] The discussion of errors for computed trajectories in the previous section is relevant here since such trajectory errors will produce an 'apparent' but unrealistic component of diffusion which may overwhelm the true diffusion (Murgatroyd, 1969).

The simplest approach is to consider the trajectories of a succession of tetroon releases. RMS values of lateral deviations of individual trajectories from the mean trajectory position at various downwind distances can then be calculated over the ensemble of trajectories in the spirit of Taylor's equation (see Eqs. 2.42, 2.54, and 2.57) [e.g., Durst et al., 1959; Angell, 1960; Murgatroyd, 1969]. Possibly the earliest and one of the best-known examples of this approach is the study by Richardson and Proctor (1925) on serial balloon releases[57]. This method requires the use of a reasonable number of trajectories for statistical significance and requires specification of a mean trajectory and a mean wind. In addition, Taylor's equation assumes stationary, homogeneous turbulence. If the sequence of tetroons is released over a significant fraction of a diurnal cycle, then significant fluctuations in the 'mean' wind will also be incorporated in the statistics (e.g., Angell and Pack, 1965). For example, Islitzer and Slade (1968) discussed series of tetroon releases from the Los Angeles Basin (see Fig. 2.20) and Yucca Flat, Nevada in which tetroon trajectories clearly showed the presence of a sea-land breeze and upslope-downslope circulation system, respectively. If a sequence of trajectories extending over a period of weeks or months is considered, then even synoptic-scale 'eddies' will contribute to the calculated σ_y's. For example, Fig. 2.21 shows composite tracks of daily geostrophic 500 hPa trajectories for a one-month period

A second approach is to consider the lateral distance between pairs of trajectories from a set of non-simultaneously-released trajectories (e.g., Angell and Pack, 1965; Thomas and Vogt, 1990). This approach does not require specification of a mean wind direction or mean trajectory centerline. If all possible pairs are used, then a greater number of data points are available compared to the first approach. In addition, the influence of different sampling times can be considered by limiting pairs to trajectories released within a certain number of hours of each other. For example, Fig. 2.22 shows lateral dispersion statistics

---

[57] Results from this study have often been used in estimating relative diffusivities, that is, the instantaneous rate of expansion of tracer clouds or clusters of particles, but most of the releases considered by Richardson and Proctor took place over periods ranging from 5 to 11 hours.

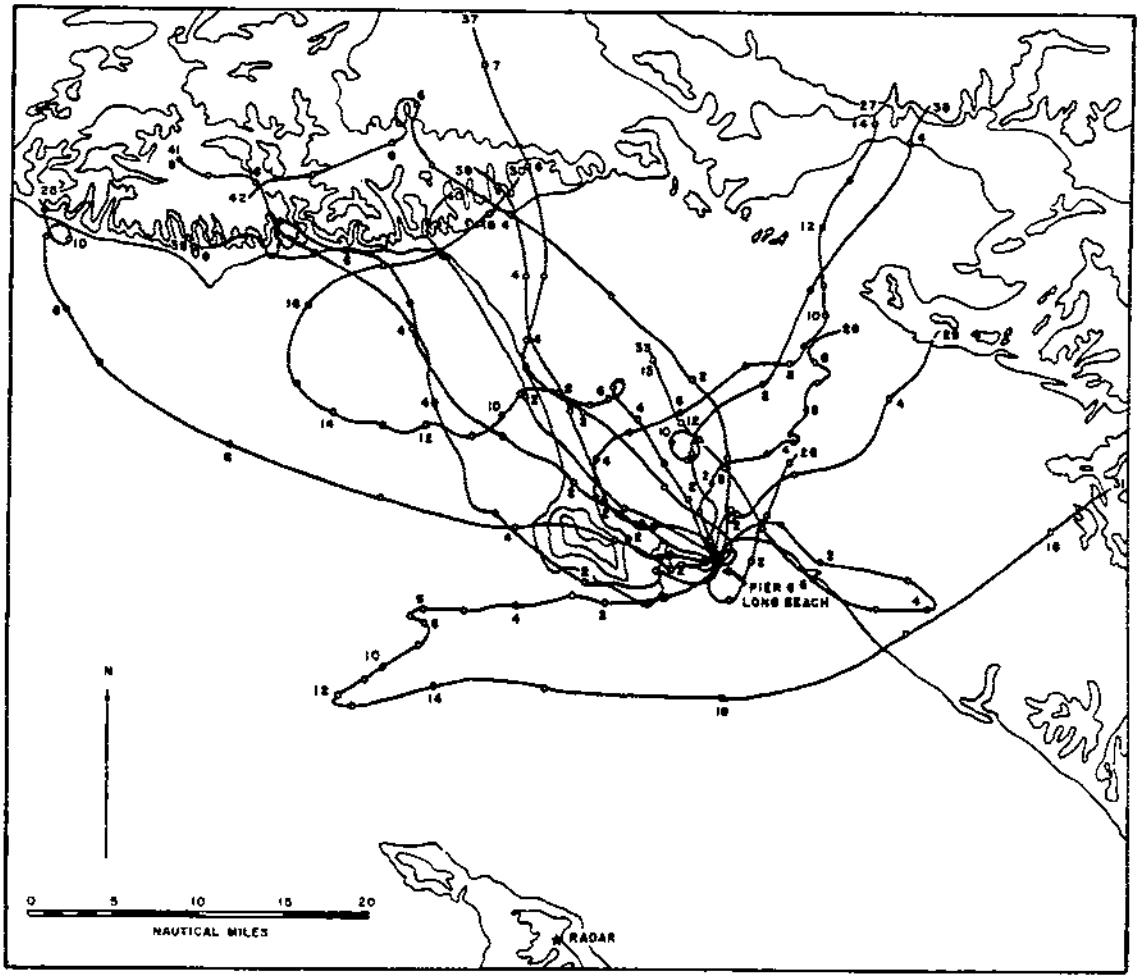

Figure 2.20: Trajectories for 18 tetroons tracked for two hours or more after release from Pier G, Long Beach, California during the six-day period May 18–23, 1963. Most releases were made either during the morning or evening hours. Float altitude was in the 305–457 m ASL range, i.e., below the tops of the highest hills to the north of the Los Angeles Basin. Tetroon positions are marked for each hour of flight and trajectory end-points are marked with the flight ID number. The contour lines mark terrain elevations of 152, 305, and 610 m (from Islitzer and Slade, 1968; adapted from Pack and Angell, 1963).

calculated by this method for tetroon releases within six hours of each other and within 24 hours of each other. The standard deviations of the latter values are almost exactly 1.4 times larger than those of the former. This figure also shows near-instantaneous (8-minute sampling time) lateral dispersion estimates made by Pasquill (1962) which are considerably smaller. These three lines for different sampling times indicate the influence of sampling time on the derived horizontal diffusivities (see also Sec. 2.3.3).

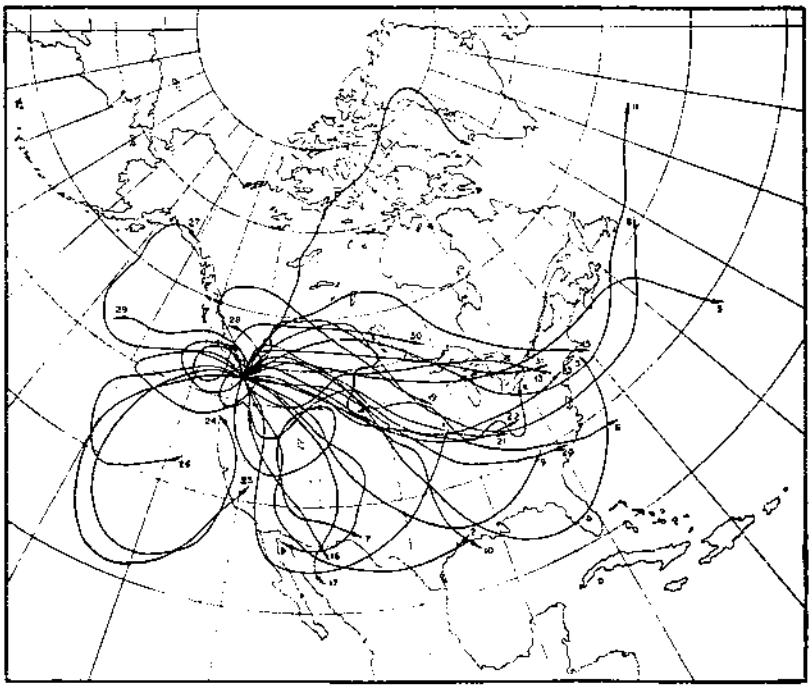

Figure 2.21: Daily 500-hPa geostrophic trajectories initiated at 0000 GMT each day during May of the International Geophysical Year, 1958, from Seattle, Washington and calculated for 72 h based on six-hourly geopotential fields. Trajectory initiation dates are indicated by the numbers at the trajectory endpoints (from Kao and Bullock, 1964).

A third approach requires calculation of the running mean of lateral wind fluctuations for different travel times for *single* tetroon flights (e.g., Angell, 1962). This method is based on Eq. 2.50; that is, σ_y is estimated by calculating $\overline{u_T'^2}$. It has the advantage of requiring only a single trajectory but travel times should be no larger than 10% of the total duration of the flight in order to get a statistically significant estimate of $\overline{u_T'^2}$ (since this is equivalent to estimating $R(\xi)$ up to $\xi = T/10$; e.g., Gifford, 1968). Gage and Jasperson (1976) carried out a related calculation in which they used the formula

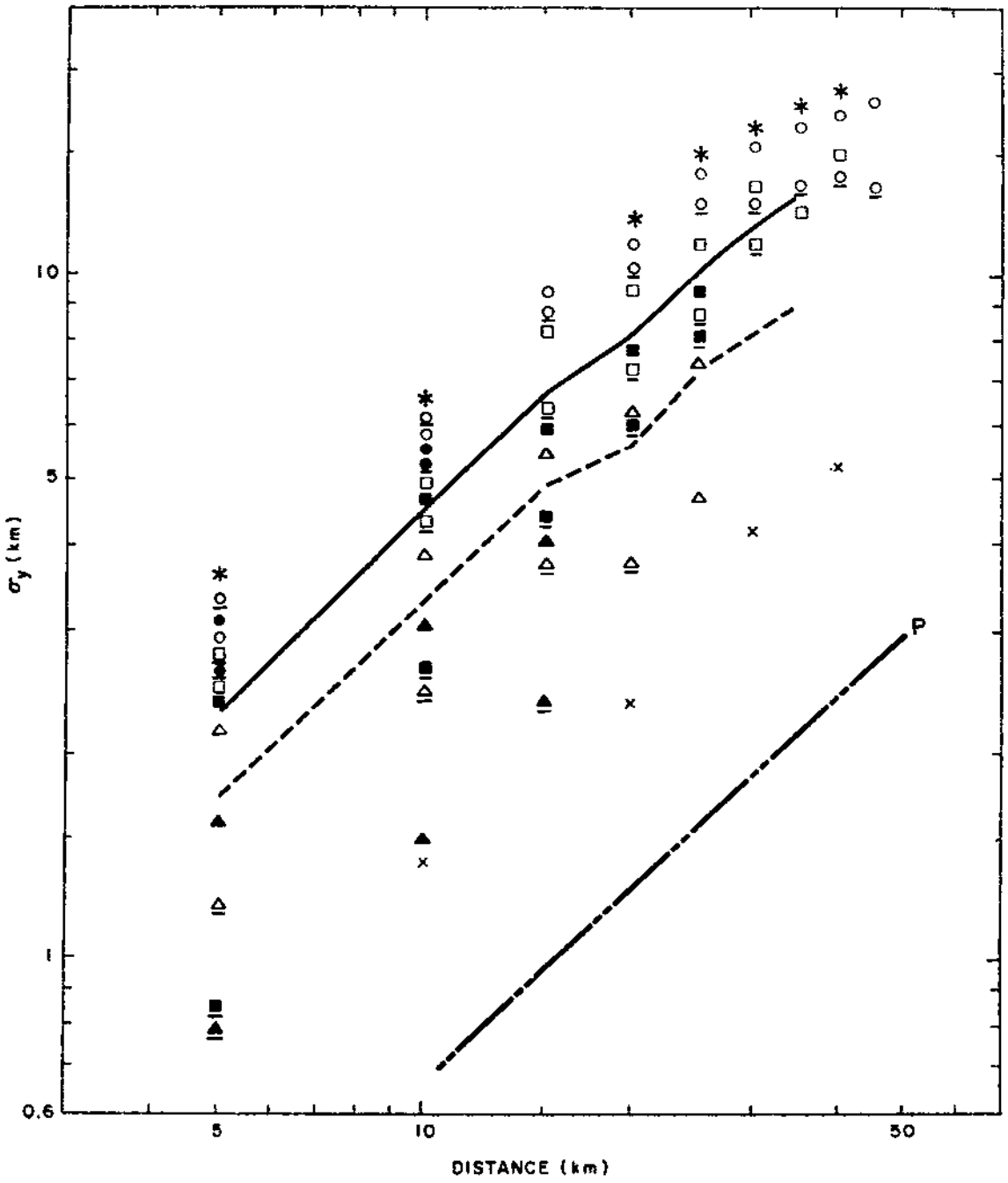

Figure 2.22: Tetroon trajectory lateral standard deviations as a function of downwind distance for flights from Cardington, England (filled triangles), Las Vegas, Nevada (filled circles), Wallops Island, Virginia (filled boxes), and from Marineland (open triangles), Long Beach (open circles), and Venice (open boxes) within the Los Angeles Basin. Underlined symbols indicate statistics calculated for tetroons released within six hours of each other; plain symbols indicate statistics calculated for flights within 24 hours of each other. The means for all flights within six hours and within 24 hours of each other are indicated by the dashed and solid lines, respectively. The line marked by the symbol 'P' was obtained by Pasquill (1962) at Porton, England from tracer releases with 8-minute sampling time (from Islitzer and Slade, 1968).

$K = \overline{v^2} T_L$ (see Eq. 2.56) and values of $\overline{v^2}$ and T_L estimated based on three-dimensional balloon positions from two test flights to estimate eddy diffusivities K_x, K_y, and K_z.

A fourth approach is based on Eqs. 2.42, 2.55, and 2.56. Velocity components along trajectories are used to determine velocity variances $\overline{u'^2}$ and $\overline{v'^2}$ and Lagrangian velocity autocorrelation functions $R_u(\xi)$ and $R_v(\xi)$. These quantities can then be used to determine Lagrangian integral time scales T_{Lu} and T_{Lv}, lateral standard deviations σ_x and σ_y, and horizontal diffusivities K_x and K_y (e.g., Edinger and Rapp, 1957; Durst et al., 1959; Kao and Bullock, 1964; Murgatroyd, 1969). Both Kao and Bullock (1964) and Murgatroyd (969a) also calculated corresponding Eulerian quantities to determine the appropriate value of the Eulerian–Lagrangian scale ratio $\beta = T_L/T_E$ proposed by Hay and Pasquill (1959) for the synoptic scale. They obtained values in the range 0 to 1, much smaller than the 4 to 6 range for microscale turbulence determined by Hay and Pasquill[58]. They also found Lagrangian integral time scales for the zonal and meridional directions to range from 5 to 50 h.

The four schemes just mentioned determine *Eulerian* (or *one-particle*) eddy diffusivities, which are dependent upon the sampling time used. *Simultaneous* balloon and tetroon releases, on the other hand, can be analyzed to estimate *Lagrangian* (or *two-particle* or *relative*) eddy diffusivities. A number of investigators have used this approach (e.g., Angell and Pack, 1965; Kao and al-Gain, 1968; Morel and Larcheveque, 1974; Kao et al., 1976; Er-El and Peskin, 1981). It is based on determination of the time rate of change of the mean-square separation of pairs of simultaneously-released particles with similar initial separation distances (see Eq. 2.61). This calculation was suggested by the papers of Batchelor (1950), Brier (1950), and, most importantly, Batchelor (1952). An equivalent calculation is to consider the dispersion of a cloud about any one of its volume

---

[58] Values of $\beta < 1$ indicate a strongly turbulent flow field since heuristic arguments suggest that $\beta \sim \overline{u}/\sigma_u$, the reciprocal of the relative turbulence intensity (e.g., Pasquill and Smith, 1983, p. 81).

elements, usually its center[59] (e.g., Batchelor, 1952; Gifford, 1957; Smith and Hay, 1961; Monin and Yaglom, 1975, p. 554).

To close this section on a cautionary note, anyone convinced of the necessary and concomitant existence of mesoscale lateral eddy diffusion by the form of the mesoscale energy spectra discussed in Sec. 2.1.5 (e.g., Fig. 2.4) and by the natural analogy to small-scale diffusion and the small-scale energy spectrum should consider the paper by Moore et al. (1954). These authors discussed four cases in which pairs of 300-hPa constant-level balloons released simultaneously displayed exceedingly small separation after long travel times. In the most extreme case, two balloons were recovered within 2 km of each other after travelling approximately 1800 km from Utah to Wisconsin. This points out the role of sampling time in constructing the observed mesoscale energy spectra. Mesoscale turbulence is very intermittent in nature and instantaneous flow fields are unlikely to display the monotonic *spatial* energy spectrum associated with a seamless downscale cascade of kinetic energy. Correspondingly, mesoscale diffusivities must also be averaged quantities. For example, while all of the studies of relative diffusion based on analysis of discrete particles mentioned above found mean particle separation to increase with time, Richardson and Stommel (1948) and Angell et al. (1971) presented cases in which pair separation distance decreased with time for individual realizations.

2.2.2 Tracer gases and aerosols

Measurements of the dispersion of tracer gases and aerosols over mesoscale distances have been made both for controlled releases in formal mesoscale tracer experiments and for uncontrolled releases from 'sources of opportunity'. The latter include *large industrial point sources* (e.g., Peterson, 1968; Randerson et al., 1971; Millán and Chung, 1977; Gillani, 1978; Uthe et al., 1980; Weber, 1980; Carras and Williams, 1981, 1988; Crabtree, 1984; Hoff and Gallant, 1985), *urban plumes* (Brown et al., 1972; Haagenson and Morris, 1974; Trout and Panofsky, 1974; Fiedler, 1987; Bastable et al., 1990), *major fires*

[59] Hence the term 'relative' diffusion.

(Davies, 1959; Randerson, 1968; Limaye et al., 1991), *volcanic eruptions* (Dyer, 1966; Randerson, 1977; Chung et al., 1981; Draxler, 1981; Crabtree and Kitchen, 1984), *accidental radioactive releases* (ApSimon et al., 1985; Persson et al., 1987; Smith and Clark, 1988; Wheeler, 1988), and *intentional radioactive releases* (Heffter, 1965; List et al., 1966; Randerson, 1972).

Organized mesoscale tracer experiments are more effective than uncontrolled releases for studying mesoscale dispersion because of the control they give over the strength of release, time of release, and length of release. Such control permits the design and deployment of the best possible network of fixed and mobile air samplers and the most appropriate sampling protocol given available resources, including proper transport and storage of samples, stringent quality assurance and quality control of samples, calibration of instruments before, during, and after the experiment, and laboratory checks and intercomparisons (e.g., Dabberdt and Dietz, 1986; Ferber et al., 1986; Lagomarsino et al., 1991). The effective 'sample size' is also considerably greater for tracer releases than it is for corresponding balloon releases since the cloud of tracer 'samples' a much larger atmospheric volume. Heffter (1965), Bauer (1974), Gifford (1977, 1983, 1986), and Draxler (1984) have summarized observations of boundary-layer, free-tropospheric, and stratospheric dispersion over a wide range of scales and from a variety of experiments.

Aerosol or parcel tracers have been widely used in short-range dispersion experiments (e.g., Gatz, 1984). They are less useful for longer-range dispersion experiments, however, because of removal by settling and deposition and their relatively high detection limits. Gaseous tracers have been found to be more useful in such applications, although aerosol tracers of opportunity can still be valuable sources of information on *transport* over regional-scale and continental-scale distances (e.g., Rahn, 1984).

Types of gaseous tracers

A variety of tracer gases have been used in mesoscale tracer experiments, including sulphur hexafluoride (SF_6), halocarbons ($CBrF_3$, CBr_2F_2), radioactive gases (Ar-41, Kr-85), deuterated methanes (Me-20, Me-21), and perfluorocarbons (PMCH, PDCH,

PTCH, PDCB, PDCH, PMCP). According to Pack et al. (1978), the ideal tracer should have the following properties: (a) non-toxic; (b) conservative, i.e., non-reactive and non-depositing; (c) inexpensive to acquire and release; (d) inexpensive to collect and analyze; (e) detectable at very low concentration; and (f) low atmospheric background (below detection limits if possible). Johnson (1983b) adds the requirement that the tracer must be able to follow air motions exactly, and Dabberdt and Dietz (1986) mention limited or negligible industrial use as another desirable property.

The perfluorocarbons (especially PMCH) and the deuterated methanes come the closest to being ideal tracers according to the above criteria[60] but are expensive to produce and require elaborate analytical equipment to make concentration measurements (gas chromatography in the case of the perfluorocarbons, mass spectrometry in the case of the heavy methanes). However, Dabberdt and Dietz (1986) and Dietz (1987) have argued that perfluorocarbons are the most cost-effective tracer currently available for mesoscale dispersion experiments if the criterion considered is the *amount* of tracer gas which must be released to give concentration levels 100 times background at downwind distances of 100 km or 1000 km.

Perfluoromonocyclohexane (PMCH: chemical formula C_7F_{14}) is the most popular tracer currently being used for mesoscale tracer experiments. It is inert, harmless, and can be accurately measured at its ambient background concentration (2.5–3.5 $\mathrm{fl\,l^{-1}}$ range, where one femtoliter per liter is one part per 10^{15}). PMCH is dynamically passive in the sense that it does not carry meteorologically significant energy and does not affect the atmospheric flow field. It does not react chemically in the gas phase, has a negligible deposition velocity at the earth's surface, and is not appreciably soluble in water so that it is not removed from the gas phase by clouds, haze, or precipitation scavenging. PMCH

---

[60] Although Turkevich (1984) has argued that such 'permanent' tracers have the disadvantages of background build-up with use and ambiguity in interpretation due to different transport paths and 'crosstalk' between multiple releases carried out too close together in space or time (e.g., Clark and Cohn, 1990). He suggested that non-conservative tracers with half-times longer than the experiment transport times might be preferable.

has no industrial applications or sources and it is only available from I.S.C. Chemical Ltd (ISCC) of England. Cost is about \$25 kg^{-1} for bulk purchases (say ten metric tons). If a reasonably strong PMCH signal is to be measured at a distance of 1000 km from the source, a release rate on the order of 25 $kg\,h^{-1}$ is required (Ferber et al., 1981; Brost et al., 1988a; Hidy, 1988). PMCH was used in both of the mesoscale tracer experiments selected for this numerical modelling study.

Good reviews of current tracer technologies can be found in Johnson (1983b), Barr et al. (1984), Dabberdt and Dietz (1986), and Dietz (1987). Dietz (1987) pointed out that an important component of tracer technology is the analytical methodology employed and discusses the electron-capture-detection gas chromatograph used to measure perfluorocarbon levels. He also discussed perfluorocarbon isomers, release methods, sampling techniques, gas standards, instrument calibration, and a variety of applications.

Mesoscale tracer dispersion experiments

Table 2.4 lists 25 formal mesoscale tracer experiments in which controlled, fixed-period releases were made of one or more selected tracers and a surface sampling network of stationary samplers extending to distances of at least 25 km downwind from the source was to measure tracer concentrations. Concentrations were measured out to distances as great as 3000 km. The majority of these experiments have been carried out in the last decade, reflecting both the recent development of suitable tracers and analysis techniques and the heightened interest of various research groups and funding agencies in mesoscale atmospheric dispersion. Plans, now apparently shelved, were also made for an even larger tracer experiment, the Massive Aerometric Tracer Experiment (MATEX), which was proposed as a means to derive empirical source-receptor transport matrices for the long-range transport of oxides of sulphur and nitrogen over eastern North America (Hidy, 1987, 1988). Two of the mesoscale tracer experiments listed in Table 2.4, the 1980 Great Plains experiment and CAPTEX '83, were selected for numerical simulation in this study. They are described in more detail in Chap. 3.

Table 2.4: Chronology of formal, surface-based, meso-β-scale and meso-α-scale tracer experiments.

Experiment Name	Location	Period (mm/yy)	Tracers	Release Site(s)	Domain Size (km)	No. of Mon. Sites	Mobile Monitors	No. of Tracer Rels.	Release Time (h)	Sample Time (h)	References
Idaho–1	SE Idaho	??	^{131}I	INEL, Idaho Falls	100	36	no	1	3	dose	Lange (1978)
Solent	southern England	5/73	SF_6	Fawley PGS, Calshot	40	31	no	1	1	0.25	Emberlin (1981)
Idaho–2	SE Idaho	1/74–5/74	Kr-85, Me-21	INEL, Idaho Falls, Idaho	1500	13	no	int.*	2 m	10	Cowan et al. (1976) Ferber et al. (1977) Draxler (1982, 1983)
Oxnard Plain	southern California	9/75	SF_6	Ormond Beach PGS	80	8	yes	2	9–14	1	Lamb et al. (1978a)
Savannah River–1	South Carolina	12/75	SF_6, Kr-85 Me-21,	Savannah River Plant, Aiken	90	37	no	1	4	7	Bench et al. (1978) Draxler (1979)
California Delta	central California	9/76	SF_6, $CBrF_3$	Montezuma Hills; Martinez; Pinole	100	28	yes	8	2–9	1	Lamb et al. (1978b)
Idaho–3	SE Idaho	4/77,	Kr-85, PMCH PDCH, PDCB Me-20,21	INEL, Idaho Falls, Idaho	90	82	yes	1	3	6–7	Clements (1979) Draxler (1979)
LA Basin	southern California	7/77	SF_6	El Segundo PGS	150	24	yes	2	5	1	Shair et al. (1982) Sackinger et al. (1982)
Savannah River–2	South Carolina	3/75–9/77	Kr-85	Savannah River Plant, Aiken, SC	300	13	no	int.	0.5	10–168	Telegadas et al. (1978, 1980) Weber (1980) Pepper & Cooper (1983) Fields et al. (1984) Policastro et al. (1986a,b) Carhart et al. (1989)
PMVD–1	central Illinois	4–5/80, 7/80, 5/81	SF_6	Kincaid PGS	~50	~200	yes	375 h	~9	1	Bowne et al. (1983) Cher et al. (1984) Hanna (1986) Moore et al. (1988)
Great Plains	central U.S.	7/80	SF_6, PMCH, PDCH Me-20,21	NSSL, Norman, OK	600	55	yes	2	3	0.75–3	Ferber et al. (1981) Fowler & Barr (1983) (see also Section 3.1)
SEADEX	NE Wisconsin	5/82–6/82	SF_6	Kewaunee PGS	30	130	yes	9	5	4	Johnson et al. (1985) Lewellen et al. (1987)

*intermittent

Table 2.4 (cont'd): Chronology of formal, surface-based, meso-β-scale and meso-α-scale tracer experiments.

Experiment Name	Location	Period (mm/yy)	Tracers	Release Site(s)	Domain Size (km)	No. of Mon. Sites	Mobile Monitors	No. of Tracer Rels.	Release Time (h)	Sample Time (h)	References
PMVD–2	eastern Tennessee	7–8/82, 9–10/82	SF_6	Bull Run PGS, Clinton	50	200	yes	326 h	~12	1	Bowne et al. (1985) Moore et al. (1988)
ACURATE	U.S. Atlantic coast	3/82–9/83	Kr-85	Savannah River Plant, Aiken, SC	1100	5	no	int.	0.32	12	Heffter et al. (1984) Policastro et al. (1986a,b)
CAPTEX	NE U.S., SE Canada	9/83, 10/83	PMCH	Dayton, OH Sudbury, ON	1100	86	yes	7	3	3–6	Ferber et al. (1986) (see also Section 3.2)
KfK/ TULLA	Upper Rhine Valley	4/83, 3/84, 3/85	SF_6	Karlsruhe, W. Germany	45 –60	50+	no	4	3–5	0.5	Thomas et al. (1986) Thomas & Vogt (1990)
METREX	metropolitan Washington, D.C.	11/83–11/84	PMCP, PMCH PDCH	Rockville, MD; Mt. Vernon, VA; Lorton, VA	90	93	yes	545	6	8 h – 1 mo	Draxler (1985)
Øresund	Denmark, Sweden	5/84, 6/84	SF_6	Barsebäck, S; Gladsaxe, DK	30	38	yes	9	3-5	1	Gryning (1985) Enger et al. (1985) Gryning et al. (1987) Andrén (1990b)
ASCOT '84	western Colorado	9/84–10/84	PMCH, PMCP PDCH	Brush Creek	25	100	no	5	9	0.25-1	Clements et al. (1989) Gudiksen & Shearer (1989)
Beijing	Beijing, P.R.C.	11/84	SF_6	Beijing	150	30	yes	4	2-4	$\leq$0.5	Lamb et al. (1990)
SCCCAMP	southern California	9/85–10/85	PMCH, PMCP PDCH	3 offshore, 2 onshore	200	50	yes	4	4	2, 24	Dabberdt & Viezee (1987) Dietz (1987)
SIESTA	Jura, NW Switzerland	11/85	SF_6	Gösgen NPP	90	100	yes	6	4–6	1	Gassmann & Bürki (1987)
DOPPTEX	San Luis Obispo, CA	8/86 9/86	SF_6 $CBrF_3$	Diablo Canyon NPP; Morrow Bay	50	150	no	8	2-8	1	PG&E (1988)
WHITEX	NE Arizona, SE Utah	1/87 2/87	Me-20	Navajo PGS, Page, AZ	250	8	yes	cont.	2 mo	6	SCENES (1987) Stocker & Pielke (1990) NRC (1990)
ANATEX	central, eastern NA	1/87 3/87	PMCH, PDCH PTCH	St. Cloud, MN; Glasgow, MT	3000	77	yes	66	3	6–24	Draxler & Heffter (1989) Clark & Cohn (1990) Haagenson et al. (1990) Draxler (1991)

A number of formal mesoscale tracer experiments were not included in Table 2.4 because they did not meet all of the criteria just mentioned. The first of these, possibly the earliest mesoscale tracer experiment of all, was described by Pasquill (1962): measurements were made from an aircraft of zinc-cadmium sulphide particle concentrations as far as 130 km downwind from the source at Porton Down, England but no surface sampling network was deployed. More recently, concentrations of SF_6 and PMCH released from a power station in Yorkshire, England were measured by an aircraft flying over the North Sea at downwind distances as great as 650 km but again no surface network was used (Clark et al., 1984; Crabtree, 1984; Fisher and Callander, 1984; Marsh, 1987). The Geysers tracer experiments of the ASCOT program (e.g., Gudiksen et al., 1984; Tesche et al., 1987) and the 1988 Campo dei Fiori experiment in northern Italy (Clerici et al., 1991) were excluded because the sampling domains were smaller than 25 km. Draxler (1984) and Vanderborght and Kretzschmar (1985) mentioned several other possible candidates for inclusion in Table 2.4, but these studies were excluded because few details were given and the original references were difficult to obtain.

Several elaborate mesoscale tracer studies have also been conducted using tracers of opportunity. These include TULLA[61] (Fiedler, 1987; Marsh, 1987; Vogt and Fiedler, 1987; Vogel et al., 1988), EMEFS (Bowne et al., 1991; Hansen et al., 1988), and Acid MODES (Boatman et al., 1990). The tracers considered were air pollutants, namely SO_x, NO_y, and O_3. These are important compounds for public health, agriculture, visibility, and regional acidic deposition. Accurate specification of emissions inventories (i.e., the source term) is a critical component of such studies and may entail use of census data, industrial source testing, traffic models, and surveys by government regulatory agencies. Chemical transformations and wet and dry deposition may also be important in addition to atmospheric transport and diffusion, introducing additional complications. One advantage of such studies is that they can make use of existing acidic

[61] TULLA is also mentioned in Table 2.4 since both formal tracer releases and measurements of tracers of opportunity were made in this study.

deposition and oxidants monitoring networks (e.g., Seilkop and Finkelstein, 1987; Olsen et al., 1990).

Mesoscale visual studies

Visual studies employing photography and photogrammetry have been used since the 1920s to study the relative diffusion of smoke puffs and plumes (e.g., Gifford, 1959, 1968; Viswanadham and Torsani, 1982). Such studies have the advantage of permitting 'global' measurements of the puff or plume to be made from a single remote location. The fundamental assumption underlying all quantitative visual dispersion studies is that the visible edge of a puff or plume represents a constant, line-of-sight visual threshold of integrated concentration (e.g., Gifford, 1957, 1959, 1968, 1980). Sampling time can be increased in visual studies by the use of time-exposed or composited photographs, allowing the investigator to consider absolute diffusion as well (e.g., Richardson, 1920; Gifford, 1968; Nappo, 1981). Subjectivity in discerning puff or plume edges can be a problem but may be avoided through the use of photometric techniques (Randerson et al., 1971; Nappo, 1983; Yassky, 1983).

Just as with other MAD observational techniques, however, MAD visual studies have only a relatively short history. The main obstacle in this case is that observations of mesoscale puffs or plumes have to be made from mesoscale distances in order to gain the necessary perspective. One possible observing platform is a high-altitude aircraft (e.g., Randerson, 1972; Nappo, 1979, 1981) but an even better platform for this purpose is an Earth-orbiting satellite or spacecraft. Smoke plumes have been photographed from such manned spaceflights as Gemini 7 and 11 (Randerson, 1968), Apollo 6 (Randerson et al., 1971), and Skylab 4 (Randerson, 1977) and from LANDSAT (Lyons and Pease, 1973; Lyons, 1974; Viswanadham and Torsani, 1982; Desiato and Ciminelli, 1991) and various operational weather satellites (Chung and Le, 1984; Matson, 1984; Chung, 1986; Ferrare et al., 1990). Many of these studies are qualitative in nature. However, Randerson et al. (1971), Randerson (1977) [also Gifford (1980)], Nappo (1979, 1981), Viswanadham

and Torsani (1982), and Desiato and Ciminelli (1991) all estimated lateral plume spreads based on the photographs they examined.

One inherent and significant limitation on mesoscale visual studies is the relative rarity of a cloud or plume remaining visible after experiencing dilution and mixing over mesoscale distances (Pasquill and Smith, 1983). For this reason, most mesoscale visual studies have considered plumes transported under stable conditions with little mixing, either in the stable PBL above a cold underlying surface or in the free troposphere after buoyant injection, as in the case of volcanic eruptions or major forest fires. It may also be difficult to 'see' a plume. Plumes will be the most visible when the optical density difference between the plume and the underlying surface is the greatest, as in the case of a bright plume against a dark surface or a dark plume against a bright surface. Lyons and Pease (1973) showed a number of examples of bright smoke plumes over low-albedo (i.e., dark) water surfaces and suggested, based on consideration of a number of factors, that the LANDSAT visible 'red' band would give optimum contrast over water surfaces. Smoke plumes are considerably more difficult to see over land surfaces since land generally has a higher albedo and an inhomogeneous, 'mottled' appearance.

Lateral diffusivity estimates

Fig. 1.1 shows a plot of both plume and puff observed widths[62] versus travel time[63] based on long-range measurements made in Australia, Europe, and North America. These data were compiled by Gifford (1986) and cover a range of sampling times (see Sec. 2.3.3). The aircraft measurements plotted in Fig. 1.1 correspond to near-instantaneous traverses while the CAPTEX plume-width values were determined from six-hour surface measurements. In contrast, Fig. 2.22 from the beginning of this section is based on separation rates of sequentially-released tetroon trajectories. The effective sampling times for this figure depend on the length of the period during which tetroons were launched.

A number of other atmospheric diffusion summary diagrams have been prepared over the past few decades. Gifford (1983a) contains a very similar diagram to Fig. 1.1 except that it is based exclusively on long-range Australian plume measurements. Carras and Williams (1988) presented a similar[64] diagram, shown here as Fig. 2.23, which was based on more recent Australian long-range PBL plume measurements. One significant feature

---

[62] The use of the lateral root-mean-square displacement or lateral standard deviation $\sigma_y = \overline{y^2}^{1/2}$ is more common for such plots. Many investigators have assumed (arbitrarily) that the visible edge of a plume or cloud coincides roughly with the point where the concentration has fallen to 10% of its peak or maximum value (e.g., Gifford, 1968, p. 101). If this is true and if the concentration has a Gaussian distribution, then $\sigma_y = W/4.28$, where W is the observed cloud width, and 97% of the cloud material will lie within the bounds of W. This definition is sometimes used even when plumes are defined on the basis of concentration measurements rather than opacity (e.g., Bigg et al., 1978). However, cross-plume concentrations will not always have a Gaussian distribution, particularly after mesoscale travel times. In such cases, Carras and William (1988) and Holland (1991) calculated σ_y directly after digitizing their measured concentration trace.

[63] The determination of travel time at mesoscale distances is not straightforward, either, especially when significant wind shear has occurred. The simplest way to determine this quantity is to divide the straight-line downwind distance by a mean transport wind speed (e.g., Bigg et al., 1978). However, plume material reaching that downwind point may have travelled a more tortuous path and may not all be of the same age. Carras and Williams (1981, 1988) attempted to account for these effects by calculating an *average* plume age. To do this, they selected four or eight constant-height forward trajectories for levels spaced through the depth of the daytime PBL so that each trajectory chosen reached the downwind distance of interest at the same time. The release times could vary and each trajectory was determined from a time sequence of observed winds. Averaging over the individual trajectory travel times then gave an estimate of the average plume age. In the case of one Mount Isa plume measurement made 933 km downstream of the source, the average plume age calculated by Carras and Williams (1981) was 42.5 h but travel times at different heights ranged from 35 to 45.5 h.

[64] Though plotted in terms of plume lateral standard deviation σ_y rather than plume width W.

of this diagram is that the scatter in σ_y values shrinks with increasing travel time. Carras and Williams (1988) attributed this behaviour to the greater influence of the exact history of diurnally-varying turbulence regimes experienced by the plume elements for shorter travel times. For longer travel times, the plume will have experienced three, four, or five PBL stability transitions so that the range of shear regimes associated with daytime convective mixing and nighttime stable stratification will all have had a chance to play a role.

Heffter (1965) prepared two very well known plots of mesoscale σ_y values, one versus travel time and the other versus travel distance. These plots are reproduced in Fig. 2.24. Heffter was faced with a lack of observations on these scales and as a result gathered together a very heterogeneous set of measurements. His 19 data sources included observations of tracer plumes, nuclear clouds, and multiple-balloon releases at a variety of heights. About one-third of the data sets were from classified experiments. Sampling times ranged from instantaneous to 24 h, and both individual and averaged σ_y values were included. Heffter also plotted lines of constant K_H on Fig. 2.24a to enable comparison with simple Fickian diffusion theory[65]. Based on this mixed set of observations, he suggested that an average horizontal eddy diffusivity value K_H of 4×10^8 cm^2 s^{-1} (or 4×10^4 m^2 s^{-1}) seemed most reasonable for travel times of 1 to 4 days. Later, Pack et al. (1978) and Heffter (1980) proposed a time-dependent formulation for σ_y to cover the full range of observations in Fig. 2.24a:

$$\sigma_y = 0.5T \quad , \tag{2.40}$$

where σ_y has units of meters and T has units of seconds (the constant will change to 1.8 for units of kilometers and hours). Eq. 2.40 has been used in a number of Lagrangian puff LRTAP models to parameterize horizontal diffusion (e.g., Heffter, 1980; Carhart et al., 1989) although somestudies have reported disagreements with its predictions. For

---

[65] In which K_H is a constant and equal to $\sigma_y^2/2T$ (see p. 231 for details).

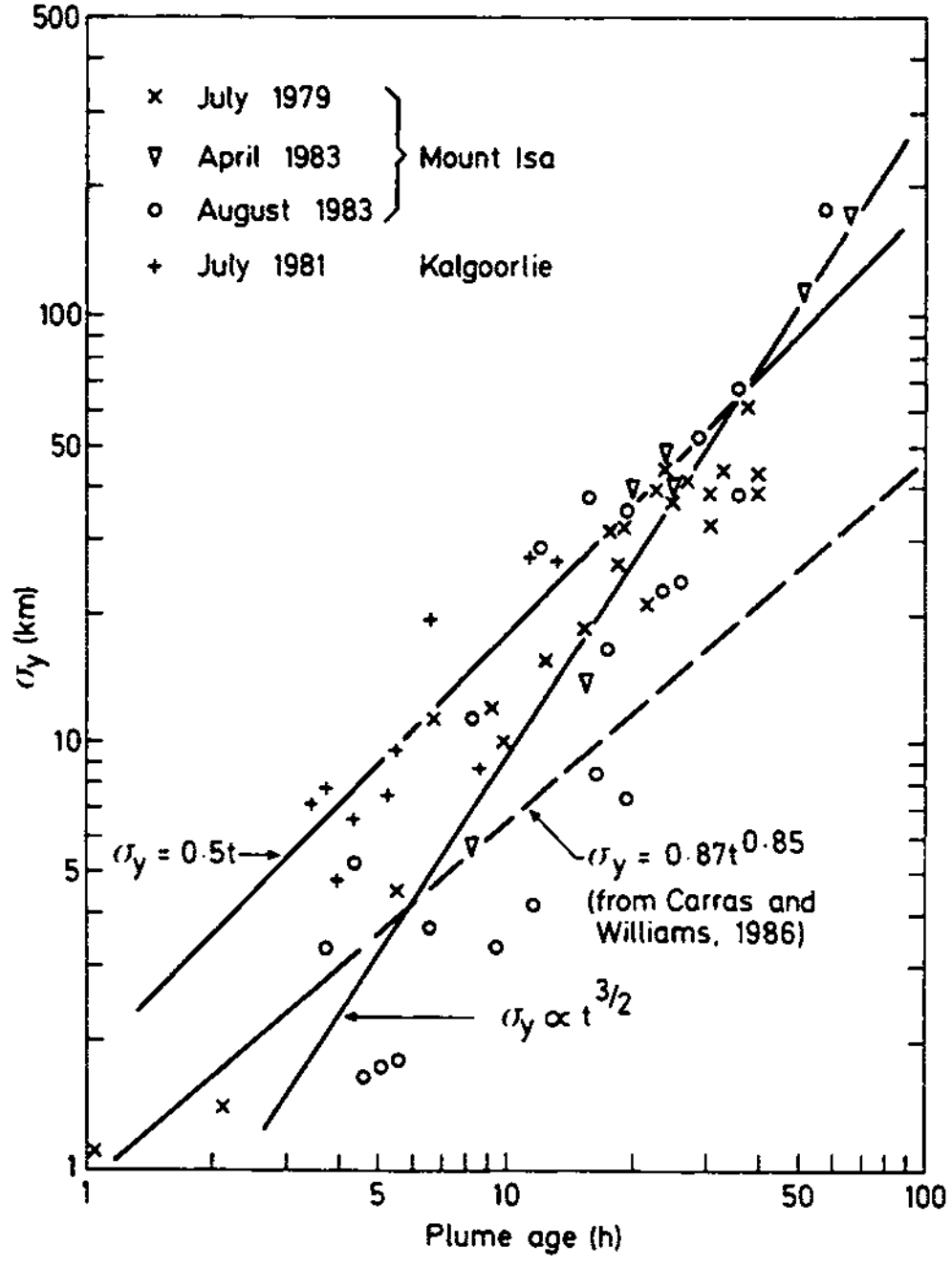

Figure 2.23: Composite of plume σ_y observations for isolated smelter plumes in northern Australia (Mount Isa) and western Australia (Kalgoorlie) over mesoscale travel times (from Carras and Williams, 1988). Three different mathematical relationships for σ_y are also plotted, including the formula $\sigma_y = 0.5T$ proposed by Pack et al. (1978).

example, Carras and Williams (1981, 1988) have reported that this formula tends to overestimate plume widths for the majority of measurements for plume ages less than about 50 h (see Figs. 1.1 and 2.23).

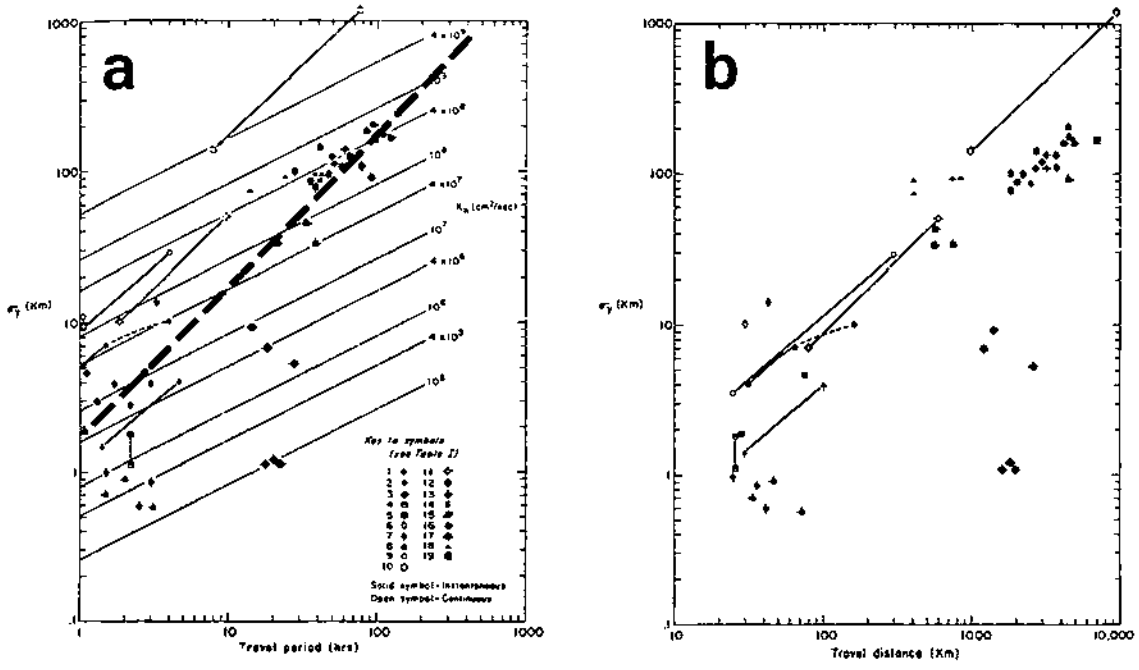

Figure 2.24: Individual and average σ_y values based on a variety of cloud, plume, and balloon measurements from the 1950s and early 1960s plus Richardson and Proctor's (1925) balloon measurements plotted as a function of (a) travel time and (b) travel distance. See Heffter (1965) or Islitzer and Slade (1968) for details. The solid lines in panel (a) indicate constant horizontal diffusivity K_H according to the relationship $K_H = \sigma_y^2/2T$. The dashed line shows the relationship $\sigma_y = 0.5T$ proposed by Pack et al. (1978).

Fig. 2.25 shows a summary diagram of horizontal *relative* diffusion compiled by Hage and Church (1967) from instantaneous and near-instantaneous measurements. This diagram covers a considerably wider temporal range than Fig. 2.24 but the two sets of diffusion data are broadly similar in the mesoscale range. Crawford (1966, 1967) presented a third diagram similar to Figs. 2.24 and 2.25 (see Fig. 2.26).

The horizontal diffusion compilations of Heffter (1965), Crawford (1966, 1967), and Hage and Church (1967) all included stratospheric as well as PBL and tropospheric measurements. Gifford (1977) argued that stratospheric diffusion is likely to be qualitatively

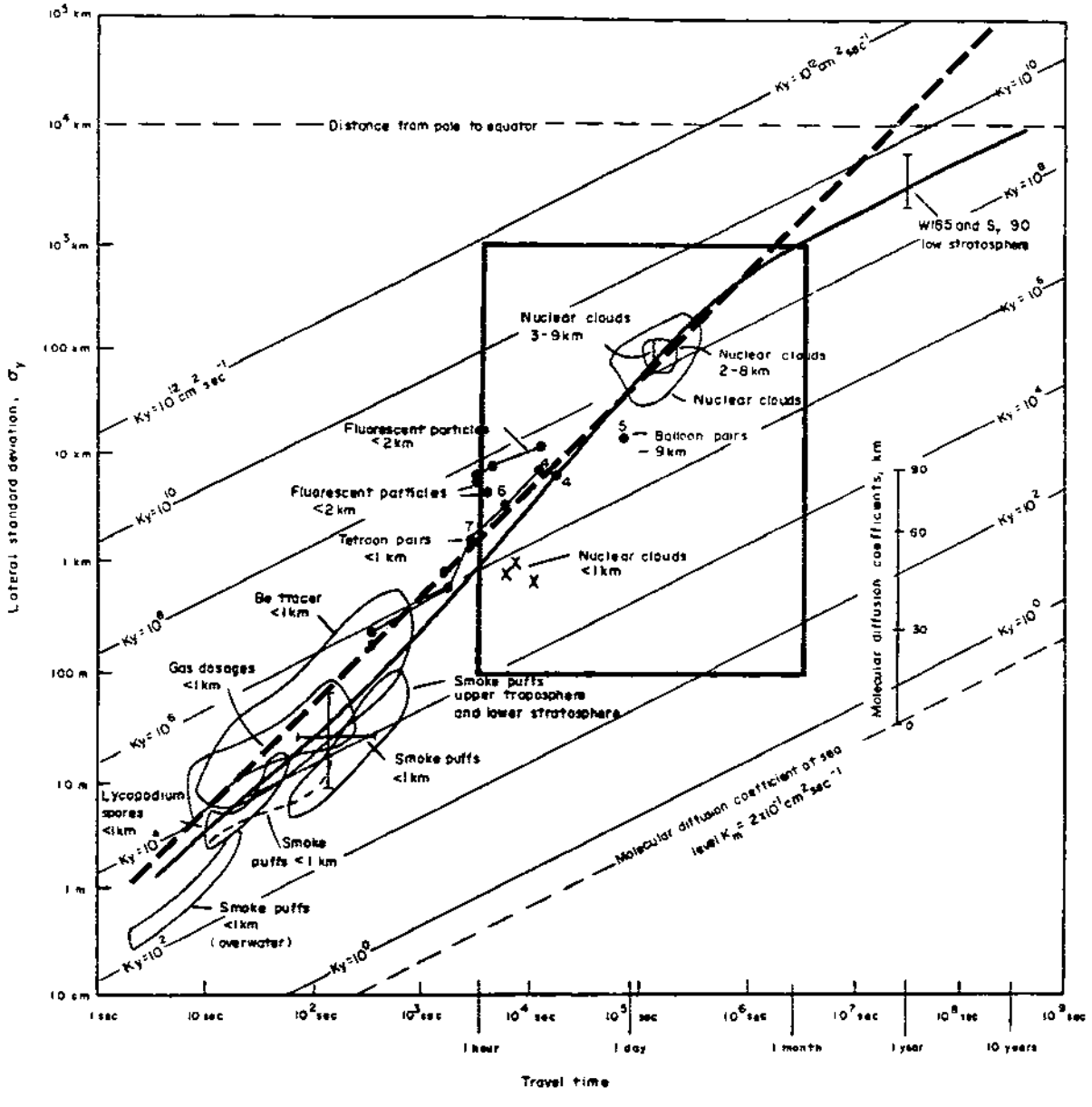

Figure 2.25: Hage and Church's (1967) summary of atmospheric horizontal relative diffusion measurements (adapted from Gifford, 1982). The solid curve is a best-fit curve to these data. The rectangle inscribed near the center of the figure indicates the range of scales plotted in Fig. 2.24. The dashed line shows the relationship $\sigma_y = 0.5T$ proposed by Pack et al. (1978).

different from tropospheric diffusion because of the much greater thermal stratification in the stratosphere (e.g., p. 140) so that stratospheric diffusion measurements should not be combined with tropospheric measurements. Fig. 2.26 shows two horizontal relative diffusion summary diagrams constructed by Gifford (1977) solely from PBL and tropospheric data. The two panels of this figure cover roughly the same scale range as Fig. 2.25. Panel (a) is a redraft of Crawford's (1966) diagram with stratospheric observations excluded while panel (b) was based on data sets not available to or overlooked by Heffter (1965), Crawford (1966, 1967), and Hage and Church (1967). Note that a line showing the empirical mesoscale horizontal diffusion curve given by Eq. 2.40 has been added to Figs. 2.25 and 2.26 to permit comparison with Figs. 1.1, 2.23, and 2.24.

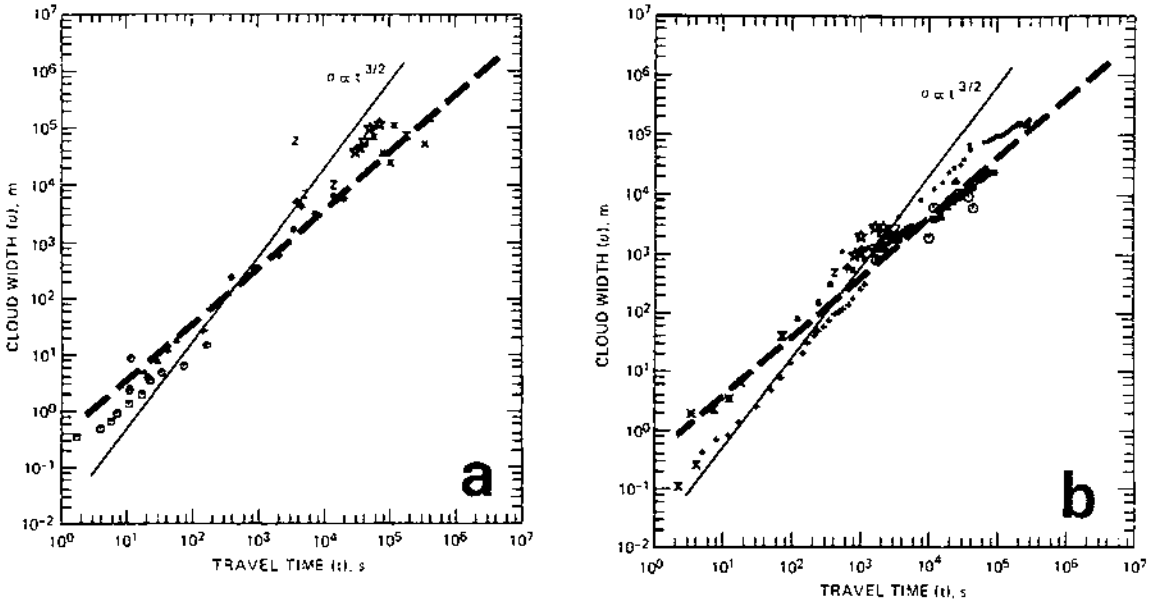

Figure 2.26: Summary of atmospheric horizontal relative diffusion measurements based on (a) Crawford's (1966) tropospheric relative diffusion data and (b) additional tropospheric relative diffusion data (adapted from Kao, 1984; based on Gifford, 1977). The dashed line shows the relationship $\sigma_y = 0.5T$ proposed by Pack et al. (1978).

Still other atmospheric horizontal diffusion summary diagrams (not shown) have been prepared by Islitzer and Slade (1968), Bauer (1974), Clarke et al. (1983), Pasquill

and Smith (1983), Draxler (1984), and Eliassen (1986). Okubo (1971) constructed a comparable diagram based on oceanic horizontal relative diffusion measurements.

Finally, Fig. 2.27 compares some tropospheric horizontal relative diffusion measurements with lateral diffusion values predicted by Csanady's (1969) model[66] of Ekman-layer shear-enhanced dispersion assuming representative flow values ($V_g = 15\ m\ s^{-1}$, $f = 10^{-4}\ s^{-1}$). This comparison suggests that shear enhancement can contribute significantly to the lateral diffusion observed after mesoscale travel times.

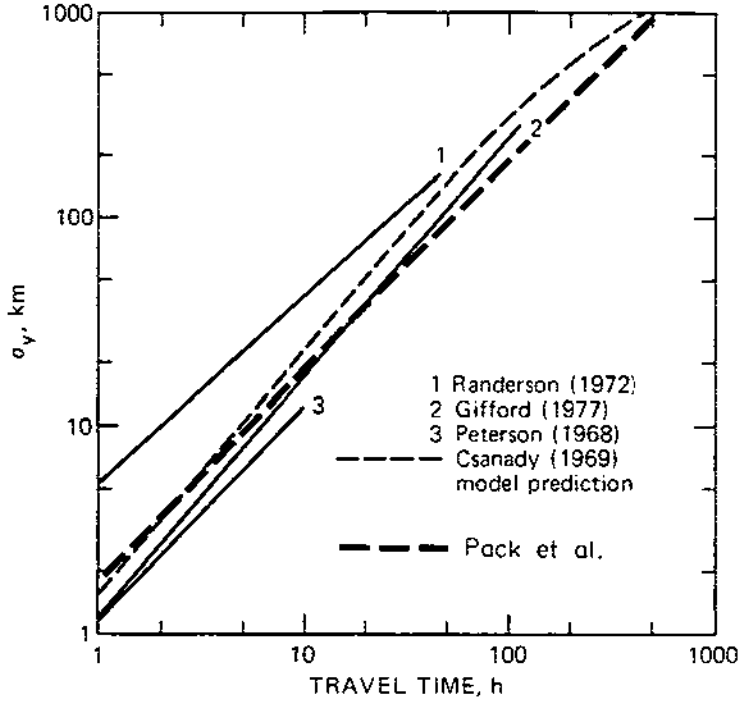

Figure 2.27: Comparison of observed horizontal mesoscale dispersion curves with a representative predicted curve from Csanady's model of shear-enhanced lateral diffusion in an atmospheric Ekman layer (adapted from Draxler, 1984). The fine dashed line shows the relationship $\sigma_y = 0.5T$ proposed by Pack et al. (1978).

---

[66] This model was discussed in Sec. 1.7.

2.2.3 Comparison of the two Lagrangian marker approaches

Let us close this section by summarizing the relative merits of the two primary Lagrangian marker techniques. One advantage of gaseous tracers over balloons is that the path of one balloon is only a single realization. A number of tetroons should be released in order to estimate an ensemble-mean trajectory. In a sense, a single tracer cloud provides a larger sample, because as it grows it is affected by an increasingly large volume of the atmospheric flow. Thus, the trajectory of the cloud center of mass is more representative of mean transport than the trajectory of the centroid of a handful of balloons.

On the other hand, after travelling for some hours, a dispersing volume of tracer gas is likely to be an elongated, possibly noncontiguous, three-dimensional object extending from the surface to some height in the free troposphere. Surface concentration measurements may give only an approximate measure (or 'footprint') of cloud size, especially at night when differential advection may be occurring. For example, Stunder et al. (1986) noted that in Release 3 of the 1983 Cross-Appalachian Tracer Experiment (see Sec. 3.2.1), aircraft measurements of PMCH tracer showed high concentrations while surface stations directly beneath the aircraft flight paths measured only background values. Neither is there any guarantee that the surface density-weighted concentration maximum will be located directly beneath the three-dimensional cloud center-of-mass location, although this may be the case for a well-mixed PBL (conceivably there might not be *any* tracer at the cloud center-of-mass location if the original tracer cloud has been fragmented). In addition, the dispersion of a gaseous tracer release is itself only a single realization, and the length of the release t_r, the travel time T, and the sampling time τ must all be considered in evaluating the inherent uncertainty in the concentration measurements (see Sec. 2.3.3).

Despite these caveats, surface measurements from mesoscale tracer experiments are still the best available means to evaluate the performance of an MAD numerical model in a cost-effective manner. It must be remembered, however, that in such comparisons it is

the *combined* treatment of mean and differential transport plus turbulent diffusion that is being evaluated and not transport alone (Draxler, 1987; Shi et al., 1990).

The use of tetroons for calculating mesoscale dispersion characteristics seems to have fallen out of favour somewhat in recent years (e.g., Islitzer and Slade, 1968 vs. Draxler, 1984) but some groups are still employing them for this purpose (e.g., Clarke et al., 1983; Vogt and Thomas, 1985; Thomas and Vogt, 1990). This approach has the advantage that very large release and sampling times can be considered based on relatively few tetroon trajectories. *In situ* tracking of tetroons is also much more easily accomplished (relatively speaking) than tracking an elevated tracer cloud. Heffter (1992; personal communication) observed that the single biggest shortcoming of mesoscale tracer technology at the present time is the lack of a remote sensing and measurement capability, although lidar has been used successfully in this role to study short-range dispersion (e.g., Uthe et al., 1980; Moore et al., 1988).

2.3 Theoretical Studies of Mesoscale Atmospheric Dispersion

There have been relatively few theoretical studies of mesoscale atmospheric dispersion *per se*. However, there have been a number of attempts to apply concepts developed in the theory of small-scale dispersion to the mesoscale case. One example of this is the analysis of tetroon trajectories to estimate mesoscale diffusivity. Another is the application of the Langevin equation, a stochastic differential equation originally used in theoretical studies of Brownian motion, to model both small-scale and mesoscale turbulent diffusion. This section reviews some of the theory of small-scale turbulent diffusion relevant to the mesoscale case.

2.3.1 Statistical theory of turbulent diffusion

The statistical theory of turbulent diffusion had its roots in studies of Brownian motion and the "drunkard's walk" problem at the beginning of this century. G.I. Taylor, in his seminal 1921 paper '*Diffusion by Continuous Movements*', referred to the subject

of these early studies as diffusion by *discontinuous* motions. Motivated by his observations that "turbulent motion is capable of diffusing heat and other diffusible properties through the interior of a fluid in much the same way that molecular agitation gives rise to molecular diffusion" (Taylor, 1921, p. 196), Taylor described his efforts to extend the theory of molecular diffusion to a turbulent flow in which the primary physical mechanism for diffusion (at least at turbulent scales) is advection by turbulent eddies rather than molecular thermal motions. He then proceeded to derive a number of now very well known results describing what he referred to as "the law of diffusion, i.e., the law which governs the average distribution of particles initially concentrated at one point, at any subsequent time" (Taylor, 1921, p. 206).

Taylor's theorem

Assuming a statistically *homogeneous*[67], *stationary*[68] turbulent flow, Taylor considered the motion of infinitesimal particles leaving the origin at $t = 0$ and being tossed back and forth by turbulent velocity fluctuations. The particles are assumed to assume the fluid velocity completely and to be passive dynamically. If a particle has velocity component u' in the x-direction, then after a period of time t, it will have reached point X. If the mean-square displacement of a large number of particles released in succession (or of many realizations of the release of a single particle) from the origin and travelling for time t is denoted by the quantity $\overline{X^2}$, then[69]

$$\begin{aligned} \frac{\mathrm{d}}{\mathrm{d}t}\overline{X^2} &= 2\overline{X\frac{\mathrm{d}}{\mathrm{d}t}X} \\ &= 2\overline{Xu'} \end{aligned}$$

---

[67] Statistical properties are independent of spatial position but are not necessarily isotropic; this requirement explains why Taylor's equation is usually applied to horizontal diffusion and less often to vertical diffusion.

[68] Homogeneous in time.

[69] Taylor had shown earlier in the paper that the laws of differentiation and integration could be applied to ensemble averages of fluctuating variables and their products.

$$= 2\int_0^t \overline{u'(t)\,u'(t+\xi)}\,\mathrm{d}\xi$$

$$= 2\overline{u'^2}\int_0^t R_L(\xi)\,\mathrm{d}\xi \quad , \tag{2.41}$$

where the assumptions of stationarity and homogeneity allowed the substitution of the Lagrangian velocity autocovariance $\overline{u'^2}R_L(\xi)$. The equation commonly known as Taylor's theorem follows by integration:

$$\overline{X^2}(T) = 2\overline{u'^2}\int_0^T\int_0^t R_L(\xi)\,\mathrm{d}\xi\,\mathrm{d}t \quad . \tag{2.42}$$

Taylor commented that Eq. 2.42 is "rather remarkable" since it reduces the problem of diffusion to consideration of a single quantity, the (one-particle, two-point) Lagrangian velocity autocovariance $\overline{u'(t)\,u'(t+\xi)}$. Taylor then showed that Eq. 2.42 approaches the expression

$$\overline{X^2} = \overline{u'^2}T^2 \tag{2.43}$$

asymptotically for small travel time T and the expression

$$\overline{X^2} = 2\overline{u'^2}T_L T \tag{2.44}$$

for large travel time, where T_L is the Lagrangian integral time scale (see Eq. 1.8). Venkatram (1988a) has used a simple random-walk model to explain the physical basis for Eq. 2.44 (see also Underwood, 1991). Note that Eq. 2.44 has the well-known parabolic time dependence of diffusion in homogeneous turbulence.

Finally, Taylor solved Eqs. 2.41 and 2.42 for the special case of $R(t) = e^{-t/T_L}$ and obtained the expressions

$$\frac{\mathrm{d}}{\mathrm{d}t}\left(\frac{1}{2}\overline{X^2}\right) = \overline{u'^2}T_L\left(1 - e^{-t/T_L}\right) \quad , \tag{2.45}$$

$$\frac{1}{2}\overline{X^2} = \overline{u'^2}\left[T_L t - T_L^2\left(1 - e^{-t/T_L}\right)\right] \quad . \tag{2.46}$$

Note too that both Eqs. 2.43 and 2.44 are easily obtained from the short and long time limits of Eq. 2.46.

Spectral representation

According to Hinze (1975) and Pasquill and Smith (1983), Kampé de Fériet was the first to show[70] that

$$\int_0^T \int_0^t R_L(\xi)\,\mathrm{d}\xi\,\mathrm{d}t = \int_0^T (T-\xi)\,R_L(\xi)\,\mathrm{d}\xi \qquad . \tag{2.47}$$

Eq. 2.47 permits restatement of Eq. 2.42 in terms of the Lagrangian energy spectrum $F_L(n)$ corresponding to $R_L(\xi)$. The lefthand-side of Eq. 2.47 is the convolution of a triangular lag function with the Lagrangian autocorrelation function $R_L(\xi)$. This suggests the use of Parseval's theorem as discussed in Sec. 1.4.6. Combining Eq. 2.47 with Eq. 1.18 then yields

$$\overline{X^2} = \overline{u'^2}T^2 \int_0^\infty F_L(n)\,\frac{\sin^2\pi nT}{(\pi nT)^2}\,\mathrm{d}n \qquad , \tag{2.48}$$

where n is the cyclic frequency. Eq. 2.48 thus relates particle dispersion to the kinetic energy spectrum of a fluid particle (e.g., Batchelor, 1949).

This frequency-domain or spectral form of Taylor's equation provides another way of looking at the asymptotic limits given by Eqs. 2.43 and 2.44. The spectral filter or weighting function $\sin^2\pi nT/(\pi nT)^2$ depends on the travel time T. When T is small, the filter function will be very broad since the first zero lies at $n = 1/T$. The energy spectrum integral in Eq. 2.48 can then be approximated as $\int_0^\infty F_L(n)\,\mathrm{d}n$ so that by Eq. 1.11, Eq. 2.48 will have the small-time limit given by Eq. 2.43. For long travel times, on the other hand, the filter function becomes very narrow so that only the contributions of very low frequencies are considered. For the large-time limit the energy spectrum integral can be approximated as $F_L(0)\int_0^\infty \sin^2\pi nT/(\pi nT)^2\,\mathrm{d}n$, which has the value[71]

---

[70] This important result can be obtained either by integration by parts (Hinze, 1975, p. 53) or by a transformation of variables with $\xi = t - t'$.

[71] Using $F_L(0) = \lim_{n\to\infty} 4\int_0^\infty R(t)\cos 2\pi nt\;\mathrm{d}t = 4T_L$ from Eq. 1.9 and the definite integral $\int_0^\infty x^{-2}\sin^2 px\,\mathrm{d}x = p\pi/2$ (e.g., Monin and Yaglom, 1975, p. 528).

$2T_L/T$, thus giving the same result as Eq. 2.44. Physically, these asymptotic limits suggest that initially eddies of all frequencies contribute to particle dispersion exactly as they do to the turbulent energy. For longer travel times, however, contributions from higher-frequency eddies diminish systematically. This is because these smaller eddies will merely oscillate a particle about its mean position while advection by lower-frequency eddies will still displace particles in a sustained fashion on that time scale (e.g., Pasquill and Smith, 1983).

Eq. 2.48 can be viewed in another way too. Let u'_T represent the mean particle fluctuation velocity over travel time T (cf. Eq. 1.12). Then

$$X(T) = u'_T T \quad , \tag{2.49}$$

$$\overline{X^2}(T) = \overline{u'^2_T} T^2 \quad . \tag{2.50}$$

Eq. 2.50 has the same form as the small-time asymptotic limit given by Eq. 2.43 but holds for all times. However, $\overline{u'^2_T}$ will be smaller than the actual turbulence intensity $\overline{u'^2}$ since the travel time T can be thought of as a finite *averaging* time which smooths out the shortest time scales contributing to $\overline{u'^2}$. Use of Eq. 1.13 then gives (Pasquill, 1975)

$$\overline{u'^2_T} = \overline{u'^2} \int_0^\infty F_L(n) \frac{\sin^2 \pi n T}{(\pi n T)^2} \, \mathrm{d}n \quad , \tag{2.51}$$

and substitution of Eq. 2.51 into Eq. 2.50 yields Eq. 2.48.

Extensions to Taylor's equation

Batchelor (1949) generalized Taylor's equation to obtain expressions for the second-order displacement tensor in both the time and frequency domains. He also derived a differential equation for the probability distribution of X and related the diffusivity tensor $K_{i,j}$ to the time derivative of the dispersion tensor $\overline{X_i X_j}$. Hinze (1975) has described the derivation of Taylor's equation for stationary but *inhomogeneous* turbulence. Pasquill and Smith (1983) discussed the significance of the shape of functions $R_L(\xi)$ and $F_L(n)$

on mean-square particle displacement $\overline{X^2}$. They determined that the autocorrelation or spectral function shape is not particularly important, especially at small travel times when $\overline{X^2}$ is effectively determined by the turbulence intensity $\overline{u'^2}$ alone.

Corrsin (1953) briefly considered the case of unbounded uniform shear flow at large times. Smith (1965) also considered the case of shear flow but for all times and including horizontal–vertical velocity covariances. He obtained a more complicated version of Eq. 2.42 consisting of three terms: one term was identical to the right-hand side of Eq. 2.42, the second term described the direct effect of wind shear independent of horizontal turbulence, and the third term incorporated the correlation of the horizontal and vertical velocity components. One advantage of Smith's statistical treatment of wind shear over other analytical approaches (see Sec. 1.7) is that it provides a convenient method by which to estimate the travel distance at which shear effects begin to outweigh simple diffusional spread (Pasquill and Smith, 1983). Recently, Venkatram (1988a) discussed a simple approximation to Smith's analysis based on a random-walk model, and Enger (1991) used the spectral form of Smith's equation to estimate σ_y in a dispersion model for sheared PBL flow over moderately complex terrain.

Smith (1968) also extended Taylor's equation in another way. Taylor's equation can be viewed as describing the dispersion of a selected or 'conditioned' set of particles, each one of which is known to have passed through a particular fixed point (the source). Smith (1968) considered the consequences of adding further selection conditions, namely (i) a specified initial velocity, (ii) passage through the source *and* a second specified location downwind of the source, and (iii) a combination of (i) and (ii). He then obtained a whole suite of statistical relations for these different selection criteria. Pasquill and Smith (1983) also noted that Gifford's (1982) Lagrangian-dynamical theory for horizontal diffusion (discussed in Sec. 2.3.5) can be viewed as an extension of this conditioned-particle approach to the case of relative diffusion.

Relationship to Fickian diffusion and K theory

Tennekes (1982) noted that the short-time and long-time asymptotic limits of Eq. 2.41 (after dividing by two) are, respectively,

$$\lim_{T\to 0} \frac{\mathrm{d}}{\mathrm{d}t}\frac{1}{2}\overline{X^2} = \overline{u'^2}T \tag{2.52}$$

and

$$\lim_{T\to \infty} \frac{\mathrm{d}}{\mathrm{d}t}\frac{1}{2}\overline{X^2} = \overline{u'^2}T_L \quad . \tag{2.53}$$

[These expressions could also be obtained from applying these same limits to Eq. 2.45 or by differentiating Eqs. 2.43 and 2.44 with respect to time.]

Eq. 2.52 suggests that the rate of growth of particle mean-square displacement increases linearly with time initially, but after long travel times the rate of growth approaches a constant value, $\overline{u'^2}T_L$. This latter limit is significant because the time derivative of mean-square displacement has units of $(\text{length})^2/(\text{distance})$, that is, units of *diffusivity.* Furthermore, in the simplest form of diffusion, Fickian diffusion, diffusivity is equal to a *constant.*

Batchelor (1949) explored the analogy between molecular diffusion and turbulent diffusion by considering what form the diffusivities in the Fickian diffusion equation for molecular diffusion would have to have in order to describe turbulent diffusion. He showed for the case of homogeneous turbulence that, by assuming the well-known Gaussian solution for an instantaneous point source to apply but using *time-dependent* mean-square displacements $\overline{X_i X_j}(t)$, the 'apparent' eddy diffusivities K_{ij} had to have the form (see also Sec. 3.8 of Csanady, 1973)

$$K_{ij} = \frac{1}{2}\frac{\mathrm{d}}{\mathrm{d}t}\overline{X_i X_j} \quad . \tag{2.54}$$

It then follows immediately from Eq. 2.41 that in the x-direction, for example,

$$K_x = \overline{u'^2} \int_0^t R_L(\xi)\, d\xi \quad . \tag{2.55}$$

This equation implies that for turbulent diffusion, the apparent eddy diffusivities, like the mean-square displacements, are time-dependent. However, for large times Eq. 2.54 reduces by Eq. 2.53 to (and Eq. 2.55 reduces to)

$$K_x = \overline{u'^2} T_L \quad . \tag{2.56}$$

This constant asymptotic limit for K_x is a real property of the turbulence field and corresponds to Fickian diffusion. It also has the form of the product of a characteristic velocity (u) and characteristic eddy size $(L = uT)$ predicted by classical mixing-length theory (e.g., Durst et al., 1959; Hinze, 1975). Moreover, for this long-time limit we have by Eq. 2.44 that

$$K_x = \frac{1}{2} \frac{\overline{X^2}}{T} \quad , \tag{2.57}$$

where Eq. 2.57 also comes from the well-known Gaussian solution for Fickian diffusion from a point source that the mean-square displacement is given by the expression $\sigma_x^2 = 2K_xT$ (e.g., Csanady, 1973; Pasquill and Smith, 1983).

The important point here is that Eq. 2.54, that is, the Fickian *form* of the diffusion equation, is true at all times if the apparent eddy diffusivities are taken to be time-dependent[72] and are determined based on equations like Eq. 2.55 but is only valid for

---

[72] Such a step leads to some logical difficulties, however, as discussed by Taylor (1959, p.105): "Roberts and others had earlier pointed out that these expressions were the solutions of a modified Eulerian diffusion equation in which the diffusion coefficient varied with the time since the diffusing material had been concentrated. It seems to me that this is an illogical conception. The one thing that seems to be agreed, whatever theory one may have about diffusion, is that diffusing distributions are superposable. If therefore you attempt to analyse the distribution of concentration from two sources which started at different times by this method, it would be necessary to assume, in places where the distributions overlapped, that the diffusion constant had two different values at the same time and at the same point in space. It seems therefore that no physical meaning can be atttached to the use of equations in which the coefficient of diffusion varies with the time of diffusion, even though the formulae produced by their use do represent adequately the concentrations in particular cases."

Fickian diffusion with its constant diffusivities in an asymptotic sense at *long* travel times $T \gg T_L$.

Why is this? Turbulent motions tend to be highly self-correlated. One interpretation of the Lagrangian integral time scale T_L is that it is a measure of the longest time, on average, during which a particle persists in moving in a particular direction, i.e., the length of the particle's 'memory'. In order for Eq. 2.57 to be true, T_L must effectively be zero, that is, the no-memory case. Csanady (1973, p. 39) has shown that the simple uncorrelated, discrete-step, stochastic diffusion model for Brownian motion (i.e., the drunkard's walk without memory) approaches the Fickian diffusion process as $\Delta t \to 0$, giving Eq. 2.57 a firmer theoretical foundation. It then follows that simple constant K theory is valid in the atmosphere when the time scale of the diffusion problem of interest, i.e., the travel time T , is much longer than the integral time scale of the diffusion process T_L (e.g., Csanady, 1973; Corrsin, 1974; Herterich and Hasselmann, 1982; Durbin, 1983). This topic is returned to in Sec. 2.3.4.

Based on Eq. 2.55, at time t = 0, the apparent eddy diffusivity K_x will actually be equal to zero (see also Eq. 2.52). It will then increase monotonically with time, at first linearly and then more slowly, finally approaching the constant value $\overline{u'^2}T_L$ asymptotically. Batchelor explained the special case of zero diffusivity at time t = 0 as a consequence of the fact that the position of a particle is known with certainty at this time. He attributed the increase in K_x with time to the fact that "... velocity oscillations of low frequency are becoming more and more effective in dispersing each particle about its original position" (Batchelor, 1949, p. 448) and noted that the magnitude of K_x was independent of scale for absolute diffusion.

It should be noted that the apparent eddy diffusivity K_x determined from Eq. 2.54 is an *Eulerian* eddy diffusivity appropriate for use in the Eulerian continuity equation. It thus describes absolute diffusion. It is clear too from Eqs. 1.16, 2.48, and 2.65 that estimates of this apparent eddy diffusivity must depend directly on the sampling times and travel times being modelled. An analogous but *Lagrangian* apparent eddy

diffusivity can be defined for relative diffusion (Eq. 2.61). The Lagrangian diffusivity is defined for ensemble-mean growth relative to the *instantaneous* center of gravity of a puff or to the *instantaneous* centerline of a plume while the Eulerian diffusivity corresponds to ensemble-mean growth for a cloud or plume relative to the fixed source. Based on the discussion in Sec. 1.6.2, it is clear that the eddy diffusivities for absolute diffusion should be larger than those for relative diffusion. Sampling time affects the magnitude of the Eulerian diffusivity because it determines which spectral components of the flow are considered to be turbulence (see Eqs. 2.65 and 2.66). Now let us examine some of the theoretical aspects of relative diffusion.

2.3.2 Two-particle diffusion

As discussed in Chap. 1, relative diffusion is also known as two-particle diffusion. It can be described by a theoretical model very similar to Taylor's theorem (Eq. 2.42). Consider two particles moving simultaneously through a stationary, homogeneous turbulent flow. Let $X_1(t)$ and $X_2(t)$ be the x-coordinates of the two particles at time t and let $X_s(t)$ be the distance separating the two particles in the x-direction, where the initial particle separation is $X_s(0)$. X_s can then be expressed as

$$X_s(t) = X_1(t) - X_2(t) = X_s(0) + \int_0^t u_1'(t_1)\,\mathrm{d}t_1 - \int_0^t u_2'(t_2)\,\mathrm{d}t_2 \quad . \tag{2.58}$$

The corresponding mean-square separation $\overline{X_s^2}$ is (Gifford, 1968)

$$\overline{X_s^2}(T) = \overline{X_s^2}(0) + 2\overline{u'^2}\int_0^T\int_0^t R(t_2 - t_1)\,\mathrm{d}t_1\,\mathrm{d}t_2 - 2\int_0^T\int_0^t \overline{u_1'(t_1)\,u_2'(t_2)}\,\mathrm{d}t_1\,\mathrm{d}t_2 \; . \tag{2.59}$$

Comparing Eq. 2.59 to Eq. 2.42, we see that the second term on the right-hand side of the former is analogous to the right-hand side of the latter but that two additional terms have appeared, a term dependent upon the initial particle separation and a term dependent upon the *two-particle*, two-point Lagrangian velocity covariance $\overline{u_1'(t_1)\,u_2'(t_2)}$. If we define δu to be the relative velocity $u_1' - u_2'$, then Eq. 2.59 can be rewritten in the form (Batchelor, 1952)

$$\overline{X_s^2}(T) = \overline{X_s^2}(0) + 2\int_0^T \int_0^t \overline{\delta u(t)\,\delta u(t-\xi)}\,\mathrm{d}\xi\,\mathrm{d}t \quad , \tag{2.60}$$

an equation which, with the exception of the initial separation term, is formally identical to Eq. 2.42. Note, however, that the integrand in Eq. 2.60 involves the correlation between velocities of *two* different fluid particles at *two* different instants (e.g., Batchelor, 1950; Smith and Hay, 1961). This is in contrast to Eq. 2.42 in which the integrand depends only upon the correlation between the velocities of a single particle at two different instants. It follows too from Eq. 2.60 that the counterpart to Eqs. 2.54 and 2.55 is (e.g., Smith and Hay, 1961; Corrsin, 1962)

$$K_{xs} = \frac{1}{2}\frac{\mathrm{d}}{\mathrm{d}t}\overline{X_s^2} = \int_0^t \overline{\delta u(t)\,\delta u(t-\xi)}\,\mathrm{d}\xi \quad . \tag{2.61}$$

It is worth noting that it is possible to use a *one*-particle approach to study relative diffusion if particles are chosen 'conditionally' at the source to account for the *initial* effects of interparticle velocity correlations. These interparticle correlations are then ignored in downwind trajectory calculations (Lee et al., 1986). This *approximate* model has generated considerable controversy but does offer an alternate and more tractable approach to relative diffusion. More information may be found in Gifford (1982, 1983b), Lee and Stone (1983), Smith (1983), and Sawford (1984). Lee et al. (1986) have compared results from a conditioned one-particle model with those from a two-particle model for simulations of the dispersion of particle pairs. They found qualitative agreement in the predictions of the two models but the one-particle model appeared to overpredict relative diffusion and underpredict meandering.

Relative diffusion regimes

It is possible to use dimensional arguments (e.g., Batchelor, 1952; Batchelor and Townsend, 1956) to obtain the time dependencies of $\overline{X_s^2}(T)$ at small and intermediate travel times T. For small T, the mean-square particle separation depends upon T^2 just as in Eq. 2.43. The intermediate regime, sometimes called the 'accelerated' regime, is of considerable interest since the time dependence is proportional to T^3. This growth rate

is consideraby faster than the T^2 dependence in the initial stages of absolute diffusion or the T dependence of molecular diffusion (or turbulent diffusion at long travel times: see Eq. 2.44). A physical explanation is that eddies contributing to the relative diffusion of two particles tend to be of the same scale as the particle separation. As the separation distance increases, larger and larger eddies contribute to particle separation — in effect, the variance of the relative velocity increases with time so long as the particle separation is still within the inertial range, that is, considerably smaller than the scale of the wavelengths of the energy-bearing eddies.

As discussed in Sec. 2.1.5, Richardson (1926) proposed an empirical relationship

$$K_H = 0.2\ell^{4/3} \tag{2.62}$$

for the 'instantaneous' horizontal eddy diffusivity, K_H, appropriate for relative diffusion. He based this formula on an empirical fit[73] to inferred K_H values over a very wide range of atmospheric length scales ℓ. Richardson estimated the values of K_H for larger scales from observed cloud size ℓ and travel time T using a formula of the form $X^2/2T$, i.e., a Fickian relation implying a constant diffusivity (cf. Eq. 2.57), even though he found K_H to vary by 12 orders of magnitude over a spatial scale range of approximately 10 orders of magnitude! Richardson and Stommel (1948) and Stommel (1949) found comparable behaviour in the ocean, although observations at scales larger than about 100 m were not available. This *Lagrangian* apparent eddy diffusivity K_H can be determined by the same relation given in Eq. 2.54 except that X_g^2 must be used rather than X^2. That is, only cloud or plume width is considered regardless of the position of the cloud centroid or plume centerline (e.g., Sec. 4.8 of Csanady, 1973 ; Walton, 1973; Gifford, 1977).

In 1941 Obukhov showed[74] that a $K_H \propto \ell^{4/3}$ relationship should follow in an inertial range based on dimensional considerations and Kolmogorov's similarity hypotheses.

---

[73] And on the practical consideration that such a power law was easily integrable (Richardson, 1952).

[74] See references in Gifford (1968), Monin and Yaglom (1975), or Pasquill and Smith (1983).

However, Richardson's data imply that this relationship holds at scales far larger than the small-scale turbulent inertial range (e.g., Gifford, 1983a; Sawford, 1984). In a paper discussing observational evidence for the accelerated regime, Gifford (1977) argued based on a number of different tropospheric relative diffusion data sets that the intermediate regime ends somewhere between 1000 and 3000 s. Gifford also acknowledged, owever, that Corrsin (1953), Saffman(1962), and Smith (1965) had derived $\overline{X_s^2}(T) \propto T^3$ laws for horizontal relative diffusion in *shear* flows which would apply at scales beyond the three-dimensional inertial range. Note also Islitzer and Slade's (1968, p. 185) comment on using simultaneously-released tetroon pairs to estimate relative diffusion: "Obviously the tetroons must possess very nearly the same equilibrium floating surface, or the wind shear in the vertical will cause a misleadingly large rate of balloon separation with time." Brier (1950), Morel and Larcheveque (1974), Monin and Yaglom (1975, p. 560), and Er-El and Peskin (1981) have also discussed this problem, and Fig. 2.27 shows an analytical model's prediction of the contribution of wind shear to mesoscale dispersion in an idealized Ekman layer.

Long-time limit

For the purposes of mesoscale dispersion, however, the most interesting regime is that of long travel times. At very large T, the pair of particles should be so far apart that their velocities are completely uncorrelated. In this case,

$$\overline{\delta u(t)\,\delta u(t-\xi)} = 2\overline{u(t)\,u(t-\xi)} \tag{2.63}$$

where u is the absolute u-velocity component of *either* particle and

$$\overline{X_s^2} = \overline{X_s^2}(0) + 4\int_0^T \int_0^t \overline{u(t)\,u(t-\xi)}\,\mathrm{d}\xi\,\mathrm{d}t \quad . \tag{2.64}$$

At what time or space scales might we expect Eq. 2.64 to hold? Based on Gifford's (1977) work, the accelerated regime does not hold past 3000 s. Fig. 2.28 shows a plot of both time-averaged (over a one-hour period) and instantaneous σ_y's vs. travel time

for an oil fog plume about 5 km long generated not long after sunrise (June 17, 1977, roughly 0700–0830 MDT). The instantaneous plume σ_y's can be seen to to obey a T^3 law at longer times and to approach the average or absolute-diffusion values as time increases. As discussed in the next section, relative and absolute diffusion will become indistinguishable as the travel time T approaches the sampling time τ. It is worth noting in this regard that Heffter (1965) did not distinguish between relative and absolute diffusion in his study of the variation of horizontal diffusivity for travel times of more than one hour.

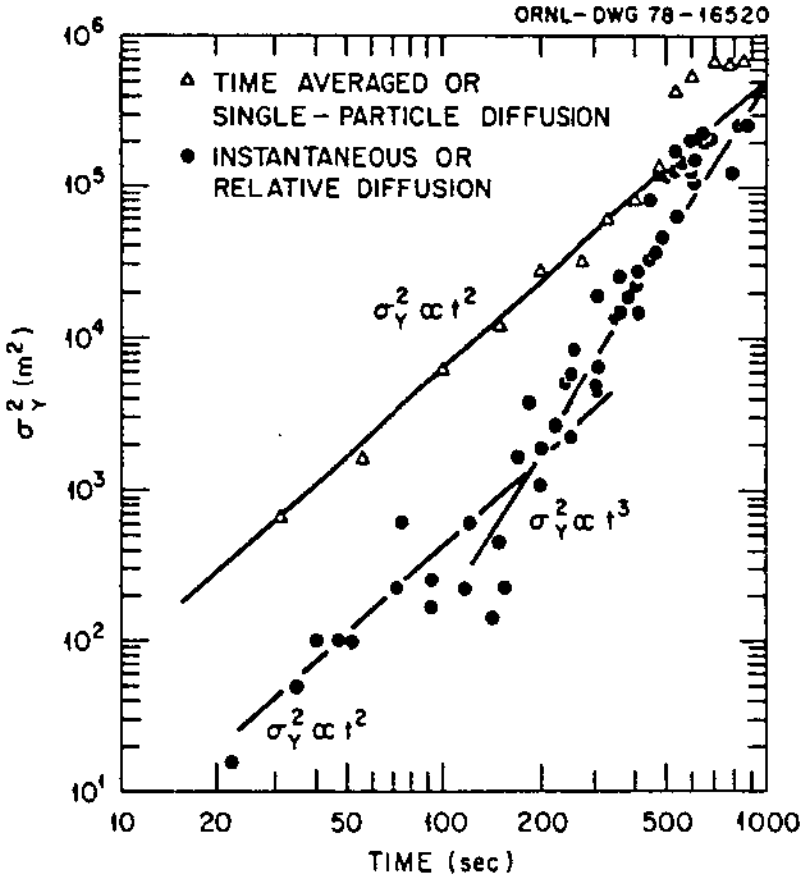

Figure 2.28: Plot of σ_y vs. travel time for both instantaneous and time-averaged plumes (from Nappo, 1981).

It should also be noted that Gifford has argued more recently (Gifford, 1983a, 1984, 1986; Barr and Gifford, 1987) that the 'accelerating diffusion' regime "... exists for 10 to 15 hours or more of downwind travel from the source, i.e., to length scales of up to several

hundred kilometers, and that the dominant time scale, T_L, is on the order of 10^4 s" (Gifford, 1984, p. 165). It is still not clear whether this is in fact true, particularly in view of the competing contributions from vertical shear (e.g., Fig. 2.27). From the point of view of a one-particle dispersion model, however, extending the time over which the velocities of two particles are correlated will not affect the results obtained provided that the scale of motion moving the two particles in concert can be resolved and included in the mean wind field used by the model (see end of next section). That is, a one-particle dispersion model is capable of treating grid-scale relative diffusion but not subgrid-scale relative diffusion.

2.3.3 Release, travel, sampling, averaging and filtering times

Release, travel, and sampling times t_r, T, and τ were defined in Sec. 1.6. These three dispersion time scales together determine the character of the dispersion problem being considered. Hanna (1982) observed that the release, travel, and sampling times each define 'windows' that are used to 'filter' turbulence in order to relate observed diffusion with turbulent flow properties (e.g., Eq. 1.16). They also indicate the nature of the diffusion: "If travel time is much greater than release time or if sampling time is much less than travel time, then puff diffusion is appropriate. If sampling time and release time are much greater than travel time, then continuous plume diffusion is important" (Hanna, 1982, p. 276).

Time scales and temporal filtering

For example, in deriving Eq. 2.42, sampling time and release time are assumed to be much larger than travel time so that absolute diffusion is being described (e.g., Hay and Pasquill, 1959). In fact, the sampling time and, correspondingly, the release time[75], are assumed to be large enough that all scales of turbulence are accounted for in $\overline{u'^2}$ and $R(\xi)$ so that $\overline{u'^2}$ corresponds to $\overline{u'^2}_{\infty,0}$ (using the notation of Sec. 1.4.6). In the real world,

[75] Since release time must be larger than sampling time for a plume release; otherwise, the plume would not be 'attached' to the source but would rather correspond to an elongated puff.

however, estimates of plume or absolute diffusion based on particles released serially from a fixed point over a certain finite sampling time will not sample much of the low-frequency end of the energy spectrum. The complementary exclusion of the high-frequency end of the energy spectrum that results from the equivalence of travel time and averaging time has already been described by Eq. 2.51. Rewriting this equation for a finite sampling time or sampling period τ then yields an equation identical in form to Eq. 1.16 (e.g., Ogura, 1959; Pasquill and Smith, 1983):

$$\overline{X^2} = \overline{u'^2}_{\infty,0} T^2 \int_0^\infty F_L(n) \left[1 - \frac{\sin^2 \pi n \tau}{(\pi n \tau)^2}\right] \frac{\sin^2 \pi n T}{(\pi n T)^2} \, \mathrm{d}n \quad . \tag{2.65}$$

Thus, spectral contributions corresponding to time scales less than the travel time T or greater than the sampling time τ are diminished or completely filtered out by one of the two sine terms. The actual reasons for the filtering are quite different, however: high-frequency contributions to $\overline{u'^2}_{\infty,0}$ are removed because they are ineffective for particle dispersion (that is, net particle displacement), but low-frequency contributions are excluded from $\overline{u'^2}_{\infty,0}$ because the sampling time is too short to allow them to contribute to $\overline{X^2}$.

Note that Eq. 2.65 can be approximated as (Kahn, 1957; Hino, 1968; Wollenweber and Panofsky, 1988)

$$\overline{X^2} \approx \overline{u'^2}_{\infty,0} T^2 \int_{1/2T}^{1/2\tau} F_L(n) \, \mathrm{d}n \quad . \tag{2.66}$$

This equation shows more clearly than Eq. 2.65 how particle diffusion or mean-square particle displacement for a finite travel time and a finite observation or sampling interval is determined by a *finite* spectral interval. To quote Ogura (1959, p. 152) on the role of sampling time in this equation: "... only eddies whose frequencies are larger than $2\pi/\tau$ contribute appreciably to the mean rate of diffusion averaged over the period of τ. In other words, for the turbulent diffusion observed during the period τ, large eddies whose frequencies are less than $2\pi/\tau$ should be regarded as a mean flow, not as turbulent components, and consequently they contribute nothing to the dispersion of

particles. Their role is no more than that of determining the center line of dispersed plumes."

Time scales and spatial filtering

The situation is somewhat different for the diffusion of a cloud or cluster of particles. In this case, the finite size of the cloud or cluster acts as an effective *spatial* band-pass filter. Spatial spectral scales larger than the scale of the cloud cannot contribute to its growth but rather can only move it as a whole (e.g., Fig. 1.4). The smallest scales are also ineffective in contributing to cloud growth since they can only oscillate particles locally and cannot maintain sustained displacement. Only the eddy scales close to the cloud size contribute significantly to its growth and dispersion. Moreover, the characteristics of this spatial 'band-pass filter' change in time as the puff grows (Smith and Hay, 1961). The combined effects of the turbulence intensity (and KE spectral slope) of the flow and the travel time determine the cloud or cluster size and hence the effective spatial filter bandwidth. Skupniewicz (1987) referred to this filter as a "sliding spectral window."

Sampling time for cloud or cluster diffusion, on the other hand, is *instantaneous* and perhaps is best thought of from the Lagrangian perspective. That is, the measurement is taken from the point of view of an observer moving with the cloud center rather than from that of an observer at a fixed point in space. However, if we compare puff diffusion to plume diffusion in spectral terms, we do better to think of the *travel* time as the effective sampling time for puff diffusion since it, like sampling time in the plume diffusion case, determines the maximum eddy time scale which can affect puff growth (though only indirectly through its influence on cloud size). Another way to think of this is to note that as T increases, the growing cloud will sample a larger spatial region than did the initial cloud, whose size was determined by the release time t_r. In fact, Ogura (1959, p. 155) stated that "... it is impossible in relative diffusion to distinguish between the (travel) time and the (sampling) time T."

Smith and Hay (1961) considered the problem of cloud growth and proposed a β approximation for the relative velocity Lagrangian and Eulerian time-correlograms

analogous to the one proposed by Hay and Pasquill (1959) for absolute diffusion. By using this assumption and by applying an ensemble average over all realizations of the velocity field and a spatial average over the cloud volume to separate relative diffusion from the mean transport, they arrived at the following expression for the rate of change of cloud size with time in terms of the filtered three-dimensional energy spectrum $E(k)$:

$$\frac{\mathrm{d}}{\mathrm{d}t}\sigma^2 = \frac{\pi\beta}{6U}\int_0^\infty E(k)\frac{1-e^{-\sigma^2k^2}}{k}\,\mathrm{d}k \quad , \tag{2.67}$$

where σ is the concentration standard deviation about the cloud center of mass, $\beta = T_L/T_E$, and U is the mean transport wind speed. The exponential term multiplying the energy spectral density function in the integrand of Eq. 2.67 has a mid-range maximum and approaches zero at both ends of the integration range. It thus acts as a band-pass filter. Moreover, as σ increases, the maximum of the filter will slide over towards smaller wavenumbers and hence to longer wavelengths.

Partitioning the kinetic energy spectrum

Gifford's fluctuating plume model. Gifford (1959) proposed an elegantly simple 'fluctuating plume' model for the absolute diffusion of material emitted from a continuous source. This model separated the contributions of relative diffusion and plume meander to total diffusion in a manner consistent with real-world experience. That is, the total lateral or vertical plume diffusion seen by a fixed observer depends upon both the width of the instantaneous plume at the downwind distance of interest *and* the fluctuations of the instantaneous plume centerline from its mean position. Gifford defined $\overline{Y^2}$ to be the variance of the instantaneous plume distribution about its instantaneous centerline and $\overline{D^2}$ to be the variance of fluctuations of the instantaneous centerline about its mean position. $\overline{Y^2}$ is assumed to be non-random, known, and time-dependent. It then follows that

$$\overline{Y^2} + \overline{D^2} = Y_0^2 + 2\overline{v^2}\int_0^T\int_0^t R_L(\xi)\,\mathrm{d}\xi\,\mathrm{d}t \quad . \tag{2.68}$$

Eq. 2.68 simply partitions the mean-square plume displacement (cf. Eq. 2.42) into two components, one due to relative diffusion and one due to plume meander. Or in Gifford's own words, "... the total dispersion, relative to a fixed time or mean-wind axis, equals the dispersion relative to the centroid plus the dispersion of the centroid" (Gifford, 1983b, p. 196). This relation is shown schematically in Fig. 2.29.

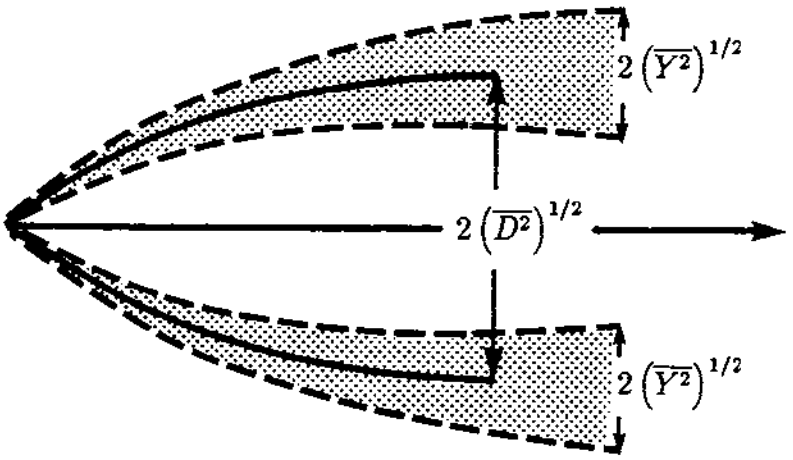

Figure 2.29: Simple schematic of Gifford's fluctuating plume model. The envelope marked as $2\overline{D^2}^{1/2}$ indicates the dispersion of the plume centerline while the envelope marked $2\overline{Y^2}^{1/2}$ indicates the relative diffusion about the instantaneous plume centerline. Note the diminishing influence of meander as travel time increases.

One significant consequence of this fluctuating plume model is that the ratio of peak (centerline) concentration c_p to mean centerline concentration $\overline{c}$ is given by

$$\frac{c_p}{\overline{c}} = \frac{\overline{Y^2} + \overline{D^2}}{\overline{Y^2}} \quad . \tag{2.69}$$

Gifford then argued based on the work of Taylor (1921) and Batchelor (1950) that this ratio should vary as T^{-1} for short travel times (i.e., in the accelerated diffusion range when $\overline{Y^2} \propto T^3$) but approach a constant value for long travel times.

Gifford (1959) did not discuss the determination of $\overline{Y^2}$ and $\overline{D^2}$ or interpret the partitioning of plume dispersion in terms of the KE spectrum, but it is clear from the

'Discussion' appended to his paper that he saw small eddies as the agents for relative diffusion (i.e., $\overline{Y^2}$) and larger eddies as the agents for plume meander. He also stated that these two processes are statistically independent regardless of whether or not a spectral gap is present. Gifford credited Brier (e.g., Brier, 1950) with the idea for this approach. Batchelor had noted too that "... when the Reynolds number is large enough the kinetic energy and mean square rate-of-strain arise from different parts of the wave-number spectrum. The big eddies do most of the translating and thus dominate the displacement p.d.f., whereas the small eddies do most of the straining and thus dominate the separation p.d.f. With the assumption (which occurs in Kolmogoroff's universal similarity theory) that these two processes are statistically independent..." (Batchelor, 1952, p. 350).

Sheih's fluctuating plume model. Sheih (1980) did try to quantify the fluctuating plume model in terms of the energy spectrum through the use of various filter functions. He started by writing expressions for the instantaneous plume center and instantaneous plume width based on the trajectories of a pair of simultaneously-released particles. He then used a time average based on sampling time τ to decompose the instantaneous plume center position into a mean position and a fluctuation from that mean. Finally, he attempted to express the variances of each of (i) instantaneous plume width, (ii) centerline fluctuation, and (iii) mean centerline position by filtering the KE spectrum with various forms of the filter functions used in Eqs. 2.65 and 2.67 after first using Hay and Pasquill's (1959) β–assumption to change from a Lagrangian energy spectrum to an Eulerian spectrum.

The results obtained by Sheih using this approach attracted considerable criticism (Gifford, 1981; Mikkelsen and Troen, 1981; Rowe, 1981). It is clear that he fell into a number of errors and misinterpretations in his application of his conceptual model, including the use of a one-dimensional speed spectrum rather than a three-dimensional velocity spectrum. The most damning criticism was the observation by Gifford (1981) that it is impossible in principle "... to extract relative diffusion information, which explicitly depends on diffusing particle velocities at two moving points separated in space and in time, by a simple filtering operation applied to one-dimensional, fixed-point,

Eulerian velocity statistics." Despite this absolutely fundamental flaw, Sheih's basic conceptual approach is still valuable. It highlights the fundamental role of sampling time in the *definition* of meander and also the difficulty of separating meander from relative diffusion due to the dependence of the characteristics of the relative-diffusion bandpass filter on travel time T (see Eq. 2.67).

Sampling time, travel time, and meander

Sheih (1980) also introduced a relative diffusion time scale, t_e, which represents the characteristic time scale of the eddies most effectively contributing to the separation of a particle pair. He defined t_e to be equal to σ_r/U, where σ_r is the standard deviation of the plume distribution about its center and U is the mean wind speed. σ_r corresponds to σ in Eq. 2.67. Figs. 2.30a-c show the three possible energy-spectrum partitionings by sampling time τ, travel time T, and relative diffusion time scale t_e for the three possible relative magnitudes of these three time scales (assuming that $t_e < T$). Fig. 2.30a is based on Sheih's Fig. 1.

One important relationship implicit in Fig. 2.30 is that the contribution of meander to absolute diffusion decreases monotonically with travel time T. Physically, this results from the dependence of the relative diffusion time scale t_e on T. As a puff (or cluster or plume section) grows in size, larger and larger eddies become effective in deforming and spreading the puff. Since meander results from the whole-body advection of the puff, correspondingly fewer eddies remain which are larger than the puff and hence capable of advecting it as a whole. For a fixed sampling time τ, the portion of the energy spectrum which can contribute to meander shrinks as T and t_e increase and approach the value of τ (Fig. 2.30a). As a result, the value of meander approaches a constant value[76] with increasing travel time. The meander component will also approach a constant value even for a very large sampling time τ provided the travel time is larger than the time scale

[76] The non-zero constant is due to the centroid displacements of individual puffs which occurred before the puffs reached a size too large to be advected by any of the turbulent eddies.

of the largest eddies (e.g., Csanady, 1973). This relationship is illustrated in Fig. 2.31, where meander is defined as the ensemble-average value over a very large set of independent puff releases of the standard deviation of the displacements of the puff centroids relative to the axis of the mean wind[77].

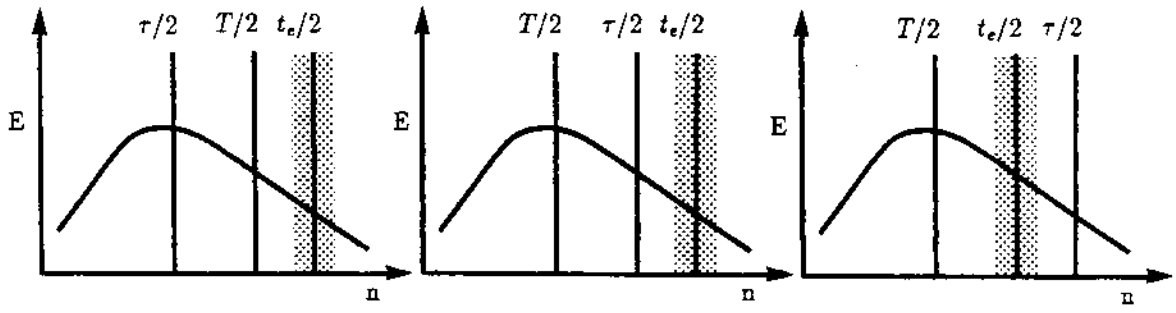

Figure 2.30: Schematic repesentation of the partitioning of the three-dimensional energy spectrum by sampling time τ, travel time T, and relative diffusion time scale t_e for the three possible combinations of these three time scales (assuming that $t_e < T$).

Sampling time and relative diffusion

Eqs. 2.65 and 2.66 can also be interpreted in terms of Fig. 2.30a. As discussed by Sheih, the sampling period τ defines the mean wind. Only the portion of the KE spectrum to the right of the vertical line marking $\tau/2$ will contribute to plume diffusion, which in this framework is the absolute or one-particle diffusion consisting of both relative diffusion and meander (see Fig. 2.32a). The portion of the spectrum to the left of this

[77] It should be noted that the meander component has a quite different long-time asymptotic behaviour for particle *pairs*. In this case, the relative diffusion and meander components approach the same T-dependent limit equal to half of the absolute diffusion (Lee et al., 1986). This difference helps to explain why Herterich and Hasselmann (1982) and Sanderson and Okubo (1988) introduced the concept of 'patch diffusion' to handle the case where a finite patch is neither small enough to move as a single particle (two-particle limit) nor large enough to be unaffected by eddy motions (one-particle limit).

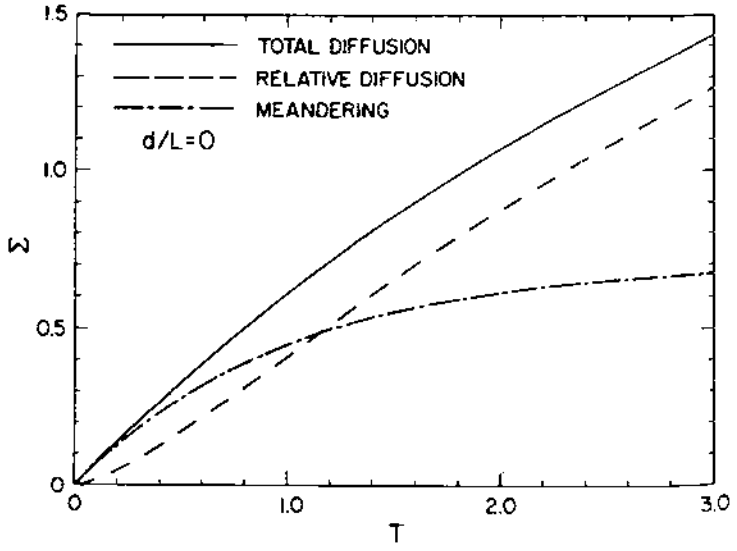

Figure 2.31: Nondimensional plots of total diffusion, relative diffusion, and meander for a point-source release and very long sampling time, based on analytical solution to a 'conditioned' one-particle model (from Lee and Stone, 1983a). Similar figures are given by Csanady (1973, Fig. 4.4a) and Pasquill and Smith (1983, Fig. 3.14).

line is responsible for the variability of the 'mean' wind and 'mean' plume centerline over many samples of length τ. This division is a consequence of the inability of a finite-length sample to 'capture' the effects of the larger, lower-frequency eddies (e.g., Ogura, 1957, 1959) and is represented in Eq. 2.65 by the $\sin^2\tau$ term and in Eq. 2.66 by the $\tau/2$ limit of integration. The travel time T, on the other hand, acts as a low-pass filter since eddies with periods smaller than T can only cause a particle to oscillate about its mean position but cannot contribute to a net displacement. Initially, all eddies do contribute to mean particle dispersion but the fraction contributing decreases as T increases. This effect is represented in Eq. 2.65 by the $\sin^2 T$ term and in Eq. 2.66 by the $T/2$ limit of integration.

When $T < \tau$, the combined effect is the band-pass filter shown schematically in Fig. 2.32a. However, how should Fig. 2.32b, which shows the complementary case when $\tau < T$, be interpreted? Ogura (1959) argued that this case is inadmissible for describing absolute diffusion because diffusion would then be occurring relative to a local,

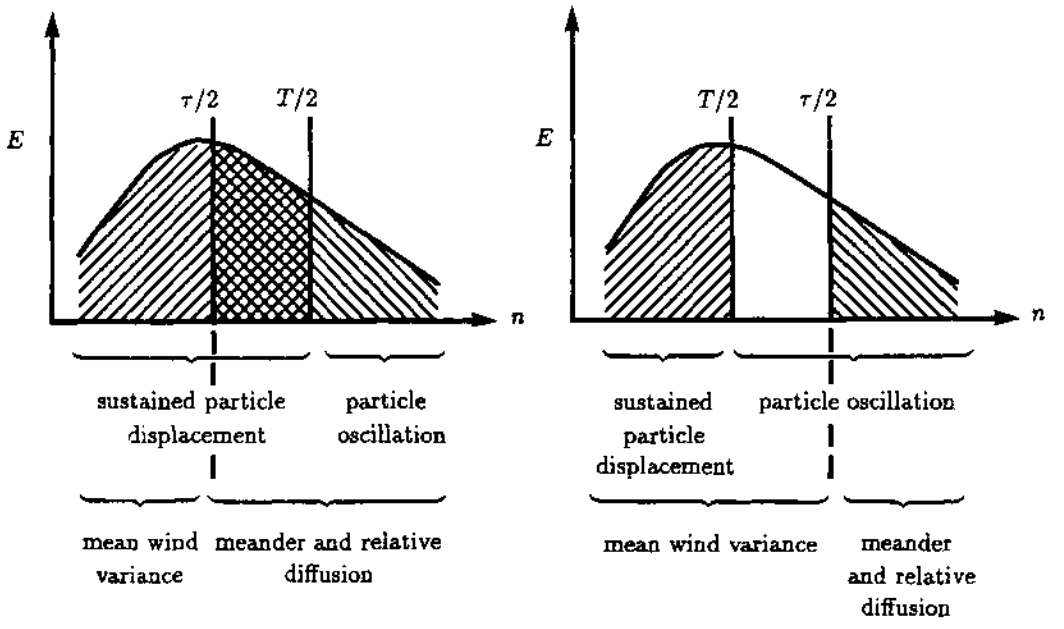

Figure 2.32: Illustration of the roles of sampling time τ in defining a high-pass spectral filter and travel time T in defining a low-pass spectral filter in the calculation of mean-square particle displacement.

possibly moving, origin rather than relative to the fixed source (consider the extreme example of $\tau = 0$). Pasquill and Smith (1983) agreed with Ogura, arguing that having $T > \tau$ introduces an *effective* sampling time larger than τ. This is important because the sampling period τ defines the mean wind direction and hence the reference frame for absolute diffusion. A larger effective sampling time would incorporate the influence of lower-frequency eddies and hence might yield a different mean wind direction. One way to see this is to suppose that the sampling time τ is equal to the release time t_r. Then for travel times T larger than τ, the plume will be detached from the source and will grow as an elongated cluster or puff. The range of relative velocities $\overline{v'^2}$ experienced by the traveling cluster will likely be larger than those sampled at the source in time τ. Alternatively, even if $t_r > T$, the plume's lateral position at downwind distance $\overline{u}T$ will be influenced by particles with a greater separation than $\overline{u}T$, and $\overline{v'^2}$ will again be determined by an effective sampling duration larger than τ (Pasquill and Smith, 1983). Thus, Eq. 2.65 is only appropriate for $T < \tau$, that is, the partition illustrated in Fig. 2.32a. Otherwise, the meander component will not be properly specified.

Meander vs. relative diffusion

The study of relative difffusion and meander by Skupniewicz (1987) illustrates some of these considerations. Continuous overwater surface tracer releases were made during the summer along the central California coast under fully developed sea-breeze conditions. Repeated cross-plume concentration measurements were made by a low-flying aircraft at downwind distances from 1–10 km. The choice of sampling time upon which to base meander calculations posed a problem since (i) tracer travel times T for a travel distance of 10 km approached 30 minutes and (ii) the wind-direction record at the source exhibited a variety of fluctuation time scales superimposed on the diurnal sea-breeze cycle, including low-frequency oscillations with periods on the order of 60 minutes. Skupniewicz finally chose to calculate meander relative to the mean wind direction at the source for 30-minute averages beginning 15 minutes before[78] the concentration measurements made over 30-minute periods. Wind fluctuations with periods longer than 15 minutes were thus not accounted for in the dispersion calculations. Skupniewicz found meander contributions to total diffusion to be at least as large as those contributions due to relative diffusion.

Kristensen et al. (1981) examined meander displacements $\overline{D^2}$ under very stable conditions for one- and three-hour sampling periods. Dispersion due to meander was anywhere from 4 to 6 times as large as that due to relative diffusion under the strongly stable, low-wind speed episodes considered. Hanna (1983) used series of nearly instantantaneous lidar observations of a tracer plume under very stable, nighttime conditions over land to estimate the contribution of meander to plume dispersion over one-hour sampling periods. He found the contribution of meander to be larger than that of relative diffusion in about 50% of the cases considered. Later, Hanna (1986) extended Gifford's fluctuating plume model by assuming that concentration fluctuations are controlled by two widely separated time scales, one the integral time scale for instantaneous in-plume

---

[78] To account for transport time.

fluctuations and the other the turbulence time scale, which is associated with meandering. In comparisons against field data he found the two processes to contribute more or less equally for a downwind distance of 70 m. Finally, Smith (1979a) analyzed over 2100 hand-drawn surface geostrophic trajectories derived from surface weather maps to study the effects of synoptic-scale plume 'swinging' or meandering. He concluded that for sampling periods of more than 24 h, synoptic meander would normally dominate small-scale turbulent diffusion in determining plume width.

Other aspects of sampling time

Sampling time and ensemble-average estimates. Another aspect to sampling time is its influence on sampling fluctuations. Gifford's fluctuating plume model, for example, was able to estimate the contribution of plume meander to concentration fluctuations (Eq. 2.69), and meander in turn depends on sampling time. As discussed in Sec. 1.4, the size of the sampling fluctuations obtained will depend upon the amount of averaging performed. Such averaging could include spatial 'smoothing', time averaging, spectral filtering, or the compositing of a number of realizations.

Eq. 1.6 showed the role of the length of the temporal or spatial sample in determining the magnitude of the variation of finite-sample means from the true ensemble-mean value. In the case of dispersion, Crawford (1967) suggested that for *absolute* diffusion from a *continuous* source, if subgrid-scale motions are to be considered random turbulence whose advective effects are represented by a diffusion equation, then time averaging should encompass a minimum of ten time scales representative of the most 'efficient' eddies contributing to subgrid-scale motions. That is, the sampling time should be related with the time scales of the turbulent processes and should be long enough to describe their contributions accurately. This requirement is recognized in the analysis of turbulence observations. A high-pass filter with cutoff period on the order of $\tau/20$ is often used to 'condition' the observed time series before spectral analysis so as to remove eddy contributions from eddies with periods in the range $\tau/20$ to $\tau/2$ (e.g., Gifford, 1968; Kaimal et al., 1976). The reason is that these eddies will have been sampled but

not sampled *significantly*. Thus, sampling time will determine a different but dependent high-pass *filter* time scale.

Sampling time and measured variances. A number of studies have determined empirical relationships for the dependence of velocity or displacement variance on sampling time. For example, Hino (1968) found based on his own measurements and those of others that the plume spread parameters σ_y and σ_z grow approximately as the fourth root of sampling time, i.e., as $\tau^{1/4}$, in the 10 minute to 5 hour range. Maximum ground-level concentrations will then vary as $\tau^{-1/2}$ since this quantity varies (in the Gaussian solution) as $(\sigma_y \sigma_z)^{-1}$. This relationship is shown in Fig. 2.33.

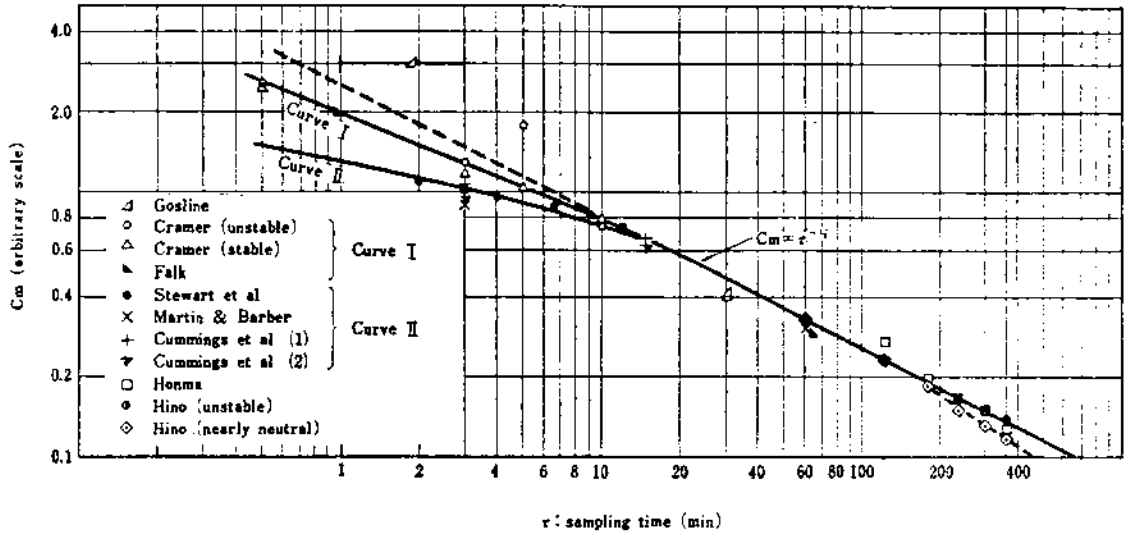

Figure 2.33: Summary plot of experimental data on the relationship between maximum ground-level concentration and sampling time (from Hino, 1968).

For stable conditions where meandering can be important, the dependence on sampling time may be even stronger. Moore et al. (1988) found σ_y to be about 3 times larger for 1 h sampling times as compared to 5 min sampling times; this would imply a $\tau^{0.4}$ dependence. Kristensen et al. (1981) suggested a $\tau^{1/3}$ dependence for strongly stable conditions. Other related discussions of sampling-time dependence for short-range diffusion may be found in Slade (1968), Doran et al. (1978), Smith (1979, 1987), Pasquill

and Smith (1983, Sec. 2.6), and Yersel et al. (1983), among others. For mesoscale and longer sampling periods, Durst et al. (1959) found σ_y to vary as the *one-half* power of sampling time τ based on puff, balloon, and geostrophic-trajectory observations in the 30 minute to 90 day range. Smith (1979a) claimed an even stronger dependence of $\tau^{0.85}$ for sampling times from 20 to 60 h based on his analysis of over 2100 hand-drawn geostrophic trajectories. The general trend for these admittedly limited and empirical relations seems to be that the power-law dependence of σ_y on sampling time τ increases as τ increases.

Sampling time and particle separation. Richardson and Stommel (1948) and Stommel (1949) studied oceanic lateral relative diffusion by considering the rate of change of the separation of a pair of particles floating on the ocean surface[79]. Assuming a classical inertial range in which their neighbour diffusivity $F(l)$ varied as $l^{4/3}$, where l was the separation distance, Stommel found that T, the time interval between successive measurements, should increase as $l^{4/3}$ as separation distance increased in order to obtain appreciable, measurable change without significantly altering the scale of separation. His suggested values for T included a 5 s interval for a 1 m separation, a 40 minute interval for a 10^3 m separation, and a 3 day interval for a 10^6 m separation[80].

Implications for particle-based parameterizations

As will be discussed in the following section, one-particle (or Lagrangian particle) dispersion models partition the atmospheric flow field into a mean field and a turbulence field by explicit or implicit *time–grid volume* averaging[81]. Thus, the 'mean' field can

---

[79] Their approach was somewhat different from other studies of relative diffusion since two observations of the same particle pair were required instead of just one. The actual particles used in their experiments included pieces of parsnips, meteorological balloons inflated with sea water, and sheets of mimeograph paper.

[80] Monin and Yaglom (1975, p. 559) have some interesting comments on Stommel's paper.

[81] And sometimes ensemble averaging in the case of most PBL parameterizations (e.g., Sec. 1.4; Wyngaard, 1982).

still vary in time and space but only at scales larger than the averaging scales (i.e., the mean fields have been low-pass filtered). The 'turbulence' field in turn corresponds to the contributions of all high-frequency and/or subgrid-scale motions, that is, unresolvable motions. Diffusion by the turbulence component is parameterized by what is sometimes called a 'Monte Carlo diffusion' model. 'Diffusion' at time and space scales larger than the averaging scales is treated entirely by explicit differential advection arising from time and space variations in the resolved (or mean) wind field (e.g., Hanna, 1982).

Hanna (1982) also observed that the definition of turbulence used in these models is based on the averaging time characteristic of the mean velocity field input to the diffusion model. He then argued that the averaging time used to determine the turbulence parameters $\overline{w'^2}$ and $R_L(\xi)$ needed by the diffusion model should be the same as the averaging time for the mean wind field determined by a prognostic or diagnostic meteorological to ensure compatibility between all of the fields. $\overline{w'^2}$ is normally taken to be the total variance or area under the band-limited vertical velocity spectrum determined in turbulence studies. Typical low-frequency limits in such studies range from 0.005 to 0.0003 Hz or from 3 to 55 minutes (e.g., Kaimal et al., 1972, 1976; Kaimal, 1973). Thus, the averaging[82] time implicit in the parameterization of turbulent diffusion by particle models will be in the 30–60 minute range, comparable to that used in the ensemble-average turbulent diffusion parametization schemes employed in mesoscale models (e.g., Pielke, 1984; Mellor, 1985).

A somewhat related concern is the distinction between relative diffusion and absolute diffusion over mesoscale travel distances and travel times since a one-particle diffusion model normally[83] simulates absolute diffusion, that is, the diffusion parameterization assumes particles to be independent of one another. This is a slippery problem conceptually (see, for example, the discussion following Moran et al., 1991) but the following

---

[82] Averaging time for calculating the mean fields but *sampling* time for calculating turbulence statistics.

[83] We note again the work of Gifford (1982), Lee and Stone (1983a,b), Sawford (1984), and Lee et al. (1986) in approximating relative diffusion through the use of a conditioned one-particle model.

points should make things clearer. Relative diffusion is in fact modelled explicitly at scales larger than the time—grid volume averaging scales in one-particle diffusion models. This is because pairs or clusters of particles being advected by the *mean* wind field are not independent; rather, they can be advected simultaneously by resolved coherent structures and other flow fluctuations. As for diffusion by the unresolved time and space scales, the parameterization does predict absolute diffusion but only for the contributions of the unresolved scales. This is a result of the spectral partitioning of the flow field as illustrated by Fig. 2.34. The use of a one-particle dispersion model will thus only be a concern for concentration sampling times smaller than the characteristic spectral partitioning time scale. For longer times, both relative diffusion and meander are resolved and the choice of concentration sampling time will determine their relative importance. The concentration sampling times used in the two mesoscale tracer experiments discussed in Chap. 3 ranged from 45 minutes to 6 hours, that is, comparable to or larger than the characteristic time scale for mean field—turbulence field partitioning.

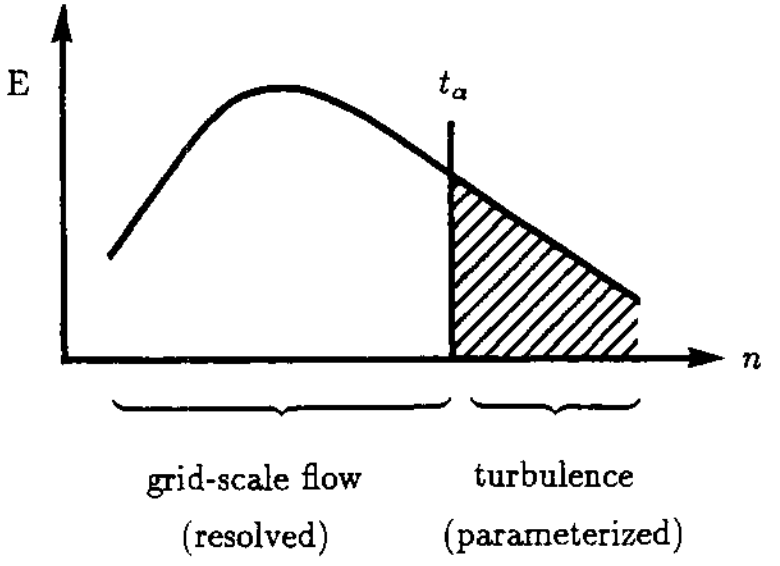

Figure 2.34: Partitioning of the atmospheric energy spectrum in mesoscale meteorological and dispersion models. t_a denotes the averaging time (for calculating the mean field – defines a low-pass filter) or sampling time (for sampling turbulence – defines a high-pass filter).

What is still a concern is the issue raised at the end of Chap. 1: are all components of the atmospheric energy spectrum represented in full by the modelled mean and turbulence wind fields? The answer is "no, not all of them will be." The turbulence parameterization should represent PBL eddies with periods less than 30 minutes reasonably well, although the contributions of lower-frequency rolls will not be represented in the turbulence statistics (e.g., Kaimal et al., 1976; Brown, 1981). Other coherent structures such as internal gravity waves and quasi-horizontal vortices, unless generated by stratified flow over topography or by explicitly-simulated convection, will not appear in the model mean wind fields. The mean fields will, however, represent and resolve diurnal and inertial oscillations, various physiographically-forced circulations, and mean PBL vertical shear. The success of these one-particle diffusion models in real-data case studies will thus depend on the relative importance of the resolved atmospheric features compared to the unresolved features in individual cases, since as discussed in Sec. 2.1, IGW and vortical modes are highly intermittent.

2.3.4 Lagrangian stochastic models

Small-scale diffusion models based on Gaussian solutions or similarity theory cannot be used to simulate mesoscale atmospheric dispersion because mesoscale flows are usually both nonstationary and inhomogeneous. The three main classes of three-dimensional *episodic* dispersion models that have been used to simulate mesoscale and larger-scale dispersion are (i) *Eulerian concentration moment* models, which require the numerical solution of some form of the Reynolds-averaged advection-diffusion equation on a fixed grid, (ii) *Lagrangian trajectory* or *Lagrangian puff* models, which treat diffusing puffs like expanding ice-hockey pucks, and (iii) *Lagrangian particle dispersion* models (LPDMs). LPDMs are also referred to in the literature as Lagrangian statistical models, Lagrangian stochastic models, Lagrangian Monte Carlo models, stochastic dispersion models, Markov chain models, random walk models, and random flight models. The CSU mesoscale atmospheric dispersion modelling system uses a Lagrangian particle dispersion model.

This section outlines the theoretical foundations of LPDMs. All three types of episodic mesoscale dispersion models are discussed and compared in Sec. 2.4, and the defining characteristics of the CSU model are described in Sec. 4.4.

Basic characteristics.

Turbulent dispersion is modeled in LPDMs by simulating the simultaneous or sequential release of a large number of pollutant point-particles and then advecting these 'virtual' particles in response to a resolved or 'mean' flow and parameterized turbulent velocity fluctuations. LPDMs are thus hybrid stochastic–deterministic models. Concentration field moments can be estimated at any time from the spatial distribution of the set of predicted particle positions through estimation of the univariate or multivariate particle-position probability density function $P(\vec{r}, t)$ (e.g., Sawford, 1985; de Baas, 1988).

Single-particle models, in which particles travel independently of one another, can only be used to estimate ensemble-mean concentration fields. Estimation of higher-order moments requires the use of multiple-particle models in which groups of particles are released whose turbulent velocities are correlated in space (e.g., Lamb, 1981; Sawford, 1982). Note that many particles may be released simultaneously in a single-particle model but such a release is still equivalent to an ensemble of independent one-particle realizations for identical external flow conditions.

Strengths and weaknesses

LPDMs have a number of advantages over Eulerian advection-diffusion models (see Sec. 2.4). First, a Lagrangian framework is a more natural framework for modeling turbulent diffusion, itself a Lagrangian phenomenon. Second, LPDMs automatically conserve tracer mass. They also do not suffer from computational diffusion or phase dispersion. Third, short-range diffusion, including emissions from point and line sources, can easily be treated by these models. The gradient-transfer hypothesis, on the other hand, limits Eulerian models to spatial scales much larger than the characteristic diffusion

length scale, that is, the product of the Lagrangian velocity integral time scale and the RMS turbulent velocity (Corrsin, 1974). Moreover, Eulerian grid models are forced either to treat subgrid-scale sources as grid-scale area sources or else employ special parameterizations (e.g., Karamchandani and Peters, 1983; Seigneur et al., 1983). Fourth, LPDMs can be shown to have an equivalent Eulerian form, the Fokker-Planck equation, which reduces to the Eulerian K-theory advection-diffusion equation for large travel times (e.g., Monin and Yaglom, 1971; Durbin, 1983; Thomson, 1987). Fifth, LPDMs are able to incorporate more turbulence properties than K-theory models at large travel times (van Dop et al., 1985). And sixth, LPDMs are flexible, conceptually simple, and, when used with a reasonable number of particles, computationally inexpensive. In principle, complex flows should be as amenable to this approach as simple ones provided that the resolvable flow, Lagrangian time scales, and turbulence statistics are known.

With respect to disadvantages, LPDMs are not well suited for modelling the dispersion of nonlinearly reacting pollutants (Lamb, 1980). Questions of statistical sampling error must also be addressed when estimating pollutant concentrations in areas of low particle density, sometimes requiring the release of very large numbers of particles in order to reduce sampling error in areas of interest to tolerable levels.

History

The origins of LPDMs lie in the early random-walk models developed by Einstein (1905) and Langevin (1908) to describe Brownian motion and molecular diffusion. Most LPDMs treat particle velocity as a stochastic process and use a discrete form of the Langevin equation (see below) to describe particle velocities as subject to a damping force and a random acceleration. Useful references on random-walk models, the Langevin equation, and stochastic processes include the books by Wax (1954), van Kampen (1981), and Gardiner (1985).

LPDMs were first applied to turbulent diffusion in the case of the surface layer and vegetation canopies and then, more recently, to the full planetary boundary layer as insight was gained into the handling of inhomogeneous turbulence and stratification

effects. Studies of small-scale dispersion conducted with LPDMs include those of Hall (1975), Hanna (1978), Lamb (1978), Reid (1979), Wilson et al. (1981a,b), Ley (1982), Legg and Raupach (1982), Thomson (1984), van Dop et al. (1985), de Baas et al. (1986), Sawford and Guest (1987), Luhar and Britter (1989, 1990), and Hurley and Physick (1990). Venkatram (1988b) used a Langevin-equation model to simulate plume centerline meandering in a study of concentration fluctuations.

All of the above studies employed *one-particle* models. Durbin (1980), Lamb (1981), Sawford (1982, 1984), Lee et al. (1986), and Thomson (1986b) have used *two-particle* Lagrangian models to study small-scale concentration fluctuations and relative dispersion. Gifford (1982), Lee and Stone (1983a,b) , and Sawford (1984) have discussed a hybrid approach using a 'conditioned' one-particle model.

Early applications of the LPDM approach to mesoscale dispersion studies include McNider et al. (1980, 1982), McNider (1981), Garrett and Smith (1982, 1984), and Pielke et al. (1983). More recent applications include those of Arritt (1985), Etling et al. (1986), Moran et al. (1986), Schorling et al. (1986), Yu and Pielke (1986), Gross et al. (1987), Kao and Yamada (1988), McNider et al. (1988), Segal et al. (1986, 1988), Yamada and Bunker (1988), Uliasz (1990a,b), Physick and Abbs (1991) and Lyons et al. (1992). All of these studies used one-particle models, but as discussed in Sec. 2.3.1 there is little distinction between absolute and relative diffusion at mesoscale times and distances.

Formulation

Let us now briefly review the continuous and discrete formulations used in one-particle LPDMs, concentrating on the effects of vertical inhomogeneities which are so important for longer travel times. An excellent and much more detailed review of this theory has been given by de Baas (1988).

Homogeneous Langevin equation. First, consider the idealized case of statistically steady, homogeneous turbulence. The Langevin equation, which describes the motion of a particle subject to a retarding or damping force and to a random acceleration, can be

written for such a flow as (e.g., Legg and Raupach, 1982; van Dop et al., 1985; de Baas, 1988)

$$\mathrm{d}w = -\frac{w}{T_L}dt + a_2^{1/2}\,\mathrm{d}\xi_t \quad , \tag{2.70}$$

where w is the particle's vertical velocity component, T_L is the Lagrangian integral time scale (e.g., Li and Meroney, 1984), and $\mathrm{d}\xi_t$ is a continuous Markov process representing the random accelerations. $\mathrm{d}\xi_t$ is modelled here as a Wiener process (e.g., Durbin, 1983) such that

$$\overline{\mathrm{d}\xi_t} = 0 \ , \qquad \overline{(\mathrm{d}\xi_t)^2} = \mathrm{d}t \ , \qquad \overline{w\mathrm{d}\xi_t} = 0 \ , \tag{2.71}$$

where the overbar denotes an ensemble average over a set of marked[84] particles (van Dop et al., 1985; de Baas, 1988).

Even though Eq. 2.70 is a stochastic differential equation because of the $\mathrm{d}\xi_t$ term, it can still be solved by application of the standard solution methods for ordinary first-order linear differential equations since T_L and a_2 are constant coefficients (e.g., Legg and Raupach, 1982; Gifford, 1984; de Baas, 1988):

$$w(t) = w(0)e^{-t/T_L} + a_2^{1/2}\int_{\xi_0}^{\xi_t} e^{(s-t)/T_L}\,\mathrm{d}\xi_s \quad . \tag{2.72}$$

It then follows (Legg and Raupach, 1982) that for an ensemble average over a set of independent particle releases, $w = \overline{w} + w'$ and

$$\overline{w}(t) \;=\; \overline{w}(0)\,e^{-t/T_L} \quad , \tag{2.73}$$

$$\overline{w'^2}(t) \;=\; \overline{w'^2}(0)\,e^{-2t/T_L} + \frac{1}{2}T_L a_2(1 - e^{-2t/T_L}) \quad , \tag{2.74}$$

and

$$T_L = \int_0^\infty \frac{\overline{w'(0)w'(t)}}{\overline{w'^2(0)}}\,\mathrm{d}t \quad . \tag{2.75}$$

---

[84] Marked, that is, by the initial condition that each particle passed through level $z = z_s$ at time t= 0 with a velocity $w(0)$ drawn from a known statistical distribution.

Based on physical reasoning, we would expect that the initial particle vertical velocity distribution, $w(0)$, whatever form it may have had, will be replaced for $t \gg T_L$ by the vertical velocity distribution of the background turbulent flow, since particles will lose their 'memory' of their initial velocities. Borrowing from the terminology of Brownian motion, de Baas (1988) referred to this asymptotic condition as "thermal equilibrium", meaning simply that the mean velocity variance of the (very large) set of marked fluid particles will eventually equal the mean velocity variance of the overall turbulent fluid.

It can be seen from Eqs. 2.73 and 2.74 that for large times $\overline{w}(t) \rightarrow 0$ and $\overline{w'^2}(t) \rightarrow T_L a_2/2$. It then follows from the thermal-equilibrium assumption and from the assumptions of statistical stationarity and homogeneity (since it will not then matter when or where the particles were released) that the constant a_2 in Eq. 2.70 will have the value $2\overline{u_3^2}/T_L$, where $\overline{u_3^2}$ is the *Eulerian* vertical velocity variance for the background turbulent flow (e.g., van Dop et al., 1985; de Baas, 1986). The magnitude of the diffusion coefficient a_2 reflects the strength of the diffusion due to the parameterized effects of unresolved subgrid-scale atmospheric motions. Such diffusion is thus modelled to be directly proportional in magnitude to the turbulence intensity of the flow (i.e., $\overline{u_3^2}$) and indirectly proportional to the timescale of a particle's 'memory' (i.e., T_L).

Generalized Langevin equation. Now consider the more general case of a horizontally homogeneous but *unsteady* and *vertically inhomogeneous* turbulent flow. The inhomogeneous Langevin equation can be written as

$$\mathrm{d}w = \left(-\frac{w}{T_L(z,t)} + a_1(z,t)\right)dt + a_2^{1/2}(z,t)\,\mathrm{d}\xi_t \quad . \tag{2.76}$$

Coefficient a_1 is the drift acceleration[85] as will become apparent shortly; it had a zero value in the case of stationary, homogeneous turbulence.

Unlike Eq. 2.70, the three coefficients T_L, a_1, and a_2 in Eq. 2.76 may vary in both time and space. One very important consequence is that even if the turbulence

---

[85] Not drift velocity since it acts on the acceleration dw and not on the velocity w.

is stationary, the stochastic process w will not be since its moments will depend on its position and hence may change with time. Similarly, Durbin (1983) has suggested that for inhomogeneous turbulence, T_L should be interpreted as the instantaneous decorrelation time scale shown in Eq. 2.77.

$$T_L = \left| \frac{1}{R(t,\tau)} \frac{\mathrm{d}R(t,\tau)}{\mathrm{d}\tau} \right|^{-1}_{\tau=0} \tag{2.77}$$

The reason for this different interpretation is that "an integral time scale is neither clearly defined nor a property of the turbulence" (Durbin, 1983, p. 53). Eq. 2.77, on the other hand, defines a *local* property of the flow. The first and second moments of dw for Eq. 2.76 are (de Baas, 1988)

$$\overline{dw} = \left(-\frac{w}{T_L} + a_1 \right) \mathrm{d}t \quad , \tag{2.78}$$

$$\overline{dw^2} = a_2 \, \mathrm{d}t \quad , \tag{2.79}$$

respectively.

Now how is a_1 defined? One striking characteristic of particle dispersion in a vertically inhomogeneous flow is that the mean particle acceleration is *not* necessarily equal to the mean flow accelleration (van Dop et al., 1985). That is, not all of the velocity characteristics of an ensemble of independent particles will be the same as those of the background turbulent flow in which the particles are moving. To see this, consider the standard Reynolds decomposition for the flow field; let u_i denote the instantaneous Eulerian velocity, let U_i denote the ensemble average[86] of this vector, i.e., $\overline{u_i}$, and let u_i' denote the instantaneous fluctuation from this mean so that $u_i = U_i + u_i'$. The vertical acceleration of a particle or marked fluid element $\mathrm{d}w/\mathrm{d}t$ at a particular point will be equal to the acceleration induced by the local Eulerian vertical velocity component u_3 at that same point:

---

[86] Not an ensemble average over Lagrangian particles but rather over an infinite set of flow realizations with identical external conditions.

$$\frac{\mathrm{d}w}{\mathrm{d}t} \equiv \frac{\mathrm{d}\tilde{u}_3}{\mathrm{d}t} = \frac{\partial \tilde{u}_3}{\partial t} + \tilde{u}_i \frac{\partial \tilde{u}_3}{\partial x_i} \quad . \tag{2.80}$$

Let us now decompose u_i into mean and fluctuating quantities U_i and u_i' in Eq. 2.80 and then take a *conditioned* ensemble average, denoted by $< \ >$, over an infinite set of flow realizations where in each realization a single particle has been released from some point at some time, possibly varying from realization to realization. If at time t the particle is located at height z, we obtain[87] the equation

$$< \frac{\mathrm{d}w}{\mathrm{d}t} >= \frac{\mathrm{d}U_3}{\mathrm{d}t} + \frac{\partial}{\partial x_i} \overline{u_i' u_3'} \quad , \tag{2.81}$$

where

$$\frac{\mathrm{d}U_3}{\mathrm{d}t} = \frac{\partial U_3}{\partial t} + U_i \frac{\partial U_3}{\partial x_i} \tag{2.82}$$

and we have used the continuity equation

$$\frac{\partial \tilde{u}_i}{\partial x_i} = 0 \quad . \tag{2.83}$$

Thus, even if dU_3/dt is equal to zero (i.e., no mean vertical flow acceleration), there may still be a mean acceleration over the ensemble of particles at height z if the turbulence field is inhomogeneous. Finally, if we assume that the turbulence is only inhomogeneous in the z-direction, it follows from Eq. 2.81 that the drift acceleration a_1 is given by the expression (van Dop et al., 1985)

$$a_1 = \frac{\partial}{\partial z} \overline{u_3^2} \quad . \tag{2.84}$$

Physically, particles moving into a layer with larger $\overline{u_3^2}$ tend to acquire larger velocity fluctuations and hence will disperse more quickly. This in turn generates a mean

---

[87] If we also assume that the Eulerian ensemble averages of flow quantities for this subensemble of realizations are the same as for the full ensemble.

acceleration up-gradient into this more turbulent layer since more particles will be located outside the region and hence an ensemble average over a set of particles at a particular height will be weighted by the more numerous particles in lower-energy regions moving into the higher-energy layer. Hunt (1982, p. 241) explained it this way: "Think of marking the edges of an agitated region of fluid; the marked elements move preferentially into the agitated region, even if there is no mean flow in that direction." If this drift acceleration term is not present, then particles will tend to collect in low-turbulence regions, a persistent problem in early LPDMs which did not include such a term (e.g., McNider, 1981; Hanna, 1982). Legg and Raupach (1983) suggested that the role of the drift acceleration in a Lagrangian framework was equivalent in an Eulerian framework to a pressure gradient force from low- to high-turbulence regions.

Gradients in T_L cause similar behaviour. The velocity of particles moving into regions in which T_L is larger maintain their direction of motion longer on average than particles moving into a region of smaller T_L. This is dispersive since particles will then tend to continue out of the region, resulting in a mean acceleration into these regions of larger T_L (Durbin, 1983; de Baas, 1988). The effect of such height variations in T_L is handled implicitly in Eq. 2.76 in the 'friction' term $T_L^{-1}w$. Durbin (1983, P. 64) noted that gradients in T_L constitute a higher-order (i.e., less significant) effect than gradients in $\overline{u_3^2}$, essentially because Eq. 2.76 is linear in T_L but quadratic in σ_z (through a_1). Legg and Raupach (1982) noted that inhomogeneities in T_L can be handled in a discrete formulation (see below) with a constant time step if the time step used is small enough that T_L does not vary significantly over one time step.

Discrete formulation. The preceding discussion dealt with continuous stochastic processes. A discrete form of Eq. 2.76 can also be integrated in time using finite-difference approximations (e.g., de Baas, 1988):

$$w_{i+1} = e^{-\Delta t/T_L} w_i + (1 - e^{-\Delta t/T_L}) T_L \frac{\mathrm{d}}{\mathrm{d}z}\sigma_w^2 + (1 - e^{-2\Delta t/T_L})^{1/2} \sigma_w r_i \quad , \qquad (2.85)$$

where r_i is a random variate from an $N(0,1)$ distribution and $\sigma_w^2 = \overline{u_3^2}$. To first order in Δt, Eq. 2.85 is equal to

$$\mathrm{d}w = -\frac{w}{T_L}dt + \frac{\mathrm{d}\sigma_w^2}{\mathrm{d}z}dt + \left(\frac{2\sigma_w^2}{T_L}\right)^{1/2}\mathrm{d}\xi_t \quad . \tag{2.86}$$

Note that the Lagrangian autocorrelation function has been assumed to have the form

$$R_L(t) = e^{-t/T_L} \tag{2.87}$$

so that the factor $e^{-\Delta t/T_L}$ corresponds to $R_L(\Delta t)$.

Application to the mesoscale.

Mesoscale LPDMs have generally used the coupled, single-particle Markov-chain equations

$$X_i(t+\Delta t) = X_i(t) + [u_i(t) + u_i'(t)]\Delta t \quad , \quad i = 1,2,3 \tag{2.88}$$

$$u_i'(t) = u_i'(t-\Delta t)R_i(\Delta t) + u_i''(t) + w_c(t)\delta_{i3} \quad , \quad i = 1,2,3, \tag{2.89}$$

to determine the position of each of the independent virtual tracer particles, where $X_i(t)$ is the i-th component of the particle location at time t, Δt is the time step, and $u_i(t)$ is the i-th component of the resolvable or grid-scale wind vector at time (t) and location $X_i(t)$. $u_i'(t)$ is a turbulent velocity fluctuation component determined by means of the discrete Langevin equation (Eq. 2.89), where $R_i(\Delta t)$ is the i-th velocity component Lagrangian autocorrelation coefficient for lag Δt (see Eq. 2.87), and $u_i''(t)$ is a random, normally-distributed turbulent component which is independent of $u_i'(t)$. From Eq. 2.85, $u_i''(t)$ has the form $(1 - R_i^2(\Delta t)^{1/2}\sigma_w$. Term $w_c(t)$ in the vertical velocity component equation is the so-called drift correction. From Eq. 2.85, it can be seen to have the form $R_i(\Delta t)T_L\,\mathrm{d}\sigma_w^2/\mathrm{d}z$.

If $w_c(t)$ is uniformly zero, then Eqs. 2.88 and 2.89 are appropriate for homogeneous, stationary turbulence. In the real boundary layer, however, a particle moving

away from the ground experiences motions with longer Lagrangian time scales and varying turbulent energy. Legg and Raupach (1982) introduced the drift correction term as a way of dealing with the model-predicted but unrealistic accumulation of particles in low-turbulent-energy flow zones. Since then, a number of papers have explored the appropriate formulation of Eq. 2.89 for inhomogeneous and nonstationary turbulence (Wilson et al., 1983; Ley and Thomson, 1983; Thomson, 1984, 1986a, 1987; van Dop et al., 1985; de Baas et al., 1986; Sawford and Guest, 1987, 1988; Luhar and Britter, 1989). The preferred form for $w_c(t)$ is still under debate but some combination of terms based on higher-order turbulence moments and their temporal and spatial derivatives are required for an accurate treatment of inhomogeneous, nonstationary turbulence.

Several studies have pointed out practical difficulties with some proposed forms of $w_c(t)$, however. First, some of the required statistical quantities (e.g., third-order velocity moments) may not be available from either observations or model predictions (Brusasca et al., 1989). Second, accurate treatment of some of these quantities may require very small model time steps to be used (Hurley and Physick, 1990). The primary constraint on the time step Δt used in an LPDM is that it be considerably smaller than the Lagrangian integral time scale T_L (e.g., Hall, 1975; Legg and Raupach, 1982; Wilson and Zhuang, 1989). However, in mesoscale applications where particles may have to be tracked for days, computational cost will be sensitive to the choice of Δt and tradeoffs may have to be made between inaccuracies in the trajectory calculations and the number of particles released and followed. Note that if Δt is set to a value much larger than T_L, then the Langevin stochastic model reduces to a true random-walk model where velocity is treated as white noise and has no memory (e.g., Hall, 1975). This is equivalent to the Eulerian K-theory model (Durbin, 1983).

Several groups have in fact tried to reduce computational costs by using such a random-walk model, where particle *displacement* is considered to be a stochastic process rather than particle velocity (e.g., Runchal, 1980; Shi et al., 1990; Uliasz and Pielke, 1991). This approach involves more assumptions but may be satisfactory in some

cases for mesoscale studies and does permit much longer time steps to be used in the particle trajectory calculations. For example, Shi et al. (1990) used 900-second time steps, orders of magnitude larger than the 10–20 second time steps commonly employed in LPDMs.

Velocity component covariances.

Eq. 2.88 is written very generally in that turbulent diffusion is considered in all three flow directions. In practice, cross-stream and streamwise diffusion are often neglected and only vertical diffusion is considered. However, a number of investigators have treated the more general case, including velocity covariance terms (Ley, 1982; Davis, 1983; Legg, 1983; Ley and Thomson, 1983; Zannetti, 1984, 1986; Thomson, 1986a). Longitudinal velocity variations tend to have a small but not insignificant effect (5–10%) in the near field (Davis, 1983; Legg, 1983) but their importance at longer distances has not been evaluated.

Fig. 2.35 shows particle plumes from a fumigation simulation in a coastal environment using the Mesoscale Dispersion Modeling System (MDMS) of Uliasz (1990a). Three variants of turbulent diffusion parameterizations of increasing complexity were used: I – only vertical diffusion of particles; II – both vertical and horizontal diffusion (Eq. 2.89); III – vertical and horizontal diffusion including velocity component covariances (Zannetti, 1984). In the near field, use of Scheme I results in a narrower plume than the other two schemes but this difference decreases with travel time. The turbulent velocity covariances appear to contribute little for this case.

Meteorological input fields.

One very important but frequently overlooked aspect of LPDMs is the method by which meteorological information is supplied. Many of the assumptions and approximations underlying LPDMs arise in this step. As Lagrangian models, LPDMs require Lagrangian meteorological inputs which are seldom available. However, such quantities may be estimated from Eulerian measurements if certain simplifying assumptions are

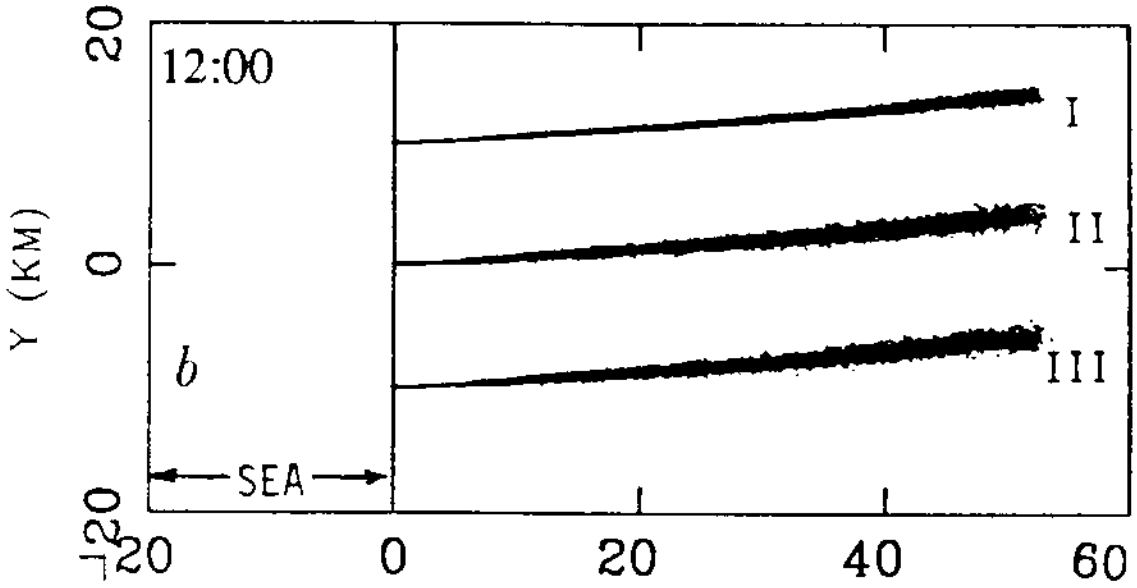

Figure 2.35: Comparison of plan views of three particle plumes from a coastal zone fumigation simulation using three different turbulence parameterizations: (a) Scheme I — vertical diffusion only; (b) Scheme II — both vertical and horizontal diffusion; (c) Scheme III — full three-dimensional diffusion, including covariance terms (from Pielke et al., 1991).

made. The most fundamental of these is that particles are fully caught up in the mean flow so that a particle's deterministic velocity can be interpolated based on its position within the mean flow field. Second, particle turbulent velocity variances and covariances are assumed to be equal to the local Eulerian values, e.g., $< W^2 >= \sigma_w^2 = \sigma_{wE}^2$, although this relation does not always hold (Legg, 1983; Sawford, 1985). Third, various expressions are assumed for the Lagrangian integral time scales T_{Lu}, T_{Lv}, and T_{Lw}, often in terms of the Eulerian integral time scales T_{Eu}, T_{Ev}, and T_{Ew} (Hanna, 1981; Davis, 1983; Legg, 1983; Sawford, 1985; McNider et al., 1988). Fourth, a functional form must be assumed for the Lagrangian autocorrelation functions $R_{Lu}(\Delta t)$, $R_{Lv}(\Delta t)$, and $R_{Lw}(\Delta t)$ (Durbin, 1983; Sawford, 1985). Fifth, when mesoscale models are used to supply meteorological input to the LPDM, expressions for such Eulerian turbulence quantities as σ_{wE}^2 and T_{Ew} must be constructed in a fashion consistent with the turbulence parameterization employed by the mesoscale model, including level of parameterization

complexity (first-order, second-order) and averaging type (ensemble, volume) (e.g., McNider et al., 1988; Uliasz, 1990a).

Other processes.

Most LPDMs to date have assumed that the Lagrangian particles are passive and nonbuoyant but several investigators have considered buoyant particles (Cogan, 1985; Schorling et al., 1986; Gaffen et al., 1987; Walklate, 1987; Wilson et al., 1988). Applications include LPDM simulations of crop spraying, cooling tower plume dispersal, heavy gas dispersion, dry deposition, and battlefield visibility. As has been reported for other regional-scale and long-range transport models (e.g., Kuo et al., 1985; Martin et al., 1987), LPDMs are sensitive to the value of large-scale vertical velocity imposed. Uliasz (1990b) has presented results from one such sensitivity test using three different large-scale vertical velocities which clearly showed this dependence.

Estimation of concentration.

Several approaches have been employed to estimate ensemble-mean concentration fields based on particle positions. The simplest is to count the number of particles in a sampling volume to arrive at a particle number density or to weight the particles by their mass and obtain a mass density (i.e., concentration). This cell-average approach has several weaknesses. First, there is the question of what size the sampling volume should be. If the size of the sampling volume is too small, the resulting concentration estimates become too noisy as a result of random sampling fluctuations. If the size of the sampling volume is too large, then the concentration distribution is oversmoothed and significant smaller-scale features may be lost. Lamb (1982) and Davis (1983) have suggested several approaches to this problem. Second, the cell-average method is discrete in the sense that the concentration estimate is implicitly assumed to be constant everywhere within the sampling volume rather than varying smoothly with position.

A new approach which makes use of a statistical technique called kernel density estimation (KDE) has been applied to this concentration estimation problem (Lorimer,

1986; Lorimer and Ross, 1986; Yamada and Bunker, 1988). The kernel density estimation technique overcomes the two weaknesses of the cell-average approach just mentioned and may require fewer tracer particles to make equally accurate concentration estimates (Grossman, 1989). It also provides a firmer statistical foundation on which to calculate estimation error bounds. However, influence bandwidths must be specified for this technique, and these present much the same problem as the specification of sampling volume mentioned above, especially for continuous plume releases where the particle distribution is elongated (Uliasz, 1990b). Pielke et al. (1991) have shown a comparison of four different KDE implementations for an idealized fumigation case. Choice of bandwidth can lead to oversmoothed or undersmoothed concentration estimates in analogy to the choice of cell size in the simple cell-average approach.

2.3.5 Two-dimensional dispersion

As discussed in Sec. 2.1, large-scale atmospheric flows are quasi-horizontal, suggesting that the kinematics of large-scale mixing will be more two- than three-dimensional. Vertical shear processes will only be a factor to the extent that they enhance the effective lateral diffusivity, although shear may still play a direct role through the interaction of lateral shear with lateral diffusion (e.g., Okubo, 1966). Moreover, as discussed in Sec. 2.1, large-scale atmospheric energy spectra can have quite a different form than microscale energy spectra. Eq. 2.48 showed the connection between absolute particle dispersion and the turbulent energy spectrum for stationary, homogeneous turbulence. It might be expected, then, that dispersion in a two-dimensional or quasi-two-dimensional flow may behave differently than dispersion in a three-dimensional flow.

Kao (1962, 1965, 1974) used some of the tools of small-scale turbulent diffusion, namely Eulerian and Lagrangian autocorrelations and energy spectra, to consider diffusion by large-scale atmospheric motions. He found that large-scale atmospheric flow on the synoptic scale and larger is anisotropic and that large-scale wave motion is strongly dispersive. He also concluded that Richardson's 4/3 power law does not generally apply to large-scale relative diffusion. Other early studies of large-scale diffusion include

Edinger and Rapp (1957), Kao and Bullock (1964), Mesinger (1965), Kao and al-Gain (1968), Murgatroyd (1969), Kao and Hill (1970), and Kao et al. (1976).

Lin (1972) considered relative diffusion in the k^{-3} enstrophy-cascading inertial range (see Sec. 2.1.2). Following the dimensional analysis of Obukhov for the small-scale energy-cascading inertial range, Lin obtained the relation that the mean-square dispersion grows *exponentially* in time compared to the t^3 dependence found in the small-scale inertial range (see Sec. 2.3.2). Observations of the rate of separation of constant-volume balloon pairs in the upper troposphere from the Eole experiment (Morel and Larcheveque, 1974) and TWERL Experiment (Er-El and Peskin, 1981) offer support for this relation. Carras and Williams (1988) analyzed Australian long-range measurements of plume relative σ_y's for travel times greater than 20 h in this framework. A reasonable if inconclusive fit was obtained.

Gifford (1988) and Gifford et al. (1988) discussed observations taken during a very-long-range tracer experiment carried out in the Antarctic in 1984 with deuterated methane. Measured ground-level tracer concentrations began to show an exponential decay in tracer concentration with time after four or five days of travel. This behaviour is somewhat surprising since two-dimensional motions quickly distort and deform diffusing clouds but conserve cloud area (e.g., Fig. 1.5). Gifford and his co-workers offered the phenomenological explanation that the large-scale, enstrophy-cascading motions draw a cloud out into long filaments so that cloud length grows exponentially. At the same time, cloud width contracts in response to the elongation in order to conserve area but also increases due to horizontal diffusion caused by smaller-scale motions. According to their argument, the net result is that the combination of exponential elongation and constant diffusion produces an exponential growth in cloud area and corresponding dilution in tracer concentration.

Other studies of the diffusion of passive scalars in two-dimensional and geostrophic turbulence include Garrett (1983), Haidvogel and Keffer (1984), Holloway and Kristmannsson (1984), Lesieur and Herring (1985), Sadourny (1986), Babiano et al. (1985,

1990), , and Bartello and Holloway (1991). See Lesieur (1990) for a recent review of this subject.

Gifford (1982) proposed a Lagrangian-dynamical theory of horizontal diffusion based on Langevin's equation that he referred to as the 'random force' theory. An important component of this theory is that an appropriate outer scale for atmospheric turbulence is the inertial period f^{-1} (e.g., Gifford, 1989b). Although subject to some questions (e.g., Smith, 1983; Sawford, 1984), this theory or components of it have been applied with apparent success to studies of mesoscale and large-scale atmospheric diffusion (e.g., Gifford, 1984; Barr and Gifford, 1987; Gifford et al., 1988; Mikkelsen et al., 1988). Hanna (1982) observed that this theory is appropriate for larger-scale averages and very long sampling times (e.g., several days or more) due to the assumptions made in selecting the Lagrangian time scale T_L of the model. See the above references for more details.

2.4 Numerical Studies of Mesoscale Atmospheric Dispersion

According to Fox and Fairobent (1981; p. 219), numerical air quality models are at best "an abstraction of reality, based on a limited understanding of the complex physical and chemical processes involved in the dispersion and possible transformation of pollutants". On the other hand, numerical air quality models are also predictive tools which (at least in some cases) combine the best available mathematical parameterizations of physical and chemical processes in a general, unified, flexible package. As such they can be used to test hypotheses, fill in gaps between observations, help to interpret data, evaluate the consequences of various 'what if' scenarios, and give guidance to the design and assessment of observing programs, making them important tools in air quality studies, environmental impact assessments, and environmental policy development and decision-making.

2.4.1 Types of mesoscale air quality models

Numerical modelling studies of mesoscale atmospheric dispersion have a short history. Numerical air quality models which considered atmospheric transport and diffusion over

mesoscale space and time scales were not developed until the mid 1970s, when interest began to grow in the long-range[88] transport of air pollutants (LRTAP) due to concerns over the occurrence of 'acid rain' and regional ozone episodes in North America and Europe. Despite this late start, LRTAP models have proliferated rapidly. Bass (1980) listed 21 LRTAP models, Pasquill and Smith (1983) discussed and compared 28 LRTAP models, and more recently, Thomson et al. (1987) listed 90 such models.

MAD and LRTAP models are based on a range of different approaches but may be divided on the basis of their prediction period length and chosen coordinate system into four broad groupings : (i) *long-term Eulerian* models; (ii) *long-term Lagrangian* models; (iii) *episodic Eulerian* models; and (iv) *episodic Lagrangian* models. All of these models, however, are based simply on the conservation-of-mass equations[89] for one or more pollutant species (e.g., Eliassen, 1980; Knox and Walton, 1984) and must represent or deal with the four primary terms of the (Reynolds-averaged) conservation-of-mass equation — mass sources, advection, diffusion, and mass sinks — in some fashion. In one sense, however, LRTAP modelling is more demanding than smaller-scale atmospheric dispersion modelling since slow-acting physical processes such as dry deposition, wet deposition, and chemical transformations may have to be considered due to the longer transport times involved.

Long-term models are intended to predict long-term (e.g., seasonal and annual) mean concentration and deposition patterns. They often make use of long-term average wind fields rather than instantaneous wind fields to calculate long-term pollutant transport and deposition. In some long-term LRTAP models, for example, a single wind rose may be used to describe the transport wind field (e.g., Fisher, 1975; Clark et al., 1989). *Episodic* models, on the other hand, predict time-dependent concentration and deposition fields resulting from the transport and diffusion of pollutant releases over a one- or two-

---

[88] Usually implying meso-α- or regional-scale distances.

[89] Also referred to as 'mass balance', 'continuity', or 'advection–diffusion' equations.

day period. They use either objectively analyzed wind fields based on available hourly, six-hourly, or twelve-hourly meteorological observations or meteorological-model-derived prognostic wind fields to predict mesoscale transport. As a rule, episodic LRTAP models require much more detailed meteorological data than do long-term LRTAP models.

Eulerian models calculate pollutant concentrations within a fixed two-dimensional or three-dimensional grid and apportion the pollutant mass amongst various grid boxes (e.g., NCAR, 1983; Brost et al., 1988b; Venkatram et al., 1988). *Lagrangian* models, on the other hand, calculate numerous trajectories or travel paths for either individual, independent pollutant 'particles' or 'puffs' or for consecutive plume 'segments' that have been emitted from one or more sources. Overall concentration fields can then be obtained either by calculating particle-position density fields or by adding up the individual puff concentration fields.

As already mentioned (Sec. 2.3.4), Lagrangian particle models and Lagrangian puff or plume models are quite different. Lagrangian particle models use zero-dimensional (i.e., point) particles which can move in all three spatial directions while most Lagrangian puff models (also known as Lagrangian trajectory models) use finite-volume puffs which are advected by a two-dimensional[90] wind field and grow horizontally in time according to an empirical or semi-empirical formula (e.g., Draxler, 1987; Carhart et al., 1989). A few models, such as the particle-in-cell models (e.g., Lange, 1978; Lee, 1987; Rodriguez, 1988), are hybrid Eulerian–Lagrangian approaches.

Useful reviews of mesoscale and long-range air quality models may be found in Bass (1980), Eliassen (1980), Fisher (1983), Johnson (1983), NCAR (1983), and Pasquill and Smith (1983). In addition, Pack et al. (1978) and Smith and Hunt (1978) have discussed some meteorological aspects of LRTAP and Demerjian (1985, 1986) has summarized some sources of error and uncertainty in current LRTAP models.

---

[90] As will be discussed shortly, some Lagrangian puff models do consider vertical shear and a few (e.g., Draxler, 1987; Martin et al., 1987) consider synoptic-scale vertical motions.

2.4.2 Characteristics of mesoscale air quality models

Most long-term LRTAP models are at best only useful for estimating mean concentration fields for long-duration releases. Episodic models may also be used for estimating long-term concentration fields by carrying out simulations of many consecutive episodes, but their much higher computer requirements have made such applications impractical up to the present. Instead, episodic LRTAP models are normally used for studying severe, short-term episodes. In medical terms, long-term models are appropriate for treating *chronic* air pollution problems while episodic models are suitable for *acute* air pollution problems.

An Eulerian model adopts a fixed frame of reference, usually the surface of the Earth, while a Lagrangian model employs a moving frame of reference, usually that of an air parcel of interest. From a purely theoretical viewpoint, these two approaches are equivalent if physical parameterizations are not considered (NCAR, 1983). The Lagrangian framework has the significant advantage that no advection terms need to be considered in the mass conservation equations for any atmospheric species. In contrast, the treatment of advection in Eulerian models usually introduces artificial numerical diffusion and, sometimes, spurious oscillatory behaviour, a problem when advecting nonnegative physical quantities such as concentrations (Eliassen, 1980; NCAR, 1983). However, geographically-fixed processes such as mass sources and sinks are better represented in an Eulerian framework.

In addition, Lagrangian puff models usually ignore entrainment, cloud venting, and other mixing effects with the ambient environment, and they cannot accommodate nonlinear chemistry. Treatment of vertical wind shear and multiple pollutant sources in a Lagrangian puff model quickly becomes very complicated though this is *not* true in the case of a Lagrangian particle model. Eulerian models are thus better suited for complex simulations with three-dimensional advection and diffusion processes and nonlinear chemistry but are generally more computationally demanding, both in terms of computer CPU time and storage requirements (Eliassen, 1980; Johnson, 1983a). If a large number

of sources must be modelled, however, Eulerian models may be more efficient since their grid-point calculations are independent of the number of sources (e.g., van Egmond and Kesseboom, 1983b).

Eulerian air quality models must of necessity employ Reynolds-averaged mass continuity equations. Reynold averaging leads in turn to a hierarchical set of equations for the concentration moments $\overline{u_i^n c}$ due to the closure problem (e.g., Lamb, 1980, 1982; van Dop et al., 1985; Sawford, 1986; de Baas, 1988), although almost all Eulerian mesoscale dispersion models consider only the first statistical moment $\overline{c}$. K-theory dispersion models are the simplest of the Eulerian concentration-moment models[91] and have been widely used (e.g., van Egmond and Kesseboom, 1983a; van Dop and de Haan, 1984; Pudykiewicz et al., 1985b; Carmichael et al., 1986; Brost et al., 1988a; Venkatram et al., 1988; Piedelievre et al., 1990). They suffer from several limitations, however.

First, as already discussed in Sec. 2.3.4, use of the gradient-transfer hypothesis limits these models to time scales much larger than the turbulence integral time scale T_L and to pollutant spatial scales much larger than the turbulence integral spatial scales Λ_i (e.g., Corrsin, 1974; Pasquill and Smith, 1983). Second, the pollutant mass being modeled must have a spatial extent at the very least equal to four or more horizontal and vertical grid increments in order that gradients be adequately defined and advection phase errors minimized (Pielke, 1984; Avissar et al., 1990). Third, computational diffusion and Gibbs oscillations associated with the advection schemes used in these models make point and line sources particularly difficult to treat. A very few modelers have used higher-order Eulerian models in some simple applications (see Lamb, 1982; Pasquill and Smith, 1983).

Eulerian advection-diffusion models have been applied to urban-scale, meso-β-scale, and regional-scale air quality problems. More information on such applications may be found in Klug et al. (1985), Chang et al. (1987), Thomson et al. (1987), Dronamraju et al. (1988), and Venkatram et al. (1988), among many others, and several appli-

---

[91] They use the first-order gradient-transfer closure assumption $\overline{u_i c} = -K \frac{\partial \overline{c}}{\partial x_i}$.

cations of Eulerian advection-diffusion models to mesoscale tracer experiment simulation are described in the next chapter.

2.4.3 Wind-field specification

Most current LRTAP models employ quite coarse representations of atmospheric wind fields resolved on grids with horizontal grid intervals larger than 100 km. Almost all of these models *diagnose* the wind fields by means of various objective analyses of twice-daily observations from the upper-air synoptic observing network with its average station spacing of $\sim$ 400 km in the U.S. (e.g., Bass, 1980; Kuo et al., 1985; Kahl and Samson, 1986). Linear interpolation is generally used to obtain wind fields between the synoptic observing times. Thus, sub-synoptic flow features will not be resolved by these models in either space or time, and the LRTAP model predictions made based on these synoptic-scale meteorological fields will likely be poor in many meteorological situations (e.g., Bass, 1980; AMS/EPA, 1987; Kahl and Samson, 1988a). This problem is especially serious within the PBL and over complex terrain (e.g., Moran et al., 1990a).

Happily, this situation seems to be improving at last. There have been an increasing number of groups using three-dimensional, gridded meteorological fields produced by either research or operational prognostic numerical weather prediction (NWP) models as input to MAD or LRTAP models: the list includes McNider (1981), Pielke et al. (1983), and Segal et al. (1988); Mueller et al. (1983); Kuo et al. (1985) and Brost et al. (1988a,b); Pudykiewicz et al. (1985a,b); Chang et al. (1987); Kao and Yamada (1988); Venkatram et al. (1988); Chock and Kuo (1990); Piedelievre et al. (1990); Rolph and Draxler (1990); Uliasz (1990a,b); and Rodriguez and Cederwall (1991). Such *forecast* fields will have better spatial resolution and much better temporal resolution, will include more variables, and will possess intervariable thermodyamic and dynamic consistency amongst all of the fields. Due to inaccuracies in the initial fields and model imperfections, however, errors in the forecast fields will usually increase with time over the simulation period[92].

---

[92] Although such error growth is smaller in cases with strong surface forcing (e.g., Paegle et al., 1990).

While forecast error growth is unavoidable in an operational mode such as emergency response or field experiment management, in a 'hindcast' or research mode, archived meteorological observations may be available throughout the prediction period, not just at the beginning. Various four-dimensional data assimilation (4DDA) methods have been developed to incorporate 'current' meteorological observations throughout the NWP model's integration period so as to control error growth[93]. Some groups have recently begun to use 4DDA as a tool to provide the most accurate meteorological fields possible to MAD and LRTAP models for air quality research studies (Kao and Yamada, 1988; Yamada et al., 1989; Haagenson et al., 1990; Seaman, 1991; Seaman and Cole, 1991; Tanrikulu and Soong, 1991).

2.4.4 Treatment of shear processes

Many episodic LRTAP models, particularly Lagrangian puff and plume models and one-layer Eulerian grid models, have neglected vertical wind shear although a number of investigators have identified vertical shear as a major source of trajectory error, particularly for the transport of nighttime emissions (e.g., Smith and Hunt, 1978; Bass, 1980). It has been argued, however, that "if the Lagrangian models are reformulated to include all major effects of stratification within the air parcel, the advantages associated with their simple and elegant basic formulation is quickly lost and replaced by prohibitive complexity." (Demerjian, 1986, p. 189).

Nevertheless, the effect of wind shear on mesoscale pollutant dispersion has been incorporated to some degree in a few Lagrangian LRTAP models. Sheih (1978), Henmi (1980), Samson (1980), Bhumralkar et al. citeyearBhumralkarEA81, Draxler and Taylor (1982), Draxler (1987), and Davis et al. (1988) have all introduced a wind-shear parameterization into Lagrangian puff models by subdividing puffs vertically into two to six independent subpuffs at night to account for decoupling due to stratification and then

---

[93] This approach is consistent with many air quality modellers's perception of prognostic three-dimensional meteorological models as very sophisticated objective analysis schemes!

following each subpuff individually[94]. This strategem will account crudely for *delayed* shear dispersion from differential advection provided that wind fields with good resolution in both space and time are available.

However, as just discussed, most Lagrangian puff models to date have relied on diagnostic wind field models which can only produce gridded wind fields with synoptic space and time resolution (e.g., Kahl and Samson, 1986,1988a,b). *Simultaneous* shear dispersion is not treated by Lagrangian puff models. Lagrangian *particle* dispersion models, on the other hand, handle differential advection and both simultaneous and delayed vertical mixing directly by tracking individual virtual tracer particles, advecting them based on a resolved mean wind field, and treating subgrid-scale diffusion through a parameterization requiring knowledge of the turbulence field. Examples of this second approach include studies by Moran et al. (1987), Kao and Yamada (1988), McNider et al. (1988), Segal et al. (1988), and Shi et al. (1990).

Multi-level Eulerian MAD and LRTAP models represent the contribution of vertical wind shear and both simultaneous and delayed mixing through the interaction of advection terms and parameterized diffusion terms based on the resolved wind field. In all of these models, vertical resolution will dictate how well these models handle PBL shear effects.

To give one interesting example, Shi et al. (1990) reported good results for their simulations of three CAPTEX tracer releases with a simplified mesoscale LPDM (see Fig. 3.27). They used a fairly simple approach, employing objectively-analyzed wind fields derived from twice-daily rawinsonde data and a simplified random-walk dispersion model. Despite the coarse grid spacing (about 300 km) and time separation (12 h) of their input data, their model did include vertical shear explicitly, although vertical resolution was also coarse since vertical wind profiles were based on the objective analysis of mandatory pressure-level winds (i.e., 1000, 850, 700, 500, ... hPa). No parameterization of lateral diffusion was employed, or apparently needed, by their model, again suggesting the

---

[94] Note that this basic approach goes back at least as far as the model of Hage et al. (1967).

importance of shear-enhanced dispersion even if the nocturnal low-level jet and mesoscale terrain-forced circulations are only very crudely represented (e.g., Moran et al., 1991).

2.4.5 MAD and LRTAP model evaluations and intercomparisons

The evaluation and intercomparison of numerical air quality models is a complicated process, involving as it does widely varying model formulations and assumptions, the availability of comprehensive data sets, large personal and institutional investments of time and resources, and fragile egos. Nevertheless, such model intercomparisons are extremely valuable since they allow a side-by-side comparison of different modelling approaches and an objective and quantitative evaluation of model performance. Model developers can then identify deficiencies, modify algorithms and parameterizations, and improve model performance while the larger community gains information on model uncertainties, limitations, reliability, and credibility. Differences between model predictions and observations also provide a measure of our understanding of the problem being modelled (e.g., Clark et al., 1989).

A few such intercomparisons have been carried out to date for MAD and LRTAP models (see also Sec. 4.6). These studies may be separated into two groups, those based on tracers of opportunity such as oxides of sulfur and nitrogen for which a number of long-term operational monitoring networks exist and those based on formal but short-term mesoscale tracer experiments (Sec. 2.2). In the case of tracers of opportunity, obtaining emissions information is always a problem and model evaluation is hampered by uncertainties in the emissions inventories used. The use of mesoscale tracer experiment data sets, on the other hand, is usually restricted to comparisons of episodic air quality model performance for the idealized case of a single source.

Van Egmond and Kesseboom (1983b) compared hourly SO_2 concentration predictions made by an episodic Eulerian grid model and an episodic Lagrangian puff model over a 400 km by 400 km domain containing the Netherlands for one winter day. Observed hourly SO_2 concentrations were obtained from 100 Dutch monitoring stations. The Eulerian model grid size was 15 km, the same as the grid cell size used in the

SO_2 emissions inventory. Van Dop (1986) reported on a similar study over the same area in which predictions of hourly SO_2 made by three episodic Eulerian grid models and one episodic Lagrangian puff model were compared for three test days, a 'stagnant' day, a 'transport' day, and a 'precipitation' day. Derwent et al. (1989) recently described a third air quality model intercomparison study based on measurements of tracers of opportunity over the Netherlands. In that study, however, *annual* wet, dry, and total deposition budgets of SO_x, NO_y, and NH_x calculated by four *long-term* LRTAP models were compared against annual observations of these quantities in the Netherlands for two different years, 1980 and 1985. Clark et al. (1989) described the results of a similar North American study, the International Sulfur Deposition Model Experiment or ISDME. In ISDME, predictions of seasonal sulfur wet deposition made by 11 long-term LRTAP models were compared against observations of SO_2 and SO_4^{2-} wet deposition made across eastern North America during each season of 1980. This year was selected since it is the only year for which a detailed North American SO_x emissions inventory was available.

Ruff et al. (1985) and Bhumralkar (1986) compared three *episodic* LRTAP models, one Eulerian and two Lagrangian, for four of the seven intensive monthly observing periods carried out during the Sulfur Regional Experiment (SURE) in 1977 and 1978. The SURE program had unusually good temporal resolution: the sulfur emissions inventory accounted for variations with season, day of the week, and time of day, and three-hourly atmospheric concentrations of SO_2 and SO_4^{2-} were collected at 9 sites in eastern North America. One other intercomparison of episodic LRTAP models is a European effort currently underway to evaluate predictions made by 20 of these models against measurements made during the Chernobyl accident (van Dop, 1991).

Turning to mesoscale tracer experiments, Tesche et al. (1987) used meteorological and perfluorocarbon tracer data sets collected during the 1980 and 1981 ASCOT field experiments in the Geysers area of California to evaluate four episodic Eulerian dispersion models. The modelling domain of interest was roughly 20 km by 20 km. Weber et al. (1982) reported results from an operational evaluation of 17 simple MAD models

against measurements of Kr-85 activity made at 13 different sites within 140 km of the Savannah River Plant (SRP) during the period 1975–1977. Policastro et al. (1986a,b) and Carhart et al. (1989) compared simulations of eight episodic MAD models for two mesoscale tracer experiment data sets, one from the 1980 Great Plains experiment and a second containing measurements made during 15 separate Kr-85 releases at the Savannah River Plant in 1976 and 1977 (see Table 2.4). Concentration measurements were made up to 600 km from the release site in the Great Plains experiment[95] and up to 144 km from the SRP release site. Clark and Cohn (1990) used the extensive data base collected during the 66 tracer releases of the 1987 Across North America Tracer Experiment (ANATEX) to evaluate the performance of nine episodic Lagrangian and two episodic Eulerian LRTAP models. The ANATEX domain was 3000 km wide. In addition to these model intercomparison studies, a number of studies have evaluated the performance of individual MAD and LRTAP models against mesoscale tracer experiment data sets. Chap. 3 summarizes nine such studies for the Cross-Appalachian Tracer Experiment (CAPTEX). Other studies include Lange (1978), Draxler (1979, 1982, 1983, 1985, 1991), Fields et al. (1984), Andrén (1990b), and Haagenson et al. (1990).

2.5 Summary

Small-scale turbulent diffusion is governed by the kinematics, dynamics, and energetics of the ambient flow, and the same should be true of mesoscale atmospheric diffusion. Accordingly, mesoscale flow kinematics, dynamics, and energetics were reviewed in this chapter along with observational, theoretical, and numerical studies of mesoscale atmospheric dispersion. Aircraft and wind profiler measurements made over the past decade suggest that mesoscale energy in the free troposphere is distributed over a variety of flow modes, including internal gravity waves (IGWs), three-dimensional turbulence, quasi-

[95] The Great Plains experiment has also been modelled in this study and is described in considerable detail in Chap. 3.

horizontal vortical modes, and mesoscale and synoptic-scale circulations. A number of concepts from small-scale turbulence theory such as inertial ranges and Taylor's frozen-turbulence hypothesis also appear to have application on the mesoscale and larger scales, although the concept of turbulence must be broadened to include two-dimensional turbulence, geostrophic turbulence, and stratified (or mesoscale) turbulence.

A big difference between mesoscale and smaller-scale dynamics is the important role of buoyancy. At larger scales, the atmosphere must be considered as a normally stratified fluid in which neutral and unstable stratification is an anomaly. Due to stratification, internal gravity waves, which cannot even exist in neutral or unstably stratified fluids, are an important mesoscale flow mode and their presence must be considered in defining turbulence and dispersion on these scales. Another consequence of stratification is that characteristic horizontal space scales are much larger than the corresponding vertical space scales. As a result, two-dimensional turbulence and dispersion is a limiting case for atmospheric stratified turbulence and dispersion at the largest scales just as three-dimensional isotropic turbulence is the limiting case at the smallest scales. A very important concept from two-dimensional turbulence, one which seems to have relevance to a section of the mesoscale energy spectrum, is the idea of a downscale enstrophy inertial cascade as a result of the conservation of enstrophy as well as energy.

A number of theoretical, observational, and experimental studies of stratified fluid kinematics, dynamics, and energetics from the oceanographic and fluid dynamical literature were also reviewed in this chapter. Much work on oceanic turbulence and dispersion has relevance for atmospheric turbulent dispersion, including studies of turbulence intermittency, Kelvin-Helmholtz instabilities, IGW velocity spectra, vertical finestructure, vortical modes, and shear-enhanced dispersion. In fact, a model of the oceanic IGW spectrum has been used extensively to interpret atmospheric mesoscale energy spectra.

The second half of this chapter dealt with observational, theoretical, and numerical studies of mesoscale atmospheric dispersion. Mesoscale atmospheric dispersion (MAD) has been studied in the field by releasing and tracking both balloons and gaseous and

aerosol tracers and by observing 'tracers of opportunity' such as smoke plumes from industrial chimneys, volcanoes, and forest fires and accidental industrial releases. Formal MAD tracer experiments have the advantages that the strength, timing, and length of the release can be controlled, an optimum network of fixed and mobile samplers can be designed and deployed, and a rigorous sampling protocol can be implemented. However, MAD tracer experiments have only become feasible in the past few decades due primarily to the technological difficulties involved but also to their considerable logistical demands and expense. An ideal mesoscale tracer should be nontoxic, nonreactive and nondepositing, inexpensive to acquire and release, inexpensive to collect and analyze, detectable at very low concentrations, have low atmospheric background, and be dynamically passive. Two mesoscale tracer technologies (i.e., the tracer and its delivery, sampling, and analysis systems) which come close to meeting these demanding requirements are based respectively on the perfluorocarbon family and on two isotopes of methane. Table 2.4 provides a comprehensive summary of MAD experiments carried out to date. Two experiments from this table were then selected for use in the present study.

There have been relatively few theoretical studies specifically of mesoscale relative diffusion, although there have been attempts to apply concepts developed in the statistical theory of small-scale turbulent diffusion to the mesoscale case. The foundation of the small-scale theory of diffusion is G.I. Taylor's (1921) study of what he termed 'diffusion by continuous motions'. A major problem, however, is that Taylor's work applies only to diffusion in a statistically homogeneous, stationary turbulent flow[96], and mesoscale flows are neither homogeneous nor stationary. Despite this restriction, Taylor's theorem and related theory provides a very useful framework for considering such aspects of mesoscale dispersion as characteristic time and space scales, eddy diffusivities, meander, and filtering

---

[96] There have been some attempts to extend Taylor's theorem to the shear case by Corrsin (1953), Smith (1965), Hinze (1975), Venkatram (1988a), and Enger (1991).

This chapter concluded with a discussion of the numerical modelling of mesoscale atmospheric dispersion. The differences between long-term and episodic models, and between Lagrangian and Eulerian models, were discussed. The two approaches to the specification of wind fields by diagnosis and prognosis were reviewed too as was the treatment of shear processes in various models. Finally, the connected topics of evaluation and intercomparison of numerical air quality models were considered, and previous model intercomparisons of various types of air quality models were summarized.

Chapter 3

OBSERVATIONAL DATA SETS AND PREVIOUS STUDIES

It is a capital mistake to theorize before one has data.

Scandal in Bohemia, Sir Arthur Conan Doyle (1859-1930)

Mesoscale tracer releases from the 1980 Great Plains and the 1983 CAPTEX mesoscale dispersion experiments have been chosen as test cases for simulations with the CSU mesoscale atmospheric dispersion modelling system. The selection of these two releases was based on a number of criteria. First, both experiments are well documented, which makes model setup and evaluation much easier. Second, both releases have been used as test cases in other mesoscale dispersion modelling studies. This makes it possible to compare results from the CSU MAD modelling system against both observations *and* results from other models, providing insight into the impact of different numerical solution techniques, physical parameterizations, and temporal and spatial resolutions on model performance. Third, the combination of these two cases provides observations of lateral dispersionat downwind distances of 100, 300, 400, 500, 600, 700, 800, 900, 1000, and 1100 km. And fourth, both of these mesoscale tracer releases have characteristics which isolate specific aspects of mesoscale atmospheric dispersion. Each took place under quasi-steady, anticyclonic, warm-season synoptic conditions, a very favourable environment for terrain-forced mesoscale circulations (e.g., Pielke et al., 1987a; Moran et al., 1991). Synoptically-forced mesoscale circulations and organized convection, on the other hand,

had little effect on these releases. Such processes are often important but are beyond the scope of this study[97].

The 1980 Great Plains tracer experiment was conducted over fairly homogeneous, slightly sloping terrain[98] in the south-central United States, a region in which the nocturnal low-level jet is very common and very strong in the summer (e.g., Bonner, 1968; Bonner and Paegle, 1970). Although regional-scale slope flows were present (e.g., McNider and Pielke, 1981), the Great Plains release is valuable for examining the influence of mesoscale time scales in relative isolation from terrain effects. In contrast, Release 2 of the Cross-Appalachian Tracer Experiment was carried out in a region of mesoscale complex terrain, including mountains and large lakes. It thus allows examination of the effects of terrain-forced mesoscale circulations on mesoscale atmospheric dispersion.

The remainder of this chapter describes the designs, domains, instrumentation, sampling programs, and results of these two mesoscale tracer experiments in some detail and summarizes previous numerical modelling studies of each. The analysis of the experimental results includes a comparison with other mesoscale dispersion observations and the determination of a number of qualitative tracer-cloud characteristics for later use as evaluation criteria in Chaps. 5 and 6.

3.1 Great Plains Mesoscale Tracer Experiment

3.1.1 Experimental design

The Great Plains mesoscale tracer experiment was carried out in July 1980 by a number of research groups led by the Air Resources Laboratory (ARL) of the U.S. National Oceanic and Atmospheric Administration (NOAA) (Ferber et al., 1981;

---

[97] A recent intercomparison of LRTAP model simulations carried out for all 66 tracer releases from the 1987 ANATEX mesoscale dispersion experiment (see Table 2.4) found that model performances worsened when regional-scale flow was influenced by a frontal passage or extratropical cyclone (Clark and Cohn, 1990).

[98] Fig. 4.13 shows contour plots of terrain elevation for this region after different spatial filters have been applied.

Fowler and Barr, 1983). It was designed as a field demonstration of two newly-developed mesoscale tracer systems, a perfluorocarbon tracer system and a heavy-methane tracer system. Two perfluorocarbons, perfluoromethylcyclohexane (symbol PMCH; chemical formula C_7F_{14}) and perfluorodimethylcyclohexane (symbol PDCH; chemical formula C_8F_{16}), and two deuterated methanes, $^{12}CD_4$ (Me–20) and $^{13}CD_4$ (Me–21), were released simultaneously along with a more traditional tracer, sulphur hexafluoride (SF_6), from an open field at the National Severe Storms Laboratory (NSSL) at Norman, Oklahoma. Release height was approximately 1 m AGL. Releases of the five tracers began at 1900 GMT (or 1400 CDT) on July 8, 1980 and lasted for three hours. The tracer of primary interest in the present study is PMCH; a total of 192 kg ($\pm$4%) of this tracer was released at a nearly constant rate between 1900 and 2100 GMT (Ferber et al., 1981).

Tracer concentration measurements were made along two arcs of sequential[99] samplers, one located 100 km to the north of Norman and the other located 600[100] km to the north in Nebraska and Missouri (Fig. 3.1). Seventeen perfluorocarbon samplers were placed along the 100-km arc at 4 to 5 km intervals; these automated samplers each collected ten 45-minute samples beginning at 2100 GMT (1600 CDT) on July 8, two hours after the start of the release at NSSL. Thirty-eight perfluorocarbon samplers were deployed along the 600-km arc at roughly 22 km intervals; these sequential samplers were set to take 22 three-hour samples beginning at 0800 GMT (0300 CDT) on July 9, 13 hours after the start of the tracer release at NSSL. Whole-air samples were also collected for analysis by an aircraft along the 100-km and 600-km arcs, and six cryogenic samplers were operated along the 600-km arc to measure deuterated methane concentrations.

---

[99] That is, an unattended sampler capable of collecting a sequence of fixed-period samples.

[100] Actual station great-circle distances ranged from 568 to 627 km.

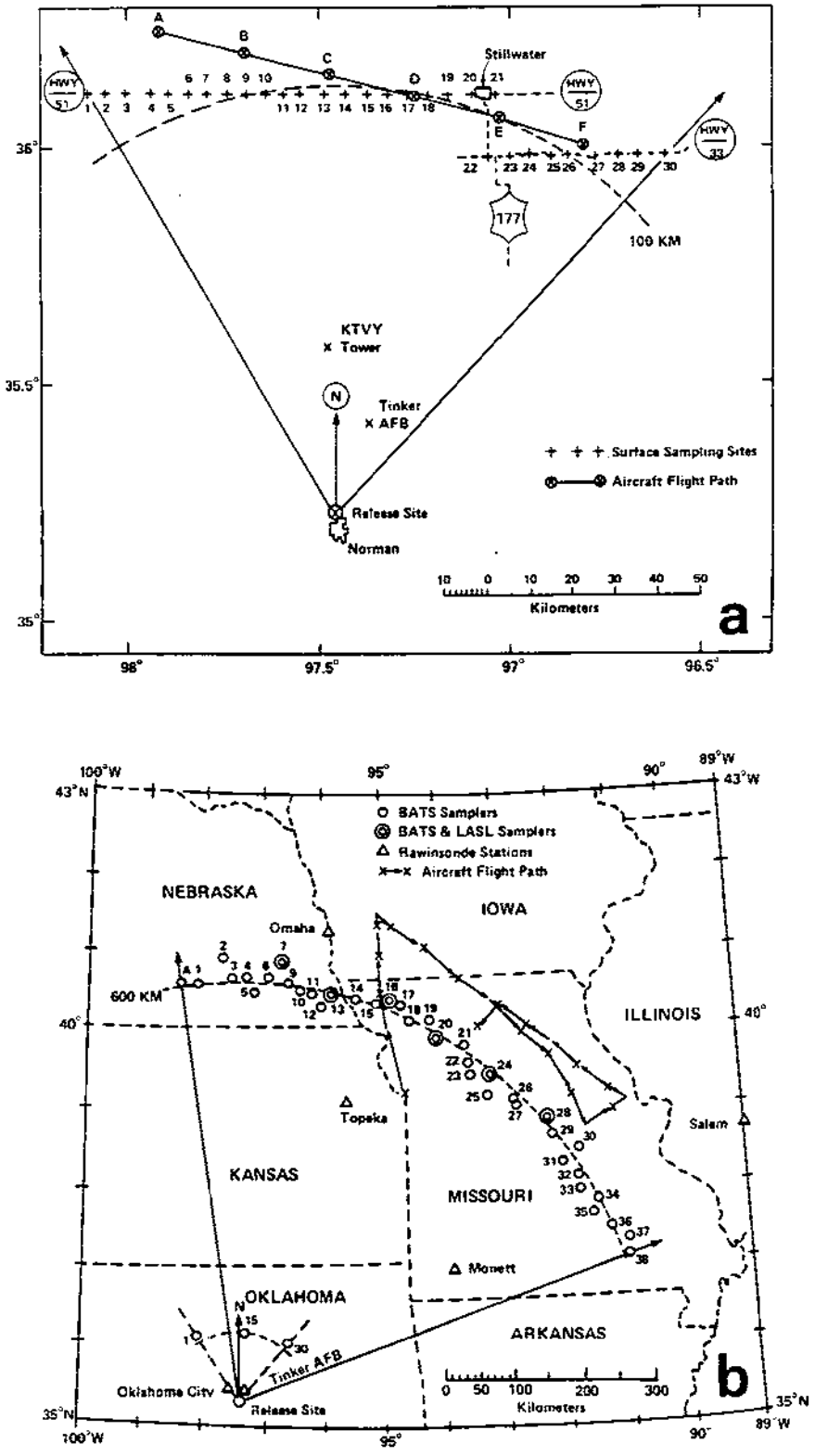

Figure 3.1: Location of perfluorocarbon sequential samplers and aircraft sampling tracks (a) 100 km north of the tracer release site at the National Severe Storms Laboratory, Norman, Oklahoma, and (b) 600 km north of the tracer release site (from Ferber et al., 1981).

3.1.2 Meteorological conditions

At the time of the tracer release, the state of Oklahoma lay under the backside of a broad area of high pressure centered over the southeastern United States, as indicated by the NMC-analyzed 850 and 500 hPa geopotential fields for this period (Figs. 3.2 and 3.3). In fact, this weather pattern was associated with a severe heat wave in the central U.S. during July 1980. Afternoon surface temperatures in the experiment domain generally rose over 38°C (100°F) during the entire period of the experiment (Ferber et al., 1981, p. 14). Fig. 3.4 shows this pattern and the associated surface winds in more detail. This figure was obtained by using the RAMS ISAN package (see Sec. 4.3) to blend the NMC gridded analysis shown in Fig. 3.2 with surface and upper-air station data.

The primary anticyclone over the south-central U.S. was quasi-stationary although a smaller secondary high-pressure system, which was located over South Dakota on July 8, moved eastward across the top of the domain during the experiment period. A west-to-east stationary front associated with a weak, eastward-moving low-pressure center was sandwiched just to the north of the 600-km arc of sampling stations between the two high-pressure systems (see Fig. 3.4). As a result, the large-scale low-level flow over Nebraska in the vicinity of the 600-km sampler arc did change significantly during the 24 h period covered by Figs. 3.2 and 3.3.

Figs. 3.5, 3.6, and 3.7 show the evolution of the low-level flow field for a 24 h period encompassing the tracer release and subsequent transport over the 100- and 600-km sampler arcs. Surface winds at Norman (marked with a letter 'N' on these figures) were south-southwesterly at 4 $m\,s^{-1}$ (see Fig. 4.9a) and the sky was clear during the tracer release on July 8 (Ferber et al., 1983). Further north, over Kansas and Missouri, the low-level flow veered[101] to southwesterly. The low-level convergence associated with the stationary front and the eastward movement of the weak surface low is evident in

[101] Rotated clockwise.

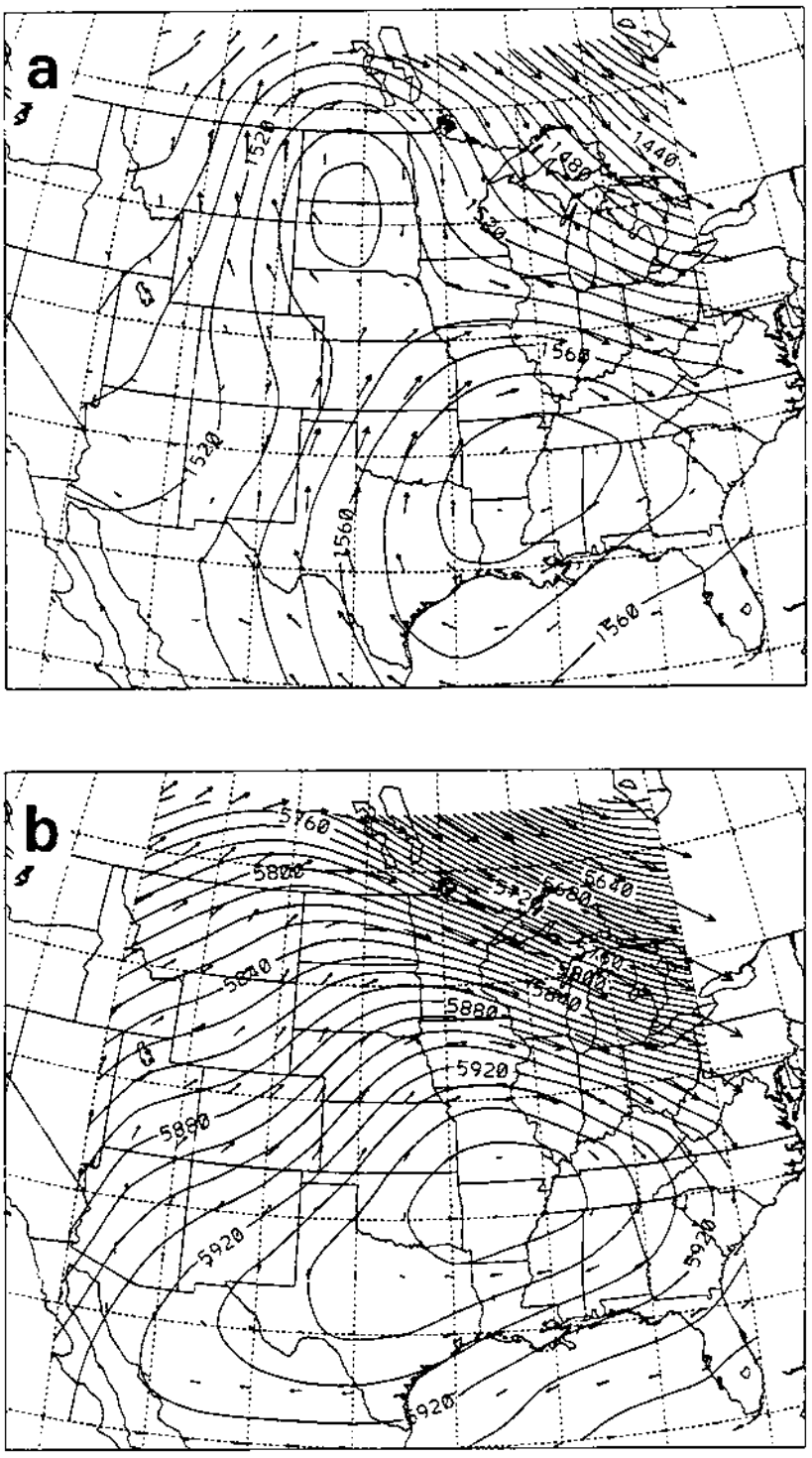

Figure 3.2: Vector winds and geopotential heights at 1200 GMT (0700 CDT), 8 July 1980 over the central United States at (a) 850 hPa and (b) 500 hPa on the NMC 2.5° by 2.5° grid. The geopotential contour interval is 10 m and the greatest wind speeds are 20.0 and 29.5 $\mathrm{m\,s^{-1}}$, respectively. Latitude and longitude lines are plotted every 5° from 125°W to 70°W and from 25°N to 50°N on this orthographic map projection.

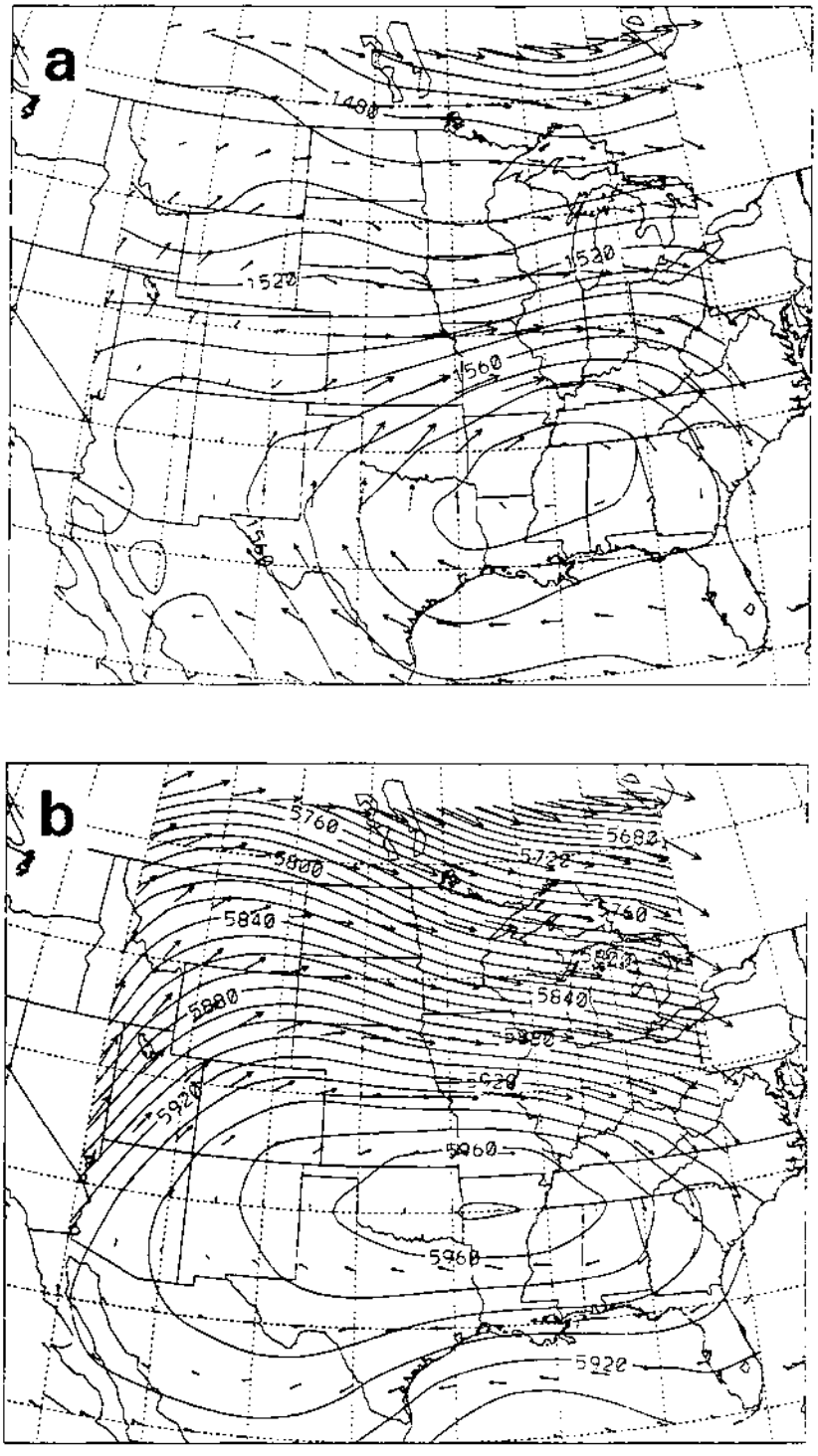

Figure 3.3: Same as Fig. 3.2 except for 1200 GMT, 9 July 1980. The greatest wind speeds are 15.4 and 26.4 $\mathrm{m\,s^{-1}}$, respectively.

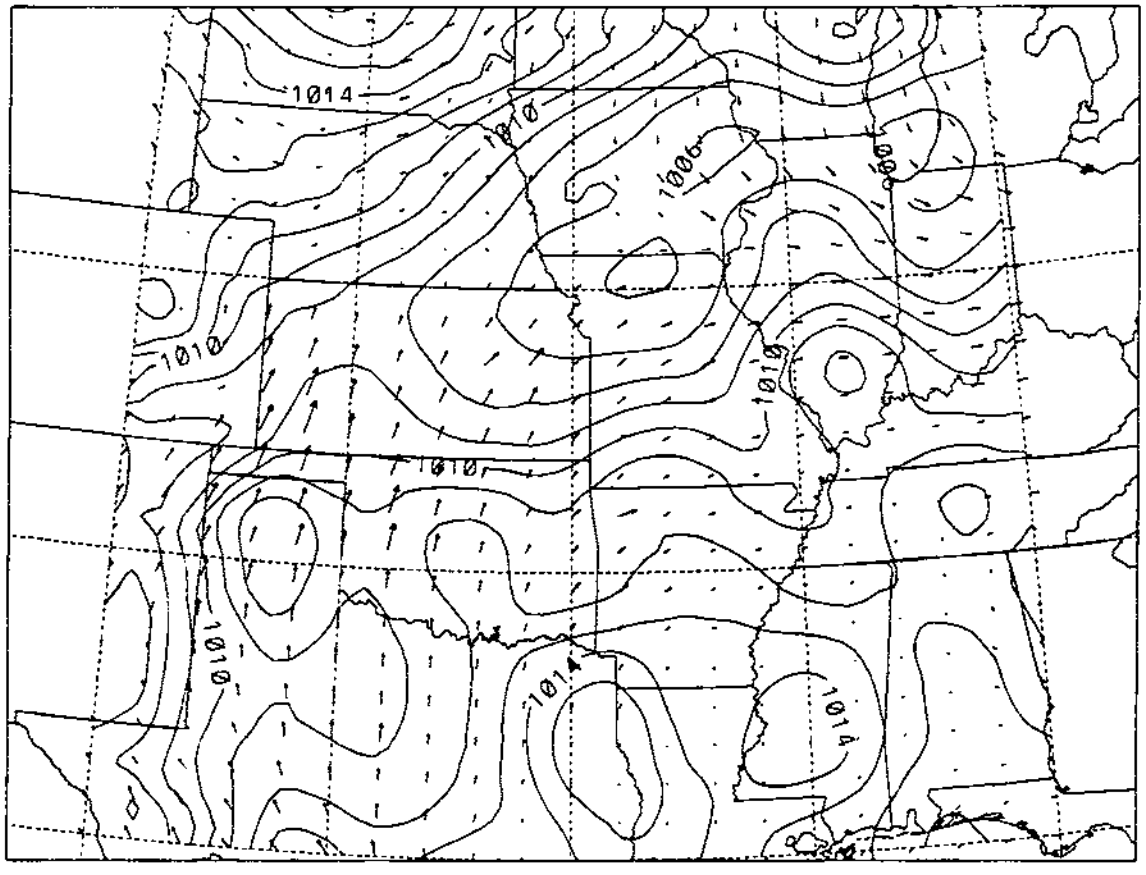

Figure 3.4: Estimated sea-level pressure field (hPa) and surface wind vectors for RAMS Great-Plains-simulation initial state at 1200 GMT, 8 July 1980 as produced by Stage 5 of the RAMS ISAN package. Contour interval is 1 hPa. Maximum wind vector is 20 $m\,s^{-1}$. Latitude and longitude lines are drawn every 5° from 105°W to 85°W and from 30°N to 40°N on the orographic base map.

Figs. 3.5b, 3.6b, and 3.7b. The veering of the winds near the 850 hPa level from southerly to westerly over this 24 h period can be seen by comparing Figs. 3.5c, 3.6c, and 3.7c.

3.1.3 Results

Strong perfluorocarbon tracer signals were obtained along both sampler arcs following the 3-hour tracer release from NSSL. Observed tracer concentration values from both sampler arcs are plotted in Fig. 3.8 and listed in Tables 3.1 and 3.2.

In the case of the 100-km arc, background levels of PMCH ($\sim$ 2.5 fll^{-1}) were measured during the first 45-minute sampling period, which began two hours after the start of the release. PMCH concentrations then increased by three orders of magnitude during the second 45-minute sampling period, reached a peak of 5900 fll^{-1} during the third 45-minute sampling period (over 2000 times background), and then returned to near-background values by the seventh 45-minute sampling period (Table 3.1). Total tracer travel time across the 100-km sampler arc was thus no more than 3.75 hours (the release duration was 3 hours).

Once the tracer had been released, a tracer trajectory was calculated by forecasters at the experiment operations center in Norman based on National Meteorological Center (NMC) synoptic-scale wind field predictions. The forecast trajectory indicated that the leading edge of the tracer cloud should reach the 600-km sampler arc at 1300 GMT (0800 CDT) on July 9, 18 hours[102] after the start of the tracer release at Norman (Ferber et al., 1981). On the basis of this forecast, the 600-km-arc samplers were turned on at 0800 GMT (0300 CDT) on July 9, five hours before the predicted tracer arrival, in order to give a margin of safety. However, the tracer cloud was transported more

[102] This estimate was entirely consistent with the measured time for the tracer cloud to reach the 100-km arc. That is, the maximum concentration measured during the third 100-km-arc sampling period was over four times that measured during the second sampling period. If we assume that the leading edge of the tracer cloud reached the sampling arc at about 2200 GMT, i.e., three-quarters of the way through the second period, then the travel time would have been 3.3 h and the mean transport speed would be 30 km h^{-1} (or 8.3 m s^{-1}), yielding a transport time of 20 h to the 600-km arc.

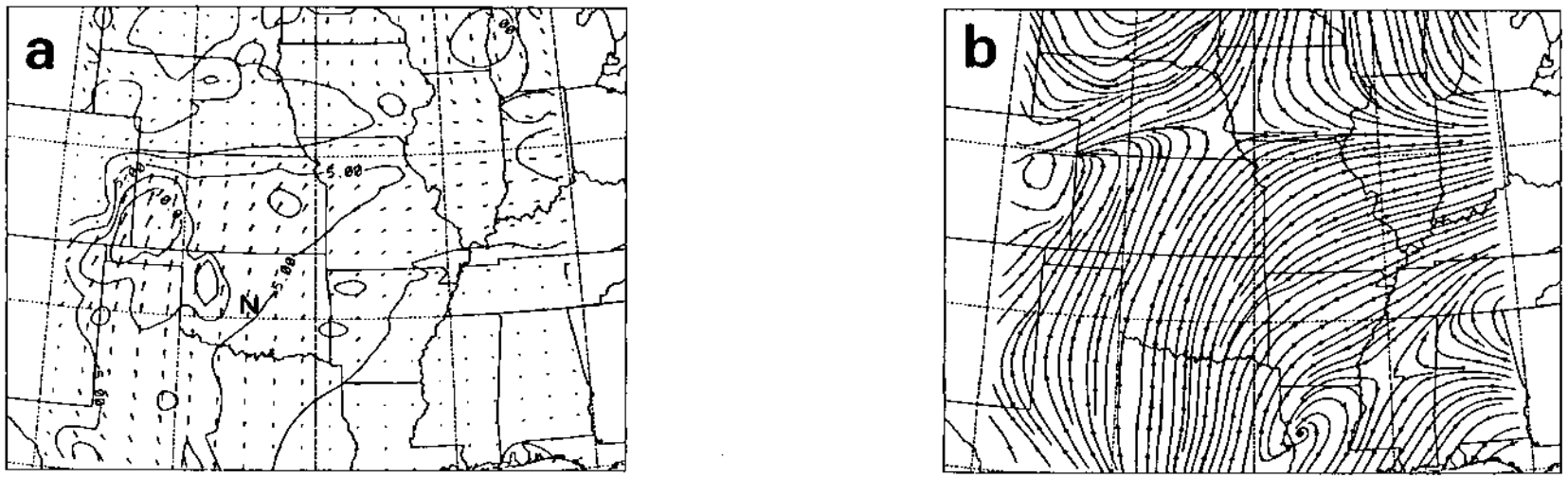

Figure 3.5: Isotach fields overlaid with wind vectors at every second grid point on July 8, 1980, 1200 GMT at (a) 50 m AGL, (c) 1470 m AGL, and (e) 3380 m AGL (in z^* coordinates) togethe r with corresponding streamline fields at (b) 50 m AGL, (d) 1470 m AGL, and (f) 3380 m AGL on the RAMS domain for the Great Plains simulations (30–45°N, 105–85°W). Isotachs are drawn every 2.5 m s^{-1} and the maximum wind vector magnitude is 20 m s^{-1}. An orthographic map projection has been used.

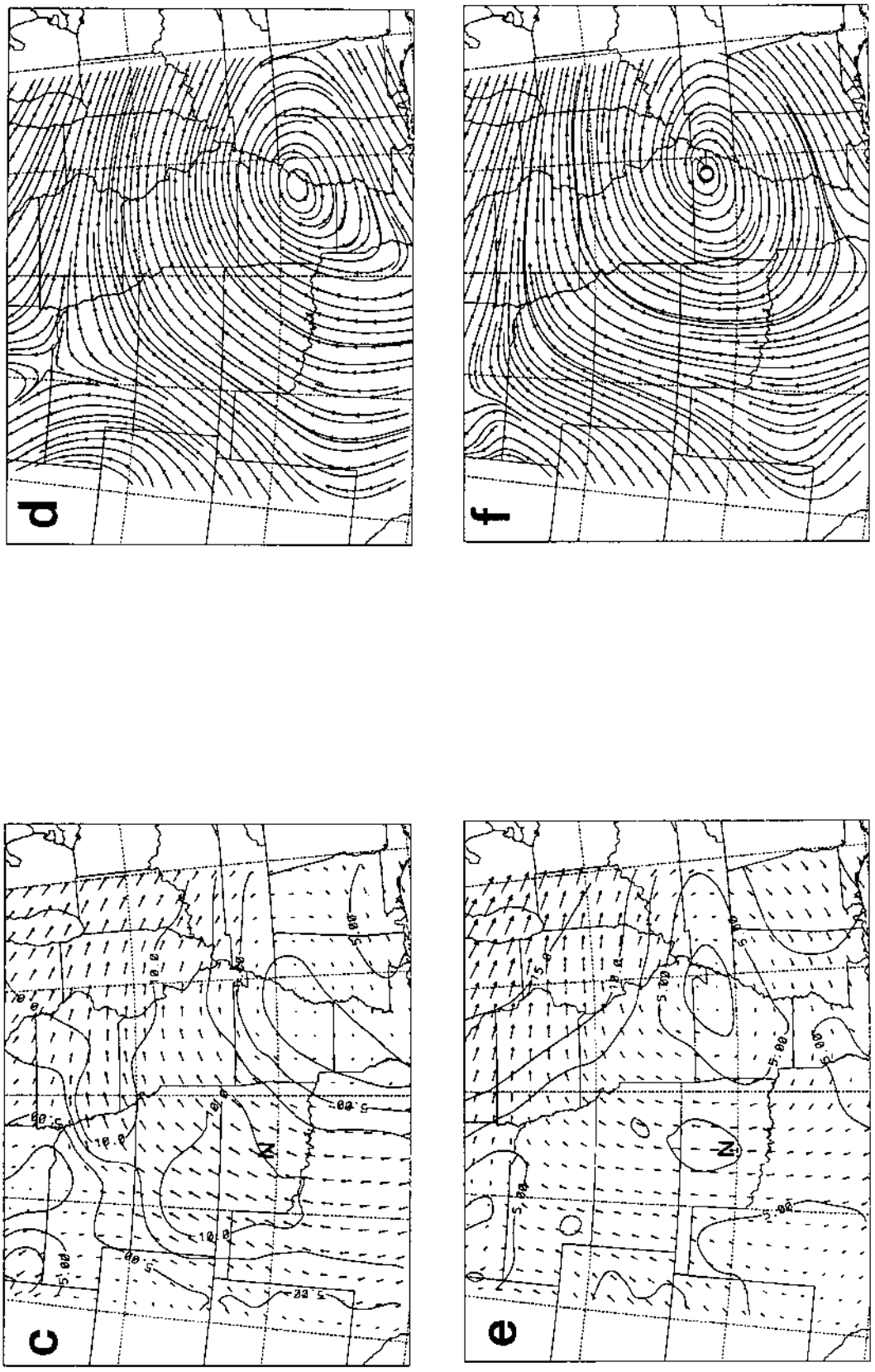

Figure 3.5: (Continued).

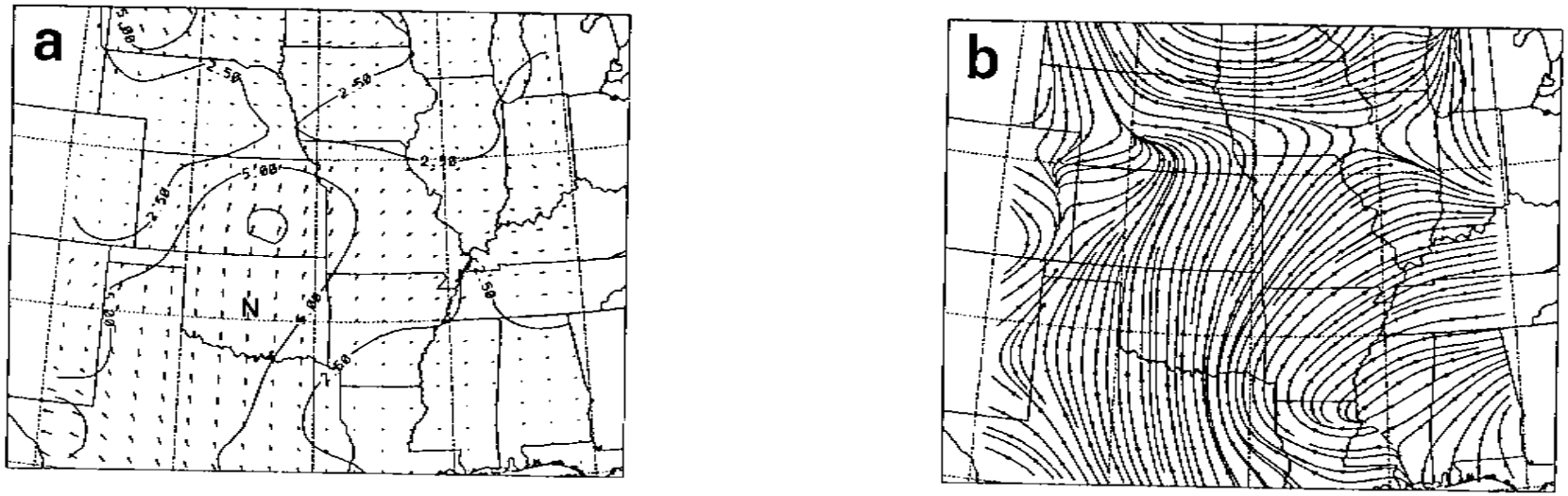

Figure 3.6: Same as Fig. 3.5 except for July 9, 1980, 0000 GMT.

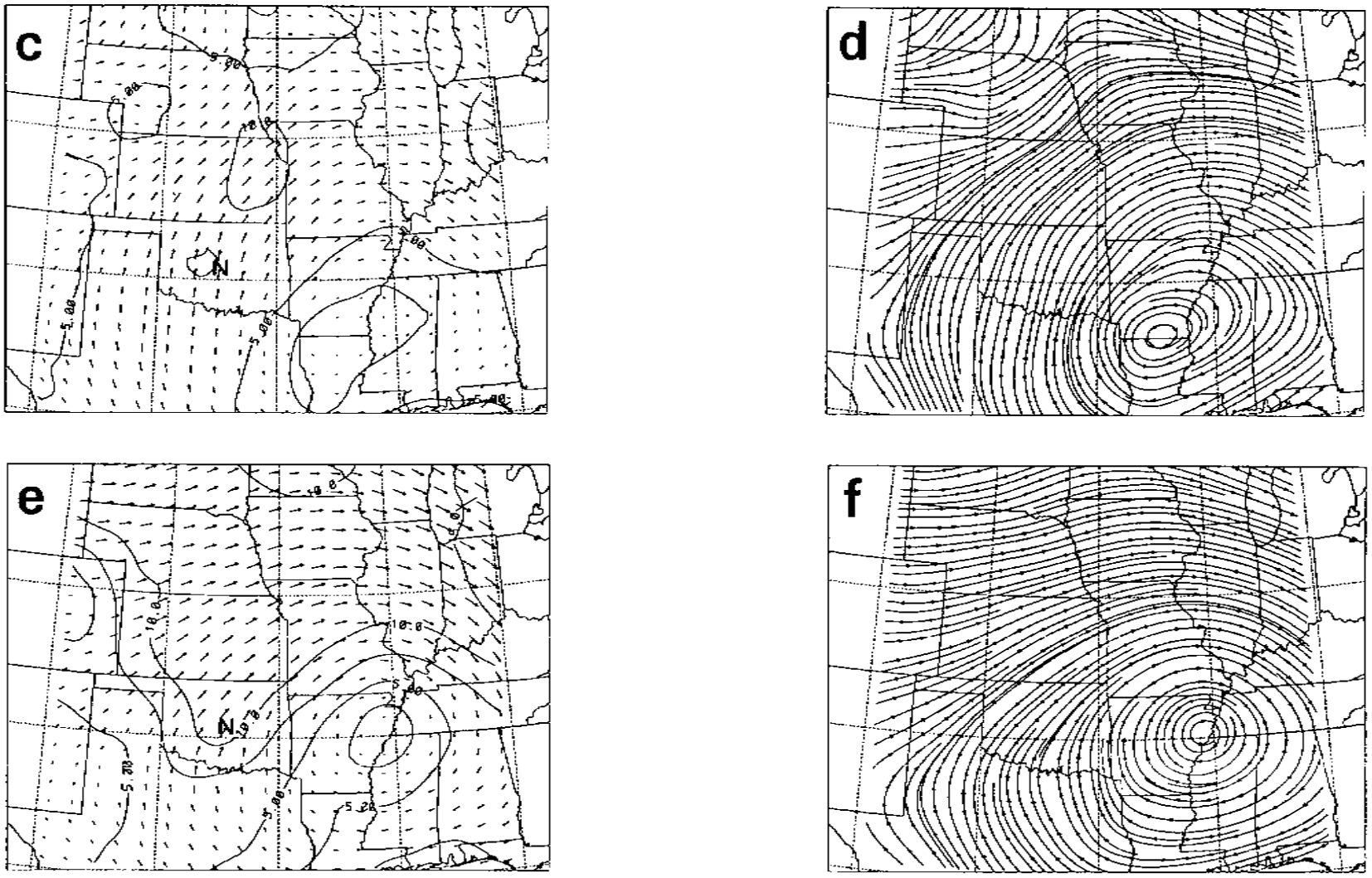

Figure 3.6: (Continued).

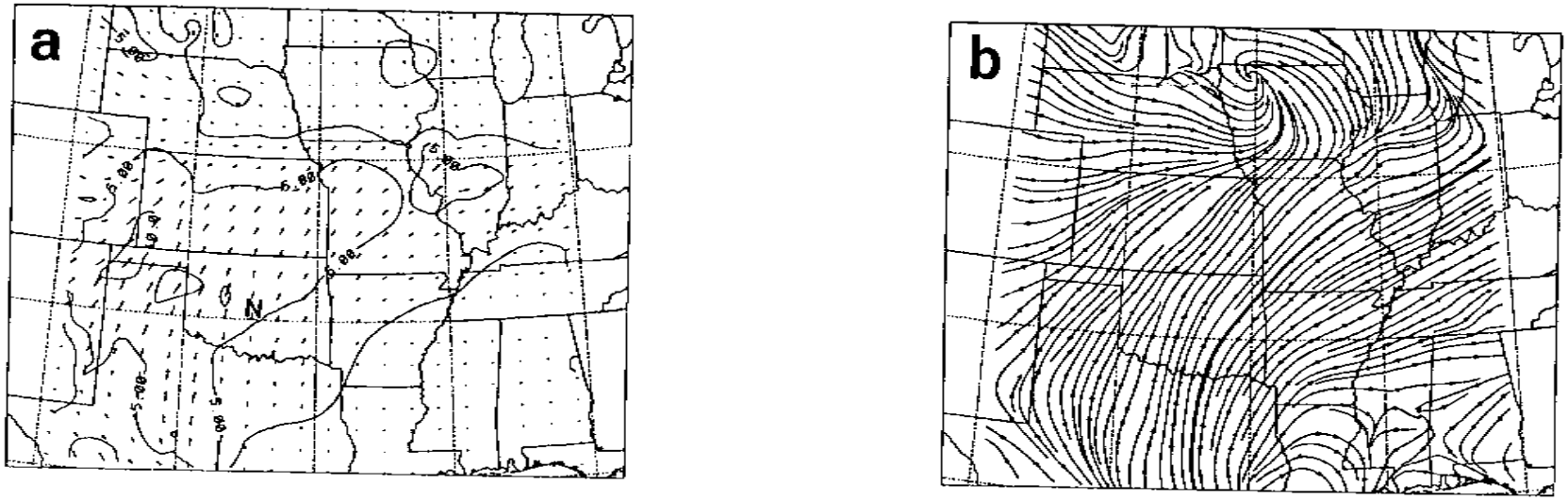

Figure 3.7: Same as Fig. 3.5 except for July 9, 1980, 1200 GMT.

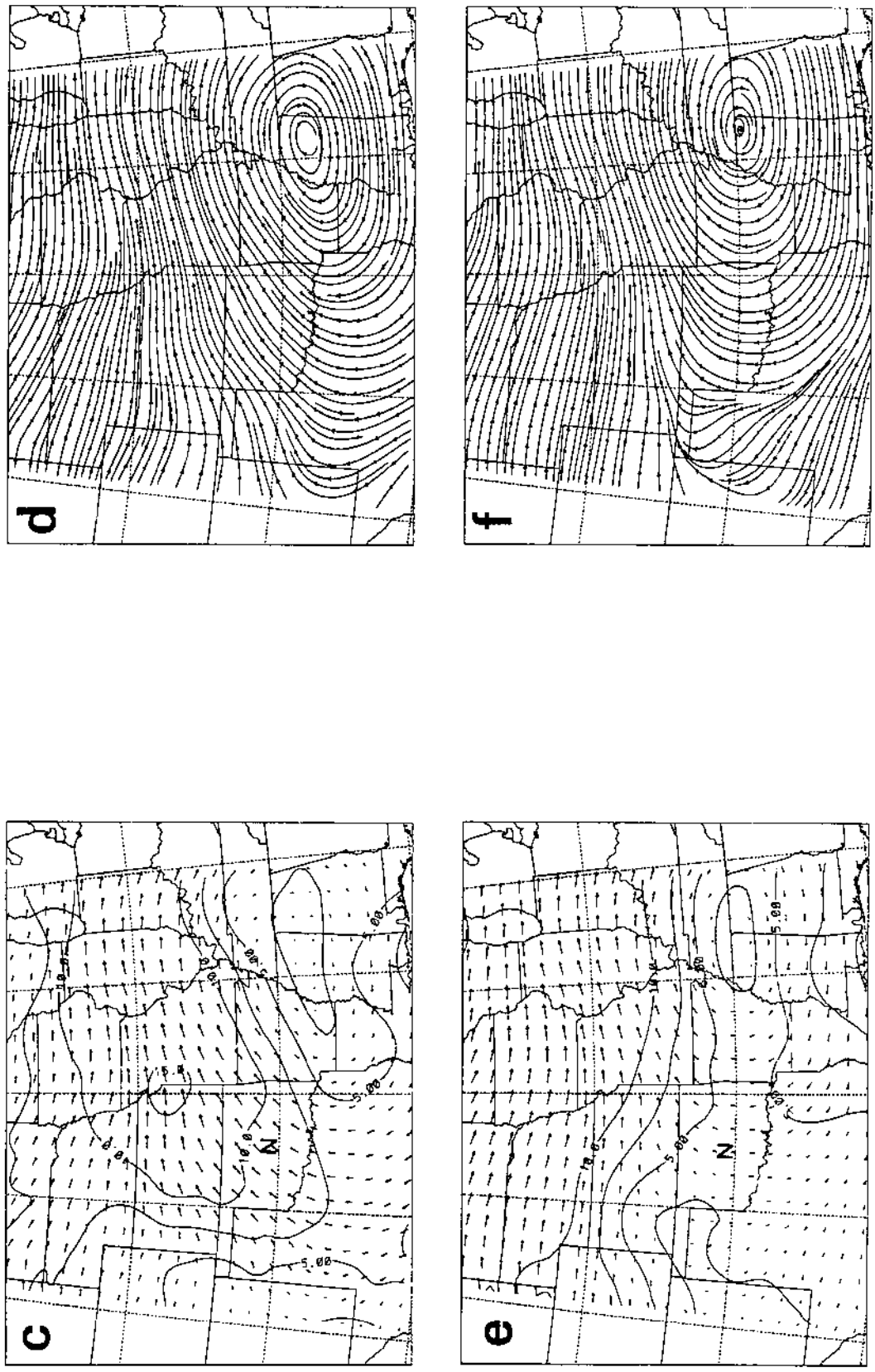

Figure 3.7: (Continued).

quickly than expected, and the first set of 3-hour samples not only showed significant PMCH levels, ranging from 627 to 1280 $fl\,l^{-1}$ at five stations along a 70-km line, but were in fact the maximum tracer concentrations measured along the 600-km arc during 66 h of observations. Measured PMCH concentrations then steadily decreased thereafter with each successive 3-h sample until near-background levels were reached on the fifth sampling period, for a cloud transit time across the arc of at least 12 h (see Fig. 3.8b and Table 3.1). The tracer cloud position indicated by the PMCH concentration measurements was supported by heavy methane measurements made at six sites[103] along the 600-km arc (Fowler and Barr, 1983).

3.1.4 Discussion

Travel time

The most surprising feature of the 600-km-arc PMCH measurements was the shorter-than-expected travel time for the tracer cloud to reach the 600-km sampler arc: 13 h (or less) vs. the 18 h predicted by the forecast trajectory based on NMC gridded forecast wind fields. The 13 h figure is uncertain because the first 600-km-arc 3-hour samples were taken beginning 13 h after the start of the release; the leading edge of the tracer puff could have arrived at any time during these three hours or even earlier. Since the synoptic pattern changed only slightly during the period of the tracer experiment (see Figs. 3.2, 3.3, 3.5, and 3.7), the likeliest explanation for the speeded-up transport is an increase in nighttime wind speed not predicted by the NMC forecast model, for example, a low-level jet.

The synoptic conditions of clear skies and a light pressure gradient which prevailed during the release were ideal for the formation of a nocturnal jet (e.g., Bonner, 1968; McNider and Pielke, 1981). Comparison of two special soundings taken at Tinker Air Force Base north of Norman (listed in Fig. 3.9; see Fig. 3.1a for the location of this site)

---

[103] Indicated in Fig. 3.1b

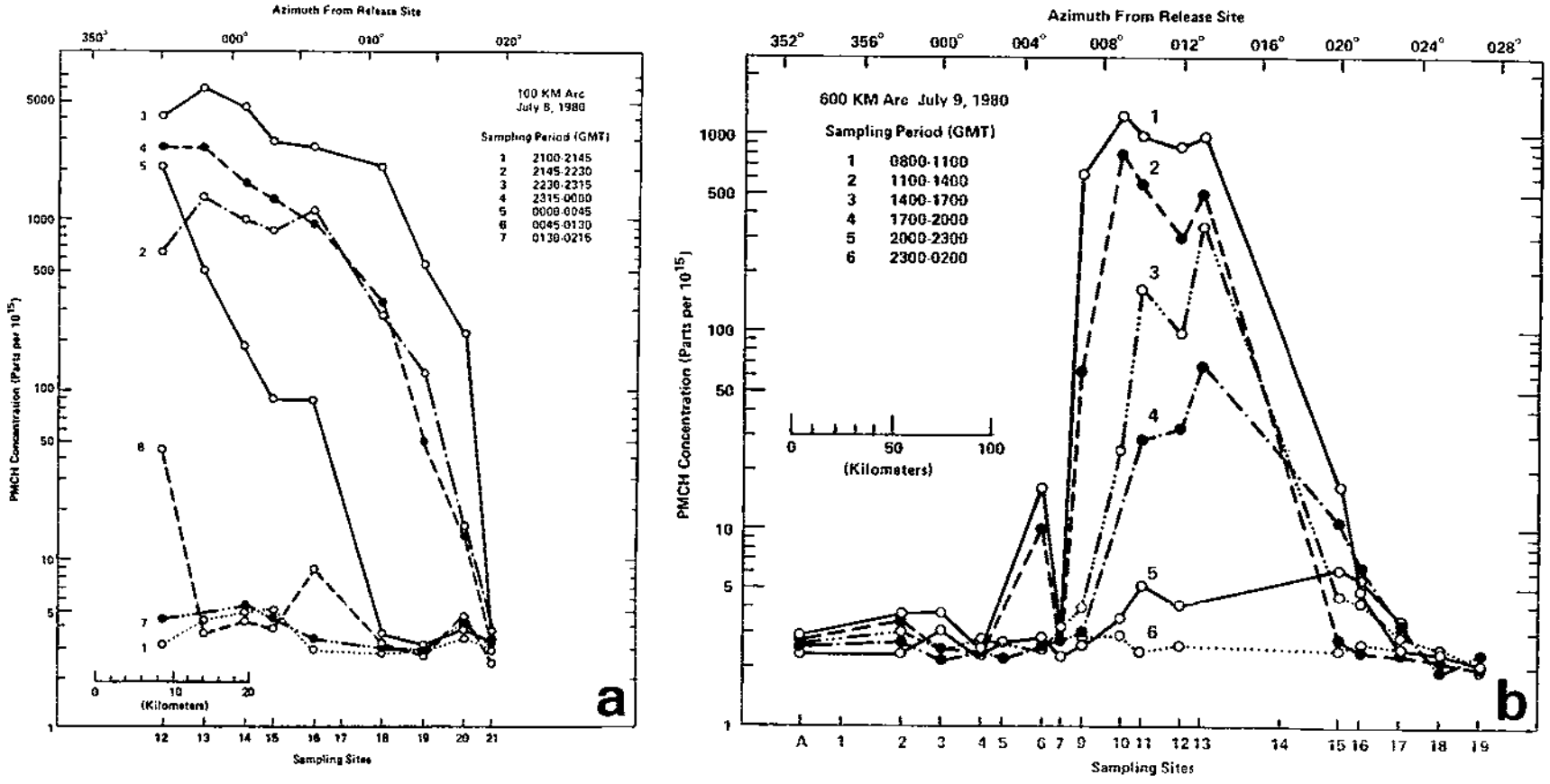

Figure 3.8: Downwind PMCH ground-level concentrations measured following the 3-hour (1900–2200 GMT) July 8, 1980 tracer release from NSSL at Norman, Oklahoma: (a) 100-km sampler arc, 45-minute samples, 7 sampling periods; (b) 600-km sampler arc, 3-hour samples, 6 sampling periods (from Ferber et al., 1981).

Table 3.1: Great Plains 100-km-arc PMCH concentration measurements in $\mathrm{fl\,l^{-1}}$ (based on Tables 3 and 8 of Ferber et al., 1981). Values have been rounded to whole numbers and no background value has been subtracted. Samplers at Stations 23–28 reported only background levels and are not listed here. No measurements were obtained from Station 17 although a sampler was deployed at that site. No samplers were deployed at Stations 1–11. The topmost line of the table lists azimuth angle (in degrees) from the release site at NSSL to the sampling sites; north corresponds to 0, east to 90, etc. The last horizontal line lists station exposures over all ten sampling periods. The rightmost vertical column lists crosswind-integrated concentrations (CWIC) for each sampling period based on an average station spacing of 5 km. Finally, the value in the lower right-hand corner is the crosswind-integrated exposure (CWIE) over all ten stations and ten sampling periods in units of $\mathrm{fl\,km\,h\,l^{-1}}$.

Azim.	355	358	1	3	6	11	14	17	19	22	
Start Time (GMT)	100-km-Arc Station Number										CWIC ($\mathrm{fl\,km\,l^{-1}}$)
	12	13	14	15	16	18	19	20	21†	22‡	
2100	3	4	5	5	3	3	3	4	–	–	150
2145	650	1300	1010	860	1110	290	130	16	–	6	26860
2230	4000	5900	4670	2730	2810	2100	560	215	27	4	115080
2315	2840	2700	1650	1260	1000	340	50	14	4	3	49305
0000	2170	500	182	88	90	*3	*3	4	3	4	15235
0045	43	4	5	4	*9	*3	*1	5	3	4	405
0130	5	–	5	5	*3	*3	*3	4	3	6	185
0215	4	4	4	*5	*4	*4	*3	4	3	4	195
0300	4	4	5	*5	*6	*3	*2	4	3	4	200
0345	3	4	4	*10	*10	–	*1	4	3	4	215
Expos. ($\mathrm{fl\,h\,l^{-1}}$)	7292	7815	5655	3729	3784	2062	567	206	37	29	155875

– No data

† Station started sampling at 2205 GMT

‡ Station started sampling at 2130 GMT

* Value uncertain due to contamination in lab analyzer

Table 3.2: Great Plains 600-km-arc PMCH concentration measurements in fl l^{-1} (based on Table 11 of Ferber et al., 1981). Values have been rounded to whole numbers and no background value has been subtracted. A dash (–) indicates 'no data'. Stations 23–38 reported only background levels for the times shown in this table and are not listed here. Stations 1 and 20 had desorption problems, Station 8 was not used, and no measurements were reported for Stations 14, 21, and 22. The topmost line of the table lists azimuth angle (in degrees) from the release site at NSSL to the sampling sites; north corresponds to 0, east to 90, etc. These azimuth angles were calculated from station positions using spherical trigonometry rather than using the cruder, map-derived values listed in Table 4 of Ferber et al. (1981). The last horizontal line lists station exposures calculated over all seven sampling periods. The rightmost vertical column lists crosswind-integrated concentrations for each sampling period based on an average station spacing of 21.5 km. Finally, the value in the lower right-hand corner is the crosswind-integrated exposure (CWIE) over all 17 stations and 7 sampling periods in units of fl km h l^{-1}.

Azim.	353	358	359	1	2	4	5	7	1	10	12	14	20	21	23	25	28	
Start Time	**600-km-arc Station Number**																	**CWIC**
(GMT)	**A**	**02**	**03**	**04**	**05**	**06**	**07**	**09**	**10**	**11**	**12**	**13**	**15**	**16**	**17**	**18**	**19**	**(fl km l^{-1})**
0800	3	4	4	3	–	17	3	627	1280	1010	900	980	16	5	3	2	3	104490
1100	3	4	2	3	–	11	3	63	820	530	186	500	3	3	2	2	3	45967
1400	3	3	2	3	–	3	–	4	26	164	99	350	5	4	3	3	3	14513
1700	2	3	2	3	2	3	3	3	3	28	32	66	11	6	3	–	3	3720
2000	3	2	3	3	3	3	2	3	4	5	4	–	6	6	3	–	2	1118
2300	–	2	–	2	3	3	3	3	3	2	3	–	3	3	3	–	2	753
0200	–	2	–	3	3	2	2	2	3	3	3	–	3	3	2	–	2	710
Expos. (fl h l^{-1})	42	60	39	60	33	126	48	2115	6417	5226	3681	5688	141	60	57	21	54	513807

at 1900 CDT and 2200 CDT on July 8, 1980, five and eight hours after the start of the tracer release, reveals a marked increase in wind speed between 200 m and 1100 m AGL over that three-hour period: e.g., 9.2 $m\,s^{-1}$ vs. 16.0 $m\,s^{-1}$ at 223 m AGL. Fifteen-minute wind-speed measurements made on the very tall, instrumented KTVY broadcast tower near Norman (Fig. 3.1a) up until 2100 CDT on July 8 also showed increasing wind speeds at the 177 m, 266 m, and 444 m levels as night fell. For example, reported wind-speed values at the 266 m level on the hour from 1400 CDT to 2100 CDT were 6.6, 7.0, 6.8, 8.2, 7.2, 8.3, 11.3, and 15.3 $m\,s^{-1}$, respectively (Appendix A of Ferber et al., 1981). Policastro et al. (1986b; Appendix E) concluded based on these measurements plus special supplemental 0600 and 1800 GMT soundings from the NWS rawinsonde stations at Monett, Topeka, and Omaha (see Fig. 3.1b) that there was strong evidence for the occurrence of a low-level jet on the night of July 8–9 with an approximate doubling of average wind speeds from their daytime values and higher values in the northern half of the study domain. (The sequence of twice-daily Oklahoma City rawinsonde wind profiles shown in Fig. 5.5 also supports this conclusion.)

Transit time

A second surprising feature was the marked increase in transit time (i.e., tracer duration; cloud time-of-passage) at the 600-km sampler arc as compared to the 100-km sampler arc: 9 h vs. 3 h or 15 h vs. 3.75 h (depending upon the cloud-edge criterion used -- see discussion of lateral diffusion). This difference suggests that the tracer cloud underwent considerable elongation in the along-wind direction in the ten hours or so of travel between the two sampler arcs. Fowler and Barr (1983) discussed this 'plume' elongation and suggested that speed shear was probably the primary agent. Draxler and Taylor (1982) had argued earlier that speed shear would completely dominate *alongwind* diffusion over mesoscale travel times, and Draxler and Stunder (1988) explored this topic further using a simple advection-diffusion model. The presence of the nocturnal low-level jet ensured that vertical shear was particularly strong in this case.

08 JUL 80 17GMT

HT M,MSL	DIR DEG	SPD M/SEC
387	190	2.0
610	210	7.7
915	205	7.2
1220	210	6.6
1551	210	6.6
1830	210	6.6
2135	215	7.7
2440	205	9.7
2745	195	11.2
3050	185	12.8
3215	185	14.4
3660	185	15.4
4270	185	9.2
4880	195	5.6
5490	190	8.2

HT M,MSL	PRES MB	TEMP DEG K
387	969	305
1551	850	295
3215	700	287
4351	609	278
5212	548	274
5960	500	271

TLH M,MSL	DIR DEG	SPD M/SEC
2270	209	7

08 JUL 80 19GMT

HT M,MSL	DIR DEG	SPD M/SEC
387	170	3.0
610	170	5.1
915	185	6.1
1220	200	5.6
1550	205	6.1
1830	210	6.1
2135	215	8.2
2440	210	9.7
2745	200	11.3
3211	195	15.4
3660	195	16.9
4270	210	10.2
4880	235	5.6
5795	210	6.1

HT M,MSL	PRES MB	TEMP DEG K
387	969	307
1550	850	295
1888	817	291
2004	806	292
2329	776	291
3211	700	286
4470	600	277
5960	500	271

TLH M,MSL	DIR DEG	SPD M/SEC
1990	196	5

08 JUL 80 21GMT

HT M,MSL	DIR DEG	SPD M/SEC
387	170	4.1
610	170	10.8
915	180	10.3
1220	190	9.8
1623	190	9.3
1830	195	8.8
2135	205	9.3
2440	200	12.9
2745	195	12.9
3288	205	16.0
3355	205	17.0
3660	215	15.9
3965	225	9.3
4270	220	7.2
4880	240	3.6
5795	235	4.6

HT M,MSL	PRES MB	TEMP DEG K
387	976	309
1623	850	296
2089	805	292
2294	786	292
3288	700	286
5297	547	273
6030	500	271

TLH M,MSL	DIR DEG	SPD M/SEC
2280	188	9

09 JUL 80 00GMT

HT M,MSL	DIR DEG	SPD M/SEC
387	180	5.1
610	175	9.2
915	175	9.7
1220	170	9.7
1525	175	10.2
1531	175	10.2
1830	180	10.8
2135	185	10.2
2440	195	11.3
2745	210	12.3
3194	220	13.3
3355	220	13.3
3660	230	9.2
4270	205	2.0
4880	260	3.6
5490	280	5.1

HT M,MSL	PRES MB	TEMP DEG K
387	966	309
516	952	307
1531	850	297
2256	781	290
2683	743	288
3194	700	286
5940	500	270

TLH M,MSL	DIR DEG	SPD M/SEC
2630	180	10

09 JUL 80 03GMT

HT M,MSL	DIR DEG	SPD M/SEC
387	170	2.6
610	170	16.0
915	175	15.4
1220	180	13.9
1526	190	12.4
1830	200	11.3
2135	205	11.3
2440	210	10.8
2745	220	9.8
3192	250	4.6
3660	210	2.6
4270	205	4.6
4880	285	1.5
5490	315	2.1

HT M,MSL	PRES MB	TEMP DEG K
387	966	304
500	952	304
550	945	306
1526	850	298
2530	755	288
2830	728	289
3192	700	287
3460	673	286
3960	628	281
5594	500	271

Figure 3.9: Tinker Air Force Base special sounding data for Great Plains mesoscale tracer release (reproduction of Table 5 from Ferber et al., 1981). The quantity 'TLH' listed at the bottom of each sounding is the transport-layer height computed from the temperature profile (Heffter, 1980).

Secondary concentration maximum

A third surprising feature of the 600-km-arc observations is shown in Fig. 3.10. As already mentioned, PMCH and PDCH concentrations were measured along the 600-km sampling arc for 66 hours in total (22 samples $\times$ 3 h/sample). Eighteen hours after the passage of the trailing edge of the primary tracer cloud across this sampler arc and 43 h after the start of the tracer release at NSSL, a second tracer-cloud passage was detected beginning with the eleventh 3-hour sampling period (July 10, 1980, 1400–1700 GMT). The maximum PMCH concentrations measured in this secondary cloud were two orders of magnitude below the maximum values measured in the primary cloud (16 fll^{-1} vs. 1280 fll^{-1}) but were still five times the background level. The secondary tracer cloud covered a much larger area than the primary cloud (Stations 4–24 vs. 6–16 or 408 km vs. 178 km) and lasted considerably longer, about 30 hours.

This secondary 'puff' was entirely unexpected and has not yet been explained satisfactorily. Policastro et al. (1986a, p. 3-9) mentioned two possible explanations: (i) return of a portion of the cloud; and (ii) nighttime capture of the tracer on vegetation with a subsequent next-day release. The first explanation seems inconsistent with the observed flow field (e.g., Fig. 3.7) and subsequent plant physiology studies in the laboratory have discounted a vegetation absorption/release mechanism (J.L. Heffter, 1992, personal communication). This intriguing topic is returned to again in Sec. 5.5 where a third possible explanation is proposed.

Lateral spread

How does the tracer cloud lateral spread measured in this experiment compare against the measurements discussed in Section 2.2.2? First, it is necessary to determine how large that spread was. As discussed on p. 218, there is some arbitrariness inherent in the determination of plume or puff width. Two commonly-used approaches are to measure the distance between the two outermost[104] points on opposite edges of the cloud at which the concentration has fallen to (a) the larger of 10% of the peak value in the interior and a minimum value based either on background level or minimum detectable level or (b) a threshold value[105] independent of the interior concentration. The first of these approaches is a relative measure while the second is an absolute one. When they are applied to the PMCH concentration observations listed in Tables 3.1 and 3.2 to calculate cloud widths, sometimes identical and sometimes different values are obtained. Tables 3.3 and 3.4 summarize the calculated *surface* cloud widths determined by these two approaches for the 100-km and 600-km arcs, respectively. A PMCH concentration of 3 fl l^{-1} *above*

---

[104] Allows for the possibility of secondary peaks.

[105] The problem of edge determination is in fact encountered in a number of disciplines and is a fundamental concern in image processing (e.g., Lewis, 1990; Jahne, 1991). 'Thresholding' is the simplest of the various edge-detection algorithms currently available.

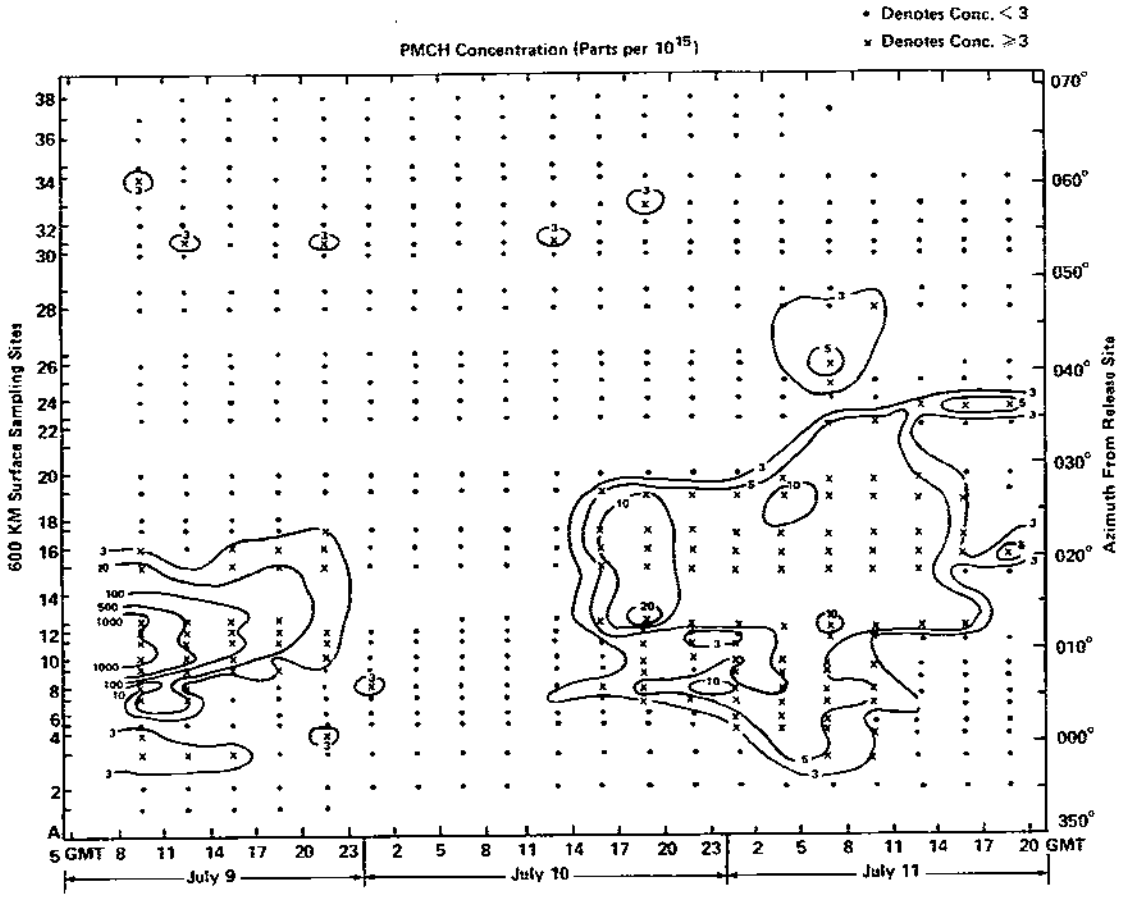

Figure 3.10: Time—sampler azimuth angle cross section of average 3-hour PMCH ground-level concentrations from the 1980 Great Plains experiment 600-km sampler arc for the 60-hour period from July 9, 0800 GMT to July 11, 2000 GMT. Contour interval values are in units of fl^{-1} (i.e., parts per 10^{15} by volume). Elevated PMCH levels marking the primary cloud passage across the 600-km sampler arc are located on the lefthand side of the figure; the lower values corresponding to the passage of the secondary tracer cloud lie on the righthand side (from Ferber et al., 1981).

background was used as both[106] the threshold value and minimum value; this level is thus twice the 1980 background level of PMCH, 3 fl l^{-1}, reported by Ferber et al. (1986).

As might be expected, the cloud widths calculated based on edge values taken to be the larger of 10% of the peak value and a minimum value are less than or equal to those based solely on a threshold value equal to the minimum value. However, the difference is less than 50% for most of the observing times in Table 3.3, somewhat larger for those in Table 3.4. To place the lateral cloud dispersion observed in this experiment in the context of other experiments discussed in Sec. 2.2.2, we first need to calculate an observed σ_y value by using the formula $\sigma_y = W/4.28$, where W is the observed cloud width based on the 10%-of-peak-value criterion. For the 100-km arc, 35 km is a representative value for W (Table 3.3). This yields a σ_y value of 8.2 km. The corresponding σ_y value predicted by Heffter's formula (Eq. 2.40) for a travel time of 12000 s (i.e., 100 km distance, 30 km h^{-1} travel speed) is 6 km. For the 600-km arc, on the other hand, a representative value for W from Table 3.4 is 100 km, which gives an observed σ_y value of 23.4 km. Given a travel time of 13 h, Heffter's formula yields a value for σ_y of 23.4 km. However, the minimum travel times for the next three sampling periods were 16, 19, and 22 h, which have corresponding predicted σ_y's of 29, 34, and 40 km. Thus, the observed cloud spread was greater than that predicted by Heffter's empirical formula for the travel times to the 100 km arc but overall was smaller than expected for the travel times to the 600 km arc.

It is worth noting the following points of methodology in the construction of Tables 3.3 and 3.4. The geometry of the 100-km 'arc' was actually linear: the samplers were deployed at approximately equal intervals along east-west Highway 51 (Fig. 3.1a). The distance from the Station 11–12 midpoint to the Station 21–23 midpoint is 48.5 km, yielding an approximate station spacing of 5 km for the ten stations within this interval. This latter value has been used for calculating cross-wind integrated concentrations (see

---

[106] Cloud widths were not calculated for sampling periods when no station reported a reading of more than 3 fl l^{-1} above background.

Table 3.1). It also provides a nominal cloud width when only a single sampler reported above-threshold values; in such cases, the cloud could have had almost zero width or could have reached almost to the two neighbouring samplers, for an average width of one station spacing. In the case of the 600-km sampler arc, the stations do lie along an approximate arc 600 km from the release site. The azimuth angles from Table 3.2 have been used to calculate the azimuth ranges and arc lengths[107] given in Table 3.4. Cloud-edge uncertainty has been accounted for by using the azimuth of the midpoint between stations on either side of the cloud edge.

Note too that at these mesoscales it is necessary to consider the properties of the map projection being used, since any two-dimensional map of a three-dimensional surface will distort length, angle, shape, area, or a combination thereof. The base map in Fig. 3.1b is a Lambert conformal projection. Pearson (1990, p. 351) has suggested that conformal projections preserve distance and azimuth reasonably well at such scales. For example, for the 10° latitude band from 35° to 45°, distance on a Lambert conformal projection with one standard parallel at 40° will be exact at the standard parallel and will be distorted by less than a half-percent[108] at 35° and 45°. The Lambert conformal projection has the additional advantage over another commonly-used conformal projection, the Mercator projection, that it does represent the convergence of meridians towards the poles. Haagenson et al. (1987) also chose to use a Lambert conformal projection in their objective analysis of surface concentration measurements from CAPTEX.

Aircraft measurements

The surface sampling network in the Great Plains tracer experiment was augmented by aircraft sampling flights over both surface sampling arcs. The aircraft flight paths are marked on Fig. 3.1. Whole-air 'grab' samples were collected in plastic bags during

---

[107] Using the formula $s = r\theta$ with r equal to 600 km.

[108] Compare this to a maximum distortion of over 40% for a Mercator projection of the same latitude band.

Table 3.3: Estimated 100-km-arc PMCH cloud widths as determined by using two different cloud-edge criteria for each of the first seven 45-minute sampling periods. Nominal station spacings of 3° and 5 km have been used in assigning the azimuth range (°) and arc-length width (km) of the cloud based on the average values of these quantities for Stations 12–21, including Site 17. Cloud widths were not calculated for sampling periods when no station reported a reading of more than 3 fl l^{-1} above background.

Obs. No.	Start Time (GMT)	Conc. Max. (fl l^{-1})	St'n No.	Max. Width (10% of peak) St'n Range	Azim. Range	Arc Length	Max. Width (> 3 fl l^{-1}) St'n Range	Azim. Range	Arc Length
1	2100	5	–	–	–	–	–	–	–
2	2145	1300	13	12–19	24	40	12–20	27	45
3	2230	5900	13	12–18	21	35	12–21	30	50
4	2315	2840	12	12–18	21	35	12–20	27	45
5	0000	2170	12	12–13	6	10	12–16	15	25
6	0045	43	12	12	3	5	12	3	5
7	0130	5	–	–	–	–	–	–	–

Table 3.4: Estimated 600-km-arc PMCH cloud widths as determined by using two different cloud-edge criteria for each of the first five 3-hour sampling periods. The azimuth range (°) is based on azimuth values from Table 3.2, and the arc-length width (km) is determined from the azimuth range and a nominal radial distance of 600 km.

Obs. No.	Start Time (GMT)	Conc. Max. (fl l^{-1})	St'n No.	Max. Width (10% of peak) St'n Range	Azim. Range	Arc Length	Max. Width (> 3 fl l^{-1}) St'n Range	Azim. Range	Arc Length
1	0800	1280	10	9–13	11	115	6–15	16	178
2	1100	820	10	10–13	9	94	6–13	14	147
3	1400	350	13	11–13	7	73	10–13	9	94
4	1700	66	13	11–13	7	73	11–15	10	105
5	2000	6	–	–	–	–	–	–	–

these flights and frequent wind measurements were also made. Three sampling passes were made by the DC-3 at the 100-km arc along line AF at an altitude of 900 m AGL (1250 m MSL) on July 8 from 2300 to 0000 GMT (1800–1900 CDT), 4 h after the start of the release. A second flight was made by the same aircraft the next day north of the 600-km arc from 1240 to 1630 GMT (0740–1130 CDT) at an altitude of 1200 m AGL (1525 m MSL).

It is difficult to use the aircraft concentration measurements for quantitative comparisons with model output. However, they provide qualitative information complementary to the surface measurements. Five-minute PMCH concentrations as high as 5400 fl^{-1} were measured along the 100-km arc at 900 m AGL, comparable to peak surface concentrations, indicating a deep, well-mixed cloud. Aircraft measurements west of the westernmost surface site on the 100-km arc were used by Ferber et al. (1981) to infer the western extent of the tracer cloud (see below). Only background PMCH levels were detected on the four-hour 600-km arc flight. Nevertheless, this seemingly negative result provides an upper limit on the time of transit of the elevated back edge of the tracer cloud past this point. That is, the elevated cloud must have completely passed the northern end of the aircraft sampling path (see Fig. 3.1b) by 1230 GMT (0730 CDT), 18.5 h after the start of the release, and passed the southern end of the flight path by no later than 1500 GMT (since the DC-3 took about 2.5 h to fly to the southern end). Note that significant PMCH concentrations were measured by some surface samplers on the 600-km arc after 1400 GMT, and even after 1700 GMT, but these stations were located west of the DC-3 flight path.

Cloud cross-wind shape

What can be said about cross-wind cloud structure at mesoscale downwind distances? At the 100-km sampler arc, Fig. 3.8a and Table 3.1 portray a classical single-peaked structure. There are suggestions of some asymmetry and skewness with a more abrupt, shortened 'wing' on the west side of the cloud and a broader wing on the east side as might be expected from a veering wind profile. However, it is difficult to say much more,

particularly as the western edge of the tracer cloud was located beyond the western end of the 100-km sampler arc for the entire sampling period. At the 600-km sampler arc, examination of Fig. 3.8b and Table 3.2 reveals an even more complicated situation. There was a weak secondary peak present in each of the first four 3-hour sampling periods. It further appears that the primary peak shifted from the western side of the cloud during the first and second sampling periods to the eastern side during the third and fourth periods.

Mass-balance analysis

One important feature of Table 3.1 is the fact that the peak concentration at the third and fourth sampling periods occurred at the *westernmost* sampler on the 100-km arc. That is, the cloud appeared to move westward with time and the full width of the plume wasn't sampled on the 100-km arc at any time but especially for the later periods. Ferber et al. (1981) discussed this problem and concluded, based on an analysis of the concurrent aircraft measurements, that concentrations west of Station 12, the westernmost active sampler site, probably decreased very rapidly. This contention is supported by the 600-km-arc measurements (Fig. 3.8b), where the westernmost cloud edge is very abrupt. However, it is relatively straightforward to estimate the mass of tracer released based on the measured concentration values and a simple model, as described below. This calculation too suggests that most of the cloud mass passed over and was sampled on the 100-km arc.

Table 3.1 gives tabulations of cross-wind integrated concentrations and time-integrated station concentrations (recall Eq. 1.23) for the 100-km sampler arc. From these values we can then calculate the cross-wind integrated *surface* exposure for the cloud passage across this sampler arc. Assuming a three-hour transit time (2145–0045 GMT) and a 50-km cloud width (Stations 12–21), the value[109] of the cross-wind integrated

[109] Subtracting a 3 fl l^{-1} background value only reduces this value by 450 fl km hl^{-1}.

exposure (CWIE) is 154,850 fl km h l^{-1}. The corresponding cloud-mean concentration $\bar{c}$ is then given by the formula

$$\bar{c} = \frac{\int\int c \, dy \, dt}{\int dy \int dt} \quad . \tag{3.1}$$

If we now multiply the value of $\bar{c}$ obtained from Eq. 3.1 by the volume of tracer-containing air which was sampled as it crossed the sampler arc, we obtain the total mass of tracer transported across the arc. However, we need to know both the depth of the tracer cloud and the transport speed *normal* to the sampler arc in order to estimate the cloud volume. Sackinger et al. (1982) gave an equivalent formulation of this control-surface approach which accounts for both of these factors:

$$m_t = \int \int_S c \vec{V} \cdot d\vec{S} \, dt \quad , \tag{3.2}$$

where m_t is the tracer mass carried in the cloud, $\vec{V}$ is the horizontal velocity, and S is the control surface. In our case, the width of the sampler arc and the depth of the cloud define the control surface of interest.

If we assume a constant normal transport speed V of 30 km h^{-1} across the 100-km arc, the along-wind cloud length will be 90 km. Further assuming a cloud depth (equal to the PBL height) of 3 km for this late afternoon, summertime case, we can multiply Eq. 3.1 by the (rectangular) cloud volume of 50 km $\times$ 3 km $\times$ 90 km to obtain[110] the total mass of the tracer release. This rough calculation yields a value of 190 kg, which compares very well with the actual amount of PMCH released, 192 kg (Ferber et al., 1981) and suggests that not too much of the tracer cloud lay to the west of Station 12, the westernmost active sampler site on the 100-km arc.

How well does this same mass-balance calculation work for the 600-km-arc measurements (Table 3.2)? Assuming a 12-hour transit time (0800–2000 GMT) and a 168 km

---

[110] After converting from fl l^{-1} to kg m^{-3} by multiplying by a factor of 7×10^{13} — see Sec. 4.6.

width (Stations 6–15), the CWIE value with background removed is 500,262 fl km h l^{-1}. Use of the same transport speed and cloud depth as in the previous calculation then yields a value of 643 kg for the total amount of PMCH tracer released, a value more than three times larger than the actual amount released. Examination of the mass-balance equations above reveals that the only two independent quantities besides the CWIE value are the transport wind speed V and the cloud depth H; somewhat surprisingly, the use of a shorter transit time or a narrower plume width will not affect the estimate. However, one assumption which may have been violated in the 600-km-arc calculation was the assumption that the measured surface concentrations are representative of the assumed full depth of the cloud (i.e., 3 km). Unlike the case of the 100-km arc, where it is reasonable to expect that the tracer was uniformly mixed throughout the depth of the afternoon boundary layer at all sampling times, the large concentration values measured along the 600-km arc during the 0800 GMT sampling period may have been associated with a shallow cloud 'nose'.

A second assumption was the use of the same transport speed as for the case of the 100-km arc. However, since the cloud transit time was four times longer for the case of the 600-km arc, the effective transport speed clearly varies from sampling period to sampling period. From Eq. 3.2 we can also see that we have to consider the product of concentration and transport speed. However, if we redo the mass-balance calculation and take this factor into account, we end up with an even higher estimated mass value since the high concentrations in the first sampling period are weighted with a transport speed of 41 km h^{-1}. Thus, the likely source of the overestimate seems to be a lack of representativeness on the part of the surface concentration measurements. If we were to use a value of 1 km for the cloud depth, for example, the estimated mass would be reduced by a factor of three to a value of 214 kg.

3.1.5 Previous Great Plains tracer experiment numerical simulations

Fowler and Barr (1983) compared time-integrated concentrations of heavy methane measured up to 8 days after the July 8 release and up to 2500 km from the release site

in Oklahoma with predictions made using a very simple Gaussian puff model for exposure from an instantaneous release. By using σ_y values suggested by Gifford (1982) for long-range transport and NOAA ATAD-model trajectories and mixing heights, they obtained very good agreement for *exposure* (i.e., within a factor of two at three out of four sites) although cloud *duration* and travel time were severely underestimated.

Policastro et al. (1986a,b,c) and Carhart et al. (1989) have described a LRTAP model intercomparison study conducted for the U.S. Environmental Protection Agency (EPA) which demonstrated problems with LRTAP models that rely on synoptic-scale meteorological fields to simulate mesoscale atmospheric dispersion. Eight episodic LRTAP models, seven Lagrangian and one hybrid, were tested against observations from two mesoscale tracer experiments, the 1980 Great Plains experiment and a long (1976–1977) tracer experiment carried out at the Savannah River Plant in South Carolina using krypton-85.

After running seven of the eight LRTAP models for each experiment[111], Policastro et al. (1986a,b) and Carhart et al. (1989) concluded that paired comparisons of model-predicted concentrations with observed concentrations were generally poor. Correlation coefficient (Pearson's R) values were low overall and were actually negative in some cases. Fig. 3.11 compares model-predicted puff center-of-mass positions and puff widths for seven of the models with the observed puff position and puff width for the Great Plains experiment at the first 600-km-arc sampling time. Fig. 3.12 shows the corresponding model-predicted surface concentration patterns for the seven individual models which were used to construct Fig. 3.11. None of the model puffs has travelled far enough or spread widely enough and several show significant directional errors, although some predictions are relatively good.

It has been suggested (AMS/EPA, 1987; Carhart et al., 1989; Moran et al., 1991) that these errors can be at least partly explained by (i) the inability of the twice-per-day upper-air soundings used by the models to resolve adequately the formation and erosion

---

[111] Two of the models could not be applied to one or the other of the two experiments.

of the nocturnal, low-level jet, (ii) corresponding neglect of differential advection due to vertical wind shear, and (iii) problems with the empirical parameterizations employed to treat lateral diffusion.

All of the models tested, with the exception of the ARRPA model (Mueller et al., 1983), relied on diagnostic wind fields generated by the objective analysis of 12-hourly upper-air soundings and all models except RADM[112] employed the well-mixed PBL assumption. The ARRPA model uses winds at 10 levels from the NWS Boundary Layer Model and RADM employs a random-walk approach for dispersion. Five of the seven models used a combination of Pasquill-Gifford-Turner dispersion curves for short travel times and Heffter dispersion curves (Heffter, 1965; see Fig. 2.24 and Eq. 2.40) for longer travel times to parameterize lateral diffusion σ_y while two specified horizontal diffusivity K_H. As shown in Fig. 1.3, 12-h temporal resolution is not adequate to represent the inertial oscillation and supergeostrophic low-level jet. Linear interpolation between the two synoptic sampling times would give too low a transport wind speed and a transport direction biased to the east, both problems with the LRTAP model predictions shown in Fig. 3.11. Moreover, differential advection due to the inertial oscillation and subsequent vertical mixing will produce a wider puff than predicted by the models.

3.2 Cross-Appalachian Tracer Experiment

3.2.1 Experimental design

The Cross-Appalachian Tracer Experiment (CAPTEX) carried out in the autumn of 1983 was in many ways a successor to the 1980 Great Plains tracer experiment. The main objectives of CAPTEX were to test the perfluorocarbon tracer technology used in the Great Plains experiment over longer distances and over more complex terrain, to provide insight into the physical mechanisms involved in long-range (i.e., 1000-km scale)

---

[112] Random-walk Advection and Dispersion Model, not the Regional Acid Deposition Model discussed in the next section.

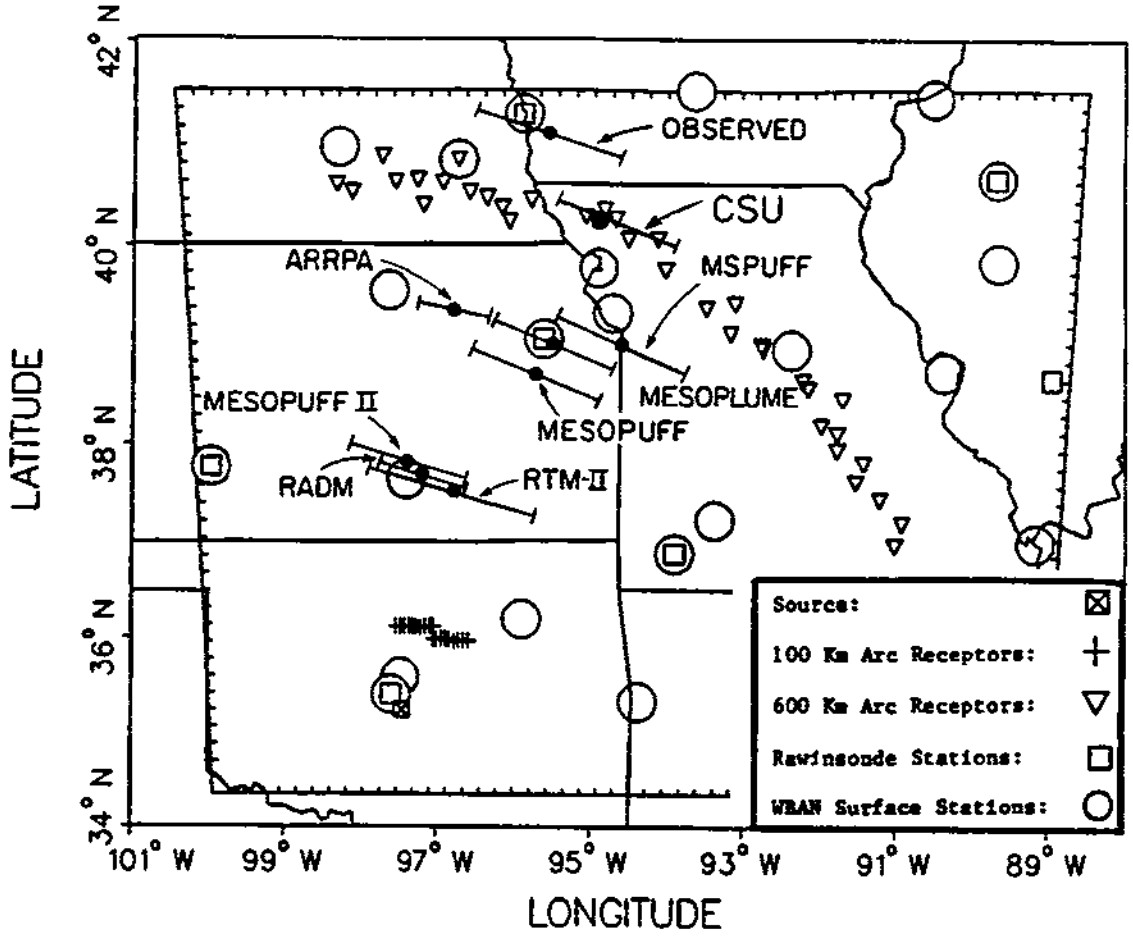

Figure 3.11: Schematic showing tracer puff centers (indicated by solid black dots) and approximate puff widths (indicated by bars passing through puff centers) predicted by eight RSDMs for the first 3-hour sampling period of the Great Plains experiment (0800–1100 GMT, 9 July 1980). The CSU modelling system result corresponds to Exp. GP4b. An estimate of the actual tracer puff position is also shown based on an extrapolation of 600-km-arc sampler measurements since it is impossible to tell from the measurements when the tracer material first arrived at this arc. The 3-hour release of perfluorocarbon tracer took place at Norman, Oklahoma (lower lefthand corner) beginning at 1900 GMT, 8 July 1980 (adapted from Moran et al., 1991).

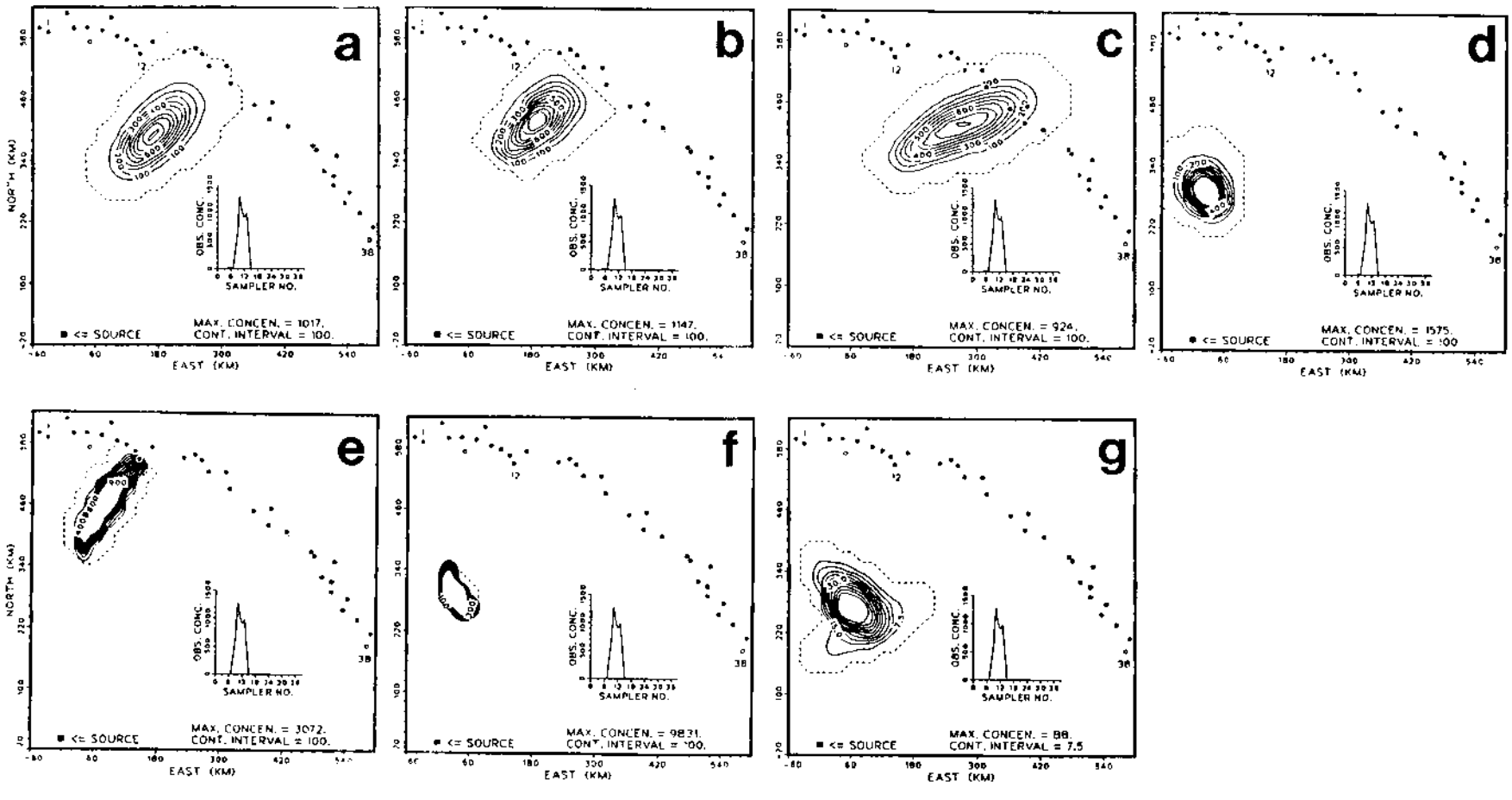

Figure 3.12: Surface concentration patterns predicted by seven RSDMs for the first 3-hour sampling period of the Great Plains experiment (0800–1100 GMT, 9 July 1980): (a) MESOPUFF; (b) MESOPLUME; (c) MSPUFF; (d) MESOPUFF-II; (e) ARRPA; (f) RADM; and (g) RTM-II (from Carhart et al., 1989). The grid increment for the 33 by 33 grid is 20 km. The concentration contour interval is 100 fl l^{-1} and only the 10 lowest contours are shown. The dotted contour represent a line drawn the the centers of nearest-neighbour grid cells to the cloud with zero predicted concentration.

atmospheric transport and diffusion, and to provide a data set with which to evaluate and improve numerical LRTAP models (Ferber et al., 1986). As in the Great Plains experiment, NOAA's Air Resources Laboratory served as the lead agency but twelve other American and Canadian organizations also participated in the six-week experiment.

The CAPTEX domain, illustrated in Fig. 3.13, covers the northeastern United States and southeastern Canada. Major topographic features include two of the Great Lakes (Lake Ontario and Lake Erie), the northern end of the Appalachian Mountains, and the western North Atlantic Ocean. Seven different releases of the perfluorocarbon PMCH were made during CAPTEX, five from Dayton, Ohio and two from Sudbury, Ontario[113]. Six of the releases were 3 hours in length and one was 30 minutes long (Ferber, 1985; Ferber et al., 1986). Automatic sequential air samplers operated at 86 sites in ten states and three provinces. The sampling sites were arranged in nine arcs which were located northeast of Dayton, Ohio at approximately 100-km intervals between 300 and 1100 km. Sampler separation along each individual arc increased linearly with distance from Dayton and approximated two expected plume standard deviations. However, station density was doubled in New York state and New Jersey along the 800-km arc in order to obtain more detail on cloud structure. Six consecutive 3-h samples were collected at the sampling sites closest to the release site while twelve 6-h consecutive samples were made at the other sites; the start of sampling lagged the release time and varied with distance from the release site.

In addition to the surface air samplers, seven instrumented aircraft made plume transects at distances from 200 to 900 km downwind of the release sites (Ferber, 1985; Stunder et al., 1986; Draxler and Stunder, 1988). Operations of the normal ten upper-air stations in the CAPTEX domain were also enhanced during the course of the experiment. Eight of the NWS/AES upper-air sites carried out special supplemental launches at 0600 and 1800 GMT. A ten-station supplementary rawinsonde network with four soundings

---

[113]The choice of these release sites was not arbitrary; both the coal-fired power plants located in the Ohio Valley and nickel smelters in Sudbury are major SO_2 sources (e.g., Ferber, 1985; Mohnen, 1988)

per day was also operated for the duration of the field program (see Fig. 3.13). Thus, the spatial and temporal resolution of the upper-air network within the CAPTEX domain were both improved by a factor of two during release periods (e.g., Kahl and Samson, 1986, 1988a). Some insight into the planning, organization, coordination, and logistics involved in mounting such a complex field program may be gleaned from the post-experiment operations review document (Ferber, 1985). As one example, the aircraft sampling paths were restricted by the decision, for safety reasons, not to fly any of the single-engine aircraft over the Great Lakes or Atlantic Ocean.

The second of the seven CAPTEX tracer releases, Release 2 made on September 25, 1983, was selected as a second test case for the CSU mesoscale dispersion modelling system for several reasons. First, examination of daily synoptic maps for the seven CAPTEX releases (e.g., Brown et al., 1984) suggested that Release 2, which took place on the back of a slow-moving high pressure system over eastern North America, was the release most likely to have been influenced by terrain-forced mesoscale circulations and the least likely to have been affected by frontal dynamics and precipitation processes. Ferber et al. (1986, p. 16) noted that this release "... was conducted under the lightest wind conditions of the seven releases and produced the most widespread plume." A second reason was that this release had been simulated by a number of other LRTAP models, including two other prognostic Eulerian air-quality modelling systems (see Brost et al., 1988a, and Kao and Yamada, 1988).

3.2.2 Meteorological conditions

Fig. 3.14 shows a plot of sea-level pressure and surface winds five hours before the start of the release of perfluorocarbon tracer from Dayton. An elongated high-pressure system, which was associated with very weak surface winds, lay over eastern North America. The tracer release site at Dayton International Airport (indicated by the letter 'D') was located on the backside of this system in southerly to southwesterly flow. Fig. 3.15 shows the corresponding NMC-analyzed geopotential fields at 1000 hPa and 500 hPa while Figs. 3.16 and 3.17 show the same fields 24 and 48 hours later.

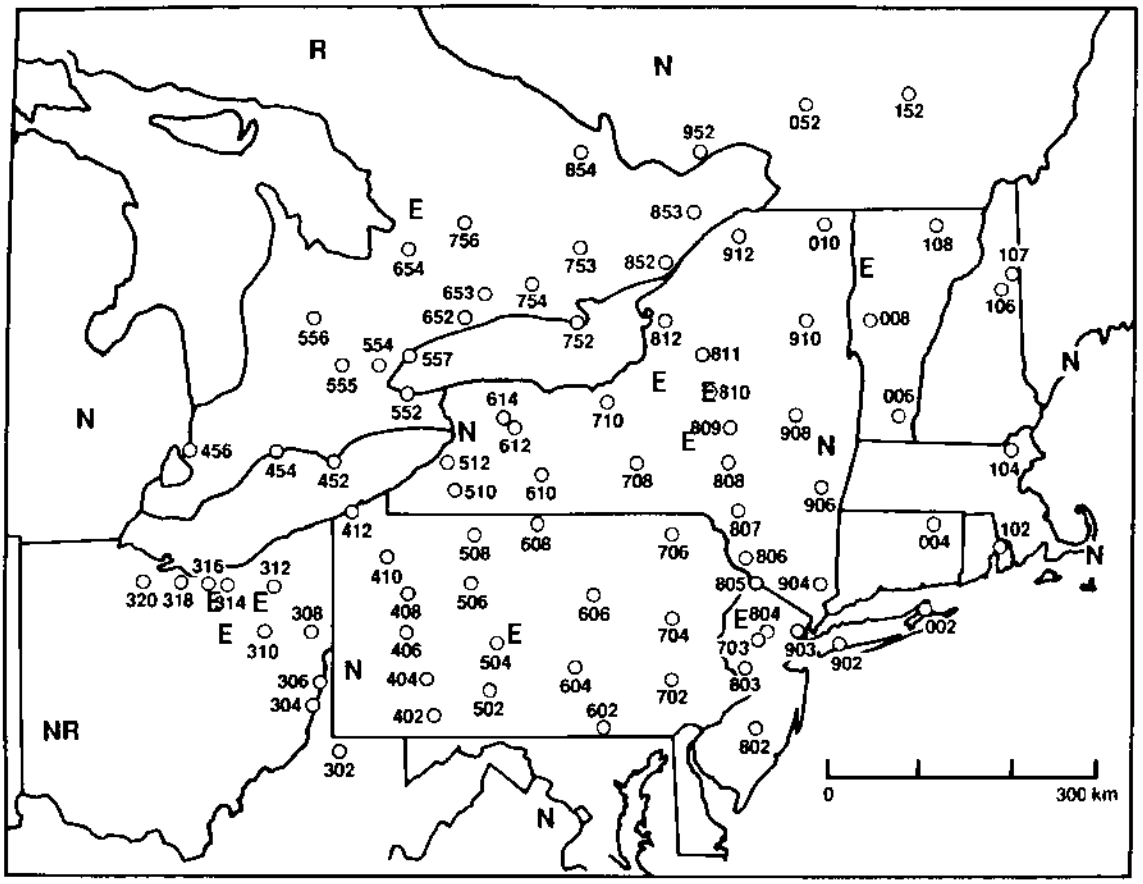

Figure 3.13: Locations of the two CAPTEX tracer release sites (R), the 86 surface sampling sites (circles with site numbers), the standard U.S. and Canadian upper-air stations (N), and the supplementary EPRI-sponsored upper-air stations (E) (adapted from Rodriguez, 1988).

The passage of a trough to the north of the Great Lakes during this period caused the upper-level flow (500 hPa) over the Lakes to veer from westerly to northwesterly. The corresponding low-level flow (1000 hPa) over the Lakes also veered during this period, changing from southwesterly to northwesterly.

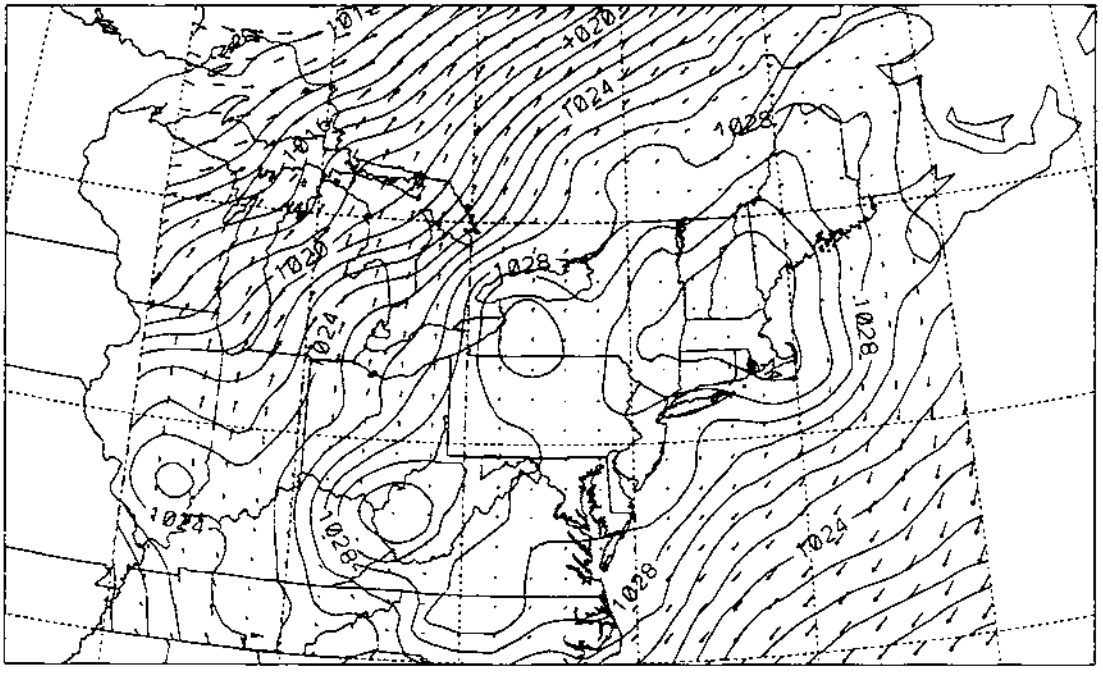

Figure 3.14: Estimated sea-level pressure field (hPa) and surface wind vectors for RAMS CAPTEX-simulation initial state at 1200 GMT, 25 September 1983 as produced by Stage 5 of the RAMS ISAN package. The contour interval is 1 hPa and the maximum wind vector is 20 $m\,s^{-1}$. Latitude and longitude lines are drawn every 5° from 95°W to 60°W and from 35°N to 45°N on the orthographic base map.

Figs. 3.18, 3.19, and 3.20 show the evolution of the low-level flow field over the CAPTEX domain for a 48 h period encompassing the 3-h tracer release and the first 43 h of transport. Low-level winds at Dayton were generally from the southwest on the

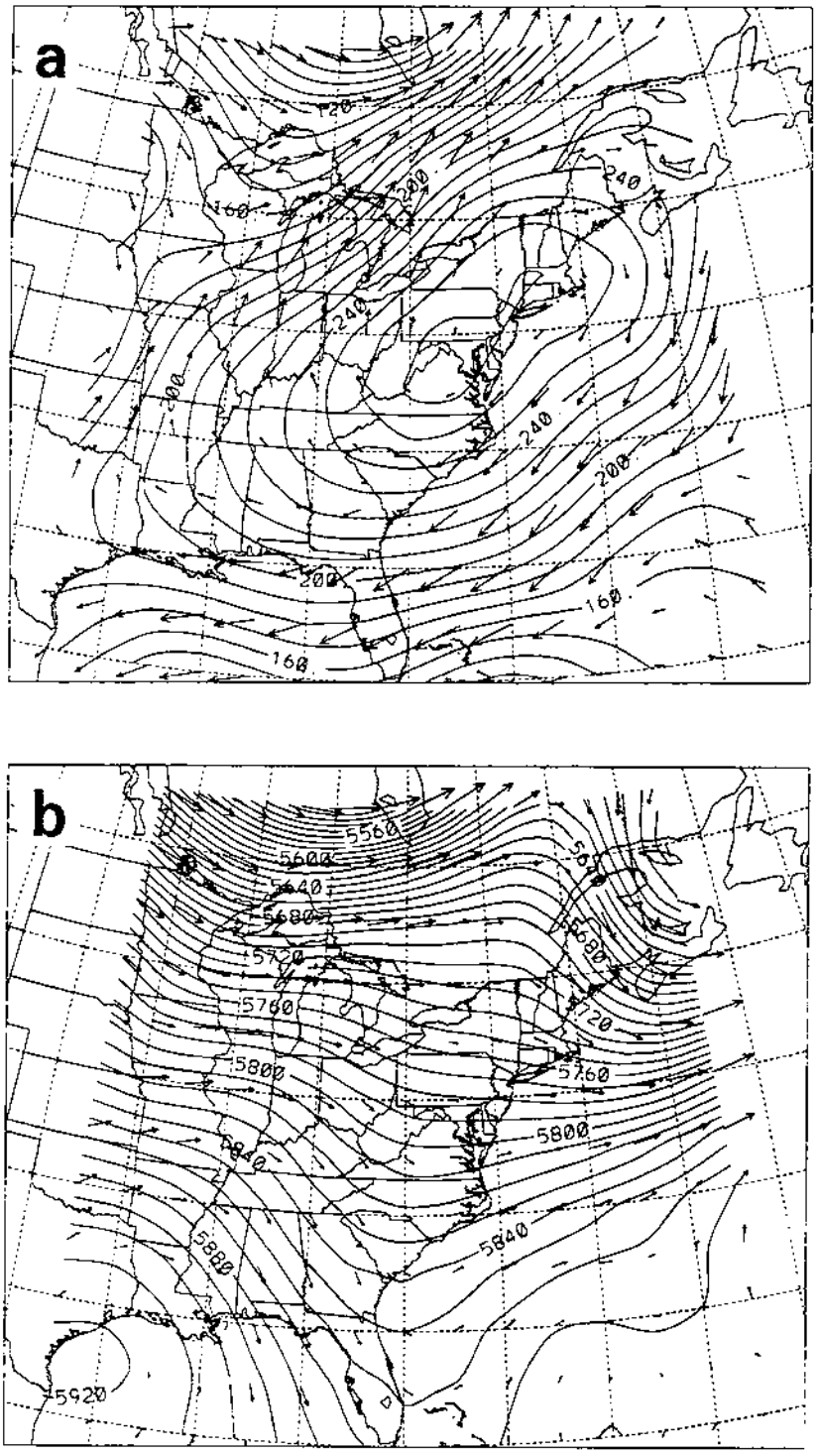

Figure 3.15: ISAN Stage 1 vector winds and geopotential heights at 1200 GMT (0800 EDT), 25 September 1983 over eastern North America at (a) 1000 hPa and (b) 500 hPa, five hours before the start of the tracer release. The geopotential height contour interval is 10 m, and the greatest wind speeds are 16.1 and 28.0 $\mathrm{m\,s^{-1}}$, respectively. Latitude and longitude lines are plotted every 5° from 110°W to 50°W and from 30°N to 55°N on the orthographic base map.

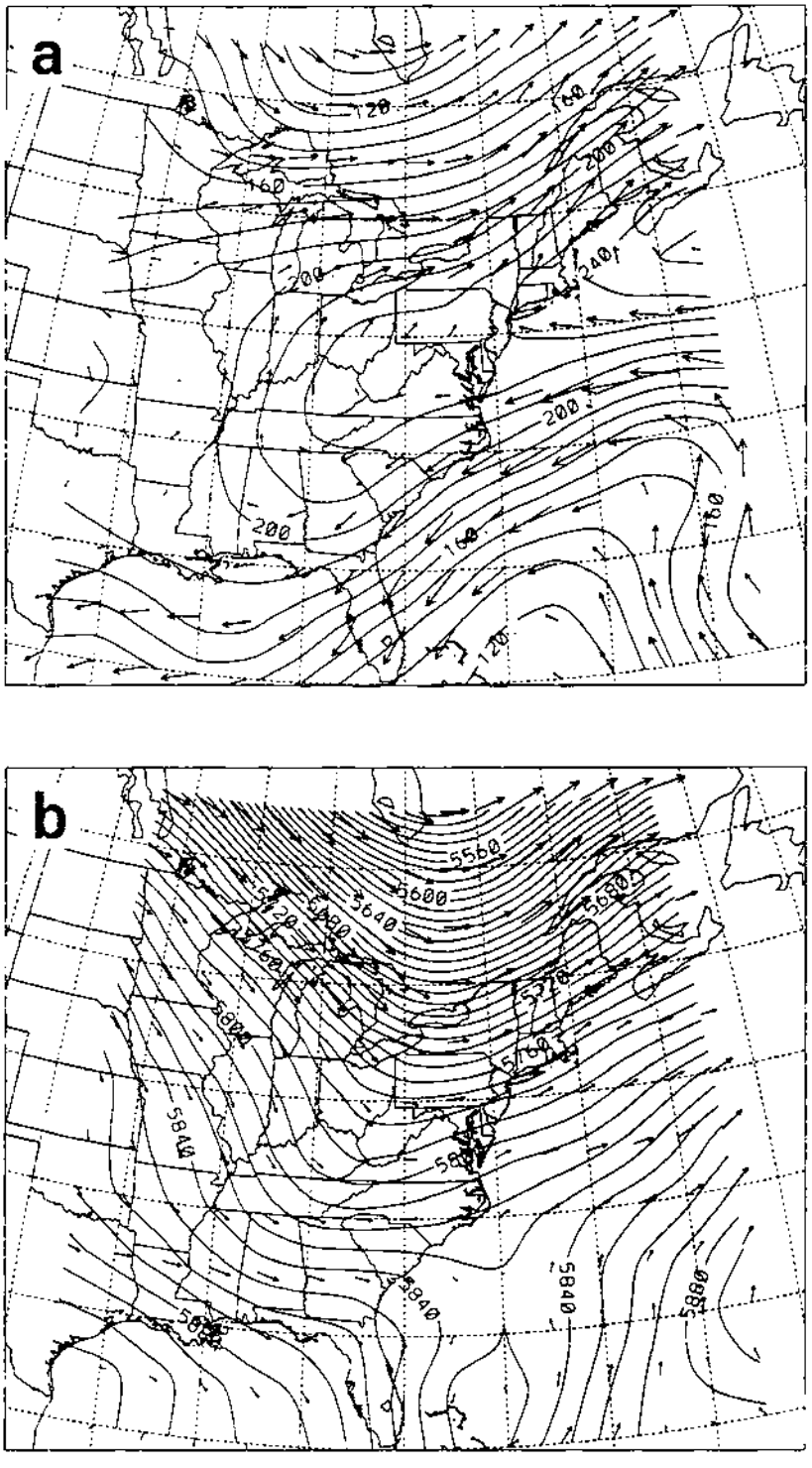

Figure 3.16: Same as Fig. 3.15 except for 1200 GMT, 26 September 1983, 19 hours after the start of the tracer release. The greatest wind speeds are 15.6 and 29.5 $\mathrm{m\,s^{-1}}$, respectively.

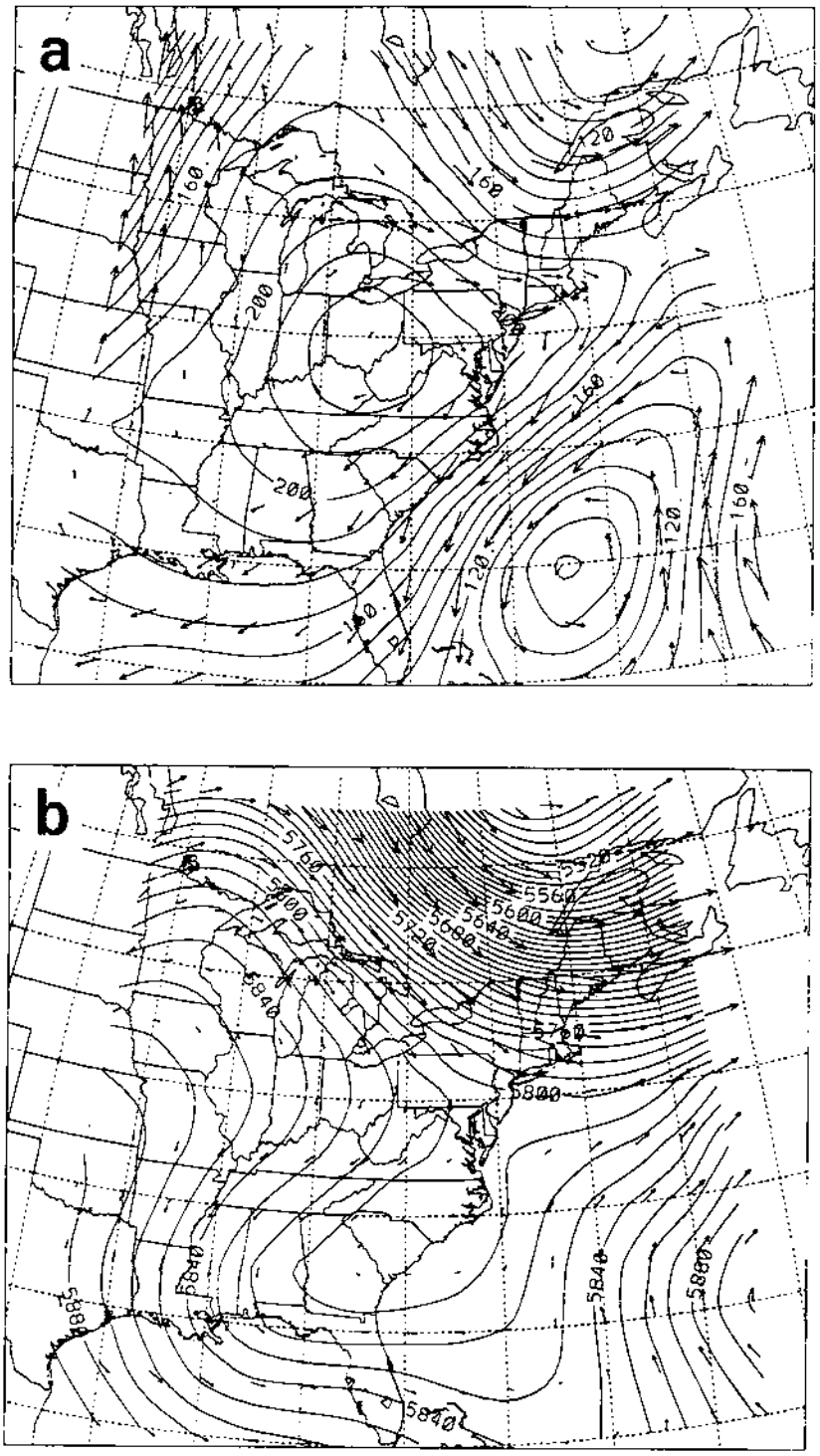

Figure 3.17: Same as Fig. 3.15 except for 1200 GMT, 27 September 1983, 43 hours after the start of the tracer release. The highest wind speeds are 17.0 and 34.3 $\mathrm{m\,s^{-1}}$, respectively.

25th at the time of the tracer release. Downwind of Dayton, the 850 hPa (i.e., 1579 m level) flow over Lakes Erie and Ontario veered from southwesterly on the 25th to westerly on the 26th to northwesterly on the 27th. A weak cold front entered the sampling area from the northwest on the 26th but then dissipated by evening. No other frontal passages occurred during the study period (Brown et al., 1984).

One important aspect of Figs. 3.18–3.20 is that the synoptic pattern over the CAPTEX domain for the two-day period following the tracer release can in no way be considered steady. Most significant is the passage of the domain-scale trough across the top of the domain. This hard fact poses a significant challenge to modelling this case as will be discussed further in Chap. 6.

3.2.3 Results

Fig. 3.21 lists above-background PMCH levels measured during CAPTEX Release 2. Peak PMCH ground-level concentrations over 300 times background were measured at some of the sampler sites closest to the source for this release while GLCs over 30 times background were measured at some of the more distant sites. The tracer puff was detected as far as 1100 km away from the source and up to 3 days after the release. Fig. 3.22 shows the time evolution of the tracer GLC pattern for this release over a 42 h period. The plume is initially quite narrow as it travels over Lakes Erie and Ontario during the early-morning hours of Sept. 26 but then broadens considerably. A secondary concentration maximum is noticeable for two of the sampling periods. Fig. 3.23 shows a time-composited tracer 'plume' based on the set of largest period-average concentration measured by each sampler during the Release 2 experimental period. Note (i) the steep dropoff in PMCH concentration from a maximum of 1575 fl l^{-1} on the 300-km arc[114]

[114] Only nominally 300 km in this case — the station reporting the maximum, No. 318, was actually located 203 km from Dayton. This problem likely arose because of the difficulty of siting stations in the vicinity of Lake Erie (Fig. 3.13). The downwind distances of stations on other sampling arcs were much more likely, with a few exceptions, to correspond to the distance indicated by their sampling arc's name (e.g., Table 3.5).

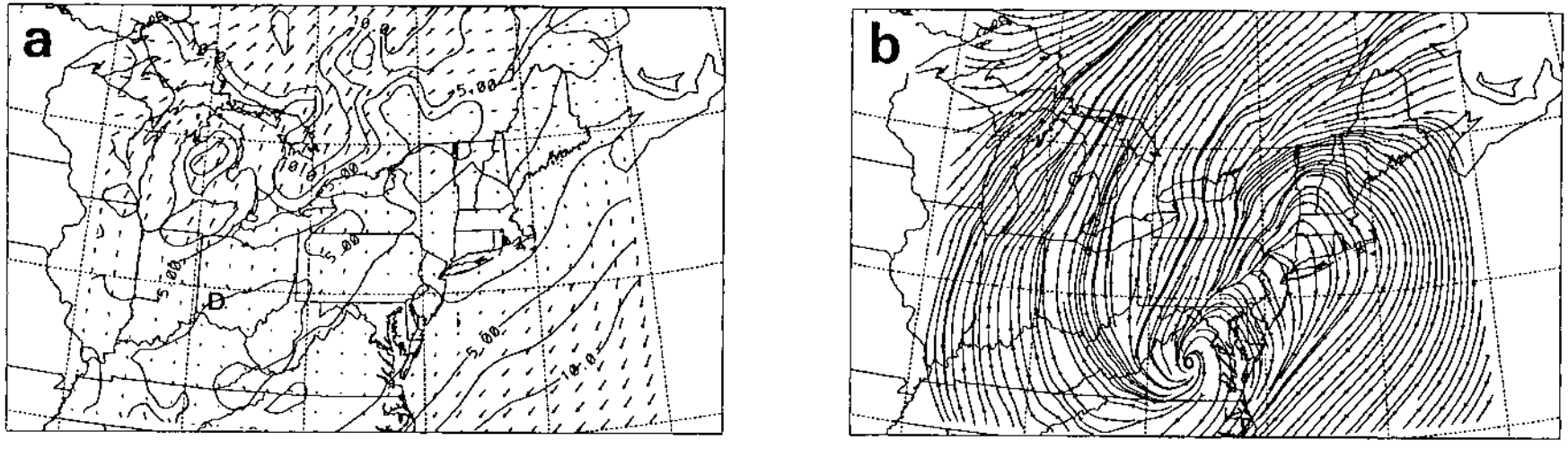

Figure 3.18: Isotach fields overlaid with wind vectors at every second grid point on the CAPTEX-simulation RAMS domain (35–50°N, 90–65°W) on Sept. 25, 1983, 1200 GMT at (a) 50 m AGL, (c) 1470 m AGL, and (e) 3380 m AGL (in z^* coordinates) together with corresponding streamline fields at (b) 50 m AGL, (d) 1470 m AGL, and (f) 3380 m AGL. Isotachs are drawn every 2.5 m s^{-1} and the maximum wind vector magnitude is 20 m s^{-1}. An orthographic map projection has been used.

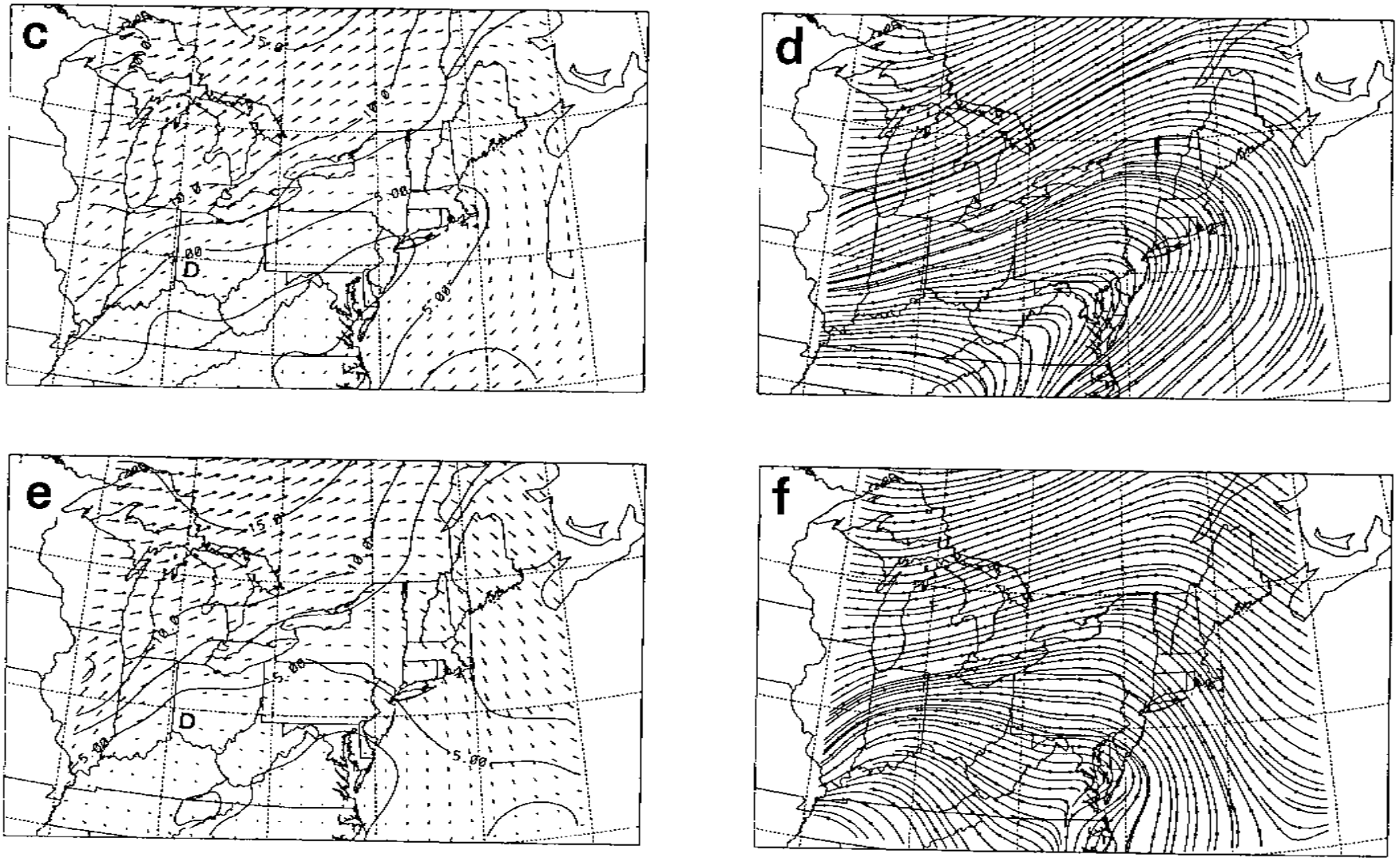

Figure 3.18: (Continued).

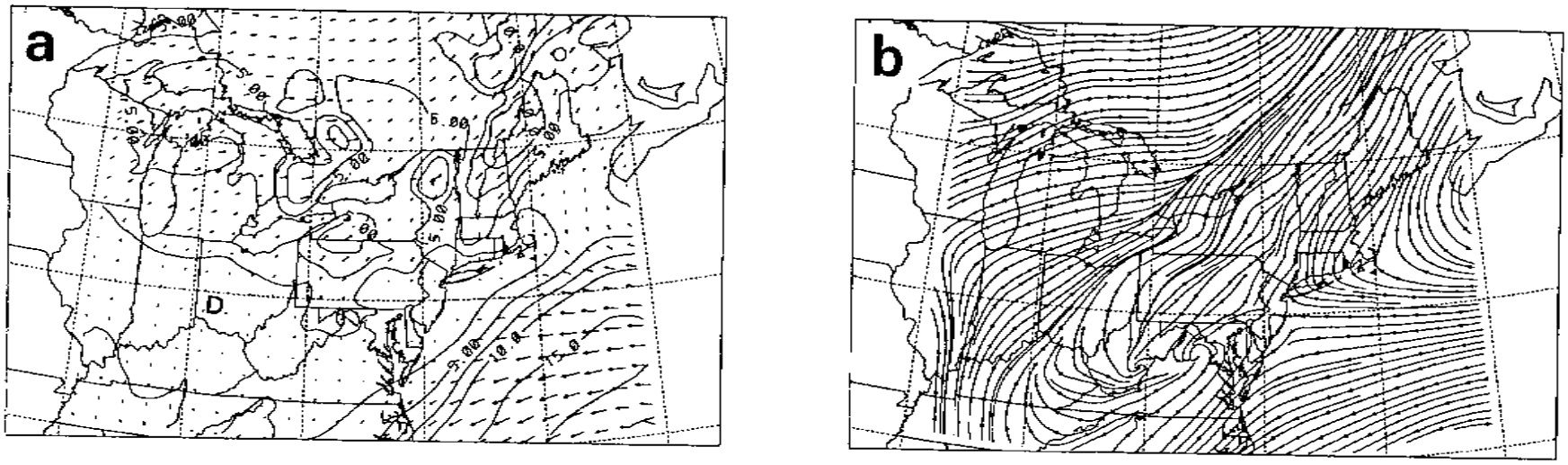

Figure 3.19: Same as Fig. 3.18 except for Sept. 26, 1983, 1200 GMT.

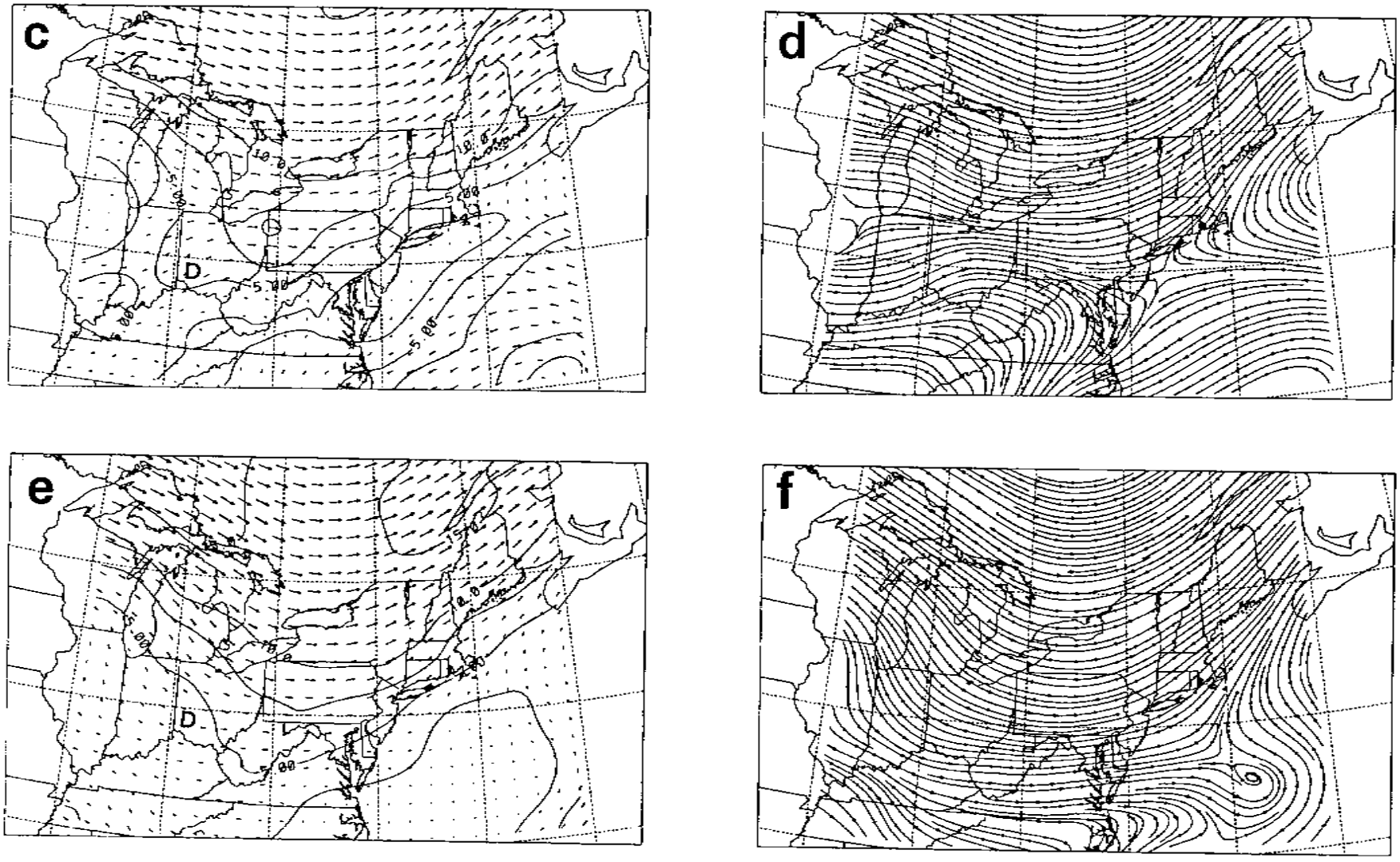

Figure 3.19: (Continued).

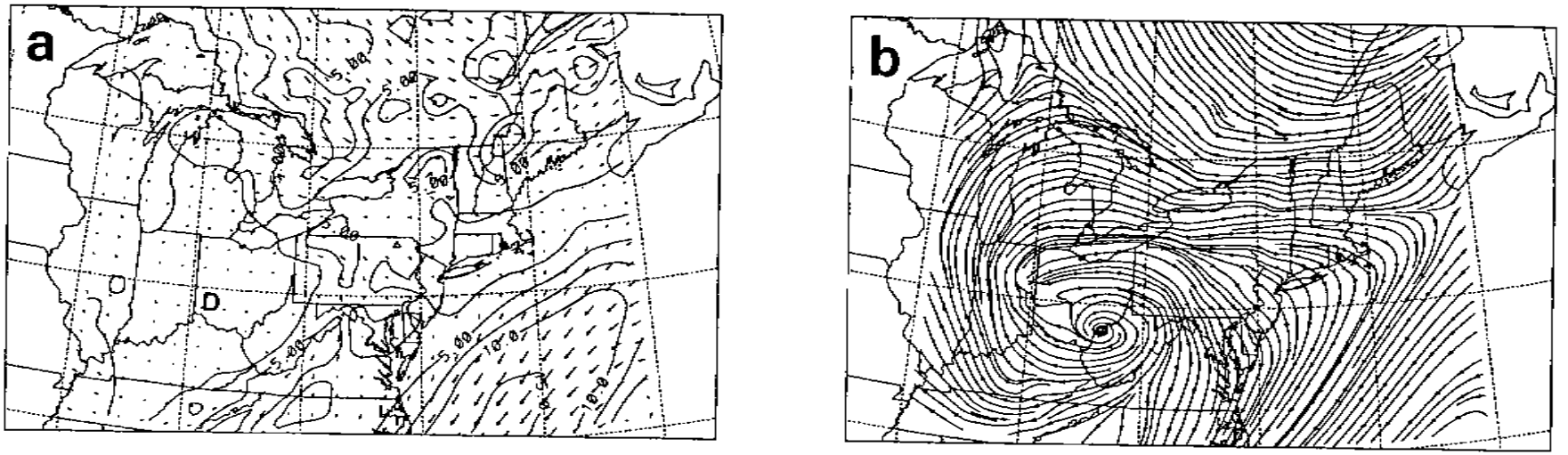

Figure 3.20: Same as Fig. 3.18 except for Sept. 27, 1983, 1200 GMT.

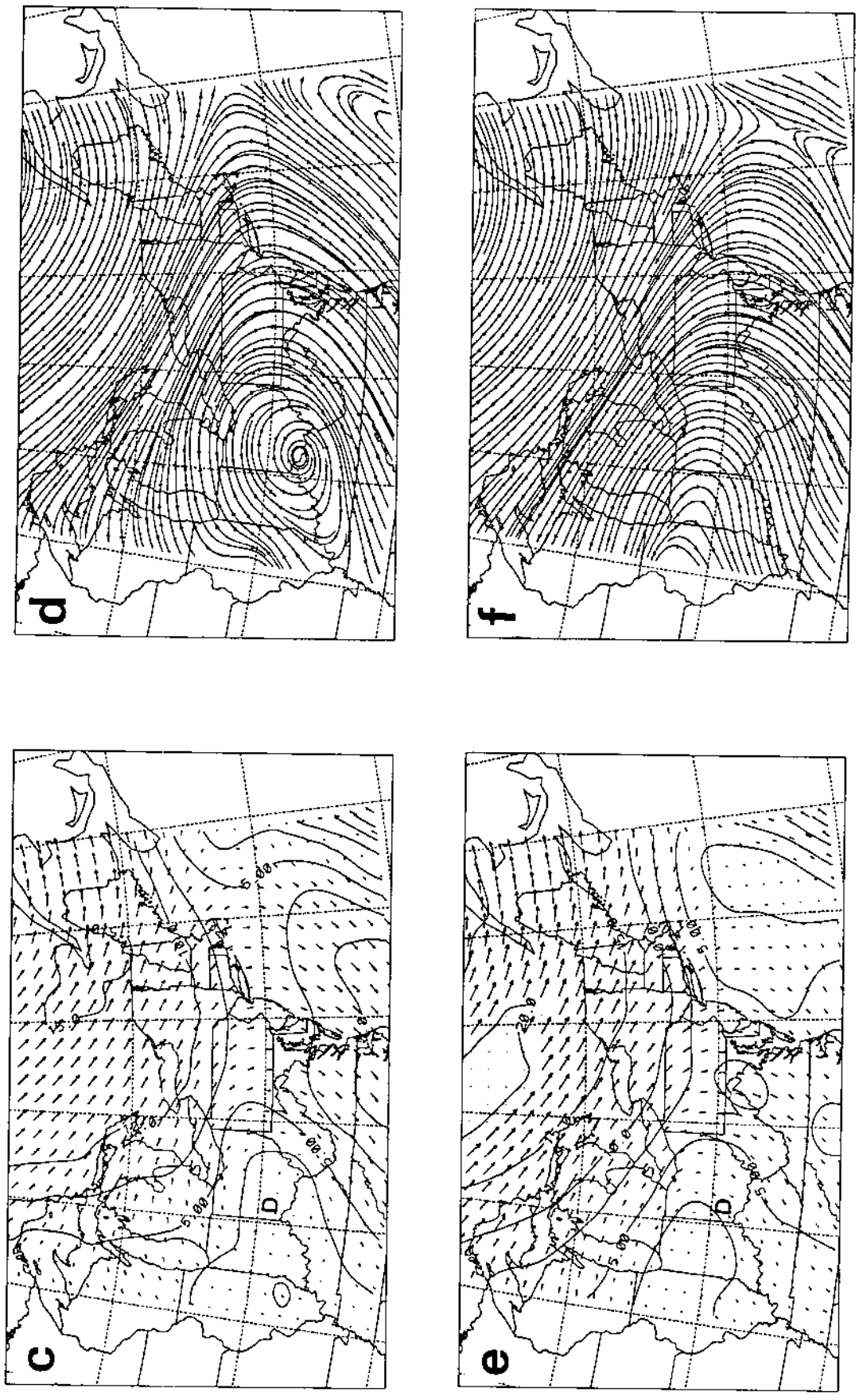

Figure 3.20: (Continued).

to a maximum of 200 fl l^{-1} on the 400-km arc[115] and (ii) the secondary maximum in western New York state. Fig. 3.24, on the other hand, shows the average ground-level plume; this is based on the average PMCH ground-level concentration at each station for its full 18-h or 36-h period of operation. It is clear from both Figs. 3.23 and 3.24 that *every* operating U.S. station on the 700-, 800-, 900-, 1000-, and 1100-km arcs sampled measurable levels of PMCH, suggesting that the cloud was both broad and unfragmented after more than a full day of transport, deformation, and diffusion.

Table 3.5 lists concentration measurements from the 800-km-arc stations plus Stations 703 and 753, which were actually located on the 800-km arc[116], in the same format as used in Tables 3.1 and 3.2. The 800-km arc was the sampler arc with doubled spatial density and is worth a little special attention. Note too that Stations 703 and 804 were located only about 14.6 km apart (Fig. 3.13); that is, they were effectively co-located in a mesoscale sense. Similar PMCH concentration levels were in fact measured at these two sites during the four 6-hour sampling periods that they had in common.

Fig. 3.25 compares observed and RADM's predicted 'event-total' (total time-integrated station sampler concentration values minus a uniform background concentration, that is, total elevated exposure; see Eqs. 1.22 and 1.23) PMCH 'plumes' for six of the seven CAPTEX releases. Although the four Dayton releases shown in Fig. 3.25 were all made at midday under relatively homogeneous meteorological conditions (southwesterly anticyclonic flow), the resulting ground-level maximum concentration patterns varied considerably, particularly the one for Release 3, which showed a markedly bimodal tracer distribution. The two releases from Sudbury were made at night into strong northwesterly flow following a cold front. In all cases, good vertical mixing was expected at the time of release.

---

[115] Note, though, that the sampling period for the 300-km-arc stations was 3 h vs. the 6-h periods used on the other arcs.

[116] The first digit in each three-digit CAPTEX station number was supposed to indicate the sampling arc on which the station was located.

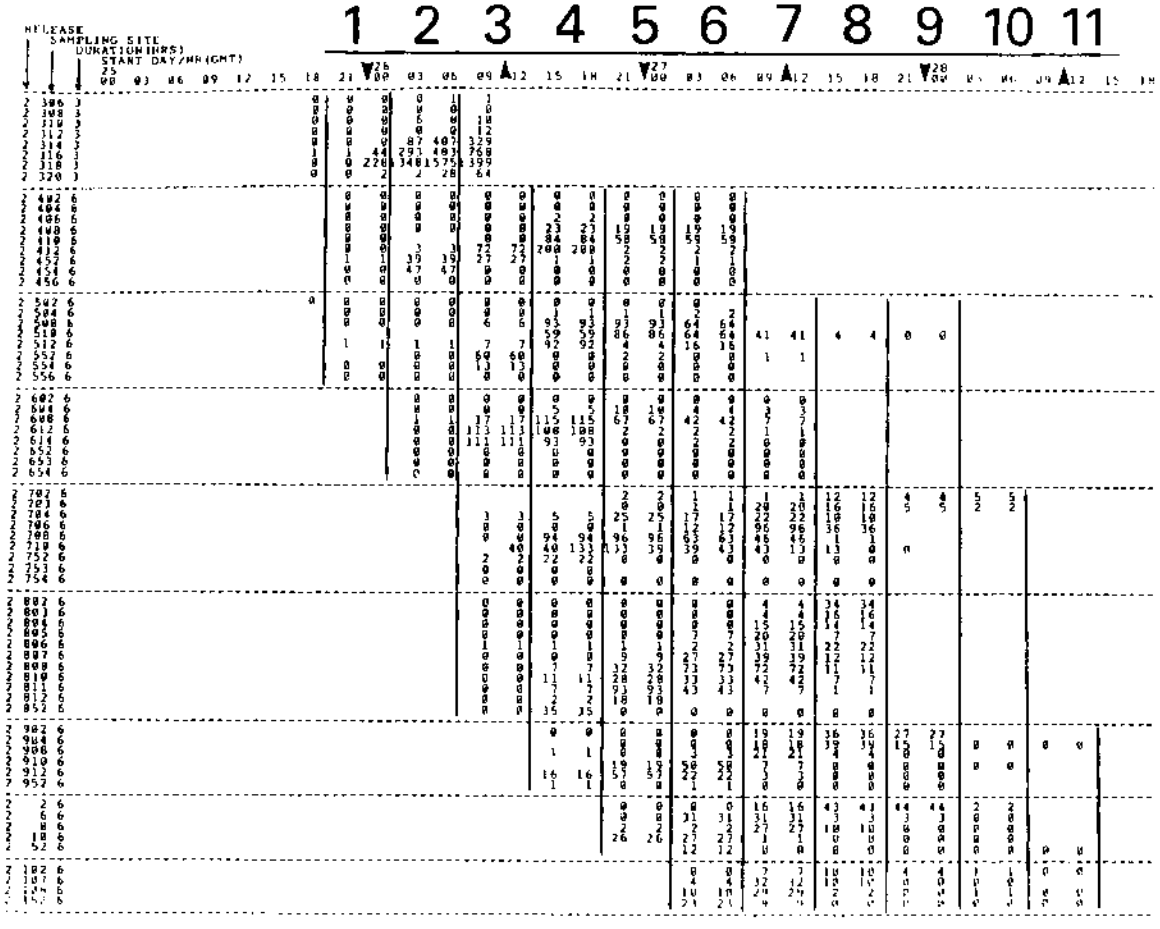

Figure 3.21: Ground-level measured PMCH concentrations (fl l^{-1}) for CAPTEX release 2 on Sept. 25, 1983 (from Ferber et al., 1986). A value of 3.4 fl l^{-1} has been subtracted from these measured concentrations to remove the background level and sampling 'noise'. Only observations from the 300-km arc are true 3-hour samples; all others are 6-hour samples which have been listed in this table as two identical 3-hour values. Only 68 stations are listed in this table; no valid data were obtained at the other 18 stations.

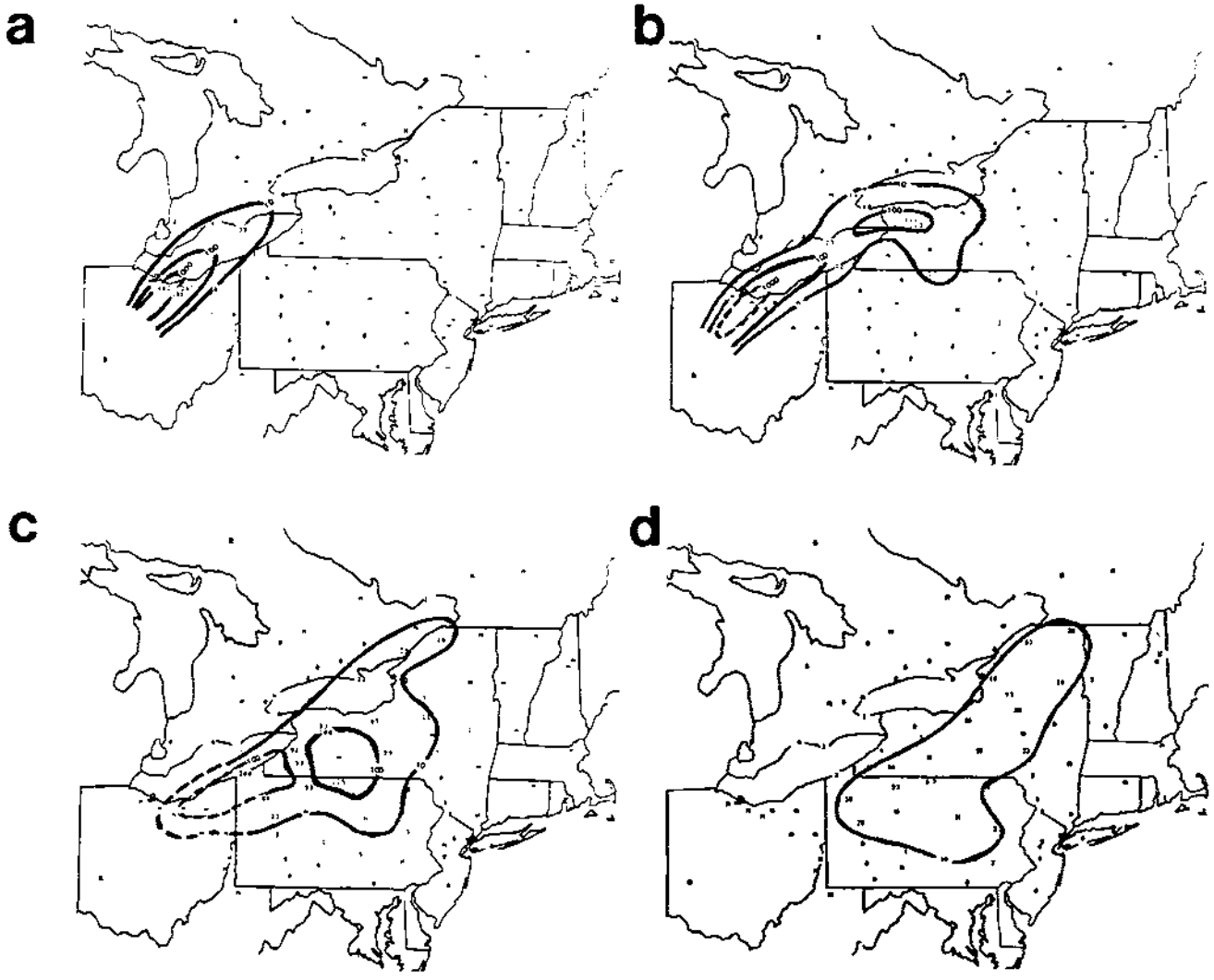

Figure 3.22: Average 6-hour PMCH surface concentration patterns (fll^{-1}) for seven of the sampling periods (Nos. 2–8) following the Sept. 25, 1983 CAPTEX tracer release (1705–2005 GMT) at Dayton, Ohio: (a) Sept. 26, 0300–0900 GMT, 10–16 h after start of release (ASOR); (b) Sept. 26, 0900–1500 GMT, 16–22 h ASOR; (c) Sept. 26, 1500–2100 GMT, 22–28 h ASOR; (d) Sept. 26-27, 2100–0300 GMT, 28–34 h ASOR; (e) Sept. 27, 0300–0900 GMT, 34–40 h ASOR; (f) Sept. 27, 0900–1500 GMT, 40–46 h ASOR; (g) Sept. 27, 1500–2100 GMT, 46–52 h ASOR (adapted in part from Ferber et al., 1986).

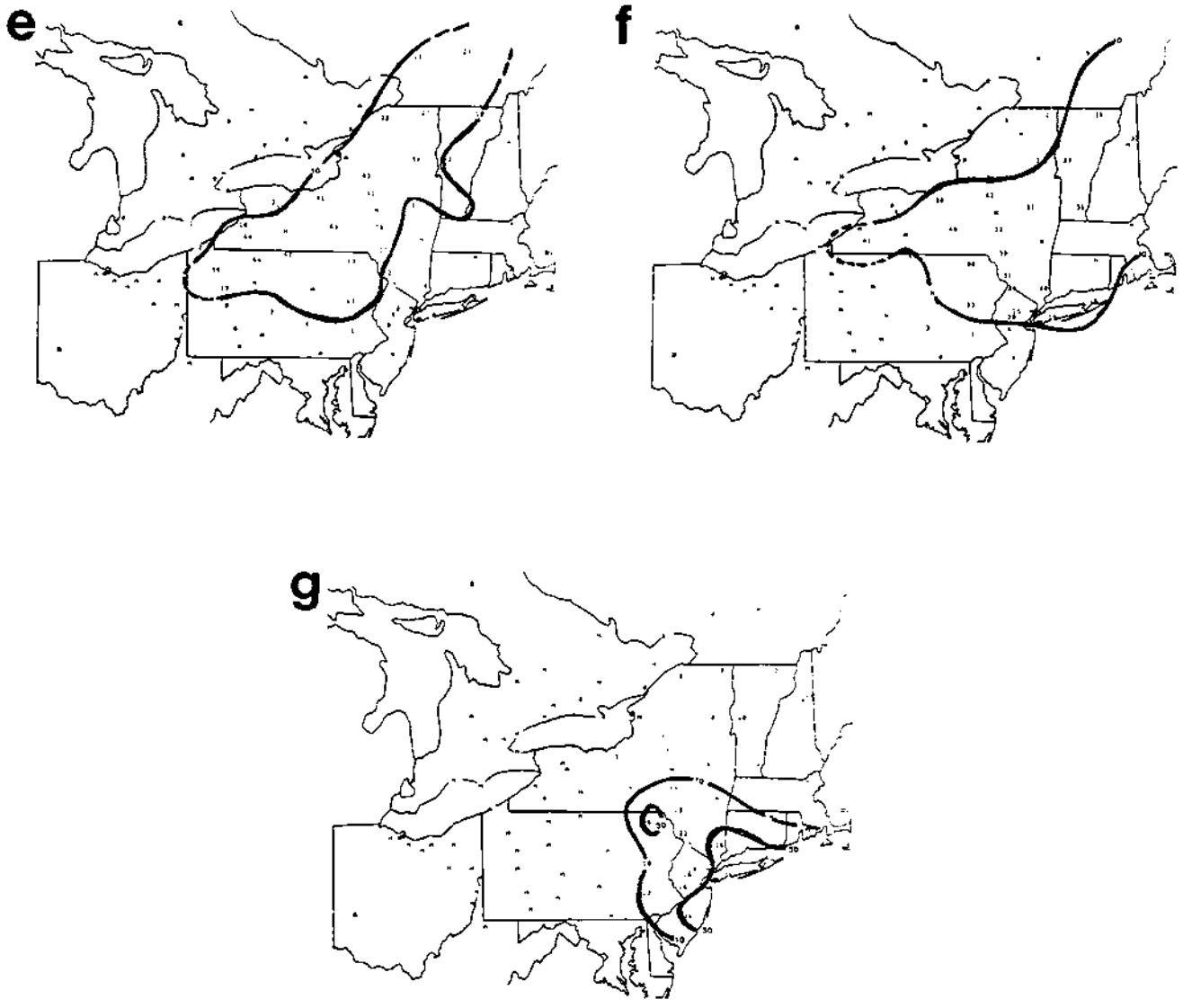

Figure 3.22: Continued.

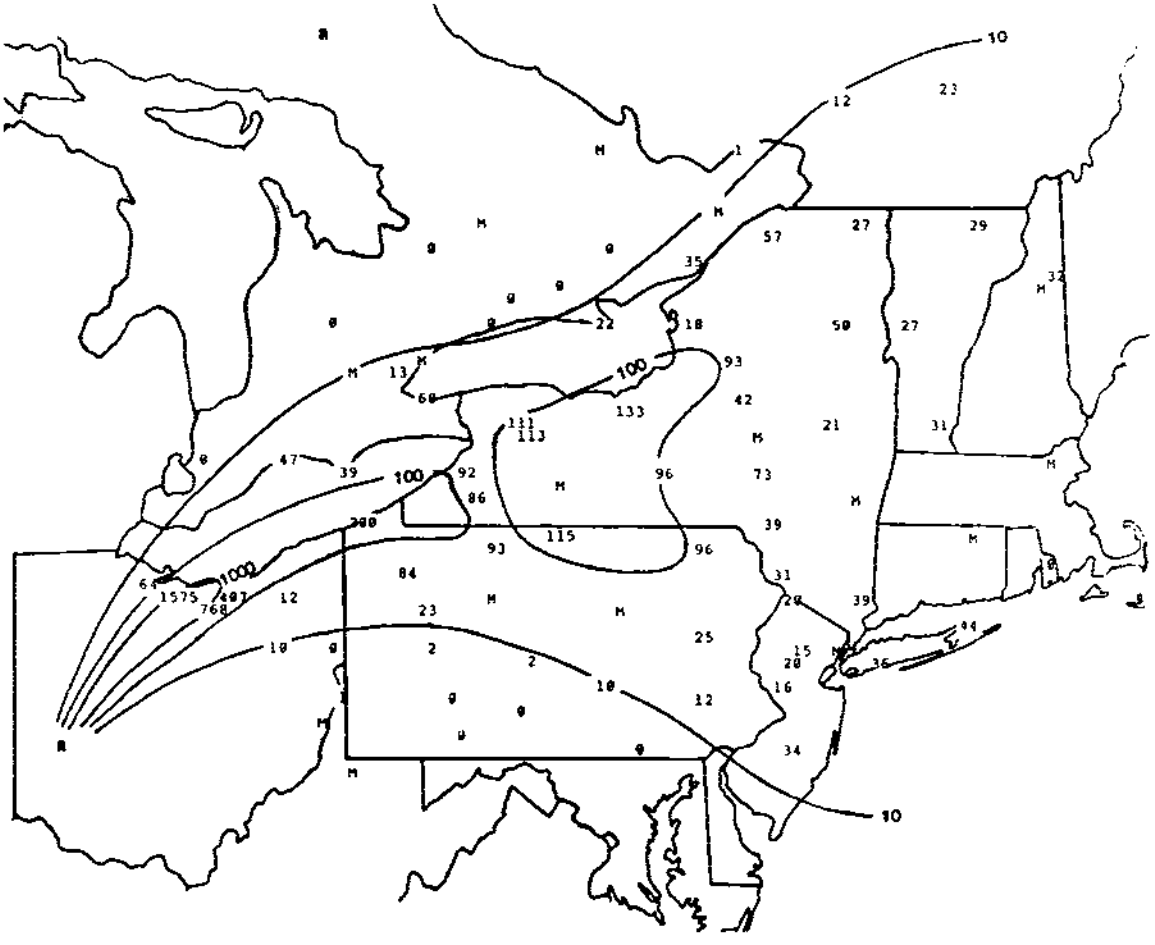

Figure 3.23: Maximum 3-hour or 6-hour PMCH ground-level concentration value (fl^{-1}) measured over the entire sampling period at each CAPTEX surface sampling site after CAPTEX Release 2 on Sept. 25, 1983, 1705–2000 GMT, from Dayton, Ohio (from Ferber et al., 1986).

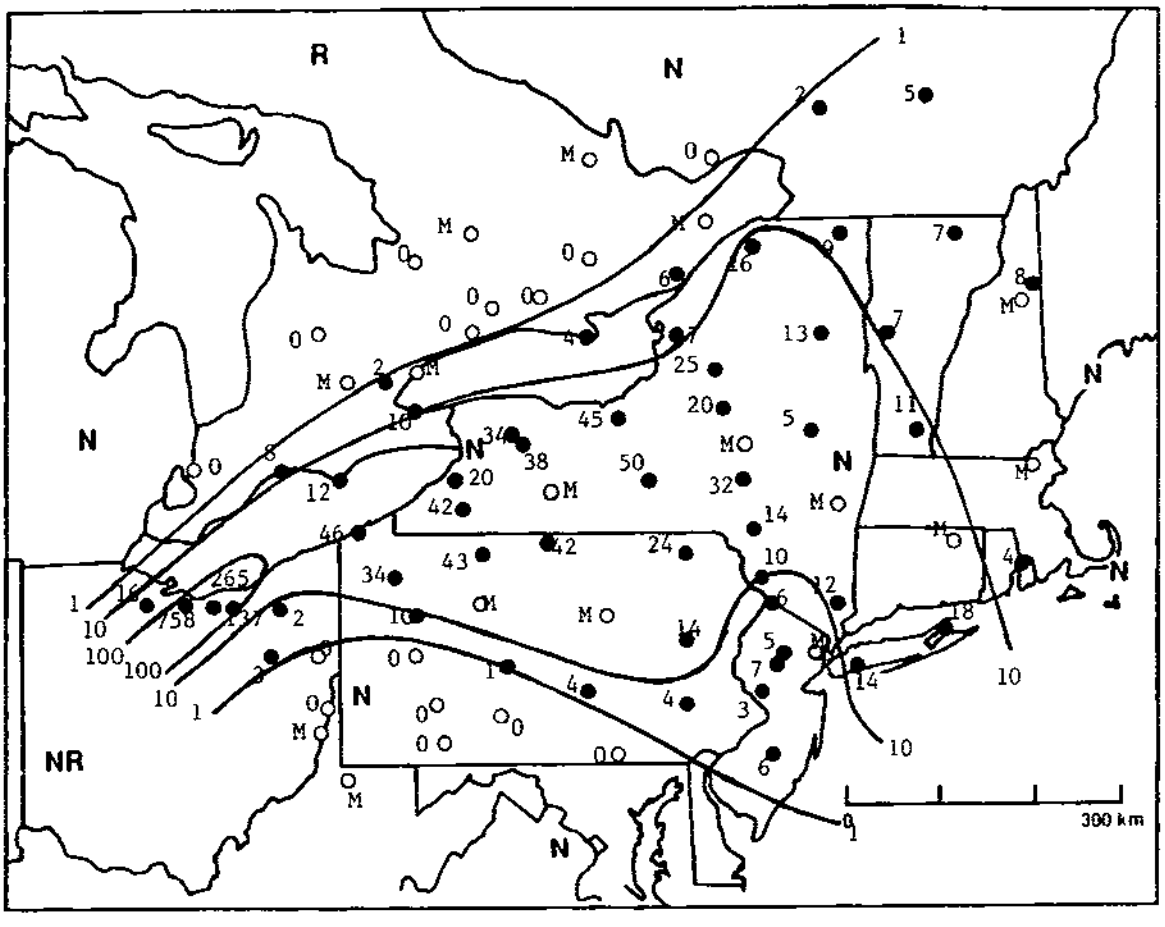

Figure 3.24: Average 3-hour or 6-hour PMCH ground-level concentrations (fll^{-1}) measured over the entire sampling period at each CAPTEX surface sampling site after CAPTEX Release 2 on Sept. 25, 1983, 1705–2000 GMT, from Dayton, Ohio.

Table 3.5: CAPTEX 800-km-arc PMCH concentration measurements in $\mathrm{fl\,l^{-1}}$ (extracted from Fig. 3.21). The topmost line of the table lists azimuth angle (in degrees) from the release site at Dayton, Ohio to the sampling sites as determined by spherical trigonometry; north corresponds to 0, east to 90, etc. The next line gives the corresponding great-circle distance (km) from the release site to the sampler sites. The main body of the table lists the concentration measurements; a dash (–) indicates 'no data'. The very last horizontal line of the table lists station exposures calculated over the 8 sampling periods listed. The rightmost vertical column gives crosswind-integrated concentrations for each six-hour sampling period based on an average 800-km-arc station spacing of 47.5 km (determined from the average downwind distance of 812 km and average azimuthal spacing of 3.35° of the 11 interior stations). Finally, the value in the lower right-hand corner is the crosswind-integrated exposure (CWIE) over all 13 stations and 8 sampling periods in units of $\mathrm{fl\,km\,h\,l^{-1}}$.

Azim.	44.0	49.2	52.3	56.5	59.3	65.5	68.7	72.4	75.1	78.3	79.2	81.8	86.0	
Dist.	785	841	812	823	814	808	803	805	809	810	803	789	798	
Start Time	**800-km-arc Station Number**													**CWIC**
(GMT)	753	852	812	811	810	808	807	806	805	804	703	803	802	($\mathrm{fl\,km\,l^{-1}}$)
0900	0	0	0	0	0	0	0	1	0	0	–	0	0	48
1500	0	35	2	7	11	7	0	1	0	0	–	0	0	2993
2100	–	0	18	93	28	32	9	1	0	0	0	0	0	8598
0300	–	0	–	43	33	73	27	2	7	0	1	0	0	8835
0900	–	0	–	7	42	72	39	31	20	15	20	4	4	12065
1500	–	0	–	1	7	11	12	22	7	14	16	16	34	6650
2100	–	–	–	–	–	–	–	–	–	–	5	–	–	238
0100	–	–	–	–	–	–	–	–	–	–	2	–	–	95
Expos. ($\mathrm{fl\,h\,l^{-1}}$)	0	210	120	906	726	1170	522	348	204	174	264	120	228	237120

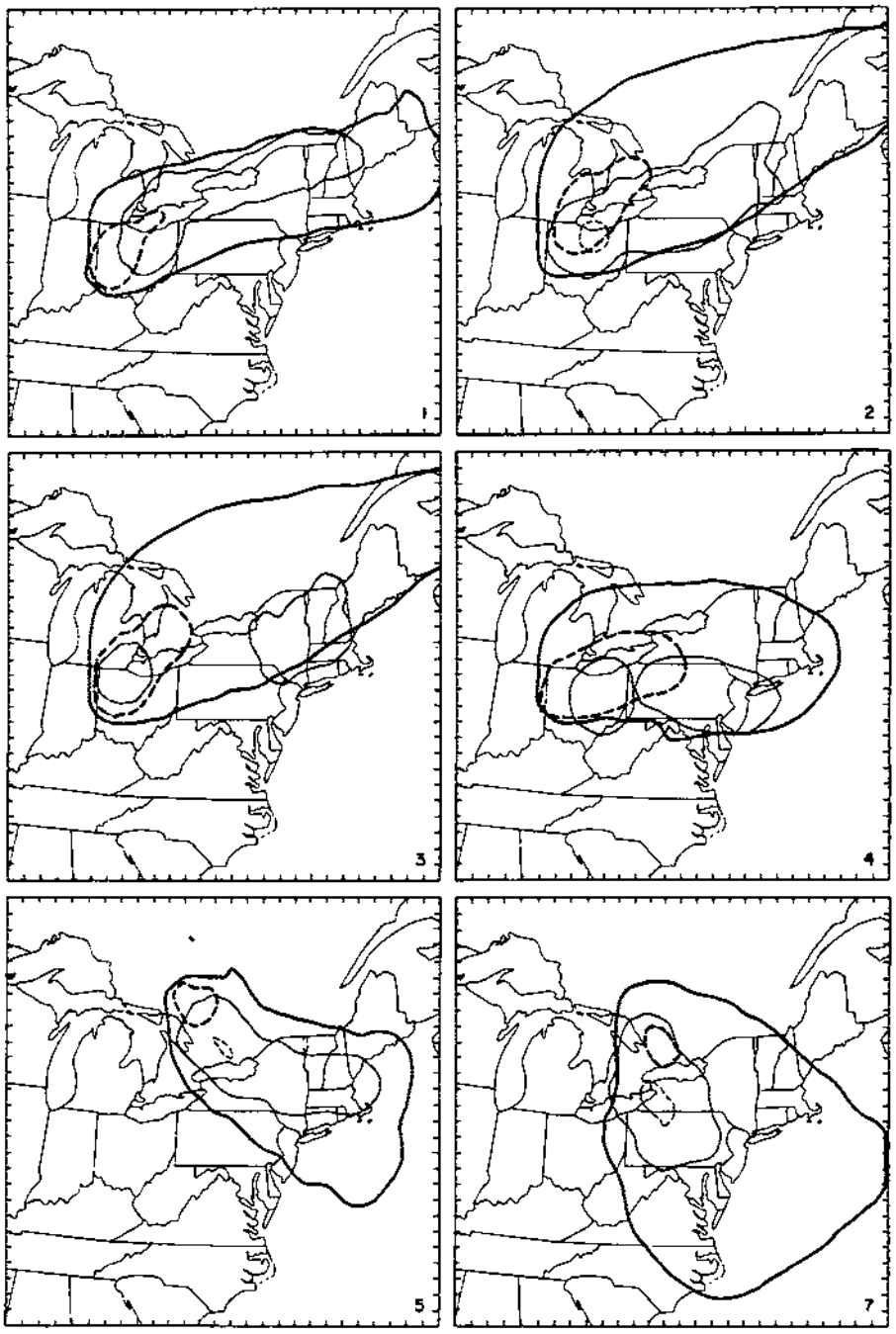

Figure 3.25: Comparison of observed and simulated (experiment G) event-total (i.e., total dose) plumes for CAPTEX releases 1–5 and 7. The heavy lines denote model-predicted PMCH concentrations and the light lines denote observed PMCH concentrations. Solid lines correspond to $10\,\mathrm{fl\,l^{-1}}$ and dashed lines to $300\,\mathrm{fl\,l^{-1}}$. The dispersion model used for these simulations was the NCAR RADM with 70 km horizontal grid spacing. Prognostic meteorological fields with 70 km horizontal grid spacing were obtained from the Penn State/NCAR mesoscale model. Tick marks on the panel edges show the grid spacing. Note that each of the simulations was halted when any of the tracer material reached the edge of the model domain. For the six panels shown, the lengths of the simulations were 30 h, 30 h, 30 h, 24 h, 30 h, and 18 h, respectively (from Brost et al., 1988a).

3.2.4 Discussion

Travel time

PMCH tracer released from 1700–2000 GMT (1200–1500 EST) on Sept. 25, 1983 during CAPTEX Release 2 was first detected at the 300-km sampler arc[117] during the third 3-h sampling period from 0000–0300 GMT (1900–2200 EST), which began seven hours after the start of the release. Examination of the concentration levels listed in Fig. 3.21 suggests that the leading edge of the tracer cloud likely reached the sampler arc late in this period, giving a transport time of about 9.25 h or a transport wind speed of about 22 $\mathrm{km\,h^{-1}}$, considerably slower than the estimate of daytime transport speed for the Great Plains experiment.

Fig. 6.18a shows the advance of the leading edge of the ground-level tracer cloud across the other sampling arcs both in terms of clock time (GMT) and travel time relative to the start of the release. Although the temporal resolution of this figure is crude, the leading edge of the cloud seems to be travelling at a fairly speedy rate in a northeasterly direction.

Transit time

One significant difference between the measurements made in the Great Plains experiment along the 100-km and 600-km arcs was the increase in transit time across the two arcs: 3 h vs. 12 h. As in the Great Plains release, PMCH tracer was released for a three-hour period for CAPTEX Release 2. The cloud transit time was also markedly greater than the tracer release time even at the first CAPTEX sampler arc 300 km downwind from the release site. Significant concentration levels were measured for four consecutive 3-hour sampling periods along this arc (Fig. 3.21). Using the same estimate as above for the time of arrival of the cloud leading edge then gives a transit time of 10 h *or more.*

---

[117] Note that the 300-km distance is only a nominal value (see Fig. 3.13). Stations 320, 318, 316, 312, and 310 were located 187, 203, 227, 257, 296, and 255 km downwind, respectively, as calculated by spherical trigonometry.

The uncertainty arises because the largest cross-wind integrated concentration measured at this arc actually occurred on the sixth and last sampling period. There is no way to be certain when the trailing edge of the tracer cloud actually crossed the arc but it may well have been after the end of sampling at 1200 GMT on September 26.

Based on the concentration values listed in Fig. 3.21, arc transit times were on the order of 30 h across the 400-km arc, 30 h across the 500-km arc, 24 h across the 600-km arc, 33 h across the 700-km arc, 30 h across the 800-km arc, 36 h across the 900-km arc, 30 h across the 1000-km arc, and 18 h or more across the 1100-km arc. These values are only rough estimates because the sampling period may not have included the transit of the cloud's leading or trailing edge in every case. However, the general trend is clear: remarkable distortion and elongation of the cloud as evidenced by the order-of-magnitude difference between cloud release time and arc transit times.

Lateral spread

Table 3.6 is based on an analysis of the measured PMCH concentrations given in Fig. 3.21 and lists cloud widths for the CAPTEX 300-km sampling arc as determined by the two methods used before. The largest tracer measurements were taken during the 0300, 0600, and 0900 GMT 3-hour sampling periods, corresponding to mean travel times of 11.5, 14.5, and 17.5 h, respectively. Estimated plume widths for these three periods based on peak-relative thresholds are 54, 77, and 77 km, respectively (Table 3.6). The σ_y's corresponding to these widths are 13, 18, and 18 km. Heffter's formula (Eq. 2.40) yields predicted σ_y values of 21, 26, and 31 km for these three mean travel times. For the first downwind CAPTEX sampling arc, then, the observed cloud was narrower than expected when compared to Heffter's empirical formula, even more so considering the three-hour sampling period employed. Note, however, that the cloud widths determined using the twice-background threshold were up to twice as large as those estimated using the 10%-of-peak threshold.

Table 3.7 is based on Table 3.5 and shows the corresponding estimated cloud widths for the 800-km arc. If we take the third and sixth sampling periods in Table 3.7 as

representative, we obtain observed σ_y values of 53 and 92 km for mean travel times of 31 and 49 h, respectively. The corresponding σ_y values from Eq. 2.40 for these travel times are 56 and 88 km, that is, very similar.

Aircraft measurements

Gifford (1986) included cloud σ_y values from four of the CAPTEX releases (Nos. 2, 4, 5, and 7) for travel times ranging from 14 to 29 h on an atmospheric diffusivity summary diagram (Fig. 1.1). He obtained these values from an analysis of CAPTEX *aircraft* measurements[118] presented by Raynor et al. (1984). The σ_y value reported for Release 2 was 62 km based on an estimated cloud width of 250 km at a downwind distance of 827 km from the source after a travel time in the 27–31 h range[119]. This was by far the largest of the four pairs plotted. The σ_y values for the other three releases ranged from 13 to 18 km although the travel times were about half of that for Release 2. However, Raynor et al. 1984) estimated that wind directional shear was greater than 90° for Release 2 compared with values of about 20° or less for the other releases. The presence of this directional shear is supported by Fig. 3.19.

Fig. 3.26a shows the two tracks flown by multiple aircraft during CAPTEX Release 2. Two aircraft flew a total of three sorties and five passes at three elevations on the Toledo–Canton track while *four* aircraft flew two sorties and a total of five passes on the Wilkes-Barre—Watertown track in a vertical formation[120] (Ferber, 1985). Several of the aircraft made wind measurements in addition to tracer measurements (Michael et al., 1984). The aircraft flying the Toledo–Canton track between 0030 and 0500 GMT on Sept. 26 measured significant PMCH tracer amounts at 1220 m and 1525 m (as high as 1919 fl l^{-1} for a 10-minute flight segment at 1220 m at about 0300 GMT). However, the maximum

---

[118] I have not seen CAPTEX *surface*-concentration-based σ_y's plotted in a similar manner to date.

[119] Presumably reflecting the sum of the release time (3 h) and the aircraft flight time.

[120] At 4000, 5000, 6000, and 7000 feet ASL (or about 1220, 1525, 1830, and 2135 m).

Table 3.6: Estimated 300-km-arc PMCH cloud widths for CAPTEX Release 2 as determined by using two different cloud-edge criteria for each of the six 3-hour sampling periods. Cloud widths were not calculated for sampling periods when no station reported a reading of more than 3 fl l^{-1} above background. Cloud-edge uncertainty has been accounted for by using the azimuth of the midpoint between stations on either side of the cloud edge. The azimuth values used for Stations 320 to 310 were 24.5°, 36.0°, 42.2°, 44.9°, 54.8°, and 59.9°, respectively. Arc length (km) is based on the product of the azimuth range (°) and a downwind distance of 220 km (the average for Stations 314, 316, 318, and 320). Sampling started on Sept. 25, 1983, 1 h after the start of the tracer release at Dayton, Ohio.

Obs. No.	Start Time (GMT)	Conc. Max. (fl l^{-1})	St'n No.	Max. Width (10% of peak)			Max. Width (> 3 fl l^{-1})		
				St'n Range	Azim. Range	Arc Length	St'n Range	Azim. Range	Arc Length
1	1800	1	–	–	–	–	–	–	–
2	2100	1	–	–	–	–	–	–	–
3	0000	228	318	316–318	14	54	316–318	14	54
4	0300	1348	318	316–318	14	54	310–318	24	92
5	0600	1575	318	314–318	20	77	314–320	26	100
6	0900	1399	318	314–318	20	77	310–320	40	153

Table 3.7: Estimated 800-km-arc PMCH cloud widths for CAPTEX Release 2 as determined by using two different cloud-edge criteria for each of the six 6-hour sampling periods. Cloud widths were not calculated for sampling periods when no station reported a reading of more than 3 fl l^{-1} above background. Cloud-edge uncertainty has been accounted for by using the azimuth of the midpoint between stations on either side of the outermost cloud edge. Arc length (km) is based on the azimuth range (°) and a downwind distance of 808 km (the average for the 800-km-arc stations — see Table 3.5). Sampling started on Sept. 26, 1983, 16 h after the start of the tracer release at Dayton International Airport.

Obs. No.	Start Time (GMT)	Conc. Max. (fl l^{-1})	St'n No.	Max. Width (10% of peak) St'n Range	Azim. Range	Arc Length	Max. Width (> 3 fl l^{-1}) St'n Range	Azim. Range	Arc Length
1	0900	1	–	–	–	–	–	–	–
2	1500	35	852	808–852	20	282	808–852	20	282
3	2100	93	811	808–812	16	226	807–812	20	282
4	0300	73	808	807–811	16	226	805–811	22	310
5	0900	72	808	703–810	23	324	802–810	28	395
6	1500	34	802	802–810	28	395	802–810	28	395
7	2100	5	703	–	–	–	–	–	–
8	0300	2	–	–	–	–	–	–	–

concentration measured at the 1830 m level was only 6 fll^{-1} (Ferber, 1985; Ferber et al., 1986), possibly indicating the vertical limit of mixing. The four-aircraft stacked passes on the Wilkes-Barre—Watertown track detected significant amounts of PMCH tracer at all four levels, although the concentrations measured tended to decrease with height (Ferber et al., 1986; Stunder et al., 1986; Draxler and Stunder, 1988). Figs. 3.26b-c show PMCH concentration measurements made by one aircraft on the first and second sorties, respectively, on the Wilkes-Barre—Watertown track. Based on these profiles, it appears that the aircraft crossed the southern edge of the elevated tracer cloud but not the northern edge. Fig. 3.22c shows isopleths of the six-hour *surface* concentrations measured during the first aircraft sortie along the Wilkes-Barre—Watertown track; the surface footprint also has the northern portion of the track lying entirely within the tracer cloud but shows the southern end of the aircraft track extending past the southern edge of the cloud.

It is more difficult to use aircraft concentration measurements than sequential time-averaged surface measurements for a quantitative comparison against MAD model results because the former are infrequent and relatively short-term and short-range. Good agreement thus requires very high accuracy in modelling both vertical diffusion and cloud spatial position (and hence cloud transport direction and speed). However, aircraft measurements provide valuable complementary information about cloud position and structure at a few times and downwind distances and unique information about cloud vertical structure. Stunder et al. (1986) and Draxler and Stunder (1988) have used stacked crosswind-integrated concentration measurements from aircraft horizontal flight legs to study the observed vertical tracer profiles and to compare them with the CWIC profiles predicted by the ARL-ATAD trajectory model.

Cloud cross-wind shape

It is of course impossible to make a definitive statement about the cross-wind shape of a tracer cloud on the basis of three surface-based data points as in the case of the 300-km arc measurements listed in Fig. 3.21. It is still worth noting, nonetheless, that these

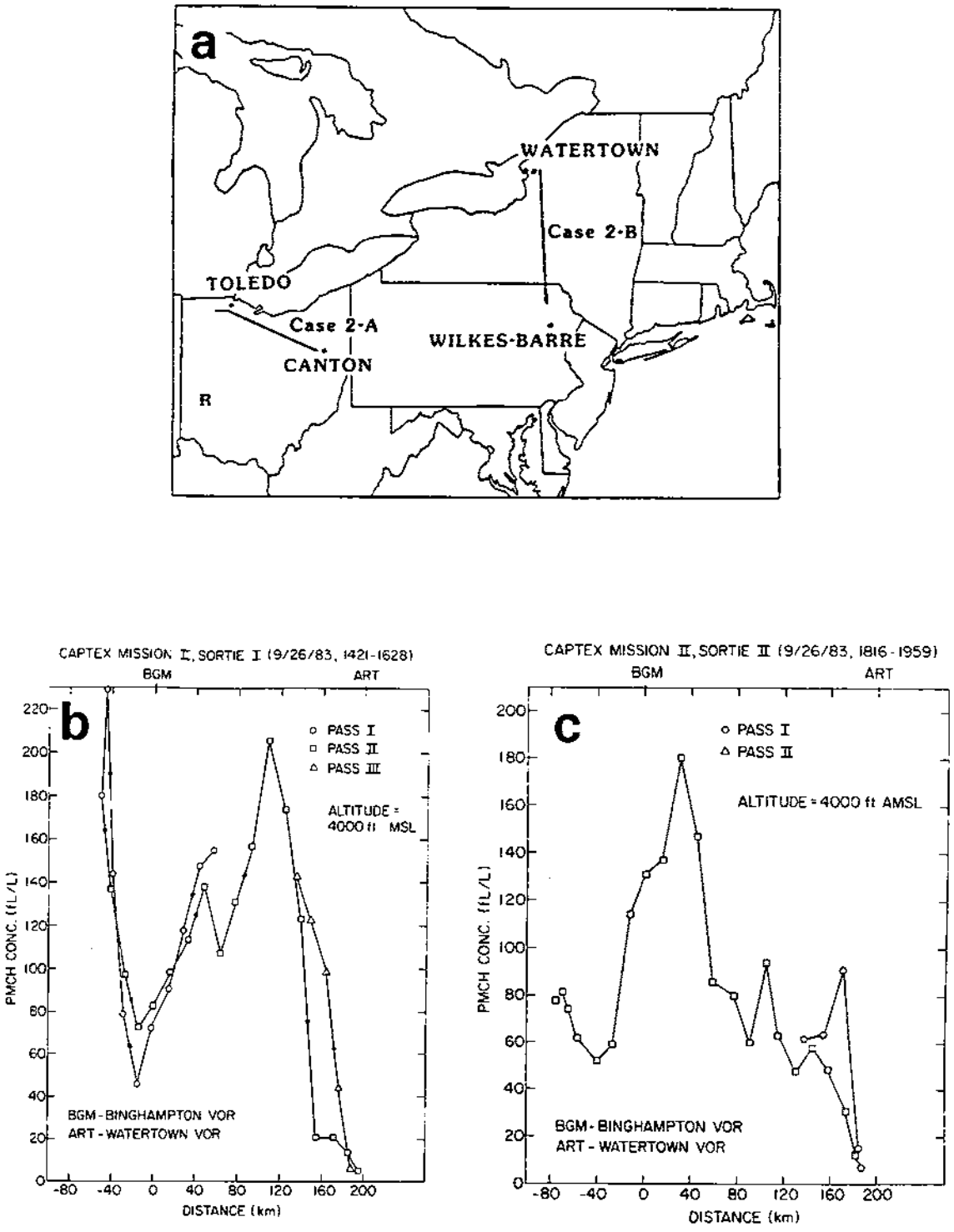

Figure 3.26: (a) Aircraft flight paths for CAPTEX Release 2; and some measured cross-plume PMCH concentration profiles about 750 km from Dayton at 1220 m ASL from (b) Sortie I and (c) Sortie II [from Stunder et al. (1986), Ferber (1985), and Raynor et al. (1984), respectively].

measurements suggest a non-Gaussian cross-wind structure even on the first day of travel. Concentrations are highest on the northern edge of the cloud, indicative of a skewed distribution with a sharply defined northern boundary and a more gradual decrease in concentration to the south. Such a distribution would be consistent with shear-enhanced dispersion in a veering wind profile (cf. Fig. 1.9). Measurements further from the source suggest an even more complicated lateral cloud structure after longer travel times. Examples include the last sampling time on the 800-km surface arc (Table 3.5) and the aircraft flights across upstate New York (Fig. 3.26b). Note that the multiple peaks in Fig. 3.26b persist across three sampling passes. One other interesting characteristic of the 800-km-arc GLC measurements is the southward shift with time of the location of the concentration peak from Station 852 to 811 to 808 to 801 (Table 3.5). Somewhat similar behaviour was seen in the Great Plains 600-km-arc measurements (Table 3.2).

Mass-balance analysis

We can also carry out mass-balance calculations for the 300 and 800 km CAPTEX sampler arcs similar to those done for the Great Plains experiment. From Fig. 3.21 the cross-wind integrated exposure at the 300-km arc is 545,791 fl km h l^{-1}, where we have used a mean station spacing value of 25.7 km. Then using a mean transport wind speed of 22 km h^{-1}, cloud transit time of 9.75 h, cloud/PBL depth of 1 km, cloud width of 103 km (i.e., 4 stations $\times$ 25.7 km/station), cloud length of 214 km (i.e., 9.75 h $\times$ 22 km h^{-1}), and fl l^{-1}–to–kg m^{-3} conversion factor of 6.4×10^{13} (see Sec. 4.6) yields 188 kg as an estimate of the total mass of PMCH tracer released during CAPTEX Release 2. The actual mass released was 201 kg, suggesting that the values used in the mass-balance calculations are reasonable. In particular, the PBL depth of about 1 km is much lower than the PBL depth of 3 km assumed in the Great Plains calculations but is consistent with the meteorogical conditions. Note that the CWIE value used in the above calculation might have missed some tracer mass since it is very possible that concentration measurements taken along the 300-km arc from 1200-1500 GMT on Sept. 26, 1983 might have sampled the trailing edge of the tracer cloud.

The corresponding CWIE value for the 800-km arc obtained from Table 3.5 is 237,120 fl km h l^{-1}. Assuming a cloud transit time of 30 h, average station spacing of 47.5 km, and cloud width of 570 km (i.e., 12 stations $\times$ 47.5 km/station) but otherwise using the same values as used in the 300-km calculation, yields a cloud length of 660 km and an estimated total mass release of 82 kg. Note, however, that the non-zero concentration measurements made at Station 703 after 2100 GMT on Sept. 27, 1083 suggest the CWIE value for the 800-km arc was probably low, though it is unlikely that enough tracer was missed to increase the estimate of total mass released by the factor of more than two needed to match the actual value. Another possible reason for this underestimate is that nocturnal surface concentrations may have been lower than concentrations in the residual layer above.

Draxler and Stunder (1988) made a somewhat similar calculation using aircraft CWIC values rather than surface CWIE values. They obtained an estimated tracer mass of 170 kg for CAPTEX Release 2. Brost et al. (1988a) also carried out mass-balance calculations for CAPTEX but used purely spatial integration rather than temporal-spatial integration. For each of the first five 6-hour observing periods of six CAPTEX releases, they summed the products of measured surface concentrations at each CAPTEX station and contiguous, exhaustive volumes centered on each station for which the station concentration was assumed to be representative. The PBL depths used to obtain the volumes were determined from actual soundings from nearest-neighbour rawinsonde stations. For CAPTEX Release 2, this approach gave them underestimates of the source strength of 0.86, 0.71, and 0.68 for sampling periods 3, 4, and 5, respectively. The 800-km-arc mass balance calculation described above used concentration measurements from sampling periods 4 through 8.

3.2.5 Previous CAPTEX numerical simulations

A variety of episodic LRTAP models have been used to simulate the transport and diffusion of one or more of the perfluorocarbon tracer releases made during CAPTEX. Eulerian *diagnostic* wind-field models have been run coupled with (i) Lagrangian puff

models (Davis et al., 1986; Draxler, 1987; Heffter et al., 1987; Viessman and Raman, 1988; Godowitch, 1989a,b), (ii) particle-in-cell dispersion models (Lee, 1987; Rodriguez, 1988), and (iii) Lagrangian particle dispersion models (Shi et al., 1990). Pudykiewicz et al. (1985a) and Brost et al. (1988a,b) employed Eulerian *prognostic* meteorological models coupled with Eulerian advection-diffusion models to simulate one and six CAPTEX releases, respectively. Kao and Yamada (1988), on the other hand, used an Eulerian prognostic meteorological model coupled to a Lagrangian particle dispersion model to simulate two CAPTEX releases.

In addition, Kahl and Samson (1986, 1988a,b), Draxler (1987), Heffter et al. (1987), and Haagenson et al. (1987) have all used Lagrangian trajectory models to study the sensitivity and/or accuracy of the trajectories calculated by these models to the temporal and spatial rawinsonde data density available in CAPTEX. Chock and Kuo (1990) compared observed CAPTEX tracer surface trajectories with isobaric trajectories predicted at three levels by three different wind-field models: (i) the MM4 primitive-equations model run in a 'forecast mode'; (ii) a very simple linear-interpolation diagnostic analysis scheme; and (iii) a quasi-geostrophic forecast model run diagnostically. Finally, Draxler and Stunder (1988) used a simple two-dimensional Eulerian advection–diffusion model to simulate CAPTEX *vertical* concentration profiles measured by aircraft 600–900 km downwind of the release locations.

These last seven papers will not be discussed further because they were concerned only with modelling horizontal transport or vertical diffusion and did not consider the full three-dimensional *dispersion* problem. Model results for the CAPTEX simulations which did consider the full problem were varied, to say the least (see Fig. 3.27), and comparison of the results is hampered by the wide range of qualitative and quantitative model performance measures employed[121] by the various authors (see Sec. 4.6 for a discussion of some of

---

[121] Or *not* employed!

these measures). Nevertheless, much can still be learned by presenting these results side by side.

Diagnostic-wind-field-based simulations

Davis et al. (1986) applied their Lagrangian trajectory puff model to two CAPTEX cases, Releases 3 and 4, with reasonable success. They were able to reproduce the strongly bimodal surface concentration pattern observed in CAPTEX Release 3 (see Fig. 3.25c), apparently through the use of a potential temperature constraint to limit daytime vertical mixing. However, they did not calculate any quantitative performance measures.

Draxler (1987) applied the ARL/ATAD Lagrangian trajectory puff model to six[122] CAPTEX releases, Releases 1–5 and 7. He considered five different meteorological input data sets of varying degrees of spatial and temporal resolution. These input data sets were obtained using different objective analysis procedures and observational data sets; four used observations from CAPTEX's enhanced upper-air network. Draxler's simulation results appear to be qualitatively reasonable. Fig. 3.27a shows a succession of predicted and observed cloud surface concentration centroid positions and time-averaged 3 fll^{-1} concentration contours from one of Draxler's five Release 2 simulations. Draxler also calculated a number of statistical performance measures for his entire set of six releases and all observing periods, including surface concentration frequency and cumulative frequency distributions, scatter plots, correlation coefficients, and centroid position errors. One of the more sobering statistics was that for predicted and measured surface concentrations paired in both space and time in which at least one member of the pair had a value greater than 3 fll^{-1}, the predicted concentration was within a factor of two of the measured surface concentration in no more than 18% of the pairs. If this comparison was restricted to pairs in which both concentrations were greater than 3 fll^{-1}, then this value rose to

[122] Release 6 was much shorter than the other six CAPTEX releases (Ferber et al., 1986) and has been ignored by most CAPTEX modelling studies.

45%. Godowitch (1989b) suggests that spatial offsets were likely responsible for many of these order-of-magnitude discrepancies between measured and predicted concentrations. Heffter et al. (1987) presented some additional information about the performance of the ARL/ATAD Lagrangian trajectory puff model for these CAPTEX simulations, including a scatter diagram for spatial position error and another for time- and space-averaged concentration pairs for Release 2, and concluded that the model was performing in a reasonable manner. Draxler and Stunder (1988) compared the vertical concentration profile predicted by the trajectory model against CAPTEX aircraft data for all six releases and obtained good agreement in three of them.

Viessman and Raman (1988) tested a parameterization of mean boundary-layer flow with the Ontario Ministry of the Environment Lagrangian puff model on four CAPTEX releases, 1, 4, 5, and 7. They based their diagnostic transport wind calculations on objectively-analyzed hourly surface *pressures* from the higher-resolution[123] surface observational network instead of on wind observations from the upper-air network. Sub-geostrophic, backed mean boundary-layer winds were estimated from surface geostrophic winds using empirical relationships developed by Viessman and Raman using the Wangara and Koorin Expedition data sets. Frictional effects were thus accounted for though not speed and curvature accelerations arising from unevenly spaced or curved isobars were not. Their calculated trajectories deviated considerably from the CAPTEX observed surface concentration fields in most cases, especially for longer travel times. One reason for the poor model performance may have been the neglect of vertical wind shear in the PBL, especially at night.

Godowitch (1989a) briefly described some results obtained with the MESOPUFF II Lagrangian puff model[124] for CAPTEX Releases 1–5 and 7. This mesoscale dispersion model was run in an 'operational' mode using meteorological input from 25 hourly NWS

---

[123] In both time and space.

[124] This is the only MAD model which has been applied to both the 1980 Great Plains and 1983 CAPTEX data sets for which results have been reported.

surface stations and standard twice-daily soundings from 6 NWS upper-air stations. In general, the values of various statistics for concentration residuals were larger than observed mean concentrations, and correlations were close to zero for non-zero measurements paired in space and time. However, actual surface concentration pattern and cloud path were predicted fairly well though transport speed was not, resulting in spatial plume offsets. The plume overlap region (percentage of modeled and observed concentration pairs when both were nonzero) varied from 16% to 50% over the six cases considered. Fig. 3.27f shows this comparison for CAPTEX Release 2; the overlap in this case was 34% (over 247 observed-predicted pairs from all observing periods). Godowitch (1989b) gave a much more detailed description of the same study and emphasized the contribution of spatial displacements of the modelled tracer cloud relative to the observed cloud to the large scatter and low correlations found in the evaluation statistics. He also discussed some sensitivity tests carried out with simplified wind fields. Similar to the experience of Viessman and Raman (1988), Godowitch found that use of a surface wind field as the transport wind field produced a modelled plume which travelled more slowly and generally to the left of the observed plume. Use of only the 850 hPa wind field, on the other hand, shifted the modelled plume to the right of the observed plume.

Lee (1987) simulated all seven CAPTEX releases using the Argonne National Laboratory particle-in-cell dispersion model with diagnosed wind fields generated from the enhanced six-hourly upper-air soundings. In addition to presenting reasonable-looking time-sequence plots of puff envelope positions based on the $2\ \mathrm{fl}^{-1}$ contour line[125], Lee also calculated model performance statistics based on his full set of seven simulations, including scatter plots of observed vs. predicted ground-level concentration and observed concentration vs. residuals, concentration frequency distributions, and residual frequency distribution (see Fig. 4.20). He concluded that the simulations showed small bias and general agreement with the CAPTEX observations. However, correlation coefficients of

---

[125] Approximately twice background.

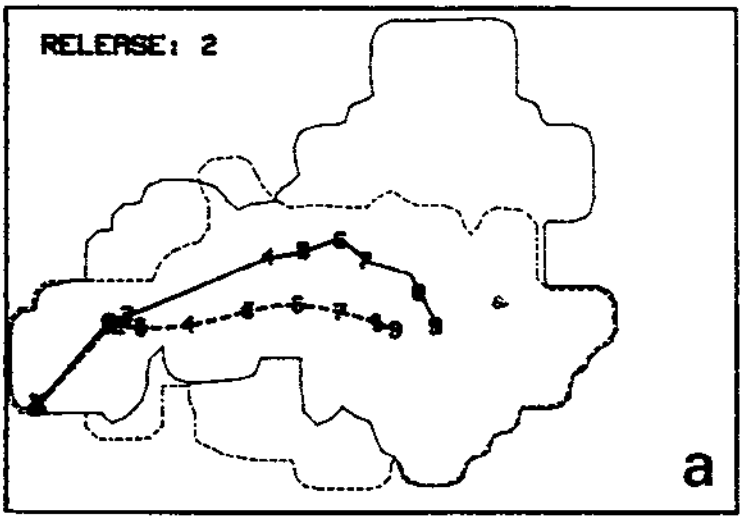

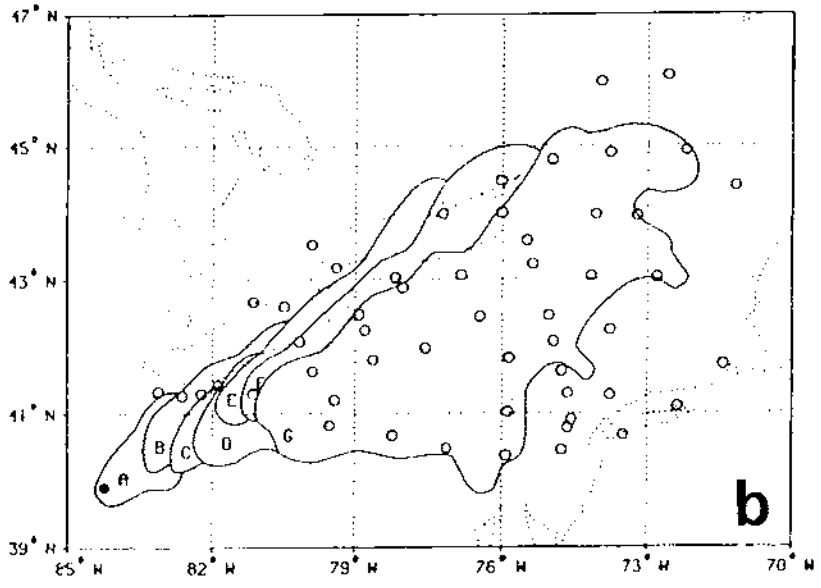

Figure 3.27: Comparison of simulations made by six different mesoscale dispersion models for CAPTEX Release 2 from Dayton, Ohio on Sept. 25, 1983, 1705–2005 GMT: (a) figure from Draxler (1987) showing 3 fll^{-1} PMCH contour intervals for observations [solid lines] and model predictions [dashed lines] for the *average* (i.e., total dose divided by total sampling time) tracer plume as well as concentration centroid positions at six-hourly intervals; (b) figure from Lee (1987) showing 2 fll^{-1} PMCH contour intervals at 0300[A], 0900[B], 1500[C], and 2100[D] GMT on Sept. 26 and at 0300[E], 0900[F], and 1500[G] GMT on Sept. 27, 1983 as well as those samplers which measured 2 fll^{-1} or more in a six-hour period (continued on next page).

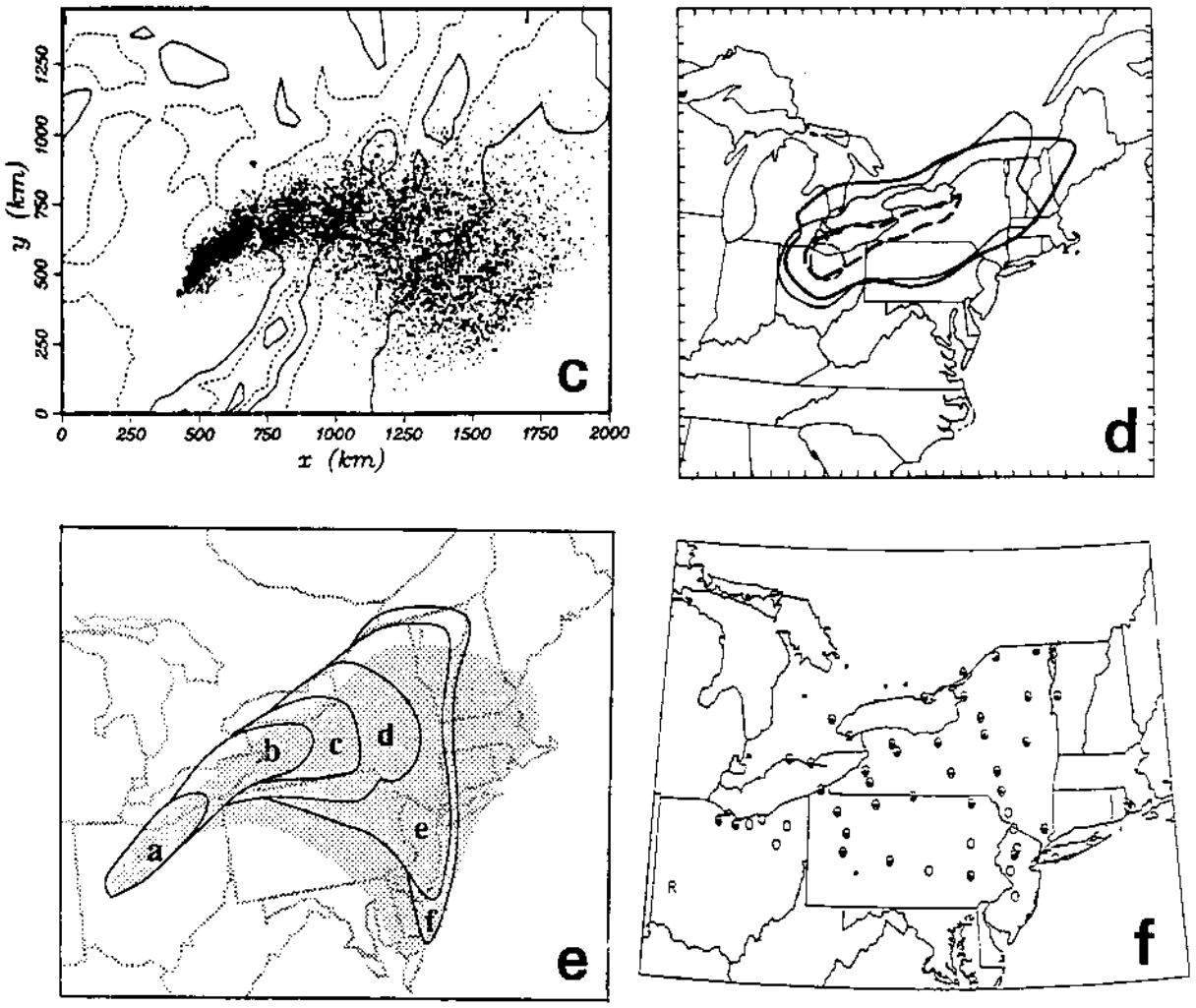

Figure 3.27: (Continued) (c) figure from Kao and Yamada (1988) showing trajectory of tracer particle set projected onto surface at six-hour intervals from Sept. 25, 1705 GMT until Sept. 27, 1705 GMT for run with full 4DDA; (d) figure from Brost et al. (1988a) showing *event-total* (i.e., total dose) 10 fl^{-1} PMCH contour intervals [heavy solid line for model, light solid line for observations] and 300 fl^{-1} PMCH contour intervals [heavy dashed line for model, light dashed line for observations] for experiment F [best results, 70 km grid interval, MM4 forecast fields plus all observations] on Sept. 26, 1983, 1800 GMT; (e) figure from Shi et al. (1990) showing 2 fl^{-1} PMCH average concentration contours for surface footprint on Sept. 26 from 0000–0600 GMT [a], 0600–1200 GMT [b], 1200–1800 GMT [c], and 1800–2400 GMT [d], and on Sept. 27 from 0000—0600 GMT [e] and 0600-1200 GMT [f] along with 1400-m time-composited maximum plume from Sept. 26 at 0000 GMT to Sept. 27 at 0900 GMT (stippled area); (f) figure from Godowitch (1989b) showing stations predicted by MESOPUFF II (*) and observed (O) to have nonzero concentrations during any sampling period. Corresponding observations are shown in Figs. 3.23 and 3.22.

predicted and observed concentrations paired in time and space were poor, likely as a result of differences in puff location and orientation as suggested by the difference in cloud position between Figs. 3.22f and 3.27b and by the large number of zero concentrations for either observed or predicted values evident in Fig. 4.20b. Heffter et al. (1987) and Lee (1987) have both referred to this latter phenomenon as an "L-shaped" scattergram.

Rodriguez (1988) used the Lawrence Livermore National Laboratory advection-diffusion particle-in-cell (ADPIC) model in conjunction with an Eulerian diagnostic wind-field model named MEDIC to simulate all seven CAPTEX releases. Like Lee (1987), Rodriguez presented several graphical measures of model performance, including a scatter plot of observed surface concentrations vs. residuals, frequency distributions for observed and predicted concentrations, and a residual frequency distribution for the full set of simulations plus residual box plots for each individual simulation. He also concluded that *unpaired* statistical measures of model performance were encouraging while poorer paired measure values appeared to result from misalignments of the plume centerlines.

Shi et al. (1990) used a displacement-based[126] LPDM to simulate three CAPTEX releases (1, 2, and 5) in conjunction with diagnosed gridded horizontal wind and potential temperature fields generated with a successive-correction objective-analysis scheme from twice-daily upper-air soundings and diagnosed values of L, u_*, w_*, and z_i. Horizontal diffusion, unlike vertical diffusion, was *not* parameterized or modelled in any way. Instead, horizontal spreading arose solely from the interaction of horizontal differential advection and vertical diffusion. Quite good qualitative agreement was obtained between simulated and observed patterns of maximum surface concentration and sequential plots of 6-hour surface concentrations (Fig. 3.28). Threat scores were also calculated as a quantitative measure based on a $2\ \mathrm{fl}^{-1}$ threshold value. Resulting threat-score values ranged from 0.10 for the Release 5 simulation to 0.30 for the Release 2 simulation. Shi et al. (1990, p. 3701) concluded that "... the dominant dispersion mechanism over

---

[126] That is, particle *displacements* rather than particle velocities are treated as a stochastic process and much longer time steps are used compared to a Langevin-equation-based LPDM.

long distances is the combination of vertical mixing and vertical wind shears." They also noted that the surface footprint of the tracer did not always match the movement of the bulk of the tracer cloud very well. Fig. 3.27e shows a time composite of model-predicted surface footprints at five successive 6-hour observing periods from Shi et al.'s CAPTEX Release 2 simulation.

Prognostic-wind-field-based simulations

Brost et al. (1988a,b) used the NCAR Regional Acid Deposition Model (RADM) to simulate six of the seven CAPTEX releases (1–5, 7). RADM is a multi-level Eulerian acid deposition model which calculates advection based both on prognostic, three-dimensional resolved wind fields and on subgrid-scale turbulent transfer using a gradient transport parameterization (NCAR, 1985, 1986; Chang et al., 1987). It is one of the most comprehensive and sophisticated regional-scale acid deposition model currently available. Brost et al. (1988a) undertook a wide-ranging suite of ten numerical experiments for each of the six releases in order to test the impact of different meteorology sources, different spatial and temporal resolution of the meteorological fields, different spatial resolution of the RADM grid, and different parameterizations of subgrid-scale vertical turbulent transfer in the tracer model.

Perhaps their most interesting experiments were those comparing meteorology sources, where the meteorological fields could come from either observations, mesoscale meteorological model simulations, or a combination of the two: that is, from a diagnostic wind-field model, from a prognostic meteorological model run in a 'forecast' mode, or from a prognostic meteorological model run in a '4DDA' mode. Prognostic, limited-area meteorological models have better spatial and temporal resolution than diagnostic meteorological models but suffer from decreasing accuracy with time due to forecast errors and boundary problems. In terms of root-mean-square (RMS) trajectory error based on surface tracer puff centroid position, the purely diagnostic meteorology experiment (their Exp. B) and the purely prognostic meteorology experiment (their Exp. G) were comparable for a 48-hour run. The best results were obtained from their Experiment F, which used a

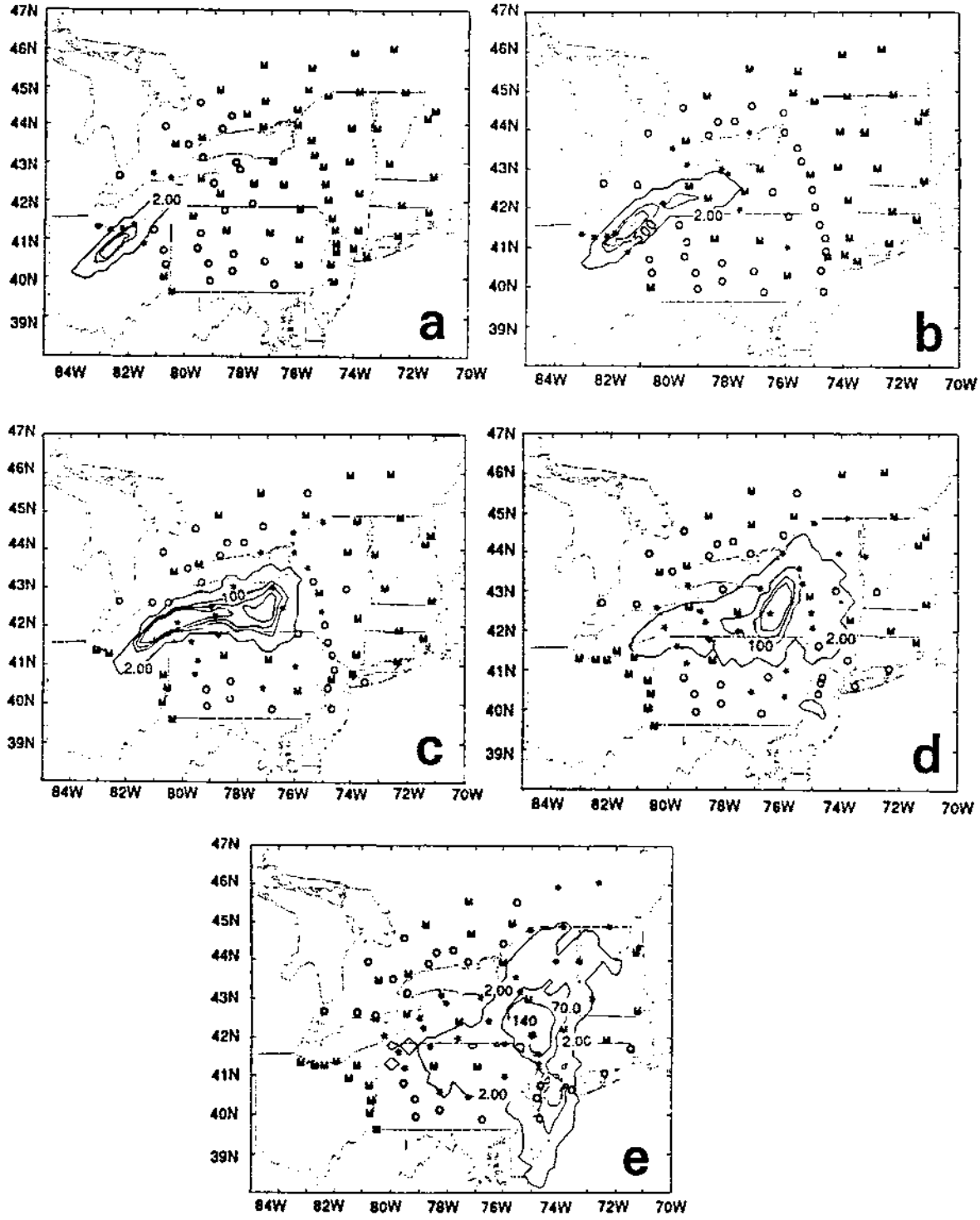

Figure 3.28: Comparison of simulated 6-hour average surface tracer concentrations for CAPTEX Release 2 made by Shi et al. (1990) against observations for five consecutive observing periods: Sept. 26, 1983 from (a) 0000–0600 GMT, (b) 0600–1200 GMT, (c) 1200–1800 GMT, and (d) 1800–2400 GMT, and (e) Sept. 27, 0000—0600 GMT. Asterisks mark stations reporting PMCH surface concentrations greater than 2 fll^{-1} above background, circles mark stations reporting concentrations less than this value, and 'M's denote stations which were turned off during the sampling period.

blend of CAPTEX enhanced-rawinsonde-network wind observations and model-predicted temperature profiles, a sort of four-dimensional-data-assimilation (4DDA) meteorology.

Besides RMS trajectory errors, Brost et al. (1988a) presented plots of puff 'envelopes' for 10 and 300 fll^{-1} thresholds and tables of bias and threat scores, correlation coefficients, and maximum concentration ratios. Their best experiments had statistically significant correlation coefficients at the 95% level over their full set of six CAPTEX releases and all observing periods. Fig. 3.25 shows tracer puff event-total concentration envelopes for the six CAPTEX releases simulated by Brost et al. (1988a) for their Exp. G. Fig. 3.27d shows the corresponding puff event-total concentration envelopes for their Exp. F. Some problems with overly large horizontal diffusion are evident. These arise both because of the artificial numerical diffusion associated with the RADM advection scheme and the assumption that tracer emitted from a point source immediately filled a RADM grid square[127] (either 35 km by 35 km or 70 km by 70 km). The use of a better advection scheme in Exp. F reduced the problem with artificial diffusion somewhat (compare Figs. 3.25b and 3.27c).

Kao and Yamada (1988) used Yamada's prognostic mesoscale meteorological model (Yamada, 1985) together with a Lagrangian particle dispersion model to simulate two CAPTEX releases, 2 and 5. By using a Lagrangian particle dispersion model, they were able to avoid the problems mentioned above associated with solving the tracer advection-diffusion equation in an Eulerian framework. They also tested a simple 4DDA approach to 'nudge' their mesoscale-model-predicted wind fields towards wind observations from the CAPTEX enhanced rawinsonde network. Particle position fields predicted using this 'research-mode' meteorology were quite different from ones obtained using 'operational-mode' meteorology (i.e., meteorological fields prognosed after mesoscale model initialization without the use of later rawinsonde observations). These differences were likely due in large part to the assumption of zero-gradient lateral boundary conditions and fixed upper-

[127] See also Karamchandani and Peters (1983).

boundary conditions for a 2000 km by 1500 km domain over a 48-h simulation period. The 'research mode' concentration fields were much closer to observations. Fig. 3.27c shows a composite plan view of particle positions for eight consecutive 6-hour intervals. However, the only quantitative measure of model performance provided by the authors was a single scatter plot of two-day, time-integrated computed and observed concentrations for their best (i.e., full 4DDA) experiment. Scatter was quite large even for these time-integrated[128] concentration pairs. 57% of the computed concentrations were within a factor of 4 of the observed concentrations.

Comparison of CAPTEX simulation results

Fig. 3.27 shows either tracer puff concentration envelopes or virtual particle positions calculated in the six CAPTEX modelling studies which considered CAPTEX Release 2. All six models predicted roughly similar concentration patterns, but it is difficult to say much more than that because of differences in domain sizes, map projections, and quantities plotted. All six models were run in a 'research' or '4DDA' mode, using meteorological observations obtained *throughout* the experimental period either directly through preparation of gridded wind fields at different times by objective analysis or indirectly by assimilation into gridded wind fields predicted by a meteorological model. Less favourable results would be expected in a real-time 'operational' mode where forecasts of mesoscale pollutant dispersion were required and the future wind fields were unknown. However, there were differences between the different model simulations over whether supplemental upper-air data from either the ten EPRI rawinsonde stations or the special NWS 0600 and 1800 GMT soundings were used.

These six CAPTEX simulations, which are representative of the present state of the science in LRTAP modelling, illustrate some current limitations. The most important limitation is the insufficient resolution of the meteorological fields needed for transport

---

[128] Temporal or spatial integration of concentration predictions and observations before comparison normally improves agreement (e.g., Heffter et al., 1987).

and diffusion calculations. Three of the models rely on diagnostic wind fields obtained from the objective analysis of rawinsonde observations. Even with the enhanced observing network sometimes deployed in mesoscale field experiments, diagnostic wind fields will only be available based on soundings taken every 12, 6, or, rarely, 3 hours. Spatial resolution will be similar to that of the regular U.S. upper-air network: several hundred kilometers. The two prognostic wind-field models do somewhat better in terms of resolution. Their model physics include a parameterized diurnal cycle, so that their time resolution will be much better than the two Lagrangian models, but their horizontal grid spacing was in the 35-50 km range. This gives at best a horizontal spatial resolution of 140–200 km (i.e., $4\Delta x$ features) and precludes consideration of the meso-β-scale terrain-forced mesoscale circulations which can contribute to mesoscale dispersion in the PBL (e.g., Moran et al., 1986, 1991; Pielke et al., 1987b).

Treatment of mesoscale diffusion is also problematic. Draxler (1987) used expanding puffs growing at a rate based on Heffter's (1965) empirical mesoscale dispersion curves to parameterize mesoscale diffusion. Lee (1987) employed horizontal eddy diffusivities based on Gifford's (1982) empirical mesoscale dispersion curves. Neither of these empirical data sets consider the effects of PBL stability, age of pollutant, or time of release of pollutant but rather lump all available observations together. Recent observations by Carras and Williams (1988) suggest that these factors may be important (see Sec. 2.2.2). RADM cannot resolve pollutant sources on scales less than its horizontal grid scale, and hence must assume that pollutant released from a point source is immediately well mixed throughout a grid cell (where it is immediately resolved as a $2\Delta x$ feature!) This restriction introduces considerable artificial diffusion near the source[129]. The two Lagrangian particle models seem to give the best treatment of difusion, avoiding numerical diffusion.

Finally, there is the problem of comparing different model results due to the differences in, and sometimes lack of, reported performance measures as well as differences in model

---

[129] In fact Brost et al. (1988b) estimated that numerical diffusion was larger than actual diffusion and hence Brost et al. (1988a) did not explicitly parameterize subgrid-scale horizontal diffusion.

domains, model map projections, and averaging periods. As well, the studies just reviewed relied for the most part on operational performance measures. Most[130] did not consider such qualitative diagnostic measures as cloud travel time, transit time, cloud width, and peak value which were used to good effect in the Great Plains model intercomparison study (Policastro et al., 1986a; Carhart et al., 1989) to augment the operational measures. Oddly enough, this may be in part a result of the better sampling network deployed in CAPTEX, that is, a two-dimensional network vs. the linear network used in the Great Plains experiment. However, even for the CAPTEX observations, the use of a linear analysis framework (e.g., 300-km arc or 800-km arc observations) provides additional insights as should have been demonstrated by the analysis of this chapter and the analyses to be presented in Chap. 6.

3.3 Summary

Releases from the 1980 Great Plains mesoscale tracer experiment and the 1983 Cross-Appalachian tracer experiment (CAPTEX) were selected as test cases for this study because they (a) were well documented, (b) have been used as test cases by a number of other mesoscale dispersion modellers, (c) together cover dispersion over downwind distances from 100 to 1100 km, and (d) have characteristics which make them suitable for examining the influence of mesoscale time scales and terrain-forced mesoscale circulations on mesoscale atmospheric dispersion. Both of these mesoscale dispersion field experiments were carried out in North America under warm-season anticyclonic conditions.

The Great Plains mesoscale tracer experiment was conducted in July 1980 over the Plains states of Oklahoma, Kansas, Nebraska, and Missouri. The physiography of this region is relatively simple and uniform: the major topographical feature is the regional-scale east-west slope from the Mississippi Valley to the Rockies. The synoptic pattern remained nearly steady during the tracer release and transport for this case. Ground-level

---

[130] Godowitch (1989b) is an exception.

concentration measurements were made along two arcs of samplers, one located 100 km north and one located 600 km north and of the PMCH tracer release site at Norman, Oklahoma. Some aircraft samples were also taken.

In CAPTEX Release 2, PMCH tracer was released from Dayton, Ohio in late September 1983 and tracked eastward across the northeastern United States and southern Canada. The physiography of this region is considerably more complex and larger than the Great Plains experiment region and includes major lakes and the Appalachian Mountain range. The synoptic pattern also changed considerably over the period of the experiment. Ground-level tracer concentration measurements were made on nine arcs of samplers at successively greater downwind distances from Dayton. Aircraft measurements were also taken by multiple aircraft flying in 'stacked' vertical formations.

These two MAD tracer experiments and their data sets were described in this chapter, including the experimental design, observational domain, network topology, sampling strategy, the meteorological conditions which prevailed during the release and transport of the tracer, and the characteristics of the actual concentration measurements. New analyses of cloud kinematics, cloud structure, and mass balance carried out for this study were described; results from these analyses will be used to evaluate the simulated tracer-cloud characteristics discussed in Chaps. 5 and 6.

This chapter also summarized previous numerical simulations of these two experiments by other MAD modelling groups. A variety of types of models have been employed, including Lagrangian puff models and a no-memory Lagrangian particle dispersion model used with diagnostic wind-field models, and an Eulerian advection-diffusion model and an LPDM used with prognostic wind-field models run in a 4DDA mode. All of these models demonstrated at least some skill was shown, although the evaluation criteria used were not the most demanding ones available. In many cases, the basis for evaluation was the area considered to be covered by the cloud regardless of concentration levels.

Chapter 4

NUMERICAL MODELS AND INPUT DATA SETS

Although this may seem a paradox, all exact science is dominated by the idea of approximation.

Bertrand Russell (1872–1970)

4.1 CSU Mesoscale Atmospheric Dispersion Modelling System

The mesoscale atmospheric dispersion simulations to be described in Chaps. 5 and 6 were carried out with the aid of a large, complex computer code, the CSU mesoscale atmospheric dispersion modelling system. The core of this modelling *system* consists of a coupled pair of numerical models: (i) a prognostic mesoscale meteorological model which can predict the time evolution of three-dimensional atmospheric mean flow and turbulence fields over complex terrain; and (ii) a mesoscale Lagrangian particle dispersion model which, given a description of mean flow and turbulence fields, can simulate the release and dispersion of a number of non-buoyant, passive pollutants from multiple sources of various geometries. In addition, the CSU mesoscale dispersion modelling system includes (iii) an isentropic analysis package for preparation of the initial meteorological model fields and, if required, lateral boundary tendencies[131], and (iv) a visualization and analysis package

[131] For larger-scale or longer-term simulations when the horizontal homogeneity of background meteorological fields cannot be assumed (if it ever can be – recall the discussion of mesoscale wavenumber spectra in Chap. 2).

for the plotting and display of model-predicted meteorological and concentration fields and particle positions and trajectories.

These various components of the CSU mesoscale dispersion modelling system are described in the rest of this chapter. Emphasis has been given to the particular model configuration selected for this study. Secs. 4.2 and 4.3 cover the RAMS mesoscale meteorological model and the isentropic data analysis package and input and special-purpose data sets, respectively. Sec. 4.4 describes the mesoscale Lagrangian particle dispersion model (MLPDM) and relevant aspects of the plotting package are covered in Sec. 4.5. Various measures of numerical-model performance are reviewed in Sec. 4.6: a number have been used in this study. To close this chapter, some preliminary tests of the selected modelling system configuration are discussed in Sec. 4.7. Additional details on the modelling system configuration may be found in the descriptions of the various numerical experiments given in Chaps. 5 and 6.

4.2 Mesoscale Meteorological Model

The Regional Atmospheric Modelling System (RAMS) is an extremely flexible limited-area, finite-difference meteorological model created from the merger of a nonhydrostatic cloud-scale model (Tripoli and Cotton, 1980, 1982, 1989a,b; Cotton et al., 1982) and two hydrostatic mesoscale meteorological models (Pielke, 1974a,b; Mahrer and Pielke, 1977; McNider and Pielke, 1981; McCumber and Pielke, 1981; Tremback et al., 1985). The use of a FORTRAN preprocessor permits RAMS to be easily configured at run time into one of a very wide variety of different models simply by choosing from a lengthy menu of physical and numerical options.

These options include the choice of the form of the vertical momentum equation (hydrostatic or nonhydrostatic) and the mass continuity equation (incompressible, anelastic, or fully compressible), the time differencing scheme (leapfrog time-split or forward-backward time-split), the turbulence closure scheme (deformation K, O'Brien K/Blackadar K, or Deardorff TKE), the radiation parameterization (none, Mahrer–Pielke

[1977] scheme, or Chen–Cotton [1983] scheme), the treatment of moist processes (no moisture, passive water vapour, stable precipitation, convective parameterization, explicit warm-rain microphysics, or explicit full-ice-phase microphysics), the complexity of the background meteorological fields (barotropic or baroclinic), the control of computational nonlinear instability (by numerical filtering or horizontal diffusion), and a number of vertical and horizontal grid discretizations and lateral, upper, and lower boundary conditions.

One very powerful feature of RAMS is its ability to run with several levels of interactive, two-way nested grids. Such a grid hierarchy allows different grid resolutions to be employed in different portions of the modelling domain at the discretion of the user. RAMS also has an explicit memory management capability that permits simulations to be run with more grid points than can be stored simultaneously in the allotted main memory segment by employing disk I/O, effectively a model-driven 'virtual memory' scheme. More details concerning RAMS may be found in Tremback et al. (1986, 1987), Tripoli (1986), Bader et al. (1987), Cotton et al. (1988), Cram (1990), Tremback (1990), Walko and Tremback (1991), Cram et al. (1992a), Pielke et al. (1992), and Tremback and Cotton (1992).

What follows is not a complete description of RAMS but rather a summary of the main RAMS options and characteristics selected for this study. Many of these model-configuration characteristics are listed in Table 4.1. Some additional discussion is provided where an explanation seems warranted for the choice made. In general, RAMS was configured so as to provide a good description of mesoscale boundary-layer transport over complex terrain under dry, anticyclonic summertime synoptic conditions. Such physical processes as radiation, surface exchanges of momentum, heat, and moisture, and turbulent diffusion were thus emphasized while cloud and precipitation processes were ignored. The terrain-forced atmospheric circulations of primary interest, the nocturnal low-level jet, lake-land breezes, and mountain-plains flows, are meso-β-scale in size. This uniformity of phenomenological spatial scale permitted the use of a single grid with uniform horizontal resolution over the domains of interest, avoiding the additional complexities of nesting

although conflicting domain size and grid resolution requirements still had to be balanced (e.g., Avissar et al., 1990).

Three-dimensional RAMS production runs were carried out at NCAR on an eight-processor, 64-Mword Cray Y-MP, permitting the model to be run entirely *in core* on a single processor. One- and two-dimensional RAMS computer runs and much development and testing was carried out locally on a Stardent Titan graphics workstation.

4.2.1 Model version

An 'unfrozen', updated version of the RAMS Version 2A model production code was used in this study. Post-release code modifications were collected and implemented by either Dr. Craig Tremback or the author. In particular, a number of changes were made to subroutine MXCOEFP, the O'Brien K/Blackadar K vertical exchange coefficient subroutine, for the present study. PBL height was also added as an analysis and history variable for subsequent input to the mesoscale Lagrangian particle dispersion model and solar albedo was changed from a constant to a variable surfacecharacteristic. The Ekman initialization option was implemented for the variable-initialization (VI) option. The RVARI module was also modified to handle the non-standard surface-characteristics data sets and soil-model initialization used in this study (Secs. 4.2.6 and 4.3) and the low-level wind time-averaging option (Sec. 5.2.2).

Three other components of the CSU mesoscale dispersion modelling system were also modified in the course of this study as well. Changes to Version 2A of the RAMS Isentropic Analysis (ISAN) package included enhancement of the plotting capabilities and modifications for running on a Cray computer under the UNICOS operating system (see Sec. 4.3). Version 2A of the Lagrangian particle dispersion model was modified to make it compatible with the use of latitude-longitude coordinates and the O'Brien K/Blackadar K turbulence parameterization in RAMS, to implement the drift velocity correction, user-specified 'test meteorology', and calculation of particle position and velocity statistics, and to expand its plotting and interpolation options, including plotting sampling stations and interpolating concentrations at station locations, among other changes (see Sec. 4.4).

Table 4.1: Table 4.1: RAMS meteorological model configuration for Great Plains and CAPTEX simulations.

Model Characteristic	Option/Value Chosen
Basic equations	
w-momentum equation	hydrostatic
continuity equation	anelastic
Numerics	
Time differencing	forward-backward time-split
Space differencing	sixth-order flux form
Horizontal coordinates	latitude-longitude
Vertical coordinate	terrain-following
Grid dimensions	41 × 46 × 29 (Great Plains); 51 × 46 × 29 (CAPTEX)
Horizontal spacing	1/2° long. × 1/3° lat.
Vertical spacing	Δz =50 m at surface, 1.15 stretch factor, 16 km top
Time step	60 s long, 20 s short
Physical parameterizations	
Radiation	Chen-Cotton shortwave, longwave schemes
Moist processes	passive water vapour only: no condensation or Cu param.
Horizontal diffusion	deformation K (first-order)
Vertical diffusion	O'Brien K/Blackadar K (first-order)
Surface layer	Louis scheme
Soil model	Tremback-Kessler scheme, 11 levels, Δz =0.01 m to 0.1 m, 0.5 m total depth
Boundary conditions	
Lateral boundaries	Klemp–Lilly radiative, Davies external
Upper boundary	Prognostic surface pressure
Bottom boundary	5' terrain, 10' land-cover, 1° soil texture, 1° SST data
Initialization	
OA scheme	Tremback isentropic-analysis package
Input data	NMC analyses, upper-air and surface station data, USDA weekly crop bulletin
Other aspects	
Start time	0600 CST
Simulation length	48 h

Finally, a greatly increased set of possible analysis variables for post-simulation output processing and analysis was added to Version 2A of the RAMS Visualization and Analysis (VAN) package (see Sec. 4.5).

4.2.2 Governing equations

The hydrostatic version of RAMS without explicit microphysics integrates four partial differential equations in time simultaneously (two horizontal momentum equations, a moist-air thermodynamic equation, and a water-vapour mixing-ratio continuity equation). The four prognostic variables are the horizontal velocity components u and v, the ice-liquid water potential temperature θ_{il} (Tripoli and Cotton, 1981), and the water-vapour mixing ratio r_v. These equations are listed in Chap. 3 of Tremback (1990) and in Tremback and Cotton (1992). Since the hydrostatic version of RAMS was used in this study, no prognostic vertical momentum equation was needed. Instead, vertical velocity w was diagnosed from the anelastic continuity equation and the Exner function[132] was diagnosed from the hydrostatic equation.

The RAMS governing equations describe perturbations about a steady, moist, hydrostatic base state. The base state is taken to be horizontally homogeneous and may have a *non-zero* wind profile if the horizontally-homogeneous-initialization (HHI) option is selected but is taken to be *at rest* and to be horizontally *inhomogeneous* if the variable-initialization option is selected. Base-state density ρ_0 is determined from the initial temperature and Exner function fields by means of the ideal gas law. In keeping with the quasi-Boussinesq form of the governing equations (e.g., Pielke, 1984; Tripoli, 1986), no further calculations, either prognostic or diagnostic, are performed for density. The horizontal pressure-gradient-force (PGF) terms are calculated for Exner function perturbations π' from this base state. Buoyancy perturbations are described by the quantities θ'_{il} and π'. The actual base state used corresponds to the 'sounding' for the grid point

---

[132] Pielke (1984) has summarized the advantages of using the Exner function Π $\left[= c_p (p/p_{00})^{R/c_p}\right]$ instead of pressure p in mesoscale models.

with the lowest elevation[133] at time zero if the variable-initialization option is selected (Tremback, 1990) or to the input sounding if the HHI option is selected.

The model equations used in this study included terms for the horizontal components of Coriolis force, for horizontal and vertical turbulent diffusion, and for radiative heating and cooling. Although only the vapour phase of water was considered in this study, the horizontal and vertical distribution of moisture could still be significant for radiation processes and buoyancy processes, the latter since water vapour can modify both density and vertical stability. The use of a prognostic soil model permitted the calculation of momentum, energy, and moisture fluxes at the earth-air interface based on both atmospheric and subsurface conditions. Horizontal diffusion was included primarily as a numerical control on computational nonlinear instability rather than as a realistic physical process but vertical diffusion was an important mechanism for vertical mixing.

4.2.3 Physical parameterizations

Moist processes

Water vapour was treated as a passive scalar except for its role as an optically-active gas in the radiation calculations. Phase changes were not considered in this study, which meant that cloud and precipitation processes were not modelled. This simplification was not considered too serious, however, since daily precipitation summaries for the two cases of interest showed little precipitation over the simulation domains. Surface moisture exchanges were considered, however (see the discussion of the soil model).

Radiation

The Chen–Cotton radiation parameterization was used for both shortwave and longwave radiation. The decision to use this scheme was based on the results of a number of one-dimensional sensitivity tests (see also Sec. 4.7). Both of the RAMS radiation param-

[133] This ensures that base-state values are available at all heights at other grid points.

eterizations implemented in Version 2A[134] were found to give vertical cooling rate profiles considerably different from profiles predicted by a state-of-the-art longwave narrow-band model (Tjemkes and Nieuwstadt, 1990) for a set of standard atmospheric soundings, with the Chen–Cotton scheme cooling too much and the Mahrer–Pielke scheme cooling too little near the surface (Moran, 1989a). Mahrer–Pielke scheme predictions of net surface radiation and 50 m temperature agreed better with observed values than Chen–Cotton values for a one-dimensional, 24-hour, Wangara Day 33 test simulation while Chen–Cotton scheme predictions of screen (i.e., 1.2 m) temperature and surface virtual temperature flux agreed better with the Wangara observations than did the corresponding Mahrer–Pielke scheme values (Moran, 1989a).

However, in a one-dimensional intercomparison of the two schemes for a three-day simulation beginning with the July 8, 1980 Oklahoma City morning sounding (1200 GMT), the run using the Mahrer–Pielke radiation scheme produced excessively high Day 3 surface temperatures (50°C), a very deep PBL (4600 m), and a spurious unstable layer near the tropopause (not shown). Net radiative flux at the surface was as much as 110 $\mathrm{W\,m^{-2}}$ higher for the Mahrer–Pielke run compared to the Chen–Cotton run and surface sensible heat flux as much as 100 $\mathrm{W\,m^{-2}}$ higher.

The choice between the two schemes was thus something of a toss-up since both displayed shortcomings during these sensitivity tests. The Chen–Cotton scheme was selected because of its apparently more realistic longwave flux divergence profile (Fig. 12 of Moran, 1989a), an important quantity for the nighttime stabilization of the elevated residual layer, and its qualitatively better performance for the Oklahoma summer-season test (the Mahrer–Pielke scheme performed better overall for the Wangara winter-season test).

One modification was made to the radiation parameterization for the simulations described in Chaps. 5 and 6: surface solar albedo was set up as a two-dimensional field

---

[134] T.-M. Wong proposed some changes to improve the implementation of the Chen–Cotton scheme after most of the simulations in this study had been completed.

dependent upon surface vegetative cover (see Table 4.3). In the standard 2A version of RAMS, this quantity is assumed to be a single value modulated by bare-soil surface moisture (McCumber and Pielke, 1981), but in this work, vegetation was assumed to dominate and to shade the bare soil (see also the discussion of the soil model below). A capability was also added to the variable-initialization option of specifying uniform surface characteristics, including solar albedo. Two-dimensional surface solar albedo values are listed in Fig. 4.4. Great Plains simulations with uniform surface characteristics used an albedo value of 0.20 while CAPTEX simulations with uniform surface characteristics used a value of 0.18.

Variation of solar time with longitude was accounted for in the two- and three-dimensional simulations. Great Plains and CAPTEX simulations were all started at 0600 Local Solar Time (LST); sunrise occurred at 0522 CST at Oklahoma City, Oklahoma and at 0605 EST at Buffalo, New York on the respective simulation start days (see p. 415 and 426).

Vertical diffusion

The choice of vertical diffusion parameterization is obviously important in an atmospheric dispersion modelling study. Version 2A of RAMS offers a choice of three[135] different vertical-diffusion parameterizations: (a) deformation K scheme, (b) O'Brien K/Blackadar K scheme, and (c) Deardorff TKE-based K scheme. The first two are first-order, Mellor–Yamada Level 2 schemes (Mellor and Yamada, 1974, 1982) while the last is a second-order, Level 2.5 scheme which employs a prognostic TKE equation.

The O'Brien K/Blackadar K scheme (McNider and Pielke, 1981; Pielke, 1984) with prognostic equation for PBL height (Deardorff, 1974; Mahrer and Pielke, 1977; Smeda, 1979) was selected for this study for several reasons. First of all, it had been used in

[135] An experimental implementation of the Mellor–Yamada TKE-based K scheme was also available in Version 2A.

an earlier version of the mesoscale atmospheric dispersion modelling system, especially in the Lagrangian particle dispersion model to diagnose turbulence parameters such as T_{Lw} and σ_w (McNider, 1981; Pielke, 1984; Moran et al., 1986; McNider et al., 1988; Segal et al., 1988). Second, it had been used with considerable success in many previous PBL modelling studies (e.g., McNider and Pielke, 1981; Mahfouf et al., 1987; Steyn and McKendry, 1988; Physick and Abbs, 1991).

Third, it had been shown to perform well relative to other vertical diffusion schemes in quantitative intercomparisons. Yu (1977) evaluated 14 different vertical diffusion parameterizations, including a simple TKE scheme and five variants of the O'Brien K scheme. He found the O'Brien K scheme with a prognostic equation for mixed-layer height to give the best overall performance in one-dimensional simulations of the O'Neill fifth observing period and Wangara Day 32. Mahfouf et al. (1987) compared a TKE scheme, the O'Brien K/Blackadar K scheme, and a mixed-layer model formulation (Zhang and Anthes, 1982) for a one-dimensional Wangara Day 33 simulation and a three-dimensional Florida sea-breeze simulation. They concluded that as far as mean variables were concerned, the TKE and O'Brien K/Blackadar K schemes gave nearly identical results. Holt and Raman (1988) tested eleven Level 2 and Level 2.5 PBL parameterizations against MONEX 79 observations. They found the O'Brien K scheme with diagnosed PBL height to perform as well as any of the four first-order schemes tested and to do as well as the higher-order schemes in predicting mean PBL structure. Moran (1989b) came to a similar conclusion in a test of the four RAMS vertical-diffusion parameterizations in one-dimensional Wangara Day 33 simulations.

For the purposes of this study, the O'Brien K/Blackadar K scheme had several advantages over the other RAMS first-order parameterization, the deformation K scheme (Smagorinsky, 1963; Tripoli, 1986; Moran, 1989c). First, the O'Brien K/Blackadar K scheme includes a prognostic equation for PBL height z_i (Segal et al., 1987), a quantity needed by the Lagrangian particle dispersion model. The deformation K scheme does not predict z_i directly; as a result, this quantity must be estimated diagnostically in

the LPDM based on potential temperature lapse rates (e.g., Anthes, 1978) or vertical eddy diffusivity thresholds if the deformation K scheme was used in RAMS. Second, the deformation K scheme predicts a maximum in eddy vertical diffusivity K_z near z_i rather than below $0.5z_i$ as is commonly observed (e.g., Pielke et al., 1983; Moran, 1989c). The resulting PBL turbulence profiles diagnosed in the LPDM would then also be in error. And third, the deformation K scheme is a local scheme, whereas the convective boundary layer is generally recognized as being non-local in character.

As far as the other two RAMS vertical-diffusion parameterizations were concerned, the Deardorff TKE scheme is an LES subgrid-scale scheme and is inappropriate for the present application (Deardorff, 1980; Moran, 1989c). The Mellor-Yamada TKE scheme, on the other hand, offers some advantages over the O'Brien K/Blackadar K scheme. First of all, inconsistencies can occur in the first-order scheme as a result of switching between stability regimes, either by diurnal heating variations or by horizontal advection across a surface temperature gradient such as may occur at a coast (e.g., Arritt, 1987; Pitts and Lyons, 1987; Moran, 1989b; Physick et al., 1989). A TKE scheme avoids the need for such switching and can handle internal boundary layers much better. In addition, a TKE scheme predicts one second-order turbulence quantity directly, permitting a more direct specification of turbulence parameters in the LPDM (e.g., Uliasz, 1990a). And third, the Mellor-Yamada scheme, unlike a surface-driven profile scheme, can respond to internal changes in atmospheric stability caused by heat sources or sinks such as radiative flux convergence or condensation.

Unfortunately, the Mellor-Yamada TKE scheme was not available in the standard release of RAMS Version 2A nor was the LPDM set up to use this parameterization. For the purposes of this study, however, the use of a first-order turbulence scheme was not expected to be a serious shortcoming since mechanisms such as the diurnal variation of differential advection were the primary focus of the study and these are treated satisfactorily by the O'Brien K/Blackadar K scheme. In addition, for the scales of motion considered here, horizontal advection of TKE should be much less important than vertical processes.

The O'Brien K/Blackadar K option in RAMS had not been used prior to the present study. It was tested extensively for this study (see Sec. 4.7) and a number of modifications and corrections were made to it as well as adding PBL height z_i as a history and analysis variable. Initialization of z_i and the Ekman initialization option for variable-initialization simulations also had to be implemented for this study. Initial PBL height was specified to be 400 m, a compromise between the presence of the nocturnal surface inversion and the low-level jet at the near-sunrise model start time.

Horizontal diffusion

Horizontal diffusion was used in this study primarily for noise control. Tripoli (1986) recommended the use of the RAMS fourth-order horizontal filter option for this purpose because of its greater scale selectivity but horizontal diffusion should perform better near steep terrain in Version 2A because it accounts for the slope of terrain-following z^* surfaces (e.g., Physick, 1988). The fourth-order filter as presently coded is a horizontal operator on z^* surfaces, not z surfaces, and hence will produce vertical as well as horizontal diffusion over slopes.

The deformation-based K_H option of RAMS was used to parameterize horizontal diffusion. Only horizontal deformation was considered in these simulations because of the large difference in the horizontal and vertical resolutions used (e.g., Tripoli, 1986; Tremback, 1990; Walko and Tremback, 1991). An eddy Prandtl number ($= K_m/K_h$) of unity was assumed (cf. Deardorff, 1980). The minimum or background K_H value was set equal to $0.075\,(\Delta x)^{4/3}$ m^{2}s^{-1} (where Δx is in meters) even in regions of zero deformation in order to damp high wavenumber modes throughout the model domain. For horizontal grid increments of 10 km, this corresponds to a horizontal eddy diffusivity[136] of about 1.6×10^4 m^{2}s^{-1}.

---

[136] A very interesting discussion of the impact of changes in the background K_H value on RAMS results may be found in Chap. 7 of Tremback (1990).

Surface layer

Version 2A of RAMS offers a choice of two surface-layer parameterizations, the Businger et al. (1971) formulation, as implemented by Mahrer and Pielke (1977), and the Louis (1979) formulation. Comparisons and sensitivity tests of these two parameterizations have been discussed by Moran (1991a). Both schemes appear to have shortcomings.

The Businger et al. formulation must be solved iteratively to obtain surface fluxes and frequently fails to converge for convective, light-wind conditions. The Louis scheme is solved in one pass and hence is more robust and computationally efficient. However, it often predicts too weak downward surface fluxes at night, resulting in the development of an unrealistically strong surface-based nocturnal inversion. It also does not include water-vapour buoyancy contributions to Monin-Obukhov length (e.g., Moran, 1992a).

The Louis scheme was selected for the present simulations. Minimum threshold values of surface friction velocity and surface wind speed were set to $0.1\ \mathrm{m\,s^{-1}}$ and $0.5\ \mathrm{m\,s^{-1}}$, respectively. The specification of gridded aerodynamic surface roughness values is discussed in Sec. 4.2.6, and summertime values are listed in Fig. 4.4 for central and eastern North America. For the Great Plains simulations in which uniform surface characteristics were assumed, a surface roughness value of 0.1 m was used while CAPTEX simulations which assumed uniform surface characteristics used a value of 0.35 m.

Soil model

The Tremback-Kessler soil model (Tremback and Kessler, 1985) was selected for this study, although, unfortunately, the explicit treatment of field capacity and the modified wetness function suggested by Lee and Pielke (1992) and incorporated into Version 2C was not available in Version 2A of RAMS. Both soil temperature and soil moisture profiles were prognosed. Eleven soil levels were specified to a depth of 0.5 m; the soil levels were located at 0.0, 0.01, 0.02, 0.04, 0.07, 0.10, 0.15, 0.20, 0.30, 0.40, and 0.50 m. Only the *vertical* diffusion of heat and moisture within the soil layer was considered. Both of the resulting one-dimensional diffusion equations were solved using a modified Crank-Nicholson implicit scheme (Paegle et al., 1976).

Variations in soil properties resulting from different types of soil were addressed by assigning a dominant soil texture category to each grid square. The 11-category U.S. Department of Agriculture soil texture classification plus peat was used for this purpose (e.g., U.S. Department of Agriculture, 1951; Clapp and Hornberger, 1978; Pielke,1984). Soil-model parameters which depend upon soil texture category include specific heat capacity, density, thermal conductivity, hydraulic conductivity, wilting point, field capacity, porosity, and saturated moisture potential.

Vegetation is not modelled explicitly in Version 2A of RAMS but the contribution from land cover was considered in assigning aerodynamic roughness, albedo, and soil moisture values. The first two quantities and the soil-texture and land-cover data sets used to infer them are described in more detail for the variable-surface-characteristic simulations in Sec. 4.2.6 while the initialization of soil temperature and soil moisture is discussed in Sec. 4.3.

Great Plains simulations carried out with uniform surface characteristics assumed silt-loam soil texture (USDA category 4) and a sea surface temperature of 289 K. CAPTEX simulations carried out with uniform surface characteristics assumed silt-loam soil texture and a sea surface temperature of 285 K.

4.2.4 Model coordinates, domain, and grid structure

The RAMS grid is staggered and corresponds to a standard Arakawa C grid (Mesinger and Arakawa, 1976; Haltiner and Williams, 1980). Scalar variables such as temperature, pressure, and mixing ratio are assigned to the centres of grid boxes while individual velocity components are assigned to the midpoints of the grid-box faces or sides normal to their direction of motion. Eddy diffusivities were assigned to scalar points in these simulations. Grid-box corner points ('M' points) do not represent any variable but are important as reference points for nesting multiple grids and for assigning particle coordinates.

The latitude-longitude coordinate option was chosen for the horizontal grid in three-dimensional simulations run in this study. Since map factors are not included in Version 2A of RAMS, the convergence of v-momentum with latitude was not accounted for al-

though the latitudinal variation of longitudinal grid increments was considered (e.g., Cram, 1990). However, this discrepancy is expected to be a minor inconsistency for the mid-latitude meso-α-scale model domains used in this study (see Figs. 4.1 and 4.2).

Horizontal domain/horizontal discretization

Different horizontal domains and grid sizes were used for the two case studies. The Great Plains tracer experiment simulation domain extended from 30°N to 45°N (a 1667 km distance) and from 105°W to 85°W (a 1924 km distance at 30°N, a 1571 km distance at 45°N). This area and its corresponding topography are shown in Figs. 4.1 and 4.13a, respectively. The smoothed topography data set which was employed is described on p. 400. The actual Great Plains experiment observational domain is shown in Fig. 3.1. Horizontal grid spacing was chosen to be 0.333° in the north-south direction (37 km) and 0.5° in the east-west direction (44.1 km at 37.5°N) for a horizontal grid size of 41 × 46.

The CAPTEX model domain was larger and extended from 35°N to 50°N (a 1667 km distance) and from 90°W to 65°W (a 2275 km distance at 35°N, a 1785 km distance at 50°N). This area and its corresponding topography are shown in Figs. 4.2 and 4.19b, respectively. Fig. 3.13 shows the CAPTEX observational domain. Two previous three-dimensional Eulerian CAPTEX modelling studies (Brost et al., 1988a; Kao and Yamada, 1988) used very similar domains in their simulations. As in the Great Plains case, horizontal grid spacing for this case was chosen to be 0.333° in the north-south direction (37 km) and 0.5° in the east-west direction (41.0 km at 42.5°N). The horizontal grid size was thus 51 × 46.

Vertical domain/vertical discretization

The terrain-following σ_z coordinate system was used for the vertical coordinate (e.g., Clark, 1977; Pielke, 1984). Twenty-nine levels with telescoping spacing were used to discretize the vertical axis and the model top was located at 16.2 km in both case studies. The actual levels are listed in Table 4.2. This particular choice of vertical discretization

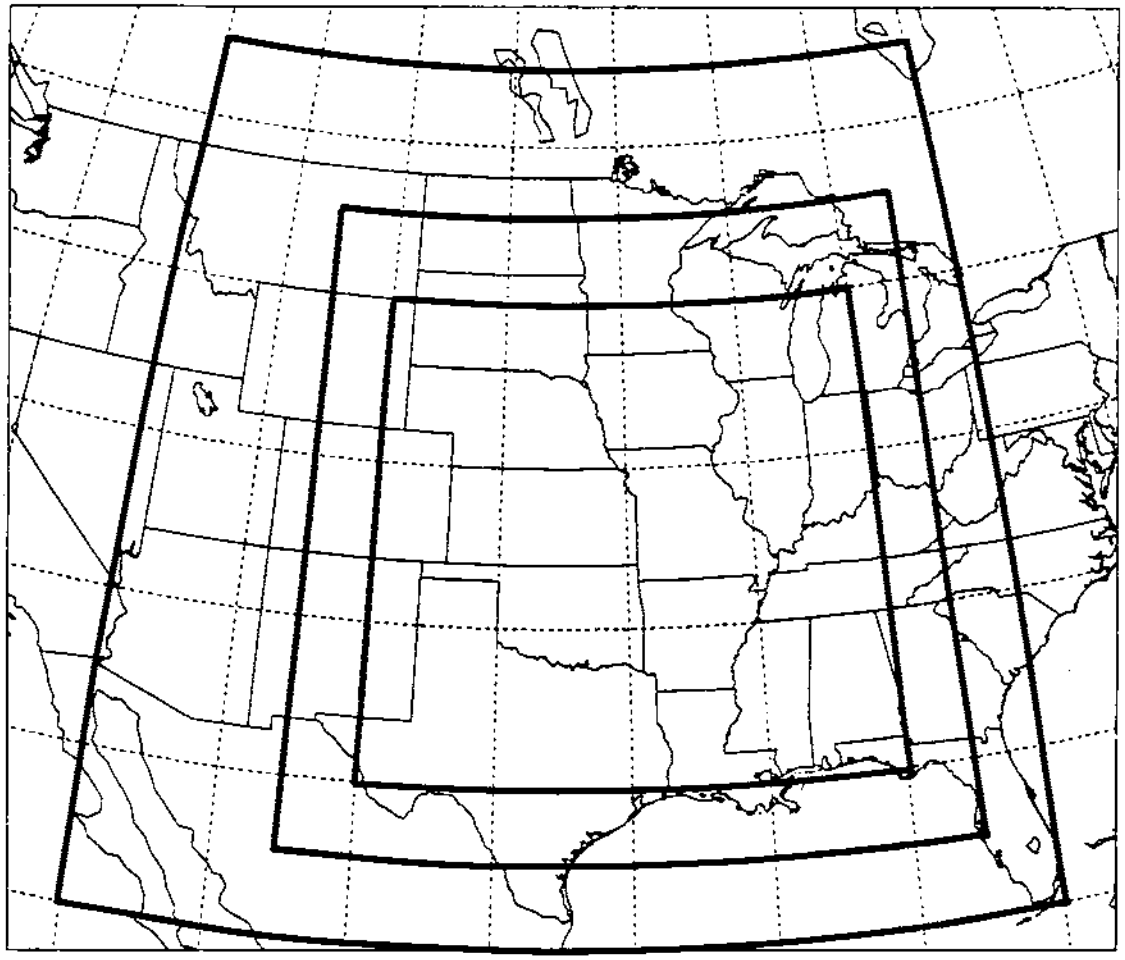

Figure 4.1: ISAN package domains and RAMS model domain for the Great Plains tracer experiment simulations. The outermost domain (25–52.5°N, 115–80°W) was used by Stages 1 and 2 of the isentropic analysis (or ISAN) package (see Sec. 4.3). The middle domain (27.5–47.5°N, 107.5–82.5°W) was used by Stages 3 and 5 of the ISAN package. The innermost domain (30–45°N, 105–85°W) is the RAMS model domain for this case. The heavy horizontal dashed line shows the west-east cross section used for the two-dimensional RAMS simulation. Lines of latitude and longitude are marked every 5° from 25°N to 50°N and from 125°W to 70°W, respectively, and an orthographic map projection has been used.

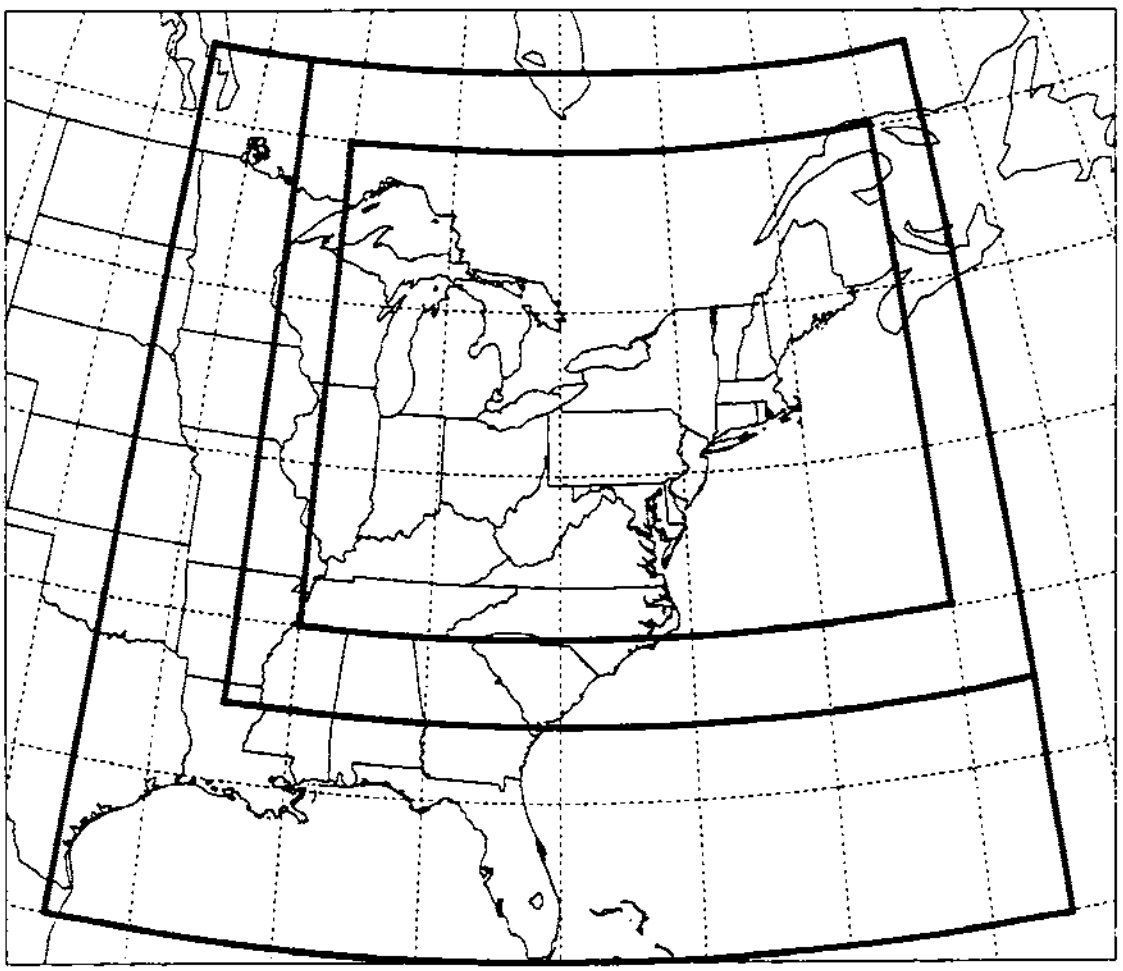

Figure 4.2: ISAN package domains and RAMS model domain for the CAPTEX simulations. The outermost domain (25–52.5°N, 97.5–62.5°W) was used by Stages 1 and 2 of the ISAN package. The middle domain (27.5–52.5°N, 92.5–62.5°W) was used by Stages 3 and 5 of the ISAN package. The innermost domain (35–50°N, 90–65°W) is the RAMS model domain for this case. Lines of latitude and longitude are marked every 5° from 25°N to 50°N and from 105°W to 55°W, respectively, and an orthographic map projection has been used.

was very much a compromise between the conflicting requirements of (a) good low-level resolution (for compatibility with the surface-layer parameterization and resolution of the low-level nocturnal jet), (b) gradually and smoothly varying spacing (to avoid loss of accuracy in the vertical diffusion calculations), (c) as high a model top as possible (for compatibility with variable initialization, the upper boundary condition, and the longwave radiation parameterization), (d) minimal truncation error in the hydrostatic calculations (to avoid spurious horizontal pressure gradient forces), (e) physical consistency between vertical and horizontal resolution (to avoid generation of spurious numerical modes), and (f) acceptable computational costs in the three-dimensional runs.

Let us consider each of these requirements in more detail:

(a) Taylor and Delage (1971) have described problems that can arise in solving the PBL equations by finite difference methods due to the 'near singularity' at height $z = 0$. The most common way to avoid such inaccuracies is to consider a 'wall layer', $0 \leq z \leq \mathrm{Z}(1)$, where $\mathrm{Z}(1)$ is the height of the first model level above the Earth's surface. Fluxes within this *shallow* layer are assumed to be constant with height and velocity and temperature profiles are assumed to be described exactly by Monin-Obukhov similarity theory. However, these assumptions require that $\mathrm{Z}(1)$ lie within the atmospheric surface layer, which is typically considered to make up less than a tenth of the total PBL depth (e.g., Danard, 1981; Holtslag and Nieuwstadt, 1986) and which may be as shallow as 10 m under stable conditions (e.g., Högström, 1988).

Delage (1988a) considered the case of coarse vertical resolution where the first model level $\mathrm{Z}(1)$ lies *above* the top of the stable surface layer. He found that significant *underestimates* of surface stress and surface heat flux resulted due to the implicit extension of the surface-layer profiles to heights well above their actual range of applicability.

Table 4.2: RAMS vertical discretization employed in all simulations for both case studies. 'Z' denotes scalar levels and 'ZZ' denotes vertical velocity levels in the RAMS Arakawa C stagger in meters. The values of DELTAZ, DZRAT, and DZMAX which were used were 50 m, 1.15, and 2000 m, respectively. Values of the July 8, 1980 Oklahoma City 1200 GMT sounding which were used in the one-dimensional and two-dimensional Great Plains case-study simulations are also listed. Sounding variable units for pressure, potential temperature, water vapour mixing ratio, and the two horizontal wind components are hPa, K, $\mathrm{g\,kg^{-1}}$, $\mathrm{m\,s^{-1}}$, and $\mathrm{m\,s^{-1}}$, respectively.

N	Z	ZZ	p	θ	r	u	v
1	-22.5	0.0	971.0	301.6	13.2	0.6	5.0
2	24.1	50.0	965.9	301.6	13.2	0.6	5.0
3	77.7	107.5	960.0	302.2	13.4	2.1	8.0
4	139.4	173.6	953.3	302.9	13.6	3.7	11.5
5	210.3	249.7	945.7	303.7	13.8	5.3	14.8
6	291.9	337.1	937.0	304.6	14.0	6.0	16.4
7	385.6	437.7	927.1	305.4	14.1	6.2	17.0
8	493.5	553.3	915.8	306.0	14.1	6.4	17.6
9	617.5	686.3	903.0	306.4	13.8	6.4	16.1
10	760.1	839.3	888.5	306.8	13.5	6.3	14.5
11	924.2	1015.2	871.9	307.2	13.1	6.5	12.4
12	1112.8	1217.5	853.2	307.7	12.7	6.9	9.7
13	1329.7	1450.1	832.1	308.2	12.2	6.6	8.2
14	1579.2	1717.6	808.3	308.5	11.5	5.6	7.8
15	1866.0	2025.2	781.6	308.9	10.6	4.4	7.4
16	2195.9	2379.0	751.7	311.1	5.6	4.1	9.4
17	2575.3	2785.9	718.4	312.6	3.2	4.0	11.5
18	3011.6	3253.8	681.6	313.7	2.3	3.8	13.3
19	3513.4	3791.8	641.1	315.5	1.7	0.4	10.2
20	4090.4	4410.6	597.0	317.7	1.1	-1.0	7.2
21	4754.0	5122.2	549.2	319.2	0.7	-0.1	5.0
21	5517.1	5940.5	498.6	329.2	1.0	0.5	1.4
23	6394.6	6881.6	445.5	330.4	0.6	0.3	0.5
24	7403.8	7963.8	389.9	333.7	0.5	-0.5	-3.0
25	8564.4	9208.4	332.9	337.3	0.3	0.0	-6.0
26	9899.0	10639.7	275.5	340.9	0.2	1.2	-8.3
27	11433.9	12285.6	219.3	344.4	0.0	1.6	-9.4
28	13209.0	14178.4	165.7	349.9	0.0	1.0	-8.3
29	15164.7	16178.4	119.8	370.8	0.0	9.3	-4.4

(b) Many atmospheric models employ nonuniformly-spaced vertical levels in order to obtain maximum resolution near the Earth's surface where vertical gradients are typically large without the computational expense associated with high-resolution *uniform* vertical grid spacing throughout the depth of the model domain. One disadvantage of such a *nonuniform* (or *variable*, *stretched*, *expanding*, or *telescoping*) vertical discretization, however, is the introduction of a lower-order truncation error[137] in Δz (Crowder and Dalton, 1971; Kálnay de Rivas, 1972; Roache, 1972). Delage (1988b) showed that truncation error due to large changes in vertical grid spacing near the Earth's surface can result in large errors in the calculated surface stress.

In the case of geometric stretching where the ratio of two adjacent grid layers Δz_k and Δz_{k+1} is constant and equal to s, the truncation error associated with the centered finite-difference approximation to the second derivative $\partial^2\phi/\partial z^2$ is $O[4(\Delta z_{k+1} - \Delta z_k),\ \Delta z^2]$. For a uniform grid (i.e., $s = 1$), however, the truncation error is simply $O(\Delta z^2)$. If $4(s-1)$ is larger than unity, then the finite-difference approximation of the second derivative will only be first-order accurate. However, Kálnay de Rivas (1972) noted that even first-order truncation errors may be acceptable if Δz is itself very small, and Sundqvist and Veronis (1970) argued that Δz_k can be chosen so that $\Delta z_{k+1} - \Delta z_k$ is $O(\Delta z_k^2)$, i.e., still second-order accurate[138].

(c) Regardless of the model vertical resolution, there are at least three good reasons for the model top to reach to the lower stratosphere. First, for variable-initialization runs, the full tropospheric circulation should be represented to ensure depth-averaged nondivergence. Otherwise, spurious circulations may form. Second, the prognostic

---

[137] Roache (1972) suggests that this problem can be avoided by performing a 'stretching' transformation and using a uniform grid spacing in the transformed coordinate. Such a transformation frequently introduces additional terms, however (e.g., Anthes, 1970).

[138] Although there is still a need to evaluate the phase behaviour of such nonuniform grids.

surface pressure boundary condition requires that mass divergence above the model top be small compared to divergence in the model interior (see Sec. 4.2.6). And third, the radiation parameterizations used in Version 2A of RAMS do not account for shortwave attenuation or longwave emissions in the atmosphere above the model top. Significant spurious longwave cooling can result at the model top if it is placed too low (e.g., Moran, 1989a).

(d) Too coarse vertical resolution can cause truncation errors in the pressure-gradient-force (PGF) terms through both vertical interpolation error (e.g., Sundqvist, 1979) and small residuals between the two terms of the PGF in sigma coordinates (e.g., Achtemeier, 1991). However, Mahrer (1984) also showed that too fine vertical resolution may lead to a numerically inconsistent approximation of the horizontal pressure gradient terms. To avoid this problem, he showed that at the surface the smallest vertical grid interval must satisfy the requirement that $\Delta z_1 \geq \Delta z_G$, where Δz_1 is the vertical grid spacing in the first model layer and Δz_G is the elevation difference between two horizontally adjacent grid points[139].

(e) Pecnick and Keyser (1989), Lindzen and Fox-Rabinovitz (1989), and Persson and Warner (1991) have recently suggested that the vertical grid resolution must be selected to be *physically* consistent with the horizontal grid resolution. That is, all vertical scales that are physically related to the resolved horizontal scales in such features as narrow sloping thermal structures or critical layers must themselves be resolved. For typical frontal slopes s of 0.005–0.02, Pecnick and Keyser's consistency relationship suggests 50–200 m vertical grid spacings for horizontal grid spacing of 10 km (i.e., $\Delta z_{opt} = s\Delta x$).

---

[139] This requirement could pose a problem at a few grid points in the simulations described herein. The RAMS ISAN package returns $(\Delta z_G)_{max}$ values when it interpolates model grid topography in Stage 5: these values were 491 m for the Great Plains simulation grid and 339 m for the CAPTEX simulation grid, considerably larger than the near-surface vertical spacing.

(f) The number of grid points and hence the computational cost increases in direct proportion to the number of vertical levels chosen. Moreover, the computational cost of most emissivity-based longwave radiation calculations, including the two schemes implemented in RAMS, is $O(N^2)$ where N is the number of levels, thus imposing an even greater computational cost if a large number of vertical levels are chosen (e.g., Lacis and Oinas, 1991).

Basically, then, most of the numerical and scientific considerations discussed above [points (a)–(d)] argue for as many vertical levels and as deep a simulation domain as possible while computer-cost considerations [point (f)] suggest that as few vertical levels and as shallow a domain as possible be used. One reasonable rule of thumb to balance these conflicting requirements is Pielke's (1984) suggestion that the representative vertical length scale of the circulation of interest should be spanned by about ten grid increments. In the case of a terrain-forced mesoscale circulation, the corresponding characteristic vertical length scale would normally fall into the 0.5–4 km range, suggesting a vertical spacing in the 50–400 m range. The shallowest significant circulation feature of interest in the two cases considered in this study is probably the nocturnal low-level jet, which typically has a vertical scale of about 700 m, the distance from the Earth's surface to the 'nose' of the jet in the vicinity of the top of the nocturnal stable layer[140].

Only a few sensitivity tests to examine the impact of a reduction in the number of model vertical levels on the simulated PBL structure have been reported in the literature. Pielke (1974b) compared a two-dimensional sea-breeze control run against two sensitivity tests, one in which the vertical resolution was held constant but the domain depth was doubled and one in which the domain depth was held constant but the vertical grid spacing was halved. He found that simulations with 8 and 13 grid levels below 4.22 km produced similar sea-breeze circulations. Pielke and Mahrer (1975) compared 2 one-dimensional

---

[140] Bonner (1968) found an overall mean of 785 m altitude for the 0600 CST low-level jet maximum for 22 Great Plains stations based on two years of rawinsonde observations. The Fort Worth, Texas jet maximum was found to occur at 600 m (Bonner and Paegle, 1970).

Wangara Day 33 simulations, one with 31 levels and one with 8 levels in the first 2 km. The time evolution of the potential temperature and specific humidity profiles during the day was very similar for the two runs. Mahfouf et al. (1987) obtained comparable results in a 36-h one-dimensional test of a TKE turbulence parameterization for the same Wangara case, this time with 9 and 30 levels in the lowest 2500 m.

As shown in Table 4.2, the vertical discretization chosen for this study based on all of the above considerations was a stretched grid with $\Delta z = 50$ m and a stretch factor of 1.15.

4.2.5 Numerical techniques

A hydrostatic time-split time differencing scheme with both a short (or 'fast') time step and a long (or 'slow') time step was used in this study (Tremback et al., 1985). Such a scheme permits the use of different numerical schemes for different flow modes so that all terms in the governing equations are not subjected to the time-step constraint imposed by the fastest-moving modes, in this case the external gravity wave and the Lamb wave (e.g., Gadd, 1978). Horizontal advection, Coriolis force, horizontal turbulent diffusion, radiation, and surface processes were handled during the long time-step calculations. Vertical advection, horizontal pressure gradient force, and surface pressure tendency were computed during the short time-step calculations. The long time step was set to 60 s in the present simulations while the short time step was set to 20 s.

The sixth-order, flux-form forward upstream advection scheme was selected as the horizontal advection operator. This scheme is more efficient and less dispersive than the centered-in-space leapfrog scheme and avoids a computational mode (Tremback et al., 1987). The Coriolis term is linearly unstable for a forward scheme but this is a very weak instability (Pielke, 1984; Tremback, 1990). A second-order, centered-in-space scheme was used for the vertical advection operator. Use of a lower-order scheme avoids problems with 'ringing' associated with sharp vertical gradients (e.g., Tripoli, 1986).

Vertical diffusion can be a rate-limiting step because of the large diffusivities which may occur in the convective PBL. In order to maintain computational stability, it is

sometimes necessary to use a smaller time step for calculating this term. The time step used in RAMS for this term is calculated automatically based on Fourier number considerations, where the Fourier number $F = K_z \Delta t (\Delta z)^{-2}$ is required to be less than 0.25. However, the long time step was small enough to ensure the stability of this term most of the time and in most of the domain.

As mentioned earlier, radiation calculations are time-consuming. Since radiative fluxes normally change relatively slowly with time, radiation tendencies were only calculated once every six time steps. The horizontal pressure gradient terms were computed using the standard transformed form (e.g., Tripoli and Cotton, 1982). RAMS also has an option to evaluate the horizontal PGF as the difference between the local pressure and the vertically interpolated pressure at an adjacent point at the same geometric height. Tremback (1990) compared these two methods and found little difference in the results.

4.2.6 Boundary conditions

Boundary conditions are an integral and important component of a limited-area model since time-dependent boundary conditions must be specified in order to close any initial-boundary value problem. While specification of the bottom boundary conditions is relatively straightforward, specification of the lateral and upper boundary conditions has been a thorny problem since the earliest days of numerical weather prediction (e.g., Charney et al., 1950; Platzman, 1954, 1979; Oliger and Sundström, 1978). This is not too surprising considering the artificiality of conceptually 'cutting out' a finite volume of the atmosphere. The model boundaries must then be perfectly transparent, i.e., 'open', both to flow 'information' travelling from the atmospheric exterior into the model interior by advection or wave propagation and to flow structures or disturbances generated within the model domain and propagating away from their source. Ideally, the lateral and upper boundaries should not be reflective or refractive in any way nor should they themselves be the source of any disturbances or noise.

Lateral boundary conditions

In the real atmosphere, the flow within a finite volume will both influence and be influenced by the flow outside the volume. However, when running a limited-area model, time-dependent lateral boundary information will often be obtained beforehand from either observations or from separate runs of a larger-scale prediction model. As a result, boundary values will not respond to flow features generated within the model domain. In other cases the limited-area model may be coupled to, and run simultaneously with, a larger-scale model, thus permitting feedbacks between the two model domains. The first approach is known as *one-way nesting* while the second is termed *two-way nesting* (e.g., Phillips and Shukla, 1973; Miyakoda and Rosati, 1977; Sundström and Elvius, 1979; Haltiner and Williams, 1980; Koch and McQueen, 1987).

Clearly, two-way nesting is a more physical approach. RAMS employs a two-way nesting scheme developed by Clark and Farley (1984) to handle interior fine grids. However, the outermost or largest-scale grid of even a two-way nested model must still employ one-way lateral boundary conditions (unless it is a global model). RAMS offers a variety of lateral boundary condition (LBC) options, including cyclic conditions in either or both horizontal directions, three different radiative boundary conditions on the normal velocity component and radiative, zero-gradient, or constant conditions on other variables, and two schemes to incorporate large-scale boundary time tendencies. These various options will be discussed shortly, but it is appropriate to mention some general theoretical concerns about lateral boundary conditions in numerical hydrodynamical models first.

Well-posedness and overspecification. All LBC schemes used in current limited-area models have been termed 'pragmatic' boundary conditions by Davies (1976, 1983) and Sundström and Elvius (1979) since all of these schemes are over-specified. That is, due to the finite-difference schemes employed, too many variable values are specified on outflow boundaries[141] for the overall initial-boundary value problem to be *well-posed.* Sundström

---

[141] Boundaries where flow normal to the boundary is directed *away from* the model interior.

and Elvius (1979) described well-posed boundary conditions as those initial and boundary conditions which determine a *unique* solution and for which small errors in the boundary data should produce errors of a *comparable* size in the solution.

Oliger and Sundström (1978) showed that for a hyperbolic system of equations, the number of boundary conditions should be equal to the number of inward characteristics. For the adiabatic inviscid Eulerian equations of fluid dynamics[142], this corresponds to four boundary conditions at inflow points and one boundary condition at outflow points[143]. If viscous terms are added, the character of the Eulerian equations changes from hyperbolic to incompletely parabolic and the number of boundary conditions required increases to five at inflow points and four at outflow points. Making the hydrostatic assumption also destroys the hyperbolic character of the system since it effectively introduces infinite phase speeds, leading Oliger and Sundström (1978, p. 431) to conclude that "local, pointwise boundary conditions cannot yield a well-posed problem for the open boundary problem for the hydrostatic equations."

Despite these theoretical concerns, specification of well-posed lateral boundary conditions has been impractical even in *nonhydrostatic* limited-area models due to discretization considerations and to a lack of practical methods to calculate characteristics (e.g., Davies, 1976, 1983; Clark, 1979). By default, a variety of pragmatic or utilitarian boundary-condition formulations have been used instead. Nevertheless, Davies (1983) noted that despite the "spectre of rabid ill-posedness", regional NWP models using these various pragmatic LBC formulations have shown significant skill.

Two problems can arise from boundary-condition overspecification, however. First, the influence of the boundary, that is, the flow exterior to the model domain, is exaggerated. Second, computational modes, gravity waves, and other disturbances can be

---

[142] Consisting of three momentum equations, a continuity equation, and a thermodynamic equation in variables u, v, w, ρ, and p.

[143] For example, the tangential velocities and potential temperature at inflow boundaries and a characteristic *combination* of normal velocity and pressure at both inflow and outflow boundaries.

generated at the boundaries and propagate into the model domain, contaminating the interior solution (Sundström and Elvius, 1979). Davies (1983) identified four approaches which have been developed to circumvent such overspecification problems: (a) boundary or 'sponge' zones of artificially large diffusion; (b) sponge zones with a blending of tendencies from externally-specified and internally-determined fields (e.g., Perkey and Kreitzberg, 1976); (c) boundary zones with a Newtonian relaxation of prognostic variables towards externally-specified values (e.g., Davies, 1976); and (d) outflow extrapolation or radiation schemes. The goal of all of these approaches is to reduce the 'noise' at model boundaries which results from the spurious *reflection* of outgoing waves and from the *generation* of noise at the boundaries themselves. The first three approaches damp incoming and outgoing waves in the boundary zone while the fourth approach attempts to let outgoing waves pass through the boundary with minimum reflection. Detailed reviews of these various pragmatic approaches have been given by Sundström and Elvius (1979) and by Davies (1983).

RAMS radiative boundary conditions. The three outflow radiative boundary conditions available in RAMS for nonperiodic open boundaries were developed by Orlanski (1976b), Klemp and Lilly (1978), and Klemp and Wilhelmson (1978), respectively. The first two have been called 'floating' radiative conditions and the last a 'fixed' radiative condition by Clark (1979) since the Orlanski and Klemp–Lilly schemes estimate phase speeds for each flow variable from *local* flow values while the Klemp–Wilhelmson scheme employs *fixed*, user-specified phase speeds. Orlanski's scheme was one of the earliest attempts to model an 'open' boundary. The Klemp–Lilly and Klemp–Wilhelmson schemes as well as others proposed by Miller and Thorpe (1981), Kurihara and Bender (1983), Raymond and Kuo (1984), and Hedley and Yau (1988) are all modifications to Orlanski's basic approach, and differ primarily in their specification of the phase speed c and in the number of flow variables to which this boundary condition is applied.

Questions have been raised about the performance of all three of these formulations. Clark (1979) compared simulations of airflow over a bell-shaped mountain which used

the Orlanski and Klemp–Wilhelmson radiative boundary conditions and found that the Klemp–Wilhemson 'fixed phase speed' run developed an unphysical, domain-scale mean vertical velocity due to the occurrence of low-level inflow and upper-level outflow on the same lateral boundary. Clark also found the Orlanski condition to suffer from this 'run-away circulation' problem but to a lesser degree.

Cho and Clark (1981) and Clark and Gall (1982) introduced a relaxation term for the basic state velocity at the boundary to address this shortcoming. Tripoli and Cotton (1980), on the other hand, reported reasonable results with the Klemp–Wilhelmson scheme. Lilly (1981) suggested that Clark (1979) had set the phase speed c to too large a value (45 $\mathrm{m\,s^{-1}}$). In contrast, Klemp and Wilhelmson (1978) had used a value of 30 $\mathrm{m\,s^{-1}}$ for c and Klemp et al. (1981) a value of 15 $\mathrm{m\,s^{-1}}$. Klemp and Lilly (1978) proposed calculating a vertically-averaged c at each boundary *column* to avoid the large spatial variations in c which can often occur and to prevent a model column changing from inflow to outflow or vice versa with height. This approach has been adopted by Durran and Klemp (1983) and Tripoli (1986). Sundström and Elvius's (1979, p. 400) comment on this scheme, however, was that "the whole boundary value specification became rather obscure." And of course all of these schemes implicitly assume the existence of a single dominant internal gravity wave (IGW) mode by their use of a single phase speed whereas a variety of IGW modes may be present (Klemp and Lilly, 1978; Hack and Schubert, 1981).

Tripoli and Cotton (1982) introduced a novel and physically-based approach to the problem of domain-scale circulations by introducing a 'mesoscale compensation region' (MCR) at their lateral boundaries. This region is basically a very wide grid box which is placed just outside of each lateral-boundary grid box and which acts as a 'mass reservoir'. Atmospheric mass leaving and entering the model domain at each vertical level is tallied and compensating lateral and vertical motion is specified to occur in the MCR which in turn feeds back into the model domain through an MCR pressure perturbation. Radiative lateral boundary conditions are still used at the domain boundaries inside the

MCR but are modified by the MCR pressure term. Tripoli and Cotton (1982) found for a two-dimensional thunderstorm simulation that the use of the MCR with the Orlanski scheme gave results closer to a larger-domain simulation than a simulation made with the Klemp–Wilhelmson scheme. In general, the MCR is most useful for simulations of significant convective activity within a small domain, for example, modelling a single isolated thunderstorm (Walko and Tremback, 1991).

More recently, Raymond and Kuo (1984) suggested the calculation of a multi-dimensional phase speed, that is, a vector phase speed with tangential as well as normal components, in multi-dimensional model simulations to avoid problems exhibited by the Orlanski scheme when horizontal gradients at the boundary are very small. Hedley and Yau (1988) addressed this same problem by introducing a minimum phase speed for the Orlanski scheme, yielding a hybrid fixed–floating radiative boundary condition. Clearly, the treatment of open boundaries in limited-area atmospheric models must still be regarded as an 'open' problem.

External forcing. Another complication which must be addressed in limited-area models is the fact that the atmosphere outside the model domain will probably also change during a simulation. Two pragmatic boundary-zone schemes have been proposed to incorporate external flow tendencies into a limited-area model solution. These are the tendency modification scheme of Perkey and Kreitzberg (1976) and the boundary relaxation scheme of Davies (1976, 1983). Both of these schemes have been implemented in RAMS.

An artificial relaxation term of the form $(\phi - \phi_{\text{ext}})/\tau$ is introduced into the governing equations in the boundary zone in both of these schemes, where τ is a relaxation time, ϕ is the model interior value, and ϕ_{ext} is the prescribed exterior value[144]. In the Perkey–Kreitzberg scheme, ϕ and ϕ_{ext} correspond to the time *tendencies* of a model variable and its external value, respectively. Internal and external tendencies are blended together at each time step using a boundary-zone weighting which varies from zero at the

[144] The Rayleigh friction term discussed in the next subsection also has this form.

domain boundary for an interior tendency ϕ to unity well inside the model interior for ϕ (actual weights from the boundary inward are 0.0, 0.4, 0.7, 0.9, 1.0, 1.0, 1.0, ...). As discussed by Perkey and Kreitzberg (1976) and Davies (1983), this tendency blending technique leads to the trapping and wavelength shortening in the boundary zone of waves propagating outward from the model interior. To complete this scheme, it is thus necessary to increase the diffusivity coefficient near the boundary in order to remove short-wave energy.

In the Davies scheme, on the other hand, ϕ and ϕ_{ext} correspond to actual variable *values* rather than tendencies so that the pure relaxation equation has the form

$$\frac{\partial \phi}{\partial t} = \frac{1}{\tau}(\phi - \phi_{\text{ext}}) \quad . \tag{4.1}$$

Model interior tendencies are thus considered in full right up to the domain boundary so that other LBC schemes can be used in conjunction with the Davies scheme (e.g., Kurihara and Bender, 1983). The Davies scheme, unlike the Perkey–Kreitzberg scheme, is self-damping and does not require the use of an additional filter or damping operator. In addition, at inflow boundaries, only *departures* of the field of interest away from specified values are relaxed whereas in the Perkey–Kreitzberg scheme the enhanced diffusion is applied to the *total* field (Davies, 1983).

LBC options selected for this study. Only a few comparisons of the two pragmatic schemes for handling external forcing have been reported in the literature. Miyakoda and Rosati (1977) carried out tests of the two schemes with the 9-level GFDL 1967-version full-physics GCM and reported comparable results for a March case study. Seitter (1988) presented results from idealized geostrophic-adjustment experiments carried out with a one-dimensional shallow-water model and a three-dimensional mesoscale model that showed the Davies scheme to perform better. Cram (1990) used RAMS to perform comparisons between the two schemes for real-data cases and found the Davies scheme to produce less computational noise at the lateral boundaries. The Davies external-forcing scheme has also been used in the Australian operational limited-area forecast system

(Leslie et al., 1981) and in the NCAR/Penn State regional-scale research model (Anthes et al., 1987). It was selected without further testing for use in the present study in the *three*-dimensional simulations with time-dependent boundary conditions.

As suggested by Cram (1990), a five-point boundary zone was used with a gradual nonlinear variation in the relaxation weights w_i of, beginning at the boundary, 0.75, 0.56, 0.32, 0.10, and 0.01. The relaxation-term contribution is thus zero at points more than four grid *lengths* from any lateral boundary. Following the analysis of Kurihara and Bender (1983), if the relaxation time $\tau = A\Delta t$, then the relaxation weight $w = 1/A$ so that these particular weights w_i correspond to relaxation times of $1.33\Delta t$, $1.79\Delta t$, $3.13\Delta t$, $10\Delta t$, and $100\Delta t$. In comparison, Leslie et al. (1981) used relaxation times of $0\Delta t$, $1.72\Delta t$, $6.39\Delta t$, $19.08\Delta t$, and $53.60\Delta t$, and Anthes et al. (1987) used relaxation times of $10\Delta t$, $15\Delta t$, and $30\Delta t$. Kurihara and Bender (1983) used relaxation times of $5\Delta t$ or $10\Delta t$ at the boundary to introduce external values and relaxation times of $20\Delta t$, $20\Delta t$, $40\Delta t$, $60\Delta t$, $90\Delta t$, and $120\Delta t$ in a six-point boundary zone to control boundary noise.

Users of the Davies scheme should be aware that some w_i values will produce oscillatory or unstable solutions for some time-differencing schemes. As discussed by Mesinger and Arakawa (1976), for the Euler (or forward) time-differencing scheme used in RAMS, solutions of Eq. 4.1 will approach ϕ_{ext} in an oscillatory fashion if τ lies in the range $(0.5\Delta t, \Delta t)$ and will not converge at all if τ is smaller than $0.5\Delta t$ (i.e., $w > 2$). For the special case of $\tau = 1\Delta t$ (i.e., $w = 1$), $\phi(t + \Delta t)$ will be exactly equal to ϕ_{ext}. For values of τ larger than Δt, τ will correspond approximately to the e-folding time for the relaxation of ϕ towards ϕ_{ext}. Leslie et al. (1981) and Kurihara and Bender (1983) avoided this stability problem by using fully implicit time differencing to solve Eq. 4.1.

The LBC temporal resolution in the Great Plains and CAPTEX simulations which employed the Davies boundary-zone scheme (see Tables 5.1 and 6.1) was 12 hours, i.e., the resolution of the operational synoptic upper-air network. The preparation of the re-

quired LBC input data sets is described in Sec. 4.3. In addition, the Klemp–Lilly radiative LBC scheme was applied in all simulations for normal velocity components at the lateral boundaries while fixed-inflow, outward-extrapolated outflow conditions were applied to other variables. Cram (1990) and Tremback (1990) used the Klemp–Wilhelmson LBC for the normal velocity component and fixed-inflow, fixed-outflow conditions for the other variables, but the difference is expected to be small in simulations with time-dependent LBC due to the dominance of the Davies external-forcing relaxation term. The MCR was not used in any of these simulations.

Upper boundary conditions

Wurtele et al. (1971) observed that a very common problem in numerical hydrodynamical calculations arises when the corresponding theoretical model applies to a semi-infinite or infinite region since it then becomes necessary to employ one or more 'false' boundaries where none really exists. Accordingly, the *upper* boundary condition has presented a problem for *all* atmospheric models, including global models. Choices for a dynamic[145] upper-boundary condition (UBC) basically reduce to either truncating the domain at a certain height or specifying the boundary conditions at a singularity (e.g., $p \rightarrow 0$) in the differential system of governing equations (Rasch, 1986).

As in the case of the lateral boundaries in a limited-area atmospheric model, imposition of an UBC at a *finite* height or pressure level can result in reflections *from* or the generation of spurious disturbances *at* the boundary. However, σ_p models[146] which use the boundary condition $\omega = 0$ at the singular boundary p = 0 also suffer from upper-boundary reflection due to discretization effects (e.g., Kirkwood and Derome, 1977).

---

[145] Referring here to vertical velocity or kinetic energy rather than pressure.

[146] $\sigma_p = p/p_s$ where p is the pressure, p_s is the surface pressure, and $\omega = dp/dt$.

Available approaches. The simplest dynamic[147] UBCs in a finite-depth model such as RAMS are a rigid lid[148] or an impervious material surface (e.g., Eliassen, 1962; Pielke, 1984). A material surface is somewhat more realistic than a rigid lid in that it moves in response to divergence in the atmospheric column below. Klemp and Lilly (1978) claimed that both conditions are perfectly reflecting but Pielke (1991: personal communication) has noted that a material surface cannot be perfectly reflecting since there is no buoyancy restoring force present in its formulation.

To avoid spurious reflections from the upper boundary, some modelers have placed an artificial layer, known variously as an absorbing layer, viscous layer, diffusion layer, damping layer, or sponge layer, at the model top. Two basic approaches have been employed. The first is to increase the effective mean kinematic viscosity in the absorbing layer by an arbitrarily large amount but to do so gradually with height so as to minimize reflections due to sudden vertical changes in the propagative medium (e.g., Klemp and Lilly, 1978; Mahrer and Pielke, 1978). A horizontal numerical filter could be used in a similar manner with the filter coefficients increasing with height. The second approach is to introduce Rayleigh friction or Rayleigh damping terms[149] into the governing equations in the absorbing layer (e.g., Houghton and Jones, 1969; Clark, 1977; Durran and Klemp, 1983; Cram, 1990). These terms will have the form $(\chi - \overline{\chi})/\tau$, where χ is the local value and $\overline{\chi}$ is the undisturbed background value of some quantity and τ is a relaxation time which *decreases* with height within the absorbing layer. Klemp and Lilly (1978) carried out a damping and reflectivity analysis for a viscous layer and noted that their analysis is also valid for a Rayleigh-friction layer.

---

[147] That is, related to velocity or kinetic energy.

[148] Sometimes referred to as a 'wall on top'.

[149] Also called *Newtonian cooling* when applied to temperature (e.g., Dickinson, 1969; Kirkwood and Derome, 1977), *Newtonian relaxation* or *nudging* when applied to initialization and data assimilation (Davies and Turner, 1977; Haltiner and Williams, 1980), and *residual relaxation* when used to solve elliptic equations (e.g., Haltiner and Williams, 1980).

While model results suggest that the absorbing-layer approach works quite well, its major drawback is its considerable computational expense since a sizable fraction of the model domain must be dedicated to this artificial layer. To be effective, the consensus seems to be that the absorbing layer should extend over at least one vertical wavelength of all the vertically-propagating waves of concern and should have at least 8 to 10 vertical levels (Rasch, 1986). As in the case of open lateral boundaries, then, a natural alternate approach is to consider the use of local radiative boundary conditions at the model top. Klemp and Durran (1983) and Bougeault (1983) independently devised approximate radiative UBCs applicable to vertically propagating gravity waves. However, these conditions assume the atmosphere above the model domain to be horizontally homogeneous, limiting their application to smaller domains.

Another approach used in hydrostatic models is the prognostic surface pressure UBC. This scheme is derived from the substitution of the fully compressible mass continuity equation into the integrated form of the hydrostatic equation (e.g., Haltiner and Martin, 1957, p. 320; Tremback, 1990, p. 15) and assumes for a finite-depth model that divergence above the model top is small compared to divergence within the model interior. As a result, in σ_z coordinates this condition is like a rigid lid while in σ_p coordinates it is equivalent to a material surface[150]. The prognostic surface pressure UBC has been used extensively in a variety of hydrostatic mesoscale meteorological models, including the operational NMC Nested Grid Model (Phillips, 1979), the NCAR/Penn State regional-scale model (Anthes et al., 1987), the Mesoscale Atmospheric Simulation System (MASS) model (Kaplan et al., 1982), the Canadian operational regional finite-element model (Benoit et al., 1989), and RAMS (Tremback, 1990). The upper boundary is typically located at or above 100 mb in these models in order to satisfy the small-divergence assumption.

---

[150] Since the upper limit of integration will be z_{top} or p_{top}, respectively.

RAMS upper boundary conditions. Version 2A of the RAMS model supports four UBCs: (i) a 'wall on top'; (ii) a material surface; (iii) the Klemp–Durran radiative UBC, and (iv) a prognostic-surface-pressure UBC. All four of these UBCs can be used with or without Rayleigh friction. However, the 'wall-on-top' condition can only be used for non-hydrostatic simulations and the last two are only compatible with hydrostatic simulations. While the standard RAMS Rayleigh-layer option only works for HHI model runs, code modifications have also been made in Version 2A to add a Rayleigh-friction layer and a viscous damping layer for variable-initialization model runs (Cram, 1990). The prognostic surface pressure UBC has been adopted in the present study as a compromise between computational cost and reflectivity problems. While this UBC is reflective, Anthes and Warner (1978), Tripoli and Cotton (1982), and Pielke (1984) have all argued that an absorbing layer is probably not required in many cases, i.e., that upper-boundary reflection can be tolerated so long as the vertical propagation of internal gravity wave energy is markedly smaller than the energy of advective processes.

The use of the prognostic surface pressure UBC does introduce the Lamb wave as a flow mode (e.g., Washington and Baumhefner, 1975). However, the presence of the Lamb wave does not restrict the maximum allowable time step any further since it is comparable in speed to the external gravity wave mode. The treatment of these fast-moving modes with the hydrostatic time-split scheme was discussed already in Sec. 4.2.5.

Bottom boundary conditions

Realistic specification of bottom boundary conditions is important when terrain forcing is a significant factor as it was expected to be in this study. The imposed kinematic bottom boundary conditions used were the 'no slip' condition in the tangential direction and zero velocity (i.e., a rigid boundary) in the normal direction. Surface temperature and surface soil moisture were prognosed using the multi-level soil model and a surface energy budget. Surface fluxes and near-surface profiles of momentum, heat, and water vapour were diagnosed based on surface-layer similarity theory and the values of these quantities at the lowest model level.

These bottom-boundary calculations require information on (a) terrain height, (b) land-cover class, (c) shortwave albedo, (d) aerodynamic surface roughness length, (e) soil texture class, and (f) water surface temperature. NCAR data sets (see Jenne, 1975, 1989) were used to specify gridded fields of each of these surface characteristics. Some of these quantities were available directly from the NCAR data sets while others had to be inferred. In the case of the three-dimensional simulations employing variable surface characteristics, computer programs were written or modified to prepare individual input data files for each of these surface quantities and modified subroutine VARMISC of RAMS to read them in. Solar albedo was also added as a two-dimensional variable in RAMS. Each of the six surface characteristics listed above will now be discussed in turn.

Terrain height data set. A number of terrain-height data sets with different horizontal resolutions and covering different parts of the world are available at NCAR. DSS data set 755.0, originally prepared by the U.S. Air Force, contains 5' latitude by 5' longitude (approximately 10 km resolution) terrain-height data for most of North America. This data set also contains information on land–water–ice cover fractions but gridded 'water' land-cover class values from another surface data set were used instead in this study to specify fractional water coverage (see following discussion of the EPA land-cover data set).

A subset of the Air Force terrain elevation data set with limits from 24° to 55°N and from 52° to 134°W was extracted to match the EPA land-cover data set domain. Terrain heights for the Great Lakes were then set equal to lake *surface* heights taken from an atlas (Espenshade and Morrison, 1979) because the archived U.S. Air Force terrain-height data set contains lake *bottom* elevation values (in fact several grid-point terrain height values for Lake Ontario are negative, that is, below sea level). Moreover, the lake-bottom height values, unlike lake-surface height values, are not equal across individual lakes; that is, there would be a 'terrain' slope to the water surfaces if these values were used without modification.

Finally, after creating the 5' terrain-height data set, I modified the RAMS isentropic analysis or ISAN package to read it in. These gridded terrain heights were then interpo-

lated linearly to the specified assimilation and model grids and smoothed as appropriate in Stages 2, 3, and 5 of the ISAN package. See Sec. 4.3 for more details. Contoured terrain height plots for the Great Plains and CAPTEX simulation grids based on this 5' data set are shown in Fig. 4.13b and Fig. 4.19b, respectively.

Land-cover data set. Much of the Earth's land area is covered by a layer or canopy of vegetation. Such 'land cover' can significantly modulate surface fluxes of momentum, heat, and moisture due both to its structural characteristics and to biological activity. 'Land use' is sometimes used as a synonym for 'land cover', but the former term connotes a modification of natural terrestrial vegetation by such human activities as farming, grazing, logging, mining, and construction while the latter term includes both natural and modified landscapes.

A few gridded land-cover data sets are available for weather and climate models (e.g., Matthews, 1983; Wilson and Henderson-Sellers, 1985; Henderson-Sellers et al., 1986). Vegetation classes in these data sets are based on such vegetation characteristics as canopy height, structure/architecture, density, seasonality, and rooting depth. Most of the available digitized land-cover data sets have been developed for general circulation models and have horizontal grid resolutions of no more than 1° latitude by 1° longitude. However, one digital land-cover data set archived at NCAR has 1/6° latitude by 1/4° longitude grid resolution over a domain covering much of North America.

This data set (DSS No. 766.0) was produced for the U.S. Environmental Protection Agency as an input data set for a mesoscale meteorological model used by that agency (Page, 1980; Sheih et al., 1986). Its domain covers the 48 contiguous U.S. states, southern Canada, and northern Mexico. The actual domain boundaries lie at longitudes 52°W and 134°W and at latitudes 24°N and 55°N. Eleven categories, listed in Table 4.3, were used to classify land cover. Percentage values of surface coverage for *each* land-cover category are given for all 61,523 of the approximately 20 km by 20 km grid squares. Values were obtained by hand analysis of a combination of U.S. Geological

Survey *Land Use and Land Cover* series maps, Landsat regional mosaic images (Bands 5 and 7), and single-scene Landsat spot coverage (Page, 1980).

One immediate use of this data set is to specify the fraction of each model surface grid square covered by water since water surfaces are treated differently than land surfaces in the RAMS surface module. Fig. 4.3a shows the distribution of surface water in central and eastern North America as described by the EPA land-cover data set (Fig. 4.7 gives a more detailed view of the *complement* of this field, land fractional coverage). The other panels in Fig. 4.3 show corresponding distributions of five of the other EPA land-cover categories: agricultural land; deciduous forest; coniferous forest; mixed forest; and urban areas.

Inferred surface fields. With the exception of the 'water' category, the actual land-cover or vegetation category fractional distributions stored in the EPA land-cover data set cannot used directly as RAMS input variables. However, standard model input variables can be inferred from known land-cover types. This approach has been used by other modellers in the case of *surface roughness* (e.g., van Dop, 1983; Dickinson et al., 1986; Walcek et al., 1986; Hsie, 1987; Sellers and Dorman, 1987; Wilson et al., 1987; Godowitch, 1989b; Seaman et al., 1989), *albedo* (Hsie, 1987; Wilson et al., 1987; Seaman et al., 1989), *emissivity* (Hsie, 1987; Seaman et al., 1989), *deposition velocity* (van Dop, 1983; Walcek et al., 1986; Walcek, 1987; Arritt et al., 1988), and various vegetation parameters (Dickinson et al., 1986; Wilson et al., 1987).

In the present study, grid-square mean values of aerodynamic surface roughness z_0 and solar or shortwave albedo a have been estimated for the two case-study domains based on the EPA land-cover data set. Table 4.3 lists characteristic summertime surface roughness and solar albedo values associated with the individual land-cover classes. Grid-square mean aerodynamic roughnesses were calculated as the weighted *logarithmic* averages of individual land-cover-category values based on the fractional areal coverage of each of the eleven land-cover categories within a grid square (e.g., Walcek et al., 1986). Grid-square mean albedos were based on weighted linear averages of individual

Table 4.3: Land-cover categories and three corresponding surface characteristics for the summer season. Surface roughness values are based on Walcek et al. (1986). Solar albedo and fractional vegetation cover (remainder is assumed to consist of unshielded bare soil) values are based on Wilson et al. (1987) and Pielke (1984), assuming that 0.7 μm divides the solar radiation spectrum evenly since vegetation albedos vary significantly between visible and infrared wavelengths (e.g., Liou, 1980, p. 39; Henderson-Sellers and Wilson, 1983). See also Henderson-Sellers et al. (1986), Hsie (1987), and Seaman et al. (1989).

Land-cover Category	Category Description	Surface Roughness (m)	Albedo (%)	Fractional Cover
1	Urban land	1.00	18	0.00
2	Agricultural land	0.25	20	0.85
3	Rangeland	0.05	19	0.80
4	Deciduous forest	1.00	18	0.80
5	Coniferous forest	1.00	14	0.80
6	Mixed forest	1.00	16	0.80
7	Water	0.0006*	8	0.00
8	Barren land	0.10	18	0.60
9	Non-forested wetland	0.15	12	0.80
10	Mixed agriculture/rangeland	0.10	19	0.80
11	Rocky open places	0.10	25	0.10

*varies with surface friction velocity (e.g., Charnock, 1955)

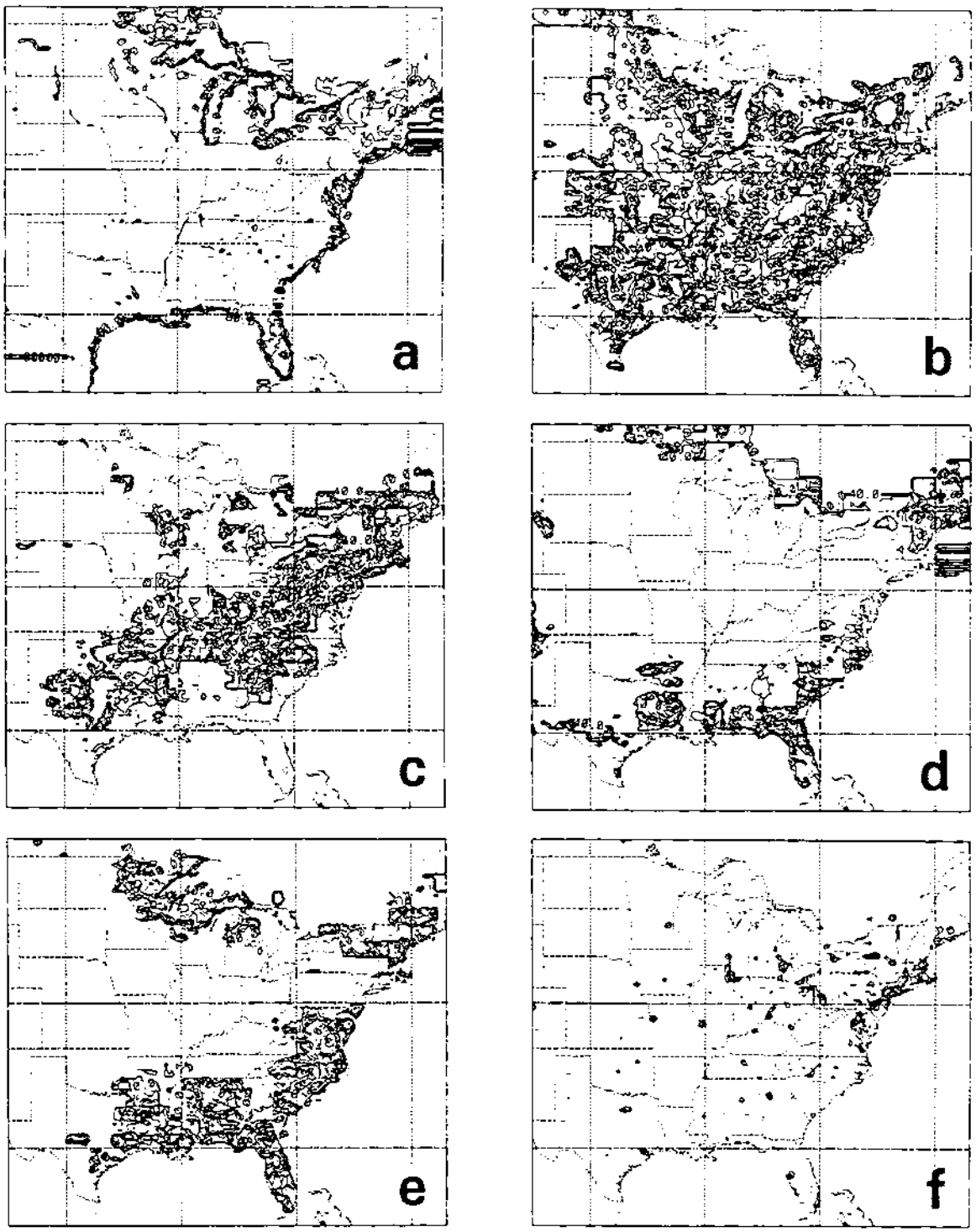

Figure 4.3: Distribution of fractional coverage (as a percentage) of six EPA land-cover categories over central and eastern North America (67°W–105°W, 24°N–50°N): (a) water; (b) agricultural land; (c) deciduous forest; (d) coniferous forest; (e) mixed forest; and (f) urban land. The contour interval is 10%. Latitude lines are indicated at 30°N and 40°N; longitude lines are indicated at 100°W, 90°W, 80°W, and 70°W. The resolution of the gridded fields shown here on a Mercator projection is 1/4° longitude by 1/6° latitude.

land-cover-category albedos, where the fractional vegetation cover value was considered so as to incorporate the contribution of unshaded bare-soil albedo as well as that of the vegetation. Bare-soil albedo in turn is well correlated with soil moisture content (McCumber and Pielke, 1981). The albedo of a water surface is strongly dependent on solar zenith angle (e.g., Henderson-Sellers and Wilson, 1983). However, this quantity is not used in RAMS since no surface energy budget is computed for water surfaces. Instead, a grid-square mean water surface temperature is specified and is assumed to remain unchanged over the simulation period (see p. 410).

Finally, the EPA land-cover data set resolution was converted to the RAMS simulation domain resolution (1/2° longitude by 1/3° latitude) by averaging[151] the EPA grid-square mean values over 2 by 2 blocks of grid squares. Fig. 4.4a shows a plot of block-averaged aerodynamic surface roughness values over central and eastern North America as derived from the gridded EPA land-cover data set. The corresponding plot of surface solar albedo is shown in Fig. 4.4b. Surface roughness values lie in the 0.10–0.25 m range in the open northwestern half of the Great Plains case-study domain but reach values as large as 1.0 m in the forested southeastern half of the domain. Forested areas also dominate surface roughness values in most of the CAPTEX case-study domain. Albedos are about 0.19 in much of Fig. 4.4b, a little bit less in forested areas (see Table 4.3).

Soil texture data set. RAMS specifies soil properties based on the 11-category (plus peat) USDA soil texture classification scheme (U.S. Department of Agriculture, 1951). These soil texture categories are determined by their composition in terms of relative fractions of three size ranges of mineral particles: *clay* (particle diameters < 0.002 mm), *silt* (0.002 to 0.05 mm), and *sand* (0.05 to 2 mm). However, available soil-type data sets do not use the USDA texture classification directly. In general, modern soil surveys classify soils based on the important processes (e.g., weathering, leaching, humification) which created

---

[151] All of the gridded land-cover data set input, calculations, and plotting were performed using a program which I wrote for this purpose. I then modified subroutine VARMISC of RAMS to input the resulting percent land, solar albedo, and surface roughness data files.

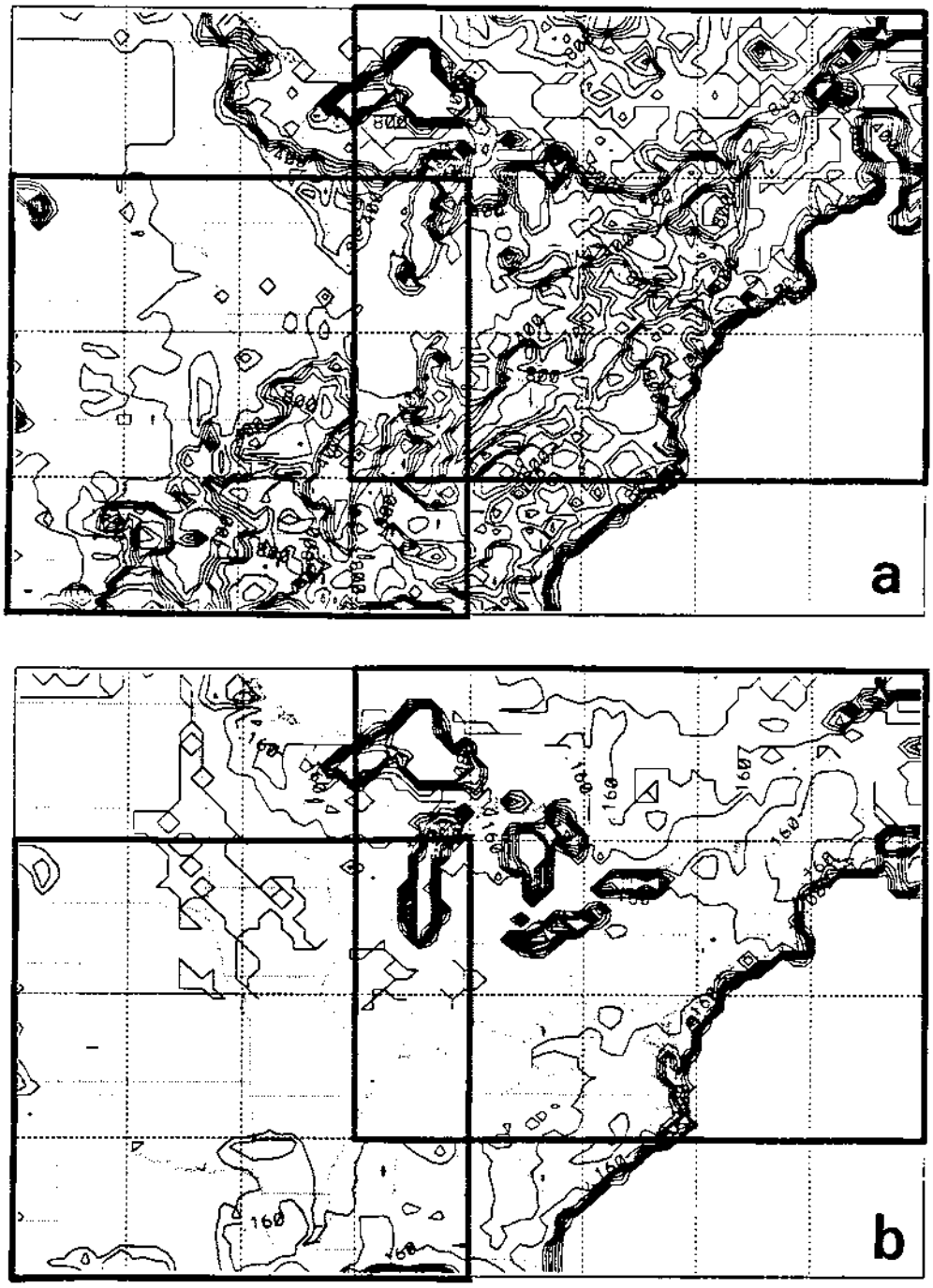

Figure 4.4: Inferred surface fields for central and eastern North America based on the EPA land-cover data set: (a) aerodynamic surface roughness (meters); and (b) solar albedo. The contour interval and range are 0.1 m and 0.0–1.0 m for surface roughness and 0.02 and 0.0–0.20 for solar albedo. The region shown stretches from 105°W to 65°W and from 30°N to 50°N. Grid resolution is 1/2° longitude by 1/3° latitude. Latitude and longitude lines are marked by dashed lines every 5° on this Mercator projection. The two heavy rectangles outline the boundaries of the two case-study RAMS domains.

the soils (Papadakis, 1969; Gardiner, 1981). The best known of these, the FAO–UNESCO world soil survey (e.g., FAO–UNESCO, 1974; Gardiner, 1981; Wilson and Henderson-Sellers, 1985; Staub and Rosenzweig, 1987), employs 26 major soil groups, including Gleysols, Phaezoms, Solonchaks, Yermosols, and Rendzinas. Specification of soil textures from such soil taxa is a job best left to a professional pedologist. Fortunately, a few gridded soil texture data sets do exist, although they do not use the USDA categories either.

NCAR data set 767.0 provides a global 1° by 1° description of soil texture in terms of *three* texture classes: coarse, medium, and fine (Wilson and Henderson-Sellers, 1985; Henderson et al., 1986). This data set also contains three-class gridded fields of soil colour (light, medium, dark) and soil drainage (freely draining, poorly draining, impeded). NCAR data set 770.0 also contains digitized global soil texture values on a 1° by 1° grid along with fields of soil type (e.g., eutric[152] regosols[153], plinthic[154] luvisols[155]), soil phase (e.g., cerrado[156], duripan[157], sodic[158]), and terrain slope (Staub and Rosenzweig, 1987). Nine texture classes are considered in this data set (see Table 4.4).

---

[152] Good, fertile (FAO–UNESCO, 1974).

[153] Skeletal soils with weak or no development, e.g., tundra of northern Canada (FAO–UNESCO, 1974).

[154] Connotative of mottled clayey materials which harden irreversibly upon exposure (FAO–UNESCO, 1974).

[155] Soils in which the essential characteristic is the illuvial accumulation of clay under conditions of high base saturation (FAO–UNESCO, 1974).

[156] Strongly depleted soils on old land surfaces; from Brazilian name for level open country of tropical savannas (FAO–UNESCO, 1974).

[157] A continuous subsurface horizon cemented by silica (FAO–UNESCO, 1974).

[158] Containing exchangeable sodium (FAO–UNESCO, 1974).

Table 4.4: Assigned correspondence between Staub and Rosenzweig (1987) soil texture classes (S-R) and USDA soil texture classes.

S-R Texture Class Code	S-R Class Description	USDA Class Description	USDA Texture Class Code
'1'	coarse	loamy sand	'2'
'2'	medium	silt loam	'4'
'3'	fine	clay	'11'
'4'	coarse-medium	sandy loam	'3'
'5'	coarse-fine	sandy clay	'9'
'6'	medium-fine	silty clay loam	'7'
'7'	coarse-medium-fine	clay loam	'8'
'8'	organic	peat	'12'
'9'	land-ice	–	' '
' '	water	–	' '

Cram (1990) used NCAR data set 767.0 to specify soil texture in her RAMS Great Plains squall-line simulation after first constructing a correspondence table between the Wilson–Henderson-Sellers texture classes and the USDA texture classes. Figs. 4.5a and 4.5c show the relationship between the three Wilson–Henderson-Sellers texture classes and the eleven USDA classes. Cram tried to obtain greater soil-texture-class resolution by simultaneously considering the associated values of the soil colour and drainage classes. Presumably, poor or impeded drainage may be an indication of greater clay content. Soil colour, on the other hand, depends largely on organic content, a quantity not considered in the definition of soil texture.

Due to such uncertainties, the Staub–Rosenzweig soil data set (NCAR data set 770.0) with its nine texture classes seemed to be a better choice for this study. However, it was still necessary to create a correspondence table, this time between the Staub–Rosenzweig and USDA soil texture classes. Table 4.4 shows the somewhat *ad hoc* equivalences used. These texture-class 'mappings' were based on Fig. 4.5 and the association of fine soil texture with clay, intermediate soil texture with silt, and coarse soil texture with sand.

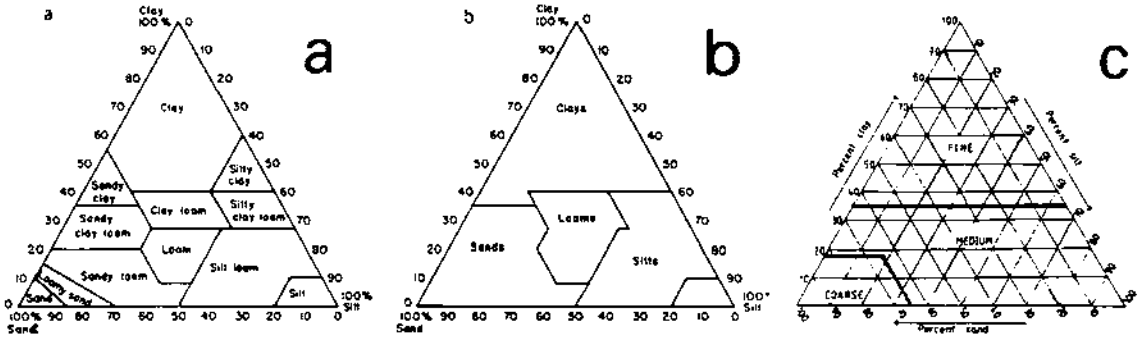

Figure 4.5: Three versions of the USDA soil texture triangle: (a) standard triangle (from Cosby et al., 1984); (b) reclassification into four broad textural classes (from Cosby et al., 1984); and (c) reclassification into three broad textural classes (from Wilson and Henderson-Sellers, 1985).

Fig. 4.6 shows the inferred[159] USDA soil texture class values for eastern North American on a 1° by 1° grid after extraction of the Staub–Rosenzweig texture class values from NCAR data set 770.0, file 2, and conversion using Table 4.4. Soil textures were then assumed to be homogeneous within each of the 1° by 1° data-set squares when interpolating to the RAMS model grids for the two case studies[160]. Note that the Staub–Rosenzweig texture classes themselves only indicate the dominant or representative soil texture for a 1° by 1° grid square and contain no information about texture-class *variability* within the grid square. Based on Fig. 4.6, USDA soil texture class 4 (sandy loam) was selected as the representative soil texture for both the Great Plains and CAPTEX simulations with uniform surface characteristics.

Sea surface temperature data set. The RAMS Isentropic Analysis package was used to access a slightly modified version of NCAR data set 270.2, a global climatological data set of mean monthly sea surface temperatures (SSTs) on a 1° by 1° latitude-longitude grid, in order to assign SST values within the case-study model domains. The creation of data set 270.2 has been described by Alexander and Mobley (1974, 1976). Some of the characteristics of this data set have implications for its use in this study.

First, the true resolution of the Alexander–Mobley SST data set is actually coarser than implied by the 1° by 1° grid resolution since it was compiled from two coarser-resolution SST data sets, the NCAR global[161] monthly SST data set on a 2.5° by 5° grid (NCAR data set 270.0) and a U.S. Navy Northern Hemisphere monthly SST data set on a 125 by 125 rectangular grid overlaying a polar stereographic hemispheric map projection true at 60°N (very roughly a 1.5° by 1.5° grid). Basically, the NCAR data

---

[159] Input and conversion of the Staub–Rosenzweig texture class data set was performed using a small program which I wrote for this purpose. I then modified subroutine VARMISC of RAMS to input this data set and interpolate soil texture values to the RAMS model grid.

[160] Unlike most gridded data sets where points correspond to grid-square *centres*, points in this data set correspond to grid-square northwest *corners*.

[161] Actually only from 60°S to 60°N.

Figure 4.6: Inferred USDA soil texture class values over central and eastern North America on a 1° by 1° grid stretching from 115°W to 62°W and from 25°N to 63°N. The two rectangles mark the Great Plains and CAPTEX modelling domains. See Table 4.4 for a description of the different USDA class codes.

set was used to assign SST values in the Southern Hemisphere and the U.S. Navy data set was used for the Northern Hemisphere. Moreover, once these two SST data sets had been merged, a nine-point, two-dimensional smoother was applied to remove small-scale features, whatever their source.

Second, the Alexander–Mobley SST data set contains values at each latitude-longitude grid point regardless of whether that point is an ocean point or not. Land-point values were obtained by *interpolation* between the nearest ocean values and are *not* indicative of the temperature of surface waters such as lakes or rivers contained within these grid squares. For example, over eastern North America, inland SST values would be based on SST values for the Gulf of Mexico, Hudson Bay, and the western Atlantic Ocean! Accordingly, it would be desirable to obtain surface water temperature values over North America from another source.

The major inland surface water features in the Great Plains and CAPTEX domains are the Great Lakes. Maps of monthly climatological Great Lake surface temperatures

based on satellite IR and ship measurements are contained in Saulesleja (1986). I abstracted SST values for July and September by hand from these maps at 1° grid points and inserted the values in place of the Alexander–Mobley data set values during the appropriate RAMS ISAN package runs. SST values at other land grid-points were left alone after comparing them against maps of monthly mean temperatures for July and September for the United States (ESSA, 1968). Differences were at most 10 K, and as can be seen from Fig. 4.7, water fractional coverage is small enough at these other points that the error introduced should be negligible. Fig. 4.8 lists the September SST values used in the CAPTEX simulations.

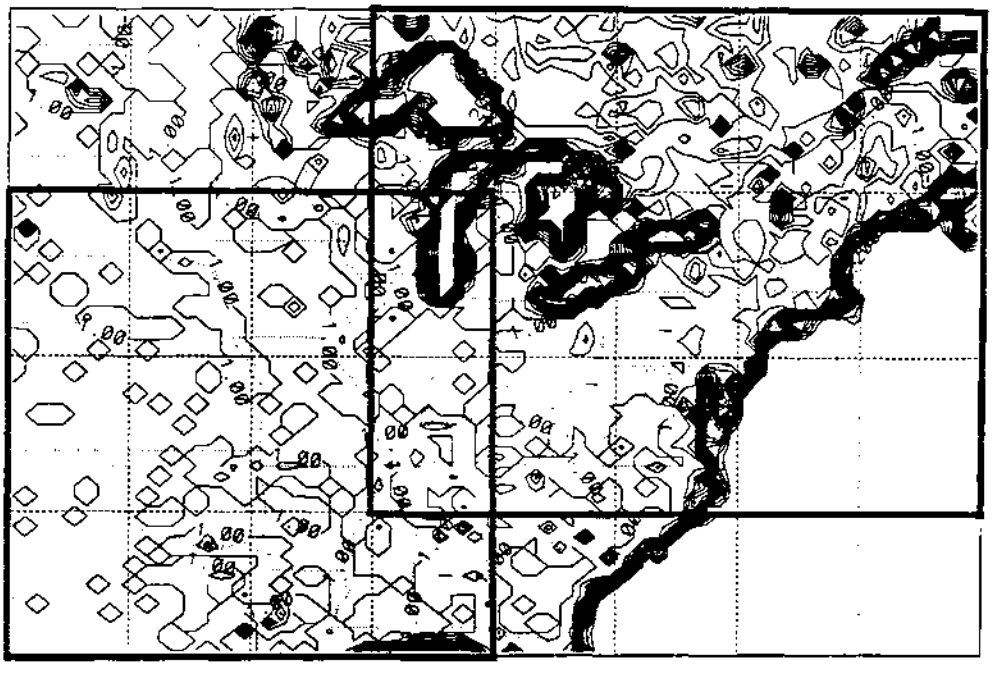

Figure 4.7: Same as Fig. 4.4 except for fraction of 0.333° latitude by 0.5° longitude grid squares covered by land. The contour interval is 0.05 and the contour range is 0.0 to 1.0.

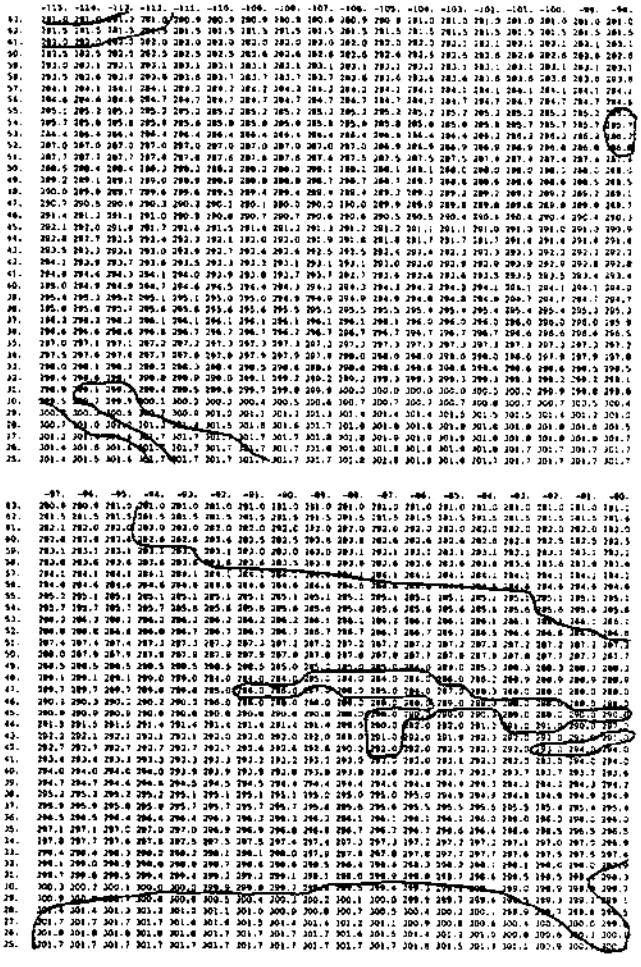

Figure 4.8: Modified gridded 1° by 1° monthly climatological sea surface temperature fields over central and eastern North America, including both case-study simulation domains, for September. The entire grid, shown here in three separate blocks, stretches from 115°W to 62°W and from 25°N to 63°N. Values were extracted from NCAR data set 270.2 and modified based on a figure in Saulesleja (1986). Latitude is indicated by the leftmost column and longitude by the topmost row of each block. Major coastlines have been drawn in by hand.

4.3 Initial Conditions and the Isentropic Analysis Package

Any prognostic numerical model requires the specification of a set of initial conditions. For the RAMS simulations described in Chaps. 5 and 6, the prognostic variables requiring initial values were ice–liquid water potential temperature, water vapour mixing ratio, the horizontal wind components, surface pressure, soil temperature, and soil moisture content. Let us first consider the initialization of the atmospheric variables and then the more *ad hoc* initialization of the soil variables for the two case studies.

4.3.1 Atmospheric variables

RAMS has two initialization options for atmospheric variables: horizontally-homogeneous initialization (HHI) and 'variable' initialization (VI). In horizontally-homogeneous initialization, atmospheric fields are defined on the basis of a single atmospheric sounding and are assumed to be uniform along constant Cartesian height surfaces in all horizontal directions[162]. In variable, or horizontally inhomogeneous, initialization, on the other hand, horizontal gradients are permitted in the initial atmospheric fields. This second option is clearly more realistic but requires a much more complicated objective analysis (OA) procedure to compute the initial fields. The RAMS Isentropic Analysis (ISAN) package is used to prepare both the three-dimensional gridded atmospheric fields required in the VI option and also the gridded fields needed at later times for the specification of time-dependent lateral boundary conditions. It can also access individual archived upper-air soundings. The RAMS ISAN package was developed by Dr. Craig Tremback (e.g., Tremback, 1990).

In general, the HHI option is useful for one- or two-dimensional simulations, idealized three-dimensional simulations, and for small-scale real-data case studies in which the background synoptic environment can be approximated as horizontally homogeneous *and*

---

[162] If non-uniform topography is being considered, the input sounding must be defined down to the lowest surface elevation present in the simulation domain. Also, initial fields will vary horizontally along constant z^* surfaces since Cartesian height z will also vary on these surfaces.

steady. Any other situation requires the use of the VI option. HHI was used in this study for the two-dimensional Great Plains tracer experiment and CAPTEX RAMS runs and for some idealized three-dimensional runs while VI was used in the remaining three-dimensional simulations (see Tables 5.1 and 6.1).

As discussed by Tremback (1990), the RAMS meteorological model does not employ any algorithm to balance the initial velocity and mass fields. Moreover, conventional synoptic-scale data sources have neither sufficient horizontal resolution to capture horizontal mesoscale features nor sufficient vertical resolution to describe PBL vertical structure (e.g., Moran et al., 1991). Thus, the early stages of a RAMS run must be viewed as a 'dynamic initialization' stage during which (i) model fields come into near balance through the generation and propagation of transient internal gravity waves and (ii) smaller-scale flow features and structures are generated by external boundary forcing and by nonlinear wave-wave interactions internally.

Horizontally-homogeneous initialization

Since the tracer release in the Great Plains tracer experiment began at 1900 GMT (1400 CDT) on July 8, 1980, the 1200 GMT (0700 CDT) Oklahoma City, Oklahoma sounding for July 8 was used to initialize RAMS and the simulation was started at this time[163] (0600 CST/0700 CDT). This early start allowed time for the model initial fields to adjust to the topography and for the growth and development of the daytime boundary layer to be simulated before the start of the tracer release.

Sunrise occurred at Oklahoma City (OKC) at 0622 CDT (1122 GMT) on July 8 and sunset occurred at 2048 CDT (0148 GMT) (Gale Research Co., 1977). Fig. 4.9a shows the morning OKC sounding and Table 4.2 lists the actual RAMS sounding input values. (Fig. 5.5 shows a time series of OKC low-level wind profiles for the Great Plains experimental period.) The OKC sounding was extracted from the NMC operational

[163] The value of STRTIM, the RAMS start time as a local solar time at the model's western boundary, was actually 0530 LST.

upper-air data set archived at NCAR (DSS data set 353.4) using Stage 3 of the RAMS Isentropic Analysis package. All standard and significant thermodynamic and wind levels were included.

However, as discussed in Sec. 5.2, the low-level winds measured by both the morning (12Z) and evening (00Z) OKC rawinsonde launches during the experimental period probably contained a significant oscillatory ageostrophic component and hence were neither steady nor representative of the synoptic-scale gradient balance (see Fig. 5.5). It was thus necessary to modify the OKC 1200 GMT low-level winds before using them in RAMS. This problem is discussed in more detail in Chap. 5. As a final step, winds in the first 400 m were adjusted for surface friction using the Ekman initialization procedure described by Mahrer and Pielke (1976).

Variable initialization

The gridded three-dimensional atmospheric variable fields needed for the VI option were prepared using the full RAMS Isentropic Analysis (ISAN) package and some of the standard NMC operational data sets contained in the NCAR meteorological data archives. Isentropic coordinates offer a number of advantages for synoptic data analysis. First, in the absence of diabatic processes such as water phase changes, radiative flux divergence, and vertical mixing, atmospheric flow is adiabatic and follows isentropic surfaces (e.g., Danielsen, 1961; Tremback, 1990; Benjamin et al., 1991). Synoptic features such as jet streaks, moist and dry tongues, and frontal surfaces are thus represented well in a flow-following isentropic framework. Second, subsynoptic-scale *horizontal* gradients can be resolved if the detailed *vertical* information contained in synoptically-spaced upper-air soundings is analyzed in an isentropic framework. For example, isentropes tend to be 'packed' near fronts; the associated gradients of wind and moisture found in frontal regions are thus resolved in greater detail (e.g., Shapiro and Hastings, 1973; Tremback, 1990; Benjamin et al., 1991). Two disadvantages of this coordinate system are that resolution is low in regions of weak static stability such as the planetary boundary layer

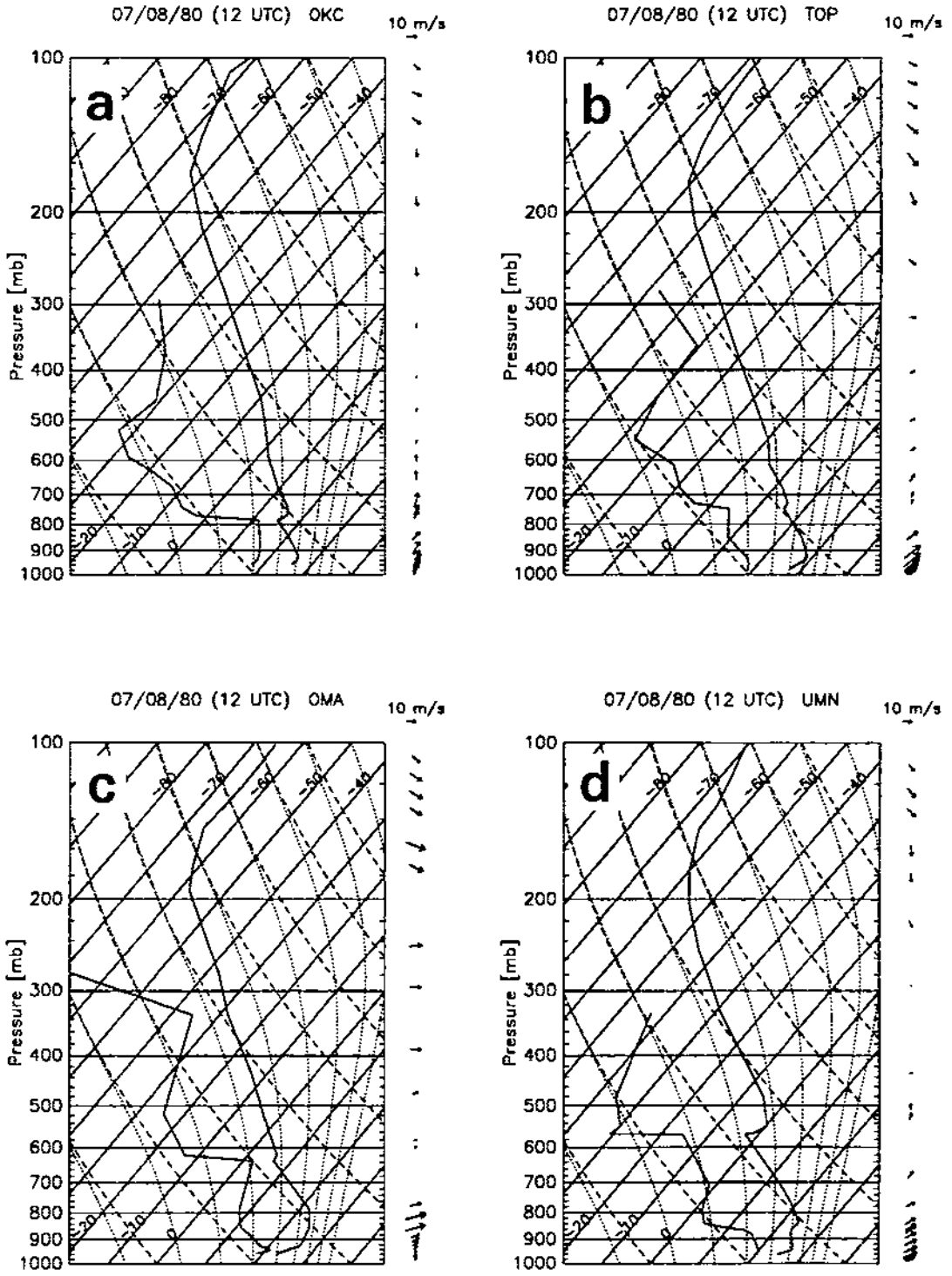

Figure 4.9: Skew-T diagrams of 1200 GMT upper-air soundings on July 8, 1980 at eight midwestern cities: (a) Oklahoma City, Oklahoma [OKC; 72353]; (b) Topeka, Kansas [TOP; 72456]; (c) Omaha, Nebraska [OMA; 72553]; (d) Monett, Missouri [UMN; 72349]; (e) Fort Sill, Oklahoma [FSI; 72355]; (f) Amarillo, Texas [AMA; 72363]; (g) Dodge City, Kansas [DDC; 72451]; and (h) North Platte, Nebraska [LBF; 72562]. The two quantities in the brackets following each station name are the three-letter station identifier and the WMO station ID number. See Fig. 4.11a for the locations of these stations.

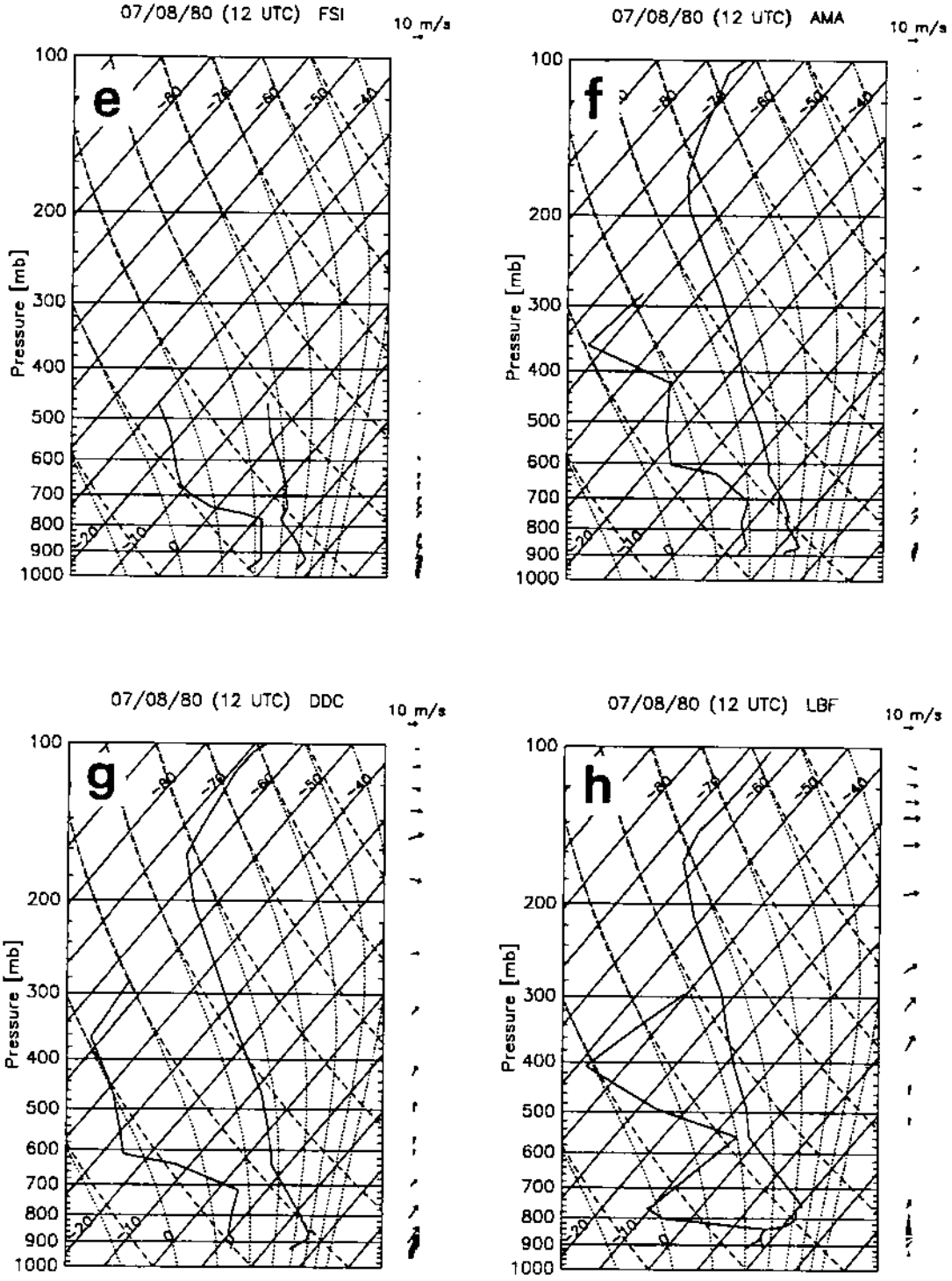

Figure 4.9: Continued.

and some isentropic surfaces may intersect the Earth's surface. However, these drawbacks are outweighed by the benefits offered by this analysis framework.

Version 2A of the RAMS ISAN package consists of five basic 'stages': (i) Stage 1 inputs gridded NMC spectral-model analyses of virtual temperature T_v, relative humidity RH, geopotential height z, and u and v horizontal velocity components on mandatory pressure surfaces; (ii) Stage 2 interpolates these fields in the vertical to user-specified isentropic surfaces; (iii) Stage 3 interpolates the gridded fields horizontally to a finer, or higher, resolution latitude-longitude grid, and, if desired, assimilates upper-air and surface *station* data; (iv) Stage 4 handles plotting for the first three stages; and (v) Stage 5 performs horizontal and vertical interpolations from the ISAN Stage 3 isentropic grid to the RAMS terrain-following grid. More detailed descriptions of the ISAN package have been given by Tremback (1990), Cram (1990), and Walko and Tremback (1991).

Several modifications were made to the standard Version 2A ISAN package for this study. The vertical cross-section plotting capability contained in pre-RAMS versions of the package, added station ID number, terrain elevation, land fraction, and SST as plot options, switched to the U.S. Air Force 5' terrain-height data set (described in Sec. 4.2.6), and added code to replace the unrepresentative Alexander–Mobley SSTs for the Great Lakes with observed values (see Sec. 4.2.6).

Great Plains experiment atmospheric fields. For the Great Plains experiment VI objective analysis, the ISAN coarse-resolution NMC domain with a 2.5° latitude-longitude grid mesh which was used in Stage 1 stretched from 25°N to 52.5°N and from 115°W to 80°W, completely covering the RAMS simulation domain for this case (Fig. 4.1). Gridded fields were input for ten standard pressure levels (1000, 850, 700, 500, 400, 300, 250, 200, 150, and 100 hPa) for the appropriate times (80/7/8/12, 80/7/9/00, 80/7/9/12) from the NMC gridded global analysis data set (DSS data set no. 082.0: see NMC, 1979; Jenne, 1989). The NMC synoptic-field quantitative analyses have been prepared since May 1980 using the Optimum Interpolation method with

the NMC global spectral model providing first-guess fields (Kistler and Parrish, 1982; Kanamitsu, 1989).

The resolution of the NMC data set is indicated by the spatial density of the plotted wind vectors in Figs. 3.2 and 3.3. The anticyclonic synoptic pattern over the study area discussed in Sec. 3.1.2 is evident in these figures. The pattern was quasi-stationary although the small high-pressure system located over South Dakota on July 8 moved eastward across the top of the domain with time.

In Stage 2, the NMC gridded pressure-level data were vertically interpolated to isentropic surfaces. There were 41 isentropic levels specified in all, with 1 K spacing from 295–325 K, 5 K spacing from 325–350 K, and 10 K spacing from 350–400 K. Values at grid points on *subterranean* isentropic surfaces were set to 'missing'. Gridded terrain elevation and SST fields were also accessed in this stage (these surface data sets were described in the previous section). Since the terrain elevation and SST data sets had different horizontal resolutions compared to the NMC data set, a third-order implementation of the overlapping polynomial technique (Bleck and Haagenson, 1968; Whittaker and Petersen, 1977) was used to interpolate these quantities to the 2.5° by 2.5° NMC grid.

Fig. 4.10 shows a south-north vertical cross section from the Gulf of Mexico to northern Ontario through eastern Oklahoma and Kansas (34–40°N) of horizontal wind speed which was produced (in Stage 4) from Stage 2 interpolated wind fields. Note the weak winds throughout the troposphere in the southern portion of the domain.

The Barnes (1973) mesoscale objective analysis scheme was then used in Stage 3 to (a) blend the NMC gridded fields with same-time upper-air and surface station reports and (b) interpolate the blended fields to a higher-resolution 0.4° by 0.5° latitude-longitude grid. The Stage 3 horizontal domain was smaller than the Stage 1 and 2 domain (see Fig. 4.1) and stretched from 27.5°N to 47.5°N and from 107.5°W to 82.5°W. However, the isentropic levels considered in Stage 3 were the same as those used in Stage 2 and, as in Stage 2, linear vertical interpolation was used to convert vertical soundings from

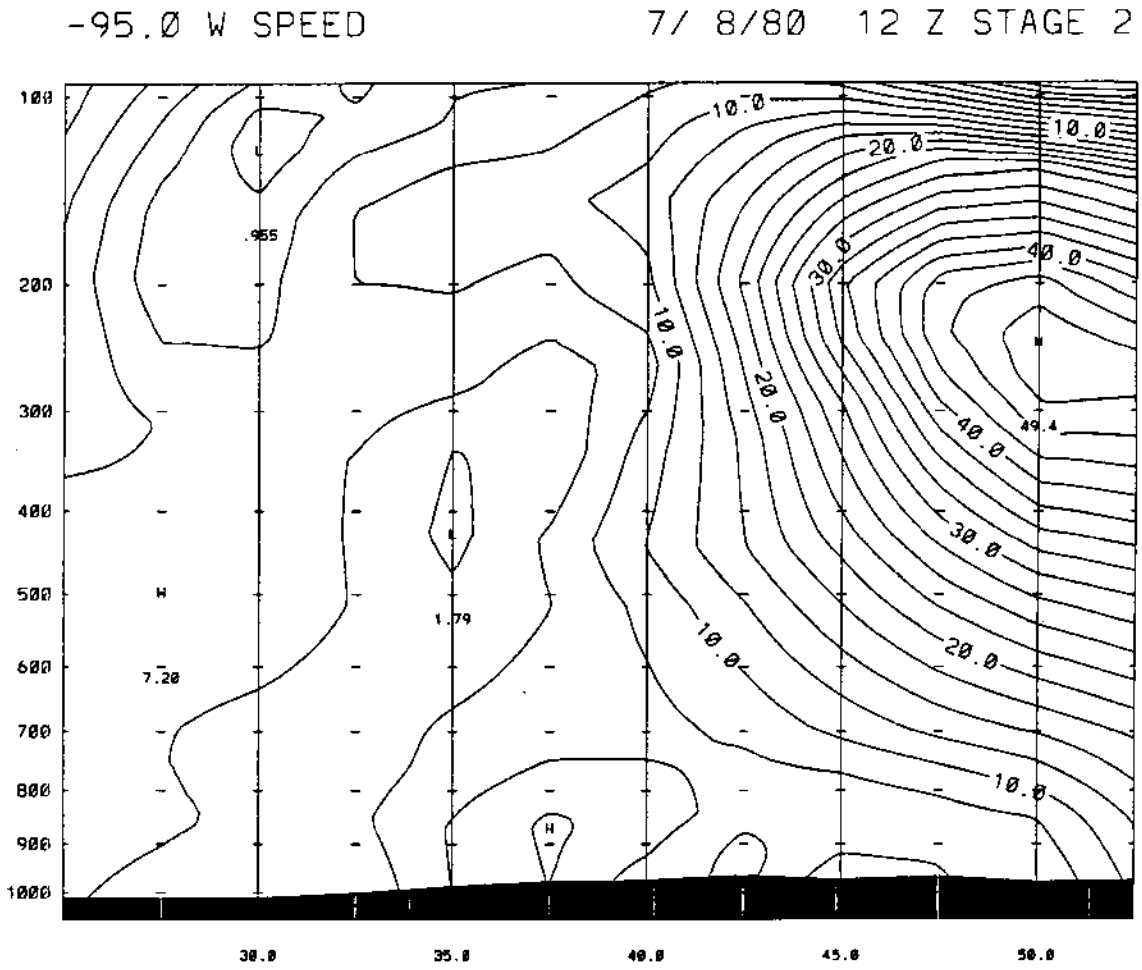

Figure 4.10: South-north vertical cross section of wind speed along 95°W at 1200 GMT, 8 July 1980. Abscissa units are degrees of latitude (N); ordinate units are hPa. The wind-speed contour interval is 2.5 $\mathrm{m\,s^{-1}}$.

p^{κ} coordinates to θ coordinates. Barnes scheme parameters included (i) the use of *all* NMC grid and NWS station data with *equal*[164] weighting (IGRIDFL=1) and (ii) response functions with the 1000 km wavelength retained at 90% amplitude (RESPON=0.9) for all of the NWS upper-air and surface station data (see Cram, 1990; Tremback, 1990; Walko and Tremback, 1991). A minimum station separation of 0.1° (STASEP=0.1) was specified for the surface station data. The Montgomery streamfunction ψ was calculated by hydrostatic integration both upwards and downwards from the 360 K level (LBCHYD=360).

Fig. 4.11 shows the locations of the upper-air and surface stations used in Stage 3 for the Great Plains case. Data from these stations were read in from the NMC operational upper-air data set (DSS No. 353.4) and from the NMC operational surface-report data set (DSS No. 464.0), both of which are archived at NCAR. The former contains pressure, geopotential height, temperature, dewpoint depression, wind speed, and wind direction values at both mandatory and significant levels while the latter contains surface pressure, temperature, dewpoint depression, wind speed, and wind direction values (see NMC, 1973, 1982, and NCAR/SCD/DSS online documentation).

Fig. 4.12 shows a plot of *surface* wind vectors and calculated *sea-level* pressure based on Stage 3 blended fields. Wind vectors are plotted at every fifth grid point. A comparison with Fig. 3.2 reveals the difference in horizontal resolution between Stages 1/2 and Stage 3 (and also the smaller analysis domain employed in Stage 3). The strong, stagnant surface high-pressure system and southerly to southwesterly low-level flow over the Great Plains tracer experiment domain are clearly visible in Fig. 4.12 as is the low-level convergence zone associated with the quasi-stationary front over Nebraska, Missouri, and Illinois. These winds can also be compared against the low-level winds plotted in the Fig. 4.9 soundings.

---

[164] I tried an experiment with IGRIDFL=2, GOBRAD=5., and GOBSEP=2. so as to ignore NMC values in the vicinity of upper-air stations but decided that the resulting transport fields were too 'blocky' or piecework.

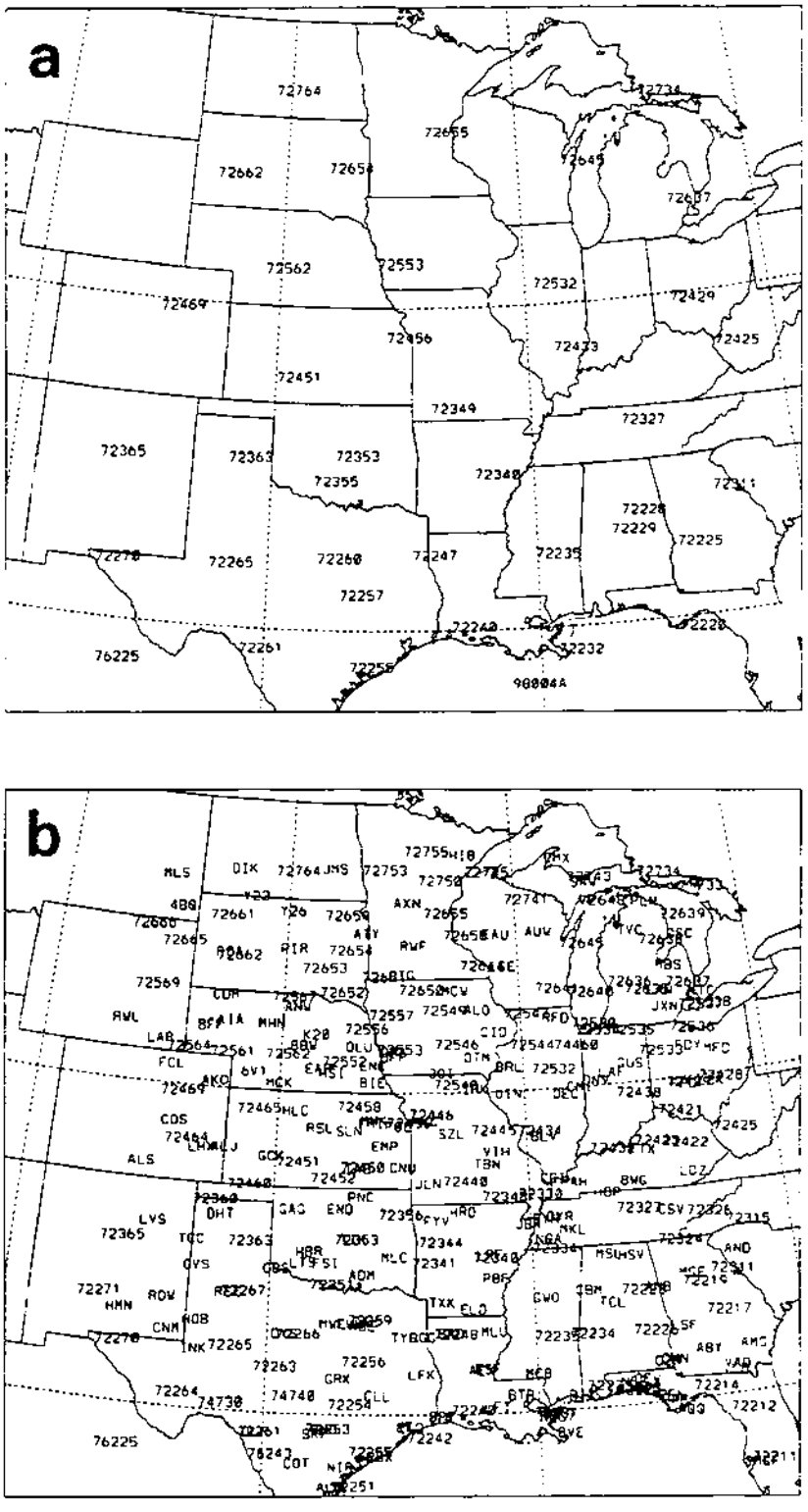

Figure 4.11: Location and station IDs of NWS (a) upper-air stations, and (b) surface stations used in the Barnes objective analysis of atmospheric fields for 1200 GMT, 8 July 1980 (Great Plains experiment). The middle of the left edge of the leftmost character of the ID number indicates the station location. Longitudes 110°W, 100°W, 90°W, and 80°W and latitudes 30°N and 40°N are marked on both panels, and an orthographic map projection has been used.

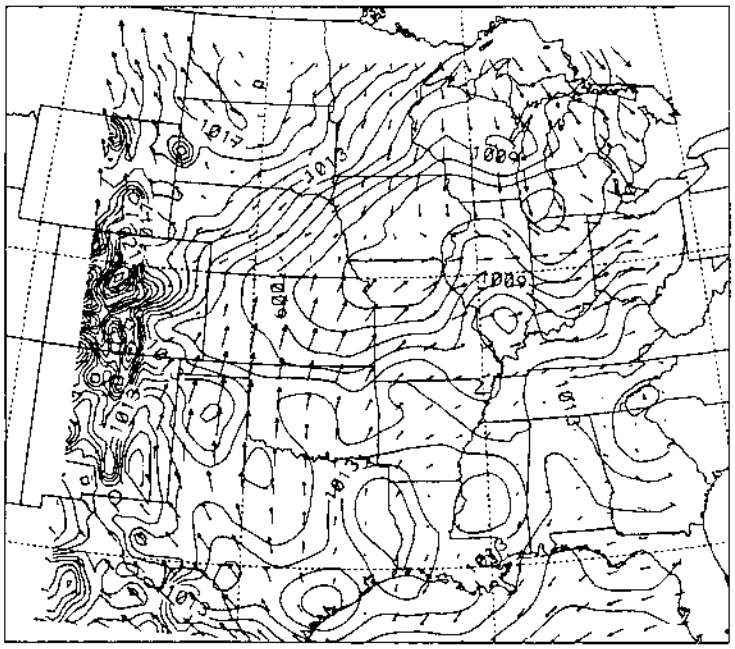

Figure 4.12: Estimated sea-level pressure field (hPa) and surface wind vectors based on Stage 3 blended fields for 1200 GMT, 8 July 1980. Contour interval is 1 hPa. Maximum wind speed is 7.3 m s^{-1}. Lines of latitude are drawn at 30°N and 40°N; lines of longitude are drawn at 80°W, 90°W, 100°W, and 110°W.

The gridded terrain-height field used in the RAMS model was produced in Stage 5 of the ISAN package by linear interpolation from the gridded terrain-height field created in Stage 3. The Stage 3 field in turn was created by first linearly interpolating terrain heights from the modified U.S. Air Force 5' terrain-height data set (described in previous section) to the Stage 3 grid and then filtering the resulting field with the same Barnes-scheme filter used on the various atmospheric fields. Fig. 4.13 shows four Stage 3 terrain-height fields produced with four different terrain-filter wavelength values. Increasing the filter wavelength removes small-scale terrain features but reveals the large-scale terrain structure. The field produced with the 200 km filter wavelength (Fig. 4.13b) was the one actually accessed by Stage 5 to produce the RAMS gridded terrain-height field.

In Stage 5, blended Stage 3 atmospheric fields were interpolated to the RAMS model grid. The major interpolation in this procedure was in the vertical to go from isentropic surfaces to terrain-following surfaces. Fig. 4.12, which shows Stage 3 fields, can be

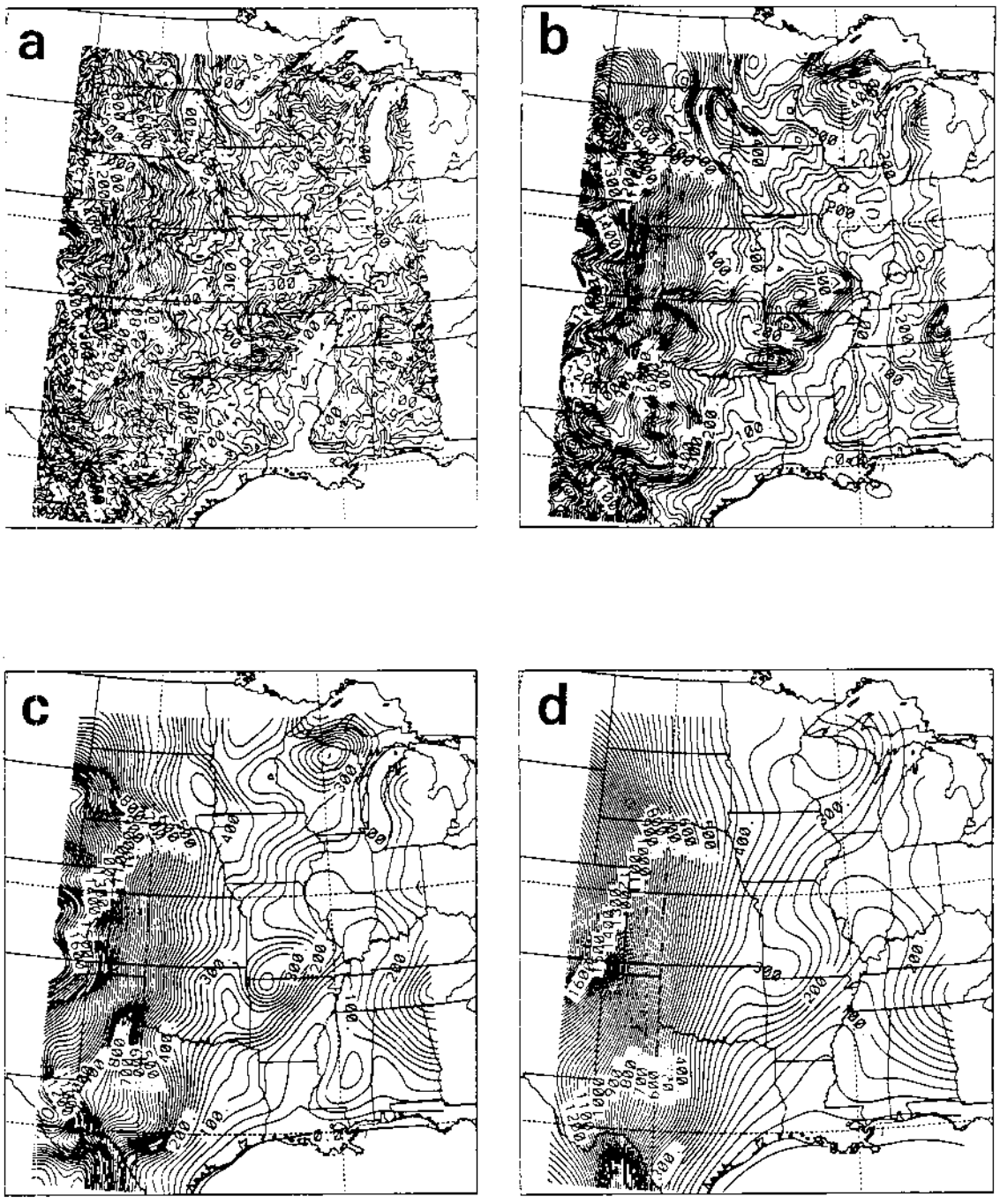

Figure 4.13: Influence of the terrain-filter wavelength value TWVLNTH on the Stage 3 gridded terrain-height field for the Great Plains case: (a) TWVLNTH = 0 km; (b) TWVLNTH = 200 km; (c) TWVLNTH = 500 km; (d) TWVLNTH = 1000 km. Contour interval is 25 m. The terrain field boundaries are 27.5°N, 47.5°N, 105°W, and 85°W (i.e., the field has been cropped in the west-east direction). Lines of latitude at 30°N and 40°N are marked by dashed lines as are lines of longitude at 100°W and 90°W.

compared to Fig. 3.4, which was produced by Stage 5, to see the results of this process. Figs. 3.5, 3.6, and 3.7 are also plots of Stage 5 fields.

CAPTEX atmospheric fields. For the CAPTEX variable-initialization objective analysis, the Stage 1 NMC analysis grid stretched from 25°N to 52.5°N and from 97.5°W to 62.5°W (see Fig. 4.2). The same ten pressure levels used in the Great Plains Stage 1 analysis were also used in the CAPTEX Stage 1 analysis. Fig. 3.15 shows plots of NMC 2.5° by 2.5° gridded height fields and wind vectors at the 1000 and 500 hPa levels at 1200 GMT (0800 EDT) on September 25, 1983. The second CAPTEX tracer release started approximately 5 hours later at 1705 GMT (1305 EDT). Again, the first few hours of RAMS model integration before the tracer release allowed adjustment of initial imbalances and simulation of the morning development of the convective PBL. Sunrise occurred at 0705 EDT on this day at Buffalo, New York and sunset occurred at 1907 EDT (Gale Research Co., 1977).

Figs. 3.16 and 3.17 show the same fields 24 and 48 hours later. As discussed in Sec. 3.2.2, the synoptic situation over eastern North America during this period was characterized by the slow eastward progression of a high-pressure system followed by a cold-frontal passage and accompanying upper-level trough.

Stages 2 and 3 of the CAPTEX variable-initialization analysis also followed the Great Plains VI analysis closely. The same gridded terrain elevation, land-water percentage, and SST data sets were accessed. A 0.4° by 0.5° latitude-longitude 'fine' grid was used in Stage 3 as in the Great Plains experiment analysis and the same Barnes scheme parameter values were employed.

There were 46 isentropic levels specified, with 1 K spacing from 274–302 K, 2 K spacing from 302–310 K, 5 K spacing from 310–350 K, and 10 K spacing from 350–400 K. This isentropic range was considerably cooler than the one employed for the Great Plains simulation and reflects the colder nighttime temperatures expected over northeastern North America in late September.

The Stage 3 horizontal grid stretched from 27.5°N to 52.5°N and from 92.5°W to 62.5°W (Fig. 4.2). Fig. 4.14 shows west-east vertical cross sections from the Mississippi to the Atlantic Ocean of wind speeds along two lines of latitude which 'bracket' the CAPTEX release site at Dayton, Ohio (latitude 39.8°N). There is considerable low-level speed variation evident in these figures with weaker winds present along the southern of the two cross sections (cf. Fig. 3.15a).

Fig. 4.15 shows the locations of the upper-air and surface stations accessed from the NMC operational upper-air and surface data sets and used in the Barnes assimilation step in Stage 3. Soundings from four of the upper-air stations in the CAPTEX domain are shown in Figs. 4.16 and 4.17 for the two 12-h synoptic observing times bracketing the tracer release period at Dayton, Ohio. A general strengthening of the low-level winds is apparent over the 12-h period between the two sets of soundings, although low-level wind direction remains fairly constant. Fig. 4.18 shows a plot of *surface* wind vectors and calculated *sea-level* pressure the morning of the tracer release. This figure is based on the Stage 3 blended fields (cf. Fig. 3.14). Wind vectors are plotted at every fifth grid point (cf. Fig. 3.15). Surface wind speeds range up to 16 $\mathrm{m\,s^{-1}}$.

The gridded terrain-height field used in the RAMS CAPTEX simulations was produced in Stage 5 of the ISAN package as already described for the Great Plains case. Fig. 4.19 shows four Stage 3 CAPTEX terrain-height fields produced with four different terrain-hfilter wavelength values. The field produced with the 200 km filter wavelength was the one actually accessed by Stage 5 to produce the RAMS gridded terrain-height field.

Atmospheric fields were also interpolated to the RAMS model grid in Stage 5. Fig. 4.18, which shows CAPTEX Stage 3 surface fields, can be compared to Fig. 3.14, which was produced by Stage 5. Figs. 3.18, 3.19, and 3.20 are also plots of Stage 5 fields.

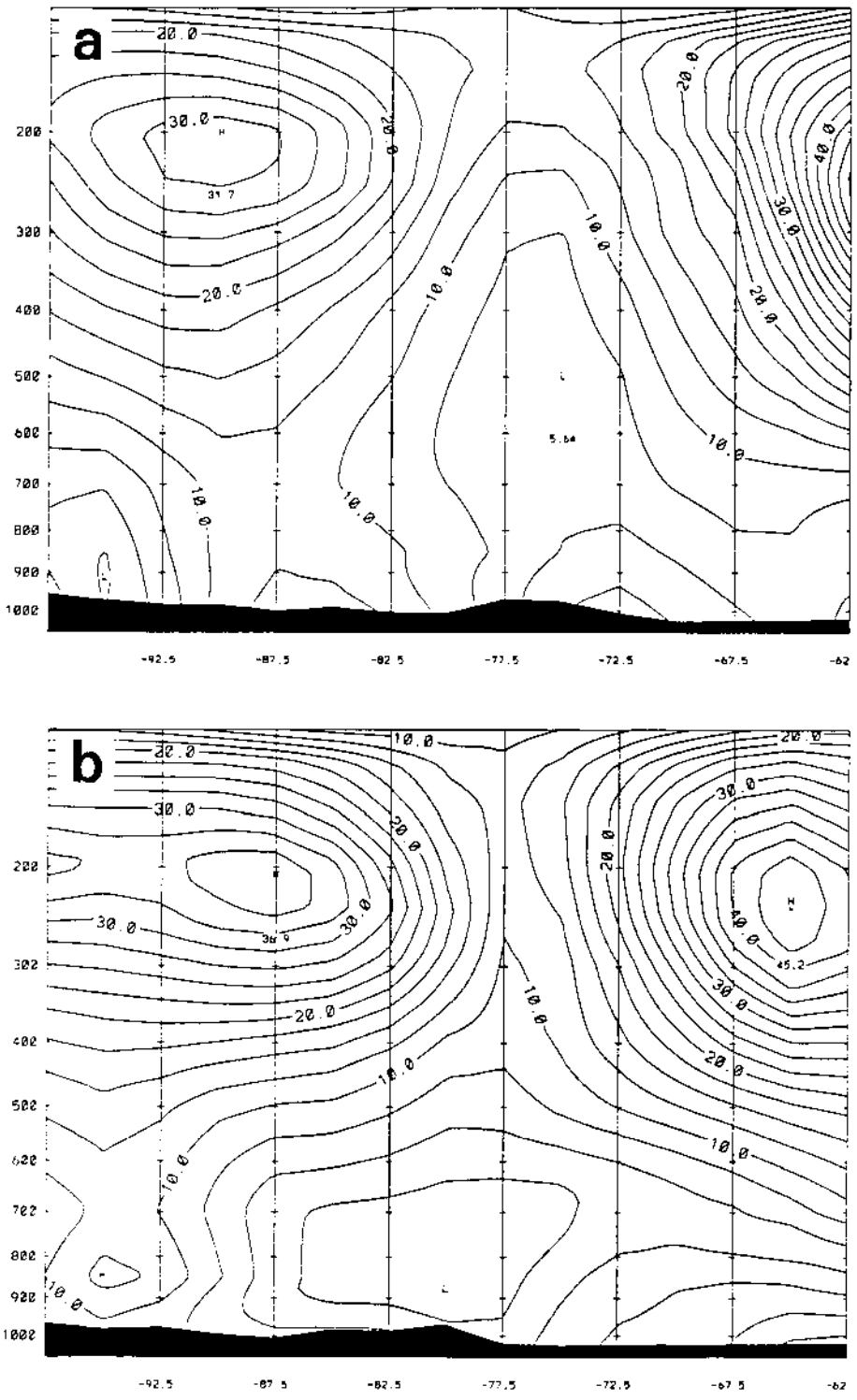

Figure 4.14: West-east vertical cross sections of wind speed along (a) 42.5°N and (b) 37.5°N at 1200 GMT, 25 September 1983. Abscissa units are degrees of longitude (W); ordinate units are hPa. The wind-speed contour interval is 2.5 $\mathrm{m\,s^{-1}}$.

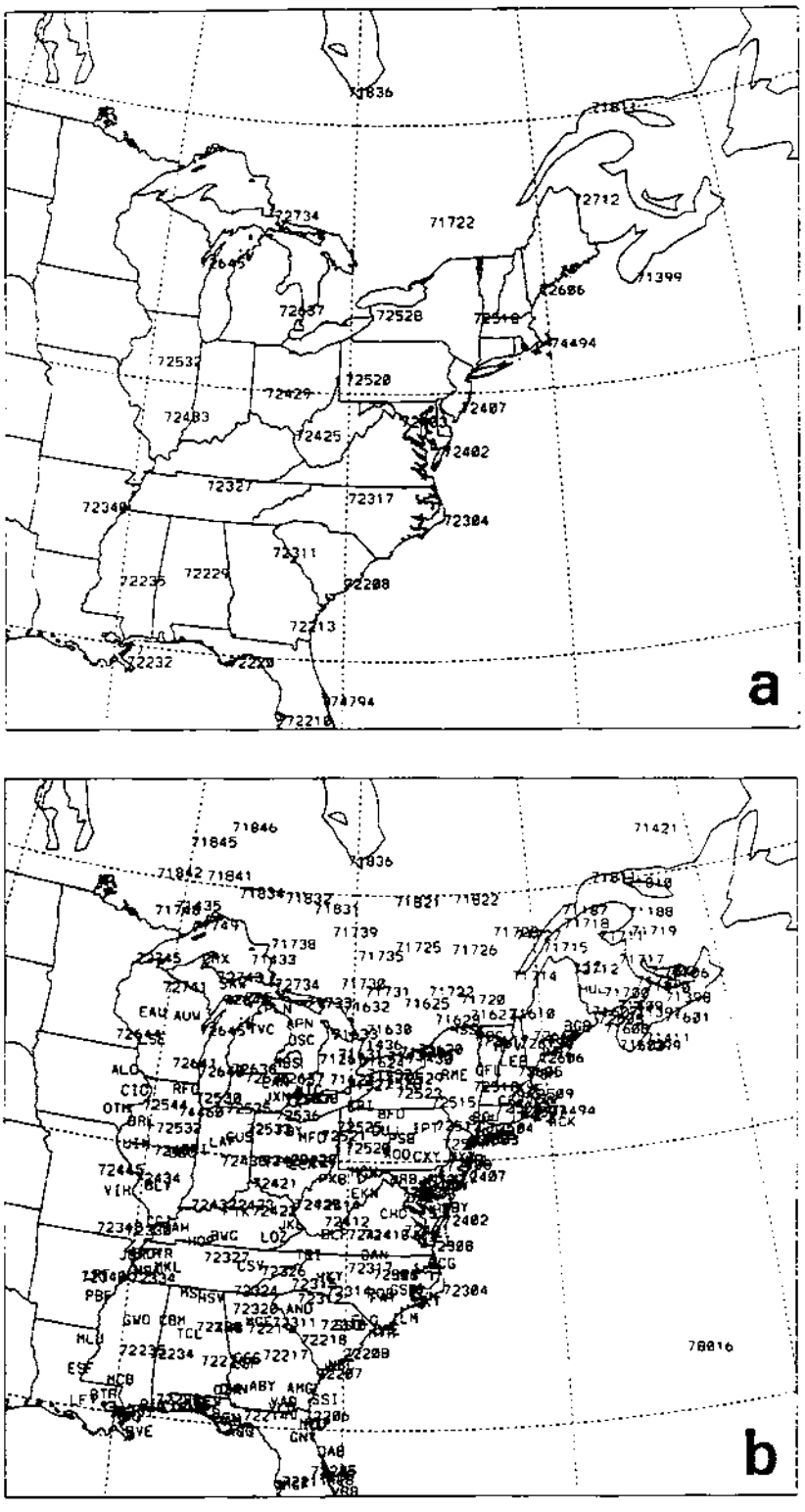

Figure 4.15: Location and station IDs of NWS (a) upper-air stations and (b) surface stations used in the Barnes objective analysis of atmospheric fields for 1200 GMT, 25 September 1983 (CAPTEX case study). Longitudes 90°W, 80°W, 70°W, and 60°W and latitudes 40°N and 50°N are marked in both panels by dashed lines.

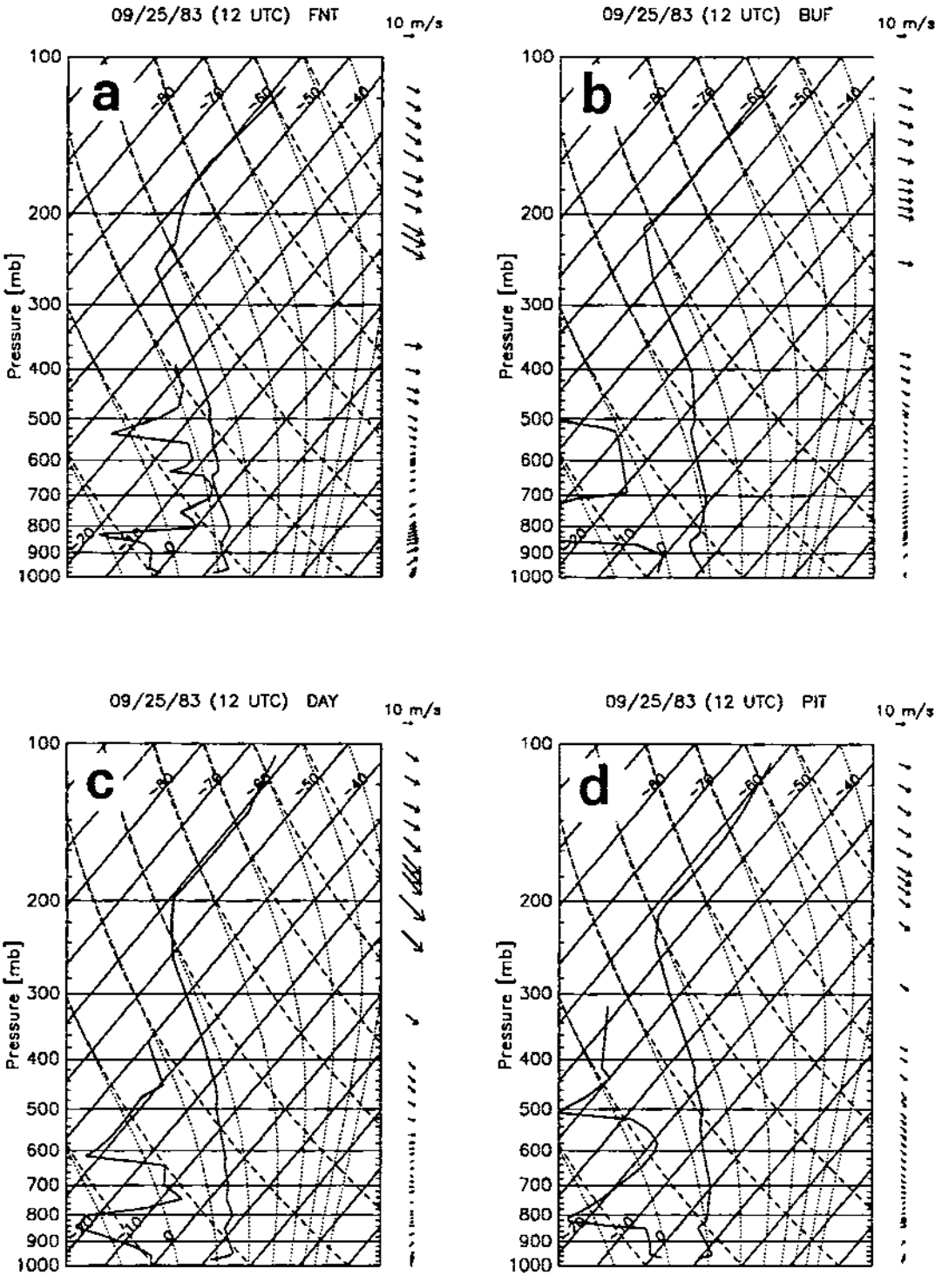

Figure 4.16: Skew-T diagrams of 1200 GMT upper-air soundings on September 25, 1983 at Great Lakes region cities: (a) Flint, Michigan [FNT; 72637]; (b) Buffalo, New York [BUF; 72528]; (c) Dayton, Ohio [DAY; 72429]; (d) Pittsburgh, Pennsylvania [PIT; 72520]. The two quantities in the brackets following each station name are the three-letter station identifier and the WMO station ID number. See Fig. 4.15a for the locations of these stations.

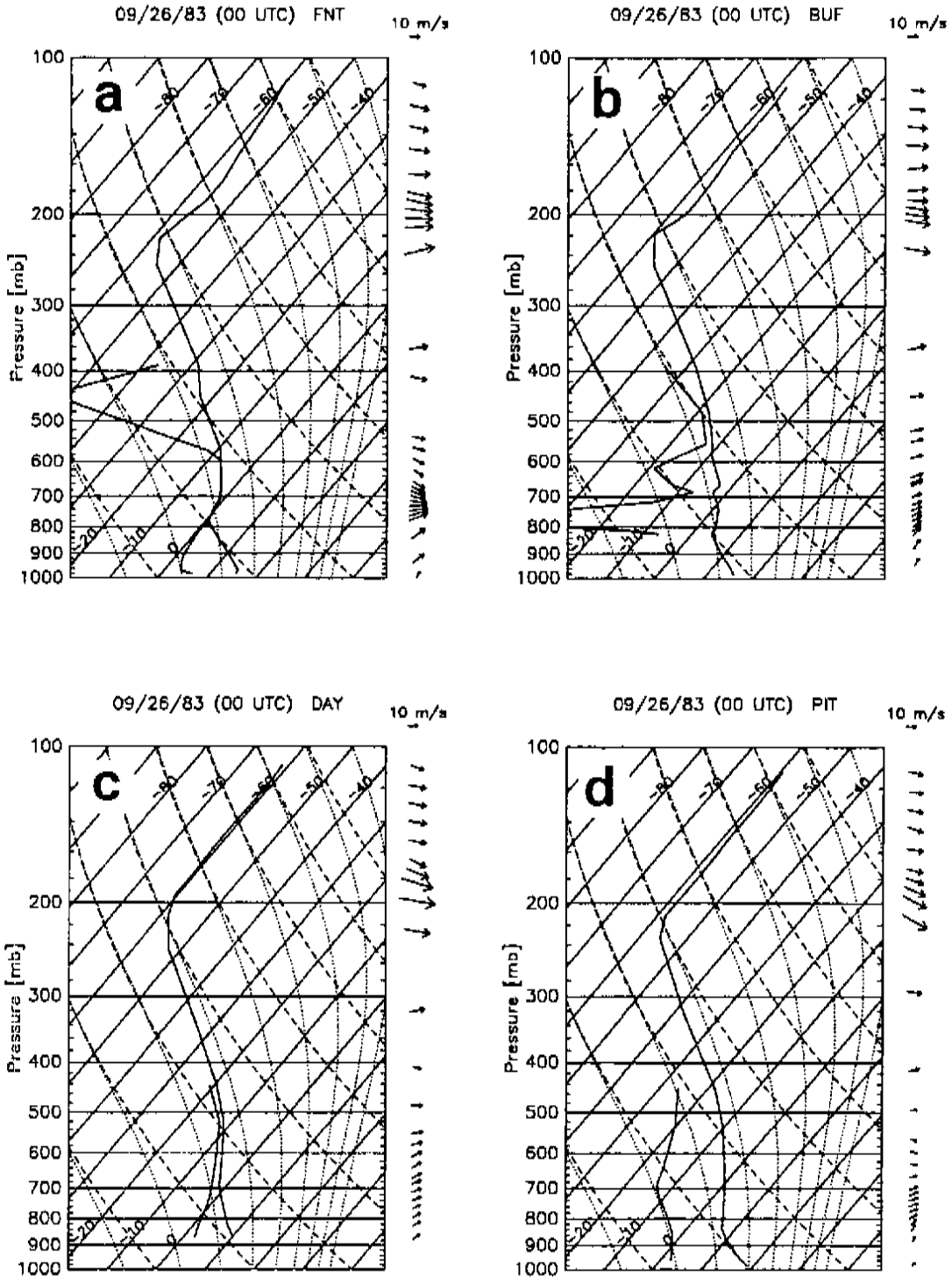

Figure 4.17: Same as Fig. 4.16 except for September 26, 0000 GMT

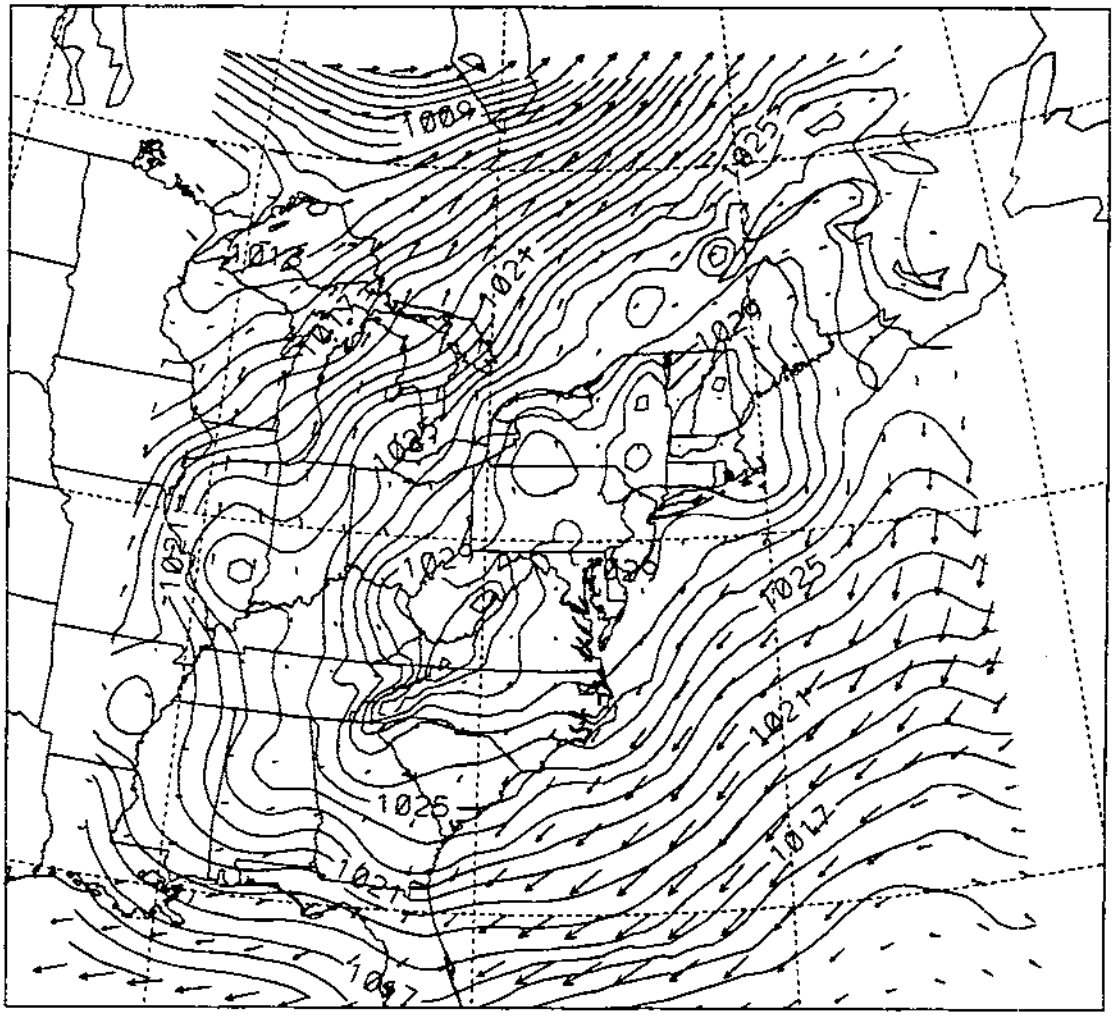

Figure 4.18: Estimated sea-level pressure field (hPa) and surface wind vectors based on Stage 3 blended fields for 1200 GMT, 25 September 1983. The contour interval is 1 hPa. Maximum wind speed is 16.1 m s^{-1}. Latitude and longitude lines are drawn every 10° from 30°N to 50°N and from 100°W to 60°W.

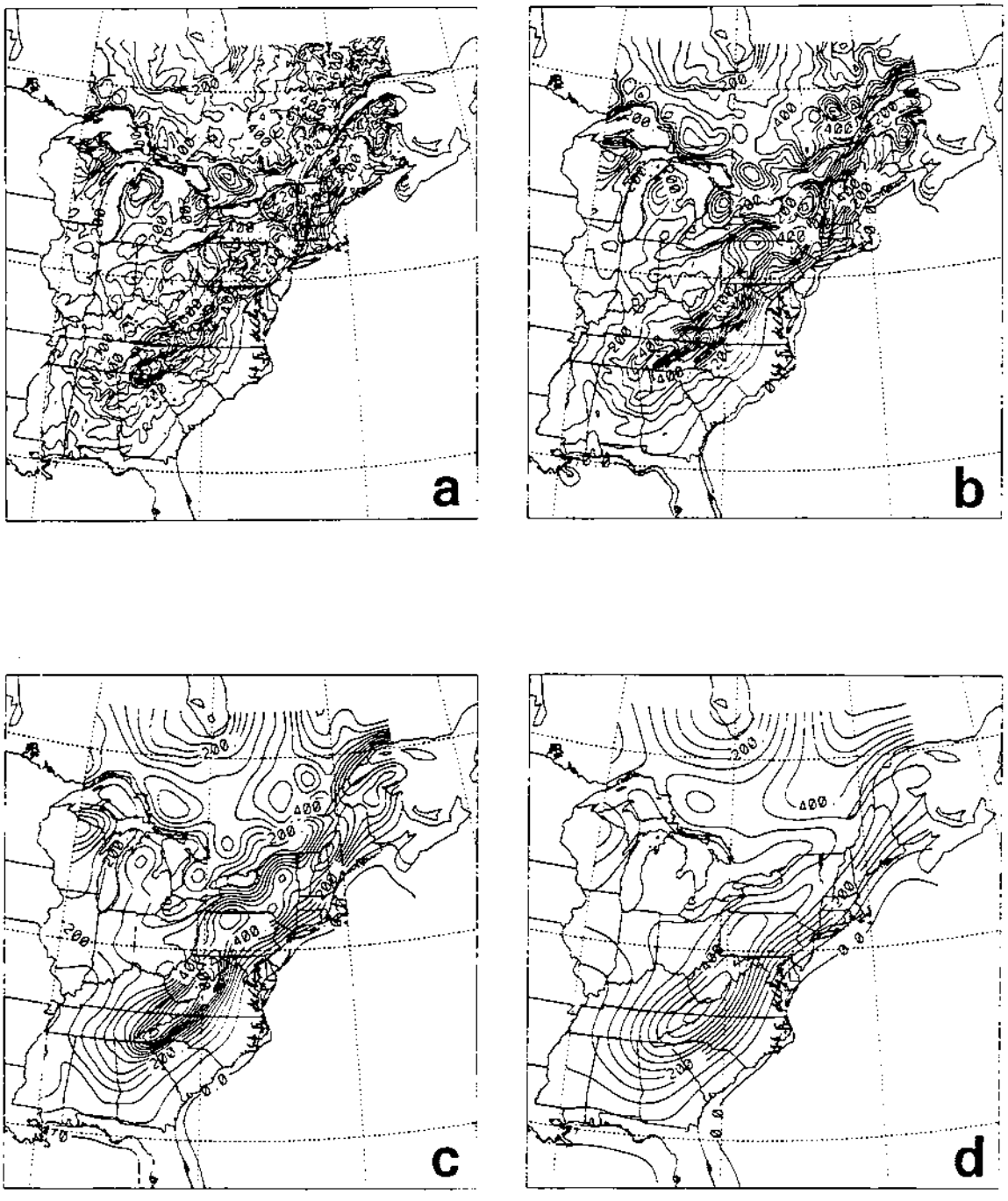

Figure 4.19: Influence of the terrain-filter wavelength value TWVLNTH on Stage 3 gridded terrain-height field for the CAPTEX case: (a) TWVLNTH = 0 km; (b) TWVLNTH = 200 km; (c) TWVLNTH = 500 km; (d) TWVLNTH = 1000 km. Contour interval is 50 m. The terrain field boundaries are 27.5°N, 52.5°N, 90°W, and 65°W (i.e., the field has been cropped in the west-east direction). Lines of latitude at 30°N, 40°N, and 50°N are marked by dashed lines as are lines of longitude at 90°W, 80°W, 70°W, and 60°W.

4.3.2 Soil variables

Unlike atmospheric measurements, soil temperature and soil moisture measurements are not made routinely in North America on a daily basis over a continental-scale network. Moreover, soil properties and, consequently, surface fluxes are likely to exhibit even larger subgrid-scale horizontal variability than atmospheric variables (e.g., Wetzel and Chang, 1988). A simple procedure was thus chosen to initialize the two soil variables in the RAMS soil model in keeping with the lack of data and inherent variability.

Soil temperature

Soil temperature was defined relative to the atmospheric temperature field at the lowest model level. Since the RAMS simulations for both case studies began approximately at sunrise, the surface soil temperature was assumed to be slightly colder than the overlying air temperature, consistent with low-level stable stratification. The subsurface temperature profile was then specified based on a climatological soil temperature profile given by Sellers (1965), which included a nearly constant deep subsurface temperature and a descending pulse of warmer temperature closer to the surface from the previous day's heating. Thus, soil temperature initially increased, then decreased, with increasing soil depth. The actual temperature 'offsets' used were, beginning from the surface, -0.1, -0.2, -0.7, -1.2, -2.0, -0.5, 1.0, 4.0, 5.0, 3.0, and 0.0 K (see the discussion of parameter STGOFF in Walko and Tremback, 1991). This same profile was used across the entire domain in both case studies.

Soil moisture

Soil moisture fields were inferred from examination of maps of total precipitation and crop moisture index for the United States as published in the joint NOAA/USDA *Weekly Weather and Crop Bulletin.*

In the case of the 1980 Great Plains simulation, the study area received virtually no rain during the three-week period leading up to and including the July 8 tracer release. In fact, the southern and central Plains sweltered under a record-breaking heat wave during

this period. For the week of July 7–13 the *Weekly Weather and Crop Bulletin* classified eastern Kansas as "extremely dry, most crops ruined". Accordingly, the volumetric soil moisture ratio as a fraction of saturation (SLMSTP) was set to a value of 0.250, a value well below the permanent wilting point value of 0.370 for sandy loam (USDA category 4), throughout the depth of the soil model (e.g., Lee and Pielke, 1992).

For the 1983 CAPTEX simulation, the *Weekly Weather and Crop Bulletin* for the week of September 18–24 indicated that about 2.5 cm of precipitation fell over Ohio, Pennsylvania, and New York. The corresponding crop moisture index map for this period showed a narrow range of conditions from 'slightly dry' to 'favourably moist' over the CAPTEX domain. Accordingly, the volumetric soil moisture ratio as a fraction of saturation was set to 0.440, a value midway between the wilting-point and field-capacity values of 0.369 and 0.562, respectively, for sandy loam, throughout the depth of the soil model everywhere in the domain.

4.4 Mesoscale Lagrangian Particle Dispersion Model

The RAMS mesoscale Lagrangian particle dispersion model (MLPDM)is based on the MLPDM developed by McNider (1981) and belongs to that varied group of models known collectively as 'air quality' models. It uses a discrete form of the Langevin equation (see Sec. 2.3.4, Eq. 2.89). Meteorological information is supplied by RAMS: these meteorological fields are used both to specify the resolved grid-scale flow field and to parameterize subgrid-scale turbulence quantities required by the MLPDM. More detailed descriptions of the formulation of this model are given in Pielke (1984) and McNider et al. (1988). A more detailed description of the RAMS MLPDM code going beyond the overview provided in this section is available in two online RAMS documentation files (Moran, 1991a,b).

4.4.1 Previous applications

The MLPDM has been applied to puff or plume dispersion in *homogeneous turbulence* (McNider et al., 1980; McNider, 1981), in *nocturnal drainage flows* (Arritt, 1985; Moran et al., 1986), in *land-sea breeze circulation systems* (Moran et al., 1986; Segal et

al., 1986, 1988), and in *regional-scale flows* over *homogeneous* terrain (Moran et al., 1987; McNider et al., 1988) and *inhomogeneous* terrain (Pielke et al., 1987c; Physick and Abbs, 1991; Lyons et al., 1992).

A few of these studies have included evaluations of this model. McNider (1981) compared MLPDM predictions against Willis and Deardorff's (1978) water-tank dispersion experiments and Lamb's (1978) numerical dispersion model results for vertical diffusion in a convective boundary layer. McNider et al. (1988) compared MLPDM simulations of plume dispersion over distances up to 1000 km against an Australian long-range plume data set. And Segal et al. (1986, 1988) calculated ground-level SO_2 concentration fields over south Florida using the MLPDM although no observations were available for comparison.

4.4.2 Software overview

The RAMS implementation of the McNider MLPDM is compatible with the RAMS meteorological model, including multiple nested grids, and has been coded as a component of the RAMS Visualization and Analysis (VAN) postprocessing package (see next section) since it relies on fields generated by RAMS as input. The MLPDM reads RAMS analysis files, uses the same staggered grid structure as the RAMS meteorological model, and, like other parts of the RAMS VAN package, calls some RAMS model subroutines. It can be run with meteorological-field plotting turned on or off just as the plotting/animation component of the VAN package can be run with the MLPDM turned on or off.

The version of the RAMS MLPDM used in the present study, Version 2A, was originally coded by Drs. Craig Tremback and Robert Walko based on the description in McNider et al. (1988). This version was actually the first RAMS version of the particle model, and because of development time constraints, it did not contain all of the features of the original. It was therefore necessary to augment the basic Version 2A code extensively in order to carry out the simulations described herein. The basic Version 2A RAMS MLPDM consists of 23 subroutines stored in two source-code modules. I wrote a third module, which contained an additional 21 subroutines, in the course of implement-

ing the following features: compatibility with the RAMS O'Brien/Blackadar turbulence parameterization (the basic version was only set up to work with the deformation K scheme) and with a latitude-longitude grid; the drift velocity correction for vertically inhomogeneous turbulence; reflective upper and lower boundary conditions; realizability checks on diagnosed turbulence parameters; user-assigned particle masses; input namelist 'echo' prints; a one-dimensional test meteorology option; particle screening and selection based on particle ID number, source ID number, and release time; calculation of particle ensemble position and velocity statistics; and greatly augmented plotting capabilities, including particle position plots, trajectory plots, concentration point-value plots, and overlays of particle positions with meteorological fields and with concentration fields. Perhaps not surprisingly, the new module had more lines of FORTRAN code than the other two combined.

The basic Version 2A MLPDM allows concentration estimates to be made based on particle position and number density using either the kernel density estimation technique (e.g., Lorimer, 1986; Lorimer and Ross, 1986) or a simple particle-in-cell count. The new MLPDM module implements four different definitions of concentration: (i) particle mass per volume; (ii) particle mass per cell (i.e., one grid box, whatever its size); (iii) number of particles per volume; and (iv) number of particles per cell. Furthermore, any of instantaneous concentrations, time-average concentrations, or exposure (see Eq. 1.23) can be calculated. All of these MLPDM post-processing options use particle position information obtained from MLPDM particle history files (the primary MLPDM output). An MLPDM 'restart' feature was also added whereby an MLPDM calculation could be continued from the particle positions and velocities contained in a specified particle history file.

Grid structure

MLPDM particle coordinates are treated differently from the RAMS meteorological model grid coordinates. The RAMS grid is based on physical distances (X,Y,Z) while the MLPDM particle coordinates are expressed in terms of the first (or outermost or coarse)

grid's M-point cardinal grid numbers (I,J,K). The 'M' grid (see Walko and Tremback, 1991) is used even though no prognostic variables are defined at these grid points because (i) grid nesting is implemented with respect to these points and (ii) some fine-grid M points also fall on coarse-grid M points. Particle coordinates are based on grid-point cardinal numbers rather than grid distances because particle segregation and sorting is easier in the former coordinate system. Another advantage is that only one coordinate system is needed to describe particle locations even if multiple nests are being used.

In addition to the RAMS coarse grid, the MLPDM makes use of a conceptually separate *concentration analysis grid* (or CAG) for estimating ensemble-mean concentrations and various statistics based on particle positions and velocities. Use of the CAG permits attention to be focussed on a subdomain of the RAMS coarse grid with finer resolution without any changes being required to the RAMS grids themselves. Specification of the concentration analysis grid is still made in terms of the RAMS coarse-grid cardinal units, however. Figs. 5.9 and 6.7 show the CAGs used in the present study.

Run control parameters

MLPDM runs are primarily controlled by parameters contained in the $LPDM namelist. The product of two $LPDM parameters, NLPSTEP and DTLP, gives the length of time that the particle model will run. The MLPDM time-step length DTLP must be chosen to be small enough that it is considerably smaller than the shortest Lagrangian velocity time scale likely to be encountered during the simulation. If this is not the case, then the assumption in the governing Langevin equation that particles have 'memory' will be violated. DTLP values should typically not be larger than about 10 s, since even in the convective boundary layer T_L values are on the order of 60–90 s (e.g., Pasquill and Smith, 1983, p. 87). The number of MLPDM timesteps NLPSTEP must be large enough to include the time from the beginning of the RAMS meteorological run to the start of the particle release, the entire release period, and any additional transport time to be considered after the release has ended.

Like the RAMS meteorological model, the MLPDM can be run in two or three dimensions (as specified by the value of ILPDIMEN). However, even if RAMS was run in a two-dimensional mode, the MLPDM can still be run in three dimensions. This is done simply by duplicating the RAMS meteorological fields in the Y direction. The MLPDM can also be run with or without the turbulence parameterization activated. This choice is controlled by the ILPTURB parameter. Other run-control parameters in the $LPDM namelist include the names of the input and output files and flags (METTYPE, TURBTYP) to control the use of the test meteorology option (where turbulence fields and/or resolved flow fields can be specified by the user in a namelist rather than being read from RAMS analysis files).

Source characteristics

A wide variety of source *geometries*, including point, line, area, or volume sources, and *release durations*, including instantaneous, finite, or continuous releases, may be specified using relatively few $LPDM namelist variables. $LPDM variable NLPSRC specifies the number of sources. Source geometry is defined by six variables, three that give the location of the source center in RAMS coarse-grid M-point cardinal coordinates (SRCX, SRCY, SRCZ) and three that give the source dimensions in the same units (XSIZE, YSIZE, ZSIZE). For instance, a point source may be defined by specifying its center location and setting all three size parameters to zero. A rectangular area source, on the other hand, may be defined by specifying its center location and setting two of the three size parameters equal to the length of the sides of the rectangular source and the third size parameter equal to zero. Irregular source geometries can be approximated by specifying multiple contiguous regular sources.

Another $LPDM variable, RELTYPE, controls the type of release. It can have one of two values, 'LATTICE' or 'RANDOM'. In a lattice release, particles are released simultaneously from each of the nodal points of a 1D, 2D, or 3D lattice. The lattice geometry is defined by specifying the number of nodal points in each spatial direction (i.e., NXLATT, NYLATT, NZLATT). For instance, a five-point vertical linear lattice

may be specified by setting NXLATT and NYLATT to '0' and NZLATT to '5'. If RELTYPE is set to 'RANDOM', however, each particle is released at a different randomly-chosen point within the confines of the source boundaries. In essence, this latter option corresponds to a spatially continuous release while the 'LATTICE' option corresponds to a spatially discrete release.

Release duration is governed by two time parameters, RELSTRT, the time of the start of the release, and RELEND, the time of the end of the release. These parameters will be equal in the case of an instantaneous release. If an intermittent source is being modelled, for example, if a short release occurs every hour, it can be handled by specifying multiple sources with the same location and geometry but with different RELSTRT and RELEND values. One last source parameter, RELRATE, specifies the number of lattice or random releases per MLPDM time step. If RELRATE is set to a value of 1/N, where N is a positive integer, then a release will be made every N time steps. Note that a RELRATE value of unity will correspond to the release of one particle per MLPDM time step if RELTYPE has been set to 'RANDOM' but will correspond to the release of NXLATT*NYLATT*NZLATT particles if RELTYPE has been set to 'LATTICE'. In the enhanced MLPDM, an additional source parameter, RELMASS, the mass per particle, has been added for concentration calculation purposes.

Data structure

The MLPDM particle data structure has been devised to minimize processing time but at the same time allow use of the particle model within a multiple-grid RAMS environment. Each particle is assigned its own data record, which consists of a number of integer and real 'attribute' fields. For example, the first three particle integer attributes are (i) the particle's own unique ID number (based on the order and location of release starting with particle 1), (ii) the ID of the innermost grid in which the particle is currently located, and (iii) the ID of the source from which the particle was emitted. The first three real attributes give the I, J, and K coordinates of the particle in terms of the coarse or outermost RAMS grid mesh. Any of the integer attributes can be used as sort 'keys'. The

particle grid ID number (integer attribute 2) is used for this purpose at each time step so that particle data records can be pre-sorted by grid, allowing advection calculations to be carried out together for all particles located within a particular model grid.

A further distinction is made between particle attributes that vary with time and particle attributes that are constant with time. For instance, particle grid ID number (integer attribute 2) may change as the particle travels through the MLPDM domain but the ID of the source from which a particle was released (integer attribute 3) will not depend on either time or particle position. Treating the constant-in-time particle attributes separately reduces the amount of sorting and memory manipulation required at each timestep. However, a complicating side effect which can arise is that individual particle records may contain the 'variable' attributes of one particle and the 'constant' attributes of an entirely different particle. This difficulty is addressed by using particle ID number to link the variable and constant attributes associated with each particle. Version 2A of the basic MLPDM uses 3 integer and 7 real attributes, but others can be added as required. For example, the enhanced MLPDM employs three additional real attributes to store particle position standard deviations.

Temporal and spatial interpolation

One obvious difference between the Eulerian coordinate system of the RAMS meteorological model and the intrinsically Lagrangian coordinate system of the MLPDM is the question of interpolation. In the RAMS meteorological model, calculations are restricted to grid points whose values are assumed to represent volume means. In the particle model, however, particles may be distributed throughout the model domain and are seldom located exactly at RAMS model grid points. Moreover, RAMS meteorological fields are only available every FRQANL seconds, whereas the MLPDM timestep DTLP is typically much shorter. It is thus necessary to determine values of the grid-scale velocity field (and the subgrid-scale turbulence field if ILPTURB=1) both at locations between RAMS grid points and at times between RAMS analysis file times.

In its current form the MLPDM interpolates linearly in time but does not interpolate in space. The linear time interpolation is likely to be quite accurate provided that the value of FRQANL used is small enough to resolve significant temporal variations in the modelled meteorological fields. For example, FRQANL should probably be no larger than 3600 s in order to represent realistically variations in the meteorological fields due to diurnal forcing. This value, however, is still far too coarse to capture intermittent events such as turbulence mixing in the stratified PBL due to Richardson-number breakdown (i.e., KHI). Moreover, time interpolation is only applied to the RAMS mean velocity fields. 'Past' values of turbulence-related fields such as K_z and σ_w are used without time interpolation.

The decision not to consider spatial interpolation was made based on a weighing of computational costs vs. accuracy benefits. Spatial interpolation must be done in *three* dimensions and is thus considerably more expensive than temporal interpolation. The treatment of the value of a model variable as constant throughout a grid-box volume is also consistent with some large-eddy simulation model formulations (e.g., Moran, 1989c). However, as in the case of temporal interpolation, the lack of spatial interpolation will cause accuracy or realism to suffer in the vicinity of small-scale but significant *nonlinear* gradients, for example, in the surface layer, at the top of the PBL, or at coastlines.

Concentration calculations and plots

Concentrations are calculated based on the distribution of tracer particles within the concentration analysis grid. Concentration values are taken to be located at the centers of CAG volumes, not at CAG grid points (i.e., grid-box corners), when sending the two-dimensional concentration field to the contouring routine. Parameter CNTYPE determines whether concentrations are based on counting particles in CAG volumes or on applying a simple kernel density estimator (a three-dimensional parabolic kernel – see Grossman, 1989) at CAG points.

A new source parameter, RELMASS (i.e., release mass in kg/particle) was added to the $LPDM namelist in the enhanced MLPDM. Source strength Q is determined by

the values of RELMASS and RELRATE. For an instantaneous release, Q will have units of mass and is given by the product of RELMASS and the total number of particles released (RELRATE for a random release, RELRATE*NXLATT*NYLATT*NZLATT for a lattice release). For a continuous release, Q has units of mass per unit time and is given by the total mass of the particles released per time step.

In calculating concentrations, four different definitions of concentration can be selected in the enhanced LPDM by specifying values for parameters CNUNITS and CNPLOTU: either particle number density or mass density can be selected (CNUNITS) and density can be defined either per spatial volume or per unit grid box (CNPLOTU). Having this choice is useful for debugging and also permits examination of the number of particles used to make concentration estimates in different parts of the domain. It is also possible to use the screening option[165] to select a subset of particles for concentration calculations.

Parameters XCPLT, YCPLT, and ZCPLT in the $POSTLPM namelist[166] together determine (a) the projection (i.e., XY, XZ, or YZ view), (b) the portion of the analysis grid to be shown (i.e., the 'window'), and (c) the range to be considered in the third direction. CAG units are used. The two projection-plane axes are indicated by an 'R' range character while the projection/averaging normal direction is indicated by a 'V' range character. The 'V' range specifies the 'thickness' of the concentration averaging volume, e.g., whether it goes from the Earth's surface to the first RAMS model level or to the top of the PBL.

The user can also control the number, range, and spacing of concentration contour intervals. Parameter CNCLL specifies the contour spacing: there are two choices at present, linear spacing or logarithmic spacing. The latter may be the better choice if the

---

[165] Particles can be selected on the basis of their individual ID number, source ID number, or release time.

[166] Two completely new namelists, $POSTLPM and $METINP, were added in the enhanced version of the Version 2A MLPDM as well as six new entries in the $LPDM namelist.

entire distribution of pollutant or tracer is of primary interest while the former is more appropriate if the detailed structure in the vicinity of the concentration maximum is of more interest. Another parameter included in the $POSTLPM namelist, DOSAGE, allows the user to specify that a time-integrated exposure be calculated rather than a time-average concentration. The integration, or averaging period, for calculating exposures, or time-average concentrations, is set by parameter NCNFRAV, which gives the number of particle-history-file times to be used.

4.5 Visualization and Analysis Package

The RAMS Visualization and Analysis (VAN) package is the post-processing component to the meteorological model. It can be used to plot RAMS meteorological fields in a variety of graphical formats, including contour plots on XY, XZ, or YZ 'slices', time-height cross sections, and space and time line plots of a selected variable. Wind vectors or streamlines may also be plotted separately or overlaid on a contour plot of a 'scalar' field. As mentioned above, the MLPDM was integrated into this package because the particle model may also be regarded as a post-processor to the RAMS meteorological model. The VAN package was used to prepare the plots of meteorological fields and tracer-related fields presented in this dissertation. The best description of the VAN package to date has been given by Walko and Tremback (1991).

A modified version of the standard Version 2A VAN package was used in this study. These modifications included the use of the extended MLPDM described in the previous section. A number of new plot variables were also added, including density, perturbation potential temperature, wind direction, vertical eddy diffusivity, Brunt-Väisälä frequency, horizontal and total deformation, Richardson number, radiation flux divergence, turbulence kinetic energy, soil temperature, soil moisture, surface heat flux, surface friction velocity, Lagrangian velocity time scale, and vertical turbulence intensity.

In addition, some code modifications were made in order to allow the overlaying of plots of meteorological fields with plots of (a) particle positions and (b) other me-

teorological fields (e.g., Fig. 4.22). User specification of vector spatial density and two additional namelists, $POSTLPM and $METINP, were also added. The former controls MLPDM plotting and statistical analysis while the latter specifies meteorological and turbulence profiles for the one-dimensional 'test meteorology' option. Finally, an additional map projection option, the cylindrical equidistant projection, was added to the existing options of orthographic, Mercator, and Lambert conformal projections. The cylindrical equidistant (or plate Carrée) projection is useful when a latitude-longitude grid is being used (e.g., Pearson, 1990).

4.6 Model Performance Evaluation Measures

The last decade has seen increasing interest within the geophysics community concerning the systematic, uniform assessment and evaluation of the performance of *individual* numerical models. This has been especially true for NWP models because of their important operational role in weather forecasting and for air quality models because of their major role in the environmental regulatory process in various countries (e.g., Fox, 1981; Anthes, 1983; Pielke, 1984; Willmott et al., 1985). For example, Steyn and McKendry (1988) and Ulrickson and Mass (1990a,b) used a number of quantitative statistical measures suggested by Willmott et al. (1985) to evaluate the performance of the CSU mesoscale model, one of the progenitors of RAMS, for two complex-terrain simulations.

A closely related topic is the choice of methodology to be used in the *intercomparison* of the performances of two or more numerical models in order to determine which model is 'best'. Model intercomparison exercises have been conducted for *urban air quality* models (NATO/CCMS, 1980; Moore et al., 1982; Londergan et al., 1983; White, 1984; Rao et al., 1989), *rural air quality* models (Londergan et al., 1982; Fox et al., 1983; Smith, 1984), *complex terrain air quality* models (Londergan and Wackter, 1984; Tesche et al., 1987), *episodic LRTAP*[167] models (Policastro et al., 1983, 1986a,b; Ruff

---

[167] Discussed in Sec. 2.4.5.

et al., 1985; van Dop, 1986; AMS/EPA, 1987; Carhart et al., 1989; Clark and Cohn, 1990; van Dop, 1991), *long-term LRTAP* models (Clark et al., 1989; Derwent et al., 1989), and *regional-scale meteorological* models (NCAR, 1988). This topic is still attracting considerable interest and no consensus has yet emerged on the best way(s) to compare model performances (e.g., Willmott, 1982; Preisendorfer and Barnett, 1983; Downton and Dennis, 1985; Willmott et al., 1985; Cox and Tikvart, 1986; Hanna and Heinold, 1986; Cox, 1987; NCAR, 1988; Carhart et al., 1989).

Three related but distinct terms are frequently encountered when discussing model performance assessment: (a) model *verification*, (b) model *evaluation*, and (c) model *validation*. Fox (1981; p. 600) distinguished between these three terms in a discussion about the appraisal of air quality model performance:

> Verification is proof of the accuracy, reality, or truth of a model. Evaluation is the process of examining and appraising the performance by comparing the model's concentration estimates to measured air quality data. Validation is the establishment of a conclusion by detailed and copious evidence that leads to formal recognition. This may include several evaluations. Models are evaluated in the hope that they will be validated.

4.6.1 Operational vs. diagnostic evaluations

Two main approaches have been taken in model evaluations: 'operational' evaluations and 'diagnostic' evaluations. The first approach quantifies model accuracy and precision through the calculation of various measures of bias, scatter, correlation, and significance. The second approach examines model predictions and algorithms in a problem- and model-dependent way in order to understand the underlying reasons for model errors. Operational evaluations tend to consider model performance over many cases while diagnostic evaluations tend to consider individual episodes or cases in detail.

Fox (1981) has discussed a wide variety of paired and unpaired statistical measures that can be used in operational evaluations of air quality models. Only a few of these measures will be employed in this study because of both the intrinsic redundancy of many of these measures and the relative paucity of available observational data. Relatively

large data sets are required to produce meaningful values for most of these quantities. Paired statistics compare model predictions with observations at common points in space and time and are more stringent than unpaired statistics. For example, a high correlation coefficient value requires the model to predict the correct size, shape, *and* position of the tracer cloud, a difficult job (Brost et al., 1988a). Two other statistical measures commonly used in weather forecast evaluations, bias scores and threat scores, have also been used in LRTAP model evaluations (e.g., Brost et al., 1988a; Shi et al., 1990). These two quantities give some indication of the goodness of the prediction of cloud size and cloud position, respectively.

Willmott et al. (1985) have argued for the use of graphical displays to supplement basic statistical performance measures. Such displays very often help to reveal systematic model errors. Fig. 4.20 shows some possible graphical displays. With the exception of the concentration frequency histogram, all are paired displays. For example, residuals, by definition, require predicted-observed pairs of values.

4.6.2 Evaluation strategy adopted in this study

In the present study, the performance of the CSU mesoscale atmospheric dispersion modelling system has been evaluated against two observational mesoscale air-quality data sets over a suite of numerical experiments.

The two evaluation data sets, which were described in Chap. 3, consist mainly of time-averaged tracer concentration observations made at a number of fixed surface stations plus some nearly instantaneous aircraft concentration measurements. It is important to remember that the evaluation data set consists mainly of concentration 'footprints', that is, surface values, even though the dispersion modelling system predicts three-dimensional pollutant concentrations. Thus, any evaluation with such a data set can only consider a small fraction of the model predictions. However, this is still a valid test because predicted surface concentrations are only likely to be correct if the full three-dimensional concentration pattern is correct.

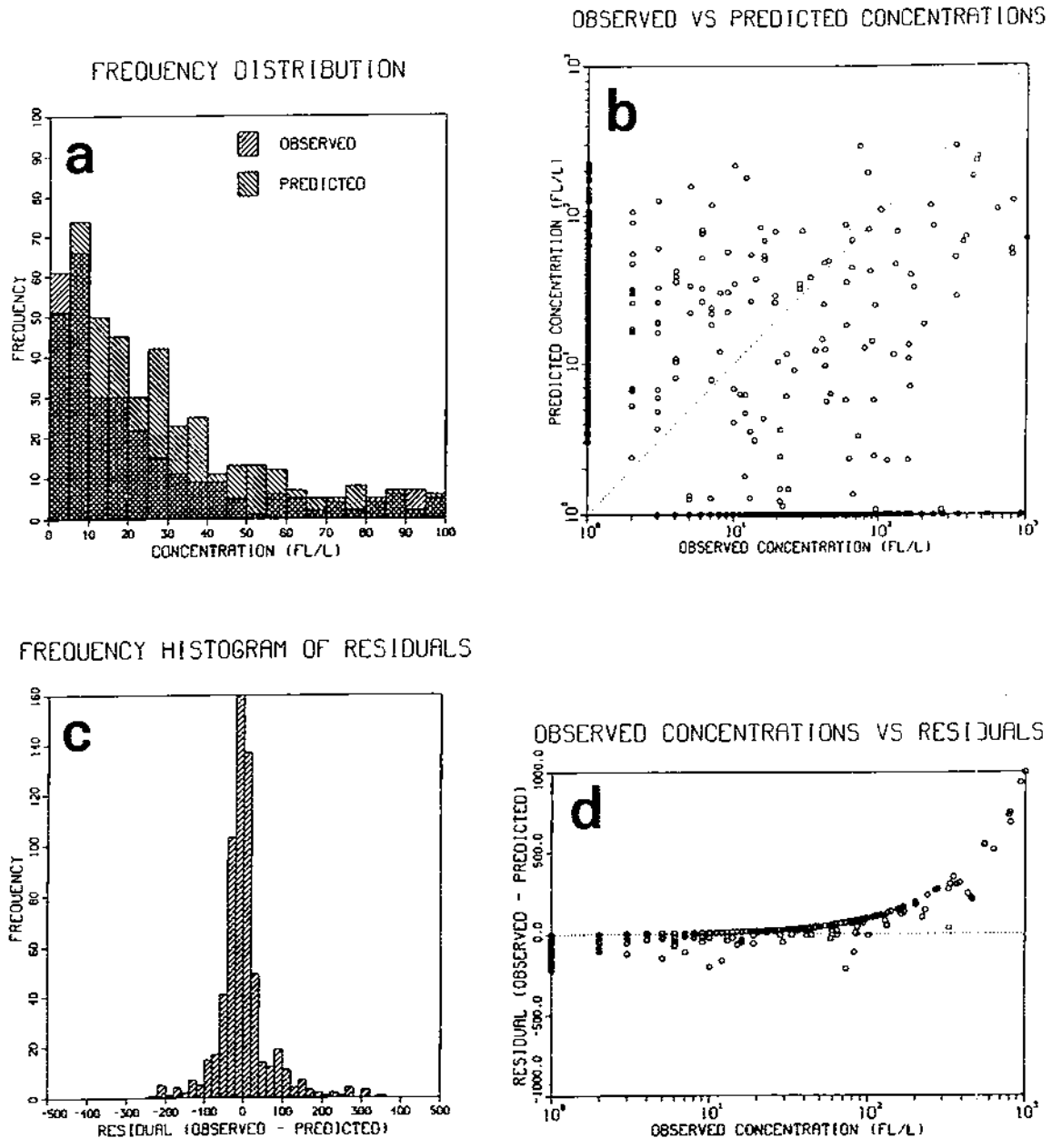

Figure 4.20: Sample model performance graphical displays: (a) superposed frequency distribution histograms for observed and model-predicted concentrations; (b) log-log scatter plot of observed concentrations vs. model-predicted concentrations; (c) frequency histogram of concentration residuals; (d) semilog plot of observed CAPTEX concentrations vs. residuals (i.e., observed minus model-predicted concentrations) (from Lee, 1987).

The number of available concentration measurements is relatively small in this study since only two episodes have been considered. This suggests the adoption of a more diagnostic evaluation approach which focuses on predicted surface concentration *patterns*. Such an approach is consistent with many of the previous studies discussed in Chap. 3, and quite a number of observed and predicted tracer-cloud 'qualitative' characteristics can be compared (e.g., Fowler and Barr, 1983; Carhart et al., 1989; Clark and Cohn, 1990). These include (a) cloud arrival time, (b) peak concentration, (c) duration of tracer cloud passage, (d) cloud size, (e) cloud structure and shape, (f) cloud mean transport speed, and (g) cloud mean transport direction.

One important consideration in designing the evaluation strategy was the geometry of the surface observing networks in the two tracer experiments considered. In the Great Plains experiment, measurements were taken along two 'one-dimensional' sampler arcs 500 km apart (Fig. 3.1). This geometry makes it difficult to impossible to estimate some quantities such as cloud concentration-weighted centroid position and cloud size. The CAPTEX observing network, on the other hand, was two-dimensional and had fairly uniform sampler separation (Fig. 3.13). Haagenson et al. (1987) estimated that the average CAPTEX sampler separation was about 86 km.

Sampling period must also be taken into account in the model performance evaluation. The Great Plains experiment used two sampling periods: 45 minutes along the 100-km arc and 180 minutes (3 h) along the 600-km arc. Six-hour samples were taken during the CAPTEX program except for stations nearest the release site (i.e., 300-km arc), which took three-hour samples. Such time-integrated measurements introduce uncertainty into the estimation of the time of an event such as the arrival of the cloud or the time at which the peak concentration occurred. However, averaging measurements and model predictions in time and/or space tends to improve agreement (e.g., Heffter et al., 1987). Unless otherwise specified, sample times referred to in Chaps. 5 and 6 will correspond to the *starting time* of the sampling interval. MLPDM particle positions were saved every 15 minutes. This permitted predicted 45-minute concentrations to be calculated based

on 3 samples[168], 3-hour concentrations to be calculated based on 12 samples, and 6-hour concentrations to be based on 24 samples. There was a slight trade-off involved between the frequency of saving particle position information and the number of particles followed but effectively the same number of particles would be considered in calculating a *time-integrated* concentration. For this study, time resolution was considered to be more important than total number of particles followed given the more detailed information gained on cloud arrival time and on cloud duration.

The ambient 'background' concentration of PMCH must be subtracted from observed PMCH concentrations or added to model predictions before comparing them since the MLPDM predicts tracer concentration levels *above* background. A value[169] of 3.4 fll^{-1} was subtracted from reported concentration values for the Great Plains simulations following Ferber et al. (1983, 1986), Policastro et al. (1986a), Draxler (1987), and Haagenson et al. (1987). The PMCH concentration values tabulated in Ferber et al. (1986) for the CAPTEX releases had already had a value of 3.4 fll^{-1} subtracted in order to remove background *and* most of the 'noise' associated with the sampling and analysis of near-background concentrations. This procedure also points out the fact that the concentration measurements themselves are subject to uncertainty. Ferber et al. (1981) suggested that for the Great Plains experiment, concentration measurements made along the 600-km arc would be accurate to ±10% at levels near background while 100-km arc samples (which were one-quarter of the volume) would have an uncertainty of ±25% near background. To address this problem, various investigators have considered only concentration values above some *threshold* value, generally 2–3 fll^{-1}, in calculating some statistics (e.g., Draxler, 1987; Heffter et al., 1987; Lee et al., 1987; Shi et al., 1990). A similar approach has been adopted in this study (e.g., Tables 3.3, 3.3).

---

[168] That is, on instantaneous concentrations calculated from particle positions at three different times.

[169] Ferber et al. (1983) give a value of 2.4 fll^{-1} for PMCH background

One other small source of uncertainty arose from the required conversion of model-predicted concentration units of $\mathrm{kg\,m^{-3}}$ to the volume-mixing-ratio units of $\mathrm{fl\,l^{-1}}$ (i.e., $10^{-15}\ \mathrm{l^{-1}}$ or parts per 10^{15}; *fl* is an abbreviation of 'femtoliter') used by Ferber et al. (1981, 1986). Following Seinfeld (1986), a conversion factor of $10^{15}\,R^*T/pM_{\mathrm{PMCH}}$ was used, where R^* is the universal gas constant ($0.08314\ \mathrm{hPa\,m^3\ K^{-1}\ mol^{-1}}$), T is temperature, p is pressure, and M_{PMCH} is the molecular weight of PMCH ($350\ \mathrm{g\,mol^{-1}}$). Using reasonable values for p and T for a summertime anticyclone[170], this expression yielded a factor of 7×10^{13} for the Great Plains experiment data. For the CAPTEX measurements, Ferber et al. (1986) recommended a value of 6.4×10^{13}, consistent with the cooler temperatures which might be expected in autumn at higher latitudes under comparable anticyclonic conditions. This second value was used for converting CAPTEX concentration values.

4.6.3 Inherent uncertainty

It is important to recognize that atmospheric model predictions can never be perfect. Differences between model predictions and atmospheric observations may occur due to errors in model input fields, errors due to model physics and model numerics, and errors in the observations themselves. However, even for perfect input data, a perfect model, and perfect observations, there will still be differences due to the comparison of time-averaged, space-averaged, model-predicted ensemble means with point measurements from a single atmospheric flow realization (Fox, 1984; Venkatram, 1988b). That is, model predictions can never be perfect due to *inherent uncertainties* arising from the stochastic nature of turbulent atmospheric flow. Of course, it is extremely unlikely that all other sources of error will be zero in a modelling study since neither models nor observations are ever perfect, but the inevitability of differences between model ensemble-mean predictions and single-realization observations should be kept in mind when evaluating numerical model results (e.g., Demerjian, 1985).

---

[170] 297 K, 1010 hPa.

4.7 Tests of the Modelling System Configuration

A number of tests of various components of the CSU mesoscale atmospheric dispersion modelling system were carried out before beginning the simulations described in the next two chapters. These baseline tests served several purposes. First, they helped in the selection of the particular RAMS options for the 'production' model by providing a comparison of the performances of different RAMS parameterizations. Second, they permitted the standard code and my own code modifications to be checked and tested. Third, they confirmed for simple flows that reasonable results could be achieved using the particular mix of RAMS options selected for this study (i.e., a synergy/compatibility check). And fourth, they demonstrated that results produced by this particular RAMS configuration were comparable to results obtained in previous studies.

4.7.1 Isentropic analysis package

The ISAN package blends together three complex data sets — (i) the gridded, objectively-analyzed, three-dimensional NMC synoptic-scale data set, (ii) a set of irregularly-spaced synoptic surface station observations, and (iii) a set of irregularly-spaced synoptic upper-air soundings — to create a three-dimensional, multivariate initial state for RAMS. Given the interpolations between different horizontal grids, different vertical coordinates, and individual station locations required in the four ISAN Version 2A analysis stages or modules, this is a difficult package to test under idealized conditions. Instead, results were checked at each stage for internal consistency, for consistency with results from the other stages, and for consistency with available observations. The (augmented) plotting capabilities of ISAN Stage 4 and the VAN package were used extensively to this end.

External benchmarks included published daily weather maps and sounding listings. The *U.S. Daily Weather Map* series contains daily surface and 500 hPa 1200 GMT weather maps. ISAN plots of reduced sea-level pressure could be checked against the published surface map at each stage. The 500 hPa geopotential field could also be

plotted in Stage 1 and compared against the published 500 hPa chart. In subsequent ISAN stages, upper-air fields were only available on isentropic and not isobaric surfaces. However, the VAN package could be used to plot the RAMS initial geopotential field on a constant-height surface close to 500 hPa for an additional qualitative check. In addition, vertical cross sections of both ISAN Stage 3 and RAMS initial fields could be plotted using ISAN Stage 4 and the VAN package, respectively, as a check on Stage 5 of the ISAN package.

ISAN Stage 3 accesses station data. Upper-air soundings could be listed in this stage and compared against published soundings in the dispersion experiment reports (e.g., Ferber et al., 1981) to check that upper-air data were being accessed correctly. Surface station data values could also be plotted in Stage 4 and compared to the *U.S. Daily Weather Map Series* surface maps, and Stage 3 horizontal cross sections could be plotted in Stage 4 and examined for 'bull's-eyes', that is, locations where station observations differed greatly from the gridded NMC first-guess fields. In such cases the station data were likely erroneous and the offending station could be flagged and discarded in a rerun of Stage 3. Fortunately, this last action was not required for the two cases considered in this study.

Code had to be added to the ISAN Version 2A package to implement the vertical cross sections and some surface variable plots. These additional features proved to be very valuable, permitting the detection of a number of problems in the ISAN code, particularly in the processing of upper-air data. Failure to have carried out this testing would have resulted in incorrect initial fields being used in the RAMS simulations.

4.7.2 Meteorological model

Having a wide range of choices of physical-process parameterizations to choose from is an advantage provided that the model user can make informed choices in configuring RAMS for a particular application. Some parameterization schemes have a dozen or more internal parameters for which values must be specified, and model results can be strongly dependent upon the values chosen. For example, Tremback (1990) found RAMS

simulations of a Great Plains mesoscale convective complex to be sensitive to the values specified for several cumulus parameterization scheme parameters and for the horizontal diffusion coefficient. Setting a RAMS run up for a new application thus requires some preparatory tests.

One-dimensional tests

Adopting a similar approach to Tremback (1990), 15 one-dimensional model runs were made in order to compare different options for the radiation, turbulence, and surface-layer parameterizations against each other and against observations (Moran, 1989a,b,c, 1992a). The test case selected for these runs was the well-known Wangara Day 33–34 observational period (e.g., Clarke et al., 1971; Hess et al., 1981).

A number of the test results are relevant here. First, the two shortwave radiation schemes currently used in RAMS performed badly when compared against Wangara measurements[171] (Moran, 1989a, 1991a). Second, the four turbulence parameterization schemes gave similar predictions of first-order dynamic and thermodynamic variables for this one case study (Moran, 1989b). Third, the Louis surface-layer formulation was shown to be more robust than the Mahrer-Pielke formulation but did not perform realistically under stable, light-wind conditions (Moran, 1992a). Fourth, the deformation K scheme was very sensitive to the specification of some of its internal parameters (Moran, 1989c). See the referenced reports for details .

Two-dimensional tests

As will be shown in the next chapter, the nocturnal low-level jet frequently observed over the Great Plains played an important role in the transport of the tracer cloud during the 1980 Great Plains mesoscale tracer experiment. McNider and Pielke (1981), hereafter MP81, carried out an idealized two-dimensional simulation of the Great Plains low-level

---

[171] The Chen-Cotton schemes for shortwave and longwave radiation were finally selected for this study after two additional one-dimensional RAMS simulations initialized with a summertime Oklahoma City sounding (see p. 372).

jet system using what was then known as the University of Virginia mesoscale model, one of the 'parents' or 'ancestors' of the RAMS meteorological model. Their case study was rerun for this study using three different configurations of RAMS both to ensure compatibility between current and previous results and to evaluate the impact of intrinsic differences between the two models.

In one run, RAMS was configured to be as close to the form of the mesoscale model used by MP81 as possible (the 'look-alike' simulation). In the second RAMS run, the 'deformation K' simulation, the O'Brien-Blackadar turbulence parameterization described in MP81 and used in the 'look-alike' simulation was replaced by the RAMS deformation K turbulence parameterization in order to compare the performance of these two schemes over the relatively complex terrain considered in this test. In addition, the deformation-K-based horizontal diffusion was used in this run (with AKMIN set to 1.0) in place of Long's filter (with FXLONG set to 0.025). The third run, which will be referred to hereafter as the 'updated' run, employed the same RAMS configuration[172] used in the simulations described in Chaps. 5 and 6. It differed from the 'look-alike' run in its use of (a) horizontal diffusion rather than Long's filter, (b) the anelastic rather than the incompressible form of the continuity equation, (c) the Klemp-Lilly radiative lateral boundary condition rather than the zero-gradient condition, (d) longitude-dependent solar heating, (e) Chen-Cotton rather than Mahrer-Pielke shortwave and longwave radiation schemes, and (f) non-zero surface moisture fluxes.

Note that even the 'look-alike' run differed in some respects from the original MP81 simulation. All three RAMS runs employed the sixth-order forward advection scheme rather than the cubic-spline scheme, the Louis rather than the Mahrer-Pielke surface-similarity-theory formulation, the Tremback-Kessler soil model rather than the Mahrer-Pielke soil model, and the Klemp-Durran upper boundary condition rather than the material surface UBC. The three RAMS runs also used 27 vertical levels rather than the 14

---

[172] Except for the upper boundary condition, since the Klemp-Durran UBC was used in place of the prognostic surface pressure UBC.

levels used by MP81. There were two reasons for using the different vertical discretization. First, there was no description of the original vertical discretization in either McNider (1981) or MP81[173]. Second, as discussed earlier, when using a stretched vertical grid, it is preferable to use a smoothly varying one. In these runs, DELTAZ was set to 61 m, DZRAT was set to 1.1, and DZMAX was set to 1000 m (see Walko and Tremback, 1991).

MP81 used the 0635 LST O'Neill experiment sounding from August 31, 1953 (see Lettau and Davidson, 1957a,b) to initialize their model. This same sounding was used to initialize the RAMS simulations, although there turned out to be a difference at about 3 km compared to the sounding used by MP81 which resulted in a less stable layer above that height in the RAMS simulations (Fig. 4.21a,b). This difference is difficult to explain since the RAMS sounding was taken directly from Lettau and Davidson (1957b, p. 531)[174]. All simulations used 43 grid points in the horizontal with 50 km grid spacing, 60 s time step, approximately the same start time (local sunrise for MP81 vs. 0600 LST for RAMS), and the same idealized two-dimensional 'ramp' topography with 0.0018 slope tapering to flat ends (see Fig. 4.21).

Differences between the results of the four simulations were relatively small. Fig. 4.22 shows an overlay of the v component and potential temperature (θ) fields at mid-afternoon, nine hours into the simulations. The 'look-alike' and 'updated' RAMS runs using the O'Brien K/Blackadar K turbulence parameterization produced PBLs which were deeper than the one predicted by the 'deformation K' run but similar in depth to the MP81 prediction. Horizontal differences within the PBL between the RAMS θ fields and the MP81 θ field at this time are probably due in large part to the differences between the initial θ fields (Fig. 4.21). The MP81 v field at 1500 LST had a slightly

---

[173] The 14 levels used by MP81 were probably 2, 8, 30, 100, 200, 300, 500, 700, 1200, 1600, 2200, 3000, 4000, and 6000 m (McNider, 1992, personal communication).

[174] There may have been a decision made in MP81 simply to assume constant stratification above 3 km because of the very coarse resolution used at upper levels; values in the first 500 m agree within 0.1 K and values in the first 2000 m agree within 1 K.

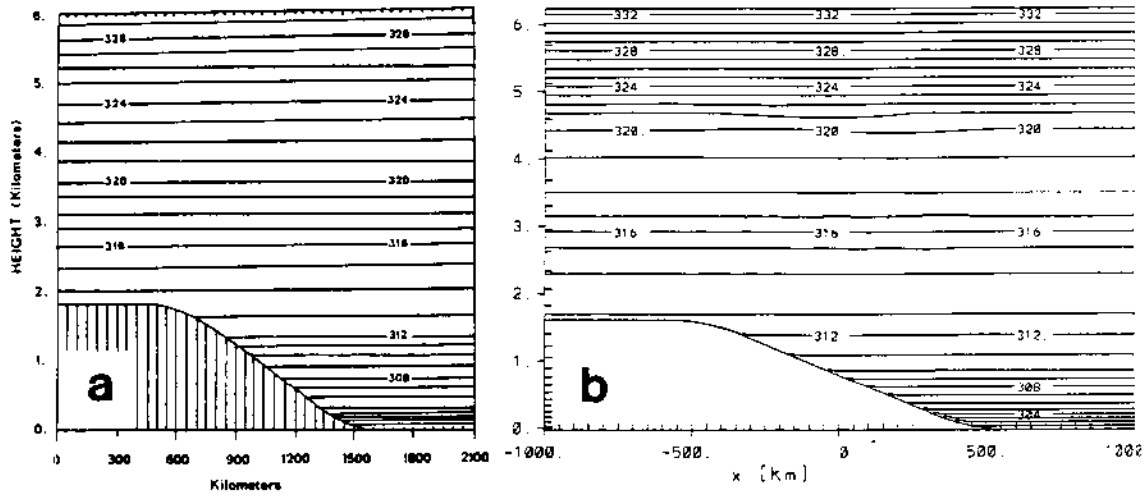

Figure 4.21: Comparison of initial temperature fields for (a) MP81 Great Plains experiment run (their Fig. 11) and (b) three RAMS Great Plains experiment runs. The contour interval is 1 K.

larger low-level maximum value than the RAMS runs (Fig. 4.22). This difference is also likely due to the difference in the initial θ fields since vertical mixing in the MP81 run would produce a stronger mesoscale, low-level, horizontal temperature gradient and hence a stronger daytime easterly upslope flow component which would in turn contribute to the northerly v flow component through Coriolis turning. Of the three RAMS simulations, the 'look-alike'-run v field most closely resembled the MP81 v field at low levels.

Fig. 4.23 shows (u,w)-vector fields and the corresponding streamline fields for the three RAMS simulations at 1500 LST. All six panels show a daytime upslope circulation superimposed on the synoptic-scale southerly flow. The transition at the top of the PBL to free-tropospheric conditions seems to be smoother in the 'look-alike' and 'updated' runs than in the 'deformation K' run. Vertical velocities also seem to be somewhat stronger at upper levels in the 'updated' run compared to the other two runs, likely due to the anelastic continuity equation used in this run. I tested this conjecture by rerunning this simulation with the incompressible continuity equation and did find a reduction in vertical velocities at upper levels (not shown).

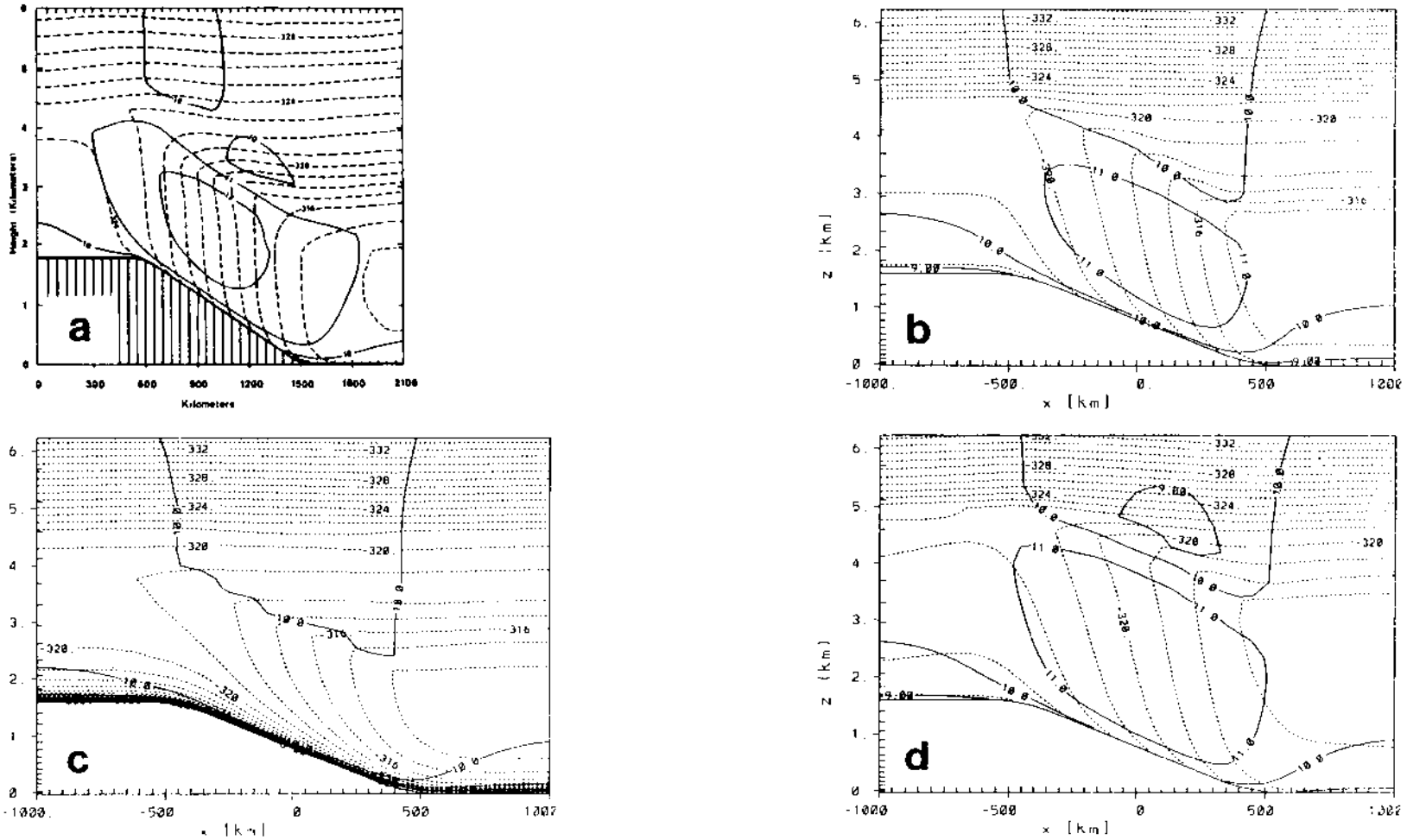

Figure 4.22: Comparison of MP81 plot of v and θ at 1500Z for idealized two-dimensional Great Plains experiment simulation with three RAMS simulations of same case: (a) Fig. 12 from McNider and Pielke (1981); (b) RAMS 'look-alike' simulation; (c) RAMS 'deformation K' simulation; (d) RAMS 'updated' simulation. Dashed lines denote isentropes with 1 K spacing; solid lines denote northerly v-component isopleths with 1 $\mathrm{m\,s^{-1}}$ spacing.

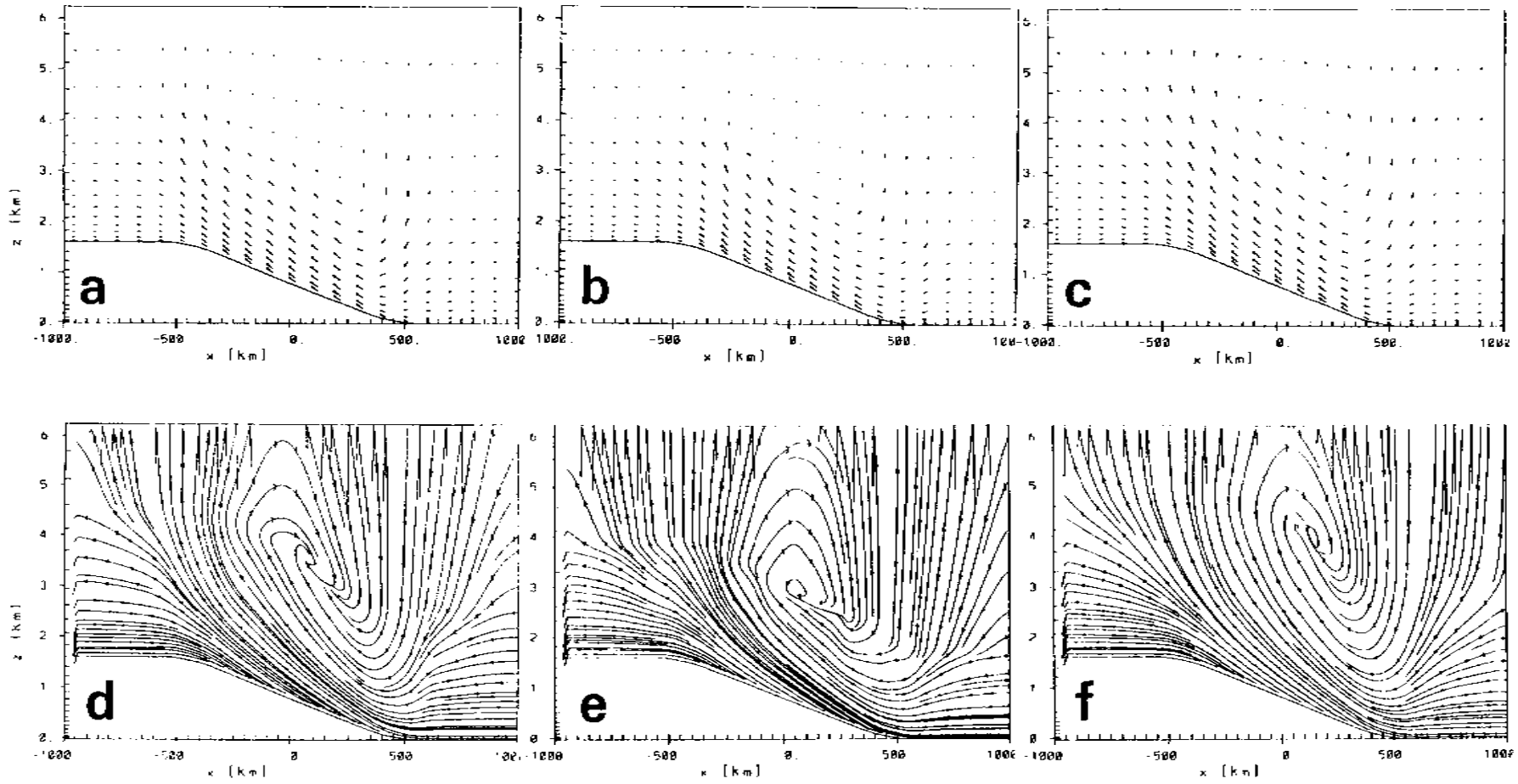

Figure 4.23: Comparison of 1953 O'Neill-case (u,w)-component vector fields/streamline fields at 1500 LST, nine hours into the simulation, for (a/d) 'look-alike' run, (b/e) 'deformation K' run, and (c/f) 'updated' run. Vertical velocity components are scaled by a factor of 236, the reciprocal of the aspect ratio for this plot. Maximum vector speed is 7.5 m s^{-1}.

Fields at 2300 LST exhibited larger differences. Fig. 4.24 shows overlays of the v component and θ for the four simulations. The MP81 simulation predicted the strongest nighttime low-level jet with the 'updated' run predicting the second strongest jet. The 'look-alike' RAMS run jet maximum was also quite a bit larger than the 'deformation K' RAMS run maximum (17.1 vs. 15.4 $\mathrm{m\,s^{-1}}$). Again, part of the difference between the MP81 and RAMS low-level velocity fields may be attributed to the difference in the initial potential temperature field. One difference in the potential temperature fields between the three RAMS runs is evident in the varying strength of the low-level nocturnal inversion over the flat eastern portion of the domain.

Fig. 4.25 shows the (u,w)-component vector fields and the corresponding streamline fields for the three RAMS simulations at 2300 LST. The biggest differences are again located at the top of the residual layer. Note that the low-level west-east flows are still upslope, due most likely to frictional turning of the strong synoptic southerly wind in the nocturnal inversion.

Three-dimensional tests

Before trying any full-blown three-dimensional RAMS production runs, several tests were carried out with a three-dimensional 'toy' grid. The 'toy' grid used for these tests was $10 \times 10 \times 10$, just large enough to accommodate the Davies lateral boundary condition and a two-point model interior. A real case was considered: July 8, 1980 over the Great Plains. This is the same case discussed in Chap. 5. Running these small-grid simulations was a good way to experiment with the ISAN package, the variable initialization option of RAMS, and the VAN package for a three-dimensional case study.

One lesson learned from these tests was the need to locate the model top above the tropopause in a three-dimensional, real-data case. In the first small-grid runs, the model top only reached to 6 km. The main synoptic feature present in the domain, a quasi-stationary summer anticyclone, was strongly divergent in the lower troposphere. To compensate, RAMS spun up a corresponding but unrealistic cyclonic circulation at the very top of the model.

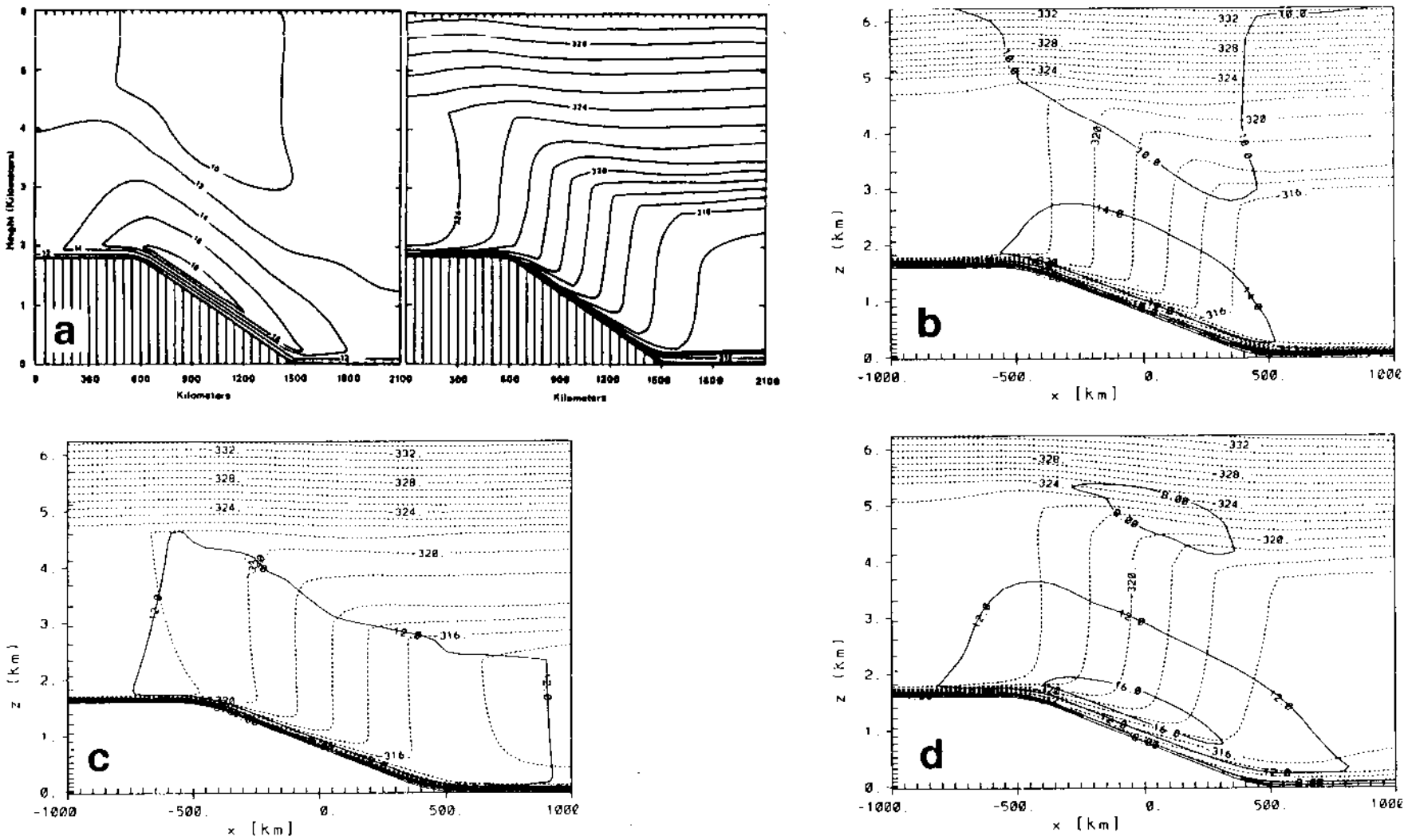

Figure 4.24: Same as Fig. 4.22 except panel (a) has been split into panels (a1) and (a2) and corresponds to 2230 LST while panels (b), (c), and (d) correspond to 2300 LST. The northerly v-component contours (solid lines) are drawn every 2 $m\,s^{-1}$ in these panels.

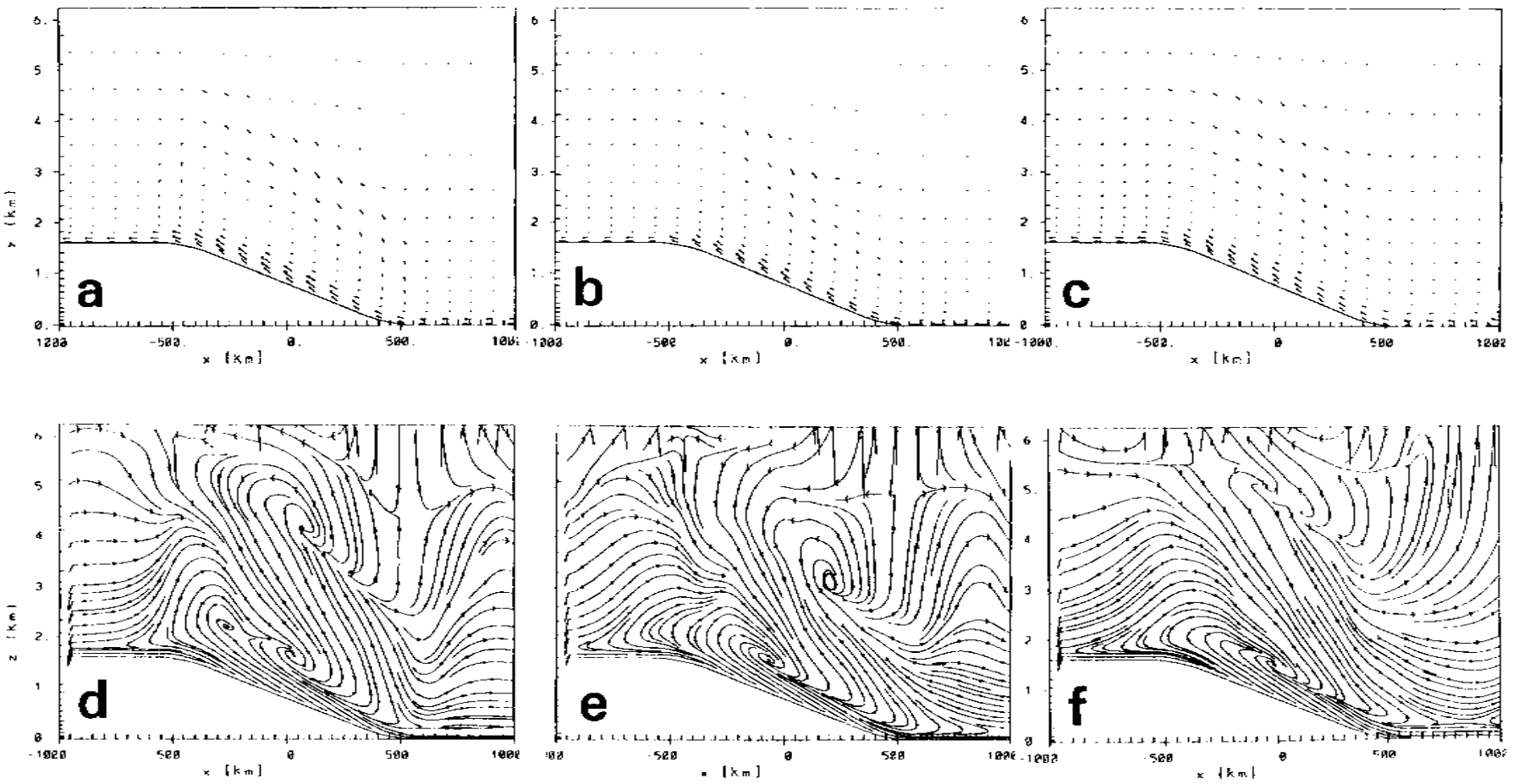

Figure 4.25: Same as Fig. 4.23 except for 2300 LST.

4.7.3 Mesoscale Lagrangian particle dispersion model

Even an idealized, one-dimensional RAMS simulation will usually produce a time-varying, vertically-inhomogeneous input data set for the MLPDM. Meaningful tests of the MLPDM code, on the other hand, require simple, steady wind and turbulence profiles. To this end, I added a *1D test* capability to the MLPDM to allow the user to specify one-dimensional profiles of all of the required meteorological variables (u, v, w, Ri, K_z, ℓ, $|\partial\vec{V}/\partial z|^2$, z_i, z_s, L, u_*) and to specify rather than diagnose the required turbulence quantities (σ_w, σ_u, T_{Lu}, T_{Lw}).

As a first test, I tried the 'well-mixed' experiment suggested by Thomson (1987): for an initially well-mixed set of particles in a steady, homogeneous turbulent flow, can the particle model maintain this well-mixed state over an indefinite period of time? I considered a 2.4 km deep domain with 49 uniformly-spaced vertical levels. Both the model top and bottom were specified to be perfectly reflecting. The mean wind was set to zero, σ_w was set to 1 m s^{-1}, and T_{Lw} was set to a value of 50 s at all levels. In the first experiment (Run A), 2000 particles were released instantaneously as a uniformly distributed, 2.4-km-high vertical column and then tracked for 12 hours. The vertical distribution of particles after 12 h is shown in Fig. 4.26a for twelve 200-meter-thick layers. There is some suggestion of more particles being located in the lower half of the domain than in the upper half, and particle distribution statistics at earlier 2-hour intervals (not shown) indicated that this tendency was strengthening with time. There were a number of possible explanations for this behaviour, including a boundary condition problem, an error in the advection calculations or in the specification of grid structure, or some sort of bias or asymmetry in the normal random numbers used. To narrow the possibilities, another run was made which was identical to Run A except that the random numbers had their signs reversed. This time there was a preponderence of particles in the upper half of the domain, suggesting that the problem lay with the set of random numbers being used.

In order to save computer time, the RAMS MLPDM creates a table of normally-distributed random numbers at the beginning of a run (the size of the table is specified by the user and should be a prime number) and then uses these numbers over and over rather than generating as needed the millions of normal variates which are frequently required in a many-particle MLPDM run. One danger of this approach is that the random-number table values may be cycled through *in the same order* thousands and thousands of times. To check if this was a problem, a short subroutine was added which rearranged a few percent of the table entries following each complete pass through the random-number table. Run B in Fig. 4.26a shows the effects of rerunning Run A with the new subroutine turned on. Although sampling fluctuations are still present, the vertical distribution of particles in Run B is improved compared to Run A.

A second experiment was carried out to check my implementation of the drift acceleration correction term. Run C was identical to Run B except that (i) 3000 particles were released instead of 2000, and (ii) σ_w varied linearly in the vertical from a value of $0.50\ \mathrm{m\,s^{-1}}$ at the bottom level to a value of $2.95\ \mathrm{m\,s^{-1}}$ at the top level. The drift acceleration correction was *not* activated in this run. As can be seen from Fig. 4.26b, the presence of a monotonically increasing σ_w profile results in the accumulation of the vast majority of particles in the least turbulent fluid near the Earth's surface. Run D was identical to Run C except the drift acceleration correction was activated. The impact of the drift acceleration correction is remarkable; in Run D the initially well-mixed particle distribution was maintained throughout the 12-h simulation.

4.8 Summary

The MAD modelling system used in the present study was described in this chapter. More detailed and comprehensive descriptions of the RAMS mesoscale meteorological model, isentropic analysis package, and visualization and analysis package have been given elsewhere. The approach adopted in this chapter was to summarize the main RAMS options and characteristics selected for this study, that is, the particular modelling

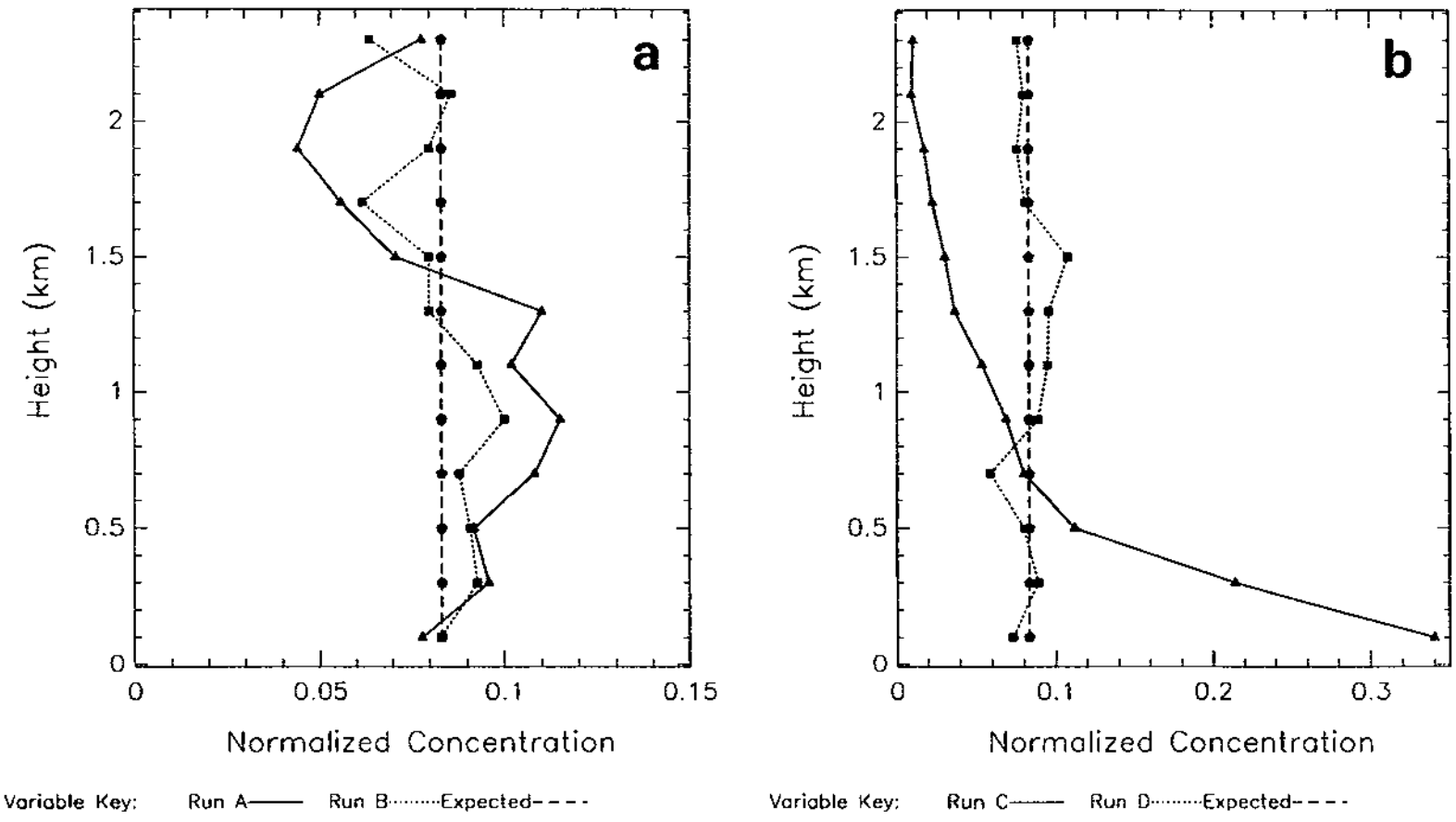

Figure 4.26: MLPDM idealized test results showing vertical distribution of particles normalized by total number of particles after 12 hours of mixing: (a) Run A had homogeneous turbulence, 2000 particles, and *no* in-run shuffling; Run B was the same as Run A except in-run shuffling was activated; (b) Run C had inhomogeneous turbulence, 3000 particles, in-run shuffling, and *no* drift correction; Run D was the same as Run C except the drift velocity correction was activated. The long-dash vertical line indicates the initial particle concentration distribution of 1/12.

system configuration used. These options are summarized in Table 4.1. However, the discussion did include the reasons for the choice of certain options over others and changes and modifications made to the standard modelling system. In addition, one section focussed on the RAMS mesoscale Lagrangian particle dispersion model (MLPDM) since this particular component of the CSU mesoscale dispersion modelling system has not be described in detail elsewhere.

The modelling philosophy followed in this study was to choose the model configuration best suited for simulating physiographically-forced mesoscale circulations and PBL transport under dry, anticyclonic conditions. Accordingly, physical processes such as turbulent diffusion, radiation, and surface exchanges of momentum, heat, and moisture were emphasized while cloud and precipitation processes were not considered. Considerable effort was spent on specifying realistic surface characteristics such as terrain elevation, solar albedo, aerodynamic surface roughness, soil moisture content, and soil texture class. The underlying assumption behind this work was that the model boundary conditions as well as the atmospheric initial state should be as realistic as possible in a real-data simulation.

Performance measures for numerical model evaluation were also discussed in this chapter along with the design and results of preliminary tests and simulations carried out to check model setup and performance before beginning the simulations described in the next two chapters. These preliminary tests helped in the selection of model options for the 'production' runs, permitted existing code and code modifications to be checked, provided a 'synergism/compatibility' check for the particular mix of model options selected, and demonstrated agreement with results from previous studies. The most important preliminary test was a comparison of the predictions from three RAMS configurations against an earlier simulation of the PBL diurnal cycle over the Great Plains made by McNider and Pielke (1981) using one of the RAMS ancestral models.

Chapter 5

GREAT PLAINS TRACER EXPERIMENT SIMULATIONS

The purpose of computing is insight, not numbers.

R.W. Hamming (1973)

This chapter and the next present results from a suite of MAD numerical simulations carried out for the two mesoscale atmospheric tracer experiments described in Chap. 3 using the CSU mesoscale atmospheric dispersion modelling system described in Chap. 4. Results from a suite of ten simulations of varying complexity of the 1980 Great Plains mesoscale tracer experiment are discussed in this chapter while the results of six numerical simulations of the 1983 CAPTEX Release 2 mesoscale tracer experiment are discussed in Chap. 6. These two case studies have added significance in that they constitute the first quantitative evaluation of the present CSU mesoscale dispersion modelling system against mesoscale dispersion data.

5.1 Outline of the Numerical Simulations

The 1980 Great Plains mesoscale tracer experiment was as simple an example of mesoscale atmospheric dispersion as one is likely to encounter in the real world. The prevailing large-scale synoptic pattern, a stagnant high-pressure system covering the central United States, was nearly steady (Figs. 3.2 and 3.3) and approximately barotropic[175] during the period of the tracer experiment. The terrain in this region (Oklahoma,

[175] In the sense that horizontal synoptic-scale temperature gradients were weak.

Kansas, Nebraska, Missouri) is fairly homogeneous. The most significant topographic feature is two-dimensional, that is, the gradual downward slope across the region from west to east (e.g., Fig. 4.13).

A priori, we would expect the diurnal and inertial time scales and the mesoscale pressure gradient induced by the daily heating and cooling of the sloping, approximately two-dimensional, topography to be important factors for the mesoscale dispersion of tracer gas in the Great Plains experiment. Ferber et al. (1981), Policastro et al. (1986a,b), AMS/EPA (1987), and Carhart et al. (1989) have all discussed the importance of the nocturnal Great Plains low-level jet to the northward transport of tracer in this experiment. In addition, smaller three-dimensional topographic features such as the Ozark Plateau, a time-varying synoptic environment, and variations in soil moisture content and other surface characteristics may also affect low-level transport (e.g., Lanicci et al., 1987; Lenschow et al., 1988; McCorcle, 1988; Parish et al., 1988; Fast and McCorcle, 1990).

The suite of six numerical experiments listed in Table 5.1 was devised to investigate the relative contributions of (i) topography, (ii) other surface inhomogeneities, (iii) atmospheric baroclinicity, and (iv) synoptic-scale flow evolution to PBL structure and variability and to mesoscale dispersion in the PBL. Results from a similar but simpler and smaller suite of experiments have been reported by Moran et al. (1987) and McNider et al. (1988) for an Australian case study based on an earlier version of the CSU mesoscale atmospheric dispersion modelling system.

Table 5.1 lists one effectively[176] one-dimensional meteorological experiment, one two-dimensional experiment with topography, and 4 three-dimensional experiments. Additional subexperiments have also been performed for Exps. GP1, GP2, and GP4, for a total of ten subexperiments. The RAMS simulation for Exp. GP1 essentially modelled the time evolution of a vertical atmospheric column (a 'Z' simulation) while the RAMS simulation for Exp. GP2 modelled a west-east vertical cross section with sloping

---

[176] That is, a two-dimensional simulation with horizontally-homogeneous initial state and no topography but longitude-dependent solar heating.

Table 5.1: Distinguishing characteristics for the suite of Great Plains mesoscale tracer experiment RAMS simulations.

Exper. Number	Space Dimen.	Terrain Type	Surface Properties	Type of Initializ.	Initialization Time	Lateral Boundary
GP1a	2D	flat	homogeneous	HHI	80/07/08/12Z	steady
GP1b	2D	flat	homogeneous	HHI	80/07/09/00Z	steady
GP1c	2D	flat	homogeneous	HHI	80/07/08/18Z	steady
GP2a	2D	sloping	homogeneous	HHI	80/07/08/12Z	steady
GP2c	2D	sloping	homogeneous	HHI	80/07/08/18Z	steady
GP3	3D	complex	homogeneous	VI	80/07/09/00Z	steady
GP4a	3D	complex	heterogeneous	VI	80/07/08/12Z	steady
GP4b	3D	complex	heterogeneous	VI	80/07/09/00Z	steady
GP4c	3D	complex	heterogeneous	VI	80/07/08/18Z	steady
GP5	3D	complex	heterogeneous	VI	80/07/08/12Z	time-dependent

topography (an 'XZ' simulation). Both simulations assumed a latitude of 35.24°N, the latitude of the release site at Norman, Oklahoma. Albedo, surface roughness, and soil textural class were assigned values of 0.20, 0.10 m, and USDA Category 4 (silt loam), respectively, in these two runs. The Oklahoma City sounding for July 8, 1980, 1200 GMT was used to initialize runs GP1a and GP2a while other soundings were used for the other Exp. GP1 and GP2 subexperiments (see the discussion in Sec. 5.2). The MLPDM was run in its three-dimensional mode for all ten subexperiments. For the GP1 and GP2 experiments, the gridded two-dimensional RAMS velocity and turbulence fields input to the MLPDM were simply duplicated in the y-direction (cf. p. 438).

These five numerical experiments are arranged in Table 5.1 approximately in order of increasing complexity and realism. The pseudo-one-dimensional RAMS simulations (Exp. GP1) included the contributions of the steady mean synoptic flow, the diurnal

heating cycle, and the inertial oscillation of the nocturnal low-level jet[177] but could not represent the contributions of differential-heating-induced mesoscale pressure gradients and slope flows, horizontal synoptic-scale flow gradients, or synoptic-scale flow evolution. By including changes in terrain height (Exp. GP2), it was possible to include the influence of regional-scale terrain slope, which McNider and Pielke (1981) showed to be capable of modifying the evolution of the low-level flow significantly.

The three-dimensional RAMS simulations permitted the inclusion of complex geographical variations in (i) surface characteristics, including terrain height, soil texture, aerodynamic surface roughness, solar albedo, and sea surface temperature, and in (ii) the synoptic-scale atmospheric fields, including baroclinicity and time changes. There are some natural groupings amongst the 5 three-dimensional subexperiments. Exps. GP3 and GP4b differ only in the homogeneity of the surface properties other than terrain elevation: surface properties are uniform in the former experiment and heterogeneous in the latter, providing a test of the importance of landscape variability. Exps. GP4a, GP4b, and GP4c differ only in their initialization times, thus isolating the contribution of synoptic-scale evolution and mesoscale temporal oscillations. Exp. GP5 can be thought of as a 'boundary 4DDA' simulation since it used time-dependent lateral boundary conditions based on observations while the other three-dimensional simulations were pure[178] 'forecast' simulations and only used observed meteorology in their initialization stage. Exp. GP4a and Exp. GP5 constitute another natural pairing, since they are identical except for the time-dependence of the lateral boundary conditions.

There are natural groupings between the two- and three-dimensional subexperiments as well. Exps. GP1b and GP3 are related by initialization time and surface properties other than terrain elevation; differences between these two subexperiments will arise

---

[177] At 35.24°N, the inertial period is 20.7 h, quite close to the 24-h diurnal period.

[178] However, some were purer than others. In order to model the tracer experiment in a true forecast mode, the RAMS initial fields must be based on an observation time prior to the time of the tracer release. This point will be mentioned again later in the chapter.

primarily from slope effects and baroclinicity. Similarly, the GP1 and GP4, and GP2 and GP4, subexperiments can be paired by initialization time, though differing in their treatment of landscape variability and atmospheric baroclinicity. Finally, subexperiments GP1a, GP2a, GP4a, and GP5 are linked by their initialization time in a simulation 'chain' of increasing complexity and realism. Subexperiments GP1b, GP3, and GP4b, and GP1c, GP2c, and GP4c form similar chains.

Together, these five experiments allow examination of the impact of increasing realism in the treatment of the regional-scale flow field from steady barotropic to steady baroclinic to time-dependent baroclinic conditions and in the treatment of regional-scale physiography from an idealized flat homogeneous surface to a realistic heterogeneous one. This is not an exhaustive suite of experiments for the evaluation of the influences of terrain slope, landscape variability, atmospheric baroclinicity, and large-scale flow pattern evolution on mesoscale dispersion for this case but it should be a revealing suite. The chapter closes with the discussion of the results of an additional MLPDM experiment to investigate a hypothesis for the cause of the secondary tracer cloud observed along the 600-km arc well after the passage of the primary cloud (see Fig. 3.10).

5.2 Results of the One-Dimensional Experiment

Table 5.1 lists 2 two-dimensional experiments, Exps. GP1 and GP2. Exp. GP1, however, was essentially a one-dimensional simulation since it was initialized with a horizontally homogeneous atmosphere over a flat, uniform surface. While Exp. GP1 might appear extremely idealized as compared to the three-dimensional Great Plains experiments listed in Table 5.1, it exhibits fundamental flow structures and behaviour found in the other experiments as well. Moreover, the temporal evolution of the regional-scale flow is most easily seen for this case. It is thus worthwhile examining the meteorological and concentration fields for this experiment in some detail in order to see the process of mesoscale dispersion in its most basic form. We will then be able to see how mesoscale dispersion is modified by other factors in the more complicated experiments to follow.

5.2.1 One-dimensional-experiment meteorological simulations

Table 5.1 lists only a single pseudo-one-dimensional experiment, Exp. GP1. However, three RAMS pseudo-one-dimensional simulations were actually run, differing only in their starting times and in the initial atmospheric profiles selected. The original reason for carrying out two of these GP1 subexperiments was that there was some leeway and hence uncertainty in the choice of initial conditions and starting time for the RAMS meteorological simulation. Oklahoma City (OKC) soundings were available for July 8, 1980 at 1200 GMT and July 9, 1980 at 0000 GMT, that is, 7 h before the release began and 2 h after it ended. RAMS could be initialized with either sounding. The tracer release took place during the mid afternoon (1900–2200 GMT) so that the greater portion of the transport to the 600-km sampler arc occurred during the evening and nighttime hours. This suggested that the evening (0000 GMT) sounding might be preferable since it should be representative of actual transport conditions. However, initializing RAMS with the July 9 0000 GMT sounding (Exp. GP1b) meant starting the model on July 8 at 0000 GMT and running 12 h longer, possibly resulting in larger forecast errors and definitely applying the assumption of synoptic stationarity for a longer period. It thus seemed best simply to try both possibilities.

As it turned out, and as will be shown shortly, the MLPDM dispersion simulations were very sensitive to the sounding used in the RAMS initialization. After determining the probable reason for this sensitivity, *both* observed soundings were used to create a composite third 'sounding' (Exp. GP1c).

One-dimensional-experiment meteorological model configuration

The RAMS simulations for Exps. GP1 and GP2 had to be configured slightly differently from the three-dimensional experiments. The primary difference was in the value specified for RLAT, the latitude of the lower lefthand corner of the grid. A value of 35.24°N, the latitude of the release site at Norman, was used for the two-dimensional simulations vs. the value of 30.0°N used for the three-dimensional simulations. All eight RAMS simulations used 29 vertical levels, 41 east-west grid points with 0.5° longitude

spacing, and Klemp-Lilly lateral boundary conditions (see Sec. 4.2). Exp. GP1 could have been run with only five horizontal grid points, cyclic lateral boundary conditions, and no longitudinal variation of solar heating because it was in essence a one-dimensional simulation, but keeping the RAMS model setup as close to that for Exp. GP2 as possible made comparison of results and attribution of differences more straightforward and the MLPDM setup simpler. The surface height for Exp. GP1 was set to a constant value of 392 m ASL, the OKC station height.

Exp. GP1a employed the OKC 1200 GMT sounding from July 8, 1980 and a start time[179] of 0530 LST (0600 CST/1200 GMT). Fig. 4.9a shows this sounding and Table 4.2 lists its representation by the RAMS 29 vertical levels. Exp. GP1b used the OKC 0000 GMT sounding from July 9, 1980 and a start time of 1730 LST on July 7 (or 0000 GMT, July 8). The wind profile from this sounding is shown in Fig. 5.5. Exp. GP1c used a composite OKC sounding, nominally for 1800 GMT on July 8, 1980, and a start time of 0600 LST. The construction of this sounding will be described shortly.

One-dimensional-experiment meteorological results

Fig. 5.1 shows time–height cross sections of four aspects of the GP1a wind profile, namely, horizontal wind speed, wind direction, u component, and v component, for the first 48 h of the simulation. Fig. 5.2a shows the corresponding wind-vector time-height cross section. Sunrise and sunset times for July 8 at Oklahoma City (0622 CDT and 2048 CDT, respectively) are indicated on each panel. The upward growth of the convective PBL and the accompanying decrease in vertical shear due to vertical mixing during the daytime is evident in Fig. 5.1a as is the development of the nocturnal low-level jet on two successive nights. The simulated jet maximum is located at a height of about

---

[179] Interpreting RAMS model times in terms of real-world times is a bit tricky when the modelling domain is large enough to straddle several time zones. Model start time is in terms of a local solar time and hence has to apply to a reference longitude. In the case of Version 2A of RAMS, this reference longitude is the western boundary of the model domain. The western boundary chosen for the Great Plains simulations was 105°W, which is located in the Mountain time zone (Fig. 4.1). Tracer release times and sampling times, on the other hand, applied to the Central time zone in the middle of the model domain. To allow for this fact, the model start time was set to be roughly equivalent to 0600 CST/0700 CDT.

500 m AGL and has a peak value of 15.5 $m\,s^{-1}$. The role that the inertial oscillation in the decoupled nighttime residual layer plays in the development of the low-level jet is suggested by the nighttime variation in wind direction and in the u- and v-components (Figs. 5.1b-d). Recall that the inertial period[180] at this latitude (35.24°N) is 20.7 h. It can also be seen from Fig. 5.1b that the mean transport direction is southerly to south-southwesterly during the day but that strong directional shear as well as speed shear (Fig. 5.1a) occurs at night, with low-level backing[181] and upper-level veering. This diurnal variation in transport direction is also evident in the parcel trajectories plotted in Fig. 5.3.

Figs. 5.2b-d portray corresponding time-height cross sections of potential temperature, water-vapour mixing ratio, and gradient Richardson number for Exp. GP1a for the same 48-h period. Of particular interest in these three panels is the formation of a very deep daytime boundary layer (about 3 km deep) due to the very strong heating for this summertime drought/heatwave case. Comparison of Fig. 5.2b with Fig. 5.1a also shows the close relationship between the location of the low-level jet 'nose' and the top of the nocturnal stable layer.

5.2.2 One-dimensional-experiment mesoscale tracer transport

As a first step in the investigation of mesoscale dispersion for this Great Plains case, the mesoscale Lagrangian particle dispersion model or MLPDM was run in a 'trajectory' mode to calculate grid-scale trajectories at different elevations. These trajectories show what difference the use of the different RAMS wind fields calculated in the Exp. GP1a and GP1b simulations makes to mesoscale transport by the resolved wind field.

---

[180] Or one-half pendulum day.

[181] That is, counter-clockwise rotation.

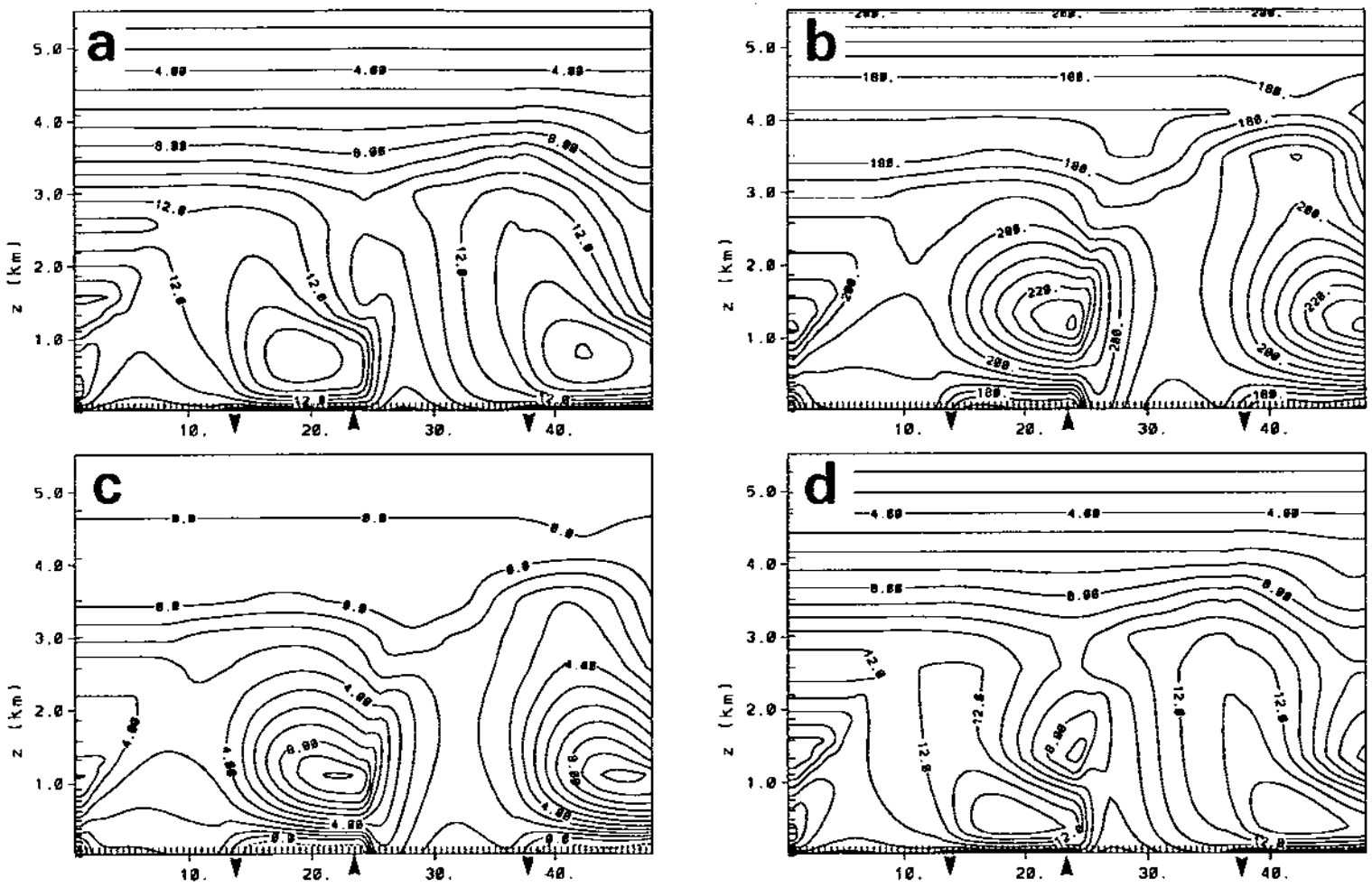

Figure 5.1: Four views of the time evolution of the Exp. GP1a vertical wind profile over the first 48 h of simulation starting at 0600 LST: (a) wind speed; (b) wind direction; (c) u-component; and (d) v-component. Contour intervals are 1 $\mathrm{m\,s^{-1}}$ in panels (a), (c), and (d) and 5° in panel (b). The meteorological convention for wind direction has been used with 0° corresponding to a north wind, 90° corresponding to an east wind, etc. The 'up' and 'down' arrowheads indicate sunrise and sunset, respectively.

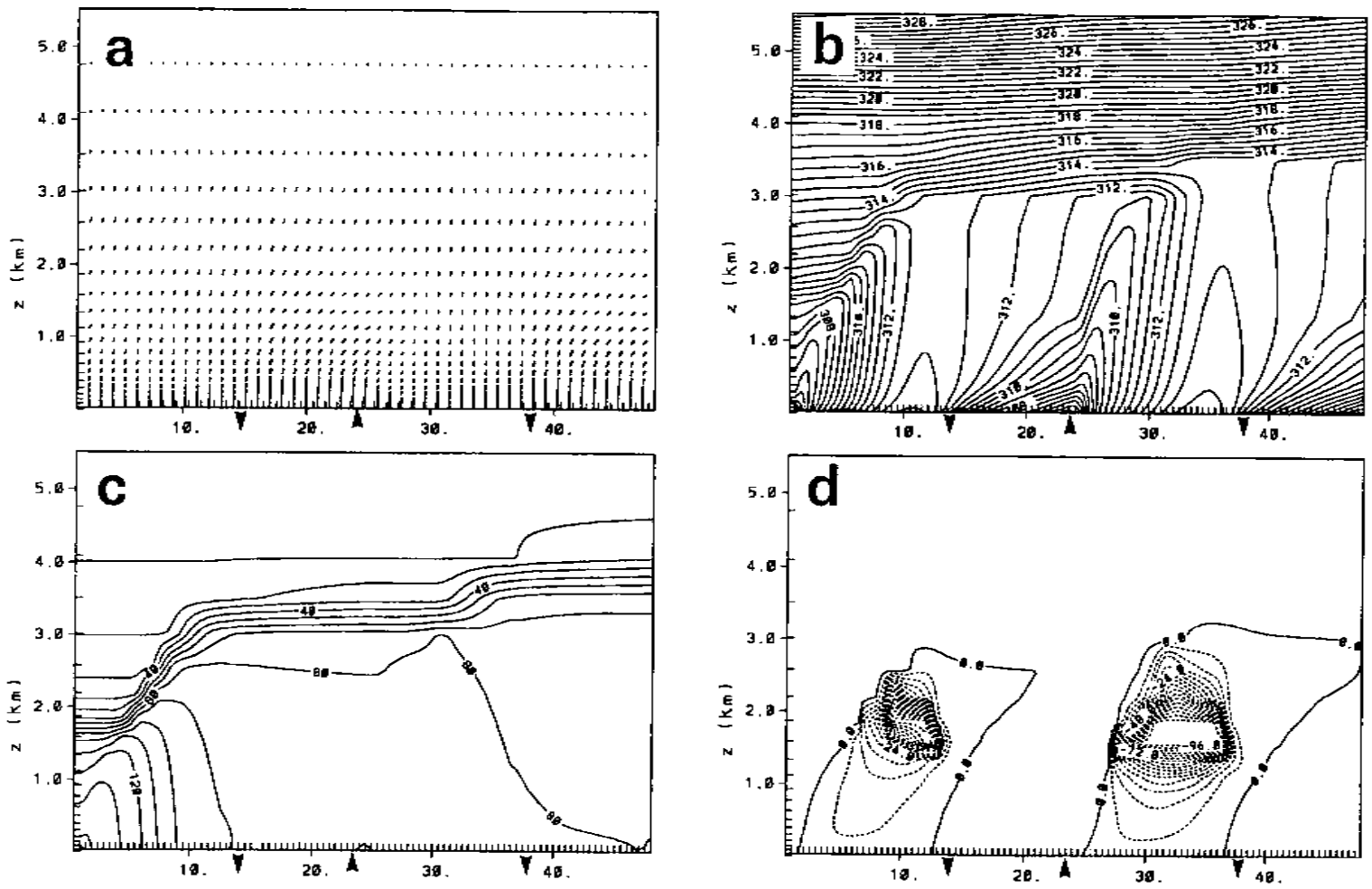

Figure 5.2: Same as Fig. 5.1 except for (a) wind vectors, (b) potential temperature, (c) water-vapour mixing ratio, and (d) gradient Richardson number. Contour intervals in panels (b), (c), and (d) are 0.5 K, 0.001 kg kg^{-1}, and 2, respectively. The longest wind vector corresponds to a wind speed of 20 m s^{-1}. An upward-pointing wind vector denotes a south wind, a rightward-pointing wind vector denotes a west wind, etc. The 'up' and 'down' arrowheads indicate sunrise and sunset, respectively.

One-dimensional-experiment MLPDM setup

The overall design of the CSU MLPDM and its various input parameters were described in Sec. 4.4. Only specific details relevant to the Great Plains experiment simulations will be mentioned here.

In the trajectory mode, the MLPDM turbulence parameterization described in Sec. 4.4 is turned off and particles are advected by the time-varying grid-scale RAMS wind fields alone. RAMS wind fields were available every 0.5 h and linear interpolation was employed in time to ensure a gradual transition between consecutive wind fields. The MLPDM time step was set to a value of 60 s for calculating these 'grid-scale' trajectories. The role of vertical wind shear was investigated by releasing five particles in a vertical column above the release site at Norman, Oklahoma at five different heights above ground level: 50 m, 293 m, 686 m, 1334 m, and 2379 m. The particle release time was selected to be 1900 GMT (1400 CDT) on July 8, 1980 to coincide with the start of the Great Plains PMCH tracer release.

One-dimensional-experiment grid-scale trajectories

The two resulting sets of grid-scale trajectories are shown in Figs. 5.3a-b. The influence of vertical wind shear is evident in both panels, with the trajectories rotating clockwise with height (with the exception of the topmost trajectory in Fig. 5.3a) just as the winds do in a classical Northern Hemisphere Ekman spiral (e.g., Holton, 1972). However, the paths of the two sets of trajectories are markedly different: all of the GP1a trajectories cross the 100-km and 600-km sampling arcs while only one of the GP1b trajectories does. This large difference was unexpected since the synoptic environment sampled by the GP1a and GP1b soundings was quasi-stationary. What then might be the source of the difference?

One possibility is the time-dependent ageostrophic component introduced by an inertial oscillation. As can be seen from Fig. 1.3, boundary-layer winds sampled at different times of day in the presence of an inertial oscillation can have quite different directions and speeds and will not be representative of the geostrophic background flow at *any* time

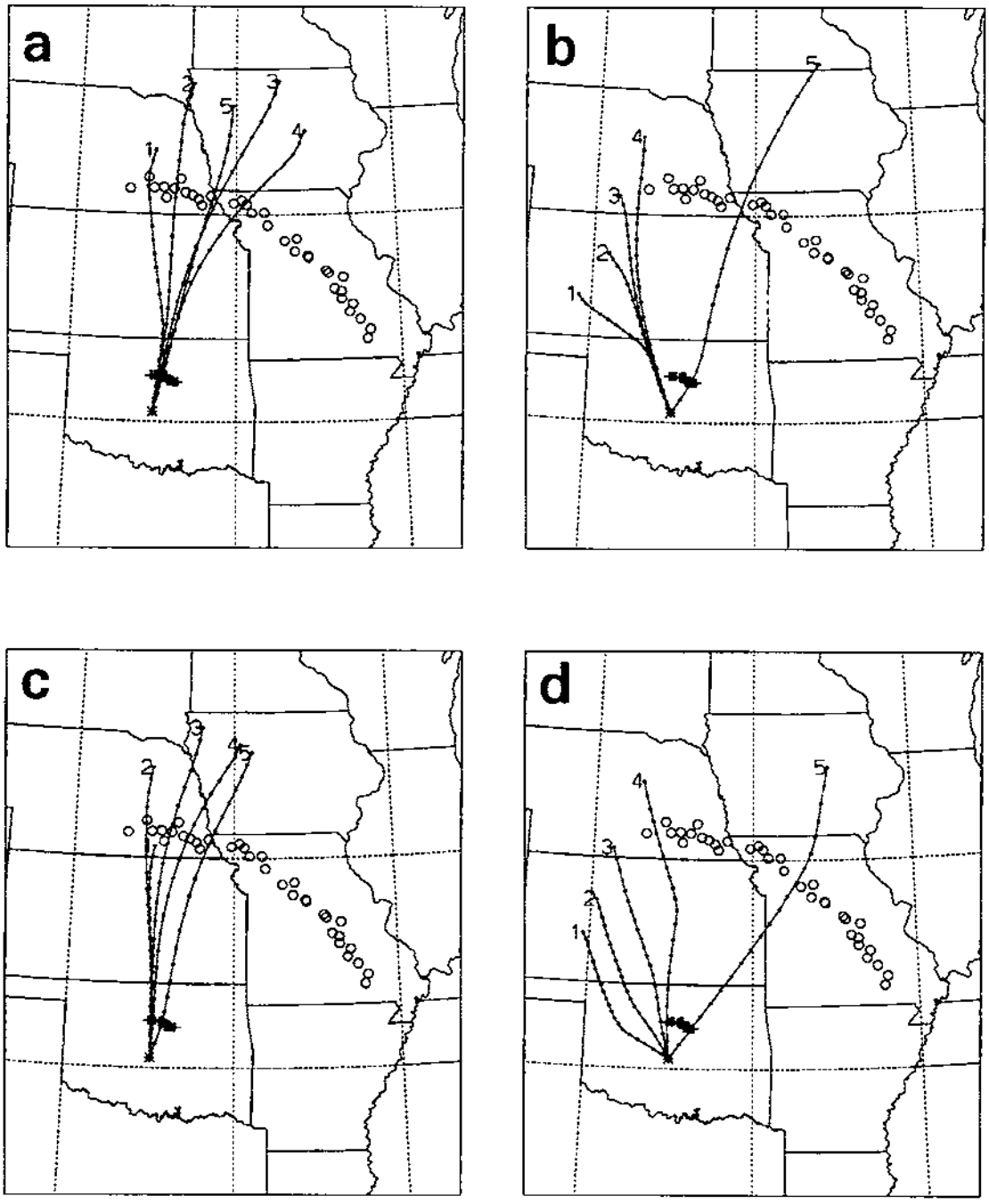

Figure 5.3: Plan view of four sets of three-dimensional grid-scale trajectories followed for 20 h at five different heights: (a) Exp. GP1a wind fields, 1900 GMT release; (b) Exp. GP1b wind fields, 1900 GMT release; (c) Exp. GP1c wind fields, 1900 GMT release; and (d) Exp. GP1b wind fields, 0700 GMT release. The small filled squares mark the hourly trajectory positions. Trajectory endpoint labels '1', '2', '3', '4', and '5' indicate the five release heights 50 m, 293 m, 686 m, 1334 m, and 2379 m AGL, respectively. Plus signs mark the locations of 100-km-arc sampling stations while open circles mark 600-km-arc station locations. The release site is indicated by the asterisk. The domain shown covers the range 32–45°N and 102–88°W; parallels at 35°N and 40°N and meridians at 90°W, 95°W, and 100°W are marked by short dashed lines. The map is a Lambert conformal conical projection with one standard parallel (at 38.5°N).

of day. Moreover, as shown in Fig. 5.4, the experimental domain coincides with a region known to have a high frequency of strong nocturnal low-level jets. However, a high climatological frequency is no guarantee of the presence of a strong inertial oscillation on a particular day. Accordingly, Fig. 5.5, a time-series plot of low-level wind profiles measured at the Oklahoma City upper-air station, was prepared for the experimental period. The wind profiles in this figure do in fact exhibit a significant low-level diurnal oscillation like the one shown in Fig. 1.3 for three days running. This suggests that each of these profiles does have a significant oscillatory ageostrophic component. However, the vertical wind profile used to initialize the RAMS wind fields in a horizontally-homogeneous initialization should be stationary and geostrophic. It is not so surprising, then, that the use of two of the upper-air profiles shown in Fig. 5.5 to initialize RAMS for the GP1a and GP1b simulations should result in such different trajectories. Even though the two soundings were taken only twelve hours apart, they sampled opposite phases of the ageostrophic oscillation.

How should the RAMS meteorological model be initialized for the two-dimensional Great Plains simulations, then, if individual soundings are not representative of the synoptic-scale flow? Consider Fig. 1.3 again. By inspection it would appear that an average of any two horizontal-wind vectors at one level which were measured 12 h apart would give a good estimate of the geostrophic wind at that level. In effect, the inertial oscillation is filtered out by averaging the wind fields at opposite phases of the oscillation. Clearly, this approach assumes an inertial period of approximately 24 h, but any location in the latitude band from 24° to 41° will have an inertial period in the 18–30 h range. Synopticians have used this same technique to filter out diurnal variations in meteorological case studies (e.g., Maddox, 1980).

Based on this approach, a composite Oklahoma City sounding was constructed from the July 8 1200 GMT sounding by averaging the horizontal winds in the first 3 km AGL from this sounding with those from the July 9 0000 GMT sounding. A value of 3 km was chosen because it is a bit deeper than the maximum PBL depth of 2630 m

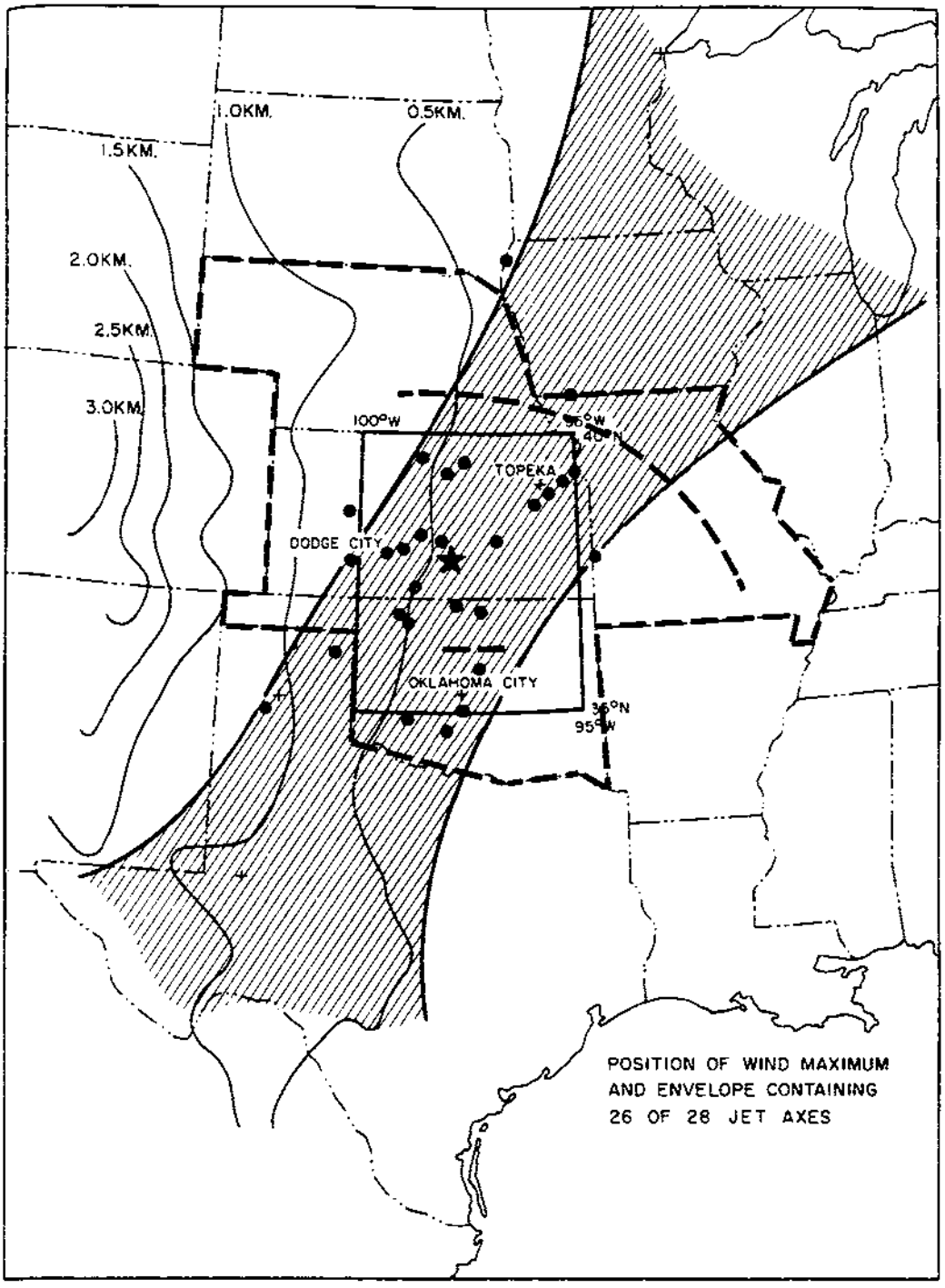

Figure 5.4: Position of jet core for 28 cases of very strong and widespread low-level jets over the Great Plains during the period 1959-1960. The shaded area includes the jet axis in 26 of the cases. The four-state Great Plains tracer experiment domain and the location of the 100-km and 600-km arcs are also marked by dashed lines (adapted from Bonner, 1968).

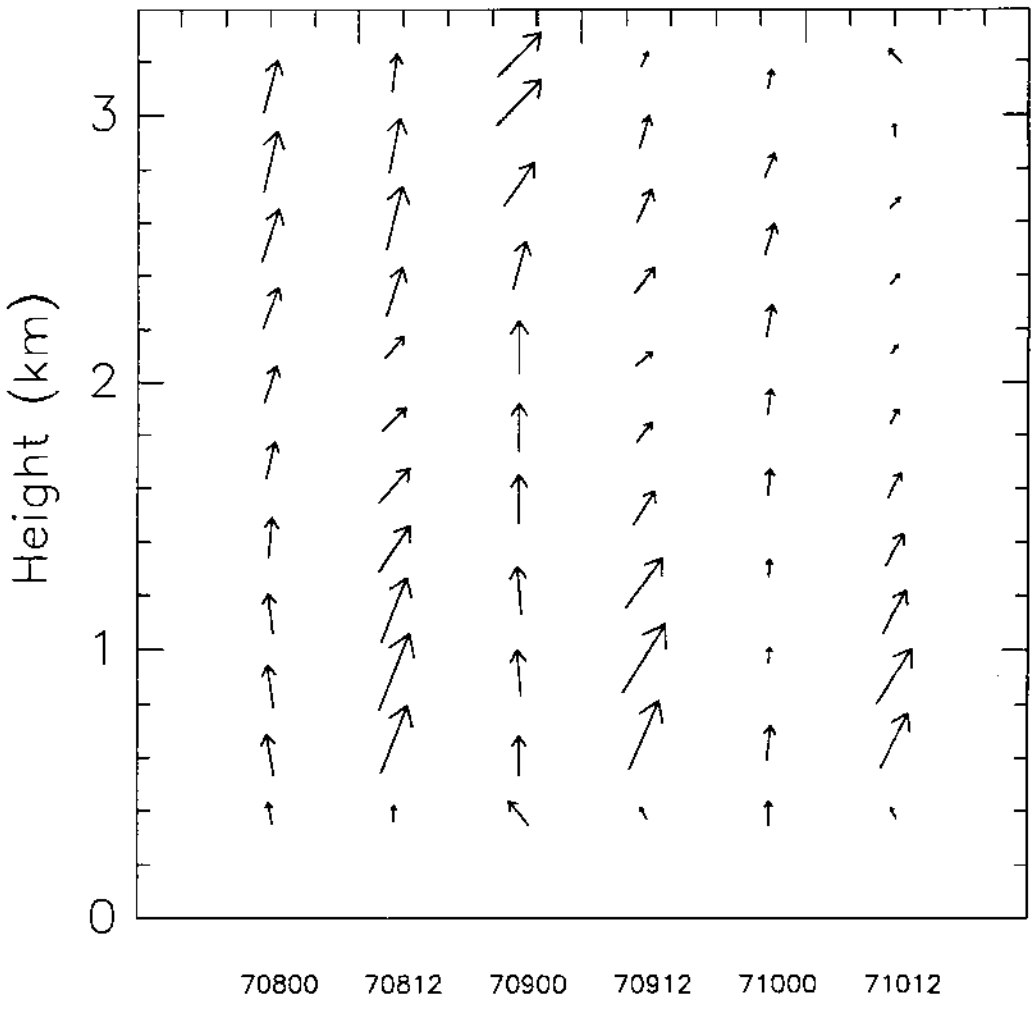

Figure 5.5: Time series of six consecutive 12-hourly Oklahoma City horizontal wind profiles for the first 3000 m AGL for the period July 8–10, 1980. A wind vector pointing upwards corresponds to a south wind, a wind vector pointing to the right corresponds to a west wind, etc. Vector length is linearly dependent on wind speed; the highest wind speed shown is 19 $m\,s^{-1}$.

calculated for this period (Fig. 3.9) and hence is an upper bound to the depth of the layer in which an ageostrophic perturbation due to surface friction and upslope heating and a resultant inertial oscillation might be expected. This composite sounding was then used to initialize RAMS for Exp. GP1c; the model starting time was 0600 LST, the same as for the Exp. GP1a RAMS simulation. The mean trajectories calculated for this third pseudo-one-dimensional subexperiment are shown in Fig. 5.3c. This set of trajectories does lie between the other two sets (Fig. 5.3a-b) as expected but is much closer to the morning sounding (1200 GMT) set than to the evening one. There is also less endpoint separation of the GP1c trajectories compared to the other two sets, which indicates less vertical shear in this subexperiment.

Fig. 5.3d shows the impact of a different release time. This second set of Exp. GP1b grid-scale trajectories was calculated for a nighttime release at 0700 GMT (0200 CDT), 12 h earlier than the daytime trajectory release at 1900 GMT (1400 CDT). Directional changes with transport time seen in Fig. 5.3d are essentially reversed from those in Fig. 5.3b. Because the initial transport occurs at night under stable conditions in Fig. 5.3d, vertical shear is large and the trajectories travel in different directions at the outset. Later, as daytime vertical mixing reduces wind shear and effectively couples different vertical levels together, the trajectories move in similar directions. Just the opposite is true in Fig. 5.3b.

5.2.3 One-dimensional-experiment mesoscale tracer dispersion

Grid-scale trajectories provide valuable information about mean transport direction and speed at different levels, and, as will be shown shortly, grid-scale trajectory 'envelopes' created by travel-time isochrons can describe mesoscale differential advection and cloud distortion processes to first order. Moreover, grid-scale trajectories have the advantage of being relatively quick and easy to compute. However, Lagrangian particle dispersion model simulations, though much more computationally intensive when carried out for large numbers of virtual tracer particles, (a) describe interactions between wind shear and turbulent diffusion more realistically and (b) allow quantitative estimates to be made of

the three-dimensional tracer concentration field. This subsection describes and compares the concentration fields predicted by the CSU mesoscale Lagrangian particle dispersion model (MLPDM) based on the RAMS pseudo-one-dimensional wind, temperature, and turbulence fields for Exps. GP1a and GP1c against concentration observations from the Great Plains experiment.

MLPDM setup

RAMS meteorological data were available for every 0.5 h of RAMS simulation time. A fixed 15 s time step was used in the MLPDM runs. Five particles were released every MLPDM time step from a point one meter above ground level at 35.24°N, 97.46°W over a three-hour period (1900–2200 GMT) beginning 8 h after the start of the Exp. GP1 RAMS meteorological simulations. A total of 3600 tracer particles were released in each MLPDM simulation. Each particle was assigned a mass of 53.33 g of PMCH for a total release of 192 kg of PMCH tracer. The full three-dimensional turbulent diffusion parameterization of the MLPDM, including the drift acceleration correction, was used. Initial particle velocity perturbations were assumed to be zero. Particles were tracked until July 9 at 2000 GMT, 25 h after the start of the release, and particle positions were archived after every 15 minutes of MLPDM simulation.

Grid-scale trajectory envelopes and particle clouds

A natural extension to the sets of grid-scale trajectories shown in Fig. 5.3 is to release a second set of five particles at the time corrresponding to the *end* of the tracer release, thus bracketing the release period. The two sets of trajectories together should then give a rough idea of the mesoscale mean transport *and* the differential advection due to vertical shear acting on the leading and trailing edges of the tracer cloud. This first-order estimate of the tracer cloud position, size, and shape resulting from transport and deformation due to the grid-scale flow field can be presented graphically by projecting the two sets of grid-scale trajectories onto either an XY, XZ, or YZ plane and then drawing isochrons of travel time for a given observation time. Haagenson and Morris (1974) used

a somewhat similar approach, based on horizontal streaklines, to forecast the behaviour of the St. Louis urban plume at downwind distances as large as 120 km from the city center.

Clearly, this method neglects subgrid-scale advection (i.e., turbulent diffusion) and can only approximate the actual projected cloud boundaries. It is of interest, though, to see how well this technique performs since its adequacy or inadequacy will reflect the relative contributions of grid-scale and subgrid-scale transport to mesoscale dispersion.

Figs. 5.6, 5.7, and 5.8 show XY, XZ, and YZ projections, respectively, of grid-scale horizontal trajectories superimposed on (i) travel-time isochrons (i.e., trajectory envelopes) and (ii) particle ensembles or particle clouds for Exp. GP2a (described in Sec. 5.3). Two observing times are considered, one at night, 10 h after the start of the release, and one in the morning, 19 h after the start of the release. In these examples, the trajectory envelopes match[182] the boundaries of the particle cloud quite closely both at night and, with the proper interpretation, in the morning. The interpretation for the growing CBL in the morning is that the horizontal extremes of the trajectory envelopes bound the surface projection of the particle cloud but the envelopes themselves may lie within the particle cloud as a result of vertical subgrid-scale mixing.

Figs. 5.7 and 5.8 suggest the important role of mesoscale deformation in determining the overall *shape* of the tracer cloud when significant vertical shear is present. Many of the Lagrangian puff LRTAP models discussed in Sec. 2.4 assume a pollutant puff to be an upright cylinder expanding uniformly radially about the puff's center of mass. Such an idealized conceptual model is inconsistent with the tilted horseshoe- or banana-shaped cloud evident in these figures[183]. It is also clear from Figs. 5.7a-b that turbulent diffusion does contribute to overall cloud expansion; the particle cloud extends noticeably beyond the bounds of the trajectory envelope in these panels. However, the contribution of

---

[182] Note that some particles appear to be located beneath the Earth's surface in Fig. 5.8 because these particles are close to ground level over the lower terrain east of the meridian selected for this south-north cross section.

[183] And also in the CAPTEX simulations – see, for example, Fig. 6.4.

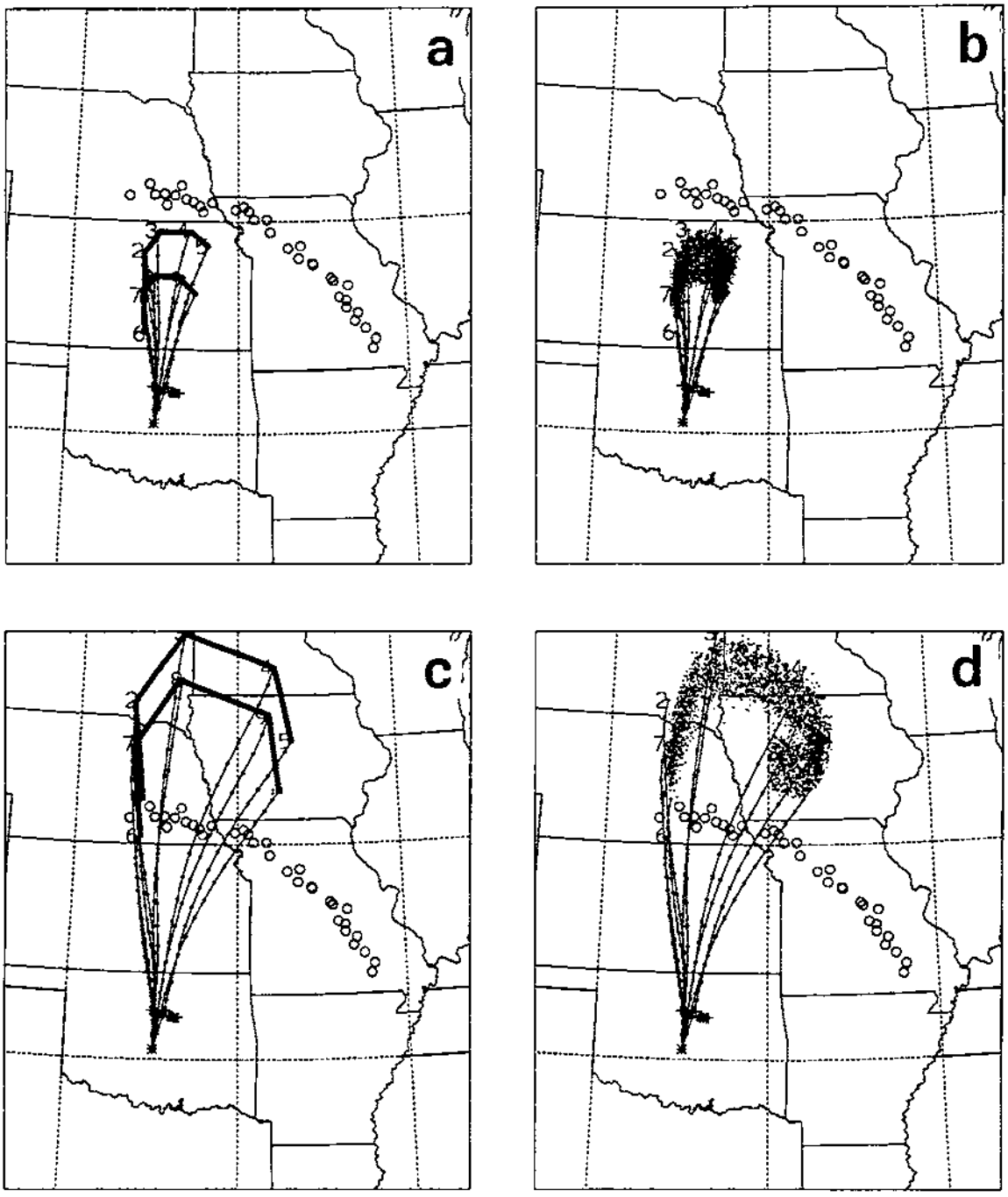

Figure 5.6: XY projections of Exp. GP2a three-dimensional grid-scale trajectories for two release times, 1900 GMT and 2200 GMT, overlaid with travel-time isochrons (thick black lines) or with particle ensembles (3600 particles) at two observing times: (a) travel-time isochrons, 0500 GMT; (b) particle cloud, 0500 GMT; (c) travel-time isochrons, 1400 GMT; (d) particle cloud, 1400 GMT. 0500 GMT corresponds to travel times of 10 h and 7 h for the cloud leading and trailing edges; 1400 GMT corresponds to travel times of 19 h and 16 h for the cloud leading and trailing edges. The small filled squares mark the hourly trajectory positions. Trajectory endpoint labels '1' and '6', '2' and '7', '3' and '8', '4' and '9', and '5' and '10' indicate the five release heights 50 m, 293 m, 686 m, 1334 m, and 2379 m AGL, respectively, for the two release times.

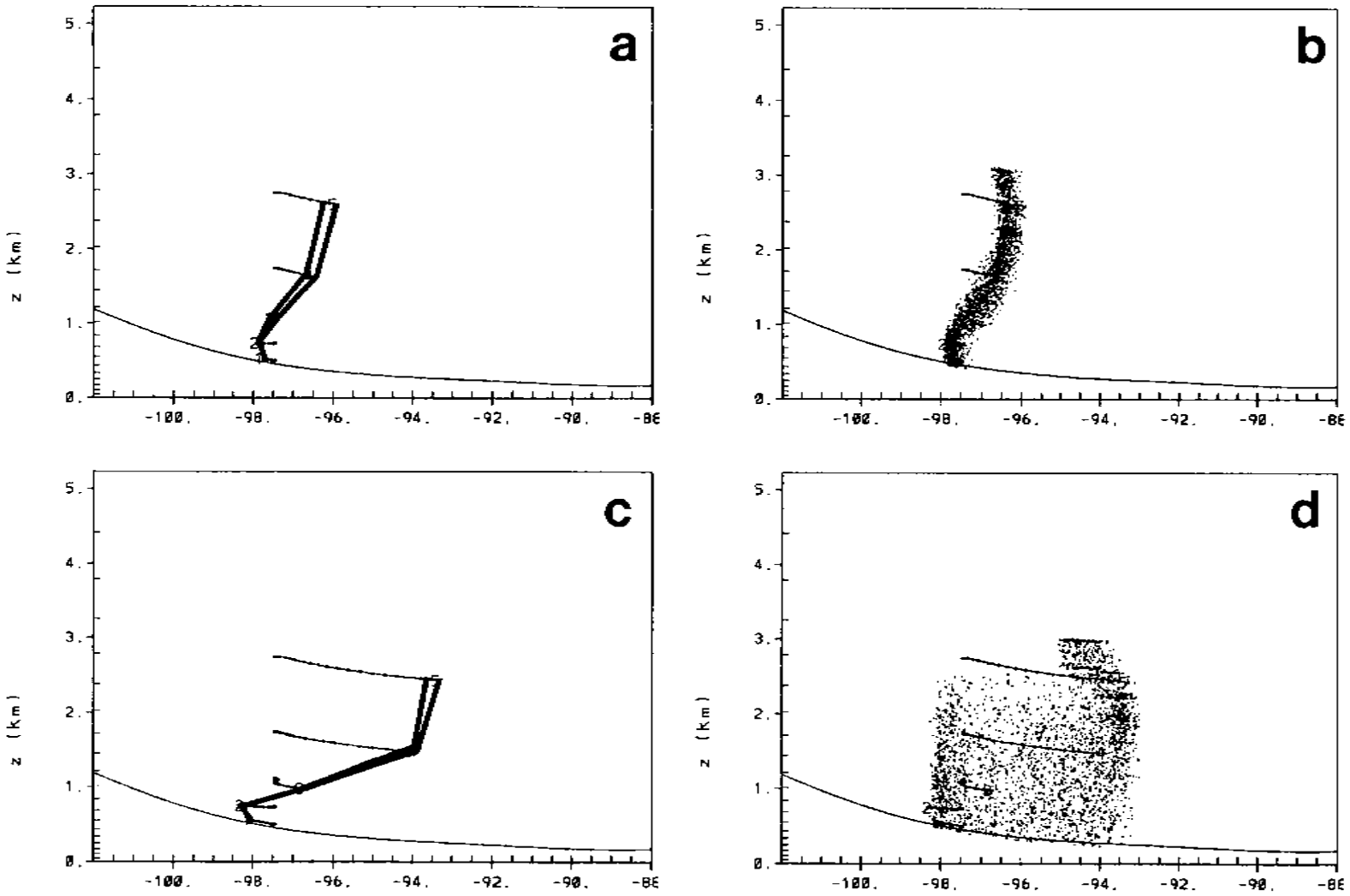

Figure 5.7: Same as Fig. 5.6 except for an XZ projection looking northwards. Topography cross section is the same for all latitudes for this two-dimensional meteorological simulation.

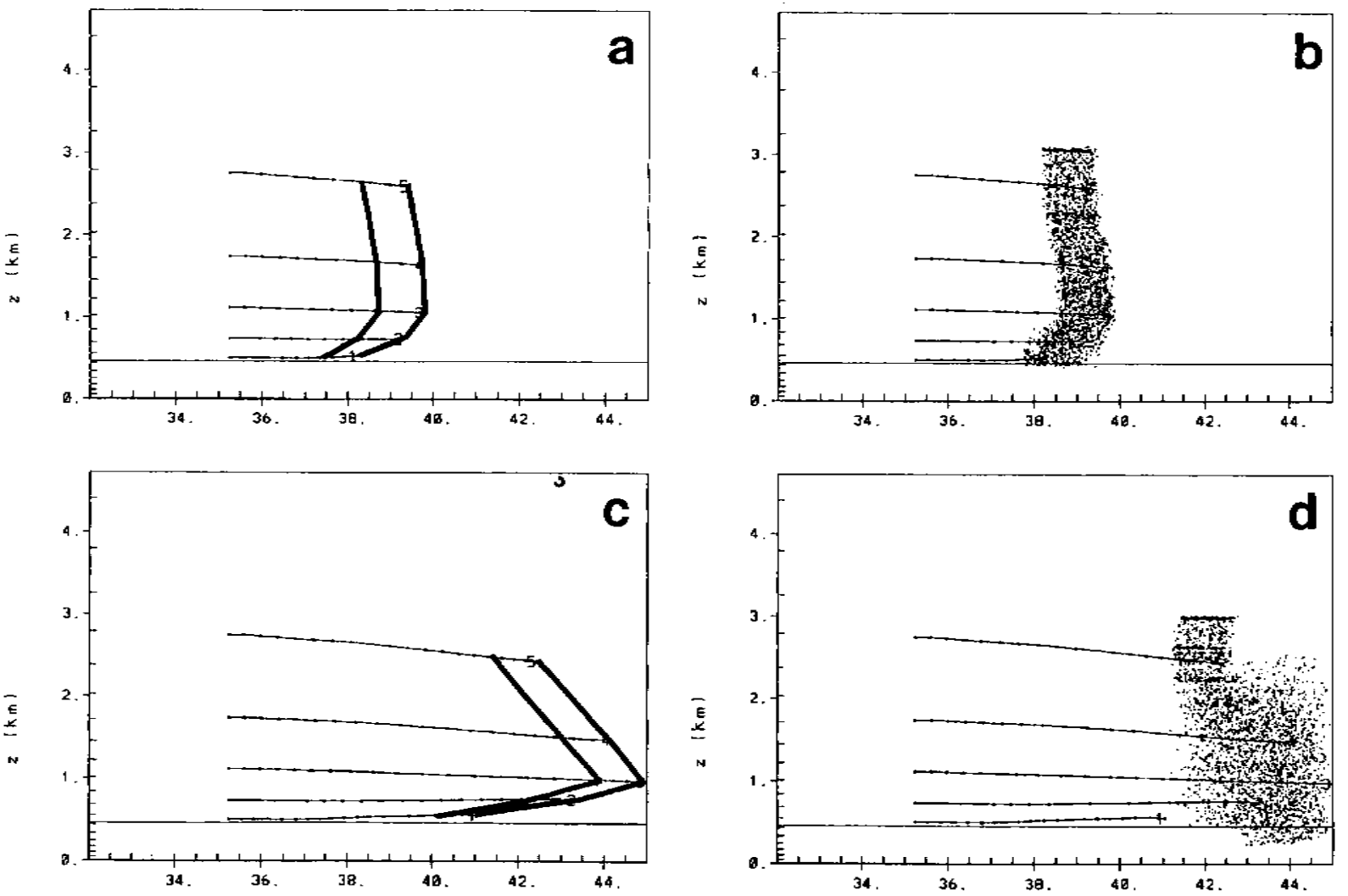

Figure 5.8: Same as Fig. 5.6 except for a YZ projection looking westwards. Topography slice is taken along 97.5°.

turbulent diffusion to cloud expansion is less pronounced in the other figures of this series, suggesting that *grid-scale* transport and deformation plays a larger role in mesoscale dispersion, at least in this shear case. It is also worth noting that the upward growth of the morning CBL can be seen in Figs. 5.7d and 5.8d, where only a small column of tracer still remains in the quiescent residual layer above the top of the growing CBL. This material too should be entrained into the CBL as the latter continues to deepen.

Although the trajectory envelopes predicted the tracer cloud position, size, and shape remarkably well in this particular case, there are situations where this method should not work as well. For example, it was implicitly assumed that the tracer substance was well-mixed throughout the vertical layer in which the five particles were released at the time of release. This would not be the case for a release under stable conditions. Resolved downstream recirculation zones, e.g., a sea-breeze circulation, will pose a problem since grid-scale trajectories will not cross a grid-scale dividing streamline even though subgrid-scale motions might advect a particle across such a grid-scale internal boundary. Subgrid-scale circulations, such as an unresolved sea-breeze system, that might retard tracer transport will not be accounted for, nor will such surface trapping processes as canopy decoupling or stomatal uptake be represented (e.g., Sec. 5.5). Nonetheless, trajectory envelopes can be used to estimate the behaviour of an MLPDM particle cloud to first order in many cases. This method will be used a number of times in this chapter and again in Chap. 6.

Concentration analysis grid

The surface concentration analysis grid (CAG) used to estimate PMCH concentrations from particle positions consisted of a $41 \times 31 \times 40$ latitude-longitude mesh. However, two different CAGs were used. CAG horizontal grid increments were set to 0.05° of longitude (about 4.5 km at 36°N) and 0.0625° of latitude (about 6.9 km) for the 100-km sampler arc and to 0.2° of longitude (about 17.0 km at 40°N) and 0.25° of

latitude (about 27.8 km) for the 600-km arc[184]. CAG vertical grid increments were set to $0.5\Delta z^*$, where Δz^* is a RAMS vertical grid increment. A CAG sampling-volume depth of 1842 m (28 vertical CAG grid increments) was used for the 100-km arc while one of 378 m (12 vertical increments) was used for the 600-km arc. Figs. 5.9a–b show plan views[185] of the two CAGs while Figs. 5.9c–d show side views of the larger CAG.

The reason for the difference in grid-cell size between the two CAGs was simply to enclose the portion of the domain which was of interest for each arc entirely within the CAG while keeping the horizontal grid size as small as possible to maximize resolution. The difference in depth between the two CAGs arose from a desire to specify as deep a sampling volume as possible while enclosing only a well-mixed surface-based layer in which all particles could be expected to contribute to the surface concentration. The greater the box depth, the more particles sampled, and thus the smaller the expected sampling fluctuations and the greater the statistical significance of the concentration estimates. For the 100-km sampler arc, concentration measurements were taken in the late afternoon in a deep and presumably well-mixed boundary layer. However, in the case of the 600-km arc, the first two sampling periods took place from 0200–0500 CST and from 0500–0800 CST. Sunrise occurred at 0522 CST (p. 415) so that the depth of the well-mixed surface layer for these two periods depended more on shear instabilities and mechanical mixing below the nose of the nocturnal low-level jet than on convective mixing. Surface concentrations after 0800 CST (1400 GMT), on the other hand, were likely also influenced by convective mix-down (i.e., fumigation) of tracer from the elevated residual layer.

Fig. 5.10 shows the effect of choosing different CAG depths on the Exp. GP1c surface *exposure* pattern calculated from 100 files of instantaneous particle positions for a 25-h

---

[184] In comparison, the average station spacing was approximately 5 km on the 100-km arc and 21.5 km on the 600-km arc.

[185] Note that individual sampling volumes are in fact true rectangular boxes. The diagonal lines in these figures are associated with the contouring routine used to plot concentrations; this routine (CONRAN) was designed for use with data points scattered randomly in space and uses data-point triangles to first interpolate data values to a regular grid.

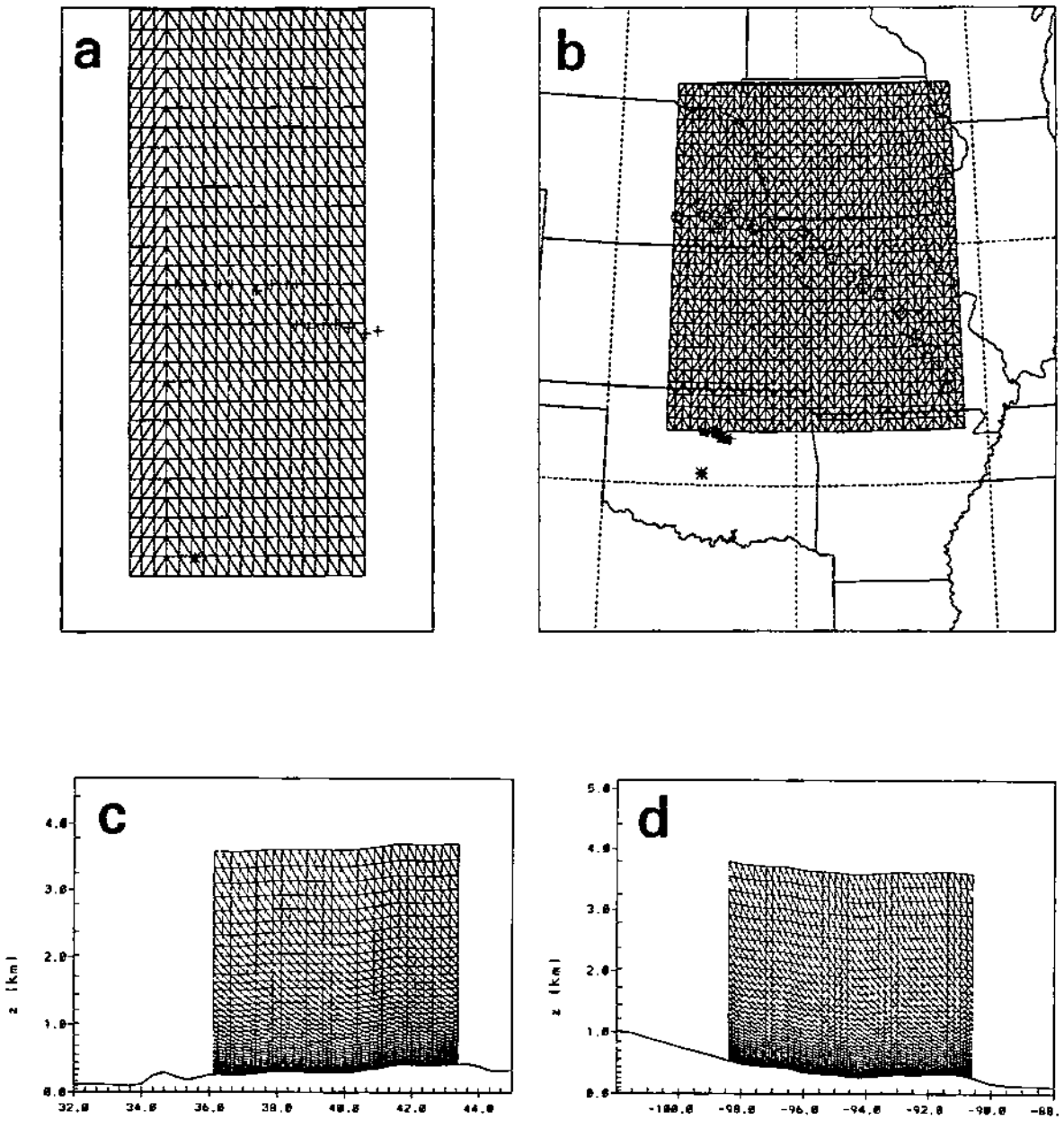

Figure 5.9: Location and size of the concentration analysis grids for the Great Plains simulations: (a) plan view of 100-km-arc CAG (21×31) ; (b) plan view of 600-km-arc CAG (41×31) ; (c) XZ view looking north at 600-km arc CAG (41×36 mesh) ; (d) YZ view looking west at 600-km arc CAG (31×36 mesh). The 100-km-arc CAG is plotted on a Mercator projection and encloses the region 35.15°–37.025°N and 97.75°–96.75 °W. The 600-km-arc CAG is plotted on a Lambert conformal projection with one standard parallel (at 38.5°N) and encloses the region 36°–43.5°N and 98.5°–90.5°W.

period. Not much difference is evident between the patterns in the first three panels. Examination of exposure values calculated at stations along the 600-km arc supports this view: for the first three CAG depths tested, non-zero exposures were found[186] only at Stations 2–5 (see Fig. 3.1b). Cross-wind integrated exposures (CWIEs) were also fairly similar, with values of approximately 300,600, 336,500, and 414,600 fl km h l^{-1} for CAG depths of 73, 204, and 378 m, respectively. However, the exposure plume was two, three, and six stations wider for the other three depths tested (607, 911, and 1312 m) and the cross-wind integrated dosages were about 40% larger. This result is consistent with Fig. 5.3c, which shows a clockwise rotation of grid-scale trajectories with increasing height; a deeper sampling volume would thus include particles transported further to the east by the winds at these higher levels, producing a wider surface footprint. It is also consistent with the eastward tilt of the particle column with height evident in Fig. 5.7b after 10 h of travel. Based on the differences shown in Fig. 5.10, a CAG depth of 378 m was used for all 600-km-arc time-average concentration estimates. This value maximized the sampling volume while still giving a surface exposure footprint similar to those given by the two shallower CAG depths tested.

Note that all six panels show a similar surface exposure pattern in the region north of the 600-km arc. The tracer cloud passes over this area during the daytime so that particles at all levels in the convective PBL can be brought to the surface by downdrafts. Consequently, sampling depth plays little role here provided the depth chosen lies within the PBL. It is worth noting too from Fig. 5.10 that a ground-based observer would measure a sudden widening of the plume as the convective PBL grew deeper during the morning. This is an example of the mechanism of delayed shear-enhanced dispersion first proposed by Pasquill (see Sec. 1.7).

---

[186] By interpolating from the gridded CAG values to the sampling-station locations using the same third-order overlapping polynomial interpolation scheme employed in the RAMS ISAN package (see Sec. 4.3). Note that this higher-order scheme can occasionally produce negative values at points located very near the cloud edge. The interpolated concentration is simply set to zero in such cases.

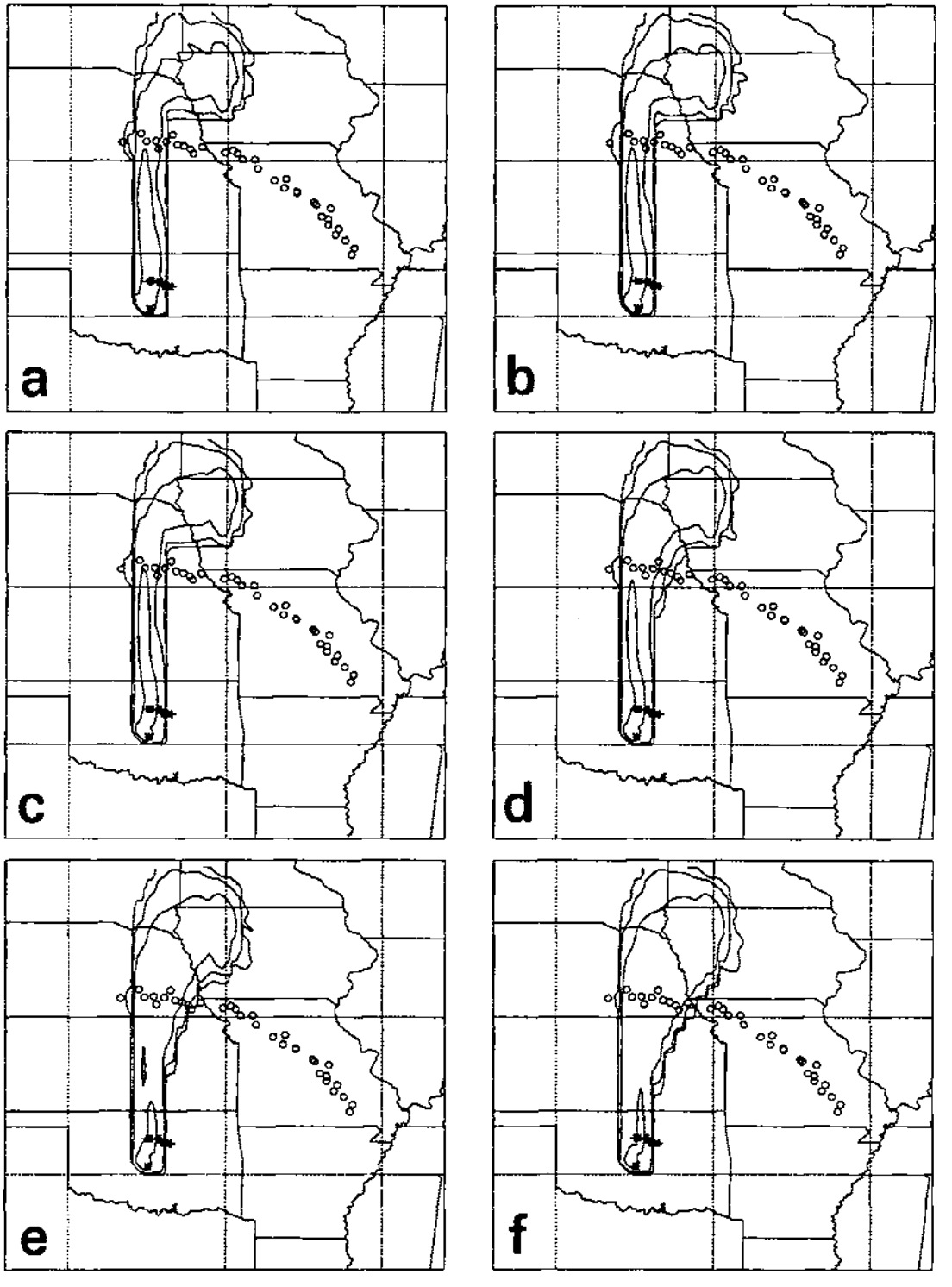

Figure 5.10: Exp. GP1c simulated surface exposure pattern (fl $h l^{-1}$) for a 25-h period beginning at 1900 GMT, July 8, 1980 as calculated for six different CAG depths: (a) 73 m; (b) 204 m; (c) 378 m; (d) 607 m; (e) 911 m; (f) 1312 m. The region shown in each panel stretches from 32–45°N and from 102–88°W; parallels at 35°N and 40°N and meridians at 90°W, 95°W, and 100°W are marked by short dashed lines. The map is a cylindrical equidistant projection.

One-dimensional-experiment concentration estimates

Estimates were made of ground-level concentrations (GLCs) for both the 100-km and 600-km sampler arcs. The results are quite different for these two sets of estimates and indicate a change in the qualitative behaviour of atmospheric dispersion over these travel times and travel distances. Tracer transport and diffusion on the way to the 100-km sampler arc occurred under relatively constant daytime conditions. Tracer was released from 1900–2200 GMT (or 1400–1700 CDT). Elevated tracer concentrations were measured along the 100-km sampler arc from 2145–0130 GMT (Table 3.1). Sunset at Oklahoma City occurred at 0148 GMT. Travel times were in the 2.75–3.50 h range. Along the 600-km arc, on the other hand, elevated tracer concentrations were measured from 0800–2000 GMT (Table 3.2). Sunrise at Oklahoma City occurred at 1122 GMT. Travel times thus fell in the much wider 13–22 h range. Early-arriving tracer material had dispersed during travel through an unstable–stable stability-regime sequence while later-arriving tracer had undergone dispersion during an unstable–stable–unstable sequence.

100-km arc. MLPDM simulations, each using 3600 particles, were run for Exps. GP1a and GP1c. Based on Fig. 5.3b, no MLPDM run was made for Exp. GP1b since the particle ensemble would not have been carried over either sampler arc. This directional error could have been dealt with (see p. 501) but two very idealized simulations (i.e., GP1a and GP1c) were probably already enough. Sampling periods on the 100-km arc were 45 minutes long. Corresponding time-averaged concentrations were estimated by first estimating instantaneous concentration fields from instantaneous particle positions. The particle positions had been archived during the MLPDM run and were available at 15-minute intervals. Three consecutive instantaneous concentration fields were then averaged together to obtain an estimate of the 45-minute-average concentration field. For example, the 2100–2145 GMT concentration field was estimated by averaging together the estimated instantaneous concentration fields for 2100, 2115, and 2130 GMT. This same approach was also used to estimate three-hour and six-hour concentration fields by using 12 and 24 consecutive instantaneous concentration fields, respectively.

(a) GLC patterns. Figs. 5.11a-b show *logarithmically-spaced* isopleths of PMCH 45-minute ground-level concentrations (GLCs) for the third[187] 100-km-arc sampling period for Exps. GP1a and GP1c. The two surface concentration patterns are quite similar at this time. However, one difference is that the leading edge of the GP1a cloud is located a bit ahead of the GP1c cloud. Another is that the alongwind axis of the GP1a cloud lies to the east of the GP1c axis. Both differences might have been expected based on Fig. 5.5, since the composited GP1c initial low-level flow field had lower wind speeds and wind directions rotated to the west relative to the 1200 GMT GP1a initial low-level wind field. These differences are also consistent with the trajectories plotted in Fig. 5.3.

Fig. 5.12 shows a sequence of GP1c surface concentration patterns for the first six 100-km-arc sampling periods. The approach of the tracer cloud to the sampling arc, the end of the tracer release and detachment of the tracer cloud from the release site, and the weaker surface concentration gradient on the leading and trailing edges of the cloud compared to the sides can all be seen in this figure. One difference between the predicted tracer-cloud behaviour and the observed cloud behaviour is that significant tracer concentrations were predicted to occur one sampling period too soon. We can see from Table 3.1 that virtually no tracer was observed to reach the 100-km arc during the first sampling period (2100–2145 GMT). However, it is clear from Fig. 5.12a that some tracer was predicted to reach the 100-km arc during this first period in the Exp. GP1c simulation.

(b) Station values. Fig. 5.13 shows Exps. GP1a and GP1c predicted PMCH ground-level concentrations plotted station by station across the 100-km sampler arc along with the actual observations for the first six observing times. Fig. 5.14 presents many of the same data in a complementary way[188], showing the time history of the predicted and

---

[187] The observing period during which the highest PMCH ground-level concentration was measured on the 100-km arc (Table 3.1).

[188] After first making the crosswind spatial offset – see discussion

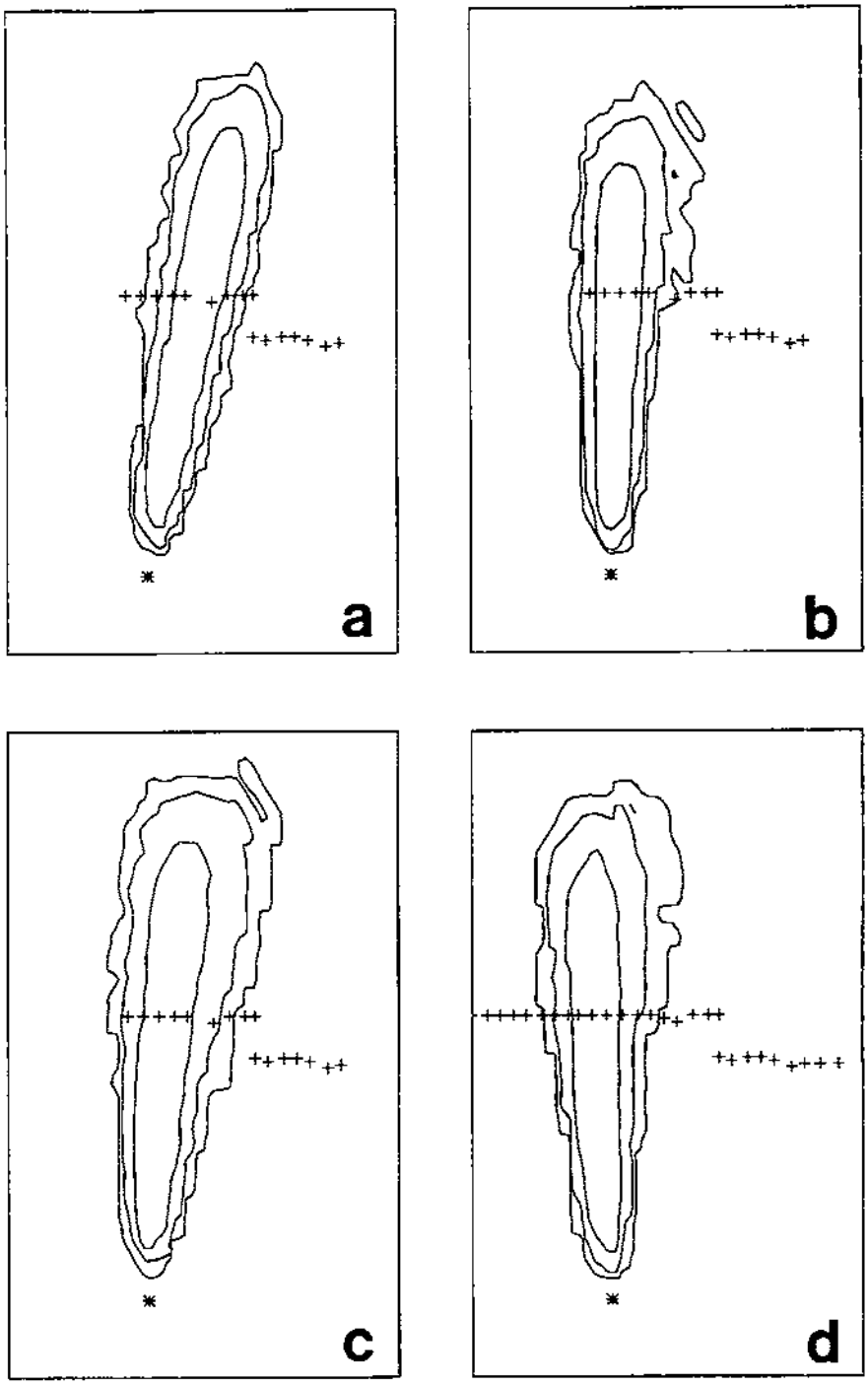

Figure 5.11: Plan views of estimated 45-minute-average PMCH ground-level concentration patterns for the third 100-km-arc sampling period, 2230–2315 GMT, which began 3.5 h after the start of the release, for four different MLPDM simulations: (a) Exp. GP1a; (b) Exp. GP1c; (c) Exp. GP2a; (d) Exp. GP2c. 10, 100, 1000, and 10000 fl^{-1} isopleths are shown. The release site is indicated by the asterisk, the active 100-km-arc samplers by plus signs. The active-sampler arc is about 90 km across; the original planned sampler arc, plotted in panel (d), is wider. The Mercator projection covers the region from 35°–37°N and 98°–96.5°W.

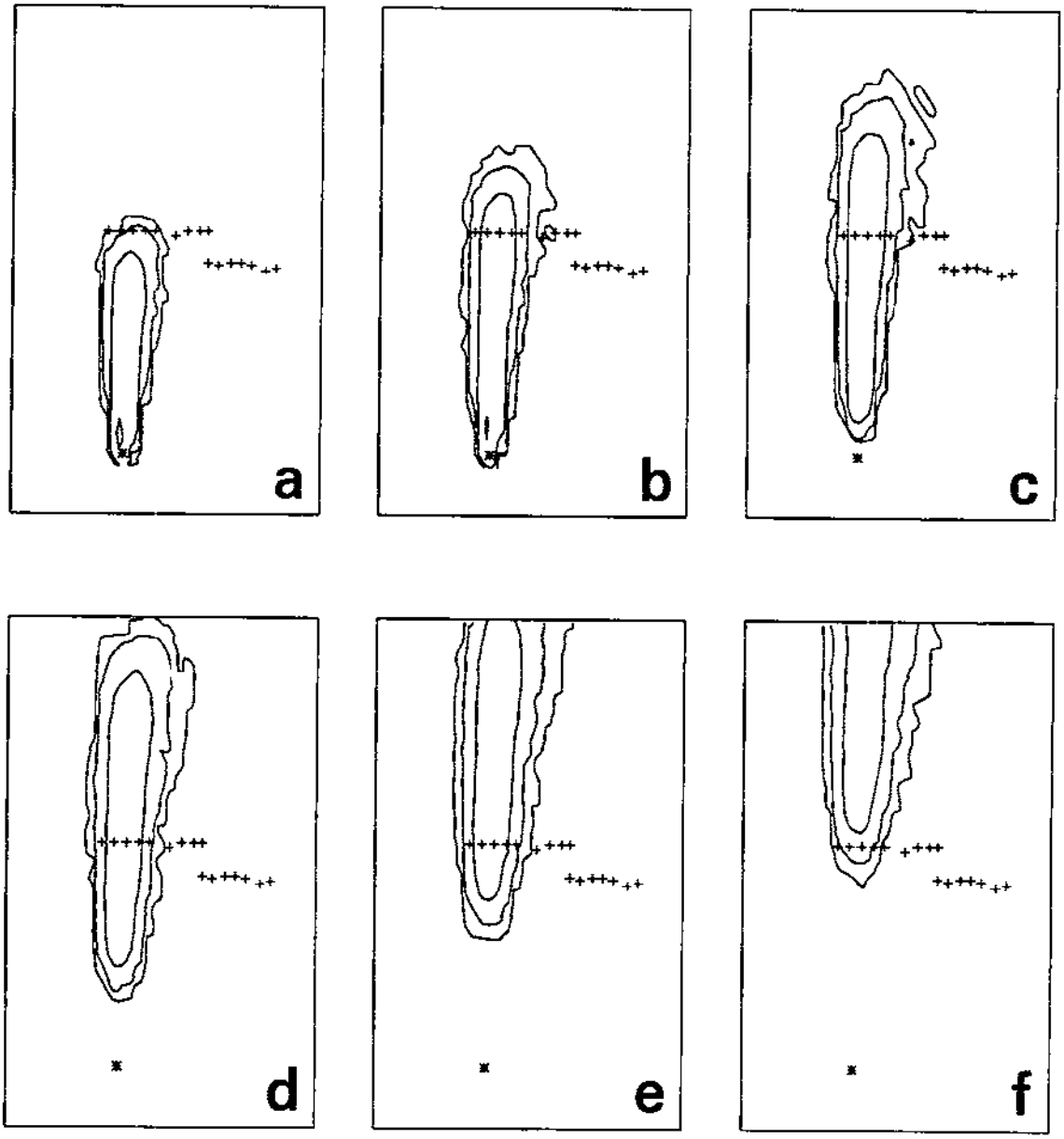

Figure 5.12: Time sequence of plan views of estimated 45-minute-average PMCH surface concentration patterns for the first six 100-km-arc sampling periods based on particle positions from the Exp. GP1c MLPDM simulation: (a) 2100–2145 GMT; (b) 2145–2230 GMT; (c) 2230–2315 GMT; (d) 2315–0000 GMT; (e) 0000–0045 GMT; and (f) 0045–0130 GMT. Otherwise identical to Fig. 5.11.

observed concentrations at six of the 100-km arc stations. Examination of these two figures suggests that the Exp. GP1 predicted clouds are narrower and more elongated than the observed cloud, since the predicted clouds arrive sooner (Fig. 5.13a) and linger longer (Fig. 5.13f) than the observed cloud and have elevated concentration values at fewer stations. However, peak concentrations for both subexperiments and centerline location for Exp. GP1c are in very good agreement with the observations.

Table 5.2 compares 100-km-arc station exposure and total cross-wind integrated exposure (CWIE) values for a 5.25 h period predicted in Exps. GP1a and GP1c and other experiments against the observed values. These integrated quantities are useful measures of the *overall* dispersion simulation. For example, predicted station exposures may agree well with actual values even though any or all of cloud arrival time, cloud transit time, or peak concentration levels are in error since these latter time-dependent quantities are 'integrated out'. Similarly, a spatially-integrated value like CWIE is independent of the exact centerline location or crosswind shape within the integration domain.

The Table 5.2 station-exposure values determined from the two Exp. GP1 MLPDM simulations are consistent with the discussion of Figs. 5.11–5.14. There is certainly 'ball-park' agreement between the Exps. GP1a and GP1c predicted station exposures and the observed values. The predicted maximum station exposures are similar and larger than the observed value (11881 and 12308 vs. 7791) while the observed exposure 'plume' is wider than the plume predicted by either GP1 subexperiment. The GP1c exposure maximum is located only one station to the east of the observed maximum at Station 13 while the GP1a exposure maximum was located four stations to the east of the observed maximum. Interestingly, the GP1a exposure plume can be argued to be either smaller or larger than the GP1c plume, depending upon the criterion used. If the criterion is the total number of stations with an non-zero exposure, then the GP1a plume is only 6 stations wide vs. 8 stations for the GP1c plume (and 11 stations[189] for the observed

[189] Assuming a non-zero exposure at Station 17.

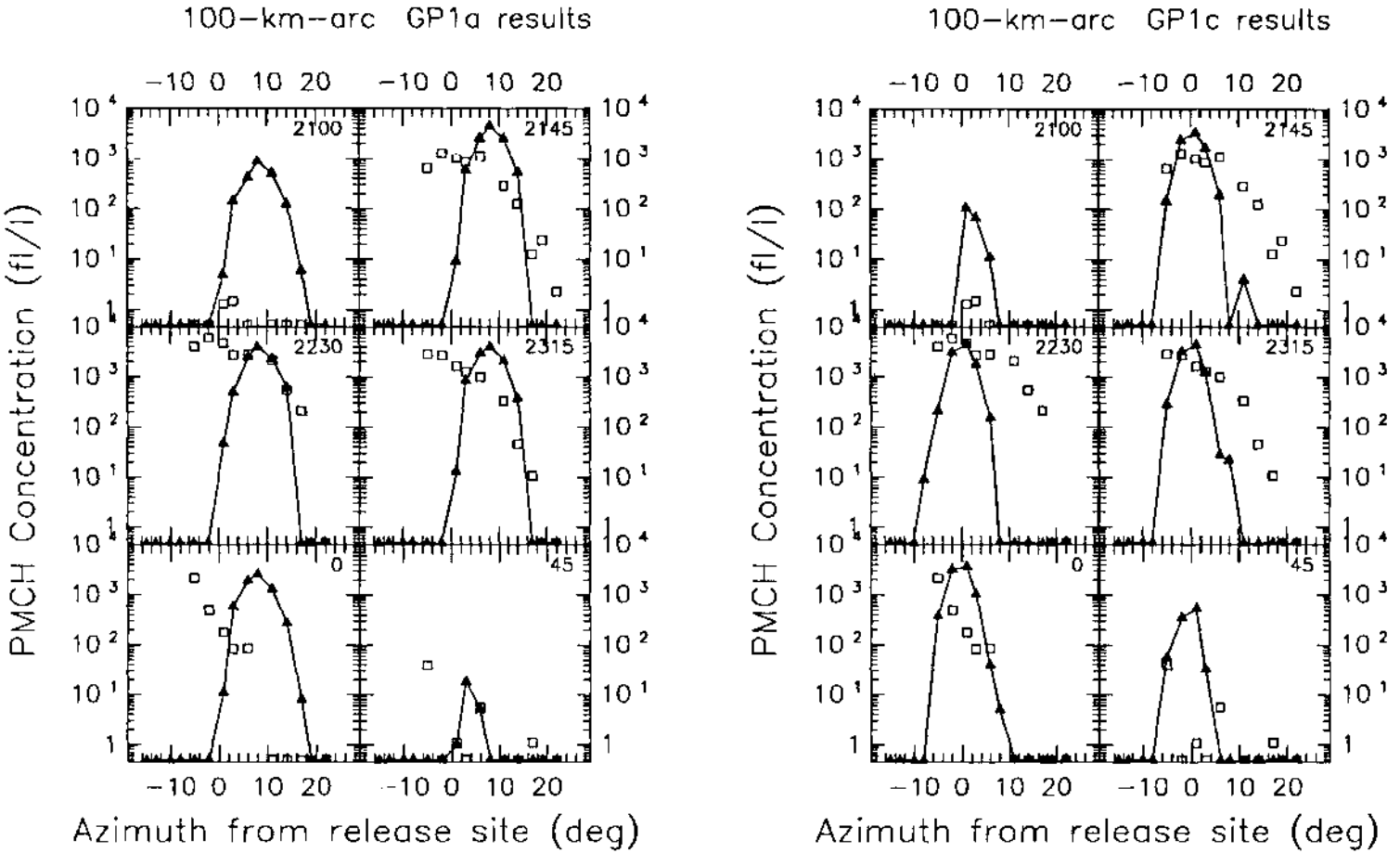

Figure 5.13: Time sequence of concentration–azimuth plots of observed vs. Exp. GP1a (lefthand panel: 'L') and observed vs. Exp. GP1c (righthand panel: 'R') estimated PMCH 45-minute-average concentrations for the Great Plains experiment 100-km sampling arc for the first six sampling periods: (a) 2100–2145 GMT; (b) 2145–2230 GMT; (c) 2230–2315 GMT; (d) 2315–0000 GMT; (e) 0000–0045 GMT; and (f) 0045–0130 GMT. Observed values are indicated by open squares; predicted values are indicated by filled triangles connected by a solid line. The starting time for each sampling period (GMT) is plotted in the upper righthand corner of each panel.

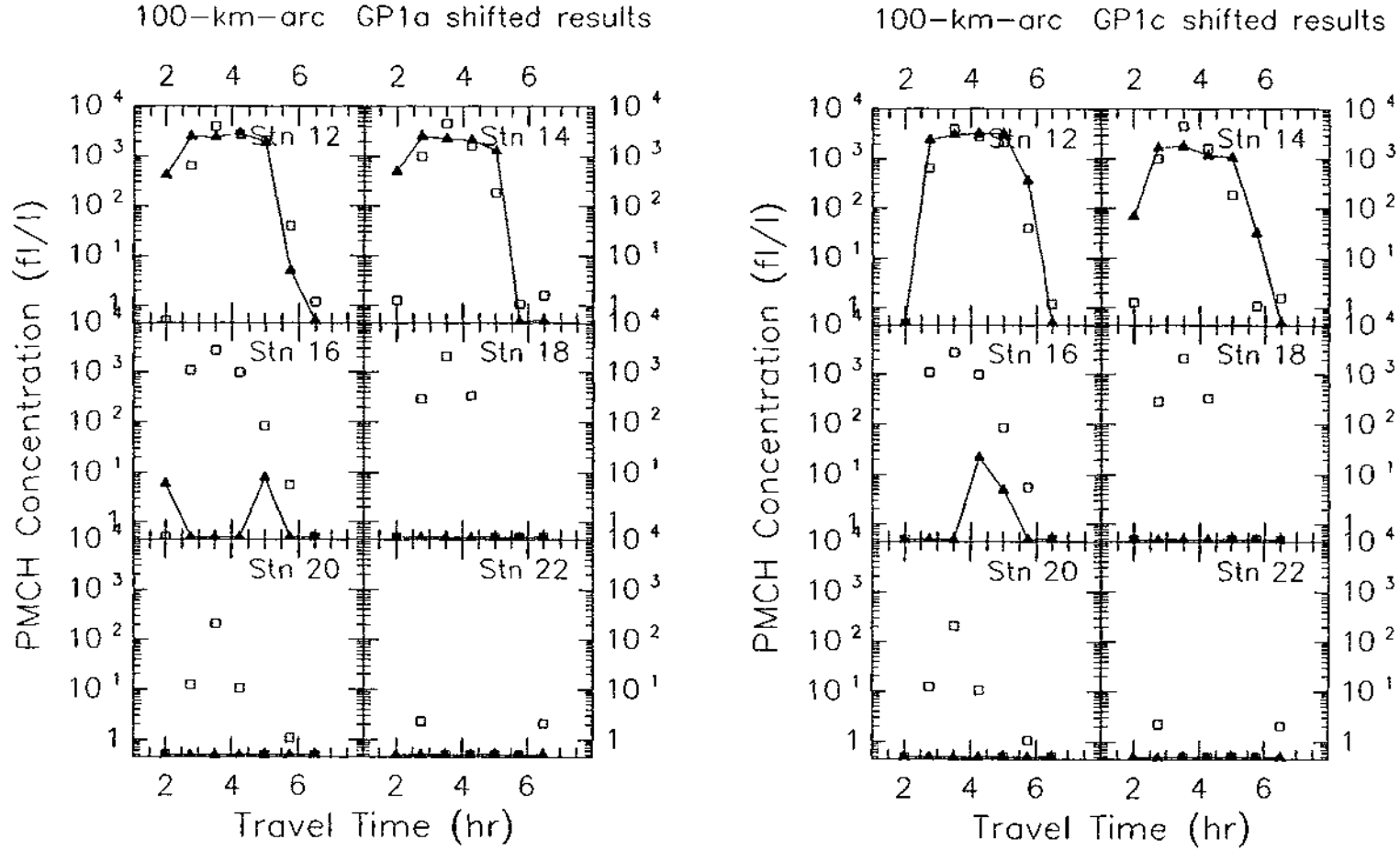

Figure 5.14: Concentration–time plots of observed vs. Exp. GP1a (lefthand panel: 'L') and observed vs. Exp. GP1c (righthand panel: 'R') estimated PMCH 45-minute-average concentrations for six 100-km-arc sampling stations: (a) Station 12; (b) Station 14; (c) Station 16; (d) Station 18; (e) Station 20; and (f) Station 22. Observed values for Stations 12–20 are indicated by open squares; predicted values are indicated by filled triangles connected by a solid line. The station ID number is plotted in the upper righthand corner of each panel. The GP1a station values were shifted westward by four station lengths while the GP1c station values were shifted westward by one station length.

Table 5.2: Comparison of predicted 100-km-arc station ground-level exposures (fl hl^{-1}) with observed values for the 5.25-h period from 2100–0215 GMT, July 8–9, 1980. A threshold value of 3.4 fll^{-1} has been subtracted from the observed ground-level concentrations listed in Table 3.1 in obtaining the 'Obs.' values listed in the last horizontal line of the table. A dash (–) indicates 'no data'. The rightmost vertical column gives crosswind-integrated exposures (CWIE) in fl km hl^{-1} over Stations 8–27, assuming a mean cross-wind station spacing of 5 km. The CWIE values have been reduced by the following obliquity factors: cos 1°=0.9998, cos 2°=0.9994, cos 5°=0.9962, cos 8°=0.9903, cos 17°=0.9563, cos 19°=0.9455.

Azim.	345	347	350	352	355	358	1	3	6	8	11	14	17	19	22	25	28	30	33	36	
Exp. No.	100-km-arc Station Number																				CWIE
	8	9	10	11	12	13	14	15	16	17	18	19	20	21	22	23	24	25	26	27	
GP1a	0	0	0	0	0	0	64	2000	7720	11881	6561	1424	10	0	0	0	0	0	0	0	148300
GP1c	0	0	0	7	800	9182	12308	4360	316	20	3	0	0	0	0	0	0	0	0	0	134980
GP2a	0	0	0	32	400	2968	9139	8897	4340	1331	415	86	3	0	0	0	0	0	0	0	138055
GP2c	0	202	2007	7078	11688	6975	1768	236	53	2	11	0	0	0	0	0	0	0	0	0	150100
GP3	0	0	0	0	0	0	0	2	22	668	3506	7991	9559	7440	3131	1067	230	44	4	0	161000
GP4a	0	0	0	0	0	0	0	0	28	407	1838	5412	9394	10060	7518	3058	776	154	16	0	182800
GP4b	0	0	0	0	0	0	0	0	56	1012	3958	7967	10064	8420	4138	1253	402	170	50	0	179300
GP5	0	0	0	0	0	0	0	4	209	1317	4091	8050	9986	8396	4299	1373	162	38	8	0	181500
Obs.	–	–	–	–	7265	7791	5627	3696	3752	–	2040	548	178	18	4	0	0	0	0	0	154595

plume). If the criterion is the number of stations with exposures above 1000 fl h l^{-1}, however, then the GP1a plume is 5 stations wide versus 3 stations for the GP1c plume (and 7 stations for the observed plume). This 'reversible' inequality is consistent with the values listed in Table 5.3, in which maximum cloud widths were determined from station *concentrations* using different cloud-edge criteria.

Table 5.2 and Fig. 5.13 both illustrate a perennial problem in evaluating air-quality models which was referred to in Sec. 3.2.5. That is, Exp. GP1c station predictions can be compared directly against the 100-km-arc station observations whereas the Exp. GP1a predictions contain a significant centerline position error, making a direct station-to-station comparison problematic at best. In general, position errors are important for evaluating an air-quality model's treatment of mean transport but are nearly irrelevant for evaluations of the model's treatment of diffusion (e.g., Draxler, 1987; Godowitch, 1989b). However, their effects have to be removed before size and shape errors can be considered properly, i.e., in isolation. This problem is related to the discussion of analysis framework and absolute dispersion vs. relative dispersion contained in Chap. 1. One way to remove position error before comparing cloud size and shape is to 'match' the location of the predicted concentration peak or centroid to the observed location as is done in a relative-diffusion analysis (e.g., Andrén, 1990). Station concentrations can then be paired in time and space and compared or plotted after first shifting each predicted value in space by the distance required to match the peaks.

Such a matching was employed in constructing Fig. 5.14. Based on Table 5.2, the overall centerline position error for Exp. GP1a was determined to be four stations distance (about 20 km). Thus, Fig. 5.14L actually shows Exp. GP1a Station 16 concentration predictions plotted against Station 12 observations, Station 18 predictions plotted against Station 14 observations, and so on. In the case of Exp. GP1c, the centerline error was only one station so Exp. GP1c Station 13 concentration predictions are plotted against Station 12 observations, Station 17 predictions are plotted against Station 16 observations, and so on, in Fig. 5.14R. Note that this approach requires equally-spaced

stations. Meeting this requirement was straightforward in the case of the 100-km sampling arc because the experimental design had specified equally-spaced stations (Fig. 3.1a). Samplers were not in fact deployed at all of the sites but values can still be estimated at all sites for the different model runs. This is the reason why Table 5.2 lists predicted values for Stations 8–11 and 17, none of which had observational data. In the case of the 600-km arc, however, stations were not evenly spaced (Fig. 3.1b). Instead, GLC values were estimated along an idealized arc of sites with equal azimuthal spacing and located exactly 600 km from the release site.

CWIE was used in Sec. 3.1.4 in the mass-balance analysis of the 100-km-arc ground-level concentration measurements to compare the amount of tracer measured with the amount released. The CWIE values listed in Table 5.2 for the two Exp. GP1 subexperiments are smaller than, but are within 15% of, the observed CWIE value for the 100-km arc. If concentrations had been measured at Stations 11 and 17, this difference would have been larger but the predicted CWIE values would still very likely be within about 20% of the measured value.

Note too that the CWIE values listed in Table 5.2 have been reduced slightly by an obliquity factor. As discussed by Sackinger et al. (1982) and Holland (1988), this factor accounts for the overestimate caused when the cloud centerline is not perpendicular to the line of samplers. For example, since the peak GP1a station exposure was predicted at Station 17, whose azimuth angle is 8°, the calculated GP1a CWIE value before multiplying by the adjustment factor of $\cos 8°$ was 148300 fl km hl^{-1}.

(c) Quantitative pattern characteristics. Table 5.3 summarizes some of the quantitative cloud characteristics estimated from the observed station concentrations and from the GP1a and GP1c predicted concentrations at all 100-km-arc *sites*. These values support the previous discussion: the two GP1 clouds are longer (by roughly 25%) and narrower (by roughly 40%) than the observed cloud but peak values are comparable (4475 vs. 5900 fll^{-1}). Predicted arrival time is one sampling period too soon but departure time is in good agreement as is the time of peak concentration. The mean centerline azimuth

values give one measure of cloud position error. As was done earlier in Chap. 3, two independent criterion have been used to determine the cloud edges in obtaining the values listed in this table. Cloud arrival time, transit time, and maximum width (the second through sixth columns) all depend on this criterion, and many of the values listed in Table 5.3 for the same experiment and quantity differ slightly depending upon which edge criterion was used. This result points out again the importance of the way in which the cloud edge is determined.

(d) Scattergrams. Fig. 5.15 presents two types of scatter diagrams (or 'scattergrams') of the correspondence of the Exp. GP1a and GP1c predicted concentrations with measured values along the 100-km arc. Figs. 5.15a,c might be termed 'absolute-dispersion' scattergrams. They show predicted and observed station concentrations paired in time and space. One serious disadvantage of such a comparison has already been mentioned: if the predicted *position* of the tracer cloud is in error, then the predicted and observed clouds may overlap little or not at all. This will result in an 'L-shaped' scattergram with many zero–nonzero concentration pairs. As already discussed, one way to avoid the effect of position errors and permit a comparison of cloud size and shape is to 'match' the location of the predicted concentration peak or centroid to the observed location. Concentrations are thus still paired in both time and space but all predicted values will have first been shifted or translated in space by the same distance required to match the peaks. Figs. 5.15b,d replot the data from Figs. 5.15a,c in this way.

The result of this matching or spatial offset is that the non-zero concentration pairs in the 'relative-dispersion' scattergrams do seem to cluster more tightly around the one-to-one correspondence line and lie within the factor-of-four lines. The numbers plotted above the top of each panel are a summary of the concentration-pair statistics for that scattergram. 'Pr' stands for 'predicted' while 'Ob' denotes 'observed. Thus for Fig. 5.15a, there were 21 concentration pairs considered where both predicted and observed station values were zero; these pairs are all plotted on the scattergram origin (lower lefthand corner). There were 19 pairs where the predicted value was zero but the observed value

Table 5.3: Tracer cloud characteristics from Great Plains numerical experiments — 100 km arc. Cloud arrival time, transit time, and maximum width all depend on the criterion used to determine the cloud edges. Azimuth range and arc length have units of degrees and kilometers, respectively, and have been obtained assuming a crosswind station spacing of 3° and 5 km. Mean center-line azimuth values are based on Table 5.2. An exposure value of 2896 fl l^{-1} has been assumed for the missing Station 17 observed value (cf. Tables 3.1, 5.2).

Exp. No.	Arrival Time (GMT)	Transit Time (h)	Maximum Width St'n Range	Maximum Width Azim. Range	Maximum Width Arc Length	Max. Conc. (fl l^{-1})	Time of Max'm (GMT)	CWIE (fl km h l^{-1}) ($\times 10^{-3}$)	Mean CL Azimuth (°)
10%-of-peak threshold									
GP1a	2100–2145	3.75	15–19	15	25	4475	2145–2230	148	8
GP1c	2145–2230	3.75	13–15	9	15	4477	2230–2315	135	1
GP2a	2100–2145	3.75	13–17	15	25	3681	2145–2230	138	1
GP2c	2100–2145	3.75	10–14	15	25	4214	2230–2315	150	355
GP3	2145–2230	3.75	18–23	18	30	3711	2230–2315	161	17
GP4a	2230–2315	3.75	18–23	18	30	4401	0000–0045	183	19
GP4b	2145–2230	3.75	18–23	18	30	3821	2315–0000	179	17
GP5	2145–2230	3.75	17–22	18	30	4538	2315–0000	182	17
Obs'd	2145–2230	3.00	12–19	24	40	5900	2230–2315	169	358
3 fl l^{-1} threshold									
GP1a	2100–2145	4.50	14–20	21	35	4475	2145–2230	148	8
GP1c	2100–2145	4.50	12–17	18	30	4477	2230–2315	135	1
GP2a	2100–2145	3.75	11–19	27	45	3681	2145–2230	138	1
GP2c	2100–2145	4.50	10–18	27	45	4214	2230–2315	150	355
GP3	2100–2145	4.50	17–26	30	50	3711	2230–2315	161	17
GP4a	2145–2230	4.50	16–26	33	55	4401	0000–0045	183	19
GP4b	2145–2230	4.50	16–26	33	55	3821	2315–0000	179	17
GP5	2145–2230	4.50	16–25	30	50	4538	2315–0000	182	17
Obs'd	2145–2230	3.75	12–21	30	50	5900	2230–2315	169	358

was greater than zero; these points fall along the abscissa. There were 8 pairs where the predicted value was greater than zero but the observed value was zero; these points fall along the ordinate axis. Finally, there were 22 pairs where both pair members were non-zero; these are the points plotted along the one-to-one correspondence line. One conclusion suggested by Figs. 5.15b,d, the two 'relative-dispersion' scattergrams, is that the observed cloud was wider than the predicted clouds. The basis for this statement is the considerably greater number of 'Pr=0, Ob>0' concentration pairs than 'Pr>0, Ob=0' concentration pairs for the two subexperiments: 21 vs. 3 and 19 vs. 2. The larger centerline position error for Exp. GP1a is also suggested by the number of zero–nonzero pairs in Fig. 5.15a, 27, versus the number of zero–nonzero pairs in Fig. 5.15c, 19.

600-km arc. Sampling periods on the 600-km arc were 3 h long. Corresponding time-averaged MLPDM concentrations were computed by averaging 12 consecutive instantaneous concentration fields which in turn were based on instantaneous particle positions available every 15 minutes.

(a) GLC patterns. Figs. 5.16a-b show *logarithmically-spaced* isopleths of PMCH 3 h GLCs for the first[190] 600-km-arc sampling period. This three-hour period ended just before sunrise (1100 GMT vs. 1122 GMT) and corresponds to cloud travel times of 13–16 h. The time-averaged GP1a surface concentration pattern during this period is considerably wider than the GP1c pattern, reaches further northward, and crosses the 600-km sampler arc slightly further to the east. These differences are reflected in the summary of quantitative tracer-cloud characteristics given in Table 5.5.

The differences between the surface concentration patterns for the two GP1 subexperiments shown in Figs. 5.16a,b seem to be consistent with the grid-scale trajectories plotted for these two experiments in Figs. 5.3a,c (or Figs. 5.26c,d). The CAG sampling

---

[190] The observing period during which the highest PMCH ground-level concentration was measured on this arc (Table 3.2).

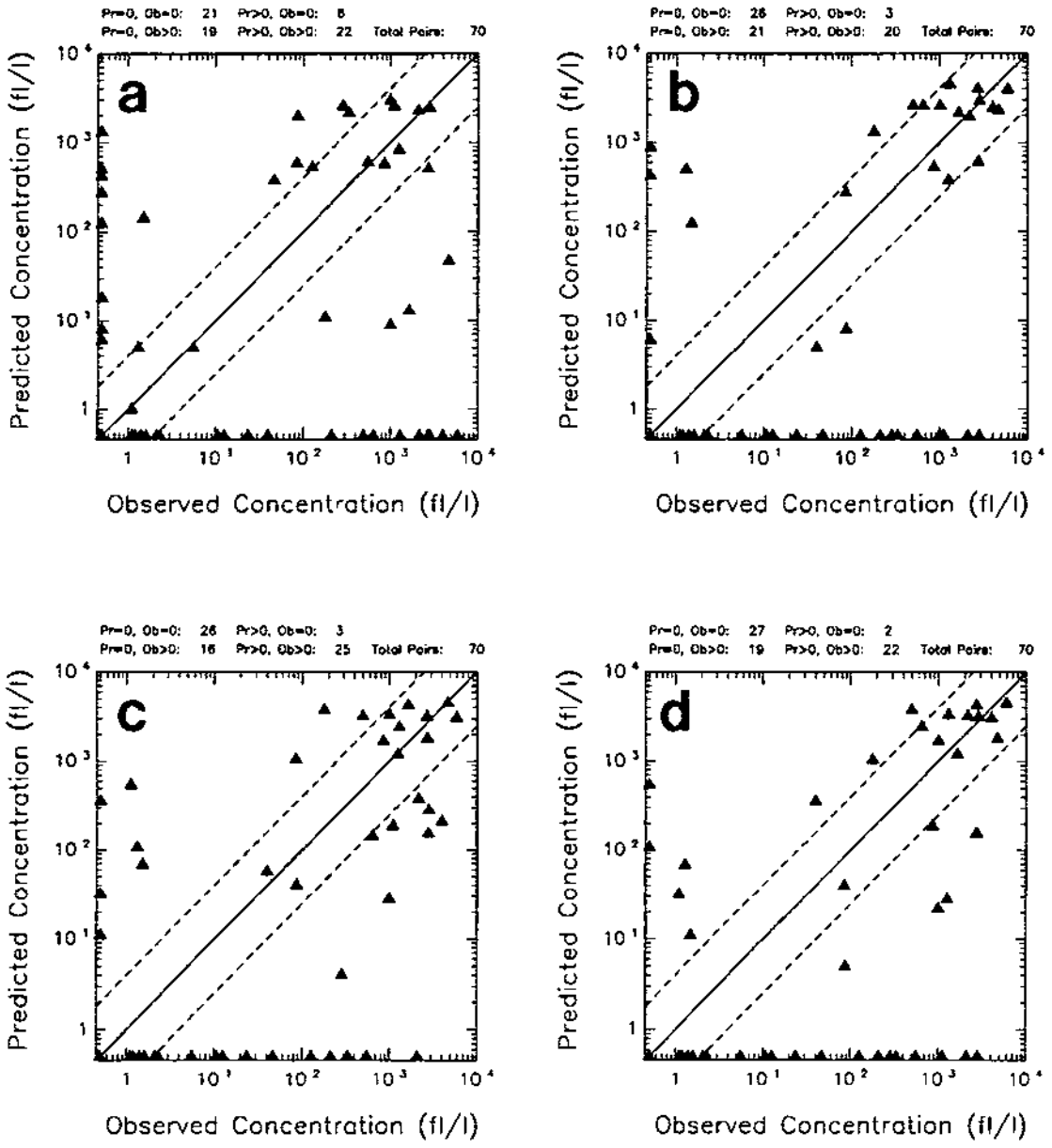

Figure 5.15: Scattergrams for observed 100-km-arc PMCH concentrations (less 3.4 fl^{-1}) vs. (a) unshifted Exp. GP1a estimated concentrations, (b) center-line-shifted Exp. GP1a estimated concentrations, (c) unshifted Exp. GP1c estimated concentrations, and (d) center-line-shifted Exp. GP1c estimated concentrations. Plotted pairs have been drawn from the set of concentrations for Stations 12–21 and the first seven 45-minute observing periods from 2100–0215 GMT, July 8–9, 1980. The GP1a station values were shifted westward by four station lengths in (b) while the GP1c station values were shifted westward by one station length in (d). The diagonal lines are the one-to-one correspondence line and two factor-of-4 lines (that is, 1:4 and 4:1).

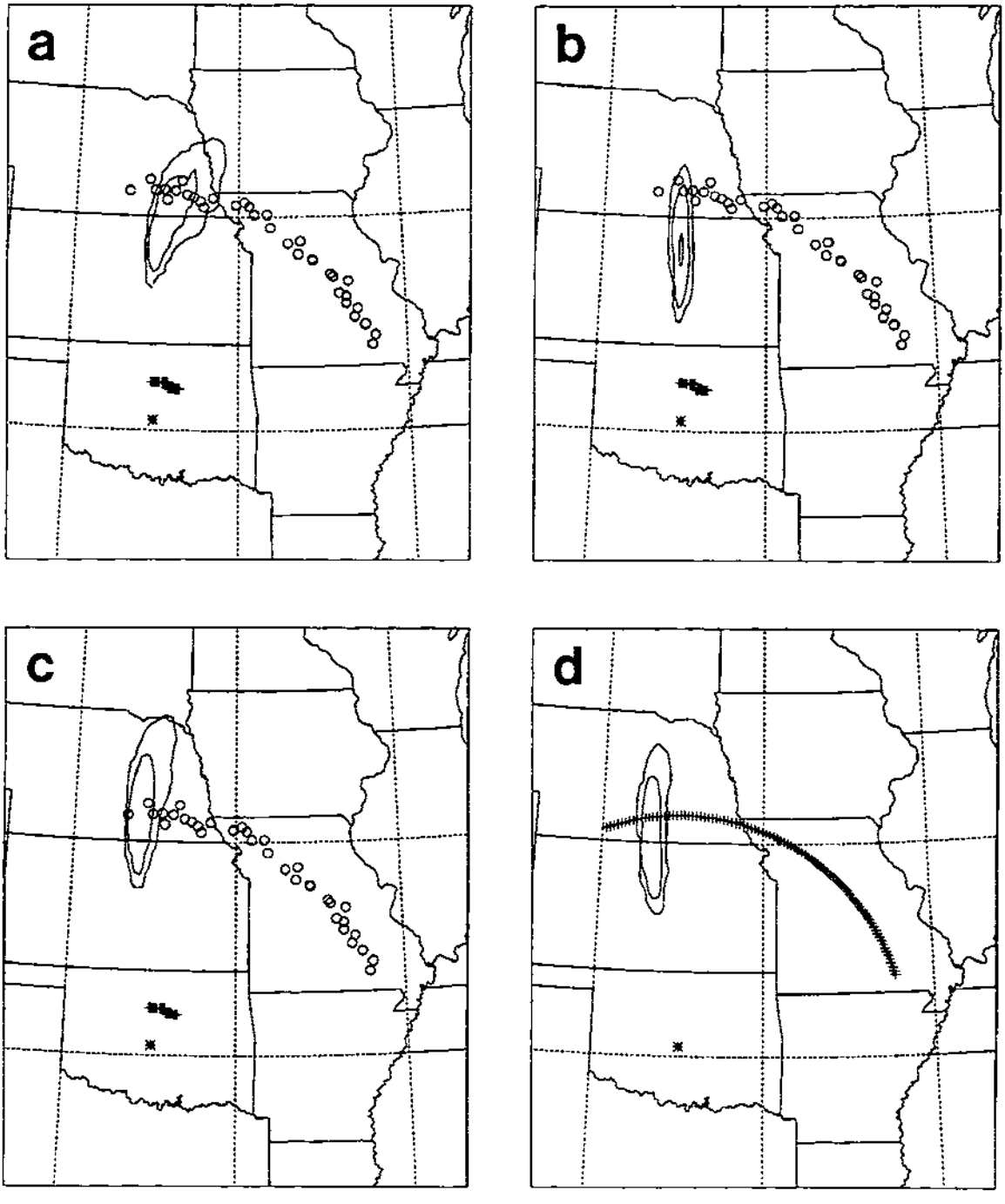

Figure 5.16: Plan views of the estimated 3-hour-average PMCH surface concentration patterns for the first 600-km-arc sampling period (0800–1100 GMT), which began 13 h after the start of the release, for four different MLPDM simulations: (a) Exp. GP1a; (b) Exp. GP1c; (c) Exp. GP2a; and (d) Exp. GP2c. The 10, 100, and 1000 fll^{-1} isopleths are shown. The release site is indicated by the asterisk, the active 100-km-arc samplers by plus signs, and the active 600-km-arc samplers by open circles. The Lambert conformal projection with one standard parallel (at 38.5°N) covers the region from 32–45°N and 102–88°W. Parallels at 35°N and 40°N and meridians at 100°W, 95°W, and 90°W are indicated by dashed lines. Panel (d) shows the equally-spaced sampler arc instead of the actual active sampler locations.

depth used to calculate the 600-km-arc concentrations was 378 m, a value in between the trajectory '2' and trajectory '3' release heights of 293 and 686 m AGL. The travel-time isochron for GP1a is both wider and located further north of the source than the corresponding GP1c isochron. From the discussion of Figs. 5.6–5.8, this difference should correspond to a difference in cloud width and cloud position similar to that seen in Figs. 5.16a,b.

Figs. 5.17 and 5.18 show time sequences of PMCH ground-level concentration patterns for the first four 600-km-arc sampling periods for Exps. GP1a and GP1c, respectively. Note the marked change in the shape of the GLC patterns from the first to the second and from the second to the third sampling periods. As the CBL develops after sunrise (1122 GMT), tracer travelling in the nighttime residual layer is brought down to the surface by vertical turbulent mixing, resulting in an elongation and widening of the surface concentration pattern. The modification of the surface 'footprint' by this process is not uniform, however. Rather, it occurs preferentially along the front and eastern flank of the surface cloud, i.e., those regions over which the upper-level leading edge of the cloud has been carried by the faster and more easterly upper-level winds (cf. Fig. 5.3). These two figures suggest that (a) the cloud width measured by surface samplers should increase during the morning period near the front of the cloud due to the downward mixing of the elevated cloud and (b) the width of the surface footprint actually measured during the Great Plains tracer experiment along the 600-km arc was *not* representative of the width of the three-dimensional cloud. The timing of the tracer release on the previous afternoon also appears to have been significant. If the tracer had been released three hours later (i.e., 2200–0100 GMT), these simulations suggest that fumigation might have occurred as the leading edge of the tracer cloud approached the 600-km arc. The measured cloud width would then have been considerably greater. Interestingly, the shape and timing of the passage of the cloud in these two figures is also consistent with the background tracer levels measured during the July 9 DC-3 flight along the 600-km arc (see Sec. 3.1.4). The elevated cloud lay just westward and northward of the aircraft track in these simulations.

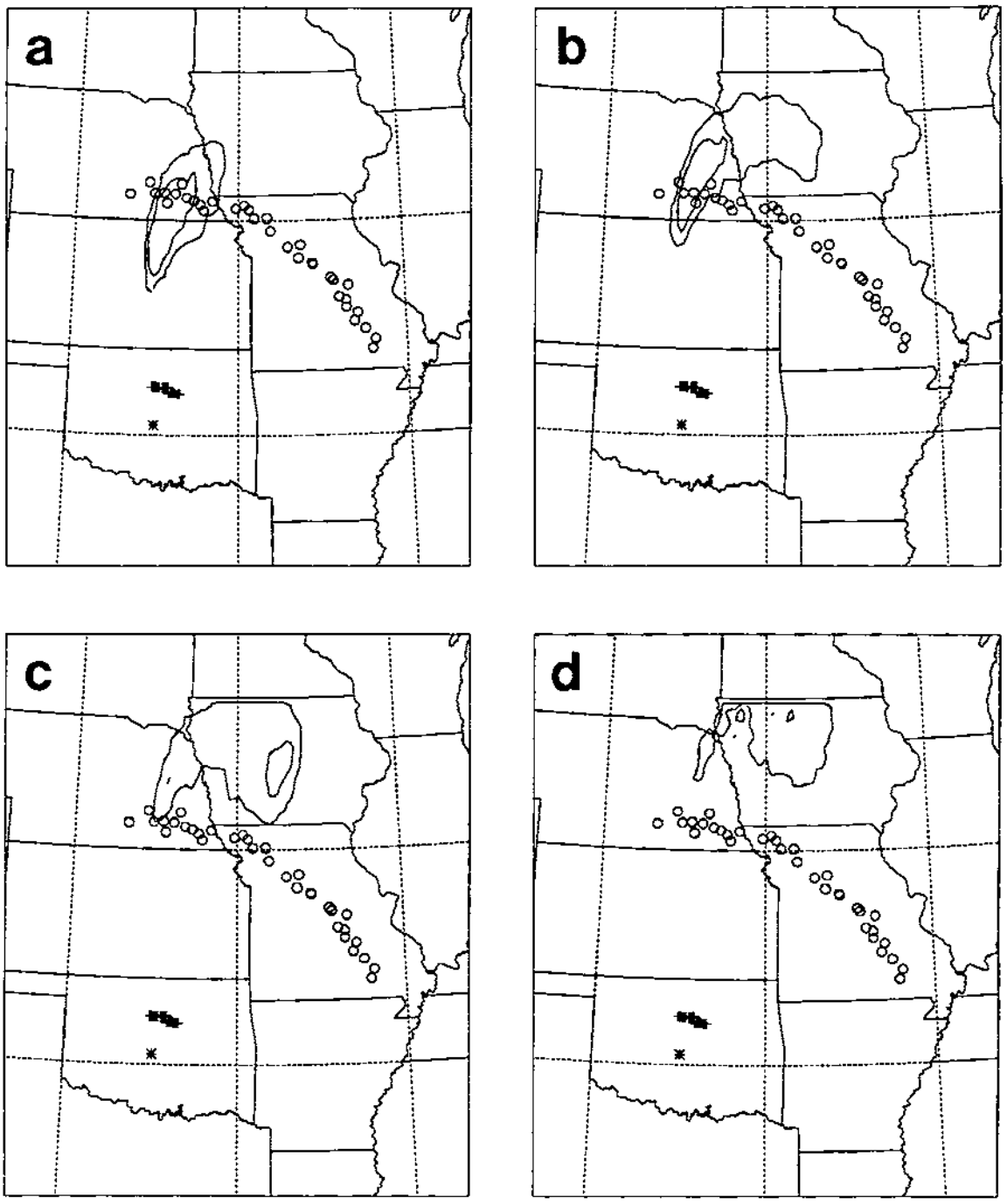

Figure 5.17: Time sequence of plan views of estimated PMCH 3-h-average GLC patterns for the first four 600-km-arc sampling periods based on particle positions from the Exp. GP1a MLPDM simulation: (a) 0800–1100 GMT; (b) 1100–1400 GMT; (c) 1400–1700 GMT; and (d) 1700–2000 GMT on July 9, 1980. Otherwise identical to Fig. 5.16.

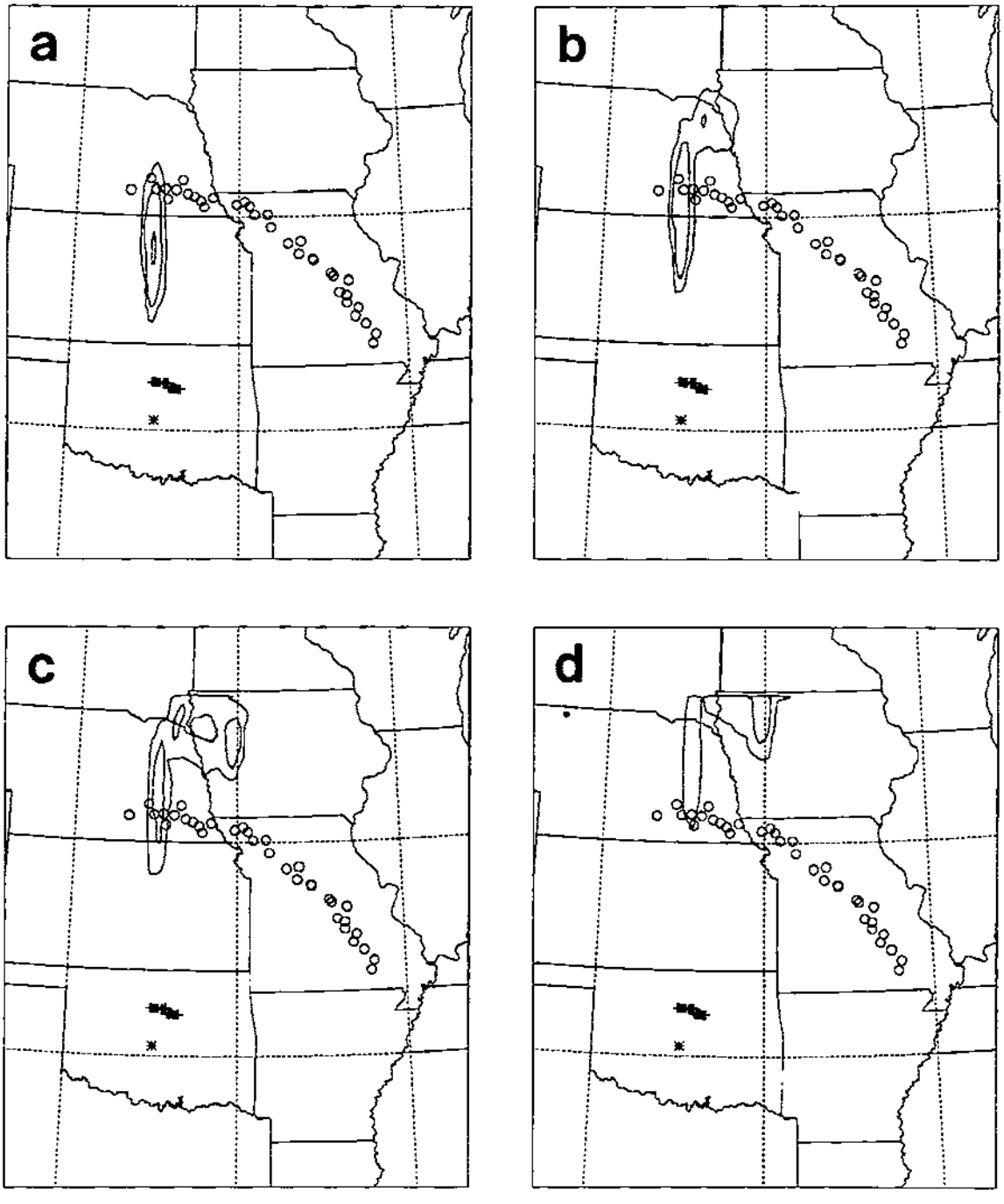

Figure 5.18: Same as Fig. 5.16 except for Exp. GP1c.

(b) Station values. The discussion of the 100-km-arc results mentioned the need to offset station values in space and match the location of the peak values in order to compare observed and predicted cloud size and shape. To do this successfully, it was necessary to interpolate model-predicted concentrations along an 'enhanced' equally-spaced arc of sampler sites because the arc of active samplers had some missing data and did not extend far enough to the west to cover the range of predicted cloud positions (Fig. 5.11). This problem arose in an even more pronounced form in the analysis of the 600-km-arc concentrations. As is evident in Fig. 5.16, the active 600-km-arc stations were irregularly spaced and again did not extend far enough to the west to sample the full width of all of the simulated tracer clouds. To deal with this problem, model-predicted concentrations were calculated at *both* the 38 active sampler locations *and* along an arc of 91 sites with 1° azimuth spacing ranging from 340° to 70° and located exactly 600 km away from the release site along a great circle. This arc of equally-spaced sites is plotted in Fig. 5.16d. In terms of arc length, the site spacing on this second 600-km arc is about 10.5 km, half the average 21 km spacing of the actual 600-km-arc sampler sites.

Fig. 5.19 shows Exps. GP1a and GP1c predicted PMCH ground-level concentrations plotted against azimuth angle and the actual observations for the first four 600-km-arc observing times. Fig. 5.20 presents many of the same data in a complementary way, plotted against travel time. Model-predicted values correspond to the equally-spaced 91-site arc, and predicted station values in Fig. 5.14 have been offset in the same fashion that those in Fig. 5.14 were. Exp. GP1a station values were offset by 8° and Exp. GP1c station values were offset by 10° based on Tables 5.6 and 5.5.

Some of the differences between Exps. GP1a and GP1c are clearly shown in these two figures. The GP1a cloud is obviously wider than the GP1c plume, although the former narrows with time (as did the observations – Table 3.2). The GP1c cloud takes longer to cross the 600-km arc than the GP1a cloud and has a higher peak value. For both subexperiments, the time of the predicted peak value is one sampling period later than the time of the observed peak value. The center of the GP1c cloud also shifts

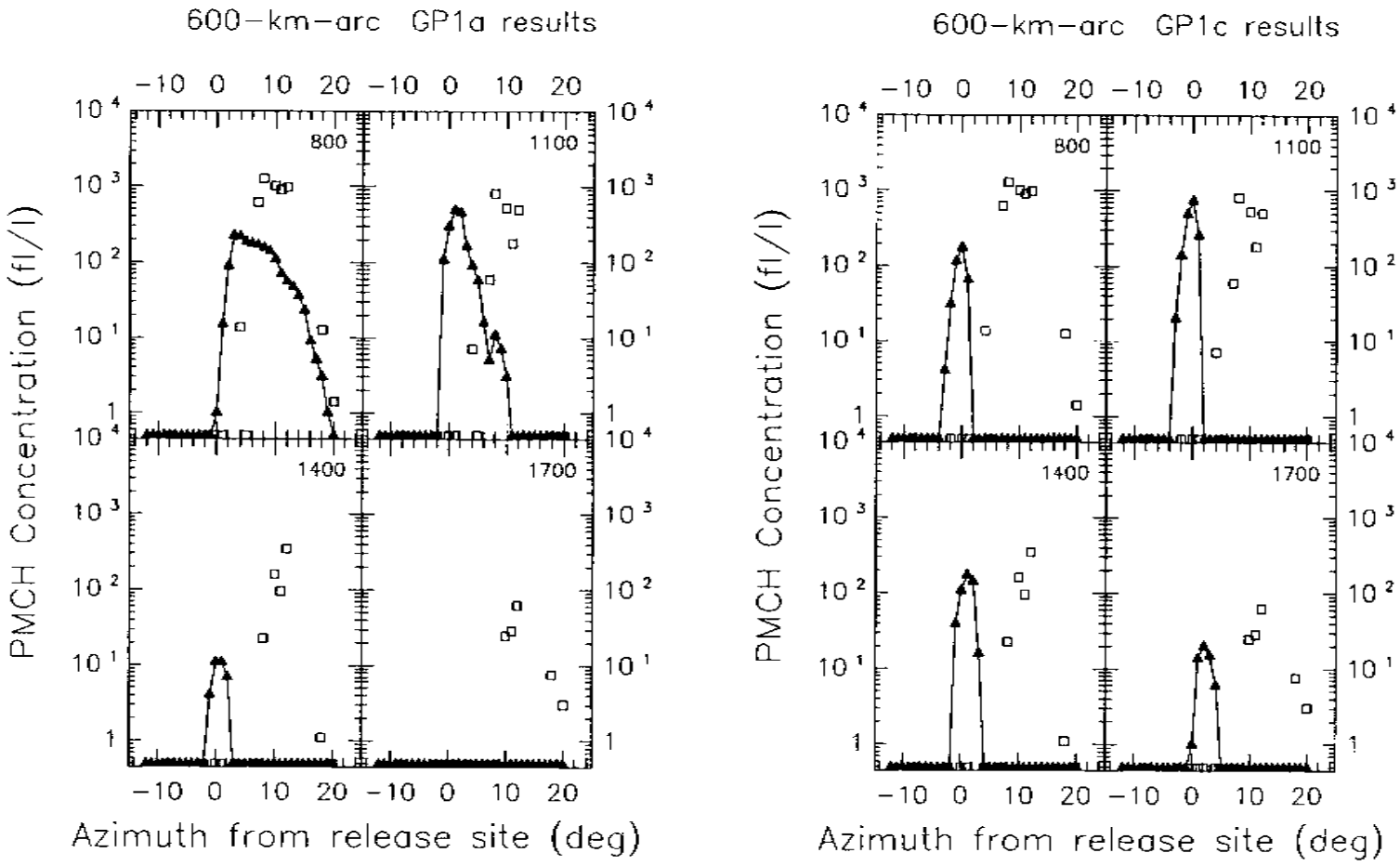

Figure 5.19: Time sequence of concentration–azimuth plots of observed vs. Exp. GP1a (lefthand panel: 'L') and observed vs. Exp. GP1c (righthand panel: 'R') estimated PMCH concentrations for the 600-km sampling arc for the first four sampling periods: (a) 0800–1100 GMT; (b) 1100–1400 GMT; (c) 1400–1700 GMT; and (d) 1700–2000 GMT. Observed values are indicated by open squares; predicted values are indicated by filled triangles connected by a solid line. The starting time of each sampling period (GMT) is plotted in the upper righthand corner of each panel.

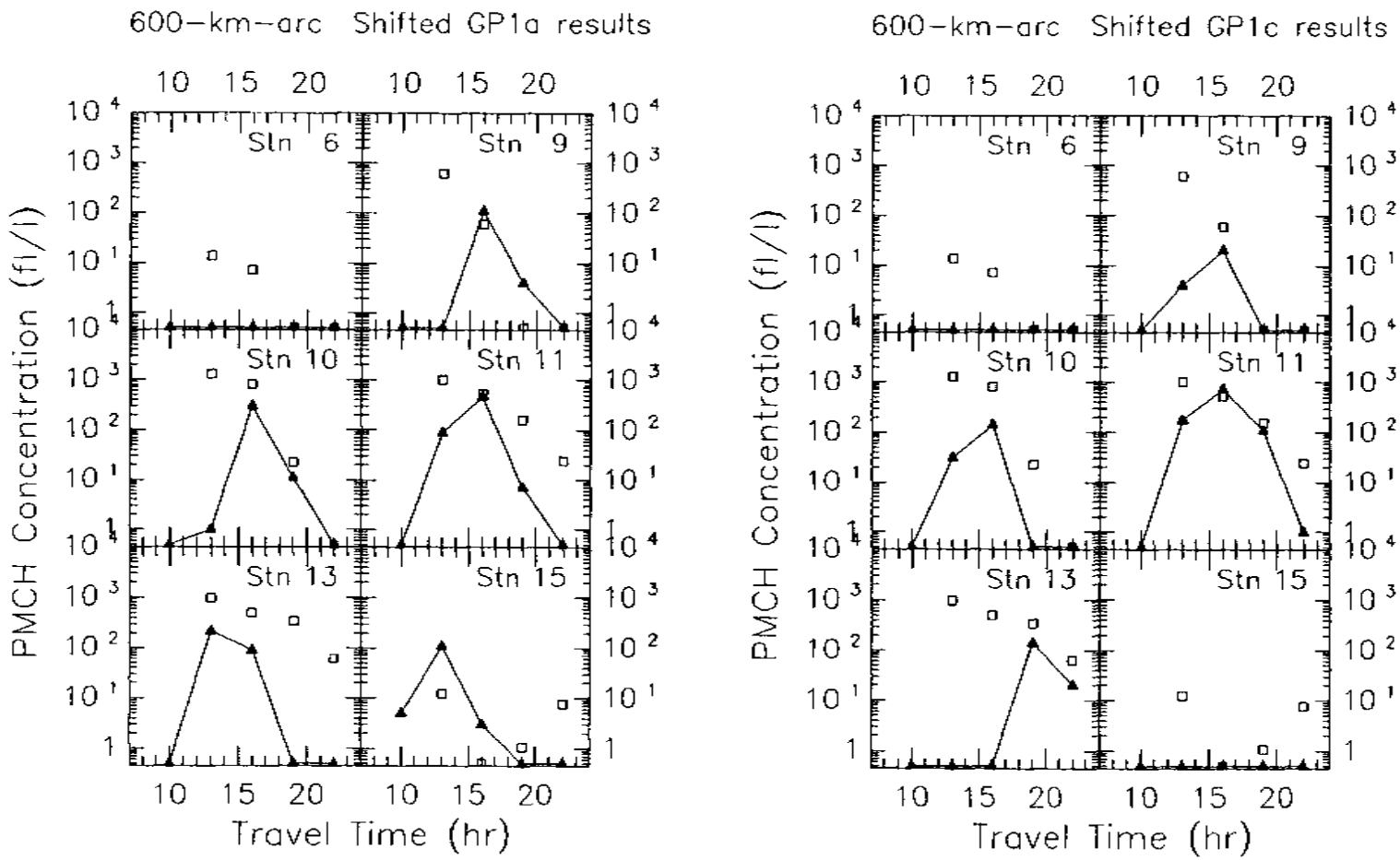

Figure 5.20: Concentration–time plots of observed vs. Exp. GP1a (lefthand panel: 'L') and observed vs. Exp. GP1c (righthand panel: 'R') estimated PMCH concentrations for six 600-km-arc sampling stations: (a) Station 6; (b) Station 9; (c) Station 10; (d) Station 11; (e) Station 13; and (f) Station 15. Observed values are indicated by open squares; predicted values are indicated by filled triangles connected by a solid line. The station ID number is plotted in the upper righthand corner of each panel.

slightly to the east with time as did the observed cloud center. Cross sections through the Exp. GP1c cloud are more symmetrical than GP2a cross sections. Finally, although the mean centerlines of these two clouds are quite close together (Table 5.5), the large difference in width makes it possible for the GP1a predicted cloud to have considerable overlap with the observed cloud (Fig. 5.19L) while the GP1c predicted cloud has *no* overlap at all with the observed cloud (Fig. 5.19R).

Table 5.4 compares 600-km-arc station exposure and total cross-wind integrated exposure (CWIE) values for a 12 h period predicted in Exps. GP1a and GP1c and other experiments against the observed values. There are a number of differences between the Exp. GP1 predicted 600-km-arc station exposures and the observed exposures evident in this table. First, the predicted exposure peaks are located about 9° west of the observed peak at Station 10. Second, the GP1c predicted exposure peak is about one-half the observed value while the GP1a exposure peak is about one-quarter the observed value. Third, the width of the GP1a exposure 'plume' is comparable to the observed plume's width but the GP1c exposure plume is much narrower. And fourth, the CWIE values for the two Exp. GP1 simulations are about 20% of the observed value. Clearly, some fraction of these differences could be due simply to sampling fluctuations arising the location of the sampling sites in space relative to the GLC pattern. However, when CWIE values are calculated for the equally-spaced 91-site arc for Exp. GP1, even smaller values are obtained (Table 5.6).

(c) Quantitative pattern characteristics. Table 5.5 summarizes some of the quantitative cloud characteristics estimated from the observed 600-km-arc station concentrations and from the GP1a and GP1c predicted concentrations along the arc of 91 equally-spaced sites. In contrast to the 100-km arc measurements (Table 5.3), many of the Exp. GP1a simulation predictions listed in Table 5.5, including maximum width, CWIE value, and centerline azimuth, agree better with the 600-km-arc observations than do the Exp. GP1c predictions. However, the Exp. GP1c peak concentration value agrees better with the

Table 5.4: Comparison of predicted 600-km-arc station ground-level exposures (fl h l^{-1}) with observed values for the 12-h period from 0800–2000 GMT, July 9, 1980. A threshold value of 3.4 fl l^{-1} has been subtracted from the observed ground-level concentrations listed in Table 3.2 in obtaining the 'Obs.' values listed in the last horizontal line of the table. A dash (–) indicates 'no data'. The rightmost vertical column gives crosswind-integrated exposures (CWIE) over Stations A–32, assuming a mean cross-wind station spacing of 21.5 km. The two-line entries 'wrap-around'; that is, the second line of exposures for an experiment corresponds to the second line, marked by slashes, of station numbers and station azimuths.

Azim.	353 /38	358 /40	359 /43	1 /44	2 /49	4 /50	5 /53	7 /54	9 /56	11	12	14	20	21	23	25	28	30	36	
Exp. No.	600-km-arc Station Number																			CWIE (fl km h^{-1})
	A /24	2 /25	3 /26	4 /27	5 /28	6 /29	7 /30	9 /31	10 /32	11	12	13	15	16	17	18	19	20	23	
GP1a	0	51	951	1422	1134	720	606	510	357	171	123	96	0	0	0	0	0	0	0	132000
GP1c	0	957	3066	297	75	0	0	0	0	0	0	0	0	0	0	0	0	0	0	95000
GP2a	420	960	276	3	0	0	0	0	0	0	0	0	0	0	0	0	0	0	0	36000
GP2c	1626	0	0	0	0	0	0	0	0	0	0	0	0	0	0	0	0	0	0	35000
GP3	0	0	0	0	0	0	0	0	0	0	0	0	1371	750	447	45	12	0	0	
	0	0	0	0	0	12	3	0												57000
GP4a	0	0	0	0	0	0	0	0	0	0	0	0	0	0	0	0	6	675	1539	
	1122	501	1083	1152	2733	2301	534	45	0											251000
GP4b	0	0	0	0	0	0	0	0	0	0	0	0	1569	1743	1305	591	207	6	0	
	0	0	0	0	0	0	9	0												117000
GP5	0	0	0	0	0	0	0	0	0	0	0	0	0	0	0	0	201	2097	156	
	81	0	9	27	315	327	252	12	0											75000
Obs.	0	1	1	0	0	63	0	2051	6347	5455	3610	5647	64	16	0	0	0	0	0	500000

observed peak value. The choice of edge criterion also has a large effect on the estimated cloud width for Exp. GP1a.

(d) Scattergrams. Following the format of Fig. 5.15, Fig. 5.21 presents unmatched-peak and matched-peak scattergrams of the correspondence of the Exp. GP1a and GP1c predicted concentrations with measured values along the 600-km arc. The position error in the location of the predicted clouds centerlines is particularly evident in Fig. 5.21c, a pure 'L-shaped' scattergram. The narrowness of the GP1c predicted cloud is suggested by the fact that in Fig. 5.21d, there are no 'Pr>0, Ob=0' or non-zero 'Pr > Ob' concentration pairs.

5.3 Results of the Two-Dimensional Experiment

Table 5.1 lists 2 two-dimensional experiments, Exps. GP1 and GP2. Exp. GP1, however, was effectively a one-dimensional simulation since it was initialized with a horizontally homogeneous atmosphere over a flat, uniform surface. This experiment was discussed in the previous section. The major difference between Exps. GP1 and GP2 was the specification of sloping two-dimensional terrain in Exp. GP2. With this exception and the sounding extension (see below), the RAMS setup for the GP2 simulation was the same as for the GP1 simulation (Sec. 5.2). Results from the Exp. GP2 RAMS and MLPDM simulations will be discussed in this section.

5.3.1 Two-dimensional-experiment meteorological simulations

As was the case with Exp. GP1, two GP2 subexperiments were actually run, differing only in their starting times and in the initial atmospheric profiles selected. Exp. GP2a, like Exp. GP1a, used the 1200 GMT sounding from Oklahoma City for July 8, 1980 to initialize the RAMS meteorological model. Exp. GP2c[191], like Exp. GP1c, used the composited 'geostrophic' sounding to initialize the RAMS meteorological model.

---

[191] Rather than Exp. GP2b so as to identify the initial field.

Table 5.5: Tracer cloud characteristics from Great Plains numerical experiments — 600 km arc. Cloud arrival time, transit time, and maximum width all depend on the criterion used to determine the cloud edges. Azimuth range and arc length have units of degrees and kilometers, respectively, and have been determined from the equally-spaced site (1° or 10.5 km spacing) concentrations. Mean center-line azimuth values are based on Table 5.6.

Exp. No.	Arrival Time (GMT)	Transit Time (h)	Maximum Width			Max. Conc. ($fl\,l^{-1}$)	Time of Max'm (GMT)	CWIE ($fl\,km\,h\,l^{-1}$) ($\times 10^{-3}$)	Mean CL Azimuth (°)
			St'n Range	Azim. Range	Arc Length				
10%-of-peak threshold									
GP1a	0800–1100	6	4–11	11	116	494	1100–1400	111	1
GP1c	0800–1100	9	2–3	4	42	731	1100–1400	80	359
GP2a	0800–1100	6	A–3	7	74	800	0800–1100	106	356
GP2c	0800–1100	6	A	4	42	746	1100–1400	126	351
GP3	0800–1100	6	15–17	8	84	639	1100–1400	136	17
GP4a	1100–1400	9	20–29‡	22	230	591	1400–1700	331	34/49*
GP4b	0800–1100	9	15–19	9	94	428	1100–1400	106	21
GP5	0800–1100	9	19–20	11	115	451	1100–1400	139	32/50*
Obs'd	0800–1100†	9	9–13	11	115	1280	0800–1100	500	9
3 $fl\,l^{-1}$ threshold									
GP1a	0500–0800	12	4–13	20	210	494	1100–1400	111	1
GP1c	0800–1100	12	2–5	5	53	731	1100–1400	80	359
GP2a	0500–0800	9	2–6	9	95	800	0800–1100	106	356
GP2c	0500–0800	12	A	7	74	746	1100–1400	126	351
GP3	0500–0800	12	15–19	10	105	639	1100–1400	136	17
GP4a	0800–1100	9	20–31‡	28‡	294	591	1400–1700	331	34/49*
GP4b	0800–1100	9	15–19	13	136	428	1100–1400	106	21
GP5	0800–1100	12	19–30‡	27‡	284	451	1100–1400	139	32/50*
Obs'd	0800–1100†	15	6–15	17	178	1280	0800–1100	500	9

†Or earlier ‡Including gap * Bimodal (see Table 5.6)

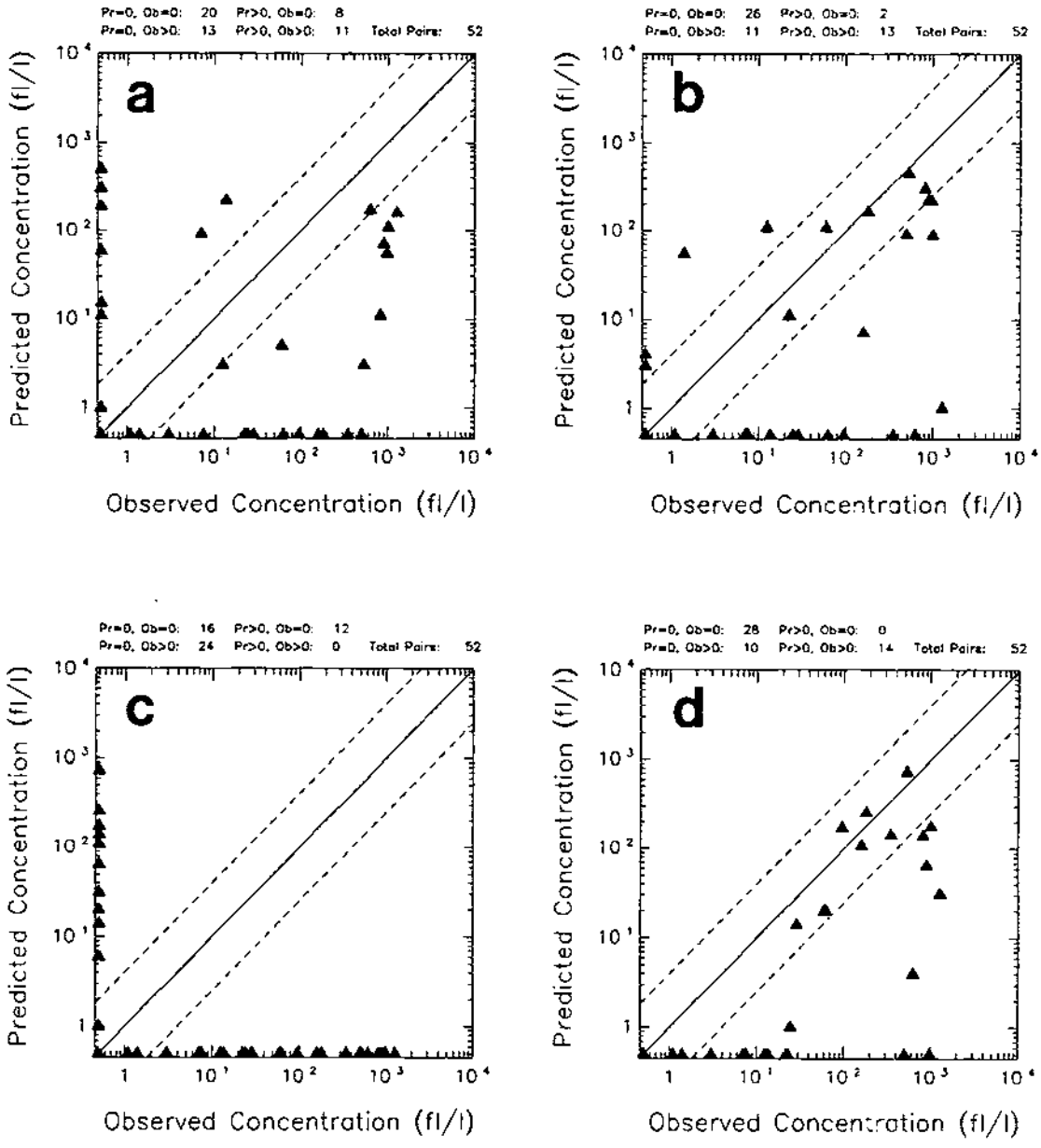

Figure 5.21: Scattergrams for observed 600-km-arc PMCH concentrations (less 3.4 $fl\,l^{-1}$) vs. (a) unshifted Exp. GP1a estimated concentrations, (b) center-line-shifted Exp. GP1a estimated concentrations, (c) unshifted Exp. GP1c estimated concentrations, and (d) center-line-shifted Exp. GP1c estimated concentrations. Plotted pairs have been drawn from the set of concentrations for Stations A–24 and the first four 3-hour observing periods from 0800–2000 GMT, July 9, 1980. The diagonal lines are the one-to-one correspondence line and two factor-of-4 (i.e., 1:4 and 4:1) lines.

Two-dimensional-experiment meteorological model configuration

The terrain heights used in Exp. GP2 were extracted from a west-east cross section at 39.1°N across the low-pass-filtered topographic field plotted in Fig. 4.13d. This terrain cross section can be seen in Figs. 5.7 and 5.25c,d. Because the lowest elevation on this cross section was 171 m and the surface elevation at Oklahoma City is 392 m, it was also necessary to extend the OKC 1200 GMT sounding downwards slightly. This was done simply by extrapolating the temperature profile at the first two measured levels downwards. The pressure at the low point was obtained by reducing the OKC surface pressure based on the standard atmosphere. Wind speed was reduced by about 40%; wind direction was held constant.

Two-dimensional-experiment meteorological results

Fig. 5.22 displays time–height cross sections of four aspects of the GP2a wind profile, namely, horizontal wind speed, wind direction, u-component, and v-component, for the first 48 h of the RAMS simulation at a point near the center of the domain corresponding to the location of Oklahoma City. Fig. 5.23a shows the wind-vector time-height cross section and Figs. 5.23b-d portray corresponding time-height cross sections of potential temperature, water-vapour mixing ratio, and gradient Richardson number for Exp. GP2a for the same 48-h period. Differences between these two figures and Figs. 5.1 and 5.2, the corresponding figures for Exp. GP1a, are directly attributable to the influence of topography.

The two sets of figures are broadly similar. It is clear from Figs. 5.22a,d, owever, that the nocturnal low-level jet was stronger in the GP2a RAMS simulation. This is consistent with the presence of topography, since daytime upslope flow generated by differential surface heating should create a stronger daytime horizontal ageostrophic component and thus a stronger nighttime inertial oscillation (cf. Fig. 1.3 and Sec. 4.7). The presence of west-east sloping terrain also means that west-east and vertical advection can now have a non-zero contribution, as suggested by the time-varying behaviour of the upper two kilometers shown in Figs. 5.22 and 5.23 and differences in the vertical structure of

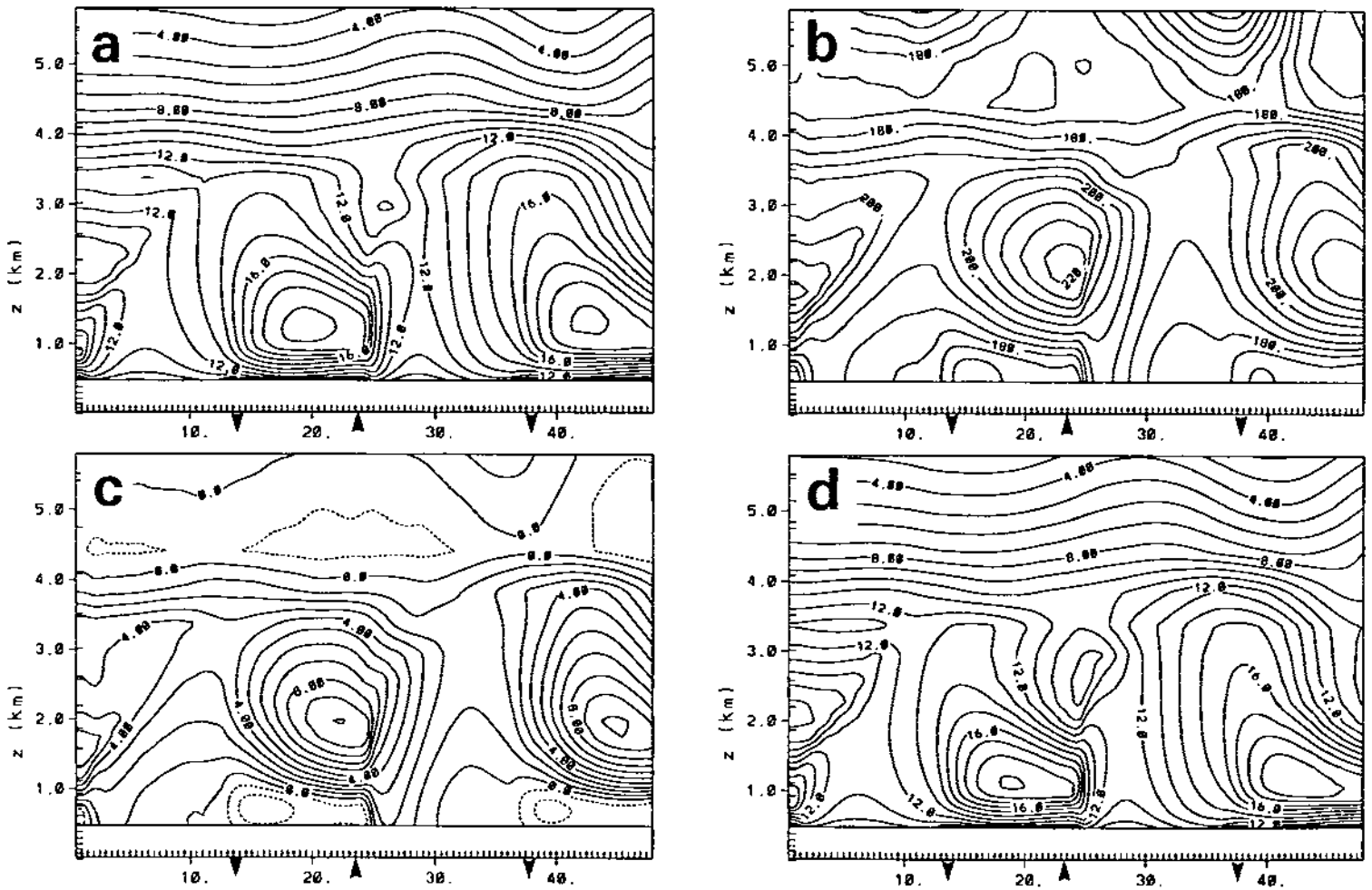

Figure 5.22: Four views of the time evolution of the Exp. GP2a vertical wind profile over the first 48 h of simulation starting at 0600 LST: (a) wind speed; (b) wind direction; (c) u-component; and (d) v-component. Contour intervals are 1 m s^{-1} in panels (a), (c), and (d) and 5° in panel (b). The meteorological convention for wind direction has been used with 0° corresponding to a north wind, 90° corresponding to an east wind, etc. The 'up' and 'down' arrowheads indicate sunrise and sunset, respectively.

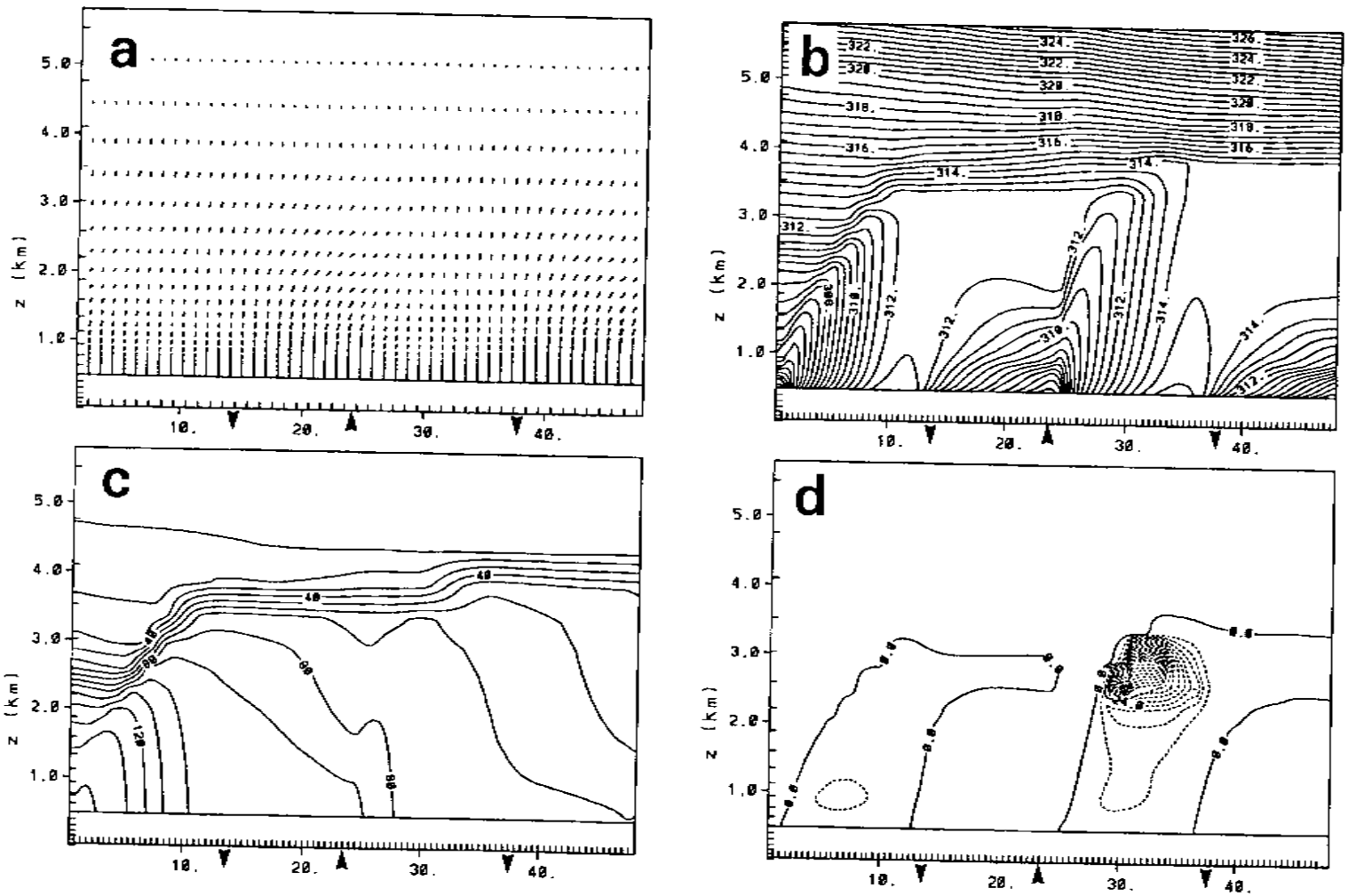

Figure 5.23: Same as Fig. 5.22 except for (a) wind vectors, (b) potential temperature, (c) water-vapour mixing ratio, and (d) gradient Richardson number. Contour intervals in panels (b), (c), and (d) are 0.5 K, 0.001 kg kg^{-1}, and 2, respectively. The longest wind vector corresponds to a wind speed of 20 m s^{-1}. An upward-pointing wind vector denotes a south wind, a rightward-pointing wind vector denotes a west wind, etc. The 'up' and 'down' arrowheads along the abscissa indicate sunrise and sunset, respectively.

potential temperature and water-vapour mixing ratio on the second day of the simulation between Exps. GP1a and GP2a (Figs. 5.2b,c vs. 5.23b,c).

Vertical cross sections of the Exp. GP2a horizontal velocity components at mid afternoon, night, and early morning after 9, 17, and 25 hours of simulation, respectively, are shown in Fig. 5.24. The first two times are the same as those in the O'Neill simulation figures (Figs. 4.22 and 4.24) and there is a strong 'family resemblance' between the fields plotted for these two summertime Great Plains cases. The strengthening of the low-level jet and then weakening at different phases of the inertial oscillation is evident in Figs. 5.24d–f. The development of a daytime upslope component is not so marked in the u-component panels. In fact, the only easterly flow shown in these panels occurs at night in association with the backing of the decoupled low-level flow (Fig. 5.24b). The presence of the inertial oscillation is again in evidence as that easterly flow changes to westerly flow by morning (Fig. 5.24c).

5.3.2 Two-dimensional-experiment mesoscale tracer transport

Three projections of Exp. GP2a grid-scale trajectories were plotted in Figs. 5.6, 5.7, and 5.8, respectively. One feature of these figures was not discussed earlier but was left instead until this section because it is related to the presence of topography. Careful examination of Figs. 5.8a,c reveals the lowest two trajectories to be slowly ascending and the upper three trajectories to be descending. There are two reasons for this behaviour. First, as can be seen in Fig. 5.7, the topography in this experiment slopes downward from west to east. Thus, an air parcel with an eastward velocity component will travel downslope while an air parcel with a westward velocity component will travel upslope. From the plan view of Fig. 5.6c, it can be seen that the trajectories at the lowest two levels (Nos. 1, 2, 6, and 7) did in fact travel westward while the trajectories at the top two levels (Nos. 4, 5, 9, and 10) traveled eastward. This partially explains the observed behaviour. However, the presence of sloping topography coupled with the diurnal heating cycle also generated slope flows with accompanying vertical motions (e.g., Figs. 4.23, 4.25). During the daytime, one would thus expect ascending motion over the

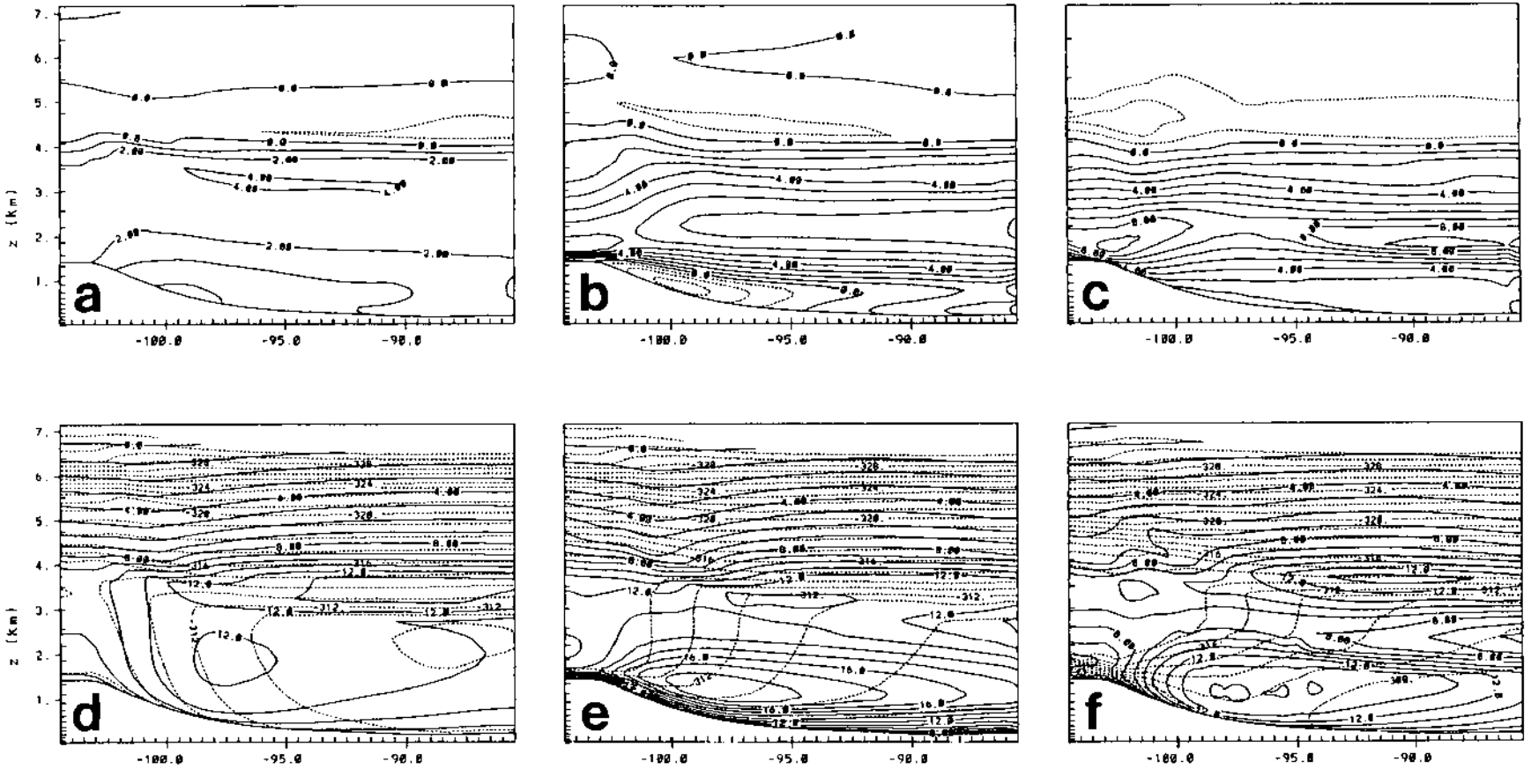

Figure 5.24: Horizontal velocity components and potential temperature θ for Exp. GP2a RAMS simulation at three times: (a) u-component, 1500 LST; (b) u-component, 2300 LST; (c) u-component, 0700 LST; (d) v-component and θ, 1500 LST; (e) v-component and θ, 2300 LST; (f) v-component and θ, 0700 LST. The dashed lines in panels (d)–(f) denote isentropes with 1 K spacing; the solid lines in the same panels denote southerly v-component isopleths with 1 $\mathrm{m\,s^{-1}}$ spacing.

higher terrain in the western portion of the domain and descending motion over the eastern portion of the domain, again consistent with the observed behaviour of the trajectories.

A special trajectory calculation was carried out in order to determine the relative importance of these two mechanisms. The grid-scale trajectories are normally calculated using RAMS *three*-dimensional wind fields. However, a second set of trajectories was calculated for Exp. GP2c in which the trajectories were constrained to stay on z^* surfaces[192]. These *two*-dimensional trajectories were thus affected by ascent or descent following z^* surfaces over sloping topography but not by vertical motions *across* z^* surfaces. The two sets of trajectories are shown in Fig. 5.25. They are very similar, indicating that the contribution of vertical advection due to the east-west slope-flow circulation is quite small in this simulation. However, there are some noticeable differences. The two lowest trajectories are slightly shorter in the three-dimensional case while the uppermost trajectory lie farther to the west, presumably as a result of sinking to levels with more easterly winds.

Fig. 5.26 compares plan views of the start-of-release grid-scale trajectories for the two Exp. GP2 subexperiments with the corresponding trajectories from Exps. GP1a and GP1c[193]. Any differences between the upper and lower panels are due to the influence of topography. The GP2 trajectory endpoints lie further to the north than their GP1 counterparts and have greater horizontal separation, consistent with the presence of a stronger nocturnal low-level jet and larger vertical wind shear. The presence of daytime upslope flow is suggested by the westward displacement of the points where the Exp. GP2 trajectories cross the 100-km and 600-km sampler arcs. One other noticeable difference between Figs. 5.26a,c is the position of the uppermost trajectory, No. 5, relative to the other trajectories. In Fig. 5.26c this particle, which was released at 2379 m AGL, followed a nearly straight path, suggesting that it was located above or close to the top

---

[192] Which are nearly terrain-following close to the ground.

[193] The Exp. GP1 panels were also included in Fig. 5.3.

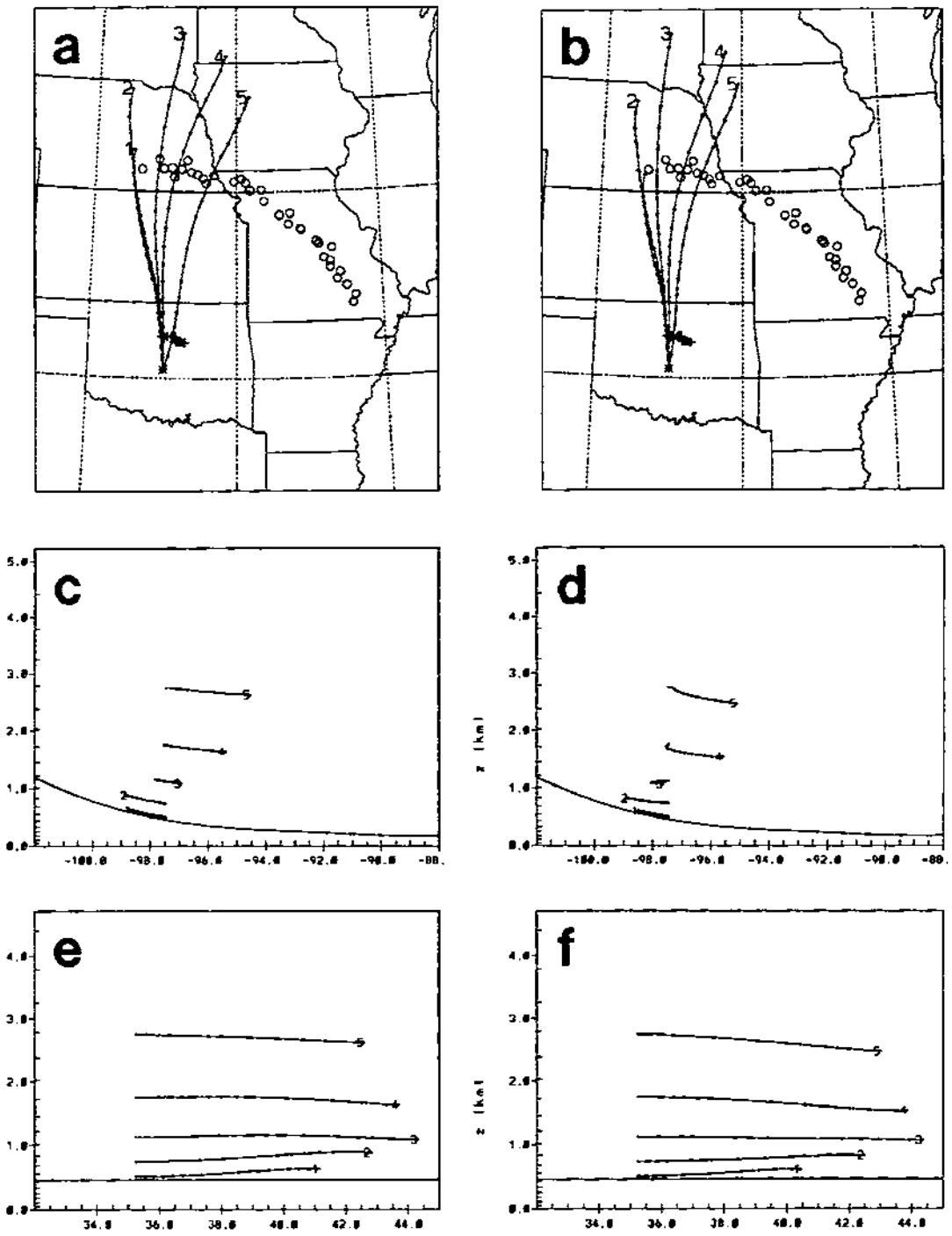

Figure 5.25: Three views of Exp. GP2c two-dimensional and three-dimensional grid-scale trajectories: (a) two-dimensional trajectories, XY projection; (b) three-dimensional trajectories, XY projection; (c) two-dimensional trajectories, XZ projection; (d) three-dimensional trajectories, XZ projection; (e) two-dimensional trajectories, YZ projection; (f) three-dimensional trajectories, YZ projection. The small filled squares mark the hourly trajectory positions. Trajectory-endpoint labels '1', '2', '3', '4', and '5' indicate the five release heights 50 m, 293 m, 686 m, 1334 m, and 2379 m AGL, respectively. Viewpoints are downward, northward, and westward for the three projections.

of the PBL and did not experience the inertially-oscillating winds that the lower particles experienced, as indicated by their *curved* trajectories. However, in Fig. 5.26a the uppermost particle also followed a curved path and was located further to the east than the other particles. This behaviour would suggest either that the PBL was deeper in Exp. GP2a compared to Exp. GP1a or else that subsidence brought this particle down into the PBL (or both).

5.3.3 Two-dimensional-experiment mesoscale tracer dispersion

MLPDM simulations, each using 3600 particles, were run for Exps. GP2a and GP2c.This section follows the same format as the section describing Exp. GP1 mesoscale dispersion. The same CAG, same sampling-volume depth, and same time averaging procedure have been used as well.

Two-dimensional-experiment concentration estimates

100-km arc.

(a) GLC patterns. Figs. 5.11c-d show *logarithmically-spaced* isopleths of PMCH 45-minute GLCs for the third 100-km-arc sampling period for these two subexperiments. The two surface concentration patterns are quite similar at this time and are both broader than the Exp. GP1 GLC patterns (Figs. 5.11a-b). The centerline axis of the Exp. GP2c GLC pattern is the most westerly oriented of the four GLC patterns shown in this figure.

(b) Station values. Exp. GP2a and GP2c predicted GLCs are plotted against azimuth angle across the 100-km sampler arc in Fig. 5.27 along with the actual observed station GLCs for the first six observing times. Fig. 5.28 presents some of the same values in a complementary way, showing the time history of the predicted and observed concentrations at six of the 100-km arc station sites. These two figures suggest that the predicted GLC values are comparable to the observed values for this experiment as well. However, just as in the case of Exp. GP1, Fig. 5.28 indicates that the GP2 predicted clouds are narrower than the observed cloud. These two figures also show that the GP2 simulated clouds arrive one sampling period too early.

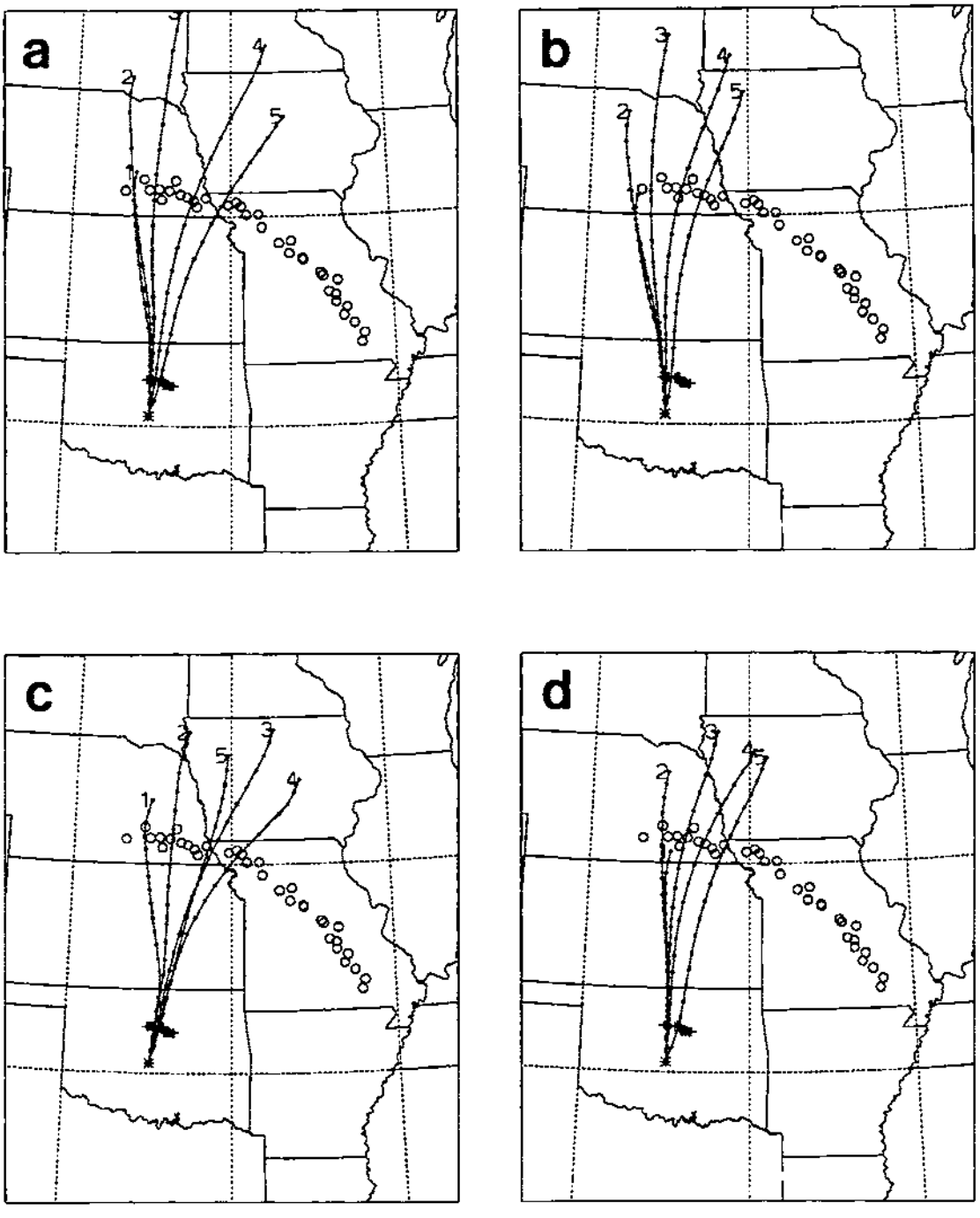

Figure 5.26: Same as Fig. 5.3 except for Exp. GP2 grid-scale trajectories vs. Exp. GP1 grid-scale trajectories: (a) Exp. GP2a wind fields; (b) Exp. GP2c wind fields; (c) Exp. GP1a wind fields; and (d) Exp. GP1c wind fields.

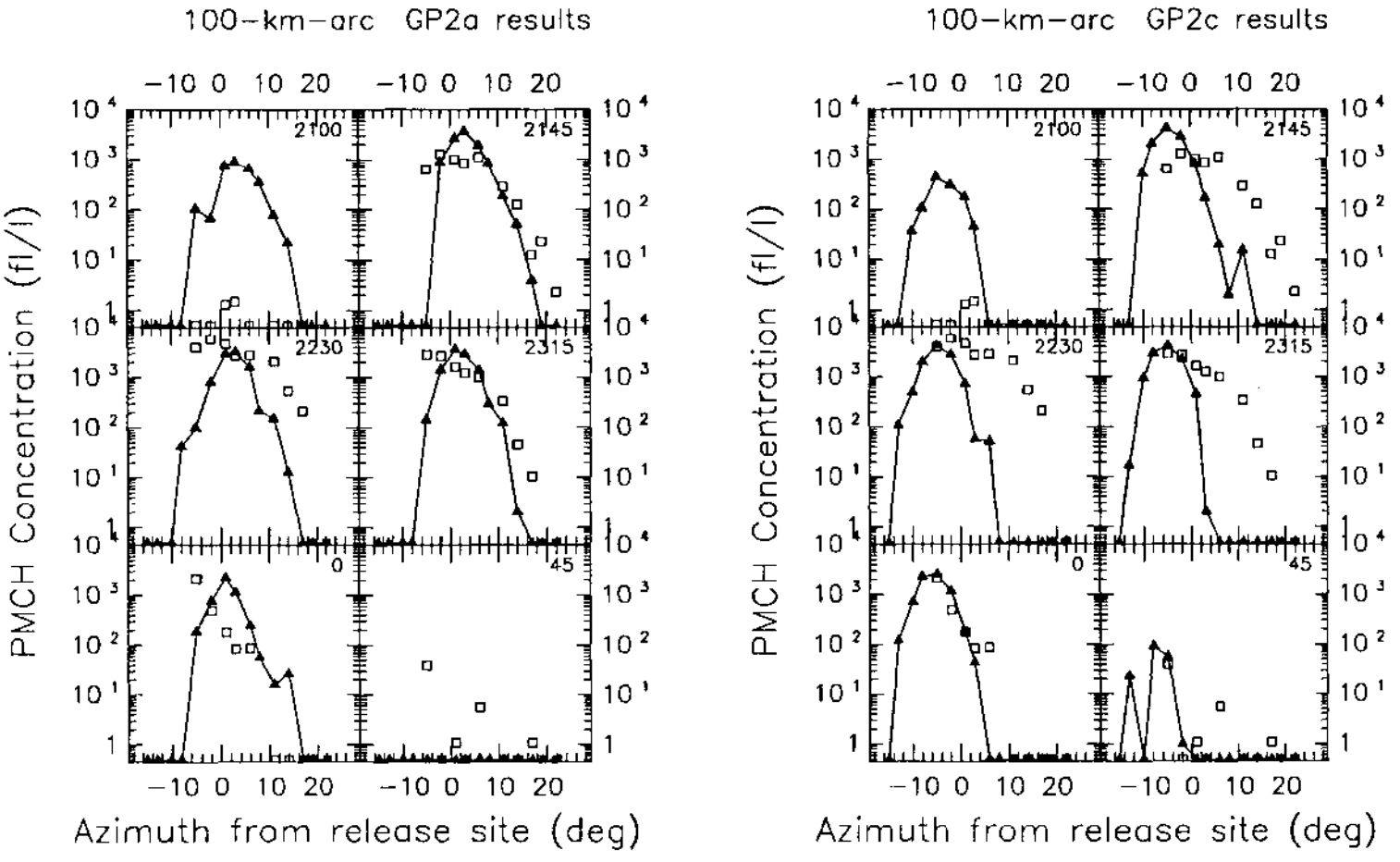

Figure 5.27: Time sequence of concentration–azimuth plots of observed vs. Exp. GP2a (lefthand panel: 'L') and observed vs. Exp. GP2c (righthand panel: 'R') estimated PMCH 45-minute-average concentrations for the Great Plains experiment 100-km sampling arc for the first six sampling periods: (a) 2100–2145 GMT; (b) 2145–2230 GMT; (c) 2230–2315 GMT; (d) 2315–0000 GMT; (e) 0000–0045 GMT; and (f) 0045–0130 GMT. Observed values are indicated by open squares; predicted values are indicated by filled triangles connected by a solid line. The starting time for each sampling period (GMT) is plotted in the upper righthand corner of each panel.

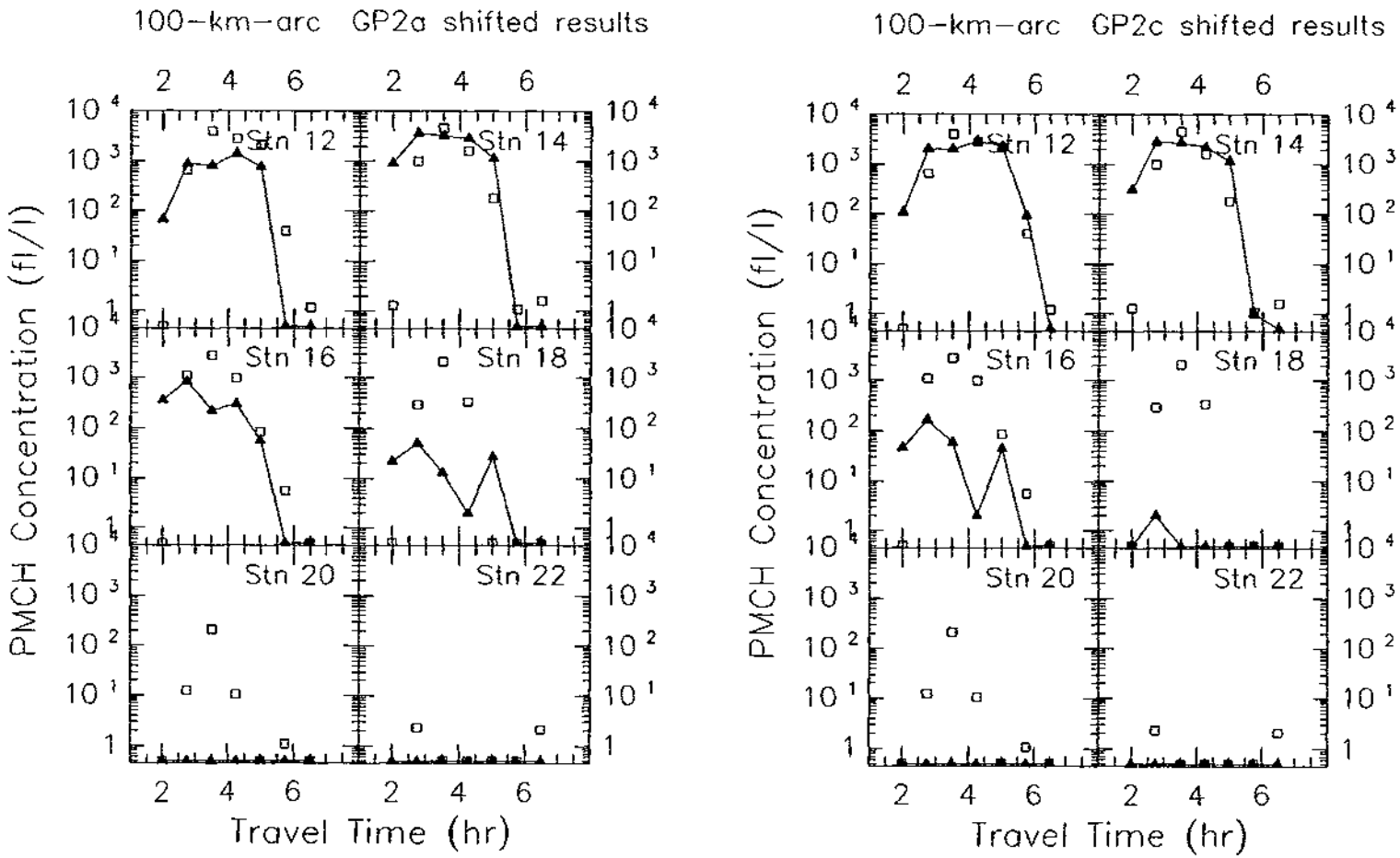

Figure 5.28: Concentration-time plots of observed vs. Exp. GP2a (lefthand panel: 'L') and observed vs. Exp. GP2c (righthand panel: 'R') estimated PMCH 45-minute-average concentrations for six 100-km-arc sampling stations: (a) Station 12; (b) Station 14; (c) Station 16; (d) Station 18; (e) Station 20; and (f) Station 22. Observed values for Stations 12–20 are indicated by open squares; predicted values are indicated by filled triangles connected by a solid line. The station ID number is plotted in the upper righthand corner of each panel. Note that the GP2a station values were shifted westward by one station length while the GP2c station values were shifted eastward by one station length.

The Table 5.2 station exposure values determined from the two Exp. GP2 MLPDM simulations help to quantify the model's performance. The predicted maximum station exposures are larger than the observed value (9139 and 11688 vs. 7791) while the observed exposure 'plume' is wider than the plume predicted by either GP2 subexperiment. However, the two GP2 exposure plumes are both wider than the two GP1 plumes, consistent with Fig. 5.11. The GP2a exposure maximum, like the GP1c maximum, is located only one station to the east of the observed maximum at Station 13 while the GP2c exposure maximum is located one station to the west of the observed maximum. In fact, Table 5.2 suggests that the GP1c and GP2a clouds were quite similar as they crossed the 100-km arc (cf. Fig. 5.11). The estimated CWIE values for the two Exp. GP2 simulations were both also smaller than but close to the observed value (with the caveat again that the latter would have been larger had Station 17 collected good data).

(c) Quantitative pattern characteristics. Table 5.3 includes some of the quantitative cloud characteristics estimated from the observed and from the GP2a and GP2c predicted 100-km-arc station concentrations. The peak concentration values predicted by the two GP2 subexperiments were smaller than both the observed peak and the Exp. GP1 predicted peaks. As was the case with the GP1 predicted clouds, the GP2 clouds's arrival times were one sampling period too early and the transit time was one period too long (except for Exp. GP2a and the 3 fll^{-1} threshold). Comparison of the cloud widths determined for the two edge criteria indicates, consistent with Table 5.2, that the GP2 clouds had wider 'wings' than the GP1 clouds, possibly as a result of larger vertical wind shear (cf. Fig. 5.26). Note that cloud centerline azimuths for Exps. GP1c and GP2a were identical (cf. Fig. 5.11). The difference in cloud centerline azimuths between Exps. GP1a and GP2a and between Exps. GP1c and GP2c suggests that daytime upslope winds induced by differential heating across the west-east terrain slope backed the low-level horizontal winds by 6–7°.

(d) Scattergrams. Fig. 5.29 presents both 'unmatched' and 'peak-matched' scattergrams of Exp. GP2a and GP2c predicted concentrations vs. measured values along the 100-km arc. Unlike the case for Exp. GP1a (see Figs. 5.15a-b), the peak-matched scattergrams for Exp. GP2 exhibit only a slight improvement in the distribution of matched non-zero concentration pairs. This is undoubtedly due to the small centerline position errors for these two simulations (3° on either side of the observed cloud centerline: Table 5.3). On the other hand, the number of 'Pr=0, Ob>0' concentration pairs was again considerably larger than the number of 'Pr>0, Ob=0' concentration pairs for the two subexperiments (15 vs. 5 and 15 vs. 4), supporting the other evidence that the predicted clouds were narrower than the observed cloud.

600-km arc.

(a) GLC patterns. Fig. 5.16 compares the predicted GLC patterns for the two GP2 subexperiments with the corresponding GLC patterns for the two GP1 subexperiments. The differences are consistent with the earlier discussion of Fig. 5.26. First, the Exp. GP2 transport winds were stronger than the Exp. GP1 transport winds so that more of the surface cloud in Figs. 5.16c-d has crossed the 600-km arc during the first sampling period. Second, both GP2 patterns are located farther westward than their GP1 counterparts as a result of the low-level easterly upslope winds present in Exp. GP2 but not in Exp. GP1. And third, the relative widths of the four surface clouds shown in Fig. 5.16 are consistent with the trajectory endpoint spread of the three lowest trajectories plotted in Fig. 5.26.

(b) Station values. Fig. 5.30 shows Exps. GP2a and GP2c predicted PMCH ground-level concentrations and the observed concentrations plotted against azimuth angle for the first four 600-km-arc observing times. Fig. 5.31 presents many of the same data in a complementary fashion, showing the time history of the predicted and observed concentrations at six of the 600-km arc stations. Model-predicted values correspond to locations on the equally-spaced 91-site arc, and predicted values in Fig. 5.28 have been offset in

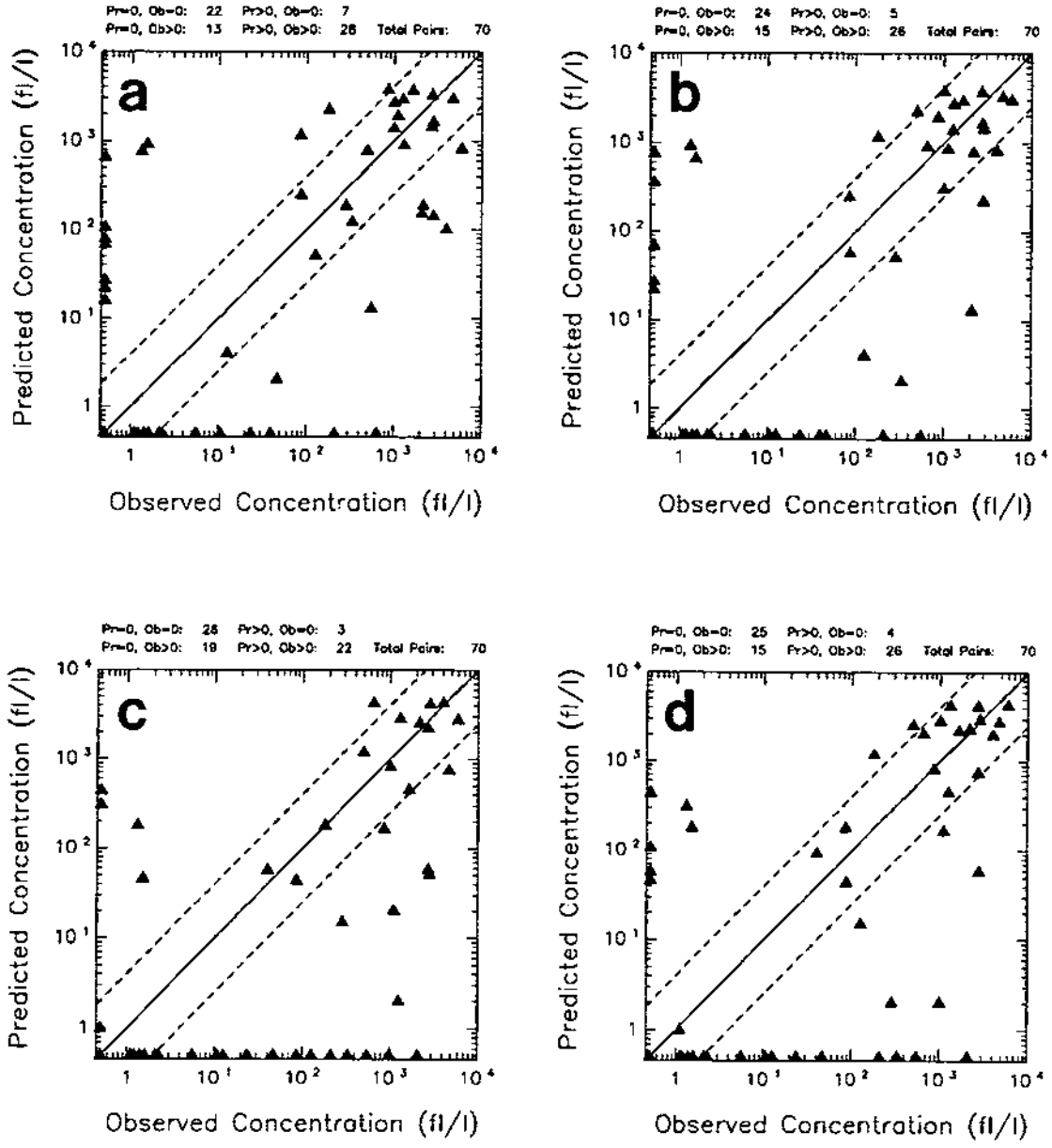

Figure 5.29: Scattergrams for observed 100-km-arc PMCH concentrations (less 3.4 fl^{-1}) vs. (a) unshifted Exp. GP2a estimated concentrations, (b) center-line-shifted Exp. GP2a estimated concentrations, (c) unshifted Exp. GP2c estimated concentrations, and (d) center-line-shifted Exp. GP2c estimated concentrations. Plotted pairs have been drawn from the set of concentrations for Stations 12–21 and the first seven 45-minute observing periods from 2100–0215 GMT. The GP2a station values were shifted westward by one station length in (b) while the GP2c station values were shifted eastward by one station length in (d). The diagonal lines are the one-to-one correspondence line and two factor-of-4 (i.e., 1:4 and 4:1) lines.

the same fashion that those in Fig. 5.28 were. Exp. GP2a station values were offset by 14° and Exp. GP2c station values were offset by 18° based on Tables 5.6 and 5.5.

These two figures suggest some of the similarities and differences between the two subexperiments. Both predicted clouds are located too far to the west and do not overlap the observed cloud at all. The GP2a cloud is a bit wider while the GP2c cloud takes longer to cross the 600-km arc. Peak values are comparable for the two simulations but the GP2a peak occurs one sampling period earlier than the GP2c peak. The Exp. GP2c cross sections are more symmetrical than the GP2a cross sections.

Table 5.4 compares 600-km-arc station exposure and total cross-wind integrated exposure (CWIE) values for a 12 h period predicted in Exps. GP2a and GP2c and other experiments against the observed station exposure values. However, as can be seen from Fig. 5.16c, the Exp. GP2a GLC pattern was situated over the western end of the 600-km arc while the Exp. GP2c GLC pattern was located even farther to the west. Accordingly, Table 5.4 lists only four non-zero station exposure values for Exp. GP2a and only one non-zero value for Exp. GP2c. The corresponding CWIE values are also about one-third of the Exp. GP1 values. The utility of calculating concentrations or exposures along an arc of equally-spaced sites has already been discussed with respect to 'peak matching'. However, the Exp. GP2 600-km-arc GLC patterns illustrate a second advantage of calculating concentrations along a line or arc of equally-spaced stations: that is, complete and regular spatial sampling.

Accordingly, GLC concentrations were also calculated for the 600-km-arc sampling periods[194] along the arc of 91 equally-spaced sites in addition to the actual 600-km-arc sampler sites (see Fig. 5.16d). Table 5.6 lists ground-level exposures calculated for the portion of the 600-km equally-spaced sites beneath the predicted tracer clouds in the various Great Plains experiment simulations. Using this table it is now possible

---

[194] Actually for the first four sampling periods plus the 3-hour period just before the start of sampling on the 600-km arc since tracer was predicted to arrive early in Exps. GP1a, GP2a, and GP2c (cf. Table 5.5).

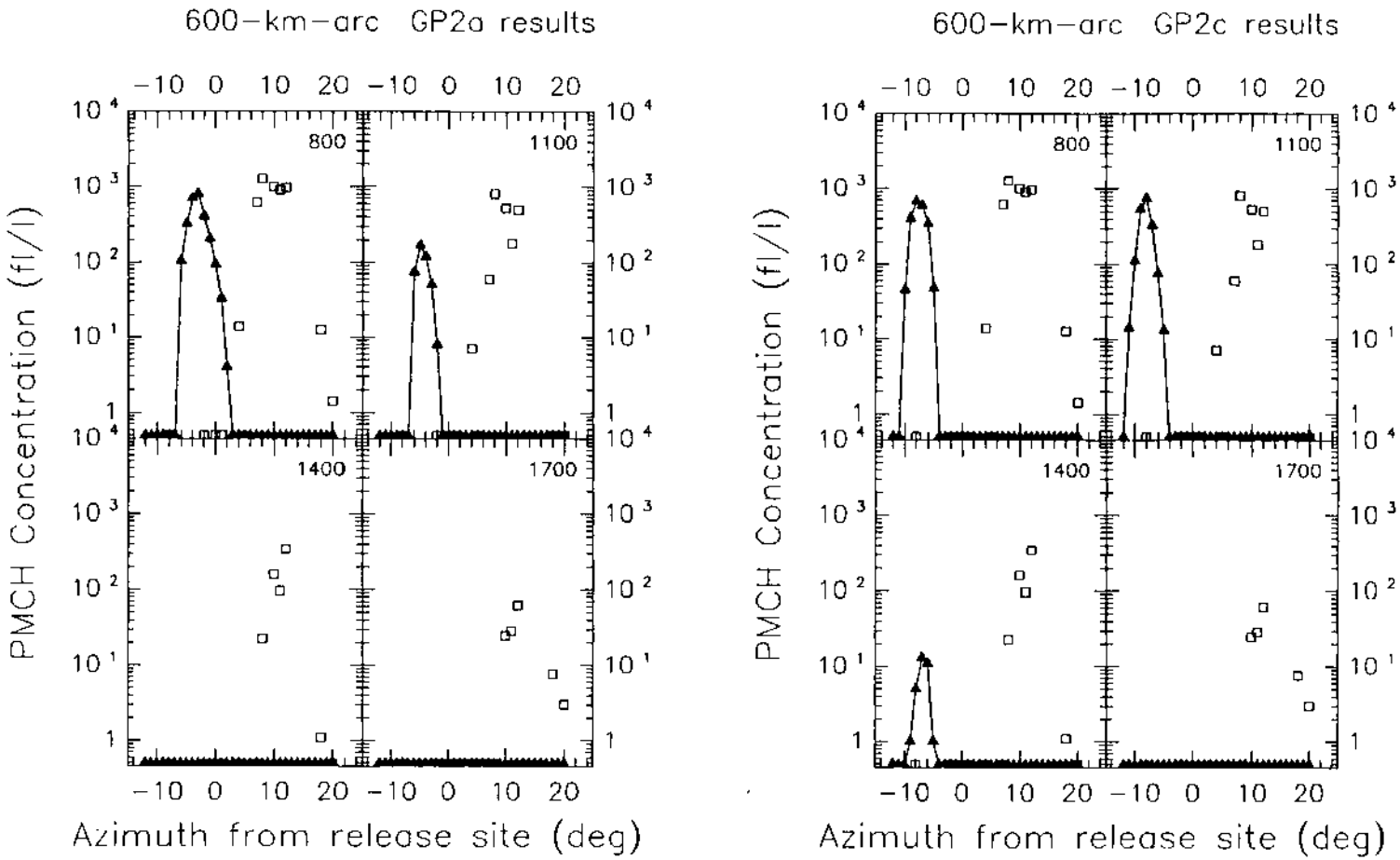

Figure 5.30: Time sequence of concentration–azimuth plots of observed vs. Exp. GP2a (lefthand panel: 'L') and observed vs. Exp. GP2c (righthand panel: 'R') estimated PMCH concentrations for the 600-km sampling arc for the first four sampling periods: (a) 0800–1100 GMT; (b) 1100–1400 GMT; (c) 1400–1700 GMT; and (d) 1700–2000 GMT. Observed values are indicated by open squares; predicted values are indicated by filled triangles connected by a solid line. The starting time of each sampling period (GMT) is plotted in the upper righthand corner of each panel.

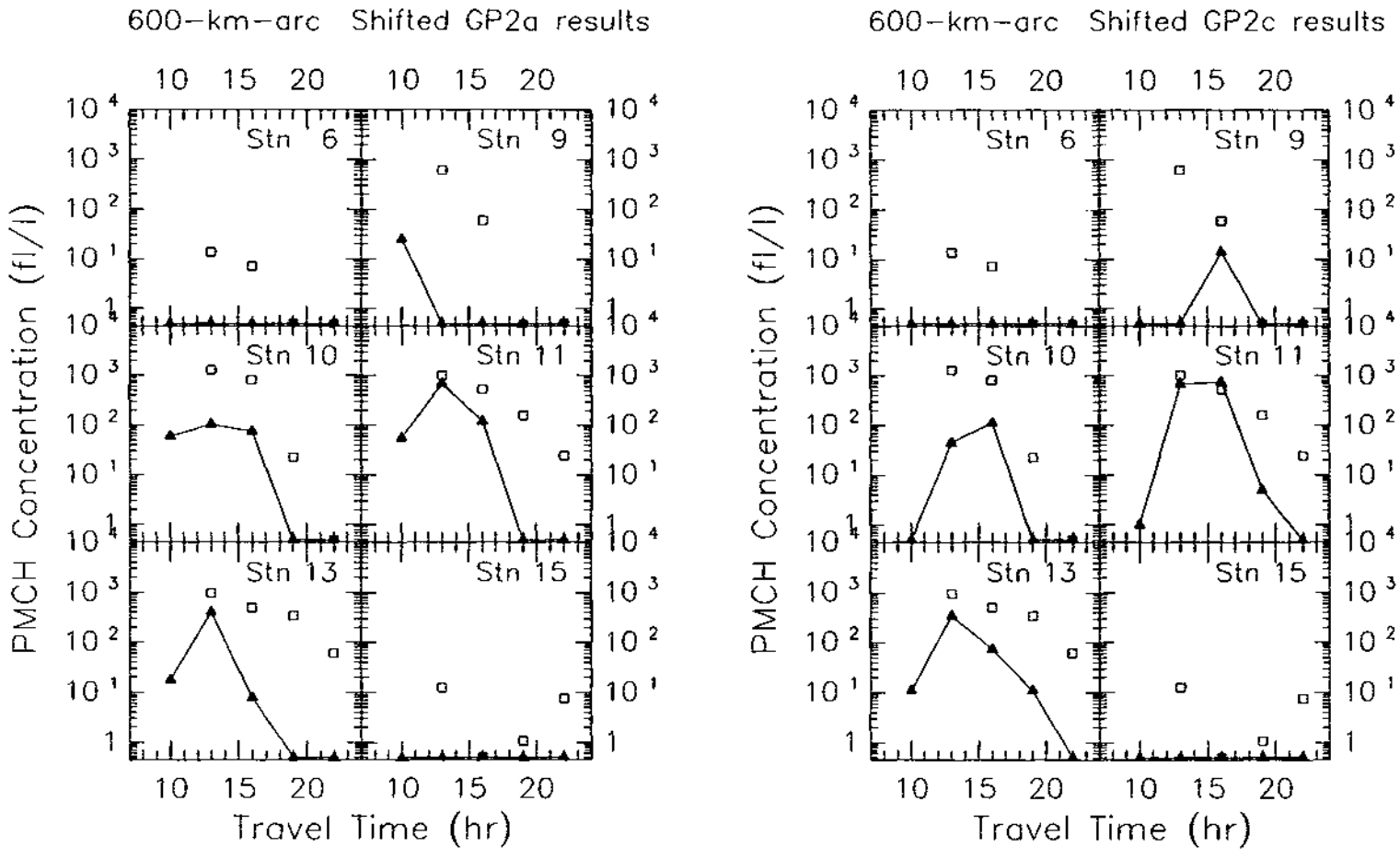

Figure 5.31: Concentration–time plots of observed vs. Exp. GP2a (lefthand panel: 'L') and observed vs. Exp. GP2c (righthand panel: 'R') estimated PMCH concentrations for six 600-km-arc sampling stations: (a) Station 6; (b) Station 9; (c) Station 10; (d) Station 11; (e) Station 13; and (f) Station 15. Observed values are indicated by open squares; predicted values are indicated by filled triangles connected by a solid line. The station ID number is plotted in the upper righthand corner of each panel.

to compare the Exp. GP2c exposure plume to the other experiment plumes and to the observations.

There are a number of interesting features apparent in this table. First, the full coverage and more regular sampling along this second arc of 600-km sites has markedly narrowed the differences in the CWIE values between the four GP1 and GP2 subexperiments. In fact, the CWIE values for both Exps. GP1a and GP1c are lower than those listed in Table 5.4, illustrating the sensitivity of this quantity to the sampling locations used[195]. Consistent with Fig. 5.16, the exposure plumes for Exps. GP1a and GP2a are wider than those for Exps. GP1c and GP2c. These last two subexperiments, however, have larger peak exposures than the first two. Interestingly, the peak exposure occurs at the same station relative to the western edge of the exposure plume in all four of these subexperiments and also quite close to the location of the actual observed peak exposure. The line for the observed station exposure plume in Table 5.6 also indicates the coarser resolution and more irregular station spacing of the actual measurements. The observed CWIE value listed in this table is an underestimate obtained by assuming zero exposures at the missing stations. Compare this value to the value of 500000 given in Table 5.4, which was obtained assuming an average station spacing of 21.5 km.

(c) Quantitative pattern characteristics. Table 5.5 summarizes some of the quantitative cloud characteristics estimated from the observed 600-km-arc station concentrations and from the GP2a and GP2c predicted concentrations along the arc of 91 equally-spaced sites. The predicted peak concentrations for these two simulations are larger than the Exp. GP1 peaks but are still about 35% lower than the observed peak concentration. Only Exp. GP2a agreed with the observations in the timing of the peak concentration. The predicted transit time for the two GP2 subexperiments was also less than the observed time for both cloud-edge criteria.

---

[195] Holland (1991) has discussed the general problem of estimating concentration moments from sparse measurements in detail.

Table 5.6: Comparison of predicted 600-km-arc ground-level exposures (fl h l^{-1}) at 1°-azimuth equally-spaced sites with the observed station exposures for the 15-h period from 0500–2000 GMT, July 9, 1980. All of the exposure values have been left-justified relative to the westernmost non-zero exposure site. The column 'Left-Edge Azimuth' gives the azimuth angle relative to the source of that westernmost site. A threshold value of 3.4 fl l^{-1} has been subtracted from the observed ground-level concentrations listed in Table 3.2 in obtaining the 'Obs.' values listed in the last horizontal line of the table. As well, observations were not available for the 0500-0800 GMT period. A dash (–) indicates 'no data'. The rightmost vertical column gives crosswind-integrated exposures (CWIE) over Stations 8–27, assuming a mean cross-wind station spacing of 10.5 km. The two-line entries 'wrap-around'; that is, the second line of exposures for an experiment corresponds to the second line, marked by slashes, of station relative azimuths.

Exp. No.	Left-Edge Azim.	600-km-arc Relative Azimuth																			CWIE (fl km $h l^{-1}$)
		0 /19	1 /20	2 /21	3 /22	4 /23	5 /24	6 /25	7 /26	8 /27	9 /28	10 /29	11 /30	12 /31	13	14	15	16	17	18	
GP1a	358	339	936	1560	1641	1158	924	735	585	522	510	453	351	213	177	168	126	78	30	15	
		9	3	0																	110600
GP1c	356	72	510	1923	3046	1515	486	93	18	0	0	0	0	0	0	0	0	0	0	0	80450
GP2a	353	534	1491	2478	2628	1422	822	444	204	66	12	6	9	3	0	0	0	0	0	0	106250
GP2c	348	42	468	2835	4278	2841	1320	231	18	0	0	0	0	0	0	0	0	0	0	0	126350
GP3	14	63	459	1650	2865	2679	2007	1197	759	606	393	174	39	0	9	6	0	0	0	0	135500
GP4a	27	6	18	24	63	330	684	1041	1287	1263	1224	1197	1140	1101	1023	942	933	1062	1293	1602	
		1911	2307	2775	2796	2466	1701	858	300	102	27	6	0								330550
GP4b	17	39	477	1074	1644	1737	1560	1170	810	615	468	285	129	42	12	0	0	0	0	0	105650
GP5	25	9	54	198	537	1101	1572	1830	1866	1623	1131	756	441	252	93	24	12	9	6	6	
		33	87	114	150	225	303	330	273	153	45	18	3	0							139150
Obs.	4	63	–	–	2051	–	6347	–	5455	3610	–	5647	–	–	–	–	–	64	16	0	244160

(d) Scattergrams. Unmatched-peak and matched-peak scattergrams are presented in Fig. 5.32. As was the case in Fig. 5.21c–d, these scattergrams are representative of too narrow, non-overlapping predicted clouds.

5.4 Results of Three-Dimensional Experiments

The predicted GLCs in the two-dimensional simulations were quite similar to the observed GLCs despite the considerable simplifications employed in those experiments (e.g., flat or two-dimensional topography and otherwise uniform surface characteristics, horizontally-homogeneous initialization, steady synoptic environment). Let us now turn to the three-dimensional experiments listed in Table 5.1. Given the much more realistic simulations possible with the full three-dimensional version of the modelling system, we might hope for improved concentration predictions. Not surprisingly, though, perfection remains elusive.

The approach adopted in this section has been to designate Exp. GP4b as the three-dimensional control or baseline experiment. We will first discuss the results from this experiment in the most detail. The other 3 three-dimensional experiments will be treated as sensitivity experiments relative to this base case, and their results will be discussed from the point of view of their differences from the Exp. GP4b results.

5.4.1 Three-dimensional-experiments meteorological simulations

As discussed in Sec. 5.2, the modelling system configuration for the three-dimensional simulations was kept as close as possible to the two-dimensional configuration. However, some differences were unavoidable. One difference was that the value specified for RLAT, the latitude of the lower lefthand corner of the grid, in the RAMS meteorological-model simulations was 30°N compared to the value of 35.24°N used in the two-dimensional RAMS simulations. Of course, Coriolis force and solar heating will vary with latitude, and in some of the three-dimensional runs, surface characteristics, including terrain elevation, soil texture, aerodynamic surface roughness, solar albedo, and sea surface temperature, were also specified to vary with location.

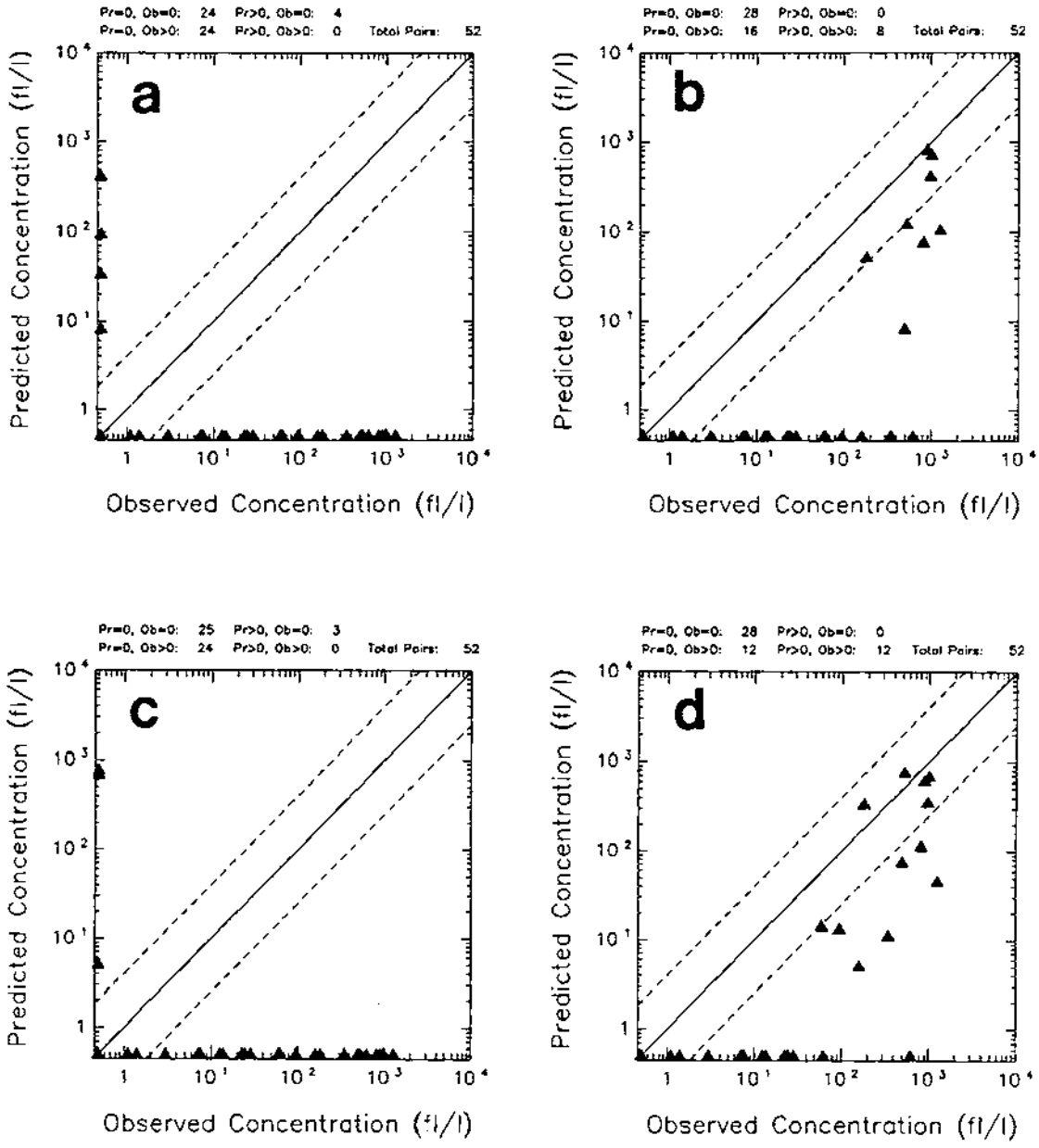

Figure 5.32: Scattergrams for observed 600-km-arc PMCH concentrations (less 3.4 fl^{-1}) vs. (a) unshifted Exp. GP2a estimated concentrations, (b) center-line-shifted Exp. GP2a estimated concentrations, (c) unshifted Exp. GP2c estimated concentrations, and (d) center-line-shifted Exp. GP2c estimated concentrations. Plotted pairs have been drawn from the set of concentrations for Stations A–24 and the first four 3-hour observing periods from 0800–2000 GMT, July 9, 1980. The diagonal lines are the one-to-one correspondence line and two factor-of-4 (i.e., 1:4 and 4:1) lines.

However, the most significant differences arose in model initialization. The RAMS variable-initialization (VI) option is only applicable to three-dimensional simulations so that the three-dimensional simulations which employed the VI option differed in a fundamental way from the two-dimensional simulations. More importantly, though, the compositing technique employed in the two-dimensional simulations to modify the low-level wind field had to be abandoned in the three-dimensional simulations.

The problems encountered in initializing RAMS for the two-dimensional runs with either a morning or evening Oklahoma City upper-air sounding were discussed in Sec. 5.2.2. The oscillatory ageostrophic component present in both of these soundings was minimized by averaging the morning and evening low-level wind fields. It was not unexpected, then, to find that this same oscillation was present in the large-scale, objectively-analyzed flow fields obtained with the RAMS ISAN package by blending the NMC analyses[196] and upper-air soundings. Fig. 5.33 presents sequences of three consecutive 12-hourly streamline fields at two heights; individual panels were extracted from Figs. 3.5–3.7. There are of course changes due to synoptic evolution in these sequences, particularly in the north of the region. However, focussing on the flow field over Oklahoma, it is clear that the streamlines back at both heights between the first and second times (morning–evening), then veer between the second and third times (evening–morning), consistent with Fig. 5.5.

Given this behaviour, it seemed best to apply the same low-level time averaging to consecutive three-dimensional VI wind fields that was applied for the pair of consecutive individual OKC soundings in the horizontally-homogeneous initialization (Sec. 5.2.2). That is, the ageostrophic oscillation is probably initiated by mesoscale low-level flow perturbations driven by differential surface heating (e.g., McNider and Pielke, 1981). It would seem preferable to start the model in a state of gradient balance and then let

---

[196] This oscillation was also evident in the three consecutive 12-hourly 850 mb gridded wind-vector fields produced in the ISAN Stage 1 analysis for this period (not shown) *before* upper-air data were assimilated in Stage 3.

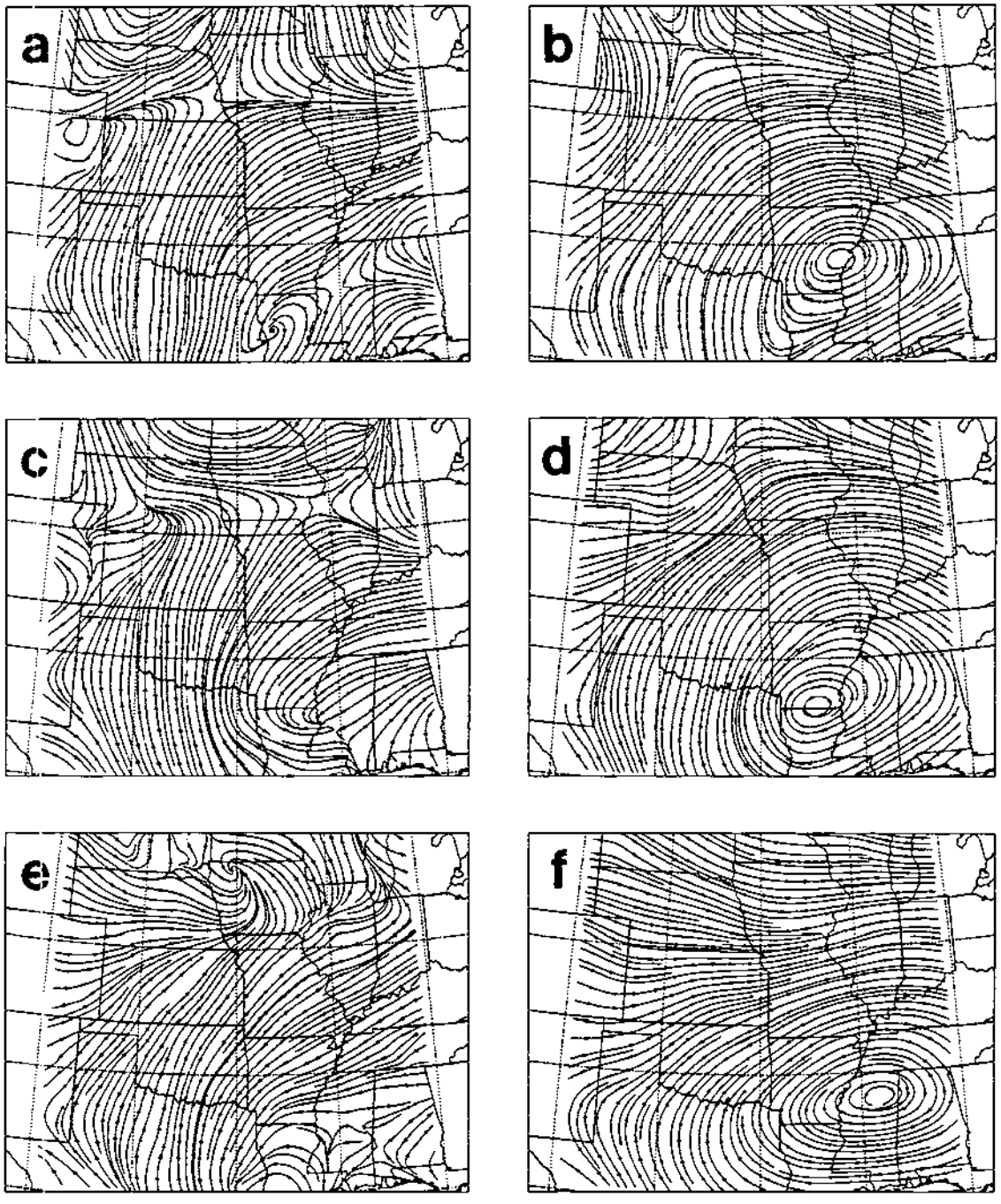

Figure 5.33: Observed streamline fields over central North America on 24 m and 1579 m z^* surfaces for three consecutive synoptic observing times: (a) 24 m, 1200 GMT, July 8, 1980; (b) 1579 m, 1200 GMT, July 8; (c) 24 m, 0000 GMT, July 9; (d) 1579 m, 0000 GMT, July 9; (e) 24 m, 1200 GMT, July 9; (f) 1579 m, 1200 GMT, July 9. Otherwise identical to Fig. 3.5.

differential surface heating do the rest rather than start the model with fields which contain an extreme of the oscillation. Such low-level time averaging was not available in the standard 2A version of RAMS, but the VI module was modified to implement this option. Fig. 5.34 shows isotachs and streamlines for the time-averaged low-level wind fields obtained from the July 8, 1200 GMT and July 9, 0000 GMT low-level fields. Notice how the saddlepoint over Iowa at the 24 m level (Fig. 5.34b) lies midway between its positions at the two synoptic observing times (Figs. 3.5b and 3.6b). It was thus both disappointing and interesting to discover after all this effort and the initialization subexperiments carried out as part of Exps. GP1 and GP2 that the use of the July 9, 0000 GMT analyses alone for initialization produced more realistic transport than the carefully prepared composite wind fields. This finding will be discussed shortly.

Exp. GP4b meteorological results

The Exp. GP4b RAMS baseline run was started at 1730 LST (1800 CST/0000 GMT) on July 7, 1980 using initial fields based on NMC 0000 GMT analyses for July 9 (and invoking the assumption of synoptic stationarity again). Fig. 5.35 shows sequences of three consecutive 12-hourly RAMS predicted streamline fields at two heights, the same format as used in Fig. 5.33 to display the observational analyses. The three synoptic observing times shown in this figure correspond to RAMS simulation times of 12, 24, and 36 hours.

Qualitatively, the predicted streamline fields agree very well with the observed streamline fields, with the exception of the evolution of the quasi-stationary front in the north of the domain. This good agreement is another indication of the quasi-stationarity of the synoptic environment since the Exp. GP4b lateral boundary conditions were held fixed in time. The directional oscillation in the flow field over Oklahoma which was remarked upon in the discussion of Fig. 5.33 is also present in these streamline sequences. The predicted isotach fields (not shown) also agree quite well with the observed fields (Figs. 3.5–3.7a,c).

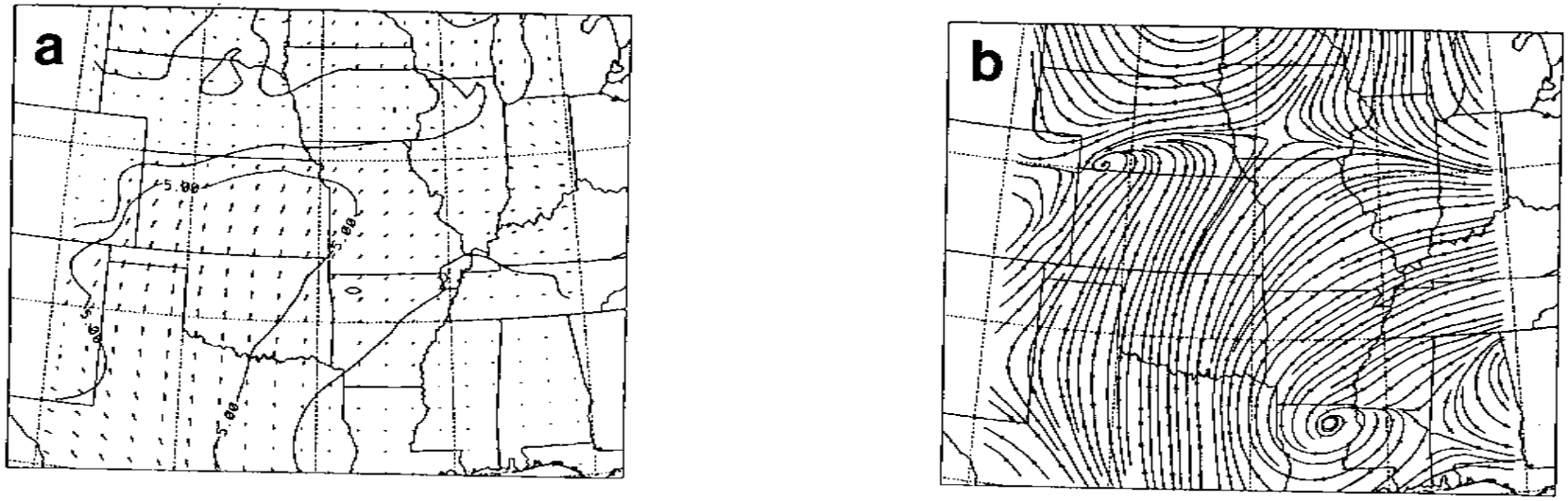

Figure 5.34: Isotach fields overlaid with wind vectors and corresponding streamline fields at three heights for the July 8, 1980 composited 'geostrophic' sounding. Otherwise same as Fig. 3.5.

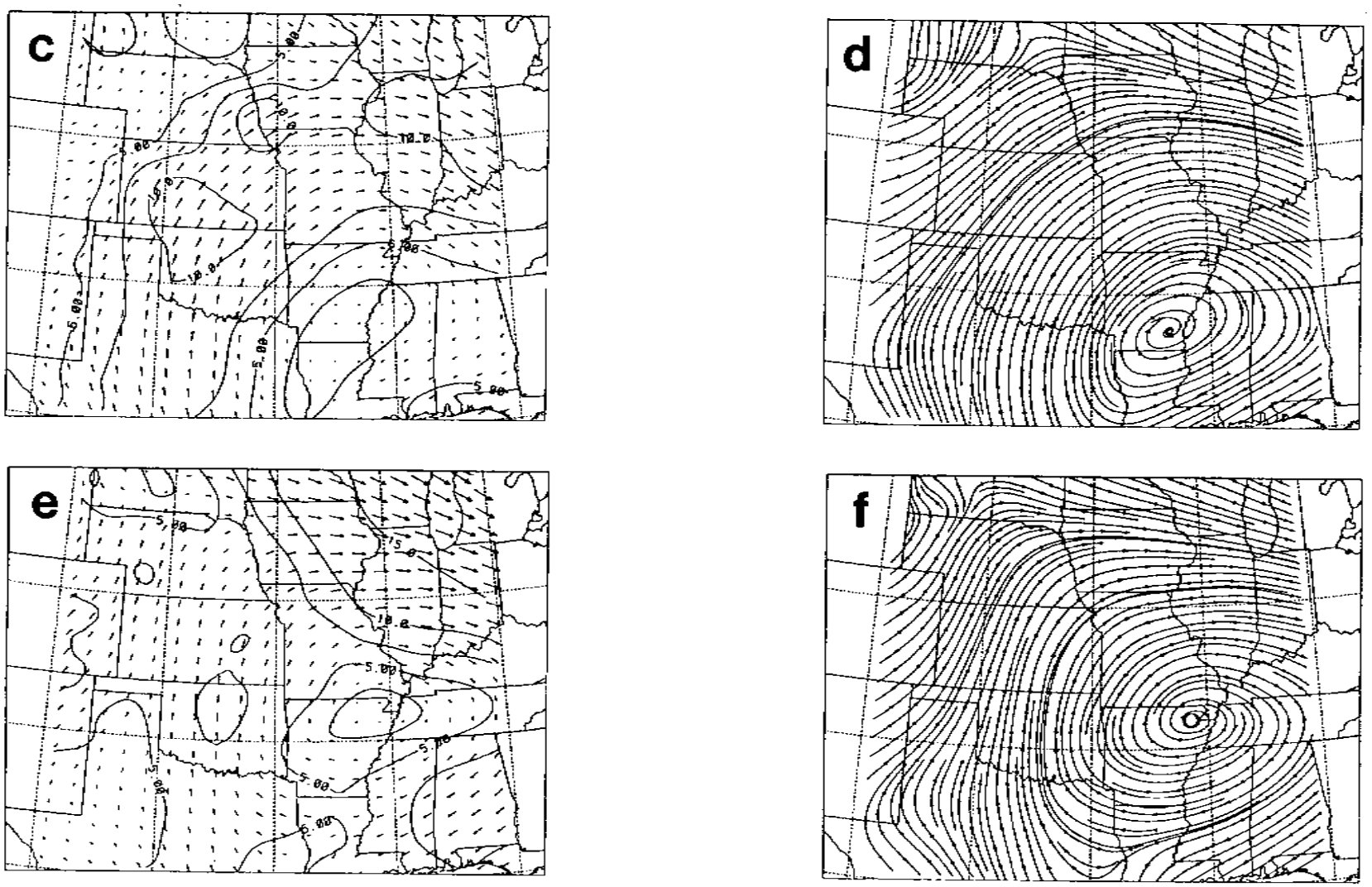

Figure 5.34: (Continued).

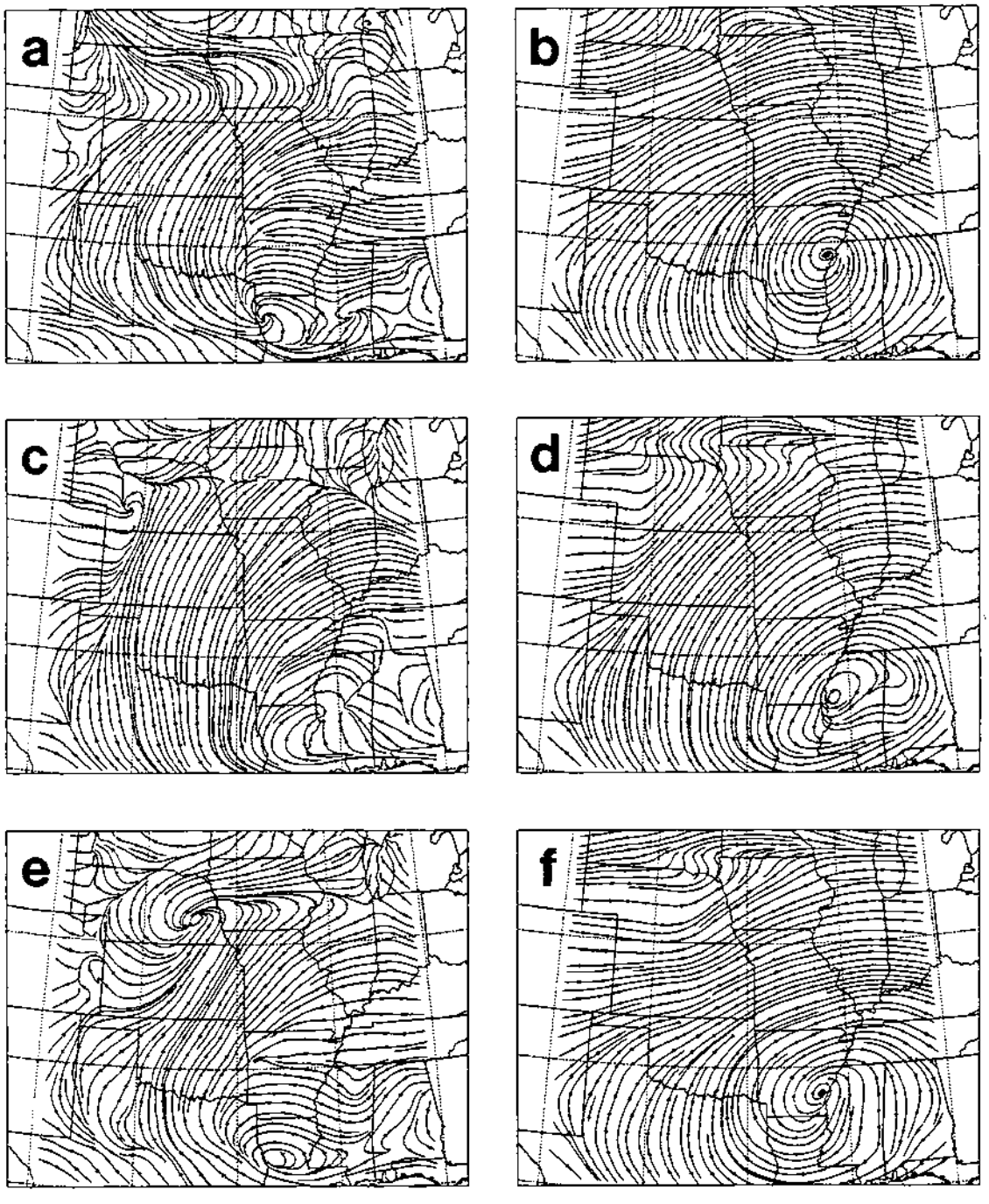

Figure 5.35: Predicted Exp. GP4b streamline fields at two z^* heights after 12, 24, and 36 hours of simulation: (a) 24 m AGL, 1200 GMT, July 8, 1980; (b) 1579 m AGL, 1200 GMT, July 8; (c) 24 m AGL, 0000 GMT, July 9; (d) 1579 m AGL, 0000 GMT, July 9; (e) 24 m AGL, 1200 GMT, July 9; (f) 1579 m AGL, 1200 GMT, July 9. Otherwise identical to Fig. 5.33.

5.4.2 Exp. GP4 mesoscale tracer transport

As discussed in Sec. 5.2.2, there was some question concerning the choice of initialization time for Exp. GP1. Three different possibilities were tested as a result (Exps. GP1a, GP1b, and GP1c). With these results as a guide plus the knowledge that the RAMS ISAN package-produced analyses also contained an oscillatory ageostrophic component (Fig. 5.33), it seemed best to adopt the time-averaging procedure used in Exps. GP1c and GP2c to construct the initial low-level wind fields for the three-dimensional simulations. Accordingly, the RAMS Exp. GP4c simulation started from the time-averaged wind fields shown in Fig. 5.34. Unfortunately, the grid-scale trajectories calculated from the Exp. GP4c meteorological fields did not agree very well with the locations at which the real tracer cloud was detected as it crossed the 100-km and 600-km surface arcs. Fig. 5.36c shows the Exp. GP4c grid-scale trajectories. The actual tracer cloud crossed the 100-km arc at its western edge (cf. Fig. 5.12) and crossed the 600-km arc in eastern Nebraska just west of the Missouri state line (Figs. 5.37 and 3.1b). Moreover, the Exp. GP4c simulated tracer transport was too slow. The 20-h trajectories shown in Fig. 5.36c have just reached the 600-km sampler arc whereas the peak GLC along this arc was actually measured during the first sampling period 13–16 h after the start of the release (Table 3.2).

Faced with this discrepancy, a natural step seemed to be to follow the example of Exp. GP1 and try two more RAMS simulations initialized with meteorological fields obtained from the NMC analyses at 1200 GMT, July 8 (Exp. GP4a) and 0000 GMT, July 9 (Exp. GP4b), the two synoptic analysis times bracketing the tracer release. The grid-scale trajectories for these two additional Exp. GP4 RAMS simulations are shown in Figs. 5.36a–b, respectively. The trajectories for Exp. GP4a are very similar to those for Exp. GP4c while the Exp. GP4b trajectories are in better agreement with the observations although they are still located too far to the east.

How can we explain these differences in both transport direction and transport speed? The initialization used in Exp. GP4c appeared to be the best choice *a priori* since it best

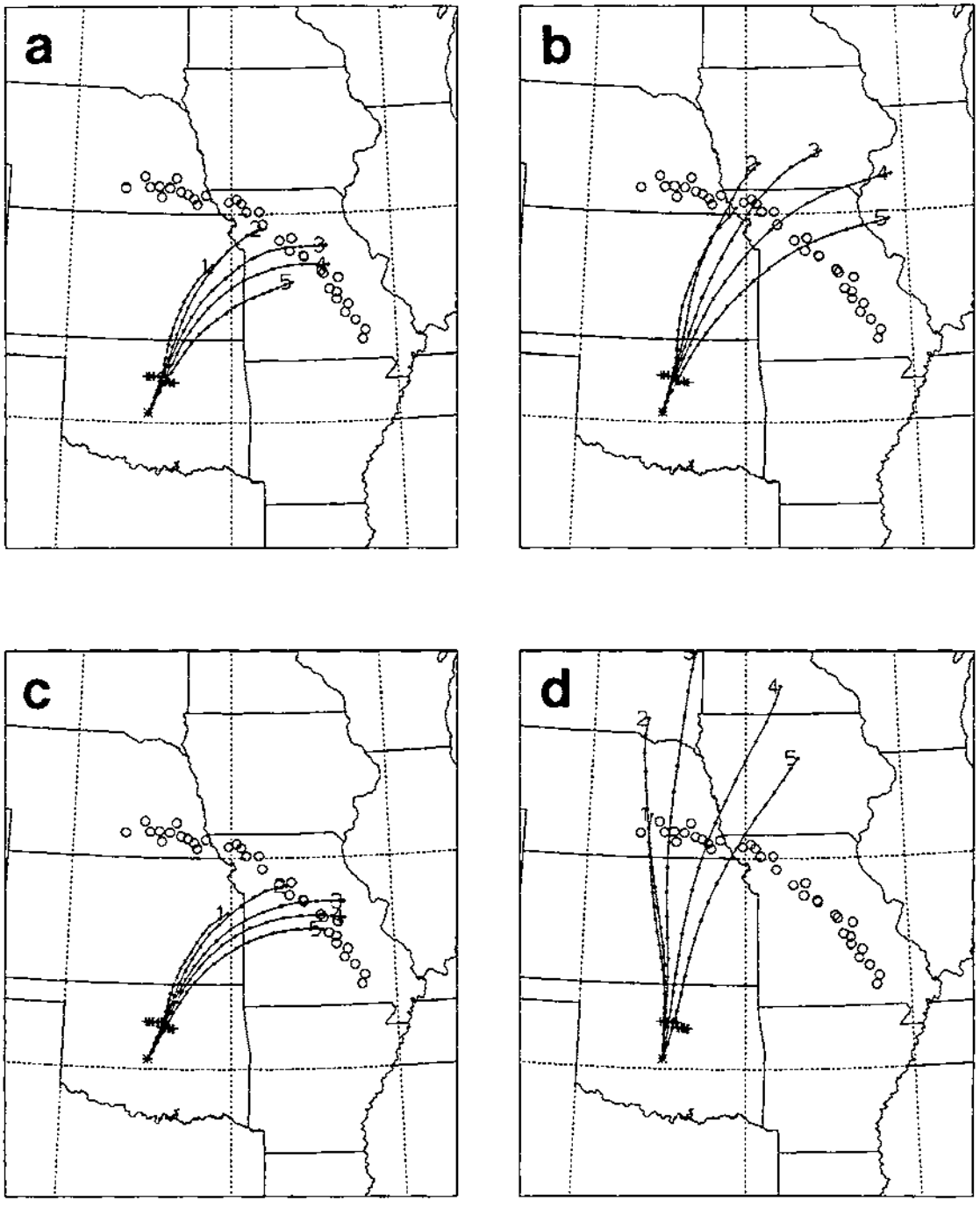

Figure 5.36: Plan view of four sets of three-dimensional grid-scale trajectories followed for 20 h at five different heights: (a) Exp. GP4a wind fields; (b) Exp. GP4b wind fields; (c) Exp. GP4c wind fields; and (d) Exp. GP2a wind fields. Otherwise, the same as Fig. 5.3.

approximated the synoptic-scale background flow and minimized the magnitude of the oscillatory ageostrophic component contained in the initial flow fields. The 0000 GMT wind field for July 9, on the other hand, was more representative of the transport wind field after the tracer release (1900–2200 GMT, July 8). However, the Exp. GP4b RAMS simulation using the July 9 0000 GMT wind fields started at July 8 at 0000 GMT and passed through the other two initialization times of 1200 GMT and 1800 GMT before the start of the tracer release at 1900 GMT. Moreover, the low-level wind speeds were *weaker* at 0000 GMT than at 1200 GMT (e.g., Fig. reffig:OKCwinds). It is also clear from Fig. 5.36 that all three Exp. GP4 subexperiments had a significant directional transport error during the initial daytime transport of tracer to the 100-km arc of roughly 20° to the east (see Table 5.3). This error is consistent with the difference between the ISAN package streamlines at Oklahoma City (Figs. 5.33d) and the observed OKC upper-air winds (Fig. reffig:OKCwinds) at 0000 GMT on July 9. Apparently, even after the OKC sounding was blended with the NMC grid-point first-guess field in Stage 3 of the ISAN analysis, the blended, gridded flow at that location still differed from the observed upper-air winds.

A possible explanation may lie in the fact that the Exp. GP4b RAMS simulation started 12 h sooner than the Exp. GP4a and GP4c meteorological simulations. The 1730 LST start time means that this simulation would experience both an evening and morning PBL transition before the start of the tracer release. The inertial oscillation initiated by the evening transition would then be present in the Exp. GP4b wind fields at 0530 LST when the other two Exp. GP4 simulations were started but would not be present in the Exp. GP4a and GP4c wind fields. Using Fig. 1.3 as a guide, the ageostrophic oscillation should cause the low-level winds in Exp. GP4b to rotate counter-clockwise during the evening and to speed up, consistent with Fig. 5.36. This mechanism should be much less pronounced in the Exp. GP4a and GP4c wind fields since they will pass through their first evening transition after the tracer release and the inertial oscillation will only be starting up.

The main reason that Exp. GP4 differed from the two-dimensional experiments in the success of the time-averaging procedure was that the latter only considered the large-scale wind at the release site while Exp. GP4 accounted for horizontal variations in the large-scale wind field. As can be seen from Fig. 5.33, the low-level streamlines curved significantly to the east with increasing latitude. Exp. GP1b, the two-dimensional counterpart to Exp. GP4b, was discarded because the tracer cloud was transported too far to the west due to the inertial oscillation (Fig. 5.3b). In Exp. GP4b, however, this process was counteracted by the synoptic-scale flow curvature. Fig. 5.36d shows the Exp. GP2a trajectories. There are two features of interest in this panel. First, the Exp. GP2a trajectories cross the 100-km arc further west than they do in Figs. 5.36a–c, consistent with the directional error discussed above. Second, the Exp. GP2a trajectories are longer than even the Exp. GP4b trajectories. This points out the fact that wind speeds are reduced to the north of Oklahoma City as the flow approaches the quasi-stationary front across the upper Plains states.

Most of the other LRTAP models that have been applied to this case have also had an easterly centerline bias (Figs. 3.11, 3.12). All of these models used wind fields diagnosed from the operational, twice-daily upper-air soundings. Ferber et al. (1981) compared *post-facto* mean trajectories calculated by the ARL–ATAD trajectory model to the 600-km-arc concentration observations. They tried two approaches for specifying the transport-layer wind. When they used winds averaged vertically in a layer of variable thickness bounded below by the Earth's surface and above by the computed PBL height to calculate the mean transport-layer trajectory, the trajectory crossed the 600-km sampling arc about 200 km east of the observed concentration peak. When they used winds averaged vertically in a constant layer from 150–600 m AGL, the computed mean transport-layer trajectory crossed the 600-km arc about 100 km east of the observed

peak[197]. These trajectories are plotted in Fig. 5.37. Note also that the timing of these two trajectories does not agree with the observations. The computed trajectories had not even reached the 600-km sampling arc by the end of the first 3-h observing period, the period during which the peak concentration levels were measured. This error is consistent with the inability of the twice-daily upper-air soundings over the central U.S. to sample the stronger winds associated with the nocturnal low-level jet when it is present (e.g., Moran et al., 1991).

As was done for Exp. GP2c, special two-dimensional grid-scale trajectories constrained to remain on z^* surfaces were calculated for Exp. GP4b in addition to the three-dimensional trajectories. Fig. 5.38 follows the format of Fig. 5.25 in comparing these two sets of trajectories. Differences arise from the effects of vertical advection. The differences are more pronounced for this experiment than for Exp. GP2c, partly because the topography varies in the north-south direction as well as in the east-west direction and partly because there are synoptic-scale as well as mesoscale vertical motions present. There is slightly less spread in the three-dimensional trajectory endpoints compared to the two-dimensional ones. The upper-level three-dimensional trajectories have also experienced considerable subsidence and hence have been transported by lower-level winds than the corresponding two-dimensional upper-level trajectories. The lower three-dimensional trajectories, on the other hand, began to ascend near the end of the travel period.

Based on the results of this Exp. GP4 trajectory intracomparison, I decided to use Exp. GP4b as the three-dimensional baseline simulation. Note, though, that Exp. GP4a is the subexperiment of interest for evaluating the performance of the CSU dispersion modelling package in a pure forecast mode. I also decided not to carry out a full particle dispersion simulation for Exp. GP4c because of the similarity of its grid-scale trajectories to the Exp. GP4a trajectories (Figs. 5.36a,c).

---

[197] Interestingly, these trajectories probably agreed reasonably well with the location of the *three-dimensional* cloud centroid and hence the cloud's vertical projection but less well with the nighttime surface footprint.

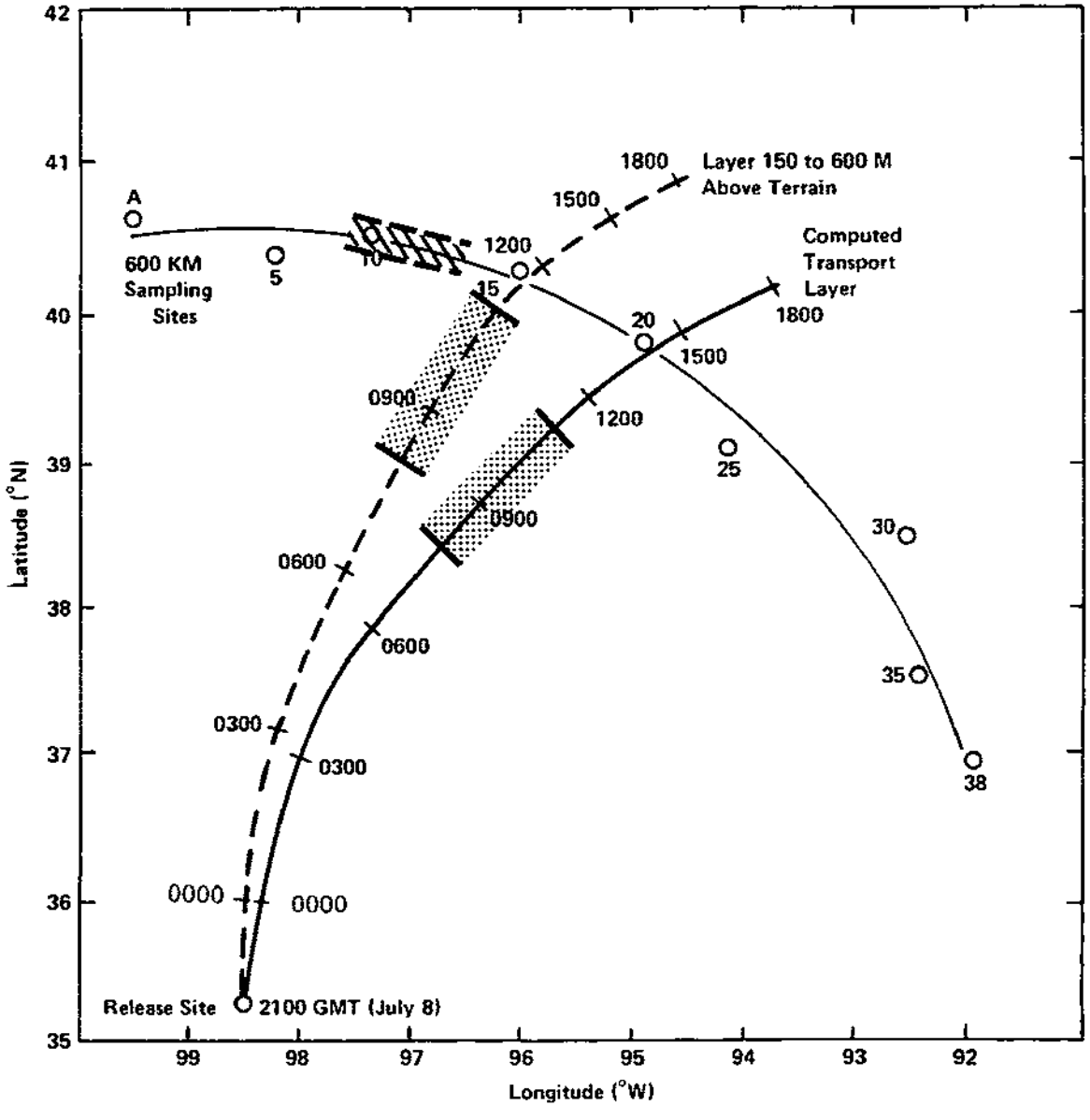

Figure 5.37: Comparison of ARL–ATAD variable-transport-layer trajectory with mean trajectory for layer 150–600 m AGL. The stippled rectangles mark the 3-hour section along each trajectory corresponding to the first 600-km-arc sampling period from 0800–1100 GMT, July 9, 1980. The hatched–dashed region on the 600-km arc marks the stations reporting significantly elevated GLCs (adapted from Fig. 9 of Ferber et al., 1981).

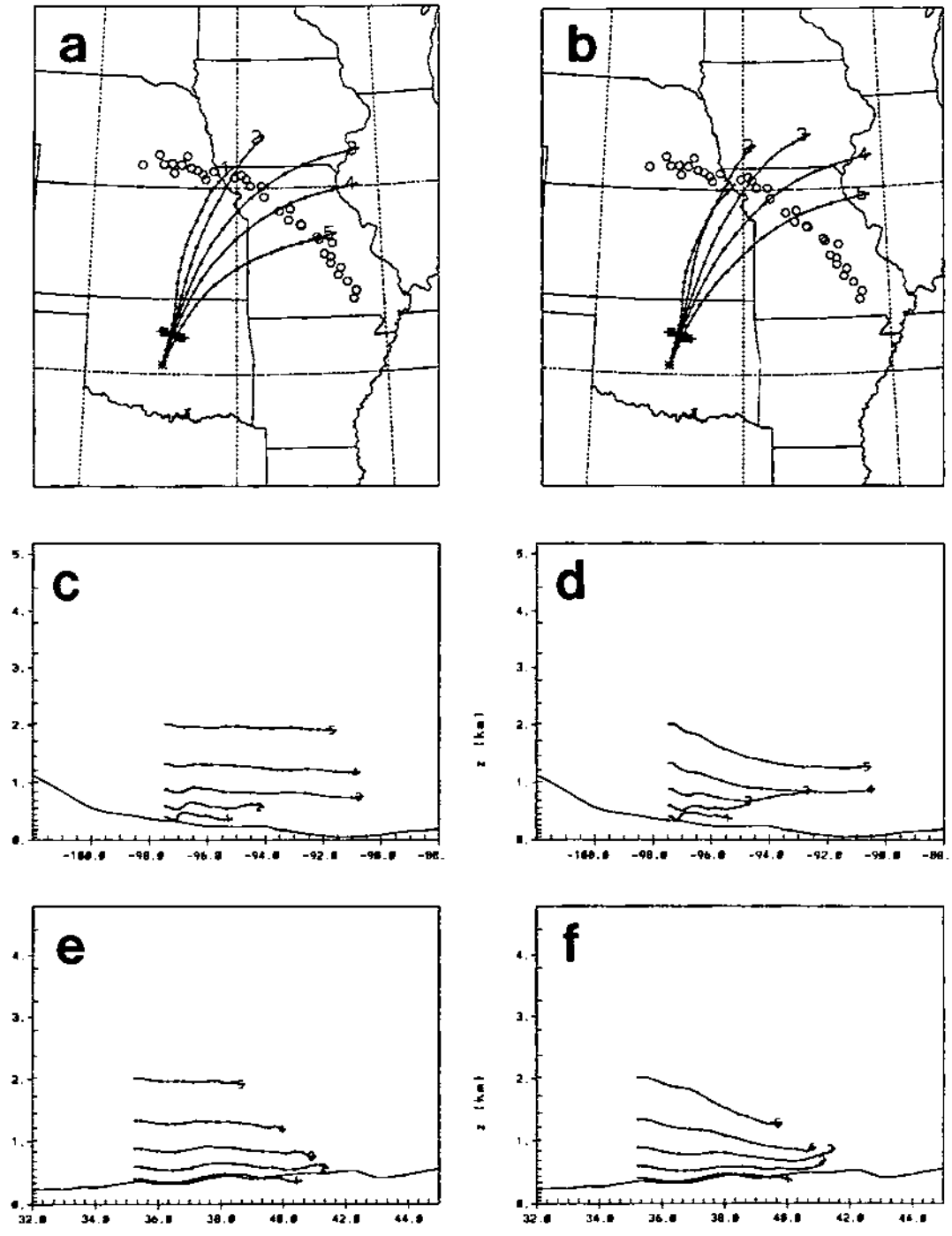

Figure 5.38: Three views of Exp. GP4b two-dimensional and three-dimensional grid-scale trajectories: (a) two-dimensional trajectories, XY projection; (b) three-dimensional trajectories, XY projection; (c) two-dimensional trajectories, XZ projection; (d) three-dimensional trajectories, XZ projection; (e) two-dimensional trajectories, YZ projection; (f) three-dimensional trajectories, YZ projection. The small filled squares mark the hourly trajectory positions. Trajectory endpoint labels '1', '2', '3', '4', and '5' indicate the five release heights 50 m, 293 m, 686 m, 1334 m, and 2379 m AGL, respectively. The west-east topography slice for the XZ projection corresponds to 35°N while the south-north topography slice for the YZ projection corresponds to 97.5°W. Viewpoints are downward, northward, and westward for the three projections.

5.4.3 Exp. GP4b mesoscale tracer dispersion

100-km arc.

(a) GLC patterns. Fig. 5.39 is a direct counterpart to Fig. 5.12 and shows Exp. GP4b estimated GLC patterns as the tracer cloud is carried across the 100-km sampler arc. Comparison of these two figures and comparison of Fig. 5.39c with Fig. 5.11 suggests that the Exp. GP4b tracer cloud is less elongated and slightly wider than the Exp. GP1 and GP2 clouds. The GP4b cloud also arrives at the 100-km arc one 45-minute sampling period later than the GP1 and GP2 clouds and its centerline lies east of the other clouds's centerlines.

(b) Station values. Exp. GP4b predicted GLCs are shown plotted against azimuth angle across the 100-km sampler arc in Fig. 5.40b along with the actual observed station GLCs for the first six observing times. Fig. 5.41b presents some of the same values in a complementary way, showing the time history of the predicted and observed concentrations at six of the 100-km arc station sites. Taken together, these two figures suggest good overall agreement between the simulated and observed cloud with the primary exception of the obvious centerline error in Fig. 5.40b. The simulated cloud is also a bit narrower than the observed cloud and does not tail off as quickly with time.

Examination of Table 5.2 supports the above discussion. The Exp. GP4b station exposures lie to the east of the corresponding observed exposures and the estimated station exposures for Exps. GP1 and GP2. There is a 19° azimuthal difference in the location of the Exp. GP4b peak exposure and the observed peak station exposure. In addition, the magnitude of the Exp. GP4 peak station exposure is comparable to the GP1 and GP2 peaks and all are higher than the observed peak exposure value. However, the CWIE value for Exp. GP4b is greater than the CWIE estimates for Exps. GP1 and GP2 by about 25%, even after reduction by an obliquity factor of $\cos 17°$. This Exp. GP4b value is comparable to the CWIE value estimated from the 100-km-arc observations if a value is assumed for Station 17 (Table 5.3).

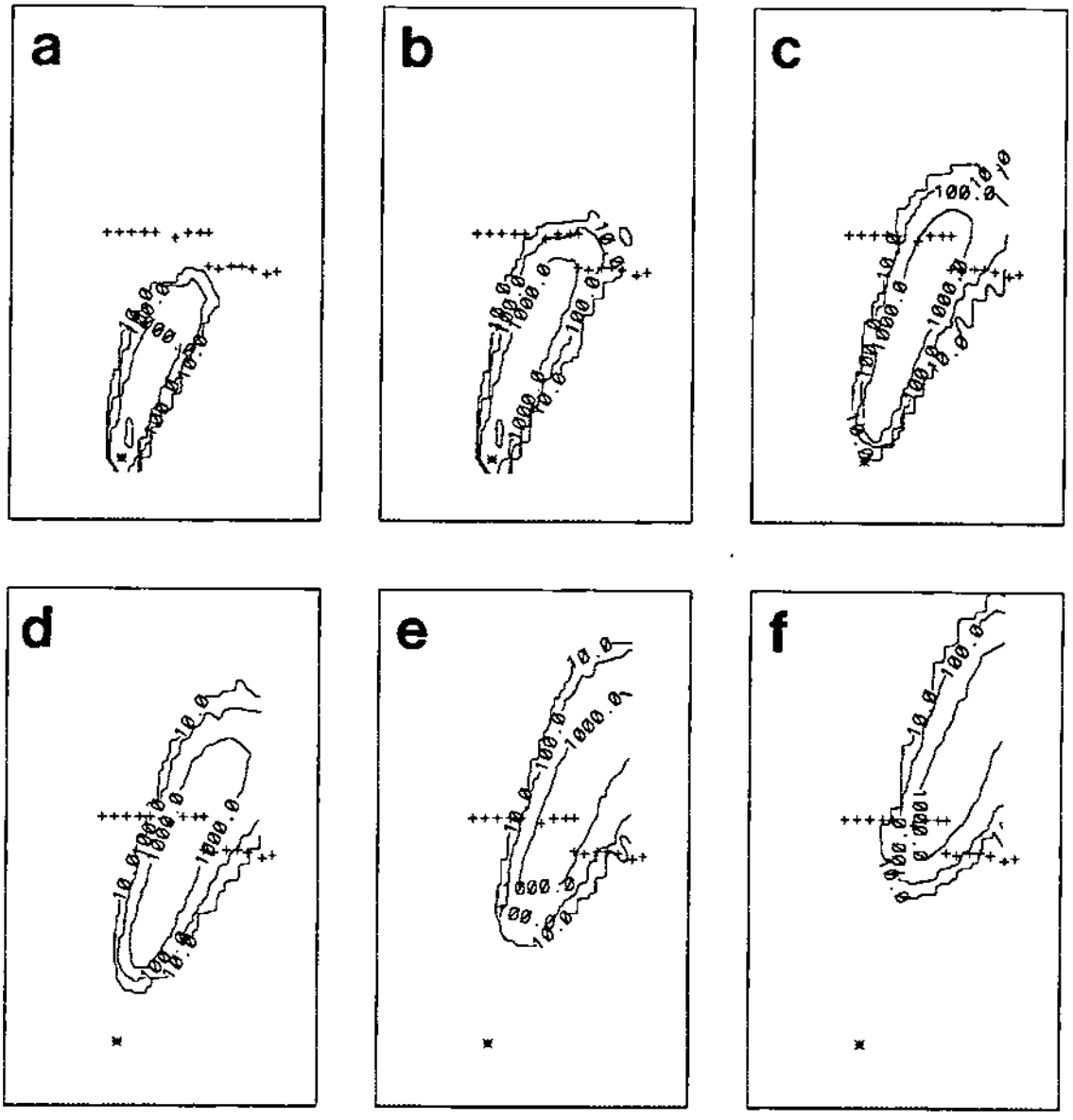

Figure 5.39: Time sequence of plan views of estimated 45-minute-average PMCH surface concentration patterns for the first six 100-km-arc sampling periods based on particle positions from the Exp. GP4b MLPDM simulation: (a) 2100–2145 GMT; (b) 2145–2230 GMT; (c) 2230–2315 GMT; (d) 2315–0000 GMT; (e) 0000–0045 GMT; and (f) 0045–0130 GMT. Otherwise identical to Fig. 5.11.

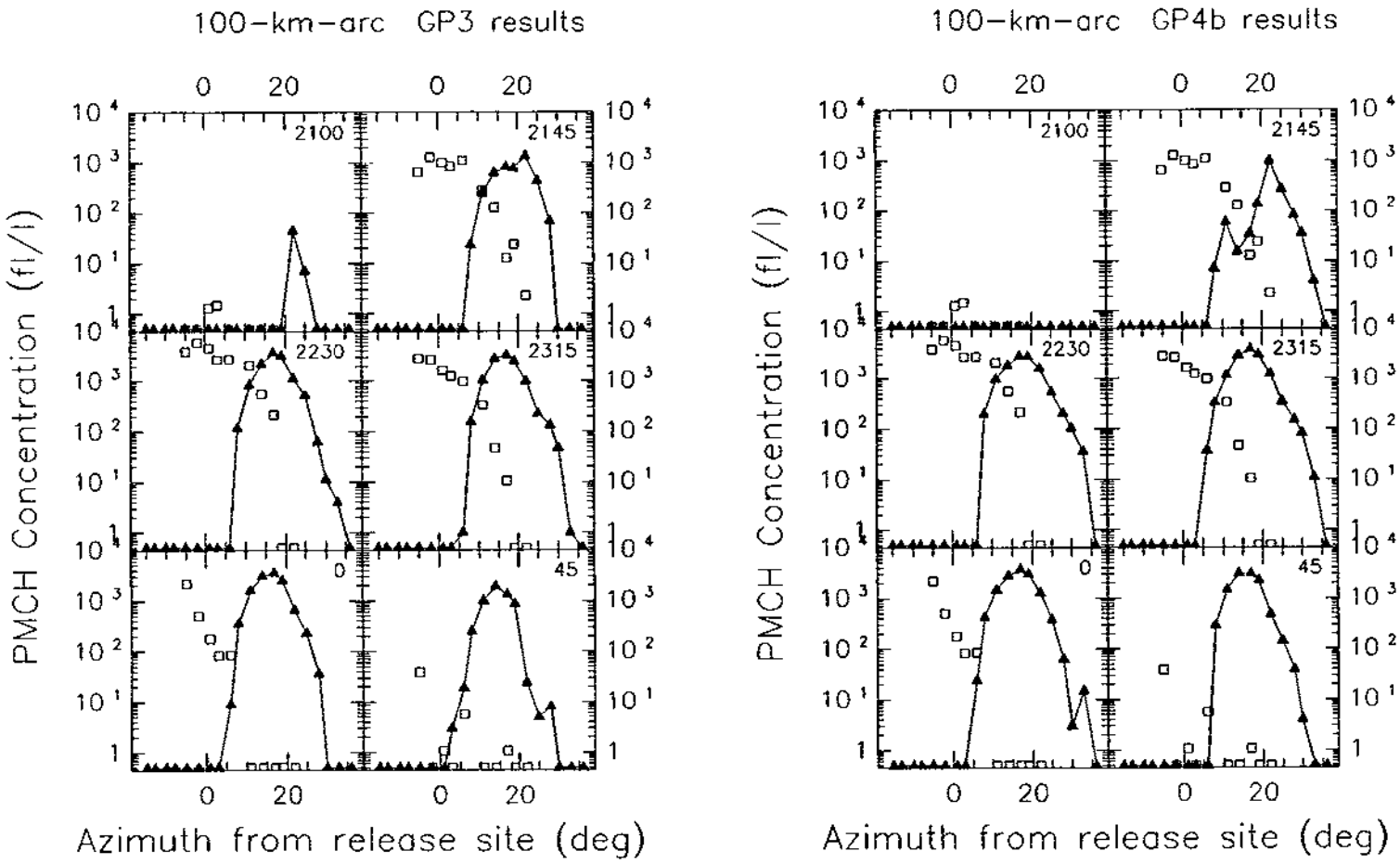

Figure 5.40: Time sequence of concentration–azimuth plots of observed vs. Exp. GP3 (lefthand panel: 'L') and observed vs. Exp. GP4b (righthand panel: 'R') estimated PMCH 45-minute-average concentrations for the Great Plains experiment 100-km sampling arc for the first six sampling periods: (a) 2100–2145 GMT; (b) 2145–2230 GMT; (c) 2230–2315 GMT; (d) 2315–0000 GMT; (e) 0000–0045 GMT; and (f) 0045–0130 GMT. Observed values are indicated by open squares; predicted values are indicated by filled triangles connected by a solid line. The starting time for each sampling period (GMT) is plotted in the upper righthand corner of each panel.

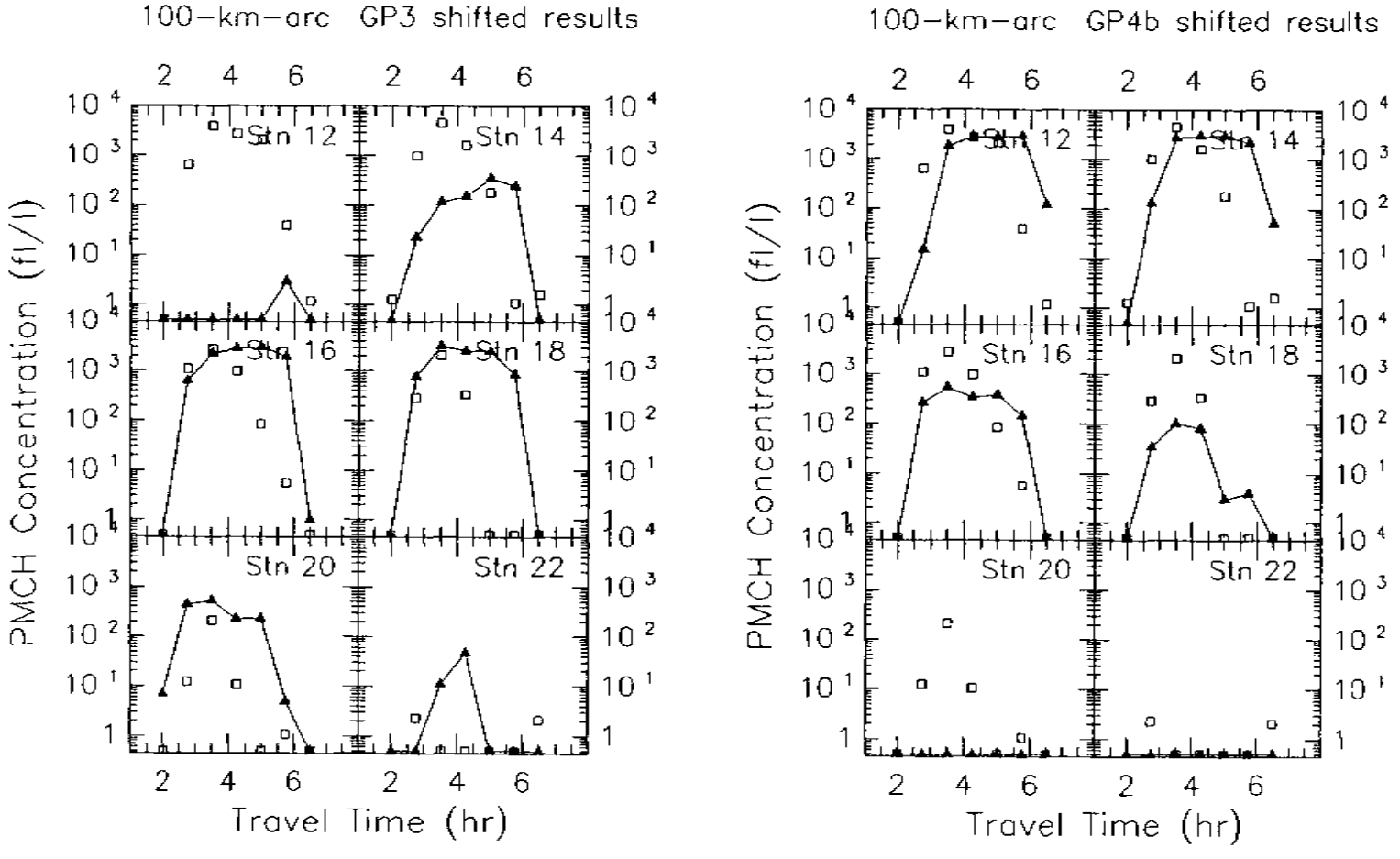

Figure 5.41: Concentration-time plots of observed vs. Exp. GP3 (lefthand panel: 'L') and observed vs. Exp. GP4b (righthand panel: 'R') estimated PMCH 45-minute-average concentrations for six 100-km-arc sampling stations: (a) Station 12; (b) Station 14; (c) Station 16; (d) Station 18; (e) Station 20; and (f) Station 22. Observed values for Stations 12–20 are indicated by open squares; predicted values are indicated by filled triangles connected by a solid line. The station ID number is plotted in the upper righthand corner of each panel. Note that the GP3 and GP4b station values have been shifted eastward by 7 station positions in order to match the observed exposure peak (cf. Table 5.2).

(c) Quantitative pattern characteristics. Table 5.3 lists some of the quantitative cloud characteristics estimated from the Exp. GP4b 100-km-arc equally-spaced-site predicted concentrations and from the 100-km-arc observed concentrations. The peak concentration value predicted for Exp. GP4b is smaller than the observed peak value by almost half and, as mentioned above, the centerline position error is large, about 19°. Despite these disagreements between peak concentration levels, however, the estimated Exp. GP4b CWIE value still agrees very well with the observed value. The predicted time of arrival of the tracer cloud at the 100-km arc also agrees well with the observations, although the transit time was one period too long. And the Exp. GP4b cloud widths determined using the two edge criteria agree very well with the observed cloud width.

(d) Scattergrams. Given the significant centerline error present in all four of the three-dimensional experiments, it seemed pointless to prepare 'unmatched' scattergrams. Thus, Fig. 5.42 presents only peak-matched scattergrams for the 4 three-dimensional experiments. The wider plume predicted by Exp. GP4b as compared to Exps. GP1 and GP2 is suggested by the slightly larger number of non-zero pairs in Fig. 5.42c as compared to Figs. 5.15 and 5.29.

600-km arc.

(a) GLC patterns. Fig. 5.43 shows a sequence of Exp. GP4b predicted time-averaged GLC patterns for the first four 3-h sampling periods on the 600-km sampling arc. This is a good simulation. The tracer cloud has reached the sampling arc by the first sampling period. Its position crossing the arc lies just to the east of the observed crossing in the southeastern corner of Nebraska (Fig. 3.1b, Table 3.2). Transit time across the arc is three sampling periods, which compares quite well against the observed value of four periods.

A sudden widening of the plume after sunrise due to fumigation of elevated tracer is evident in Figs. 5.43c–d. However, this mixdown occurs at the leading edge of the plume past the 600-km arc. The existence of this feature cannot be confirmed. The

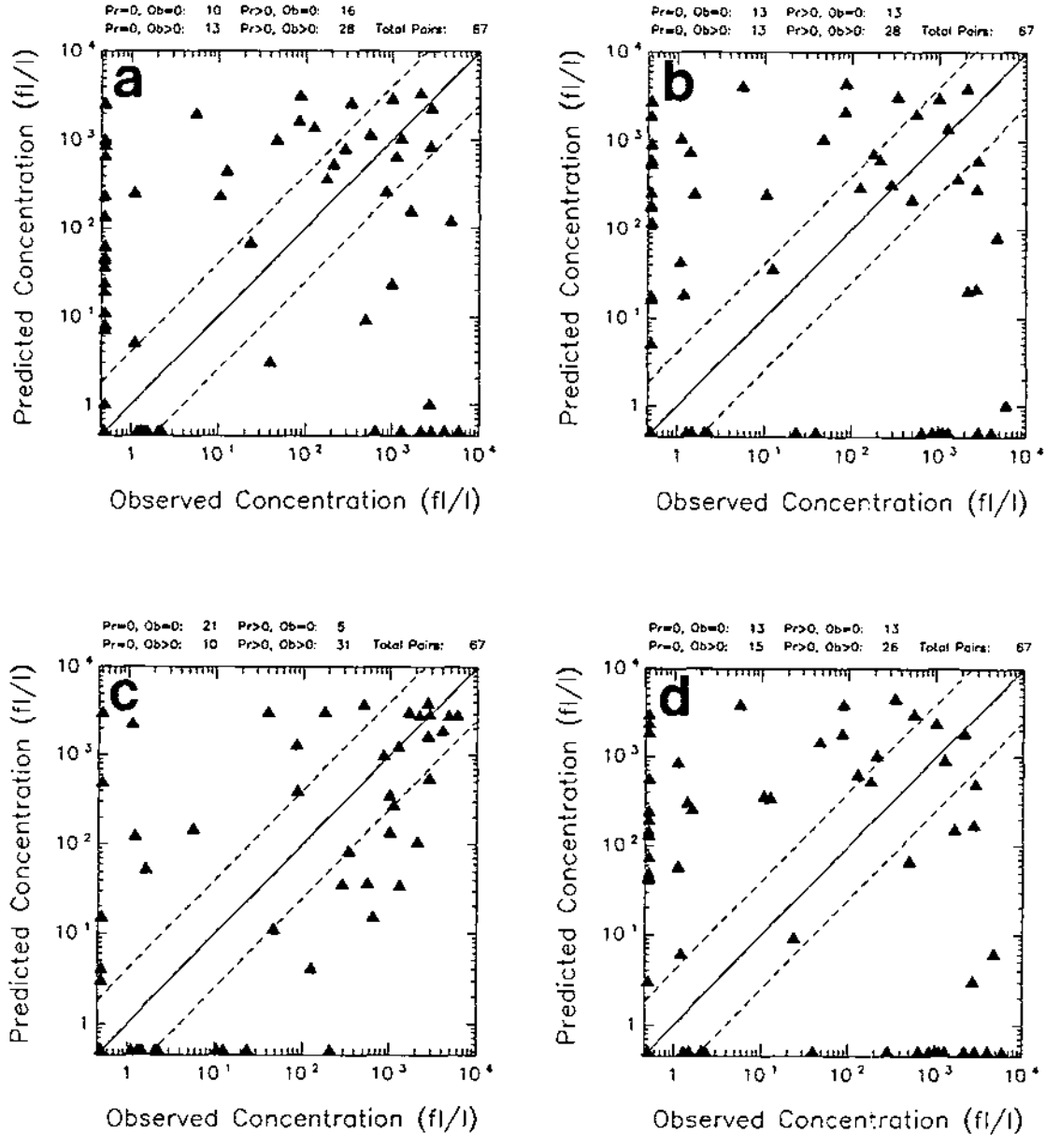

Figure 5.42: Scattergrams for observed 100-km-arc PMCH concentrations (less 3.4 fl^{-1}) vs. three-dimensional-experiment computed center-line-shifted concentrations: (a) Exp. GP3; (b) Exp. GP4a; (c) Exp. GP4b; and (d) Exp. GP5. Plotted pairs have been drawn from the set of concentrations for Stations 12–21 and the first seven 45-minute observing periods from 2100–0215 GMT. The GP3, GP4b, and GP5 station values were all shifted westward by seven station positions while the GP4a station values were shifted westward by eight station positions. The diagonal lines are the one-to-one correspondence line and two factor-of-4 (i.e., 1:4 and 4:1) lines.

Great Plains concentration data do not contain such a widening. On the other hand, the Exp. GP4b simulation predicts that they should not, a sort of negative confirmation. It is worth mentioning, though, that such a morning widening *was* detected in the CAPTEX concentration data. This is discussed in the next chapter.

Fig. 3.11 compares the Exp. GP4b GLC pattern prediction for the first 600-km arc sampling period against predictions made by seven other mesoscale dispersion models in a model intercomparison study carried out for this same case by Policastro et al. (1986a,b,c) and Carhart et al. (1989). The Exp. GP4b prediction looks very good relative to the other models's predictions. None of the GLC footprints predicted by the other models had reached the 600-km arc by this time. This result supports the value of using a prognostic meteorological model with good PBL physics and good vertical resolution in the PBL. The RAMS simulation did predict a nocturnal low-level jet and hence increased low-level transport speeds. Six of the seven other models relied on diagnostic wind fields based on the objective analysis of twice-daily upper-air soundings. As a result, they did not represent the nocturnal low-level jet or enhanced nocturnal low-level transport observed in this case study very well.

(b) Station values. Fig. 5.44b shows Exp. GP4b predicted PMCH ground-level concentrations and the observed 600-km-arc station concentrations plotted against azimuth angle for the first four 600-km-arc observing times. Fig. 5.45b presents many of the same data in a complementary fashion, showing the time history of the predicted and observed concentrations at six of the 600-km arc stations. Model-predicted values correspond to locations on the equally-spaced 91-site arc, and predicted values in Fig. 5.41b have been offset by 14° (see Table 5.6).

A number of Exp. GP4b qualitative cloud characteristics are evident in Fig. 5.44b: (i) there is a centerline error but it is not too large; (ii) the cloud is quite symmetric; (iii) the peak concentration occurs during the second sampling period; and (iv) transit time is three sampling periods (i.e., 9 hours). Compared to Exps. GP1 and GP2, Exp. GP4b appears most similar to Exps. GP1a (Fig. 5.19a) and GP2c (Fig. 5.30b).

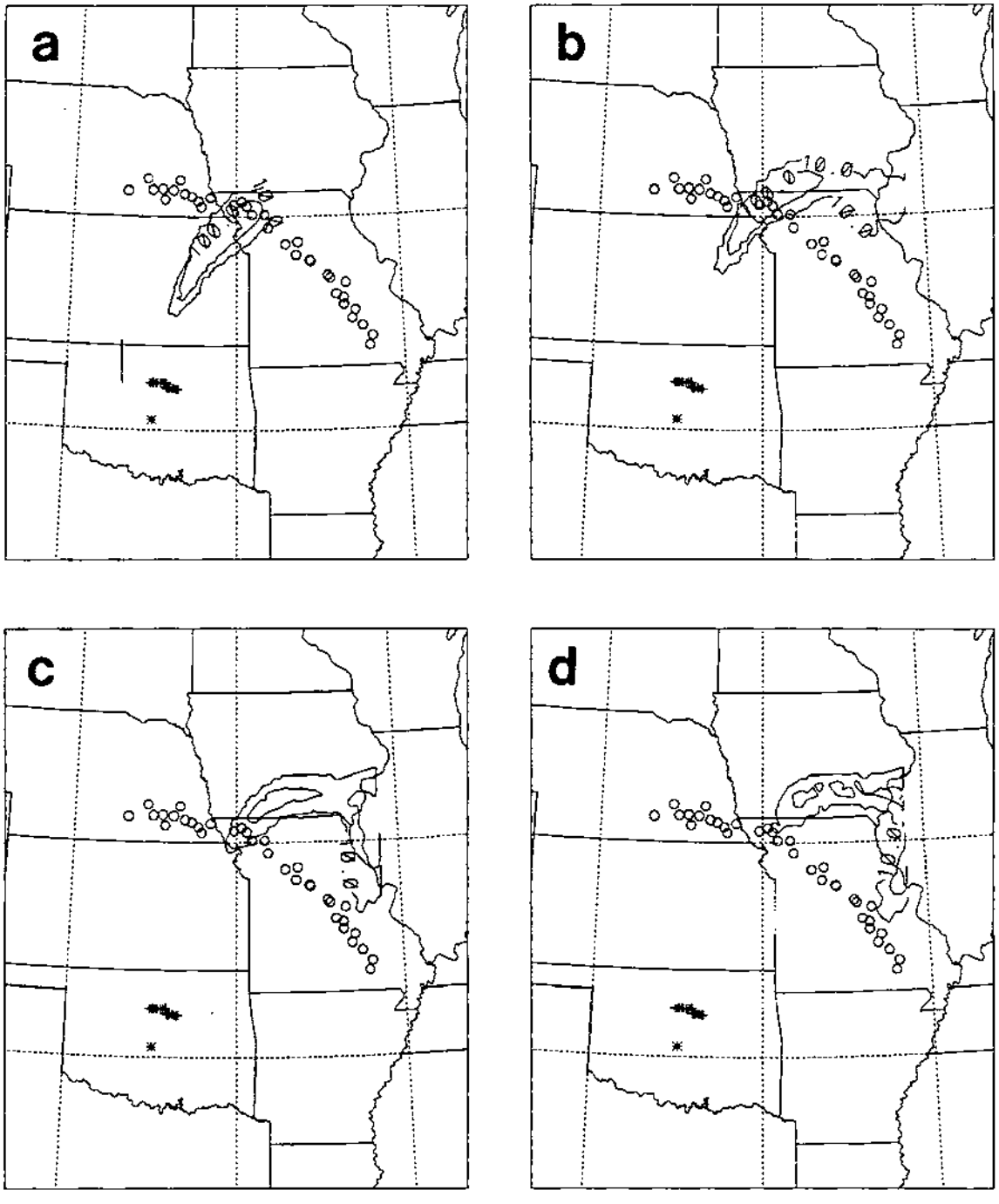

Figure 5.43: Time sequence of plan views of estimated PMCH 3-h-average GLC patterns for the first four 600-km-arc sampling periods based on particle positions from the Exp. GP4b MLPDM simulation: (a) 0800–1100 GMT; (b) 1100–1400 GMT; (c) 1400–1700 GMT; and (d) 1700–2000 GMT on July 9, 1980. Otherwise identical to Fig. 5.16.

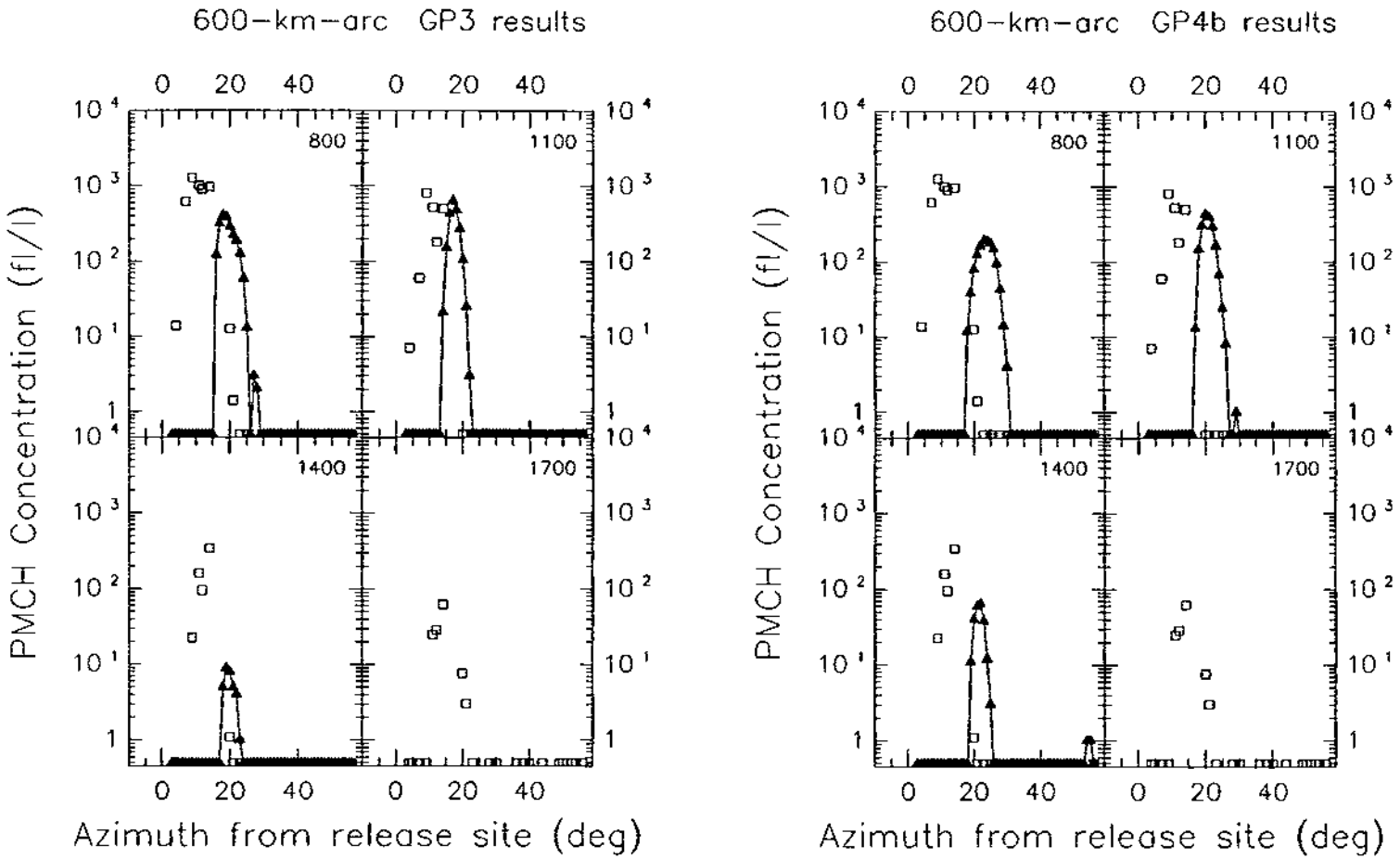

Figure 5.44: Time sequence of concentration–azimuth plots of observed vs. Exp. GP3 (lefthand panel: 'L') and observed vs. Exp. GP4b (righthand panel: 'R') estimated PMCH concentrations for the 600-km sampling arc for the first four sampling periods: (a) 0800–1100 GMT; (b) 1100–1400 GMT; (c) 1400–1700 GMT; and (d) 1700–2000 GMT. Observed values are indicated by open squares; predicted values are indicated by filled triangles connected by a solid line. The starting time of each sampling period (GMT) is plotted in the upper righthand corner of each panel. The predicted site estimates were first shifted westward by 8° and 12°, respectively, to match the observed exposure peak.

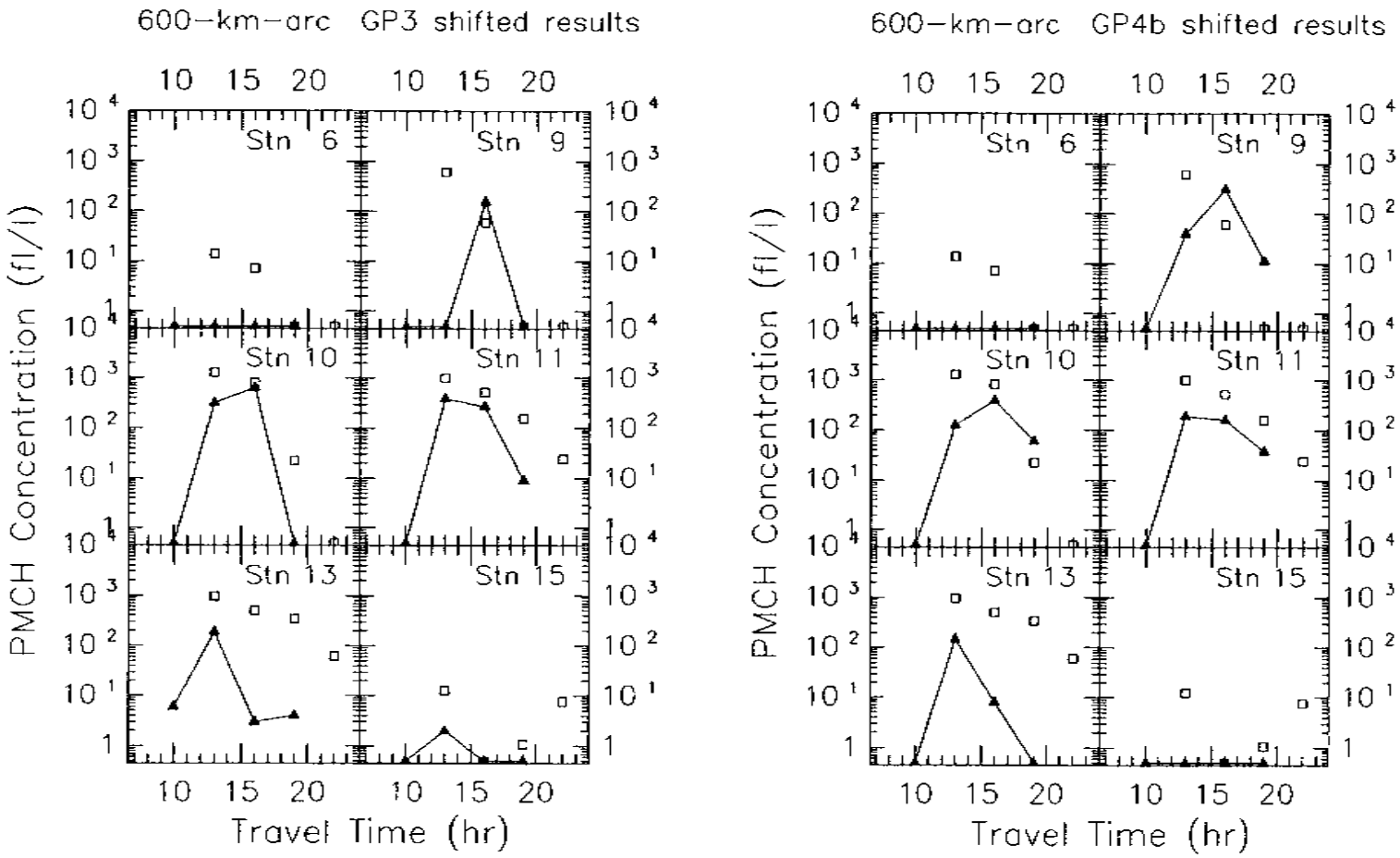

Figure 5.45: Concentration–time plots of observed vs. Exp. GP3 (lefthand panel: 'L') and observed vs. Exp. GP4b (righthand panel: 'R') estimated PMCH concentrations for six 600-km-arc sampling stations: (a) Station 6; (b) Station 9; (c) Station 10; (d) Station 11; (e) Station 13; and (f) Station 15. Observed values are indicated by open squares; predicted values are indicated by filled triangles connected by a solid line. The station ID number is plotted in the upper righthand corner of each panel.

Table 5.4 lists estimated 600-km-arc station exposure and total cross-wind integrated exposure (CWIE) values for a 12 h period for Exp. GP4b while Table 5.6 lists complementary values along the equally-spaced 91-site arc. It is clear from the first of these tables that the predicted exposure plume overlaps with the easternmost portion of the observed exposure plume, while the second table suggests that the angular gap between the two peak station exposures is 14°. It can also be seen from Table 5.6 that the predicted and observed exposure plumes are comparable in width although the Exp. GP4b predicted plume is narrower: 14° vs. 17°. A larger difference is apparent in the magnitude of the peak exposures: 1737 fl hl^{-1} vs. 6347 fl hl^{-1}. The Exp. GP4b estimated CWIE value is also smaller than the observed value by about 60%.

(c) Quantitative pattern characteristics. Table 5.5 summarizes some of the quantitative cloud characteristics estimated from the Exp. GP4b predicted concentrations along the arc of 91 equally-spaced sites. The predicted peak concentration for this simulations is only about one-third of the observed peak concentration. The timing of the peak concentration was also off by one sampling period. One interesting finding listed in this table is that the Exp. GP 4b predicted transit time matched the observed time for one cloud-edge criterion but was considerably shorter than was observed on the basis of the second criterion.

(d) Scattergrams. Fig. 5.46c shows the peak-matched scattergram for Exp. GP4b for the active 600-km-arc samplers. Corresponding unmatched scattergrams were not prepared for the three-dimensional experiments, however, because of the sizable centerline errors present in these simulations.

5.4.4 Other three-dimensional experiments

Three other three-dimensional experiments were run in addition to Exp. GP4b. Each can be paired with Exp. GP4b to investigate one aspect of the mesoscale dispersion problem. Exp. GP3 was identical to Exp. GP4b except that all surface properties other than terrain elevation were assumed to be uniform. Thus, differences between these two

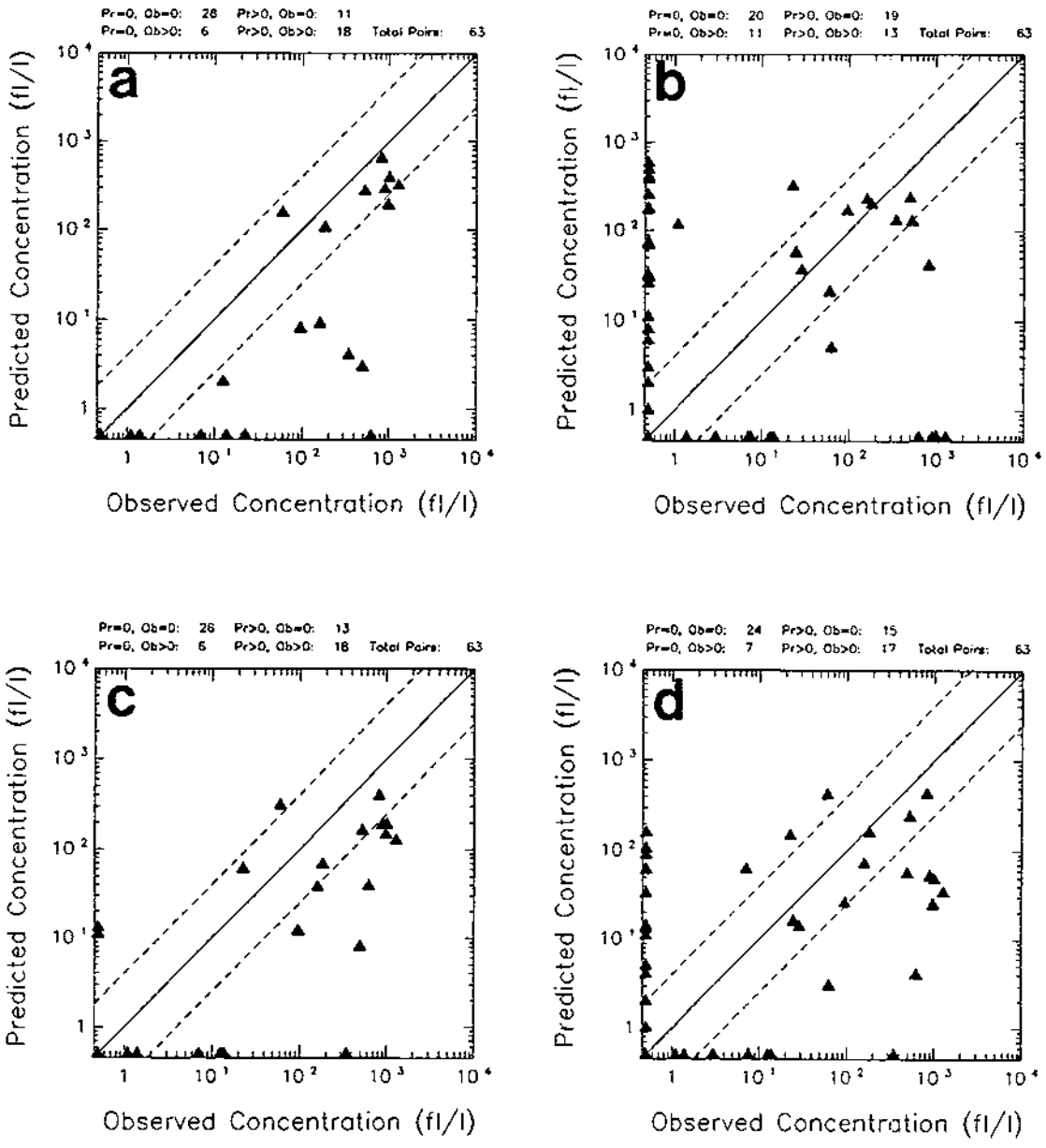

Figure 5.46: Scattergrams for observed 600-km-arc PMCH concentrations (less 3.4 fl^{-1}) vs. three-dimensional-experiment, computed, center-line-shifted concentrations: (a) Exp. GP3; (b) Exp. GP4; (c) Exp. GP4b; and (d) Exp. GP5. Plotted pairs have been drawn from the set of concentrations for Stations A–24 and the first four 3-hour observing periods from 0800–2000 GMT, July 9, 1980. Center-line-shift factors were 12°, 21°, 14°, and 19° for the four experiments. The diagonal lines are the one-to-one correspondence line and two factor-of-4 (i.e., 1:4 and 4:1) lines.

simulations are related solely to landscape heterogeneity and variability. Exp. GP4a was identical to Exp. GP4b with the exception of the choice of initial fields and starting time. The former simulation started at 1200 GMT on July 8 and used NMC gridded objective analyses and upper-air soundings for that time to create the RAMS initial fields. The Exp. GP4b RAMS simulation, on the other hand, began at 0000 GMT on July 8 and used the NMC analyses and upper-air soundings from 0000 GMT on July 9 to prepare the RAMS initial fields. Differences in grid-scale trajectories for these two subexperiments have already been discussed in Sec. 5.4.2. Exp. GP5 was identical to Exp. GP4b in all but two respects. Like Exp. GP4a, the Exp. GP5 RAMS simulation started at 1200 GMT on July 8 and the RAMS initial fields were based on the NMC analyses for that time. In addition, though, the lateral boundary conditions for this simulation were time-dependent. The Davies nudging lateral boundary scheme was used and four boundary meteorological files with 12-h spacing were prepared with the ISAN package for the 36-h RAMS simulation. Exp. GP5 was the experiment was referred to in Sec. 5.1 as the 'boundary 4DDA' experiment.

Three-dimensional-experiments mesoscale tracer transport

The sets of grid-scale trajectories calculated using the RAMS predicted wind fields from these 4 three-dimensional experiments are compared in Fig. 5.47. The differences between the Exp. GP4a and GP4b trajectories (panels 'b' and 'c') have already been considered in the discussion of Fig. 5.36. The Exp. GP3 grid-scale trajectories (panel 'a') are similar but not identical to the GP4b trajectories (panel 'c'), indicating that landscape variability did influence the low-level flow. The Exp. GP5 trajectories (panel 'd') are very interesting. They most closely resemble the Exp. GP4a trajectories (panel 'b'), which is not surprising since these two subexperiments differed only in the time dependence of the lateral boundary conditions. However, they are slightly longer than and are rotated counter-clockwise to the Exp. GP4a trajectories. In effect, they lie somewhere in between the Exp. GP4a and GP4b trajectories, consistent with the fact that the Exp. GP5 boundary conditions varied linearly with time from the observed fields

along the domain edges at 1200 GMT, July 8 to those at 0000 GMT, July 9 to those at 1200 GMT, July 9 to those at 0000 GMT, July 10. The first two of these times correspond to the analysis times used to initialize the Exp. GP4a and GP4b RAMS simulations, respectively.

Note that all of these trajectory sets display the obvious directional error between the source and the 100-km arc already discussed in connection with Exp. GP4b. In terms of the 600-km-arc crossing, Exps. GP3 and GP4b are the closest, followed by Exp. GP5 and finally Exp. GP4.

Three-dimensional-experiments mesoscale tracer dispersion

100-km arc.

(a) GLC patterns. Fig. 5.48 compares GLC patterns for the third 100-km-arc sampling period. The discussion for Fig. 5.47 carries over to this figure. The four simulated clouds look quite similar. All have a similar centerline direction (and directional error). The Exp. GP3 and GP4b clouds are slightly more elongated than the other two, consistent with faster transport speeds and longer grid-scale trajectories.

(b) Station values. Predicted GLCs are shown plotted against azimuth angle and the observed GLCs across the 100-km sampler arc for all 4 Great Plains three-dimensional experiments in Figs. 5.40 and 5.49 for the first six observing times. Some of the same values are presented in a complementary way, showing the time history of the predicted and observed concentrations at six of the 100-km arc station sites, in Figs. 5.41 and 5.50.

Overall, the agreement is good between the simulated tracer clouds and the observed cloud after travel over 100 km distance except for the obvious centerline error in Fig. 5.40. The simulated tracer clouds are a bit narrower than the observed tracer cloud and do not 'tail off' as abruptly with time. The predicted peak concentrations are also roughly 25% smaller than the observed peak concentrations (see Table 5.3). These three differences together suggest that speed shear may have been overemphasized somewhat in the simulations. One feature of the observed concentrations that was discussed in Sec. 3.1.4, the

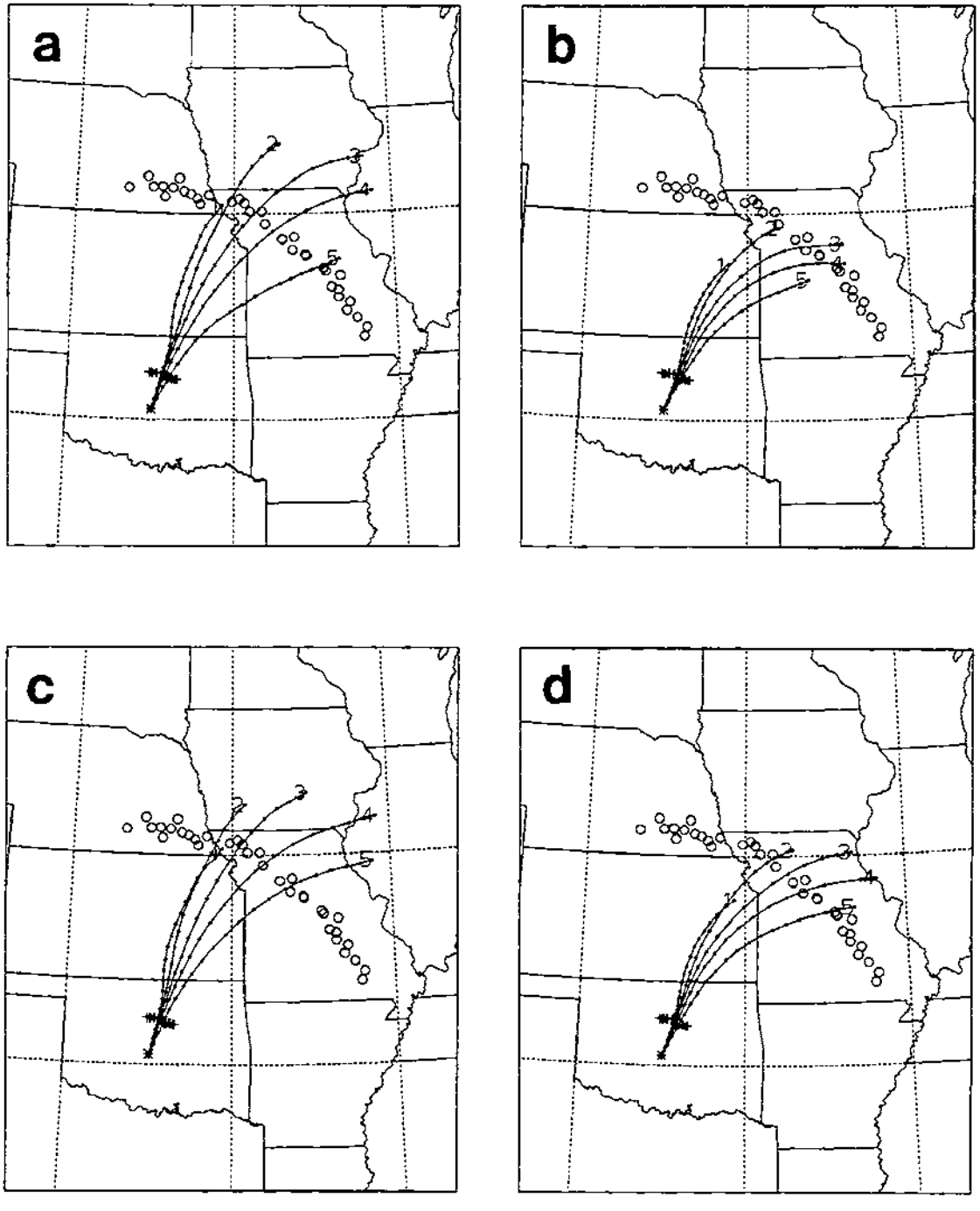

Figure 5.47: Plan view of grid-scale trajectories followed for 20 h at five different heights for the 4 three-dimensional Great Plains experiments: (a) Exp. GP3 wind fields; (b) Exp. GP4a wind fields; (c) Exp. GP4b wind fields; and (d) Exp. GP5 wind fields. Otherwise, the same as Fig. 5.36.

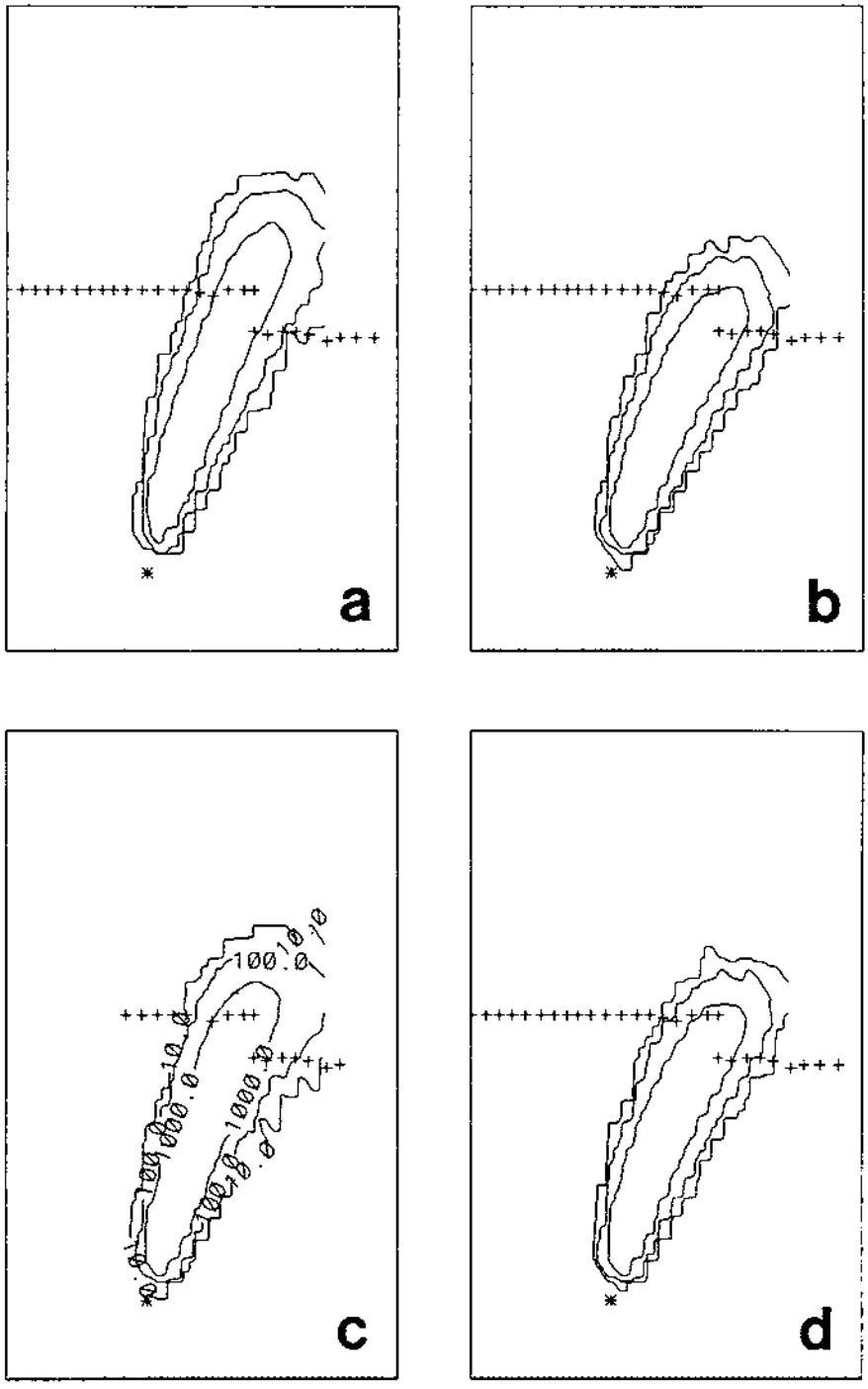

Figure 5.48: Plan views of estimated 45-minute-average PMCH ground-level concentration patterns for the third 100-km-arc sampling period, 2230–2315 GMT, which began 3.5 h after the start of the release, for the 4 three-dimensional-experiment MLPDM simulations: (a) Exp. GP3; (b) Exp. GP4a; (c) Exp. GP4b; and (d) Exp. GP5. 10, 100, 1000, and 10000 fl l^{-1} isopleths are shown. Otherwise similar to Fig. 5.3.

westward shift in the peak concentration with time, was mirrored in the predicted concentrations. This behaviour may be the result of wind shear too, since the leading edge of the cloud would be transported by the fastest PBL winds, which in the classic Ekman spiral are veered relative to the slower near-surface winds. Presumably, the trailing edge of the cloud is transported by these lower, slower, backed winds.

Station exposures and CWIE values are listed in Table 5.2 for the 100-km-arc stations for all 4 three-dimensional Great Plains experiments. The exposure plumes are very similar in terms of plume width, peak magnitude, and peak location. All four MLPDM exposure plumes lie to the east of the observed exposure plume, and all four peak exposures are 20–25% larger than the observed peak station exposure. The CWIE values for subexperiments GP4a, GP4b, and GP5 are very similar in magnitude. The estimated CWIE value for Exp. GP3 is somewhat smaller than the other three, but all are larger than the values predicted for Exps. GP1 and GP2.

One possible explanation for the higher CWIE values of the three-dimensional simulations (GP3–GP5) relative to the two-dimensional simulations might be that synoptic-scale subsidence associated with the anticyclonic circulation over the south-central U.S (cf. Figs. 5.38d,f) was represented in the former but not the latter simulations. Such large-scale sinking motion will suppress PBL depth and hence result in higher predicted concentrations since the tracer will be mixed and diluted through a shallower layer. Note in Table 5.3 that the predicted peak concentrations for the two-dimensional and three-dimensional MLPDM simulations are comparable in magnitude even though the three-dimensional clouds are wider. This difference is consistent with the larger CWIE values predicted by the three-dimensional subexperiments.

One slight difference between Exps. GP3 and GP4b on the one hand and Exps. GP4a and GP5 on the other is that the former two clouds seem slightly more skew than the other two, with wider eastside wings. This can been seen by careful comparison of Fig. 5.40 with Fig. 5.49 and by examining pairs of exposures in Table 5.2 at equal distances from the peak exposure.

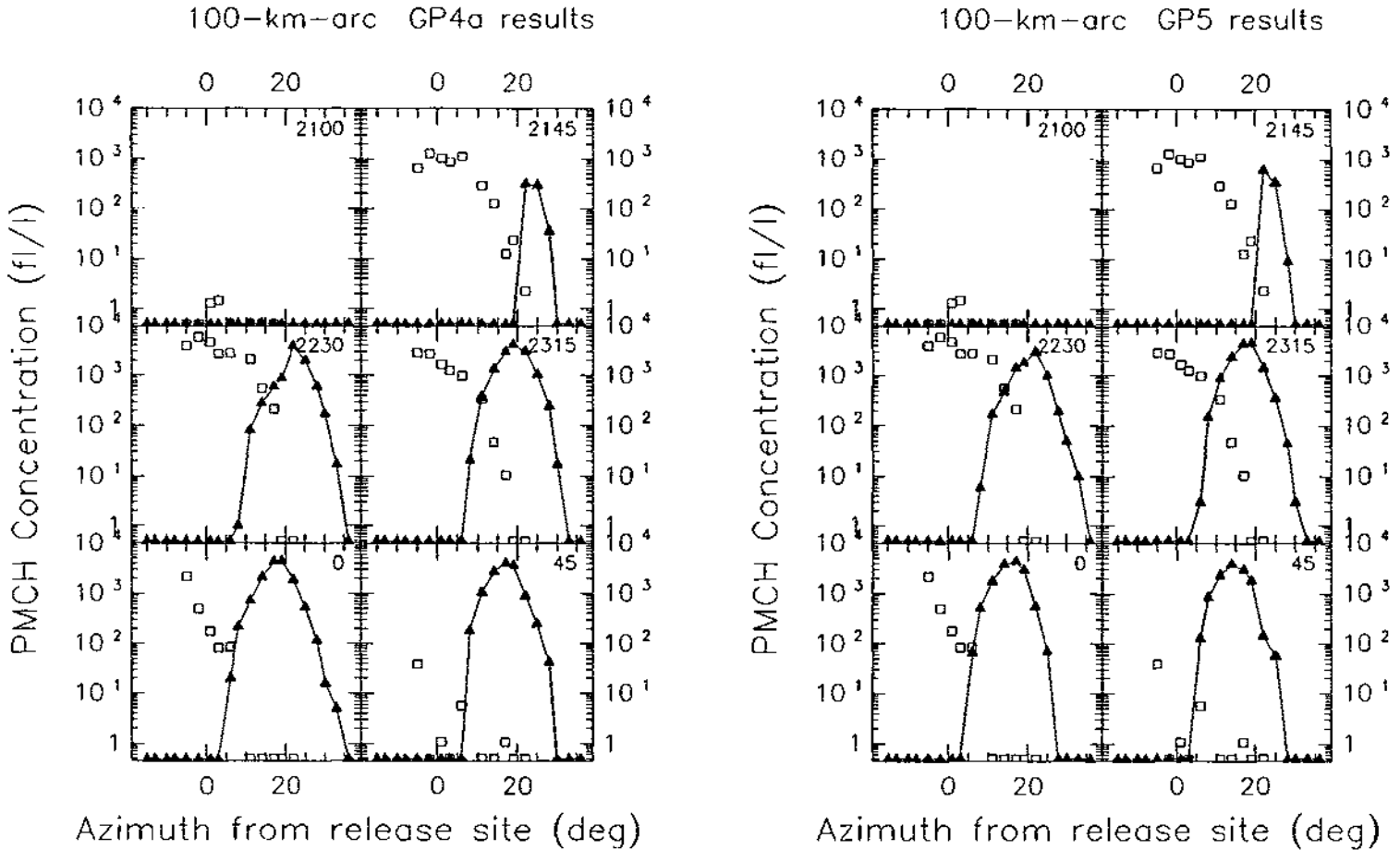

Figure 5.49: Time sequence of concentration–azimuth plots of observed vs. Exp. GP4a (lefthand panel: 'L') and observed vs. Exp. GP5 (righthand panel: 'R') estimated PMCH 45-minute-average concentrations for the Great Plains experiment 100-km sampling arc for the first six sampling periods: (a) 2100–2145 GMT; (b) 2145–2230 GMT; (c) 2230–2315 GMT; (d) 2315–0000 GMT; (e) 0000–0045 GMT; and (f) 0045–0130 GMT. Observed values are indicated by open squares; predicted values are indicated by filled triangles connected by a solid line. The starting time for each sampling period (GMT) is plotted in the upper righthand corner of each panel.

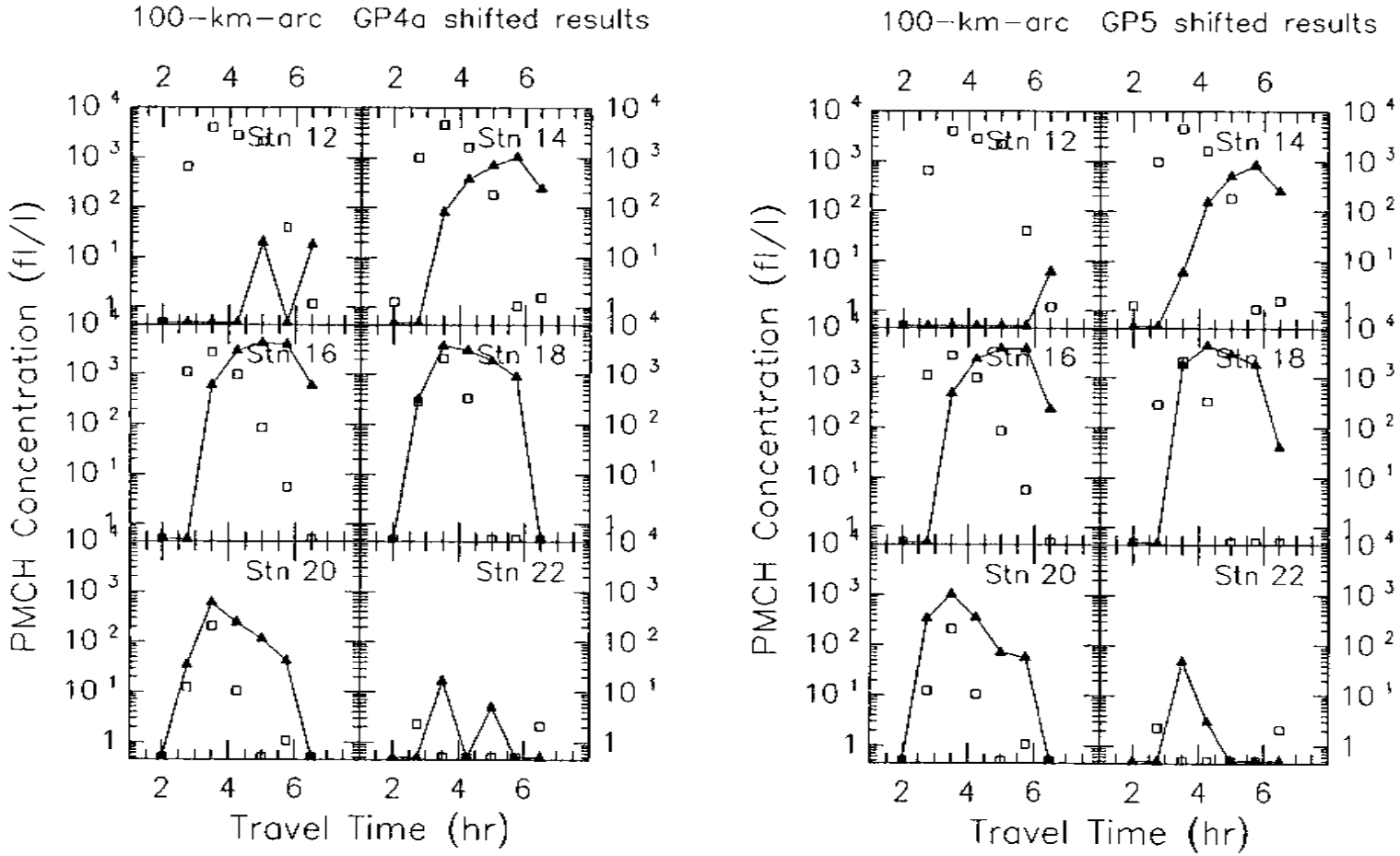

Figure 5.50: Concentration–time plots of observed vs. Exp. GP4a (lefthand panel: 'L') and observed vs. Exp. GP5 (righthand panel: 'R') estimated PMCH 45-minute-average concentrations for six 100-km-arc sampling stations: (a) Station 12; (b) Station 14; (c) Station 16; (d) Station 18; (e) Station 20; and (f) Station 22. Observed values for Stations 12–22 are indicated by open squares; predicted values are indicated by filled triangles connected by a solid line. The station ID number is plotted in the upper righthand corner of each panel. Note that the GP4a station values have been shifted westward by 8 station positions while the GP5 station values have been shifted westward by 7 station positions to match the observed exposure peak.

(c) Quantitative pattern characteristics. Table 5.3 lists some of the quantitative cloud characteristics estimated from the 100-km-arc predicted station concentrations for all of the three-dimensional Great Plains experiments. The characteristics of the four experiments are basically very similar, and what differences there are seem consistent with differences between these simulations which have already been discussed. The peak concentrations for Exps. GP3 and GP4b are smaller than those for Exps. GP4a and GP5; this is consistent with the faster transport speeds of the first two subexperiments. In a similar vein, Exp. GP4a, which has the slowest transport speeds, has a later arrival time at the 100-km arc and later time of peak concentration than the other three three-dimensional subexperiments.

(d) Scattergrams. Fig. 5.42 shows peak-matched scattergrams for all 4 three-dimensional Great Plains subexperiments. The scattergrams are quite similar, although Exp. GP5 seems to have fewer high-concentration matches than the others. Also, Exp. GP4b has significantly fewer zero–nonzero pairs than the other three subexperiments: that is, 15 vs. 29, 26, and 28.

600-km arc.

(a) GLC patterns. Fig. 5.51 compares GLC patterns for the 4 three-dimensional subexperiments for the first 600-km-arc sampling period. Differences in this figure are similar to the differences in the grid-scale trajectories for these same subexperiments (Fig. 5.47). That is, the tracer surface concentration footprints have travelled further in Exps. GP3 and GP4b and are rotated counter-clockwise as compared to the other two footprints. The GLC pattern for Exp. GP4a has not even reached the 600-km arc by this time, but this footprint is wider than the others. Interestingly, there are small but noticeable differences between the patterns for Exps. GP3 and GP4b. These differences are entirely attributable to landscape variability, which Exp. GP4b considers and Exp. GP3 ignores.

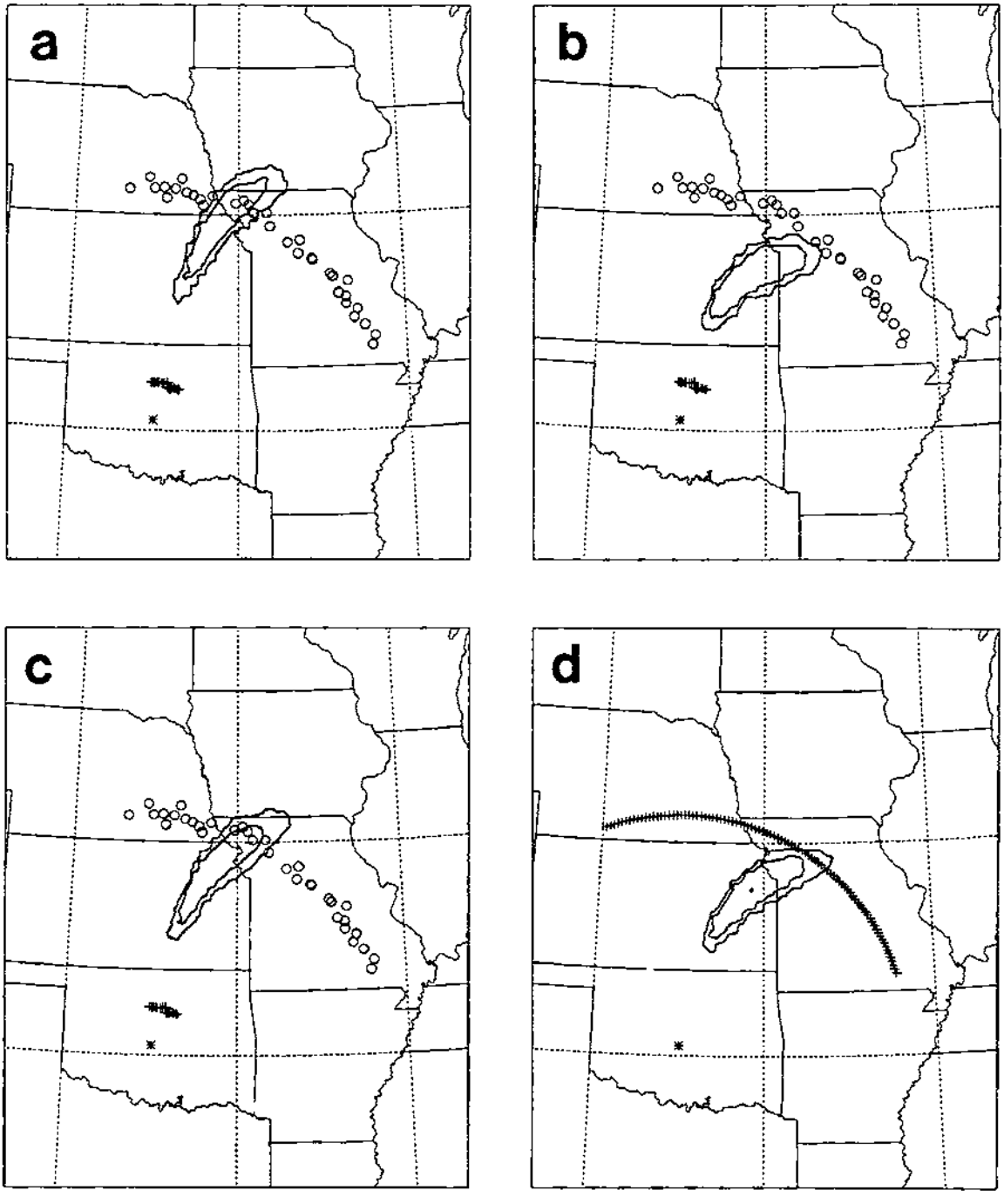

Figure 5.51: Plan views of the estimated 3-hour-average PMCH surface concentration patterns for the first 600-km-arc sampling period (0800–1100 GMT), which began 13 h after the start of the release, for the 4 4 three-dimensional-experiment MLPDM simulations: (a) Exp. GP3; (b) Exp. GP4a; (c) Exp. GP4b; and (d) Exp. GP5. The 10, 100, and 1000 fl l^{-1} isopleths are shown. The release site is indicated by the asterisk, the active 100-km-arc samplers by plus signs, and the active 600-km-arc samplers by open circles. The Lambert conformal projection with one standard parallel (at 38.5°N) covers the region from 32–45°N and 102–88°W. Parallels at 35°N and 40°N and meridians at 100°W, 95°W, and 90°W are indicated by dashed lines. Panel (d) shows the equally-spaced sampler arc instead of the actual active sampler locations.

(b) Station values. Figs. 5.44 and 5.52 show both predicted PMCH ground-level concentrations for the equally-spaced 600-km arc sites and observed 600-km-arc station concentrations plotted against azimuth angle for the first four 600-km-arc observing times. Figs. 5.45 and 5.45 present many of the same data in a complementary fashion, showing the time history of the predicted and observed concentrations at six of the 600-km arc stations.

There is quite a difference between the plots for Exps. GP3 and GP4b on the one hand and for Exps. GP4a and GP5 on the other. The latter two subexperiments exhibit a marked bimodal structure during the daytime sampling periods (Fig. 5.52) while the first two subexperiments are narrower and unimodal (Fig.5.44).

This unimodal vs. bimodal crosswind structure is also apparent in Table 5.4, which lists estimated 600-km-arc station exposure and CWIE values for a 12 h period for all 4 three-dimensional Great Plains experiments, and in Table 5.6, which lists complementary estimated values along the equally-spaced 91-site arc. Moreover, while the Exp. GP3 and GP4a 600-km-arc exposure plumes are narrower than the observed plume, the Exp. GP4a and GP5 plumes are much broader than the observed plume. The centerline locations are also more varied for the 600-km arc than for the 100-km arc (cf. Table 5.2).

What is the cause of the bimodal cross-plume structure of Exps. GP4a and GP5? Fig. 5.54 presents a time sequence of GLC patterns for Exp. GP4a in the same format used in Fig. 5.43 for Exp. GP4b. As expected from the discussion of Fig. 5.51, the Exp. GP4a surface cloud lags considerably behind the Exp. GP4b cloud. This difference in mean transport speed means that the bulk of the Exp. GP4a cloud crosses the 600-km sampler arc after sunrise whereas the Exp. GP4b cloud has nearly passed the sampler arc by this time. Accordingly, fumigation of elevated tracer occurs *over* the 600-km sampler arc in the case of Exp. GP4a but *past* the sampler arc in the case of Exp. GP4b. In addition, vertical directional shear appears to be greater in Exp. GP4a than Exp. GP4b (Figs. 5.36a,b). As a result, the Exp. GP4a cloud has a greater centerline tilt relative to the mean transport direction than does the Exp. GP4b cloud. This means that it

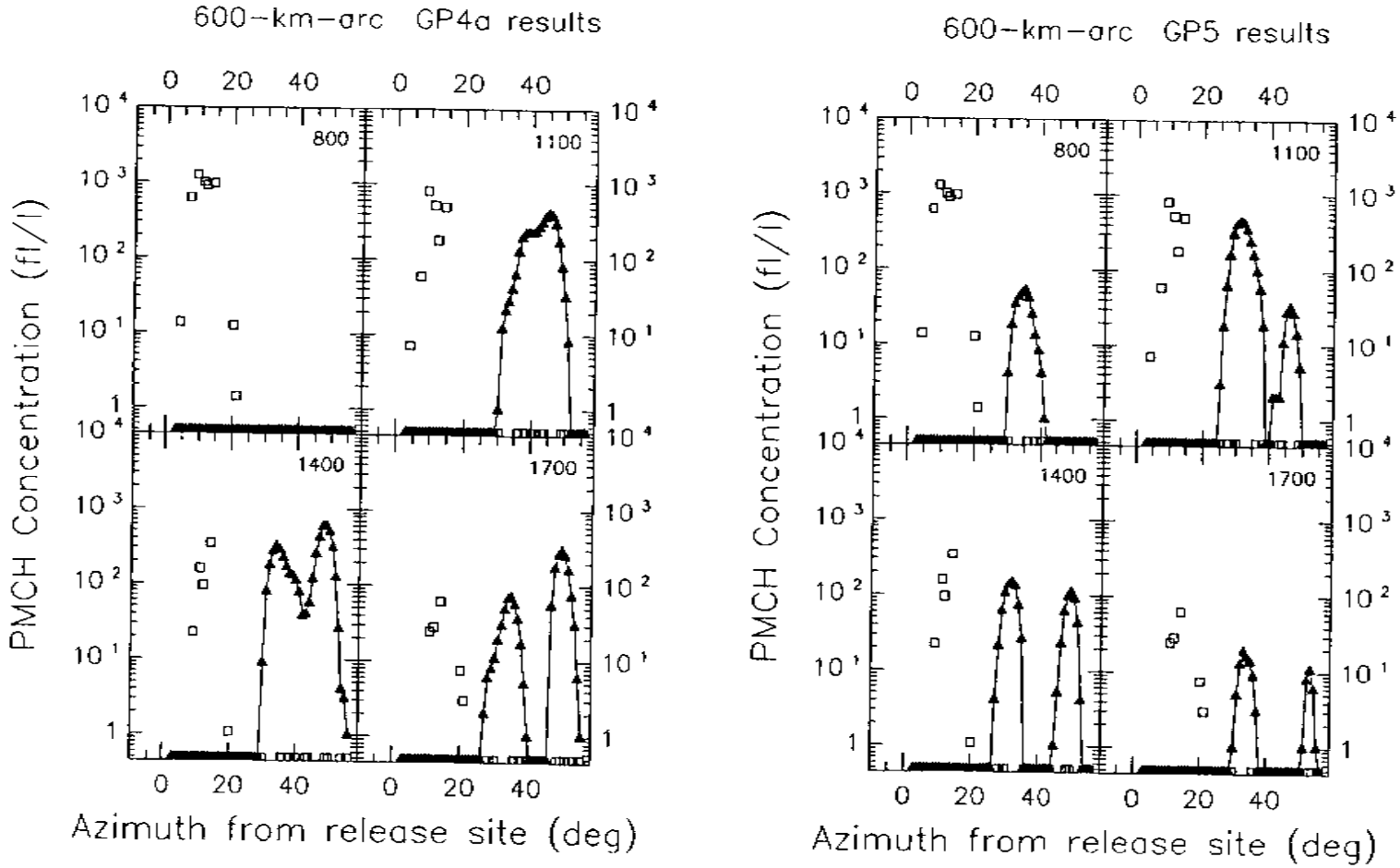

Figure 5.52: Time sequence of concentration–azimuth plots of observed vs. Exp. GP4a (lefthand panel: 'L') and observed vs. Exp. GP5 (righthand panel: 'R') estimated PMCH concentrations for the 600-km sampling arc for the first four sampling periods: (a) 0800–1100 GMT; (b) 1100–1400 GMT; (c) 1400–1700 GMT; and (d) 1700–2000 GMT. Observed values are indicated by open squares; predicted values are indicated by filled triangles connected by a solid line. The starting time of each sampling period (GMT) is plotted in the upper righthand corner of each panel.

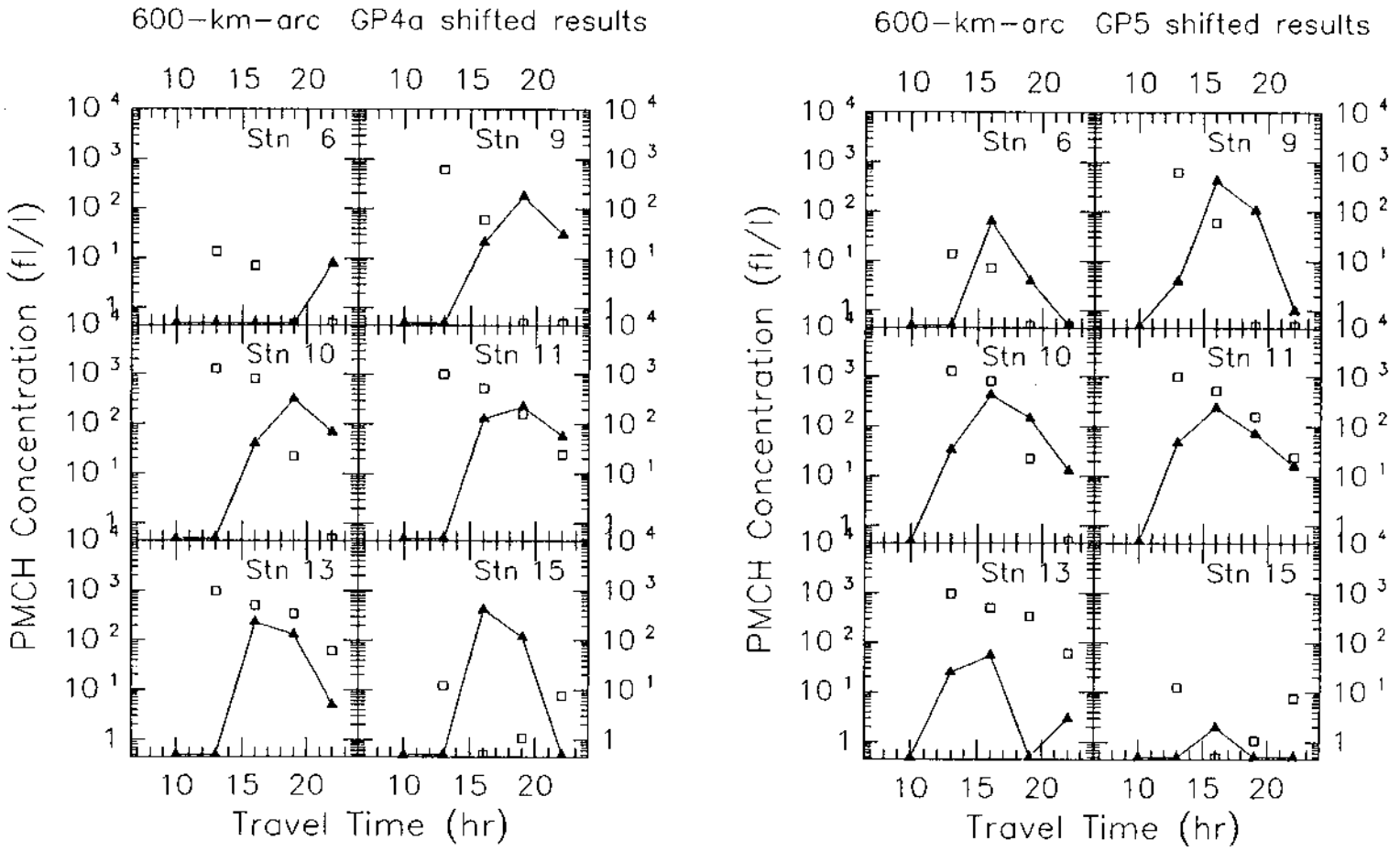

Figure 5.53: Concentration–time plots of observed vs. Exp. GP4a (lefthand panel: 'L') and observed vs. Exp. GP5 (righthand panel: 'R') estimated PMCH concentrations for six 600-km-arc sampling stations: (a) Station 6; (b) Station 9; (c) Station 10; (d) Station 11; (e) Station 13; and (f) Station 15. Observed values are indicated by open squares; predicted values are indicated by filled triangles connected by a solid line. The station ID number is plotted in the upper righthand corner of each panel. The predicted site estimates were first shifted westward by 25° and 23°, respectively, in order to match the observed exposure peak.

crosses the sampler arc more broadside than the Exp. GP4b cloud and hence is seen to be much wider. The Exp. GP3 cloud behaves similarly to the GP4b cloud while the Exp. GP5 cloud behaves similarly to the GP4a cloud.

(c) Quantitative pattern characteristics. Table 5.5 summarizes some of the quantitative cloud characteristics estimated from predicted concentrations along the arc of 91 equally-spaced sites for the 4 three-dimensional subexperiments. A few features are worth noting. As just discussed, the slower transport speeds for Exps. GP4a and GP5 with the resulting fumigation over the 600-km arc has made the determination of centerline angle and cloud width more complicated since *two* portions of the cloud with a gap between are detected during several sampling periods. The peak concentration predicted for Exp. GP3 is 50% larger than the corresponding value for Exp. GP4b. Because these two simulations are so similar, it is hard to know whether this difference arises solely from sampling fluctuations or if at least some of the difference is real and corresponds to the influence of mesoscale landscape variations. The estimated CWIE value for Exp. GP4a is over twice as large as the values for the other 3 three-dimensional subexperiments and is much closer to the observed value. But whereas the observed CWIE value was the result of high concentrations at only a narrow band of stations, the Exp. GP4a value results from lower concentrations over a much wider band of stations. This is very interesting nonetheless since the biggest difference between the MLPDM predicted clouds and the observed cloud is probably this difference in CWIE values.

(d) Scattergrams. Fig. 5.46 shows peak-matched scattergrams for all 4 three-dimensional Great Plains subexperiments based on concentration data from the active 600-km-arc samplers. Corresponding unmatched scattergrams were not prepared for the three-dimensional experiments, however, because of the sizable centerline errors present in these simulations.

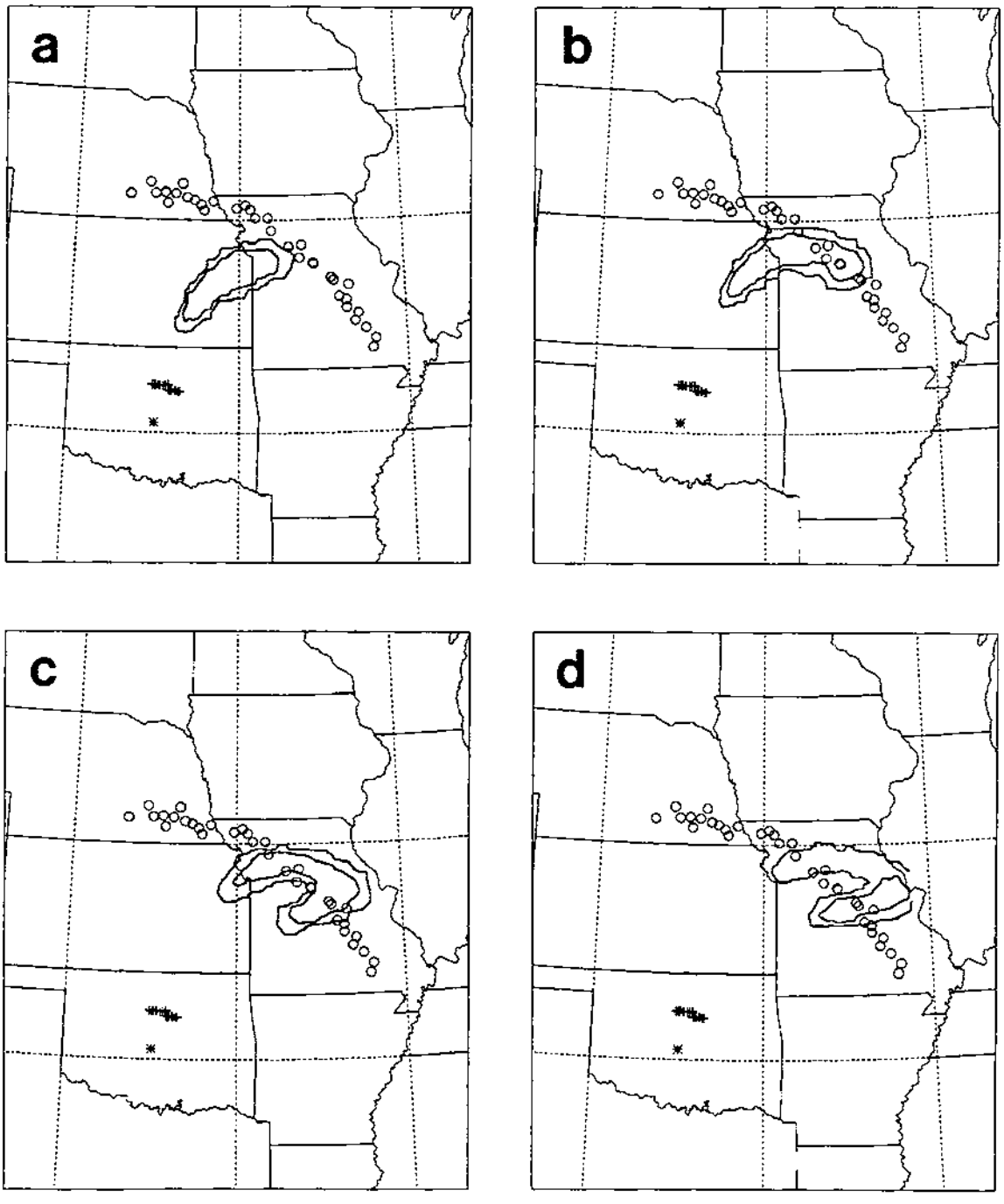

Figure 5.54: Time sequence of plan views of estimated PMCH 3-h-average GLC patterns for the first four 600-km-arc sampling periods based on particle positions from the Exp. GP4a MLPDM simulation: (a) 0800–1100 GMT; (b) 1100–1400 GMT; (c) 1400–1700 GMT; and (d) 1700–2000 GMT on July 9, 1980. Otherwise identical to Fig. 5.16.

5.5 Speculation on Canopy Storage Under Stable Conditions

Fig. 3.10 revealed a remarkable aspect of the Great Plains tracer experiment 600-km-arc measurements, namely the existence of a secondary concentration maximum which was first detected during the eleventh 3-h sampling period, 18 h after the passage of the trailing edge of the primary tracer cloud across the 600-km-arc stations. This secondary cloud was over twice as broad as the primary cloud (408 km vs. 178 km) and took twice as long to cross the 600-km sampler arc (30 h vs. 15 h). The peak PMCH concentration reported for the secondary cloud was 16 fl^{-1}, two orders of magnitude lower than the 1280 fl^{-1} maximum reported for the primary cloud but still over five times greater than background levels (Sec. 3.1.4).

Any explanation for the existence of the secondary cloud should explain the large gap between its arrival at the 600-km arc and the passage of the primary cloud, its greater size, and its observed concentration levels. The two possible explanations for this phenomenon mentioned in Chap. 3 were (a) a return crossing of the 600-km arc by a portion of the primary tracer cloud and (b) some type of vegetation absorption/release mechanism. Both of these explanations have been discounted (Policastro et al., 1986a). However, a third possible mechanism to explain this secondary cloud is the nighttime trapping and subsequent next-day release of near-surface tracer by the surface vegetation *canopy* upwind of the 600-km arc due to stability effects, i.e., an aerodynamical rather than a plant-physiological mechanism.

One very important characteristic of canopies is that the temperature stratification within the canopy has the opposite phase to the stratification above the canopy (e.g., Pielke, 1984, p. 417). That is, air within and below the foliage is stably stratified during the day and unstably stratified at night. The air flow within a vegetation canopy is thus coupled to airflow above the canopy mainly by the action of above-canopy coherent eddies with length scales of the order of the canopy thickness or greater (Raupach, 1988). Tracer can be carried or injected into the canopy by 'sweeps' or 'gusts' and be carried out of the canopy by 'bursts' or 'ejections' (e.g., Shaw et al., 1983). According to

this conceptual model, it then follows that the coupling between the sub-canopy flow and the above-canopy flow should decrease with decreasing above-canopy turbulence intensity and increasing above-canopy stability. Raupach (1988) briefly mentioned some unpublished Canadian data which support this conclusion. Baldocchi and Meyers (1988) found a nocturnal reduction in turbulence intensities measured above and below a deciduous forest canopy as well as a reduction in turbulence variances. Moreover, they found a corresponding reduction in the magnitude of vertical-velocity skewness at night. This quantity is normally negative within the canopy because turbulent above-canopy downdrafts are common whereas turbulence is weaker near the canopy floor and there is no near-surface source of updrafts. A weaker vertical-velocity skewness within the canopy thus implies weaker canopy–atmosphere coupling.

Let us hypothesize, then, that the PMCH tracer will be well-mixed throughout the daytime CBL, including any vegetation canopy and subcanopy layers. As night approaches, however, vertical mixing will decrease and fewer and fewer above-canopy eddies will penetrate into the canopy and subcanopy layers. Tracer carried into the canopy during the day will thus be stranded as the canopy air becomes decoupled from the airflow above. The above-canopy tracer cloud will continue onwards while tracer within the canopy remains behind, trapped[198] until vigorous new eddies develop after sunrise the next morning and again mix canopy air with above-canopy air. This scenario can be viewed as a special case of the more general problem discussed by Purnama (1988).

Of course, for canopy trapping to be relevant to the Great Plains case, there must be a canopy[199]. Fig. 5.55 shows the distribution of forests across North America. Some forested areas do exist in eastern Oklahoma and Missouri. In addition, extensive plant

---

[198] The unstable stratification within the canopy at night may allow some tracer to 'bleed' out of the canopy into the stagnant stable air immediately above the canopy but horizontal advection will still be small.

[199] An alternate or complementary mechanism to canopy trapping which might also have played a role is the pooling of tracer gas in local valleys and low spots on the evening of July 8 due to local cold-air drainage (W. Lyons, personal communication, 1992). The terrain in this region is undulating.

canopies associated with agriculture will also be present during the growing season in this area (Fig. 4.3b).

To test this hypothesis, the following numerical experiment was carried out. The instantaneous ground-level PMCH concentration pattern for Exp. GP4b was calculated at 0000 GMT on July 9, five hours after the start of the tracer release from Norman, for the first 134 m of air above the ground (Fig. 5.56). This time was approximately 1.75 h before sunset (0148 GMT/2048 CDT). The MLPDM was then rerun for a 2.5-h ground-level areal release beginning at 1330 GMT, approximately two hours after sunrise (1122 GMT/0622 CDT) the next morning. The release area corresponded to the sunset GLC pattern. The time-integrated strength of the release was set to a value of 0.75 kg. This was equal to the product of 1/250, the vertical fraction of a 2500-m-deep daytime CBL occupied by a nominal 10-m-thick canopy, and the amount of tracer released initially, 192 kg. A total of 3600 particles were released during the July 9[200] areal release and were then followed for 24 h.

Fig. 5.57 shows a time-sequence composite of the predicted GLC pattern as the canopy tracer cloud approaches and crosses the 600-km sampler arc. The simulated secondary tracer cloud arrives at the 600-km sampler arc at approximately 0400 GMT on July 10, 14.5 hours after the start of the canopy areal release and 11 hours after the trailing edge of the Exp. GP4b primary cloud had reached reached the 600-km arc at 1700 GMT on July 9 (see Fig. 5.43c–d). Again, the observed secondary cloud arrived at 1400 GMT on July 10, 18 hours after the departure of the primary cloud. The simulated canopy cloud takes 6 hours to cross the sampler arc, has a maximum station concentration of just over 1 fll^{-1}, and is roughly five stations wide based on a 10% threshold criterion. The corresponding observed values were 30 hours, 16 fll^{-1}, and ten stations wide.

---

[200] The actual wind fields used were from the Exp. GP4b RAMS simulation for the 24-h period beginning July 8 at 1200 GMT; this was done because the GP4b simulation was not carried out far enough in time to follow a July 9 morning release (60 h would have been required) but the approximation is reasonable given the assumption of synoptic stationarity in this run.

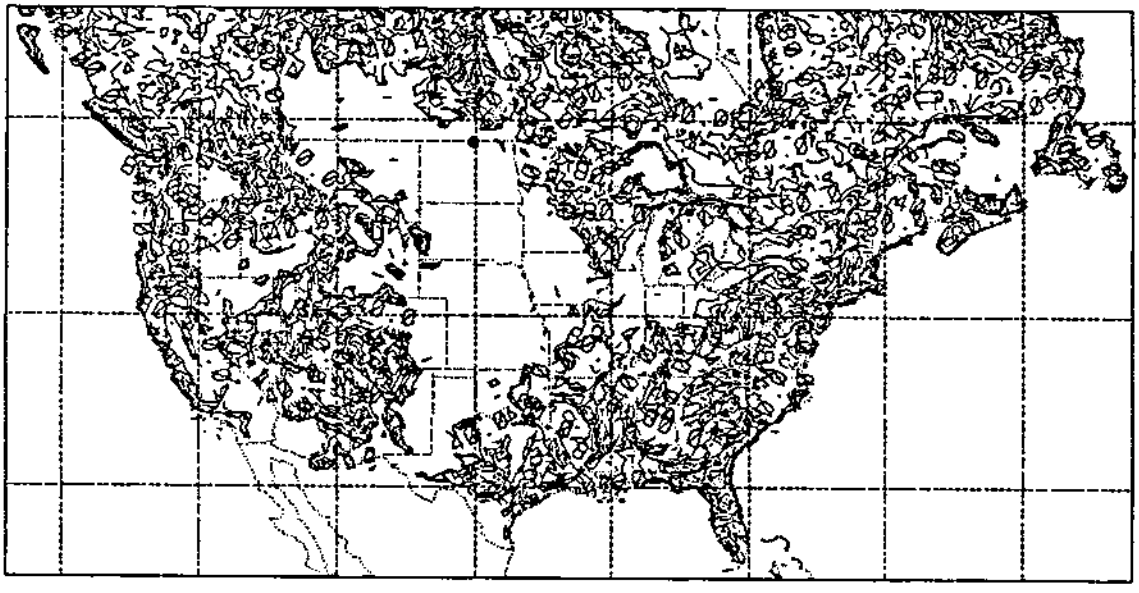

Figure 5.55: Distribution of fractional coverage (as a percentage) of a composited EPA 'forest' land-cover category over North America. This field is the summation of the three forest subcategories (see Fig. 4.3). The resolution of this gridded field, shown here on a Mercator projection, is 1/4° longitude by 1/6° latitude.

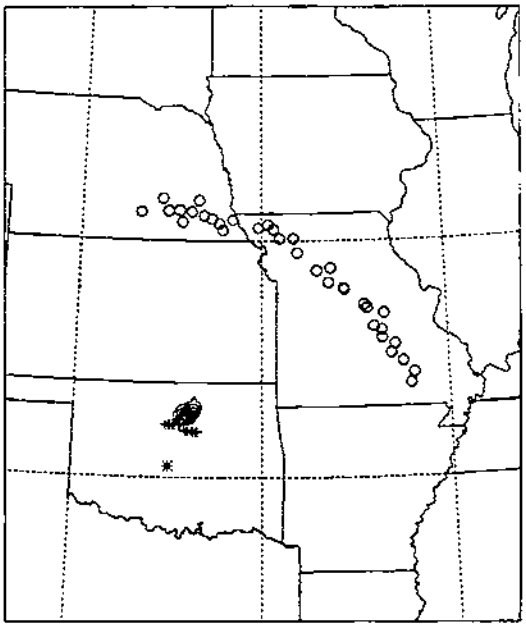

Figure 5.56: Plan view of instantaneous GLC pattern 1.75 h before sunset on July 8, 1980 for a CAG depth of 134 m. Concentration isopleths are linearly spaced over 200 fll^{-1} intervals. Maximum GLC value was 2541 fll^{-1}.

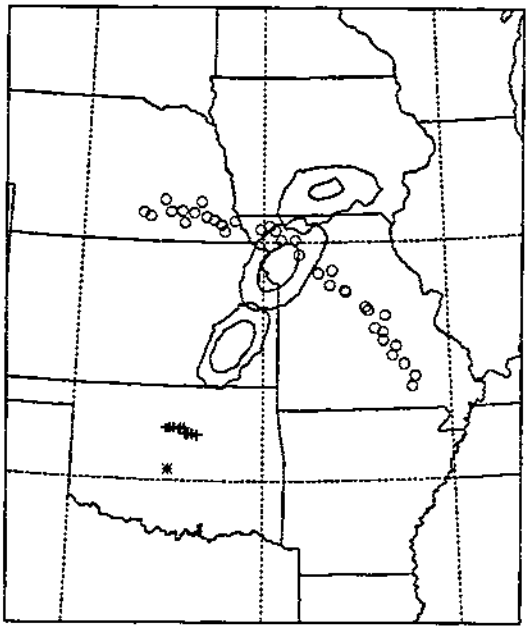

Figure 5.57: Plan view of a composite of three 3-h-average GLC patterns, July 9 at 2000–2300 GMT and July 10 at 0200–0500 and 0800–1100 GMT, for a CAG depth of 378 m. The 0.1 and 1 fll^{-1} concentration isopleths are plotted.

In summary, the simulated secondary cloud for the proposed canopy-trapping scenario displays some of the quantitative characteristics of the observed secondary cloud, particularly the delayed arrival of the secondary cloud. Transit time, peak concentration level, and cloud width were all too low. However, it should be noted that the primary-cloud simulations also suffered from too low peak values and too short transit times (Table 5.5). These results suggest that canopy trapping remains a possible candidate mechanism to explain the observed occurrence of the secondary tracer cloud at the 600-km sampler arc. And if it is not a perfect explanation, it is still the only possible one advanced to date.

Moreover, this phenomenon of a secondary cloud is worthy of further study for several reasons. For example, the occurrence of detectable secondary tracer clouds would have to be considered when designing a mesoscale tracer field study with multiple releases. The response to the accidental release of a particularly toxic or virulent substance should also recognize the possibility of overnight trapping and next-day re-release of smaller but possibly still harmful amounts of the hazardous substance.

5.6 Summary

A suite of six meteorological experiments and ten subexperiments of varying degrees of complexity and realism were conducted for the Great Plains mesoscale tracer experiment case. The meteorological experiments consisted of a flat-terrain two-dimensional simulation, a sloping-terrain two-dimensional simulation, and 4 three-dimensional simulations. These numerical experiments permitted an examination of the impact of terrain elevation and other land-surface characteristics, atmospheric baroclinicity, and synoptic flow evolution on the predicted tracer dispersion.

Quite realistic results were obtained with the idealized two-dimensional simulations, even though these were initialized with only a single Oklahoma City sounding. The main effect of introducing the regional-scale terrain slope characteristic to the Great Plains (Exp. GP1 vs. Exp. GP2) was to increase the mean PBL transport speed. However, it was also found in these experiments that the simulated tracer-cloud dispersion was very

sensitive to the time of the sounding used to initialize the RAMs meteorological model. Examination of a sequence of consecutive 12-hourly Oklahoma City soundings for the experimental period showed that the soundings contained a significant ageostrophic oscillation superimposed on the background synoptic profile. This finding was not surprising since the Great Plains are well known for having strong nocturnal low-level jets much of the year as a result of a slope-flow-enhanced inertial oscillation. The RAMS initial state in a horizontally-homogeneous simulation should be steady and geostrophic, however. Best results were obtained by averaging the morning and evening Oklahoma City velocity profiles from the soundings bracketing the Great Plains experiment release time. The averaged velocity profile so obtained is in fact a reasonable estimate of the background geostrophic wind profile.

The main difference between the two-dimensional and three-dimensional numerical experiments for this case was the latter's representation of regional-scale flow curvature and flow speed changes. Not surprisingly, a single sounding is unlikely to be representative of the atmospheric flow hundreds of kilometers away. In the case of the Great Plains mesoscale tracer experiment, the tracer was transported on the backside of a large high-pressure system centered just north of Louisiana so that the flow direction tended to veer with travel time. The three-dimensional-experiment grid-scale trajectories were shorter than the two-dimensional ones and had significant anticyclonic curvature (Fig. 5.36). The NMC analyses used to initialize the RAMS three-dimensional-experiment simulations were also found to contain an unsteady ageostrophic oscillation. However, the same averaging procedure used in the two-dimensional experiments was considerably less successful in the three-dimensional experiments. What seemed to be more important in these runs was to start the meteorological model the night before the tracer release so as to allow the inertial oscillation time to develop.

A total of 3600 virtual particles were released over a three-hour period in each MLPDM simulation for the Great Plains numerical subexperiments. This is a fairly small number of particles from which to make quantitative concentration estimates. However,

composites of archived instantaneous particle-position sets were used to estimate time-averaged concentrations for comparison against the observed values. Particle positions were archived after every 15 minutes of MLPDM simulation. Thus, up to 10800 particle positions were available for estimating 45-minute ground-level concentrations (GLCs) on the 100-km arc while 43200 particle positions were considered in making 3-hour GLC estimates on the 600-km sampler arc. Not all of these particle positions contributed to the *ground-level* concentration estimates, however. It seems unreasonable to expect that particles well above the surface would affect ground-level concentrations, especially under stable conditions. It was thus necessary to specify a sampling depth[201] in making GLC estimates as well as a sampling-box length and width. After conducting some sensitivity tests, a value of 1842 m was chosen for the sampling depth used to make the daytime 100-km-arc GLC estimates while a shallower value of 378 m was selected for the nighttime and daytime 600-km arc GLC estimates. Once areal GLC estimates were made over the selected concentration analysis grid with this simple box-count method, values were then interpolated at selected points using a third-order, bidirectional, overlapping-polynomical technique.

A number of analysis techniques were employed to evaluate the tracer dispersion simulations. Sets of grid-scale trajectories were calculated for five different PBL release heights at the beginning and end of the tracer release period for each numerical subexperiment. These trajectory sets provided information on the speed and direction of mesoscale transport and the magnitude and direction of ambient grid-scale vertical shear. Travel-time isochrons could then be drawn through these trajectories to obtain cloud 'envelopes', that is, bounded regions defining the position, size, and shape of the grid-scale cloud. It was shown that these trajectory envelopes provided a first-order estimate of the position, size, and shape of the corresponding particle cloud. If we think of the MLPDM as a stochastic–deterministic numerical model, then the trajectory envelopes will describe

---

[201] Or a vertical bandwidth in the case of the kernel density estimation technique.

tracer transport and deformation by the deterministic component of the flow. However, these envelopes cannot describe cloud growth, which results from subgrid-scale mixing.

Predicted GLC patterns were compared to the observed GLC patterns on the two sampling arcs in a space-time sense by means of a number of quantitative measures. These included cloud arrival time and transit time, mean travel direction, maximum cloud width, peak time-average station concentration, time of peak station concentration, peak station exposure, and cross-wind integrated exposure or CWIE. The last quantity is related to the total mass of the tracer cloud. Two different cloud-edge criteria, (a) fixed fraction of maximum concentration (a relative measure) and (b) fixed concentration threshold (an absolute measure), were used in estimating cloud width since this quantity is sensitive to the criterion chosen. Predicted station concentrations on each sampling arc were also compared to observed values using three different graphical presentations: concentration–azimuth angle (CA) plots for each sampling period, concentration–travel time (CT) plots for selected sampling stations, and concentration–concentration (CC) scatterplots for all sampling periods and stations. As has been found in other mesoscale dispersion studies (e.g., Draxler, 1987; Godowitch, 1989b; Carhart et al., 1989; Andren, 1990b), the biggest source of error between the predicted and observed tracer clouds is positional error due to the cloud being transported in the wrong direction. Even a slight directional offset can produce poor comparison statistics for data points paired in space and time. The influence of this directional offset error can be minimized, however, by 'matching' or overlaying the predicted cloud centerline with the observed centerline. The errors which remain will then be due to problems with the representation of diffusion. This peak matching approach was used in constructing many of the CT and CC concentration plots in Chaps. 5 and 6.

It was also found to be very useful to estimate GLC values at sites along computational arcs with equal azimuthal spacing and identical downwind distance. While observations were not available at these equally-spaced-arc sites, sampling stations could be matched to individual sites. The advantages of the equally-spaced arcs were azimuthal coverage

across the full width of the predicted tracer cloud, arbitrarily high spatial resolution[202], and uniform spacing. The quantitative pattern comparison measures and graphical plots employed both station GLC estimates and equally-spaced-arc GLC estimates.

The mesoscale dispersion modelling system displayed both quantitative and qualitative skill for this case. The 100-km-arc predictions in particular agreed well with the observations in both quantitative and qualitative terms (e.g., Table 5.3). The two-dimensional experiments with their idealized single-sounding initialization were at much less of a disadvantage relative to the three-dimensional experiments for this meso-/*beta*-scale travel distance. In fact, the NMC analysis used to initialize the three-dimensional RAMS simulations was found to have a significant error in low-level flow direction with the result that the three-dimensional simulations had a considerably larger tracer-cloud longitudinal centerline error than the two-dimensional simulations. The three-dimensional-experiment cloud widths and CWIE values, on the other hand, agreed better with the 100-km-arc observations than the two-dimensional-experiment values did, possibly as a result of the inclusion of large-scale subsidence.

Agreement between model predictions and observations was not as good on the 600-km arc but was still qualitatively reasonable. Exp. GP4b had the best prediction overall in terms of quantitative pattern characteristics. Predicted cloud arrival time agreed well. Predicted cloud transit time either agreed well or was too short, depending upon the edge criterion used. Time of peak concentration was predicted to be one 3-h sampling period too late. The peak predicted concentration was about one-third of the observed value and the predicted CWIE value was only about one-fifth of the observed value. Predicted maximum cloud width was 15–20% on the low side and the predicted centerline was displaced 12° too far east. On the other hand, the Exp. GP4b simulation was more successful than simulations made by seven other mesoscale dispersion models in terms of predicted arrival time (see Fig. 3.11). Clouds predicted by the other models all arrived

---

[202] Though limited implictly by the sampling box size used to make the CAG concentration estimates.

late at the 600-km arc. Some of the other models predicted cloud widths comparable to the MLPDM value (Carhart et al., 1989). Most of these other models, however, assumed a vertically well-mixed cloud and would not have predicted the sudden widening of the MLPDM cloud after sunrise as elevated tracer was mixed downwards (e.g., Fig. 5.10). But as discussed in Chap. 5, this widening, if it did in fact occur, happened downwind of the 600-km arc and was not evident in the observations.

The major differences between the observations and model predictions on the 600-km arc were in the peak concentration and CWIE values. It is worth noting, however, that both observed quantities were higher than expected based on the 100-km arc measurements. Peak concentrations on the 100-km and 600-km arcs were 5900 and 1280 fl l^{-1}, respectively, while the CWIE values on the two arcs were 156000 and 500000 fl km h l^{-1}. If we assume peak concentration to decrease linearly with travel time T (e.g., a vertically bounded cloud with $\sigma_y \propto T$), then the peak concentration values agree very well. The threefold increase in CWIE is much more difficult to explain, however.

Finally, a hypothesis to explain the observed but very unexpected secondary tracer cloud measured at the 600-km sampler arc beginning 18 h after the primary cloud had passed the arc was tested. It was proposed that tracer gas could become trapped within the vegetation canopy at night due to stratification effects and then not be released until the following morning. The hypothesis was tested with a numerical simulation in which tracer was released from an area source over a 2.5-h period beginning approximately two hours after sunset. The location of the area source corresponded to the surface footprint of the primary tracer cloud five hours after the start of the release and 1.75 h before sunset. The resulting transit time, peak concentration level, and maximum cloud width at the 600-km arc were all too low compared to the observed values, and the delay between the departure of the trailing edge of the primary tracer cloud and the arrival of the simulated secondary cloud was only 11 h as compared to the 18 h observed delay. The simulated scenario did provide qualitative agreement nonetheless.

Chapter 6

CROSS-APPALACHIAN TRACER EXPERIMENT SIMULATIONS

Does the wind possess a velocity? This question, at first foolish, improves on acquaintance.

L.F. Richardson (1926)

The second MAD case considered in this study was Release 2 of the Cross-Appalachian Tracer Experiment (CAPTEX), which was carried out over eastern North America from September 25–28, 1983. This case complements the Great Plains case nicely: the sampling period was longer, the sampling network was larger, the experimental domain was considerably more inhomogeneous, and the large-scale synoptic pattern changed considerably during the experimental period. As a result, synoptic nonstationarity and three-dimensional flow perturbations induced by terrain-forced mesoscale circulations played a much more significant role in this mesoscale tracer experiment than in the Great Plains experiment.

6.1 Outline of the Numerical Experiments

As discussed in Chap. 3, CAPTEX was inherently more complex than the Great Plains experiment due to its larger domain and more complicated topography, which included several of the Great Lakes and a portion of the Appalachian Mountains. Accordingly, the two-dimensional sensitivity experiment carried out for the Great Plains case study (Exp. GP2) was not as appropriate for this case since the physiography of eastern

North America varies significantly both latitudinally and longitudinally. Some of the other Great Plains experiments, however, could be carried over.

Knowledge gained from the Great Plains simulations described in the previous chapter and from CAPTEX simulations made by a number of other modelling groups (Davis et al., 1986; Draxler, 1987; Lee, 1987; Brost et al., 1988a,b; Kao and Yamada, 1988; Shi et al., 1990) was also useful in designing the suite of experiments for this case study. None of the Lagrangian and Eulerian mesoscale dispersion models run for CAPTEX Release 2 to date (see Chap. 3) have had fine enough horizontal spatial resolution to simulate realistically the terrain-forced mesoscale circulations likely to have occurred over the Great Lakes and Appalachian Mountains during this period. Kao and Yamada employed 50 km horizontal grid spacing and Brost et al. (1988a) ran several experiments with 35 km horizontal grid spacing. However, Lakes Erie and Ontario are at most only about 100 and 80 km wide, respectively, that is, barely resolved with these grid spacings since at least four grid increments are required to resolve meteorological and surface features properly (e.g., Avissar et al., 1990). Nevertheless, lake-breeze circulations on these large lakes are likely to have had some impact on the resulting tracer transport (e.g., Moran et al., 1986; Pielke et al., 1987b). The CAPTEX simulations described in this chapter have the same horizontal resolution limitations. As discussed in Sec. 4.2.5, the 0.5° longitude by 0.333° latitude grid spacing used was roughly equivalent to 41 km by 37 km grid spacing.

Table 6.1 lists the six numerical experiments carried out for this case. Together, they allow an examination of the influence of topography and other land-surface characteristics and of spatial and temporal variations in the synoptic-scale environment on the dispersion of the simulated tracer cloud. Exp. CAP1 was the most idealized of the six CAPTEX numerical experiments. Like Exp. GP1, it assumed flat terrain and horizontally homogeneous atmospheric flow at the start of the simulation. However, unlike Exp. GP1, geographical variations in land-surface properties other than terrain elevation were considered (i.e., sea-surface temperature, albedo, surface roughness, and

soil texture class). Thus, the presence of Lakes Erie and Ontario was accounted for in Exp. CAP1 but not the presence of the Appalachian Mountains or other significant *orographic* features. Another difference between the RAMS configurations for Exp. CAP1 and Exp. GP1 was that latitudinal variations of solar radiation and Coriolis force were accounted for in Exp. CAP1. Exp. CAP2 differed from Exp. CAP1 only in its inclusion of variations in terrain elevation. Exp. CAP2 thus employed a realistic representation of physiography but an idealized representation of the regional-scale atmospheric flow (due to its use of the single-sounding model initialization option).

Exps. CAP3a and CAP3b used the VI option for model initialization so that spatial variations in the synoptic-scale flow pattern were accounted for. These two Exp. CAP3 subexperiments differed only in their choice of initialization fields. Exp. CAP3a used the NMC analysis and upper-air soundings from the morning of the tracer release (Sept. 25, 1983) to construct the RAMS initial fields while Exp. CAP3b used the analysis and soundings from the morning after the tracer release (Sept. 26). Differences between these two subexperiments are thus an indication of the magnitude of time changes in the synoptic-scale flow pattern. Exp. CAP5 was very similar to Exp. CAP3a but employed the time-dependent lateral boundary condition option. Exp. CAP5 thus accounted at least in part for the evolution of the synoptic-scale pattern. Exp. CAP4 was a sensitivity experiment to investigate the influence of mesoscale landscape variability on mesoscale dispersion. It was identical to Exp. CAP5 except that all surface properties other than terrain elevation were assumed to be uniform.

As in the Great Plains simulation suite, there are some natural pairings amongst the experiments listed in Table 6.1. The first pair of experiments, CAP1 and CAP2, isolate the role of terrain slope. The importance of spatial variations in the large-scale flow field can be investigated by comparing Exp. CAP2 with Exp. CAP3. The importance of temporal variations in the large-scale flow field can be investigated by comparing Exp. CAP3a with Exp. CAP3b. Exps. CAP4 and CAP5 isolate the influence of

Table 6.1: Distinguishing characteristics for the suite of CAPTEX numerical experiments.

Exper. Number	Terrain Type	Surface Properties	Type of Initializ.	Initialization Time	Lateral Boundary
CAP1	flat	heterogeneous	HHI	80/09/25/12Z	steady
CAP2	complex	heterogeneous	HHI	80/09/25/12Z	steady
CAP3a	complex	heterogeneous	VI	80/09/25/12Z	steady
CAP3b	complex	heterogeneous	VI	80/09/26/12Z	steady
CAP4	complex	homogeneous	VI	80/09/25/12Z	time-dependent
CAP5	complex	heterogeneous	VI	80/09/25/12Z	time-dependent

mesoscale landscape variability. Finally, Exps. CAP2, CAP3a, and CAP5 form a trio of experiments with identical surface characteristics but increasingly realistic meteorology.

The approach adopted in the rest of this chapter to discuss the results of this complex experimental suite will be to designate Exp. CAP5 as the control experiment. Exp. CAP5 was the most realistic of the six experiments. We will discuss the results of this experiment in detail in the next section. The other suite members will be treated as sensitivity experiments, and their results will be discussed from the point of view of their differences from those of Exp. CAP5 in the last section, which is divided into subsections around the roles of (a) topography, (b) inhomogeneities of land-surface characteristics other than topography, (c) synoptic-scale flow inhomogeneities, and (d) synoptic-scale flow evolution.

6.2 Control Experiment Results: Experiment CAP5

6.2.1 Meteorological simulation

Meteorological model configuration

The Exp. CAP5 RAMS simulation was carried out using a detailed specification of terrain elevation and other land-surface characteristics, including aerodynamic surface

roughness, solar albedo, soil type, land-water fraction, and sea surface temperature. The variable-initialization option was used in this run. RAMS initial fields were produced by the ISAN package based on the NMC Sept. 25, 1983 1200 GMT gridded analyses and upper-air soundings. Later 12-hourly NMC analyses for Sept. 26, 0000 GMT and 1200 GMT, and for Sept. 27, 0000 GMT and 1200 GMT, were used with the Davies time-dependent lateral boundary conditions to account for large-scale flow changes outside of the domain during the simulation period.

The model start time was 0600 LST at the RAMS domain's western boundary. The release site at Dayton, Ohio (84.22°) and the entire CAPTEX sampling network lie within the Eastern time zone although the western boundary of the RAMS domain at 90° is located in the Central time zone. The model start time thus corresponds at least nominally to 0600 CST/0700 CDT, 0700 EST/0800 EDT, and 1200 GMT. Sunrise at Buffalo, New York (78.8°W) occurs at 0705 EDT (1105 GMT) on September 25. The 3-h tracer release began at 1300 EDT, five hours after the start of the RAMS meteorological simulation and less than six hours after sunrise at Dayton.

Meteorological results

Exp. CAP5 predicted isotach and streamline fields after one day and two days of simulation are shown for three heights in Figs. 6.1 and 6.2, respectively. The same format used in Figs. 3.19–3.20 to display the analyzed observed wind fields has also been used in these two figures to allow easy comparison. The RAMS predicted fields show good agreement overall with the observed fields although the forecast does deteriorate with time.

The z^*=24 m predicted winds plotted in Figs. 6.1a–b agree very well overall with the observed winds plotted in Figs. 3.19a–b. The predicted low-level fields do display more horizontal structure, but this is consistent with the finer grid spacing of the RAMS grid as compared to the NMC grid (0.5° × 0.333° vs. 2.5° × 2.5°). Agreement is quite good too for the z^*=1579 m wind field. However, one noticeable difference is the positioning of the col over northern Virginia in the RAMS 24-hour predicted fields (Fig. 6.1d) versus its

analyzed location south of Long Island (Fig. 3.19d). A second difference, and a significant one for the transport of the CAPTEX tracer cloud, is the shift in the position of the trough line at the top of the predicted Sept. 26 1200 GMT z^*=1579 m wind field as compared to the analyzed position. The result is that the analyzed westerly winds over Lake Erie and Lake Ontario were predicted to be west-southwesterly. Comparison of Fig. 3.18d with Fig. 3.19d reveals, however, that the large-scale flow changed considerably over this 24 h period, especially over the Atlantic Ocean. The col mentioned above was not even present in the domain 24 h earlier and the trough line was located some distance beyond the western boundary of the RAMS domain. All in all, the Davies boundary condition performed commendably in communicating changes in the larger-scale flow outside of the model domain to the predicted interior flow. Comparison of the predicted and analyzed z^*=3012 m wind fields (Figs. 6.1e–f and 3.19e–f) supports this conclusion. Agreement is very good with the one exception of the lagging trough line over the Great Lakes.

It is clear from comparing Figs. 3.19 and 3.20 that the observed synoptic pattern continued to evolve on the second day of the simulation, with the northern trough moving eastward across the domain and a high-pressure center drifting in from the southwestern boundary. In addition, what appears to be boundary noise[203] is evident in Fig. 6.2 over the Great Lakes. This feature is an unfortunate development, but its location and timing is such that it probably did not affect the MLPDM simulation of the CAPTEX tracer cloud transport and dispersion adversely. For example, comparison of the predicted 48 h z^*=1579 m and z^*=3012 m streamlines with the analyzed streamline field still indicates good agreement (Figs. 6.2d,f and 3.20d,f).

---

[203] Comparison of the Exp. CAP5 RAMS simulations with those for Exps. CAP3a, CAP3b, and CAP4 suggest that this 'noise' is an artifact of the time-dependent lateral boundary conditions. Flow on the northern lateral boundary strengthens considerably and rotates from southwesterly to northwesterly during the simulation as the synoptic-scale trough crosses the domain. The problem seems to develops after the boundary flow changes from outgoing to incoming.

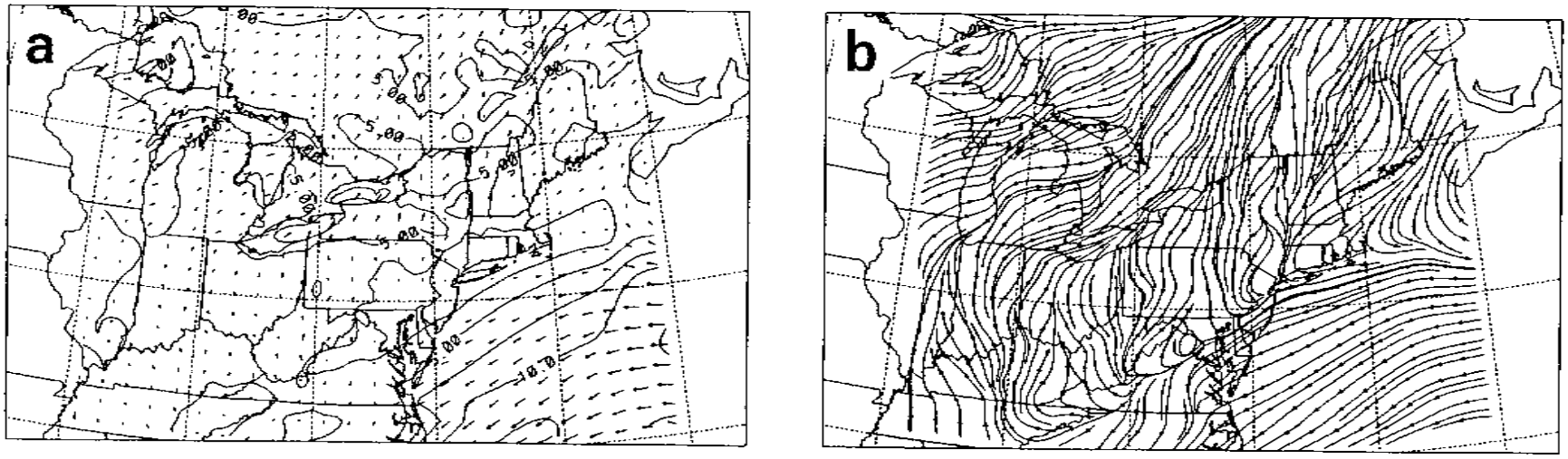

Figure 6.1: Isotach plots overlaid with wind vectors at every second grid point on the CAPTEX-simulation RAMS domain (35–50°N, 90–65°W) as predicted by Exp. CAP7 for Sept. 26, 1983, 1200 GMT at three heights, (a) 24 m AGL, (c) 1579 m AGL, and (e) 3012 m AGL (in z^* coordinates), together with corresponding streamline fields at (b) 24 m AGL, (d) 1579 m AGL, and (f) 3012 m AGL. Otherwise same as Fig. 3.19.

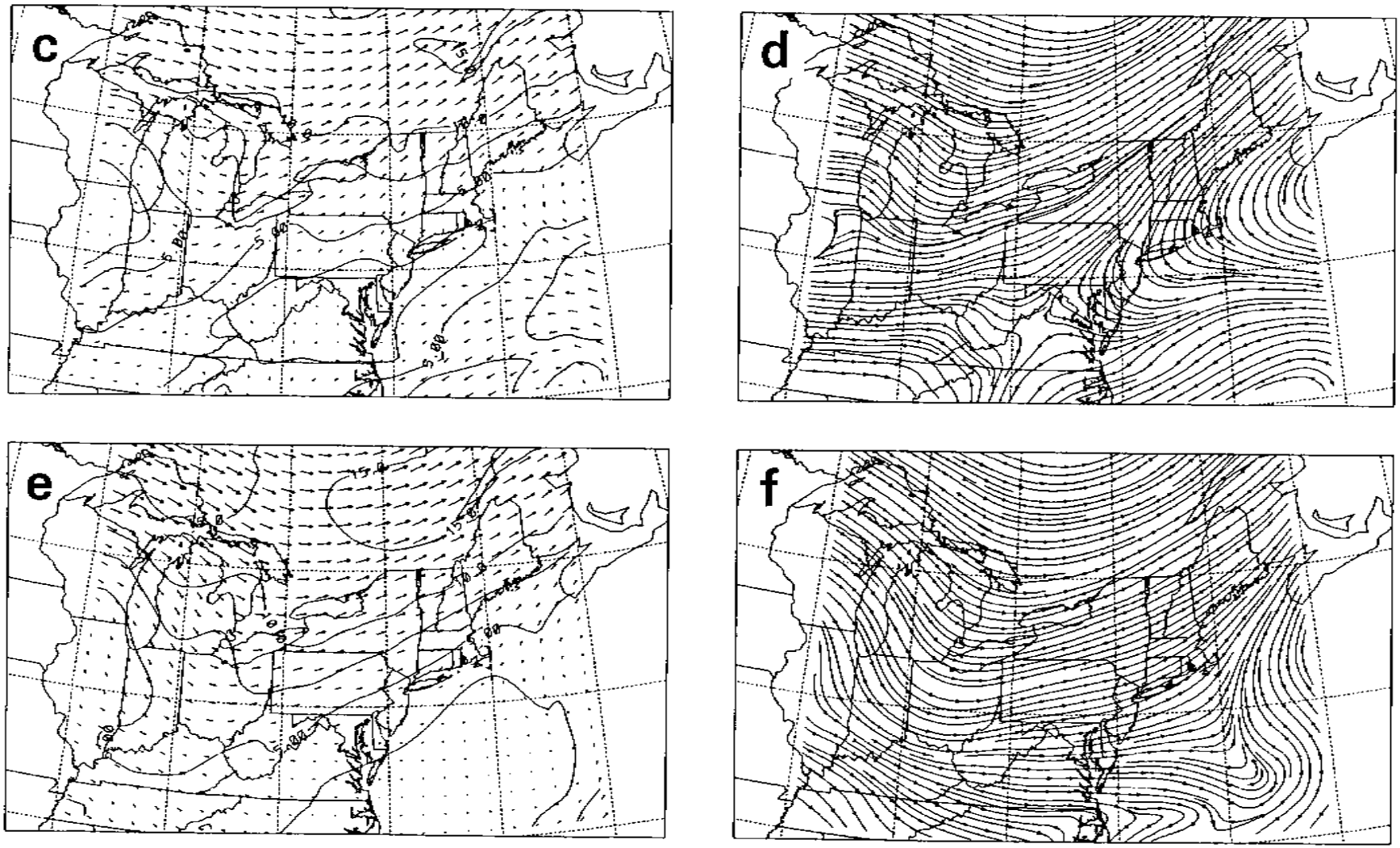

Figure 6.1: (Continued).

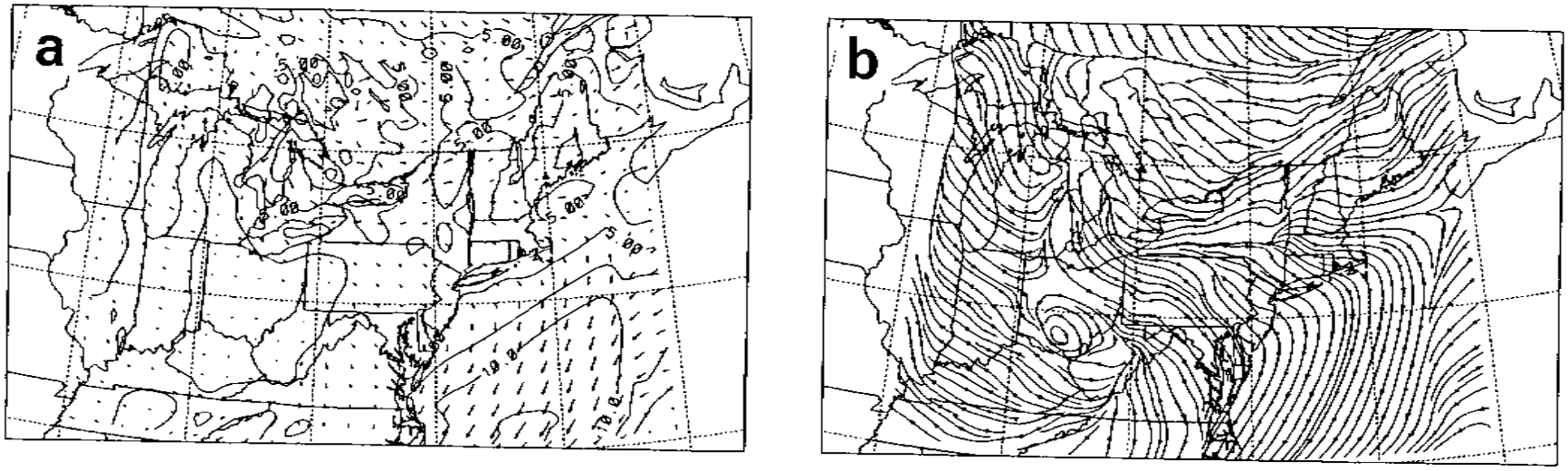

Figure 6.2: Same as Fig. 6.1 except for Sept. 27, 1983, 1200 GMT.

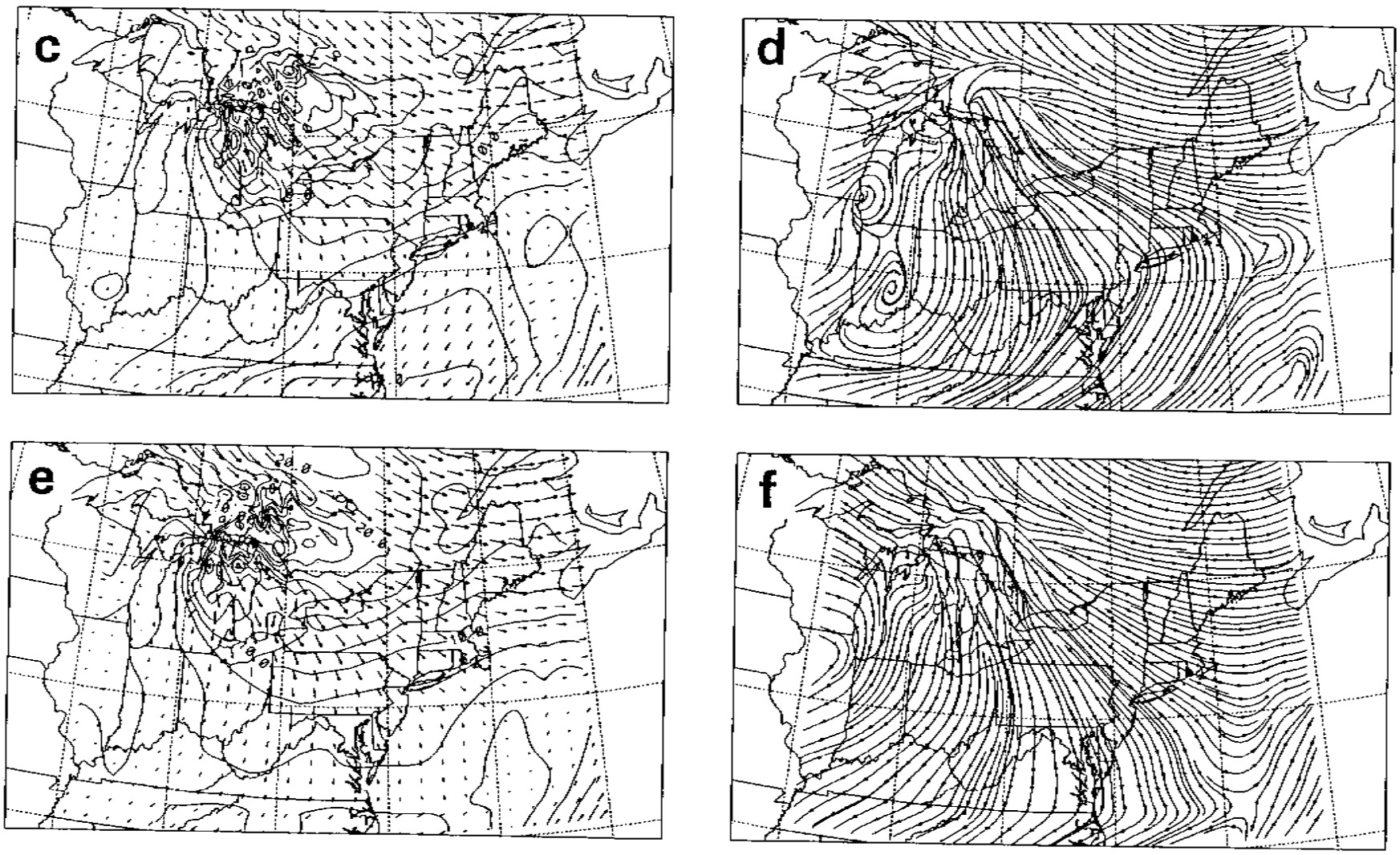

Figure 6.2: (Continued).

6.2.2 Mesoscale tracer transport

MLPDM setup

The first step in modelling mesoscale dispersion for this case was to examine the predicted mesoscale transport. Accordingly, grid-scale trajectories were calculated for Exp. CAP5 following the same approach used for the Great Plains experiments. Five particles stacked in a vertical lattice were released from the point corresponding to Dayton International Airport at 1700 GMT, Sept. 25, 1983, the time of the start of CAPTEX Release 2. Five more were released at 2000 GMT on the same day, the time of the end of the tracer release. All ten particles were followed either until 1200 GMT on Sept. 27 or until they reached the edge of the domain, whichever came first. Note that these trajectories span a shallower layer than the grid-scale trajectories calculated in the Great Plains case study (1718 m vs. 2379 m) because of the shallower mixing depth expected for this autumn case.

Grid-scale trajectories

The 10-hour-increment travel-time isochrons plotted in Fig. 6.3a on the five Exp. CAP5 release-start grid-scale trajectories indicate the significant speed and directional shear present in this simulation within just the first 1700 m. It is also evident from this panel that the predicted speed maximum occurs at mid levels (trajectory 3 was released at 553 m).

Figs. 6.3b–d display three different projections of the ten release-bounding Exp. CAP5 grid-scale trajectories. A good indication of the agreement of the simulated mesoscale transport with the observed transport can be gained by comparing the trajectory plan views shown in Fig. 6.3a with Figs. 3.22, 3.23, and 3.24. The initial transport to the 300-km arc looks very realistic. Peak concentrations were measured at Station 318 (see Table 3.6) and most of the predicted grid-scale trajectories lie between Stations 318 and 320. Further downwind, however, the trajectories seem to lie too far to the north as compared to the concentration observations. Analysis of the predicted GLCs

confirms this centerline rotational error, which was probably associated with the too slow propagation of the northern trough across the domain discussed in the previous section. Note that the time trend evident in the release-start and release-end trajectory pairs is for a clockwise rotation of the trajectories with time. Note too that the two trajectories corresponding to the lowest release level at 50 m (nos. 1 and 6) follow a rough 'zig-zag' path due to the backing of the low-level winds at night during the evening transition and subsequent veering during the morning transition.

The trajectory side views presented in Figs. 6.3c–d provide some additional insights. The greater complexity of the topography in this case as compared to the Great Plains case is suggested by the greater number of upward and downward excursions[204] by various particles as they pass over different terrain features (cf. Fig. 5.36). For example, all of the trajectories sink initially as they approach Lake Erie[205]. Near the end of the period shown, on the other hand, most of the Exp. CAP5 mid-level trajectories are rising, probably as a result of vertical advection in the ascending air ahead of the trough, while at the same time the uppermost trajectories, which lag the mid-level ones, are sinking. Note also that the release-start/release-end trajectory pairs at the five release heights move pretty much in concert in the vertical. The differences which are present are due in part to their horizontal paths passing over different terrain.

6.2.3 Mesoscale tracer dispersion

MLPDM setup

The RAMS predicted meteorological fields for Exp. CAP5 were available on the hour for every hour of RAMS simulation time. A fixed 15 s time step was used in the MLPDM particle dispersion run. Five particles were released at each MLPDM time step from a

---

[204] Note that some trajectories appear to travel *through* elevated terrain in Fig. 6.3c because these particles are close to ground level over the lower terrain north of the line of latitude selected for this west–east projection.

[205] The elevation of Dayton is 298 m while the mean Lake Erie lake-surface elevation is at 174 m.

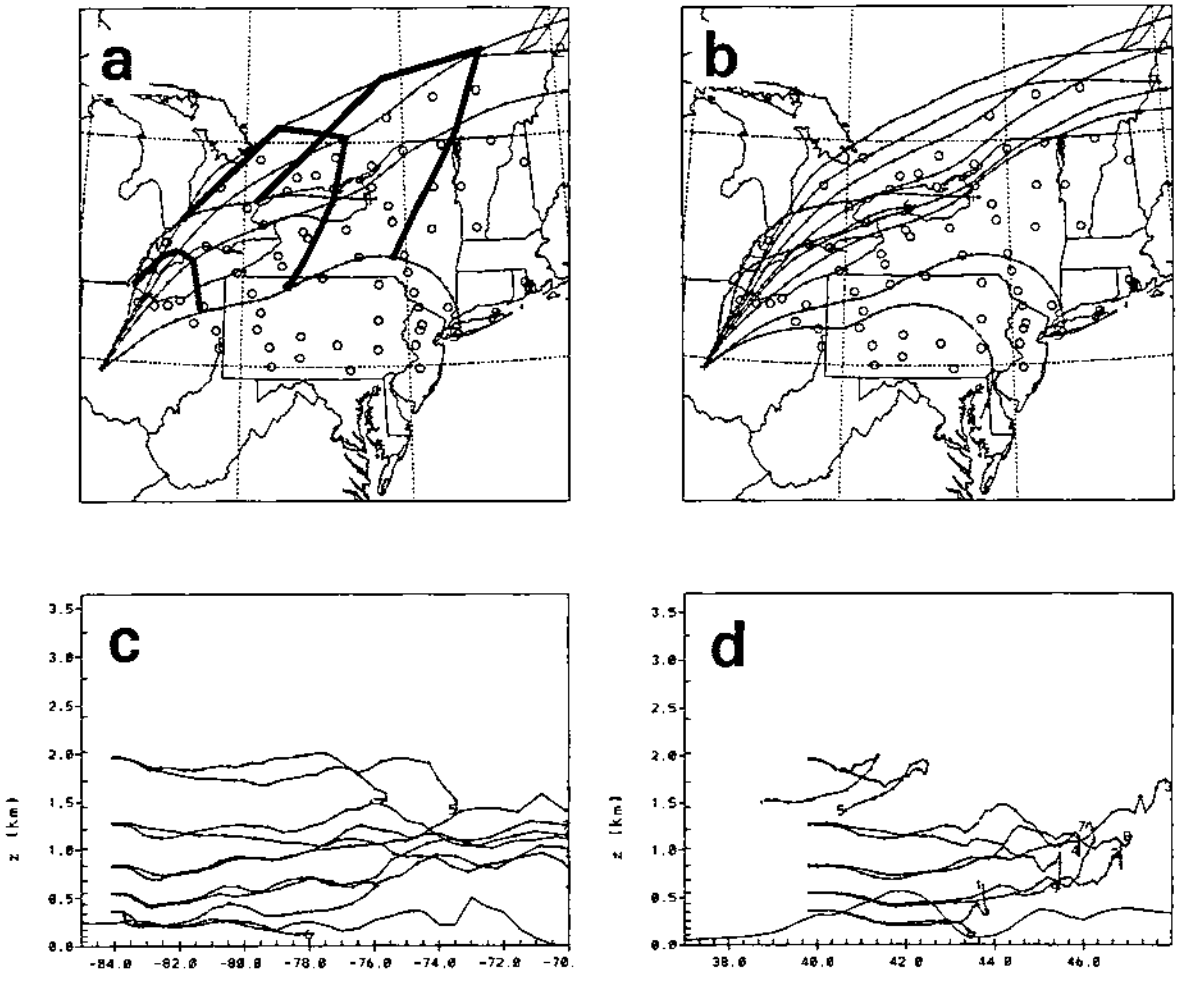

Figure 6.3: Two sets of Exp. CAP5 grid-scale trajectories followed for 40 h at five different heights: (a) XY projection of release-start trajectories with travel-time isochrons marked every ten hours; (b) XY projection, all ten trajectories; (c) XZ projection, view looking north from southern boundary; (d) YZ projection, view looking west from eastern boundary. The small squares mark the hourly trajectory positions. Endpoint labels '1' and '6', '2' and '7', '3' and '8', '4' and '9', and '5' and ':' indicate the five release heights 50 m, 250 m, 553 m, 1015 m, and 1718 m, respectively. The XZ topography slice lies along 43°N while the YZ slice is taken along 77.5°W.

point one meter above the ground at 39.90°N, 84.22°W over a three-hour period from 1705 GMT to 2005 GMT on Sept. 25, 1983. The release began 5.08 h after the start of the RAMS simulation. A total of 3600 particles were released, and each particle was assigned a mass of 55.83 g for a total release of 201 kg of PMCH tracer. The full three-dimensional turbulent diffusion parameterization of the MLPDM, including the drift acceleration correction, was used. Initial particle velocity perturbations were assumed to be zero. Particles were followed either until 1200 GMT on Sept. 27 (i.e., up to travel times of 43 h) or until they reached the edge of the domain, whichever came first. Particle positions were archived after every 15 minutes of MLPDM simulation.

Particle clouds

Figs. 6.4–6.6 show plan views and side views of Exp. CAP5 particle positions every six hours for the first 36 h following the start of the release. The evolution of the modelled particle cloud for this case is somewhat similar to the evolution of the simulated Great Plains cloud (cf. Figs. 5.6–5.8). The particle cloud is initially a well-mixed, block-like structure during the first hours of transport within the daytime PBL. The time of sunset at Buffalo, New York on Sept. 25[206] is 1907 EDT (2307 GMT) so that Fig. 6.4a, which is a 'snapshot' of the particle cloud at 1900 EDT (2300 GMT), corresponds to a time shortly before sunset in central Ohio. The modelled tracer cloud has reached a height of approximately 1500 m AGL by this time and the leading edge of the cloud is located just to the south of the sampler stations at the western end of the 300-km sampling arc. Elevated tracer levels were first measured along this arc during the 2000–2300 EDT (0000–0300 GMT) sampling period (see Fig. 3.21), but the simulated transport is probably too fast since considerably higher concentrations were measured during the next three sampling periods (i.e., 2300–0800 EDT). Note that the tracer release at Dayton ended at 1605 EDT (2005 GMT) so that the leading edge of

[206] Since this experiment took place just after the Northern Hemisphere autumnal equinox, sunrise and sunset occur approximately twelve hours apart.

the particle cloud has travelled for approximately six hours while the trailing edge has travelled just under three hours.

Six hours after the time shown in Fig. 6.4a, vertical directional shear and speed shear have deformed the particle cloud considerably (Fig. 6.4b). The beginnings of the 'horseshoe' shape so pronounced in Figs. 6.4c–d are already discernible at this time (0100 EDT/0500 GMT). By considering Fig. 6.4b in conjunction with Figs. 6.5b and Fig. 6.6b, it is possible to envisage the three-dimensional structure of the cloud. The particles on the leading edge of the cloud at the Ohio–Pennsylvania state line turn out to be the most elevated while the particles on the trailing edge over the western end of Lake Erie and southwestern tip of Ontario are nearest the ground. The northernmost particles in Fig. 6.4b are located at mid-cloud levels. Note that at this time, the simulated cloud has just about completely crossed the 300-km-arc stations. In fact, elevated tracer levels were measured along the 300-km arc for another seven hours (Fig. 3.21).

The time of sunrise at Buffalo, New York on Sept. 26 is 0705 EDT (1105 GMT). Figs. 6.4c, 6.5c, and 6.6c show different views of the Exp. CAP5 particle cloud at 0700 EDT, before the start of daytime vertical mixing. Speed shear has clearly caused alongwind elongation but in a somewhat complicated fashion: the occurrence of a speed maximum or jet at cloud mid-height has produced elongation on one 'leg' of the horseshoe due to positive speed shear and elongation on the second leg due to *negative* speed shear. Figs. 6.4d, 6.5d, and 6.6d, on the other hand, show the particle cloud in the early afternoon (1300 EDT/1700 GMT). Convective mixing has reached to the top of the previous day's residual layer from the by this time. As a result, tracer levels should have increased abruptly south of Lake Ontario as elevated tracer was mixed downwards (e.g., see Fig. 6.9). Note also the dislocation (or 'fracture') on the lower half of the 'horseshoe' at the eastern end of Lake Ontario (Fig. 6.4d). This may have been caused by a delay in the vertical mixdown of elevated particles travelling over the lake as compared to particles travelling just to the south over land.

The particle-cloud plan view at 1900 EDT (2300 GMT) shown in Fig. 6.4e is more diffuse than that in the previous panel, suggesting that lateral turbulent diffusion in the convective boundary layer increased the total lateral dispersion during the daylight hours. Further widening is also evident in Fig. 6.4f but the responsible mechanism for this period was likely vertical shear associated with nighttime low-level stabilization, just as it was 24 h earlier in Figs. 6.4a–b. This figure thus suggests that for cloud dispersion over a long enough period to include two PBL evening transitions, alongwind cloud elongation due to speed shear can be augmented by diurnally-varying directional shear in a three-step process. In the first step, tracer material is transported laterally by low-level backing (upper-level veering) on the first night. The second step consists of vertical redistribution of the tracer by vertical mixing the next day. Finally, in the third step, tracer material returns to the original cloud axis by upper-level veering (low-level backing) on the second night. This sequence thus constitutes a sort of shear-based crosswind secondary circulation with a diurnal period. Fig. 6.6f shows southward transport at the top of the cloud along its southern edge by 0500 GMT on Sept. 27. This is consistent with the northwesterly flow at the 850 and 700 hPa levels over the northeastern U.S. plotted in Fig. 3.20.

Concentration analysis grid

As in Chap. 5, the concentration analysis grid (CAG) used to stimate PMCH surface concentrations from particle positions consisted of a $41 \times 31 \times 40$ mesh. Two different sets of grid sizes were again used, one for the 300-km sampler arc and the second for the full sampler network. CAG horizontal grid increments were set to 0.125° of longitude (about 10.6 km at 40°N) and 0.117° of latitude (about 13.0 km) for the 300-km-arc CAG and to 0.35° of longitude (about 28.7 km at 40°N) and 0.25° of latitude (about 27.8 km) for the whole-domain CAG[207]. CAG vertical grid increments were set

[207] In comparison, the average station spacing was approximately 25.7 km on the 300-km arc and 47.5 km on the 800-km arc.

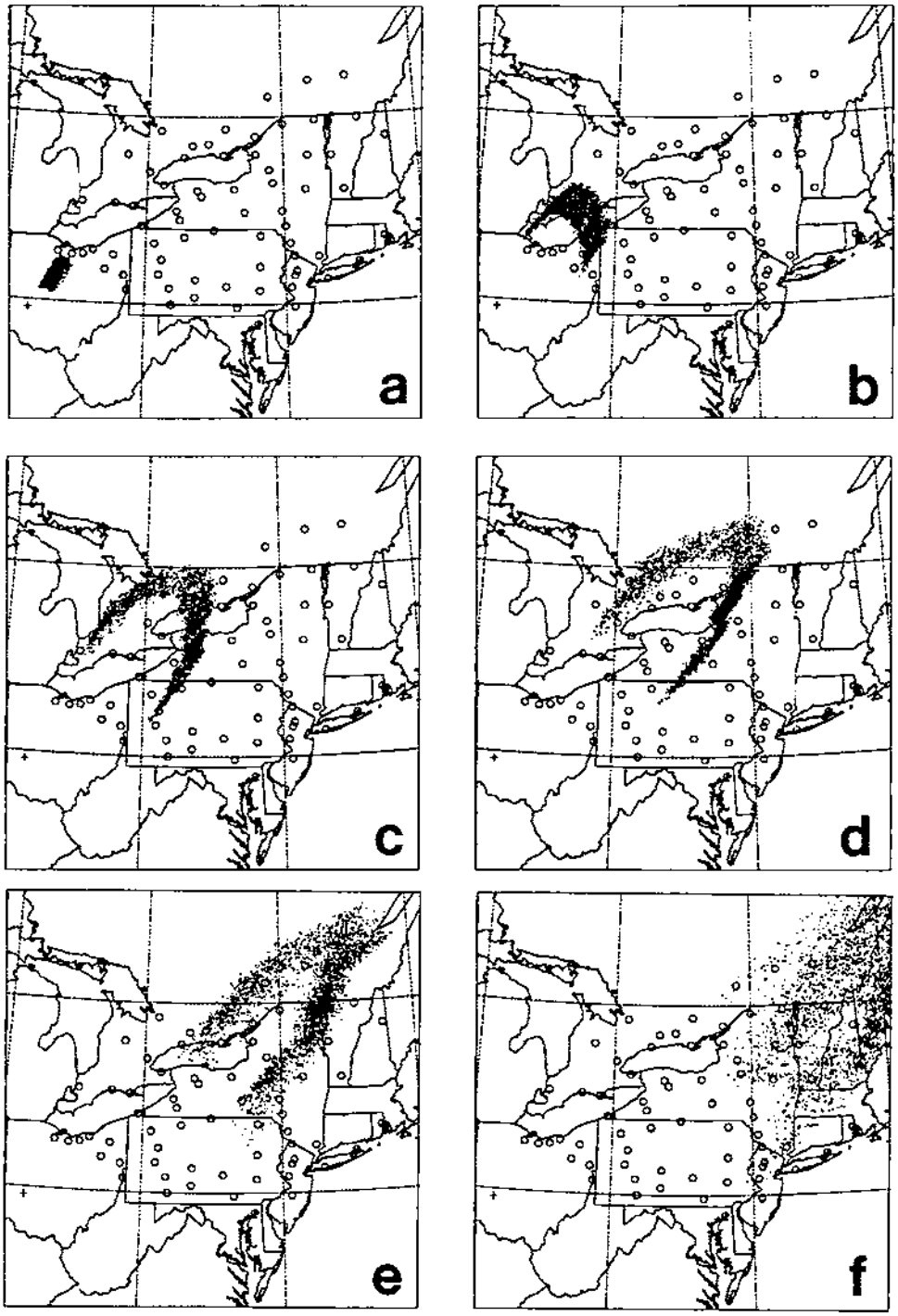

Figure 6.4: Six plan views of particle positions for Exp. CAP5 at six-hour intervals: (a) Sept. 25, 2300 GMT (travel time T=6 h); (b) Sept. 26, 0500 GMT (T=12 h); (c) Sept. 26, 1100 GMT (T=18 h); (d) Sept. 26, 1700 GMT (T=24 h); (e) Sept. 26, 2300 GMT (T=30 h); (f) Sept. 27, 0500 GMT (T=36 h). The release site is indicated by a plus sign. The region shown in each panel stretches from 37–48°N and from 85–70°W; parallels at 40°N and 45°N and meridians at 85°W, 80°W, 75°W, and 70°W are marked by short dashed lines. The map is a Lambert conformal projection with one standard parallel at 42.5°N.

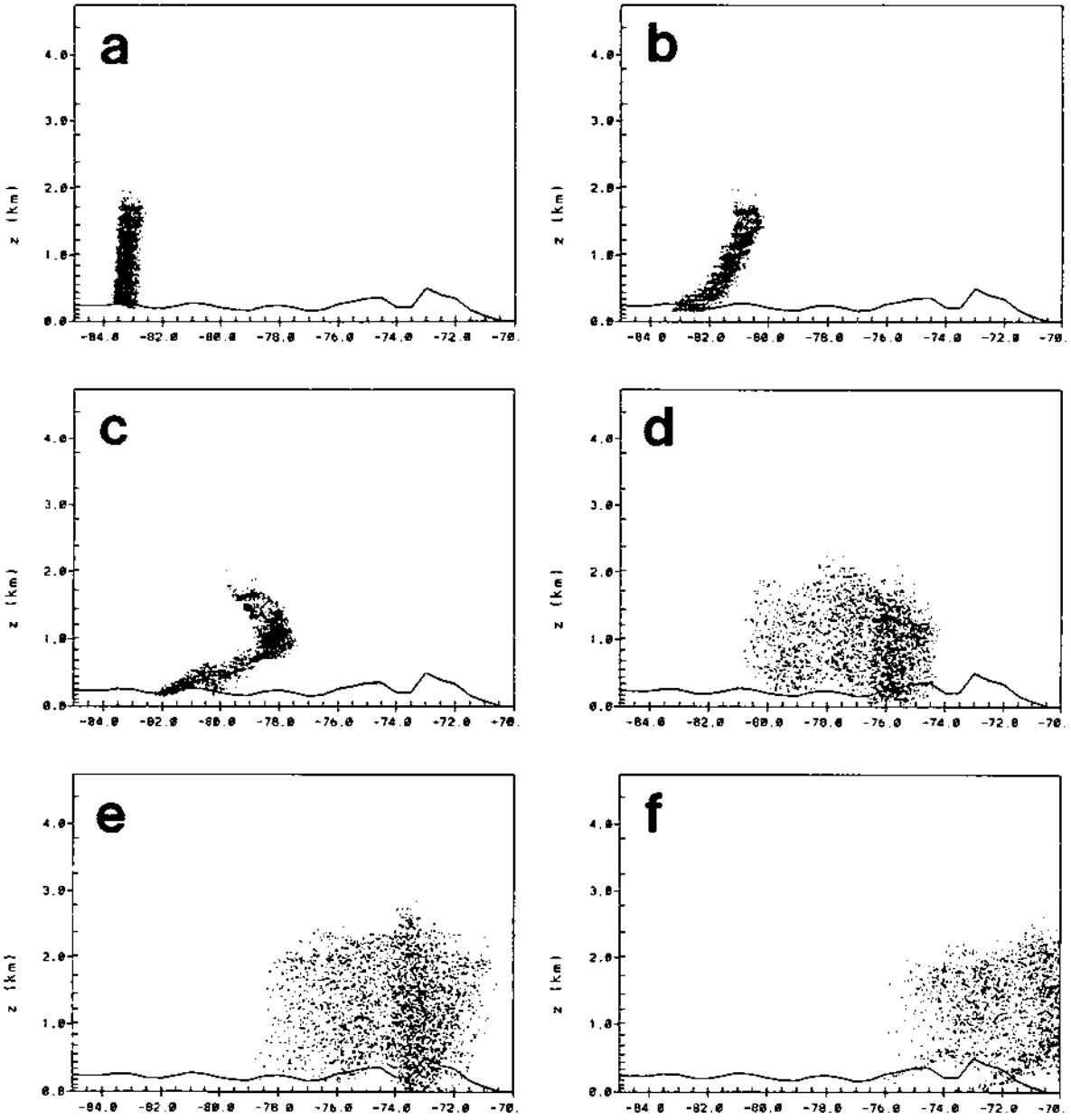

Figure 6.5: Same as Fig. 6.4 except for XZ view. Topography slice corresponds to 43°N.

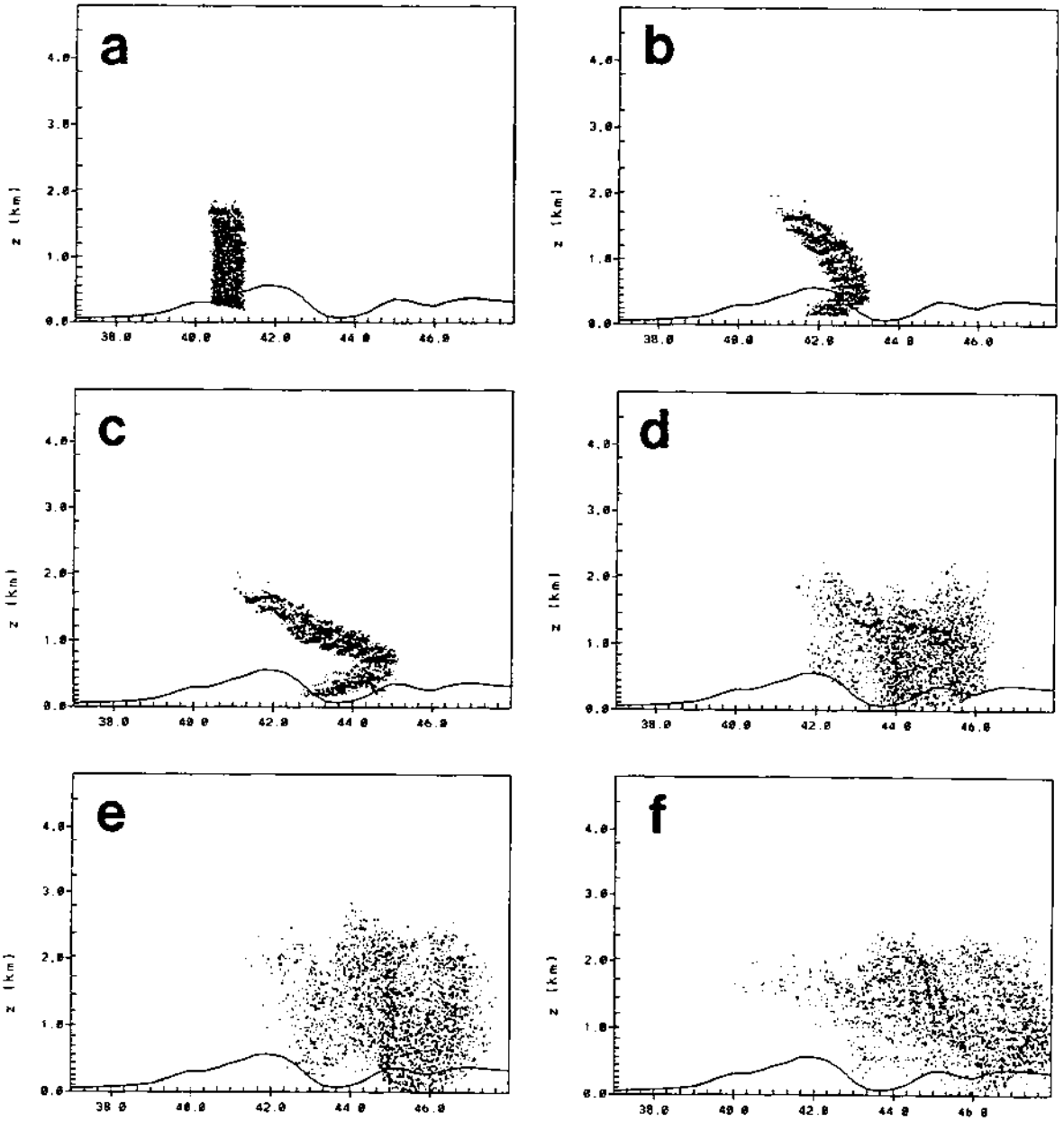

Figure 6.6: Same as Fig. 6.4 except for YZ view. Topography slice corresponds to 77.5°W.

to $0.5\Delta z^*$. A CAG sampling-volume depth of 134 m (6 vertical grid increments) was selected after some experimentation (see below). Plan and side views[208] of these two CAG grids are shown in Fig. 6.7.

For comparison with previous studies, Lee (1987) used a sampling volume of 0.5° longitude by 0.5° latitude by about 800 m depth, Kao and Yamada (1988) used one of 20 km × 20 km × 50 m, and Shi et al. (1990) used one of 22 km × 22 km × 50 m.

The discussion accompanying Fig. 5.10 described the problem of choosing a CAG sampling depth appropriate for both nighttime and daytime GLC estimates. The competing requirements are (i) to select as deep a sampling volume as possible so as to maximize the number of particles considered and minimize sampling fluctuations but (ii) to choose as shallow a sampling volume as possible so that the only particles sampled are ones which might reasonably be expected to influence the ground-level concentration. At night or under other stably stratified situations, elevated tracer material will effectively be decoupled from the surface and will not influence GLCs.

As was done in Fig. 5.10 for Exp. GP1c, ground-level exposures were calculated for the first 24 hours of transport of the Exp. CAP5 particle cloud for a number of different CAG depths to see how sensitive the predicted exposures were to this quantity. Fig. 6.8 shows a plan view of an Exp. CAP5 24-hour *composited* particle cloud based on a sequence of 12 instantaneous plan views at successive two-hour intervals[209]. This figure indicates the maximum possible horizontal extent of the 24-hour ground-level exposure pattern. As already discussed for Figs. 6.4–6.6, however, particles on the southern and northern extremes of this composite cloud were likely to have been located in the middle or top of the cloud and hence were not likely to have influenced surface concentrations under stably stratified conditions.

---

[208] As in Fig. 5.9, the sampling cells were quasi-rectangular, terrain-following boxes. The diagonal lines in these panels are an artifact of the contouring routine used.

[209] The diagonal banded structure evident in this figure corresponds to the 'legs' of the horseshoe-shaped instantaneous clouds later in the period (cf. Figs. 6.4c–d).

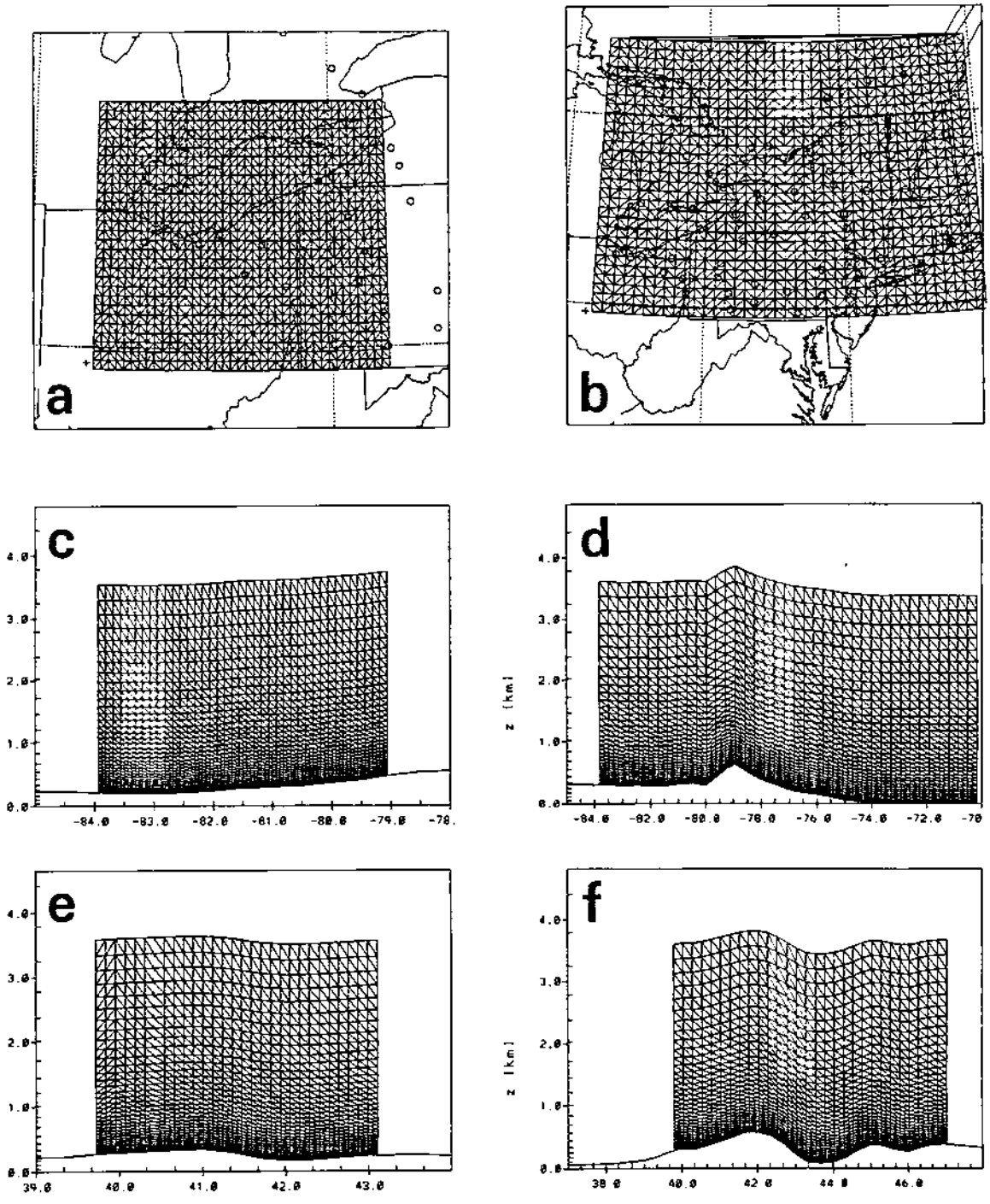

Figure 6.7: Plan and side views of the location and size of the two concentration analysis grids used to estimate surface concentrations for the CAPTEX Release 2 simulations: (a) 300-km-arc domain, XY view, 41×31 mesh; (b) full domain, XY view, 41×31 mesh; (c) 300-km-arc domain, XZ view, 41×36 mesh; (d) full domain, XZ view, 41×36 mesh; (e) 300-km-arc domain, YZ view, 31×36 mesh; (f) full domain, YZ view, 31×36 mesh. XZ topography slices are along 41.3°N and 40°N while the YZ slices lie along 81.5°W and 77.5°W. Other map characteristics are the same as Fig. 6.4.

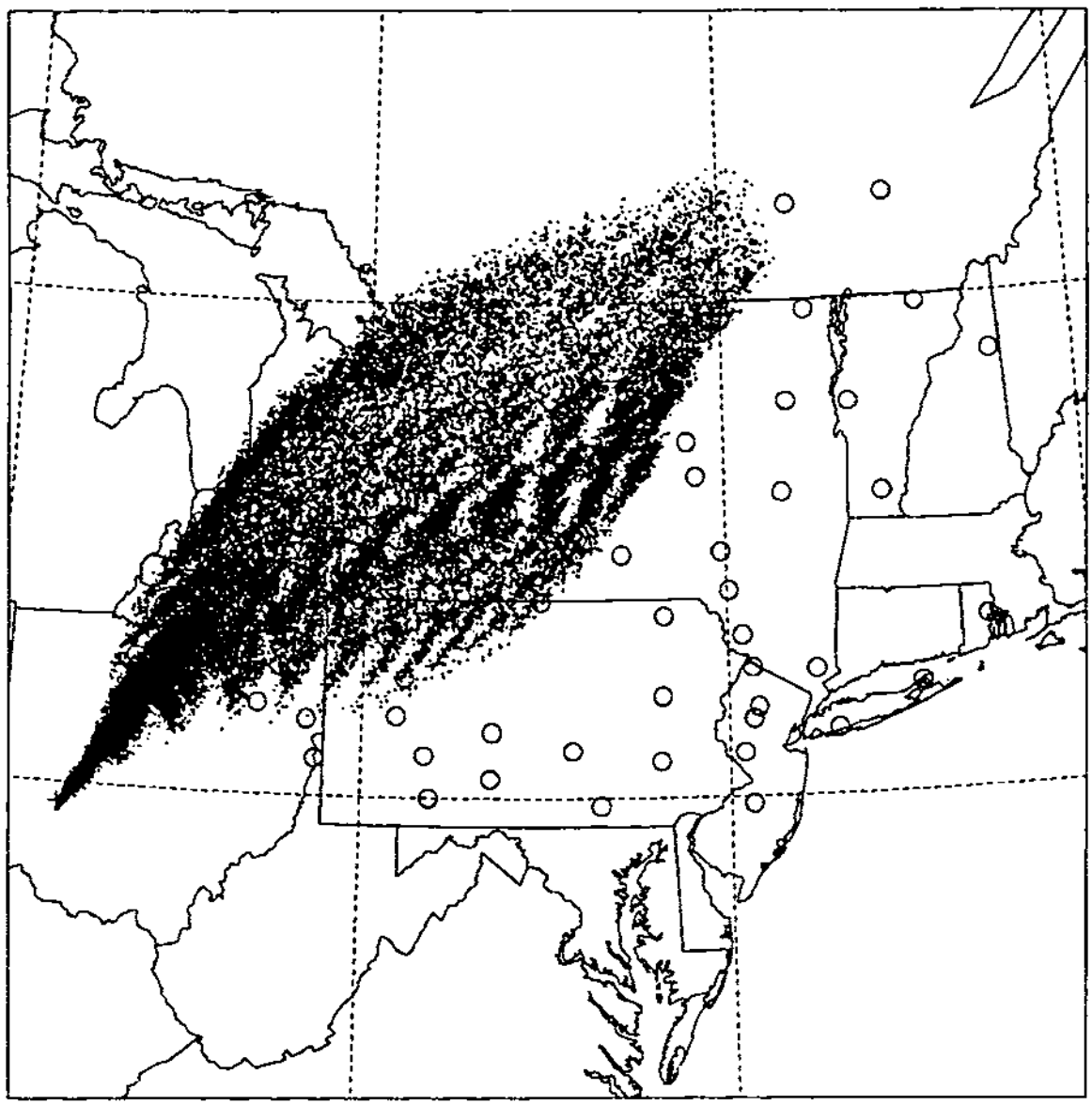

Figure 6.8: Plan view of a composited set of 12 instantaneous particle clouds at two-hour intervals for the first 24 hours of travel. The actual times used were 1900 GMT, 2100 GMT, 2300 GMT, ..., 1300 GMT, 1500 GMT, and 1700 GMT, Sept. 25–26, 1983. Map characteristics are the same as in Fig. 6.4.

This expectation is borne out by Fig. 6.9, which shows the 24-h ground-level exposure patterns obtained using four different CAG depths. As the sampling depth employed increases, the surface exposure footprint increases in size until, for a CAG sampling depth of 1312 m, virtually all particles are sampled (compare Fig. 6.9d with Fig. 6.8). The overall exposure patterns are very similar for the first three sampling depths (134, 378, and 607 m), however, suggesting that the particles contributing to the exposure pattern south of Lake Erie in Fig. 6.9d were located in the upper portion of the particle cloud. This inference is consistent with Figs. 6.6b–c. Note also that the plume 'hook' located over the eastern end of Lake Ontario and upstate New York in Figs. 6.9a–c results from vertical mixdown of elevated plume material after sunrise (cf. Figs. 6.4d and 6.6d). Such a feature is certainly not consistent with a classical Gaussian plume model but does resemble an observed feature in Fig. 3.22b.

Despite the overall similarity between the ground-level-exposure patterns for the first three CAG sampling depths (Fig. 6.9), individual station values varied significantly with the sampling depth used. Table 6.2 lists ground-level exposures[210] calculated at five CAPTEX station locations for the four CAG sampling-volume depths considered. Exposures at three of the stations increase with increasing sampling-volume depth while exposures at the other two stations decrease with increasing sampling-volume depth. Of particular interest is the dependence for Stations 318 and 320. These two stations are adjacent to each other (see Fig. 3.13), but the estimated ground-level exposure at Station 318 increases twelve-fold when the sampling-volume depth is increased from 134 m to 1312 m while the ground-level exposure at Station 320 decreases by roughly a three-fold factor. Which then is the best sampling depth to use? All of the exposure values listed in Table 6.2 are 'correct' in so far as being *layer-average* estimates for layers of different thicknesses, but the wide range of values obtained indicates the importance

---

[210]The value listed in this table for Station 320 for a sampling depth of 134 m differs from the value in Table 6.3 for the same station because the horizontal sample box dimensions used to calculate these two values were different. The first exposure value was calculated on the full-domain CAG while the second exposure was calculated on the smaller 300-km-arc CAG (see Fig. 6.7).

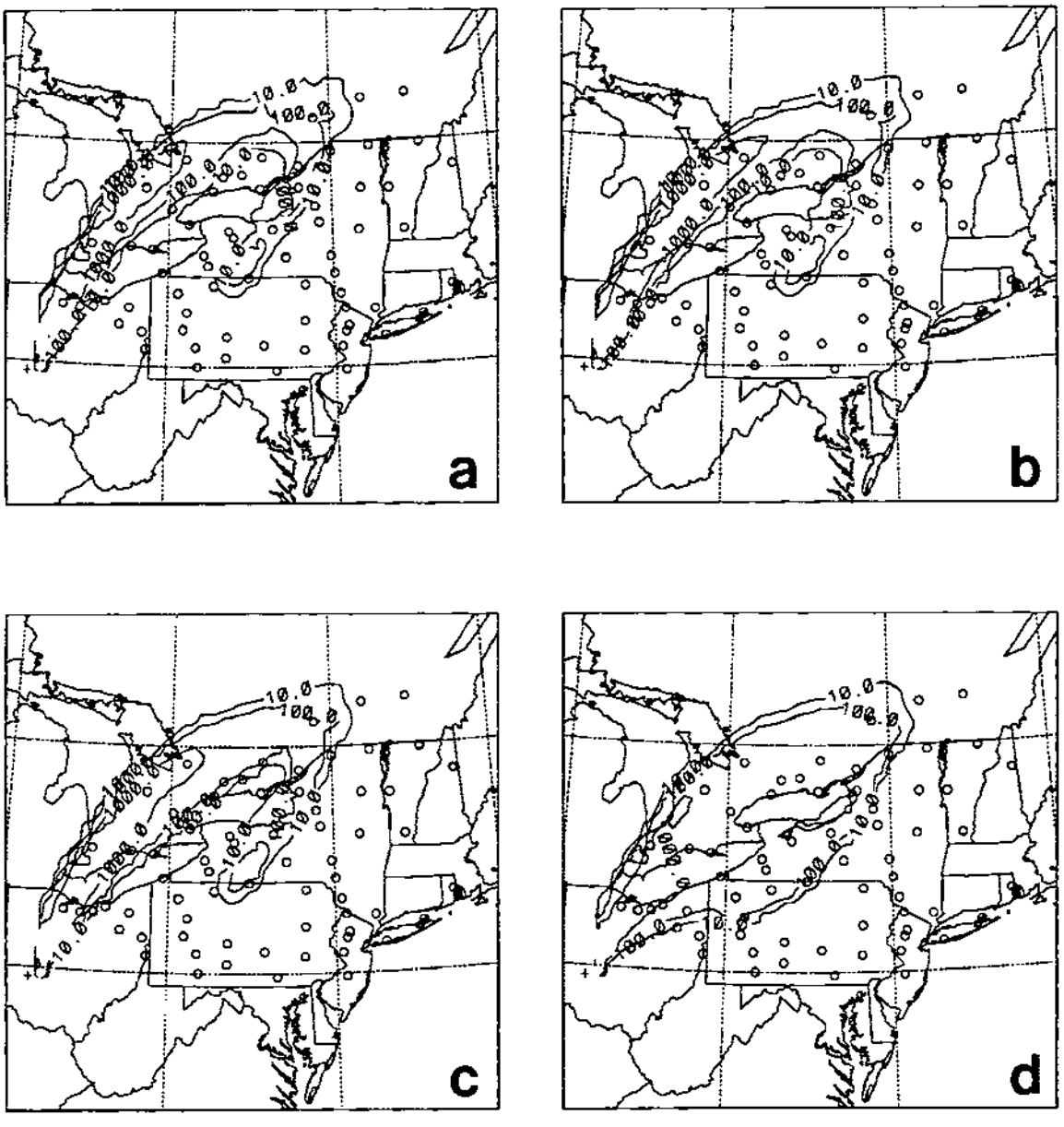

Figure 6.9: Sensitivity of the Exp. CAP5 simulated surface exposure pattern (fl h l^{-1}) for a 24-h period beginning at 1900 GMT, Sept. 25, to the choice of CAG sampling-volume depth: (a) 134 m; (b) 378 m; (c) 607 m; (d) 1312 m. Map characteristics are the same as in Fig. 6.4.

of vertical wind shear and differential advection for this case. Accordingly, the best correspondence of layer-average exposure (concentration) with ground-level exposure (concentration) should be found for the shallowest sampling-volume depth. The CAG sampling-volume depth selected based on the above considerations, 134 m, spans six CAG vertical increments.

Table 6.2: Variation of estimated station 24-h ground-level exposure with sampling-volume depth.

Depth	CAPTEX Station Number				
(m)	318	320	556	710	812
134	267	6496	5200	50	597
378	782	5233	3359	83	699
607	1789	3922	2124	104	730
1312	3189	1921	1000	551	1004

Concentration estimates

Let us now consider the Exp. CAP5 predicted ground-level concentrations. We begin by following the format of the previous chapter and considering concentration values along two arcs of samplers: the 300-km arc and the 800-km arc. We then examine the full two-dimensional surface concentration footprint; this second step was not possible in the Great Plains case because of the limited coverage of the surface sampler network.

300-km arc. The six sampling periods on the CAPTEX 300-km arc were each 3 hours in length[211] and spanned the 18-h period from 1800 GMT (1400 EDT) on Sept. 25, 1983, one hour after the start of the tracer release at Dayton International Airport,

[211] The 300-km arc was a special case. Sampling periods for all of the other eight CAPTEX sampler arcs were 6 hours in length.

to 1200 GMT (0800 EDT) on Sept. 26, 1983, 16 h after the end of the the 3-h tracer release. MLPDM instantaneous particle positions had been archived at 15-minute intervals. Time-average ground-level concentrations were estimated from these MLPDM archives by first calculating instantaneous GLC patterns for twelve consecutive sets of particle positions and then averaging these instantaneous GLC patterns together to produce a three-hour average GLC pattern.

(a) GLC patterns. Fig. 6.10 shows logarithmically-spaced isopleths of PMCH estimated ground-level concentrations for the second through fifth 300-km arc sampling periods for the Exp. CAP5 simulation. The overall qualitative agreement of this figure with the 300-km-arc observations is quite good. According to the observations, no tracer was measured until close to the end of the third 3-hour sampling period and the plume centerline remained over Station 318[212] for all four of the sampling periods during which elevated PMCH levels were measured (Fig. 3.21, Table 3.6). In Fig. 6.10, the leading edge of the simulated surface cloud has just reached Stations 318 and 320 by the end of the second sampling period (panel A) and the cloud has passed the 300-km arc by the fifth sampling period (panel A). Thus, the predicted arrival time for this simulation is too early (7 h vs. 9.25 h) and the transit time is too short (9 h vs. 12 h). The simulated cloud's centerline remains to the west of Station 318 and closer to Station 320[213], but not too far[214] from the observed position.

One interesting prediction of this simulation is the change in low-level transport direction after sunset (2307 GMT at Buffalo, New York). The cloud centerline is oriented roughly southwest–northeast at all four times shown in this figure. After sunset, however, the low-level winds decouple from the winds aloft and back from southwesterly to south-

---

[212] The second most westerly station south of Lake Erie.

[213] The westernmost station on the 300-km arc.

[214] Although the mean centerline position error was 11° (Table 6.5), indicating the station sparsity.

southwesterly as a result of the changed force balance in this near-surface stable layer (cf. Thorpe and Guymer, 1977). This change in low-level wind direction is evident in the movement of the GLC pattern in Figs. 6.10b–d. Note also the weaker horizontal concentration gradient on the leading and trailing edges of the cloud as compared to the sides, suggesting the significant contribution of speed-shear-enhanced alongwind diffusion.

(b) Station values.

Table 6.3 compares 300-km-arc predicted ground-level station exposure and total cross-wind integrated exposure (CWIE) values for the suite of CAPTEX numerical experiments with observed station values for the complete 18-hour sampling period. The situation in the case of Exp. CAP5 is somewhat reminiscent of the Exp. GP1 and GP2 predictions for the Great Plains 100-km sampler arc: that is, the observed plume crossed the 300-km arc at its western end and the simulated plume was located too far to the west so that a significant tracer exposure was predicted at only the westernmost station, Station 320 (see Fig. 6.10). The predicted peak station exposure value and CWIE value are smaller than the observed values by a factor of two or so. This difference is not terribly significant in and of itself, however, given that the predicted tracer cloud was only 'sampled' by two CAPTEX stations. Note that the observed CWIE value had to be corrected for the off-perpendicular angle of the 300-km sampler arc relative to the transport wind, i.e., the obliquity correction. No comparable correction was applied to the Exp. CAP5 predicted CWIE value since it is based effectively on a single value.

The approach used in the Great Plains GLC analysis to address this problem of sparse, incomplete, and/or uneven spatial sampling, namely, the estimation of concentrations along a wide arc of numerous, equally-spaced sites, was used here too. Concentrations were calculated along an arc of 51 equally-spaced sites located 200 km downwind of Dayton at 1° azimuthal increments from 10° to 60°. The corresponding site separation distance along this arc is 3.5 km, much smaller than the mean 300-km-arc station spacing of approximately 25 km. The location and distribution of the equally-spaced sites can be seen in Fig. 6.10. Note that the apparent conflict in comparing observed GLCs along

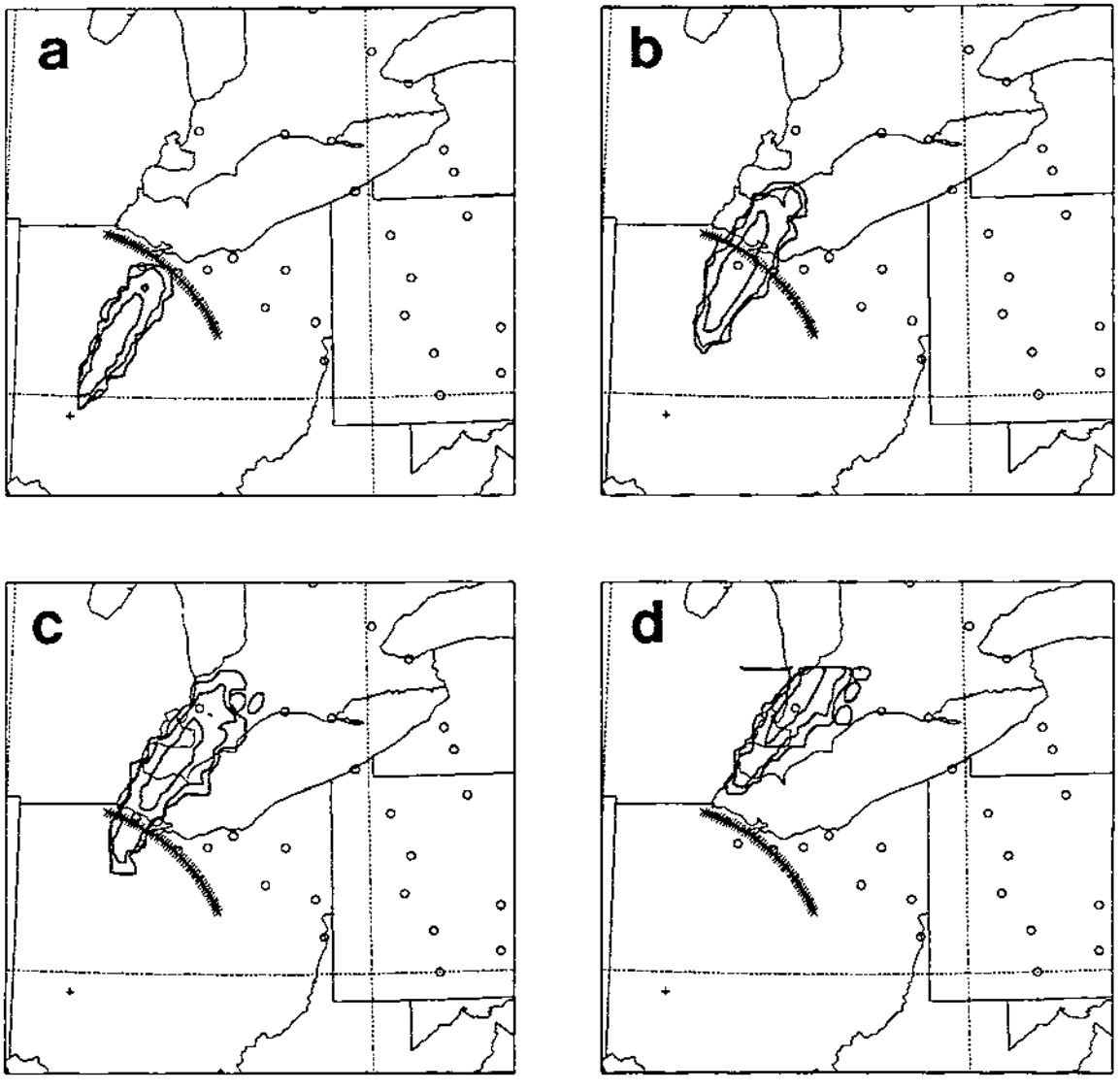

Figure 6.10: Time sequence of plan views of estimated 3-hour-average PMCH surface concentration patterns for the first four 300-km-arc sampling periods (Sept. 25–26) based on particle positions from the Exp. CAP5 MLPDM simulation: (a) 2100–0000 GMT; (b) 0000–0300 GMT; (c) 0300–0600 GMT; (d) 0600–0900 GMT. The 10, 100, and 1000 fl^{-1} concentration isopleths are plotted. Only a portion of the simulation domain is shown: the panel boundaries approximately frame the region from 85–77°W and from 39–44°N. The 40°N parallel and 85°W and 80°W meridians are indicated by short dashed lines. The map projection is a Lambert conformal projection with one standard parallel at 41.5°N. The release site at Dayton is indicated by the plus sign. The locations of active 300-km-, 400-km-, and 500-km-arc samplers are marked by open circles while the fifty-one 200-km 1°-azimuthally-spaced sites are marked by X's.

Table 6.3: Comparison of predicted 300-km-arc station ground-level exposures (fl h l^{-1}) with observed values for the 18-h period from 1800–1200 GMT, Sept. 25–26, 1983. A dash (–) indicates 'no data'. The rightmost vertical column gives crosswind-integrated exposures (CWIE) over Stations 306–320, assuming a mean cross-wind station spacing of 25 km (or 7.1°). Azimuth angles are in degrees (clockwise from north) and great-circle distances from the release site at Dayton are given in kilometers. The western end of the sampler line is oriented obliquely at a 27° angle from the perpendicular to the cloud centerline.

Azimuth	24.5	36.0	42.2	44.9	54.8	59.9	67.9	76.4	82.9	88.1	
Distance	187	203	227	257	296	255	300	298	285	311	
Experiment	**300-km-arc Station Number**										**CWIE**
Number	320	318	316	314	312	310	308	306	304	302	(fl km h l^{-1})
CAP2	1467	0	0	57	0	0	0	0	0	0	38100
CAP3a	5148	0	0	0	0	0	0	0	0	0	128700
CAP3b*	0	11082	5349	6090	0	0	0	0	0	0	563000
CAP4	10395	0	0	0	0	0	0	0	0	0	259900
CAP5	8781	6	0	0	0	0	0	0	0	0	219700
Obs.	288	13650	4770	2469	36	48	0	6	–	–	†473700

* Had nonzero concentrations from 1200–1500 GMT as well

†Equal to 531700 cos 27°

a 300-km arc of sampler stations and predicted GLCs along an idealized 200-km arc of equally-spaced sites arises because of the wide variation in downwind distance of the 300-km samplers (Table 6.3). As discussed in Sec. 3.2.1, the average distance from Dayton of the four 300-km-arc stations that measured significant PMCH levels during CAPTEX Release 2 is 220 km, and Station 318, the sampler station at which the peak GLC and peak exposure were actually measured, is located 203 km from Dayton.

Table 6.4 presents corresponding exposure predictions for the 200-km equally-spaced-arc sites for the suite of CAPTEX numerical experiments. (Only every other predicted exposure value is listed in this table in order to be able to fit it onto a broadside page.) In the case of Exp. CAP5, the predicted exposure plume is considerably narrower than the observed exposure plume: 20° vs. 36°. The predicted peak exposure is less than half the observed value: 5214 vs. 13650 fl h l^{-1}. The predicted peak exposure is also located 11° to the west of the observed[215] peak. These last two differences are probably due in part to the predicted advection of the tracer cloud at an oblique angle to its longitudinal centerline after sunset. Coincidentally, the CWIE value calculated from the 11 equally-spaced site exposure values for Exp. CAP5 is very close to the value estimated in Table 6.3 from only two point values.

Fig. 6.11R shows Exp. CAP5 predicted GLC values for the 200-km equally-spaced arc plotted site by site against azimuth angle together with observed 300-km arc station GLC values. Fig. 6.12R presents some of the same data in a complementary way, plotted against travel time (the predicted values have been peak-matched by shifting them eastward 11° before plotting this figure). Note that all of the 300-km-arc stations reporting non-zero concentrations above the 3 fl l^{-1} threshold are shown in Fig. 6.12R. Many of the features mentioned in the discussion of Fig. 6.10 are supported by these two figures, including the too early arrival time, too short transit time, and the centerline offset error. Predicted concentration levels, on the other hand, are of the correct magnitude,

---

[215] Of course, it is unlikely that the true peak value occurred at Station 318 so the true centerline error might be smaller or greater than 11°.

Table 6.4: Comparison of predicted ground-level exposures (fl h l^{-1}) along the 200-km equally-spaced-site arc (2° azimuthal spacing; every second site) with the observed 300-km-arc station exposures for the 18-h period from 1800–1200 GMT, Sept. 25–26, 1983. All of the exposure values on each horizontal line have been left-justified beginning with the westernmost site with a non-zero value. The column labelled 'Left-Edge Azimuth' gives the azimuth angle (° from the north) relative to the source of that westernmost site. The relative azimuths give clockwise rotations of the arc sites relative to the left-edge azimuth. A dash (–) indicates 'no data'. The rightmost vertical column gives crosswind-integrated exposures (CWIE) over the equally-spaced-site arc; the mean cross-wind site spacing is 7 km. Actual downwind distances for the nominal 300-km-arc stations ('Obs.' horizontal data line) range from 187 to 311 km; see Table 6.3 for these distances.

Exp. No.	Left-Edge Azim.	200-km-arc Relative Azimuth																			CWIE (fl km h l^{-1})
		0	2	4	6	8	10	12	14	16	18	20	22	24	26	28	30	32	34	36	
CAP2	7	21	294	1011	1803	2100	2373	1944	1701	1791	1809	1104	180	117	210	90	0	0	0	0	115800
CAP3a	15	195	2445	9432	13128	6984	2640	960	180	0	0	0	0	0	0	0	0	0	0	0	251700
CAP3b	29	39	852	6144	12096	10389	5067	2994	4185	6195	5760	2850	747	219	3	0	0	0	0	0	402800
CAP4	12	33	171	81	1755	5391	7293	9342	9732	6930	3951	1509	144	0	0	0	0	0	0	0	324300
CAP5	15	657	2478	3537	4119	4485	5214	4623	3291	1590	651	96	0	0	0	0	0	0	0	0	215200
Obs.	24	288	–	–	–	–	–	13650	–	–	4770	2469	–	–	–	–	36	–	–	48	†473700

†From Table 6.3.

and Fig. 6.12R suggests that the predicted cloud core width is of the right size although the lateral 'wings' are too narrow. The westward movement of the predicted GLC peak with time due to the backing of the low-level winds after sunset is apparent in Fig. 6.11R. So too is the quite sparse station spacing on the 300-km arc.

(c) Quantitative pattern characteristics.

Table 6.5 compares some of the quantitative cloud characteristics estimated from (i) observed concentration measurements made along the 300-km sampler arc and from (ii) predicted concentrations along the 200-km equally-spaced arc for the various CAPTEX numerical experiments. As mentioned above, the Exp. CAP5 tracer cloud crossed the sampler arc more quickly than did the observed cloud, was narrower (especially for the 3 fl l^{-1} edge criterion), had a slightly higher peak concentration value but significantly lower CWIE value, and was located west of the observed tracer cloud. The predicted time of the peak station concentration was also two sampling periods early.

(d) Scattergrams. Figs. 6.13c–d show the 300-km-arc unmatched and matched-peak scattergrams for Exp. CAP5. Relatively few observed concentrations were available for constructing this diagram (i.e., six stations $\times$ six sampling periods). The two non-zero concentration pairs plotted in Fig. 6.13c are apparent in Fig. 6.12R and correspond to the 0000–0300 GMT sampling period. It has been mentioned already that a large number of zero–nonzero pairs on only one axis is an indication that one of the clouds is considerably narrower than the other. In this case, 'narrower' refers partly to temporal extent as well as to spatial extent. That is, the predicted cloud's transit time across the sampler arc was shorter and earlier than the observed cloud's transit time, resulting in many concentration pairs in which the predicted cloud station concentration was zero while the observed cloud station concentration was greater than zero.

This generalization can be extended to peak-matching. That is, the *time* of the peak concentration can be matched as well as the spatial location. This was done in constructing Fig. 6.13d. The predicted concentrations were both shifted eastward and

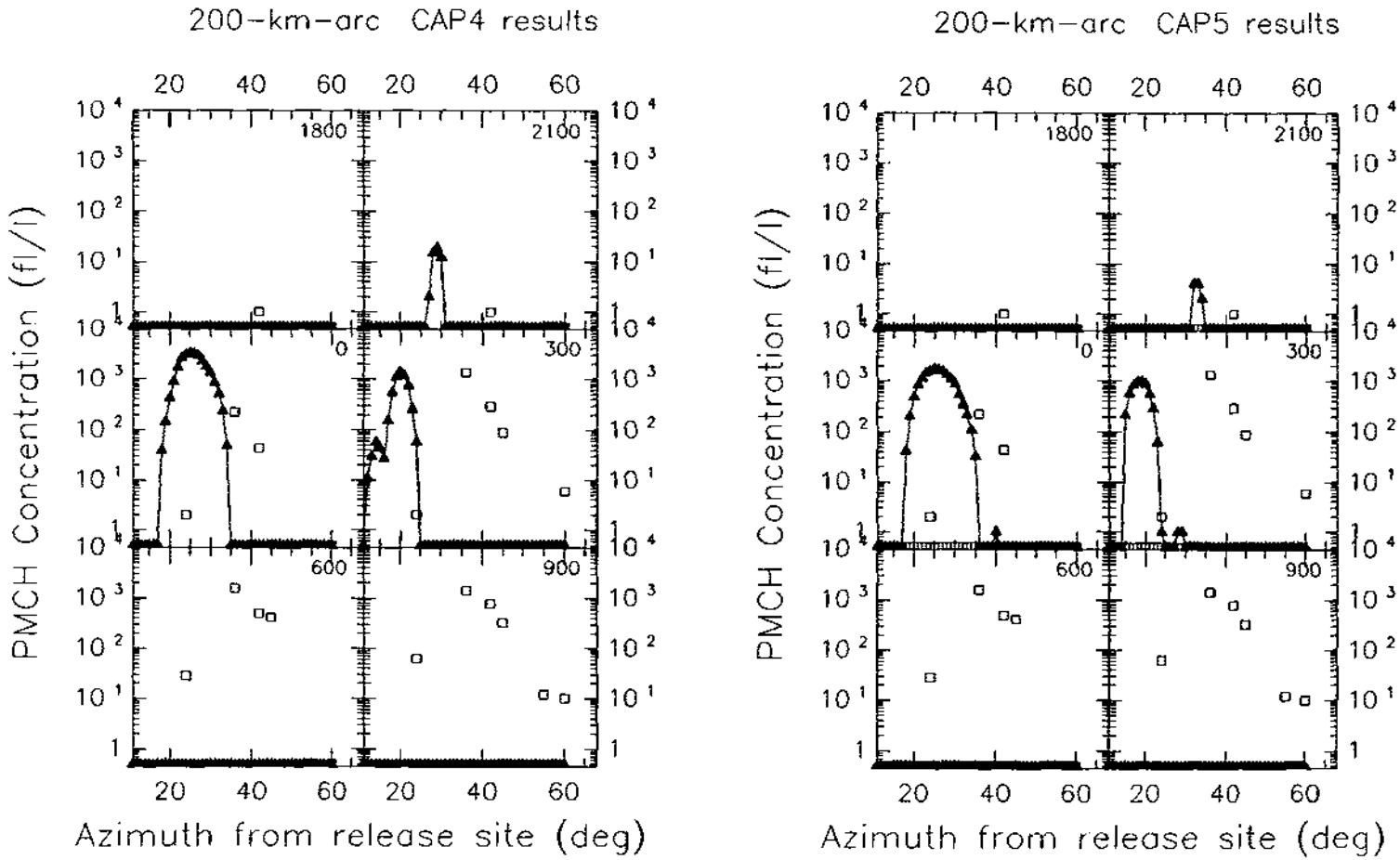

Figure 6.11: Observed and Exps. CAP4 (lefthand side: 'L') and CAP5 (righthand side: 'R') predicted PMCH concentration–azimuth plots for the 300-km sampling arc for all six 3-hour sampling periods (Sept. 25–26): (a) 1800–2100 GMT; (b) 2100–0000 GMT; (c) 0000–0300 GMT; (d) 0300–0600 GMT; (e) 0600–0900 GMT; and (f) 0900–1200 GMT. Observed values are indicated by open squares; predicted 200-km equally-spaced-site values are indicated by filled triangles connected by a solid line. The starting time of each sampling period (GMT) is plotted in the upper righthand corner of each panel.

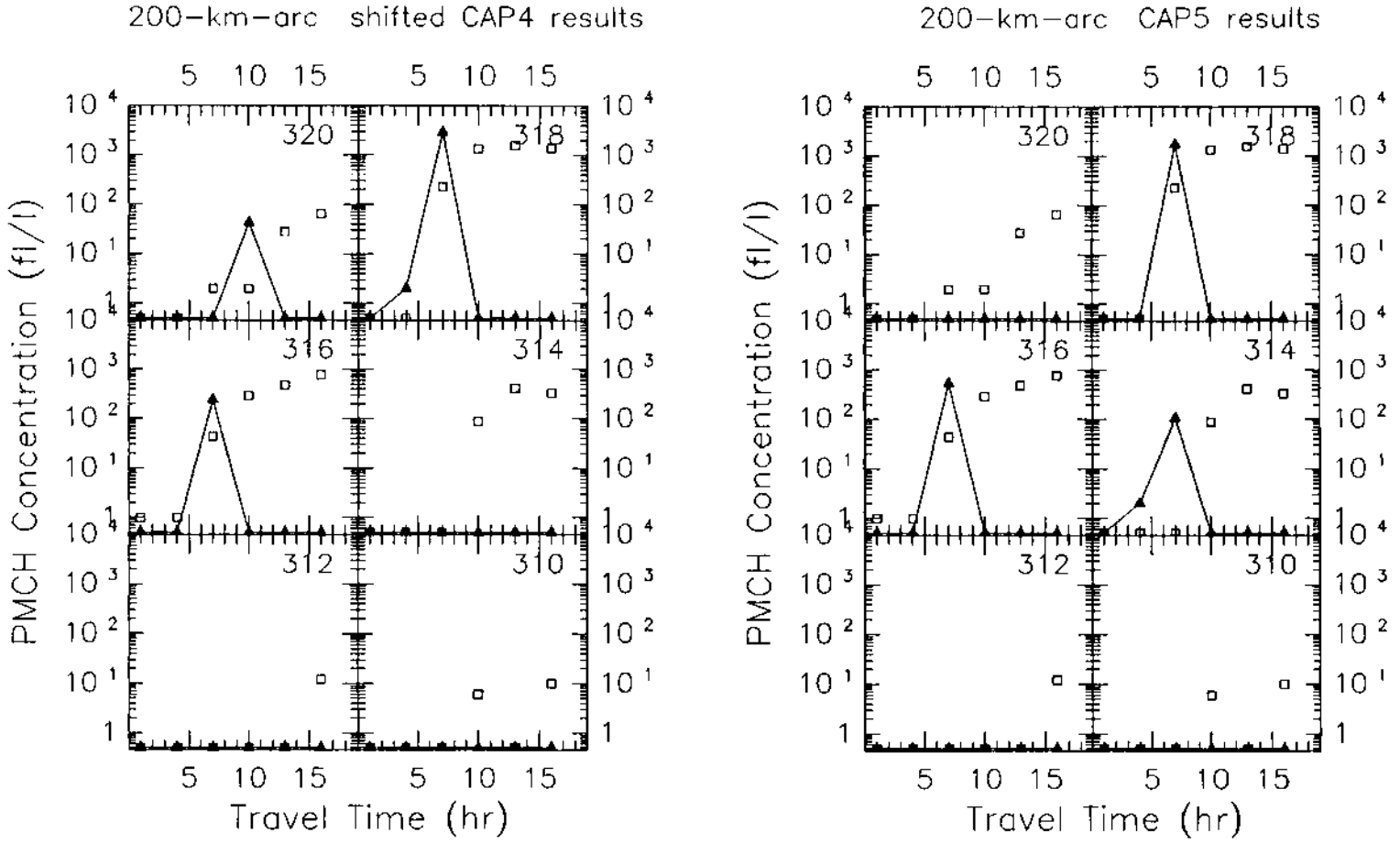

Figure 6.12: Observed and Exp. CAP4 (lefthand side: 'L') and CAP5 (righthand side: 'R') predicted PMCH concentration–time plots for six 300-km-arc sampling stations: (a) Station 310; (b) Station 312; (c) Station 314; (d) Station 316; (e) Station 318; and (f) Station 320. Observed values for Stations 310–320 are indicated by open squares; predicted 200-km equally-spaced-site values are indicated by filled triangles connected by a solid line. The station number is plotted in the upper righthand corner of each panel. The time period shown extends from Sept. 25 at 1700 GMT until Sept. 26 at 1200 GMT and includes all six 3-hour sampling periods. The Exp. CAP4 site values have been shifted eastward 9° and the Exp. CAP5 site values have been shifted eastward 11° in constructing this figure.

Table 6.5: Tracer-cloud characteristics estimated from CAPTEX Release 2 numerical experiments — 200 km equally-spaced-site arc. Cloud arrival time, transit time, and maximum width all depend on the criterion used to determine the cloud edges. 0000 GMT corresponds to Sept. 26, 1983. Azimuth range and arc length have units of degrees and kilometers, respectively, and have been determined from the equally-spaced-site predicted concentrations. Mean center-line azimuth values correspond to stations with maximum exposures in Table 6.4. Some 'Observed' data-line values are based on values given in Fig. 3.21 and Table 3.6.

Exp. No.	Arrival Time (GMT)	Transit Time (h)	Maximum Width			Max. Conc. ($fl\,l^{-1}$)	Time of Max'm (GMT)	CWIE ($fl\ km\ h\ l^{-1}$) ($\times 10^{-3}$)	Mean CL Azimuth (°)
			St'n Range	Azim. Range	Arc Length				
10%-of-peak threshold									
CAP2	0600–0900	9	314–320	19	67	622	0900–1200	116	17
CAP3a	0000–0300	6	320	9	32	2447	0000–0300	252	21
CAP3b	0300–0600	9	314–318	11	38	3127	0600–0900	403	35
CAP4	0000–0300	6	320	13	46	3329	0000–0300	324	27
CAP5	0000–0300	6	320	15	53	1738	0000–0300	215	25
Obs'd	0000–0300	12†	314–318	20	70	1575	0600–0900	493	36
3 $fl\,l^{-1}$ threshold									
CAP2	0600–0900	9	314–320	28	98	622	0900–1200	116	17
CAP3a	0000–0300	9	320	16	56	2447	0000–0300	252	21
CAP3b	0300–0600	9	314–318	21	74	3127	0600–0900	403	35
CAP4	2100–0000	9	320	17	59	3329	0000–0300	324	27
CAP5	2100–0000	9	320	18	63	1738	0000–0300	215	25
Obs'd	0000–0300	12†	310–320	40	140	1575	0600–0900	493	36

†Or longer. Significant PMCH levels were reported on the last sampling period.

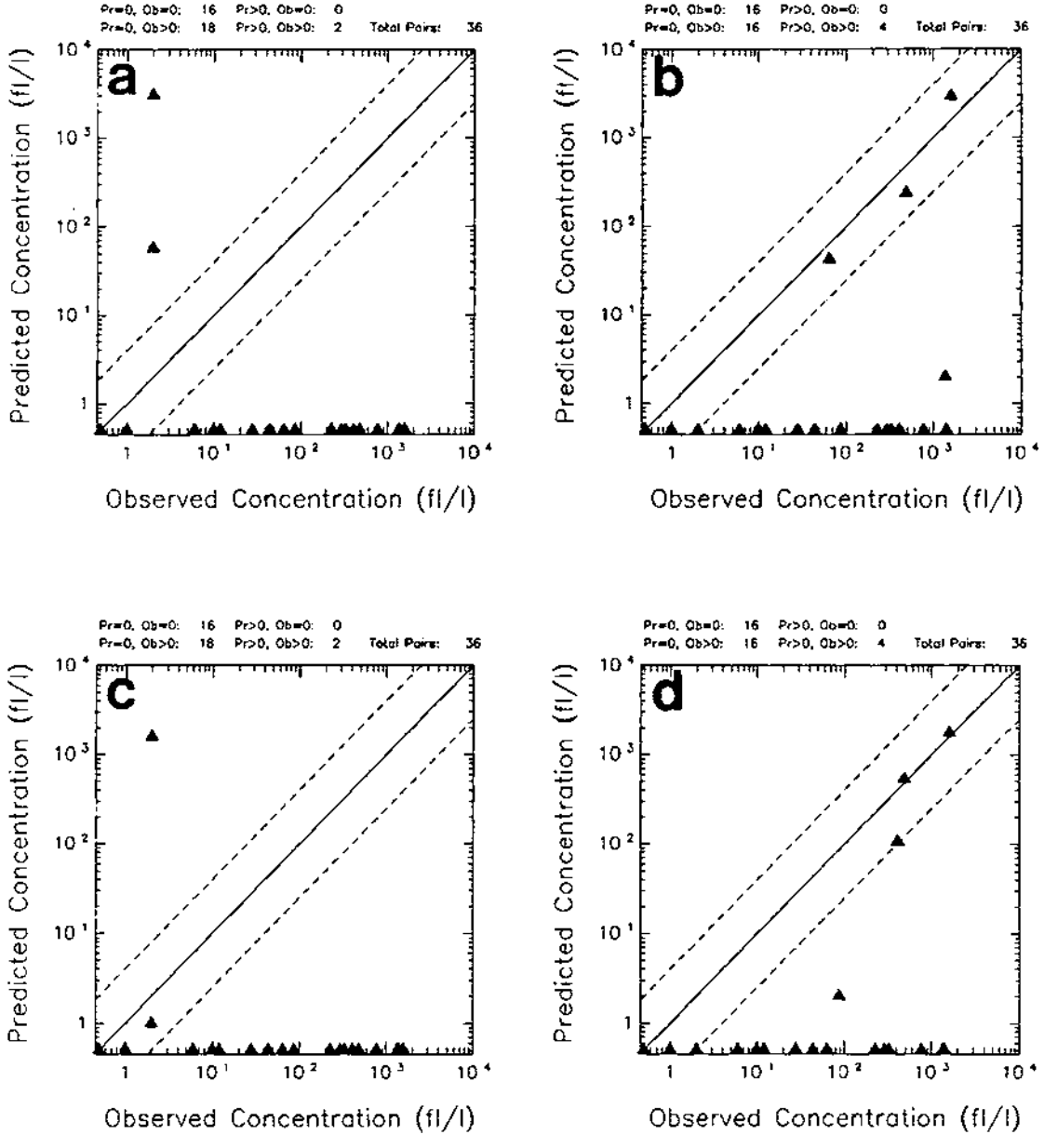

Figure 6.13: Scattergram for observed 300-km-arc PMCH concentrations vs. Exp. CAP4 and Exp. CAP5 200-km equally-spaced-arc computed concentrations. Plotted pairs have been drawn from the set of concentrations for Stations 310–320 and all six 3-hour observing periods from 1800–1200 GMT, Sept. 25–26. The diagonal lines are the one-to-one correspondence line and two factor-of-4 (i.e., 1:4 and 4:1) lines. The Exp. CAP4 site values have been shifted eastward 9° in space and ahead two sampling periods in time; the Exp. CAP5 site values have been shifted eastward 11° in space and ahead two sampling periods in time in constructing this figure.

advanced in time to correspond to a later sampling period. Peak matching only resulted in a slight improvement in this case. The reasons for this are the sparseness of the sampling stations coupled with the too short transit time predicted by the Exp. CAP5 simulation.

800-km arc. The six primary sampling periods on the CAPTEX 800-km sampler arc, Periods[216] III–VIII, were each 6 h in length. They spanned the 36-h period from 0900 GMT (0500 EDT) on Sept. 26, 1983, 16 hours after the start of the tracer release at Dayton International Airport, to 2100 GMT (1700 EDT) on Sept. 27, 1983, 49 hours after the end of the the 3-h tracer release. Six-hour-average GLCs were estimated from the particle positions stored in the MLPDM archives by first calculating instantaneous GLC patterns from 24 consecutive sets of particle positions and then averaging these instantaneous GLC patterns together to produce a six-hour-average GLC pattern.

(a) GLC patterns. Fig. 6.14 shows logarithmically-spaced isopleths of estimated PMCH ground-level concentrations for the second through fifth CAPTEX six-hour sampling periods for the Exp. CAP5 simulation. This figure can be compared directly against the observed GLC patterns for the same periods that were plotted in Figs. 3.22a–d. Both similarities and differences are evident. The overall shape of the predicted and observed surface footprints are similar for Periods II (0300–0900 GMT: 'a' panels) and III (0900–1500 GMT: 'b' panels), although the predicted pattern continues to suffer from the counterclockwise rotational error seen for the 300-km arc. The small closed contour over southeastern Lake Ontario in Fig. 6.14b suggests the development of the southern leg on the cloud leading edge evident in Fig. 3.22b. This southward expansion continues during Period IV (1500–2100 GMT) as shown in Figs. 6.14c and 3.22c. The agreement between predicted and observed cloud shape is less good for Periods IV and V (2100–0300 GMT), however: the predicted cloud resembles a horseshoe while the observed cloud might better

---

[216] Fig. 3.21 shows the division of the full 69-hour CAPTEX sampling period for Release 2 into 11 six-hour periods. These periods will be denoted by Roman numerals and referred to as Period I, Period II, Period III, etc., in the rest of this chapter.

be described as 'amoeboid'. This difference in shape is also consistent with a difference between the predicted and observed station values which will be discussed shortly; namely, that the predicted cloud transit time across the 800-km arc is considerably shorter than the observed transit time. Such a difference would be expected if the longitudinal extent of the simulated cloud were too short. The predicted cloud also appears to outrun the observed cloud. This aspect is considered further in Fig. 6.18.

The first 14 h of the 18 h period spanned by Figs. 6.14a–c also coincide with the last 14 h of the 24-h period used to calculate ground-level exposure in Fig. 6.7a. It is straightforward to see how the sum of the first three panels resemble the latter panel. Another feature of interest pictured in Fig. 6.14 is the veering of the surface concentration maximum with time. In Figs. 6.14a–b the maximum is located to the north of Lake Erie while in Figs. 6.14c–d the surface maximum has migrated to the south shore of the St. Lawrence River. The backing of the low-level wind at night and resulting transport at an angle to the cloud centerline was remarked upon in the discussion of Fig. 6.10. Similarly, transport at an angle to the cloud centerline can occur if the synoptic-scale wind direction shifts. This was the case during this release as the 850 hPa wind direction over the lower Great Lakes veered from southwesterly to westerly to northwesterly over a two-day period (Figs. 3.18–3.19). One result is that the southern 'leg' of the horseshoe-shaped cloud in Fig. 6.14c passes over more and more southerly stations on the 800-km-arc as the cloud is carried eastward. Such a southward shift in the measured peak concentrations can in fact be seen in Table 3.5.

(b) Station values. Measurements were made along the 800-km arc beginning with sampling Period III (0900-1500 GMT) but significant tracer levels were not detected until Period IV (Table 3.5). This is consistent with the predicted cloud positions plotted in Fig. 6.14. In panel 'b', the cloud's leading edge just touches the (northern extension of the) 800-km sampler arc while in panels 'c' and 'd' the cloud straddles this arc.

Fig. 6.15R shows Exp. CAP5 GLC values predicted for the 800-km equally-spaced arc plotted site by site against azimuth angle together with observed 800-km arc station

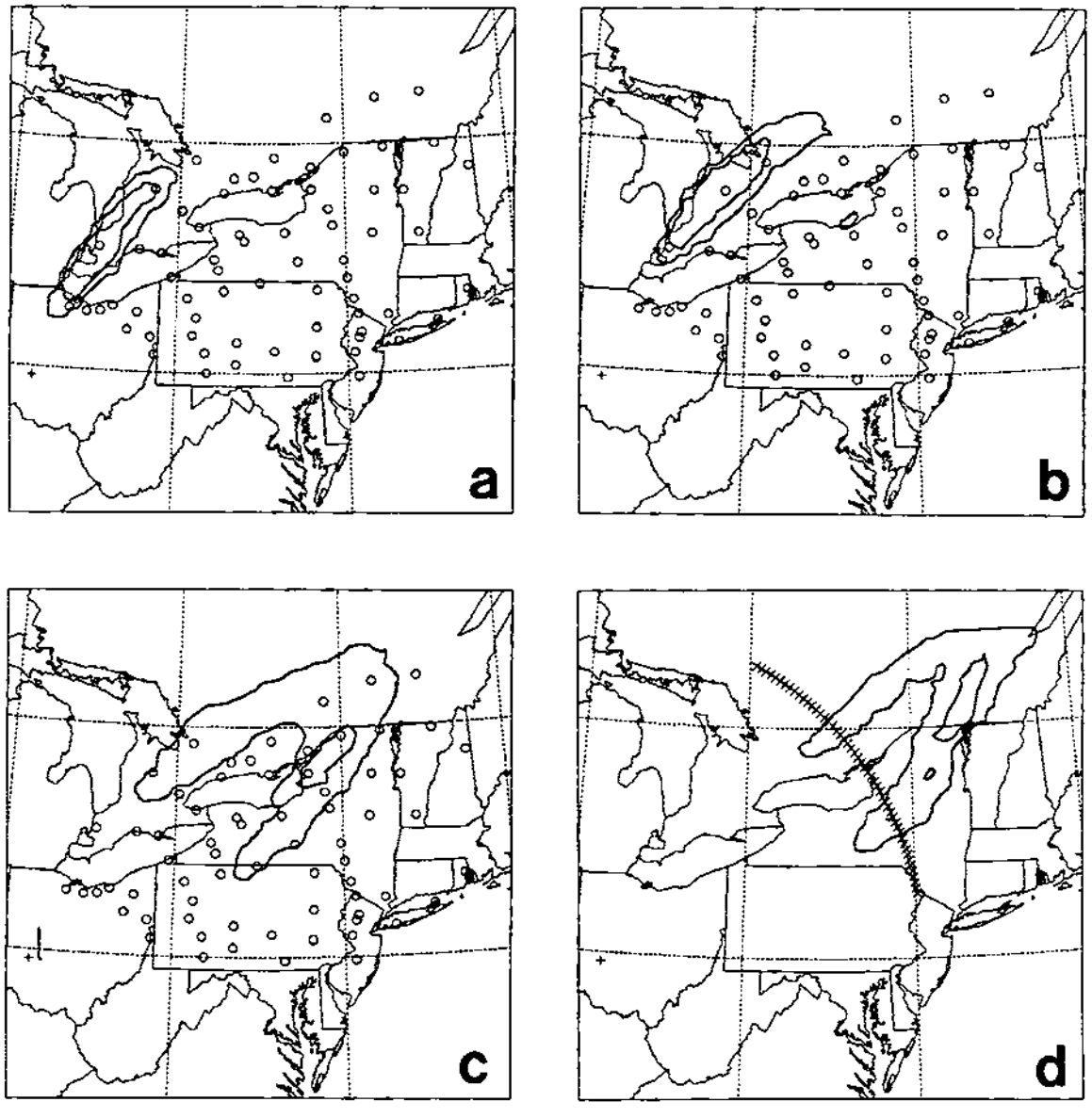

Figure 6.14: Time sequence of plan views of estimated PMCH surface concentration patterns for the second through fifth 6-hour Release 2 sampling periods (Sept. 26–27, 1983) based on particle positions from the Exp. CAP5 MLPDM simulation: (a) 0300–0900 GMT; (b) 0900–1500 GMT; (c) 1500–2100 GMT; (d) 2100–0300 GMT. The 10 fl l^{-1} and 100 fl l^{-1} concentration isopleths are indicated by triple-thick contour lines. Map characteristics are the same as Fig. 6.4. The last panel shows the locations of the 62 equally-spaced sites 800 km downwind from Dayton, Ohio.

GLC values. Fig. 6.16R presents some of the same data in a complementary way, plotted against travel time. Several of the features mentioned in the discussion of Fig. 6.14 can be seen clearly in these two figures. These include the arrival of the simulated cloud one sampling period too early and predicted peak concentration levels of comparable magnitude to the observed values. It is also clear from Fig. 6.15R that the predicted cloud is located to the north of the observed cloud. The striking predicted bimodal concentration patterns at the two middle sampling periods in Fig. 6.15R are due to the passage of the two 'horseshoe legs' of the simulating tracer cloud across the 800-km arc. Note that the observed concentration values for each of the last three sampling periods presented in this figure also have a bimodal, though much less pronounced, structure. Interestingly, Fig. 6.16R suggests that the predicted cloud width is of the right size when the two 'legs' are considered together (see Table 6.8). The predicted cloud transit time across this arc is 24 h, somewhat shorter than the observed 30 to 36 h transit time but much greater than the original 3-h release time.

Table 6.6 compares the 800-km-arc ground-level station exposure and cross-wind integrated exposure (CWIE) values predicted in the various CAPTEX numerical experiments with observed 800-km-arc station values for the complete 36-hour sampling period on this arc. As expected from Fig. 6.15R, the Exp. CAP5 exposure plume is located north of the observed plume and is not sampled on its northern flank by the 800-km-arc stations. The predicted CWIE value for Exp. CAP5 is less than half the observed value but the predicted peak exposure is comparable in magnitude to the peak observed station exposure: 1092 vs. 1170 $\mathrm{fl\,h\,l^{-1}}$. But note too that the observed CWIE value for the 800-km arc is itself about half the value estimated on the 300-km arc (see Table 6.3). This difference suggests that the representativeness of the surface measurements relative to the entire cloud was different along these two arcs. It would be tempting to say that this difference arose because sampling on the 800-km arc included a nighttime period and tracer carried aloft in the previous day's residual layer was not sampled. However, most of the tracer measured on the 300-km arc was also measured at night (Table 3.21).

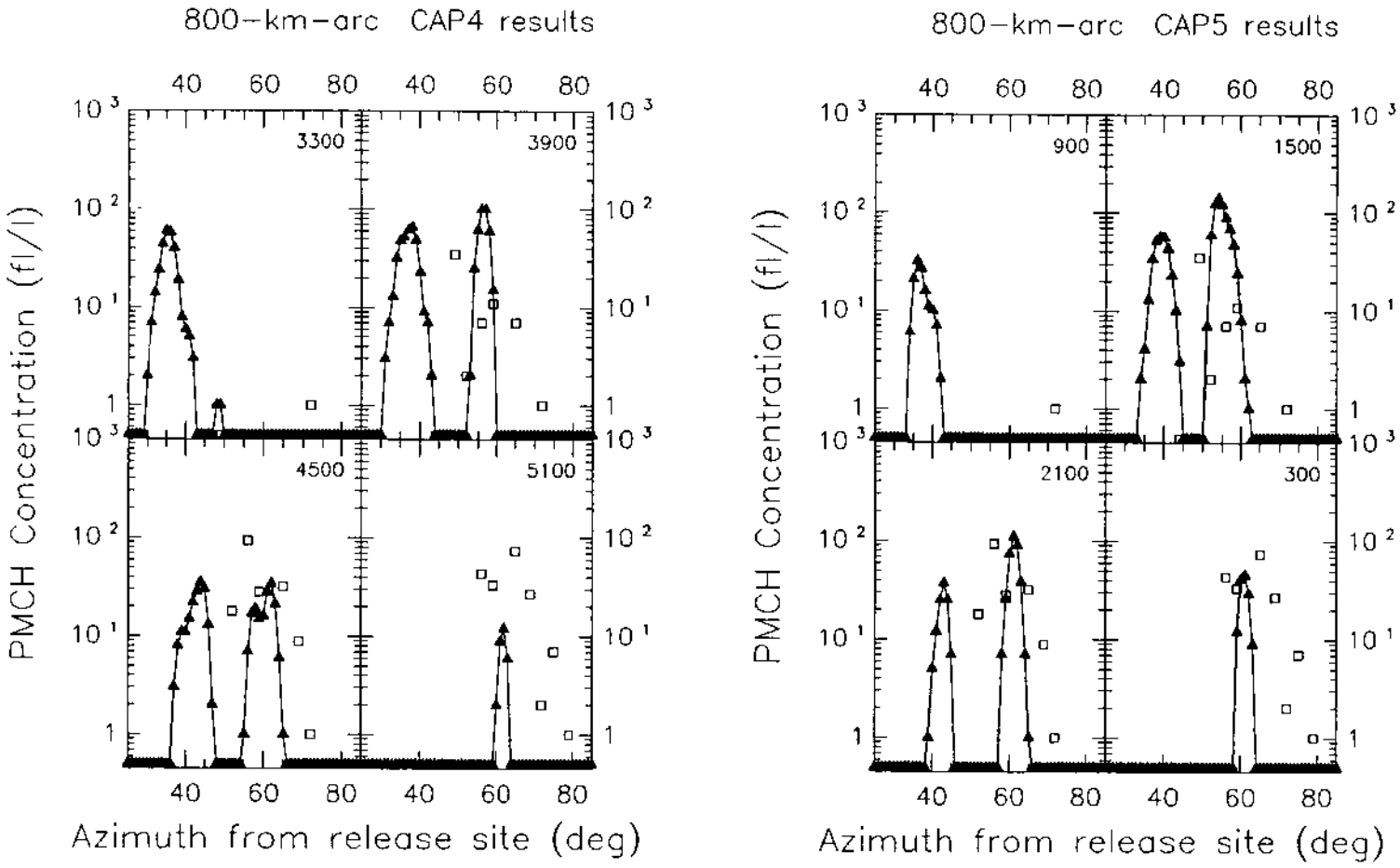

Figure 6.15: Observed and Exps. CAP4 (lefthand side: 'L') and CAP5 (righthand side: 'R') predicted PMCH concentration–azimuth plots for the 800-km sampling arc for the first four 6-hour sampling periods (Sept. 26–27, 1983) on this arc: (a) 0900–1500 GMT; (b) 1500–2100 GMT; (c) 2100–0300 GMT; and (d) 0300–0900 GMT. Observed values are indicated by open squares; predicted values are indicated by filled triangles connected by a solid line. The starting time of each sampling period (GMT) is plotted in the upper righthand corner of each panel.

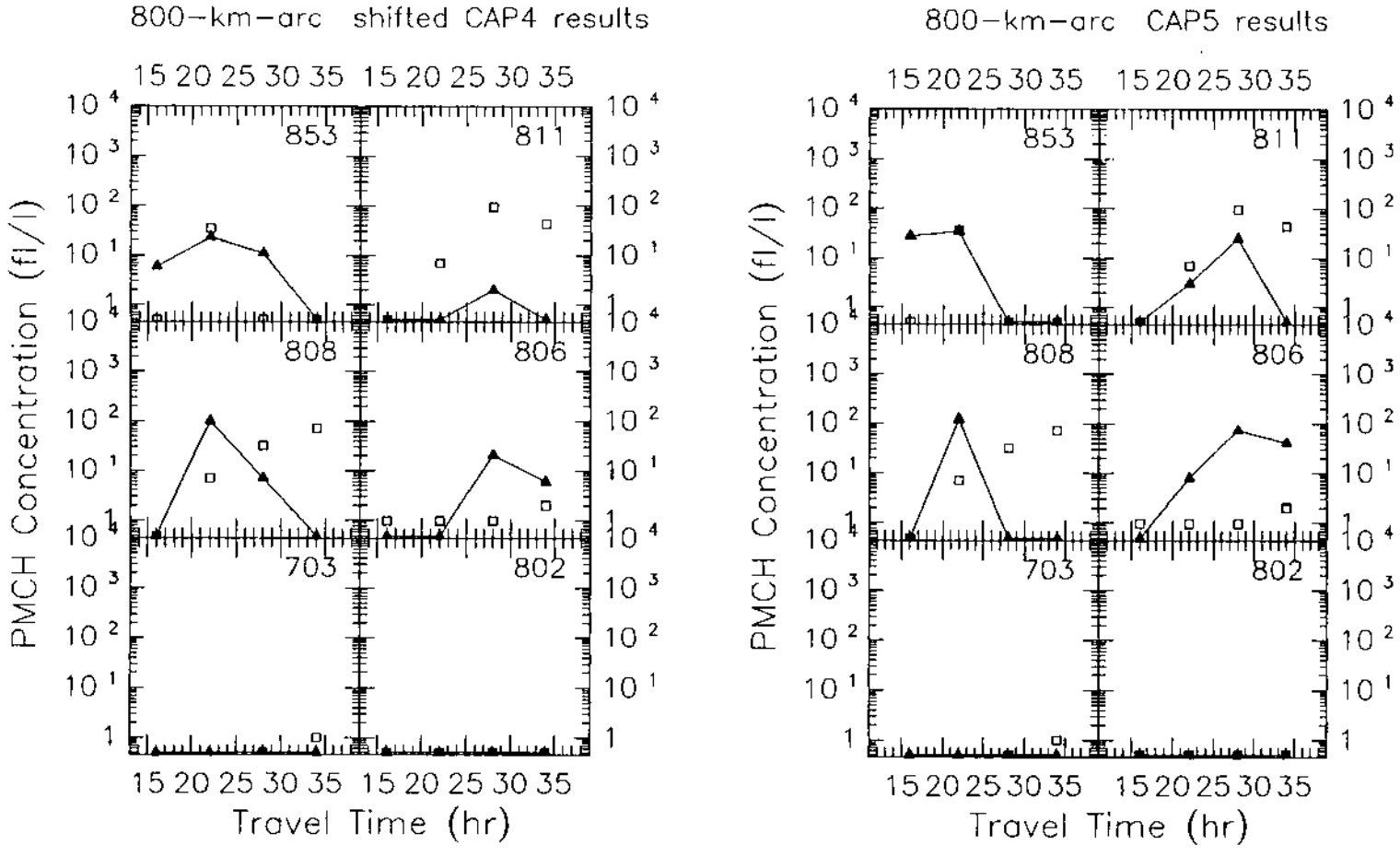

Figure 6.16: Observed and Exp. CAP4 (lefthand side: 'L') and CAP5 (righthand side: 'R') predicted PMCH concentration–time plots for six 800-km-arc sampling stations: (a) Station 853; (b) Station 811; (c) Station 808; (d) Station 806; (e) Station 703; and (f) Station 802. Observed values are indicated by open squares; predicted values are indicated by filled triangles connected by a solid line. The station number is plotted in the upper righthand corner of each panel. The time period shown extends from Sept. 26 at 0600 GMT until Sept. 27 at 0800 GMT and includes the first four 6-hour sampling periods on this sampler arc. The Exp. CAP4 site values have been shifted southward 9° and the Exp. CAP5 site values have been shifted southward 12° in constructing this figure.

Table 6.6: Comparison of predicted 800-km-arc station ground-level exposures (fl h l^{-1}) for the 24-h period from 0900–0900 GMT, Sept. 26–27, 1983 with observed values for the 36-h period from Sept. 26, 0900 GMT to Sept. 27, 2100 GMT. A dash (–) indicates 'no data'. The rightmost vertical column gives crosswind-integrated exposures (CWIE) over Stations 753–802, assuming a mean cross-wind station spacing of 47.5 km (or 3.35°). Azimuth angles are in degrees (clockwise from north) and great-circle distances from the release site at Dayton are given in kilometers.

Azimuth	44.0	49.2	52.3	56.5	59.3	65.5	68.7	72.4	75.1	78.3	79.2	81.8	86.0	
Distance	785	841	812	823	814	808	803	805	809	810	803	789	798	
Experiment	**800-km-arc Station Number**													**CWIE**
Number	753	852	812	811	810	808	807	806	805	804	703	803	802	(fl km l^{-1})
CAP2	0	0	0	0	0	0	0	0	0	0	0	0	0	†0
CAP3a	312	2220	708	0	0	0	0	0	0	0	0	0	0	153900
CAP3b	0	69	160	54	0	0	0	0	0	0	0	0	0	67800
CAP4	138	54	114	444	156	0	0	0	0	0	0	0	0	43000
CAP5	36	168	1092	498	1098	0	0	0	0	0	0	0	0	137400
Obs.	0	210	120	906	726	1170	522	348	204	174	264	120	228	237100

†Exp. CAP2 cloud had not reached 800-km arc by end of Period VI (Sept. 27, 0300–0900).

Six-hourly GLCs were also calculated along an arc of 62 equally-spaced sites located exactly 800 km downwind of Dayton at 1° azimuthal increments from 25° to 86°. The corresponding site separation distance along this equally-spaced arc is 14 km, much smaller than the mean 800-km-arc station spacing of approximately 47.5 km (Table 3.5). This equally-spaced arc is shown in Fig. 6.14d.

Table 6.7 lists the ground-level exposures calculated at the 800-km equally-spaced sites for the CAPTEX numerical experiments. (Only every other predicted exposure value is listed in this table in order to be able to fit it onto a broadside page.) The results for Exp. CAP5 look somewhat different when presented in this format. The predicted width of the exposure plume now more closely resembles the observed exposure plume width, as compared to Table 6.6, because the equally-spaced arc samples the tracer located north of the northern limit of the CAPTEX 800-km-arc stations (Fig. 6.14). The predicted CWIE value obtained from this denser and nontruncated computational arc, on the other hand, is close to the value given in Table 6.6 and still 40% smaller than the CWIE value estimated from the 800-km-arc concentration observations. Note that the gap between the predicted cloud's two legs can be clearly seen in Table 6.7.

(c) Quantitative pattern characteristics. Table 6.8 compares some of the quantitative cloud characteristics estimated from (i) the observed 800-km-arc sampler measurements and from (ii) predicted concentrations along the 62-site 800-km equally-spaced arc for Exp. CAP5. Values for most of the characteristics are in reasonable agreement. Plume widths are comparable at this distance, unlike the 300-km arc where the predicted plume was too narrow (Table 6.5). The predicted maximum concentration value is also comparable to (and larger than) the observed maximum value, although the predicted 800-km-arc CWIE value is almost half as small as the value estimated from the observed station exposures. The predicted cloud arrival time and time of maximum concentration are both one six-hour sampling period too early. The predicted and observed transit times agree quite well, however: 24 h vs. 30–36 h. The centerline error in the location

Table 6.7: Comparison of predicted ground-level exposures (fl h l^{-1}) along the 800-km equally-spaced-site arc (2° azimuthal spacing) for the 24-h period from 0900–0900 GMT, Sept. 26–27, 1983 with the observed 800-km-arc station exposures for the 36-h period from Sept. 26, 0900 GMT to Sept. 27, 2100 GMT. All of the exposure values on each horizontal line have been left-justified beginning with the westernmost site with a non-zero value. The column labelled 'Left-Edge Azimuth' gives the azimuth angle (° from the north) relative to that westernmost site. The relative azimuths give clockwise rotations of the arc sites relative to the left-edge azimuth. A dash (–) indicates 'no data'. The rightmost vertical column gives crosswind-integrated exposures (CWIE) over the equally-spaced-site arc; the mean cross-wind site spacing in this table is 28 km.

Exp. No.	Left-Edge Azim.	800-km-arc Relative Azimuth																			CWIE (fl km h l^{-1})
		0	2	4	6	8	10	12	14	16	18	20	22	24	26	28	30	32	34	36	
CAP2	0	0	0	0	0	0	0	0	0	0	0	0	0	0	0	0	0	0	0	0	*0
CAP3a	29	6	336	624	522	216	150	162	180	318	666	1536	2742	1578	0	0	0	0	0	0	†253000
CAP3b	50	48	594	1128	1128	270	0	0	0	0	0	0	0	0	0	0	0	0	0	0	†88700
CAP4	30	12	126	456	660	558	240	192	210	78	6	0	0	150	642	474	108	276	36	0	118300
CAP5	34	48	270	408	426	300	168	0	0	0	354	846	534	324	612	630	42	0	0	0	138900
Obs.	50	210	–	120	–	906	726	–	–	1170	–	522	–	348	204	174	264	–	120	228	‡237100

*Exp. CAP2 cloud had not reached 800-km arc by end of Period VI (Sept. 27, 0300–0900).
†Value is an underestimate since cloud was still crossing the 800-km sampling arc at 0900 GMT, Sept. 27. ‡From Table 6.6.

of the simulated Exp. CAP5 cloud is reflected by differences in the 'Station Range' and 'Mean Azimuth' column values.

(d) Scattergrams. Figs. 6.17c–d show the 800-km-arc unmatched and matched-peak[217] scattergrams for Exp. CAP5. Like Fig. 6.13, relatively few observed concentrations were available for constructing this figure (i.e., 13 stations × four sampling periods minus 5 missing values). Peak-matching doubled the number of non-zero concentration pairs on the scattergram for this arc, too. The large number of concentration pairs on the observed-concentration axis is partly due to the gap between the Exp. CAP5 predicted cloud's 'legs', partly due to the predicted cloud being narrower than the observed cloud, and partly due to the predicted cloud crossing the 800-km sampler arc faster than the observed cloud.

Full domain. With the exception of Godowitch (1989b), previous CAPTEX studies have not compared their predictions against observations along a single sampler arc. Rather, comparisons were made for the full two-dimensional sampler network. A number of these comparisons are shown in Fig. 3.27. Several similar graphical comparisons will be shown here.

Fig. 6.18 shows the position of the leading edge of the Release 2 tracer cloud for successive six-hour sampling periods as determined from station GLC observations and Exp. CAP5 predictions. Comparison of the two panels reveals that the predicted surface cloud consistently leads[218] the observed cloud. This problem with too fast transport in the Exp. CAP5 simulation has been mentioned already in the discussion of some of the previous figures in this section. Presumably, it is related to an overprediction of low-level wind speed in the RAMS simulation, but the reasons for this overprediction are not clear.

---

[217] In both time and space.

[218] The apparent jump in the position of the leading edge of the predicted cloud in Fig. 6.18b between 1200 GMT and 1800 GMT on September 26 is due to the fact that the Exp. CAP5 cloud did not lie over any active 700-km-arc stations at 1200 GMT even though it was located this far downwind (Fig. 6.14b).

Table 6.8: Tracer-cloud characteristics estimated from CAPTEX Release 2 numerical experiments — 800 km sampler arc. Cloud arrival time, transit time, and maximum width all depend on the criterion used to determine the cloud edges. GMT times before midnight correspond to Sept. 26, 1983 except for time of Exp. CAP3b peak concentration. Azimuth range and arc length have units of degrees and kilometers, respectively, and have been determined from the equally-spaced-site predicted concentrations. Mean center-line azimuth values correspond to stations with maximum exposures in Table 6.7. Some 'Observed' data-line values are based on values given in Tables 3.5 and 3.7.

Exp. No.	Arrival Time (GMT)	Transit Time (h)	Maximum Width			Max. Conc. ($fl\,l^{-1}$)	Time of Max'm (GMT)	CWIE ($fl\ km\ h\ l^{-1}$) ($\times 10^{-3}$)	Mean CL Azimuth (°)
			Sl'n Range	Azim. Range	Arc Length				
10%-of-peak threshold									
CAP2	–	–	–	–	–	–	–	–	–
CAP3a	0900–1500	18+	812–753	†23	321	269	2100–0300	253	51
CAP3b	2100–0300	12+	812–852	8	112	156	0300–0900	89	55
CAP4	0900–1500	24	811–852	†27	378	100	1500–2100	118	57
CAP5	0900–1500	24	811–852	†22	308	141	1500–2100	139	54
Obs'd	1500–2100	30	802–810	28	395	93	2100–0300	237	66
3 $fl\,l^{-1}$ threshold									
CAP2	–	–	–	–	–	–	–	–	–
CAP3a	0900–1500	24+	812–753	†26	363	269	2100–0300	253	51
CAP3b	2100–0300	12+	811–852	10	140	156	0300–0900	89	55
CAP4	0900–1500	24	811–852	†29	406	100	1500–2100	118	57
CAP5	0900–1500	24	811–852	†25	350	141	1500–2100	139	54
Obs'd	1500–2100	36	802–810	28	395	93	2100–0300	237	66

– Exp. CAP2 cloud had not reached 800-km arc by the end of Period VI (Sept. 27, 0300–0900 GMT).
+ Cloud was still crossing the 800-km arc at 0900 GMT on Sept. 27. †Split cloud (e.g., Fig. 6.14c).

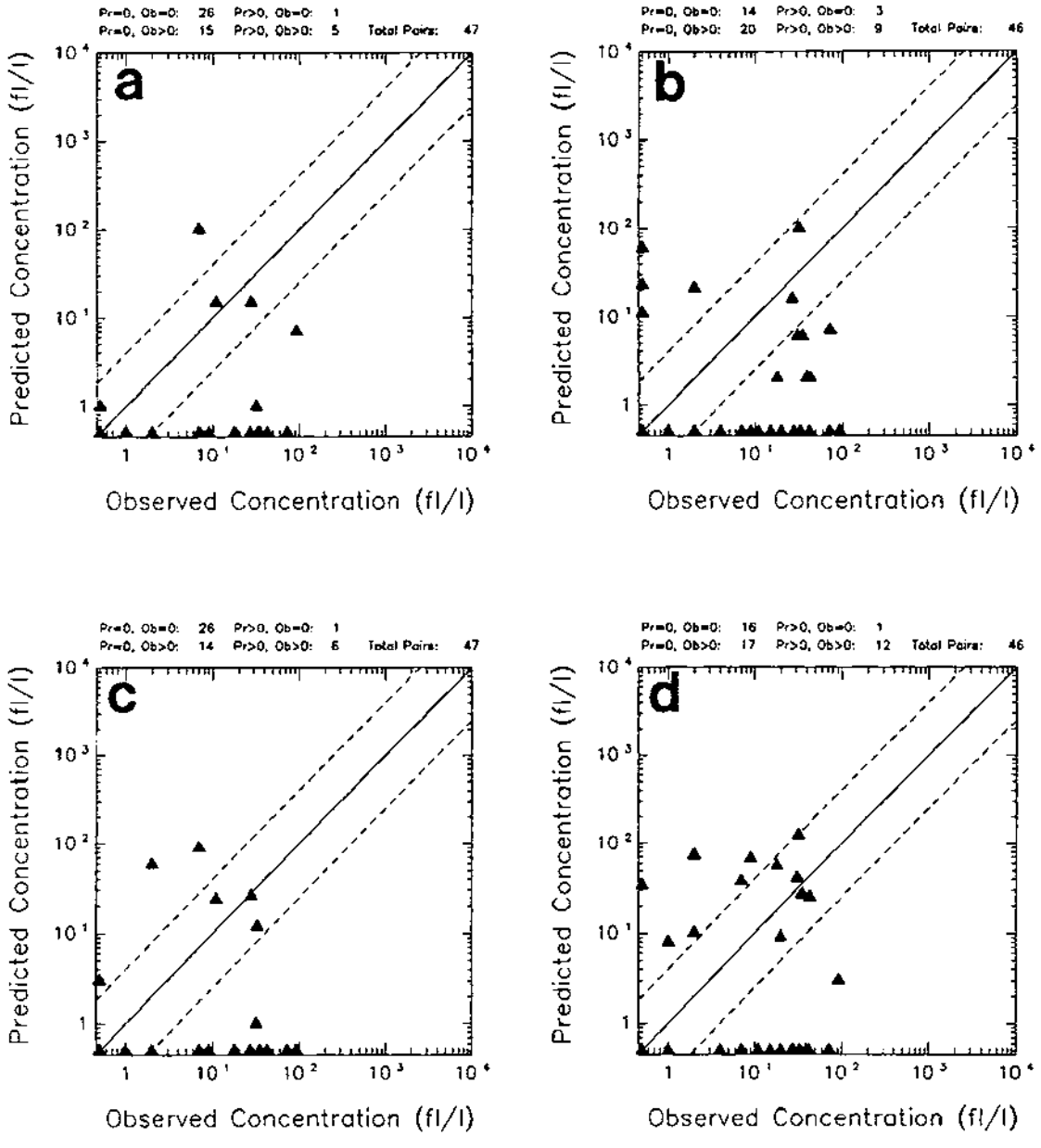

Figure 6.17: Scattergrams for observed 800-km-arc PMCH concentrations vs. Exp. CAP4 and Exp. CAP5 computed concentrations: (a) unmatched Exp. GP4 estimated concentrations; (b) peak-matched Exp. GP4 estimated concentrations; (c) unmatched Exp. GP5 estimated concentrations; and (d) peak-matched Exp. GP5 estimated concentrations. Plotted pairs have been drawn from the set of concentrations for Stations 802–853 and the first four 6-hour observing periods on this arc (from 0900–0900 GMT, Sept. 26–27) for panels (a) and (c). The Exp. CAP4 site values have been shifted southward 9° in space and ahead one 6-hour sampling period in time while the Exp. CAP5 site values have been shifted southward 12° and ahead one sampling period in constructing this figure. The diagonal lines are the one-to-one correspondence line and two factor-of-4 (i.e., 1:4 and 4:1) lines.

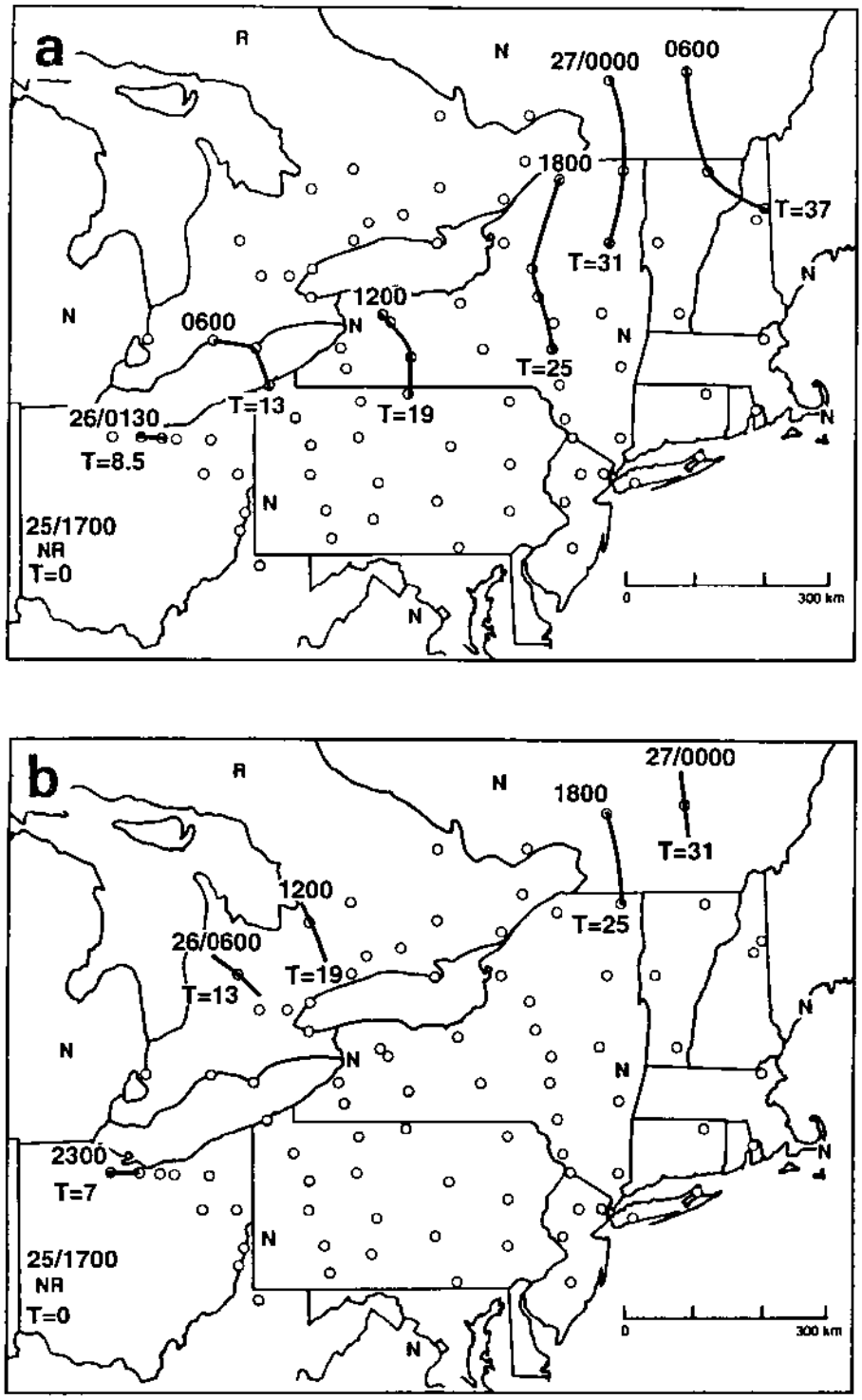

Figure 6.18: Mean arrival-time isochrons for ground-level tracer cloud as determined from CAPTEX station (a) observations and (b) Exp. CAP5 predictions. Only stations reporting values above 3 fl l^{-1} are connected. Numbers at the tops of the isochrons give the mean arrival time (GMT) while numbers at the bases of the isochrons give the mean travel time from the start of the release on Sept. 25, 1983 at 1700 GMT.

Most of the results presented in Fig. 3.27 from simulations made of this case by other mesoscale dispersion models are in the form of ground-level exposure or concentration envelopes. Using a similar format, Fig. 6.19 presents 36-hour time composites of the predicted GLC patterns for five of the CAPTEX numerical experiments carried out in the present study. Panel E of this figure shows the Exp. CAP5 composite plume. Compared to Panel F, we see that the the Exp. CAP5 composite plume has the correct alongwind extent and a comparable crosswind extent at later sampling periods. The counter-clockwise centerline rotational error in the predicted composite plume can also be seen clearly, however, as can the too narrow crosswind extent south of Lakes Erie and Ontario. It is interesting to compare Figs. 6.19e–f with Figs. 6.8 and 6.9. The projected footprints in the latter, which include tracer above the sampling-volume depth of 134 m used in constructing Fig. 6.19e, seem to agree better with Fig. 6.19f. This suggests that the too narrow crosswind extent over Pennsylvania may be related to the too fast alongwind transport predicted in Exp. CAP5. Examination of Fig. 3.21 reveals that the measured values along the southern ends of the 400-, 500-, and 600-km arcs occurred during Periods III–VI, that is, after sunrise on Sept. 26, so that sheared, elevated tracer may have been mixed down to the surface over these stations.

6.3 Sensitivity Experiment Results: Experiments CAP1–CAP4

Let us now compare the results from the five CAPTEX sensitivity experiments, Exps. CAP1, CAP2, CAP3a, CAP3b, and CAP4, with the Exp. CAP5 results. The distinguishing characteristics of the RAMS simulations for all of these numerical dispersion experiments are listed in Table 6.1. By simplifying the specification of either the land-surface characteristics or the initial meteorological fields, it was possible to isolate the influence of terrain elevation, other land-surface properties, and spatial variations and temporal variations in the synoptic-scale flow field. This set of sensitivity experiments does not exhaust all possible combinations of the simplifications to be discussed, so the results of these experiments can only be suggestive, not definitive. But bear in

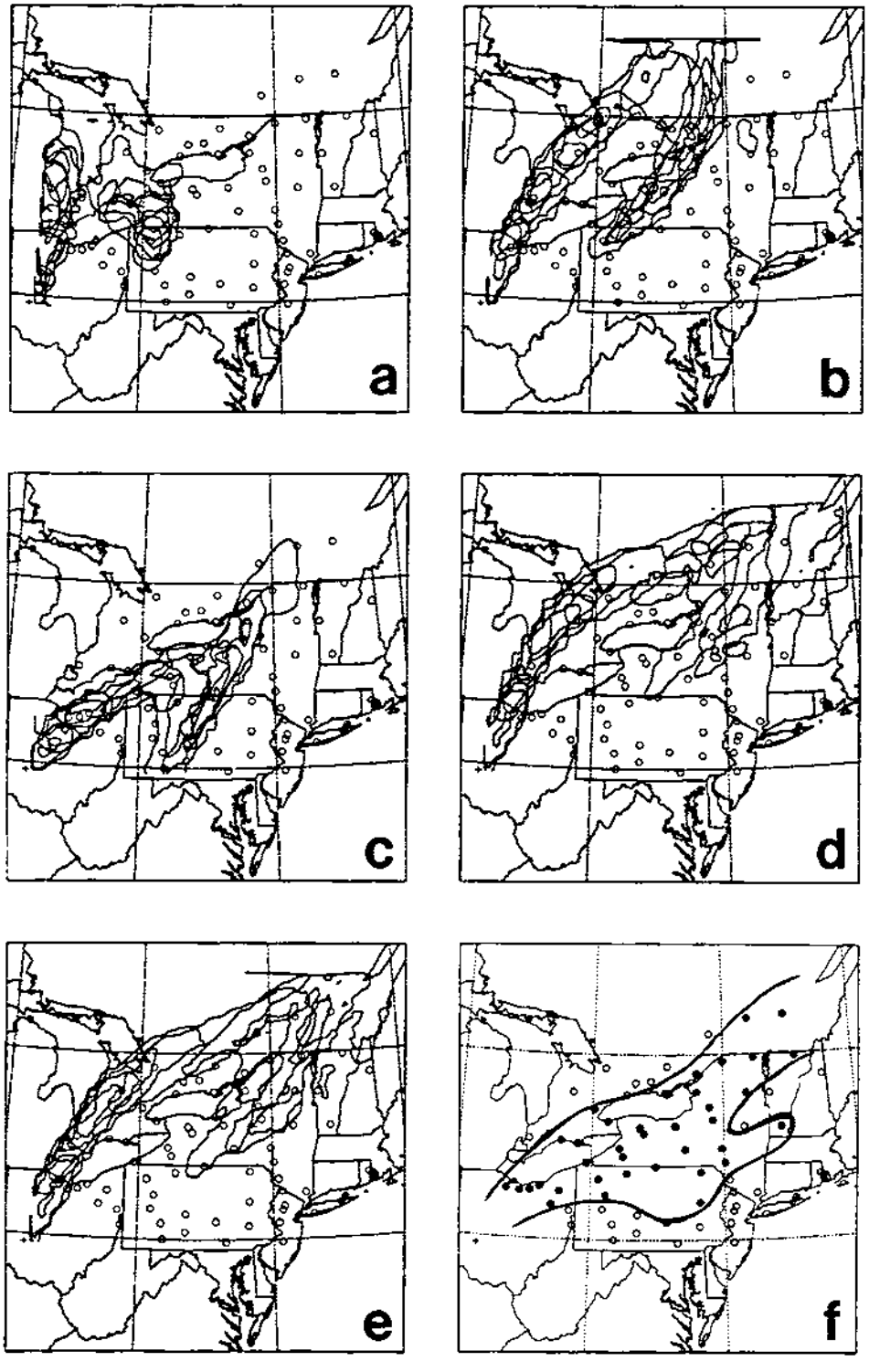

Figure 6.19: Time composites of predicted GLC patterns over 36 hours (i.e., Periods I–VI) for five of the CAPTEX numerical experiments: (a) Exp. CAP2; (b) Exp. CAP3a; (c) Exp. CAP3b; (d) Exp. CAP4; (e) Exp. CAP5. The concentration isopleths plotted in panels (a)–(e) are the 10 fll^{-1}, 100 fll^{-1}, and 1000 fll^{-1} levels. Filled station circles in panel (f) mark sampling stations reporting concentrations of 10 fll^{-1} or more for at least one six-hour sampling period. Otherwise the same as Fig. 6.4.

mind too that results from a single case study cannot be considered definitive either when generalizing about the relative importance of various processes.

6.3.1 Effects of Terrain Forcing

The first two CAPTEX sensitivity experiments, CAP1 and CAP2, were the simplest members of the CAPTEX numerical suite. The RAMS simulations for both were initialized using the HHI option, that is, with horizontally homogeneous meteorological fields; the input sounding employed was the Sept. 25 1200 GMT sounding from Dayton, Ohio (see Fig. 4.16c). The three-hour tracer release began at Dayton at 1700 GMT, five hours later. Exps. CAP1 and CAP2 differed, however, in their treatment of terrain elevation. Exp. CAP1 assumed flat, sea-level terrain elevations everywhere whereas Exp. CAP2 employed realistic terrain (Fig. 4.19b). Other land-surface property fields were identical, however, so that Exp. CAP1 did take into account the presence of the Great Lakes and the Atlantic Ocean.

One other difference between these two experiments arose due to their treatment of the input sounding. Because the terrain height assumed for the entire domain in Exp. CAP1 was 0 m and terrain heights in Exp. CAP2 were also as low as sea level, the Dayton sounding had to be extrapolated down to sea level in order to initialize RAMS. The elevation of Dayton, Ohio is 298 m. (A similar procedure was followed for the Oklahoma City sounding in Exp. GP2: see Sec. 5.3.) This was done simply by extrapolating the temperature profile at the first two measured levels downwards. The pressure at the low point was obtained by reducing the DAY surface pressure based on the standard atmosphere. Wind speed was reduced by about 40%; wind direction was held constant.

Fig. 6.20 compares low-level streamlines from the RAMS simulations for these two experiments on two (terrain-following) surfaces, one close to ground level and the other close to the top of the daytime PBL. The z^*=24 m streamline fields are quite different for the two simulations. Fig. 6.20a corresponds to Exp. CAP1. Although this was the flat-terrain simulation, variations in other land-surface properties still caused changes in wind

direction and produce some areas of convergence and divergence. When terrain elevation variations are also considered, as in Exp. CAP2, the near-surface streamline field shows more mesoscale horizontal structure (Fig. 6.20b). The corresponding streamline fields at z^*=1579 m for the two experiments are shown in Figs. 6.20c–d. The differences between the two experiments are not as pronounced at this height but the influence of the Appalachian Mountains is still evident in Fig. 6.20d.

Mesoscale transport

How do the grid-scale trajectories compare for these two numerical experiments? Figs. 6.21a–b show the stacked grid-scale trajectories corresponding to the start of the Dayton tracer release. The Exp. CAP1 trajectories at the three lowest levels are rotated counter-clockwise relative to their Exp. CAP2 counterparts. Two of the middle trajectories are also longer, indicating faster transport speeds at these heights.

Some of these differences between the low-level trajectories for the two experiments arose from the fact that the low-level transport fields in the vicinity of Dayton were different because of the different terrain heights assumed in this area. The surface winds at Dayton for Exp. CAP1 corresponded to the *extrapolated* sounding winds at $z = 0$ whereas the surface winds at Dayton for Exp. CAP2 corresponded to the measured surface winds at Dayton (z = 298 m ASL). As a result, grid-scale trajectories '2', '3', and '4' for Exp. CAP1 correspond roughly to grid-scale trajectories '1', '2', and '3' for Exp. CAP2 in terms of height above sea level. This correspondence does not account for modification of the input sounding by PBL processes, however.

Since Exp. CAP1 was so idealized and since the tracer transport across the 300-km arc suggested by Fig. 6.21a was markedly west (by about 40°) of its observed position, particle dispersion calculations were not undertaken for this experiment. Essentially, this experiment served its purpose in investigating the contribution of terrain elevation through the comparison shown in Fig. 6.20.

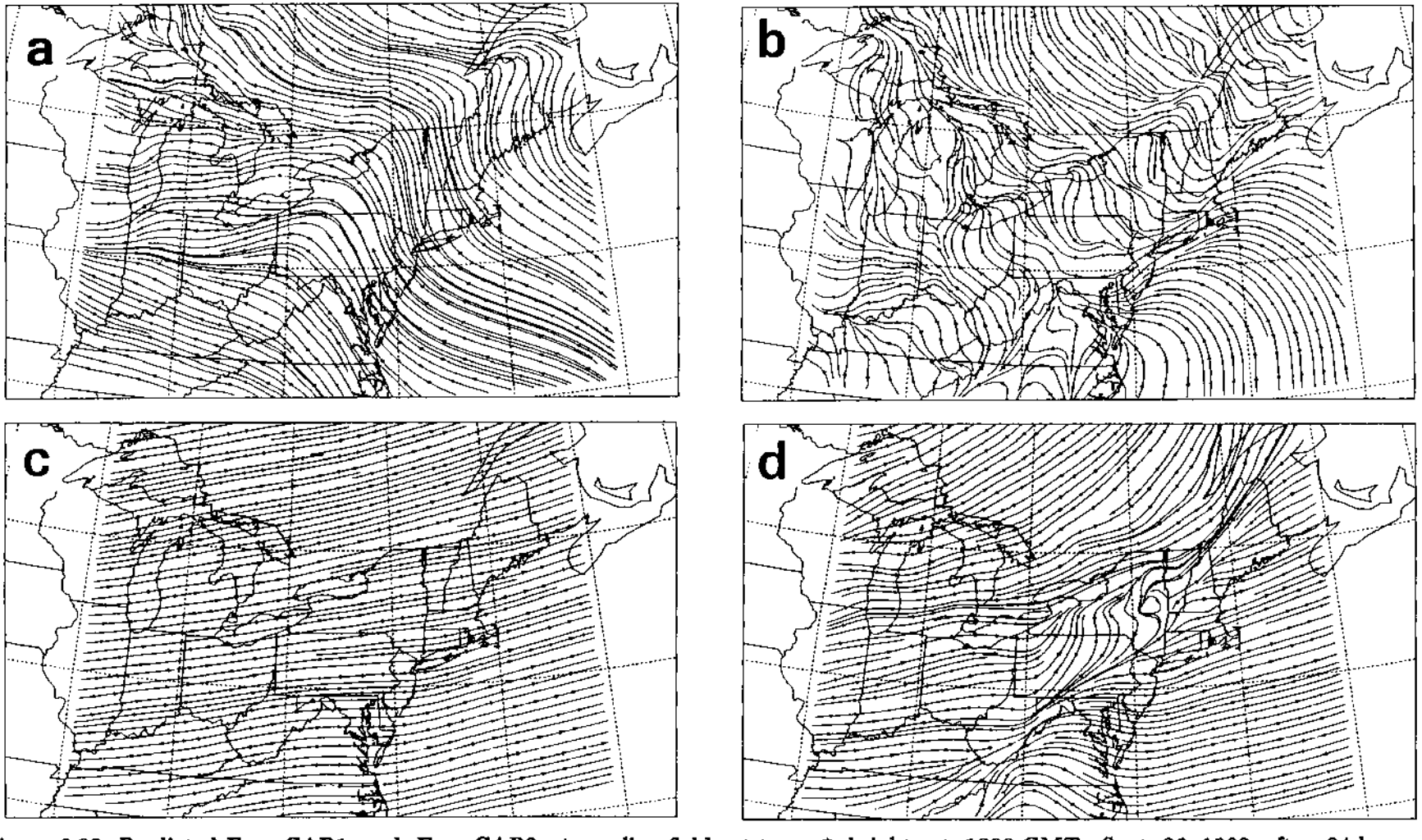

Figure 6.20: Predicted Exp. CAP1 and Exp. CAP2 streamline fields at two z^* heights at 1200 GMT, Sept. 26, 1983 after 24 hours of simulation: (a) 24 m AGL, Exp. CAP1; (b) 24 m AGL, Exp. CAP2; (c) 1579 m AGL, Exp. CAP1; (d) 1579 m AGL, Exp. CAP2. Otherwise identical to Fig. 6.1.

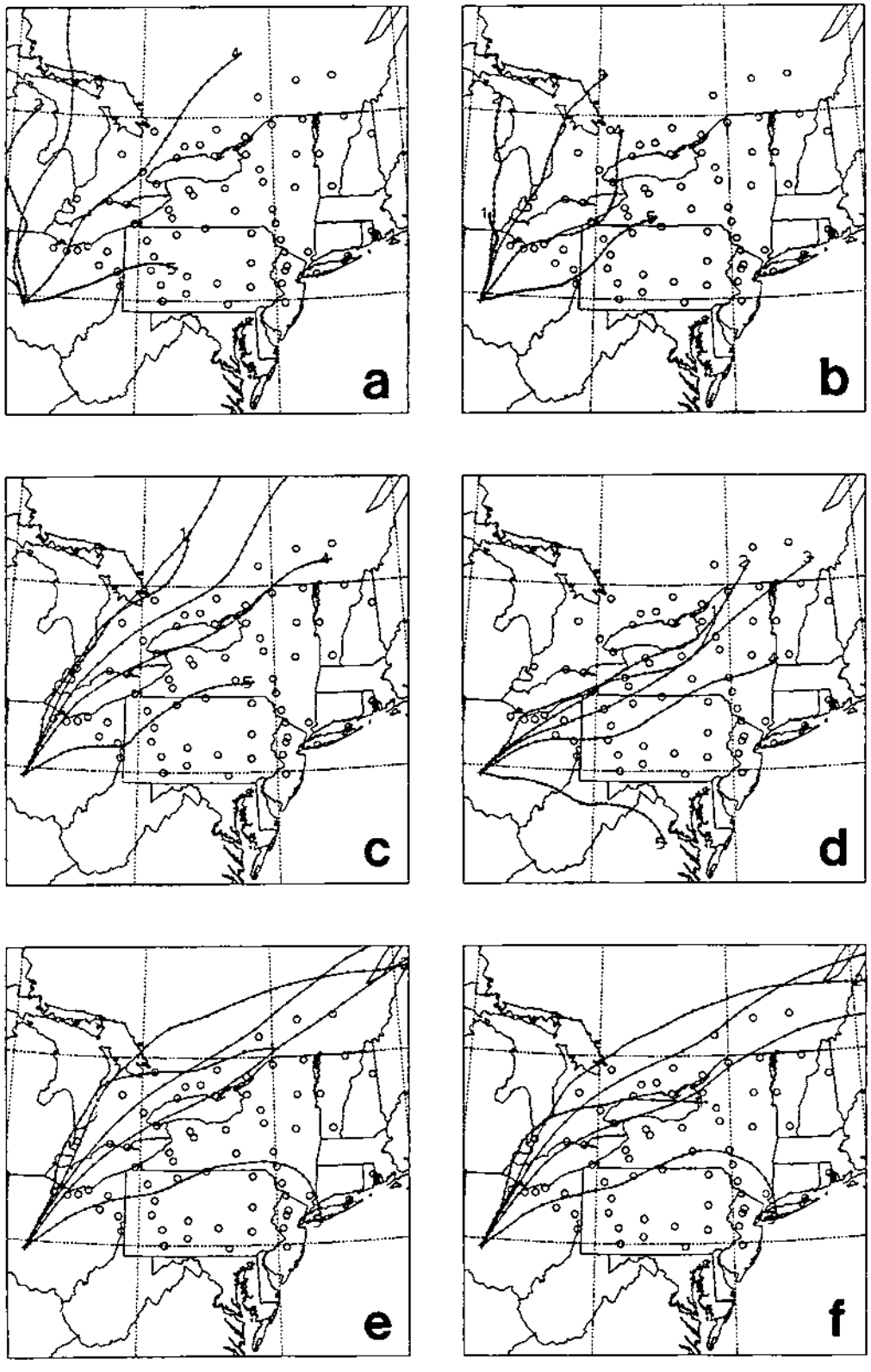

Figure 6.21: Plan views of 40-hour grid-scale trajectories for six CAPTEX numerical experiments: (a) Exp. CAP1; (b) Exp. CAP2; (c) Exp. CAP3a; (d) Exp. CAP3b; (e) Exp. CAP4; and (f) Exp. CAP5. Otherwise same as Fig. 6.3.

6.3.2 Effects of Land-Surface Inhomogeneities

The only difference between Exp. CAP4 and Exp. CAP5, the control experiment, was in their treatment of land-surface characteristics. Both experiments used realistic topography but Exp. CAP4 assumed the other land-surface characteristics needed by RAMS to be uniform: i.e., all land, silt-loam soil, solar albedo of 0.18, and aerodynamic surface roughness of 0.35 m. Differences between these two experiments could thus be attributed entirely to mesoscale landscape variability. Of particular interest were differences arising from neglect of the surface properties of Lakes Erie and Ontario in Exp. CAP4, since the tracer-cloud trajectory passed over these large bodies of water on the night following the tracer release from Dayton.

Mesoscale transport

Figs. 6.21e–f show plan views of the grid-scale trajectories released from Dayton at the beginning of the tracer release for these two experiments. The overall trajectory patterns are very similar. Close examination reveals, however, that the lowest trajectories (at 50 m AGL) diverge on the second day. It seems reasonable that differences in surface characteristics should affect the lowest levels of the atmosphere the most. In contrast, even the next pair of trajectories, at 250 m AGL, display much smaller deviations.

Concentration estimates

Given these minor differences between the grid-scale trajectories, how similar are the predicted GLC patterns and station values for these two experiments?

300-km arc. Figs. 6.22d and 6.10c show the predicted time-integrated GLC patterns in the vicinity of the 300-km arc for Exps. CAP4 and CAP5, respectively, for the three-hour period beginning 10 hours after the start of the release. The patterns are very similar. One noticeable difference is the slight counter-clockwise rotation of the Exp. CAP4 longitudinal centerline relative to the Exp. CAP5 centerline (see also Table 6.5). Figs. 6.11 and 6.12 compare the 200-km-arc concentration–azimuth and

concentration–travel time plots, respectively, for these two experiments. It appears from Fig. 6.11 that the Exp. CAP4 cloud reaches the 200-km range a bit sooner than the Exp. CAP5 cloud, is slightly narrower, and has a higher peak concentration value. Table 6.5 confirms this. In fact, the Exp. CAP4 peak concentration value is nearly double the Exp. CAP5 value. On the other hand, cloud arrival time, transit time, and time of peak concentration are the same for these two experiments.

Table 6.4 reveals some additional differences. The Exp. CAP4 *exposure* plume peak value is also nearly double the Exp. CAP5 peak value and the Exp. CAP4 CWIE value is 50% larger than the Exp. CAP5 value. The west side of the Exp. CAP5 exposure plume drops off more abruptly than does the Exp. CAP4 plume, but the two exposure plumes have almost the same width on the 200-km equally-spaced arc. The 200-km-arc concentration scattergrams for these two experiments are presented in Fig. 6.13 and are quite similar in appearance. Again, the very few non-zero concentration pairs, even for the peak-matched scattergrams, are due to the coarse 300-km-arc sampler spatial distribution relative to the cloud width and to the too-short cloud transit time predicted by the MLPDM for both experiments.

800-km arc. Figs. 6.23d and 6.14c show the six-hour-average GLC patterns for the two experiments for the afternoon of the second day of transport. Again, the patterns are broadly similar. Careful examination reveals the Exp. CAP4 predicted cloud to be located slightly to the northeast of the Exp. CAP5 cloud. The closed 100 fl l^{-1} isopleth is also located noticeably further north in the Exp. CAP4 cloud. Figs. 6.19d–e compare the 36-hour time composite GLC patterns for the two experiments. Differences are small between these two panels.

Fig. 6.15, which shows the 800-km-arc concentration–azimuth time plots for these two experiments, and Fig. 6.16, which shows the corresponding concentration–travel time plots, are also very similar overall. In fact, it requires some study of Table 6.8 to find any significant quantitative differences between Exps. CAP4 and CAP5 at this downwind distance. That both clouds are offset to the north relative to the observed cloud is clear

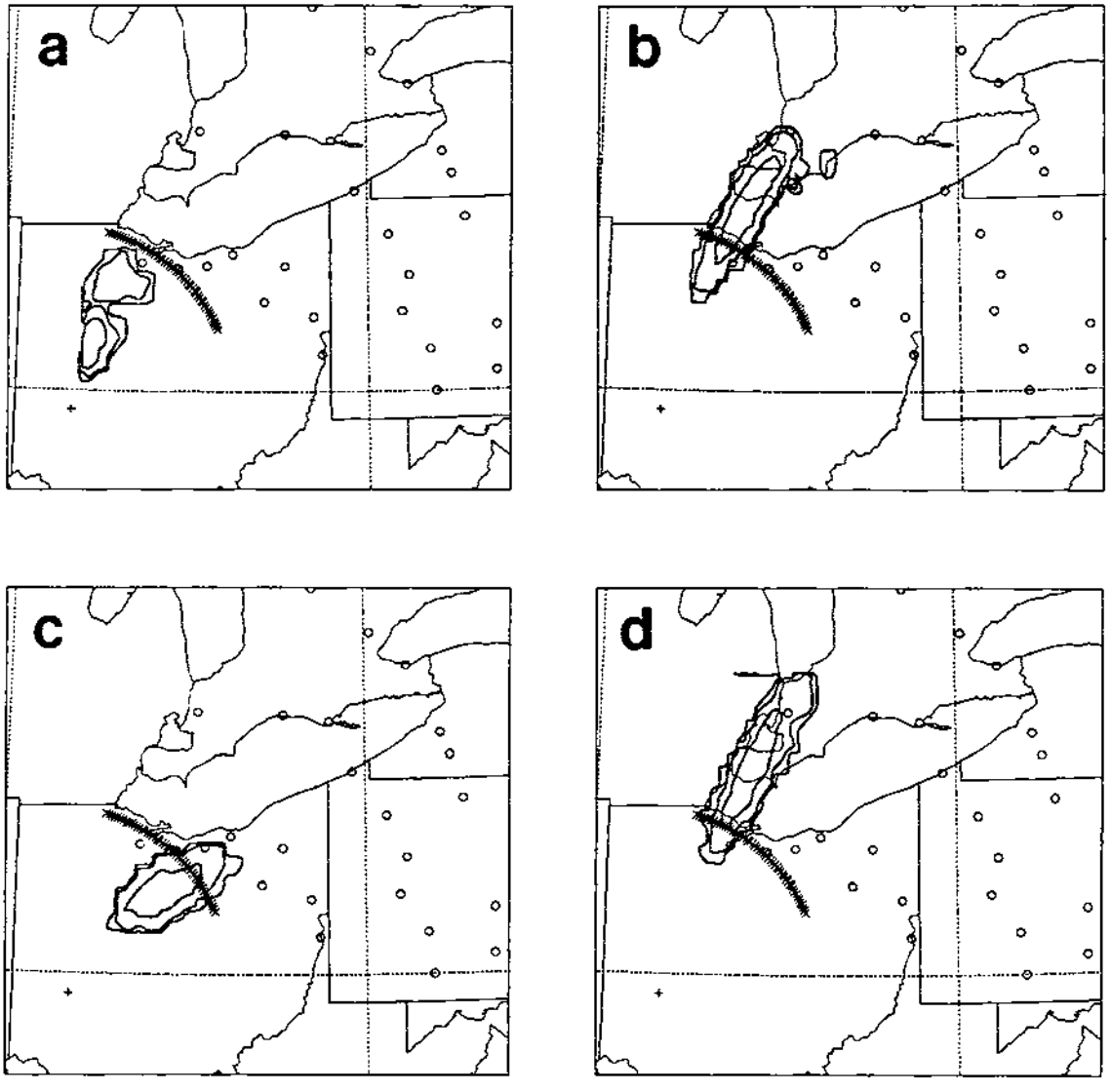

Figure 6.22: Plan views of estimated 3-hour-average PMCH surface concentration patterns for the fourth 300-km-arc sampling period (0300–0600 GMT, Sept. 26) based on particle positions from four of the sensitivity experiments: (a) Exp. 2; (b) Exp. 3a; (c) Exp. 3b; and (d) Exp. 4. Otherwise the same as Fig. 6.10

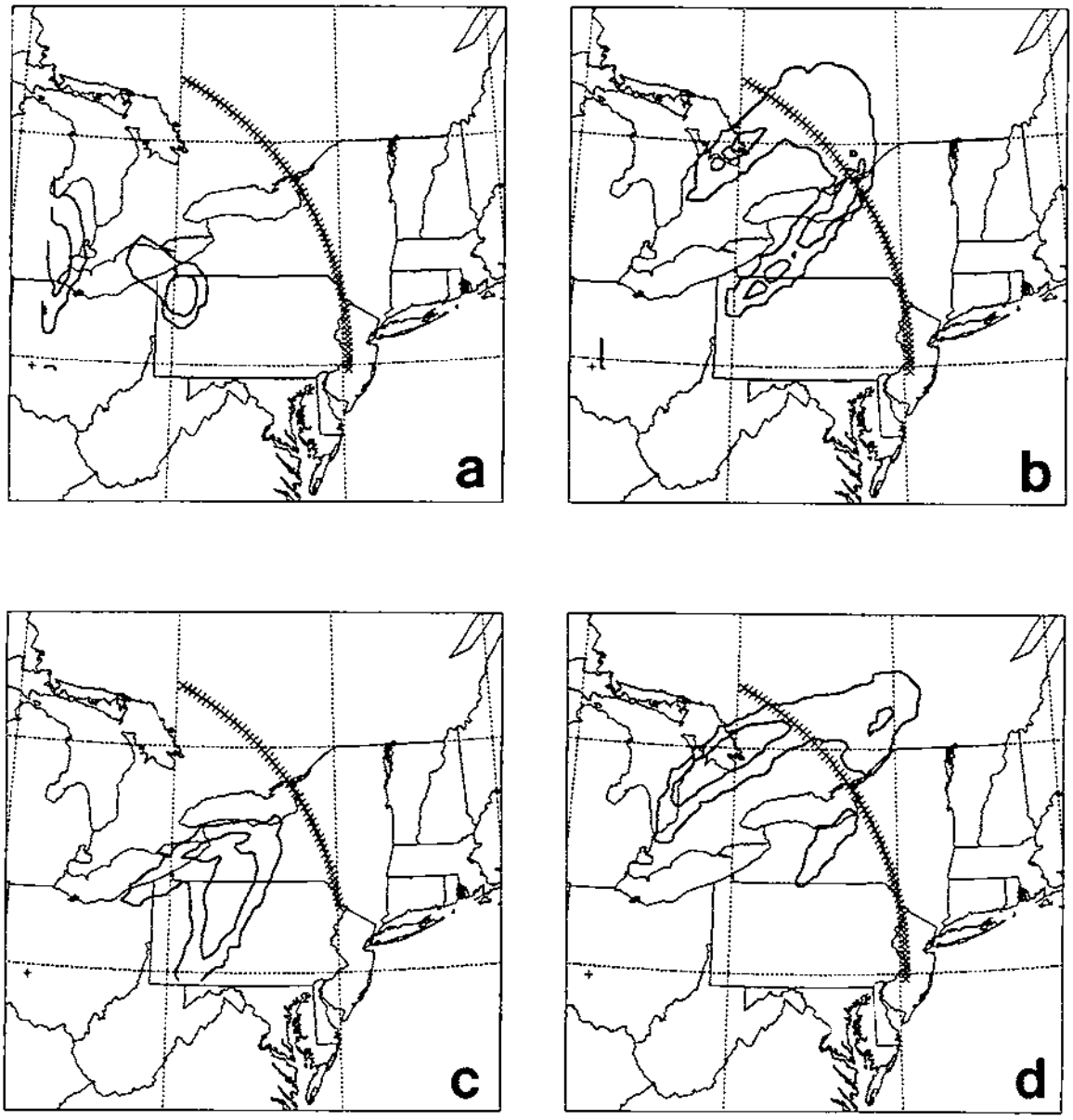

Figure 6.23: Plan views of estimated PMCH surface concentration patterns for sampling Period IV (1500–2100 GMT, Sept. 26) based on particle positions from four of the CAPTEX sensitivity experiments: (a) Exp. CAP2; (b) Exp. CAP3a; (c) Exp. CAP3b; (d) Exp. CAP4. Otherwise the same as Fig. 6.23.

from Table 6.6. Table 6.8 suggests that the Exp. CAP4 cloud is roughly 20% wider[219] than the Exp. CAP5 cloud at 800 km and has a lower peak concentration and lower CWIE value. Cloud arrival time, transit time, and time of peak concentration are all the same, however. From Table 6.7, we find that the exposure plume is also wider for Exp. CAP4. This table also suggests that the northern leg of the Exp. CAP4 cloud is wider than the corresponding Exp. CAP5 leg while just the opposite is true for the southern leg. Finally, the unmatched and peak-matched concentration scattergrams for these two experiments are shown in Fig. 6.17. They too are similar overall, although the peak-matched scattergram for Exp. CAP5 shows slightly better agreement with the observations than its Exp. CAP4 counterpart.

In summary, differences between these two cases as a result of the influence of mesoscale land variability were small but measurable, particularly for the 200-km-arc peak concentrations. It is quite likely, however, that the differences would have been larger if a grid with smaller horizontal spacing had been used for the RAMS meteorological simulations. As mentioned at the beginning of the chapter, even for approximately 40 km grid spacing, Lakes Erie and Ontario are very poorly represented on the grid used for the CAPTEX RAMS simulations.

6.3.3 Effects of Synoptic-Scale Flow Inhomogeneity

Differences between the dispersion predictions of Exps. CAP2 and CAP3a provide some insight into the importance of representing spatial variations in the synoptic-scale flow field when modelling mesoscale dispersion. These two experiments differed only in the RAMS initialization option used. Both were initialized using Sept. 25 1200 GMT observations, but Exp. CAP2 used the HHI option so that the initial RAMS atmospheric fields were horizontally homogeneous and based solely on the Dayton morning upper-air sounding. The initial atmospheric fields for Exp. CAP3a, on the other hand, were created using the VI option; they were based on blended fields produced using the NMC

---

[219] Counting both 'legs' and the gap between them.

gridded analysis for this synoptic time plus approximately 20 upper-air soundings from stations located within the RAMS domain (see Fig. 4.15a).

As can be seen from Figs. 3.18 and 4.16c, the wind direction at Dayton at 1200 GMT on Sept. 25 is actually quite representative of the synoptic-scale flow direction over much of the CAPTEX domain. Flow speed, by contrast, increases with distance from the center of the high-pressure system over the mid-Atlantic states (e.g., Fig. 3.18c). This is confirmed by Fig. 4.16: winds at Dayton, Buffalo, and Pittsburgh are all similar and very light but wind speeds are higher to the northwest at Flint, Michigan.

Mesoscale transport

Grid-scale trajectories for these two experiments for the start of the tracer release are shown in Figs. 6.21b–c. The initial trajectory directions are similar at first, but then the Exp. CAP3a particles begin to display anticyclonic curvature as they travel further downstream from Dayton (cf. Fig. 3.18b). Moreover, the lowest four trajectories for Exp. CAP3a are considerably longer than their Exp. CAP2 counterparts since the low-level winds strengthen as the Exp. CAP3a particles travel further to the north. Note, too, that the same inertial 'wiggles' are present in the trajectories for both experiments; even though the synoptic-scale flow fields may differ, these two numerical experiments pass through the same sequence of diurnal stability regimes.

Concentration estimates

Figs. 6.22a–b show plan views of the Exps. CAP2 and CAP3a predicted clouds for the fourth 300-km-arc 3-hour sampling period. There are a number of differences apparent. The Exp. CAP2 predicted tracer cloud has travelled about half as far as the Exp. CAP3a cloud. The slower horizontal transport predicted for Exp. CAP2 results in a much wider exposure plume as compared to Exp. CAP3a (Table 6.4) since crosswind-sheared tracer in the upper part of the tracer cloud is mixed down *over* the 200-km arc in Exp. CAP2 but *past* this arc in Exp. CAP3a. One reason for the smaller CWIE value predicted for Exp. CAP2 is that the Exp. CAP2 had still not crossed the 200-km

equally-spaced arc entirely by the end of the sixth 3-hour sampling period so that not all the cloud tracer material was sampled[220].

Differences are even greater at the 800-km arc. As shown in Figs. 6.14a–b, the Exp. CAP3 GLC footprint has again travelled only about half as far from the release site as the Exp. CAP3a GLC footprint and has followed a more northerly track. The predicted cloud width, however, is comparable. Figs. 6.19b–c show the corresponding 36-hour time composite GLC patterns for the two experiments. These panels reinforce the differences seen in Figs. 6.14a–b. Note that no Exp. CAP2 values are listed in Tables 6.6, 6.7, or 6.8 since the tracer cloud had not reached the 800-km sampler arc by the end of Period VI.

Comparison of the GLC predictions for Exps. CAP2 and CAP3a thus suggest that horizontal variations in the large-scale flow field can have a significant impact on mesoscale dispersion predictions after after travel over distances of 200 km.

6.3.4 Effects of Synoptic-Scale Flow Nonstationarity

The trio of experiments CAP3a, CAP3b, and CAP5 together shed some light on the importance on large-scale flow nonstationarity in this mesoscale tracer dispersion case. As mentioned earlier in the discussion of the results of Exp. CAP5, the synoptic-scale flow over eastern North America changed considerably over the three days of interest. This is in contrast to the Great Plains case, where the large-scale flow was nearly stationary during the period of tracer transport.

Exp. CAP5 employed time-dependent lateral boundary conditions. Exps. CAP3a and CAP3b, on the other hand, used steady lateral boundary conditions so that any changes to the flow field should only arise from internal surface forcing due to the diurnal cycle. The RAMS simulations for all three numerical experiments were initialized using the VI option so that spatial variations in the large-scale flow field were represented. Both

---

[220] In fact, the maximum concentration value predicted for Exp. CAP2 for the 1200–1500 GMT period was over twice the maximum value during the 0900–1200 GMT sampling period.

Exps. CAP3a and CAP5 used the Sept. 25 1200 GMT NMC analyzed fields as the basis for their initial fields (see Fig. 3.18). The RAMS simulation for Exp. CAP3b was started at the same time as those for the other two experiments (Sept. 25, 1983, 1200 GMT) but its initial fields were based on the Sept. 26 1200 GMT NMC analyses, that is, on the synoptic conditions prevailing on the morning after the tracer release from Dayton. Differences between the Exp. CAP3a and CAP3b dispersion predictions were thus due solely to the differences between the initial meteorological fields (and to their subsequent evolution). Exp. CAP5 started with the same initial fields as Exp. CAP3a, but then the flow at its lateral boundaries was linearly adjusted in time by the observed flow for Sept. 26 at 0000 GMT, then 1200 GMT, and then Sept. 27 at 0000 GMt and 1200 GMT. *A priori*, we would thus expect Exp. CAP5 results to fall somewhere between those for Exp. CAP3a and CAP3b. This expectation turns out to agree reasonably well with the predicted results.

Mesoscale transport

Figs. 6.21c–d show plan views of the grid-scale trajectories released from Dayton at the beginning of the tracer release for Exps. CAP3a and CAP3b. Fig. 6.21f shows the corresponding trajectories for Exp. CAP5. As expected from comparing Figs. 3.18 and 3.19, the Exp. CAP3b grid-scale trajectories are rotated clockwise with respect to the Exp. CAP3a trajectories. Instead of crossing Lake Erie at its western end as in Exp. CAP3a, the Exp. CAP3b trajectories travel south of the lake. Not surprisingly, perhaps, the Exp. CAP3a trajectories match the observed tracer cloud concentrations initially but the Exp. CAP3b agree better with the observed GLC patterns at later sampling periods (see Fig. 3.23). The Exp. CAP5 trajectories start off very much like the Exp. CAP3a trajectories but then curve anticyclonically towards the east like the Exp. CAP3b trajectories. The Exp. CAP5 trajectories are also the longest of the three sets.

Concentration estimates

300-km arc. Figs. 6.22b–c show plan views of the Exps. CAP3a and CAP3b predicted clouds for the fourth 3-hour sampling period. Panel 'd' of the same figure shows the Exp. CAP4 cloud. (As discussed already, the Exp. CAP4 and CAP5 predictions were very similar so that the Exp. CAP4 panel can be used as a surrogate for Exp. CAP5.) The Exp. CAP3a and CAP4 clouds are very similar as might have been expected since the respective RAMS simulations should have been very similar for the first 6–9 hours (i.e., until the changing conditions at the Exp. CAP4 lateral boundaries began to be felt). The Exp. CAP3b cloud, though, is shorter and wider than the other two, has traveled a shorter distance, and is rotated clockwise relative to the other two cloud GLC patterns (consistent with the grid-scale trajectories).

Figs. 6.24 and 6.25 compare the 200-km-arc concentration–azimuth and concentration–travel time plots for Exps CAP3a and CAP3b, respectively. Figs. 6.11R and 6.12R show the corresponding plots for Exp. CAP5. Again, the panels for Exps. CAP3a and CAP5 are similar and different from the Exp. CAPP3b results. The Exp. CAP3a cloud is a bit slower than the Exp. CAP5 cloud but has the same transit time across the 200-km equally-spaced arc. Cloud centerline errors are also similar for these two experiments (see Table 6.5). The Exp. CAP3b predicted tracer cloud can be seen to have behaved differently from the other two in these figures as well. It has travelled more slowly than the Exp. CAP3a and CAP5 predicted clouds, is wider (for the absolute-threshold edge criterion), and has almost no centerline error.

From Tables 6.3 and Table 6.4, we find that Exp. CAP3b also has the highest CWIE value of the three experiments, although Exp. CAP3a has the highest peak station exposure value of the three. The Exp. CAP3b exposure plume is the widest of the three while the Exp. CAP3a exposure plume is the narrowest (Table 6.4). Similarly, we see from Table 6.5 that Exp. CAP3b has the highest peak concentration value of the three while Exp. CAP5 has the lowest value (and the nearest to the observed peak station concentration). Finally, Fig. 6.26 shows the unmatched and peak-matched concentration

scattergrams for Exps. CAP3a and CAP3b while Fig. 6.13 shows the corresponding scattergrams for Exp. CAP5. Again, the plots for Exps. CAP3a and CAP5 are similar. The pair of Exp. CAP3b scattergrams are almost identical because no time shift and only a 1° spatial shift were required. The greater number of non-zero concentration pairs for this experiment are probably due to the Exp. CAP3b predicted cloud's relatively longer transit time and greater width.

800-km arc. Figs. 6.23b–c show plan views of the Exps. CAP3a and CAP3b predicted clouds for the fourth 6-hour sampling period (i.e., Period IV). Fig. 6.23d shows the Exp. CAP4 cloud. Differences between the time-integrated GLC patterns are even more noticeable for this time period. The Exp. CAP3a and CAP4 patterns are both roughly horseshoe-shaped but the former has strong central cores in both its 'legs'. The Exp. CAP3b GLC pattern, in contrast, is more compact and bears more of a resemblance to the observed GLC pattern for this period (see Fig. 3.23c).

Figs. 6.27 and 6.28c compare the 800-km-arc concentration–azimuth and concentration–travel time plots for Exps CAP3a and CAP3b, respectively. Figs. 6.15R and 6.16R present the corresponding plots for Exp. CAP5. The Exp. CAP3a concentration–azimuth plot is quite similar to that for Exp. CAP5. The most interesting difference occurs for Period IV (1500–2100 GMT, Sept. 26) when the concentration–azimuth plot for Exp. CAP3a exhibits a bimodal structure but no gap between the two legs of the 'horseshoe' as in Fig. 6.15R. Compared to the other two experiments, the Exp. CAP3b cloud is clearly slower reaching the 800-km arc, is narrower as it crosses it, and is unimodal.

Table 6.7 also shows some differences between these three experiments. Exp. CAP3b has the narrowest exposure plume on this arc while Exp. CAP5 has the widest one. Exp. CAP3a has the highest peak station exposure and CWIE values of these three experiments; Exp. CAP5 has the lowest peak station exposure value while Exp. CAP3b has the lowest CWIE value. We see from Table 6.8 that Exp. CAP3a also has the highest peak concentration value of the three experiments. The Exp. CAP3a CWIE value agrees

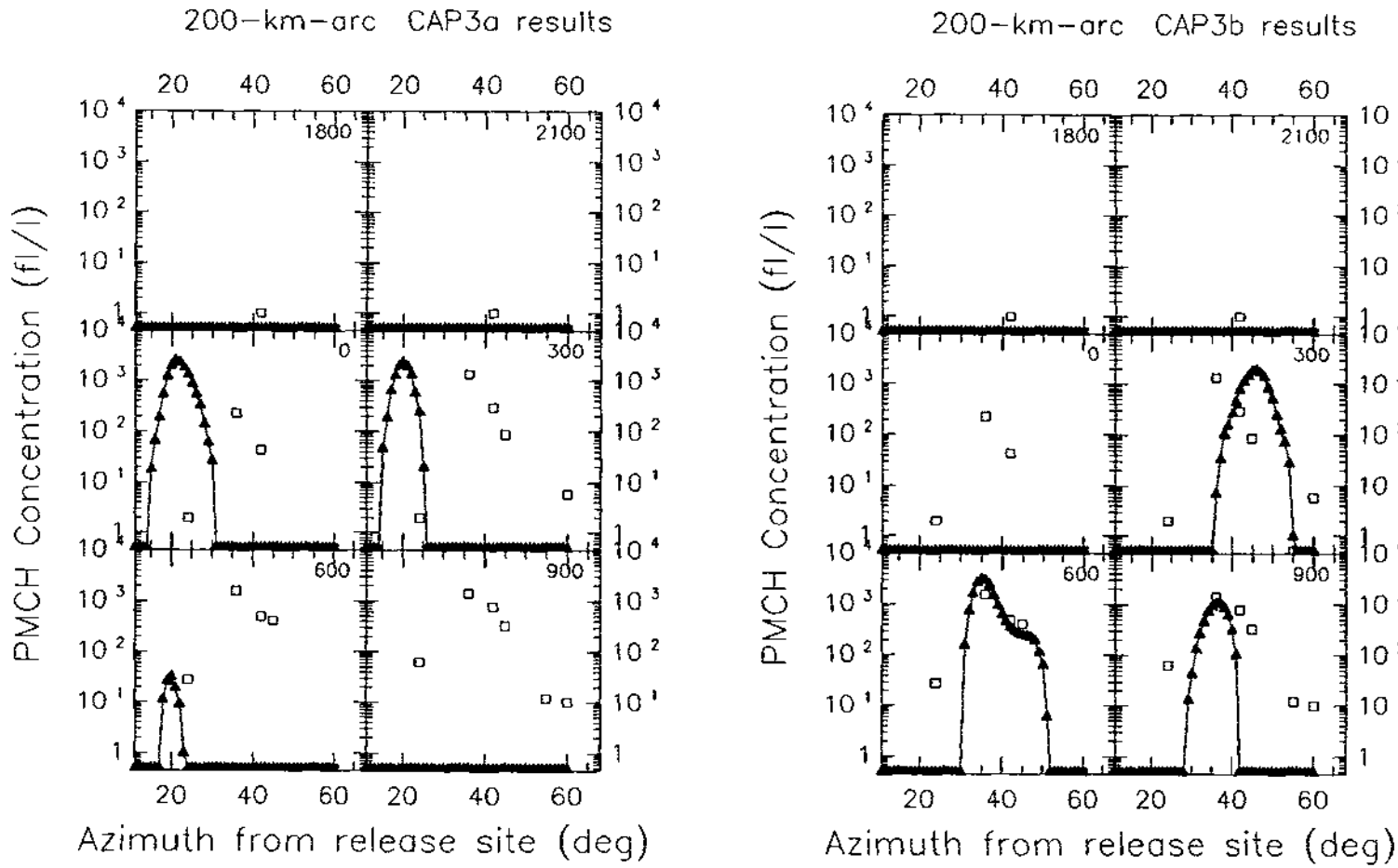

Figure 6.24: Observed and Exps. CAP3a (lefthand side; 'L') and CAP3b (righthand side; 'R') predicted PMCH concentration–azimuth plots plots for the 300-km sampling arc for all six 3-hour sampling periods (Sept. 25–26): (a) 1800–2100 GMT; (b) 2100–0000 GMT; (c) 0000–0300 GMT; (d) 0300–0600 GMT; (e) 0600–0900 GMT; and (f) 0900–1200 GMT. Observed values are indicated by open squares; predicted 200-km equally-spaced-site values are indicated by filled triangles connected by a solid line. The starting time of each sampling period (GMT) is plotted in the upper righthand corner of each panel.

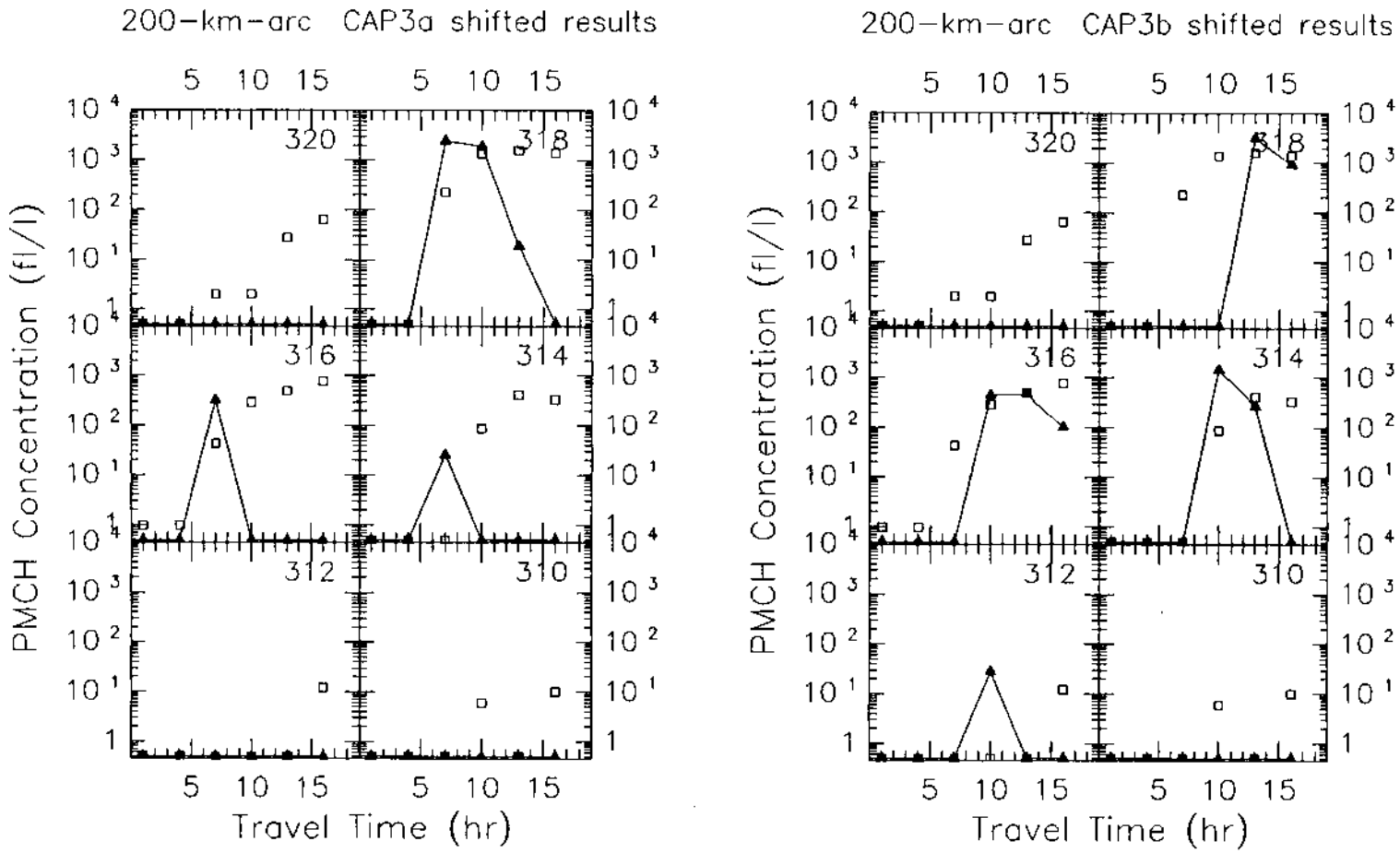

Figure 6.25: Observed and Exp. CAP3a (lefthand side; 'L') and CAP3b (righthand side; 'R') predicted PMCH concentration–time plots for six 300-km-arc sampling stations: (a) Station 310; (b) Station 312; (c) Station 314; (d) Station 316; (e) Station 318; and (f) Station 320. The Exp. CAP3a site values have been shifted eastward 15° and the Exp. CAP3b site values have been shifted eastward 1° in constructing this figure. Otherwise the same as Fig. 6.12.

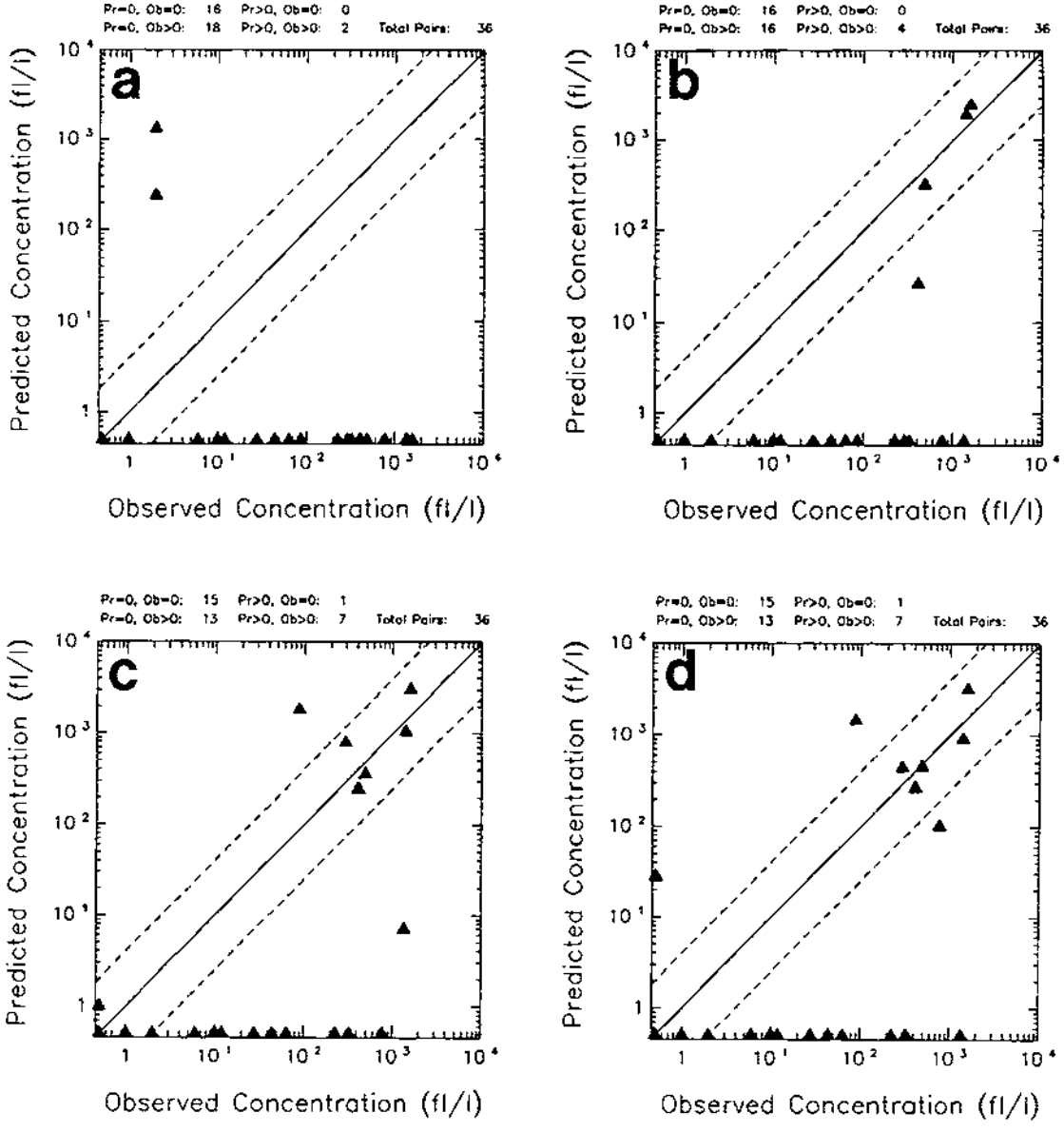

Figure 6.26: Scattergram for observed 300-km-arc PMCH concentrations vs. Exp. CAP3a (lefthand side; 'L') and Exp. CAP3b (righthand side; 'R') computed concentrations. The Exp. CAP3a site values have been shifted eastward 15° in space and ahead two sampling periods in time while the Exp. CAP3b site values have been shifted eastward 1° in space in constructing this figure. Otherwise the same as Fig. 6.13.

well with the observed value but the Exp. CAP3a peak concentration and exposure values are over twice the observed values. Finally, Fig. 6.29 shows the unmatched and peak-matched concentration scattergrams for Exps. CAP3a and CAP3b while Fig. 6.17 shows the corresponding scattergrams for Exp. CAP5.

The results of these three numerical experiments demonstrate the sensitivity of mesoscale dispersion to the evolution of the synoptic flow and also to different shear profiles (Exp. CAP3a vs. Exp. CAP3b). The Exp. CAP3a and Exp. CAP5 clouds behaved very similarly at the beginning of the simulations but began to show differences in their respective cloud characteristics on the second day of travel as the simulated surface clouds crossed the 800-km sampler arc. These differences arose from the evolution of the synoptic-scale flow pattern, which Exp. CAP5 accounted for but Exp. CAP3a did not. Exp. CAP3b gave significantly different results from the other two experiments. The low-level transport winds in this simulation were more westerly and slower than in the other two experiments. In terms of cloud arrival time at the 800-km arc, the Exp. CAP3b predicted cloud was late while the predicted clouds in the other two experiments were early (Table 6.8). Overall, the Exp. CAP5 simulation gave the best agreement with the observations, suggesting the importance of accounting for the evolution of the large-scale flow pattern in a dispersion simulation over several days. For transport over 24 hours or less, however, it may be possible to ignore synoptic evolution, barring significant changes such as a frontal passage.

6.4 Summary

A suite of six meteorological–dispersion experiments undertaken for the CAPTEX Release 2 case has been discussed in this chapter. The CAPTEX numerical suite was slightly smaller than the numerical suite run for the Great Plains case, but all of the RAMS simulations for the CAPTEX case were three-dimensional simulations and were run over a larger domain and longer time period than the Great Plains simulations. The

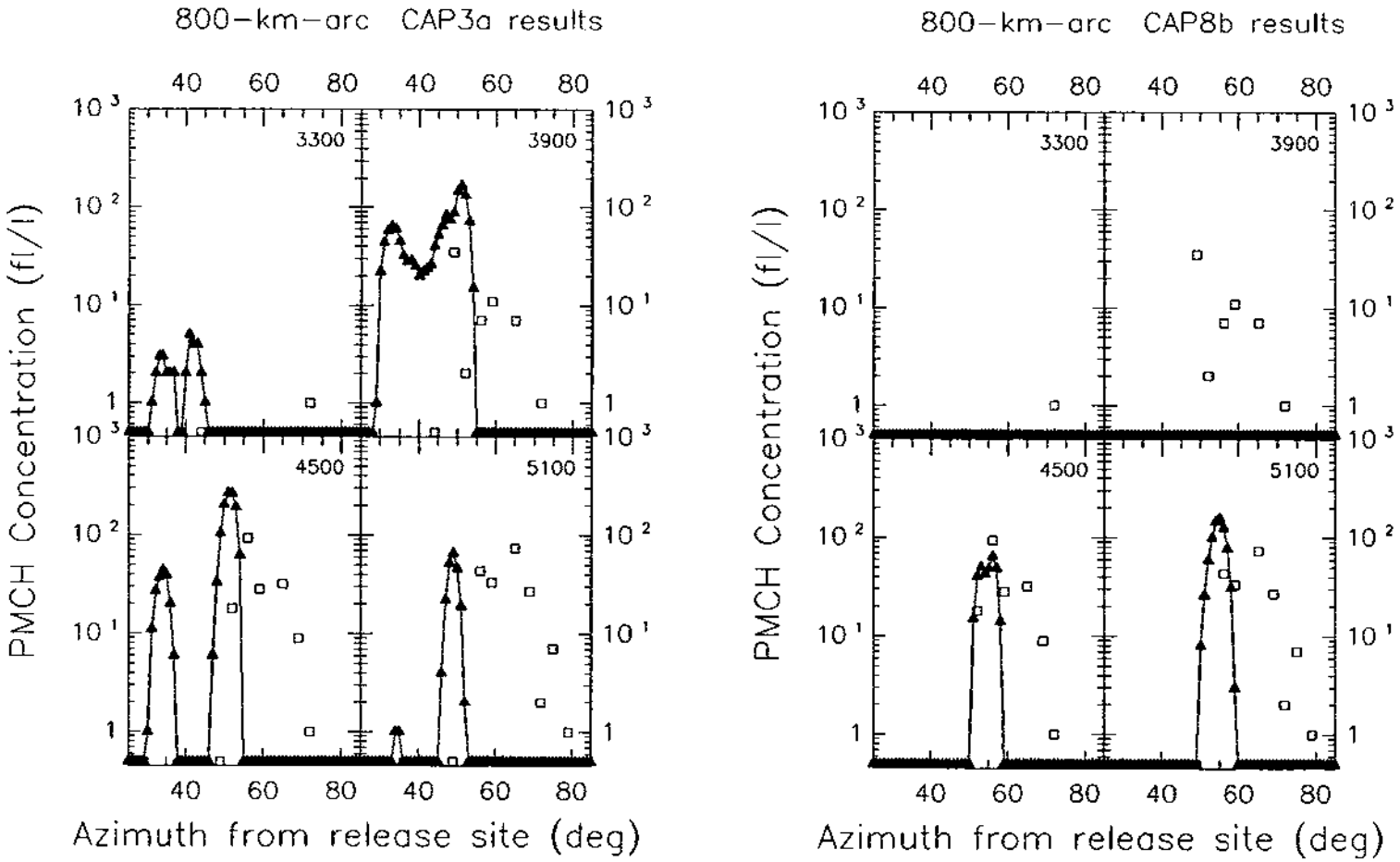

Figure 6.27: Observed and Exps. CAP3a (lefthand side; 'L') and CAP3b (righthand side; 'R') predicted PMCH concentration–azimuth plots for the 800-km sampling arc for the first four 6-hour sampling periods (Sept. 26–27, 1983) on this arc: (a) 0900–1500 GMT; (b) 1500–2100 GMT; (c) 2100–0300 GMT; and (d) 0300–0900 GMT. Observed values are indicated by open squares; predicted values are indicated by filled triangles connected by a solid line. The starting time of each sampling period (GMT) is plotted in the upper righthand corner of each panel.

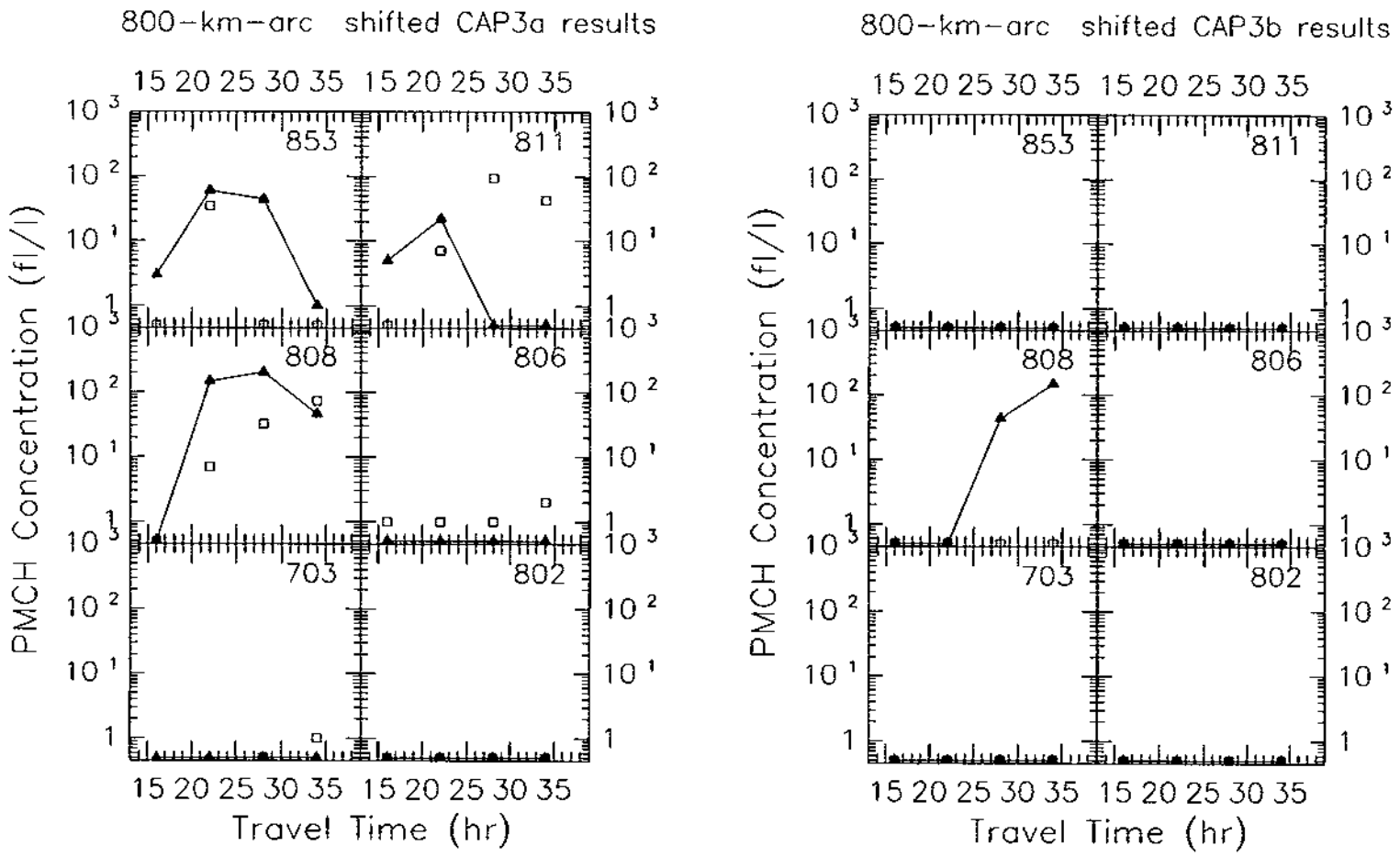

Figure 6.28: Observed and Exp. CAP3a (lefthand side; 'L') and CAP3b (righthand side; 'R') predicted PMCH concentration–time plots for six 800-km-arc sampling stations: (a) Station 853; (b) Station 811; (c) Station 808; (d) Station 806; (e) Station 703; and (f) Station 802. The Exp. CAP3a site values have been shifted southward 15° and the Exp. CAP3b site values have been shifted southward 11° in constructing this figure. Otherwise the same as Fig. 6.28.

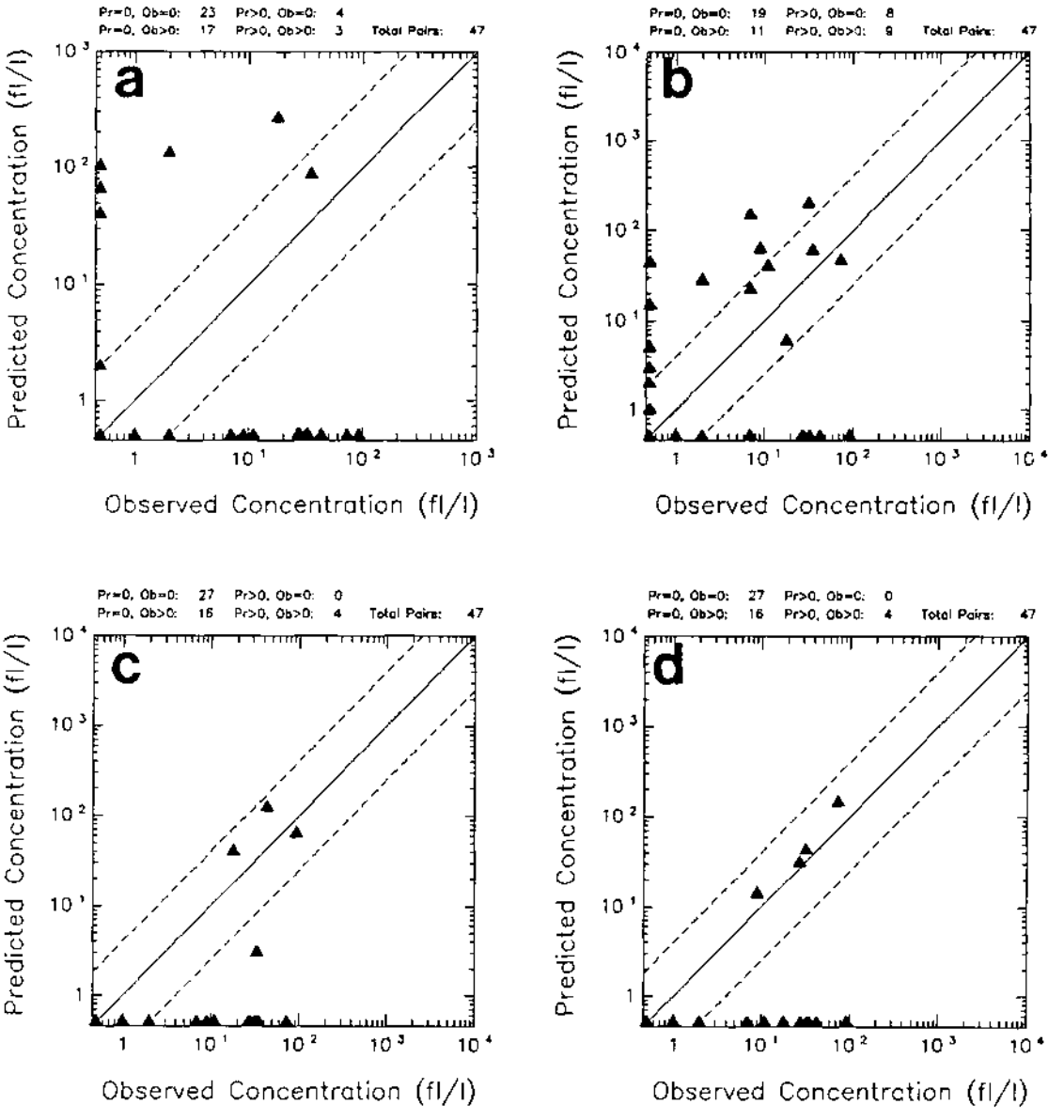

Figure 6.29: Scattergrams for observed 800-km-arc PMCH concentrations vs. Exp. CAP3a and Exp. CAP3b computed concentrations: (a) unmatched Exp. GP3a estimated concentrations; (b) peak-matched Exp. GP3a estimated concentrations; (c) unmatched Exp. GP3b estimated concentrations; and (d) peak-matched Exp. GP3b estimated concentrations. Plotted pairs have been drawn from the set of concentrations for Stations 802–853 and the first four 6-hour observing periods on this arc (from 0900–0900 GMT, Sept. 26–27) for panels (a) and (c). The Exp. CAP3a site values have been shifted southward 15° while the Exp. CAP3b site values have been shifted southward 11° in constructing this figure. The diagonal lines are the one-to-one correspondence line and two factor-of-4 (i.e., 1:4 and 4:1) lines.

same number of virtual particles, 3600, and same time step, 15 s, were used in the MLPDM runs for the two cases.

The most realistic of these six CAPTEX numerical mesoscale dispersion experiments, Exp. CAP5 (see Table 6.1), was treated as the control experiment. Exp. CAP5 used realistic gridded land-surface properties and was initialized with real-data meteorological fields based on a blending of NMC gridded analyses and upper-air soundings; the Davies external boundary condition was then employed in this simulation to incorporate observed temporal changes in the synoptic-scale flow at the lateral boundaries of the RAMS model domain during the simulation period.

The other five numerical experiments were sensitivity experiments for Exp. CAP5. All made at least one simplification to the Exp. CAP5 RAMS model configuration. Exp. CAP1, the most idealized experiment of the suite, assumed flat terrain. Both Exps. CAP1 and CAP2 assumed horizontally-homogeneous RAMS initial meteorological fields based on the Dayton upper-air sounding from the morning of the tracer release. Unlike the first two experiments, Exps. CAP3a and CAP3b were initialized with horizontally heterogeneous, real-data meteorological fields. But unlike Exp. CAP5, Exps. CAP3a and CAP3b did not use the Davies external lateral boundary condition and instead assumed stationary lateral boundary conditions (and hence a steady synoptic pattern). Exps. CAP3a and CAP5 were identical otherwise, so that differences between these two simulations would be entirely attributable to the evolution of the synoptic-scale flow field. Exp. CAP4 was identical to Exp. CAP5 as well, except for the neglect in Exp. CAP4 of geographical variations of surface properties other than terrain elevation. Differences between these two experiments could thus be attributed to the influence of mesoscale land-surface variability.

The analysis of results for the CAPTEX Release 2 suite of experiments followed that carried out in Chap. 5 for the Great Plains experiments. First, the Exp. CAP5 predicted meteorological fields and ground-level concentration fields were compared to the corresponding observed fields. The RAMS low-level wind-speed and wind-direction fields

agreed very well overall with NMC analyzed fields for Day 1 and Day 2 (i.e., Sept. 26 and 27, 1983). The Davies external lateral boundary condition was successful in bringing a large-scale trough across the RAMS model domain during the 48-hour simulation period. The MLPDM was then used to calculate grid-scale trajectories for five particles launched over a 1700-meter-thick layer at the start of the 3-hour tracer release from Dayton International Airport. These grid-scale trajectories crossed the 300-km sampling arc at nearly the observed crossing point but then travelled somewhat too far to the north compared to GLC measurements made later during the experimental period. The end-point spread of the five trajectories also showed the significant speed and directional shear present in just the first 1700 m during this period. The middle trajectories were the longest, suggesting the presence of a low-level jet during the simulation.

Plots of projections of the MLPDM particle cloud for Exp. CAP5 (Figs. 6.4–6.4) reveal the evolution of the cloud into a 'horseshoe' shape due to the interplay of mesoscale deformation and diurnally-modulated vertical mixing. Wind shear effects were very significant in this evolution; the bending back of the upper leg of the 'horseshoe' occurred as a result of the lighter winds above the mid-level jet nose. Note that a similar horseshoe shape was evident towards the end of the Great Plains simulations (see Figs. 5.43 and 5.43). The particle-cloud plots also suggested that alongwind cloud elongation due to speed shear can be augmented by diurnally-varying directional shear in a three-step process for cloud dispersion over a long enough period to include two PBL evening transitions.

Some exposure-calculation experiments were carried out to test the sensitivity of the ground-level exposure estimates to the choice of sampling-volume depth (Fig. 6.9). The calculated exposure patterns were quite sensitive to this choice. As a result, a shallow sampling-volume depth (134 m) was used for all subsequent concentration and exposure calculations.

GLC estimates for Exp. CAP5 were then compared against measurements made on the 300-km and 800-km sampling arcs. The quantitative tracer-cloud characteristics calculated for the 300-km arc were in good agreement overall. The peak concentration

values were comparable in magnitude as were the cloud widths based on the 10%-of-peak edge criterion. The predicted cloud width based on the 3 fll^{-1} edge criterion, however, was narrower than the observed cloud by half (Table 6.5). The predicted CWIE value for Exp. CAP5 was also less than half the observed value. This difference might have been due to the shorter-than-observed transit time across the 300-km arc predicted by the Exp. CAP5 simulation, that is, 6–9 h vs. 12+ h (depending upon the choice of cloud-edge criterion). It is worth noting, however, that it was the *observed* cloud transit time across the 300-km sampling arc which was surprisingly *long*. Consider that in the Great Plains tracer experiment, where the release time t_r was also 3 hours, that the cloud transit time across the 600-km sampler arc was equal to or shorter than the transit time in the CAPTEX Release 2 case across what was effectively (at its western end) a 200-km sampler arc.

Comparison of GLC patterns from later in the Exp. CAP5 simulation with observed patterns (Fig. 6.14 vs. Fig. 3.22) revealed both similarities and differences. Probably the most significant similarity from the point of view of evaluating the importance of the role played by Pasquill's delayed-mixing mechanism for shear-enhanced dispersion was the change in GLC pattern between sampling Periods II and III. Both the observations and Exp. CAP5 simulation suggest an explosive lateral growth of the surface footprint after the morning PBL transition, consistent with the convective mix-down of elevated, differentially-advected tracer material. The observed concentrations along the 800-km arc also displayed a bimodal structure, though weaker than the predicted (and probably exaggerated) Exp. CAP5 'split' plume. In terms of differences, the Exp. CAP5 cloud was transported too quickly and too far to the north. The quantitative tracer-cloud characteristics calculated for Exp. CAP5 for the passage of the predicted GLC footprint across the 800-km arc are given in Table 6.8. Predicted peak concentration levels and maximum cloud width are comparable (141 vs. 93 fll^{-1} and 350 vs. 395 km) but the predicted CWIE value is lower than the observed value by close to a factor of two.

Results from the five sensitivity experiments carried out in addition to Exp. CAP5 provide some additional insight into the influence of terrain elevation variations, land-surface characteristic variability, and spatial and temporal variations in the synoptic-scale flow pattern on the predicted mesoscale dispersion. The use of the single-sounding initialization option for RAMS based on the Dayton upper-air sounding for the morning of the tracer release produced quite different dispersion predictions from the variable-initialization runs, which accounted for horizontal variations in the large-scale flow field, even after only 200 km of travel (e.g., Exp. CAP2 vs. Exp. CAP3a). Temporal changes in the synoptic-scale pattern were less important initially but produced significant differences by the second day of transport (e.g., Exp. CAP3a vs. Exp. CAP5). Comparison of Exps. CAP3a and Exp. CAP3b provides one example of the effect of changing the vertical shear characteristics of the initial large-scale flow field on subsequent mesoscale dispersion. Finally, mesoscale variations in land-surface properties were found to produce small but significant differences in mesoscale dispersion over a two-day period (Exp. CAP4 vs. Exp. CAP5).

Chapter 7

CONCLUSIONS AND RECOMMENDATIONS

This is the end ...

Jim Morrison (1943–1971)

This chapter attempts to distill the material presented in the last two chapters and to highlight the main points therein by listing the major and minor conclusions of this study. The conclusions are then followed by recommendations for further research.

7.1 Conclusions

A number of conclusions can be drawn from the results of this study. They will be presented in two groups, with major conclusions first followed by minor conclusions.

- *The CSU mesoscale dispersion modelling system demonstrated skill when its ground-level concentration predictions were compared against observed concentrations from the two case studies considered in this study and against the GLC predictions of other modelling studies of these same two cases.*

  For example, the CSU system gave a better estimate of the arrival time of the tracer cloud at the 600-km sampler arc in the Great Plains case than did seven other models. The success of this prediction is probably attributable to the prediction of the development of the nocturnal low-level jet in the RAMS meteorological simulation. The CSU mesoscale dispersion modelling system also predicted the explosive daytime widening of the tracer surface footprint on the second day of transport in the

CAPTEX Release 2 simulation. Quantitative pattern comparison results were generally good for both cases. Some qualitative features such as crosswind shifting of the concentration peak with time along the sampling arcs were also reproduced. The main source of error in modelling the dispersion of the tracer clouds for the two cases arose from directional errors in the low-level wind fields, which in turn produced tracer-cloud centerline offsets.

- *Pasquill's (1962) delayed-mixing mechanism for the shear enhancement of lateral diffusion was found to be important for the two case studies considered.*

  As hypothesized in Chap. 1, mesoscale atmospheric flow features did contribute significantly to dispersion in the planetary boundary layer over mesoscale and longer distances through the interplay of shear processes, differential advection, and Pasquill's (1962) delayed-mixing mechanism for the two case studies considered in this study. This is likely to be true in general for warm-season mesoscale dispersion in the PBL over land. The critical component is the diurnally-modulated coupling and interaction between differential advection and turbulent mixing. In cases of mesoscale dispersion over relatively uniform terrain with a weak diurnal PBL cycle, such as cold-season dispersion or overwater dispersion, this mechanism will probably play a smaller role.

  The GLC measurements made during the Great Plains and CAPTEX tracer releases provide indirect and direct evidence, respectively, of the occurrence of shear-enhanced lateral dispersion due to delayed mixing. In the Great Plains case, the numerical simulations suggest that the timing of the tracer release and transport was such that the convective mixdown of elevated tracer from the sheared cloud did not occur until most of that material had been carried past the 600 km arc. The observed eastward shift of the concentration peak with time is consistent with this mechanism, however. It is worth noting too that most of the predictions of the simpler LRTAP models for this case (see Figs. 3.11, 3.12) had the *surface* tracer cloud located further to the east than was observed. However, most of these models

handled vertical diffusion crudely. They actually performed better in terms of locating the *three-dimensional* (but elevated) cloud center of mass. In the CAPTEX case, the significant role played by delayed mixing is strongly suggested in Fig. 3.22 by the explosive widening of the cloud in phase with the transition from night to day.

The delayed-mixing mechanism will likely be very important too for mesoscale and synoptic-scale dispersion in the free troposphere, where both vertical and horizontal shear are large in magnitude and nearly ubiquitous. The major difference between this shear environment and the PBL is that vertical or horizontal coupling and mixing is intermittent. There is no equivalent to the modulation of PBL turbulence and mixing by the diurnal cycle of surface heating and cooling. Other processes will provide the vertical transport and mixing. One such process, which is likely to be significant throughout the year, is Kelvin-Helmholtz instability and subsequent turbulent mixing associated with the jet stream and travelling or standing internal gravity waves (e.g., Sec. 2.1.8). Moist convection will also be important on a variety of scales of organization: thunderstorms, mesoscale convective systems, and extratropical and tropical cyclones (e.g., Lyons et al., 1986; Cotton and Anthes, 1989). A third process is large-scale vertical motions associated with atmospheric waves. Mesoscale free-tropospheric dispersion for a PBL source is at least partly similar to the injection and dispersion of stratospheric material as in the case of stratospheric intrusions of ozone and nuclear fallout (e.g., Danielsen, 1961; List et al., 1965; Feely et al., 1966; Bamber et al., 1984; Holton, 1990; Ebel et al., 1991).

- *The neglect of wind shear by models of mesoscale atmospheric dispersion can result in significant errors in the prediction of cloud size, cloud shape, cloud centroid location, and surface footprint pattern if the tracer cloud has experienced a sequence of at least two PBL stability regimes.*

  The horseshoe-shaped cloud seen at night in the daytime residual layer in both case studies is quite different from the traditional conception in LRTAP modelling of

a vertically well-mixed cylindrical puff expanding uniformly in all directions. The surface footprint will also differ in size and shape from the cloud's *projected* footprint after differential advection and deformation under stable conditions. Consistent with this, examination of observed and predicted crosswind-integrated exposure (CWIE) values in this study suggests that surface GLC measurements will not always be representative of the entire tracer cloud, especially at night. Brost et al. (1988a) and Holland (1991) have also raised this concern.

- *Three mesoscale time scales, the diurnal period, the daylight period, and the inertial period, can be significant in episodic mesoscale atmospheric dispersion because they control the time variations of the PBL wind-shear profile.*

  These three time scales collectively determine the timing of the morning and evening PBL transitions, the formation and evolution of the nocturnal low-level jet, and the daytime erosion of the elevated residual layer. As a result, time of release, time of sampling, and latitude may all affect the characteristics of observed or simulated mesoscale dispersion. For example, this study adds support to Carras and Williams's (1988) suggestion that the particular sequence of daytime and nighttime periods experienced by a dispersing cloud will affect its size and shape. It also points out some limitations inherent in mesoscale dispersion diagrams such as Figs. 2.23–2.26 that do not stratify their data points based on parcel stability history, release time, and observing time. The results of this study suggest that the large variability observed in these composite diagrams probably arises at least in part due to the wide range of atmospheric synoptic conditions over which the dispersion observations were made and is not due only to sampling fluctuations. Accordingly, empirical dispersion relationships such as Heffter's (1965) equation (Eq. 2.40) may not perform very well for many synoptic scenarios. The good news is that by accounting for release time, observing time, and the characteristics of the synoptic-scale and mesoscale flow fields explicitly, it should be possible to explain much of the variability in observed dispersion found in the empirical studies.

- *Both of the case studies considered herein illustrate the significant role of along-wind cloud elongation in mesoscale dispersion.*

  After transport over meso-α-scale distances (e.g., 500–1000 km), the alongwind length of the Great Plains and CAPTEX tracer clouds had increased by a factor of 4 to 10, a value much greater than would be expected due to turbulent diffusion alone. Draxler and Taylor (1982) and Fowler and Barr (1983) have suggested that the responsible mechanism for such elongation is speed shear. The CSU mesoscale dispersion modelling system simulations of these releases, which were described in Chaps. 5 and 6, also predicted considerable alongwind elongation due to speed shear, although not quite as pronounced as that observed (see the predicted and observed transit times listed in Tables 5.5, 6.5, and 6.8). Note too from Figs. 6.4c–d and 6.5c–d that in the case of delayed mixing, such elongation might not be measurable at ground-level until the next period of fumigation. For cloud dispersion over a long enough period to include two PBL evening transitions, the numerical simulations indicated that alongwind elongation could be augmented by directional shear as well due to upper-level veering on the first night followed by vertical mixing during the day and low-level backing on the second night (see Fig. 6.4).

- *Modelling mesoscale dispersion is a particularly demanding test of a mesoscale meteorological model as well as the air-quality model with which it is coupled.*

  Minor errors in grid-scale wind direction which would not even be noticeable in other contexts become significant for this application, since wind direction is the single most important meteorological quantity in atmospheric dispersion modelling. Other important meteorological quantities for mesoscale dispersion modelling include mean horizontal wind speed, low-level shear strength, mean vertical motion, turbulence intensity, and PBL height. Each of these quantities depends on many aspects of the meteorological model. For example, good predictions of turbulence intensity require good predictions of low-level wind and temperature structure, which in turn require good predictions of surface temperature, vertical

diffusion, radiation, and horizontal advection. Surface temperature alone depends on the contributions of shortwave and longwave fluxes, sensible and latent heat fluxes, and soil heat fluxes. These quantities in turn are influenced by surface characteristics such as soil moisture distribution, soil texture, surface roughness, albedo, and plant physiology and by atmospheric characteristics such as low-level wind speed and relative humidity, cloud shading, and vertical moisture distribution. Predicting the correct timing for such major changes as the morning and evening PBL transitions is also important.

The preceding conclusions were the primary conclusions of this study. A number of secondary conclusions can also be drawn.

- A mesoscale dispersion modelling system which employs a prognostic meteorological model in a pure forecast mode to estimate grid-scale wind and turbulence fields can be at a disadvantage compared to one which incorporates wind-field observations throughout the simulation period when the synoptic pattern is changing rapidly, since wind-field forecast errors will cause larger and larger errors in the dispersion prediction as time passes. This, of course, is only relevant in post-event analysis. For purposes of emergency response to an accident or for operational planning and management of a mesoscale tracer experiment in the field, however, only wind forecasts will be available, not observations of what has yet to happen. In such cases, a mesoscale dispersion modelling system which employs a prognostic meteorological model in a pure forecast mode will be the best available tool. Moreover, as shown in this study, the use of time-dependent lateral boundary conditions can improve prognosed wind fields in either a research or operational[221] application. Although not tested here, full four-dimensional assimilation of meteorological observations by the prognostic meteorological model should reduce errors in the grid-scale wind fields

[221] If such time-dependent LBCs can be obtained from a larger-scale forecast.

even further, thus leading to improved mesoscale transport and diffusion predictions. Exps. GP4a and CAP3a were the two simulations carried out in this study for the Great Plains and CAPTEX case studies in which the CSU mesoscale dispersion modelling system was run in a pure forecast mode with realistic atmospheric initial fields.

- The presence of an oscillatory ageostrophic component in both the NMC analyzed synoptic-scale low-level wind fields and in individual upper-air sounding for the Great Plains case made RAMS initialization more difficult. This component was most likely due to the superposition of an inertial oscillation on the synoptic-scale flow field. The fact that this oscillation has not been widely recognized as requiring special treatment in summertime simulations over the Great Plains probably reflects the particular emphasis on low-level wind direction in the present study.

- Mesoscale variations in land-surface characteristics were found to influence simulations of mesoscale dispersion for both case studies, although the magnitude of the changes to the predicted GLC pattern were relatively small. Larger changes might be seen for simulations using finer-scale horizontal resolution than used here (see next section).

- Trajectory envelopes can give good first-order estimates of the size, shape, and location of an ensemble mesoscale tracer cloud. The limitations of this method must be borne in mind, however. That is, it cannot represent subgrid-scale advection, particularly vertical turbulent diffusion or terrain-locked coherent circulations such as lake breezes. It presumes that the tracer is mixed throughout the depth of the vertical layer in which the trajectory particles are released. And it cannot represent subgrid-scale surface processes such as canopy trapping.

- Mesoscale deformation and differential advection should dominate small-scale turbulence diffusion in terms of their relative contributions to mesoscale lateral dispersion

when vertical wind shear is present. In such cases, the shear horizontal length scale $t\,\Delta V$ will be much greater than the corresponding small-scale turbulence length scale $(t\,K_x)^{1/2}$ (cf. Eq. 2.44), where ΔV is the maximum of the change in the lateral velocity component from the Earth's surface to the top of the PBL or residual layer[222]. Moreover, the strongest vertical shear normally occurs at night when turbulent diffusion is weakest. The success of trajectory envelopes (e.g., Fig. 5.6) in predicting tracer-cloud size, shape, and location supports this conclusion.

- The success of these mesoscale dispersion simulations suggests that the truncation of the mesoscale energy spectrum due to the relatively coarse horizontal grid resolution employed in these simulations was not a major problem (cf. Sec. 1.8). Similarly, the use of a first-order turbulence parameterization appeared to be sufficient for these mesoscale dispersion cases. For Pasquill's delayed-shear mechanism, first-order characteristics of vertical mixing such as duration and depth should in general much more important than the second-order characteristics which would be better modelled by a higher-order turbulence closure scheme.

- A one-particle dispersion model for small-scale turbulent absolute diffusion can be used successfully in conjunction with a mesoscale meteorological model to make quantitative concentration estimates in mesoscale *relative* diffusion episodes. The reason for this is that relative to mesoscale temporal averaging scales of days, the grid-scale mesoscale flow field predicted by the mesoscale meteorological model corresponds to a single time-dependent realization of the mesoscale flow field. That is, mesoscale 'eddies' are represented explicitly on the model grid even though small-scale turbulent eddies are fully parameterized and completely subgrid-scale. Pairs of particles are thus not independent at grid scale but rather can be advected in unison by the same coherent grid-scale flow structures. Thus, the small-scale one-

---

[222] Recall the discussion in Sec. 1.7 of the studies of Högström (1964), Smith (1965), Tyldesley and Wallington (1965), and Csanady (1969).

particle model becomes a two-particle model on the mesoscale. One restriction on this interpretation, however, is that the effects of some mesoscale eddies, namely, those smaller in horizontal scale than $4\Delta x$ but larger than one or two PBL depths, will not be represented even though they would contribute to mesoscale diffusion.

- There is circumstantial evidence from the Great Plains tracer observations and numerical simulation of the secondary tracer cloud to suggest that tracer material or pollutant may become trapped in a vegetation canopy overnight and then be released after sunrise. In effect, the canopy acts as a temporary tracer 'reservoir'. If this is in fact a real phenomenon, it will have implications for designing future mesoscale tracer experiments and for planning and managing the emergency response to an accidental release of hazardous airborne material. In both cases, a secondary tracer cloud may appear well after the primary cloud has passed.

- It is important to specify clearly and explicitly the criterion used to determine the location of the edge of a tracer cloud since estimates of cloud size are sensitive to the edge criterion chosen.

- As discussed by Holland (1988, 1991), the estimation of dispersion parameters from a network of sampler measurements can be complicated by the sparseness, unevenness, or incompleteness of the sampling network. The concentration measurements from the Great Plains experiment and from CAPTEX suffered from all three problems. The estimation of concentrations along artificial equally-spaced sampler arcs[223] in the numerical experiments permitted better estimates to be made of quantitative characteristics of the simulated cloud because the cloud was sampled uniformly and with high resolution over its entire width.

---

[223] Concentration estimates were also made for actual sampler locations.

7.2 Recommendations for Further Research

As noted by Mark Pattison[224], "... research is always incomplete." In that spirit, then, here are some thoughts on directions in which the present study could be extended.

- The large-scale flow in CAPTEX Release 2 initially carried the tracer cloud over Lakes Erie and Ontario. It is likely that lake breezes were present during the daytime and modified the low-level synoptic flow. These large lakes were still just barely represented by the grid spacing used in the Chap. 6 experiments, however. The importance of the physiographically-forced mesoscale circulations due to these lakes could be investigated by carrying out a RAMS and MLPDM nested-grid experiment. The inner, higher-resolution grid would be set up to contain both lakes. The results from such a simulation could then be compared against the Exp. CAP5 results.

- All of the numerical experiments described in this study used RAMS in a prognostic or forecast mode. CAPTEX employed an unusually high-resolution rawinsonde network with twice the normal number of stations and twice the normal frequency of soundings. It would be of interest to try some 4DDA experiments for the CAPTEX Release 2 case to see if incorporation of upper-air observations directly into the interior dynamic and thermodynamic fields could improve the CSU mesoscale dispersion modelling system simulation of this case.

- One strength of this study was its consideration of two dissimilar but complementary cases. General principles begin to reveal themselves and new phenomena may be seen if a number of varied cases are examined. Other candidates for future study and simulation include some of the other six CAPTEX releases. CAPTEX Release 1 was quite similar to Release 2 in terms of synoptic situation and transport path (e.g., Ferber et al., 1986). However, the Release 1 cloud remained much narrower than the Release 2 cloud as it travelled, and it would be interesting to explore the

---

[224] Chap. 10 of *Isaac Casaubon: 1559–1614*, Second Edition, 1892, Clarendon Press, Oxford.

reasons for this difference. CAPTEX Release 3 would provide another interesting case-study candidate: in this release most of the tracer remained aloft and did not mix down to the surface, even though this release was again broadly similar to Release 2 in terms of synoptic environment and transport path (Davis et al., 1986; Ferber et al., 1986; Draxler, 1987). CAPTEX Releases 5 and 7 are of interest because they are significantly different than Releases 1–4: (a) they took place later in the year (late October); (b) the synoptic environment was different (post-cold frontal vs. backside of a high); and (c) the tracer was released at night rather than during the day. Another set of candidates are the numerous (66) ANATEX releases (e.g., Draxler and Heffter, 1989; Haagenson et al., 1990). These are winter and early spring cases and the perfluorocarbon tracers released were tracked about three times as far (3000 km) as in CAPTEX (see Table 2.4). One factor which could be examined in an ANATEX case study is the role of synoptic-scale wind shear due to warm or cold advection in mesoscale dispersion (e.g., Holt et al., 1990).

- It might be possible to streamline the RAMS mesoscale Lagrangian particle dispersion model for some mesoscale applications. For the experiments carried out in the present study, this component of the MAD modelling system took more computer time and required more computer memory than the RAMS meteorological model. Shi et al. (1990) and Uliasz and Pielke (1991) have used a random-walk-with-no-memory approach to increase the allowable time step. The advantages of the more complicated finite-memory formulation decrease rapidly with downwind distance from the source so this simpler approach may be satisfactory provided that (a) it produces similar results to the current MLPDM formulation and (b) that it does not lead to unrealistic behaviour such as particle accumulation above the PBL. Another modification which may be required is the formulation and addition of a parameterization of vegetation canopy trapping. There have been numerous Lagrangian particle model studies of flow and dispersion within a canopy (e.g., Raupach, 1988) but I am not aware of any to date which have considered tracer

fluxes between the canopy and the air above. Given the relatively shallow canopy thickness, the canopy may have to be parameterized as a single layer for mesoscale air pollution applications.

REFERENCES

Acheson, D. J., 1976: On over-reflexion. *J. Fluid Mech.*, **77**, 433–472.

Achtemeier, G. L., 1991: Reducing hydrostatic truncation error in a mesobeta boundary layer model. *Mon. Wea. Rev.*, **119**, 223–229.

Aguado, E., 1990: Effect of advected pollutants on solar radiation attenuation: Mojave Desert, California. *Atmos. Environ.*, **24B**, 153–157.

Alexander, R. C. and R. L. Mobley, 1974: Monthly average sea-surface temperatures and ice-pack limits on a 1° global grid. Report No. R-1310-ARPA, December, The Rand Corporation, Santa Monica, California, 30 pp.

Alexander, R. C. and R. L. Mobley, 1976: Monthly average sea-surface temperatures and ice-pack limits on a 1° global grid. *Mon. Wea. Rev.*, **104**, 143–148.

Amen, R. and T. Maxworthy, 1980: The gravitational collapse of a mixed region into a linearly stratified fluid. *J. Fluid Mech.*, **96**, 65–80.

AMS/EPA, 1987: Review of short-term long-range models. Unpublished report, June, American Meteorological Society/Environmental Protection Agency Steering Committee on Air Quality Models, 20 pp. [Available from Prof. R.T. McNider, Dept. of Mathematics and Statistics, University of Alabama at Huntsville, Huntsville, AL 35899].

Andrén, A., 1990a: Evaluation of a turbulence closure scheme suitable for air-pollution applications. *J. Appl. Meteor.*, **29**, 224–239.

Andrén, A., 1990b: A meso-scale plume dispersion model: preliminary evaluation in a heterogeneous area. *Atmos. Environ.*, **24A**, 883–896.

Angell, J. K., 1961: Use of constant level balloons in meteorology. *Adv. Geophys.*, **8**, 137–219.

Angell, J. K., 1962: On the use of tetroons for the estimation of atmospheric dispersion on the mesoscale. *Mon. Wea. Rev.*, **90**, 263–270.

Angell, J. K. and D. H. Pack, 1960: Analysis of some preliminary low-level constant level balloon (tetroon) flights. *Mon. Wea. Rev.*, **88**, 235–248.

Angell, J. K. and D. H. Pack, 1965: Atmospheric lateral diffusion estimates from tetroons. *J. Appl. Meteor.*, **4**, 418–425.

Angell, J. K., P. W. Allen, and E. A. Jessup, 1971: Mesoscale relative diffusion estimates from tetroon flights. *J. Appl. Meteor.*, **10**, 43–46.

Angell, J. K., D. H. Pack, L. Machta, C. R. Dickson, and W. H. Hoecker, 1972: Three-dimensional air trajectories determined from tetroon flights in the planetary boundary layer of the Los Angeles Basin. *J. Appl. Meteor.*, **11**, 451–471.

Anthes, R. A., 1970: Numerical experiments with a two-dimensional horizontal variable grid. *Mon. Wea. Rev.*, **98**, 810–822.

Anthes, R. A., 1983: Regional models of the atmosphere in middle latitudes. *Mon. Wea. Rev.*, **111**, 1306–1335.

Anthes, R. A., 1986: The general question of predictability. In *Mesoscale Meteorology and Forecasting*, Ray, P. S., Editor, American Meteorological Society, Boston, 636–656.

Anthes, R. A. and T. T. Warner, 1978: Development of hydrodynamic models suitable for air pollution and other mesometeorological studies. *Mon. Wea. Rev.*, **106**, 1045–1078.

Anthes, R. A., E.-Y. Hsie, and Y.-H. Kuo, 1987: Description of the Penn State/NCAR mesoscale model version 4 (MM4). NCAR Tech. Note NCAR/TN-282+STR, May, National Center for Atmospheric Research, Boulder, Colorado, 66 pp.

ApSimon, H. M., A. J. H. Goddard, and J. Wrigley, 1985: Long-range atmospheric dispersion of radioisotopes — I. The MESOS model. *Atmos. Environ.*, **19**, 99–111.

Arakawa, A. and W. H. Schubert, 1974: Interaction of a cumulus cloud ensemble with the large-scale environment: Part I. *J. Atmos. Sci.*, **31**, 674–701.

Aris, R., 1956: On the dispersion of a solute in a fluid flowing through a tube. *Proc. Roy. Soc. Lond.*, **A235**, 67–77.

Arritt, R. W., 1985: Numerical studies of thermally and mechanically forced circulations over complex terrain. Final Report, Contract No. NA81RAH00001, Amendment 17, Item 15, December, National Park Service, U.S. Department of the Interior, Denver, Colorado, 201 pp.

Arritt, R. W., 1987: The effect of water surface temperature on lake breezes and thermal internal boundary layers. *Boundary-Layer Meteor.*, **40**, 101–125.

Arritt, R. W., R. A. Pielke, and M. Segal, 1988: Variations of sulfur dioxide deposition velocity resulting from terrain-forced mesoscale circulations. *Atmos. Environ.*, **22**, 715–723.

Atkinson, B. W., 1981: *Meso-scale Atmospheric Circulations.* Academic Press, New York, 495 pp.

Augustine, J. A. and E. J. Zipser, 1987: The use of wind profilers in a mesoscale experiment. *Bull. Amer. Meteor. Soc.*, **87**, 4–17.

Avissar, R., M. D. Moran, G. Wu, R. N. Meroney, and R. A. Pielke, 1990: Operating ranges of mesoscale numerical models and meteorological wind tunnels for the simulation of sea and land breezes. *Boundary-Layer Meteor.*, **50**, 227–275.

Axford, D. N., 1968: On the accuracy of wind measurements using an inertial platform in an aircraft, and an example of a measurement of the vertical mesostructure of the atmosphere. *J. Appl. Meteor.*, **7**, 645–666.

Axford, D. N., 1971: Spectral analysis of an aircraft observation of gravity waves. *Quart. J. Roy. Meteor. Soc.*, **97**, 313–321.

Babiano, A., C. Basdevant, and R. Sadourny, 1985: Structure functions and dispersion laws in two-dimensional turbulence. *J. Atmos. Sci.*, **42**, 941–949.

Babiano, A., C. Basdevant, P. Le Roy, and R. Sadourny, 1990: Relative dispersion in two-dimensional turbulence. *J. Fluid Mech.*, **214**, 535–557.

Bader, D. C., T. B. McKee, and G. J. Tripoli, 1987: Mesoscale boundary layer evolution over complex terrain. Part I: Numerical simulation of the diurnal cycle. *J. Atmos. Sci.*, **44**, 2823–2838.

Baer, F., 1972: An alternate representation of atmospheric energy spectra. *J. Atmos. Sci.*, **29**, 649–664.

Baer, F., 1974: Hemispherical spectral statistics of APE. *J. Atmos. Sci.*, **74**, 932–941.

Baines, P. G., 1987: Upstream blocking and airflow over mountains. *Ann. Rev. Fluid Mech.*, **19**, 75–97.

Baldocchi, D. D. and T. P. Meyers, 1988: Turbulence structure in a deciduous forest. *Boundary-Layer Meteor.*, **43**, 345–364.

Baldwin, L. V. and G. R. Johnson, 1974: An estimate of space-time correlations. *Boundary-Layer Meteor.*, **5**, 373–377.

Balsley, B. B. and D. A. Carter, 1982: The spectrum of atmospheric velocity fluctuations at 8 km and 86 km. *Geophys. Res. Lett.*, **9**, 465–468.

Balsley, B. B. and K. S. Gage, 1982: On the use of radars for operational wind profiling. *Bull. Amer. Meteor. Soc.*, **63**, 1009–1018.

Bamber, D. J., P. G. W. Healey, B. M. R. Jones, S. A. Penkett, A. F. Tuck, and G. Vaughan, 1984: Vertical profiles of tropospheric gases: chemical consequences of stratospheric intrusions. *Atmos. Environ.*, **18**, 1759–1766.

Barat, J., 1983: The fine structure of the stratospheric flow revealed by differential sounding. *J. Geophys. Res.*, **88**, 5219–5228.

Barat, J. and C. Cot, 1989: Simultaneous measurements of wind shear and temperature gradient spectra in the stratosphere. *Geophys. Res. Lett.*, **16**, 1161–1164.

Barnes, S. L., 1973: Mesoscale objective map analysis using weighted time-series observations. NOAA Tech. Memo. ERL NSSL-62, March, National Severe Storms Laboratory, National Oceanic and Atmospheric Administration, Norman, Oklahoma, 38 pp.

Barr, S. and C. W. Kreitzberg, 1975: Horizontal variability and boundary-layer modeling. *Boundary-Layer Meteor.*, **8**, 163–172.

Barr, S. and F. A. Gifford, 1987: The random force theory applied to regional scale tropospheric diffusion. *Atmos. Environ.*, **21**, 1737–1741.

Barr, S., W. E. Clements, and P. R. Guthals, Editors, 1984: *Atmospheric Tracer Workshop, Santa Fe, New Mexico, May 21–25, 1984.* Report No. LA-10301-C, December, Los Alamos National Laboratory, Los Alamos, New Mexico, 381 pp.

Barrie, L. A., M. P. Olson, and K. K. Oikawa, 1989: The flux of anthropogenic sulphur into the Arctic from mid-latitudes in 1979/80. *Atmos. Environ.*, **23**, 2505–2512.

Bartello, P. and G. Holloway, 1991: Passive scalar transport in β-plane turbulence. *J. Fluid Mech.*, **223**, 521–536.

Bass, A., 1980: Modeling long range transport and diffusion. In *Proc. 2nd Joint AMS/APCA Conf. on Applications of Air Pollution Meteorology*, March 24-27, New Orleans, American Meteorological Society, Boston, 193–215.

Bastable, H. G., D. P. Rogers, and D. E. Schorran, 1990: Tracers of opportunity and pollutant transport in southern California. *Atmos. Environ.*, **24B**, 137–151.

Batchelor, G. K., 1949: Diffusion in a field of homogeneous turbulence. *Austral. J. Sci. Res.*, **A2**, 437–450.

Batchelor, G. K., 1950: The application of the similarity theory of turbulence to atmospheric diffusion. *Quart. J. Roy. Meteor. Soc.*, **76**, 133–146.

Batchelor, G. K., 1952: Diffusion in a field of homogeneous turbulence. II: The relative motion of particles. *Proc. Camb. Phil. Soc.*, **48**, 345–362.

Batchelor, G. K., 1953: *The Theory of Homogeneous Turbulence.* Cambridge University Press, 197 pp.

Batchelor, G. K., 1959: Small-scale variation of convected quantities like temperature in a turbulent fluid. Part 1: General discussion and the case of small conductivity. *J. Fluid Mech.*, **5**, 113–133.

Batchelor, G. K., 1969: Computation of the energy spectrum in homogeneous two-dimensional turbulence. *Phys. Fluids Suppl. II,* 233–239.

Batchelor, G. K. and A. A. Townsend, 1956: Turbulent diffusion. In *Surveys in Mechanics*, Batchelor, G. K. and R. M. Davies, Editors, Cambridge University Press, Cambridge, 352–399.

Bauer, E., 1974: Dispersion of tracers in the atmosphere and ocean: survey and comparison of experimental data. *J. Geophys. Res.*, **79**, 789–795.

Bench, H. L., R. W. Bench, W. P. Elliott, G. J. Ferber, R. N. Dietz, S. Barr, W. E. Clements, M. M. Fowler, P. R. Guthals, W. A. Sedlacek, C. D. Kern, D. P. Pepper, and A. L. Turkevich, 1978: Heavy methane—SF_6 tracer test conducted at the Savannah River Plant, December 10, 1975. Report DP-1469, Savannah River Laboratory, Aiken, South Carolina.

Benjamin, S. G., K. A. Brewster, R. Brümmer, B. F. Jewett, T. W. Schlatter, T. L. Smith, and P. A. Stamus, 1991: An isentropic three-hourly data assimilation system using ACARS aircraft observations. *Mon. Wea. Rev.*, **119**, 888–906.

Bennett, A. F. and D. B. Haidvogel, 1983: Low-resolution numerical simulation of decaying two-dimensional turbulence. *J. Atmos. Sci.*, **40**, 738–748.

Benoit, R., J. Côté, and J. Mailhot, 1989: Inclusion of a TKE boundary layer parameterization in the Canadian regional finite-element model. *Mon. Wea. Rev.*, **117**, 1726–1750.

Benton, G. S. and A. B. Kahn, 1958: Spectra of large-scale atmospheric flow at 300 millibars. *J. Meteor.*, **15**, 404–410.

Beran, D. W., W. H. Hooke, and S. F. Clifford, 1973: Acoustic echo-sounding techniques and their application to gravity-wave, turbulence, and stability studies. *Boundary-Layer Meteor.*, **4**, 133–153.

Bhumralkar, C. M., 1986: Regional air quality model assessment and evaluation. In *Air Pollution Modeling and Its Application V*, de Wispelaere, C., Editor, Plenum Press, New York, 483-500.

Bigg, E. K., G. P. Ayers, and D. E. Turvey, 1978: Measurement of the dispersion of a smoke plume at large distances from the source. *Atmos. Environ.*, **12**, 1815–1818.

Blackadar, A. K., 1957: Boundary layer wind maxima and their significance for the growth of nocturnal inversions. *Bull. Amer. Meteor. Soc.*, **38**, 283–290.

Blackall, R. M. and J. Gloster, 1981: Forecasting the airborne spread of foot and mouth disease. *Weather*, **36**, 162–167.

Bleck, R. and P. L. Haagenson, 1968: Objective analysis on isentropic surfaces. Tech. Note NCAR-TN-39, National Center for Atmospheric Research, Boulder, Colorado, 27 pp.

Bluestein, H. B., 1986: Fronts and jet streaks: a theoretical perspective. In *Mesoscale Meteorology and Forecasting*, Ray, P. S., Editor, American Meteorological Society, Boston, 173–215.

Blumen, W., 1972: Geostrophic adjustment. *Rev. Geophys. Space Phys.*, **10**, 485–528.

Boatman, J. F., N. Laulainen, J. Ray, C. Van Valin, L. Gunter, R. Lee, D. Luecken, and K. Busness, 1990: Acid precursor concentrations above the northeastern United States during summer 1987: three case studies. *J. Geophys. Res.*, **95**, 11831–11845.

Boer, G. J., 1983: Homogeneous and isotropic turbulence on the sphere. *J. Atmos. Sci.*, **40**, 154–163.

Boer, G. J. and T. G. Shepherd, 1983: Large-scale two-dimensional turbulence in the atmosphere. *J. Atmos. Sci.*, **40**, 164–184.

Bonner, W. D., 1968: Climatology of the low level jet. *Mon. Wea. Rev.*, **96**, 833–850.

Bonner, W. D. and J. Paegle, 1970: Diurnal variations in boundary layer winds over the south central United States in summer. *Mon. Wea. Rev.*, **98**, 735–744.

Booker, J. R. and F. P. Bretherton, 1967: The critical layer for internal gravity waves in a shear flow. *J. Fluid Mech.*, **27**, 513–539.

Bougeault, P., 1983: A non-reflective upper boundary condition for limited-height hydrostatic models. *Mon. Wea. Rev.*, **111**, 420–429.

Bowden, K. F., 1965: Horizontal mixng in the sea due to a shearing current. *J. Fluid Mech.*, **21**, 83–95.

Bowne, N. E., D. J. McNaughton, and M. A. Allan, 1991: A summary of the Operational Evaluation Network. In *Seventh Joint AMS/AWMA Conf. on Applications of Air Pollution Meteorology*, Jan. 14-18, New Orleans, Louisiana, American Meteorological Society, Boston, 152–155.

Brachet, M. E., M. Meneguzzi, H. Politano, and P. L. Sulem, 1988: The dynamics of freely decaying two-dimensional turbulence. *J. Fluid Mech.*, **194**, 333–349.

Bretherton, C. S. and P. K. Smolarkiewicz, 1989: Gravity waves, compensating subsidence and detrainment around cumulus clouds. *J. Atmos. Sci.*, **46**, 740–759.

Bretherton, F. P., 1969a: Waves and turbulence in stably stratified fluids. *Radio Sci.*, **4**, 1279–1287.

Bretherton, F. P., 1969b: Momentum transport by gravity waves. *Quart. J. Roy. Meteor. Soc.*, **95**, 213–243.

Bretherton, F. P., 1969c: The spectral gap. *Radio Sci.*, 4, 1361–1363.

Brier, G. W., 1950: The statistical theory of turbulence and the problem of diffusion in the atmosphere. *J. Meteor.*, **7**, 283–290.

Briscoe, M. G., 1975: Introduction to collection of papers on oceanic internal waves. *J. Geophys. Res.*, **80**, 289–290.

Brost, R. A., P. L. Haagenson, and Y.-H. Kuo, 1988a: Eulerian simulation of tracer distribution during CAPTEX. *J. Appl. Meteor.*, **27**, 579–593.

Brost, R. A., P. L. Haagenson, and Y.-H. Kuo, 1988b: The effect of diffusion on tracer puffs simulated by a regional scale Eulerian model. *J. Geophys. Res.*, **93**, 2389–2404.

Browand, F. K. and E. J. Hopfinger, 1985: The inhibition of vertical turbulent scale by stable stratification. In *Turbulence and Diffusion in Stable Environments*, Hunt, J. C. R., Editor, Clarendon Press, Oxford, 15–27.

Brown, Jr., P. S. and G. D. Robinson, 1979: The variance spectrum of tropospheric winds over Eastern Europe. *J. Atmos. Sci.*, **36**, 270–286.

Brown, R. A., 1980: Longitudinal instabilities and secondary flows in the planetary boundary layer: a review. *Rev. Geophys. Space Phys.*, **18**, 683–697.

Brown, R. M., L. A. Cohen, and M. E. Smith, 1972: Diffusion measurements in the 10–100 km range. *J. Appl. Meteor.*, **11**, 323–334.

Brown, R. M., M. J. Leach, G. S. Raynor, and P. A. Michael, 1984: A summary and index of the weather documentation for the 1983 Cross-Appalachian Tracer Experiments. Informal Report No. BNL 36879, December, Department of Applied Science, Brookhaven National Laboratory, Upton, New York, 41 pp.

Brusasca, G., G. Tinarelli, and D. Anfossi, 1989: Comparison between the results of a Monte Carlo atmospheric diffusion model and tracer experiments. *Atmos. Environ.*, **23**, 1263–1280.

Buell, C. E., 1957: Synoptic scale motion of the atmosphere as two dimensional isotropic turbulence. *J. Meteor.*, **14**, 471–472.

Busch, N. E., 1969: Waves and turbulence. *Radio Sci.*, **4**, 1377–1379.

Bushnell, R. H. and P. O. Huss, 1958: A power spectrum of surface winds. *J. Meteor.*, **15**, 180–183.

Businger, J. A., J. C. Wyngaard, Y. Izumi, and E. F. Bradley, 1971: Flux-profile relationships in the atmospheric surface layer. *J. Atmos. Sci.*, **28**, 181–189.

Cadet, D., 1978: The superpressure balloon sounding technique for the study of atmospheric meso- and microscale phenomena. *Bull. Amer. Meteor. Soc.*, **59**, 1119–1127.

Camp, D. W., 1971: The Jimsonde — a high resolution temperature sensor. *J. Geophys. Res.*, **76**, 8613–8620.

Canavero, F. G. and F. Einaudi, 1987: Time and space variability of spectral estimates of atmospheric pressure. *J. Atmos. Sci.*, 44, 1589–1604.

Carhart, R. A., A. J. Policastro, M. Wastag, and L. Coke, 1989: Evaluation of eight short-term long-range transport models using field data. *Atmos. Environ.*, **23**, 85–105.

Carmichael, G. R., L. K. Peters, and T. Kitada, 1986: A second generation model for regional-scale transport/chemistry/deposition. *Atmos. Environ.*, **20**, 173–188.

Carras, J. N. and D. J. Williams, 1981: The long-range dispersion of a plume from an isolated point source. *Atmos. Environ.*, **15**, 2205–2217.

Carras, J. N. and D. J. Williams, 1986: Experimental studies of plume dispersion in convective conditions — II. Horizontal plume dispersion. *Atmos. Environ.*, **20**, 2307–2314.

Carras, J. N. and D. J. Williams, 1988: Measurements of relative σ_y up to 1800 km from a single source. *Atmos. Environ.*, **22**, 1061–1069.

Carruthers, D. J. and J. C. R. Hunt, 1985: Turbulence and wave motions near an interface between a turbulent region and a stably stratified region. In *Turbulence and Diffusion in Stable Environments*, Hunt, J. C. R., Editor, Clarendon Press, Oxford, 29–60.

Carruthers, D. J. and C.-H. Moeng, 1987: Waves in the overlying inversion of the convective boundary layer. *J. Atmos. Sci.*, **44**, 1801–1808.

Caughey, S. J. and C. J. Readings, 1975: An observation of waves and turbulence in the Earth's boundary layer. *Boundary-Layer Meteor.*, **9**, 279–296.

Chadwick, R. B. and E. E. Gossard, 1986: Radar probing and measurement of the planetary boundary layer: I. Scattering from refractive index irregularities. In *Probing the Atmospheric Boundary Layer*, Lenschow, D. H., Editor, American Meteorological Society, Boston, 163–182.

Chang, J. S., R. A. Brost, I. S. A. Isaksen, S. Madronich, P. Middleton, W. R. Stockwell, and C. J. Walcek, 1987: A three-dimensional Eulerian acid deposition model: physical concepts and formulation. *J. Geophys. Res.*, **92**, 14681–14700.

Charney, J. G., 1971: Geostrophic turbulence. *J. Atmos. Sci.*, **28**, 1087–1095.

Charney, J. G., R. Fjørtoft, and J. von Neumann, 1950: Numerical integration of the barotropic vorticity equation. *Tellus*, **2**, 237–254.

Charnock, H., 1955: Wind stress on a water surface. *Quart. J. Roy. Meteor. Soc.*, **81**, 639–640.

Chatwin, P. C., 1971: On the interpretation of some longitudinal dispersion experiments. *J. Fluid Mech.*, **48**, 689–702.

Chatwin, P. C. and P. J. Sullivan, 1980: The core-bulk structure associated with diffusing clouds. In *Turbulent Shear Flows 2*, Bradbury, L. J. S., F. Durst, B. E. Launder, F. W. Schmidt, and J. H. Whitelaw, Editors, Springer-Verlag, New York, 379–389.

Chatwin, P. C. and P. J. Sullivan, 1979a: The basic stucture of clouds of diffusing contaminant. In *Mathematical Modelling of Turbulent Diffusion in the Environment*, Harris, C. J., Editor, Academic Press., New York, 3–32.

Chatwin, P. C. and P. J. Sullivan, 1979b: The relative diffusion of a cloud of passive contaminant in incompressible turbulent flow. *J. Fluid Mech.*, **91**, 337–355.

Chatwin, P. C. and P. J. Sullivan, 1979c: Measurements of concentration fluctuations in relative turbulent diffusion. *J. Fluid Mech.*, **94**, 83–101.

Chen, C. and W. R. Cotton, 1983: A one-dimensional simulation of the stratocumulus-capped mixed layer. *Boundary-Layer Meteor.*, **25**, 289–321.

Chen, T.-C. and A. Wiin-Nielsen, 1978: On nonlinear cascades of atmospheric energy and enstrophy in a two-dimensional spectral index. *Tellus*, **30**, 313–322.

Chimonas, G. and J. R. Grant, 1984a: Shear excitation of gravity waves. Part I: Modes of a two-scale atmosphere. *J. Atmos. Sci.*, **41**, 2269–2277.

Chimonas, G. and J. R. Grant, 1984b: Shear excitation of gravity waves. Part II: Upscale scattering from Kelvin-Helmholtz waves. *J. Atmos. Sci.*, **41**, 2278–2288.

Ching, J. K. S. and A. J. Alkezweeny, 1986: Tracer study of vertical exchange by cumulus clouds. *J. Climate Appl. Meteor.*, **25**, 1702–1711.

Ching, J. K. S., S. T. Shipley, and E. V. Browell, 1988: Evidence for cloud venting of mixed layer ozone and aerosols. *Atmos. Environ.*, **22**, 225–242.

Cho, H.-R. and T. L. Clark, 1981: A numerical investigation of the structure of vorticity fields associated with a deep convective cloud. *Mon. Wea. Rev.*, **109**, 1654–1670.

Chock, D. P. and Y.-H. Kuo, 1990: Comparison of wind-field models using the CAPTEX data. *J. Appl. Meteor.*, **29**, 76–91.

Chopra, K. P., 1973: Atmospheric and oceanic flow problems introduced by islands. *Adv. Geophys.*, **16**, 297–421.

Chung, Y. S., 1986: Air pollution detection by satellites: the transport and deposition of air pollutants over oceans. *Atmos. Environ.*, **20**, 617–630.

Chung, Y.-S. and H. V. Le, 1984: Detection of forest-fire smoke plumes by satellite imagery. *Atmos. Environ.*, **18**, 2143–2151.

Chung, Y. S., A. Gallant, F. Fanaki, and M. Millán, 1981: On the observations of Mount St Helens volcanic emissions. *Atmos. Ocean*, **19**, 172–178.

Clapp, R. B. and G. M. Hornberger, 1978: Empirical equations for some soil hydraulic properties. *Water Resources Res.*, **14**, 601–604.

Clark, P. A., I. S. Fletcher, A. S. Kallend, W. J. McElroy, A. R. W. March, and A. H. Webb, 1984: Observations of cloud chemistry during long-range transport of power plant plumes. *Atmos. Environ.*, **18**, 1849–1858.

Clark, T. L., 1977: A small-scale dynamic model using a terrain-following coordinate transformation. *J. Comp. Phys.*, **24**, 186–215.

Clark, T. L., 1979: Numerical simulations with a three-dimensional cloud model: lateral boundary condition experiments and multicellular severe storm simulations. *J. Atmos. Sci.*, **36**, 2191–2215.

Clark, T. L. and R. Gall, 1982: Three-dimensional numerical model simulations of airflow over mountainous terrain: a comparison with observations. *Mon. Wea. Rev.*, **110**, 766–791.

Clark, T. L. and W. R. Peltier, 1984: Critical level reflection and the resonant growth of nonlinear mountain waves. *J. Atmos. Sci.*, **41**, 3122–3134.

Clark, T. L. and R. D. Farley, 1984: Severe downslope windstorm calculations in two and three spatial dimensions using anelastic interactive grid nesting: a possible mechanism for gustiness. *J. Atmos. Sci.*, **41**, 329–350.

Clark, T. L. and R. D. Cohn, 1990: The Across North America Tracer Experiment (ANATEX) model evaluation study. Technical Report EPA/600/3-90/051, June, U. S. Environmental Protection Agency, Research Triangle Park, North Carolina, 141 pp.

Clark, T. L., T. Hauf, and J. P. Kuettner, 1986: Convectively forced internal gravity waves: results from two-dimensional numerical experiments. *Quart. J. Roy. Meteor. Soc.*, **112**, 899–925.

Clark, T. L., E. C. Voldner, R. L. Dennis, S. K. Seilkop, M. Alvo, and M. P. Olson, 1989: The evaluation of long-term sulfur deposition models. *Atmos. Environ.*, **23**, 2267–2288.

Clarke, J. F., T. L. Clark, J. K. S. Ching, P. L. Haagenson, R. B. Husar, and D. E. Patterson, 1983: Assessment of model simulation of long-distance transport. *Atmos. Environ.*, **17**, 2449–2462.

Clarke, R. H., A. J. Dyer, R. R. Brook, D. G. Reid, and A. J. Troup, 1971: The Wangara experiment: boundary layer data. Division of Meteorological Physics Technical Paper 19, Commonwealth Scientific and Industrial Research Organization, Melbourne, Australia, 21 pp. + Appendices.

Clements, W. E., Editor, 1979: Experimental design and data of the April 1977 multitracer atmospheric experiment at the Idaho National Engineering Laboratory. Informal Report LA–7795–MS, Los Alamos Scientific Laboratory, P.O. Box 1663, Los Alamos, NM 87545, 96 pp.

Clements, W. E., J. A. Archuleta, and P. H. Gudiksen, 1989: Experimental design of the 1984 ASCOT field study. *J. Appl. Meteor.*, **28**, 405–413.

Clerici, G., R. Salerno, and S. Sandroni, 1991: Time evolution of breeze circulations in alpine valleys. In *Air Pollution Modeling and Its Application VIII*, van Dop, H. and D. G. Steyn, Editors, Plenum Press, New York, 349–360.

Cogan, J. L., 1985: Monte Carlo simulation of buoyant dispersion. *Atmos. Environ.*, **19**, 867–878.

Colwell, R. C. and A. W. Friend, 1939: Reflection of medium and short radio waves in the troposphere. *Nature*, **144**, 31.

Comte-Bellot, G. and S. Corrsin, 1971: Simple Eulerian time correlation of full- and narrow-band velocity signals in grid-generated "isotropic" turbulence. *J. Fluid Mech.*, **48**, 272–337.

Cooke, T. H., 1962: A smoke-trail technique for measuring wind. *Quart. J. Roy. Meteor. Soc.*, **88**, 82–88.

Corrsin, S., 1953: Remarks on turbulent heat transfer. In *Proc. First Iowa Symp. on Thermodynamics*, University of Iowa, Iowa City, Iowa, 5–30.

Corrsin, S., 1959: Outline of some topics in homogeneous turbulent flow. *J. Geophys. Res.*, **64**, 2134–2150.

Corrsin, S., 1962: Theories of turbulent dispersion. In *Mécanique de la turbulence*, Centre National de la Recherche Scientifique, Paris, 27–52.

Corrsin, S., 1974: Limitations of gradient transport models in random walks and in turbulence. *Adv. Geophys.*, **18A**, 25–60.

Cosby, B. J., G. M. Hornberger, R. B. Clapp, and T. R. Ginn, 1984: A statistical exploration of the relationships of soil moisture characteristics to the physical properties of soils. *Water Resources Res.*, **20**, 682–690.

Cot, C. and J. Barat, 1989: Spectral analysis of high resolution temperature profiles in the stratosphere. *Geophys. Res. Lett.*, **16**, 1165–1168.

Cotton, W. R., 1986: Averaging and the parameterization of physical processes in mesoscale models. In *Mesoscale Meteorology and Forecasting*, Ray, P. S., Editor, American Meteorological Society, Boston, 614–635.

Cotton, W. R. and R. A. Anthes, 1989: *Storm and Cloud Dynamics*. Academic Press, Inc., San Diego, 883 pp.

Cotton, W. R., M. A. Stephens, T. Nehrkorn, and G. J. Tripoli, 1982: The Colorado State University three-dimensional cloud/mesoscale model — 1982. Part II: An ice phase parameterization. *J. Rech. Atmos.*, **16**, 295–320.

Cotton, W. R., C. J. Tremback, and R. L. Walko, 1988: CSU RAMS – a cloud model goes regional. In *Proc. NCAR Workshop on Limited-Area Modeling Intercomparison*, Nov. 15–18, Boulder, Colorado, National Center for Atmospheric Research, Boulder, 202–211. (Available from Dr. Y.-H. Kuo, Mesoscale and Microscale Meteorology Division, NCAR, P.O. Box 3000, Boulder, CO 80307).

Coulman, C. E., 1973: Vertical profiles of small-scale temperature structure in the atmosphere. *Boundary-Layer Meteor.*, 4, 169–177.

Court, A., 1965: Undulence and turbulence. *Quart. J. Roy. Meteor. Soc.*, **91**, 234–235.

Courtney, M. and I. Troen, 1990: Wind speed spectrum from one year of continuous 8 Hz measurements. In *Proc. Ninth AMS Symp. on Turbulence and Diffusion*, Apr. 30–May 3, Roskilde, Denmark, American Meteorological Society, Boston, 301–304.

Cowan, G. A., D. G. Ott, A. Turkevich, L. Machta, G. J. Ferber, and N. R. Daly, 1976: Heavy methanes as atmospheric tracers. *Science*, **191**, 1048–1050.

Cox, W. M., 1987: Protocol for determining the best performing model. Unpublished manuscript, September, U.S. Environmental Protection Agency, Research Triangle Park, North Carolina, 14 pp. + App.

Cox, W. M. and J. A. Tikvart, 1986: Assessing the performance level of air quality models. In *Air Pollution Modeling and Its Application V*, De Wispelaere, C., F. A. Schiermeier, and N. V. Gillani, Editors, Plenum Press, New York, 425–440.

Crabtree, J., 1959: The travel and diffusion of the radioactive material emitted during the Windscale accident. *Quart. J. Roy. Meteor. Soc.*, **85**, 362–370.

Crabtree, J., 1984: Studies of plume transport and dispersion over distances of travel up to several hundred kilometers. In *Air Pollution Modeling and Its Application III*, De Wispelaere, C., Editor, Plenum Press, 129–138.

Crabtree, J. and M. Kitchen, 1984: The long-range travel and dispersion of the plume from the Mount St Helens volcano. *Atmos. Environ.*, **18**, 1073–1079.

Cram, J. M., 1990: Numerical simulation and analysis of the propagation of a prefrontal squall line. Atmospheric Science Paper 471, Department of Atmospheric Science, Colorado State University, Fort Collins, Colorado, 332 pp.

Cram, J. M., R. A. Pielke, and W. R. Cotton, 1992a: Numerical simulation and analysis of a prefrontal squall line. Part I: Propagation of the squall line as an internal gravity wave. *J. Atmos. Sci.*, **49**, 189–208.

Cram, J. M., R. A. Pielke, and W. R. Cotton, 1992b: Numerical simulation and analysis of a prefrontal squall line. Part II: Propagation of the squall line as an internal gravity wave. *J. Atmos. Sci.*, **49**, 209–225.

Crawford, K. C. and H. R. Hudson, 1973: The diurnal wind variation in the lowest 1500 ft in central Oklahoma: June 1966 – May 1967. *J. Appl. Meteor.*, **12**, 127–132.

Crawford, T. V., 1966: A computer program for calculating the atmospheric dispersion of large clouds. Technical Report UCRL-50179, Lawrence Radiation Laboratory, University of California, Livermore, Calif., 56 pp.

Crawford, T. V., 1967: Atmospheric diffusion of large clouds. In *Proc. USAEC Meteor. Info. Meeting*, Sept. 11–14, Chalk River, Ontario, Canada, Doc. AECL-2787, Chalk River Nuclear Laboratories, Atomic Energy of Canada, Ltd, Ottawa, Canada, 191–214.

Crowder, H. J. and C. Dalton, 1971: Errors in the use of nonuniform mesh systems. *J. Comput. Phys.*, **7**, 32–45.

Csanady, G. T., 1966: Accelerated diffusion in the skewed shear flow of lake currents. *J. Geophys. Res.*, **71**, 411–420.

Csanady, G. T., 1969: Diffusion in an Ekman layer. *J. Atmos. Sci.*, **26**, 414–426.

Csanady, G. T., 1972: Crosswind shear effects on atmospheric diffusion. *Atmos. Environ.*, **6**, 221–232.

Csanady, G. T., 1973: *Turbulent Diffusion in the Environment.* D. Reidel Publishing Co., Dordrecht, 248 pp.

Dabberdt, W. F. and R. N. Dietz, 1986: Gaseous tracer technology and applications. In *Probing the Atmospheric Boundary Layer*, American Meteorological Society, Boston, 103–128.

Dabberdt, W. F. and W. Viezee, 1987: South Central Coast Cooperative Aerometric Monitoring Program (SCCCAMP). *Bull. Amer. Meteor. Soc.*, **68**, 1098–1110.

Dalaudier, F. and C. Sidi, 1987: Evidence and interpretation of a spectral gap in the turbulent atmospheric temperature spectra. *J. Atmos. Sci.*, **44**, 3121–3126.

Dalaudier, F., J. Barat, F. Bertin, E. Brun, M. Crochet, and F. Cuq, 1985: Comparison between S.T. radar and *in situ* balloon measurements. In *Proc. 7th ESA Symp. on European Rocket & Balloon Programmes and Related Research*, May 5–11, Loen, Norway, ESA SP-229, European Space Agency, Paris, 247–251.

D'Almeida, G. A., 1986: A model for Saharan dust transport. *J. Climate Appl. Meteor.*, **25**, 903–916.

Dalu, G. A. and R. A. Pielke, 1989: An analytical study of the sea breeze. *J. Atmos. Sci.*, **46**, 1815–1825.

Dalu, G. A., R. A. Pielke, R. Avissar, G. Kallos, M. Baldi, and A. Guerrini, 1991: Linear impact of thermal inhomogeneities on mesoscale atmospheric flow with zero synoptic wind. *Ann. Geophysicae*, **9**, 641–647.

Danard, M. B., 1981: A note on estimating the height of the constant flux layer. *Boundary-Layer Meteor.*, **20**, 397–398.

Danielsen, E. F., 1959: The laminar structure of the atmosphere and its relation to the concept of a tropopause. *Arch. Meteor. Geophys. Bioklim*, **11**, 293–332.

Danielsen, E. F., 1961: Trajectories: isobaric, isentropic and actual. *J. Meteor.*, **18**, 479–486.

Davies, H. C., 1976: A lateral boundary formulation for multi-level prediction models. *Quart. J. Roy. Meteor. Soc.*, **102**, 405–418.

Davies, H. C., 1983: Limitations of some common lateral boundary schemes used in regional NWP models. *Mon. Wea. Rev.*, **111**, 1002–1012.

Davies, H. C. and R. E. Turner, 1977: Updating prediction models by dynamical relaxation: an examination of the technique. *Quart. J. Roy. Meteor. Soc.*, **103**, 225–245.

Davies, R. W., 1959: Large-scale diffusion from an oil fire. *Adv. Geophys.*, **6**, 413–415.

Davis, P. A., 1983: Markov chain simulations of vertical dispersion from elevated source into the neutral planetary boundary layer. *Boundary-Layer Meteor.*, **26**, 355–376.

Davis, P. A. and W. R. Peltier, 1976: Resonant parallel shear instability in the stably stratified planetary boundary layer. *J. Atmos. Sci.*, **33**, 1287–1300.

Davis, P. A. and W. R. Peltier, 1979: Some characteristics of the Kelvin-Helmholtz and resonant overreflection modes of shear flow instability and of their interaction through vortex pairing. *J. Atmos. Sci.*, **36**, 2394–2412.

Davis, W. E., A. R. Olsen, B. T. Didier, and D. W. Damschen, 1986: A comparison of meso-alpha MLAM model results with observations from CAPTEX. In *Proc. Fifth AMS/APCA Conf. on Applications of Air Pollution Meteorology*, Nov. 18-21, Chapel Hill, North Carolina, American Meteorological Society, Boston, 69–72.

Davis, W. E., A. R. Olsen, and B. T. Didier, 1988: MLAM assessment of radionuclide air concentration and deposition for the Chernobyl reactor accident. In *Proc. 17th NATO/CCMS Intern. Tech. Mtg on Air Pollution Modelling and Its Application*, Sept. 19–22, Cambridge, England, Committee on the Challenges of Modern Society, North Atlantic Treaty Organization, Brussels.

de Baas, A. F., 1988: Some properties of the Langevin model for dispersion. Report No. Risø-M-2627, January, Risø National Laboratory, DK-4000, Roskilde, Denmark, 250 pp.

de Baas, A. F. and A. G. M. Driedonks, 1985: Internal gravity waves in a stably stratified boundary layer. *Boundary-Layer Meteor.*, **31**, 303–323.

de Baas, A. F., H. van Dop, and F. T. M. Nieuwstadt, 1986: An application of the Langevin equation for inhomogeneous conditions to dispersion in a convective boundary layer. *Quart. J. Roy. Meteor. Soc.*, **112**, 165–180.

Deardorff, J. W., 1969: Numerical study of heat transport by internal gravity waves above a growing unstable layer. *Phys. Fluids Suppl. II* 184–194.

Deardorff, J. W., 1973: The use of subgrid transport equations in a three-dimensional model of atmospheric turbulence. *J. Fluids Engineering*, **95**, 429–438.

Deardorff, J. W., 1974: Three-dimensional numerical study of turbulence in an entraining mixed layer. *Boundary-Layer Meteor.*, **7**, 199–226.

Deardorff, J. W., 1980: Stratocumulus-capped mixed layers derived from a three-dimensional model. *Boundary-Layer Meteor.*, **18**, 495–527.

Deardorff, J. W., G. E. Willis, and D. K. Lilly, 1969: Laboratory investigation of non-steady penetrative convection. *J. Fluid Mech.*, **35**, 7–31.

Defant, A., 1921: Die Bestimmung der Turbulenzgrössen der atmosphärischen Zirkulation aussertropischer Breiten. *Sitz.-Ber. Akad. Wiss. Wien*, **130**, 383–403.

Delage, Y., 1988a: A parameterization of the stable atmospheric boundary layer. *Boundary-Layer Meteor.*, **43**, 365–381.

Delage, Y., 1988b: The position of the lowest levels in the boundary layer of atmospheric circulation models. *Atmos. Ocean*, **26**, 329–340.

Delisi, D. P. and G. Corcos, 1973: A study of internal waves in a wind tunnel. *Boundary-Layer Meteor.*, **5**, 121–137.

DeMandel, R. E. and J. R. Scoggins, 1967: Mesoscale wave motions as revealed by improved wind profile measurements. *J. Appl. Meteor.*, **6**, 617–620.

Demerjian, K. L., 1985: Quantifying uncertainty in long-range-transport models. *Bull. Amer. Meteor. Soc.*, **66**, 1533–1540.

Demerjian, K. L., Editor, 1986: Quantifying uncertainty in long-range transport models: workshop report on sources and evaluation of uncertainty in long-range transport models. Workshop proceedings, American Meteorological Society, Boston, 210 pp.

Derwent, R. G., Ø. Hov, W. A. H. Asman, J. A. van Jaarsveld, and F. A. A. M. de Leeuw, 1989: An intercomparison of long-term atmospheric transport models; the budgets of acidifying species for the Netherlands. *Atmos. Environ.*, **23**, 1893–1909.

Desaubies, Y. and M. C. Gregg, 1981: Reversible and irreversible finestructure. *J. Phys. Ocean.*, **11**, 541–556.

Desbois, M., 1975: Large-scale kinetic energy spectra from Eulerian analysis of EOLE wind data. *J. Atmos. Sci.*, **32**, 1838–1847.

Desiato, F. and M. G. Ciminelli, 1991: Plume dispersion investigated by LANDSAT imagery. *Atmos. Environ.*, **25A**, 965–978.

Dester, G. D., C. H. Liu, S. J. Franke, and J. L. Green, 1990: Simultaneous observations of the troposphere and lower stratosphere by the Flatland and Urbana ST radars. *Radio Sci.*, **25**, 917–931.

Dewan, E. M., 1979: Stratospheric wave spectra resembling turbulence. *Science*, **204**, 832–835.

Dewan, E. M., 1985: On the nature of atmospheric waves and turbulence. *Radio Sci.*, **20**, 1301–1307.

Dewan, E. M., N. Grossbard, A. F. Quesada, and R. E. Good, 1984: Spectral analysis of 10 m resolution scalar velocity profiles in the stratosphere. *Geophys. Res. Lett.*, **11**, 80–83 and 624.

Dickerson, R. R., G. J. Huffman, W. T. Luke, L. J. Nunnermacker, K. E. Pickering, A. C. D. Leslie, C. G. Lindsey, W. G. N. Slinn, T. J. Kelly, P. H. Daum, A. C. Delany, J. P. Greenberg, P. R. Zimmerman, J. F. Boatman, J. D. Ray, and D. H. Stedman, 1987: Thunderstorms: An important mechanism in the transport of air pollutants. *Science*, **235**, 460–465.

Dickey, T. D. and G. L. Mellor, 1980: Decaying turbulence in neutral and stratified fluids. *J. Fluid Mech.*, **99**, 13–31.

Dickinson, R. E., 1969: Vertical propagation of planetary Rossby waves through an atmosphere with Newtonian cooling. *J. Geophys. Res.*, **74**, 929–938.

Dickinson, R. E., A. Henderson-Sellers, P. J. Kennedy, and M. F. Wilson, 1986: Biosphere-atmosphere transfer scheme (BATS) for the NCAR Community Climate Model. NCAR Technical Note NCAR/TN-275+STR, December, National Center for Atmospheric Research, Boulder, Colorado, 69 pp.

Dietz, R. N., 1987: Perfluorocarbon tracer technology. In *Regional and Long-range Transport of Air Pollution*, Sandroni, S., Editor, Elsevier Science Publishers B.V., Amsterdam, 215–247.

Dong, B. and K. C. Yeh, 1988: Resonant and nonresonant wave-wave interactions in an isothermal atmosphere. *J. Geophys. Res.*, **93**, 3729–3744.

Donn, W. L., P. L. Milic, and R. Brilliant, 1956: Gravity waves and the tropical sea breeze. *J. Meteor.*, **13**, 356–361.

Doran, J. C., T. W. Horst, and P. W. Nickola, 1978: Variations in measured values of lateral diffusion parameters. *J. Appl. Meteor.*, **17**, 825–831.

Dougherty, J. P., 1961: The anisotropy of turbulence at the meteor level. *J. Atmos. Terrest. Phys.*, **21**, 210–213.

Doviak, R. J. and M. Berger, 1980: Turbulence and waves in the optically clear planetary boundary layer resolved by dual-Doppler radars. *Radio Sci.*, **15**, 297–317.

Downton, M. W. and R. L. Dennis, 1985: Evaluation of urban air quality models for regulatory use: refinement of an approach. *J. Climate Appl. Meteor.*, **24**, 161–173.

Draxler, R. R., 1979: Modeling the results of two recent mesoscale dispersion experiments. *Atmos. Environ.*, **13**, 1523–1533.

Draxler, R. R., 1981: Observing and forecasting motions of volcanic emissions shortly after the initial Mt. St. Helens eruptions. NOAA Tech. Memo. ERL ARL–95, February, Air Resources Laboratories, National Oceanic and Atmospheric Administration, Silver Spring, Maryland, 14 pp.

Draxler, R. R., 1982: Measuring and modeling the transport and dispersion of krypton–85 1500 km from a point source. *Atmos. Environ.*, **16**, 2763–2776.

Draxler, R. R., 1983: Model validation using krypton-85 air concentration data from the 1500 km long-range dispersion experiment. In *Proc. 6th AMS Symp. on Turbulence and Diffusion*, March 22–25, Boston, Massachusetts, American Meteorological Society, Boston, 139–141.

Draxler, R. R., 1984: Diffusion and transport experiments. In *Atmospheric Science and Power Production*, Randerson, D., Editor, Report No. DOE/TIC-27601, Office of Scientific and Technical Information, U.S. Department of Energy, Washington, D.C., 367–422.

Draxler, R. R., 1985: Metropolitan Tracer Experiment (METREX). NOAA Tech. Memo. ERL ARL–101, October, Air Resources Laboratory, National Oceanic and Atmospheric Administration, Silver Spring, Maryland, 102 pp.

Draxler, R. R., 1987: Sensitivity of a trajectory model to the spatial and temporal resolution of the meteorological data during CAPTEX. *J. Climate Appl. Meteor.*, **26**, 1577–1588.

Draxler, R. R., 1988: The persistence of pollutants downwind of a point source following termination of the emission. *Boundary-Layer Meteor.*, **42**, 43–53.

Draxler, R. R., 1989: Overview and preliminary results from the Across North America Tracer Experiment (ANATEX). In *Proc. Sixth AMS/APCA Conf. on Applications of Air Pollution Meteorology*, Jan. 30–Feb. 3, Anaheim, California, American Meteorological Society, Boston, 82–85.

Draxler, R. R., 1991: The accuracy of trajectories during ANATEX calculated using dynamic model analyses versus rawinsonde observations. *J. Appl. Meteor.*, **30**, 1446–1467.

Draxler, R. R. and A. D. Taylor, 1982: Horizontal dispersion parameters for long-range transport modelling. *J. Appl. Meteor.*, **21**, 367–372.

Draxler, R. R. and B. J. B. Stunder, 1988: Modeling the CAPTEX vertical tracer concentration profiles. *J. Appl. Meteor.*, **27**, 617–625.

Draxler, R. R. and J. L. Heffter, Editors, 1989: *Across North America Tracer Experiment (ANATEX). Volume I: Description, ground-level sampling at primary sites, and meteorology.* NOAA Tech. Memo. ERL ARL-167, January, Air Resources Laboratory, National Oceanic and Atmospheric Administration, Silver Spring, Maryland, 83 pp.

Drazin, P. G. and L. N. Howard, 1966: Hydrodynamic stability of parallel flow of inviscid fluid. *Adv. Appl. Mech.*, **9**, 1–89.

Dronamraju, M., L. K. Peters, G. R. Carmichael, P. Kasibhatla, and S.-Y. Cho, 1988: An Eulerian transport/transformation/removal model for SO_2 and sulfate – III: Comparison with the July 1974 SURE database. *Atmos. Environ.*, **22**, 2003–2011.

Durbin, P. A., 1980: A stochastic model of two-particle dispersion and concentration fluctuations in homogeneous turbulence. *J. Fluid Mech.*, **100**, 279–302.

Durbin, P. A., 1983: Stochastic differential equations and turbulent dispersion. NASA Ref. Pub. 1103, April, National Aeronautics and Space Administration, Washington, D.C., 73 pp.

Durran, D. R., 1986: Mountain waves. In *Mesoscale Meteorology and Forecasting*, Ray, P. S., Editor, American Meteorological Society, Boston, 472–492.

Durran, D. R., 1990: Mountain waves and downslope winds. In *Atmospheric Processes Over Complex Terrain*, Blumen, W., Editor, American Meteorological Society, Boston, 59–81.

Durran, D. R. and J. B. Klemp, 1983: A compressible model for the simulation of moist mountain waves. *Mon. Wea. Rev.*, **111**, 2341–2361.

Durst, C. S., A. F. Crossley, and N. E. Davis, 1959: Horizontal diffusion in the atmosphere as determined by geostrophic trajectories. *J. Fluid Mech.*, **6**, 401–422.

Dyer, A. J., 1966: Artificial radio-activity, ozone and volcanic dust as atmospheric tracers in the Southern Hemisphere. *Tellus*, **18**, 416–419.

Ebel, A., H. Hass, H. J. Jakobs, M. Laube, M. Memmesheimer, and A. Oberreuter, 1991: Simulation of ozone intrusion caused by a tropopause fold and cut-off low. *Atmos. Environ.*, **25A**, 2131–2144.

Eckart, C., 1948: An analysis of the stirring and mixing processes in incompressible fluids. *J. Mar. Res.*, **7**, 265–275.

Ecklund, W. L., K. S. Gage, G. D. Nastrom, and B. B. Balsley, 1986: A preliminary climatology of the spectrum of vertical velocity observed by clear-air Doppler radar. *J. Climate Appl. Meteor.*, **25**, 885–892.

Ecklund, W. L., D. A. Carter, and B. B. Balsley, 1988: A UHF wind profiler for the boundary layer: brief description and initial results. *J. Atmos. Oceanic Technol.*, **5**, 432–441.

Edinger, J. G. and R. R. Rapp, 1957: Dispersion in the upper atmosphere. *J. Meteor.*, **14**, 421–425.

Eilts, M. D., R. J. Doviak, and A. Sundara-Rajan, 1984: Comparison of winds, waves, and turbulence as observed by airborne lidar, ground-based radars, and instrumented tower. *Radio Sci.*, **19**, 1511–1522.

Einaudi, F., D. P. Lalas, and G. E. Perona, 1979: The role of gravity waves in tropospheric processes. *Pure Appl. Geophys.*, **117**, 627–663.

Einaudi, F., W. L. Clark, D. Fua, J. L. Green, and T. E. VanZandt, 1987: Gravity waves and convection in Colorado during July 1983. *J. Atmos. Sci.*, **44**, 1534–1553.

Einaudi, F., A. J. Bedard, Jr., and J. J. Finnigan, 1989: A climatology of gravity waves and other coherent disturbances at the Boulder Atmospheric Observatory during March-April 1984. *J. Atmos. Sci.*, **46**, 303–329.

Einstein, A., 1905: Über die von der molekular-kinetischen Theorie der Wärme geforderte Bewegung von in ruhenden Flüssigkeiten suspendierten Teilchen. *Ann. Physik*, **17**, 549–560.

Elder, J. W., 1959: The dispersion of marked fluid in turbulent shear flow. *J. Fluid Mech.*, **5**, 544–560.

Eliassen, A., 1962: On the use of a material layer model of the atmosphere in numerical prediction. In *Proc. Int'l. Symp. on Numerical Weather Prediction in Tokyo*, Meteorological Society of Japan, Tokyo, 207–211.

Eliassen, A., 1980: A review of long-range transport modeling. *J. Appl. Meteor.*, **19**, 231–240.

Eliassen, A., 1986: Sources of uncertainty in Lagrangian long range transport model calculation. In *Quantifying Uncertainty in Long Range Transport Models*, Demerjian, K. L., Editor, American Meteorological Society, Boston, 77–96.

Eliassen, A. and E. Palm, 1961: On the transfer of energy in stationary mountain waves. *Geofysiske Publikasjoner*, **22**, 1–23.

Ellsaesser, H. W., 1969a: A climatology of epsilon (atmospheric dissipation). *Mon. Wea. Rev.*, **97**, 415–423.

Ellsaesser, H. W., 1969b: Wind variability as a function of time. *Mon. Wea. Rev.*, **97**, 424–428.

Elsberry, R. L., 1989: Observation and analysis of tropical cyclones. In *A Global View of Tropical Cyclones*, University of Chicago Press, Chicago, 1–12. (Available from Prof. R. L. Elsberry, Naval Postgraduate School, Monterey, California 93943).

Emanuel, K. A., 1986: Overview and definition of mesoscale meteorology. In *Mesoscale Meteorology and Forecasting*, Ray, P. S., Editor, American Meteorological Society, Boston, 1–17.

Emberlin, J. C., 1981: A sulphur hexafluoride tracer experiment from a tall stack over complex topography in a coastal area of southern England. *Atmos. Environ.*, **15**, 1523–1530.

Endlich, R. M., R. C. Singleton, and J. W. Kaufman, 1969: Spectral analysis of detailed vertical wind profiles. *J. Atmos. Sci.*, **26**, 1030–1041.

Enger, L., 1991: Simulation of dispersion in moderately complex terrain. In *Air Pollution Modelling and Its Application VIII*, van Dop, H. and D. G. Steyn, Editors, Plenum Press, New York, 321–328.

Enger, L., S.-E. Gryning, E. Lyck, and U. Widemo, 1985: Simulations of a tracer experiment in the ø resund region. In *Air Pollution Modeling and Its Application IV*, De Wispelaere, C., Editor, Plenum Press, New York, 295–309.

Er-El, J. and R. L. Peskin, 1981: Relative diffusion of constant-level balloons in the Southern Hemisphere. *J. Atmos. Sci.*, **38**, 2264–2274.

Erickson, C. O. and L. F. Whitney, Jr., 1973: Picture of the month: gravity waves following severe thunderstorms. *Mon. Wea. Rev.*, **101**, 708–711. (see also pp. 2379–2380).

Eriksson, E., 1975: On the representation of frequency spectra in meteorology. *Boundary-Layer Meteor.*, **8**, 221–226.

Espenshade, Jr., E. B. and J. L. Morrison, Editors, 1979: *Goode's World Atlas, 15th Edition, Revised.* Rand McNally &. Co., Chicago, 372 pp.

ESSA, 1968: *Climatic Atlas of the United States.* Environmental Science Services Administration, U.S. Dept. of Commerce, Washington, D.C., 80 pp. (Available from National Climatic Data Center, Federal Building, Asheville, NC 28801).

Etling, D., 1988: Vortex streets behind large islands – an atmospheric example of turbulent wake collapse in stably stratified flows? In *Proc. 8th AMS Symp. on Turbulence and Diffusion*, April 25-29, San Diego, American Meteorological Society, Boston, 224–225.

Etling, D., 1989: On atmospheric vortex streets in the wake of large islands. *Met. Atmos. Phys.*, **41**, 157–164.

Etling, D., 1990a: Turbulence collapse, vortical modes and mesoscale turbulence. In *Proc. Fourth AMS Conf. on Mesoscale Processes*, June 25-29, Boulder, Colorado, American Meteorological Society, Boston, 176–177.

Etling, D., 1990b: On plume meandering under stable stratification. *Atmos. Environ.*, **24A**, 1979–1985.

Etling, D., J. Preuss, and M. Wamser, 1986: Application of a random walk model to turbulent diffusion in complex terrain. *Atmos. Environ.*, **20**, 741–747.

Fackrell, J. E. and A. G. Robins, 1990: The effects of source size on concentration fluctuations in plumes. *Boundary-Layer Meteor.*, **22**, 335–350.

Fairall, C. W., A. B. White, and D. W. Thomson, 1991: A stochastic model of gravity-wave-induced clear-air turbulence. *J. Atmos. Sci.*, **48**, 1771–1790.

FAO-UNESCO, 1974: *Soil Map of the World: Vol. I. Legend.* United Nations Educational, Scientific, and Cultural Organization, Paris, 59 pp. + Legend Sheet.

Fast, J. D. and M. D. McCorcle, 1990: A two-dimensional numerical sensitivity study of the Great Plains low-level jet. *Mon. Wea. Rev.*, **118**, 151–163.

Feely, H. W., H. Seitz, R. J. Lagomarsino, and P. E. Biscaye, 1966: Transport and fallout of stratospheric radioactive debris. *Tellus*, **18**, 316–327.

Ferber, G. J., 1985: Cross-Appalachian Tracer Experiment (CAPTEX) operations review. NOAA Technical Memorandum ERL ARL-138, May, Air Resources Laboratory, National Oceanic and Atmospheric Administration, Silver Spring, Maryland, 106 pp.

Ferber, G. J., K. Telegadas, J. L. Heffter, and M. E. Smith, 1977: Air concentrations of krypton–85 in the midwest United States during January–May 1974. *Atmos. Environ.*, **11**, 379–385.

Ferber, G. J., K. Telegadas, J. L. Heffter, C. R. Dickson, R. N. Dietz, and P. W. Krey, 1981: Demonstration of a long-range atmospheric tracer system using perfluorocarbons. NOAA Tech. Memo. ERL ARL-101, April, Air Resources Laboratory, National Oceanic and Atmospheric Administration, Silver Spring, Maryland, 74 pp.

Ferber, G. J., J. L. Heffter, R. R. Draxler, R. J. Lagomarsino, F. L. Thomas, R. N. Dietz, and C. M. Benkovitz, 1986: Cross-Appalachian Tracer Experiment (CAPTEX '83) final report. NOAA Tech. Memo. ERL ARL-142, January, Air Resources Laboratory, National Oceanic and Atmospheric Administration, Silver Spring, Maryland, 60 pp.

Ferrare, R. A., R. S. Fraser, and Y. J. Kaufman, 1990: Satellite measurements of large-scale air pollution: measurements of forest fire smoke. *J. Geophys. Res.*, **95**, 9911–9925.

Fiedler, F., 1971: The variance spectrum of the horizontal wind velocity at 50 m above the ground. *Beitr. Phys. Atmos.*, **44**, 187–200.

Fiedler, F., 1987: Atmospheric transport of air pollutants in the mesoscale over hilly terrain: a review of the TULLA experiment. In *Regional and Long-range Transport of Air Pollution*, Sandroni, S., Editor, Elsevier Science Publishers B. V., Amsterdam, 281–304.

Fiedler, F. and H. A. Panofsky, 1970: Atmospheric scales and spectral gaps. *Bull. Amer. Meteor. Soc.*, **51**, 1114–1119.

Fields, D. E., C. W. Miller, and S. J. Cotter, 1984: Validation of the AIRDOS–EPA computer code by simulating intermediate range transport of ^{85}Kr from the Savannah River Plant. *Atmos. Environ.*, **18**, 2029–2036.

Finnigan, J. J., 1988: Kinetic energy transfer between internal gravity waves and turbulence. *J. Atmos. Sci.*, **45**, 486–505.

Finnigan, J. J. and F. Einaudi, 1981: The interaction between an internal gravity wave and the planetary boundary layer. Part II: Effect of the wave on the turbulence structure. *Quart. J. Roy. Meteor. Soc.*, **107**, 807–832.

Finnigan, J. J., F. Einaudi, and D. Fua, 1984: The interaction between an internal gravity wave and turbulence in the stably-stratified nocturnal boundary layer. *J. Atmos. Sci.*, **41**, 2409–2436.

Fisher, B. E. A., 1975: The long range transport of sulphur dioxide. *Atmos. Environ.*, **9**, 1063–1070.

Fisher, B. E. A., 1983: A review of the processes and models of long-range transport of air pollutants. *Atmos. Environ.*, **17**, 1865–1880.

Fisher, B. E. A. and B. A. Callander, 1984: Mass balances of sulphur and nitrogen oxides over Great Britain. *Atmos. Environ.*, **18**, 1751–1757.

Fisher, M. J. and P. O. A. L. Davies, 1964: Correlation measurements in a non-frozen pattern of turbulence. *J. Fluid Mech.*, **18**, 97–116.

Fjørtoft, R., 1953: On the changes in the spectral distribution of kinetic energy for twodimensional, nondivergent flow. *Tellus*, **5**, 225–230.

Fowler, M. M. and S. Barr, 1983: A long-range atmospheric tracer field test. *Atmos. Environ.*, **17**, 1677–1685.

Fox, D. G., 1981: Judging air quality model performance. *Bull. Amer. Meteor. Soc.*, **62**, 599–609.

Fox, D. G., 1984: Uncertainty in air quality modeling. *Bull. Amer. Meteor. Soc.*, **65**, 27–36.

Fox, D. G. and J. E. Fairobent, 1981: NCAQ panel examines uses and limitations of air quality models. *Bull. Amer. Meteor. Soc.*, **62**, 218–221.

Fox, D. G., D. Randerson, M. E. Smith, F. D. White, and J. C. Wyngaard, 1983: Synthesis of the rural model reviews. Report No. EPA-600/S3-83-109, December, Environmental Protection Agency, Research Triangle Park, North Carolina.

Frenkiel, F. N., 1952: Application of the statistical theory of turbulent diffusion to micrometeorology. *J. Meteor.*, **9**, 252–259.

Frenkiel, F. N., 1953: Turbulent diffusion: mean concentration distribution in a flow field of homogeneous turbulence. *Adv. Appl. Mech.*, **3**, 61–107.

Frenkiel, F. N. and P. S. Klebanoff, 1966: Space-time correlations in turbulence. In *Dynamics of Fluids and Plasmas*, Pai, S. I., Editor, Academic Press, New York, 257–274.

Frisch, A. S., B. B. Stankov, B. E. Martner, and J. C. Kaimal, 1991: Midtropospheric wind speed spectra from long-term wind profiler measurements. *J. Appl. Meteor.*, **30**, 1646–1651.

Fritts, D. C., 1982: Shear excitation of atmospheric gravity waves. *J. Atmos. Sci.*, **39**, 1936–1952.

Fritts, D. C., 1989: A review of gravity wave saturation processes, effects, and variability in the middle atmosphere. *Pure Appl. Geophys.*, **130**, 343–371.

Fritts, D. C., 1984a: Gravity wave saturation in the middle atmosphere: a review of theory and observations. *Rev. Geophys. Space Phys.*, **22**, 275–308.

Fritts, D. C., 1984b: Shear excitation of atmospheric gravity waves. Part II: Nonlinear radiation from a free shear layer. *J. Atmos. Sci.*, **41**, 524–537.

Fritts, D. C. and P. K. Rastogi, 1985: Convective and dynamical instabilities due to gravity wave motions in the lower and middle atmosphere: theory and observations. *Radio Sci.*, **20**, 1247–1277.

Fritts, D. C. and T. E. VanZandt, 1987: Effects of Doppler shifting on the frequency spectra of atmospheric gravity waves. *J. Geophys. Res.*, **92**, 9723–9732.

Fritts, D. C. and Z. Luo, 1992: Gravity wave excitation by geostrophic adjustment of the jet stream. Part I: Two-dimensional forcing. *J. Atmos. Sci.*, **49**, 681–697.

Fritts, D. C., T. Tsuda, T. Sato, and S. Fukao, 1988: Observational evidence of a saturated gravity wave spectrum in the troposphere and lower stratosphere. *J. Atmos. Sci.*, **45**, 1741–1759.

Fua, D., F. Einaudi, and D. P. Lalas, 1976: The stability analysis of an inflexion-free velocity profile and its application to the night-time boundary layer in the atmosphere. *Boundary-Layer Meteor.*, **10**, 35–54.

Gadd, A. J., 1978: A split explicit integration scheme for numerical weather prediction. *Quart. J. Roy. Meteor. Soc.*, **104**, 569–582.

Gaffen, D. J., C. Benocci, and D. Olivari, 1987: Numerical modeling of buoyancy dominated dispersal using a Lagrangian approach. *Atmos. Environ.*, **21**, 1285–1293.

Gage, K. S., 1979: Evidence for a $k^{-5/3}$ law inertial range in mesoscale two-dimensional turbulence. *J. Atmos. Sci.*, **36**, 1950–1954.

Gage, K. S., 1990: Radar observations of the free atmosphere: structure and dynamics. In *Radar in Meteorology*, Atlas, D., Editor, American Meteorological Society, Boston, 534–565.

Gage, K. S. and W. H. Jasperson, 1976: Diffusion coefficients estimated from turbulence data measured by the METRAC^{tm} positioning system in Minneapolis field test. In *Proc. Third AMS Symp. on Atmospheric Turbulence, Diffusion, and Air Quality*, Oct. 19–22, Raleigh, North Carolina, American Meteorological Society, Boston, 114–121.

Gage, K. S. and W. L. Clark, 1978: Mesoscale variability of jet stream winds observed by the Sunset VHF Doppler radar. *J. Appl. Meteor.*, **17**, 1412–1416.

Gage, K. S. and B. B. Balsley, 1978: Doppler radar probing of the clear atmosphere. *Bull. Amer. Meteor. Soc.*, **59**, 1074–1093.

Gage, K. S. and W. H. Jasperson, 1979: Mesoscale wind variability below 5 km as revealed by sequential high-resolution wind soundings. *Mon. Wea. Rev.*, **107**, 77–86.

Gage, K. S. and B. B. Balsley, 1980: On the scattering and reflection mechanisms contributing to clear air radar echoes from the troposphere, stratosphere, and mesosphere. *Radio Sci.*, **15**, 243–257.

Gage, K. S. and G. D. Nastrom, 1988: Further discussion of the dynamical processes that contribute to the spectrum of mesoscale atmospheric motions. In *8th AMS Symp. on Turbulence and Diffusion*, April 25-29, San Diego, American Meteorological Society, Boston, 217–220.

Gage, K. S. and G. D. Nastrom, 1990: A simple model for the enhanced frequency spectrum of vertical velocity based on tilting of atmospheric layers by lee waves. *Radio Sci.*, **25**, 1049–1056.

Gage, K. S. and G. D. Nastrom, 1985a: On the spectrum of atmospheric velocity fluctuations seen by MST/ST radar and their interpretation. *Radio Sci.*, **20**, 1339–1347.

Gage, K. S. and G. D. Nastrom, 1985b: Evidence for coexisting spectra of stratified turbulence and internal waves in mesoscale atmospheric velocity fields. In *Proc. 7th AMS Symp. on Turbulence and Diffusion*, Nov. 12-15, Boulder, Colorado, American Meteorological Society, Boston, 176–179.

Gage, K. S. and G. D. Nastrom, 1986a: Theoretical interpretation of atmospheric wavenumber spectra of wind and temperature observed by commercial aircraft during GASP. *J. Atmos. Sci.*, **43**, 729–739.

Gage, K. S. and G. D. Nastrom, 1986b: Spectrum of atmospheric vertical displacements and spectrum of conservative scalar passive additives due to quasi-horizontal atmospheric motions. *J. Geophys. Res.*, **91**, 13211–13216.

Gage, K. S., B. B. Balsley, and R. Garello, 1986: Comparisons of horizontal and vertical velocity spectra in the mesosphere, stratosphere, and troposphere: observations and theory. *Geophys. Res. Lett.*, **13**, 1125–1128.

Gale Research Co., 1977: *Sunrise and Sunset Tables for the United States.* Gale Research Co., Detroit, 375 pp.

Gall, R. L., R. T. Williams, and T. L. Clark, 1988: Gravity waves generated during frontogenesis. *J. Atmos. Sci.*, **45**, 2204–2219.

Gardiner, C. W., 1985: *Handbook of Stochastic Methods for Physics, Chemistry and the Natural Sciences, Second Edition.* Spring-Verlag, New York, 442 pp.

Gardiner, M. J., 1981: Use of regional and global soils data for climate modelling. In *Proc. WCRP Study Conf. on Land Surface Processes in Atmospheric General Circulation Models*, Eagleson, P. S., Editor, World Climate Research Programme, World Meteorological Organization, Cambridge University Press, Cambridge, 361–393.

Gargett, A. E., 1989: Ocean turbulence. *Ann. Rev. Fluid Mech.*, **21**, 419–451.

Garratt, J. R., R. A. Pielke, W. F. Miller, and T. J. Lee, 1990: Mesoscale model response to random, surface-based perturbations — a sea-breeze experiment. *Boundary-Layer Meteor.*, **52**, 313–334.

Garrett, A. J. and F. G. Smith, III, 1982: A two-dimensional dynamical drainage flow model with Monte Carlo transport and diffusion calculations. ASCOT Report 82-6, September, Savannah River Laboratory, Aiken, South Carolina, 67 pp.

Garrett, A. J. and F. G. Smith, III, 1984: Two-dimensional simulations of drainage winds and diffusion compared to observations. *J. Climate Appl. Meteor.*, **23**, 597–610.

Garrett, C., 1979: Mixing in the ocean interior. *Dyn. Atmos. Ocean*, **3**, 239–265.

Garrett, C., 1983: On the initial streakiness of a dispersing tracer in two- and three-dimensional turbulence. *Dyn. Atmos. Oceans*, **7**, 265–277.

Garrett, C. and W. Munk, 1972: Space-time scales of internal waves. *Geophys. Fluid Dyn.*, **2**, 225–264.

Garrett, C. and W. Munk, 1975: Space-time scales of internal waves: a progress report. *J. Geophys. Res.*, **80**, 291–297.

Garrett, C. and W. Munk, 1979: Internal waves in the ocean. In *Annual Review of Fluid Mechanics, Vol. 11*, Annual Reviews, Inc., Palo Alto, California, 339–369.

Gassmann, F. and D. Bürki, 1987: Experimental investigation of atmospheric dispersion over the Swiss plain — Experiment 'Siesta'. *Boundary-Layer Meteor.*, **41**, 295–307.

Gatz, D. F., 1984: Review of particle tracers of atmospheric processes. In *Proc. Atmospheric Tracer Workshop*, Barr, S., W. E. Clements, and P. R. Guthals, Editors, May 21–25, Santa Fe, New Mexico, Report No. LA-10301-C, December, Los Alamos National Laboratory, Los Alamos, New Mexico, 201–225.

Gedzelman, S. D., 1983: Short-period atmospheric gravity waves: a study of their statistical properties and source mechanisms. *Mon. Wea. Rev.*, **111**, 1293–1299.

Gedzelman, S. D. and R. A. Rilling, 1978: Short-period atmospheric gravity waves: a study of their dynamic and synoptic features. *Mon. Wea. Rev.*, **106**, 196–210.

Gedzelman, S. D. and W. L. Donn, 1979: Atmospheric gravity waves and coastal cyclones. *Mon. Wea. Rev.*, **107**, 667–681.

Geisler, J. E. and F. P. Bretherton, 1969: The sea-breeze forerunner. *J. Atmos. Sci.*, **26**, 82–95.

Ghil, M., R. Benzi, and G. Parisi, Editors, 1985: *Turbulence and Predictability in Geophysical Fluid Dynamics and Climate Dynamics*. North-Holland, Amsterdam, 440 pp. (Proc. of International School of Physics "Enrico Fermi", Varenna on Lake Como, Italy, June 1983, Italian Physical Society).

Gibson, C. H., 1981: Fossil turbulence and internal waves. In *Nonlinear Properties of Internal Waves*, West, B. J., Editor, American Institute of Physics, New York, 159–179. (La Jolla Institute, 1981, AIP Conf. Proc. No. 76).

Gibson, C. H., 1987: Fossil turbulence and intermittency in sampling oceanic mixing processes. *J. Geophys. Res.*, **92**, 5383–5404.

Gifford, F. A., 1956: The relation between space and time correlations in the atmosphere. *J. Meteor.*, **13**, 289–294.

Gifford, F. A., 1957: Relative atmospheric diffusion of smoke puffs. *J. Meteor.*, **14**, 410–414.

Gifford, F. A., 1959: Statistical properties of a fluctuating plume dispersion model. *Adv. Geophys.*, **6**, 117–137.

Gifford, F. A., 1968: An outline of theories of diffusion in the lower layers of the atmosphere. In *Meteorology and Atomic Energy 1968*, Slade, D., Editor, U.S. Atomic Energy Commission, Washington, D.C., 65–116. (Available as Publication TID-24190 from the National Technical Information Service, U.S. Department of Commerce, Springfield, Virginia 22161).

Gifford, F. A., 1977: Tropospheric relative diffusion observations. *J. Appl. Meteor.*, **16**, 311–313.

Gifford, F. A., 1980: Smoke as a quantitative atmospheric diffusion tracer. *Atmos. Environ.*, **14**, 1119–1121.

Gifford, F. A., 1981: Comments on "Lateral Dispersion Coefficients as a Function of Averaging Time". *J. Appl. Meteor.*, **20**, 213.

Gifford, F. A., 1982: Horizontal diffusion in the atmosphere: a Lagrangian-dynamical theory. *Atmos. Environ.*, **16**, 505–512.

Gifford, F. A., 1983a: Atmospheric diffusion in the mesoscale range: the evidence of recent plume width observations. In *Proc. 6th AMS Symp. on Turbulence and Diffusion*, March 22-25, American Meteorological Society, Boston, 300–304.

Gifford, F. A., 1983b: Author's reply. *Atmos. Environ.*, **17**, 196–197. (See Smith, 1983).

Gifford, F. A., 1984: The random force theory: applications to meso- and large-scale atmospheric diffusion. *Boundary-Layer Meteor.*, **30**, 159–175.

Gifford, F. A., 1986: Atmospheric diffusion in the range 20 to 2000 kilometers. In *Air Pollution Modeling and Its Application V*, De Wispelaere, C., F. A. Schiermeier, and N. V. Gillani, Editors, Plenum Press, New York, 247–252.

Gifford, F. A., 1988: A similarity theory of the tropospheric turbulence energy spectrum. *J. Atmos. Sci.*, **45**, 1370–1379.

Gifford, F. A., 1989b: Does atmospheric turbulence have an outer scale? *Agric. Forest Meteor.*, **47**, 155–161.

Gifford, F. A., S. Barr, R. C. Malone, and E. J. Mroz, 1988: Tropospheric relative diffusion to hemispheric scales. *Atmos. Environ.*, **22**, 1871–1879.

Gill, A. E., 1982: *Atmosphere–Ocean Dynamics.* Academic Press, Inc., New York, 662 pp.

Gill, G. C., E. W. Bierly, and J. N. Kerawalla, 1963: An inexpensive rocket technique for obtaining low-level wind profiles. *J. Appl. Meteor.*, **2**, 457–462.

Gillani, N. V., 1978: Project MISST: mesoscale plume modeling of the dispersion, transformation and ground removal of SO_2. *Atmos. Environ.*, **12**, 569–588.

Godowitch, J. M., 1989a: Evaluation and testing of the MESOPUFF II model system with CAPTEX measurements. In *Proc. 6th AMS/AWMA Conf. on Applications of Air Pollution Meteorology*, Jan. 30–Feb. 3, Anaheim, Calif., American Meteorological Society, Boston, 56–59.

Godowitch, J. M., 1989b: Evaluation and sensitivity analyses results of the MESOPUFF II model with CAPTEX measurements. Report EPA/600/3-89/056, April, Atmospheric Sciences Modeling Division, Atmospheric Research and Exposure Assessment Laboratory, U.S. Environmental Protection Agency, Research Triangle Park, NC 27711, 99 pp.

Goff, R. C. and C. E. Duchon, 1974: Low-frequency temperature from a 444 meter tower. *J. Atmos. Sci.*, **31**, 1164–1166.

Goldstein, S., 1931: On the stability of superposed streams of fluid of different densities. *Proc. Roy. Soc. London*, **A132**, 524–548.

Golitsyn, G. S., 1974: Introduction to the dynamics of planetary atmospheres. NASA Tech. Translation TT F-15,627, National Aeronautics and Space Administration, Washington, D. C., 103 pp. (Russian title: "Vvdeniye v Dinamiku Planetnykh Atmosfer").

Gossard, E. E., 1960: Spectra of atmospheric scalars. *J. Geophys. Res.*, **65**, 3339–3351.

Gossard, E. E., 1990: Radar research on the atmospheric boundary layer. In *Radar in Meteorology*, Atlas, D., Editor, American Meteorological Society, Boston, 477–527.

Gossard, E. E. and W. Munk, 1954: On gravity waves in the atmosphere. *J. Meteor.*, **11**, 259–269.

Gossard, E. E. and W. B. Sweezy, 1974: Dispersion and spectra of gravity waves in the atmosphere. *J. Atmos. Sci.*, **31**, 1540–1548.

Gossard, E. E. and W. H. Hooke, 1975: *Waves In The Atmosphere.* Elsevier Scientific Publishing Co., Amsterdam, 456 pp.

Gossard, E. E., J. H. Richter, and D. Atlas, 1970: Internal waves in the atmosphere from high-resolution radar measurements. *J. Geophys. Res.*, **75**, 3523–3536.

Gossard, E. E., D. R. Jensen, and J. H. Richter, 1971: An analytical study of tropospheric structure as seen by high-resolution radar. *J. Atmos. Sci.*, **28**, 794–807.

Gossard, E. E., J. H. Richter, and D. R. Jensen, 1973: Effect of wind shear on atmospheric wave instabilities revealed by FM/CW radar observations. *Boundary-Layer Meteor.*, **4**, 113–131.

Gossard, E. E., W. D. Neff, R. J. Zamora, and J. E. Gaynor, 1984: The fine structure of elevated refractive layers: implications for over-the-horizon propagation and radar sounding systems. *Radio Sci.*, **19**, 1523–1533.

Gossard, E. E., J. E. Gaynor, R. J. Zamora, and W. D. Neff, 1985: Finestructure of elevated stable layers observed by sounder and *in situ* tower sensors. *J. Atmos. Sci.*, **42**, 2156–2169.

Green, J. L. and K. S. Gage, 1980: Observations of stable layers in the troposphere and stratosphere using VHF radar. *Radio Sci.*, **15**, 395–405.

Green, J. L., K. S. Gage, T. E. VanZandt, W. L. Clark, J. M. Warnock, and G. D. Nastrom, 1988: Observations of vertical velocity over Illinois by the Flatland radar. *Geophys. Res. Lett.*, **15**, 269–272.

Gregg, M. C., 1987: Diapycnal mixing in the thermocline: a review. *J. Geophys. Res.*, **92**, 5249–5286.

Gregg, M. C. and M. G. Briscoe, 1979: Internal waves, finestructure, microstructure and mixing in the ocean. *Rev. Geophys. Space Phys.*, **17**, 1524–1548.

Grimshaw, R. H. J., 1976: Nonlinear aspects of an internal gravity wave co-existing with an unstable mode associated with a Helmholtz velocity profile. *J. Fluid Mech.*, **76**, 65–83.

Groll, A. and W. aufm Kampe, 1983: Single particle and relative diffusion over sea areas. In *Proc. Sixth AMS Symp. on Turbulence and Diffusion*, March 22–25, Boston, American Meteorological Society, Boston, 5–8.

Groll, A., W. aufm Kampe, and H. Weber, 1985: Downwind hazard distances for pollutants over land and sea. In *Air Pollution Modeling and Its Application IV*, De Wispelaere, C., Editor, Plenum Press, New York, 585–600.

Gross, G., H. Vogel, and G. Wippermann, 1987: Dispersion over and around a steep obstacle for varying thermal stratification — numerical simulations. *Atmos. Environ.*, **21**, 483–490.

Grossman, P. A., 1989: Kernel density estimation applied to a Lagrangian particle dispersion model. Draft report, Chisholm Institute of Technology, Melbourne, Victoria, Australia, 36 pp. + App.

Gryning, S.-E., 1985: The ø experiment — a Nordic mesoscale dispersion experiment over a land-water-land area. *Bull. Amer. Meteor. Soc.*, **66**, 1403–1407.

Gryning, S.-E., S. Joffre, and J. C. Doran, 1987: The ø resund experiment — wind and temperature structure over a land-water-land area. *Boundary-Layer Meteor.*, **41**, 309–318.

Gudiksen, P. H. and D. L. Shearer, 1989: The dispersion of atmospheric tracers in nocturnal drainage flows. *J. Appl. Meteor.*, **28**, 602–608.

Haagenson, P. L. and A. L. Morris, 1974: Forecasting the behavior of the St. Louis, Missouri, pollutant plume. *J. Appl. Meteor.*, **13**, 901–909.

Haagenson, P. L., Y.-H. Kuo, M. Skumanich, and N. L. Seaman, 1987: Tracer verification of trajectory models. *J. Climate Appl. Meteor.*, **26**, 410–426.

Haagenson, P. L., K. Gao, and Y.-H. Kuo, 1990: Evaluation of meteorological analyses, simulations, and long-range transport calculations using ANATEX surface tracer data. *J. Appl. Meteor.*, **29**, 1268–1283.

Haase, S. P. and R. K. Smith, 1984: Morning glory wave clouds in Oklahoma: a case study. *Mon. Wea. Rev.*, **112**, 2078–2089.

Hack, J. J. and W. H. Schubert, 1981: Lateral boundary conditions for tropical cyclone models. *Mon. Wea. Rev.*, **109**, 1404–1420.

Hadfield, M. G., W. R. Cotton, and R. A. Pielke, 1991: Large-eddy simulations of thermally forced circulations in the convective boundary layer. Part I: A small-scale circulation with zero wind. *Boundary-Layer Meteor.*, **57**, 79–114.

Hage, K. D. and H. W. Church, 1967: A computer programmed model for calculation of fall and dispersion of particles in the atmosphere. In *Proc. USAEC Meteor. Info. Meeting*, Sept. 11–14, Chalk River, Ontario, Canada, Doc. AECL-2787, Chalk River Nuclear Laboratories, Atomic Energy of Canada, Ltd, Ottawa, Canada, 320–333.

Haidvogel, D. B. and T. Keffer, 1984: Tracer dispersal by mid-ocean mesoscale eddies: Part I. Ensemble statistics. *Dyn. Atmos. Oceans*, **8**, 1–40.

Hall, C. D., 1975: The simulation of particle motion in the atmosphere by a numerical random-walk model. *Quart. J. Roy. Meteor. Soc.*, **101**, 235–244.

Haltiner, G. J., 1971: *Numerical Weather Prediction.* John Wiley & Sons, Inc., New York, 317 pp.

Haltiner, G. J. and F. L. Martin, 1957: *Dynamical and Physical Meteorology.* McGraw-Hill Book Co., New York, 470 pp.

Haltiner, G. J. and R. T. Williams, 1980: *Numerical Weather Prediction and Dynamic Meteorology, Second Edition.* John Wiley & Sons, Inc., New York, 477 pp.

Hamming, R. W., 1973: *Numerical Methods for Scientists and Engineers, Second Edition.* McGraw-Hill Book Co., Inc., New York, 721 pp.

Hanna, S. R., 1978: A statistical diffusion model for use with variable wind fields. In *Proc. Fourth AMS Symp. on Turbulent Diffusion and Air Pollution*, Jan. 15-18, Reno, American Meteorological Society, Boston, 15-18.

Hanna, S. R., 1981: Lagrangian and Eulerian time-scale relations in the daytime boundary layer. *J. Appl. Meteor.*, **20**, 242–249.

Hanna, S. R., 1982: Applications in air pollution modeling. In *Atmospheric Turbulence and Air Pollution Modelling*, Nieuwstadt, F. T. M. and H. van Dop, Editors, D. Reidel Publishing Co., Dordrecht, 275-310.

Hanna, S. R., 1983: Lateral turbulence intensity and plume meandering during stable conditions. *J. Climate Appl. Meteor.*, **22**, 1424–1430.

Hanna, S. R., 1984: Concentration fluctuations in a smoke plume. *Atmos. Environ.*, **18**, 1091–1106.

Hanna, S. R., 1986: Spectra of concentration fluctuations: the two time scales of a meandering plume. *Atmos. Environ.*, **20**, 1131–1137.

Hanna, S. R., 1986a: Spectra of concentration fluctuations: the two time scales of a meandering plume. *Atmos. Environ.*, **20**, 1131–1137.

Hanna, S. R., 1986b: Lateral dispersion from tall stacks. *J. Climate Appl. Meteor.*, **25**, 1426–1433.

Hanna, S. R. and D. W. Heinold, 1986: Simple statistical methods for comparative evaluation of air quality models. In *Air Pollution Modeling and Its Application V*, De Wispelaere, C., F. A. Schiermeier, and N. V. Gillani, Editors, Plenum Press, New York, 441–453.

Hanna, S. R., G. A. Briggs, and R. P. Hosker, Jr., 1982: *Handbook on Atmospheric Diffusion.* DOE/TIC-11223, U.S. Department of Energy, Washington, D.C., 102 pp. (Available from the National Technical Information Service, U.S. Department of Commerce, Springfield, Virginia 22161).

Hansen, D. A., H. M. Barnes, M. Lusis, and K. J. Puckett, 1988: A North American field study to evaluate Eulerian models. In *Proc. 17th NATO/CCMS Intern. Tech. Mtg. on Air Pollution and Its Applications*, Sept. 19-22, Cambridge, England, Committee on the Challenges of Modern Society, North Atlantic Treaty Organization, Brussels.

Hardy, K. R. and K. S. Gage, 1990: The history of radar studies of the clear atmosphere. In *Radar in Meteorology*, Atlas, D., Editor, American Meteorological Society, Boston, 130–142.

Hasselmann, K., 1966: Feynman diagrams and interaction rules of wave-wave scattering processes. *Rev. Geophys.*, 4, 1–32.

Hasselmann, K., 1967: Nonlinear interactions treated by the methods of theoretical physics (with applications to the generation of waves by wind). *Proc. Roy. Soc. London*, **A299**, 77–100.

Hay, J. S. and F. Pasquill, 1959: Diffusion from a continuous source in relation to the spectrum and scale of turbulence. *Adv. Geophys.*, **6**, 345–365.

Hayashi, T., 1991: The horizontal distribution of space correlation coefficients of wind fluctuations in the atmospheric surface layer. *Boundary-Layer Meteor.*, **55**, 125–140.

Hazel, P., 1967: The effect of viscosity and heat conduction on internal gravity waves at a critical level. *J. Fluid Mech.*, **30**, 775–783.

Hedley, M. and M. K. Yau, 1988: Radiation boundary conditions in numerical modeling. *Mon. Wea. Rev.*, **116**, 1721–1736.

Heffter, J. L., 1965: The variation of horizontal diffusion parameters with time for travel periods of one hour or longer. *J. Appl. Meteor.*, **4**, 153–156.

Heffter, J. L., 1980: Air Resources Laboratory Atmospheric Transport and Dispersion model (ARL-ATAD). NOAA Tech. Memo. ERL ARL-81, February, Air Resources Laboratory, National Oceanic and Atmospheric Administration, Silver Spring, Maryland, 17 + App.

Heffter, J. L., J. F. Schubert, and G. A. Mead, 1984: Atlantic Coast Unique Regional Atmospheric Tracer Experiment (ACURATE). NOAA Tech. Memo. ERL ARL–130, Air Resources Laboratory, National Oceanic and Atmospheric Administration, Silver Spring, Maryland, 15 pp. + Appendices.

Heffter, J. L., T. Yamada, and R. N. Dietz, 1987: Long-range (CAPTEX) and complex terrain (ASCOT) perfluorocarbon tracer studies. In *Regional and Long-range Transport of Air Pollution*, Sandroni, S., Editor, Elsevier Science Publishers B.V., Amsterdam, 437–465.

Helfand, H. M. and J. C. Labraga, 1988: Design of a nonsingular level 2.5 second-order closure model for the prediction of atmospheric turbulence. *J. Atmos. Sci.*, **45**, 113–132.

Henderson-Sellers, A. and M. F. Wilson, 1983: Surface albedo data for climatic modeling. *Rev. Geophys. Space Phys.*, **21**, 1743–1778.

Henderson-Sellers, A., M. F. Wilson, G. Thomas, and R. E. Dickinson, 1986: Current global land-surface data sets for use in climate-related studies. NCAR Technical Note NCAR/TN-272+STR, September, National Center for Atmospheric Research, Boulder, Colorado, 110 pp.

Henmi, T., 1980: Long-range transport model of SO_2 and sulfate and its application to the eastern United States. *J. Geophys. Res.*, **85**, 4436–4442.

Herring, J. R., 1980: Statistical theory of quasi-geostrophic turbulence. *J. Atmos. Sci.*, **37**, 969–977.

Herring, J. R. and O. Metais, 1989: Numerical experiments in forced stably stratified turbulence. *J. Fluid Mech.*, **202**, 97–115.

Herring, J. R., S. A. Orszag, R. H. Kraichnan, and D. G. Fox, 1974: Decay of two-dimensional homogeneous turbulence. *J. Fluid Mech.*, **66**, 417–444.

Herron, T. J. and I. Tolstoy, 1969: Tracking jet stream winds from ground level pressure signals. *J. Atmos. Sci.*, **26**, 266–269.

Herron, T. J., I. Tolstoy, and D. W. Kraft, 1969: Atmospheric pressure background fluctuations in the mesoscale range. *J. Geophys. Res.*, **74**, 1321–1329.

Herterich, K. and K. Hasselmann, 1982: The horizontal diffusion of tracers by surface waves. *J. Phys. Ocean.*, **12**, 704–711.

Heskestad, G., 1965: A generalized Taylor hypothesis with application for high Reynolds number turbulent shear flows. *J. Appl. Mech., Trans. ASME, Ser. E*, **32**, 735–739.

Hess, G. D. and R. H. Clarke, 1973: Time spectra and cross-spectra of kinetic energy in the planetary boundary layer. *Quart. J. Roy. Meteor. Soc.*, **99**, 130–153.

Hess, G. D., B. B. Hicks, and T. Yamada, 1981: The impact of the Wangara experiment. *Boundary-Layer Meteor.*, **20**, 135–174.

Hidy, G. M., 1987: Conceptual design of a massive aerometric tracer experiment (MATEX). *J. Air Pollu. Control Assoc.*, **37**, 1137–1157.

Hidy, G. M., 1988: Scientific considerations for empirical determination of regional source-receptor relationships. *Atmos. Environ.*, **22**, 1801–1820.

Hines, C. O., 1960: Internal atmospheric gravity waves at ionospheric heights. *Can. J. Phys.*, **38**, 1441–1481.

Hines, C. O., 1972: Gravity waves in the atmosphere. *Nature*, **239**, 73–78.

Hino, M., 1968: Maximum ground-level concentration and sampling time. *Atmos. Environ.*, **2**, 149–165.

Hinze, J. O., 1975: *Turbulence, 2nd Edition.* McGraw-Hill Book Co., New York, 790 pp.

Hobbs, P. V., 1978: Organization and structure of clouds and precipitation on the mesoscale and microscale in cyclonic storms. *Rev. Geophys. Space Phys.*, **16**, 741–755.

Hoecker, W. H., 1981: A model for predicting diurnal height variations of quasi-constant-density tetroons. *J. Appl. Meteor.*, **20**, 1095–1104.

Hoff, R. M. and A. J. Gallant, 1985: The use of an available SO_2 tracer during the 1983 CAPTEX experiment. *Atmos. Environ.*, **19**, 1573–1575.

Hogg, D. C., M. T. Decker, F. O. Guiraud, K. B. Earnshaw, D. A. Merritt, K. P. Moran, W. B. Sweezy, R. G. Strauch, E. R. Westwater, and C. G. Little, 1983: An automatic profiler of the temperature, wind and humidity in the troposphere. *J. Climate Appl. Meteor.*, **22**, 807–831.

Högström, U., 1964: An experimental study on atmospheric diffusion. *Tellus*, **16**, 205–251.

Högström, U., 1972: A method for detecting odour frequencies from a point source. *Atmos. Environ.*, **6**, 103–121.

Högström, U., 1988: Non-dimensional wind and temperature profiles in the atmospheric surface layer: a re-evaluation. *Boundary-Layer Meteor.*, **42**, 55–78.

Holland, J. Z., 1988: Truncation effects on estimated parameters of tracer distributions sampled on finite domains. *J. Appl. Meteor.*, **27**, 280–294.

Holloway, G., 1986: Eddies, waves, circulation, and mixing: statistical geofluid mechanics. *Ann. Rev. Fluid Mech.*, **18**, 91–147.

Holloway, G. and B. J. West, Editors, 1984: *Predictability of Fluid Motions.* American Institute of Physics, New York, 610 pp. (AIP Conf. Proceedings No. 106, LaJolla Institute – 1983).

Holloway, G. and S. S. Kristmannsson, 1984: Stirring and transport of tracer fields by geostrophic turbulence. *J. Fluid Mech.*, **141**, 27–50.

Holmboe, J., 1962: On the behavior of symmetric waves in stratified shear layers. *Geofysiske Publikasjoner*, **24**, 68–113.

Holt, E. H., R. A. Pielke, R. L. Walko, S. A. Luces, and W. H. Ohmstede, 1991: Methodology for modeling extreme effects of aerosol particles transported on a regional scale. In *Proc. Seventh Joint AMS/APCA Conf. on Applications of Air Pollution Meteorology*, Jan. 14–18, New Orleans, American Meteorological Society, Boston, 131–134.

Holt, T. and S. Raman, 1988: A review and comparative evaluation of multilevel boundary layer parameterizations for first-order and turbulent kinetic energy closure schemes. *Rev. Geophys.*, **26**, 761–780.

Holton, J. R., 1972: *An Introduction to Dynamic Meteorology.* Academic Press, Inc., New York, 319 pp.

Holton, J. R., 1990: On the global exchange of mass between the stratosphere and troposphere. *J. Atmos. Sci.*, **47**, 393–395.

Holtslag, A. A. M. and F. T. M. Nieuwstadt, 1986: Scaling the atmospheric boundary layer. *Boundary-Layer Meteor.*, **36**, 201–209.

Hooke, W. H., 1986: Gravity waves. In *Mesoscale Meteorology and Forecasting*, Ray, P. S., Editor, American Meteorological Society, Boston, 272–288.

Hooke, W. H. and K. R. Hardy, 1975: Further study of the atmospheric gravity waves over the eastern seaboard on 18 March 1969. *J. Appl. Meteor.*, **14**, 31–38.

Hooke, W. H. and R. M. Jones, 1986: Dissipative waves excited by gravity-wave encounters with the stably stratified planetary boundary layer. *J. Atmos. Sci.*, **43**, 2048–2060.

Hopfinger, E. J., 1987: Turbulence in stratified fluids: a review. *J. Geophys. Res.*, **92**, 5287–5303.

Horn, L. H. and R. A. Bryson, 1963: An analysis of the geostrophic kinetic energy spectrum of large-scale atmospheric turbulence. *J. Geophys. Res.*, **68**, 1059–1064.

Houghton, D. D. and W. L. Jones, 1969: A numerical model for linearized gravity and acoustic waves. *J. Comput. Phys.*, **3**, 339–357.

Howard, L. N., 1961: Note on a paper of John W. Miles. *J. Fluid Mech.*, **10**, 509–512.

Howard, L. N., 1963: Neutral curves and stability boundaries in stratified flow. *J. Fluid Mech.*, **16**, 333–342.

Howard, L. N. and S. A. Maslowe, 1973: Stability of stratified shear flows. *Boundary-Layer Meteor.*, **4**, 511–523.

Hsie, E.-Y., 1987: MM4 (Penn State/NCAR) mesoscale model version 4 documentation. NCAR Tech. Note NCAR/TN-293+STR, National Center for Atmospheric Research, Boulder, Colorado, 215 pp.

Hsueh, Y., 1968: Mesoscale turbulence spectra over the Indian Ocean. *J. Atmos. Sci.*, **25**, 1052–1057.

Huang, X.-Y. and E. Källén, 1990: Grouping of clouds and internal gravity waves in a three-dimensional model of moist convection. In *Fourth AMS Conf. on Mesoscale Processes*, June 25-29, Boulder, CO, American Meteorological Society, Boston, 234–235.

Hunt, J. C. R., J. C. Kaimal, and J. E. Gaynor, 1985: Some observations of turbulence structure in stable layers. *Quart. J. Roy. Meteor. Soc.*, **111**, 793–815.

Hurley, P. and W. Physick, 1990: A fumigation model incorporating a Lagrangian particle approach. *Atmos. Environ.*, **25A**, 1313–1325.

Hutchings, J. W., 1955: Turbulence theory applied to large-scale atmospheric phenomena. *J. Meteor.*, **12**, 263–271.

Hwang, H. J., 1970: Power density spectrum of surface wind speed on Palmyra Island. *Mon. Wea. Rev.*, **98**, 70–74.

Islitzer, N. F. and D. H. Slade, 1968: Diffusion and transport experiments. In *Meteorology and Atomic Energy 1968*, Slade, D. H., Editor, U.S. Atomic Energy Commission, Washington, D.C., 117–188. (Available as Publication TID-24190 from the National Technical Information Service, U.S. Department of Commerce, Springfield, Virginia 22161).

Itsweire, E. C. and K. N. Helland, 1989: Spectra and energy transfer in stably stratified turbulence. *J. Fluid Mech.*, **207**, 419–452.

Itsweire, E. C., K. N. Helland, and C. W. Van Atta, 1986: The evolution of grid-generated turbulence in a stably stratified fluid. *J. Fluid Mech.*, **162**, 299–338.

Jähne, B., 1991: *Digital Image Processing*. Springer-Verlag, New York, 383 pp.

James, P. K., 1980: A review of radar observations of the troposphere in clear air conditions. *Radio Sci.*, **15**, 151–175.

Jasperson, W. H., 1982: Mesoscale time and space wind variability. *J. Appl. Meteor.*, **21**, 831–839.

Jasperson, W. H., G. D. Nastrom, and D. C. Fritts, 1990: Further study of terrain effects on the mesoscale spectrum of atmospheric motions. *J. Atmos. Sci.*, **47**, 979–987.

Jenne, R. L., 1975: Data sets for meteorological research. Tech. Note NCAR-TN/IA-111, July, National Center for Atmospheric Research, Boulder, Colorado, 194 pp.

Jenne, R. L., 1989: Data availability at NCAR. SCD UserDoc, June, Scientific Computing Division, National Center for Atmospheric Research, Boulder, Colorado, 45 pp.

Johnson, W. B., 1983a: Interregional exchanges of air pollution: model types and applications. *J. Air Pollut. Control Assoc.*, **33**, 563–574.

Johnson, W. B., 1983b: Meteorological tracer techniques for parameterizing atmospheric dispersion. *J. Climate Appl. Meteor.*, **22**, 931–946.

Johnson, W. B., E. E. Uthe, C. R. Dickson, G. Start, R. L. Coulter, and R. A. Kornasiewicz, 1985: The Shoreline Environment Atmospheric Dispersion Experiment (SEADEX). In *Air Pollution Modeling and Its Application IV*, De Wispelaere, C., Editor, Plenum Press, New York, 311–326.

Jones, W. L., 1967: Propagation of internal gravity waves in fluids with shear flow and rotation. *J. Fluid Mech.*, **30**, 439–448.

Jones, W. L., 1968: Reflexion and stability of waves in stably stratified fluids with shear flow: a numerical study. *J. Fluid Mech.*, **34**, 609–624.

Julian, P. R. and A. K. Cline, 1974: The direct estimation of spatial wavenumber spectra of atmospheric variables. *J. Atmos. Sci.*, **31**, 1526–1539.

Julian, P. R., W. M. Washington, L. Hembree, and C. Ridley, 1970: On the spectral distribution of large-scale atmospheric kinetic energy. *J. Atmos. Sci.*, **27**, 376–387.

Kahl, J. D. and P. J. Samson, 1986: Uncertainty in trajectory calculations due to low resolution meteorological data. *J. Climate Appl. Meteor.*, **25**, 1816–1831.

Kahl, J. D. and P. J. Samson, 1988a: Trajectory sensitivity to rawinsonde data resolution. *Atmos. Environ.*, **22**, 1291–1299.

Kahl, J. D. and P. J. Samson, 1988b: Uncertainty in estimating boundary-layer transport during highly convective conditions. *J. Appl. Meteor.*, **27**, 1024–1035.

Kahl, J. D. and P. J. Samson, 1988c: Shear effects on wind interpolation accuracy. *J. Appl. Meteor.*, **27**, 1299–1301.

Kahn, A. B., 1957: A generalization of average-correlation methods of spectrum analysis. *J. Meteor.*, **14**, 9–17.

Kaimal, J. C., 1973: Turbulence spectra, length scales and structure parameters in the stable surface layer. *Boundary-Layer Meteor.*, **4**, 289–309.

Kaimal, J. C. and J. E. Gaynor, 1983: The Boulder Atmospheric Observatory. *J. Climate Appl. Meteor.*, **22**, 863–880.

Kaimal, J. C., J. C. Wyngaard, Y. Izumi, and O. R. Coté, 1972: Spectral characteristics of surface-layer turbulence. *Quart. J. Roy. Meteor. Soc.*, **98**, 563–589.

Kaimal, J. C., J. C. Wyngaard, D. A. Haugen, O. R. Coté, Y. Izumi, S. J. Caughey, and C. J. Readings, 1976: Turbulence structure in the convective boundary layer. *J. Atmos. Sci.*, **33**, 2152–2169.

Kálnay de Rivas, E., 1972: On the use of nonuniform grids in finite-difference equations. *J. Comput. Phys.*, **10**, 202–210.

Kampé de Fériet, J., 1951: Averaging processes and Reynolds equations in atmospheric turbulence. *J. Meteor.*, **8**, 358–361.

Kampé de Fériet, J., 1954: Introduction to the statistical theory of turbulence: Part I. *J. Soc. Indust. Appl. Math.*, **2**, 1–9.

Kampé de Fériet, J., 1974: Turbulent atmospheric diffusion: the first twenty-five years, 1920–1945. *Adv. Geophys.*, **18A**, 1–23.

Kanamitsu, M., 1989: Description of the NMC global data assimilation and forecast system. *Wea. Forecasting*, **4**, 335–342.

Kao, C.-Y. J. and T. Yamada, 1988: Use of the CAPTEX data for evaluations of a long-range transport numerical model with a four-dimensional data assimilation technique. *Mon. Wea. Rev.*, **116**, 293–306.

Kao, S.-K., 1962: Large-scale turbulent diffusion in a rotating fluid with applications to the atmosphere. *J. Geophys. Res.*, **67**, 2347–2359.

Kao, S.-K., 1965: Some aspects of the large-scale turbulence and diffusion in the atmosphere. *Quart. J. Roy. Meteor. Soc.*, **91**, 10–17.

Kao, S.-K., 1970: Wavenumber-frequency spectra of temperature in the free atmosphere. *J. Atmos. Sci.*, **27**, 1000–1007.

Kao, S.-K., 1974: Basic characteristics of global scale diffusion in the troposphere. *Adv. Geophys.*, **18B**, 15–32.

Kao, S. K., 1984: Theories of atmospheric transport and diffusion. In *Atmospheric Science and Power Production*, Randerson, D., Editor, Report No. DOE/TIC-27601, Office of Scientific and Technical Information, U.S. Department of Energy, Washington, D.C., 189–239.

Kao, S.-K. and H. D. Woods, 1964: Energy spectra of meso-scale turbulence along and across the jet stream. *J. Atmos. Sci.*, **21**, 513–519.

Kao, S.-K. and W. S. Bullock, 1964: Lagrangian and Eulerian correlations and energy spectra of geostrophic velocities. *Quart. J. Roy. Meteor. Soc.*, **90**, 166–174.

Kao, S.-K. and A. A. al-Gain, 1968: Large-scale dispersion of clusters of particles in the atmosphere. *J. Atmos. Sci.*, **25**, 214–221.

Kao, S.-K. and L. L. Wendell, 1970: The kinetic energy of the large-scale atmospheric motion in wavenumber - frequency space: I. Northern Hemisphere. *J. Atmos. Sci.*, **27**, 359–375.

Kao, S.-K. and W. R. Hill, 1970: Characteristics of the large-scale dispersion of particles in the Southern Hemisphere. *J. Atmos. Sci.*, **27**, 126–132.

Kao, S.-K., R. L. Jenne, and J. F. Sagendorf, 1970: The kinetic energy of large-scale atmospheric motion in wavenumber - frequency space: II. Mid-troposphere of the Southern Hemisphere. *J. Atmos. Sci.*, **27**, 1008–1020.

Kao, S.-K., C.-N. Chi, and W. M. Washington, 1976: Statistical characteristics of three-dimensional particle movement in the NCAR general circulation model. *J. Atmos. Sci.*, **33**, 1042–1049.

Kaplan, M. L., J. W. Zack, V. C. Wong, and J. J. Tuccillo, 1982: Initial results from a mesoscale atmospheric simulation system and comparisons with the AVE-SESAME I data set. *Mon. Wea. Rev.*, **110**, 1564–1590.

Karamchandani, P. and L. K. Peters, 1983: Analysis of the error associated with grid representation of point sources. *Atmos. Environ.*, **17**, 927–934.

Keliher, T. E., 1975: The occurrence of microbarograph-detected gravity waves compared with the existence of dynamically unstable wind shear layers. *J. Geophys. Res.*, **80**, 2967–2976.

Keyser, D., 1986: Atmospheric fronts: an observational perspective. In *Mesoscale Meteorology and Forecasting*, Ray, P. S., Editor, American Meteorological Society, Boston, 216–258.

Kirkwood, E. and J. Derome, 1977: Some effects of the upper boundary condition and vertical resolution on modeling forced stationary planetary waves. *Mon. Wea. Rev.*, **105**, 1239–1251.

Kistler, R. E. and D. F. Parrish, 1982: Evolution of the NMC data assimilation system: September 1978 – January 1982. *Mon. Wea. Rev.*, **110**, 1335–1346.

Klaassen, G. P. and W. R. Peltier, 1989: The role of transverse secondary instabilities in the evolution of free shear layers. *J. Fluid Mech.*, **202**, 367–402.

Klemp, J. B. and D. K. Lilly, 1978: Numerical simulation of hydrostatic mountain waves. *J. Atmos. Sci.*, **35**, 78–107.

Klemp, J. B. and R. B. Wilhelmson, 1978: The simulation of three-dimensional convective storm dynamics. *J. Atmos. Sci.*, **35**, 1070–1096.

Klemp, J. B. and D. R. Durran, 1983: An upper boundary condition permitting internal gravity wave radiation in numerical mesoscale models. *Mon. Wea. Rev.*, **111**, 430–444.

Klemp, J. B., R. B. Wilhelmson, and P. S. Ray, 1981: Observed and numerically simulated structure of a mature supercell thunderstorm. *J. Atmos. Sci.*, **38**, 1558–1580.

Klug, W., P. J. H. Builtjes, H. van Dop, N. D. van Egmond, H. Glaab, D. Gömer, B. J. de Haan, K. D. v.d. Hout, N. Kesseboom, R. Röckle, and C. Veldt, 1985: Comparison between four different interregional air pollution models. In *Interregional Air Pollution Modelling: The State of the Art*, Zwerver, S. and J. van Ham, Editors, Plenum Press, New York, 149-273.

Knox, J. B. and J. J. Walton, 1984: Modeling regional to global air pollution. In *Atmospheric Science and Power Production*, Randerson, D., Editor, Technical Information Center, Office of Scientific and Technical Information, U. S. Department of Energy, Oak Ridge, Tennessee, 621–651. [Available as DE84005177 (DOE/TIC-27601) from National Technical Information Service, U.S. Department of Commerce, Springfield, Virginia 22161].

Koch, S. E. and J. T. McQueen, 1987: A survey of nested grid techniques and their potential for use within the MASS weather prediction model. NASA Technical Memorandum 87808, February, National Aeronautics and Space Administration, Washington, D. C., 25 pp.

Kogan, Z. N. and N. P. Shakina, 1973: Numerical investigation of internal waves in jet streams including nonlinear effects. *Boundary-Layer Meteor.*, **5**, 79–93.

Kolesnikova, V. N. and A. S. Monin, 1965: Spectra of meteorological field fluctuations. *Bull. USSR Acad. Sci. Atmos. Oceanic Phys.*, **1**, 377–386. (English translation).

Kolmogorov, A. N., 1941: The local structure of turbulence in incompressible viscous fluids for very large Reynolds numbers. *C. R. Acad. Sci. URSS*, **30**, 301–305.

Koop, C. G. and F. K. Browand, 1979: Instability and turbulence in a stratified fluid with shear. *J. Fluid Mech.*, **93**, 135–159.

Kraichnan, R. H., 1967: Inertial ranges in two-dimensional turbulence. *Phys. Fluids*, **10**, 1417–1423.

Kraichnan, R. H., 1971: Inertial-range transfer in two- and three-dimensional turbulence. *J. Fluid Mech.*, **47**, 525–535.

Kraichnan, R. H. and D. Montgomery, 1980: Two-dimensional turbulence. *Rep. Prog. Phys.*, **43**, 547–619.

Kristensen, L., N. O. Jensen, and E. L. Petersen, 1981: Lateral dispersion of pollutants in a very stable atmosphere — the effect of meandering. *Atmos. Environ.*, **15**, 837–844.

Kropfli, R. A. and P. H. Hildebrand, 1980: Three-dimensional wind measurements in the optically clear planetary boundary layer with dual-Doppler radar. *Radio Sci.*, **15**, 283–296.

Kubota, S. and M. Iida, 1954: Statistical characteristics of the atmospheric disturbances. *Pap. Meteor. Ocean.*, **5**, 22–34.

Kuettner, J. P., P. A. Hildebrand, and T. L. Clark, 1987: Convection waves: observations of gravity wave systems over convectively active boundary layers. *Quart. J. Roy. Meteor. Soc.*, **113**, 445–467.

Kullenberg, G., 1972: Apparent horizontal diffusion in stratified vertical shear flow. *Tellus*, **24**, 17–28.

Kuo, Y.-H., M. Skumanich, P. L. Haagenson, and J. S. Chang, 1985: The accuracy of trajectory models as revealed by the observing system simulation experiments. *Mon. Wea. Rev.*, **113**, 1852–1867.

Kurihara, Y. and M. A. Bender, 1983: A numerical scheme to treat the open lateral boundary condition of a limited area model. *Mon. Wea. Rev.*, **111**, 445–454.

Lacis, A. A. and V. Oinas, 1991: A description of the correlated k distribution method for modeling nongray gaseous absorption, thermal emission, and multiple scattering in vertically inhomogeneous atmospheres. *J. Geophys. Res.*, **96**, 9027–9063.

Lagomarsino, R. J., T. J. Weber, and N. Latner, 1991: The Across North America Tracer Experiment (ANATEX). Volume IV: Quality assurance of ground-level samplers and quality assessment of EML analysis of surface samples. Report No. EML-523, February, Environmental Measurements Laboratory, U. S. Department of Energy, New York, New York, 70 pp.

Lalas, D. P. and F. Einaudi, 1976: On the characteristics of gravity waves generated by atmospheric shear layers. *J. Atmos. Sci.*, **33**, 1248–1259.

Lalas, D. P., F. Einaudi, and D. Fua, 1976: The destabilizing effect of the ground on Kelvin-Helmholtz waves in the atmosphere. *J. Atmos. Sci.*, **33**, 59–69.

Lamb, B. K., X.-F. Zhang, R. E. Eskridge, R. Benner, H. Westberg, J. Mitchell, X.-C. Zou, and J. Li, 1990: Elevated plume transport and dispersion: 20–150 km downwind of Beijing, P.R.C. *Atmos. Environ.*, **24A**, 859–870.

Lamb, B. K., A. Lorenzen, and F. H. Shair, 1978a: Atmospheric dispersion and transport within coastal regions — Part I. Tracer study of power plant emissions from the Oxnard Plain. *Atmos. Environ.*, **12**, 2089–2100.

Lamb, B. K., F. H. Shair, and T. B. Smith, 1978b: Atmospheric dispersion and transport within coastal regions — Part II. Tracer study of industrial emissions in the California Delta Region. *Atmos. Environ.*, **12**, 2101–2118.

Lamb, R. G., 1978: A numerical simulation of dispersion from an elevated point source in the convective planetary boundary layer. *Atmos. Environ.*, **12**, 1297–1304.

Lamb, R. G., 1980: Mathematical principles of turbulent diffusion modeling. In *Atmospheric Planetary Boundary Layer Physics*, Longhetto, A., Editor, Elsevier Scientific Publishing Co., New York, 173-210.

Lamb, R. G., 1981: A scheme for simulating particle pair motions in turbulent fluid. *J. Comp. Physics*, **39**, 329–346.

Lamb, R. G., 1982: Diffusion in the convective boundary layer. In *Atmospheric Turbulence and Air Pollution Modelling*, Nieuwstadt, F. T. M. and H. van Dop, Editors, D. Reidel Publishing Co., Boston, 159-229.

Lamb, R. G., 1984: Air pollution models as descriptors of cause-effect relationships. *Atmos. Environ.*, **18**, 591–606.

Lamb, R. G. and S. K. Hati, 1987: The representation of atmospheric motions in models of regional-scale air pollution. *J. Climate Appl. Meteor.*, **26**, 837–846.

Lambert, S. J., 1981: A diagnostic study of global energy and enstrophy fluxes and spectra. *Tellus*, **33**, 411–414.

Lane, J. A., 1968: Small-scale variations of radio refractive index in the troposphere: I. Relationship to meteorological conditions. *Proc. IEE*, **115**, 1227–1234.

Lane, J. A., 1969: Some aspects of the fine structure of elevated layers in the troposphere. *Radio Sci.*, **4**, 1111–1114.

Lange, R., 1978: ADPIC — a three-dimensional particle-in-cell model for the dispersal of atmospheric pollutants and its comparison to regional tracer studies. *J. Appl. Meteor.*, **17**, 320–329.

Langevin, P., 1908: Sur la théorie du mouvement brownien. *Comptes rendus, Academie des Sciences*, **146**, 530–533.

Lanicci, J. M., T. N. Carlson, and T. T. Warner, 1987: Sensitivity of the Great Plains severe-storm environment to soil-moisture distribution. *J. Atmos. Sci.*, **115**, 2660–2673.

Larsen, M. F., M. C. Kelley, and K. S. Gage, 1982: Turbulence spectra in the upper troposphere and lower stratosphere at periods between 2 hours and 40 days. *J. Atmos. Sci.*, **39**, 1035–1041.

Larsen, M. F., R. F. Woodman, T. Sato, and M. K. Davis, 1986: Power spectra of oblique velocities in the troposphere and lower stratosphere observed at Arecibo, Puerto Rico. *J. Atmos. Sci.*, **43**, 2230–2240.

Larsen, M. F., J. Röttger, and D. N. Holden, 1987: Direct measurements of vertical-velocity power spectra with the Sousy-VHF-radar wind profiler system. *J. Atmos. Sci.*, **44**, 3442–3448.

Lee, I. Y., 1987: Numerical simulations of cross-Appalachian transport and diffusion. *Boundary-Layer Meteor.*, **39**, 53–66.

Lee, J. T. and G. L. Stone, 1983a: The use of Eulerian initial conditions in a Lagrangian model of turbulent diffusion. *Atmos. Environ.*, **17**, 2477–2481.

Lee, J. T. and G. L. Stone, 1983b: Eulerian–Lagrangian relationships in Monte Carlo simulations of turbulent diffusion. *Atmos. Environ.*, **17**, 2483–2487.

Lee, J. T., G. L. Stone, R. E. Lawson, Jr., and M. Shipman, 1986: Monte Carlo simulation of two-particle relative diffusion using Eulerian statistics. *Atmos. Environ.*, **20**, 2185–2197.

Lee, T. D., 1951: Difference between turbulence in a two-dimensional fluid and in a three-dimensional fluid. *J. Appl. Phys.*, **22**, 524.

Lee, T. J. and R. A. Pielke, 1992: Estimating the soil surface specific humidity. *J. Appl. Meteor.*, **31**, 480–484.

Lefohn, A. S. and S. V. Krupa, Editors, 1988: *Acidic Precipitation: A Technical Amplification of NAPAP's Findings*, January. Air Pollution Control Association, Pittsburgh, 239 pp.

Legg, B. J., 1983: Turbulent dispersion from an elevated line source: Markov chain simulations of concentration and flux profiles. *Quart. J. Roy. Meteor. Soc.*, **109**, 645–660.

Legg, B. J. and M. R. Raupach, 1982: Markov-chain simulation of particle dispersion in inhomogeneous flows: the mean drift velocity induced by a gradient in Eulerian velocity variance. *Boundary-Layer Meteor.*, **24**, 3–13.

Leith, C. E., 1968: Diffusion approximation for two-dimensional turbulence. *Phys. Fluids*, **11**, 671–673.

Leith, C. E., 1971: Atmospheric predictability and two-dimensional turbulence. *J. Atmos. Sci.*, **28**, 145–161.

Leith, C. E. and R. H. Kraichnan, 1972: Predictability of turbulent flows. *J. Atmos. Sci.*, **29**, 1041–1058.

Lelong, M.-P. and J. J. Riley, 1991: Internal wave–vortical mode interactions in strongly stratified flows. *J. Fluid Mech.*, **232**, 1–19.

LeMone, M. A., 1973: The structure and dynamics of horizontal roll vortices in the planetary boundary layer. *J. Atmos. Sci.*, **30**, 1077–1091.

Lenschow, D. H., X. S. Li, C. J. Zhu, and B. B. Stankov, 1988a: The stably stratified boundary layer over the Great Plains: I. Mean and turbulence structure. *Boundary-Layer Meteor.*, **42**, 95–121.

Lenschow, D. H., S.-F. Zhang, and B. B. Stankov, 1988b: The stably stratified boundary layer over the Great Plains: II. Horizontal variations and spectra. *Boundary-Layer Meteor.*, **42**, 123–135.

Lesieur, M., 1990: *Turbulence In Fluids, Second Edition.* Kluwer Academic Publishers, Dordrecht, 412 pp.

Lesieur, M. and J. Herring, 1985: Diffusion of a passive scalar in two-dimensional turbulence. *J. Fluid Mech.*, **161**, 77–95.

Leslie, L. M., G. A. Mills, and D. J. Gauntlett, 1981: The impact of FGGE data coverage and improved numerical techniques in numerical weather prediction in the Australian region. *Quart. J. Roy. Meteor. Soc.*, **107**, 629–642.

Lettau, H. H. and B. Davidson, Editors, 1957a: *Exploring the Atmosphere's First Mile. Volume I: Instrumentation and Data Evaluation.* Pergamon Press, New York, 376 pp.

Lettau, H. H. and B. Davidson, Editors, 1957b: *Exploring the Atmosphere's First Mile. Volume II: Site Description and Data Tabulation.* Pergamon Press, New York, 202 pp.

Lewellen, W. S., 1987: Parameterization of subgrid-scale fluxes and estimation of dispersion. In *Modeling the Urban Boundary Layer*, ??, American Meteorological Society, Boston, 381–409.

Lewellen, W. S., R. I. Sykes, C. P. Cerasoli, and F. C. Kornegay, 1987: Comparison of the 1982 SEADEX dispersion data with results from a number of different models. NRC Report NUREG/CR-4820, February, Nuclear Regulatory Commission, Washington, D.C., 24 pp. + App.

Lewis, R., 1990: *Practical Digital Image Processing.* Ellis Horwood, New York, 261 pp.

Ley, A. J., 1982: A random walk simulation of two-dimensional turbulent diffusion in the neutral surface layer. *Atmos. Environ.*, **16**, 2799–2808.

Ley, A. J. and D. J. Thomson, 1983: A random walk model of dispersion in the diabatic surface layer. *Quart. J. Roy. Met. Soc.*, **109**, 847–880.

Ley, B. E. and W. R. Peltier, 1978: Wave generation and frontal collapse. *J. Atmos. Sci.*, **35**, 3–17. (see also pp. 2379–2380).

Li, W.-W. and R. N. Meroney, 1984: Estimation of Lagrangian time scales from laboratory measurements of lateral dispersion. *Atmos. Environ.*, **18**, 1601–1611.

Li, X.-S., J. E. Gaynor, and J. C. Kaimal, 1983: A study of multiple stable layers in the nocturnal lower atmosphere. *Boundary-Layer Meteor.*, **26**, 157–168.

Lilly, D. K., 1969: Numerical simulation of two-dimensional turbulence. *Phys. Fluids (Suppl. II)*, 240–249.

Lilly, D. K., 1971: Numerical simulation of developing and decaying two-dimensional turbulence. *J. Fluid Mech.*, **45**, 395–415.

Lilly, D. K., 1978: A severe downslope windstorm and aircraft turbulence event induced by a mountain wave. *J. Atmos. Sci.*, **35**, 59–77.

Lilly, D. K., 1981: Wave-permeable lateral boundary conditions for convective cloud and storm simulations. *J. Atmos. Sci.*, **38**, 1313–1316.

Lilly, D. K., 1984: The atmospheric noise spectrum ~ waves or stratified turbulence? In *Internal Gravity Waves and Small-Scale Turbulence*, Müller, P. and R. Pujalet, Editors, Hawaii Institute of Geophysics, University of Hawaii, Honolulu, Hawaii, 285–294. (Proc. 'Aha Huliko'a Hawaiian Winter Workshop, University of Hawaii at Manoa, Jan. 17-20, 1984).

Lilly, D. K., 1988: Cirrus outflow dynamics. *J. Atmos. Sci.*, **45**, 1594–1605.

Lilly, D. K., 1972a: Numerical simulation studies of two-dimensional turbulence: I. Models of statistically steady turbulence. *Geophys. Fluid Dyn.*, **3**, 289–319.

Lilly, D. K., 1972b: Numerical simulation studies of two-dimensional turbulence: II. Stability and predictability studies. *Geophys. Fluid Dyn.*, **4**, 1–28.

Lilly, D. K., 1983a: Stratified turbulence and the mesoscale variability of the atmosphere. *J. Atmos. Sci.*, **40**, 749–761.

Lilly, D. K., 1983b: Mesoscale variability of the atmosphere. In *Mesoscale Meteorology — Theories, Observations and Models*, Lilly, D. K. and T. Gal-Chen, Editors, D. Reidel Publishing Company, Boston, 13–24.

Lilly, D. K., 1989a: Two-dimensional turbulence generated by energy at two scales. *J. Atmos. Sci.*, **46**, 2026–2030.

Lilly, D. K., 1989b: Turbulence in stably stratified fluids. In *Lecture Notes on Turbulence*, Herring, J. R. and J. C. McWilliams, Editors, World Scientific, Singapore, 191–196.

Lilly, D. K. and P. J. Kennedy, 1973: Observations of a stationary mountain wave and its associated momentum flux and energy dissipation. *J. Atmos. Sci.*, **30**, 1135–1152.

Lilly, D. K. and P. F. Lester, 1974: Waves and turbulence in the stratosphere. *J. Atmos. Sci.*, **31**, 800–812.

Lilly, D. K. and E. L. Petersen, 1983: Aircraft measurement of atmospheric kinetic energy spectra. *Tellus*, **35A**, 379–382.

Limaye, S. S., V. E. Suomi, C. Velden, and G. Tripoli, 1991: Satellite observations of smoke from oil fires in Kuwait. *Science*, **252**, 1536–1539.

Lin, C. C., 1953: On Taylor's hypothesis and the acceleration terms in the Navier-Stokes equation. *Quart. Appl. Math.*, **10**, 294–306.

Lin, J.-T., 1972: Relative dispersion in the enstrophy-cascading inertial range of homogeneous two-dimensional turbulence. *J. Atmos. Sci.*, **29**, 394–396.

Lin, J.-T. and S. D. Veenhuizen, 1975: Measurements of the decay of grid-generated turbulence in a stratified fluid. *Flow Res. Note*, **85**.

Lin, J.-T. and Y.-H. Pao, 1979: Wakes in stratified fluids. In *Annual Review of Fluid Mechanics, Vol. 11*, Annual Reviews, Inc., Palo Alto, California, 317–338.

Lin, Y.-H. and R. C. Goff, 1988: A study of a mesoscale solitary wave in the atmosphere originating near a region of deep convection. *J. Atmos. Sci.*, **45**, 194–205.

Lindzen, R. S., 1974: Stability of a Helmholtz velocity profile in a continuously stratified, infinite Boussinesq fluid — applications to clear air turbulence. *J. Atmos. Sci.*, **31**, 1507–1514.

Lindzen, R. S. and K.-K. Tung, 1976: Banded convective activity and ducted gravity waves. *Mon. Wea. Rev.*, **104**, 1602–1617.

Lindzen, R. S. and A. J. Rosenthal, 1976: On the instability of Helmholtz velocity profiles in stably stratified fluids when a lower boundary is present. *J. Geophys. Res.*, **81**, 1561–1571.

Lindzen, R. S. and K.-K. Tung, 1978: Wave overreflection and shear instability. *J. Atmos. Sci.*, **35**, 1626–1632.

Lindzen, R. S. and M. Fox-Rabinovitz, 1989: Consistent vertical and horizontal resolution. *Mon. Wea. Rev.*, **117**, 2575–2583.

Liou, K.-N., 1980: *An Introduction to Atmospheric Radiation.* Academic Press, Inc., Orlando, Florida, 392 pp.

List, R. J., L. P. Salter, and K. Telegadas, 1966: Radioactive debris as a tracer for investigating stratospheric motions. *Tellus*, **18**, 345–353.

Liu, Y. N., T. Maxworthy, and G. R. Spedding, 1987: Collapse of a turbulent front in a stratified fluid: I. Nominally two-dimensional evolution in a narrow tank. *J. Geophys. Res.*, **92**, 5427–5433.

Londergan, R. J. and D. J. Wackter, 1984: Evaluation of complex terrain air quality simulation models. Report No. EPA-450/4-84-017, June, Environmental Protection Agency, Research Triangle Park, North Carolina.

Londergan, R. J., D. H. Minott, D. J. Wackter, T. Kincaid, and D. Bonitata, 1982: Evaluation of rural air quality simulation models. Report No. EPA-450/4-83-003, October, Environmental Protection Agency, Research Triangle Park, North Carolina.

Londergan, R. J., D. H. Minott, D. J. Wackter, and R. R. Fizz, 1983: Evaluation of urban air quality simulation models. Report No. EPA-450/4-83-020, July, Environmental Protection Agency, Research Triangle Park, North Carolina.

Lorenz, E. N., 1953: The interaction between a mean flow and random disturbances. *Tellus*, **5**, 238–250.

Lorenz, E. N., 1969: The predictability of a flow which possesses many scales of motion. *Tellus*, **21**, 289–307.

Lorimer, G. S., 1986: The kernel method for air quality modelling — I. Mathematical foundation. *Atmos. Environ.*, **20**, 1447–1452.

Lorimer, G. S. and D. G. Ross, 1986: The kernel method for air quality modelling — II. Comparison with analytic solutions. *Atmos. Environ.*, **20**, 1773–1780.

Louis, J.-F., 1979: A parametric model of vertical eddy fluxes in the atmosphere. *Boundary-Layer Meteor.*, **17**, 187–202.

Lu, D., T. E. VanZandt, and W. L. Clark, 1984: VHF Doppler radar observations of buoyancy waves associated with thunderstorms. *J. Atmos. Sci.*, **41**, 272–282.

Lu, N.-P., W. D. Neff, and J. C. Kaimal, 1983: Wave and turbulence structure in a disturbed nocturnal inversion. *Boundary-Layer Meteor.*, **26**, 141–155.

Luhar, A. K. and R. E. Britter, 1989: A random walk model for dispersion in inhomogeneous turbulence in a convective boundary layer. *Atmos. Environ.*, **23**, 1911–1924.

Luhar, A. K. and R. E. Britter, 1990: An application of Lagrangian stochastic modelling to dispersion during shoreline fumigation. *Atmos. Environ.*, **24A**, 871–881.

Lumley, J. L., 1964: The spectrum of nearly inertial turbulence in a stably stratified fluid. *J. Atmos. Sci.*, **21**, 99–102.

Lumley, J. L., 1965: Interpretation of time spectra measured in high-intensity shear flows. *Phys. Fluids*, **8**, 1056–1062.

Lyons, T. J., 1975: Mesoscale wind spectra. *Quart. J. Roy. Meteor. Soc.*, **101**, 901–910.

Lyons, W. A., 1974: Inadvertent weather modification by Chicago–Northern Indiana pollution sources observed by ERTS-1. *Mon. Wea. Rev.*, **102**, 503–508.

Lyons, W. A., 1980: Evidence of transport of hazy air masses from satellite imagery. *Ann. N. Y. Acad. Sci.*, **338**, 418–433.

Lyons, W. A. and S. R. Pease, 1973: Detection of particulate air pollution plumes from major point sources using ERTS-1 imagery. *Bull. Amer. Meteor. Soc.*, **54**, 1163–1170.

Lyons, W. A. and H. S. Cole, 1976: Photochemical oxidant transport: mesoscale lake breeze and synoptic-scale aspects. *J. Appl. Meteor.*, **15**, 733–743.

Lyons, W. A., R. H. Calby, and C. S. Keen, 1986: The impact of mesoscale convective systems on regional visibility and oxidant distributions during persistent elevated pollution episodes. *J. Climate Appl. Meteor.*, **25**, 1518–1531.

Lyons, W. A., J. L. Eastman, R. A. Pielke, C. J. Tremback, and G. W. Wilkerson, 1992: The use of a mesoscale prognostic model to design a field tracer experiment for the Lake Michigan Ozone Study. In *Proceedings*, Paper No. 92–87.10, 85th Annual Meeting, June 21–26, Kansas City, Air & Waste Management Assoc., Pittsburgh, 16 pp.

Mackas, D. L., W. R. Crawford, and P. P. Niiler, 1989: A performance comparison for two Lagrangian drifter designs. *Atmos. Ocean*, **27**, 443–456.

Madden, T. R. and J. F. Claerbout, 1968: Jet stream associated gravity waves and implications concerning jet stream stability. In *Acoustic-Gravity Waves in the Atmosphere*, Georges, T. M., Editor, July 15-17, Boulder, Colorado, Superintendent of Documents, U.S. Government Printing Office, Washington, D. C., 121–134.

Maddox, R. A., 1980: An objective technique for separating macroscale and mesoscale features in meteorological data. *Mon. Wea. Rev.*, **108**, 1108–1121.

Maenhaut, W., P. Cornille, J. M. Pacyna, and V. Vitols, 1989: Trace element composition and origin of the atmospheric aerosol in the Norwegian Arctic. *Atmos. Environ.*, **23**, 2551–2569.

Mahfouf, J. F., E. Richard, P. Mascart, E. C. Nickerson, and R. Rosset, 1987: A comparative study of various parameterizations of the planetary boundar y layer in a numerical mesoscale model. *J. Climate Appl. Meteor.*, **26**, 1671–1695.

Mahrer, Y., 1984: An improved numerical approximation of the horizontal gradients in a terrain-following coordinate system. *Mon. Wea. Rev.*, **112**, 918–922.

Mahrer, Y. and R. A. Pielke, 1976: Numerical simulation of the airflow over Barbados. *Mon. Wea. Rev.*, **104**, 1392–1402.

Mahrer, Y. and R. A. Pielke, 1977: A numerical study of the airflow over irregular terrain. *Beitr. Phys. Atmos.*, **50**, 98–113.

Mahrer, Y. and R. A. Pielke, 1978: A test of an upstream spline interpolation technique for the advective terms in a numerical model. *Mon. Wea. Rev.*, **106**, 818–830.

Mahrt, L., 1987: Grid-averaged surface fluxes. *Mon. Wea. Rev.*, **115**, 1550–1560.

Mahrt, L., 1988: Turbulence in stratified flow. In *Proc. 8th AMS Symp. on Turbulence and Diffusion*, April 25-29, San Diego, American Meteorological Society, Boston, 131–135.

Mahrt, L. and H. Frank, 1988: Eigenstructure of eddy microfronts. *Tellus*, **40A**, 107–119.

Mahrt, L., R. C. Heald, D. H. Lenschow, B. B. Stankov, and I. Troen, 1979: An observational study of the structure of the nocturnal boundary layer. *Boundary-Layer Meteor.*, **17**, 247–264.

Maitani, T., Y. Hiramatsu, and T. Seo, 1984: Wave-like wind fluctuations observed in the stable surface layer over a plant canopy. *Boundary-Layer Meteor.*, **29**, 273–283.

Manney, G. L. and J. L. Stanford, 1990: Wave number spectra from temperature-humidity infrared radiometer 6.7-μm water vapor data. *J. Geophys. Res.*, **95**, 909–913.

Mantis, H. T., 1963: The structure of winds in the upper troposphere at mesoscale. *J. Atmos. Sci.*, **20**, 94–106.

Mantis, H. T. and T. J. Pepin, 1971: Vertical temperature structure of the free atmosphere at mesoscale. *J. Geophys. Res.*, **76**, 8621–8628.

Marsh, A. R., 1987: Airborne measurements. In *Regional and Long-range Transport of Air Pollution*, Sandroni, S., Editor, Elsevier Science Publishers B.V., Amsterdam, 195–213.

Martin, D., C. Mithieux, and B. Strauss, 1987: On the use of the synoptic vertical wind component in a transport trajectory model. *Atmos. Environ.*, **21**, 45–52.

Martner, B. E. and R. A. Kropfli, 1989: TRACIR: A radar technique for observing the exchange of air between clouds and their environment. *Atmos. Environ.*, **23**, 2715–2721.

Masmoudi, M. and A. Weill, 1988: Atmospheric mesoscale spectra and structure functions of mean horizontal velocity fluctuations measured with a Doppler sodar network. *J. Appl. Meteor.*, **27**, 864–873.

Mastrantonio, G., F. Einaudi, D. Fua, and D. P. Lalas, 1976: Generation of gravity waves by jet streams in the atmosphere. *J. Atmos. Sci.*, **33**, 1730–1738.

Matson, M., 1984: The 1984 El Chichón volcano eruptions — a satellite perspective. *J. Volcanology Geotherm. Res.*, **23**, 1–10.

Matsumoto, S., 1961: A note on geostrophic adjustment and gravity wave in the atmosphere. *J. Meteor. Soc. Japan*, **39**, 18–28.

Matthews, E., 1983: Global vegetation and land use: new high-resolution data bases for climate studies. *J. Climate Appl. Meteor.*, **22**, 474–487.

Maul, P. R., 1978: The effect of the turning of the wind vector with height on the ground level trajectory of a diffusing cloud. *Atmos. Environ.*, **12**, 1045–1050.

Maxworthy, T., 1980: On the formation of nonlinear internal waves from the gravitational collapse of mixed regions in two and three dimensions. *J. Fluid Mech.*, **96**, 47–64.

Maxworthy, T., P. Caperan, and G. R. Spedding, 1990: Two dimensional turbulence and vortex dynamics in a stratified fluid. In *Stratified Flows*, List, E. J. and G. H. Jirka, Editors, American Society of Civil Engineers, New York, 398–407.

McBean, G. A., K. Bernhardt, S. Bodin, Z. Litynska, A. P. Van Ulden, and J. C. Wyngaard, 1979: The planetary boundary layer. WMO Tech. Note No. 165, World Meteorological Organization, Geneva, Switzerland, 201 pp.

McComas, C. H. and F. P. Bretherton, 1977: Resonant interaction of oceanic internal waves. *J. Geophys. Res.*, **82**, 1397–1412.

McComas, C. H. and P. Müller, 1981: The dynamic balance of internal waves. *J. Phys. Ocean.*, **11**, 970–986.

McCorcle, M. D., 1988: Simulation of surface-moisture effects on the Great Plains low-level jet. *Mon. Wea. Rev.*, **116**, 1705–1720.

McCumber, M. C. and R. A. Pielke, 1981: Simulation of the effects of surface fluxes of heat and moisture in a mesoscale numerical model. Part I: Soil layer. *J. Geophys. Res.*, **86**, 9929–9938.

McElroy, J. L., J. A. Eckert, and C. J. Hager, 1981: Airborne downlooking lidar measurements during STATE 78. *Atmos. Environ.*, **15**, 2223–2230.

McEwan, A. D., 1983: Internal mixing in stratified fluids. *J. Fluid Mech.*, **128**, 59–80.

McFarlane, N. A., 1987: The effect of orographically excited gravity wave drag on the general circulation of the lower stratosphere and troposphere. *J. Atmos. Sci.*, **44**, 1775–1800.

McIntyre, M. E. and M. A. Weissman, 1978: On radiating instabilities and resonant overreflection. *J. Atmos. Sci.*, **35**, 1190–1196.

McNider, R. T., 1981: *Investigation of the impact of topographic circulations on the transport and dispersion of air pollutants.* Ph.D dissertation, University of Virginia, Charlottesville, Virginia, 210 pp.

McNider, R. T. and R. A. Pielke, 1981: Diurnal boundary-layer development over sloping terrain. *J. Atmos. Sci.*, **38**, 2198–2212.

McNider, R. T., S. R. Hanna, and R. A. Pielke, 1980: Sub-grid scale plume dispersion in coarse resolution mesoscale models. In *Proc. 2nd AMS/APCA Conf. on Applications of Air Pollution Meteorology*, March, New Orleans, Louisiana, American Meteorological Society, Boston, 424–429.

McNider, R. T., K. J. Anderson, and R. A. Pielke, 1982: Numerical simulations of plume impaction. In *Proc. 3rd AMS Conf. Applications of Air Pollution Meteorology*, January, San Antonio, Texas, American Meteorological Society, Boston, 126–129.

McNider, R. T., M. D. Moran, and R. A. Pielke, 1988: Influence of diurnal and inertial boundary-layer oscillations in long-range dispersion. *Atmos. Environ.*, **22**, 2445–2462.

McWilliams, J. C., 1985: A uniformly valid model spanning the regimes of geostrophic and isotropic, stratified turbulence: balanced turbulence. *J. Atmos. Sci.*, **42**, 1773–1774.

McWilliams, J. C., 1989: Statistical properties of decaying geostrophic turbulence. *J. Fluid Mech.*, **198**, 199–230.

McWilliams, J. C., 1990a: The vortices of two-dimensional turbulence. *J. Fluid Mech.*, **219**, 361–385.

McWilliams, J. C., 1990b: The vortices of geostrophic turbulence. *J. Fluid Mech.*, **219**, 387–404.

Mellor, G. L., 1985: Ensemble average turbulence closure. *Adv. Geophys.*, **28B**, 345–358.

Mellor, G. L. and T. Yamada, 1974: A hierarchy of turbulence closure models for planetary boundary layers. *J. Atmos. Sci.*, **31**, 1791–1806.

Mellor, G. L. and T. Yamada, 1982: Development of a turbulence closure model for geophysical fluid problems. *Rev. Geophys. Space Phys.*, **20**, 851–875.

Merilees, P. E. and H. Warn, 1975: On energy and enstrophy exchanges in two-dimensional non-divergent flow. *J. Fluid Mech.*, **69**, 625–630.

Meroney, R. N., 1990: Fluid dynamics of flow over hills/mountains — insights obtained through physical modeling. In *Atmospheric Processes Over Complex Terrain*, Blumen, W., Editor, American Meteorological Society, Boston, 145–171.

Merrill, J. T. and J. R. Grant, 1979: A gravity wave–critical level encounter observed in the atmosphere. *J. Geophys. Res.*, **84**, 6315–6320.

Mesinger, F., 1965: Behavior of a very large number of constant-volume trajectories. *J. Atmos. Sci.*, **22**, 479–492.

Mesinger, F. and A. Arakawa, 1976: Numerical methods used in atmospheric models: Vol. I. GARP Publications Series No. 17, August, Global Atmospheric Research Programme, World Meteorological Organization, Case Postale No. 5, CH-1211, Geneva 20, Switzerland, 64 pp.

Metais, O. and J. R. Herring, 1989: Numerical simulations of freely evolving turbulence in stably stratified fluids. *J. Fluid Mech.*, **202**, 117–148.

Metcalf, J. I., 1975a: Gravity waves in a low-level inversion. *J. Atmos. Sci.*, **32**, 351–361.

Metcalf, J. I., 1975b: Microstructure of radar echo layers in the clear atmosphere. *J. Atmos. Sci.*, **32**, 362–370.

Michael, P. A., R. M. Brown, and J. L. Tichler, 1984: Airborne wind measurements for CAPTEX 1983. Informal Report BNL 36878, January, Department of Applied Science, Brookhaven National Laboratory, Upton, New York, 61 pp.

Mikkelsen, T. and I. Troen, 1981: Comments on "Lateral Dispersion Coefficients as a Function of Averaging Time". *J. Appl. Meteor.*, **20**, 731–732.

Mikkelsen, T., S. E. Larsen, and H. L. Pécseli, 1988: Spectral parameterization of large-scale atmospheric diffusion. In *Air Pollution Modeling and Its Application VI*, van Dop, H., Editor, Plenum Press, New York, 579–591.

Miles, J. W., 1961: On the stability of heterogeneous shear flows. *J. Fluid Mech.*, **10**, 496–508.

Miles, J. W. and L. N. Howard, 1964: Note on a heterogeneous shear flow. *J. Fluid Mech.*, **20**, 331–336.

Millán, M. M., 1987: The regional transport of tall stack plumes. In *Regional and Long-range Transport of Air Pollution*, Sandroni, S., Editor, Elsevier Science Publishers B.V., Amsterdam, 249–280.

Millán, M. M. and Y. S. Chung, 1977: Detection of a plume 400 km from the source. *Atmos. Environ.*, **11**, 939–944.

Miller, M. J. and A. J. Thorpe, 1981: Radiation conditions for the lateral boundaries of limited-area numerical models. *Quart. J. Roy. Meteor. Soc.*, **107**, 615–628.

Miyakoda, K. and A. Rosati, 1977: One-way nested grid models: the interface conditions and the numerical accuracy. *Mon. Wea. Rev.*, **105**, 1092–1107.

Mizuno, T. and H. A. Panofsky, 1975: The validity of Taylor's hypothesis in the atmospheric surface layer. *Boundary-Layer Meteor.*, **9**, 375–380.

Moeng, C.-H. and J. C. Wyngaard, 1989: Evaluation of turbulent transport and dissipation closures in second-order modeling. *J. Atmos. Sci.*, **46**, 2311–2330.

Mohnen, V. A., 1988: The challenge of acid rain. *Sci. Amer.*, **259**, August, 30–38.

Monin, A. S., 1972: *Weather Forecasting as a Problem in Physics.* MIT Press, Cambridge, Massachusetts, 199 pp.

Monin, A. S. and A. M. Yaglom, 1971: *Statistical Fluid Mechanics, Vol. 1.* MIT Press, Cambridge, Massachusetts, 769 pp.

Monin, A. S. and A. M. Yaglom, 1975: *Statistical Fluid Mechanics, Vol. 2.* MIT Press, Cambridge, Massachusetts, 874 pp.

Moore, C. B., J. R. Smith, and A. Gaalswyk, 1954: On the use of constant-level balloons to measure horizontal motions in the atmosphere. *J. Meteor.*, **11**, 167–172.

Moore, G. E., T. E. Stoeckenius, and D. A. Stewart, 1982: A survey of statistical measures of model performance and accuracy for several air quality models. Report No. EPA-450/4-83-001, November, Environmental Protection Agency, Research Triangle Park, North Carolina.

Moore, G. E., L. B. Milich, and M. K. Liu, 1988: Plume behaviors observed using lidar and SF_6 tracer at a flat and hilly site. *Atmos. Environ.*, **22**, 1673–1688.

Moran, M. D., 1989a: An examination of the RAMS radiation schemes. Informal RAMS Report No. 1, Dept. of Atmospheric Science, Colorado State University, Fort Collins, Colorado, 19 pp. (Unpublished manuscript).

Moran, M. D., 1989b: Intercomparison of the current RAMS turbulence parameterizations. In: *Proc. 1989 RAMS Workshop*, Dept. of Atmospheric Science, Colorado State University, Fort Collins, Colorado, 29 pp. (Unpublished).

Moran, M. D., 1989c: An examination of the RAMS deformation K turbulence closure scheme. Informal RAMS Report No. 2, Dept. of Atmospheric Science, Colorado State University, Fort Collins, Colorado, 49 pp. (Unpublished manuscript).

Moran, M. D., 1991a: Lagrangian Particle Dispersion Model online documentation. Unpublished manuscript, Department of Atmospheric Science, Colorado State University, Fort Collins, Colorado.

Moran, M. D., 1991b: LPDM Extension Module online documentation. Unpublished manuscript, Department of Atmospheric Science, Colorado State University, Fort Collins, Colorado.

Moran, M. D., 1992a: An examination of the surface-layer parameterizations in RAMS. Informal RAMS Report No. 3, Dept. of Atmospheric Science, Colorado State University, Fort Collins, Colorado, ?? pp. (Unpublished manuscript).

Moran, M. D., R. W. Arritt, M. Segal, and R. A. Pielke, 1986: Modification of regional-scale pollutant dispersion by terrain-forced mesoscale circulations. In *Trans. Second APCA Int'l. Spec. Conf. on Meteorology of Acidic Deposition*, Laznow, J. and G. J. Stensland, Editors, Air Pollution Control Association, Pittsburgh, 136–157.

Moran, M. D., R. T. McNider, and R. A. Pielke, 1987: Diurnal influences on mesoscale atmospheric dispersion. In *Proc. Third AMS Conference on Mesoscale Processes*, August 21-26, Vancouver, B.C., American Meteorological Society, Boston, 220–221.

Moran, M. D., R. A. Pielke, and R. T. McNider, 1991: Temporal and spatial resolution requirements for regional-scale dispersion models. In *Air Pollution Modelling and Its Application VIII*, van Dop, H. and D. G. Steyn, Editors, Plenum Press, New York, 427–437.

Morel, P. and W. Bandeen, 1973: The Eole experiment: early results and current objectives. *Bull. Amer. Meteor. Soc.*, **54**, 298–306.

Morel, P. and M. Larcheveque, 1974: Relative dispersion of constant-level balloons in the 200-mb general circulation. *J. Atmos. Sci.*, **31**, 2189–2196.

Mori, Y., 1990: Evidence of inertial oscillations of the surface wind at Marcus Island. *J. Geophys. Res.*, **95**, 11777–11783.

Morita, O. and M. Uryu, 1989: Geostrophic turbulence in a rotating annulus of fluid. *J. Atmos. Sci.*, **46**, 2349–2355.

Morris, A. L., D. B. Call, and R. B. McBeth, 1975: A small tethered balloon sounding system. *Bull. Amer. Meteor. Soc.*, **56**, 964–969.

Mueller, S. F., R. J. Valente, T. L. Crawford, A. L. Sparks, and L. L. Gautney, Jr., 1983: Description of the Air Resources Regional Pollution Assessment (ARRPA) model. Technical report, September, Air Quality Branch, Tennessee Valley Authority, Muscle Shoals, Alabama.

Müller, P., 1984: Small-scale vortical motions. In *Internal Gravity Waves and Small-Scale Turbulence*, Müller, P. and R. Pujalet, Editors, Hawaii Institute of Geophysics, Honolulu, Hawaii, 249–262. (Proc. Second 'Aha Huliko'a Hawaiian Winter Workshop).

Müller, P., G. Holloway, F. Henyey, and N. Pomphrey, 1986: Nonlinear interactions among internal gravity waves. *Rev. Geophys. Space Phys.*, **24**, 493–536.

Müller, P., R.-C. Lien, and R. Williams, 1988: Estimates of potential vorticity at small scales in the ocean. *J. Phys. Ocean.*, **18**, 401–416.

Munk, W. H. and C. J. R. Garrett, 1973: Internal wave breaking and microstructure. *Boundary-Layer Meteor.*, **4**, 37–45.

Munk, W. H. and J. D. Woods, 1973: Remote sensing of the ocean. *Boundary-Layer Meteor.*, **5**, 201–209.

Murgatroyd, R. J., 1969a: Estimations from geostrophic trajectories of horizontal diffusivity in the mid-latitude troposphere and lower stratosphere. *Quart. J. Roy. Meteor. Soc.*, **95**, 40–62.

Murrow, H. N. and R. M. Henry, 1965: Self-induced balloon motions. *J. Appl. Meteor.*, **4**, 131–138.

Murthy, C. R. and G. T. Csanady, 1971: Experimental studies of relative diffusion in Lake Huron. *J. Phys. Ocean.*, **1**, 17–24.

Nappo, C. J., 1979: Relative and single particle diffusion estimates determined from smoke plume photographs. In *Proc. Fourth AMS Symp. on Turbulence, Diffusion, and Air Pollution*, Jan. 15–18, Reno, NV, American Meteorological Society, Boston, 46–47.

Nappo, C. J., 1981: Atmospheric turbulence and diffusion estimates derived from observations of a smoke plume. *Atmos. Environ.*, **15**, 541–547.

Nappo, C. J., 1983: Turbulence parameters derived from smoke-plume analysis. In *Proc. Sixth AMS Symp. on Turbulence and Diffusion*, Mar. 22–25, Boston, American Meteorological Society, Boston, 329–332.

Nappo, C. J., 1990: Sporadic turbulence and dispersion in the stable boundary layer. In *Proc. 18th NATO/CCMS Intern. Tech. Mtg on Air Pollution Modelling and Its Applications*, 13-17 May, Vancouver, B. C., Canada, Committee on the Challenges of Modern Society, North Atlantic Treaty Organization, Brussels, 565–571.

Narasimha, R. and S. V. Kailas, 1990: Turbulent bursts in the atmosphere. *Atmos. Environ.*, **24A**, 1635–1645.

Nastrom, G. D. and K. S. Gage, 1983: A first look at wavenumber spectra from GASP data. *Tellus*, **35A**, 383–388.

Nastrom, G. D. and K. S. Gage, 1985: A climatology of atmospheric wavenumber spectra of wind and temperature observed by commercial aircraft. *J. Atmos. Sci.*, **42**, 950–960.

Nastrom, G. D. and K. S. Gage, 1990: Enhanced frequency spectra of winds at the mesoscale based on radar profiler observations. *Radio Sci.*, **25**, 1039–1047.

Nastrom, G. D., K. S. Gage, and W. H. Jasperson, 1984: Kinetic energy spectrum of large- and mesoscale atmospheric processes. *Nature*, **310**, 36–38.

Nastrom, G. D., D. C. Fritts, and K. S. Gage, 1987: An investigation of terrain effects on the mesoscale spectrum of atmospheric motions. *J. Atmos. Sci.*, **44**, 3087–3096.

Nastrom, G. D., W. H. Jasperson, and K. S. Gage, 1986a: Horizontal spectra of atmospheric tracers measured during the Global Atmospheric Sampling Program. *J. Geophys. Res.*, **91**, 13201–13209.

Nastrom, G. D., K. S. Gage, and W. L. Ecklund, 1986b: Variability of turbulence, 4–20 km, in Colorado and Alaska from MST radar observations. *J. Geophys. Res.*, **91**, 6722–6734.

NATO/CCMS, 1980: Practical demonstration of urban air quality models. Report No. 106, NATO/CCMS Pilot Study on Air Pollution Assessment Methodology and Modeling, August, Committee on the Challenges of Modern Society, North Atlantic Treaty Organization, Brussels.

NCAR, 1983: Regional acid deposition: models and physical processes. NCAR Tech. Note NCAR/TN-214+STR, August, National Center for Atmospheric Research, Boulder, Colorado, 386 pp.

NCAR, 1985: The NCAR Eulerian regional acid deposition model. NCAR Tech. Note NCAR/TN-256+STR, June, National Center for Atmospheric Research, Boulder, Colorado, 178 pp.

NCAR, 1986: Preliminary evaluation studies with the regional acid deposition model (RADM). NCAR Tech. Note NCAR/TN-265+STR, March, National Center for Atmospheric Research, Boulder, Colorado, 202 pp.

NCAR, 1988: *Proceedings of the Workshop on Limited-Area Modeling Intercomparison.* National Center for Atmospheric Research, Boulder, Colorado, 244 pp. (Available from Dr. Y.-H. Kuo, Mesoscale and Microscale Meteorology Division, NCAR, P.O. Box 3000, Boulder, CO 80307).

Nicholls, S., M. A. LeMone, and G. Sommeria, 1982: The simulation of a fair weather marine boundary layer in GATE using a three-dimensional model. *Quart. J. Roy. Meteor. Soc.*, **108**, 167–190.

Nieuwstadt, F. T. M. and R. A. Brost, 1986: The decay of convective turbulence. *J. Atmos. Sci.*, **43**, 532–546.

NMC, 1973: NMC format for observational data (ADP reports). Office Note 29, September, National Meteorological Center, National Oceanic and Atmospheric Administration, Washington, D.C., 50 pp.

NMC, 1979: NMC 360/195 packed data fields. Office Note 84, November, National Meteorological Center, National Oceanic and Atmospheric Administration, Washington, D.C., 28 pp.

NMC, 1982: NMC format for surface reports. Office Note 124, April, National Meteorological Center, National Oceanic and Atmospheric Administration, Washington, D.C., 10 pp.

Noonan, J. A. and R. K. Smith, 1987: The generation of north Australian cloud lines and the 'morning glory'. *Aust. Met. Mag.*, **35**, 31–45.

Novikov, E. A., 1958: Concerning a turbulent diffusion in a stream with a transverse gradient of velocity. *J. Appl. Math. Mech.*, **22**, 576–579. (Translated from Russian).

NRC, 1983: *Acid Deposition: Atmospheric Processes in Eastern North America.* National Research Council, National Academy Press, Washington, D. C., 375 pp.

NRC, 1990: *Haze in the Grand Canyon: An Evaluation of the Winter Haze Intensive Tracer Experiment.* National Research Council, National Academy Press, Washington, D.C., 97 pp.

Ogura, Y., 1952: The structure of two-dimensionally isotropic turbulence. *J. Meteor. Soc. Japan*, **30**, 59–64.

Ogura, Y., 1953: The relation between the space- and time-correlation functions in a turbulent flow. *J. Meteor. Soc. Japan*, **31**, 355–369.

Ogura, Y., 1957: The influence of finite observation intervals on the measurement of turbulent diffusion parameters. *J. Meteor.*, **14**, 176–181.

Ogura, Y., 1958: On the isotropy of large-scale disturbances in the upper troposphere. *J. Meteor.*, **15**, 375–382.

Ogura, Y., 1959: Diffusion from a continuous source in relation to a finite observation interval. *Adv. Geophys.*, **6**, 149–159.

Okubo, A., 1966: A note on horizontal diffusion from an instantaneous source in a nonuniform flow. *J. Oceanogr. Soc. Japan*, **22**, 1–6.

Okubo, A., 1967: The effect of shear in an oscillatory current on horizontal diffusion from an instantaneous source. *Int. J. Oceanol. Limnol.*, **1**, 194–204.

Okubo, A., 1968: Some remarks on the importance of the 'shear effect' on horizontal diffusion. *J. Ocean. Soc. Japan*, **24**, 20–29.

Okubo, A., 1971: Oceanic diffusion diagrams. *Deep-Sea Res.*, **18**, 789–802.

Okubo, A. and M. J. Karweit, 1969: Diffusion from a continuous source in a uniform shear flow. *Limnol. Oceanogr.*, **14**, 514–520.

Olbers, D. J., 1983: Models of the oceanic internal wave field. *Rev. Geophys. Space Phys.*, **21**, 1567–1606.

Olesen, H. R., S. E. Larsen, and J. Højstrup, 1984: Modelling velocity spectra in the lower part of the planetary boundary layer. *Boundary-Layer Meteor.*, **29**, 285–312.

Oliger, J. and A. Sundström, 1978: Theoretical and practical aspects of some initial boundary value problems in fluid dynamics. *SIAM J. Appl. Math.*, **35**, 419–446.

Olsen, A. R., E. C. Voldner, D. S. Bigelow, W. H. Chan, T. L. Clark, M. A. Lusis, P. K. Misra, and R. J. Vet, 1990: Unified wet deposition data summaries for North America: data summary procedures and results for 1980–1986. *Atmos. Environ.*, **24A**, 661–672.

Onsager, L., 1949: Statistical hydrodynamics. *Nuovo Cimento (Suppl.)*, **6**, 279–287.

Oort, A. H. and A. Taylor, 1969: On the kinetic energy spectrum near the ground. *Mon. Wea. Rev.*, **97**, 623–636.

Orlanski, I., 1973: Trapeze instability as a source of internal gravity waves: Part I. *J. Atmos. Sci.*, **30**, 1007–1016.

Orlanski, I., 1975: A rational subdivision of scales for atmospheric processes. *Bull. Amer. Meteor. Soc.*, **56**, 527–530.

Orlanski, I., 1976: The trapeze instability in an equatorial β-plane. *J. Atmos. Sci.*, **33**, 745–763.

Orlanski, I., 1976b: A simple boundary condition for unbounded hyperbolic flows. *J. Comput. Phys.*, **21**, 251–269.

Orlanski, I. and K. Bryan, 1969: Formation of the thermocline step structure by large-amplitude internal gravity waves. *J. Geophys. Res.*, **74**, 6975–6983.

Orszag, S. A. and G. S. Patterson, Jr., 1972: Numerical simulation of turbulence. In *Statistical Models and Turbulence*, Rosenblatt, M. and C. Van Atta, Editors, Springer-Verlag, New York, 127–147. (Lecture Notes in Physics, Vol. 12).

Ottersten, H., K. R. Hardy, and C. G. Little, 1973: Radar and sodar probing of waves and turbulence in statically stable clear-air layers. *Boundary-Layer Meteor.*, **4**, 47–89.

Ozmidov, R. V., 1965: On the turbulent exchange in a stably stratified ocean. *Bull. USSR Acad. Sci. Atmos. Oceanic Phys.*, **1**, 493–497. (English translation).

Pack, D. H. and J. K. Angell, 1963: A preliminary study of air trajectories in the Los Angeles Basin as derived from tetroon flights. *Mon. Wea. Rev.*, **91**, 583–604.

Pack, D. H., G. J. Ferber, J. L. Heffter, K. Telegadas, J. K. Angell, W. H. Hoecker, and L. Machta, 1978: Meteorology of long-range transport. *Atmos. Environ.*, **12**, 425–444.

Paegle, J., W. G. Zdunkowski, and R. M. Welch, 1976: Implicit differencing of predictive equations of the boundary layer. *Mon. Wea. Rev.*, **104**, 1321–1324.

Paegle, J., R. A. Pielke, G. A. Dalu, W. Miller, J. R. Garratt, T. Vukicevic, G. Berri, and M. Nicolini, 1990: Predictability of flows over complex terrain. In *Atmospheric Processes over Complex Terrain*, Blumen, W., Editor, American Meteorological Society, Boston, 285–299.

Page, S. H., 1980: National land use and land cover inventory. Report prepared by Lockheed Engineering and Management Service Company, Inc. under contract No. EPA-68-03-2636 for the Office of Research and Development, U.S. Environmental Protection Agency, Las Vegas, Nevada, 11 pp. [Available from the Atmospheric Sciences Research Laboratory, U.S. Environmental Protection Agency, Research Triangle Park, North Carolina].

Palmer, T. N., G. J. Shutts, and R. Swinbank, 1986: Alleviation of a systematic westerly bias in general circulation and numerical weather prediction models through an orographic gravity wave drag parameterization. *Quart. J. Roy. Meteor. Soc.*, **112**, 1001–1039.

Panofsky, H. A., 1969: Internal atmospheric turbulence. *Bull. Amer. Meteor. Soc.*, **50**, 539–543.

Panofsky, H. A., 1978: Discussion of "A Laboratory Study of Dispersion from an Elevated Source within a Modeled Convective Planetary Boundary Layer". *Atmos. Environ.*, **12**, 2036.

Panofsky, H. A. and I. Van der Hoven, 1956: Spectra and cross-spectra of velocity components in the mesometeorological range. *Quart. J. Roy. Meteor. Soc.*, **82**, 603–606.

Panofsky, H. A. and J. A. Dutton, 1984: *Atmospheric Turbulence.* J. Wiley & Sons, New York, 397 pp.

Panofsky, H. A., D. W. Thomson, D. A. Sullivan, and D. E. Moravek, 1974: Two-point velocity statistics over Lake Ontario. *Boundary-Layer Meteor.*, **7**, 309–321.

Pao, H.-P. and T. W. Kao, 1977: Vortex structure in the wake of a sphere. *Phys. Fluids*, **20**, 187–191.

Pao, Y.-H., 1973: Measurements of internal waves and turbulence in two-dimensional stratified shear flows. *Boundary-Layer Meteor.*, **5**, 177–193.

Pao, Y.-H. and J.-T. Lin, 1973: Turbulent wakes of a towed slender body in stratified and nonstratified fluids: analysis and flow visualizations. *Bull. Amer. Phys. Soc.*, **18**, 1484.

Papadakis, J., 1969: *Soils of the World.* Elsevier Publishing Co., New York, 208 pp.

Parish, T. R., A. R. Rodi, and R. D. Clark, 1988: A case study of the summertime Great Plains low level jet. *Mon. Wea. Rev.*, **116**, 94–105.

Pasquill, F., 1961: The estimation of the dispersion of windborne material. *Meteor. Mag.*, **90**, 33–49.

Pasquill, F., 1962: Some observed properties of medium-scale diffusion in the atmosphere. *Quart. J. Roy. Meteor. Soc.*, **88**, 70–79.

Pasquill, F., 1969: The influence of the turning of wind with height on crosswind diffusion. *Proc. Royal Soc. London A*, **265**, 173–181.

Pasquill, F., 1974: Limitations and prospects in the estimation of dispersion of pollution on a regional scale. *Adv. Geophys.*, **18B**, 1–13.

Pasquill, F., 1975: The dispersion of materials in the atmospheric boundary layer — the basis for generalization. In *Lectures on Air Pollution and Environmental Impact Analyses*, Haugen, D. A., Editor, American Meteorological Society, Boston, 1–34.

Pasquill, F. and F. B. Smith, 1983: *Atmospheric Diffusion, Third Edition.* John Wiley & Sons, New York, 437 pp.

Patnaik, P. C., F. S. Sherman, and G. M. Corcos, 1976: A numerical simulation of Kelvin-Helmholtz waves of finite amplitude. *J. Fluid Mech.*, **73**, 215–240.

Pearson, F., I., 1990: *Map Projections: Theory and Applications.* CRC Press, Inc., Boca Raton, 372 pp.

Pecnick, M. J. and D. Keyser, 1989: The effect of spatial resolution on the simulation of upper- tropospheric frontogenesis using a sigma-coordinate primitive equation model. *Meteor. Atmos. Phys.*, **40**, 137–149.

Pedgley, D. E., 1982: *Windborne Pests and Diseases.* Ellis-Horwood Ltd, Chichester, 250 pp.

Pennell, W. T. and M. A. LeMone, 1974: An experimental study of turbulence structure in the fair-weather trade wind boundary layer. *J. Atmos. Sci.*, **31**, 1308–1323.

Pepper, D. W. and R. E. Cooper, 1983: Preliminary analysis of four numerical models for calculating the mesoscale transport of Kr-85. *Atmos. Environ.*, **17**, 1881–1895.

Perkey, D. J. and C. W. Kreitzberg, 1976: A time-dependent lateral boundary condition scheme for limited-area primitive equation models. *Mon. Wea. Rev.*, **104**, 744–755.

Persson, C., H. Rodhe, and L.-E. De Geer, 1987: The Chernobyl accident — a meteorological analysis of how radionuclides reached and were deposited in Sweden. *Ambio*, **16**, 20–31.

Persson, P. O. G. and T. T. Warner, 1991: Model generation of spurious gravity waves due to inconsistency of the vertical and horizontal resolution. *Mon. Wea. Rev.*, **119**, 917–935.

Peterson, K. R., 1968: Continuous point source behavior out to 160 miles. *J. Appl. Meteor.*, **7**, 217–226.

PG&E, 1988: Incorporation of Doppler acoustic radar data into a dispersion model, Phase II – field experiment. PG&E Tech. Report No. 009.5-88.3, July, Pacific Gas and Electric Company, San Ramon, California, 124 pp.

Phillips, N. A., 1979: The Nested Grid Model. NOAA Technical Report NWS 22, April, National Weather Service, National Oceanic and Atmospheric Administration, Silver Spring, Maryland, 80 pp.

Phillips, N. A. and J. Shukla, 1973: On the strategy of combining coarse and fine grid meshes in numerical weather prediction. *J. Appl. Meteor.*, **12**, 763–770.

Phillips, O. M., 1971: On spectra measured in an undulating layered medium. *J. Phys. Ocean.*, **1**, 1–6.

Phillips, O. M., 1977: *The Dynamics of the Upper Ocean, Second Edition.* Cambridge University Press, Cambridge, 336 pp.

Physick, W. L., 1988: Review: mesoscale modelling in complex terrain. *Earth-Science Reviews*, **25**, 199–235.

Physick, W. L. and D. J. Abbs, 1991: Modeling of summertime flow and dispersion in the coastal terrain of southeastern Australia. *Mon. Wea. Rev.*, **119**, 1014–1030.

Physick, W. L., D. J. Abbs, and R. A. Pielke, 1989: Formulation of the thermal internal boundary layer in a mesoscale model. *Boundary-Layer Meteor.*, **49**, 99–111.

Piedelievre, J. P., L. Musson-Genon, and F. Bompay, 1990: MEDIA - an Eulerian model of atmospheric dispersion: first validation on the Chernobyl release. *J. Appl. Meteor.*, **29**, 1205–1220.

Pielke, R. A., 1984: *Mesoscale Meteorological Modeling.* Academic Press, Orlando, Florida, 612 pp.

Pielke, R. A., 1974a: A three-dimensional numerical model of the sea breezes over south Florida. *Mon. Wea. Rev.*, **102**, 115–134.

Pielke, R. A., 1974b: A comparison of three-dimensional and two-dimensional numerical predictions of sea breezes. *J. Atmos. Sci.*, **31**, 1577–1585.

Pielke, R. A. and Y. Mahrer, 1975: Representation of the heated planetary boundary layer in mesoscale models with coarse vertical resolution. *J. Atmos. Sci.*, **32**, 2288–2308.

Pielke, R. A. and M. Segal, 1986: Mesoscale circulations forced by differential terrain heating. In *Mesoscale Meteorology and Forecasting*, Ray, P. S., Editor, American Meteorological Society, Boston, 516–548.

Pielke, R. A., H. A. Panofsky, and M. Segal, 1983: A suggested refinement for O'Brien's convective boundary layer eddy exchange coefficient formulation. *Boundary-Layer Meteor.*, **26**, 191–195.

Pielke, R. A., W. A. Lyons, R. T. McNider, M. D. Moran, D. A. Moon, R. A. Stocker, R. L. Walko, and M. Uliasz, 1991: Regional and mesoscale meteorological modeling as applied to air quality studies. In *Air Pollution Modelling and Its Application VIII*, van Dop, H. and D. G. Steyn, Editors, Plenum Press, New York, 259–289.

Pielke, R. A., W. R. Cotton, R. L. Walko, C. J. Tremback, W. Lyons, L. Grasso, M. E. Nicholls, M. D. Moran, D. A. Wesley, T. J. Lee, and J. H. Copeland, 1992: A comprehensive meteorological modeling system — RAMS. *Meteor. Atmos. Phys.* (In press).

Pielke, R. A., R. W. Arritt, M. Segal, M. D. Moran, and R. T. McNider, 1987a: Mesoscale numerical modeling of pollutant transport in complex terrain. *Boundary-Layer Meteor.*, **41**, 59–74.

Pielke, R. A., M. Segal, R. W. Arritt, and M. D. Moran, 1987b: Mesoscale influences on long-range pollutant transport. In *Compendium of Papers Presented at CIRA Workshop on Acid Deposition in Colorado*, Cooperative Institute on Research in the Atmosphere, Fort Collins, Colorado, 219–227.

Pielke, R. A., M. D. Moran, M. Segal, D. A. Wesley, and T. B. McKee, 1987c: Opportunities for nowcasting air pollution episodes and accidental toxic and radioactive releases. In *Proc. IUGG Symposium on Mesoscale Analysis and Forecasting, Incorporating Nowcasting*, August 17-19, 1987, Vancouver, B.C., International Union of Geodesy and Geophysics, Geneva, 463–470.

Pierrehumbert, R. T., 1986: Lee cyclogenesis. In *Mesoscale Meteorology and Forecasting*, Ray, P. S., Editor, American Meteorological Society, Boston, 493–515.

Pierrehumbert, R. T. and B. Wyman, 1985: Upstream effects of mesoscale mountains. *J. Atmos. Sci.*, **42**, 977–1003.

Pinus, N. Z., 1968: The energy of atmospheric macroturbulence. *Bull. USSR Acad. Sci. Atmos. Oceanic Phys.*, 4, 461–464.

Pinus, N. Z., 1977: Experimental studies of mesoscale turbulence in the upper troposphere. *Izv. Atmos. Oceanic Phys.*, **13**, 808–814.

Pinus, N. Z., 1979: Spectra of longitudinal and transverse fluctuations in wind speed at altitudes of 10-20 km. *Izv. Atmos. Oceanic Phys.*, **15**, 93–97.

Pinus, N. Z., E. R. Reiter, G. N. Shur, and N. K. Vinnichenko, 1967: Power spectra of turbulence in the free atmosphere. *Tellus*, **19**, 206–213.

Pitts, R. O. and T. J. Lyons, 1987: Switching between first-order closure schemes in a numerical mesoscale model. *Mon. Wea. Rev.*, **115**, 3188–3199.

Platzman, G. W., 1954: The computational stability of boundary conditions in numerical integration of the vorticity equation. *Arch. Met. Geophys. Biokl.*, **A7**, 29–40.

Platzman, G. W., 1979: The ENIAC computations of 1950 — gateway to numerical weather prediction. *Bull. Amer. Meteor. Soc.*, **60**, 302–312.

Pleune, R., 1990: Vertical diffusion in the stable atmosphere. *Atmos. Environ.*, **24A**, 2547–2555.

Pohle, J. F., A. K. Blackadar, and H. A. Panofsky, 1965: Characteristics of quasi-horizontal mesoscale eddies. *J. Atmos. Sci.*, **22**, 219–221.

Policastro, A. J., M. Wastag, J. D. Shannon, R. Carhart, and W. Dunn, 1983: Evaluation of two short-term long-range transport models with field data. In *Trans. APCA Specialty Conf. Meteorology of Acid Deposition*, Samson, P. J., Editor, Air Pollution Control Association, Pittsburgh, 513–521.

Policastro, A. J., M. Wastag, L. Coke, R. A. Carhart, and W. E. Dunn, 1986a: Evaluation of short-term long-range transport models. Volume I: Analysis procedures and results. Technical Report EPA-450/4-86-016a, October, U.S. Environmental Protection Agency, Research Triangle Park, North Carolina, 215 pp.

Policastro, A. J., M. Wastag, L. Coke, R. A. Carhart, and W. E. Dunn, 1986b: Evaluation of short-term long-range transport models. Volume II: Appendices A through E. Technical Report EPA-450/4-86-016b, October, U.S. Environmental Protection Agency, Research Triangle Park, North Carolina, 291 pp.

Policastro, A. J., M. Wastag, L. Coke, R. A. Carhart, W. E. Dunn, N. Possiel, and J. Tikvart, 1986c: Evaluation of eight short-term long-range transport models with field data. In *Proc. Fifth AMS/APCA Joint Conf. Applications of Air Pollution Meteorology*, Nov. 18–21, Chapel Hill, N.C., American Meteorological Society, Boston, 53–56.

Powell, D. C. and C. E. Elderkin, 1974: An investigation of the application of Taylor's hypothesis to atmospheric boundary layer turbulence. *J. Atmos. Sci.*, **31**, 990–1002.

Preisendorfer, R. W. and T. P. Barnett, 1983: Numerical model–reality intercomparison tests using small-sample statistics. *J. Atmos. Sci.*, **40**, 1884–1896.

Pudykiewicz, J., R. Benoit, and A. Staniforth, 1985a: Validating the PBL parameterization of a finite element regional model using data of the tracer experiment CAPTEX. In *Proc. 7th AMS Conf. Numerical Weather Prediction*, June 17–20, Montreal, Quebec, American Meteorological Society, Boston, 359–361.

Pudykiewicz, J., R. Benoit, and A. Staniforth, 1985b: Preliminary results from a partial LRTAP model based on an existing meteorological forecast model. *Atmos. Ocean*, **23**, 267–303.

Purnama, A., 1988: Boundary retention effects upon contaminant dispersion in parallel flows. *J. Fluid Mech.*, **195**, 393–412.

Queney, P., G. A. Corby, N. Gerbier, H. Koschmieder, and J. Zierep, 1960: The airflow over mountains. Technical Note No. 34, Secretariat of the World Meteorological Organization, Geneva, 135 pp. (WMO Number 98.TP.43).

Rahn, K. A., 1984: Some remarks on continental and global transport. In *Proc. Atmospheric Tracer Workshop*, Barr, S., W. E. Clements, and P. R. Guthals, Editors, May 21–25, Santa Fe, New Mexico, Report No. LA-10301-C, December, Los Alamos National Laboratory, Los Alamos, New Mexico, 349–352.

Randerson, D., 1968: A study of air pollution sources as viewed by earth satellites. *J. Air Pollu. Control Assoc.*, **18**, 249–253.

Randerson, D., 1972: Temporal changes in horizontal diffusion parameters of a single nuclear debris cloud. *J. Appl. Meteor.*, **11**, 670–673.

Randerson, D., 1977: Quantitative analysis of atmospheric pollution phenomena. In *Skylab Explores the Earth, NASA SP-380*, Scientific and Technical Information Office, National Aeronautics and Space Administration, Washington, D.C., 381–405.

Randerson, D., J. G. Garcia, and V. S. Whitehead, 1971: Photogrammetric and photometric investigation of a smoke plume viewed from space. *J. Appl. Meteor.*, **10**, 1122–1131.

Rao, K. S., J.-Y. Ku, and S. T. Rao, 1989: A comparison of three urban air pollution models. *Atmos. Environ.*, **23**, 793–801.

Rasch, P. J., 1986: Toward atmospheres without tops: absorbing upper boundary conditions for numerical models. *Quart. J. Roy. Meteor. Soc.*, **112**, 1195–1218.

Raupach, M. R., 1988: Canopy transport processes. In *Flow and Transport in the Natural Environment*, Steffen, W. L. and O. T. Denmead, Editors, Springer-Verlag, New York, 95–132.

Ray, P. S., Editor, 1986: *Mesoscale Meteorology and Forecasting.* American Meteorological Society, Boston, 793 pp.

Raymond, W. H. and H. L. Kuo, 1984: A radiation boundary condition for multidimensional flows. *Quart. J. Roy. Meteor. Soc.*, **110**, 535–551.

Raynor, G. S. and J. V. Hayes, 1984: Wind direction meander at a coastal site during onshore flows. *J. Climate Appl. Meteor.*, **23**, 967–978.

Raynor, G. S., R. N. Dietz, and T. W. D'Ottavio, 1984: Aircraft measurements of tracer gas during the 1983 Cross Appalachian Tracer Experiment (CAPTEX). In *Proc. Fourth AMS/APCA Joint Conf. on Applications of Air Pollution Meteorology*, Oct. 16-19, Portland, Oregon, American Meteorological Society, Boston, 162–165.

Readings, C. J. and H. E. Butler, 1972: The measurement of atmospheric turbulence from a captive balloon. *Met. Mag.*, **101**, 286–298.

Reid, J. D., 1979: Markov chain simulations of vertical dispersion in the neutral surface layer for surface and elevated releases. *Boundary-Layer Meteor.*, **16**, 3–22.

Reisinger, L. M. and S. F. Mueller, 1983: Comparisons of tetroon and computed trajectories. *J. Climate Appl. Meteor.*, **22**, 664–672.

Reiter, E. R., 1978: *Atmospheric Transport Processes. Part 4: Radioactive Tracers.* Technical Information Center, U. S. Dept. of Energy, Washington, D. C., 605 pp. (Available as TID-27114 from National Technical Information Service, U.S. Department of Commerce, Springfield, Virginia 22161.

Reiter, E. R. and A. Burns, 1966: The structure of clear-air turbulence derived from "TOPCAT" aircraft measurements. *J. Atmos. Sci.*, **23**, 206–212.

Reynolds, O., 1895: On the dynamical theory of incompressible viscous fluids and the determination of the criterion. *Phil. Trans. Roy. Soc. London, Ser. A*, **186**, 123–164.

Rhines, P. B., 1975: Waves and turbulence on a beta-plane. *J. Fluid Mech.*, **69**, 417–443.

Rhines, P. B., 1979: Geostrophic turbulence. In *Annual Review of Fluid Mechanics, Vol. 11*, Annual Reviews, Inc., Palo Alto, California, 401–441.

Richardson, L. F., 1922: *Weather Prediction by Numerical Process.* Cambridge University Press, 236 pg. (Reprinted by Dover Publications, New York, 1965).

Richardson, L. F., 1926: Atmospheric diffusion shown on a distance-neighbour graph. *Proc. Roy. Soc. London*, **A110**, 709–737.

Richardson, L. F., 1952: Transforms for the eddy-diffusion of clusters. *Proc. Roy. Soc. London, Series A*, **214**, 1–20.

Richardson, L. F. and D. Proctor, 1925: Diffusion over distances ranging from 3 km to 86 km. *Mem. Roy. Met. Soc.*, **1**, 1–15.

Richardson, L. F. and H. Stommel, 1948: Note on eddy diffusion in the sea. *J. Meteor.*, **5**, 238–240.

Richter, J. H., 1969: High-resolution tropospheric radar sounding. *Radio Sci.*, 4, 1261–1268.

Riley, J. J., R. W. Metcalfe, and M. A. Weissman, 1981: Direct numerical simulations of homogeneous turbulence in density-stratified fluids. In *Nonlinear Properties of Internal Waves*, West, B. J., Editor, American Institute of Physics, New York, 79–112. (La Jolla Institute, 1981, AIP Conf. Proc. No. 106).

Roache, P. J., 1972: *Computational Fluid Dynamics.* Hermosa Publishers, Albuquerque, New Mexico, 446 pp.

Robinson, G. D., 1967: Some current projects for global meteorological observation and experiment. *Quart. J. Roy. Meteor. Soc.*, **93**, 409–418.

Rodriguez, D. J., 1988: Long range transport: evaluation of a particle-in-cell model using sources in the U.S. and U.S.S.R. In *Proc. 17th NATO-CCMS Int. Tech. Mtg on Air Pollution and Its Applications*, Sept. 19–22, Cambridge, England, Committee on the Challenges of Modern Society, North Atlantic Treaty Organization, Brussels.

Rodriguez, D. J. and R. T. Cederwall, 1991: A preliminary evaluation of ADPIC model performance on selected ANATEX releases using observed, analyzed and dynamically predicted winds. In *Air Pollution Modeling and Its Application VIII*, van Dop, H. and D. G. Steyn, Editors, Plenum Press, New York, 439–446.

Rogallo, R. S. and P. Moin, 1984: Numerical simulation of turbulent flows. *Ann. Rev. Fluid Mech.*, **16**, 99–137.

Rolph, G. D. and R. R. Draxler, 1990: Sensitivity of three-dimensional trajectories to the spatial and temporal densities of the wind field. *J. Appl. Meteor.*, **29**, 1043–1054.

Ropelewski, C. F., H. Tennekes, and H. A. Panofsky, 1973: Horizontal coherence of wind fluctuations. *Boundary-Layer Meteor.*, **5**, 353–363.

Röttger, J. and M. F. Larsen, 1990: UHF/VHF radar techniques for atmospheric research and wind profiler applications. In *Radar in Meteorology*, Atlas, D., Editor, American Meteorological Society, Boston, 235–281.

Rowe, R. D., 1981: Comments on "On Lateral Dispersion Coefficients as Functions of Averaging Time". *J. Appl. Meteor.*, **20**, 728–730.

Ruff, R. E., K. C. Nitz, F. L. Ludwig, C. M. Bhumralkar, J. D. Shannon, C. M. Sheih, I. Y. Lee, R. Kumar, and D. J. McNaughton, 1985: Evaluation of three regional air quality models. *Atmos. Environ.*, **19**, 1103–1115.

Runchal, A. K., 1980: A random walk atmospheric dispersion model for complex terrain and meteorological conditions. In *Proc. Second AMS/APCA Conf. on Applications of Air Pollution Meteorology*, March 24-27, New Orleans, American Meteorological Society, Boston, 430-437.

Ruscher, P., 1988: Coherent structures in the very stable atmospheric boundary layer. In *Proc. 8th AMS Symp. on Turbulence and Diffusion*, April 25-29, San Diego, American Meteorological Society, Boston, 140–143.

Ruscher, P. and L. Mahrt, 1989: Coherent structures in the very stable atmospheric boundary layer. *Boundary-Layer Meteor.*, **47**, 41–54.

Sackinger, P. A., D. D. Reible, and F. H. Shair, 1982: Uncertainties associated with the estimation of mass balances and Gaussian parameters from atmospheric tracer studies. *J. Air Pollu. Contr. Assoc.*, **32**, 720–724.

Sadourny, R., 1986: Turbulent diffusion in large-scale flows. In *Large-Scale Transport Processes in Oceans and Atmosphere*, Willebrand, J. and D. L. T. Anderson, Editors, D. Reidel Publishing Co., Dordrecht, 359–373.

Saffman, P. G., 1962: The effect of wind shear on horizontal spread from an instantaneous ground source. *Quart. J. Roy. Meteor. Soc.*, **88**, 382–393.

Sakagami, J., 1961: Diffusion experiments using balloons. Natural Science Report 12, No.2, Ochanomizu Univ.

Saltzman, B., 1957: Equations governing the energetics of the larger scales of atmospheric turbulence in the domain of wave number. *J. Meteor.*, **14**, 513–523.

Saltzman, B., 1958: Some hemispherical spectral statistics. *J. Meteor.*, **15**, 259–263.

Saltzman, B., 1970: Large-scale atmospheric energetics in the wave-number domain. *Rev. Geophys. Space Phys.*, **8**, 289–302.

Saltzman, B. and A. Fleisher, 1962: Spectral statistics of the wind at 500 mb. *J. Atmos. Sci.*, **19**, 195–204.

Samson, P. J., 1980: Trajectory analysis of summertime sulfate concentrations in the northeastern United States. *J. Appl. Meteor.*, **19**, 1382–1394.

Sanderson, B. G. and A. Okubo, 1988: Diffusion by internal waves. *J. Geophys. Res.*, **93C**, 3570–3582.

Saulesleja, A., Editor, 1986: *Great Lakes Climatological Atlas.* Atmospheric Environment Service, Environment Canada, 145 pp. [Available from Canadian Government Publishing Centre, Ottawa, Canada K1A 059].

Saunders, P. M., 1972: Comments on "Wavenumber-Frequency Spectra of Temperature in the Free Atmosphere". *J. Atmos. Sci.*, **29**, 197–199.

Sawford, B. L., 1982: Lagrangian Monte Carlo simulation of the turbulent motion of a pair of particles. *Quart. J. Roy. Meteor.*, **108**, 207–213.

Sawford, B. L., 1984: The basis for, and some limitations of, the Langevin equation in atmospheric relative dispersion modelling. *Atmos. Environ.*, **18**, 2405–2411.

Sawford, B. L., 1985: Lagrangian statistical simulation of concentration mean and fluctuation fields. *J. Clim. Appl. Meteor.*, **24**, 1152–1166.

Sawford, B. L., 1986: Generalized random forcing in random-walk turbulent dispersion models. *Phys. Fluids*, **29**, 3582–3585.

Sawford, B. L. and F. M. Guest, 1987: Lagrangian stochastic analysis of flux-gradient relationships in the convective boundary layer. *J. Atmos. Sci.*, **44**, 1152–1165.

Sawford, B. L. and F. M. Guest, 1988: Uniqueness and universality of Lagrangian stochastic models of turbulent dispersion. In *Proc. Eighth AMS Symp. on Turbulence and Diffusion*, April 25-29, San Diego, American Meteorological Society, Boston, 96-99.

Sawyer, J. S., 1961: Quasi-periodic wind variations with height in the lower stratosphere. *Quart. J. Roy. Meteor. Soc.*, **87**, 24–33.

Saxton, J. A., J. A. Lane, and R. W. Meadows, 1964: Layer structure of the troposphere. *Proc. IEE*, **111**, 275–283.

SCENES, 1987: Winter Haze Intensive Tracer Experiment (WHITEX). SCENES Newsletter, Vol. 1, No. 2, 4 pp., (Available from Chuck McDade, EMSI, 4765 Calle Quetzal, Camarillo, CA 93010).

Schaefer, J. T., 1986: The dryline. In *Mesoscale Meteorology and Forecasting*, Ray, P. S., Editor, American Meteorological Society, Boston, 549–572.

Scheffler, A. O. and C. H. Liu, 1985: On observation of gravity wave spectra in the atmosphere by using MST radars. *Radio Sci.*, **20**, 1309–1322.

Scheffler, A. O. and C. H. Liu, 1986: The effect of Doppler shift on gravity wave spectra observed by MST radar. *J. Atmos. Terr. Phys.*, **48**, 1225–1231.

Schmidt, J. M. and W. R. Cotton, 1990: Interactions between upper and lower tropospheric gravity waves on squall line structure and maintenance. *J. Atmos. Sci.*, **47**, 1205–1222.

Schorling, M., H.-U. Mast, and J. Schmidt, 1986: Lagrangian simulation of neutral and heavy gases in complex terrain and streets. Technical report, April, Hauptabteilung Systemstudien, Industrieanlagen-Betriebsgesellschaft, Ottobrunn, West Germany, 35 pp. (Unpublished manuscript).

Scoggins, J. R., 1965: Spherical balloon wind sensor behavior. *J. Appl. Meteor.*, **4**, 139–145.

Scorer, R. S., 1949: Theory of waves in the lee of mountains. *Quart. J. Roy. Meteor. Soc.*, **75**, 41–56.

Scorer, R. S., 1986: *Cloud Investigation By Satellite.* Ellis Horwood Ltd, Chichester, ca. 300 pp.

Seaman, N. L., 1991: Four-dimensional data assimilation of boundary layer measurements for the 1990s. In *Proc. Seventh AMS/AWMA Conf. on Applications of Air Pollution Meteorology*, Jan. 14–18, New Orleans, American Meteorological Society, Boston, J109–J114.

Seaman, N. L. and C. D. Cole, 1991: Application of four-dimensional data assimilation for generating three-day episodic meteorological fields over the Los Angeles basin suitable for air quality modeling. In *Proc. 7th Joint AMS/AWMA Conf. on Applications of Air Pollution Meteorology*, Jan. 14-18, New Orleans, American Meteorological Society, Boston, 320–323.

Seaman, N. L., F. L. Ludwig, E. G. Donall, T. T. Warner, and C. M. Bhumralkar, 1989: Numerical studies of urban planetary boundary-layer structure under realistic synoptic conditions. *J. Appl. Meteor.*, **28**, 760–781.

Segal, M., R. A. Pielke, R. W. Arritt, M. D. Moran, C.-H. Yu, and D. Henderson, 1986: Southern Florida air pollution climatology study and selected episodic impacts. Final Report Contract No. NA81RAH00001, Amendment 17, Item 15, October, Air Quality Division, National Park Service, Department of Interior, Denver, Colorado, 237 pp.

Segal, M., R. A. Pielke, R. W. Arritt, and R. T. McNider, 1987: Comment on "Spatial Switching between First-Order Closure Schemes in a Numerical Mesoscale Model". *Mon. Wea. Rev.*, **115**, 3200–3201.

Segal, M., R. A. Pielke, R. W. Arritt, M. D. Moran, C.-H. Yu, and D. Henderson, 1988: Application of a mesoscale atmospheric dispersion modeing system to the estimation of SO_2 concentrations from major elevated sources in southern Florida. *Atmos. Environ.*, **22**, 1319–1334.

Segal, M., J. Weaver, and J. F. W. Purdom, 1989: Some effects of the Yellowstone fire smoke plume on northeast Colorado at the end of summer 1988. *Mon. Wea. Rev.*, **117**, 2278–2284.

Segal, M., J. H. Cramer, R. A. Pielke, J. R. Garrett, and P. Hildebrand, 1990: Observational evaluation of the snow-breeze. *Mon. Wea. Rev.* (Submitted).

Seigneur, C., T. W. Tesche, P. M. Roth, and M.-K. Liu, 1983: On the treatment of point source emissions in urban air quality modeling. *Atmos. Environ.*, **17**, 1655–1676.

Seilkop, S. K. and P. L. Finkelstein, 1987: Acid precipitation patterns and trends in eastern North America, 1980–84. *J. Climate Appl. Meteor.*, **26**, 980–994.

Seinfeld, J. H., 1986: *Atmospheric Chemistry and Physics of Air Pollution.* John Wiley & Sons, New York, 738 pp.

Seitter, K. L., 1988: Some aspects of the geostrophic adjustment process in meso-beta numerical models revealed by lateral boundary tests and implications for model initialization. In *Eighth AMS Conf. on Numerical Weather Prediction*, Feb. 22-26, Baltimore, Maryland, American Meteorological Society, Boston, 848–854.

Sellers, P. J. and J. L. Dorman, 1987: Testing the Simple Biosphere Model (SiB) using point micrometeorological and biophysical data. *J. Climate Appl. Meteor.*, **26**, 622–651.

Sellers, W. D., 1965: *Physical Climatology.* The University of Chicago Press, Chicago, 272 pp.

SethuRaman, S., 1977: The observed generation and breaking of atmospheric internal gravity waves over the ocean. *Boundary-Layer Meteor.*, **12**, 331–349.

SethuRaman, S., 1980: A case of persistent breaking of internal gravity waves in the atmospheric surface layer over the ocean. *Boundary-Layer Meteor.*, **19**, 67–80.

SethuRaman, S., C. Nagle, and G. S. Raynor, 1982: Seasonal variations in the formation of internal gravity waves at a coastal site. *J. Appl. Meteor.*, **21**, 237–241.

Shair, F. H., E. J. Sasaki, D. E. Carlan, G. R. Cass, W. R. Goodin, J. G. Edinger, and G. E. Schacher, 1982: Transport and dispersion of airborne pollutants associated with the land breeze—sea breeze system. *Atmos. Environ.*, **16**, 2043–2053.

Shapiro, M. A. and J. T. Hastings, 1973: Objective cross-section analyses by Hermite polynomial interpolation on isentropic surfaces. *J. Appl. Meteor.*, **12**, 753–762.

Shaw, R. H., J. Tavangar, and D. P. Ward, 1983: Structure of the Reynolds stress in a canopy layer. *J. Clim. Appl. Meteor.*, **22**, 1922–1931.

Sheih, C. M., 1978: A puff pollutant dispersion model with wind shear and dynamic plume rise. *Atmos. Environ.*, **12**, 1933–1938.

Sheih, C. M., 1980: On lateral dispersion coefficients as functions of averaging time. *J. Appl. Meteor.*, **19**, 557–561.

Sheih, C. M., M. L. Wesely, and C. J. Walcek, 1986: A dry deposition module for regional acid deposition. Report prepared by Argonne National Laboratory for the Atmospheric Sciences Research Laboratory, Office of Research and Development, U.S. Environmental Protection Agency, Research Triangle Park, North Carolina, 63 pp.

Shepherd, T. G., 1987: A spectral view of nonlinear fluxes and stationary-transient interaction in the atmosphere. *J. Atmos. Sci.*, **44**, 1166–1178.

Sherman, F. S., J. Imberger, and G. M. Corcos, 1978: Turbulence and mixing in stably stratified waters. *Ann. Rev. Fluid Mech.*, **10**, 267–288.

Shi, B.-Q., J. D. Kahl, Z. D. Christidis, and P. J. Samson, 1990: Simulation of the three-dimensional distribution of tracer during the Cross-Appalachian Tracer Experiment. *J. Geophys. Res.*, **95**, 3693–3703.

Sidi, C. and F. Dalaudier, 1989: Temperature and heat flux spectra in the turbulent buoyancy subrange. *Pure Appl. Geophys.*, **130**, 547–569.

Sidi, C., J. Lefrere, F. Dalaudier, and J. Barat, 1988: An improved atmospheric buoyancy wave spectrum model. *J. Geophys. Res.*, **93**, 774–790.

Siggia, E. D. and G. S. Patterson, 1978: Intermittency effects in a numerical simulation of stationary three-dimensional turbulence. *J. Fluid Mech.*, **86**, 567–592.

Simpson, J. E., 1987: *Gravity Currents in the Environment and the Laboratory.* Ellis Horwood Ltd, Chichester, 244 pp.

Skupniewicz, C. E., 1987: Measurements of overwater diffusion: the separation of relative diffusion and meander. *J. Climate Appl. Meteor.*, **26**, 949–958.

Slade, D. H., Editor, 1968: *Meteorology and Atomic Energy 1968.* U.S. Atomic Energy Commission, Washington, D.C., 445 pp. (Available as Publication TID-24190 from the National Technical Information Service, U.S. Department of Commerce, Springfield, Virginia 22161).

Smagorinsky, J., 1963: General circulation experiments with the primitive equations. I: The basic experiment. *Mon. Wea. Rev.*, **91**, 99–164.

Smeda, M. S., 1979: Incorporation of planetary boundary-layer processes into numerical forecasting models. *Boundary-Layer Meteor.*, **16**, 115–129.

Smedman-Högström, A. S. and U. Högström, 1975: Spectral gap in surface-layer measurements. *J. Atmos. Sci.*, **32**, 340–350.

Smith, F. B., 1962: The effect of sampling and averaging on the spectrum of turbulence. *Quart. J. Roy. Meteor. Soc.*, **88**, 177–180.

Smith, F. B., 1965: The role of wind shear in horizontal diffusion of ambient particles. *Quart. J. Roy. Meteor. Soc.*, **91**, 318–329.

Smith, F. B., 1968: Conditioned particle motion in a homogeneous turbulent field. *Atmos. Environ.*, **2**, 491–508.

Smith, F. B., 1979a: The character and importance of plume lateral spread affecting the concentration downwind of isolated sources of hazardous airborne material. In *Proc. WMO Symp. on Long-Range Transport of Pollutants and Its Relation to General Circulation Including Stratospheric/Tropospheric Exchange Processes*, WMO Publ. No. 538, October 1–5, Sofia, Bulgaria, World Meteorological Organization, Geneva, 241–251.

Smith, F. B., 1983: Discussion of "Horizontal Difusion in the Atmosphere: A Lagrangian–Dynamical Theory". *Atmos. Environ.*, **17**, 194–197.

Smith, F. B., 1987: Atmospheric turbulent transport. In *Regional and Long-range Transport of Air Pollution*, Sandroni, S., Editor, Elsevier Scientific Publishers B.V., Amsterdam, 43–69.

Smith, F. B. and J. S. Hay, 1961: The expansion of clusters of particles in the atmosphere. *Quart. J. Roy. Meteor. Soc.*, **87**, 82–101.

Smith, F. B. and R. D. Hunt, 1978: Meteorological aspects of the transport of pollution over long distances. *Atmos. Environ.*, **12**, 461–477.

Smith, F. B. and M. J. Clark, 1988: Wet and dry deposition of Chernobyl releases. *Nature*, **322**, 245–249.

Smith, M. E., 1984: Review of the attributes and performance of 10 rural diffusion models. *Bull. Amer. Meteor. Soc.*, **65**, 554–558.

Smith, R. B., 1979b: The influence of mountains on the atmosphere. *Adv. Geophys.*, **21**, 87–230.

Smith, R. K., 1988: Travelling waves and bores in the lower atmosphere: the 'morning glory' and related phenomena. *Earth-Sci. Rev.*, **25**, 267–290.

Smith, S. A., D. C. Fritts, and T. E. VanZandt, 1985: Comparison of mesoscale wind spectra with a gravity wave model. *Radio Sci.*, **20**, 1331–1338.

Smolarkiewicz, P. K., R. M. Rasmussen, and T. L. Clark, 1988: On the dynamics of Hawaiian cloud bands: island forcing. *J. Atmos. Sci.*, **45**, 1872–1905.

Smyth, W. D. and W. R. Peltier, 1989: The transition between Kelvin-Helmholtz and Holmboe instability: an investigation of the overreflection hypothesis. *J. Atmos. Sci.*, **46**, 3698–3720.

Snyder, W. H., 1990: Fluid modeling applied to atmospheric diffusion in complex terrain. *Atmos. Environ.*, **24A**, 2071–2088.

Starr, V. P., 1954: Commentaries concerning research on the general circulation. *Tellus*, **6**, 268–272.

Starr, V. P., 1968: *Physics of Negative Viscosity Phenomena.* McGraw-Hill Book Co., New York, 256 pp.

Staub, B. and C. Rosenzweig, 1987: Global digital data sets of soil type, soil texture, surface slope, and other properties: documentation of archived data tape. NASA Technical Memorandum 100685, Institute for Space Studies, NASA Goddard Space Flight Center, 2880 Broadway, New York, 19 pp.

Stewart, R. W., 1969: Turbulence and waves in a stratified atmosphere. *Radio Sci.*, **4**, 1269–1278.

Steyn, D. G. and I. G. McKendry, 1988: Quantitative and qualitative evaluation of a three-dimensional mesoscale numerical model simulation of a sea breeze in complex terrain. *Mon. Wea. Rev.*, **116**, 1914–1926.

Stilke, G., 1973: Occurrence and features of ducted modes of internal gravity waves over western Europe and their influence on microwave propagation. *Boundary-Layer Meteor.*, **4**, 493–509.

Stillinger, D. C., K. N. Helland, and C. W. Van Atta, 1983: Experiments on the transition of homogeneous turbulence to internal waves in a stratified fluid. *J. Fluid Mech.*, **131**, 91–122.

Stinner, R. E., K. Wilson, C. Barfield, J. Regniere, A. Riordan, and J. Davis, 1982: Insect movement in the atmosphere. In *Biometeorology in Integrated Pest Management*, Hatfield, J. L. and I. J. Thomason, Editors, Academic Press, New York, 193–209.

Stocker, R. A. and R. A. Pielke, 1990: Source attribution during WHITEX – a modeling study. In *Trans. AWMA/EPA Specialty Conf. on Visibility and Fine Particulates*, Air and Waste Management Association, Pittsburgh. (In press).

Stocker, R. A., R. A. Pielke, A. J. Verdon, and J. T. Snow, 1990: Characteristics of plume releases as depicted by balloon launchings and model simulations. *J. Appl. Meteor.*, **29**, 53–62.

Stolarski, R. S., 1988: The Antarctic ozone hole. *Sci. Amer.*, **258**, January, 30–36.

Stommel, H., 1949: Horizontal diffusion due to oceanic turbulence. *J. Mar. Res.*, **8**, 199–225.

Stonehouse, B., Editor, 1986: *Arctic Air Pollution.* Cambridge University Press, Cambridge, 328 + xvi pp.

Strauch, R. G., D. A. Merritt, K. P. Moran, K. B. Earnshaw, and D. van de Kamp, 1984: The Colorado wind-profiling network. *J. Atmos. Oceanic Technol.*, **1**, 37–49.

Stull, R. B., 1976: Internal gravity waves generated by penetrative convection. *J. Atmos. Sci.*, **33**, 1279–1286.

Stull, R. B., 1988: *An Introduction to Boundary Layer Meteorology.* Kluwer Academic Publishers, Dordrecht, 666 pp.

Stunder, B. J. B., J. L. Heffter, and R. R. Draxler, 1986: Long-range transport model evaluation using CAPTEX aircraft and surface data. I: Vertical tracer distribution. In *Proc. Fifth AMS/APCA Joint Conf. on Applications of Air Pollution Meteorology*, Nov. 18–21, Chapel Hill, N.C., American Meteorological Society, Boston, 65–68.

Sundqvist, H., 1979: Vertical coordinates and related discretization. In *Numerical Methods Used in Atmospheric Models, Vol. II*, Case Postale No. 5, CH-1211, Geneva 20, Switzerland, 1–50. GARP Publication Series No. 17.

Sundqvist, H. and G. Veronis, 1970: A simple finite-difference grid with non-constant intervals. *Tellus*, **22**, 26–31.

Sundström, A. and T. Elvius, 1979: Computational problems related to limited-area modeling. In *Numerical Methods Used in Atmospheric Models, Vol. II*, World Meteorological Organization, Case Postale No. 5, Geneva 20, CH-1211, Switzerland, 379–416. (GARP Publications Series No. 17).

Sykes, R. I., 1984: The variance in time-averaged samples from an intermittent plume. *Atmos. Environ.*, **18**, 121–123.

Sykes, R. I. and W. S. Lewellen, 1982: A numerical study of breaking Kelvin-Helmholtz billows using a Reynolds-stress turbulence closure model. *J. Atmos. Sci.*, **39**, 1506–1520.

Synge, J. L., 1933: The stability of heterogeneous liquids. *Trans. Roy. Soc. Canada, Series III*, **27**, 1–18.

Syono, S. and K. Gambo, 1952: On numerical prediction (II). *J. Meteor. Soc. Japan*, **30**, 264–271.

Syono, S., A. Kasahara, and Y. Sekiguti, 1955: Some statistical properties of the atmospheric disturbance on 500-mb level. *J. Meteor. Soc. Japan*, **33**, 23–30.

Tang, C.-M. and S. A. Orszag, 1978: Two-dimensional turbulence on the surface of a sphere. *J. Fluid Mech.*, **87**, 305–319.

Tanrikulu, S. and S.-T. Soong, 1991: Use of the four-dimensional data assimilation method in mesoscale meteorological models. In *Proc. Seventh AMS/AWMA Conf. on Applications of Air Pollution Meteorology*, Jan. 14–18, New Orleans, American Meteorological Society, Boston, J238–J241.

Taylor, A. D., 1982: Puff growth in an Ekman layer. *J. Atmos. Sci.*, **39**, 837–850.

Taylor, G. I., 1921: Diffusion by continuous movements. *Proc. London Math. Soc. Ser. 2*, **20**, 196–212.

Taylor, G. I., 1931: Effect of variation in density on the stability of superposed streams of fluid. *Proc. Roy. Soc. London*, **A132**, 499–523.

Taylor, G. I., 1938: The spectrum of turbulence. *Proc. Roy. Soc. London*, **A164**, 476–490.

Taylor, G. I., 1953: Dispersion of soluble matter in solvent flowing slowly through a tube. *Proc. Roy. Soc. London A*, **219**, 186–203.

Taylor, G. I., 1959: The present position in the theory of turbulent diffusion. *Adv. Geophys.*, **6**, 101–112.

Taylor, G. I., 1954a: The dispersion of matter in turbulent flow through a pipe. *Proc. Roy. Soc. London A*, **223**, 446–467.

Taylor, G. I., 1954b: Conditions under which dispersion of a solute in a stream of solvent can be used to measure molecular diffusion. *Proc. Roy. Soc. London A*, **225**, 473–477.

Taylor, P. A. and Y. Delage, 1971: A note on finite difference schemes for the surface and planetary boundary layers. *Boundary-Layer Meteor.*, **2**, 108–121.

Telegadas, K., G. J. Ferber, J. L. Heffter, and R. R. Draxler, 1978: Calculated and observed seasonal and annual krypton–85 concentrations at 30–150 km from a point source. *Atmos. Environ.*, **12**, 1769–1775.

Telegadas, K., G. J. Ferber, R. R. Draxler, M. M. Pendergast, A. L. Boni, J. P. Hughes, and J. Gray, 1980: Measured weekly and twice-daily krypton–85 surface air concentrations within 150 km of the Savannah River Plant (March 1975 through September 1977) — Final Report. NOAA Tech. Memo. ERL ARL–80, January, Air Resources Laboratory, National Oceanic and Atmospheric Administration, Silver Spring, Maryland, 32 pp. + Appendices.

Tennekes, H., 1978: Turbulent flow in two and three dimensions. *Bull. Amer. Meteor. Soc.*, **59**, 22–28.

Tennekes, H., 1982: Similarity relations, scaling laws and spectral dynamics. In *Atmospheric Turbulence and Air Pollution Modelling*, Nieuwstadt, F. T. M. and H. van Dop, Editors, D. Reidel Publishing Co., Dordrecht, 37–68.

Tennekes, H., 1985: A comparative pathology of atmospheric turbulence in two and three dimensions. In *Turbulence and Predictability in Geophysical Fluid Dynamics and Climate Dynamics*, Ghil, M., R. Benzi, and G. Parisi, Editors, North-Holland Physics Publishing, Amsterdam, 45–70.

Tennekes, H. and J. L. Lumley, 1972: *A First Course in Turbulence.* MIT Press, Cambridge, Massachussetts, 300 pp.

Tesche, T. W., J. L. Haney, and R. E. Morris, 1987: Performance evaluation of four grid-based dispersion models in complex terrain. *Atmos. Environ.*, **21**, 233–256.

Thomas, P. and S. Vogt, 1990: Mesoscale atmospheric dispersion experiments using tracer and tetroons. *Atmos. Environ.*, **24A**, 1271–1284.

Thomas, P., S. Vogt, and P. Gaglione, 1986: Field experiments with tracer and tetroons to investigate atmospheric dispersion in the mesoscale range. In *Air Pollution Modeling and Its Application V*, De Wispelaere, C., F. A. Schiermeier, and N. V. Gillani, Editors, Plenum Press, New York, 621–637.

Thompson, P. D., 1954: Prognostic equations for the mean motions of simple fluid systems and their relation to the theory of large scale atmospheric turbulence. *Tellus*, **6**, 150–164.

Thomson, D. J., 1984: Random walk modelling of diffusion in inhomogeneous turbulence. *Quart. J. Roy. Meteor. Soc.*, **110**, 1107–1120.

Thomson, D. J., 1987: Criteria for the selection of stochastic models of particle trajectories in turbulent flows. *J. Fluid Mech.*, **180**, 529–556.

Thomson, D. J., 1986a: A random walk model of dispersion in turbulent flows and its application to dispersion in a valley. *Quart. J. Roy. Meteor. Soc.*, **112**, 511–530.

Thomson, D. J., 1986b: On the relative dispersion of two particles in homogeneous stationary turbulence and the implications for the size of concentration fluctuations at large times. *Quart. J. Roy. Meteor. Soc.*, **112**, 890–894.

Thomson, R. B., R. P. Angle, and S. Sakiyama, 1987: Selecting air quality – acid deposition models for mesoscale application. *J. Air Pollu. Control Assoc.*, **37**, 260–265.

Thomson, R. E., P. H. LeBlond, and W. J. Emery, 1990: Analysis of deep-drogued satellite-tracked drifter measurements in the northeast Pacific. *Atmos. Ocean*, **28**, 409–443.

Thorpe, A. J. and T. H. Guymer, 1977: The nocturnal jet. *Quart. J. Roy. Meteor. Soc.*, **103**, 633–653.

Thorpe, S. A., 1969: Experiments on the stability of stratified shear flows. *Radio Sci.*, **4**, 1327–1331.

Thorpe, S. A., 1975: The excitation, dissipation, and interaction of internal waves in the deep ocean. *J. Geophys. Res.*, **80**, 328–338.

Thorpe, S. A., 1981: An experimental study of critical layers. *J. Fluid Mech.*, **103**, 321–344.

Thorpe, S. A., 1973a: Experiments on instability and turbulence in a stratified shear flow. *J. Fluid Mech.*, **61**, 731–751.

Thorpe, S. A., 1973b: Turbulence in stably stratified fluids: a review of laboratory experiments. *Boundary-Layer Meteor.*, **5**, 95–119.

Tjemkes, S. A. and F. T. M. Nieuwstadt, 1990: A longwave radiation model for the nocturnal boundary layer. *J. Geophys. Res.*, **95**, 867–872.

Tolefson, H. B. and R. M. Henry, 1961: A method of obtaining detailed wind shear measurements for application to dynamic response problems of missile systems. *J. Geophys. Res.*, **66**, 2849–2862.

Townsend, A. A., 1965: Excitation of internal waves by a turbulent boundary layer. *J. Fluid Mech.*, **22**, 241–252.

Townsend, A. A., 1966: Internal waves produced by a convective layer. *J. Fluid Mech.*, **24**, 307–319.

Townsend, A. A., 1968: Excitation of internal waves in a stably-stratified atmosphere with considerable wind-shear. *J. Fluid Mech.*, **32**, 145–171.

Tremback, C. J., 1990: Numerical simulation of a mesoscale convective complex: model development and numerical results. Atmospheric Science Paper 465, Department of Atmospheric Science, Colorado State University, Fort Collins, Colorado, 247 pp.

Tremback, C. J. and R. Kessler, 1985: A surface temperature and moisture parameterization for use in mesoscale numerical models. In *Proc. 7th AMS Conf. on Numerical Weather Prediction*, June 17-20, Montreal, Canada, American Meteorological Society, Boston, 355–358.

Tremback, C. J. and W. R. Cotton, 1991: Numerical simulation of the meso-α-scale aspects of a mesoscale convective complex. Part I: Model description and verification. *Mon. Wea. Rev.* (Submitted).

Tremback, C. J., G. J. Tripoli, and W. R. Cotton, 1985: A regional scale atmospheric numerical model including explicit moist physics and a hydrostatic time-split scheme. In *Proc. 7th AMS Conf. on Numerical Weather Prediction*, June 17-20, Montreal, Quebec, American Meteorological Society, Boston, 433–434.

Tremback, C. J., G. J. Tripoli, R. W. Arritt, W. R. Cotton, and R. A. Pielke, 1986: The Regional Atmospheric Modeling System. In *Proc. Internat. Conf. Development and Application of Computer Techniques to Environmental Studies*, Zannetti, P., Editor, Computational Mechanics Publications, Boston, 601–607.

Tremback, C. J., J. Powell, W. R. Cotton, and R. A. Pielke, 1987: The forward-in-time upstream advection scheme: extension to higher orders. *Mon. Wea. Rev.*, **115**, 540–555.

Tripoli, G. J., 1986: A numerical investigation of an orogenic mesoscale convective system. Atmospheric Science Paper 401, Department of Atmospheric Science, Colorado State University, Fort Collins, Colorado, 290 pp.

Tripoli, G. J. and W. R. Cotton, 1980: A numerical investigation of several factors leading to the observed variable intensity of deep convection over South Florida. *J. Appl. Meteor.*, **19**, 1037–1063.

Tripoli, G. J. and W. R. Cotton, 1981: The use of ice-liquid water potential temperature as a thermodynamic variable in deep atmospheric models. *Mon. Wea. Rev.*, **109**, 1094–1102.

Tripoli, G. J. and W. R. Cotton, 1982: The Colorado State University three-dimensional cloud/mesoscale model — 1982. Part I: General theoretical framework and sensitivity experiments. *J. Rech. Atmos.*, **16**, 185–219.

Tripoli, G. J. and W. R. Cotton, 1989a: A numerical study of an observed orogenic mesoscale convective system. Part 1: Simulated genesis and comparison with observations. *Mon. Wea. Rev.*, **117**, 273–304.

Tripoli, G. J. and W. R. Cotton, 1989b: A numerical study of an observed orogenic mesoscale convective system. Part 2: Analysis of governing dynamics. *Mon. Wea. Rev.*, **117**, 305–328.

Trivett, N. B. A., L. A. Barrie, J. W. Bottenheim, J.-P. Blanchet, G. den Hartog, R. M. Hoff, and R. E. Mickle, 1988: An experimental investigation of Arctic haze at Alert, N. W. T., March 1985. *Atmos. Ocean*, **26**, 341–376.

Trout, D. A. and H. A. Panofsky, 1974: Mesoscale dispersion from a large city. *Adv. Geophys.*, **18B**, 151–157.

Turkevich, A., 1984: Nonconservative long-range (> 1000-km) atmospheric tracers. In *Proc. Atmospheric Tracer Workshop*, Barr, S., W. E. Clements, and P. R. Guthals, Editors, May 21–25, Santa Fe, New Mexico, Report No. LA-10301-C, December, Los Alamos National Laboratory, Los Alamos, New Mexico, 353–356.

Turner, J. S., 1973: *Buoyancy Effects In Fluids.* Cambridge University Press, Cambridge, 368 pp.

Tyldesley, J. B. and C. F. Wallington, 1965: The effect of wind shear and vertical diffusion on horizontal dispersion. *Quart. J. Roy. Meteor. Soc.*, **91**, 158–174.

Uccellini, L. W. and S. E. Koch, 1987: The synoptic setting and possible energy sources for mesoscale wave disturbances. *Mon. Wea. Rev.*, **115**, 721–729.

Uliasz, M., 1990a: Development of the mesoscale dispersion modeling system using personal computers. Part I: Models and computer implementation. *Z. Meteor.*, **40**, 104–114.

Uliasz, M., 1990b: Development of the mesoscale dispersion modeling system using personal computers. Part II: Numerical simulations. *Z. Meteor.*, **40**, 285–298.

Uliasz, M. and R. A. Pielke, 1991: Lagrangian–Eulerian dispersion modeling system for real-time mesoscale applications. In *Proc. Third Topical Mtg on Emergency Preparedness and Response*, April 16–19, Chicago, American Nuclear Society, La Grange Park, Illinois, 95–98.

Ulrickson, B. L. and C. F. Mass, 1990a: Numerical investigation of mesoscale circulations over the Los Angeles basin: Part I: A verification study. *Mon. Wea. Rev.*, **118**, 2138–2161.

Ulrickson, B. L. and C. F. Mass, 1990b: Numerical investigation of mesoscale circulations over the Los Angeles basin. Part II: Synoptic influences and pollutant transport. *Mon. Wea. Rev.*, **118**, 2162–2184.

Underwood, B. Y., 1991: Discussion of "An Interpretation of Taylor's Statistical Analysis of Particle Dispersion". *Atmos. Environ.*, **25A**, 1129–1130.

U.S. AEC, 1968: *Meteorology and Atomic Energy 1968.* U.S. Atomic Energy Commission, Washington, D.C., 445 pp. (Available as Publication TID-24190 from the National Technical Information Service, U.S. Department of Commerce, Springfield, Virginia 22161).

U.S. Department of Agriculture, 1951: *Soil Survey Manual.* U.S.D.A. Handbook No. 18. Superintendent of Documents, Government Printing Office, Washington, D. C., 503 pp.

Uthe, E. E., F. L. Ludwig, and F. Pooler, Jr., 1980: Lidar observations of the diurnal behavior of the Cumberland power plant plume. *J. Air Pollu. Control Assoc.*, **30**, 889–893.

Van der Hoven, I., 1957: Power spectrum of horizontal wind speed in the frequency range from 0.0007 to 900 cycles per hour. *J. Meteor.*, **14**, 160–164.

van Dop, H., 1983: Terrain classification and derived meteorological parameters for inter-regional transport models. *Atmos. Environ.*, **17**, 1099–1105.

van Dop, H., 1986: The CCMS air pollution model intercomparison study. *Atmos. Environ.*, **20**, 1261–1271.

van Dop, H., 1991: The WMO/IAEA/CEC model intercomparison study (ATMES). In *Air Pollution Modeling and Its Application VIII*, van Dop, H. and D. G. Steyn, Editors, Plenum Press, New York, 591–593.

van Dop, H. and B. J. de Haan, 1984: Mesoscale air pollution dispersion modelling. *Atmos. Environ.*, **18**, 545–552.

van Dop, H., F. T. M. Nieuwstadt, and J. C. R. Hunt, 1985: Random walk models for particle displacements in inhomogeneous unsteady turbulent flows. *Phys. Fluids*, **28**, 1639–1653.

van Egmond, N. D. and H. Kesseboom, 1983a: Mesoscale air pollution dispersion models. I: Eulerian grid model. *Atmos. Environ.*, **17**, 257–265.

van Egmond, N. D. and H. Kesseboom, 1983b: Mesoscale air pollution dispersion models. II: Lagrangian puff model and comparison with Eulerian grid model. *Atmos. Environ.*, **17**, 267–274.

van Kampen, N. G., 1981: *Stochastic Processes in Physics and Chemistry.* North-Holland Publishing Co., New York, 419 pp.

Vanderborght, B. and J. G. Kretzschmar, 1985: A literature study on tracer experiments for atmospheric dispersion study. In *Air Pollution Modeling and Its Application IV*, De Wispelaere, C., Editor, Plenum Press, New York, 571–584.

VanZandt, T. E., 1982: A universal spectrum of buoyancy waves in the atmosphere. *Geophys. Res. Lett.*, **9**, 575–578.

VanZandt, T. E., 1985: A model for gravity wave spectra observed by Doppler sounding systems. *Radio Sci.*, **20**, 1323–1330.

VanZandt, T. E. and D. C. Fritts, 1989: A theory of enhanced saturation of the gravity wave spectrum due to increases in atmospheric stability. *Pure Appl. Geophys.*, **130**, 399–420.

Venkatram, A., 1990: Comprehensive models for environmental systems. In *Proc. 18th NATO/CCMS Intern. Tech. Mtg on Air Pollution Modelling and Its Applications*, May 13-17, Vancouver, B.C., Canada, Committee on the Challenges of Modern Society, North Atlantic Treaty Organization, Brussels, 533–544.

Venkatram, A., 1988a: An interpretation of Taylor's statistical analysis of particle dispersion. *Atmos. Environ.*, **22**, 865–868.

Venkatram, A., 1988b: Inherent uncertainty in air quality modeling. *Atmos. Environ.*, **22**, 1221–1227.

Venkatram, A., P. K. Karamchandani, and P. K. Misra, 1988: Testing a comprehensive acid deposition model. *Atmos. Environ.*, **22**, 737–747.

Viessman, S. M. and S. Raman, 1988: Boundary layer wind parameterization for use in a Lagrangian trajectory model. *Atmos. Environ.*, **22**, 839–851.

Vincent, A. and M. Meneguzzi, 1991: The spatial structure and statistical properties of homogeneous turbulence. *J. Fluid Mech.*, **225**, 1–20.

Vincent, R. A. and S. D. Eckermann, 1990: VHF radar observations of mesoscale motions in the troposphere: evidence for gravity wave Doppler shifting. *Radio Sci.*, **25**, 1019–1037.

Vinnichenko, N. K., 1970: The kinetic energy spectrum in the free atmosphere — 1 second to 5 years. *Tellus*, **22**, 158–166.

Vinnichenko, N. K. and J. A. Dutton, 1969: Empirical studies of atmospheric structure and spectra in the free atmosphere. *Radio Sci.*, **4**, 1115–1126.

Vinnichenko, N. K., N. Z. Pinus, S. M. Shmeter, and G. N. Shur, 1980: *Turbulence in the Free Atmosphere (Second Edition)*. Consultants Bureau (Plenum Press), New York, 310 pp.

Viswanadham, Y. and J. A. Torsani, 1982: A study of atmospheric diffusion from the LANDSAT imagery. *J. Geophys. Res.*, **87**, 9621–9635.

Vogel, B., K. Nester, and M. Baer, 1988: Comparison between simulated and measured concentration and dry deposition fields of SO_2. In *Air Pollution Modeling and Its Application VI*, van Dop, H., Editor, Plenum Press, New York, 37–48.

Vogt, S. and P. Thomas, 1985: Analysis of tetroon flights performed during the PUKK meso-scale experiment. In *Air Pollution Modeling and Its Application IV*, De Wispelaere, C., Editor, Plenum Press, New York, 375–388.

Vogt, S. and F. Fiedler, 1987: Measurements of air pollutants in a mesoscale region. *Ann. Geophys.*, **5B**, 487–495.

Vukovich, F. M. and J. Fishman, 1986: The climatology of summertime O_3 and SO_2 (1977-1981). *Atmos. Environ.*, **20**, 2423–2433.

Vukovich, F. M. and J. K. S. Ching, 1990: A semi-empirical approach to estimate vertical transport by nonprecipitating convective clouds on a regional scale. *Atmos. Environ.*, **24A**, 2153–2168.

Wacongne, S. and A. Babiano, 1982: Space-time turbulent characteristics in the atmospheric surface layer. *Boundary-Layer Meteor.*, **24**, 429–450.

Walcek, C. J., 1987: A theoretical estimate of O_3 and H_2O_2 dry deposition over the northeast United States. *Atmos. Environ.*, **21**, 2649–2659.

Walcek, C. J., R. A. Brost, J. S. Chang, and M. L. Wesely, 1986: SO_2, sulfate, and HNO_3 deposition velocities computed using regional landuse and meteorological data. *Atmos. Environ.*, **20**, 949–964.

Walklate, P. J., 1987: A random-walk model for dispersion of heavy particles in turbulent air flow. *Boundary-Layer Meteor.*, **39**, 175–190.

Walko, R. L. and C. J. Tremback, 1991: Regional Atmospheric Modeling System (RAMS) Version 2C User's Guide. ASTeR, Inc., P.O. Box 466, 515 S. Howes St., Fort Collins, Colorado, 80521, 84 pp. (Draft).

Walko, R. L., W. R. Cotton, and R. A. Pielke, 1991: Large eddy simulations of the effects of hilly terrain on the convective boundary layer. *Boundary-Layer Meteor.* (Accepted).

Wallace, J. M. and V. E. Kousky, 1968: Observational evidence of Kelvin waves in the tropical stratosphere. *J. Atmos. Sci.*, **25**, 900–907.

Walton, J. J., 1973: Scale-dependent diffusion. *J. Appl. Meteor.*, **12**, 547–549.

Warner, T. T., 1981: Verification of a three-dimensional transport model using tetroon data from Project STATE. *Atmos. Environ.*, **15**, 2219–2222.

Warner, T. T., R. R. Fizz, and N. L. Seaman, 1983: A comparison of two types of atmospheric transport models — use of observed winds versus dynamically predicted winds. *J. Climate Appl. Meteor.*, **22**, 394–406.

Washington, W. M. and D. P. Baumhefner, 1975: A method of removing Lamb waves from initial data for primitive equation models. *J. Appl. Meteor.*, **14**, 114–119.

Wax, N., Editor, 1954: *Selected Papers on Noise and Stochastic Processes.* Dover Publications, Inc., New York, 337 pp.

Weber, A. H., 1980: Case studies of horizontal spread of ^{85}Kr at 100 km downwind. In *Proc. Second AMS/APCA Conf. on Applications of Air Pollution Meteorology*, March 24–27, New Orleans, Louisiana, American Meteorological Society, Boston, 272–274.

Weber, A. H., M. R. Buckner, and J. H. Weber, 1982: Statistical performance of several mesoscale atmospheric dispersion models. *J. Appl. Meteor.*, **21**, 1633–1644.

Weinstein, A. I., E. R. Reiter, and J. R. Scoggins, 1966: Mesoscale structure of 11-20 km winds. *J. Appl. Meteor.*, **5**, 49–57.

Welander, P., 1955: Studies on the general development of motion in a two-dimensional ideal fluid. *Tellus*, **7**, 141–156.

Wendell, L. L., 1972: Mesoscale wind fields and transport estimates determined from a network of wind towers. *Mon. Wea. Rev.*, **100**, 565–578.

Wetzel, P. J. and J.-T. Chang, 1988: Evapotranspiration from nonuniform surfaces: a first approach for short-term numerical weather prediction. *Mon. Wea. Rev.*, **116**, 600–621.

Wheeler, D. A., 1988: Atmospheric dispersal and deposition of radioactive material from Chernobyl. *Atmos. Environ.*, **22**, 853–863.

Whelpdale, D. M., A. Eliassen, J. N. Galloway, H. Dovland, and J. M. Miller, 1988: The transatlantic transport of sulfur. *Tellus*, **40B**, 1–15.

White, F. D., 1984: Review of the attributes and performance of six urban diffusion models. Report EPA-600/S3-84-089, September, U.S. Environmental Protection Agency.

White, R. M. and D. S. Cooley, 1956: Kinetic-energy spectrum of meridional motion in the mid-troposphere. *J. Meteor.*, **13**, 67–69.

Whiteman, C. D., 1990: Observations of thermally developed wind systems in mountainous terrain. In *Atmospheric Processes Over Complex Terrain*, Blumen, W., Editor, American Meteorological Society, Boston, 5–42.

Whittaker, T. M. and R. A. Petersen, 1977: Objective cross-sectional analyses incorporating thermal enhancement of the observed winds. *Mon. Wea. Rev.*, **105**, 147–153.

Wiin-Nielsen, A., 1967: On the annual variation and spectral distribution of atmospheric energy. *Tellus*, **19**, 540–559.

Wiin-Nielsen, A., 1972: A study of power laws in the atmospheric kinetic energy spectrum using spherical harmonic functions. *Meteor. Ann.*, **6**, 107–124.

Wilczak, J. M. and J. W. Glendening, 1988: Observations and mixed-layer modeling of a terrain-induced mesoscale gyre: the Denver cyclone. *Mon. Wea. Rev.*, **116**, 2688–2711.

Williams, D. T., 1953: Pressure wave observations in the central Midwest, 1952. *Mon. Wea. Rev.*, **81**, 278–289.

Willis, G. E. and J. W. Deardorff, 1976: On the use of Taylor's translation hypothesis for diffusion in the mixe layer. *Quart. J. Roy. Meteor. Soc.*, **102**, 817–822.

Willis, G. E. and J. W. Deardorff, 1978: A laboratory study of dispersion from an elevated source within a modeled convective planetary boundary layer. *Atmos. Environ.*, **12**, 1305–1311.

Willmott, C. J., 1982: Some comments on the evaluation of model performance. *Bull. Amer. Meteor. Soc.*, **63**, 1309–1313.

Willmott, C. J., S. G. Ackleson, R. E. Davis, J. J. Feddema, K. M. Klink, D. R. Legates, J. O'Donnell, and C. M. Rowe, 1985: Statistics for the evaluation and comparison of models. *J. Geophys. Res.*, **90**, 8995–9005.

Wilson, J. D. and Y. Zhuang, 1989: Restriction on the timestep to be used in stochastic Lagrangian models of turbulent dispersion. *Boundary-Layer Meteor.*, **49**, 309–316.

Wilson, J. D., B. J. Legg, and D. J. Thomson, 1983: Calculation of particle trajectories in the presence of a gradient in turbulent-velocity variance. *Boundary-Layer Meteor.*, **27**, 163–169.

Wilson, J. D., E. P. Lozowski, and Y. Zhuang, 1988: Comments on a relationship between fluid and immersed-particle velocity fluctuations proposed by Walklate (1987). *Boundary-Layer Meteor.*, **43**, 93–98.

Wilson, J. D., G. W. Thurtell, and G. E. Kidd, 1981a: Numerical simulation of particle trajectories in inhomogeneous turbulence. I: Systems with constant turbulent velocity scale. *Boundary-Layer Meteor.*, **21**, 295–313.

Wilson, J. D., G. W. Thurtell, and G. E. Kidd, 1981b: Numerical simulation of particle trajectories in inhomogeneous turbulence. II: Systems with variable turbulent velocity scale. *Boundary-Layer Meteor.*, **21**, 423–441.

Wilson, M. F. and A. Henderson-Sellers, 1985: A global archive of land cover and soils data for use in general circulation climate models. *J. Climatology*, **5**, 119–143.

Wilson, M. F., A. Henderson-Sellers, R. E. Dickinson, and P. J. Kennedy, 1987: Sensitivity of the Biosphere-Atmosphere Transfer Scheme (BATS) to the inclusion of variable soil characteristics. *J. Climate Appl. Meteor.*, **26**, 341–362.

Wollenweber, G. C. and H. A. Panofsky, 1988: The effect of sampling time on velocity variances. In *Proc. 8th AMS Symp. on Turbulence and Diffusion*, April 25–29, San Diego, American Meteorological Society, Boston, 116–118.

Woods, J. D., 1968: Wave-induced shear instability in the summer thermocline. *J. Fluid Mech.*, **32**, 791–800.

Woods, J. D., 1969a: On Richardson's number as a criterion for laminar-turbulent-laminar transition in the ocean and atmosphere. *Radio Sci.*, **4**, 1289–1298.

Woods, J. D., 1969b: Fossil turbulence. *Radio Sci.*, **4**, 1365–1367.

Woods, J. D. and R. L. Wiley, 1972: Billow turbulence and ocean microstructure. *Deep-Sea Res.*, **19**, 87–121.

Wu, J., 1969: Mixed region collapse with internal wave generation in a density-stratified medium. *J. Fluid Mech.*, **35**, 531–534.

Wurtele, M. G., J. Paegle, and A. Sielecki, 1971: The use of open boundary conditions with the storm-surge equations. *Mon. Wea. Rev.*, **99**, 537–544.

Wyngaard, J. C., 1973: On surface-layer turbulence. In *Workshop on Micrometeorology*, Haugen, D. A., Editor, American Meteorological Society, Boston, 101–149.

Wyngaard, J. C., 1982: Boundary-layer modeling. In *Atmospheric Turbulence and Air Pollution Modelling*, Nieuwstadt, F. T. M. and H. van Dop, Editors, D. Reidel Publishing Company, Boston, 69–106.

Wyngaard, J. C. and S. F. Clifford, 1977: Taylor's hypothesis and high-frequency turbulence spectra. *J. Atmos. Sci.*, **34**, 922–929.

Yamada, T., 1985: Numerical simulation of the night 2 data of the 1980 ASCOT experiments in the California geysers area. *Arch. Met. Geophys. Bioclim.*, **34**, 223–247.

Yamada, T. and S. Bunker, 1988: Development of a nested grid, second moment turbulence closure model and application to the 1982 ASCOT Brush Creek data simulation. *J. Appl. Meteor.*, **27**, 562–578.

Yamada, T., C.-Y. J. Kao, and S. Bunker, 1989: Airflow and air quality simulations over the western mountainous region with a four-dimensional data assimilation technique. *Atmos. Environ.*, **23**, 539–554.

Yang, C.-H. and R. Shapiro, 1973: The effects of the observational system and the method of interpolation on the computation of spectra. *J. Atmos. Sci.*, **30**, 530–536.

Yassky, D., 1983: Estimation of dispersion parameters from photographic density measurements on smoke puffs. *Atmos. Environ.*, **17**, 283–290.

Yeh, K. C. and B. Dong, 1989: The non-linear interaction of a gravity wave with the vortical modes. *J. Atmos. Terr. Phys.*, **51**, 45–50.

Yersel, M., R. Goble, and J. Morrill, 1983: Short range dispersion experiments in an urban area. *Atmos. Environ.*, **17**, 275–282.

Yeung, P. K. and S. B. Pope, 1990: Lagrangian statistics from direct numerical simulations of isotropic turbulence. *J. Fluid Mech.*, **207**, 531–586.

Yoon, K. and Z. Warhaft, 1990: The evolution of grid-generated turbulence under conditions of stable thermal stratification. *J. Fluid Mech.*, **215**, 601–638.

Young, G. S., 1987: Mixed layer spectra from aircraft measurements. *J. Atmos. Sci.*, **44**, 1251–1256.

Young, W. R., P. B. Rhines, and C. J. R. Garrett, 1982: Shear flow dispersion, internal waves and horizontal mixing in the ocean. *J. Phys. Ocean.*, **12**, 515–527.

Yu, C.-H. and R. A. Pielke, 1986: Mesoscale air quality under stagnant synoptic cold season conditions in the Lake Powell area. *Atmos. Environ.*, **20**, 1751–1762.

Yu, T.-W., 1977: A comparative study on parameterization of vertical turbulent exchange processes. *Mon. Wea. Rev.*, **105**, 57–66.

Yule, A. J., 1980: Phase scrambling effects and turbulence data analysis. In *Turbulent Shear Flows 2*, Bradbury, L. J. S., F. Durst, B. E. Launder, F. W. Schmidt, and J. H. Whitelaw, Editors, Springer-Verlag, New York, 263–281.

Zannetti, P., 1984: New Monte-Carlo scheme for simulating Lagrangian particle diffusion with wind shear effects. *Appl. Math. Modeling*, **8**, 188–192.

Zannetti, P., 1986: Monte-Carlo simulation of auto- and cross-correlated turbulent velocity fluctuations (MC-LAGPAR II model). *Environmental Software*, **1**, 26–30.

Zhang, D. and R. A. Anthes, 1982: A high-resolution model of the planetary boundary layer — sensitivity tests and comparisons with SESAME-79 data. *J. Appl. Meteor.*, **21**, 1594–1609.

Zhou, L. and H. A. Panofsky, 1983: Wind fluctuations in stable air at the Boulder tower. *Boundary-Layer Meteor.*, **25**, 353–362.